# Development of Microcrystal Electron Diffraction Techniques for the Characterization of Small Molecules and Novel Materials

Thesis by

Christopher G. Jones

In Partial Fulfillment of the Requirements

for the Degree of

Doctor of Philosophy

Caltech

CALIFORNIA INSTITUTE OF TECHNOLOGY

Pasadena, California

2024

(Defended August 30, 2023)

# ABSTRACT

Traditional techniques for structural analysis, such as X-ray crystallography and Nuclear Magnetic Resonance (NMR), have been invaluable in understanding the composition of various substances. However, these methods often encounter challenges when applied to the analysis of small molecules and certain novel materials, particularly those that cannot form large, high-quality crystals. The research presented here focuses on the evolution and applications of Microcrystal Electron Diffraction (MicroED), a transformative technique that has expanded the boundaries of structural analysis. We trace the developmental trajectory of MicroED, exploring its underlying principles, technological advancements, and comparative advantages over conventional methods. A variety of data from several key studies was collected through a series of experiments utilizing MicroED to analyze a range of substances, from small organic molecules to complex novel materials and innovative inorganic complexes. MicroED offers unprecedented resolution and sensitivity, capable of structural elucidation where other methods fail. In particular, MicroED has been successful in determining the structures of several novel materials and small molecules with applications in areas such as renewable energy, advanced manufacturing, and pharmaceuticals. Furthermore, this technique is highly amenable to integration with other analytical and computational methods, including machine learning algorithms for data interpretation, enhancing its applicability and efficiency. This research contends that MicroED is not merely an alternative but a substantial upgrade to existing methodologies, holding the potential to revolutionize fields as diverse as materials science, chemistry, and medicine.

## PUBLISHED CONTENT AND CONTRIBUTIONS

Portions of the work described herein were disclosed in the following publications:

1.  Jones, C. G.; Martynowycz, M. W.; Hattne, J.; Fulton, T. J.; Stoltz, B. M.; Rodriguez, J. A.; Nelson, H. M.; Gonen, T. The CryoEM Method MicroED as a Powerful Tool for Small Molecule Structure Determination. *ACS Cent. Sci.* **2018**, 4, 1587-1592. https://doi.org/10.1021/acscentsci.8b00760. C.G.J provided scientific expertise, performed experiments, collected data, and helped prepare manuscript.

2.  Jones, C. G.; Asay, M.; Kim L. J.; Kleinsasser, J.; Saha, A.; Fulton, T. J.; Berkley K.; Cascio D.; Malyutin, A.; Conley, M.; Stoltz, B. M.; LaVallo, V.; Rodriguez, J. A.; Nelson, H. M. Characterization of reactive organometallic species via MicroED. *ACS Cent. Sci.* **2019**, 5, 1507-1513. https://doi.org/10.1021/acscentsci.9b00403. C.G.J provided scientific expertise, performed experiments, collected data, and helped prepare manuscript.

3.  Anderson, C. L.; Li, H.; Jones, C. G.; Teat, S. J.; Settineri, N. S.; Dailing, E. A.; Liang, J.; Mao, H.; Klivansky, L. M.; Li, X.; Reimer, J. A.; Nelson, H. M.; Liu, Y. Solution-Processable and Functionalizable Ultra-high Molecular Weight Polymers via Topochemical Polymerization. *Nat. Commun.* **2021**, 12, 6818. https://doi.org/10.1038/s41467-021-27090-1. C.G.J provided scientific expertise, performed experiments, collected data, and helped prepare manuscript.

4.  Meng, Z.; Jones, C. G.; Farid, S. Khan, I. U.; Nelson, H. M.; Mirica, K. A. Unraveling the Electrical and Magnetic Properties of Two-Dimensional Conductive Metal-Organic Frameworks with Atomic Precision. *Angew. Chem. Int. Ed.* **2021**, 61, e202113569. https://doi.org/10.1002/ange.202113569. C.G.J provided scientific expertise, performed experiments, collected data, and helped prepare manuscript.

5. Aykanat, A.; Jones, C. G.; Cline, E.; Stolz, R. M.; Meng, Z.; Nelson, H. M.; Mirica, K. A. Conductive Stimuli-Responsive Coordination Network Linked with Bismuth for Chemiresistive Gas Sensing. *ACS Appl. Mater. Interfaces* **2021**,13, 60306–60318. https://doi.org/10.1021/acsami.1c14453. C.G.J provided scientific expertise, performed experiments, collected data, and helped prepare manuscript.

6. Jellen, M. J.; Liepuoniute, I.; Jin, M.; Jones, C. G.; Yang, S.; Jiang, X., Nelson, H. M., Houk, K. N.; Garcia-Garibay, M. A. Enhanced Gearing Fidelity Achieved Through Macrocyclization of a Solvated Molecular Spur Gear. *J. Am. Chem. Soc.* **2021**, 143, 7740-7747. https://doi.org/10.1021/jacs.1c01885. C.G.J provided scientific expertise, performed experiments, collected data, and helped prepare manuscript.

7. Mills, H. A.; Jones, C. G.; Anderson, K. P.; Ready, A. D.; Djurovich, P. I.; Khan, S. I.; Hohman, J. N.; Nelson, H. M.; Spokoyny, A. M. Sterically Invariant Carborane-Based Ligands for the Morphological and Electronic Control of Metal Organic Chalcogenolate Assemblies. *Chem. Mater.* **2022**, 34, 6933-6943. https://doi.org/10.1021/acs.chemmater.2c01319. C.G.J provided scientific expertise, performed experiments, collected data, and helped prepare manuscript.

8. Samkian, A.; Kiel, G. R.; Jones, C. G.; Bergman, H.; Oktawiec, J.; Nelson, H. M.; Tilley, T. D. MicroED Elucidation of Diverse Solid-State Packing in a Family of Electron-Deficient Expanded Helicenes. *Angew. Chem. Int. Ed.* **2021**, 60, 2493. https://doi.org/10.1002/anie.202012213. C.G.J provided scientific expertise, performed experiments, collected data, and helped prepare manuscript.

9. Lin, S.; Oakley, C. E.; Jenkinson, C. B.; Chiang, Y.; Lee, C.; Jones, C. G.; Seidler, P.; Nelson, H. M.; Todd, R. B.; Wang, C. C.; Oakley, B. R. A heterologous expression platform

in Aspergillus nidulans for the elucidation of cryptic secondary metabolism biosynthetic gene clusters: Discovery of the Aspergillus fumigatus sartorypyrone biosynthetic pathway. *Chem. Sci.,* **2023***, Advance Article.* https://doi.org/10.1039/D3SC02226A. C.G.J provided scientific expertise, performed experiments, collected data, and helped prepare manuscript.

**TABLE OF CONTENTS**

*CHAPTER 1*

*Development of Microcrystal Electron Diffraction Techniques and Their Applications in Small Molecule Analysis and Natural Product Discovery*

**CHAPTER 2**

*The CryoEM Method MicroED as a Powerful Tool for Small Molecule Structure Determination*

**CHAPTER 3**

*Characterization of Reactive Organometallic Species via MicroED*

*CHAPTER 4*

*Solution-processable and functionalizable ultrahigh molecular weight polymers via topochemical synthesis*

*CHAPTER 5*

*Unraveling the Electrical and Magnetic Properties of Layered Conductive Metal-Organic Framework with Atomic Precision*

*CHAPTER 6*

*Conductive Stimuli-Responsive Coordination Network Linked with Bismuth for Chemiresistive Gas Sensing*

*CHAPTER 7*

*Enhanced Gearing Fidelity Achieved Through Macrocyclization of a Solvated Molecular Spur Gear*

## CHAPTER 8

*Sterically Invariant Carborane-Based Ligands for the Morphological and Electronic Control of Metal−Organic Chalcogenolate Assemblies*

## CHAPTER 9

*Elucidation of Diverse Solid-State Packing in a Family of Electron-Deficient Expanded Helicenes via Microcrystal Electron Diffraction*

*CHAPTER 10*

*A heterologous expression platform in Aspergillus nidulans for the elucidation of*

*cryptic secondary metabolism biosynthetic gene clusters: discovery of the Aspergillus fumigatus*

*sartorypyrone biosynthetic pathway*

*Chapter 1*

*Development of Microcrystal Electron Diffraction Techniques and Their*

*Applications in Small Molecule Analysis and Natural Product Discovery*

## 1.1 INTRODUCTION

Natural products (NPs), primarily derived from plants,[1] fungi,[2] bacteria,[3] and marine organisms,[4] have historically played a pivotal role in discovering and developing therapeutic agents due to their vast structural complexity, diverse molecular framework, and potent bioactivities. Serving as the foundation of traditional medicine for millennia, these bioactive compounds have contributed immensely to modern pharmacopeias.[5] In the pharmaceutical industry, they are recognized not only as primary agents for drug treatment but also as templates for synthetic modification, leading to the development of novel drugs with enhanced efficacy and reduced side effects.[6, 7] Their intrinsic structural diversity and biological activity make NPs indispensable in modern drug development, offering a vast reservoir of molecular scaffolds and pharmacophores.[8] However, the field of NP discovery suffers from many inherent challenges in structure elucidation, creating a significant bottleneck in the discovery of novel compounds and their subsequent translation into viable therapeutics. As a result, modern drug discovery efforts have largely shifted toward leveraging various computational techniques, such as machine learning[9] and fragment-based methods.[10] While these techniques have been effective, the sheer limitless diversity of compounds in nature still makes NPs a vast resource for potential drug discovery efforts. The advent of new and emerging technologies, such as microcrystal electron diffraction (MicroED),[11-16] has enabled unprecedented study and analysis of

NPs in previously inaccessible ways, potentially leading to a new revolution in our study and understanding of NPs and their properties.

Traditional NP analysis has depended on spectroscopic techniques like mass spectrometry (MS)[17] and nuclear magnetic resonance (NMR) spectroscopy.[18] While these methods don't directly reveal structural connectivity or atomic position, they offer important spectroscopic data. This data, when synthesized, helps deduce molecular structures with a high degree of accuracy. These techniques have been pivotal in our understanding of NPs for decades, but they each come with their own set of challenges. MS, for instance, is excellent in sensitivity, detecting numerous NPs in standard MS metabolomics tests.[19] Yet, identifying these metabolites becomes a hurdle due to gaps in spectral databases and minimal information regarding connectivity or stereoisomer differentiation.[20] In conjunction with MS analysis, NMR spectroscopy is often used to decipher the structure of elusive NPs. While powerful, NMR experiments typically require pure samples in milligram amounts, making them resource-intensive, especially when many NPs are available only in minute quantities.[21] Moreover, obstacles like a scant number of protons or issues with coupling can obstruct structural determination using NMR.[22] Consequently, only a fraction of MS-detected NPs get detailed structural insight through NMR.[23-25] Despite these limitations, NMR and MS have allowed researchers to infer structures for thousands of known NPs.

In contrast to traditional inference-based spectroscopic techniques, single-crystal X-ray crystallography has remained the gold standard of structural determination for small molecules, as it provides atomic position, connectivity, and in some cases, absolute configuration through the analysis of anomalous scattering.[26, 27] However, in much of the NP literature to date, only a small fraction of all reported NPs have crystallographic analysis to corroborate their spectroscopic structural assignments.[26] The absence of such crystallographic studies from the NP literature can be attributed to several limitations with traditional X-ray crystallography. Foremost is the need for growing sufficiently large single crystals, with dimensions typically greater than 100 $\mu$m, to achieve sufficient quality data.[28] While this is routinely done in various areas of synthetic chemistry and pharmaceutical development, it is rarely done in NP research as

the minute quantities of isolates are generally insufficient to grow large crystals. Furthermore, the source organism may be difficult to obtain or exceedingly rare, making large amounts of extract challenging to obtain. Even if enough material is secured, cultivating X-ray-worthy crystals can be an arduous, prolonged endeavor, spanning days to even years. Additionally, poor physical properties such as stability or solubility can preclude the formation of sizable, high-quality crystals necessary for X-ray diffraction studies. However, by leveraging recent advancements in the field of electron crystallography, it is now possible to overcome many of the inherent limitations of traditional structural analysis and facilitate new groundbreaking discoveries in the field of NP chemistry.

## 1.2 THE EMERGENCE OF MICROCRYSTAL ELECTRON DIFFRACTION

Microcrystal electron diffraction, often referred to as MicroED, represents a notable advancement in the field of electron microscopy and crystallography. This technique circumvents many limitations associated with traditional spectroscopic methods and single-crystal X-ray diffraction.[29] Rather than relying on a focused beam of photons as in X-ray crystallography, MicroED utilizes a focused electron beam inside a transmission electron microscope (TEMs), which typically operates between 120 to 300 keV.[30] Unlike photons, electrons have both charge and mass, facilitating much stronger interactions with atoms as they pass through the crystal lattice.[31] These strong interactions and scattering effects allow diffraction patterns to be obtained from crystals on the order of micro- or even nanometers, several orders of magnitude smaller than those needed for single-crystal X-ray diffraction.[29] Interestingly, these microcrystals can often be found in samples that appear amorphous, like powders resulting from purification processes, solvent evaporation, or unsuccessful crystallization attempts.[32] Furthermore, mere nanograms of material could potentially suffice for generating crystals of sufficient quality and size, making MicroED an outstanding analytic tool for studying molecules when only minuscule quantities are available.[33] This method's unique strengths pave the way for fresh exploration, granting structural chemists an unparalleled method for ascertaining the configuration of NPs and other small molecules, especially when traditional techniques fall short due to sample constraints.

*Figure 1.1* *MicroED workflow from sample preparation to data processing and refinement.*
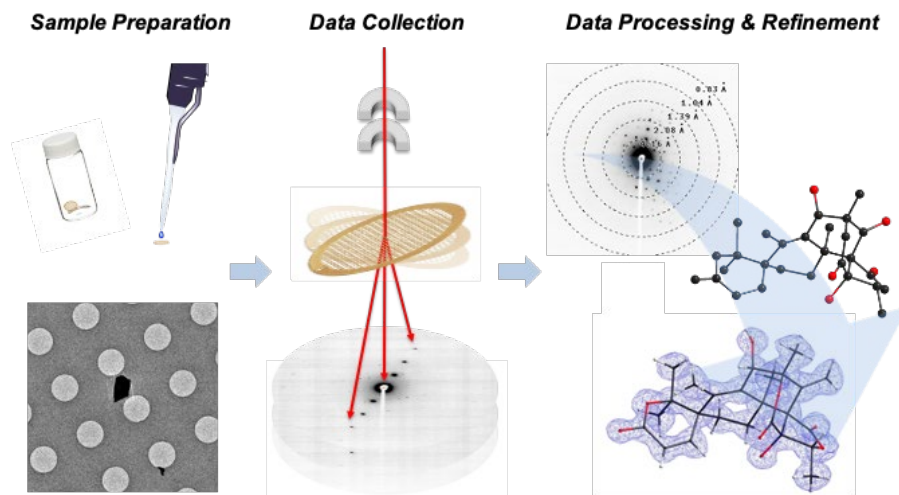


At its core, MicroED operates by directing a finely-focused electron beam, generated within a TEM, onto a crystal, often no larger than a few nanometers.[29] As these high-energy electrons traverse the sample, they interact with the atoms in the crystal lattice, and the resultant scattering creates diffraction patterns on a detector.[34] This process is typically performed as the TEM stage containing the mounted crystal is continuously rotated over several degrees.[35] Like X-ray crystallography, this diffraction data can be processed using standard crystallographic software such as XDS,[36] DIALS,[37] and SHELX.[38] By collecting multiple such patterns from various crystal orientations and integrating the data, a three-dimensional electron density map of the sample is constructed.[39] This map is then used to determine the precise atomic arrangement of the molecule in question, offering insights into its structural nuances with remarkable precision. This process thus opens up entirely new avenues to study previously inaccessible chemical structures that were once too challenging or limited by quantities of material or crystal quality.

### 1.2.1. Brief History of Electron Diffraction

While MicroED as a technique has only recently been popularized when demonstrated by Gonen and coworkers in 2013,[35] electron diffraction as a field boasts a rich historical lineage spanning several decades. The inception of electron diffraction can be traced back to 1927, when Davisson and Germer

successfully demonstrated the diffraction of an electron beam from a pure nickel single-crystal.[40] This groundbreaking experiment thus further substantiated de Broglie's theory on the wave-like properties of electrons.[41] Later that year, Thomson and Reid observed electron diffraction at heightened kinetic energies.[42] By 1931, the first electron microscope was crafted by Ruska and Knoll,[43] heralding the dawn of electron microscopy. Despite these developments, its widespread application in crystallography faced obstacles, notably the dynamical effects that complicated structural analysis.[44] This "dynamical scattering" was due to the propensity of electrons to undergo multiple scatterings within a crystal, altering the detected intensities. However, a significant milestone was achieved in 1976 when Dorset and Hauptman illustrated the feasibility of extracting crystallographic phases from electron diffraction data, paving the way for ab initio structure determination.[45] Thereafter, electron structures from an array of organic and inorganic compounds were reported, and even a protein structure derived from a 2D crystal using molecular replacement—a technique leveraging homology models for phasing diffraction data to decode macromolecular configurations.[46] Building upon these foundational discoveries, various electron diffraction methodologies, such as continuous rotation electron diffraction (cRED) and MicroED, were birthed. These methodologies are thus broadly categorized under the umbrella term "3D electron diffraction (3D ED)".[47, 48]

**Figure 1.2** *Timeline of selected historical events relevant to electron diffraction.*
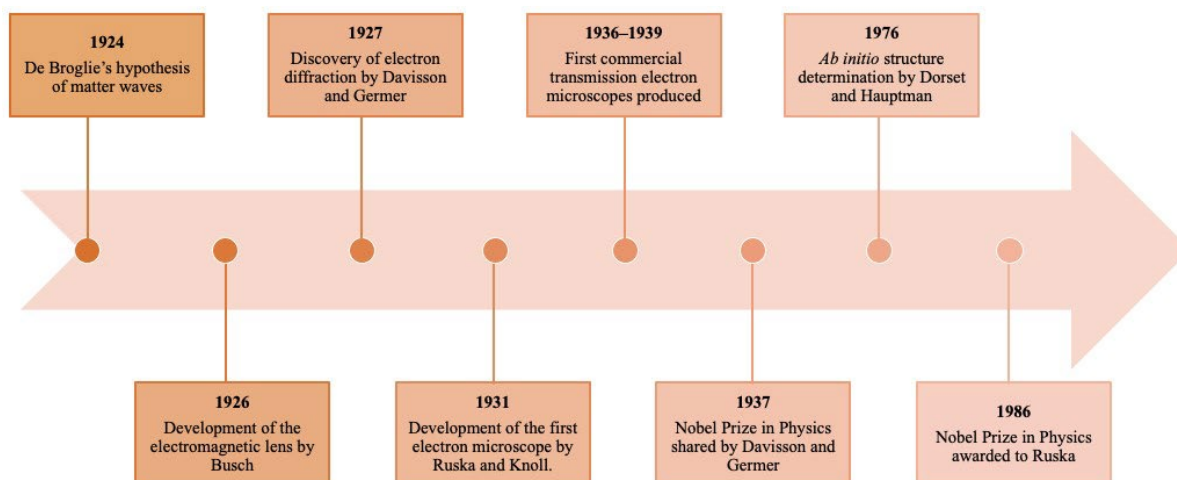
**1.2.2 The Scope of MicroED in Small Molecule Regime**

Since the initial report by Gonen and coworkers in 2013,[35] MicroED has made significant strides in determining the structures of various macromolecules, including well-known proteins like lysozyme and catalase. While impactful from a methods development standpoint, these early studies predominantly focused on proteins whose structures have been well studied for decades through traditional X-ray crystallography. Nevertheless, these studies have led to recent advancements, including the structural elucidation of a novel protein R2lox[49] and peptide fragments[50-52] using MicroED. While many of these investigations have employed molecular replacement to interpret the electron diffraction data, a handful that adopted *ab initio* methods showcased the streamlined process of handling electron diffraction data with XDS and the SHELX suite — tools frequently used in X-ray crystallography.

In 2018, the chemistry community witnessed a significant shift in the adoption of MicroED. This surge in popularity was catalyzed by two consecutive papers that showcased the effortless structural determination of various organic molecules directly from their commercially available, seemingly amorphous powder forms.[32, 53] Both studies presented a straightforward procedure for preparing grids for examination: the dry powder samples were directly mounted onto a grid and then rapidly frozen in liquid nitrogen. This deviated from the conventional approach of vitrification in liquid ethane, typical in standard cryoEM experiments, which both increased the throughput and ease of sample preparation.[32] Through this workflow, these studies demonstrated that highly accurate crystallographic structures could be achieved from microcrystals orders of magnitude smaller than those needed for X-ray and, in some cases, in as little as 30 minutes.[32] Electron diffraction-derived structures were superimposed with those from previous X-ray studies to validate the accuracy of the electron diffraction data. Remarkably, despite higher $R_1$, electron diffraction-derived structures were nearly identical to previously reported X-ray structures. Even hydrogen atoms were discernible in many structures, a feat that's particularly challenging in X-ray crystallography due to weak scattering interaction between hydrogen atoms and photons.[32] Furthermore, the technique

displayed its prowess by analyzing a blend of microcrystalline powders, successfully revealing the chemical identity of individual constituents from a multicomponent mixture.[32]

Spurred by the initial success of the 2018 study, Nelson and coworkers further refined MicroED technology with subsequent experiments. Recognizing the technique's potential, they expanded its application to include reactive organometallic compounds, underscoring MicroED's capacity to decipher structures of chemicals that are traditionally challenging due to their pronounced reactivity and poor stability outside of an inert atmosphere. A standout aspect of this research was the incorporation of a rapid and precise detector, facilitating MicroED experimentation at room temperature.[54] This removed the prerequisite of chilling the sample to cryogenic levels for data gathering, further broadening its applicability and ease of use for routine structural analysis of small molecule compounds.

**Figure 1.3** *Number of small molecule structures obtained via electron diffraction and deposited to the Cambridge Structural Database (CSD) each year from 2013 to 2020.*
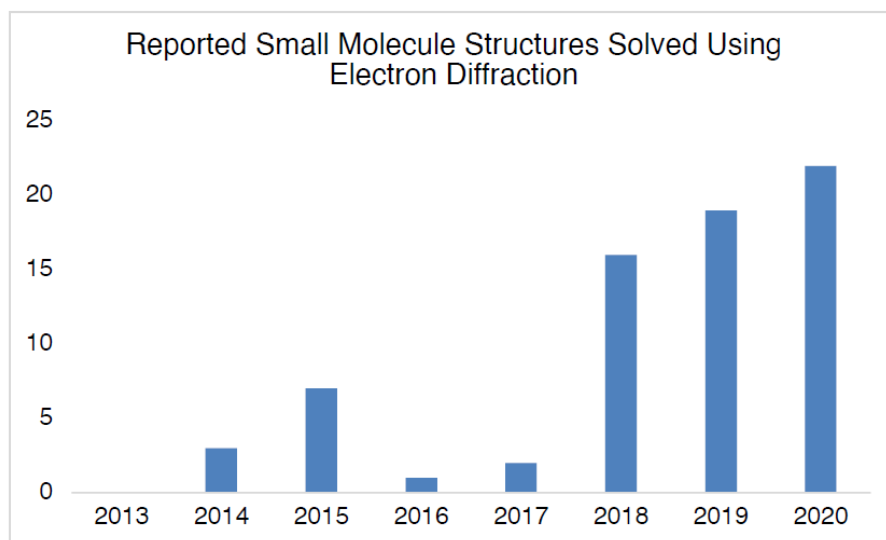


From the remarkable success of these initial small molecule studies, MicroED, and the field of electron crystallography more broadly, have been rapidly evolving, demonstrating its prowess in deducing structures across diverse fields, including metal-organic frameworks, pharmaceutical compounds, synthetic reaction products, and elusive NPs. Often, researchers have turned to MicroED precisely because other

techniques fall short of the task. By doing so, the structural insights gathered from MicroED analysis have become a pivotal and complementary piece of data in conjunction with traditional spectroscopic methods, heightening the confidence in structural assignments of complex molecules. A testament to its increasing significance in the domain of small molecule analysis is the steadily rising number of structure submissions to the Cambridge Structural Database (CSD) between 2013 and 2020, underscoring MicroED's expanding role and relevance (Figure 1.3).

**1.2.3 MicroED in NP Structure Elucidation**

MicroED has rapidly established itself as an indispensable tool for the detailed structural analysis of NPs. While both X-ray diffraction and MicroED require crystalline samples, the latter boasts the unique capability to utilize crystals several orders of magnitude smaller.[32, 53] This capability of MicroED is invaluable as growing microcrystals is typically faster, easier, and consumes far less sample than growing larger ones suitable for X-ray diffraction. This efficient approach facilitates higher experimental throughput, granting researchers more immediate access to critical structural data for NPs of interest. Beyond this, MicroED stands out for its ability to scrutinize heterogeneous mixtures, thereby offering the potential to identify minute quantities of impurities or trace components in NP isolates, which might otherwise escape detection or further convolute spectroscopic analysis.[32]

While MicroED has shown great promise in the field of chemistry, it's only recently begun to be used as a routine analytical tool in the NP characterization and analysis workflow.[55] Prior studies have showcased MicroED's potential for the accurate structural determination of known NP and NP-like molecules.[54] Thanks to these pioneering studies, there has been a growing body of research demonstrating MicroED's ability to confidently assign structures of novel natural products and even revise structures previously proposed through other methods. As the field of electron crystallography continues to grow, the widespread integration of MicroED into the NP workflow appears inevitable, driven by its proven track record and game-changing capabilities.

*Figure 1.4.* (a) Diffraction pattern of 3-thiaGlu peptide. (b) MicroED structure of 3-thiaGlu (c) Structure of chemically synthesized tetrapeptides (VFA-thiaGlu) containing D-thiaGlu and L-thiaGlu. (d) Determination of stereochemical configuration of thiaGlu by comparison with synthetic standards. (e) $^{13}C$ NMR spectra showing the β carbon of the C-terminal cysteine in $^{13}C$-labeled TglA-Cys (top) and $^{13}C$-formate after reaction with TglHI (bottom).[52]
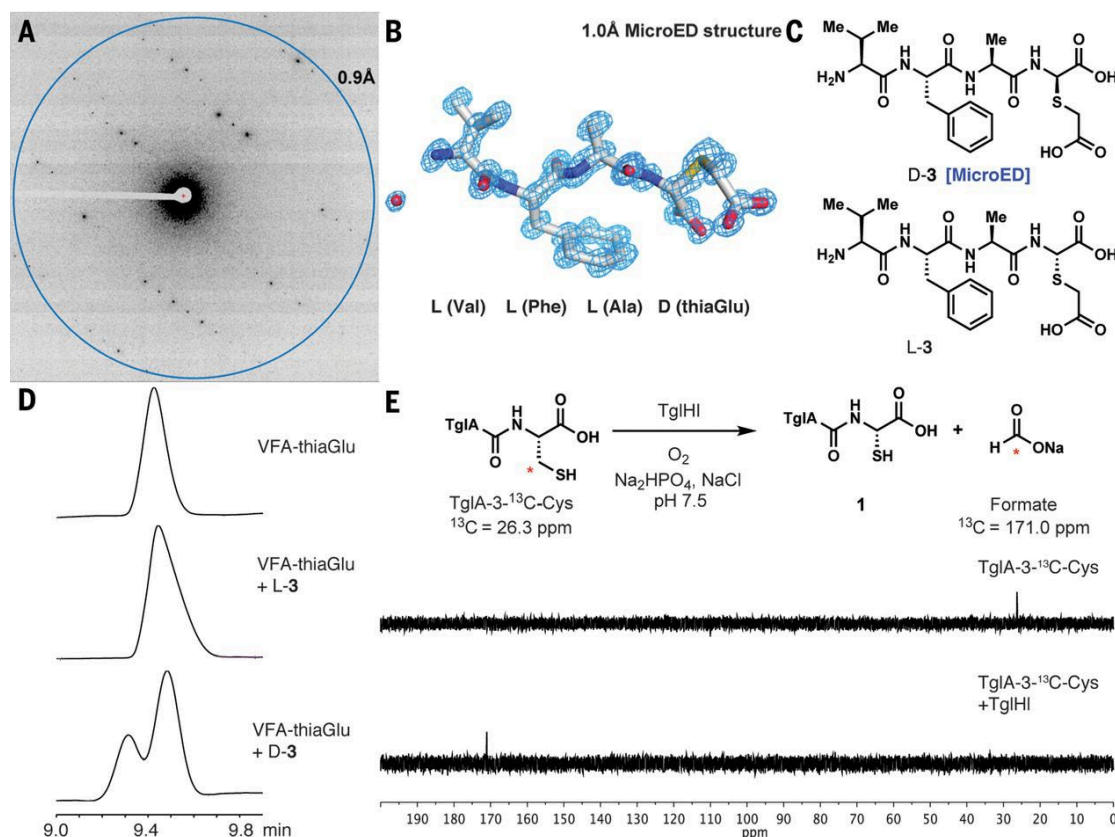


## 1.3 RECENT APPLICATIONS OF MICROED IN NATURAL PRODUCT ELUCIDATION

Recently, MicroED has gained significant attention in the chemical literature for its potential to address the challenges posed by conventional structural characterization methods, especially concerning NPs.[55] MicroED has played a pivotal role in providing essential structural insights, enabling researchers to confidently determine the structure of new NPs[56-58] and even revisit and correct structures previously deduced using NMR and other spectroscopic methods.[59, 60] The array of recent studies underscores the versatility of MicroED, revealing structures of NPs with a broad range of molecular weights, bioactivities,

and structural diversity. These NPs, derived from a spectrum of biological sources, from fungi to organisms like Caenorhabditis elegans, exemplify MicroED's expansive utility in NP research and exploration.

*Figure 1.5. (a) Chemical structures of ilicicolin H and its derivative Py-469. (b) Preliminary structure solution revealing the molecular framework of Py-469. (c) Fully refined structure of Py-469.[59]*



a)

Ilicicolin H, **(1)**

Py-469, **(2)**
*First novel non-peptidyl NP characterized by MicroED*

b)

*Preliminary structure*

c)

*0.90 Å resolution, $R_1$ = 13.7%, GooF = 1.778*
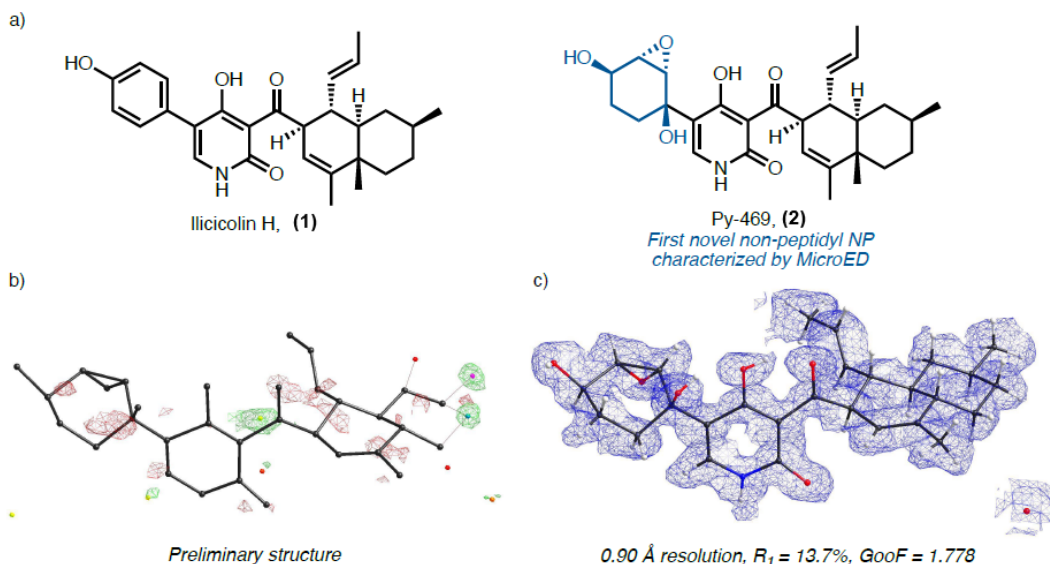
### 1.3.1 Novel NP Identification

In 2019, one of the pioneering studies showcasing MicroED's capability to resolve the structures of novel natural products was presented by van der Donk and coworkers.[52] Their investigation centered on the genome sequencing of environmental bacteria, which revealed unique biosynthetic gene clusters. These clusters encoded an intriguing ensemble of enzymes responsible for the production of previously unidentified natural products. Interestingly, they discovered a process where a ribosomally synthesized small peptide, acted as a foundation for the nonribosomal extension and subsequent chemical alterations. This process saw amino acids being appended to the peptide's carboxyl end via ATP and aminoacyl-tRNA– mediated reactions, independently of ribosomal action. The ensuing steps involved oxidative reshuffling, carboxymethylation, and the proteolytic action on a terminal cysteine, culminating in the creation of an amino acid–derived molecule. Despite thorough analysis through NMR and MS, efforts to obtain crystals

to assign stereochemistry through X-ray crystallography were fruitless. Utilizing high-performance liquid chromatography (HPLC), the team managed to procure a minuscule quantity of powder by evaporating the initially eluted diastereomer. This powder was subsequently placed on a TEM grid, and MicroED analysis of the formed nanocrystals unveiled the d configuration of the 3-thiaGlu within the studied peptide (Figure 1.4). Delving deeper, this study illuminated a similar peptide extension mechanism in the production of ammosamides, potent pyrroloquinoline alkaloids known for their cytotoxic properties. This study thus demonstrated the pivotal role of MicroED as a novel method for the exploration of natural product biosynthetic pathways and metabolite elucidation.

Following this Kim *et al*. demonstrated the use of MicroED to explore non-peptidyl natural products associated with drug-resistant pathogens. As the threat from drug-resistant pathogens grows, the quest for novel natural products to inspire the creation of new pharmaceuticals with unique molecular actions becomes increasingly critical. Synthetic biology has risen to this challenge, facilitating the generation of unique complex metabolites, such as Py-469.[61] Py-469 is a novel secondary metabolite produced from the icc biosynthetic gene cluster (BGC) found in Penicillium variabile. While this BGC is known for generating ilicicolin H, an antifungal agent that disrupts the eukaryotic respiratory chain, it also possesses three additional enzymes not linked to ilicicolin H's biosynthesis. To probe the potential chemical diversification of ilicicolin H, these surplus genes were expressed alongside the five primary genes of ilicicolin H. The result was the production of Py-469. After purification via HPLC and lyophilization, Py-469 underwent MicroED analysis. This technique shed light on Py-469's core molecular structure, albeit with some atomic ambiguity (Figure 1.5a-c). Remarkably, much of this structure was deduced solely from bond angles and lengths, without relying on prior knowledge beyond the compound's molecular formula. Subsequent NMR spectroscopy affirmed this structure but highlighted a discrepancy regarding the position of one nitrogen atom – a challenge in MicroED due to its current resolution capabilities. The final refined structure showed Py-469 as a unique derivative of ilicicolin H, featuring an epoxydiol group (Figure 1.5c). This modification arises from oxidative dearomatization, epoxidation, and a pair of reduction steps

orchestrated by the extra icc enzymes. This pioneering work marks the first instance of MicroED unveiling the structure of one of the first novel, non-peptidyl NPs.

*Figure 1.6. Sinatryptin B, a quinone derivative of sinatryptin A, and its MicroED structure. Thermal ellipsoids are drawn at 30% probability.*[56]



Sinatryptin A                    Sinatryptin B
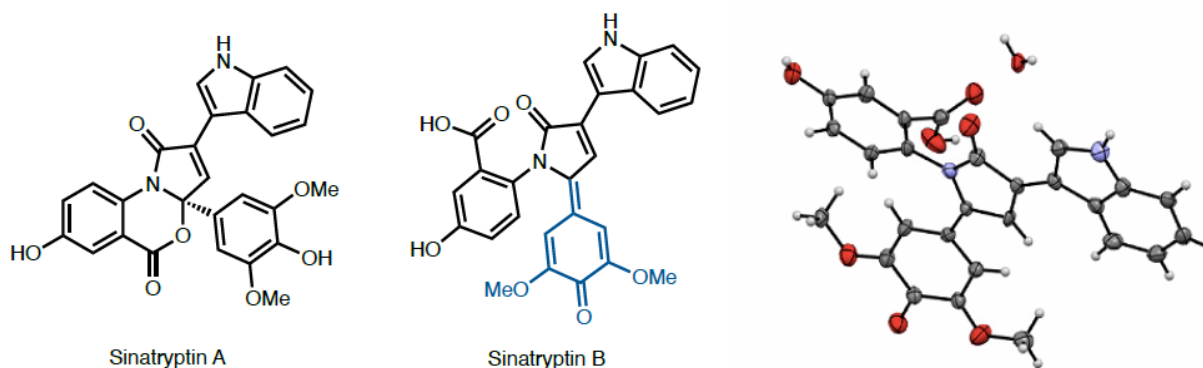
A novel approach to discovering new natural products involves altering the growth conditions of microorganisms.[62] In a 2021 study of the symbiotic relationship between the haptophyte Emiliania huxleyi and the α-proteobacterium Phaeobacter inhibens, Seyedsayamdost and coworkers observed a transition from mutualistic to parasitic interactions.[56] Initially, the algae release compounds that foster bacterial growth, and in return, the bacteria produce chemicals that aid and shield the algae. Yet, when E. huxleyi releases phenylpropanoids like sinapic acid, P. inhibens counters by emitting algaecidal secondary metabolites.[56] In a controlled setting, this mutualist-to-parasite shift was replicated by introducing sinapic acid and tryptophan (suspected to play a role in the parasitic phase) to P. inhibens. This tweak in conditions spurred the generation of various metabolites integrated with tryptophan. Among these, sinatryptin B was isolated, but in quantities too minuscule for traditional spectroscopic or X-ray crystallographic analysis. As a solution, MicroED was employed to decipher sinatryptin B's structure, identifying it as a quinone variant of sinatryptin A (Figure 1.6). This study highlights the pivotal role MicroED can play when conventional structural determination methods fall short and further cements its utility with the second documented non-peptidyl natural product structure resolved using this method.

***Figure 1.7*** *MicroED structure of compound sartorypyrone F.*[58]



Sartorypyrone F
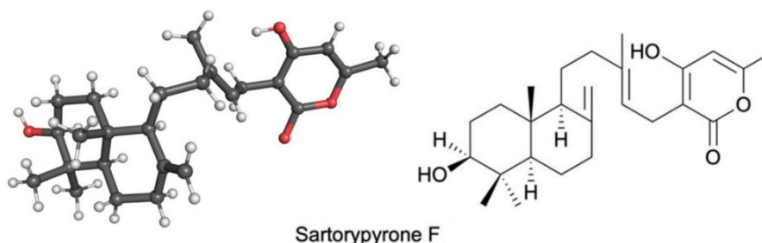
Recent work by Lin *et al*. demonstrated another instance where microED was used to study cryptic NPs expressed by a previously unknown BGC from the fungus *Aspergillus fumigatus*.[58] Aspergillosis, caused by the Aspergillus species, poses a significant threat to immunocompromised patients, with mortality rates between 30-80%.[63] A distinctive feature of *A. fumigatus* is its production of bioactive NPs, which provide it with a competitive edge in host environments. Gliotoxin, an example of such a metabolite, acts as a defense against certain immune responses.[64] The synthesis of NPs in these fungi is facilitated by BGCs, and there is significant diversity among the BGCs in different Aspergillus strains.[65] However, many SM BGCs aren't typically expressed in standard laboratory settings, making the identification of these compounds a challenging task. In this study, a previously unexplored *A. fumigatus* secondary metabolite biosynthesis pathway was expressed in *Aspergillus nidulans*. Using a genetic dereplication strategy, the researchers managed to bring the BGC genes into *A. nidulans*, allowing them to control their expression. Using MicroED analysis Lin and coworkers were able to deduce the structure of a heterologously expressed secondary metabolite which they named sartorypyrone F (Figure 1.7). This innovative approach, combining genetics and advanced electron diffraction techniques, not only revealed new compounds and pathways but also presents a promising method for exploring other cryptic secondary metabolism BGCs in fungal species.

**1.3.2 Structural Revisions**

Determining the structure of highly complex NPs often can pose a significant challenge to researchers. While NMR spectroscopy is the go-to method for characterization, it often provides an inferred rather than direct insight into the molecular structure. This can sometimes result in misinterpretations, as

evidenced by numerous instances where NP structures have had to be revised.[66] Without comprehensive total synthesis endeavors or obtaining crystal structures of the natural entities, some of these inaccuracies might remain undetected. Correcting these structural misassignments is vital, not only for ensuring the relevance of synthetic strategies but also for accurately probing their biological effects and understanding their modes of action.

**Figure 1.8**. *Initially proposed structures of (–)-lomaiviticin A and C and their revised structures based on MicroED analysis. Core carbons are numbered in blue, and atoms exchanged during structure revision are colored in orange.[60]*



(–)-lomaiviticin A
2001 structure assignment

(–)-lomaiviticin C
2012 structure assignment

(–)-lomaiviticin C
Refined MicroED structure

(–)-lomaiviticin A
2021 structure assignment

(–)-lomaiviticin C
2021 structure assignment
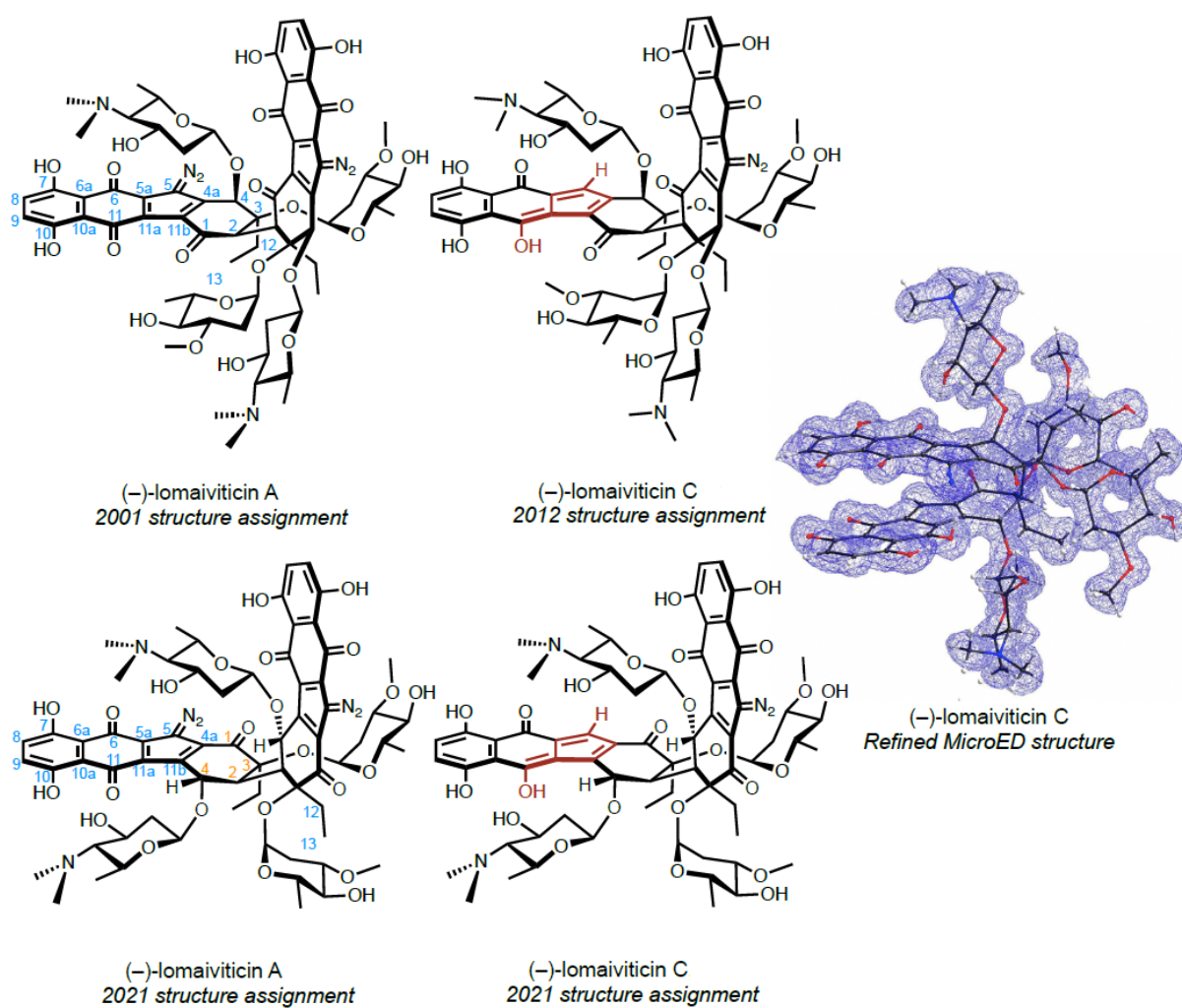
A significant instance of structural revision is the collaborative effort between the Nelson and Herzon labs, focusing on the lomaiviticins, a group of bioactive NPs derived from marine bacteria.[60] The potent cytotoxicity of (–)-lomaiviticin A has led to its extensive exploration, with numerous publications detailing its bioactivity and biosynthetic pathways.[67] Despite decades of study, the scarce proton-attached carbons comprising the core molecular structure have made NMR analysis challenging, leaving the initially suggested structure unconfirmed. Additionally, the lomaiviticins remained elusive despite two decades of attempted total synthesis. The puzzle began to unravel when MicroED analysis of (–)-lomaiviticin C, a precursor to lomaiviticin A with a similar core ring structure, revealed discrepancies in the previously suggested structure based on NMR interpretations. Following this, through computational modeling, high-field (800 MHz) NMR spectroscopy, and density functional theory (DFT) calculations, it was established that the experimental NMR data resonated more with the newly revised structure than that which was previously reported (Figure 1.7). Thus, by using MicroED to corroborate corresponding spectroscopic and computational evidence, decades of structural misinterpretation were finally corrected. This revelation underscores the inherent limitations of pure inferenced based structural determination, especially when dealing with complex NPs with highly complex structures of minimal proton-attached carbons and weak proton coupling signals.

**Figure 1.9**. *Fischerin's initially proposed relative stereochemistry based on NMR shift calculations, and the corrected relative stereochemistry based on MicroED structure.*[59]
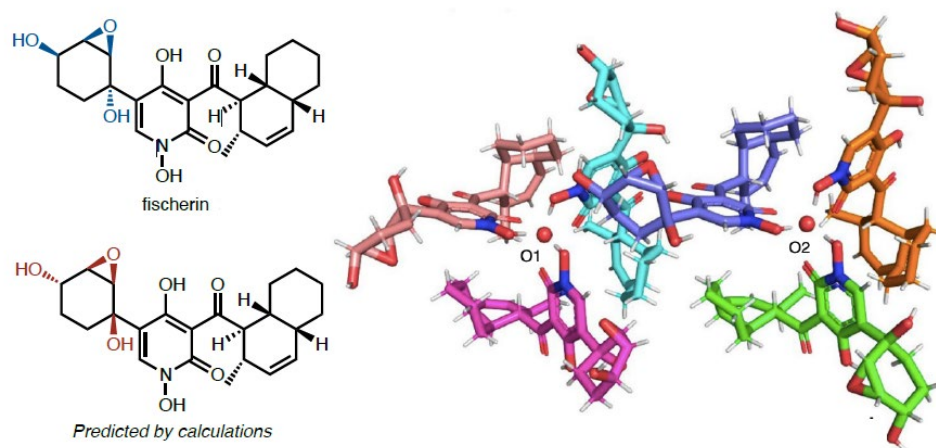
In addition to lomaiviticin, another important structural revision was provided by Kim *et at*., through the use of MicroED, in the case of the NP fischerin.[59] This a-pyridone-enriched fungal NP, derived from *Neosartorya fischeri* and known for its potent bioactivity, was initially isolated over a quarter-century ago.[68] While NMR studies elucidated its chemical structure, assigning its relative stereochemistry was challenging, primarily due to the flexible bonds linking its intricate, stereochemically rich ring systems. Though computational chemistry was used to propose a stereochemical configuration by Amini in 2015,[69] fischerin's actual crystal structure remained elusive since its initial discovery. Lacking the original fungal strain for reference, Kim *et al*. turned to genome mining, which led to a BGC capable of reproducing fischerin. In line with the findings of the original reports, traditional methods such as X-ray crystallography and NMR spectroscopy failed to provide clarity on fischerin's structure. However, a breakthrough came with MicroED, which offered a clear crystal structure, unveiling the relative stereochemistry of the epoxydiol ring components (Figure 1.8). Most notably, the revising the stereochemistry deduced varied from Amini's proposal based on NMR shift computations,[69] dispelling previous ambiguity and providing a definitive stereochemical configuration. This instance underscores the potency of MicroED as a complementary tool to other analytical methods like NMR and emphasizes the need to corroborate computed structures through experimental validation whenever feasible.

### 1.3.3 Determining connectivity via MicroED

Determining the connectivity of structural elements and functional groups in natural products is vital for deciphering their molecular architecture. A comprehensive understanding of a compound's molecular blueprint can serve as a roadmap for drug discovery, aiding in tasks such as docking simulations and probing mechanisms of action grounded on the molecule's interaction with a protein's active site. While NMR spectroscopy is often the go-to method for determining molecular structures, it sometimes falls short, especially when dealing with challenges like ambiguous spectral patterns or the presence of multiple compounds in a sample.[18, 23] Take, for instance, the case of (–)-lomaiviticin C: MicroED was pivotal in definitively establishing and revising the atomic connectivity within its core. Such precise delineations not

only propel forward synthetic methodologies but also deepen our insights into biosynthesis and the biological roles these molecules play.[60]

**Figure 1.10**. *Proposed structure of uglas#1 and the MicroED structure of gluric#1, a glucosyl uric acid NP used as a synthetic intermediate. Preliminary structure clearly reveals the $N^3$ connectivity.*



uglas#1
*Proposed structures by MS$^2$*

gluric#1
*Characterized by MicroED*

*Preliminary structure*

*1.0 Å resolution, $R_1$ = 14.0%, GooF = 1.223*
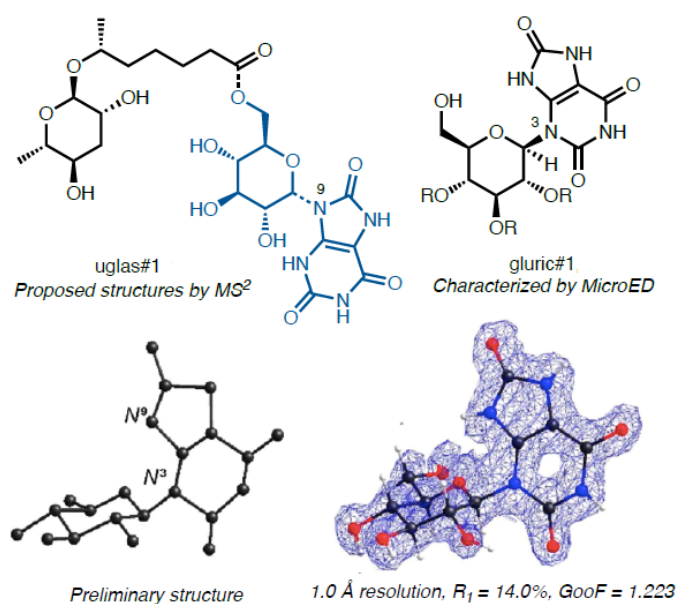
Another notable case where MicroED played a pivotal role in revealing atomic connections is illustrated in a 2020 study by the Nelson and Schroeder labs.[57] This study focused on the uric acid-incorporating gluconucleoside NP, uglas#1. Extracted from C. elegans, a well-regarded model organism in biological research, uglas#1 is believed to play a role in insulin signaling pathways.[70] Mass spectrometry analysis hinted at a structure containing components of uric acid, glucose, and an ascaroside segment. However, deciphering the precise connectivity between glucose and uric acid proved challenging, given the indistinct line shapes in the 2D NMR spectra. This obstacle was circumvented when the MicroED structure of gluric#1, a synthetic precursor to uglas#1, unveiled a preference for glucosylation of uric acid at the $N^3$ position (Figure 1.9). This investigation accentuates not only the versatility of MicroED in natural product characterization but also its potential to address limitations inherent to other techniques like NMR.

*Figure 1.11*. *MicroED structure showcasing co-crystallized sinamicin B and sinamicin C. In the asymmetric unit, sinamicin B is on the right and sinamicin C is on the left. Thermal ellipsoids drawn at 30% probability.*[56]
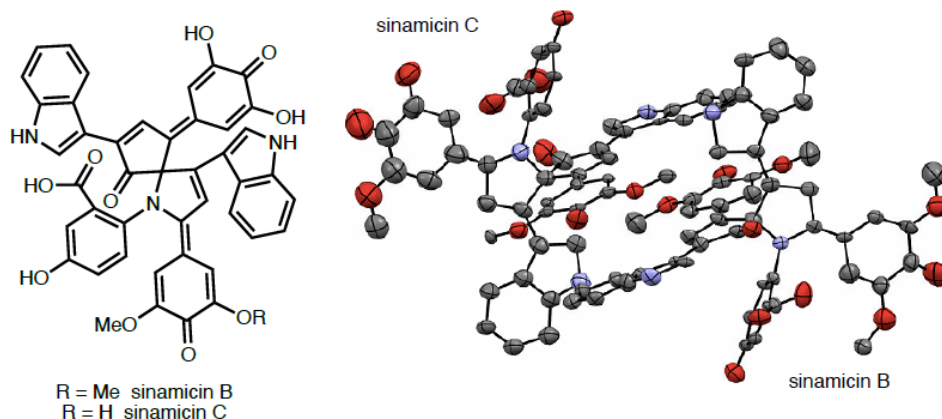


Establishing atomic connectivity with NMR spectroscopy becomes particularly challenging when a solution comprises multiple compounds, especially if these molecules possess limited proton-bound carbons to assist structural interpretation. In the study of sinatryptin A, Seyedsayamdost and colleagues encountered these such obstacles when attempting to distinguish sinamicin B from sinamicin C. Both are co-metabolites of sinatryptin A and distinct alkaloids produced when sinapic acid and tryptophan are present.[56] Adding to the challenges of purification, the minute quantities in which sinamicin B and C were available and their low proton-to-carbon ratio made NMR-based structural determination even more challenging. However, by employing MicroED, they discovered that these secondary metabolites cocrystallized, forming microcrystals and enabling the simultaneous elucidation of their structures in a single experiment (Figure 1.10).[56]

### 1.3.4. Assignment of Relative Stereochemistry

Assigning the correct relative stereochemistry to small molecules, especially bioactive ones like secondary metabolites, is crucial. Different stereoisomers can have distinct bioactivities, as exemplified by the classic examples of propoxyphene[71] and thalidomide.[72] While D-Propoxyphene functions as an

analgesic, its counterpart, L-propoxyphene, acts as an antihistamine.[71] Similarly, the (R)-enantiomer of thalidomide serves as a sedative and is effective against morning sickness, whereas its other isomer has teratogenic effects.[72] While NMR spectroscopy often reveals enough data to discern relative stereochemistry, certain molecules might lack appropriately positioned hydrogen atoms for clear analysis. This is particularly true for molecules with distant stereocenters separated by rigid structures containing rotatable bonds. Fischerin and Py-469, discussed earlier in this chapter, exhibited these very challenges, making their relative stereochemistries elusive.[59, 68, 69] However, with the precision of MicroED, their stereochemical configurations were clarified, even necessitating the revision of a previously suggested structure.

*Figure 1.12*. *Structure of (–)-sambutoxin its biosynthetic intermediate, featuring the characteristic tetrahydropyran motif.*[73]
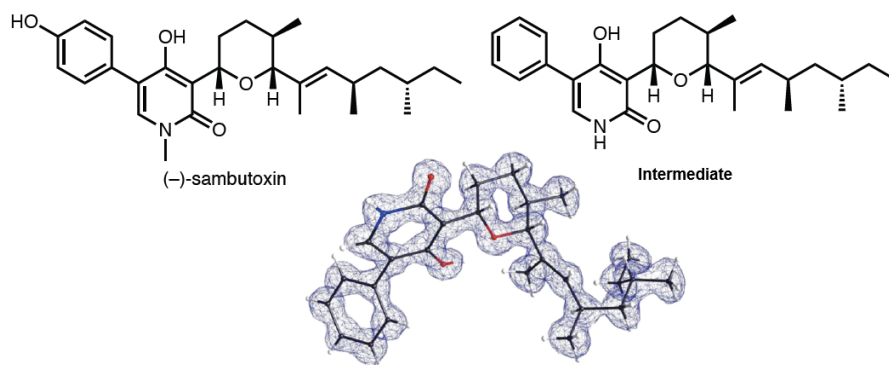


In a joint effort between the Nelson and Tang laboratories, MicroED played an essential role in affirming the relative stereochemistry assignments for a crucial intermediate in the biosynthesis of a fungal secondary metabolite. (–)-Sambutoxin, a 4-hydroxy-2-pyridone toxin, is sourced from the potato parasite, Fusarium sambucinum.[73] While various 4-hydroxy-2-pyridone alkaloids have been studied, the 3-ether subfamily, distinguished by its unique tetrahydropyran feature, has not been extensively explored compared to its counterparts. Through genome mining and sequential reconstitution, the biosynthetic route to this toxin was investigated, leading to the isolation and characterization of key intermediates. One such

intermediate, directly succeeding the formation of the tetrahydropyran, undergoes late-stage P450-catalyzed oxidation and *N*-methylation, culminating in the creation of (–)-sambutoxin. To decipher and affirm the relative stereochemistry of this intermediate, specifically between the tetrahydropyran element and the methyl groups on the polyketide chain, a combined approach of MicroED and NMR spectroscopy was employed (Figure 1.11). This collaborative effort revealed that the intermediate's stereochemistry mirrors that of (–)-sambutoxin, reinforcing its significant role in the compound's biosynthesis (Figure 1.11).

*Figure 1.13*. *Crystal structures of hakuhybotrol. (a) MicroED (thermal ellipsoids are drawn at 50% probability levels); (b) statistics calculated from the dynamical refinement result; (c) SCXRD (thermal ellipsoids are drawn at 50% probability levels); (d) superposition of (a) and (c).*[74]

**(a)**

3D ED/MicroED (kinematical refinement)

**(b)**

|  | Hakuhybotrol (**1**) | *ent*-**1** |
|---|---|---|
| $R_1$ | 0.1685 | 0.1931 |
| $wR_2$ | 0.2857 | 0.3206 |
| z-score | 4.0σ | |

**(c)**

SCXRD

**(d)**

Blue: SCXRD, Red: 3D ED/MicroED
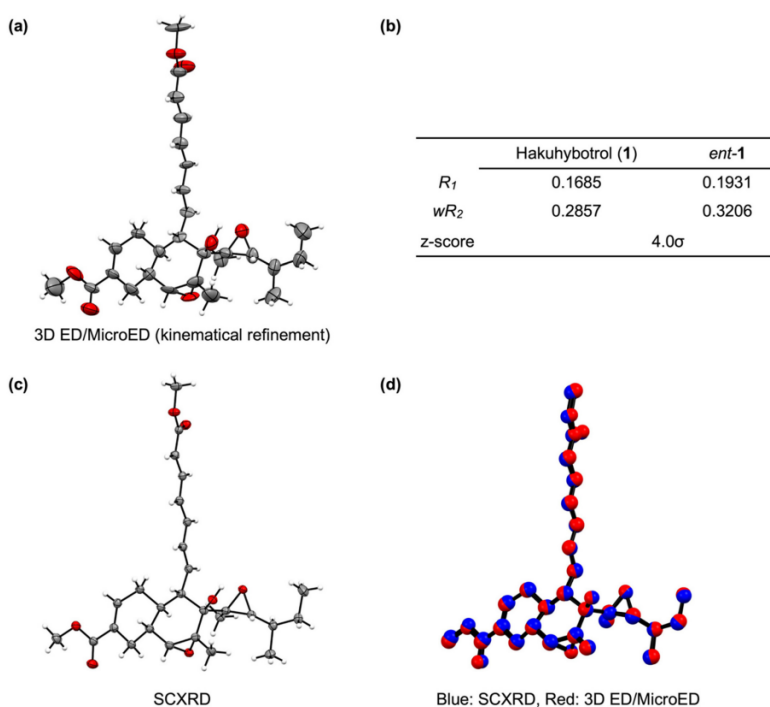
## 1.3.5 Assignment of Absolute Configuration through Dynamical Refinement

Dynamical refinement, as applied in the realm of electron diffraction, is a newly emerging technique in the structural analysis of natural products.[75] The accurate determination of absolute stereochemistry, a cornerstone in understanding biological activities and functions of organic molecules,

often presents challenges when using conventional methods. Dynamical refinement, particularly when applied to 3D ED/MicroED data, provides enhanced resolution and clarity, and precision regarding the spatial arrangement of atoms in molecular structures.[75, 76] In the context of natural products, which often possess complex and chiral structures, the technique offers a more direct pathway to establishing their absolute stereochemistry. This is particularly invaluable when working with compounds that might be available only in minute quantities or when dealing with sub-micron crystalline powders. While its application has been limited in the space of NP chemistry, it is a rapidly developing area of research within the broader crystallographic community.

One recent study by Watanabe *et al*. applied the use of dynamical refinement in the study of a novel polyketide, hakuhybotrol, extracted from the mycoparasitic fungus Hypomyces pseudocorticiicola FKA-73.[74] In this research, while the compound's structure was primarily analyzed using high-resolution mass spectrometry and both 1D and 2D NMR, its absolute configuration became discernible through a multi-faceted approach. This included the integration of chemical derivatization, SCXRD, and, crucially, MicroED. By using MicroED to analyze small crystals of compound hakuhybotrol, the absolute configurations were decisively deduced as 8S, 9R, 14R, 15R, 16R, 17S, 18S, 19R, and 20R. Remarkably, the sole reliance on MicroED data was sufficient to directly infer the absolute configuration of compound hakuhybotrol (Figure 1.12a). Post refinement, the computed $R_1$ and $wR_2$ values for compound hakuhybotrol indicated a preferable fit compared to its enantiomer, ent-1 (Figure 1.12b). This insight validates the technique's potential to discern the correct absolute configuration solely from electron diffraction data. Comparatively, the consistency and reliability of MicroED became evident when superimposed with the conventional SCXRD method (Figure 1.12c-d). The latter confirmed the absolute configuration of compound hakuhybotrol, which aligned seamlessly with data obtained through MicroED, emphasizing the congruence of the two techniques. This study thus demonstrates, to the best of our knowledge, the first time the absolute configuration of an NP has been deduced by MicroED. While current dynamical refinement software does have some constraints, and requires a certain level of expertise to perform, the field is rapidly

advancing, making these techniques more accessible to chemists. It is, therefore, likely that in the coming years, we may see the widespread adoption of such techniques in routine electron diffraction workflows, making it an all the more powerful tool for natural product exploration and analysis.

*Figure 1.14. (a) Sketch of the illumination conditions in the case of selected-area 3D electron diffraction. (b) Sketch of the illumination conditions in the case of nanobeam 3D electron diffraction. (c) Left: beam-path geometry in precession electron diffraction. Right: single pattern collected from a nanocrystal of HEWL in precession-assisted nanobeam 3D electron diffraction mode.*[77]
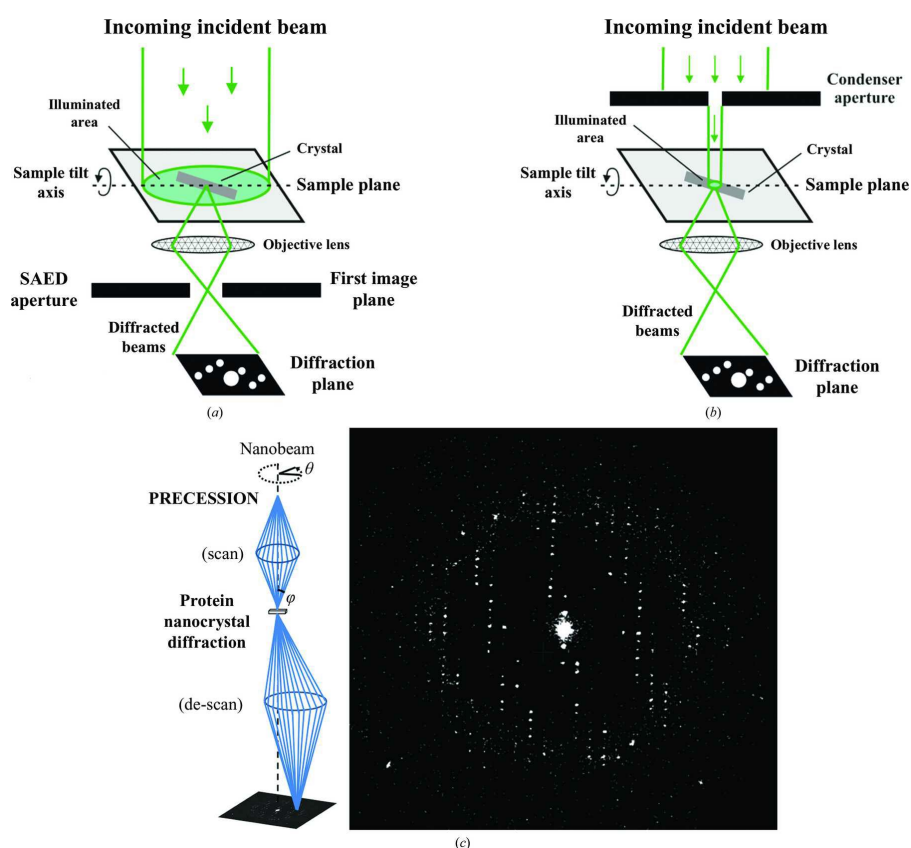


## 1.4 CHALLENGES AND OUTLOOK IN NP CHARACTERIZATION USING MICROED

Electron diffraction and MicroED have garnered significant attention in natural product research due to their potential to determine the molecular structures of complex organic compounds. However, several challenges persist. Firstly, sample preparation remains a delicate and critical step. Natural products, given their diverse and sometimes labile nature, may be susceptible to electron beam damage. The challenge

is to ensure that the sample is both thin enough for electron transmission and stable enough to resist radiation damage during data acquisition.[78] Achieving the right balance demands skill, time, and the correct sample preparation methodologies. Secondly, while MicroED has been heralded for its ability to work with nanoscale samples, there's a threshold below which the quality of the resulting diffraction pattern diminishes.[79] This presents a challenge when working with scarce or precious natural samples where only minute quantities are available. Furthermore, data processing and analysis present their own set of challenges. Differentiating between solvent molecules and structural components, accounting for dynamical scattering effects, and handling incomplete or low-resolution data all require sophisticated software and expertise. Given that natural product research often involves complex and large molecules, these challenges are magnified.

In contrast to standard electron diffraction techniques, nanobeam diffraction also present a promising avenue to probe NPs and other chemical systems. A 2019 study by Lanza *et al*. demonstrates the use of a precession-assisted nanobeam technique to examine the structure of submicrometric protein crystals, revealing novel protein polymorphs undetected by X-ray diffraction (Figure 1.13).[77] This technique's proficiency is evident in its ability to offer crucial structural insights from minimal protein nanocrystals, significantly few than what would be required for other advanced analytical techniques such as XFEL.[80] Such nanocrystals are also easier to cultivate and bear fewer defects than their macroscopic counterparts used in conventional X-ray crystallography. Notably, this method unveiled a new monoclinic polymorph of HEWL, a protein studied for over five decades, highlighting its capacity to detect protein forms, even when data completeness was under 70%.[77] The employed nanobeam precession-assisted approach, akin to strategies at synchrotron microfocus beamlines, prioritizes the undamaged sections of a crystal, ensuring enhanced diffraction pattern quality.[81] This pioneering study positions nanobeam diffraction as a potential tool for the study of challenging NPs, which are prone to forming poor-quality crystals with a large number of defects. Furthermore, these nanobeam methods have other potential uses in

the real-time monitoring of protein dynamics, shedding light on NPs and their interaction with various biological processes.[82]

*Figure 1.15*. *Workflow for using peptide fragments for phasing MicroED data. A) Electron diffraction pattern reaching atomic resolution for QYNNENNFV. Rings designate resolution ranges while arrowhead designates highest resolution spot. B) All fragments comprising the polyglycine hexapeptide library aligned in pymol. C) LLG vs InitCC plot for the fragments screened in ARCIMBOLDO-BORGES. Color indicates the wMPE of the fragment relative to the phases calculated from the final structure. Inset shows the fragment chosen for SHELXE expansion overlaid on the final structure. D) Output solution from ARCIMBOLDO-BORGES following SHELXE expansion is shown overlaid on the final structure. Maps are shown after one round of refinement in Phenix. E) Final structure and potential map for the QYNNENNFV peptide with symmetry related chains shown in gray.[83]*
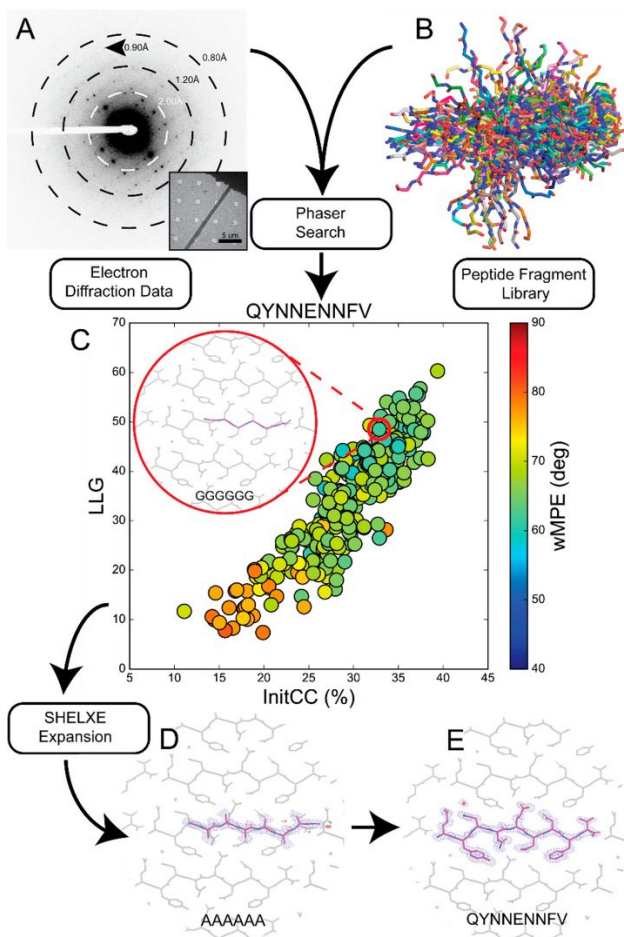
In response to the emerging demand for novel ab initio phasing solutions for MicroED, Rodriguez, and coworkers have pioneered fragment-based phasing strategies utilizing an automated, fragment-based approach to structure determination ARCIMBOLDO, successfully determining five previously inaccessible peptide structures through molecular phasing (Figure 1.14).[83] In this study, the variations in diffraction quality they observed mirror the challenges often seen in the structural analysis of NPs, including poor resolution and radiation damage. In these scenarios where atomic resolution is lacking, utilizing pre-existing solutions may circumvent the lack of high-resolution data. Here, fragments employed were successfully selected by Phaser and refined by SHELXE, resulting in consistent, unambiguous solutions. This approach demonstrates the power of verification through competition in chemical crystallography. The libraries they used for macromolecular phasing, built around a shared local fold, consistently produced accurate results. Emphasizing the efficacy of this method, single-fragment solutions consistently outperformed combined ones. Based on this method's adaptability to different structural motifs, further enhancements by leveraging libraries like AlphaFold's deep learning techniques could hold great promise for tackling a range of diverse structural challenges in other small molecule systems, such as NPs which can often have similar core structural motifs.[84] By broadening the ab initio phasing toolkit for small molecules, it may soon be possible to achieve accurate structural solutions without the strict need for atomic resolution data.

Despite these challenges, the future of electron diffraction and MicroED in natural product research appears promising. As technologies advance, there is considerable hope that many of the current challenges will be mitigated. The continuous development of hardware, especially direct electron detectors, promises to increase the sensitivity and resolution of data collection. These advancements could potentially reduce the required sample size even further while simultaneously improving data quality. In terms of software, ongoing collaborations between crystallographers, chemists, and software developers are expected to yield advanced algorithms that can more efficiently process and interpret electron diffraction data, especially from complex natural product samples. Moreover, the interdisciplinary nature of this field is likely to foster innovations in sample preparation techniques, potentially drawing from related disciplines such as

biological electron microscopy. Finally, as more researchers adopt these techniques, a collective repository of knowledge and best practices will emerge. This will not only streamline the process but also help new entrants into the field, thus expanding the scope and application of electron diffraction and MicroED in NP research.

## 1.5 CONCLUSION

The integration of advanced analytical techniques into the field of NP researcu has always presented a significant shift in our ability to uncover and understand the vast molecular complexity that nature offers. The emergence of electron diffraction and, more prominently, MicroED has presented a transformative shift in the field, revolutionizing how we approach structural elucidation challenges in NP research. Such techniques have been a boon for natural product chemists, offering an alternative pathway for the elucidation of molecular structures without the need for sizable crystals. The inherent capability of MicroED to generate high-resolution structural data from nanocrystalline samples has effectively democratized structural analysis. Now, research groups have new tools that will allow them to participate in the quest to unveil nature's molecular repertoire. The fact that such detailed structural data can be obtained from tiny crystal samples is nothing short of revolutionary, paving the way for the rapid characterization of a multitude of compounds that would have been considered challenging or even impossible to analyze in the past.

Beyond simply expanding the toolkit of the natural products researcher, the adoption of electron diffraction and MicroED has led to the discovery and elucidation of a plethora of novel compounds. This increased pace of discovery is expanding our understanding of biodiversity at the molecular level and revealing intricate pathways and mechanisms that nature employs to synthesize these compounds. Furthermore, as many natural products have therapeutic potential, the rapid and accurate structural determination facilitated by these techniques may provide an expedited route along the drug discovery pipeline, with huge implications for healthcare and medicine.

In terms of future prospects, the trajectory for electron diffraction, especially MicroED, in NP research is undoubtedly steep. As technology advances, and as methodologies become even more refined, we can expect even greater capabilities in terms of data quality, speed, and accessibility. Collaborative efforts between chemists, biologists, and physicists will be crucial in harnessing the full potential of these tools, integrating them seamlessly into the broader natural products research paradigm. The profound impact of electron diffraction and MicroED on the field of natural products cannot be overstated. Overall, these techniques have begun to reshape the landscape in the field of NP chemistry, eliminating long-standing barriers and opening up new vistas of exploration. As we continue to delve deeper into the molecular wonders that nature has to offer, it is clear that electron diffraction methods will be essential in guiding researchers into a new era of discovery and understanding for this important class of small molecules.

## 1.6 REFERENCES

(1) Nasim, N.; Sandeep, I. S.; Mohanty, S. Plant-derived natural products for drug discovery: current approaches and prospects. *Nucleus (Calcutta)* **2022**, *65* (3), 399-411.

(2) Sanchez, S.; Demain, A. L. Bioactive products from fungi. *Food bioactives: extraction and biotechnology applications* **2017**, 59-87.

(3) Sekurova, O. N.; Schneider, O.; Zotchev, S. B. Novel bioactive natural products from bacteria via bioprospecting, genome mining and metabolic engineering. *Microbial Biotechnology* **2019**, *12* (5), 828-844.

(4) Carroll, A. R.; Copp, B. R.; Davis, R. A.; Keyzers, R. A.; Prinsep, M. R. Marine natural products. *Natural Product Reports* **2021**, *38* (2), 362-413, 10.1039/D0NP00089B.

(5) Yuan, H.; Ma, Q.; Ye, L.; Piao, G. The Traditional Medicine and Modern Medicine from Natural Products. *Molecules* **2016**, *21* (5), 559.

(6) Beutler, J. A. Natural Products as a Foundation for Drug Discovery. *Current Protocols in Pharmacology* **2009**, *46* (1), 9.11.11-19.11.21.

(7) David, B.; Wolfender, J.-L.; Dias, D. A. The pharmaceutical industry and natural products: historical status and new trends. *Phytochemistry Reviews* **2015**, *14*, 299-315.

(8) Seidel, T.; Wieder, O.; Garon, A.; Langer, T. Applications of the Pharmacophore Concept in Natural Product inspired Drug Design. *Molecular Informatics* **2020**, *39* (11), 2000059.

(9) Dara, S.; Dhamercherla, S.; Jadav, S. S.; Babu, C. H. M.; Ahsan, M. J. Machine Learning in Drug Discovery: A Review. *Artificial Intelligence Review* **2022**, *55* (3), 1947-1999.

(10) Li, Q. Application of Fragment-Based Drug Discovery to Versatile Targets. *Frontiers in Molecular Biosciences* **2020**, *7*, Review.

(11) Nannenga, B. L.; Gonen, T. The cryo-EM method microcrystal electron diffraction (MicroED). *Nature Methods* **2019**, *16* (5), 369-379.

(12) Nannenga, B. L.; Gonen, T. MicroED opens a new era for biological structure determination. *Current opinion in structural biology* **2016**, *40*, 128-135.

(13) Nguyen, C.; Gonen, T. Beyond protein structure determination with MicroED. *Current opinion in structural biology* **2020**, *64*, 51-58.

(14) Mu, X.; Gillman, C.; Nguyen, C.; Gonen, T. An Overview of Microcrystal Electron Diffraction (MicroED). *Annual Review of Biochemistry* **2021**, *90* (1), 431-450.

(15) Gemmi, M.; Mugnaioli, E.; Gorelik, T. E.; Kolb, U.; Palatinus, L.; Boullay, P.; Hovmöller, S.; Abrahams, J. P. 3D Electron Diffraction: The Nanocrystallography Revolution. *ACS Central Science* **2019**, *5* (8), 1315-1329.

(16) Gruene, T.; Mugnaioli, E. 3D Electron Diffraction for Chemical Analysis: Instrumentation Developments and Innovative Applications. *Chemical Reviews* **2021**, *121* (19), 11823-11834.

(17) Bouslimani, A.; Sanchez, L. M.; Garg, N.; Dorrestein, P. C. Mass spectrometry of natural products: current, emerging and future technologies. *Natural Product Reports* **2014**, *31* (6), 718-729, 10.1039/C4NP00044G.

(18) Halabalaki, M.; Vougogiannopoulou, K.; Mikros, E.; Skaltsounis, A. L. Recent advances and new strategies in the NMR-based identification of natural products. *Current Opinion in Biotechnology* **2014**, *25*, 1-7.

(19) Demarque, D. P.; Dusi, R. G.; de Sousa, F. D. M.; Grossi, S. M.; Silvério, M. R. S.; Lopes, N. P.; Espindola, L. S. Mass spectrometry-based metabolomics approach in the isolation of bioactive natural products. *Scientific Reports* **2020**, *10* (1), 1051.

(20) Frainay, C.; Schymanski, E. L.; Neumann, S.; Merlet, B.; Salek, R. M.; Jourdan, F.; Yanes, O. Mind the Gap: Mapping Mass Spectral Databases in Genome-Scale Metabolic Networks Reveals Poorly Covered Areas. *Metabolites* **2018**, *8* (3), 51.

(21) Robinette, S. L.; Brüschweiler, R.; Schroeder, F. C.; Edison, A. S. NMR in Metabolomics and Natural Products Research: Two Sides of the Same Coin. *Accounts of Chemical Research* **2012**, *45* (2), 288-297.

(22) Fabian, M. D.; Angel, C. d. D. 1H and 13C NMR for the Profiling of Natural Product Extracts: Theory and Applications. In *Spectroscopic Analyses*, Eram, S., Fahmina, Z. Eds.; IntechOpen, 2017; p Ch. 5.

(23) Buevich, A. V.; Williamson, R. T.; Martin, G. E. NMR structure elucidation of small organic molecules and natural products: choosing ADEQUATE vs HMBC. *Journal of Natural Products* **2014**, *77* (8), 1942-1947.

(24) Kutateladze, A. G.; Kuznetsov, D. M.; Beloglazkina, A. A.; Holt, T. Addressing the challenges of structure elucidation in natural products possessing the oxirane moiety. *The Journal of Organic Chemistry* **2018**, *83* (15), 8341-8352.

(25) Riccio, R.; Bifulco, G.; Cimino, P.; Bassarello, C.; Gomez-Paloma, L. Stereochemical analysis of natural products. Approaches relying on the combination of NMR spectroscopy and computational methods. *Pure and applied chemistry* **2003**, *75* (2-3), 295-308.

(26) Wagner, U.; Kratky, C. Structure Elucidation of Natural Compounds by X-Ray Crystallography. In *Progress in the Chemistry of Organic Natural Products 100*, Kinghorn, A. D., Falk, H., Kobayashi, J. Eds.; Springer International Publishing, 2015; pp 1-75.

(27) Kong, L.-Y.; Wang, P. Determination of the absolute configuration of natural products. *Chinese Journal of Natural Medicines* **2013**, *11* (3), 193-198.

(28) Holton, J. M.; Frankel, K. A. The minimum crystal size needed for a complete diffraction data set. *Acta Crystallographica Section D: Biological Crystallography* **2010**, *66* (4), 393-408.

(29) Nannenga, B. L.; Bu, G.; Shi, D. The Evolution and the Advantages of MicroED. *Frontiers in Molecular Biosciences* **2018**, *5*, Mini Review.

(30) Nannenga, B. L. MicroED methodology and development. *Structural Dynamics* **2020**, *7* (1).

(31) Williams, D. B.; Carter, C. B. Scattering and Diffraction. In *Transmission Electron Microscopy: A Textbook for Materials Science*, Springer US, 2009; pp 23-38.

(32) Jones, C. G.; Martynowycz, M. W.; Hattne, J.; Fulton, T. J.; Stoltz, B. M.; Rodriguez, J. A.; Nelson, H. M.; Gonen, T. The CryoEM Method MicroED as a Powerful Tool for Small Molecule Structure Determination. *ACS Central Science* **2018**, *4* (11), 1587-1592.

(33) Danelius, E.; Bu, G.; Wieske, H.; Gonen, T. MicroED as a powerful tool for structure determination of macrocyclic drug compounds directly from their powder formulations. *bioRxiv* **2023**, 2023.2007.2031.551405.

(34) Dupree, T. H. Electron scattering in a crystal lattice. *Annals of Physics* **1961**, *15* (1), 63-78.

(35) Shi, D.; Nannenga, B. L.; Iadanza, M. G.; Gonen, T. Three-dimensional electron crystallography of protein microcrystals. *eLife* **2013**, *2*, e01345.

(36) Kabsch, W. xds. *Acta Crystallographica Section D: Biological Crystallography* **2010**, *66* (2), 125-132.

(37) Clabbers, M. T.; Gruene, T.; Parkhurst, J. M.; Abrahams, J. P.; Waterman, D. G. Electron diffraction data processing with DIALS. *Acta Crystallographica Section D: Structural Biology* **2018**, *74* (6), 506-518.

(38) Sheldrick, G.; Gilmore, C.; Hauptman, H.; Weeks, C.; Miller, R.; Usón, I. Shelx. **2012**.

(39) Wang, H. W.; Wang, J. W. How cryo-electron microscopy and X-ray crystallography complement each other. *Protein Science* **2017**, *26* (1), 32-39.

(40) Davisson, C.; Germer, L. H. Diffraction of Electrons by a Crystal of Nickel. *Physical Review* **1927**, *30* (6), 705-740.

(41) De Broglie, L. Waves and Quanta. *Nature* **1923**, *112* (2815), 540-540.

(42) Thomson, G. P.; Reid, A. Diffraction of Cathode Rays by a Thin Film. *Nature* **1927**, *119* (3007), 890-890.

(43) Ruska, E. The development of the electron microscope and of electron microscopy. *Reviews of Modern Physics* **1987**, *59* (3), 627-638.

(44) Uyeda, R. Dynamical effects in high-voltage electron diffraction. *Acta Crystallographica Section A: Crystal Physics, Diffraction, Theoretical and General Crystallography* **1968**, *24* (1), 175-181.

(45) Dorset, D. L.; Hauptman, H. A. Direct phase determination for quasi-kinematical electron diffraction intensity data from organic microcrystals. *Ultramicroscopy* **1976**, *1* (3-4), 195-201.

(46) Amos, L. A.; Henderson, R.; Unwin, P. N. T. Three-dimensional structure determination by electron microscopy of two-dimensional crystals. *Progress in Biophysics and Molecular Biology* **1982**, *39*, 183-231.

(47) Wang, Y.; Yang, T.; Xu, H.; Zou, X.; Wan, W. On the quality of the continuous rotation electron diffraction data for accurate atomic structure determination of inorganic compounds. *Journal of Applied Crystallography* **2018**, *51* (4), 1094-1101.

(48) Gruene, T.; Holstein, J. J.; Clever, G. H.; Keppler, B. Establishing electron diffraction in chemical crystallography. *Nature Reviews Chemistry* **2021**, *5* (9), 660-668.

(49) Xu, H.; Lebrette, H.; Clabbers, M. T. B.; Zhao, J.; Griese, J. J.; Zou, X.; Högbom, M. Solving a new R2lox protein structure by microcrystal electron diffraction. *Science Advances* **2019**, *5* (8), eaax4621.

(50) Zee, C.-T.; Saha, A.; Sawaya, M. R.; Rodriguez, J. A. Ab Initio Determination of PeptidePeptides Structures by MicroEDMicrocrystal electron diffraction (MicroED). In *cryoEM: Methods and Protocols*, Gonen, T., Nannenga, B. L. Eds.; Springer US, 2021; pp 329-348.

(51) Zee, C. T.; Glynn, C.; Gallagher-Jones, M.; Miao, J.; Santiago, C. G.; Cascio, D.; Gonen, T.; Sawaya, M. R.; Rodriguez, J. A. Homochiral and racemic MicroED structures of a peptide repeat from the ice-nucleation protein InaZ. *IUCrJ* **2019**, *6* (Pt 2), 197-205.

(52) Ting, C. P.; Funk, M. A.; Halaby, S. L.; Zhang, Z.; Gonen, T.; van der Donk, W. A. Use of a scaffold peptide in the biosynthesis of amino acid-derived natural products. *Science* **2019**, *365* (6450), 280 284.

(53) Gruene, T.; Wennmacher, J. T. C.; Zaubitzer, C.; Holstein, J. J.; Heidler, J.; Fecteau-Lefebvre, A.; De Carlo, S.; Müller, E.; Goldie, K. N.; Regeni, I.; et al. Rapid Structure Determination of Microcrystalline Molecular Compounds Using Electron Diffraction. *Angewandte Chemie International Edition* **2018**, *57* (50), 16313-16317.

(54) Jones, C. G.; Asay, M.; Kim, L. J.; Kleinsasser, J. F.; Saha, A.; Fulton, T. J.; Berkley, K. R.; Cascio, D.; Malyutin, A. G.; Conley, M. P.; et al. Characterization of Reactive Organometallic Species via MicroED. *ACS Central Science* **2019**, *5* (9), 1507-1513.

(55) Danelius, E.; Halaby, S.; van der Donk, W. A.; Gonen, T. MicroED in natural product and small molecule research. *Natural Product Reports* **2021**, *38* (3), 423-431, 10.1039/D0NP00035C.

(56) Park, J.-D.; Li, Y.; Moon, K.; Han, E. J.; Lee, S. R.; Seyedsayamdost, M. R. Structural Elucidation of Cryptic Algaecides in Marine Algal-Bacterial Symbioses by NMR Spectroscopy and MicroED. *Angewandte Chemie International Edition* **2022**, *61* (4), e202114022.

(57) Curtis, B. J.; Kim, L. J.; Wrobel, C. J. J.; Eagan, J. M.; Smith, R. A.; Burch, J. E.; Le, H. H.; Artyukhin, A. B.; Nelson, H. M.; Schroeder, F. C. Identification of Uric Acid Gluconucleoside–Ascaroside Conjugates in Caenorhabditis elegans by Combining Synthesis and MicroED. *Organic Letters* **2020**, *22* (17), 6724-6728.

(58) Lin, S.-Y.; Oakley, C. E.; Jenkinson, C. B.; Chiang, Y.-M.; Lee, C.-K.; Jones, C. G.; Seidler, P. M.; Nelson, H. M.; Todd, R. B.; Wang, C. C. C.; et al. A heterologous expression platform in Aspergillus nidulans for the elucidation of cryptic secondary metabolism biosynthetic gene clusters: discovery of the Aspergillus fumigatus sartorypyrone biosynthetic pathway. *Chemical Science* **2023**, 10.1039/D3SC02226A.

(59) Kim, L. J.; Ohashi, M.; Zhang, Z.; Tan, D.; Asay, M.; Cascio, D.; Rodriguez, J. A.; Tang, Y.; Nelson, H. M. Prospecting for natural products by genome mining and microcrystal electron diffraction. *Nature Chemical Biology* **2021**, *17* (8), 872-877.

(60) Kim, L. J.; Xue, M.; Li, X.; Xu, Z.; Paulson, E.; Mercado, B.; Nelson, H. M.; Herzon, S. B. Structure Revision of the Lomaiviticins. *Journal of the American Chemical Society* **2021**, *143* (17), 6578-6585.

(61) Zhang, H.; Guo, L.; Su, Y.; Wang, R.; Yang, W.; Mu, W.; Xuan, L.; Huang, L.; Wang, J.; Gao, W. Hosts engineering and in vitro enzymatic synthesis for the discovery of novel natural products and their derivatives. *Critical Reviews in Biotechnology* **2023**, 1-19.

(62) Pham, J. V.; Yilma, M. A.; Feliz, A.; Majid, M. T.; Maffetone, N.; Walker, J. R.; Kim, E.; Cho, H. J.; Reynolds, J. M.; Song, M. C.; et al. A Review of the Microbial Production of Bioactive Natural Products and Biologics. *Frontiers in Microbiology* **2019**, *10*, Review.

(63) Arastehfar, A.; Carvalho, A.; Houbraken, J.; Lombardi, L.; Garcia-Rubio, R.; Jenks, J. D.; Rivero Menendez, O.; Aljohani, R.; Jacobsen, I. D.; Berman, J.; et al. Aspergillus fumigatus and aspergillosis: From basics to clinics. *Studies in Mycology* **2021**, *100*, 100115.

(64) Svahn, K. S.; Göransson, U.; Chryssanthou, E.; Olsen, B.; Sjölin, J.; Strömstedt, A. A. Induction of Gliotoxin Secretion in Aspergillus fumigatus by Bacteria-Associated Molecules. *PLOS ONE* **2014**, *9* (4), e93685. 5.

(65) Dai, G.; Shen, Q.; Zhang, Y.; Bian, X. Biosynthesis of Fungal Natural Products Involving Two Separate Pathway Crosstalk. *Journal of Fungi* **2022**, *8* (3), 320.

(66) Chhetri, B. K.; Lavoie, S.; Sweeney-Jones, A. M.; Kubanek, J. Recent trends in the structural revision of natural products. *Natural Product Reports* **2018**, *35* (6), 514-531, 10.1039/C8NP00011E.

(67) Herzon, S. B. The Mechanism of Action of (−)-Lomaiviticin A. *Accounts of Chemical Research* **2017**, *50* (10), 2577-2588.

(68) Fujimoto, H.; Ikeda, M.; Yamamoto, K.; Yamazaki, M. Structure of fischerin, a new toxic metabolite from an ascomycete, Neosartorya fischeri var. fischeri. *Journal of Natural Products* **1993**, *56* (8), 1268-1275.

(69) Amini, S. Assignment of the absolute configuration of fischerin by computed nmr chemical shifts. *Journal of Structural Chemistry* **2015**, *56*, 1334-1341.

(70) Wan, Q.-L.; Fu, X.; Dai, W.; Yang, J.; Luo, Z.; Meng, X.; Liu, X.; Zhong, R.; Yang, H.; Zhou, Q. Uric acid induces stress resistance and extends the life span through activating the stress response factor DAF-16/FOXO and SKN-1/NRF2. *Aging (Albany NY)* **2020**, *12* (3), 2840.

(71) Cooper, M. J.; Anders, M. W. Metabolic and pharmacodynamic interactions of enantiomers of propoxyphene and methorphan. *Life Sciences* **1974**, *15* (9), 1665-1672.

(72) Vargesson, N. Thalidomide-induced teratogenesis: History and mechanisms. *Birth Defects Research Part C: Embryo Today: Reviews* **2015**, *105* (2), 140-156.

(73) Go, E. B.; Kim, L. J.; Nelson, H. M.; Ohashi, M.; Tang, Y. Biosynthesis of the Fusarium Mycotoxin (−)-Sambutoxin. *Organic Letters* **2021**, *23* (20), 7819-7823.

(74) Watanabe, Y.; Takahashi, S.; Ito, S.; Tokiwa, T.; Noguchi, Y.; Azami, H.; Kojima, H.; Higo, M.; Ban, S.; Nagai, K.; et al. Hakuhybotrol, a polyketide produced by Hypomyces pseudocorticiicola, characterized with the assistance of 3D ED/MicroED. *Organic & Biomolecular Chemistry* **2023**, *21* (11), 2320-2330, 10.1039/D2OB02286A.

(75) Colmont, M.; Palatinus, L.; Huvé, M.; Kabbour, H.; Saitzek, S.; Djelal, N.; Roussel, P. On the Use of Dynamical Diffraction Theory To Refine Crystal Structure from Electron Diffraction Data: Application to KLa5O5(VO4)2, a Material with Promising Luminescent Properties. *Inorganic Chemistry* **2016**, *55* (5), 2252-2260.

(76) Klar, P. B.; Krysiak, Y.; Xu, H.; Steciuk, G.; Cho, J.; Zou, X.; Palatinus, L. Accurate structure models and absolute configuration determination using dynamical effects in continuous-rotation 3D electron diffraction data. *Nature Chemistry* **2023**, *15* (6), 848-855.

(77) Lanza, A.; Margheritis, E.; Mugnaioli, E.; Cappello, V.; Garau, G.; Gemmi, M. Nanobeam precession assisted 3D electron diffraction reveals a new polymorph of hen egg-white lysozyme. *IUCrJ* **2019**, *6* (2), 178-188.

(78) Shi, D.; Huang, R. Analysis and comparison of electron radiation damage assessments in Cryo-EM by single particle analysis and micro-crystal electron diffraction. *Frontiers in Molecular Biosciences* **2022**, *9*, Review.

(79) Hattne, J.; Shi, D.; Glynn, C.; Zee, C.-T.; Gallagher-Jones, M.; Martynowycz, M. W.; Rodriguez, J. A.; Gonen, T. Analysis of global and site-specific radiation damage in cryo-EM. *Structure* **2018**, *26* (5), 759-766. e754.

(80) Johansson, L. C.; Stauch, B.; Ishchenko, A.; Cherezov, V. A bright future for serial femtosecond crystallography with XFELs. *Trends in biochemical sciences* **2017**, *42* (9), 749-762.

(81) Mazzorana, M.; Shotton, E. J.; Hall, D. R. A comprehensive approach to X-ray crystallography for drug discovery at a synchrotron facility—The example of Diamond Light Source. *Drug Discovery Today: Technologies* **2020**, *37*, 83-92.

(82) Pearson, A. R.; Mehrabi, P. Serial synchrotron crystallography for time-resolved structural biology. *Current opinion in structural biology* **2020**, *65*, 168-174.

(83) Richards, L. S.; Flores, M. D.; Millán, C.; Glynn, C.; Zee, C.-T.; Sawaya, M. R.; Gallagher-Jones, M.; Borges, R. J.; Usón, I.; Rodriguez, J. A. Fragment-Based Ab Initio Phasing of Peptidic Nanocrystals by MicroED. *ACS Bio & Med Chem Au* **2023**, *3* (2), 201-210.

(84) MIYAZONO, K.-i.; TANOKURA, M. New era in structural biology with the AlphaFold program. *Translational and Regulatory Sciences* **2022**, *4* (2), 48-52.

*Chapter 2*

*The CryoEM Method MicroED as a Powerful Tool for Small Molecule Structure*

*Determination[1]*

## 2.1 INTRODUCTION

The history of organic chemistry closely parallels the development of new methods for structural characterization. The earliest studies were driven by melting point determination, and over the past 175 years, more complex methods for the interrogation of chemical structures have been developed. Techniques such as polarimetry,[1] UV−vis,[2] and infrared spectroscopy,[3] coupled with electron paramagnetic resonance,[4] vibrational circular dichroism,[5] circular dichroism,[6] and mass spectrometry[7] have been commonly employed over the years, dramatically expanding our ability to assign structures. In the past 50 years, however, the explosion of NMR spectroscopy[8] and the accompanying abundance of individual NMR experiments have produced a wealth of detailed structural information for organic chemists. Indeed, NMR is a mainstay in chemistry and the most predominant method employed in both routine synthetic chemistry experiments and in advanced structural elucidation of complex small molecules. In the current state of the art, only single-crystal X-ray diffraction holds a higher place in terms of precision, producing unequivocal structural information about the position, orientation, connectivity, and placement of individual atoms and bonds within a given molecule. For decades, small molecule X-ray analysis has been the definitive tool for structural analysis.[9] This technique, however, is not without limitations. The process is considered by many

an art, where the production of high-quality crystals suitable for X-ray diffraction requires uncodified "tricks of the trade" as well as a certain amount of luck! Additionally, even after a substance has been successfully crystallized, there is no guarantee that the particular crystal form will be amenable to X-ray diffraction. Since crystal growth is both a slow and arduous process, X-ray diffraction has not been an effective tool for rapid, on-the-fly structural determination of small molecules. For this reason, X-ray diffraction is generally not implemented as a routine analytical tool for the practicing organic chemist, despite the fact that the structural data provided are far superior to any other characterization method to date.

*Figure 2.1. Process of applying MicroED to small molecule structural analysis. Here commercial progesterone (1) was analyzed, and an atomic resolution structure was determined at 1 Å resolution. Grid holes are 1 μm in diameter.*
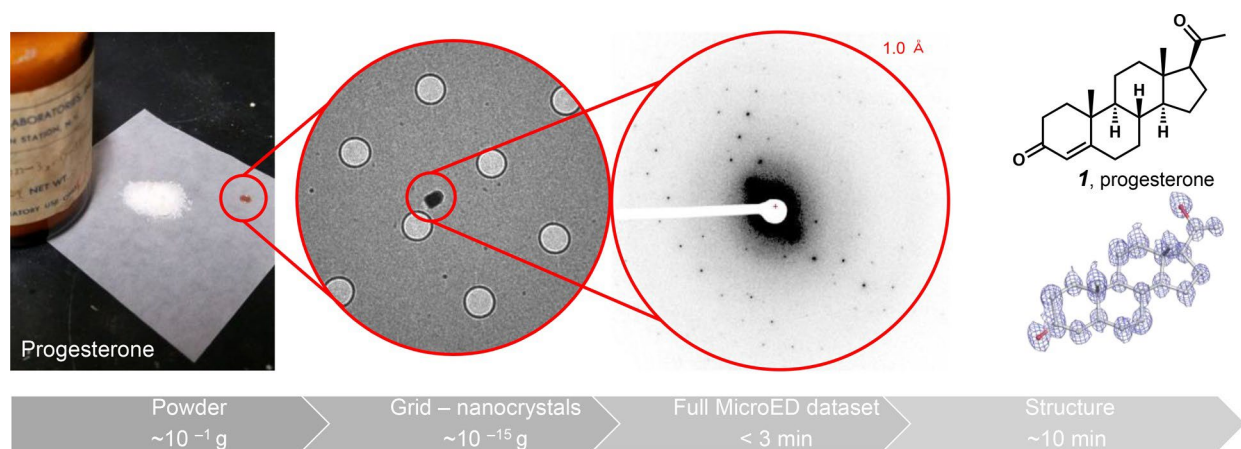


## 2.2 APPLICATION OF MICROED FOR SMALL MOLECULE ANALYSIS

Herein, we employ the recently developed electron cryomicroscopy (CryoEM) method microcrystal electron diffraction (MicroED)[10] to address the long-standing need for fast and reliable structure determination in organic chemistry. Recently, electron diffraction was used to solve the structure of a methylene blue derivative, although no scope studies were undertaken to allow the reader to assess the applicability of the methodology.[11] Moreover, a specialized detector was used for their experiments, limiting

the broad adaptability of their approach to the wider synthetic community.[11] We demonstrate that with minimal sample preparation and experiment time, simple powders and seemingly amorphous materials (in some cases, solids isolated via silica gel chromatography and rotary evaporation) could be directly used in MicroED studies, leading to rapid, high-quality structural elucidation of several classes of complex molecules with atomic resolution, in many cases better than 1 Å. Moreover, we utilize a commercially available microscope that is already in use at universities around the world. MicroED has the potential to dramatically accelerate and impact the fields of synthetic chemistry, natural product chemistry, drug discovery, and many others by delivering rapid, high-resolution atomic structures of complex, small molecules with minimal sample preparation or formal crystallization procedures.

The applicability of MicroED was initially tested on the naturally occurring steroid progesterone (**1**) as a model system (Figure 2.1). The sample was obtained as a powder from chemical supplier Preparations Laboratories Inc. (we estimate the bottle to be more than 20 years old). Small quantities of the seemingly amorphous solid were transferred directly from the bottle onto glass cover slides and ground between another slide to produce a fine powder. The powder was then deposited on a holey carbon−copper grid, cooled to liquid nitrogen temperatures, and transferred to a cryoelectron microscope operating at an acceleration voltage of 200 kV (Thermo Fisher Talos Arctica). An overview of the preparation is shown in Figure 2.1. Upon imaging, thousands of nanocrystals were easily discernible on the grid surface providing ample nanocrystals to investigate for diffraction. Typically, for samples such as these, the vast majority of nanocrystals diffracted to ∼1 Å resolution or better (Figure 2.1). Through continuous rotation of the sample stage, 140° of diffraction data could be collected from a single nanocrystal,[12] while the improved autoloader and piezo stage of the Talos Arctica allowed us to travel through the zero degree point without introducing errors in crystal position. Typically, the stage was rotated at approximately 0.6 deg/s, and an entire data set was collected in less than 3 minutes as a movie (Video 1) using a bottom mount CetaD CMOS detector (Thermo Fisher) fitted with a thick scintillator for diffraction studies. Software adapted from previous studies[13] was used to convert the diffraction movie frames into SMV format for expeditious processing in

the readily available XDS software package commonly used for X-ray crystallography. By collecting data from just a single nanocrystal, the structure of steroid **1** was resolved to an impressive 1 Å resolution. The entire process, from bottle to structure, was easily accomplished in less than 30 minutes.

*Figure 2.2. Molecules solved by MicroED. (A) Several pharmaceuticals, vitamins, commercial natural products, and synthetic samples resolved through MicroED. (B) Example of an amorphous film utilized in this study leading to 1 Å resolution data. (C) Protons could be observed for several compounds through MicroED. Green density are $F_o - F_c$ maps showing positive density belonging to hydrogen atoms of the molecule.*



**A**

acetaminophen, **2**

ibuprofen, **3**

carbamazepine, **4**

biotin, **6**

ethisterone, **7**

cinchonine, **8**

brucine, **9**

synthetic (+)-limaspermidine, **10**

synthetic oxindole, HKL-I-029, **11**

thiostrepton, **5**

**B**

1.0 Å

**C**

resolved hydrogen atoms

synthetic (+)-limaspermidine, **10**
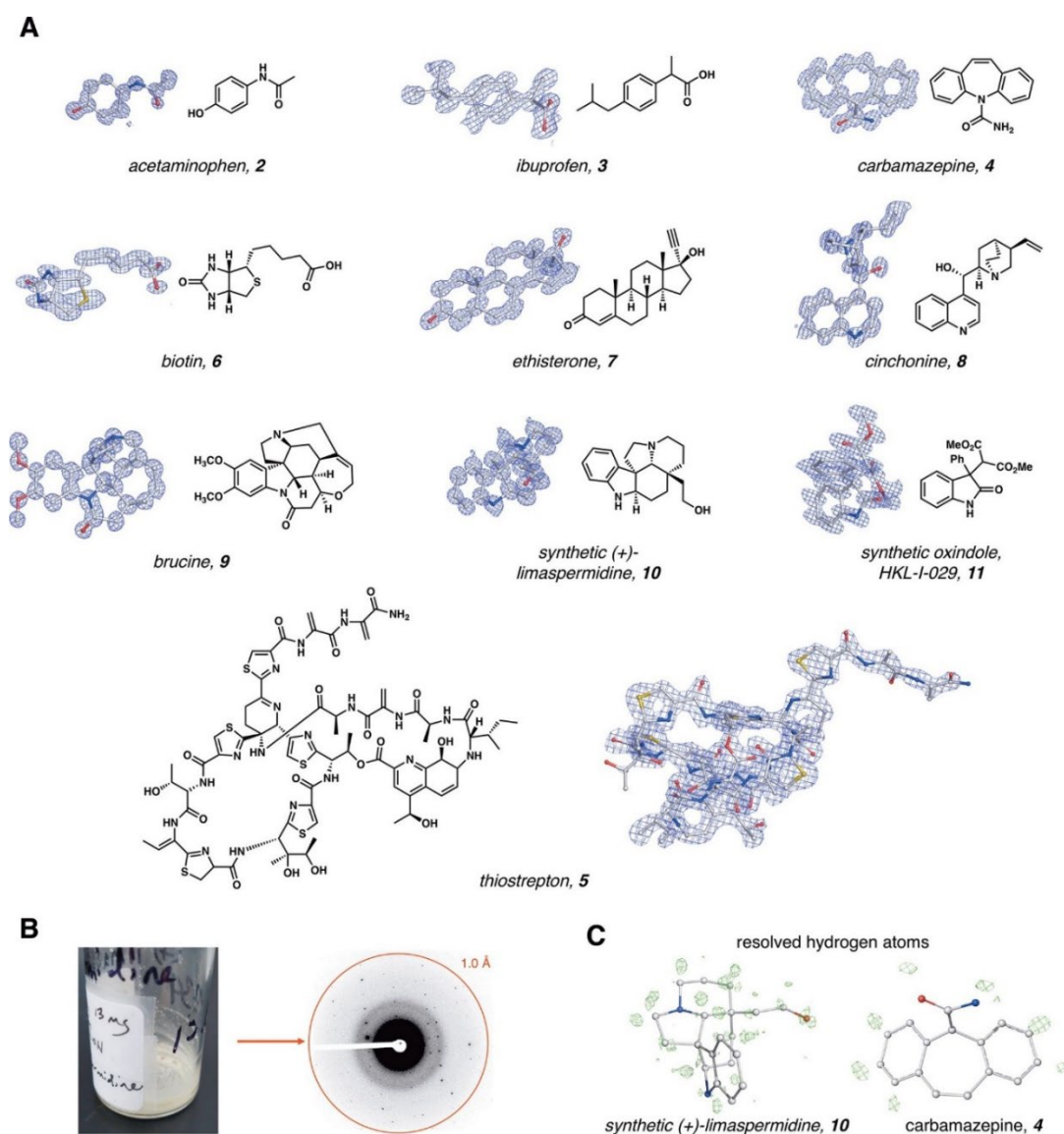
carbamazepine, **4**

*Figure 2.3*. *Identification of compounds from heterogeneous mixtures. An EM grid was prepared as above with biotin, brucine, carbamazepine, and cinchonine powders mixed together. All four compounds identified by unit cell parameters using MicroED data from within the same grid square. All structures were solved to ~1 Å resolution. Grid holes are 2 μm in diameter.*
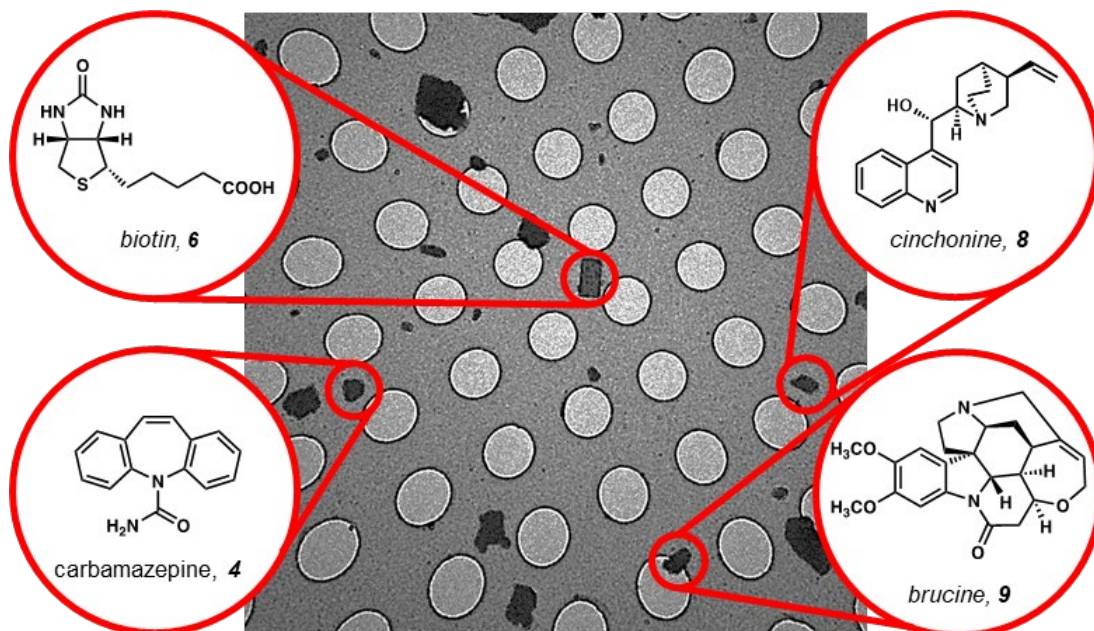


Encouraged by these results, we wanted to investigate a wide range of natural products to fully explore the scope and applicability of this powerful structural determination method for small molecules (Figure 2.2A). The Talos Arctica was particularly amenable to our studies as it is capable of storing up to 12 different grids at once, providing effortless swapping of sample grids for rapid investigation of multiple compounds. Once a reliable sample prep routine had been established, over-the-counter medications were purchased from local pharmacies for investigation. Tablets of CVS-branded acetaminophen and Kroger-branded ibuprofen were crushed using a mortar and pestle, and the ground powder was placed on electron microscopy grids as described above. Despite the heterogeneity of such pharmaceuticals, which typically include various coatings, binders, and other formulation agents, we were astonished to obtain such clearly resolved atomic resolution structures of both acetaminophen (**2**) and ibuprofen (**3**) in rapid succession. Just as impressively, structures of the sodium channel blocker

carbamazepine (**4**) and the macrocyclic polypeptide antibiotic thiostrepton (**5**) were also determined from seemingly amorphous powders used as received from Sigma-Aldrich. We went on to further study several commercially available natural products and derivatives. Once again, compounds were used as received, without any crystallization, to yield atomic resolution structures of biotin (**6**), ethisterone (**7**), cinchonine (**8**), and brucine (**9**). Of the 11 different commercial bioactives examined, all 11 yielded processable MicroED data. Of those 11 compounds, 10 were amenable to rapid structure determination by direct methods,[14] while one was determined by molecular replacement.[15] As mentioned previously, all structures were obtained without any crystallization attempts or chemical modifications to compounds examined. While these pharmaceutical and commercial natural products were likely recrystallized for purification purposes by the manufacturer, the powders examined by MicroED possessed nanocrystals a billionth the size ($\sim$100 nm) of crystals typically needed for X-ray crystallography. This was powder to structure.

Next we decided to investigate compounds that were never crystallized, but instead were purified by flash column chromatography. Since silica gel chromatography is the most common method of purification in early-stage research for complex molecules in drug discovery, natural product isolation efforts, and synthesis efforts in general, we were interested to see whether solid samples prepared in such a way would be amenable to analysis by MicroED. Four compounds, purified by chromatographic methods, were collected from our laboratories, and samples of these seemingly amorphous solids were analyzed. Here, two of four compounds diffracted, yielding atomic resolution structures at or below 1 Å (**10** and **11**, Figure 2.2A,B). While the success rate for these compounds was 50%, it is worthy to note that no crystallization procedures were employed in the isolation of these materials. Notably, (+)-limaspermidine (**10**), an alkaloid natural product synthesized by our laboratories,[16] was resolved from a residue of only milligram quantities of material following flash chromatography and rotary evaporation from a scintillation vial (Figure 2.2B). Furthermore, while it is extremely challenging to observe protons in X-ray structures, electrons interact with matter more strongly than X-rays and are affected by charge, making them relatively common to observe in MicroED data.[17-21] For all structures resolved from our samples, at least some, if not

most, protons could be observed on the molecule. In particular, the density maps obtained for limaspermidine (**10**) and carbamazepine (**4**) after refinement showed protons associated with almost all atoms in these molecules (Figure 2.2C).

Astounded by the ease with which such high-quality data were obtained and the apparent generality of MicroED to small molecules, we undertook studies to examine heterogeneous samples (mixtures of compounds). In the case of heterogeneous samples, single crystal X-ray diffraction precludes the study of mixtures, and NMR is poorly suited for this task. For this experiment, mixtures of four compounds (**4**, **6**, **8** and **9**, cf. Figure 2.3) were crushed together and deposited on a holey copper−carbon. Several crystal forms belonging to the different compounds in the mixture were visually identified on the grids (Figure 2.3). MicroED data were collected from several nanocrystals, and the identity of each species was resolved within minutes by confirmation of unit cell parameters. After compound identification, atomic resolution structures could be rapidly determined for all small molecules present in the mixture (Figure 2.3).

## 2.3 CONCLUSION

The results described here introduce a powerful new characterization tool into the organic chemist's toolbox. While MicroED was initially developed for structure determination of biological materials such as proteins in a frozen, hydrated state,[22, 23] we demonstrate that cross pollination of macromolecular structural methods of CryoEM are powerful tools for chemical synthesis, drug characterization, and drug discovery. Prior to this work, MicroED has allowed for the structural characterization of several proteins from crystals which had generally been unsuitable for X-ray crystallography due to their small size or morphologies.[22-24] Despite this success, the MicroED method has largely gone unnoticed in the small molecule communities. On the basis of our findings, we anticipate that MicroED will be enthusiastically received by many types of small molecule chemists in both academia and industry. Here we have shown that a variety of seemingly amorphous solid materials can lead to rapid atomic resolution structure determination by MicroED with little or no additional sample preparation or crystallization. The fact that a solid film in a flask, following solvent removal from a flash chromatography purification, can lead to an atomic resolution molecular

structure, is evidence that MicroED will likely have a profound effect on the structural characterization work-flow of organic chemists. Although the past 50 years have seen huge advances in the state of the art, no completely new techniques have been introduced that alter the routine structural interrogation of organic substances. NMR,[8] IR,[3] UV−vis,[2] and X-ray diffraction[9] have been routinely in place since the 1960s and are still utilized today as the most common methods for structure determination in chemistry. We believe that electron diffraction is potentially the next big advance in the field and are enthusiastic about the prospects of expanding its utility as a routine analytical technique for chemists.[25, 26]

## 2.4 REFERENCES

(1) Schreier, P.; Bernreuther, A.; Huffer, M. *Analysis of chiral organic molecules: methodology and applications*; Walter de Gruyter, 2011.

(2) Scott, A. I. *Interpretation of the ultraviolet spectra of natural products: international series of monographs on organic chemistry*; Elsevier, 2013.

(3) Coates, J. Interpretation of infrared spectra, a practical approach. 2000.

(4) Dougherty, D. A. SPIN CONTROL IN ORGANIC-MOLECULES. *Accounts of Chemical Research* **1991**, *24* (3), 88-94.

(5) Stephens, P. J.; Devlin, F. J.; Pan, J. J. The determination of the absolute configurations of chiral molecules using vibrational circular dichroism (VCD) spectroscopy. *Chirality* **2008**, *20* (5), 643-663.

(6) Berova, N.; Di Bari, L.; Pescitelli, G. Application of electronic circular dichroism in configurational and conformational analysis of organic compounds. *Chemical Society Reviews* **2007**, *36* (6), 914-931.

(7) De Hoffmann, E.; Stroobant, V. *Mass spectrometry: principles and applications*; John Wiley & Sons, 2007.

(8) Günther, H. *NMR spectroscopy: basic principles, concepts and applications in chemistry*; John Wiley & Sons, 2013.

(9) Dunitz, J. D. X-ray Analysis and the Structure of Organic Molecules. **1995**.

(10) Shi, D.; Nannenga, B. L.; Iadanza, M. G.; Gonen, T. Three-dimensional electron crystallography of protein microcrystals. *Elife* **2013**, *2*.

(11) Gruene, T.; Wennmacher, J. T. C.; Zaubitzer, C.; Holstein, J. J.; Heidler, J.; Fecteau Lefebvre, A.; De Carlo, S.; Muller, E.; Goldie, K. N.; Regeni, I.; et al. Rapid Structure Determination of Microcrystalline Molecular Compounds Using Electron Diffraction. *Angewandte Chemie International Edition* **2018**, *57* (50), 16313-16317.

(12) Nannenga, B. L.; Shi, D.; Leslie, A. G. W.; Gonen, T. High-resolution structure determination by continuous rotation data collection in MicroED. *Nature Methods* **2014**, *11* (9), 927-930.

(13) Hattne, J.; Reyes, F. E.; Nannenga, B. L.; Shi, D.; de la Cruz, M. J.; Leslie, A. G. W.; Gonen, T. MicroED data collection and processing. *Acta Crystallographica a- Foundation and Advances* **2015**, *71*, 353-360.

(14) Sheldrick, G. M. SHELXT - Integrated space-group and crystal-structure determination. *Acta Crystallographica a-Foundation and Advances* **2015**, *71*, 3-8.

(15) Vagin, A.; Teplyakov, A. MOLREP: an automated program for molecular replacement. *Journal of Applied Crystallography* **1997**, *30*, 1022-1025.

(16) Pritchett, B. P.; Donckele, E. J.; Stoltz, B. M. Enantioselective Catalysis Coupled with Stereodivergent Cyclization Strategies Enables Rapid Syntheses of (+) Limaspermidine and (+)-Kopsihainanine A. *Angewandte Chemie-International Edition* **2017**, *56* (41), 12624-12627.

(17) Henderson, R. THE POTENTIAL AND LIMITATIONS OF NEUTRONS, ELECTRONS AND X RAYS FOR ATOMIC-RESOLUTION MICROSCOPY OF UNSTAINED BIOLOGICAL MOLECULES. *Quarterly reviews of biophysics* **1995**, *28* (2), 171-193.

(18) Vergara, S.; Lukes, D. A.; Martynowycz, M. W.; Santiago, U.; Plascencia-Villa, G.; Weiss, S. C.; de la Cruz, M. J.; Black, D. M.; Alvarez, M. M.; Lopez-Lozano, X.; et al. MicroED Structure of Au 146(p-MBA)(57) at Subatomic Resolution Reveals a Twinned FCC Cluster. *Journal of Physical Chemistry Letters* **2017**, *8* (22), 5523-5530.

(19) Rodriguez, J. A.; Ivanova, M. I.; Sawaya, M. R.; Cascio, D.; Reyes, F. E.; Shi, D.; Sangwan, S.; Guenther, E. L.; Johnson, L. M.; Zhang, M.; et al. Structure of the toxic core of alpha-synuclein from invisible crystals. *Nature* **2015**, *525* (7570), 486.

(20) Sawaya, M. R.; Rodriguez, J.; Cascio, D.; Collazo, M. J.; Shi, D.; Reyes, F. E.; Hattne, J.; Gonen, T.; Eisenberg, D. S. Ab initio structure determination from prion nanocrystals at atomic resolution by MicroED. *Proceedings of the National Academy of Sciences of the United States of America* **2016**, *113* (40), 11232 11236.

(21) Hattne, J.; Shi, D.; Glynn, C.; Zee, C. T.; Gallagher-Jones, M.; Martynowycz, M. W.;Rodriguez, J. A.; Gonen, T. Analysis of Global and Site-Specific Radiation Damage in Cryo-EM. *Structure* **2018**, *26* (5), 759.

(22) de la Cruz, M. J.; Hattne, J.; Shi, D.; Seidler, P.; Rodriguez, J.; Reyes, F. E.; Sawaya, M. R.; Cascio, D.; Weiss, S. C.; Kim, S. K.; et al. Atomic-resolution structures from fragmented protein crystals with the cryoEM method MicroED. *Nature Methods* **2017**, *14* (4), 399.

(23) Nannenga, B. L.; Shi, D.; Hattne, J.; Reyes, F. E.; Gonen, T. Structure of catalase determined by MicroED. *Elife* **2014**, *3*.

(24) Gallagher-Jones, M.; Glynn, C.; Boyer, D. R.; Martynowycz, M. W.; Hernandez, E.; Miao, J.; Zee, C. T.; Novikova, I. V.; Goldschmidt, L.; McFarlane, H. T.; et al. Subangstrom cryo-EM structure of a prion protofibril reveals a polar clasp. *Nature Structural & Molecular Biology* **2018**, *25* (2), 131.

(25) Martynowycz, M. W.; Gonen, T. From electron crystallography of 2D crystals to MicroED of 3D crystals. *Current opinion in colloid & interface science* **2018**, *34*,9-16.

(26) Nannenga, B. L.; Gonen, T. Protein structure determination by MicroED. *Current opinion in structural biology* **2014**, *27*, 24-31.

<div align="right">*Chapter 3*</div>

<div align="center">*Characterization of Reactive Organometallic Species via MicroED[1]*</div>

## 3.1 INTRODUCTION

For over a century, crystallography has fueled developments in modern chemistry. Within the chemical enterprise, crystallography has played a particularly special role in organometallic chemistry. Here, NMR-silent nuclei, paramagnetic spin, diversity of bonding and coordination environments, and poor reactivity profiles hinder the application of many solution-state characterization techniques. However, the need for carefully prepared single crystals with dimensions on the order of 0.1 $mm^3$ can also limit the application of X-ray crystallography. Moreover, neutron diffraction can be limited by the requirement of even larger crystals ($\sim$0.5 $mm^3$) and incompatibility with boron-containing compounds, as a result of destructive nuclear reactions.[1] Electron diffraction, as opposed to X-ray diffraction, offers several benefits, primarily the ability to circumvent the need for such large crystals for successful structural analysis of molecular compounds. Since earlier work by Kolb *et al.[2]* and Mugnaioli *et al.*[3] to adapt 3D electron diffraction techniques for structural analysis, several studies using a variety of electron diffraction techniques have been employed to structurally characterize inorganic and organic−inorganic hybrid materials such as metal-organic frameworks.[4-10] Although these studies demonstrate the power of such techniques, we aim to adapt this method as a routine structural characterization tool for inorganic and organometallic chemists who often rely on traditional X-ray analysis as their primary means of

characterization for highly reactive and unstable compounds. Here we employ the electron diffraction technique MicroED under ambient temperature using a 300 keV TEM to structurally characterize several organometallic compounds, reactive intermediates, and transition-metal coordination complexes, which are of interest to the practicing chemist and are often employed as catalytic reagents for a variety of important synthetic transformations. Despite there being several different methods for the collection of electron diffraction data, we found that the continuous rotation technique used for MicroED is readily implemented on currently available instruments, and data obtained from this method is easily processed using standard, freely available, crystallographic software.[11] The MicroED method itself, which has typically been employed for large macromolecular structure analysis, is often performed under cryogenic conditions to preserve the hydration state of such biomolecules. However, prior studies have shown that by leveraging sensitive detectors, it is possible to use low electron doses to collect diffraction for small molecule structure determination under ambient temperatures, even for compounds that are particularly beam sensitive.[12-14] Using ambient temperature MicroED, we successfully resolve the first crystal structure of the privileged hydrozirconation reagent chloridobis($\eta^5$-cyclopentadienyl)hydridozirconium, colloquially known as Schwartz's reagent, which was obtained from bulk powder utilized as purchased and determined by direct methods. We also report an ab initio structure of a Pd(II) 1,2-dipallidated alkyl species, obtained as a precipitant from the reaction mixture of ethylene with a pseudo-low-coordinate Pd(I) dimer. As a demonstration of the broad applicability of MicroED, we also determine the structures of five other transition-metal complexes.

## 3.2 APPLICATION OF MICROED FOR ORGANOMETALLIC AND INORGANIC COMPOUNDS

Having recently reported the application of the CryoEM method MicroED to determine structures of several complex organic molecules,[15] we now evaluated the facility with which MicroED could interrogate complex organometallic species. We were particularly interested in chemical entities that failed to yield structures by conventional structural elucidation methods—crystallography or solution-state characterization. We first interrogated the structure of chloridobis($\eta^5$-cyclopentadienyl)hydridozirconium **1**

(Figure 3.1A),[16] a well-known industrial catalyst colloquially referred to as Schwartz's reagent. Schwartz's reagent sees widespread use in modern organic synthesis and is useful for a number of unique transformations mediated via hydrozirconation intermediates.[17-19] However, despite its synthetic relevance and the countervailing fact that half a century has transpired since Wailes and Weigold first discovered this species,[20, 21] no single crystal structure of this canonical zirconocene complex has been obtained. This gap in crystallographic data has been attributed to the low solubility of the complex in hydrocarbon and ethereal solvents and its reactivity with polar chlorinated solvents,[22] precluding its crystallization and hindering NMR studies. As such, the currently accepted structure of Schwartz's reagent, a centrosymmetric dimer doubly linked by two bridging hydride ligands, represents a reconstruction from a combination of FTIR spectroscopy,[20, 21] solid-state $^{35}Cl$ NMR studies,[23] and X-ray diffraction of related complexes.[24] To confirm this inferred structure, we subjected commercially acquired Schwartz's reagent to ambient temperature MicroED. Continuous-rotation data was collected from three crystals at ambient temperature (ca. 23 °C), using a low-flux 300 keV electron beam (e.g., below 0.01 $e^-/Å^2$ per second) and a TVIPS XF-416 camera in rolling shutter mode (Figure 3.3B). The resulting diffraction was reduced and merged to obtain a high-completeness (90.6%) data set resolved at 1.15 Å. The room temperature Schwartz's structure was then determined ab initio by direct methods and refined to reveal the expected centrosymmetric dimer. Importantly, refinement proceeded smoothly and required no ex post facto corrections, calculations, or molecular replacement procedures. The structure with riding hydrogens on the cyclopentadienyl ligands refined with anisotropic displacement parameters to an $R_1$ value of 14.9%. Critically, we had already observed suggestive regions of electron density consistent with bridging hydrides in the initial difference Fourier map (Figure 3.1B). To trace this more explicitly, we tracked peaks in the screened Coulomb potential within the unit cell, representing atomic locations. A sampling of consecutive two-dimensional slices in real space along the *a*-axis at the central mirror plane, which runs orthogonal to the cyclopentadienyl rings but bisects the zirconium, chlorine, and hydrogen atoms (Figure 3.1C) shows two hydrides emerging from the void space of the noise floor, thus corroborating the hydride positions observed during structural refinement (Figure 3.1D).

*Figure 3.1*. *(A) Proposed structure of Schwartz's reagent and refined structure with potential map overlay. (B) Prerefinement difference Fourier map using default X-ray scattering factors. Green lobes indicate regions of electron density consistent with bridging hydrides. (C) Unit cell of refined crystal structure after applying electron scattering parameters, viewed along the a-axis. (D) Contour map of central mirror plane depicted in (C) with Coulomb potential of hydrides visible.*
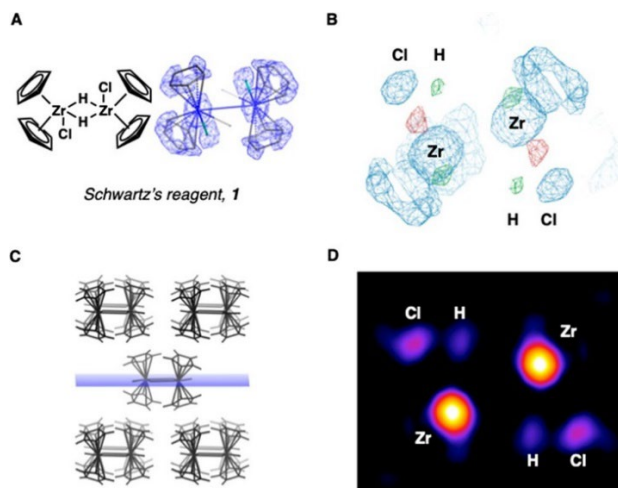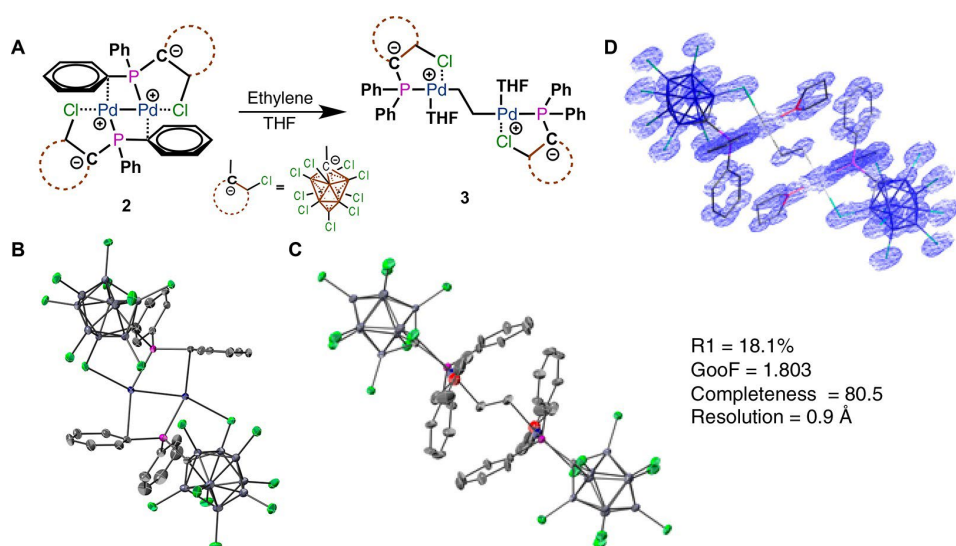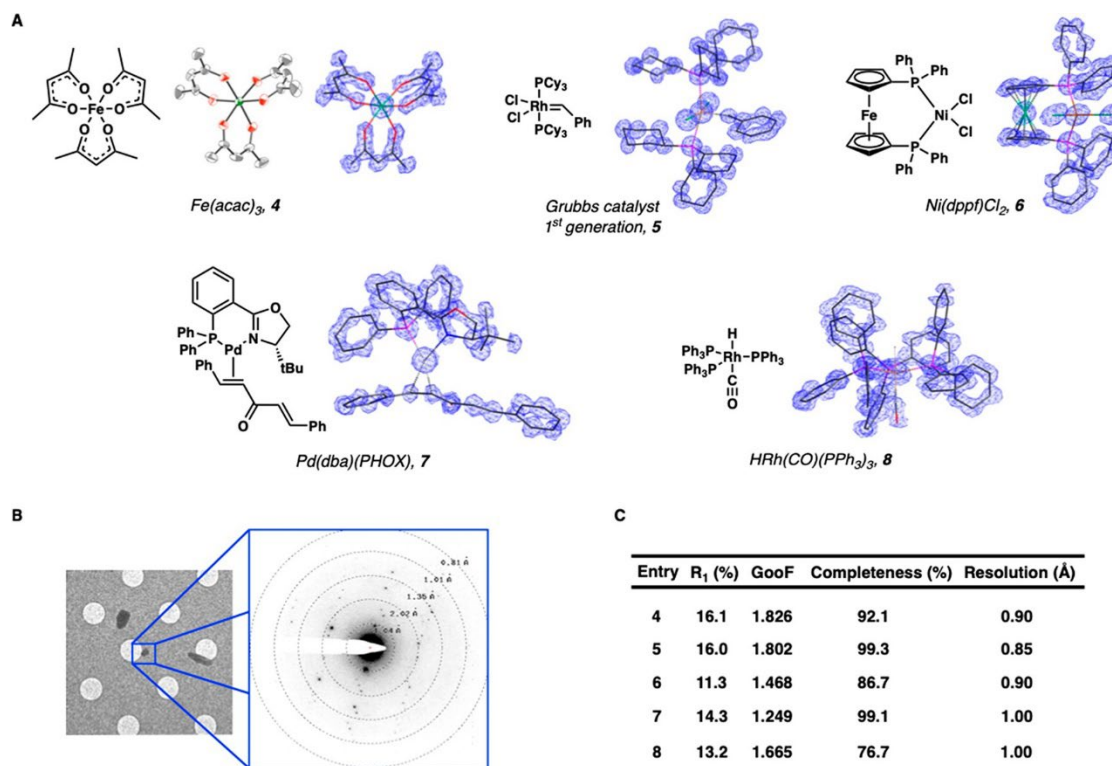


*Figure 3.2*. *(A) Reaction of Pd(I) dimer **2** to form ethylene insertion product **3**. (B) X-ray crystal structure of complex **2**. (C) Ambient temperature electron diffraction structure of the ethylene insertion product **3**. (D) Coulomb potential map overlaid on the structure of **3**. (The hydrogen atoms and solvents of crystallization omitted for clarity).*

Concurrent to our study of the application of MicroED to organometallic species, we sought to apply this powerful technique to active research problems in our groups including the reactivity of dimeric Pd(I) complexes. Dimeric palladium-(I) species featuring Pd−Pd bonds have been previously reported to react with a variety of small molecules to give homolytic cleavage[25] or insertion products.[26] Pd(I) dimer **2** (Figure 3.2), synthesized by thermolysis or UV irradiation of the methyl palladium phosphine precursor,[27] was fully characterized by single crystal XRD (Figure 3.2B) and multinuclear NMR (see Supporting Information). To study the reactivity of this species (**2**), a THF solution was treated with ethylene gas, which interestingly led to a dramatic color change and precipitation of a yellow solid (Figure 3.2A). Efforts to characterize this solid, however, were frustrated by the lack of solubility and fragile nature of the putative ethylene adduct, as treatment of the precipitant with a variety of crystallization and/or NMR solvents led to rapid gas release and reformation of starting material **2**. Typically, such physical properties of a reactive intermediate would preclude definitive structural characterization. The yellow precipitate was instead taken directly from the reaction mix and deposited on an EM grid for characterization by MicroED. Remarkably, under high magnification, the apparently amorphous solid proved to have nanocrystalline domains that yielded the electron diffraction patterns shown in Figure B.2. Diffraction movies were reduced to yield a high-completeness data set that produced an ab initio solution, which during refinement led to the definitive structural assignment of the species as the unexpected oxidative insertion product **3**. Such ethylene insertion products have been reported but remain rare.[28, 29] This structure features two Pd(II) phosphine moieties linked by the reduced ethylene linker (Figure 3.2C, D). The extended linker precludes ipso-$\pi$-arene interactions of the phosphines, and therefore, one equivalent of THF completes the coordination sphere of each palladium center. The solid-state $^{13}C\{^1H\}$ cross-polarization magic angle spinning (CPMAS) NMR spectrum of **3** contains a signal at 37 ppm assigned to the reduced ethylene fragment (Figure B.16). The $^{11}B\{^1H\}$ and $^{31}P\{^1H\}$ CPMAS NMR spectroscopy (Figures B.17 and B.18) are also consistent with the structure of **3** obtained from microED measurements. These NMR spectra also demonstrate the homogeneity of the sample.

*Figure 3.3*. *Structures obtained by ambient temperature MicroED method. (A) Chemical structures and Coulomb potential maps of common-use transition-metal complexes. ORTEP diagram of Fe(acac)₃ is provided. (B) Example of an electron diffraction pattern obtained from submicron scale crystals. Grid holes are 1 μm in diameter. (C) Data and statistics obtained by ambient temperature MicroED.*



**A**

*Fe(acac)₃, 4*

*Grubbs catalyst 1ˢᵗ generation, 5*

*Ni(dppf)Cl₂, 6*

*Pd(dba)(PHOX), 7*

*HRh(CO)(PPh₃)₃, 8*

**B**

**C**

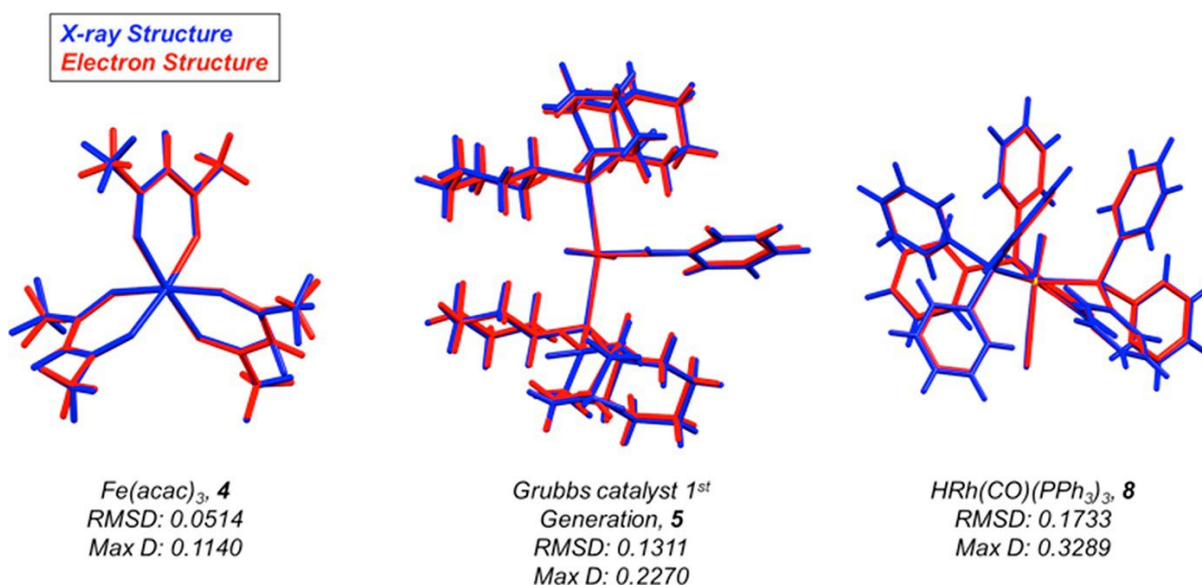| Entry | R₁ (%) | GooF | Completeness (%) | Resolution (Å) |
|-------|--------|-------|------------------|----------------|
| 4 | 16.1 | 1.826 | 92.1 | 0.90 |
| 5 | 16.0 | 1.802 | 99.3 | 0.85 |
| 6 | 11.3 | 1.468 | 86.7 | 0.90 |
| 7 | 14.3 | 1.249 | 99.1 | 1.00 |
| 8 | 13.2 | 1.665 | 76.7 | 1.00 |

To establish the generality of our approach we went on to determine structures of five additional commonly used organometallic compounds and transition-metal coordination complexes (Figure 3.3). The structures of tris(acetylacetonato)-iron(III) [Fe(acac)₃] (**4**), benzylidene-bis-(tricyclohexylphosphino)-dichlororuthenium (Grubbs' first generation catalyst) (**5**), [1,1-bis(diphenylphosphino)-ferrocene]dichloronickel(II) (**6**), Pd(dibenzylideneacetone)-((*S*)-4-*tert*-butyl-2-[2-(diphenylphosphino)phenyl]-2-oxazoline) (Pd(dba)(PHOX)) (**7**), and carbonyl(hydrido)tris-(triphenylphosphane)rhodium(I) [HRh(CO)(PPh₃)₃] (**8**), (Figure 3.3A), were all determined using direct methods from data collected at noncryogenic temperatures. Together, this set of molecular structures demonstrates the utility of ambient temperature electron diffraction for the study of transition-metal

complexes. Bulk powders of these compounds were analyzed by MicroED as described above, and data collected from one or more crystals were merged resulting in the assignment of space group and unit cell parameters that closely matched published values for XRD structures of these compounds, with the exception of compounds **6** and **7**, which are new polymorphs.[30-33] For a direct comparison, electron diffraction structures of compounds **4**, **5**, and **8** were overlaid with previously reported X-ray structures.[34-36] Root mean-square (RMS) values were calculated based on the deviation of atomic position resulting in RMS values of 0.0514, 0.1311, 0.1733 Å and a maximum deviation of 0.1140, 0.2270, and 0.3289 Å for compounds **4**, **5**, and **8**, respectively (Figure 3.4). On the basis of the overlaid structures, the position of the observed hydride in the case of the Rh−H complex (**5**) is both geometrically and symmetrically consistent with the published X-ray crystallographic data with a deviation of 0.164 Å.[37] Although the published structures of these compounds are associated with lower statistical errors in general, our ambient temperature MicroED structures were determined from bulk powders (i.e., no formal recrystallization) and maintain sufficiently accurate statistical parameters (Figure 3.3C) to unambiguously characterize the connectivity of these compounds. These considerations render electron diffraction a powerful alternative for the structural determination of transition-metal hydride structures.

Several previous studies use electron diffraction data for the determination of hydrogen atom positions[38-41] in metal hydrides, which are capable of exhibiting different chemical, electronic, and bonding properties in comparison to typical hydrogen atoms, and thus, the current quality of electron diffraction data obtained in this study does not allow for their unambiguous placement with high-enough precision to facilitate accurate discussion of bond lengths and angles. Although collecting data in continuous-rotation mode helps reduce dynamical scattering, residual dynamical scattering present in the data limits the accuracy of refinements based on a kinematical scattering approximation, and therefore, bond distances derived in this way can potentially be chemically inconsistent.[42] This problem has been well-analyzed by several other groups, including Palatinus *et al.*, who have used dynamical refinement on electron diffraction data collected in precession mode to help reduce statistical errors in atomic placement and bonding.[40, 42-44]

It is expected that such statistics of hydride localization as well as bond lengths and angles for all atomic constituents will improve with subsequent amelioration of microscopes and detectors. Furthermore, improvements in refinement software such as Jana, which has previously been used for processing of precession data, may now allow the possibility of applying dynamical refinements to continuous-rotation data, further reducing statistical error.[39, 40]

*Figure 3.4. Overlay of ambient temperature ED (red) and previously reported X-ray diffraction (blue) structures for compounds 4, 5, and 8 with calculated root-mean-square deviation (Å) and maximum deviation (Å) of atomic coordinates.*



Fe(acac)$_3$, **4**
RMSD: 0.0514
Max D: 0.1140

Grubbs catalyst 1$^{st}$
Generation, **5**
RMSD: 0.1311
Max D: 0.2270

HRh(CO)(PPh$_3$)$_3$, **8**
RMSD: 0.1733
Max D: 0.3289

## 3.3 CONCLUSIONS

Ambient temperature electron diffraction is an advantageous step toward the routine determination of organometallic species and potentially applicable to a wide array of small molecule organometallic and inorganic solids. The ability to routinely solve structures from nanocrystalline material and unambiguously determine the position of all atoms, including historically challenging hydrides attached to heavy atoms, presents chemists with a potent tool for the broad identification and characterization of elusive, but relevant, complexes. Armed with this method, we have determined structures of a diverse series of organometallic

compounds and transition-metal coordination complexes, including those obtained from both commercial and laboratory synthesis. Importantly, each of these structures was determined ab initio by direct methods and refined using methods common to XRD. Our application of ambient temperature MicroED to the structure determination of Schwartz's reagent, obtained directly from the commercial seemingly amorphous powder, highlights the power of this new approach. Despite the importance of this molecule in synthetic chemistry, no previous high-resolution crystal structures have been obtained, as a result of the seemingly amorphous nature of the white powder obtained by precipitation during its preparation. Our ambient temperature MicroED structure not only confirms the dimeric nature of the reagent but more remarkably identifies the likely locations of bridging hydrides that are visible in electrostatic potential maps and can be refined freely. This method also allows for the determination of an unusual Pd(II) intermediate that was not amenable to structure determination by solution-state NMR or single crystal X-ray diffraction. Moreover, neutron diffraction would be incompatible with this compound because of destructive boron neutron capture nuclear reactions. Importantly, although several protein structures have been determined by MicroED using molecular replacement, and structures of small molecules and polypeptides of known connectivity have been determined from MicroED data via direct methods, the reported Pd(II) complex (**3**) is a rare example of a novel complex small molecule identified by MicroED without prior knowledge of the structure or other corroborating solution-state spectroscopic methods. Although our data does not facilitate extensive discussions of bond lengths or angles because of higher-than expected statistical errors in refinement compared to traditional XRD, the fact that cryogenic temperatures are not required to obtain structural information from reactive metal complexes is ground-breaking, as many research institutions can make rapid use of readily available TEM facilities. Moreover, utilization of a more sensitive and faster detector, with shorter dead-time,[11] reduces peak overlap between frames as well. Ambient temperature measurements also dramatically simplify sample preparation and loading, eliminating issues typically associated with cryogenic cooling that often complicate crystal screening and data collection (e.g., ice deposition). We envision that microelectron diffraction will continue to improve and find new applications in the molecular sciences. Efforts directed toward a multitude of new frontiers in small molecule electron diffraction are

already underway. These efforts are expected to bring new horizons for small molecule structure determination over the coming months and years.

## 3.4 REFERENCES

(1) Nedunchezhian, K.; Aswath, N.; Thiruppathy, M.; Thirugnanamurthy, S. Boron Neutron Capture Therapy - A Literature Review. *Journal of Clinical and Diagnostic Research* **2016**, *10* (12), ZE1-ZE4.

(2) Kolb, U.; Gorelik, T.; Kubel, C.; Otten, M. T.; Hubert, D. Towards automated diffraction tomography: Part I  Data acquisition. *Ultramicroscopy* **2007**, *107* (6-7), 507-513.

(3) Mugnaioli, E.; Gorelik, T.; Kolb, U. "Ab initio" structure solution from electron diffraction data obtained by a combination of automated diffraction tomography and precession technique. *Ultramicroscopy* **2009**, *109* (6), 758-765.

(4) Portoles-Gil, N.; Lanza, A.; Aliaga-Alcalde, N.; Ayllon, J. A.; Gemmi, M.; Mugnaioli, E.; Lopez Periago, A. M.; Domingo, C. Crystalline Curcumin bioMOF Obtained by Precipitation in Supercritical CO2 and Structural Determination by Electron Diffraction Tomography. *Acs Sustainable Chemistry & Engineering* **2018**, *6* (9), 12309-12319.

(5) Yuan, S.; Qin, J. S.; Xu, H. Q.; Su, J.; Rossi, D.; Chen, Y. P.; Zhang, L. L.; Lollar, C.;  Wang, Q.; Jiang, H. L.; et al. Ti8Zr2O12(COO)(16) Cluster: An Ideal Inorganic Building Unit for Photoactive Metal-Organic Frameworks. *Acs Central Science* **2018**, *4* (1), 105-111.

(6) Denysenko, D.; Grzywa, M.; Tonigold, M.; Streppel, B.; Krkljus, I.; Hirscher, M.; Mugnaioli, E.; Kolb, U.; Hanss, J.; Volkmer, D. Elucidating Gating Effects for Hydrogen  Sorption  in  MFU-4-Type Triazolate-Based Metal-Organic Frameworks Featuring Different Pore Sizes. *Chemistry-a European Journal* **2011**, *17* (6), 1837-1848.

(7) Feyand, M.; Mugnaioli, E.; Vermoortele, F.; Bueken, B.; Dieterich, J. M.; Reimer, T.; Kolb, U.; de Vos, D.; Stock, N. Automated Diffraction Tomography for the Structure Elucidation of Twinned, Sub

micrometer Crystals of a Highly Porous, Catalytically Active Bismuth Metal-Organic Framework. *Angewandte Chemie-International Edition* **2012**, *51* (41), 10373-10376.

(8) Wang, B.; Rhauderwiek, T.; Inge, A. K.; Xu, H. Y.; Yang, T. M.; Huang, Z. H.; Stock, N.; Zou, X. D. A Porous Cobalt Tetraphosphonate Metal-Organic Framework: Accurate Structure and Guest Molecule Location Determined by Continuous Rotation Electron Diffraction. *Chemistry-a European Journal* **2018**, *24* (66), 17429-17433.

(9) Bellussi, G.; Montanari, E.; Di Paola, E.; Millini, R.; Carati, A.; Rizzo, C.; Parker, W. O.; Gemmi, M. Mugnaioli, E.; Kolb, U.; et al. ECS-3: A Crystalline Hybrid Organic Inorganic Aluminosilicate with Open Porosity. *Angewandte Chemie-International Edition* **2012**, *51* (3), 666-669.

(10) Yun, Y. F.; Zou, X. D.; Hovmoller, S.; Wan, W. Three-dimensional electron diffraction as a complementary technique to powder X-ray diffraction for phase identification and structure solution of powders. *Iucrj* **2015**, *2*, 267-282.

(11) Gemmi, M.; La Placa, M. G. I.; Galanis, A. S.; Rauch, E. F.; Nicolopoulos, S. Fast electron diffraction tomography. *Journal of Applied Crystallography* **2015**, *48*, 718-727.

(12) Gorelik, T. E.; van de Streek, J.; Kilbinger, A. F. M.; Brunklaus, G.; Kolb, U. Ab-initio crystal structure analysisand refinement approaches of oligo p-benzamides based on electron diffraction data. *Acta Crystallographica Section B-Structural Science* **2012**, *68*, 171-181.

(13) van Genderen, E.; Clabbers, M. T. B.; Das, P. P.; Stewart, A.; Nederlof, I.; Barentsen, K. C.; Portillo, Q.; Pannu, N. S.; Nicolopoulos, S.; Gruene, T.; et al. Ab initio structure determination of nanocrystals of organic pharmaceutical compounds by electron diffraction at room temperature using a Timepix quantum area direct electron detector. *Acta Crystallographica a-Foundation and Advances* **2016**, *72*, 236-242.

(14) Das, P. P.; Mugnaioli, E.; Nicolopoulos, S.; Tossi, C.; Gemmi, M.; Galanis, A.; Borodi, G.; Pop, M. M. Crystal Structures of Two Important Pharmaceuticals Solved by 3D Precession Electron Diffraction Tomography. *Organic Process Research & Development* **2018**, *22* (10), 1365-1372.

(15) Jones, C. G.; Martynowycz, M. W.; Hattne, J.; Fulton, T. J.; Stoltz, B. M.; Rodriguez, J. A.; Nelson, H. M.; Gonen, T. The CryoEM Method MicroED as a Powerful Tool for Small Molecule Structure Determination. *Acs Central Science* **2018**, *4* (11), 1587-1592.

(16) Hart, D. W.; Schwartz, J. Hydrozirconation. Organic synthesis via organozirconium intermediates. Synthesis and rearrangement of alkylzirconium(IV) complexes and their reaction with electrophiles. *Journal of the American Chemical Society* **1974**, *96* (26), 8115-8116.

(17) Schwartz, J.; Labinger, J. A. HYDROZIRCONATION - NEW TRANSITION-METAL REAGENT FOR ORGANIC-SYNTHESIS. *Angewandte Chemie-International Edition in English* **1976**, *15* (6), 333-340.

(18) Wieclaw, M. M.; Stecko, S. Hydrozirconation of C=X Functionalities with Schwartz's Reagent. *European Journal of Organic Chemistry* **2018**, *2018* (47), 6601-6623.

(19) Pinheiro, D. L. J.; de Castro, P. P.; Amarante, G. W. Recent Developments and Synthetic Applications of Nucleophilic Zirconocene Complexes from Schwartz's Reagent. *European Journal of Organic Chemistry* **2018**, *2018* (35), 4828-4844.

(20) Kautzner, B.; Wailes, P. C.; Weigold, H. HYDRIDES OF BIS(CYCLOPENTADIENYL)ZIRCONIUM. *Journal of the Chemical Society D Chemical Communications* **1969**, (19), 1105.

(21) Wailes, P. C.; Weigold, H. HYDRIDO COMPLEXES OF ZIRCONIUM .1. PREPARATION. *Journal of Organometallic Chemistry* **1970**, *24* (2), 405.

(22) Takahashi, T.; Suzuki, N.; Jayasuriya, N.; Wipf, P. Chlorobis (cyclopentadienyl) hydridozirconium. *Encyclopedia of Reagents for Organic Synthesis* **2001**.

(23) Rossini, A. J.; Mills, R. W.; Briscoe, G. A.; Norton, E. L.; Geier, S. J.; Hung, I.; Zheng, S.; Autschbach, J.; Schurko, R. W. Solid-State Chlorine NMR of Group IV Transition Metal Organometallic Complexes. *Journal of the American Chemical Society* **2009**, *131* (9), 3317-3330.

(24) Harlan, C. J.; Bott, S. G.; Barron, A. R. Methyl-hydride metathesis between Zr(cp)(2)Me(2) and HAl(mu(3) NBu(t)) (4): Molecular structures of Me(1x)H(x)Al(mu(3)-NBu(t)) (4) (x=0, 0.78 or 1) and (cp)(2)ZrMe(mu-H) (2) (cp=eta(5) C5H5). *Journal of the Chemical Society-Dalton Transactions* **1997**, (4), 637-641.

(25) Fafard, C. M.; Adhikari, D.; Foxman, B. M.; Mindiola, D. J.; Ozerov, O. V. Addition of ammonia, water, and dihydrogen across a single Pd-Pd bond. *Journal of the American Chemical Society* **2007**, *129* (34), 10318.

(26) Huacuja, R.; Graham, D. J.; Fafard, C. M.; Chen, C. H.; Foxman, B. M.; Herbert, D. E.; Alliger, G.; Thomas, C. M.; Ozerov, O. V. Reactivity of a Pd(I)-Pd(I) Dimer with O-2: Monohapto Pd Superoxide and Dipalladium Peroxide in Equilibrium. *Journal of the American Chemical Society* **2011**, *133* (11), 3820-3823.

(27) Kleinsasser, J. F.; Reinhart, E. D.; Estrada, J.; Jordan, R. F.; Lavallo, V. Ethylene Oligomerization and Polymerization by Palladium(II) Methyl Complexes Supported by Phosphines Bearing a Perchlorinated 10 Vertex closo-Carborane Anion Substituent. *Organometallics* **2018**, *37* (24), 4773-4783.

(28) Hetterscheid, D. G. H.; Kaiser, J.; Reijerse, E.; Peters, T. P. J.; Thewissen, S.; Blok, A. N. J.; Smits, J. M. M.; de Gelder, R.; de Bruin, B. Ir-II(ethene): Metal orcarbon radical? *Journal of the American Chemical Society* **2005**, *127* (6), 1895-1905.

(29) Vanvoorhees, S. L.; Wayland, B. B. FORMATION OF METALLO HYDRIDE, FORMYL, AND ALKYL COMPLEXES OF RH(TMTAA). *Organometallics* **1987**, *6* (1), 204-206.

(30) Weng, S. S.; Ke, C. S.; Chen, F. K.; Lyu, Y. F.; Lin, G. Y. Transesterification catalyzed by iron(III) beta diketonate species. *Tetrahedron* **2011**, *67* (9), 1640-1648.

(31) Torker, S.; Muller, A.; Sigrist, R.; Chen, P. Tuning the Steric Properties of a Metathesis Catalyst for Copolymerization of Norbornene and Cyclooctene toward Complete Alternation. *Organometallics* **2010**, *29* (12), 2735-2751.

(32)   Casellato,   U.;   Ajo,   D.;   Valle,   G.;   Corain,   B.;   Longato,   B.;   Graziani,   R. HETEROPOLYMETALLIC   COMPLEXES   OF   1,1'-BIS(DIPHENYLPHOSPHINO) FERROCENE (DPPF) .2. CRYSTAL STRUCTURE OF DPPF AND NICL2(DPPF). *Journal of Crystallographic and Spectroscopic Research* **1988**, *18* (5), 583-590.

(33) Sherden, N. H.; Behenna, D. C.; Virgil, S. C.; Stoltz, B. M. Unusual Allylpalladium Carboxylate Complexes: Identification of the Resting State of Catalytic Enantioselective Decarboxylative Allylic Alkylation Reactions of Ketones.*Angewandte Chemie-International Edition* **2009**, *48* (37), 6840-6843.

(34) Trnka, T. M. *Catalysts for olefin metathesis: Ruthenium alkylidene complexes with phosphine and N heterocyclic carbene ligands*; California Institute of Technology, 2003.

(35) Iball, J.; Morgan, C. A refinement of the crystal structure of ferric acetylacetonate. *Acta Crystallographica* **1967**, *23* (2), 239-244.

(36)   Laplaca,   S.   J.;   Ibers,   J.   A.   CRYSTAL   AND   MOLECULAR   STRUCTURE   OF TRISTRIPHENYLPHOSPHINE   RHODIUM   CARBONYL   HYDRIDE.   *Acta Crystallographica* **1965**, *18*, 511.

(37) Babra, I. S.; Morley, L. S.; Nyburg, S. C.; Parkins, A. W. THE CRYSTAL AND MOLECULAR-STRUCTURE   OF   A   NEW   POLYMORPH   OF CARBONYLHYDRIDOTRIS(TRIPHENYLPHOSPHINE)RHODIUM(I) HAVING A RH-H STRETCHING ABSORPTION AT 2013 CM(-1). *Journal of Crystallographic and Spectroscopic Research* **1993**, *23* (12), 997-1000.

(38) Mugnaioli, E.; Gemmi, M. Single-crystal analysis of nanodomains by electron diffraction tomography: mineralogy at the order-disorder borderline. *Zeitschrift Fur Kristallographie-Crystalline Materials* **2018**, *233* (3-4), 163-178.

(39) Hynek, J.; Brázda, P.; Rohlíček, J.; Londesborough, M. G.; Demel, J. Phosphinic acid based linkers: Building blocks in metal–organic framework chemistry. *Angewandte Chemie* **2018**, *130* (18), 5110-5113.

(40) Palatinus, L.; Brazda, P.; Boullay, P.; Perez, O.; Klementova, M.; Petit, S.; Eigner, V.; Zaarour, M.; Mintova, S. Hydrogen positions in single nanocrystals revealed by electron diffraction. *Science* **2017**, *355* (6321), 166-169.

(41) Clabbers, M. T. B.; Gruene, T.; van Genderen, E.; Abrahams, J. P. Reducing dynamical electron scattering reveals hydrogen atoms. *Acta Crystallographica a Foundation and Advances* **2019**, *75*, 82-93.

(42) Palatinus, L.; Jacob, D.; Cuvillier, P.; Klementova, M.; Sinkler, W.; Marks, L. D. Structure refinement from precession electron diffraction data. *Acta Crystallographica Section A* **2013**, *69*, 171-188.

(43) Palatinus, L.; Petricek, V.; Correa, C. A. Structure refinement using precession electron diffraction tomography and dynamical diffraction: theory and implementation. *Acta Crystallographica a Foundation and Advances* **2015**, *71*, 235-244.

(44) Palatinus, L.; Correa, C. A.; Steciuk, G.; Jacob, D.; Roussel, P.; Boullay, P.; Klementova, M.; Gemmi, M.; Kopecek, J.; Domeneghetti, M. C.; et al. Structure refinement using precession electron diffraction tomography and dynamical diffraction: tests on experimental data. *Acta Crystallographica Section B Structural Science Crystal Engineering and Materials* **2015**, *71*, 740-751.

*Chapter 4*

*Solution-processable and functionalizable ultrahigh molecular weight polymers*

*via topochemical synthesis[1]*

## 4.1 INTRODUCTION

Topochemical polymerizations (TCPs) are solid-state transformations, wherein monomers crystallize in an alignment such that some external stimulus—most often heat and/or light—causes them to polymerize.[1-5] TCP reactions are freed from many of the constraints of their solution-based counterparts and are capable of producing ultra-high molecular weight (UHMW) polymers—those with number-averaged molecular weights (Mn) above $10^6$ Dalton,[6-8] in a stereospecific, regioregular, solvent-free, and catalyst-free manner. TCP reactions are relatively rare, however, due to the fact that TCP monomers must crystallize such that the distances between their reactive sites ($d_{CC}$s) are small enough to allow for their polymerization to proceed without significant movement or deformation in each of the monomers.[1, 3, 4, 9] The vast majority of examples make use of two categories of reactions: cycloaddition reactions that involve polyolefins,[10-13] oligo(aza)anthracenes,[14-17] alkynes/azide,[18-21] and alkene/azides;[22] and addition reactions between reactive groups, such as diynes,[3, 6, 23-25] triynes,[26-28] dienes,[29-32] trienes,[33] *para*-quinodimethanes[9, 34-41] and bis(indanone)s.[8, 42, 43] In addition to linear polymers, TCP reactions have also been used to produce a number of intriguing extended materials, such as porous 2D[25, 42, 44-51] and 3D polymer crystals.[52]

---

*Figure 4.1. Single-crystal polymerization of a family of AQM ditriflates. a) The structures of the AQM ditriflates, **1**–**4**, studied herein. Monomers **1**–**3** underwent topochemical polymerization under the effects of heat and/or light to produce polymers **P1**–**P3**. NR: no reaction. b–c) Photographs and optical microscope images of vials containing crystals of (b) **1** and (c) **P1**, showing the typical morphology of crystals. Scale bar: 1 mm. d–f) $^{13}$C-NMR spectra of polymers **P1**–**P3**. Cross-polarization/magic angle spinning (CP/MAS) solid-state $^{13}$C-NMR spectra of (d) **P1**, and (e) **P2** (asterisks denote spinning side bands). (f) Solution $^{13}$C-NMR spectrum of **P3** (solvent: CDCl$_3$). All carbon resonances are annotated by colored circles. The resonances in d–f between 49–53 ppm (red) indicate the presence of the sp$^3$ carbons generated during polymerization, and the CF$_3$ multiplets (expected ratio of 1:3:3:1, but only the two highest peaks are observed) between 117 and 120 ppm (orange) show that the triflate groups remain intact.*
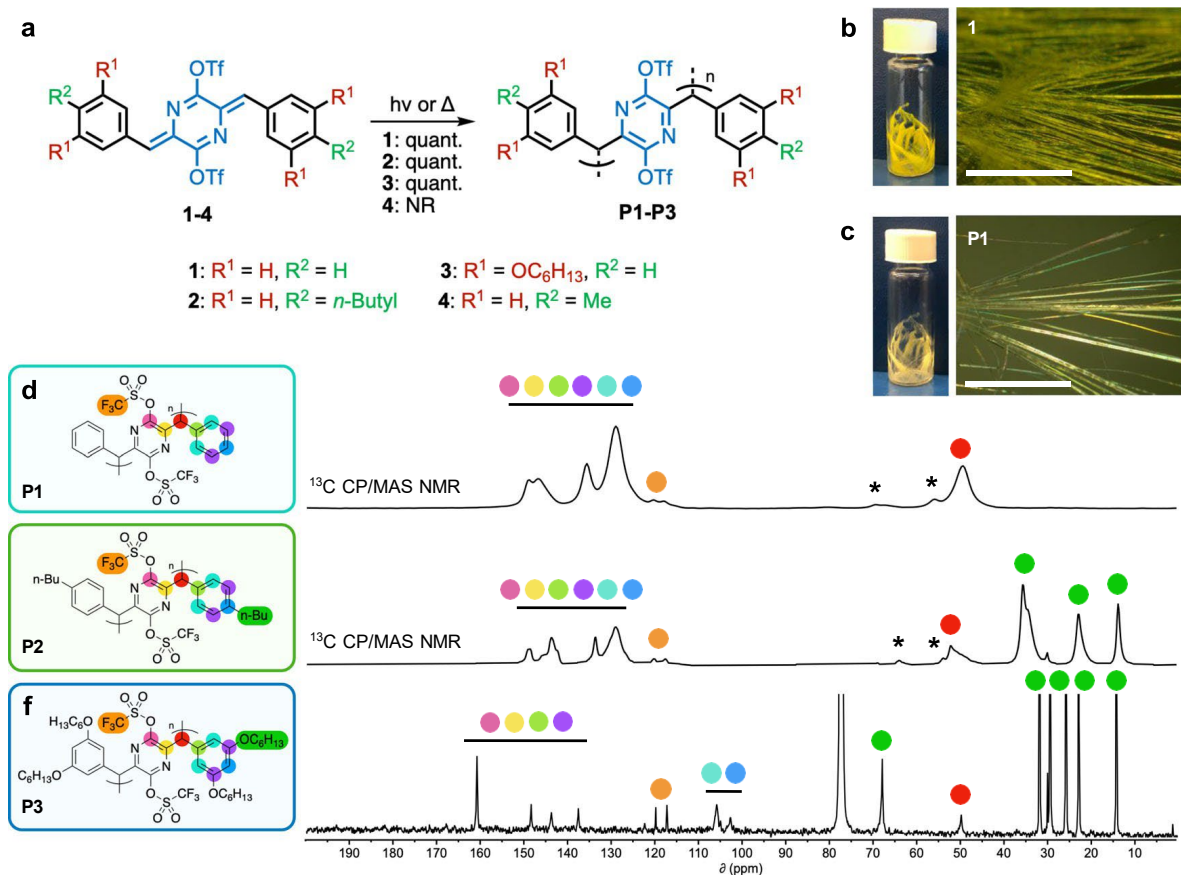


To date, the utility of TCP reactions as a polymerization technique has not been adequately demonstrated as the crystalline polymers so produced are often insoluble, or in the cases of soluble ones,

their molecular weights are typically quite limited.[12] In addition, the functional groups cannot be varied without drastically affecting their TCP reactivity.[6, 9, 42] As hinted at by others previously, an alternative strategy to produce a wide variety of useful UHMW polymers from TCP reactions would be to make use of a monomeric structure that incorporates both the solubilizing sidechains and a reactive functional group that survives the TCP reaction, allowing for post-polymerization functionalization.[3, 23, 53] If successful, this method would represent one of the few routes to soluble UHMW polymers with functionality that is not significantly restrained by the polymerization conditions.[54-57]

In this work, we demonstrate that a family of *para*-azaquinodimethanes (AQMs) shows a tempered form of the reactivity displayed by their unsubstituted structural cousin, *para*-quinodimethane, undergoing robust light and thermally initiated single-crystal polymerization while accommodating both the reactive and solubilizing groups.[58, 59] The bestowed solution processability enables the fabrication of dielectric film capacitors that show excellent capacitive energy storage properties.

## 4.2 Results

### 4.2.1 Monomer synthesis, topochemical polymerization, and characterization.

The AQM ditriflates in this study (Figure 4.1a) employ substituted phenyl or phenolic end groups, which are homologues of the previously reported thiophene-end-capped AQMs.[60, 61] The substitution of the aromatic end groups of these AQMs yielded an unexpected change in their solid-state reactivity. While the thienylidene AQMs are photochemically and thermally stable in the solid state, the new AQM series display remarkable solid-state reactivity that is suitable for TCP applications.

The synthesis of the AQM ditriflate monomers **1**–**4** was accomplished in high yield following a succinct synthetic route (Supplementary Figure C.2).[60-62] The four monomers produced long-aspect ratio yellow needle or hair-like crystals under all of the attempted crystallization conditions (Figure 4.1, Supplementary Figure C.3 and C.4). Crystals of monomers **1**–**3** decolorized when exposed to ambient sunlight or heating above 80 °C, indicating that they undergo solid-state polymerization reactions to

produce the nonconjugated poly-*p*-xylylene derivatives **P1**–**P3** (Figure 4.1 and Supplementary Figure

C.3).[9, 35, 41] The solid-state reactivity of the phenyl-substituted AQM monomers **1**–**3** differs from the

monomer **4**, which is not affected by light and/or heat. After polymerization, crystals of **P1** and **P2** become

insoluble, while those of **P3** readily dissolve in many common mid-range polarity organic solvents. In

contrast to previously reported TCP systems—including the closely related substituted *para*-

quinodimethanes and quinone methides—the solid-state reactivity of diphenylidine-substituted AQMs were

surprisingly forgiving to the inclusion of long alkyl groups.[9, 35, 36, 40, 41] Additionally, unlike many other

methods of producing UHMW polymers, this method is insensitive to the presence of water and oxygen

and requires no catalysts or auxiliaries.[54-57]

***Figure 4.2***. *Solid-state structures of monomer **2** and polymer **P2**. a) X-ray crystal structure of **2** showing*

*molecular structure, and $d_{CC}$—the distance between reactive sites of two neighboring molecules. b) CryoEM*

*structure of polymer **P2** showing the unit cell structure (top), and a dimeric unit (bottom). c) Scanning*

*electron microscopy image of crystals of **P2** on a TEM grid similar to those used to obtain its structure by*

*cryoEM. Scale bar: 10 μm. d and e Analogous views of the columnar stacks of monomer **2** and the polymeric*

*chains of **P2**. Atom color scheme: carbon = gray, nitrogen = blue, oxygen = red, sulfur = yellow, fluorine*

*= green, hydrogen = white, magenta balls represent the truncated polymer chain in polymer **P2**.*
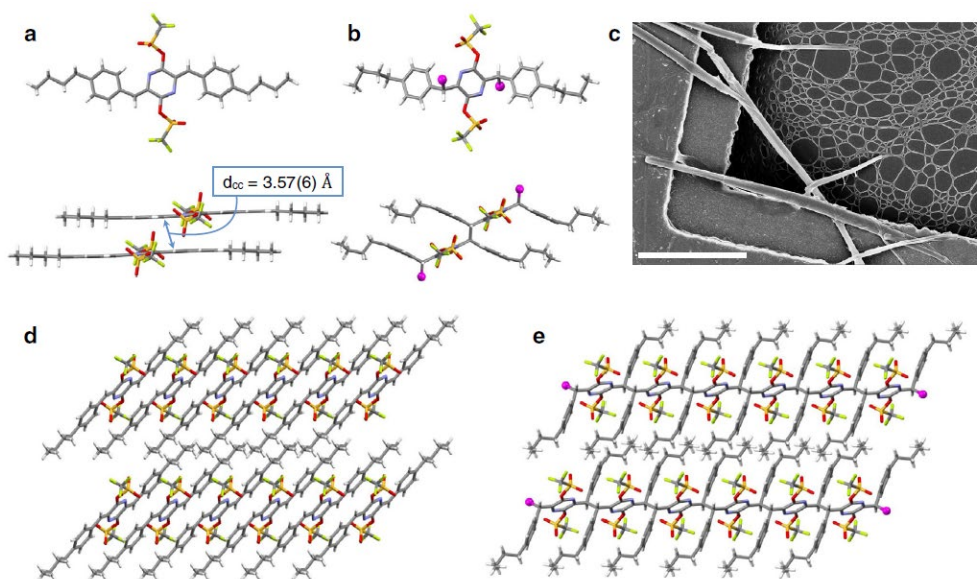
*Figure 4.3*. Optical and thermal interrogation of the topochemical polymerization of AQMs and capacitive energy storage properties of polymer *P3*. *a* UV- Vis scanning kinetic curves of a film of *1* (gold) as it polymerizes to form *P1* (ruby) over the course of roughly eight hours. *b* and *c* DSC studies of monomer *3* and the in-situ thermally polymerized *P3*. *b* the first heating (gold), and the subsequent cycle (ruby) of *3* as it polymerizes to *P3*. *c* multiple heating and cooling cycles (ruby = first four cycles, blue = final cycle) of *P3*. *d* Comparative electric displacement-electric field (D-E) loops at 200 MV m$^{-1}$ showing the effective K values derived therefrom. *e* discharged energy density plots as a function of the electric field, showing the superior energy storage properties of P3 against parylene-C and BOPP (BOPP = biaxially oriented polypropylene; error bars represent standard deviations obtained from at least three measurements using different samples).
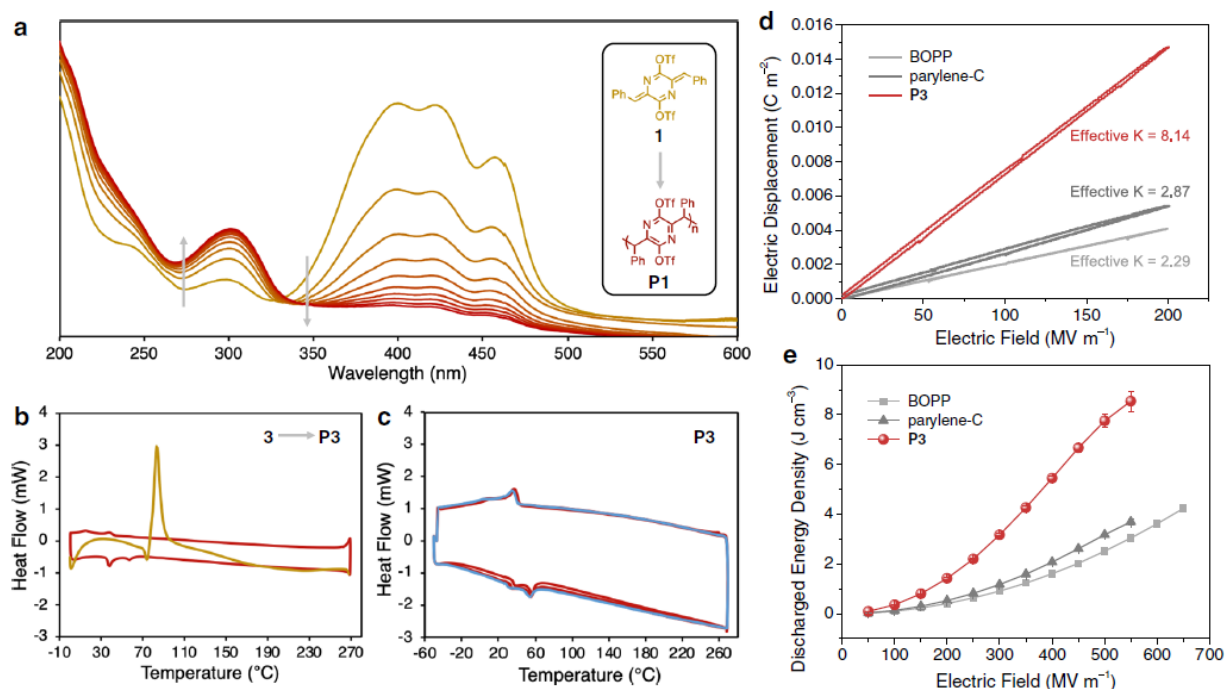


The structures of polymers **P1**–**P3** were confirmed by a variety of nuclear magnetic resonance (NMR) and infrared (IR) spectroscopic studies. The solubility of polymer **P3** allows for solution-phase $^{1}$H, $^{13}$C, and $^{19}$F NMR characterizations, which show broadened peaks typical of polymers along with chemical shifts and integrals consistent with the proposed structure (Figure 4.1d–f and Supplementary Figures C.52–

C.54). In particular, the characteristic resonance corresponding to the exocyclic methylene protons in the $^1$H NMR spectrum of **3** at $\delta = 6.82$ ppm is absent in that of **P3** (Supplementary Figure C.59). Instead, a resonance corresponding to the xylyl protons at $\delta = 4.95$ ppm is observed. The solution $^{13}$C-NMR spectrum of **P3**, along with cross-polarization/magic angle spinning (CP/MAS) solid-state $^{13}$C-NMR spectra of **P1** and **P2**, further corroborate the proposed polymer structures, showing the expected resonances corresponding to the xylyl carbons around 50 ppm and the absence of the exocyclic methylene carbon resonances of their respective monomers. As these NMR spectra are taken on unpurified polymer samples, it can be concluded that the conversions from **1**–**3** to **P1**–**P3** in the solid state proceed quantitatively. In addition, the features with a characteristic splitting at 117–121 ppm in the polymers' $^{13}$C-NMR spectra can be attributed to the $CF_3$ groups within the triflates appended to each repeat unit. This feature, together with a slightly broadened peak at –73.8 ppm in the $^{19}$F NMR spectrum of **P3**, confirms that the triflate groups appended to monomers **1**–**3** remain intact through the polymerization process (Supplementary Figure C.53).

The proposed TCP reaction was further supported by IR spectroscopic studies (Supplementary Figures C.5 and C.6). The characteristic vibrational features at 1570–1635 cm$^{-1}$ in the IR spectrum of **1** is not observed in the spectrum of **P1**.[35, 38] With the help of computations, these features can be assigned to the stretching mode of the quinoidal AQM ring, supporting the conclusion that the quinoidal rings have been consumed during the polymerization reaction.

The solid-state polymerization of monomers **1** and **2** produces insoluble polymeric products, for which molecular weight information cannot be obtained experimentally. However, the solubility of **P3** allows for the evaluation of its molecular weight information via conventional size-exclusion chromatography (SEC). Monomer **3** could be crystallized via the slow-evaporation of its solutions in different common solvents, which, when polymerized, produce a variable range of molecular weights (Supplementary Figure C.7). The highest molecular weight polymer—produced from crystals of **3** grown via the slow evaporation of a toluene solution—yields a Mn = $1.9 \times 10^6$, a Mw = $3.9 \times 10^6$, and a polydispersity index of 1.99. The differences in molar mass and polydispersity are attributed to the

variations of crystallite domain sizes in the monomer crystals, determined by defect sites in the parent crystal and fragmentation during the polymerization, which are highly solvent and process dependent.[12]

**4.2.2 Crystal structure determination by X-ray and electron diffractions.**

Single-crystal X-ray diffraction studies of monomers **1**–**4** provide more insights into their solid-state packing and polymerization. In all four monomers, the central AQM unit displays a bond-length alternation pattern characteristic of a quinoidal ring and sits coplanar with its phenyl end groups (Figure 4.2 and Supplementary Figures C.12–C.15). These $\pi$ systems further stack into extended columns with close $\pi$-$\pi$ interplanar distances in the range of 3.26–3.42 Å. Notably, the distances between the active methylenes on neighboring AQMs in the solid state ($d_{CC}$s) in the three topochemically active monomers (**1**–**3**) are 3.62(6), 3.57(6), and 3.76(8) Å, respectively. Such small $d_{CC}$ distances are a necessity in topochemical polymerizations, as they require minimal atomic movement or deformation of the unit cell in order to form the new bonds, and thus preserve macroscopic crystal integrity and produce high molecular weight polymers.[4, 8, 9] In contrast to monomers **1**–**3**, the reactive methylene carbons on each molecule of **4** are not close enough to either of its neighbors' to allow for TCP. Large $d_{CC}$ values of 4.98(3) and 5.13(8) Å—depending on which methylene carbons are presumed to react—are found in the solid-state of **4**, which are significantly larger than those in monomers **1**–**3** and other polymerizable examples in the *para*-quinodimethane family and explain its lack of topochemical reactivity.[9, 35, 36, 40, 41]

Powder X-ray diffraction (PXRD) studies of crystals of **1**–**3** and polymers **P1**–**P3** showed a retention of crystallinity upon polymerization but with apparent changes in the diffraction patterns in all three cases (Supplementary Figure C.11). In the case of **P2** and **P3**, the (100) diffraction peak position is nearly identical to that of the respective monomers, in accordance with very small lattice changes upon polymerization. Significant changes of the rest of the patterns, together with all other experimental evidences (DSC, NMR, IR, SEC, UV-vis, solubility), corroborate well with the complete monomer-to-polymer transformation. All attempts at obtaining a polymeric crystal structure using synchrotron X-ray crystallography proved unsatisfactory due to the loss of single-crystal quality after TCP reaction. As the

polymerization propagates from the outer surface to the inner zone of the monomer crystal, the strain causes the crystals to break into smaller pieces. While further optimization of the TCP reaction at different temperatures and irradiation conditions may facilitate single-crystal X-ray studies, we have sought to a convenient alternative that requires minimal crystal growth effort. Through a facile dip-coating procedure, monomer **2** microcrystals were deposited on TEM grids, and polymerized in situ to provide **P2** microcrystals (Figure 4.2, Supplementary Figures C.2, C.20 and C.21) that were structurally analyzed via the cryoelectron microscopy (cryoEM) technique of microcrystal electron diffraction (MicroED). This strategy obviates the challenges of obtaining TCP product crystal structures with X-ray diffraction and may prove useful in other contexts that were previously inaccessible through traditional structural characterization methods.[63] The successful crystallographic analysis of **P2**-coated grids yielded a 1 Å resolution structure of polymer **P2** in the solid state (Figure 4.2, Supplementary Figures C.16 and C.22). The structure of polymer **P2** shows the expected highly substituted poly-*p*-xylylene structure. Each repeat unit is joined in a single bond between two tetrahedral carbons with a regiospecificity analogous to the 1,6-addition polymerizations of *p*-QMs to form poly-*p*-xylylenes. The planar monomer **2** molecules deform upon polymerization, such that the pyrazine rings in each repeat unit of **P2** are coplanar with each other, and 66° out of plane with their appended 4-*n*-butylphenyl rings. The simulated PXRD based on the cryoEM structure of **P2** shows a similar pattern to the experimental room temperature PXRD of **P2** except a noticeable shift of all the peaks to higher angle (Supplementary Figures C.17). Such differences are ascribed to temperature-induced lattice expansion that is well observed in crystalline polymers,[64, 65] since the former is based on structures obtained at cryogenic temperature while the latter is from room temperature (RT) measurements. While we are experimentally limited to conduct PXRD measurements at cryogenic temperatures, we have verified the thermal lattice expansion behavior at above-RT conditions. Variable temperature PXRD studies conducted between room temperature and 100 °C clearly indicate a consistent lattice expansion upon increasing the temperature (Supplementary Figures C.18a and C.19), corroborating with the trend of PXRD peak shifts shown in Supplementary Figures C.17. The successful crystal structure determination represents an unprecedented TCP product structure determined with atomic resolution by

microED, which achieves a high degree of structural accuracy despite its slightly lower precision in bond length and angles. The results highlight the advantage of electron diffraction for polymer structural determination in comparison to X-ray analysis, which requires single crystals several orders of magnitude larger, as well as single-particle analysis, which requires monodisperse but rotationally-nonuniform high molecular weight compounds.[63]

*Figure 4.4*. Post-polymerization functionalization of polymer **P3** with amines. a The synthesis of two amine-functionalized polymers from reacting polymer **P3** with primary and secondary amine nucleophiles. b–d *¹H NMR spectra of (b) polymer **P3** and its post-polymerization functionalization products, (c) **P3-A** and (d) **P3-B**, showing 37%, and 57% triflate replacement, respectively. All proton resonances are annotated by colored circles.*
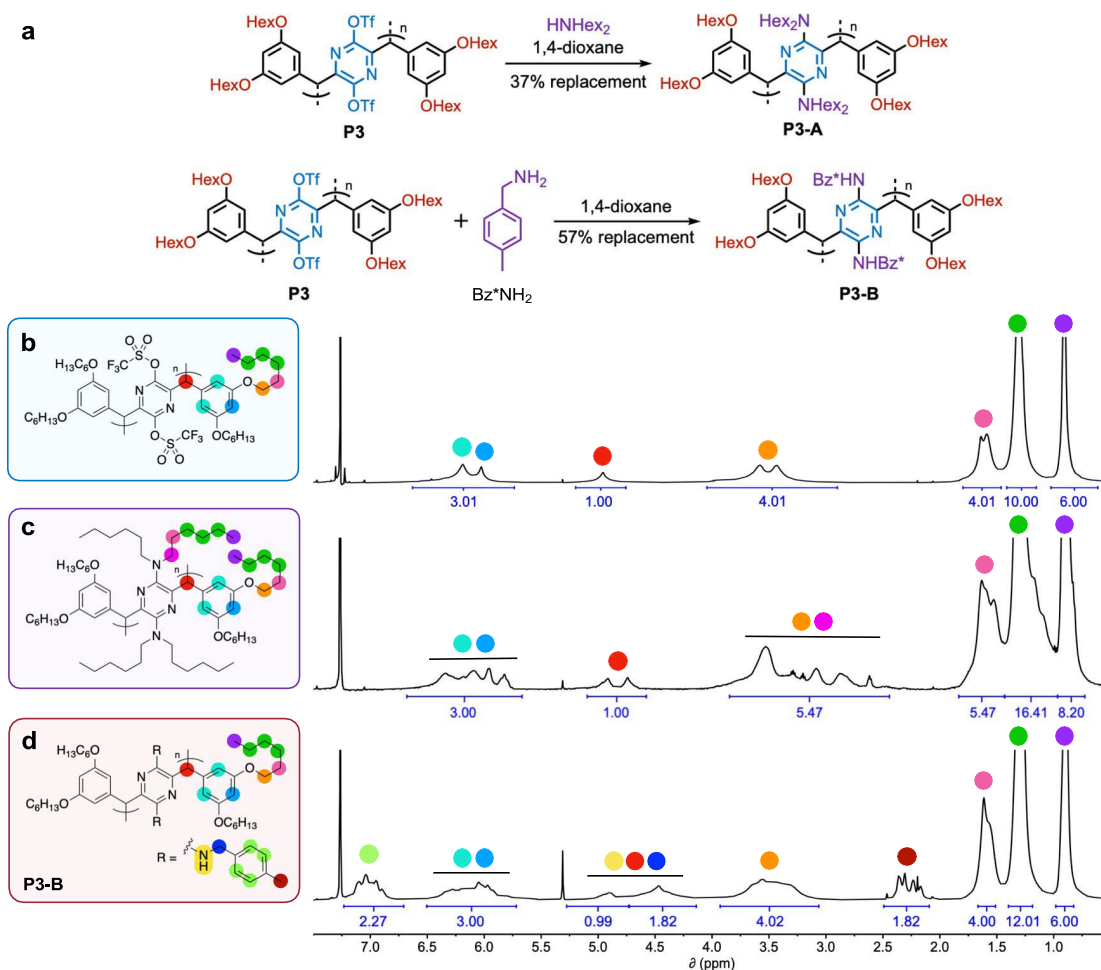
### 4.2.3 Optical and thermal characterization of the polymerization.

The polymerizations of **1**–**3** are not limited to single crystals but readily occur in polycrystalline powders and thin films as well. Films of monomers **1**–**3** could be easily obtained via spin-coating and polymerize within minutes when exposed to ambient light and overnight in the dark at room temperature to yield films of **P1**–**P3**—a transformation that can be directly observed by taking UV-Vis scans at regular intervals (Figure 4.3a and Supplementary Figure C.25). Visible-light triggered TCP reactions such as these are rare but preferable over higher-frequencies as visible light sources are comparatively safe and accessible.[8, 42] The conversions of **1**–**3** to **P1**–**P3** are accompanied by marked shifts in their absorption and fluorescence behavior (Supplementary Figures C.23 and C.24). As typified by a film of monomer **1**, upon polymerization, the three visible region absorbance subpeaks recede and one new ultraviolet absorbance appears. This shift in absorbance is consistent with the shortening of the chromophoric conjugated unit upon polymerization. During the polymerization process, no intermediate absorbances appear and then recede; instead, an isosbestic point is observed at $\lambda = 334$ nm, indicating that the polymerization occurs via a mechanism with no major intermediates or side-products. Similar features are seen in the polymerizations of **2** and **3**.

Differential scanning calorimetry (DSC) studies performed on **1**–**3** between 0 and 270 °C all show large exothermic features with their maxima centered around 100 °C on the first heating sweeps, corresponding to the thermally induced, exothermic polymerization reaction (Figure 4.3b and Supplementary Figure C.8). After the first heating, the samples were fully converted to their polymeric forms. Subsequent heating and cooling cycles give featureless traces for **P1** and **P2** (Supplementary Figures C.8 and C.9), showing the lack of thermal transitions under the degradation temperature (~300 °C as determined by thermogravimetric analysis, Supplementary Figure C.10). In contrast, **P3** shows two small repeatable peaks in both the heating and cooling sweeps of its DSC (Figure 4.3c), although variable temperature PXRD did not show significant changes of diffraction patterns during these transitions

(Supplementary Figure C.18b). It is postulated that these transitions may correspond to thermally induced reorganization of side chains though the exact reason remains undetermined.

### 4.2.4 Dielectric capacitive energy storage properties.

Polymer **P3** was anticipated to show a high dielectric constant ($K$) and other desirable properties as a polymer dielectric due to the rotatable and highly polar triflate groups on each of its repeat units.[66, 67] The facile solution processability of **P3** allows for it to be recast into thin films for dielectric capacitor devices. An effective $K$ of 8.14 is obtained for **P3**, which is notably higher than that of the structurally related poly-*p*-xylylene, parylene-C ($K = 2.87$), as well as the widely applied biaxially oriented polypropylene (BOPP) ($K = 2.29$) (Figure 4.3d and Supplementary Figure C.27). Together with a high breakdown strength of 568 $MVm^{-1}$ (Figure 4.3e and Supplementary Figure C.28) and high charge–discharge efficiencies (>97% at 200 $MVm^{-1}$) (Supplementary Figure C.29), the **P3**-based film capacitor delivers a high discharged energy density of 8.54 J $cm^{-3}$. Additionally, the energy density of **P3**-based capacitors shows less than 2% variation over 50,000 consecutive charge–discharge cycles, indicating that this polymer is highly stable under high-voltage conditions (Supplementary Figure C.30). It is widely understood in the field of dielectrics that there is a fundamental tradeoff between the charge–discharge efficiency and discharged energy density of a dielectric material.[66, 67] Despite this, polymer **P3**-based capacitors showed the best combination of these two metrics reported thus far under the benchmark condition of 200 $MVm^{-1}$ (Supplementary Figure C.31).

### 4.2.5 Post-polymerization modification.

The triflate substituents on monomers **1**–**3** remain intact through the polymerization process, allowing for the tuning of the resultant polymeric material's properties via post-polymerization functionalization. Due to its facile solution characterization, **P3** was chosen as a model polymer to explore the substitution reaction with the amine nucleophiles dihexylamine and 4-methylbenzylamine. The substitution reactions occurred readily to produce **P3-A** and **P3-B**, respectively, as verified by solution NMR spectroscopy (Figure 4.4 and Supplementary Figures C.55–C.58). The ¹H NMR spectra of **P3-A** and

**P3-B** showed that 37 and 57% of the triflate groups in **P3** were displaced by dihexylamine and 4-methylbenzylamine, respectively, with their ^{19}F NMR spectra showing the presence of the remaining intact triflates (Figure 4.4, Supplementary Figures C.56 and C.58).

## 4.3 CONCLUSION

AQM-based TCP reactions were shown to generate solution-processable UHMW polymers with excellent dielectric properties and controllable functionality. This method of synthesizing functionalized UHMW polymers exhibits notable advantages that overcome the constraints of previously reported TCP reactions, rendering it more amenable to practical use. In addition, the use of cryoEM for the structural determination of a TCP product crystal was demonstrated, obviating the need for large X-ray quality polymer single crystals. While there is inherent restraint with regard to data collection under the employed TEM conditions, which results in relatively lower data/parameter ratio and precision for microED structures than for the X-ray structures, quantitative analysis in terms of root mean square (RMS) deviation between the electron and X-ray structures has shown a high degree of accuracy[68] despite the experimental limitations of electron diffraction in its current state.[69]

The family of AQM ditriflates that undergo TCP is likely to be much larger than the few detailed here. Together with the demonstrated ability to undergo post-polymerization reactions, this reaction motif provides a wide access to diverse structures and functions, which facilitates future optimization of their capacitance properties. These advances allow TCP reactions to function as another practical tool in the toolbox of polymer chemists, opening up applications that were inaccessible before.

## 4.4 REFERENCES

(1) Cohen, M. D.; Schmidt, G. M. J. TOPOCHEMISTRY .1. SURVEY. *Journal of the Chemical Society* **1964**, (JUN), 1996.

(2) Hasegawa, M. PHOTO-POLYMERIZATION OF DIOLEFIN CRYSTALS. *Chemical Reviews* **1983**, *83* (5), 507-518.

(3) Lauher, J. W.; Fowler, F. W.; Goroff, N. S. Single-crystal-to-single-crystal topochemical polymerizations by design. *Accounts of Chemical Research* **2008**, *41* (9), 1215-1229.

(4) Hema, K.; Ravi, A.; Raju, C.; Pathan, J. R.; Rai, R.; Sureshan, K. M. Topochemical polymerizations for the solid-state synthesis of organic polymers. *Chemical Society Reviews* **2021**, *50* (6), 4062-4099.

(5) Hema, K.; Ravi, A.; Raju, C.; Sureshan, K. M. Polymers with advanced structural and supramolecular features synthesized through topochemical polymerization. *Chemical Science* **2021**, *12* (15), 5361-5380.

(6) Xu, R.; Schweizer, B.; Frauenrath, H. Soluble poly(diacetylene)s using the perfluorophenyl-phenyl motif as a supermolecule synthon. *Journal of the American Chemical Society* **2008**, *130* (34), 11437-11445.

(7) Nakanishi, H.; Kasai, H. Polydiacetylene microcrystals for third-order nonlinear optics. In *Photonic and Optoelectronic Polymers*, Jenekhe, S. A., Wynne, K. J. Eds.; ACS Symposium Series, Vol. 672; 1997; pp 183-198.

(8) Dou, L. T.; Zheng, Y. H.; Shen, X. Q.; Wu, G.; Fields, K.; Hsu, W. C.; Zhou, H. P.; Yang, Y.; Wudl, F. Single Crystal Linear Polymers Through Visible Light-Triggered Topochemical Quantitative Polymerization. *Science* **2014**, *343* (6168), 272-277.

(9) Nomura, S.; Itoh, T.; Nakasho, H.; Uno, T.; Kubo, M.; Sada, K.; Inoue, K.; Miyata, M. Crystal structures and topochemical polymerizations of 7,7,8,8-tetrakis(alkoxycarbonyl)quinodimethanes. *Journal of the American Chemical Society* **2004**, *126* (7), 2035-2041.

(10) Garai, M.; Santra, R.; Biradha, K. Tunable Plastic Films of a Crystalline Polymer by Single-Crystal-to-Single Crystal Photopolymerization of a Diene: Self-Templating and Shock-Absorbing Two-Dimensional Hydrogen-Bonding Layers. *Angewandte Chemie-International Edition* **2013**, *52* (21), 5548-5551.

(11) Coates, G. W.; Dunn, A. R.; Henling, L. M.; Ziller, J. W.; Lobkovsky, E. B.; Grubbs, R. H. Phenyl perfluorophenyl stacking interactions: Topochemical 2+2 photodimerization and

photopolymerization of olefinic compounds. *Journal of the American Chemical Society* **1998**, *120* (15), 3641-3649.

(12) Johnston, P.; Braybrook, C.; Saito, K. Topochemical photo-reversible polymerization of a bioinspired monomer and its recovery and repolymerization after photo-depolymerization. *Chemical Science* **2012**, *3* (7), 2301-2306.

(13) Guo, Q. H.; Jia, M. P.; Liu, Z. C.; Qiu, Y. Y.; Chen, H. L.; Shen, D. K.; Zhang, X.; Tu, Q.; Ryder, M. R.; Chen, H. Y.; et al. Single-Crystal Polycationic Polymers Obtained by Single-Crystal-to-Single Crystal Photopolymerization. *Journal of the American Chemical Society* **2020**, *142* (13), 6180-6187.

(14) Li, M.; Schluter, A. D.; Sakamoto, J. Solid-State Photopolymerization of a Shape-Persistent Macrocycle with Two 1,8-Diazaanthracene Units in a Single Crystal. *Journal of the American Chemical Society* **2012**, *134* (28), 11721-11725.

(15) Al-Kaysi, R. O.; Dillon, R. J.; Kaiser, J. M.; Mueller, L. J.; Guirado, G.; Bardeen, C. J. Photopolymerization of organic molecular crystal nanorods. *Macromolecules* **2007**, *40* (25), 9040 9044.

(16) Servalli, M.; Trapp, N.; Schluter, A. D. Single-Crystal-to-Single-Crystal (SCSC) Linear Polymerization of a Desymmetrized Anthraphane. *Chemistry-a European Journal* **2018**, *24* (56), 15003-15012.

(17) Khorasani, S.; Fernandes, M. A. A synthetic co-crystal prepared by cooperative single-crystal-to-single-crystal solid-state Diels-Alder reaction. *Chemical Communications* **2017**, *53* (36), 4969-4972.

(18) Pathigoolla, A.; Gonnade, R. G.; Sureshan, K. M. Topochemical Click Reaction: Spontaneous Self Stitching of a Monosaccharide to Linear Oligomers through Lattice-Controlled Azide-Alkyne Cycloaddition. *Angewandte Chemie-International Edition* **2012**, *51* (18), 4362-4366.

(19) Hema, K.; Sureshan, K. M. beta-Sheet to Helical-Sheet Evolution Induced by Topochemical Polymerization: Cross-alpha-Amyloid-like Packing in a Pseudoprotein with Gly-Phe-Gly Repeats. *Angewandte Chemie International Edition* **2020**, *59* (23), 8854-8859.

(20) Krishnan, B. P.; Rai, R.; Asokan, A.; Sureshan, K. M. Crystal-to-Crystal Synthesis of Triazole-Linked Pseudo proteins via Topochemical Azide-Alkyne Cycloaddition Reaction. *Journal of the American Chemical Society* **2016**, *138* (45), 14824-14827.

(21) Mohanrao, R.; Hema, K.; Sureshan, K. M. Topochemical synthesis of different polymorphs of polymers as a paradigm for tuning properties of polymers. *Nature Communications* **2020**, *11* (1).

(22) Khazeber, R.; Sureshan, K. M. Topochemical Ene-Azide Cycloaddition Reaction. *Angewandte Chemie International Edition* **2021**, *60* (47), 24875-24881.

(23) Tian, S. D.; Li, H. Z.; Li, Z.; Tang, H. J.; Yin, M. M.; Chen, Y. G.; Wang, S.; Gao, Y. T.; Yang, X. L.; Meng, F. L.; et al. Polydiacetylene-based ultrastrong bioorthogonal Raman probes for targeted live-cell Raman imaging. *Nature Communications* **2020**, *11* (1).

(24) Hädicke, E.; Mez, E.; Krauch, C.; Wegner, G.; Kaiser, J. The Structure of Polymeric 2, 4-Hexadiynylene-bis (phenylurethane). *Angewandte Chemie International Edition in English* **1971**, *10* (4), 266-267.

(25) Jordan, R. S.; Wang, Y.; McCurdy, R. D.; Yeung, M. T.; Marsh, K. L.; Khan, S. I.; Kaner, R. B.; Rubin, Y. Synthesis of Graphene Nanoribbons via the Topochemical Polymerization and Subsequent Aromatization of a Diacetylene Precursor. *Chem* **2016**, *1* (1), 78-90.

(26) Xiao, J.; Yang, M.; Lauher, J. W.; Fowler, F. W. A supramolecular solution to a long-standing problem: The 1,6 polymerization of a triacetylene. *Angewandte Chemie-International Edition* **2000**, *39* (12), 2132.

(27) Freitag, M.; DeCicco, R. C.; Black, A.; Ang, X. Z.; Young, C. N.; Resch, D.; Halada, G. P.; Phillips, B. L.; Gorofft, N. S. Polymerization Studies of Diiodohexatriyne and Diiodooctatetrayne Cocrystals. *Macromolecules* **2019**, *52* (22), 8563-8568.

(28) Xu, R.; Schweizer, W. B.; Frauenrath, H. Perfluorophenyl-Phenyl Interactions in the Crystallization and Topochemical Polymerization of Triacetylene Monomers. *Chemistry-a European Journal* **2009**, *15* (36),  9105-9116.

(29) Matsumoto, A.; Matsumura, T.; Aoki, S. Stereospecific polymerization of dialkyl muconates through free radical polymerization: Isotropic polymerization and topochemical polymerization. *Macromolecules* **1996**, *29* (1), 423-432.

(30) Nagahama, S.; Matsumoto, A. Synchronized propagation mechanism for crystalline-state polymerization of p xylylenediammonium disorbate. *Journal of the American Chemical Society* **2001**, *123* (49), 12176-12181.

(31) Tanaka, T.; Matsumoto, A. First disyndiotactic polymer from a 1,4-disubstituted butadiene by alternate molecular stacking in the crystalline state. *Journal of the American Chemical Society* **2002**, *124* (33), 9676-9677.

(32) Hou, X. D.; Wang, Z. H.; Lee, J.; Wysocki, E.; Oian, C.; Schlak, J.; Chu, Q. R. Synthesis of polymeric ladders by topochemical polymerization. *Chemical Communications* **2014**, *50* (10), 1218-1220.

(33) Hoang, T.; Lauher, J. W.; Fowler, F. W. The topochemical 1,16-polymerization of a triene. *Journal of the American Chemical Society* **2002**, *124* (36), 10656-10657.

(34) Itoh, T.; Nomura, S.; Uno, T.; Kubo, M.; Sada, K.; Miyata, M. Topochemical polymerization of 7,7,8,8-tetrakis(methoxycarbonyl)quinodimethane. *Angewandte Chemie-International Edition* **2002**, *41* (22), 4306-4309.

(35) Itoh, T.; Nomura, S.; Ohtake, M.; Yoshida, T.; Uno, T.; Kubo, M.; Kajiwara, A.; Sada, K.; Miyata, M. Molecular oxygen insertion polymerization into crystals of tetrakis(alkoxycarbonyl)quinodimethanes. *Macromolecules* **2004**, *37* (22), 8230-8238.

(36) Itoh, T.; Nomura, S.; Saitoh, N.; Uno, T.; Kubo, M.; Sada, K.; Inoue, K.; Miyata, M. Solid-state polymerizations of 7-alkoxycarbonyl-7-cyano-1,4-benzoquinone methides. *Macromolecules* **2004**, *37* (21), 7938-7944.

(37) Itoh, T.; Yamashita, S.; Nomura, S.; Uno, T.; Kubo, M.; Tohnai, N.; Miyata, M. Solid-State Polymerization of 7,7,8,8-Tetrakis(methoxyethoxycarbonyl)-quinodimethane under UV Irradiation. *Macromolecules* **2009**, *42* (17), 6473-6482.

(38) Itoh, T.; Suzuki, T.; Uno, T.; Kubo, M.; Tohnai, N.; Miyata, M. Cis-Specific Topochemical Polymerization: Alternating Copolymerization of 7,7,8,8-Tetrakis(methoxycarbonyl)-quinodimethane with 7,7,8,8 Tetracyanoquinodimethane in the Solid State. *Angewandte Chemie-International Edition* **2011**, *50* (10), 2253-2256.

(39) Itoh, T.; Nomura, S.; Nakasho, H.; Uno, T.; Kubo, M.; Tohnai, N.; Miyata, M. Halogen Bond Effect for Single Crystal-to-Single-Crystal Transformation: Topochemical Polymerization of Substituted Quinodimethane. *Macromolecules* **2015**, *48* (15), 5450-5455.

(40) Itoh, T.; Tachino, K.; Akira, N.; Uno, T.; Kubo, M.; Tohnai, N.; Miyata, M. Twofold Helical Polymerization: Thermal Solid-State Polymerization of 7-Cyano-7-(2 '-haloethoxycarbonyl)-1,4 benzoquinone Methides. *Macromolecules* **2015**, *48* (9), 2935-2947.

(41) Itoh, T.; Morita, E.; Takakura, R.; Nakajima, H.; Uno, T.; Kubo, M.; Tohnai, N.; Miyata, M. Formation of Bundle Assemblies of Stereoregular Polymers in Thermal Solid-State Polymerization of 7,7,8,8-Tetrakis(aryloxycarbonyl)-p-quinodimethanes. *Macromolecules* **2016**, *49* (13), 4802-4816.

(42) Samanta, R.; Ghosh, S.; Devarapalli, R.; Reddy, C. M. Visible Light Mediated Photopolymerization in Single Crystals: Photomechanical Bending and Thermomechanical Unbending. *Chemistry of Materials* **2018**, *30* (3), 577-581.

(43) Samanta, R.; Kitagawa, D.; Mondal, A.; Bhattacharya, M.; Annadhasan, M.; Mondal, S.; Chandrasekar, R.; Kobatake, S.; Reddy, C. M. Mechanical Actuation and Patterning of Rewritable Crystalline Monomer Polymer Heterostructures via Topochemical Polymerization in a Dual-Responsive Photochromic Organic Material. *Acs Applied Materials & Interfaces* **2020**, *12* (14), 16856-16863.

(44) Hsu, T. J.; Fowler, F. W.; Lauher, J. W. Preparation and Structure of a Tubular Addition Polymer: A True Synthetic Nanotube. *Journal of the American Chemical Society* **2012**, *134* (1), 142-145.

(45) Lange, R. Z.; Hofer, G.; Weber, T.; Schluter, A. D. A Two-Dimensional Polymer Synthesized through Topochemical 2+2 -Cycloaddition on the Multigram Scale. *Journal of the American Chemical Society* **2017**, *139* (5), 2053-2059.

(46) Kissel, P.; Murray, D. J.; Wulftange, W. J.; Catalano, V. J.; King, B. T. A nanoporous two-dimensional polymer by single-crystal-to-single-crystal photopolymerization. *Nature Chemistry* **2014**, *6* (9), 774-778.

(47) Kissel, P.; Erni, R.; Schweizer, W. B.; Rossell, M. D.; King, B. T.; Bauer, T.; Gotzinger, S.; Schluter, A. D.; Sakamoto, J. A two-dimensional polymer prepared by organic synthesis. *Nature Chemistry* **2012**, *4* (4), 287-291.

(48) Kory, M. J.; Worle, M.; Weber, T.; Payamyar, P.; van de Poll, S. W.; Dshemuchadse, J.; Trapp, N.; Schluter, A. D. Gram-scale synthesis of two-dimensional polymer crystals and their structure analysis by X-ray diffraction. *Nature Chemistry* **2014**, *6* (9), 779-784.

(49) Hu, F.; Hao, W. B.; Mucke, D.; Pan, Q. Y.; Li, Z. B.; Qi, H. Y.; Zhao, Y. J. Highly Efficient Preparation of Single-Layer Two-Dimensional Polymer Obtained from Single-Crystal to Single-Crystal Synthesis. *Journal of the American Chemical Society* **2021**, *143* (15), 5636-5642.

(50) Wang, Z. H.; Randazzo, K.; Hou, X. D.; Simpson, J.; Struppe, J.; Ugrinov, A.; Kastern, B.; Wysocki, E.; Chu, Q. R. Stereoregular Two-Dimensional Polymers Constructed by Topochemical Polymerization. *Macromolecules* **2015**, *48* (9), 2894-2900.

(51) Bhola, R.; Payamyar, P.; Murray, D. J.; Kumar, B.; Teator, A. J.; Schmidt, M. U.; Hammer, S. M.; Saha, A.; Sakamoto, J.; Schluter, A. D.; et al. A Two-Dimensional Polymer from the Anthracene Dimer and Triptycene Motifs. *Journal of the American Chemical Society* **2013**, *135* (38), 14134-14141.

(52) Beaudoin, D.; Maris, T.; Wuest, J. D. Constructing monocrystalline covalent organic networks by polymerization. *Nature Chemistry* **2013**, *5* (10), 830-834.

(53) Sun, A. W.; Lauher, J. W.; Goroff, N. S. Preparation of poly(diiododiacetylene), an ordered conjugated polymer of carbon and iodine. *Science* **2006**, *312* (5776), 1030-1034.

(54) Carmean, R. N.; Sims, M. B.; Figg, C. A.; Hurst, P. J.; Patterson, J. P.; Sumerlin, B. S. Ultrahigh Molecular Weight Hydrophobic Acrylic and Styrenic Polymers through Organic-Phase Photoiniferter-Mediated Polymerization. *Acs Macro Letters* **2020**, *9* (4), 613-618.

(55) Carmean, R. N.; Becker, T. E.; Sims, M. B.; Sumerlin, B. S. Ultra-High Molecular Weights via Aqueous Reversible-Deactivation Radical Polymerization. *Chem* **2017**, *2* (1), 93-101.

(56) Percec, V.; Guliashvili, T.; Ladislaw, J. S.; Wistrand, A.; Stjerndahl, A.; Sienkowska, M. J.; Monteiro, M. J.; Sahoo, S. Ultrafast synthesis of ultrahigh molar mass polymers by metal-catalyzed living radical polymerization of acrylates, methacrylates, and vinyl chloride mediated by SET at 25 degrees C. *Journal of the American Chemical Society* **2006**, *128* (43), 14156-14165.

(57) Xu, J. T.; Jung, K.; Atme, A.; Shanmugam, S.; Boyer, C. A Robust and Versatile Photoinduced Living Polymerization of Conjugated and Unconjugated Monomers and Its Oxygen Tolerance. *Journal of the American Chemical Society* **2014**, *136* (14), 5508-5519.

(58) Itoh, T.; Iwasaki, T.; Kubo, M.; Iwatsuki, S. POLYMERIZATIONS OF NITROGEN-CONTAINING HETEROPHANES BY VAPOR-DEPOSITION METHOD, TRANSFORMATION TO POLYMERIC FILMS BEARING A CONJUGATED STRUCTURE, AND THEIR PROPERTIES. *Polymer Bulletin* **1995**, *35* (3), 307-313.

(59) Errede, L. A.; Hoyt, J. M. THE CHEMISTRY OF XYLYLENES .3. SOME REACTIONS OF RHO XYLYLENE THAT OCCUR BY FREE RADICAL INTERMEDIATES. *Journal of the American Chemical Society* **1960**, *82* (2), 436-439.

(60) Anderson, C. L.; Liang, J. T.; Teat, S. J.; Garzon-Ruiz, A.; Nenon, D. P.; Navarro, A.; Liu, Y. A highly substituted pyrazinophane generated from a quinoidal system via a cascade reaction. *Chemical Communications* **2020**, *56* (32), 4472-4475.

(61) Anderson, C. L.; Dai, N.; Teat, S. J.; He, B.; Wang, S.; Liu, Y. Electronic Tuning of Mixed Quinoidal Aromatic Conjugated Polyelectrolytes: Direct Ionic Substitution on Polymer Main-Chains. *Angewandte Chemie International Edition* **2019**, *58* (50), 17978-17985.

(62) Liu, X. C.; He, B.; Anderson, C. L.; Kang, J.; Chen, T.; Chen, J. X.; Feng, S. Z.; Zhang, L. J.; Kolaczkowski, M. A.; Teat, S. J.; et al. para-Azaquinodimethane: A Compact Quinodimethane Variant as an Ambient Stable Building Block for High-Performance Low Band Gap Polymers. *Journal of the American Chemical Society* **2017**, *139* (24), 8355-8363.

(63) Jones, C. G.; Martynowycz, M. W.; Hattne, J.; Fulton, T. J.; Stoltz, B. M.; Rodriguez, J. A.; Nelson, H. M.; Gonen, T. The CryoEM Method MicroED as a Powerful Tool for Small Molecule Structure Determination. *Acs Central Science* **2018**, *4* (11), 1587-1592.

(64) Dadobayev, G.; Slutsker, A. Temperature dependence of expansion of crystalline lattices of some flexible chain polymers. *Polymer Science USSR* **1982**, *24* (8), 1837-1844.

(65) Ishige, R.; Masuda, T.; Kozaki, Y.; Fujiwara, E.; Okada, T.; Ando, S. Precise analysis of thermal volume expansion of crystal lattice for fully aromatic crystalline polyimides by X-ray diffraction method: relationship between molecular structure and linear/volumetric thermal expansion. *Macromolecules* **2017**, *50* (5), 2112-2123.

(66) Zhu, L.; Wang, Q. Novel Ferroelectric Polymers for High Energy Density and Low Loss Dielectrics. *Macromolecules* **2012**, *45* (7), 2937-2954.

(67) Zhang, Z. B.; Wang, D. H.; Litt, M. H.; Tan, L. S.; Zhu, L. High-Temperature and High-Energy-Density Dipolar Glass Polymers Based on Sulfonylated Poly(2,6-dimethyl-1,4-phenylene oxide). *Angewandte Chemie International Edition* **2018**, *57* (6), 1528-1531.

(68) Gruene, T.; Holstein, J. J.; Clever, G. H.; Keppler, B. Establishing electron diffraction in chemical crystallography. *Nature Reviews Chemistry* **2021**, *5* (9), 660-668.

(69) Gruene, T.; Mugnaioli, E. 3D Electron Diffraction for Chemical Analysis: Instrumentation Developments and Innovative Applications. *Chemical Reviews* **2021**, *121* (19), 11823-11834.

*Unraveling the Electrical and Magnetic Properties of Layered Conductive Metal-Organic Framework with Atomic Precision[1]*

## 5.1 INTRODUCTION

The emergence of layered two-dimensional (2D) electrically conductive MOFs[1, 2] as a new generation of 2D materials[3] has offered opportunities for innovation in electronics,[4, 5] magnetics,[6-8] chemiresistive sensing,[9-12] electrocatalysis,[13-16] and energy storage.[17-19] In 2D layered conductive MOFs, the connection of ligands and metal nodes determines the topology and environment of the nanochannel and governs the electronic coupling between the subunits that dictate the emergent electrical,[1, 2] and magnetic properties of the overall material.[20, 21] This electronic coupling can be extremely sensitive to the exact atomic arrangement of molecular components and the stacking of layers within the MOF crystal.[22-24] Due to electronic coupling between adjacent layers, stacking features exert dramatic influence upon the electronic properties in other 2D layered materials.[25, 26] Achieving a similar level of control in MOFs requires clear structural elucidation of the molecular details and stacking features of this class of materials with atomic precision.[22-24]

The self-assembly of 2D conductive MOFs involves multiple and interrelated processes, including deprotonation, redox reactions, and coordination polymerization. The complexity of controlling the thermodynamics and kinetics of these processes has posed considerable challenges for obtaining

---

crystals amendable for single crystal X-ray diffraction (SXRD) analysis. To date, access to single crystal structures of 2D conductive MOFs remains highly limited.[27-30] With few exceptions, 2D conductive MOFs thus far have been obtained as polycrystalline powders with moderate crystallinity, small crystallite size, disordered interlayer stacking, and/or unidentified pore environment.[1, 2] The lack of knowledge of single crystal structures with atomic precision has significantly hampered the understanding of structure-property relationships.[2, 22, 29] Although combining powder X-ray diffraction (PXRD) with quantum calculations has yielded structural insight into selected 2D conductive MOFs,[22, 31, 32] this approach offers limited information about atomic positions, geometric parameters, stacking modes, and arrangement of guest molecules within pores. While insight into these parameters can emerge from sophisticated electron microscopy techniques,[27, 28] developing and implementing additional methods that can offer direct structural insight into 2D layered MOFs with atomic precision are highly demanded.

Recently, the emerging technique of microcrystalline electron diffraction (MicroED)[33, 34] has been employed to characterize a range of compounds including large biological macromolecules,[35] small molecules,[36] and organometallic complexes.[37] Unlike X-rays, electrons possess both charge and mass, allowing them to interact more strongly with matter, thus yielding high-quality diffraction data on submicron crystals several orders of magnitude smaller than those required for SXRD analysis. Thus, MicroED is particularly advantageous for the structural determination of conductive MOFs whose synthetic routes are difficult to adapt to growing sufficiently large single crystals for conventional X-ray analysis. Indeed, several studies have shown the use of electron diffraction for the unambiguous structural characterization of several classes of materials,[38] such as zeolites,[39, 40] MOFs,[29, 41-44] and covalent organic frameworks.[45, 46] Despite these successful implementations, the application of MicroED for structural determination of 2D conductive MOFs remains extremely limited.[29]

This chapter describes an unambiguous elucidation of the structure of $Cu_3(C_6O_6)_2$ by MicroED with sub-angstrom precision (0.8 Å) to provide information on features of interlayer packing, variations of the coordination, and the presence of water guests. We demonstrate that the ligand embedded in the

two fully eclipsed layers of the MOF is cofacially stacked with a remarkably short interplanar distance of 2.73 Å. This extremely short p-stacking distance suggests the formation of the pancake bonds between the ligands, which represents the first discovery of this type of interaction in 2D layered materials. $Cu_3(C_6O_6)_2$ exhibits a bulk electrical conductivity of 1.2 x $10^{-6}$ S $cm^{-1}$ at room temperature with an activation energy of 0.47 eV. Band structure analysis suggests that the semiconductive feature of $Cu_3(C_6O_6)_2$ may be related to the localized nature of the pancake bonds. As pancake bonding leads to the formation of singlet dimers of the ligand between adjacent layers of the MOF, this structural feature leaves the spins of $Cu^{II}$ as the dominant contributor to the paramagnetism of $Cu_3(C_6O_6)_2$. The $Cu^{II}$ ions in a 2D Kagomé network of the $Cu_3(C_6O_6)_2$ MOF experience strong geometric magnetic frustration. Our study provides fundamental insights into how the unique stacking features can affect the electrical and magnetic properties of 2D layered conductive MOFs.

*Figure 5.1. The synthetic scheme, chemical structure, and electron microscopy images of $Cu_3(C_6O_6)_2$ MOF. a) The synthetic Scheme for the formation of $Cu_3(C_6O_6)_2$. b) EM and c) TEM characterization of $Cu_3(C_6O_6)_2$.*
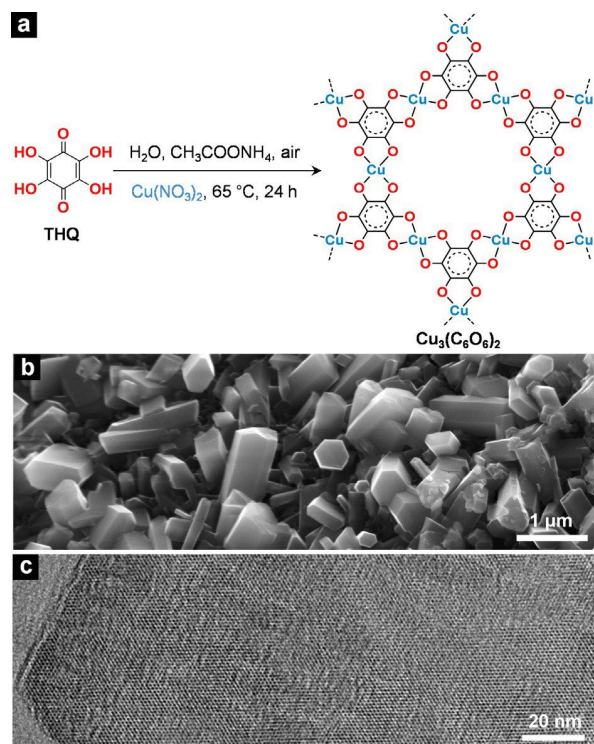
***Figure 5.2.*** *Single crystal structure of $Cu_3(C_6O_6)_2$ resolved by MicroED and pXRD analysis of the bulk powder of $Cu_3(C_6O_6)_2$. a) Front view of the crystal structure. Two types of structurally different Cu in $Cu_3(C_6O_6)_2$ were labeled by $Cu^\alpha$ and $Cu^\beta$, respectively. b) Side view of the structure showing a double-layered and mixed type of fully eclipsed and slipped parallel stacking. The purple and green arrows depict the alignment of $Cu^\alpha$ and $Cu^\beta$, respectively, along the directions of the stacking. In (a) and (b) the guest molecules in the pores are omitted. c) The slightly different geometry of $CuO_4$ unit formed by $Cu^\alpha$ and $Cu^\beta$. d) The structure of the water cluster $[(H_2O)_{12}]_n$ formed inside the channel of $Cu_3(C_6O_6)_2$. The structure was shown as the equivalent primitive cell to highlight a single-channel structure. e) Overlay of the experimental and Pawley refinement pXRD traces for $Cu_3(C_6O_6)_2$ with key diffraction planes labeled.*
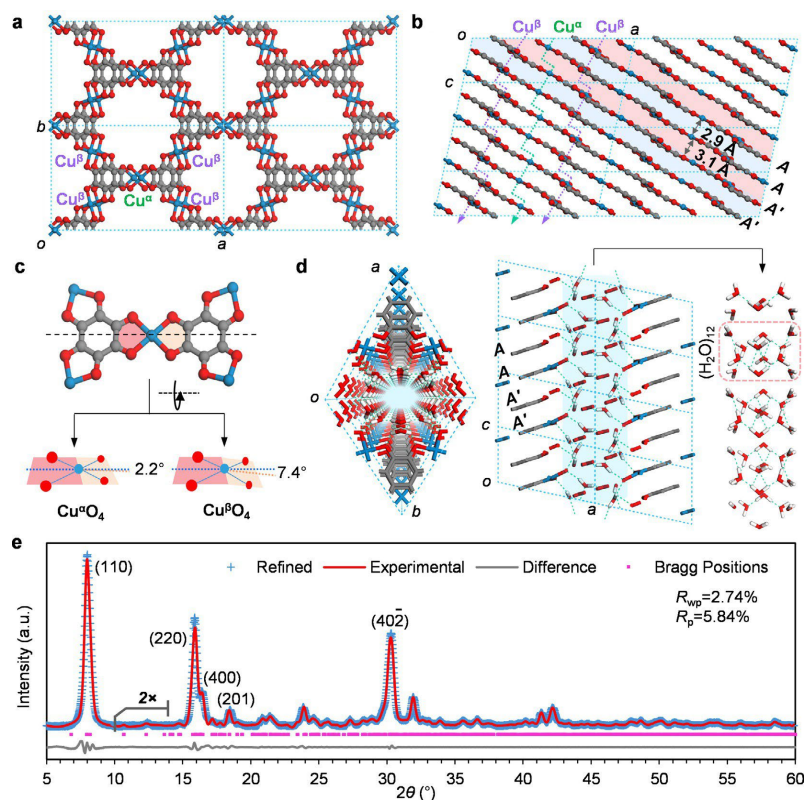


## 5.2 ANALYSIS AND INVESTIGATION OF MOF SYSTEM

In our optimized conditions, $Cu_3(C_6O_6)_2$ was synthesized by adding tetrahydroxy-1,4-benzoquinone (THQ) solid to a copper nitrate or acetate solution in water in the presence of ammonium

acetate under gentle air bubbling at 65 °C for 24 h (Figure 5.1a, see Appendix D for details). $Cu_3(C_6O_6)_2$ was obtained as a microcrystalline powder comprising crystals with hexagon-shaped rods at the submicrometer to micrometer scale and hexagonal pores, as observed by scanning electron microscopy (SEM, Figure 5.1b) and transmission electron microscopy (TEM, Figure 5.1c), respectively. Compared with the previous report,[47-49] our synthetic conditions significantly increased the crystallinity (Figures D.1, D.2) and crystallite size (nanometer vs. micrometer, Figure D.3) of $Cu_3(C_6O_6)_2$ material. This improvement of the crystallite size to micrometer dimensions was a key advance that ultimately enabled the first structure elucidation of $Cu_3(C_6O_6)_2$ MOF using MicroED with atomic-level precision.

The crystal of $Cu_3(C_6O_6)_2$ was illuminated by a low dose electron beam (<0.03 e⁻Å⁻² s), while being continuously rotated. The diffraction data were processed and refined using broadly available software for X-ray crystallography (see section 9 in Supporting Information). The structure of $Cu^3(C_6O_6)_2$ was resolved with a high resolution of up to 0.80 Å. This resolution is on par with the best resolution achieved by electron diffraction for MOF PCN-415 (0.75 Å)[42] and comparable to that of the SXRD structure of COF-300 (0.85 Å).[50] $Cu_3(C_6O_6)_2$ has a honeycomb-type network formed by the coordination between the Cu ion and $C_6O_6$ unit in a ratio of 2:3 (Figure 5.2a). Cu ions link the ligand through the chelation sites from the direction of the $C_2$ symmetry axis of the ligand. We identified two types of Cu ions, $Cu^\alpha$ and $Cu^\beta$, in a molar ratio of 1:2, which have slightly different distortions in their square planar coordination geometry (Figure 5.2c). $Cu^\alpha$ adopts a nearly perfect square planar coordination geometry in $Cu^\alpha O_4$ units with a dihedral angle of only ≈ 2.2° between the two planes established by O-$Cu^\alpha$-O atoms. The corresponding dihedral angle in $Cu^\beta O_4$ units is ≈ 7.4°. These imperfect square planar connections lead the layers of the MOF to be slightly bent. These layers exhibit a unique double-layer and mixed stacking of *AAA'A'* with an alternating fully eclipsed (*AA* and *A'A'*) and a slipped-parallel packing (*AA'* and *AA'*, relative in-plane displacement of 1.9 Å) between two adjacent layers (Figure 5.2b). This observation is in stark contrast to other layered conductive MOFs that show either fully eclipsed, slipped-parallel, or staggered packing exclusively.[22, 27, 31, 51] In $Cu_3(C_6O_6)_2$, the average layer-to-layer distance (see

Figure D.14 for definition) for the fully eclipsed and slipped-parallel packings with honeycomb pores of 2.9 Å and 3.1 Å, respectively. The value of 2.9 Å is much shorter than those observed in MOFs with honeycomb lattices based on hexaiminobenzene ($\approx$ 3.2–3.3 Å)[18, 51] and hexasubstitubed triphenylene ($\approx$ 3.3 Å).[27, 31, 52]

**Figure 5.3**. *Oxidation state analysis of the metal and ligand in $Cu_3(C_6O_6)_2$ MOF and extremely close stacking of the ligand. The high-resolution XPS scan of a) Cu 2p and b) C 1s range (after $Ar^+$ sputter etching) of $Cu_3(C_6O_6)_2$ MOF with area percentages of the deconvoluted peaks given. c) Representative resonant structures of $C_6O_6$ ligand in –2, –3, and –4 charged states (upper part). Two types of $C_6O_6$ ligands (colored in red and blue) as being incorporated in $Cu_3(C_6O_6)_2$ MOF with slightly different C–O bonds (lower part). d) The arrangement of the two types of $C_6O_6$ ligands in $Cu_3(C_6O_6)_2$.*
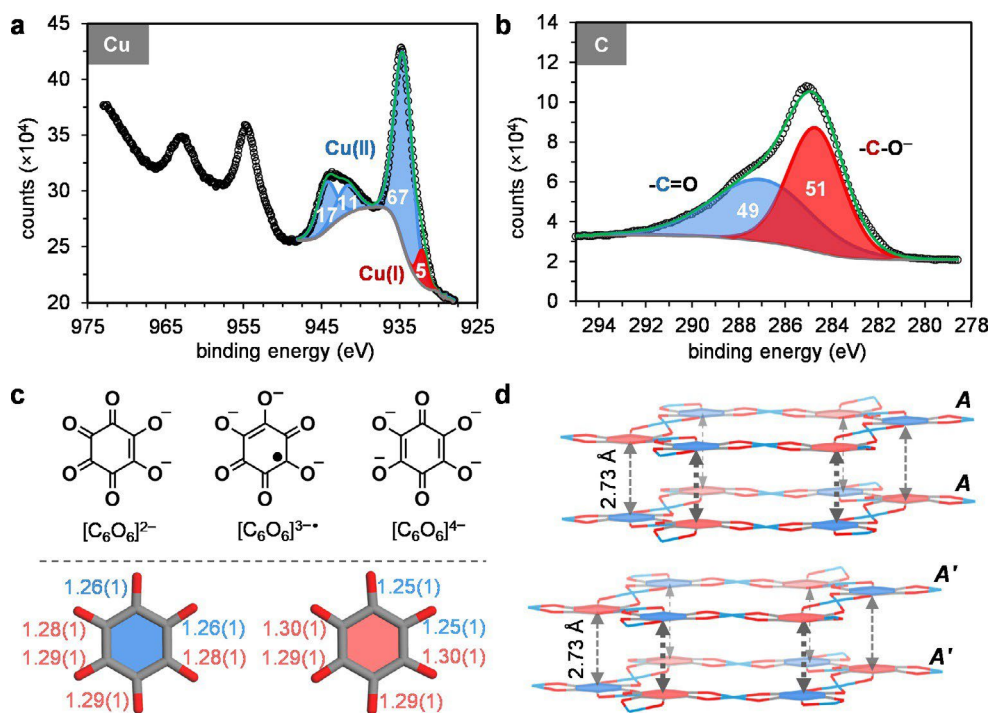


$Cu_3(C_6O_6)_2$ showed solvent-accessible nanopores with a diameter of $\approx$ 1.1 nm containing confined water clusters. Regeneration of the positions of hydrogen atoms of water molecules by DFT calculations suggested a hydrogen-bonded water assembly of dodecamer $(H_2O)_{12}$ formed within the two adjacent fully eclipsed layers. This assembly appeared aligned along the channel to form a longitudinally

extended cluster $[(H_2O)_{12}]_n$ (Figure 5.2d). The above analysis suggested a chemical formula of $Cu_3(C_6O_6)_2 \cdot 6H_2O$, which is in excellent agreement with elemental analysis (Table D.2) and thermogravimetric analysis (Figure D.24). Pawley refinement of the structure resolved by MicroED analysis against experimental pXRD ($\lambda = 1.5406$ Å) yielded an excellent match (Figure 5.2e). These results demonstrated good consistency with the structure resolved by MicroED and experimental pXRD, as well as excellent crystallinity and purity of the bulk material of $Cu_3(C_6O_6)_2$.

An accurate determination of the valency of constituents in MOFs is critical for interpreting their electronic properties, including charge transport and spin behavior. X-ray photoelectron spectroscopy (XPS) confirmed the presence of C, O, and Cu in $Cu_3(C_6O_6)_2$ sample. The deconvolution of high-resolution XPS scan of Cu 2p range[53] in $Cu_3(C_6O_6)_2$ suggested a dominant distribution of $Cu^{II}$ over $Cu^{I}$ with a $Cu^{II}$:$Cu^{I}$ ratio of 95:5 (Figure 5.3a). High-resolution XPS analysis of the C 1s revealed a nearly 1:1 distribution of -C=O and -C–O (Figure 5.3b), in line with the observation of C=O and C–O stretching in Fourier-transform infrared spectroscopy and Raman spectroscopy (see Appendix D). These results supported the existence of the ligand in a tris(semiquinone) form on average, equivalent to an anionic radical of $[C_6O_6]^{3-\cdot}$. However, the possibility of an equal distribution of ligand in –2 ($[C_6O_6]^{2-}$) and –4 ($[C_6O_6]^{4-}$) states as a mixed valency cannot be excluded (upper part in Figure 5.3c). A combination of $Cu^{2+}$ ions and the ligand with a formal averaged charge of –3 in a ratio of 3:2 should give a charge-neutral framework for $Cu_3(C_6O_6)_2$, consistent with the crystal structure resolved by MicroED and elemental analysis (Table D.2). The above analysis demonstrated that the charge neutral $Cu_3(C_6O_6)_2$ MOF in this work exhibited a more oxidized state in its skeleton than the negatively charged scaffold of this analog reported previously.[47] We attribute the charge neutrality realized in this work to continuous air bubbling during synthesis.

To gain more insights into the oxidation state of the ligand, we turned to bond-length analysis. Previous studies of metal-semiquinone complexes showed that the C–O bond length is indicative of the degree of oxidation of the semiquinone fragment.[54-56] Shorter C–O bonds correlate with more oxidized

(quinone-type) character, whereas longer C–O bonds correspond to reduced (catechol-type) character. Based on the C–O and C–C bond lengths, the structure of the $Cu_3(C_6O_6)_2$ revealed two kinds of slightly different $C_6O_6$ ligands within the MOF (lower part in Figure 5.3c) with averaged C–O bond lengths of 1.28(1) Å. This value was close to the average C–O bond lengths in a $Cu^{II}$ bissemiquinonate complex (1.288 Å)[55] and a $Cu^{II}$ triphenylene tris(semiquinone) complex (1.283 Å) (see Table D.6 and Figure D.22 for comprehensive comparison). This consistency suggested that ligands within the MOF were likely in a tris(semiquinone) state (see detailed discussion in Appendix D).

*Figure 5.4*. *Spin characteristic of MOF $Cu_3(C_6O_6)_2$. a) EPR spectra of $Cu_3(C_6O_6)_2$ at 77 K. b) DFT-calculated spin-up (pink) and spin-down (blue) density of $Cu_3(C_6O_6)_2$.*
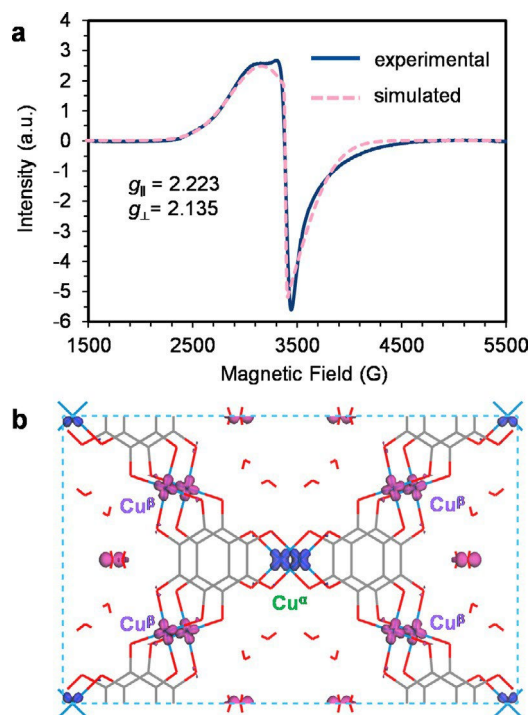


Our analysis showed that the two types of ligands were alternatively embedded in the two adjacent fully eclipsed layers within the MOF. The ligands were cofacially stacked with an interplanar distance (averaged C to C distances in the ligand) of only 2.73 Å (Figure 5.3d). This value represents one of the shortest $\pi$-$\pi$ stacking distances (plane to plane or centroid to plane)[57] that has been experimentally approached and identified in all structures reported to date.[58] Considering that conventional $\pi$-$\pi$ stacking

distances are in the range of 3.0– 3.9 Å,[57] this extremely short distance suggested the presence of strong intermolecular interactions, for example, charge transfer interaction[59, 60] or spin-spin coupling interaction,[61, 62] between the two types of $C_6O_6$ ligands.

Spin pairing has been previously observed in π-assemblies of phenalenyl,[63, 64] viologen cation,[65, 66] naphthalenediimide anion,[67] tetracyanoquinodimethane anion,[68] tetrathiafulvalene cation,[69] and others.[61, 70, 71] In these systems, efficient π-π orbital overlap provides the driving force for the stabilization of a dimer that is responsible for contact distances significantly shorter and interaction energies larger than those of typical van der Waals interactions. This interaction has been described as "pancake bonding".[61, 63, 64, 67, 68, 70, 72] We hypothesized that analogous interactions might be present within adjacent bilayers of $Cu_3(C_6O_6)_2$ MOF, considering the cofacial alignment and the very short interplanar distance between the ligands with a formal radical state.

Given that the spin state of the ligand can be significantly affected by the radical pairing interaction, electron paramagnetic resonance (EPR) spectroscopy was performed to study the spin characteristics of MOF $Cu_3(C_6O_6)_2$. EPR of $Cu_3(C_6O_6)_2$ at 77 K (Figure 5.4a) and 298 K both exhibited a broad absorbance band in the range of 2500–4500 G, which was ascribed to a Cu-centered radical in Cu catecholate-based materials (Figure D.12).[29, 56, 73] The asymmetric shape of the EPR spectra is consistent with the pseudo-square planar coordination of Cu, in which in-plane Cu···O coordination bonds are much longer than Cu to O and Cu to Cu distances along the axial direction (Figure D.33).[74] DFT calculations revealed that the spin density of $Cu_3(C_6O_6)_2$ was predominately centered on the $d_{x2-y2}$ orbital of Cu ions, with the positive and negative signs of spin density for $Cu^\alpha$ and $Cu^\beta$, respectively (Figure 5.4b). Taken together, EPR results and DFT calculations suggested that the unpaired electrons in $Cu_3(C_6O_6)_2$ MOF were centered $Cu^{II}$ centers. The lack of the spin signal from ligands was consistent with the presence of pancake-bonded singlet dimers (Figure 5.3d). This strong interlayer interaction may be beneficial in promoting ordered packing without stacking faults in $Cu_3(C_6O_6)_2$ (Figure D.5).

*Figure 5.5*. *Electrical properties of Cu(CO) MOF. a) Electrical conductivity of Cu(CO) pellets as a function of temperature. The inset is the Arrhenius fitting of conductivity to temperature. b) UV-vis-NIR spectrum of Cu₃(C₆O₆)₂ thin film deposited on quartz substrates. The inset is the Tauc plot of the UV-vis absorbance spectra for the estimation of the optical band gap. c) Calculated band structure (blue and red lines for spin-up and spin-down electron-associated bands, respectively) and projected PDOS for Cu₃(C₆O₆)₂ using the structure determined by MicroED with H atoms of water molecules regenerated. d) The first Brillouin zone and K-points of Cu₃(C₆O₆)₂ MOF. Green planes parallel to 2D layers are added to guide eyes. Calculated orbitals near the e) VBM and f) CBM.*
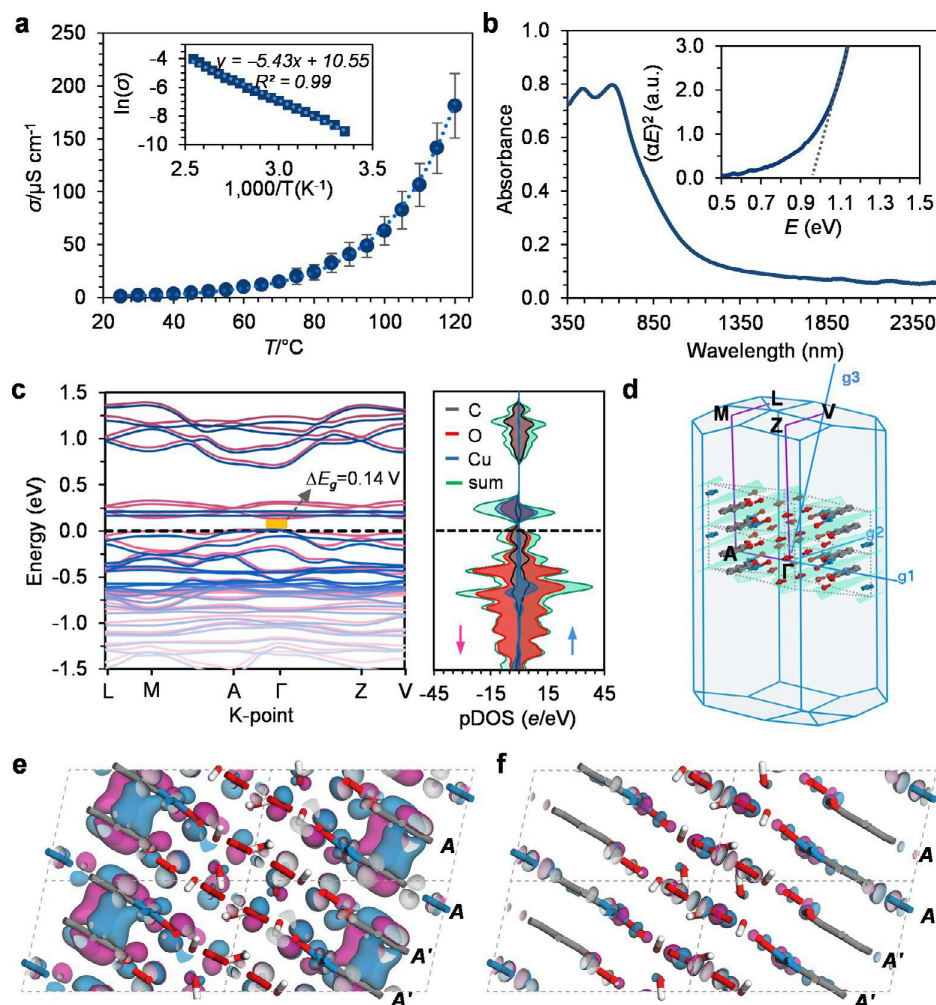


Although pancake bond, as a type of stacking interaction, has been demonstrated in several molecular systems with planar configurations as mentioned earlier,[63-67, 72] as far as we know, it has not

been previously reported in any 2D layered materials. The possible presence of pancake bonds in the $Cu_3(C_6O_6)_2$ suggested a unique type of electronic interlayer coupling between the ligands in the MOF, which can influence the electrical and magnetic properties of this material.

With a clear picture of structural features for $Cu_3(C_6O_6)_2$ in mind, we sought to investigate the electrical and magnetic properties of this material. Two-contact probe measurements of the conductivity of $Cu_3(C_6O_6)_2$ gave a bulk conductivity of 1.2 X $10^{-6}$ S cm$^{-1}$ at 298 K. This value showed more than one order of magnitude improvement compared with the MOF made from $Cu^{II}$ and THQ in previous reports.[47, 48] We attributed this increase to the improved crystallinity achieved in this study, as well as the charge-neutral skeleton of the structure in this report. Temperature-dependent conductivity tests showed that increasing the temperature to 393 K increased the conductivity of the material to 1.7x$10^{-4}$ S cm$^{-1}$ (Figure 5.5a). A plot of conductivity against temperature revealed Arrhenius-type dependence with an activation energy ($E_a$) of 0.47 eV for the charge carrier transport (inset in Figure 5.5a). UV-vis-NIR spectroscopy showed relatively broad absorption bands that extended to the NIR region (Figure 5.5b). Plotting the UV-vis-NIR spectra in Tauc coordinates resulted in an optical band gap ($E_{O, gap}$) of 0.95 eV for $Cu_3(C_6O_6)_2$ (inset in Figure 5.5b). These results suggested the semiconductive property of the bulk material of $Cu_3(C_6O_6)_2$.

To further understand the intrinsic electrical properties of $Cu_3(C_6O_6)_2$, we performed the spin-polarized DFT calculations of band structure using meta-generalized gradient approximation functional (see Appendix D). The calculated band structure of $Cu_3(C_6O_6)_2$, which included entrapped water molecules, revealed a direct band gap of 0.14 eV near gamma point, consistent with the semiconducting characteristic of $Cu_3(C_6O_6)_2$ (Figure 5.5c). Although DFT calculations can underestimate the band gap,[75] the discrepancy between the theoretical band gap (0.14 eV) and the relatively large experimental activation energy (0.47 eV) indicated charge hopping barriers between rather localized states. Domain boundaries,[2, 8, 47, 51, 76] impurities and defects may also contribute to the magnitude of the activation energy of charge transport in the polycrystalline MOF. The partial density of states (PDOS) showed that the

valence band maximum (VBM) comprised exclusive contributions from $p$ orbitals of O and C atoms. The conduction band minimum (CBM) exhibited considerable hybridization of $d$ orbitals of Cu and $p$ orbitals of O atoms. The calculated minimum carrier effective mass (see Appendix D) of VBM along the M-A direction (along reciprocal lattice vector $[0,1,\bar{1}]$) was 0.05 $m_e$, much smaller than those for L-M, A-$\Gamma$, $\Gamma$ - Z, and Z-V directions (0.15, 2.01, 0.18, and 0.40 $m_e$, respectively). These differences suggested more efficient transport of charge carriers along the M-A direction than along other directions (Figure 5.5d).

**Figure 5.6**. *Magnetic properties of Cu₃(C₆O₆)₂ MOF. a) ZFC (solid blue line) and FC (dashed orange line) magnetization for Cu₃(C₆O₆)₂ in an applied DC magnetic field of 100 Oe. The inset is molar paramagnetic susceptibility of Cu₃(C₆O₆)₂ was fit against the temperature to Curie–Weiss law. b) Magnetic hysteresis of Cu₃(C₆O₆)₂ MOF at 2 K and 5 K. c) Temperature dependence of the product of the paramagnetic susceptibility and temperature ($\chi_{m,p}T$). d) Schematic representation of the antiferromagnetic coupling interactions in Cu₃(C₆O₆)₂ MOF. The circles and triangles represent Cu ions and ligands in the MOF.*
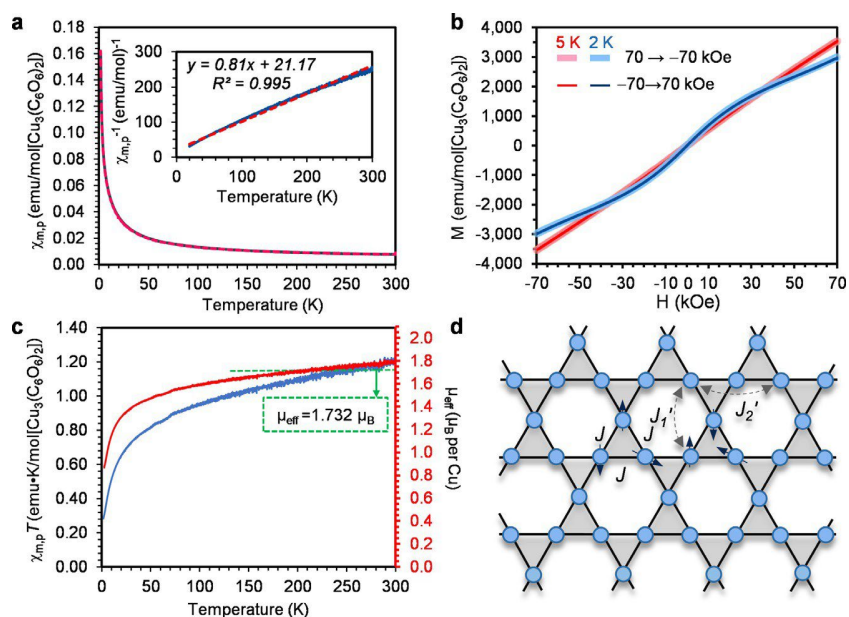


The calculated orbitals near the VBM were centered on $[C_6O_6]^{3-\cdot}$ ligand (Figure 5.5e, see also Figure D.28a) in comparison to the orbitals near the CBM that were mostly centered on CuO₄ units

(Figure 5.5f, see also Figure D.28b). The composition of these orbitals was consistent with the PDOS analysis. Importantly, we observed that in the calculated orbitals near the VBM, the $p$ orbitals of C exhibited a high degree of overlap and formed multicentered bonding orbitals. This observation further corroborated the formation of the pancake bonding of ligands in $Cu_3(C_6O_6)_2$. Because of the unique double-layer and mixed stacking mode of $Cu_3(C_6O_6)_2$, the pancake bonds were found sandwiched between the fully eclipsed layers (*AA* or *A'A'*), while absent between the slipped-parallel layers (*A'A* or *AA'*). This spatial distribution of the pancake bonds suggested the presence of a localized feature of $\pi$ electrons in the VBM. We hypothesize that this feature likely limits the long-range out-of-plane electron transport in $Cu_3(C_6O_6)_2$ and serves as an important intrinsic reason for the observed moderate conductivity and relatively large activation energy in addition to the contributing factors of domain boundaries.

To probe the magnetic properties of $Cu_3(C_6O_6)_2$ MOF, temperature-variable magnetic susceptibility measurements were performed between 1.8–300 K (Figure 5.6a). The field-cooled (FC) and zero field-cooled (ZFC) magnetization curves were almost the same in the tested temperature range, indicating a lack of long-range magnetic order down to 1.8 K and a typical paramagnetic behavior at 1.8–300 K. The magnetic hysteresis tests of $Cu_3(C_6O_6)_2$ MOF at 2 K and 5 K did not display any hysteretic behavior (Figure 5.6b and Figure D.32), demonstrating the lack of remanent magnetization due to the absence of ferromagnetic ordering. The fitting of paramagnetic susceptibility $\chi_{m,p}$ (see Appendix D) against temperature at 25–300 K according to Curie–Weiss law provided a nearly linear relationship (inset Figure 5.6a). This fitting yielded a Curie constant of 1.23 emu K mol$^{-1}$ (per mole $Cu_3(C_6O_6)_2 \cdot 6H_2O$) and a Weiss constant ($\theta$) of –26.1 K. This value of Curie constant was only slightly higher than the theoretical value expected for three independent spins of $Cu^{2+}$ with $S = 1/2$ (1.125 emu K mol$^{-1}$). However, this value was much smaller than that for five independent $S=1/2$ spins (1.875 emu K mol$^{-1}$, three $Cu^{2+}$ and two ligands). Consistently, the effective moment ($\mu_{eff}$) calculated for each Cu ion in the formula $Cu_3(C_6O_6)_2 \cdot 6H_2O$, 1.788 $\mu_B$, was reasonably close to that expected for $Cu^{2+}$ ion with S = 1/2 state, 1.73 $\mu_B$. These results supported that the paramagnetism of the $Cu_3(C_6O_6)_2$ MOF at the tested temperature

range was mostly from the spin of Cu centers. The negative Weiss temperature suggested an antiferromagnetic interaction between localized $Cu^{2+}$ ions moments.[76, 77] Further considering the Kagomé arrangement of $Cu^{II}$ ions in $Cu_3(C_6O_6)_2$, the antiferromagnetic interactions between adjacent $Cu^{II}$ spins within the layer (single arrows in Figure 5.6d) can lead to geometrical frustration.[78-81] Estimation of the frustration parameter $f$, defined as $|\theta|/T_c$,[82] gave $f > 14$, which supported a strong suppression of magnetic ordering that may result from geometrical frustration.

The antiferromagnetic exchange interactions were also reflected in the temperature dependence of the product of the paramagnetic susceptibility and temperature ($\chi_{m,p}T$), which revealed a decreasing trend with the decrease of the temperature (Figure 5.6c). Based on the computational insight that the calculated spin resides on $d_{x2-y2}$ orbital of Cu ions, which favors intralayer interaction over interlayer interaction, we hypothesized that intralayer Cu coupling would dominate over interlayer coupling (see Appendix D for details). The lack of magnetic ordering for $Cu_3(C_6O_6)_2$ down to 1.8 K was also consistent with the observed antiferromagnetic interactions of $Cu^{II}$ spins within a Kagomé layer, similar to those found in the related Cu-BHT (BHT = benzenehexathiol)[77] and $Cu_3(HHTP)_2$ (HHTP = hexahydroxytriphenylene)[83] system.

To assess the antiferromagnetic coupling interactions between the adjacent $Cu^{II}$ cations within a layer (Figure 5.6d), we analyzed the temperature-dependent $\chi_{m,p}$ data by high-temperature series expansion (see Appendix D for details).[84] The obtained exchange coupling constant for adjacent $Cu^{II}$ cations was $J//k_B = -20$ K ($-13.9$ cm$^{-1}$). This coupling constant was much larger than that in $Cu_3(HHTP)$ complex ($-2.76$ cm$^{-1}$)[56] and $Cu_3(HHTP)_2$ MOF ($J//k_B = -2$ K),[83] demonstrating a stronger antiferromagnetic coupling interaction of adjacent $Cu^{II}$ ions in $Cu_3(C_6O_6)_2$ MOF system, which was possibly ascribed to the shorter $Cu^{II}$-$Cu^{II}$ distance in $Cu_3(C_6O_6)_2$. Below 4.8 K, $\chi_{m,p}T$ value was even smaller than 0.375 emu K mol$^{-1}$ (calculated $\mu_{eff} < 1.73$ $\mu_B$ for each $Cu_3(C_6O_6)_2 \cdot 6H_2O$ unit), indicating the existence of the across-Cu antiferromagnetic coupling interactions (indicated as $J_1$' and $J_2$' in Figure 5.6d). The across-Cu antiferromagnetic couplings can be favorable in $Cu_3(C_6O_6)_2$ MOF system

considering that the across-Cu $Cu^{II}$-$Cu^{II}$ distances in this MOF (11.3 and 13.0 Å) were comparable with those in the triphenylene-bridged Cu complexes (11.1 Å).[56, 83]

## 5.3 CONCLUSION

This chapter demonstrates the unambiguous structural elucidation of $Cu_3(C_6O_6)_2$ MOF by MicroED with subangstrom precision. This achievement provides a new level of insight into the hydration, coordination variation and distortion, and stacking features of this material. Cofacial stacking of adjacent bilayers over a remarkably short interplanar distance of 2.73 Å has led us to propose pancake bonding interactions, which were not previously reported in 2D layered materials. Experimental studies and electronic band structure analysis indicated the semiconductive feature of the MOF, which was likely related to the localized feature of pancake bonds. The magnetism of $Cu_3(C_6O_6)_2$, dominated by the paramagnetic $Cu^{II}$ ions, showed strong geometric magnetic frustration resulting from the Kagomé arrangement of $Cu^{II}$ in the MOF. This property may be of further interest for evaluating this material as a potential candidate for quantum spin liquid.[78, 80, 81, 85] We anticipate that the fundamental study presented herein will open the avenue for in-depth investigation of other conductive frameworks and 2D layered materials through the exploitation and manipulation of different types of stacking forces. Future studies using devices fabricated from large single crystals and precisely controlled number of layers of the 2D layered MOFs should clarify the anisotropic and intrinsic electronic properties and minimize the nontrivial effects of structural defects, impurities, and grain boundaries in this general class of materials.[2, 28, 30]

## 5.4 REFERENCES

(1) Sun, L.; Campbell, M. G.; Dinca, M. Electrically Conductive Porous Metal-Organic Frameworks. *Angewandte Chemie-International Edition* **2016**, *55* (11), 3566-3579.

(2) Xie, L. S.; Skorupskii, G.; Dinca, M. Electrically Conductive Metal-Organic Frameworks. *Chemical Reviews* **2020**, *120* (16), 8536-8580.

(3) Tan, C. L.; Cao, X. H.; Wu, X. J.; He, Q. Y.; Yang, J.; Zhang, X.; Chen, J. Z.; Zhao, W.; Han, S. K.; Nam, G. H.; et al. Recent Advances in Ultrathin Two-Dimensional Nanomaterials. *Chemical Reviews* **2017**, *117* (9), 6225-6331.

(4) Dinca, M.; Leonard, F. Metal-organic frameworks for electronics and photonics. *Mrs Bulletin* **2016**, *41* (11), 854-857.

(5) Wu, G. D.; Huang, J. H.; Zang, Y.; He, J.; Xu, G. Porous Field-Effect Transistors Based on a Semiconductive Metal-Organic Framework. *Journal of the American Chemical Society* **2017**, *139* (4), 1360-1363.

(6) DeGayner, J. A.; Jeon, I. R.; Sun, L.; Dinca, M.; Harris, T. D. 2D Conductive Iron-Quinoid Magnets Ordering up to T-c=105 K via Heterogenous Redox Chemistry. *Journal of the American Chemical Society* **2017**, *139* (11), 4175-4184.

(7) Dong, R. H.; Zhang, Z. T.; Tranca, D. C.; Zhou, S. Q.; Wang, M. C.; Adler, P.; Liao, Z. Q.; Liu, F.; Sun, Y.; Shi, W. J.; et al. A coronene-based semiconducting two-dimensional metal-organic framework with ferromagnetic behavior. *Nature Communications* **2018**, *9*.

(8) Yang, C. Q.; Dong, R. H.; Wang, M.; St Petkow, P.; Zhang, Z. T.; Wang, M. C.; Han, P.; Ballabio, M.; Brauninger, S. A.; Liao, Z. Q.; et al. A semiconducting layered metal-organic framework magnet. *Nature Communications* **2019**, *10*.

(9) Campbell, M. G.; Liu, S. F.; Swager, T. M.; Dinca, M. Chemiresistive Sensor Arrays from Conductive 2D Metal-Organic Frameworks. *Journal of the American Chemical Society* **2015**, *137* (43), 13780-13783.

(10) Smith, M. K.; Mirica, K. A. Self-Organized Frameworks on Textiles (SOFT): Conductive Fabrics for Simultaneous Sensing, Capture, and Filtration of Gases. *Journal of the American Chemical Society* **2017**, *139* (46), 16759-16767.

(11) Yao, M. S.; Lv, X. J.; Fu, Z. H.; Li, W. H.; Deng, W. H.; Wu, G. D.; Xu, G. Layer-by-Layer Assembled Conductive Metal-Organic Framework Nanofilms for Room-Temperature Chemiresistive Sensing. *Angewandte Chemie-International Edition* **2017**, *56* (52), 16510-16514.

(12) Meng, Z.; Aykanat, A.; Mirica, K. A. Welding Metallophthalocyanines into Bimetallic Molecular Meshes for Ultrasensitive, Low-Power Chemiresistive Detection of Gases. *Journal of the American Chemical Society* **2019**, *141* (5), 2046-2053.

(13) Downes, C. A.; Marinescu, S. C. Efficient Electrochemical and Photoelectrochemical H-2 Production from Water by a Cobalt Dithiolene One-Dimensional Metal-Organic Surface. *Journal of the American Chemical Society* **2015**, *137* (43), 13740-13743.

(14) Dong, R. H.; Pfeffermann, M.; Liang, H. W.; Zheng, Z. K.; Zhu, X.; Zhang, J.; Feng, X. L. Large Area, Free-Standing, Two-Dimensional Supramolecular Polymer Single-Layer Sheets for Highly Efficient Electrocatalytic Hydrogen Evolution. *Angewandte Chemie-International Edition* **2015**, *54* (41), 12058-12063.

(15) Miner, E. M.; Fukushima, T.; Sheberla, D.; Sun, L.; Surendranath, Y.; Dinca, M. Electrochemical oxygen reduction catalysed by Ni-3(hexaiminotriphenylene)(2). *Nature Communications* **2016**, *7*.

(16) Zhong, H. X.; Ly, K. H.; Wang, M. C.; Krupskaya, Y.; Han, X. C.; Zhang, J. C.; Zhang, J.; Kataev, V.; Buchner, B.; Weidinger, I. M.; et al. A Phthalocyanine-Based Layered Two-Dimensional Conjugated Metal-Organic Framework as a Highly Efficient Electrocatalyst for the Oxygen Reduction Reaction. *Angewandte Chemie-International Edition* **2019**, *58* (31), 10677-10682.

(17) Sheberla, D.; Bachman, J. C.; Elias, J. S.; Sun, C. J.; Shao-Horn, Y.; Dinca, M. Conductive MOF electrodes for stable supercapacitors with high areal capacitance. *Nature Materials* **2017**, *16* (2), 220-224.

(18) Feng, D. W.; Lei, T.; Lukatskaya, M. R.; Park, J.; Huang, Z. H.; Lee, M.; Shaw, L.; Chen, S. C.; Yakovenko, A. A.; Kulkarni, A.; et al. Robust and conductive two-dimensional metal-organic frameworks with exceptionally high volumetric and areal capacitance. *Nature Energy* **2018**, *3* (1), 30-36.

(19) Nam, K. W.; Park, S. S.; dos Reis, R.; Dravid, V. P.; Kim, H.; Mirkin, C. A.; Stoddart, J. F. Conductive 2D metal-organic framework for high-performance cathodes in aqueous rechargeable zinc batteries. *Nature Communications* **2019**, *10*.

(20) Espallargas, G. M.; Coronado, E. Magnetic functionalities in MOFs: from the framework to the pore. *Chemical Society Reviews* **2018**, *47* (2), 533-557.

(21) Thorarinsdottir, A. E.; Harris, T. D. Metal-Organic Framework Magnets. *Chemical Reviews* **2020**, *120* (16), 8716-8789.

(22) Clough, A. J.; Skelton, J. M.; Downes, C. A.; de la Rosa, A. A.; Yoo, J. W.; Walsh, A.; Melot, B. C.; Marinescu, S. C. Metallic Conductivity in a Two-Dimensional Cobalt Dithiolene Metal-Organic Framework. *Journal of the American Chemical Society* **2017**, *139* (31), 10863-10867.

(23) Park, S. S.; Hontz, E. R.; Sun, L.; Hendon, C. H.; Walsh, A.; Van Voorhis, T.; Dinca, M. Cation Dependent Intrinsic Electrical Conductivity in lsostructural Tetrathiafulvalene-Based Microporous Metal-Organic Frameworks. *Journal of the American Chemical Society* **2015**, *137* (5), 1774-1777.

(24) Skorupskii, G.; Trump, B. A.; Kasel, T. W.; Brown, C. M.; Hendon, C. H.; Dinca, M. Efficient and tunable one-dimensional charge transport in layered lanthanide metal-organic frameworks. *Nature Chemistry* **2020**, *12* (2), 131-136.

(25) Fei, Z. Y.; Zhao, W. J.; Palomaki, T. A.; Sun, B. S.; Miller, M. K.; Zhao, Z. Y.; Yan, J. Q.; Xu, X. D.; Cobden, D. H. Ferroelectric switching of a two-dimensional metal. *Nature* **2018**, *560* (7718), 336.

(26) Cao, Y.; Fatemi, V.; Fang, S.; Watanabe, K.; Taniguchi, T.; Kaxiras, E.; Jarillo-Herrero, P. Unconventional superconductivity in magic-angle graphene superlattices. *Nature* **2018**, *556* (7699), 43.

(27) Hmadeh, M.; Lu, Z.; Liu, Z.; Gandara, F.; Furukawa, H.; Wan, S.; Augustyn, V.; Chang, R.; Liao, L.; Zhou, F.; et al. New Porous Crystals of Extended Metal-Catecholates. *Chemistry of Materials* **2012**, *24* (18), 3511-3513.

(28) Day, R. W.; Bediako, D. K.; Rezaee, M.; Parent, L. R.; Skorupskii, G.; Arguilla, M. Q.; Hendon, C. H.; Stassen, I.; Gianneschi, N. C.; Kim, P.; et al. Single Crystals of Electrically Conductive Two Dimensional Metal-Organic Frameworks: Structural and Electrical Transport Properties. *Acs Central Science* **2019**, *5* (12), 1959-1964.

(29) Dou, J. H.; Arguilla, M. Q.; Luo, Y.; Li, J.; Zhang, W. Z.; Sun, L.; Mancuso, J. L.; Yang, L. M.; Chen, T. Y.; Parent, L. R.; et al. Atomically precise single-crystal structures of electrically conducting 2D metal-organic frameworks. *Nature Materials* **2021**, *20* (2), 222.

(30) Ha, D. G.; Rezaee, M.; Han, Y. M.; Siddiqui, S. A.; Day, R. W.; Xie, L. S.; Modtland, B. J.; Muller, D. A.; Kong, J.; Kim, P.; et al. Large Single Crystals of Two-Dimensional pi-Conjugated Metal-Organic Frameworks via Biphasic Solution-Solid Growth. *Acs Central Science* **2021**, *7* (1), 104-109.

(31) Sheberla, D.; Sun, L.; Blood-Forsythe, M. A.; Er, S.; Wade, C. R.; Brozek, C. K.; Aspuru-Guzik, A.; Dinca, M. High Electrical Conductivity in Ni-3(2,3,6,7,10,11-hexaiminotriphenylene)(2), a Semiconducting Metal-Organic Graphene Analogue. *Journal of the American Chemical Society* **2014**, *136* (25), 8859-8862.

(32) Huang, X.; Sheng, P.; Tu, Z. Y.; Zhang, F. J.; Wang, J. H.; Geng, H.; Zou, Y.; Di, C. A.; Yi, Y. P.; Sun, Y. M.; et al. A two-dimensional pi-d conjugated coordination polymer with extremely high electrical conductivity and ambipolar transport behaviour. *Nature Communications* **2015**, *6*.

(33) Shi, D.; Nannenga, B. L.; Iadanza, M. G.; Gonen, T. Three-dimensional electron crystallography of protein microcrystals. *Elife* **2013**, *2*.

(34) Nannenga, B. L.; Shi, D.; Leslie, A. G. W.; Gonen, T. High-resolution structure determination by continuous-rotation data collection in MicroED. *Nature Methods* **2014**, *11* (9), 927-930.

(35) Nannenga, B. L.; Gonen, T. The cryo-EM method microcrystal electron diffraction (MicroED). *Nature Methods* **2019**, *16* (5), 369-379.

(36) Jones, C. G.; Martynowycz, M. W.; Hattne, J.; Fulton, T. J.; Stoltz, B. M.; Rodriguez, J. A.; Nelson, H. M.; Gonen, T. The CryoEM Method MicroED as a Powerful Tool for Small Molecule Structure Determination. *Acs Central Science* **2018**, *4* (11), 1587-1592.

(37) Jones, C. G.; Asay, M.; Kim, L. J.; Kleinsasser, J. F.; Saha, A.; Fulton, T. J.; Berkley, K. R.; Cascio, D.; Malyutin, A. G.; Conley, M. P.; et al. Characterization of Reactive Organometallic Species via MicroED. *Acs Central Science* **2019**, *5* (9), 1507-1513.

(38) Gemmi, M.; Mugnaioli, E.; Gorelik, T. E.; Kolb, U.; Palatinus, L.; Boullay, P.; Hovmoller, S.; Abrahams, J. P. 3D Electron Diffraction: The Nanocrystallography Revolution. *Acs Central Science* **2019**, *5* (8), 1315-1329.

(39) Jiang, J. X.; Jorda, J. L.; Yu, J. H.; Baumes, L. A.; Mugnaioli, E.; Diaz-Cabanas, M. J.; Kolb, U.; Corma, A. Synthesis and Structure Determination of the Hierarchical Meso-Microporous Zeolite ITQ-43. *Science* **2011**, *333* (6046), 1131-1134.

(40) Simancas, J.; Simancas, R.; Bereciartua, P. J.; Jorda, J. L.; Rey, F.; Corma, A.; Nicolopoulos, S.; Das, P. P.; Gemmi, M.; Mugnaioli, E. Ultrafast Electron Diffraction Tomography for Structure Determination of the New Zeolite ITQ-58. *Journal of the American Chemical Society* **2016**, *138* (32), 10116-10119.

(41) Denysenko, D.; Grzywa, M.; Tonigold, M.; Streppel, B.; Krkljus, I.; Hirscher, M.; Mugnaioli, E.; Kolb, U.; Hanss, J.; Volkmer, D. Elucidating Gating Effects for Hydrogen Sorption in MFU-4 Type Triazolate-Based Metal-Organic Frameworks Featuring Different Pore Sizes. *Chemistry-a European Journal* **2011**, *17* (6), 1837-1848.

(42) Yuan, S.; Qin, J. S.; Xu, H. Q.; Su, J.; Rossi, D.; Chen, Y. P.; Zhang, L. L.; Lollar, C.; Wang, Q.; Jiang, H. L.; et al. Ti8Zr2O12(COO)(16) Cluster: An Ideal Inorganic Building Unit for Photoactive Metal-Organic Frameworks. *Acs Central Science* **2018**, *4* (1), 105-111.

(43) Lenzen, D.; Zhao, J. J.; Ernst, S. J.; Wahiduzzaman, M.; Inge, A. K.; Frohlich, D.; Xu, H. Y.; Bart, H. J.; Janiak, C.; Henninger, S.; et al. A metal-organic framework for efficient water-based ultra-low temperature-driven cooling. *Nature Communications* **2019**, *10*.

(44) Huang, Z. H.; Ge, M.; Carraro, F.; Doonan, C.; Falcaro, P.; Zou, X. D. Can 3D electron diffraction provide accurate atomic structures of metal-organic frameworks? *Faraday Discussions* **2021**, *225* (0), 118-132.

(45) Zhang, Y. B.; Su, J.; Furukawa, H.; Yun, Y. F.; Gandara, F.; Duong, A.; Zou, X. D.; Yaghi, O. M. Single-Crystal Structure of a Covalent Organic Framework. *Journal of the American Chemical Society* **2013**, *135* (44), 16336-16339.

(46) Sun, T.; Hughes, C. E.; Guo, L. S.; Wei, L.; Harris, K. D. M.; Zhang, Y. B.; Ma, Y. H. Direct-Space Structure Determination of Covalent Organic Frameworks from 3D Electron Diffraction Data. *Angewandte Chemie-International Edition* **2020**, *59* (50), 22638-22644.

(47) Park, J.; Hinckley, A. C.; Huang, Z. H.; Feng, D. W.; Yakoyenko, A. A.; Lee, M.; Chen, S. C.; Zou, X.; Bao, Z. A. Synthetic Routes for a 2D Semiconductive Copper Hexahydroxybenzene Metal Organic Framework. *Journal of the American Chemical Society* **2018**, *140* (44), 14533-14537.

(48) Jiang, Q.; Xiong, P. X.; Liu, J. J.; Xie, Z.; Wang, Q. C.; Yang, X. Q.; Hu, E. Y.; Cao, Y.; Sun, J.; Xu, Y. H.; et al. A Redox-Active 2D Metal-Organic Framework for Efficient Lithium Storage with Extraordinary High Capacity. *Angewandte Chemie-International Edition* **2020**, *59* (13), 5273 5277.

(49) Nyakuchena, J.; Ostresh, S.; Streater, D.; Pattengale, B.; Neu, J.; Fiankor, C.; Hu, W. H.; Kinigstein, E. D.; Zhang, J.; Zhang, X. Y.; et al. Direct Evidence of Photoinduced Charge Transport Mechanism in 2D Conductive Metal Organic Frameworks. *Journal of the American Chemical Society* **2020**, *142* (50), 21050-21058.

(50) Ma, T. Q.; Kapustin, E. A.; Yin, S. X.; Liang, L.; Zhou, Z. Y.; Niu, J.; Li, L. H.; Wang, Y. Y.; Su, J.; Li, J.; et al. Single-crystal x-ray diffraction structures of covalent organic frameworks. *Science* **2018**, *361* (6397), 48-52.

(51) Dou, J. H.; Sun, L.; Ge, Y. C.; Li, W.; Hendon, C. H.; Li, J.; Gul, S.; Yano, J. K.; Stach, E. A.; Dinca, M. Signature of Metallic Behavior in the Metal-Organic Frameworks M-3(hexaiminobenzene)(2) (M = Ni, Cu). *Journal of the American Chemical Society* **2017**, *139* (39), 13608-13611.

(52) Dong, R.; Han, P.; Arora, H.; Ballabio, M.; Karakus, M.; Zhang, Z.; Shekhar, C.; Adler, P.; St Petkov, P.; Erbe, A.; et al. High-mobility band-like charge transport in a semiconducting two-dimensional metal-organic framework. *Nature Materials* **2018**, *17* (11), 1027.

(53) Biesinger, M. C.; Lau, L. W. M.; Gerson, A. R.; Smart, R. S. C. Resolving surface chemical states in XPS analysis of first row transition metals, oxides and hydroxides: Sc, Ti, V, Cu and Zn. *Applied Surface Science* **2010**, *257* (3), 887-898.

(54) Pierpont, C. G.; Lange, C. W. The Chemistry of Transition Metal Complexes Containing Catechol and Semiquinone Ligands. In *Progress in Inorganic Chemistry*, 1994; pp 331-442.

(55) Ovcharenko, V. I.; Gorelik, E. V.; Fokin, S. V.; Romanenko, G. V.; Ikorskii, V. N.; Krashilina, A. V.; Cherkasov, V. K.; Abakumov, G. A. Ligand effects on the ferro- to antiferromagnetic exchange ratio in Bis(o-Semiquinonato)copper(II). *Journal of the American Chemical Society* **2007**, *129* (34), 10512-10521.

(56) Yang, L. M.; He, X.; Dinca, M. Triphenylene-Bridged Trinuclear Complexes of Cu: Models for Spin Interactions in Two-Dimensional Electrically Conductive Metal-Organic Frameworks. *Journal of the American Chemical Society* **2019**, *141* (26), 10475-10480.

(57) Banerjee, A.; Saha, A.; Saha, B. K. Understanding the Behavior of pi-pi Interactions in Crystal Structures in Light of Geometry Corrected Statistical Analysis: Similarities and Differences with the Theoretical Models. *Crystal Growth & Design* **2019**, *19* (4), 2245-2252.

(58) Fiori, A. T. M.; Nakahata, D. H.; Cuin, A.; Lustri, W. R.; Corbi, P. P. Synthesis, crystallographic studies, high resolution mass spectrometric analyses and antibacterial assays of silver(I) complexes with sulfisoxazole and sulfadimethoxine. *Polyhedron* **2017**, *121*, 172-179.

(59) Hunter, C. A.; Sanders, J. K. M. THE NATURE OF PI-PI INTERACTIONS. *Journal of the American Chemical Society* **1990**, *112* (14), 5525-5534.

(60) Goetz, K. P.; Vermeulen, D.; Payne, M. E.; Kloc, C.; McNeil, L. E.; Jurchescu, O. D. Charge-transfer complexes: new perspectives on an old class of compounds. *Journal of Materials Chemistry C* **2014**, *2* (17), 3065-3076.

(61) Cui, Z. H.; Lischka, H.; Beneberu, H. Z.; Kertesz, M. Double Pancake Bonds: Pushing the Limits of Strong pi-pi Stacking Interactions. *Journal of the American Chemical Society* **2014**, *136* (37), 12958-12965.

(62) Molcanov, K.; Milassinovic, V.; Kojic-Prodic, B. Contribution of Different Crystal Packing Forces in pi-Stacking: From Noncovalent to Covalent Multicentric Bonding. *Crystal Growth & Design* **2019**, *19* (10), 5967-5980.

(63) Itkis, M. E.; Chi, X.; Cordes, A. W.; Haddon, R. C. Magneto-opto-electronic bistability in a phenalenyl-based neutral radical. *Science* **2002**, *296* (5572), 1443-1445.

(64) Suzuki, S.; Morita, Y.; Fukui, K.; Sato, K.; Shiomi, D.; Takui, T.; Nakasuji, K. Aromaticity on the Pancake-Bonded Dimer of Neutral Phenalenyl Radical as Studied by MS and NMR Spectroscopies and NICS Analysis. *Journal of the American Chemical Society* **2006**, *128* (8), 2530-2531.

(65) Barnes, J. C.; Fahrenbach, A. C.; Cao, D.; Dyar, S. M.; Frasconi, M.; Giesener, M. A.; Benitez, D.; Tkatchouk, E.; Chernyashevskyy, O.; Shin, W. H.; et al. A Radically Configurable Six-State Compound. *Science* **2013**, *339* (6118), 429-433.

(66) Gourlaouen, C.; Vela, S.; Choua, S.; Berville, M.; Wytko, J. A.; Weiss, J.; Robert, V. Pairing-up viologen cations and dications: a microscopic investigation of van der Waals interactions. *Physical Chemistry Chemical Physics* **2018**, *20* (44), 27878-27884.

(67) Zheng, X. J.; Zhang, Y.; Cao, N.; Li, X.; Zhang, S. Q.; Du, R. F.; Wang, H. Y.; Ye, Z. N.; Wang, Y.; Cao, F. H.; et al. Coulombic-enhanced hetero radical pairing interactions. *Nature Communications* **2018**, *9*.

(68) Cai, K.; Mao, H. C.; Liu, W. G.; Qiu, Y. Y.; Shi, Y.; Zhang, L.; Shen, D. K.; Chen, H. L.; Jiao, Y.; Wu, H.; et al. Highly Stable Organic Bisradicals Protected by Mechanical Bonds. *Journal of the American Chemical Society* **2020**, *142* (15), 7190-7197.

(69) Torrance, J. B.; Scott, B. A.; Welber, B.; Kaufman, F. B.; Seiden, P. E. OPTICAL-PROPERTIES OF THE RADICAL CATION TETRATHIAFULVALENIUM (TTF+) IN ITS MIXED-VALENCE AND MONO-VALENCE HALIDE SALTS. *Physical Review B* **1979**, *19* (2), 730-741.

(70) Kertesz, M. Pancake Bonding: An Unusual Pi-Stacking Interaction. *Chemistry-a European Journal* **2019**, *25* (2), 400-416.

(71) Cai, K.; Zhang, L.; Astumian, R. D.; Stoddart, J. F. Radical-pairing-induced molecular assembly and motion. *Nature Reviews Chemistry* **2021**, *5* (7), 447-465. DOI: 10.1038/s41570-021-00283-4.

(72) B.J.McC. Molecular complexes: R.S. Mulliken and W.B. Person, Wiley-Interscience, New York and London, 1969, pp. xv+498, price £9.25. *Journal of Molecular Structure* **1971**, *10* (1), 155.

(73) Stolz, R. M.; Mahdavi-Shakib, A.; Frederick, B. G.; Mirica, K. A. Host-Guest Interactions and Redox Activity in Layered Conductive Metal-Organic Frameworks. *Chemistry of Materials* **2020**, *32* (18), 7639-7652.

(74) Garribba, E.; Micera, G. The determination of the geometry of Cu(II) complexes - An EPR spectroscopy experiment. *Journal of Chemical Education* **2006**, *83* (8), 1229-1232.

(75) Mancuso, J. L.; Mroz, A. M.; Le, K. N.; Hendon, C. H. Electronic Structure Modeling of Metal-Organic Frameworks. *Chemical Reviews* **2020**, *120* (16), 8641-8715.

(76) Darago, L. E.; Aubrey, M. L.; Yu, C. J.; Gonzalez, M. I.; Long, J. R. Electronic Conductivity, Ferrimagnetic Ordering, and Reductive Insertion Mediated by Organic Mixed-Valence in a Ferric Semiquinoid Metal-Organic Framework. *Journal of the American Chemical Society* **2015**, *137* (50), 15703-15711.

(77) Huang, X.; Zhang, S.; Liu, L. Y.; Yu, L.; Chen, G. F.; Xu, W.; Zhu, D. B. Superconductivity in a Copper(II)-Based Coordination Polymer with Perfect Kagome Structure. *Angewandte Chemie International Edition* **2018**, *57* (1), 146-150.

(78) Anderson, P. W. THE RESONATING VALENCE BOND STATE IN LA2CUO4 AND SUPERCONDUCTIVITY. *Science* **1987**, *235* (4793), 1196-1198.

(79) Yan, S. M.; Huse, D. A.; White, S. R. Spin-Liquid Ground State of the S=1/2 Kagome Heisenberg Antiferromagnet. *Science* **2011**, *332* (6034), 1173-1176.

(80) Broholm, C.; Cava, R. J.; Kivelson, S. A.; Nocera, D. G.; Norman, M. R.; Senthil, T. Quantum spin liquids. *Science* **2020**, *367* (6475), 263.

(81) Chamorro, J. R.; McQueen, T. M.; Tran, T. T. Chemistry of Quantum Spin Liquids. *Chemical Reviews* **2021**, *121* (5), 2898-2934.

(82) Ramirez, A. P. STRONGLY GEOMETRICALLY FRUSTRATED MAGNETS. *Annual Review of Materials Science* **1994**, *24*, 453-480.

(83) Misumi, Y.; Yamaguchi, A.; Zhang, Z. Y.; Matsushita, T.; Wada, N.; Tsuchiizu, M.; Awaga, K. Quantum Spin Liquid State in a Two-Dimensional Semiconductive Metal-Organic Framework. *Journal of the American Chemical Society* **2020**, *142* (39), 16513-16517.

(84) Lohmann, A.; Schmidt, H. J.; Richter, J. Tenth-order high-temperature expansion for the susceptibility and the specific heat of spin-s Heisenberg models with arbitrary exchange patterns: Application to pyrochlore and kagome magnets. *Physical Review B* **2014**, *89* (1).

(85) Collins, K. A.; Saballos, R. J.; Fataftah, M. S.; Puggioni, D.; Rondinelli, J. M.; Freedman, D. E. Synthetic investigation of competing magnetic interactions in 2D metal-chloranilate radical frameworks. *Chemical Science* **2020**, *11* (23), 5922-5928.

*Chapter 6*

*Conductive Stimuli-Responsive Coordination Network Linked with Bismuth for*

*Chemiresistive Gas Sensing[1]*

## 6.1 INTRODUCTION

In today's densely inhabited society, there is an increasing need for the design and synthesis of new materials for low-power portable gas sensors with potential applications in monitoring atmospheric pollution,[1, 2] home and work safety,[3, 4] filtration of air for personal safety,[5] and breath diagnostics.[6] Full realization of these applications would significantly benefit from the design and fabrication of low-cost, low-power wireless gas sensors that do not rely on expensive equipment or trained technicians for analysis.[7] Nanomaterial-based chemiresistive sensors offer a unique approach toward this goal, with vast potential for addressing the increasing demand of portable sensors in environmental and healthcare applications.[8] Primary demonstrations of nanomaterial-based sensors, such as those fabricated from metal oxides,[9] carbon nanotubes (CNTs),[10] and synthetically modified graphene,[11] have confirmed the value of nanostructured materials in terms of high sensitivity,[12] low power consumption,[13] and rapid response time.[14] Yet specific limitations, such as ambiguity of sensing mechanisms, selectivity to analytes, and cost-effectiveness of device integration methods, limit the practical applications of nanomaterial-based sensors.[15]

Crystalline conductive coordination polymers (CPs), such as metal−organic frameworks (MOFs)[16] and coordination networks (CNs),[17] offer a promising alternative as a new emerging class of materials with

---

[1] Portions of this chapter have been adapted from Aylin Aykanat, Christopher G. Jones, Evan Cline, Robert M. Stolz, Zheng Meng, Hosea M. Nelson, and Katherine A. Mirica *ACS Applied Materials & Interfaces* **2021** *13* (50), 60306-60318. © American Chemical Society.

broad applicability in chemiresistive detection.[18-25] High conductivity and tunable surface chemistry, combined with modular porosity and high surface area for gas uptake—all accessible through bottom-up self-assembly—give this class of materials a set of unique attributes that are particularly well suited for applications in gas sensing.[18, 19, 23, 26] Despite this promise, most conductive coordination polymers that have thus far been employed in chemical sensing have two significant shortcomings. First, they are based on two-dimensional (2D) lattices comprising first row transition metals with square planar or octahedral coordination geometries around the metal site.[16, 18, 20, 21, 23-25, 27-31] While these low-dimensional materials exhibit high sensitivity to small reactive gases and vapors, the reliance on 2D lattices fundamentally limits gains in selectivity that can be achieved through stereoelectronic tuning of a binding site with a more complex coordination geometry. To address this fundamental limitation, we reasoned that expanding beyond first-row transition metals to create conductive networks with complex topologies and new, unsaturated coordination environments may promote gains in selectivity through simultaneous tuning of steric and electronic attributes of intermolecular interactions of sensing materials with analytes. The use of bismuth ions within a coordination network can enable solutions to these limitations by allowing tailoring of multiple useful and functional properties, such as charge delocalization and a tunable coordination environment. Additionally, flexible coordination sites capable of undergoing analyte-induced changes within the coordination environment can provide room to investigate the contributions of structural features in relation to sensing within a well-ordered material. Furthermore, the advantages of utilizing microED can help overcome the challenges associated with obtaining suitably large crystallites of 2D framework materials, where the lack of single-crystal diffraction studies in established framework systems conceals structural information and characterization studies. This limitation restricts the fundamental understanding of the interactions of host framework materials with guest analytes.[24]

## 6.2 MOLECULAR DESIGN

The molecular design of the conductive coordination network capitalizes on several unique characteristics of bismuth-containing compounds and materials and extends these characteristics to

generate a new material with promising functionality. Currently, bismuth-based materials and coordination compounds have applications in healthcare,[32] photocatalytic photocatalytic function,[33, 34] radiation technology,[35] and gas adsorption and storage.[36] The unique flexible coordination sphere of bismuth,[37] Lewis acidity,[38] nontoxicity,[39] stability,[40] as well as the high affinity for soft and hard ligands, enable desirable structure−property relationships,[41] particularly when bismuth is used as a constituent within CPs.[42] Specifically, bismuth-based CPs[43] and porous metal−organic frameworks (MOFs)[44] have demonstrated valuable structure−property relationships, such as conductivity,[43, 45] and photocatalysis.[33] These properties are tunable through the strategic selection of constituent organic linkers in bismuth-containing CPs that can dictate the coordination environment around the bismuth metal node.[43]

*Figure 6.1*. *(a) General reaction scheme and (b) structure of Bi(HHTP)-α and Bi(HHTP)-β. (c) Coordination polyhedral around two nonequivalent coordination polyhedra of Bi(HHTP)-α and Bi(HHTP)-β. In Bi(HHTP)-α, Bi$_2$ is displayed as a distorted tetragonal pyramid (CN = 5) and Bi$_1$ is shown as a distorted quadrilateral (CN = 4). In Bi(HHTP)-β, Bi$_1$ is displayed as a distorted pentagonal pyramid (CN = 5) and Bi$_2$ as a distorted one-capped octahedron (CN = 6).*
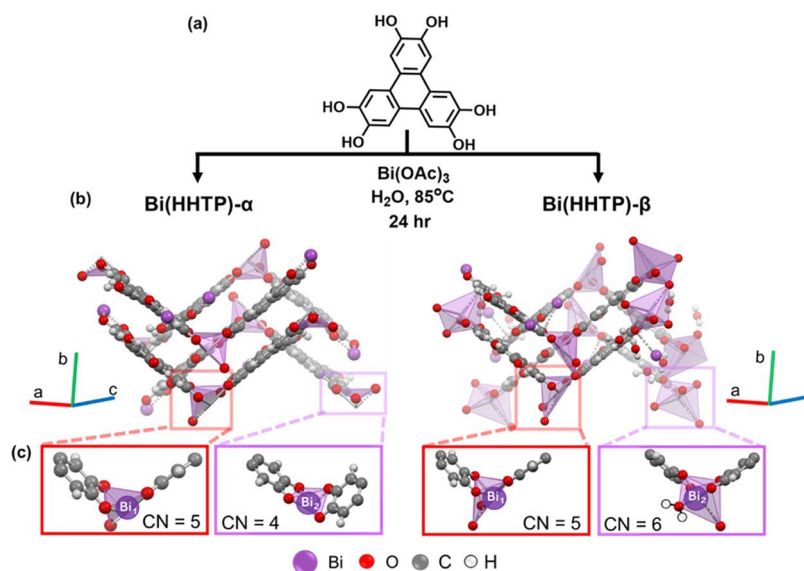


The unique nature of bismuth-based coordination networks allows for the tailoring of multiple useful and functional properties, such as charge delocalization,[45, 46] band gap, and direction of assembly, or

dimensionality through careful selection of organic ligands.[43] Several of these properties are highly desirable in the context of chemiresistive sensing. First, conductive CPs may be designed by selecting constituents that contain loosely held valence shell electrons and ligands that permit their efficient through-bond charge delocalization,[17, 43] allowing the integration of the semiconductive material into amperometric devices for chemical sensing. This charge delocalization has been well documented within both bismuth oxide lattices[47] and bismuth-based metal−organic coordination networks.[45, 46] Second, the flexible coordination geometry of bismuth provides control over dimensionality of the coordination network structure,[43] resulting in unique structure−property relationships through ligand modification strategies and through the choice of bismuth metal salt. Third, the structures of Bi(III)-containing compounds often present a vacant or flexible coordination site at the bismuth center, which may serve as an electron acceptor site.[40, 43] The coordination environment around the bismuth ion may undergo further interaction with analytes, thereby enabling selective chemical detection of analytes with a three-dimensional (3D) coordination sphere of bismuth accompanied by electronic transduction of signal. Capitalizing on these advantages can provide a path to control these functional properties in selective chemical sensing.

**Figure 6.2.** *(a) Experimental and simulated MicroED pXRD patterns of Bi(HHTP)-α and (b) corresponding (002), (20$\bar{2}$), (200), (10$\bar{2}$), and (32$\bar{1}$) crystalline planes and interatomic distances.*
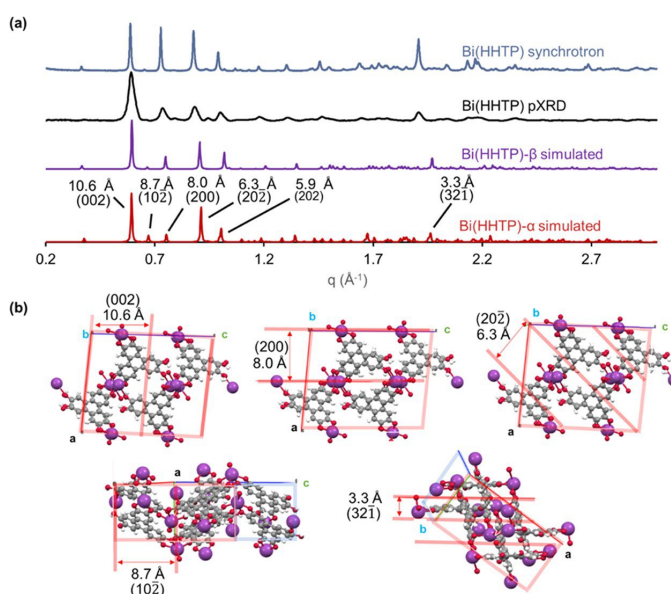
Our molecular design is inspired by previously reported literature of bismuth-based semiconductive coordination networks interconnected with triphenylene-based ligands.[46] The precedent set by Li *et al*. utilized hexakis(alkylthio)-triphenylene (alkyl: methyl, ethyl, and isopropyl) triphenylenes reacted with bismuth halides to produce semiconductive hybrid networks that featured flexible network dimensionalities and tunable electronic properties.[43] We reasoned that substituting the alkylthio substituents with hydroxy groups may promote similar coordination chemistry with bismuth ions while generating a material with good stability to water and air due to the robust nature of hydroxy-substituted triphenylenes and the strong nature of Bi−O bonds,[48] compared to their sulfur substituted analogues. The 2,3,6,7,10,11-hexahydroxytriphenylene (HHTP) ligand exhibits a large $\pi$-conjugated system and threefold symmetry (Figure 6.1) and has previously been reported to form conductive metal−organic frameworks using first-row transition metals[21, 23, 25] and lanthanides.[49]

A useful attribute of HHTP and HHTP-based MOFs is that they can undergo electron-transfer interactions that can be coupled to proton-transfer events.[50] This colocalized ability to interact with analyte protons and electrons using HHTP may provide an additional level of selectivity in sensing devices for protic guests. Despite the useful properties displayed by HHTP, CPs employing this ligand are unprecedented for metal complexes with bismuth. We aimed to achieve bottom-up assembly of a conductive CP that provides a three-dimensional (3D) ligand coordination environment around the metal center tailored for enhanced selectivity in response to specific gas-phase molecules. Thus, we subjected bismuth (III) acetate to aqueous reaction conditions and paired this node with a polyaromatic organic linker to observe a dark green microcrystalline powder. Bi(HHTP) exhibited distinct structural transformations upon dehydration and hydration of the pores within the network (here termed Bi(HHTP)-$\alpha$ and Bi- (HHTP)-$\beta$, respectively), likely driven by hydrogen-bonding interactions with the oxo groups on the ligand, which induced changes in the coordination environment of both bismuth centers and unit cell parameters. This type of dynamic flexibility, such as the slipping and/or expansion of the layers, has been previously investigated in 2D HHTP-based MOFs using quantum mechanical calculations.[51]

## 6.3 EXPERIMENTAL PROCEDURE

### 6.3.1 Synthesis and Characterization.

We used hydrothermal synthesis that combined $Bi(OAc)_3$ and HHTP to produce Bi(HHTP) (Figure 6.1). Reaction optimization procedures carried out after powder X-ray diffractometry (pXRD) analysis revealed the presence of residual starting material $Bi(OAc)_3$, when Bi(HHTP) was synthesized using a 2:1 molar ratio of Bi(OAc)3 and HHTP (see Figure E.5). This residual starting material can be removed with a purification procedure (overnight stirring in H2O at 50 °C) followed by subsequent washes with ethyl acetate (see Appendix E for details), or a Soxhlet extraction technique using ethyl acetate (only effective using small scale synthesis). Residual $Bi(OAc)_3$ starting material can be avoided altogether through the use of a stoichiometric 1:1 molar ratio of $Bi(OAc)_3$ and HHTP (see Appendix E). The resulting dark green/blue conductive, microcrystalline powder [Bi(HHTP)] was initially characterized using pXRD analysis (Figure 6.2), scanning and transmission electron microscopy (SEM and TEM, respectively), and elemental analysis. The experimental pXRD pattern of Bi(HHTP) exhibited a high-intensity peak in the low-angle range at 8.36° $2\theta$. This peak corresponds to an interatomic distance of 10.6 Å and the (002) plane, which bisects the unit cell of Bi(HHTP) (Figure 6.2).

Other major peaks appearing in the pXRD pattern included the $(10\bar{2})$, (200), $(20\bar{2})$, (202), and $(32\bar{1})$ planes, which were attributed to interatomic distances of 8.7, 8.0, 6.3, 5.9, and 3.3 Å using Bragg's law, respectively. The (002) and $(20\bar{2})$ planes intersected a section of one HHTP ligand when viewed along the crystallographic c-axis, while the (200) and the $(10\bar{2})$ planes intersected and ran parallel to the bismuth atoms (Figure 6.2b). The $(32\bar{1})$ crystalline plane runs parallel to the $\pi-\pi$ stacking distance and corresponds to an interatomic distance of 3.3 Å. We contribute the slight offset of the $(32\bar{1})$ peak to the limitations in resolution of microED and the highly disordered solvent present within the void space of the Bi(HHTP)-$\beta$ structure, which could have affected the layering of $\pi-\pi$ stacking planes. For higher-resolution crystal structure analysis, Bi(HHTP) material was analyzed using a synchrotron light source at Argonne National Laboratories (Beamline 11-BM) (Figure 6.2a).

**6.4 RESULTS AND DISCUSSION**

Morphological characterization of Bi(HHTP) via SEM analysis revealed rectangular-shaped crystallites of varying lengths (Figure 6.3a). TEM imaging, obtained after 1.0 mg of Bi(HHTP), was sonicated in acetone for 16 h and dropcasted onto a carbon grid, provided visualization of rectangular, sheetlike materials (Figure E.9). Further characterization of Bi(HHTP) using TEM analysis revealed the presence of a distinct crystallite with a length of ~2 μm (Figure 6.3b). Selected area diffraction analysis (SAED) on this crystallite showed well-ordered diffraction spots in reciprocal space (Figure 6.3c), which we used as a complementary method of measuring interatomic distances along diffraction planes. The distances between the diffraction spots were calculated according to the equation derived from Bragg's law (eq E.1). Two interatomic distances (3.3 and 6.3 Å) measured within the SAED nanocrystal were also present in the pXRD pattern (Figure 6.2). The 6.3 Å distance observed in the nanocrystal was slightly offset in the pXRD (6.6 Å) and likely corresponded to the $(20\bar{2})$ *hkl* plane, while the 3.3 Å interatomic distance corresponded to the $(32\bar{1})$ plane, which is parallel to $\pi-\pi$ stacking distances (Figure 6.2b).

***Figure 6.3***. *(a) Scanning electron micrograph (SEM), (b) transmission electron micrograph (TEM), and (c) selected area electron diffraction of Bi(HHTP).*
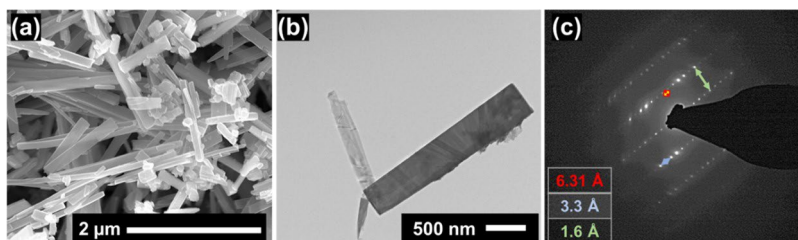


Although Bi(HHTP) displayed high crystallinity, efforts to grow a single crystal large enough for single-crystal X-ray diffraction (SCXRD) using methods such as slow evaporation, high pressure/temperature synthesis, and slow addition techniques were unsuccessful; thus, we focused our attention on microelectron diffraction (MicroED).[52] Although the MicroED method was popularized by structural biologists for the characterization of proteins, this technique has proven invaluable for the field

of small-molecule characterization,[52] and even more recently, the characterization of both coordination networks and MOFs.[53] MicroED enabled the structural characterization of Bi(HHTP) and permitted the correlation of the *hkl* planes in this structure to the ones observed in the experimental pXRD spectrum (Figure 6.2).

*Figure 6.4. (a) Bi(HHTP)-α and (b) Bi(HHTP)-β structure within one unit cell view down the crystallographic b-axis. (c) Inset of Bi(HHTP)-α depicting coordination environments Bi₁ (left) and Bi₂ (right). (d) Inset of Bi(HHTP)-β depicting a new coordination environment of Bi₁ (left) and Bi₂ (right) after hydration. (e) Space-filling model of Bi(HHTP)-α and (f) Bi(HHTP)-β*
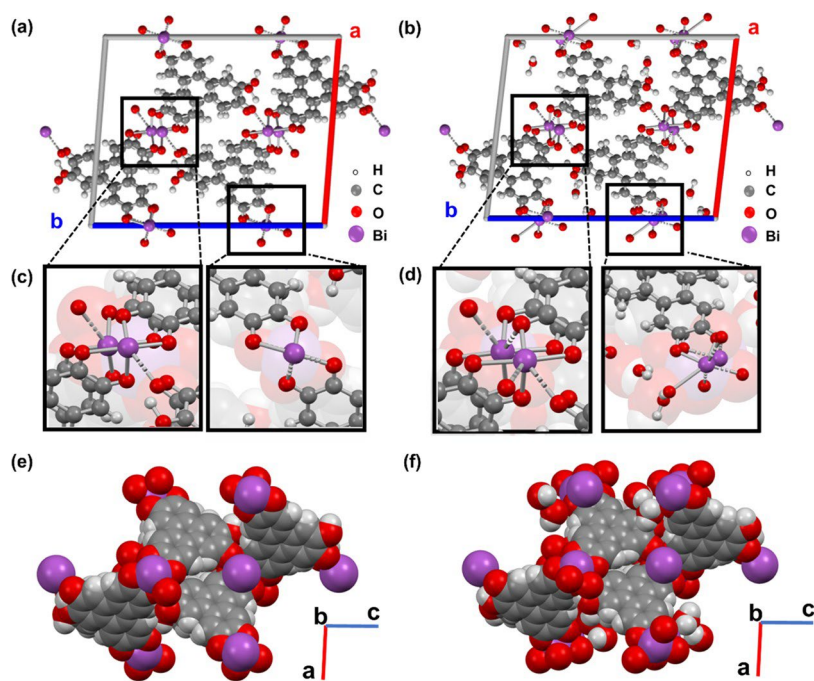


## 6.4.1 Analysis of Crystallographic Structure from MicroED.

For MicroED analysis, electron diffraction data was collected using a Talos F200C transmission electron microscope equipped with a Thermo-Fischer CetaD detector. To prepare sample grids (quantifoil or pure carbon TEM grids), a TEM grid was placed in a vial containing dry powder and gently shaken. Images were collected in a movie format as crystals were continuously rotated under a focused electron beam. Typical data collection was performed using a constant tilt rate of 0.3°/s between the minimum and

maximum tilt ranges of $-72°$ to $+72°$, respectively (see Appendix E for details). Structural characterization by MicroED revealed that Bi(HHTP) exhibited two distinct structural forms, Bi(HHTP)-$\alpha$ and Bi(HHTP)-$\beta$, respectively. Bi(HHTP)-$\alpha$ exhibited monoclinic ($\alpha$, $\gamma = 90°$, $\beta = 94°$) type Bravais lattice with symmetry group P2$_1$/$c$ and intricately connected layers (*vide infra*). Bi(HHTP)- $\beta$ displayed different cell parameters ($\alpha$, $\gamma = 90°$, $\beta = 97°$), occupied pores (likely water molecules from incomplete drying), and distinct coordination geometries, but the same symmetry group, P2$_1$/$c$ (Figure E.7). Pawley refinement was conducted using the crystallographic information file (cif) obtained from MicroED for Bi(HHTP)-$\alpha$, which provided unit cell parameters and presented a $R_{wp}$ of 7.07% and a $R$p of 12.54% (see Appendix E for details).

Topological analysis performed using a ToposPro program package[54, 55] and the Topological Types Database (TTD) collection of periodic networks was used to determine the network topology model in the coordination network (see Appendix E for details). The topological description includes a simplification procedure (graph theory approach), which was used to describe the crystal net topology and designate a 2,3-C4 topological type net for Bi(HHTP)-$\alpha$, which corresponds to this structure in its standard representation (Figure E.15). The cluster simplification procedure was also implemented to identify more complex building units of a structure and characterize their connection mode, where the fragments of Bi(HHTP)-$\alpha$ form infinite chains linked through Bi$-$O linkages (Figure E.19b) and exhibit rod packing with 2M4-1 topology and point symbol.[55]

The Bi(HHTP)-$\alpha$ sheet contains dimeric one-dimensional (1D) zigzagging chains of alternating nonplanar HHTP ligands that connect one 1D chain to another through the longest Bi$_1-$ O bond of 2.6 Å. These dimeric chains contain alternating uncoordinated semiquinone groups and stack in the crystallographic b-direction through $\pi-\pi$ stacking interactions. Binding interactions present inside one-dimensional chains connecting HHTP constituents are approximately 4.1 Å long. Both Bi(HHTP)-$\alpha$ and -$\beta$ adopt a herringbone-like packing motif, similar to HHTP (see Appendix E for details),[56] where bismuth ions cause distortions in the $\pi-\pi$ stacking of the matrix through catechol bidentate chelation and slight rotation within the coordination sphere. Compared to bismuth-based MOFs made using carboxylate ligands,

which exhibit Bi−O bond lengths ranging from 2.2 to 3.0 Å,[44] we observed a smaller array of bond lengths, 2.0−2.6 Å, commonly seen in bismuth catecholate coordination. The $\pi-\pi$ stacking distance in Bi(HHTP)-$\alpha$ was measured at 3.3 Å, which matches the interatomic distance obtained from diffraction peaks in pXRD. Bi(HHTP)-$\alpha$ displays two coordination environments (Figure 6.1c), distorted tetragonal pyramid (Bi$_2$) and distorted quadrilateral (Bi$_1$); the latter is similar to a dimeric bismuth(III) catecholate coordination complex involved in a five-coordination environment reported previously.[57] Bi(HHTP)-$\beta$ exhibited two distinct bismuth coordination spheres with six and five-coordinate environments; the former (Bi$_2$) contains an aqua ligand (Figure 6.4d). Specifically, the coordination polyhedra of Bi$_1$ and Bi$_2$ contain a distorted pentagonal pyramid (CN = 5) and distorted one-capped octahedron (CN = 6), respectively.

We hypothesize that Bi(HHTP)-$\beta$ hydrate was stabilized when water occupies the slit-like pores of the network (Figure 6.4b), altering unit cell parameters and permitting further interaction of each oxygen heteroatom in HHTP to neighboring layers. After hydration, bismuth-containing CN = 4 in Bi(HHTP)-$\alpha$ shifted from an eclipsed environment, with respect to other bismuth atoms in adjacent layers, to a staggered conformation due to oxygen now in proximity within the pores of Bi(HHTP)-$\beta$ (Figure 6.4). The presence of uncoordinated hydroxy groups facing inward within the pores (present in both structures) is likely further stabilized through hydrogen bonding (H-bonding) with the water molecules in Bi(HHTP)-$\beta$.

**6.4.2 Additional Physical and Chemical Characterization.**

*IR Analysis*. Attenuated total reflectance infrared spectroscopy (ATR-IR) of Bi(HHTP) revealed the presence of vibrational bands (Figure E.21) at 1420 and 1157 cm$^{-1}$, which are characteristic of catechol vibrational modes.[58] Because the vibrational modes strongly depend on atomic masses, heavy bismuth ions should present vibrational bands at lower frequencies (500−100 cm$^{-1}$). Thus, the appearance of new bands in this region may also be attributed to new Bi−O bond vibrational frequencies.

*Surface Area Analysis*. Structural characterization of the specific surface area of activated and degassed (at 85 °C and 635 Torr for 24 h) Bi(HHTP) using Brauner−Emmet−Teller (BET) analysis was

performed using $N_2$ adsorption−desorption isotherms, collected at 77 K on a Micromeritics 3FLEX instrument. Preliminary results indicated a surface area of 26.8 m$^2$ g$^{-1}$ (Figure E.22). The low surface area measured from BET analysis using nitrogen (probe radius of 1.8 Å) is reasonable when compared to the accessible solvent surface area calculated using Materials Studio software, where a probe radius of 1.2 Å calculated a surface area 101.6 Å$^2$ and a free volume of 22.62 Å$^3$ (Figure E.20).

**6.4.3 Elemental Composition.**

Elemental microanalysis and inductively coupled plasma mass spectrometry (ICP-MS) confirmed the elemental composition of Bi(HHTP) (Table E.2). The percent mass of carbon, hydrogen, and bismuth observed experimentally within the coordination network were 38.3, 1.51, and 33.1%, respectively. These values were closer in value to the percent mass theoretical calculations (39.0, 1.62, and 37.7%, respectively) based on the empirical formula of Bi(HHTP)-$\beta$ (($C_{36}H_{12}O_{12}$)$Bi_2$-2($H_2O$)), relative to the empirical formula for Bi(HHTP)-$\alpha$ (($C_{36}H_{12}O_{12}$)$Bi_2$), whose theoretical masses yielded values for carbon, hydrogen, and bismuth are 41.1, 1.51, and 39.4%, respectively. This comparison suggests the prevalence of the Bi(HHTP)-$\beta$ structure within the sample, although the percent volume ratio of the two structures may fluctuate depending on drying conditions and can be further investigated using systematic thermal gravimetric analysis (TGA) analysis or statistical microED techniques.

*Thermal Analysis*. The thermal gravimetric analysis (TGA) profile of Bi(HHTP) revealed a total of ~34% weight loss with the highest rate of decomposition occurring at 466 °C (Figure E.23). There was an initial mass loss of ~8% from 100 to 200°C, potentially due to the loss of volatile solvent molecules such as acetone or $H_2O$, which is consistent with the presence of Bi(HHTP)-$\beta$ or the hydration of the material. We observed a similar mass loss for Bi(OAc)$_3$ (38%) and a higher mass loss for the organic linker, HHTP (56%).

*Analysis of the Oxidation State*. X-ray photoelectron spectroscopy (XPS) enabled the analysis of bismuth in a low (3+) valence oxidation state through emission lines at binding energies of 160.1 and 165.3

eV, assigned to $Bi^{3+}$ $4f_{7/2}$ and Bi $4f_{5/2}$ (see Appendix E for details).[59] We were unable to fully deconvolute the region of the O 1s primary emission line present at 532 eV to assign C−O and C=O bonds, due to the likely presence of $H_2O$ both within the pores of the network and within the coordination sphere of Bi(HHTP)-$\beta$ creating uncertainty around the correct electronic state of the ligand. Based on the deconvoluted primary C 1s emission line (Figure E.25b) and considering the presence of $Bi^{3+}$, one possible oxidation state of the ligand to result in an overall neutral coordination network is a bis-semiquinone catechol state (sq, sq, cat) to generate $Bi^{3+}$ within the network (Figure E.25d). The C 1s spectra were consistent with this oxidation state, as they present C−O, C=O, and C−OH bonds in 2:2.6:1 ratio. Another possibility that renders a neutral framework is that bismuth atoms within the network are in a ratio of $Bi^{3+}/Bi^{2+}$ oxidation state. These two oxidation states of HHTP generate an alternating (sq, sq, sq) and (sq, sq, cat) state (Figure E.26b,c) and would generate a −2.5-overall charge on the ligand. This network structure would also create a radical ion on HHTP, which is plausibly what we are observing in electron paramagnetic resonance (EPR) spectroscopy (see Appendix E).

*Electronic Properties*. Conductivity measurements of Bi-(HHTP) were performed using a four-point probe technique, which required 100 mg of material pressed into 6 mm diameter pellet of 0.2 mm thickness. Bi(HHTP) showed a bulk conductivity of $5.3 \times 10^{-3}$ S·cm$^{-1}$ (see Appendix E eq E.2). Pellets of the precursors Bi(OAc)$_3$ and HHTP exhibited no measurable conductivity using a two-point probe digital multimeter (Extech EX430 series), which had a maximum resistance limit of measurement at 40 MΩ.

To investigate the Arrhenius activation energy for electrical conductivity of Bi(HHTP), a two-point probe on a 50 mg pressed pellet was employed to collect the current change under different temperatures (25−110 °C) with a linear sweep voltage from −2.0 to 2.0 V (Figure E.24). The activation energy determined by this method was 425 meV. The optical band gap was determined by plotting the absorbance squared vs energy (eV) and estimated to be 1.61 eV based on the value of the absorption edge (Figure E.28). Density functional theory (DFT) calculations were performed on the simulated structure of Bi(HHTP) using functional Perdew−Burke−Ernzerhof (PBE) and generalized gradient approximation (GGA)

approximations (Figure E.29). The high symmetry points in the first Brillouin zone demonstrated that the Dirac bands approached the Fermi level through the Y-A and E-C (crystallographic c) directions, where a low band gap of approximately 0.1 eV was observed for Bi(HHTP)-$\alpha$ and 0.08 eV for Bi(HHTP)-$\beta$. The partial density of states analysis showed that, compared with bismuth, the p orbitals from the C and O atoms contribute significantly to the Dirac bands.

*Chemiresistive Gas Sensing*. We hypothesized that Bi-(HHTP) would be a promising chemiresistive sensing material due to its flexible coordination sphere around the bismuth metal center, which may act as a potential binding site and accommodate gaseous probes, causing a direct perturbation of the charge transport with the semiconductive network. There is also the presence of free, uncoordinated hydroxy groups in both Bi(HHTP)-$\alpha$ and Bi(HHTP)-$\beta$ that can promote H-bonding interactions in the vicinity of the bismuth atom. To characterize the fundamental ability of Bi(HHTP) to sense small reactive gases through electronic doping interactions, we examined the chemiresistive responses of Bi(HHTP) toward both oxidizing (NO) and reducing ($NH_3$) gaseous analytes. To further probe Bi(HHTP)'s capacity to detect analytes through a combination of electronic doping and H-bonding interactions, we also examined the response of Bi(HHTP) toward a range of H-bond donors (MeOH, EtOH, iPrOH) and H-bond acceptors (acetone).

To carry out the sensing procedure, we dropcasted 10 $\mu$L of a Bi(HHTP) suspension (1−2 mg/mL in $H_2O$) onto five devices containing interdigitated 10 $\mu$m gap gold electrodes, which generated devices with resistances in ~30 M$\Omega$ range (see Appendix E for details). Since the suspension of Bi(HHTP) used for device fabrication was sonicated in $H_2O$ and dried 16 h in ambient air, we hypothesize that the Bi(HHTP)-$\beta$ structure was the dominant form within the devices. Furthermore, due to the similar band gaps of the $\alpha$ and $\beta$ structures (Figure E.29) and simulated XRD patterns (Figure 6.2a), we do not believe that the differences in the structures could lead to considerable differences in chemiresistive response. The devices were dried overnight in ambient air and then placed into an edge connector, wired to a breadboard and potentiostat (PalmSens) that applied 1.0 V voltage at room temperature. The devices were then enclosed

in a Teflon chamber with gas inlet/outlet ports connected to Smart-Trak mass flow controllers delivering target concentrations of gases from premixed tanks purchased from AirGas (tanks of 10,000 ppm of $NH_3$ in $N_2$ and 10,000 ppm of NO in $N_2$). The concentrations of gaseous analytes were modified by adjusting flow rates ($N_2$ as the balance/purging gas). Generally, five devices at a time were exposed to each gas at different concentrations (5−1000 ppm) of the chosen analyte at a $N_2$ flow rate of 0.5 L/min and then purged with dry $N_2$ to examine Bi(HHTP)'s recovery.

**Figure 6.5**. *(a) Chemiresistive responses of devices integrated with Bi(HHTP) under an applied voltage of 1.0 V and an atmosphere of dry nitrogen to 15 min of exposure to (a) $NH_3$ and (b) NO at 40, 20, 10, and 5 ppm. (c) Plot of concentration vs normalized change in conductance ($-\Delta G/G_o$). (d) Initial rate of response as a function of concentration during the first minute of exposure across two gases (NO and $NH_3$). Error bars represent standard deviations from the mean of responses from three devices.*
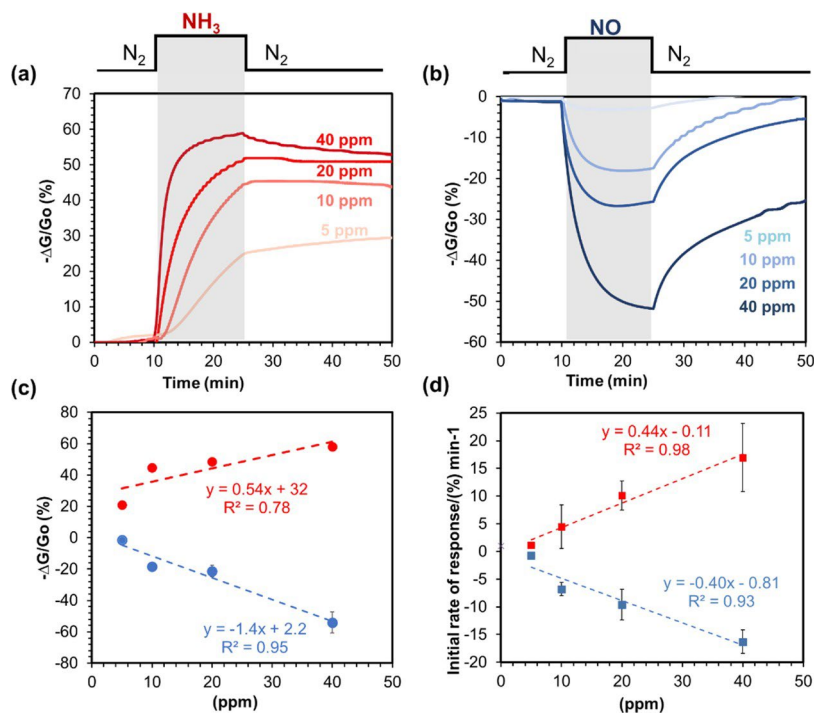


For volatile organic compound (VOC) sensing, a Kintek FlexStream gas generator was used to produce vapors of the analyte (EtOH, MeOH, acetone, or iPrOH), which was diluted in $N_2$ (4 L/min) to the desired concentration. Each organic vapor was calibrated before use in the generator by heating the internal

permeation glass chamber/tube, loading a vial of the desired VOC inside the tube and setting the span flow rate at for $N_2$ at 4 L/min (see Appendix E). Notably, we observed that altering flow rates between analytes affects the response of the material, where higher flow rates are used to deliver lower concentrations; thus, we chose to keep the flow rate constant and vary the rate of evaporation of the analyte through the control temperature within the vapor generator to acquire concentration-dependent experiments (eq E.10). In all sensing measurements, the devices were kept at ambient temperature.

**Figure 6.6**. (a) Chemiresistive response of Bi(HHTP) to varying concentrations of acetone (blue) and ethanol (orange) collected at temperatures 25−45 °C. (b) Plot of concentration vs normalized change in conductance (−ΔG/G$_o$) for exposures to acetone and EtOH. (c) Chemiresistive response of Bi(HHTP) to varying concentrations of MeOH (purple) and iPrOH (green) collected at temperatures 25−45 °C. (d) Plot of concentration vs normalized change in conductance (−ΔG/G$_o$) for exposures to MeOH and iPrOH. Error bars represent standard deviations from the mean of responses from three devices.
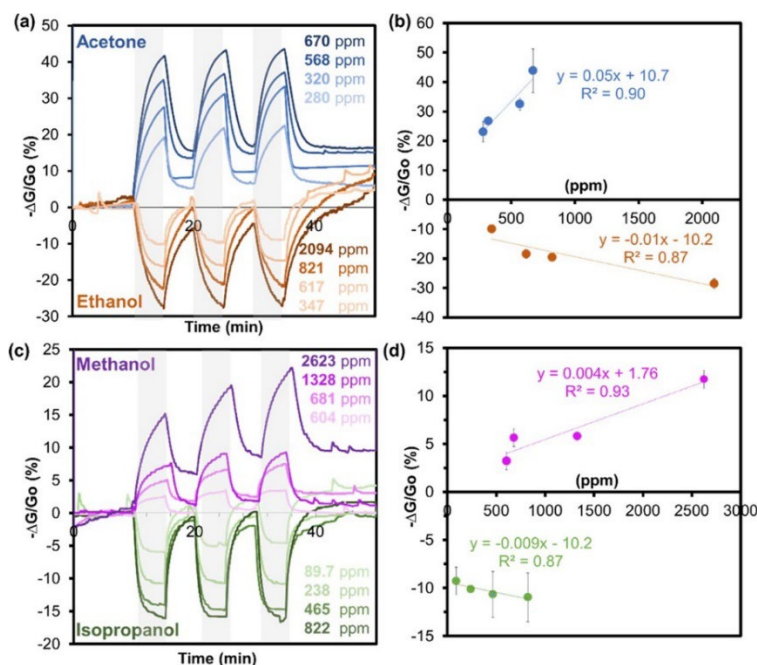


*Chemiresistive Sensing Response*. Although many examples of MOF-based sensors exist, to the best of our knowledge, this report constitutes the first example of bismuth-based CP chemiresistive sensing.

The favorable semiconductive nature of Bi(HHTP) facilitated the integration of Bi(HHTP) into devices through dropcasting to examine the chemiresistive response of Bi(HHTP) to the four VOCs (acetone, EtOH, MeOH, and iPrOH) and 40, 20, 10, and 5 ppm of NO and $NH_3$. Bi(HHTP) exhibited a decrease in conductivity to the reducing gas ($NH_3$) and an increase in conductivity to the oxidizing gas NO (Figure 6.5). Upon exposure to 40 ppm of NO, Bi(HHTP) showed a normalized response ($-\Delta G/G_o$) of $-54.8 \pm 6\%$ after 15 min of exposure with excellent reversibility. Also, upon exposure to 40 ppm of $NH_3$, Bi(HHTP) showed a normalized response ($-\Delta G/G_o$) of $58.4 \pm 2\%$ after the first 15 min of exposure. The observed chemiresistive responses to both oxidizing and reducing gases are thus consistent with the response of a p-type semiconductor.[60] We also examined the response of Bi(HHTP) to NO and $NH_3$ in the presence of humidity (5000 ppm of $H_2O$, Figures E.40 and E.41). We observed a significant decrease in response in the presence of humidity (from $-34.4 \pm 3.2$ to $-19.9 \pm 0.76\%$ $-\Delta G/G_o$) when sensing NO and a considerable increase in response for $NH_3$ (from $39.6 \pm 7.0$ to $-81.8 \pm 7.3\%$ $-\Delta G/G_o$) in the same concentration of $H_2O$. These results may point to the importance of the presence of H-bonding in the sensing mechanism of $NH_3$.

Bi(HHTP) devices exhibited unique chemiresistive responses toward VOCs that changed in the direction of normalized conductance depending on the analyte (Figure 6.6). Both MeOH and acetone displayed an increase in normalized conductance ($-\Delta G/G_o$) upon exposure, while EtOH and iPrOH demonstrated a decrease in normalized conductance ($-\Delta G/G_o$) upon exposure to specific concentrations of the analyte. All exposures to the VOCs were observed to be reversible. To better understand the responses and H-bonding interactions of Bi(HHTP) with the four VOCs, we compared the $pK_a$ values, dipole moment, and dielectric constants of each compound (Table E.5). The $pK_a$ values of the VOCs increase from MeOH to acetone. While EtOH and iPrOH have similar dipole moments (1.66D), MeOH and acetone have higher dipole moments. Other considerations include the dielectric constants ($\varepsilon$), which decrease down the line from methanol, ethanol, isopropanol, and all the way to the lowest value, acetone. The combination of these electronic and structural properties may explain the observations noted during sensing of VOCs. Furthermore, the presence of water molecules in the pores of Bi(HHTP)-$\beta$, as demonstrated by MicroED,

may compete as host sites for H-bonding with VOCs. Thus, sensing responses to VOCs may have contributions from two competing mechanisms: one involving Lewis acid and base interactions, and another one involving Brønsted acid or H-bonding interactions with the surface of Bi(HHTP), which we further investigated using several spectroscopic techniques (*vide infra*). *I−V* curves of Bi(HHTP) during exposure to 1000 ppm of EtOH vapor suggested Ohmic contacts after saturation, excluding the possibility of Schottky barrier modulation mechanism during the sensing of VOCs (Figure E.39).

Limits of Detection. To examine the limits of detection (LODs), we focused our attention on two representative biomarkers that are known to be common breath metabolites,[61] acetone and EtOH (*vide infra*). We varied the concentration of these VOCs by increasing the temperature of the chamber housing the analyte from 25 to 40 °C and recorded three sequential exposures (Figure 6.6). Bi(HHTP) had an average response of $43.8 \pm 7\%$ to 670 ppm of acetone after averaging across three devices exposed for 5 min and recovered in $N_2$ for 5 min, sequentially. To 2094 ppm of EtOH, Bi(HHTP) has an average response of $-28.5 \pm 2\%$.

To determine the LODs in response to NO and $NH_3$, we calculated the change in response of Bi(HHTP) upon 15 min of exposure toward NO at different concentrations (5−40 ppm) (for full calculation, see Appendix E, eqs E.7−E.9). The theoretical LODs, calculated based on the response after 15 min of exposure to either NO or $NH_3$ (5−40 ppm), were 0.15 and 0.29 ppm, respectively. These LOD values are comparable to $M_3(HXTP)_2$-based systems,[21, 25-28] but do not exceed previously reported MPc-based 2D framework sensitivity to NO.[22] Here, however, Bi(HHTP) displays a unique reversibility to low concentrations of NO (and partial reversibility to concentrations above 20 ppm), as observed by sensing and pXRD experiments (Figures 6.7 and E.53, respectively), that is not observed in either of these previous systems. These reversible sensing characteristics can be particularly advantageous for nanomaterial-based sensors that can be fabricated to withstand repeated exposures to NO for an enhanced long-term durability. For VOCs, the LOD values were 41.2 ppm for acetone, 278 ppm for MeOH, 50.2 ppm for iPrOH, and 185 ppm for EtOH. These values are similar to other reported chemiresistive values for alcohol sensors

fabricated from metal oxides or reduced graphene oxides.[62] Furthermore, the system we present allows for differentiation between analytes based on the direction of response using a single conductive network. These sensing responses to four VOCs using one conductive network have not been previously observed in chemiresistive sensing. Previously, an array of 2D MOFs was required to distinguish between similar analytes (e.g., MeOH and iPrOH).[19] The unique responses seen in Bi(HHTP) may arise from the interaction of these analytes within the bismuth coordination sphere, offering an exclusive advantage over 2D systems with lower-coordinate metal nodes.

*Studies of the Sensing Mechanism with NO and NH3 Using MicroED, XPS, EPR, ATR-IR, and Diffuse Reflectance Infrared Fourier Transform Spectroscopy (DRIFTS)*. We first used MicroED to elucidate structural or electronic density changes in Bi(HHTP) induced upon exposure to NO and $NH_3$ (exposed for 1 h at high concentration, 10,000 ppm or 1% of analyte in $N_2$). MicroED confirmed that the coordination network maintained its crystallinity, network topology, and space group upon exposure to the gases (Figures E.51 and E.52). Gas exposure did, however, induce a slight expansion in unit cell parameters (cell length $\alpha$ and angle $\beta$) for both structures of Bi(HHTP) (Figure E.51). We hypothesize that this change may have been induced by either occupation of the pores within the coordination network or through structural changes induced by analyte interaction with the host sites within the network. To confirm these structural changes induced by analyte exposure, we utilized pXRD analysis on samples before and after 1 h exposure to 10,000 ppm of $NH_3$ and NO (Figures E.52 and E.53, respectively). After $NH_3$ exposure, Bi(HHTP) exhibited a significant shift in the peak corresponding to the $(32\bar{1})$ plane. This plane runs parallel to $\pi-\pi$ stacking layers, which suggests that $NH_3$ exposure may be increasing the distances between these planes. This change could result from $NH_3$ occupying the available void volumes within Bi(HHTP) and on the edge sites of the structure, causing the expansion and increase in spacing of these layers. After recovery in $N_2$ for 2 h, this shift did not return to its original position, consistent with our observations in sensing that $NH_3$ induces dosimetric response Bi(HHTP). For NO exposure, we observed a slight shift in the (002), (200), $(20\bar{2})$, and $(32\bar{1})$ planes. These peak shifts partially recover after a 2 h $N_2$ exposure, which is

consistent with our observation in sensing that response to NO is partially reversible at concentrations above 20 ppm. These slight deviations in peak position could also indicate NO occupying the available volume within the pores of Bi(HHTP), which is feasible considering the bond length of N−O (1.15 Å), causing increases in distances between Bragg planes.

To gain deeper insight into the changes to the surface chemistry, oxidation states of constituents of Bi(HHTP), and material−analyte interactions, we used X-ray photoelectron spectroscopy (XPS), electron paramagnetic resonance (EPR), DRIFTS, and ATR-IR spectroscopy. XPS was used to confirm the elemental composition of Bi(HHTP), as well as identify chemical shifts typically associated with changes in the population of electronic states. EPR allowed the observation of the effective analyte binding on the location and population of unpaired spins and/or changes in the oxidation state of metal and ligand constituents within the bulk material.[24] In turn, IR techniques provided complementary details regarding the nature of the material−analyte interactions based on changes in the vibrational modes of the participating species.

*Figure 6.7. X-ray photoelectron spectroscopy of the (a) Bi 4f$_{7/2}$ and the Bi 4f$_{5/2}$ region of Bi(HHTP) of pristine and dosed with NH$_3$ and (b) the Bi 4f$_{7/2}$ and the Bi 4f$_{5/2}$ region of Bi(HHTP) of pristine and dosed with NO.*
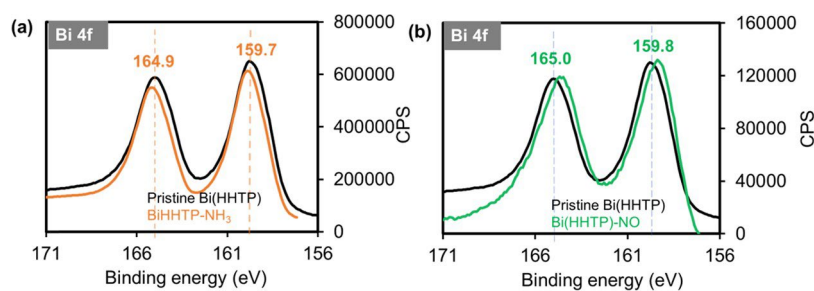


XPS comparative analysis (carried out at $10^{-9}$ Torr) was used to analyze the composition of Bi(HHTP) in its pristine state and after exposure to NO and NH$_3$. First, a pristine sample of Bi(HHTP) was purged for 1 h with N$_2$, while another batch was saturated with NO or NH$_3$ (1%, 10,000 ppm) for 1 h and sealed (left for over 24 h as samples were shipped out for analysis, see Appendix E for details). High-

resolution deconvoluted spectra of the C 1s emission line after NO dosing revealed an increase in the peak area assigned to the C−O---Bi binding energy and decrease in the peak area corresponding to the C=O---Bi binding energy (Figure E.47b), which supports the hypothesis that the interaction is occurring within the network causing a shift in the chemical environment near the semiquinone/catecholate region. Although not further oxidized, the deconvoluted region of Bi $4f_{7/2}$ and Bi $4f_{5/2}$ in the NO-doped Bi(HHTP) displayed a slight shift toward lower binding energies (Figure 6.7d). This shift may be attributed to electron density transferring from the ligand or bismuth node to NO, causing higher conductivities, less charging, and thus lower binding energies of less tightly bound emitted electrons. We attribute the observations during XPS analysis to be applicable only to the irreversible chemiresistive response to NO. For $NH_3$ exposure, the C 1s region displayed a slight increase in the area corresponding to the C=O---Bi bond (Figure E.47c), and in the region corresponding to the C−O---Bi bond. We also observed the presence of a new N 1s peak corresponding to the presence of nitrogen on $NH_3$ adsorbed within the network (Figure E.47f). Taken together, XPS data point to significant electronic perturbations near the bismuth metal node, possibly at the catechol region of the ligand after NO/$NH_3$ analyte exposure.

To complement the understanding of material−analyte interactions by XPS and EPR, we employed DRIFTS. Difference spectra were collected upon exposure to 10,000 ppm of each gaseous analyte. After exposure to NO, the presence of negative-going bands at 1255, 860, and 800 $cm^{-1}$ were attributed to the alteration of bismuth-catechol bonding and supported additional spectroscopic data acquired through ATR-IR (Figure E.45) of NO interacting at or near the bismuth center, possibly resulting in oxidative damage to the network. After exposure of pristine Bi(HHTP) to 10,000 ppm $NH_3$ followed by purging with $N_2$, positive bands remained at 1250 and 1565 $cm^{-1}$, which suggested possible chemisorbed $NH_3$ species interacting with Lewis Acid Site (LAS) within the network. Exposure to $NH_3$ caused the appearance of negative going $v$(OH) and $\delta$(HOH) bands indicating interactions with or removal of water within the network. Furthermore, we observed varying degrees of reversibility for Bi(HHTP) toward these gaseous analytes; which was quantified by the recovery to the background absorbance after exposure to an analyte and purge with $N_2$

gas (Figures E.59 and E.60). Bi(HHTP) demonstrated moderate reversibility toward NH$_3$ and no reversibility toward NO at this concentration. This concentration-dependent reversibility for NO-related DRIFTS experiments observed with 10,000 ppm may reflect a different mechanism of sensing and/or active sites at high ppm concentrations of NO compared to low ppm concentrations of NO used for chemiresistive measurements. This possibility appears to be consistent with chemiresistive measurements, which showed decreasing reversibility of response with increasing concentrations of NO. Interestingly, NH$_3$ DRIFTS experiments demonstrated negative-going bands corresponding to either dehydration of the network or disruption of H-bonding within the network; this negative-going water-related response could be related to a decrease in conductivity for NH$_3$ sensing experiments, which would be commensurate with electron donation (i.e., NH$_3$ adsorbing to LAS and Brønsted acid sites [BAS]) onto a p-type semiconductor.

EPR spectroscopy was collected at room temperature in the solid state. EPR analysis of the pristine Bi(HHTP) material displayed a broad absorbance band with low-intensity centered at g = 2.000, which indicated that unpaired electron density resided primarily in a ligand-centered orbital or possibly located on adsorbed oxygen molecules. A slight increase in the intensity of the resonant absorbance was observed when the sample was exposed to NO (10,000 ppm for 1 h, Figure E.48). This increase in absorbance was also observed for NH$_3$-exposed Bi(HHTP) (10,000 ppm for 1 h, Figure E.48). The exposure to NH$_3$ also resulted in a shift of the g-value to g = 1.991. This result suggests that NH$_3$ induced a slight change in the coordination sphere around the EPR active center, consistent with what is observed at the bismuth site in XPS.

To summarize, XPS and both methods of the infrared analysis indicated that exposure of Bi(HHTP) to NO and NH$_3$ yielded a significant variation in the electronic state of the ligand and bismuth node. Although the bismuth center was not formally oxidized beyond its pristine state, a shift of the Bi 4f$_{7/2}$ and the Bi 4f$_{5/2}$ emission lines by XPS analysis indicated a change in electron density surrounding the bismuth node. Due to the strong binding of the analyte NH$_3$ within the network, we were able to observe the presence of a N 1s peak in the XPS spectrum (Figure E.46f). For NO and NH$_3$, we also observed possible LAS and

hydrogen-bonding interactions that were likely accompanied by charge-transfer interactions with the network. DRIFTS experiments for VOC analytes revealed LAS and hydrogen-bonding interactions, with possible protonation/dehydration events occurring within the network. Furthermore, in our DRIFTS experiments, we observed a strong general correlation between negative/positive going water bands for all VOCs and the direction of chemiresistive response. This observation again may point to the importance of H-bonding interactions (either through BAS interactions or change in structural conformations) when considering the mechanism of sensing.

### 6.4.4 Mechanistic Studies with VOCs Using DRIFTS.

Because the VOC analytes in this work showed highly reversible interactions with Bi(HHTP), ex situ analysis by MicroED, XPS, and EPR proved less informative in this context. As such, we turned our attention to the in situ characterization of host−guest interactions between analytes and the coordination network using DRIFTS. This method enabled in situ IR analysis of the solid-state material, while simultaneously permitting analyte exposure, aiding in the elucidation of host−guest interactions (Figures E.55−E.58). Gas delivery for in situ DRIFTS analysis was handled with a custom-made manifold allowing delivery of vacuum, gas analytes, VOCs, and pure $N_2$ to purge samples. We observed varying degrees of reversibility for Bi(HHTP) toward VOC analytes; this reversibility was quantified by the recovery to the background absorbance after exposure to an analyte and purge with vacuum. Difference experiments revealed four distinct spectroscopic signatures of VOCs interacting with the network. First, exposure to acetone and EtOH produced negative-going Bi(HHTP) bands within the fingerprint region of the IR spectrum, whereas MeOH and iPrOH did not. Second, negative-going bands corresponding to either dehydration of the network or disruption of hydrogen bonding within the network resulted from exposure to acetone and MeOH. These bands were present in the characteristic water regions (3000 and 1600 cm$^{-1}$). Third, all of the VOCs were characterized to interact with the network at LAS, most likely at available bismuth sites. Fourth, the background absorbance of Bi-(HHTP) demonstrated high reversibility toward iPrOH and EtOH, moderate reversibility toward MeOH, and partial reversibility toward acetone. These

experiments demonstrated that both steric properties of the VOCs (e.g., MeOH versus EtOH) as well as the protic nature of the VOCs (e.g., iPrOH versus acetone) played significant roles in guiding the host−guest interactions at the network interface. We hypothesized that exposure to both MeOH and acetone would result in the depletion of charge carriers (holes) through either electron transfer, H-bonding, or proton-coupled electron-transfer interactions. Bi(HHTP)-$\beta$ contained water both within the pores and within the coordination sphere of the bismuth nodes; thus, another possible explanation for the observed sensing responses may be two VOCs interacting through different mechanisms of H-bonding to water molecules and displacing their positions within the pores, triggering a structural change that promotes the mobility of charge carriers within the network. Future studies in transistor device architectures may help clarify the details of material−VOC interactions.

## 6.5 CONCLUSIONS

This report constitutes the first demonstration of a bismuth-based coordination polymer toward chemiresistive sensing. To the best of our knowledge, Bi(HHTP) is among the first HHTP-based network structures solved using electron diffraction techniques.[63] Bi(HHTP) consisted of polyaromatic HHTP ligands interconnected with bismuth metal nodes and exhibited an unprecedented network topology with intricately connected layers, along with good electrical conductivity ($5.3 \times 10^{-3}$ S·cm$^{-1}$), when compared to other HHTP-based 2D MOFs.[25] Bi(HHTP) can be synthesized at room temperature with environmentally friendly aqueous conditions using a nontoxic metal and relatively inexpensive starting materials. Compared to other reported bismuth-based MOFs that are commonly linked using polyaromatic carboxylate linkers and secondary-building units that exhibit larger pore apertures, Bi(HHTP) adopts a herringbone-like packing (similar to HHTP packing) with slit-shaped pores. We demonstrate the utility of this material toward chemical sensing of NO and NH$_3$ with limits of detection of 0.15 and 0.29 ppm respectively, low driving voltages (0.1−1.0 V), and operation at room temperature. The LOD values for NO and NH$_3$ are like those reported using first-row transition-metal HHTP-based 2D MOF sensors[21, 23] and rival that of 2D MOFs made using layer-by-layer liquid-phase epitaxial techniques.[27] Bi(HHTP) is not as sensitive as MPc-

based 2D MOFs in response to NO (Table E.4).[18, 20, 22] What is particularly noteworthy is that Bi(HHTP) has a unique, promising selective and reversible response toward NO at concentrations of 20 ppm and below. Although reversible NO binding has been demonstrated in other MOF systems,[64] it has not been observed in chemiresistive sensing using conductive coordination networks. Current limitations of Bi(HHTP) in the context of chemiresistive sensing may be centered on the limited control over the spatial orientation on the surfaces of devices and the thickness of the film may be resolved in the future through further optimization. We also demonstrate the utility of Bi(HHTP) toward sensing four structurally analogous VOCs (acetone, MeOH, EtOH, and iPrOH) to exhibit unique and reversible responses.

## 6.6 REFERENCES

(1) Snyder, E. G.; Watkins, T. H.; Solomon, P. A.; Thoma, E. D.; Williams, R. W.; Hagler, G. S. W.; Shelow, D.; Hindin, D. A.; Kilaru, V. J.; Preuss, P. W. The Changing Paradigm of Air Pollution Monitoring. *Environmental Science & Technology* **2013**, *47* (20), 11369-11377.

(2) Baron, R.; Saffell, J. Amperometric Gas Sensors as a Low Cost Emerging Technology Platform for Air Quality Monitoring Applications: A Review. *Acs Sensors* **2017**, *2* (11), 1553-1566.

(3) Ishihara, S.; Azzarelli, J. M.; Krikorian, M.; Swager, T. M. Ultratrace Detection of Toxic Chemicals: Triggered Disassembly of Supramolecular Nanotube Wrappers. *Journal of the American Chemical Society* **2016**, *138* (26), 8221-8227.

(4) Ling, C. W.; Xian, X. J.; Qin, X. C.; Wang, D.; Tsow, F.; Forzani, E.; Tao, N. J. High Performance Colorimetric Carbon Monoxide Sensor for Continuous Personal Exposure Monitoring. *Acs Sensors* **2018**, *3* (2), 327-333.

(5) Yoo, D. K.; Woo, H. C.; Jhung, S. H. Effective removal of particulate matter from air by using zeolite coated filters. *Journal of Materials Chemistry A* **2020**, *8* (35), 17960-17968.

(6) Konvalina, G.; Haick, H. Sensors for Breath Testing: From Nanomaterials to Comprehensive Disease Detection. *Accounts of Chemical Research* **2014**, *47* (1), 66-76.

(7) Ren, F.; Pearton, S. J. *Semiconductor device-based sensors for gas, chemical, and biomedical applications*; CRC Press, 2011.

(8) Otagawa, T.; Madou, M.; Wing, S.; Richalexander, J.; Kusanagi, S.; Fujioka, T.; Yasuda, A. PLANAR MICROELECTROCHEMICAL CARBON-MONOXIDE SENSORS. *Sensors and Actuators B Chemical* **1990**, *1* (1-6), 319-325.

(9) Wang, C. X.; Yin, L. W.; Zhang, L. Y.; Xiang, D.; Gao, R. Metal Oxide Gas Sensors: Sensitivity and Influencing Factors. *Sensors* **2010**, *10* (3), 2088-2106.

(10) Schroeder, V.; Savagatrup, S.; He, M.; Ling, S. B.; Swager, T. M. Carbon Nanotube Chemical Sensors. *Chemical Reviews* **2019**, *119* (1), 599-663.

(11) Yavari, F.; Koratkar, N. Graphene-Based Chemical Sensors. *Journal of Physical Chemistry Letters* **2012**, *3* (13), 1746-1753.

(12) Choi, J. H.; Lee, J.; Byeon, M.; Hong, T. E.; Park, H.; Lee, C. Y. Graphene-Based Gas Sensors with High Sensitivity and Minimal Sensor-to-Sensor Variation. *Acs Applied Nano Materials* **2020**, *3* (3), 2257-2265.

(13) Chen, J. Q.; Chen, Z.; Boussaid, F.; Zhang, D. Q.; Pan, X. F.; Zhao, H. J.; Bermak, A.; Tsui, C. Y.; Wang, X. R.; Fan, Z. Y. Ultra-Low-Power Smart Electronic Nose System Based on Three Dimensional Tin Oxide Nanotube Arrays. *Acs Nano* **2018**, *12* (6), 6079-6088.

(14) Zhang, M. L.; Yuan, Z. H.; Song, J. P.; Zheng, C. Improvement and mechanism for the fast response of a Pt/TiO2 gas sensor. *Sensors and Actuators B-Chemical* **2010**, *148* (1), 87-92.

(15) Jian, Y. Y.; Hu, W. W.; Zhao, Z. H.; Cheng, P. F.; Haick, H.; Yao, M. S.; Wu, W. W. Gas Sensors Based on Chemi-Resistive Hybrid Functional Nanomaterials. *Nano-Micro Letters* **2020**, *12* (1).

(16) Xie, L. S.; Skorupskii, G.; Dinca, M. Electrically Conductive Metal-Organic Frameworks. *Chemical Reviews* **2020**, *120* (16), 8536-8580.

(17) Givaja, G.; Amo-Ochoa, P.; Gomez-Garcia, C. J.; Zamora, F. Electrical conductive coordination polymers. *Chemical Society Reviews* **2012**, *41* (1), 115-147.

(18) Meng, Z.; Aykanat, A.; Mirica, K. A. Welding Metallophthalocyanines into Bimetallic Molecular Meshes for Ultrasensitive, Low-Power Chemiresistive Detection of Gases. *Journal of the American Chemical Society* **2019**, *141* (5), 2046-2053.

(19) Campbell, M. G.; Liu, S. F.; Swager, T. M.; Dinca, M. Chemiresistive Sensor Arrays from Conductive 2D Metal-Organic Frameworks. *Journal of the American Chemical Society* **2015**, *137* (43), 13780-13783.

(20) Aykanat, A.; Meng, Z.; Benedetto, G.; Mirica, K. A. Molecular Engineering of Multifunctional Metallophthalocyanine-Containing Framework Materials. *Chemistry of Materials* **2020**, *32* (13), 5372-5409.

(21) Ko, M.; Aykanat, A.; Smith, M. K.; Mirica, K. A. Drawing Sensors with Ball-Milled Blends of Metal Organic Frameworks and Graphite. *Sensors* **2017**, *17* (10).

(22) Meng, Z.; Stolz, R. M.; Mirica, K. A. Two-Dimensional Chemiresistive Covalent Organic Framework with High Intrinsic Conductivity. *Journal of the American Chemical Society* **2019**, *141* (30), 11929-11937.

(23) Smith, M. K.; Mirica, K. A. Self-Organized Frameworks on Textiles (SOFT): Conductive Fabrics for Simultaneous Sensing, Capture, and Filtration of Gases. *Journal of the American Chemical Society* **2017**, *139* (46), 16759-16767.

(24) Stolz, R. M.; Mahdavi-Shakib, A.; Frederick, B. G.; Mirica, K. A. Host-Guest Interactions and Redox Activity in Layered Conductive Metal-Organic Frameworks. *Chemistry of Materials* **2020**, *32* (18), 7639-7652.

(25) Ko, M.; Mendecki, L.; Mirica, K. A. Conductive two-dimensional metal-organic frameworks as multifunctional materials. *Chemical Communications* **2018**, *54* (57), 7873-7891.

(26) Yao, M. S.; Lv, X. J.; Fu, Z. H.; Li, W. H.; Deng, W. H.; Wu, G. D.; Xu, G. Layer-by-Layer Assembled Conductive Metal-Organic Framework Nanofilms for Room-Temperature Chemiresistive Sensing. *Angewandte Chemie-International Edition* **2017**, *56* (52), 16510-16514.

(27) Campbell, M. G.; Sheberla, D.; Liu, S. F.; Swager, T. M.; Dinca, M. Cu-3(hexaiminotriphenylene)(2): An Electrically Conductive 2D Metal-Organic Framework for Chemiresistive Sensing. *Angewandte Chemie-International Edition* **2015**, *54* (14), 4349-4352.

(28) Hmadeh, M.; Lu, Z.; Liu, Z.; Gandara, F.; Furukawa, H.; Wan, S.; Augustyn, V.; Chang, R.; Liao, L.; Zhou, F.; et al. New Porous Crystals of Extended Metal-Catecholates. *Chemistry of Materials* **2012**, *24* (18), 3511-3513.

(29) Claire, F. J.; Tenney, S. M.; Li, M. Y. M.; Siegler, M. A.; Wagner, J. S.; Hall, A. S.; Kempa, T. J. Hierarchically Ordered Two-Dimensional Coordination Polymers Assembled from Redox-Active Dimolybdenum Clusters. *Journal of the American Chemical Society* **2018**, *140* (34), 10673-10676.

(30) Solomos, M. A.; Claire, F. J.; Kempa, T. J. 2D molecular crystal lattices: advances in their synthesis, characterization, and application. *Journal of Materials Chemistry A* **2019**, *7* (41), 23537-23562.

(31) Claire, F. J.; Solomos, M. A.; Kim, J.; Wang, G. Q.; Siegler, M. A.; Crommie, M. F.; Kempa, T. J. Structural and electronic switching of a single crystal 2D metal-organic framework prepared by chemical vapor deposition. *Nature Communications* **2020**, *11* (1).

(32) Singh, A. K.; Singh, R. K.; Sharma, B.; Tyagi, A. K. Characterization and biocompatibility studies of lead free X-ray shielding polymer composite for healthcare application. *Radiation Physics and Chemistry* **2017**, *138*, 9-15.

(33) Jin, X. L.; Ye, L. Q.; Xie, H. Q.; Chen, G. Bismuth-rich bismuth oxyhalides for environmental and energy photocatalysis. *Coordination Chemistry Reviews* **2017**, *349*, 84-101.

(34) Wang, G.; Sun, Q.; Liu, Y.; Huang, B.; Dai, Y.; Zhang, X.; Qin, X. A Bismuth-Based Metal–Organic Framework as an Efficient Visible-Light-Driven Photocatalyst. *Chemistry – A European Journal* **2015**, *21* (6), 2364-2367.

(35) Maghrabi, H. A.; Vijayan, A.; Deb, P.; Wang, L. J. Bismuth oxide-coated fabrics for X-ray shielding. *Textile Research Journal* **2016**, *86* (6), 649-658.

(36) Savage, M.; Yang, S. H.; Suyetin, M.; Bichoutskaia, E.; Lewis, W.; Blake, A. J.; Barnett, S. A.; Schroder, M. A Novel Bismuth-Based Metal-Organic Framework for High Volumetric Methane and Carbon Dioxide Adsorption. *Chemistry-a European Journal* **2014**, *20* (26), 8024-8029.

(37) Wibowo, A. C.; Smith, M. D.; zur Loye, H. C. New 3D bismuth-oxo coordination polymers containing terephthalate-based ligands: observation of Bi2O2-layer and Bi4O3-chain motifs. *Crystengcomm* **2011**, *13* (2), 426-429.

(38) Norman, N. C. COORDINATION CHEMISTRY OF ANTIMONY AND BISMUTH - LEWIS ACIDITY, SIGMA-ASTERISK-ORBITALS AND COORDINATION GEOMETRY. *Phosphorus Sulfur and Silicon and the Related Elements* **1994**, *87* (1-4), 167-176.

(39) Sun, H. Z.; Li, H. Y.; Sadler, P. J. The biological and medicinal chemistry of bismuth. *Chemische Berichte-Recueil* **1997**, *130* (6), 669-681.

(40) Sun, H. *Biological chemistry of arsenic, antimony and bismuth*; John Wiley & Sons, 2010.

(41) Suzuki, H.; Komatsu, N.; Ogawa, T.; Murafuji, T.; Ikegami, T.; Matano, Y. *Organobismuth chemistry*; Elsevier, 2001.

(42) Wibowo, A. C.; Smith, M. D.; zur Loye, H. C. A new Kagome lattice coordination polymer based on bismuth and pyridine-2,5-dicarboxylate: structure and photoluminescent properties. *Chemical Communications* **2011**, *47* (26), 7371-7373.

(43) Li, K. H.; Xu, Z. T.; Xu, H. H.; Ryan, J. M. Semiconductive coordination networks from 2,3,6,7,10,11 hexakis(alkylthio)triphenylenes and bismuth(III) halides: Synthesis, structure-property relations, and solution processing. *Chemistry of Materials* **2005**, *17* (17), 4426-4437.

(44) Inge, A. K.; Koppen, M.; Su, J.; Feyand, M.; Xu, H. Y.; Zou, X. D.; O'Keeffe, M.; Stock, N. Unprecedented Topological Complexity in a Metal-Organic Framework Constructed from Simple Building Units. *Journal of the American Chemical Society* **2016**, *138* (6), 1970-1976.

(45) Li, K. H.; Xu, H. H.; Xu, Z. T.; Zeller, M.; Hunter, A. D. Semiconductive coordination networks from bismuth(III) bromide and 1,2-bis(methylthio)phenylacetylene-based ligands. *Inorganic Chemistry* **2005**, *44* (24), 8855-8860.

(46) Xu, Z. T.; Li, K. H.; Fettinger, J. C.; Li, J.; King, M. M. A semiconductive coordination network based on 2,3,6,7,10,11-hexakis(methylthio)triphenylene and BiCl3. *Crystal Growth & Design* **2005**, *5* (2), 423-425.

(47) Mansfield, R. The electrical properties of bismuth oxide. *Proceedings of the Physical Society. Section B* **1949**, *62* (8), 476.

(48) Luo, Y.-R. *Comprehensive handbook of chemical bond energies*; CRC press, 2007.

(49) Skorupskii, G.; Trump, B. A.; Kasel, T. W.; Brown, C. M.; Hendon, C. H.; Dinca, M. Efficient and tunable one-dimensional charge transport in layered lanthanide metal-organic frameworks. *Nature Chemistry* **2020**, *12* (2), 131-136.

(50) Miner, E. M.; Wang, L.; Dinca, M. Modular O-2 electroreduction activity in triphenylene-based metal organic frameworks. *Chemical Science* **2018**, *9* (29), 6286-6291.

(51) Shi, Y. L.; Momeni, M. R.; Chen, Y. J.; Zhang, Z. Y.; Shakib, F. A. RETRACTED: Water-Induced Structural Transformations in Flexible Two-Dimensional Layered Conductive Metal-Organic Frameworks (Retracted article. See vol. 34, pg. 8089, 2022). *Chemistry of Materials* **2020**, *32* (22), 9664-9674.

(52) Jones, C. G.; Martynowycz, M. W.; Hattne, J.; Fulton, T. J.; Stoltz, B. M.; Rodriguez, J. A.; Nelson, H. M.; Gonen, T. The CryoEM Method MicroED as a Powerful Tool for Small Molecule Structure Determination. *Acs Central Science* **2018**, *4* (11), 1587-1592.

(53) Huang, Z. H.; Grape, E. S.; Li, J.; Inge, A. K.; Zou, X. D. 3D electron diffraction as an important technique for structure elucidation of metal-organic frameworks and covalent organic frameworks. *Coordination Chemistry Reviews* **2021**, *427*.

(54) Blatov, V. A.; Shevchenko, A. P.; Proserpio, D. M. Applied Topological Analysis of Crystal Structures with the Program Package ToposPro. *Crystal Growth & Design* **2014**, *14* (7), 3576-3586.

(55) Alexandrov, E. V.; Blatov, V. A.; Kochetkov, A. V.; Proserpio, D. M. Underlying nets in three-periodic coordination polymers: topology, taxonomy and prediction from a computer-aided analysis of the Cambridge Structural Database. *Crystengcomm* **2011**, *13* (12), 3947-3958.

(56) Thebault, F.; Ohrstrom, L.; Haukka, M. 2,3,6,7,10,11-Hexahydroxytriphenylene tetrahydrate: a new form of an important starting material for supramolecular chemistry and covalent organic frameworks. *Acta Crystallographica Section C-Structural Chemistry* **2011**, *67*, o143-o145.

(57) Smith, G.; Reddy, A. N.; Byriel, K. A.; Kennard, C. H. L. THE PREPARATION AND CRYSTAL STRUCTURE OF THE BISMUTH(III) CATECHOLATE COMPLEX ADDUCT (NH4)2 BI2(C6H4O2)4 .2C6H6O2.2H2O. *Australian Journal of Chemistry* **1994**, *47* (7), 1413-1418.

(58) Guilhaume, N.; Postel, M. Easy access to bismuth catecholates. *Heteroatom Chemistry* **1990**, *1* (3), 233-235.

(59) Guan, H. M.; Zhang, X. D.; Xie, Y. Soft-Chemical Synthetic Nonstoichiometric Bi2O2.33 Nanoflower: A New Room-Temperature Ferromagnetic Semiconductor. *Journal of Physical Chemistry C* **2014**, *118* (46), 27170-27174.

(60) Williams, D. E. Semiconducting oxides as gas-sensitive resistors. *Sensors and Actuators B-Chemical* **1999**, *57* (1-3), 1-16.

(61) Diskin, A. M.; Spanel, P.; Smith, D. Time variation of ammonia, acetone, isoprene and ethanol in breath: a quantitative SIFT-MS study over 30 days. *Physiological Measurement* **2003**, *24* (1), 107 119.

(62) Boroujerdi, R.; Abdelkader, A.; Paul, R. State of the Art in Alcohol Sensing with 2D Materials. *Nano Micro Letters* **2020**, *12* (1).

(63) Leubner, S.; Bengtsson, V. E. G.; Inge, A. K.; Wahiduzzaman, M.; Steinke, F.; Jaworski, A.; Xu, H.; Halis, S.; Rnfeldt, P.; Reinsch, H.; et al. Hexahydroxytriphenylene for the synthesis of group 13 MOFs - a new inorganic building unit in a beta-cristobalite type structure. *Dalton Transactions* **2020**, *49* (10), 3088-3092.

(64) McKinlay, A. C.; Eubank, J. F.; Wuttke, S.; Xiao, B.; Wheadey, P. S.; Bazin, P.; Lavalley, J. C.; Daturi, M.; Vimont, A.; De Weireld, G.; et al. Nitric Oxide Adsorption and Delivery in Flexible MIL-88(Fe) Metal-Organic Frameworks. *Chemistry of Materials* **2013**, *25* (9), 1592-1599.

*Chapter 7*

*Enhanced Gearing Fidelity Achieved Through Macrocyclization of a Solvated*

*Molecular Spur Gear[1]*

## 7.1 INTRODUCTION

The beginning of nanoscience and nanotechnology can be traced back to 1959 when Richard Feynman gave his famous lecture, There's Plenty of Room at the Bottom, during which he challenged scientists and engineers to make a $(1/64)^3$ in$^3$ operational electric motor.[1] Present-day synthetic chemists are involved in making molecular and supramolecular entities with both structural and functional analogies to the macroscopic objects, including gears, pumps, and switches.[2-4] Early examples of molecular gears were published by Iwamura[5] and Mislow[6] in the 1980s, when they reported molecular bevel gear **1** (Figure 7.1), with two triptycenes covalently linked to a methylene group or an oxygen atom, respectively. In these landmark studies, they were able to show that the two triptycenes display fast and correlated dynamics, resembling those of macroscopic bevel gears. Since these pioneering studies, many triptycene-based bevel gears have been developed, including systems with three linear triptycenes[7] or six cyclic triptycenes,[8] switchable two-gear systems,[9] and a four-gear system with tunable dynamics.[10] The study of molecular spur

---

gears (MSG), with two gearing cogs arranged in parallel, has seen remarkably less success than its off-parallel counterparts.

Similar to the macroscopic objects, molecular gearing occurs when the two triptycenes undergo concerted, disrotatory motion, while slippage occurs either by conrotatory motion or independent rotation. As suggested by Siegel, the primary figure of merit for determining a gear's quality is gearing fidelity, which is defined as the number of geared rotations per slippage events ($F_{gear} = \underline{k}_{gear}/k_{slip}$).[11] Bevel gears with high gearing fidelity were developed

**Figure 7.1**. *Representative triptycene-based bevel (1), spur (2-6), and macrocyclic (6-7) gears. All spur gears arrange triptycenes in parallel, while bevel gears position cogs at an off-parallel orientation.*
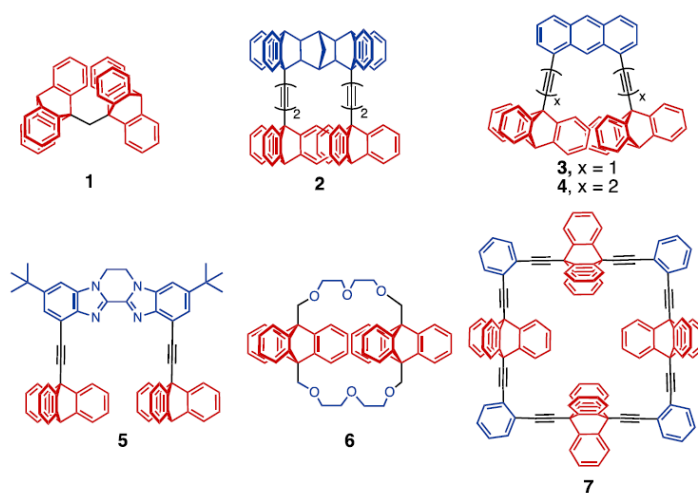


utilizing tightly meshed systems in which the transition state leading to slippage was much higher in energy than the one leading to gearing (>30 kcal mol$^{-1}$ vs 1−2 kcal mol$^{-1}$). Spur gears utilizing triptycene have strict geometric requirements to function properly, and there are no examples of structures shown to displayed high gearing fidelity. As discussed by Siegel and co-workers, the optimal distance for triptycene gearing is 8.1 Å, while the slippage transition state occurs at a distance of 7.2 Å between the rotational axes of the two gears. From this, the difficulty with achieving high-functioning spur gears becomes apparent, the transition state leading to slippage occurs at a shorter distance than does the one for gearing. This means

that in order to have a properly functioning spur gear, stabilizing, enthalpic interactions must lower the energy of the gearing transition state to cause it to be favored over slippage. This issue is only exacerbated by the entropic penalty that arises as there are many rotational processes that can lead to slippage, while there is only one gearing trajectory.

*Figure 7.2. Design of new macrocyclic MSG built with intermeshed triptycene blades held in place by a stator consisting of a bibenzimidazole and a gold-phosphine capping group.*
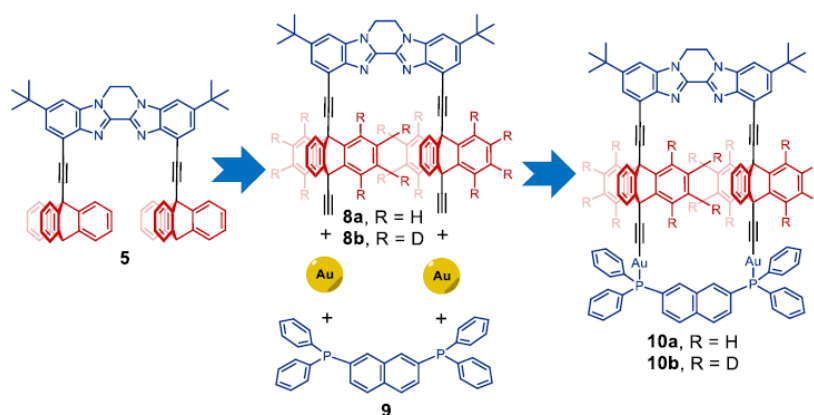


Using a combination of molecular dynamics (MD) and quantum mechanical (QM) calculations, we recently explored the gearing and slippage trajectories in MSGs **2-5** (Figure 7.1).[12] In this study, we discovered that diyne-linked gears **2** and **4**[13] have calculated barriers of 5 kcal mol$^{-1}$ for gearing and of 1−2 kcal mol$^{-1}$ for slippage, respectively. Interestingly, the monoalkyne-linked gear **3** shows the inverse preference for gearing over slippage, which we attribute to the reduction in flexibility of **3** over **4** by having only a single alkynyl linker rather than two. Our calculations also showed that the flexibility of **5** might reduce its gearing efficiency, dropping the gearing barrier to 2.4 kcal mol$^{-1}$, which is quite close to that of slippage at 3.5 kcal mol$^{-1}$ (down from 3.4 and 7.6 kcal mol$^{-1}$, respectively, when calculated with DFT). Clearly, when one considers the many different vibrational and torsional modes accessible to various MSGs rather than simply the transition state (TS) energies, a more complicated picture of gearing emerges. From this vein, the design of MSGs requires not only careful engineering of gearing and slippage barriers but also designing highly rigid structures where torsional degrees of freedom are limited to gearing processes.[14]

**Scheme 7.1**. *Synthesis of Macrocyclic MSGs **10a** and **10b***
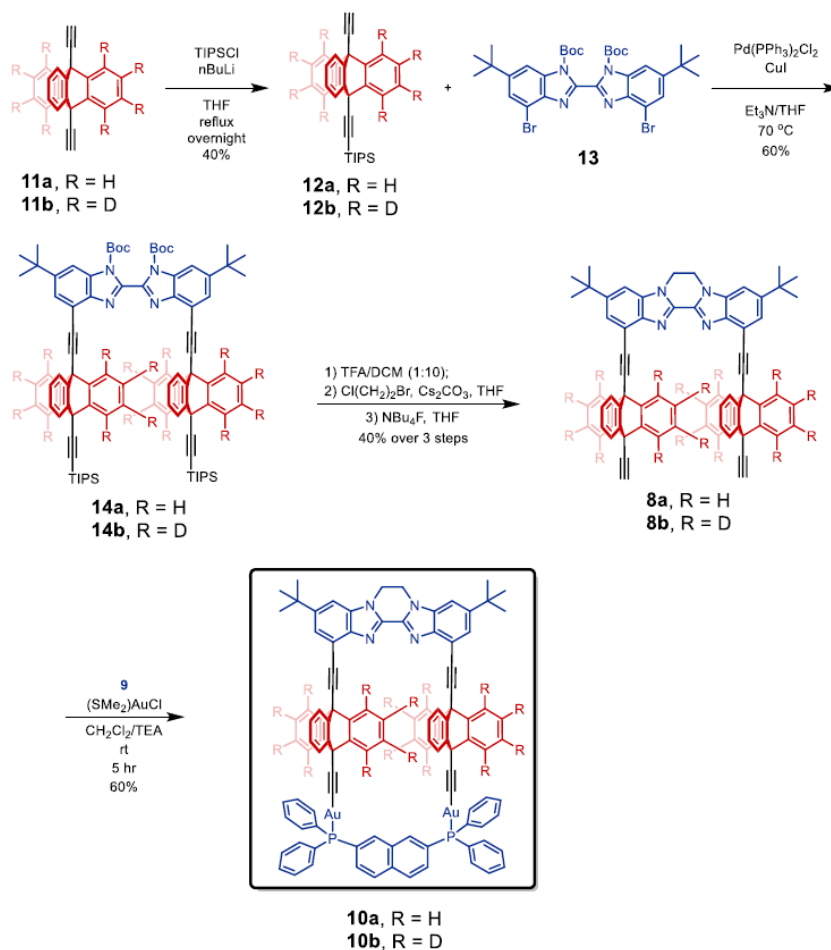


One method to reduce the number of degrees of freedom present in a linear or branched molecule is to convert it into a cyclic structure. This is particularly true for macrocyclization reactions, as evidenced by the need for templating agents to overcome the high entropic penalties present in their syntheses.[15] While macrocyclic MSGs such as **6** and **7** from the Bryan[16] and Toyota[17] laboratories, respectively, have been developed, there was no systematic study of how the macrocyclization affects gearing efficiency in either case. We envisioned that locking the triptycene cogs into the proper orientation for gearing using a cyclic structure would restrict high amplitude bending modes that might reduce gearing efficiency or facilitate independent rotation of either triptycene, and ultimately enhance gearing fidelity. From this understanding, we sought to synthesize a new macrocyclic MSG and characterize its dynamics using a combination of

molecular dynamics (MD) simulations and density functional theory (DFT) calculations. Our design utilizes **5**, the bibenzimidazole stator developed by Siegel and co-workers, which places two triptycenes in parallel, 8 Å apart (). We prepared **8a** and its deuterated analogue **8b**[18] with two parallel ethynyl groups to form the desired macrocycle by linking **8a/8b** with digold complex **9**. The use of deuterated gears was envisioned as a tool to simplify the $^2$H NMR spectrum by removing potential overlapping of aromatic signals from the two components of the stator. Our group's experience with gold complexes inspired us to bond the naphthyl diphosphine **9** to **8** via an $Au^{1+}$ coordination bond.[19] Compound **9** was chosen as the 2,7-naphthyl substitution pattern to place the two phosphine groups 8.07 Å apart, a close fit for the idealized bibenzimidazole stator. Complexation with Au(I) conveniently coordinates alkyne and phosphine ligands at an angle of 180°, allowing for the construction of MSG **10a/b** with the two triptycenes oriented in parallel and separated by ∼8.1 Å.

## 7.2 EXPERIMENTAL DETAILS AND ANALYSIS OF MSG SYSTEM

### 7.2.1 Synthesis and Electron Diffraction Structure

With the above design principles in mind, we set out to synthesize MSG **10a** (Scheme 1). Synthesis for **10a** started with 9,10-diethynyltriptycene **11a**, which was treated with 1 equiv of *n*-BuLi followed by 1.15 equiv of triisopropylsilyl chloride at −78 °C. Subsequent overnight reflux followed by chromatographic separation resulted in the isolation of **12a** in 40% yield with the double protected and unprotected compounds recollected and used in proceeding reactions. Compound **12a** was then reacted with the boc-protected bibenzimidazole stator **13** using standard Sonogashira conditions to afford **14a** in 60% yield. Both boc-protecting groups could then be removed by treatment with a 1:10 mixture of trifluoroacetic acid (TFA) and dichloromethane (DCM). This crude mixture was reacted with an excess of 1-bromo-2-chloroethane in the presence of $Cs_2CO_3$ and THF at elevated temperatures. A short silica column was run on this mixture to remove any excess 1-bromo-2-chloroethane before reaction with TBAF in THF to yield macrocyclization precursor **8a**

*Figure 7.3*. *Crystal structure of 10a (A) face on with key distances measured, (B) side on showing the effects of utilizing tetrahedral phosphines as stators, and (C) space-filling model with the phosphine ligand and alkynes hidden to show alignment of the triptycenes. (D) Crystal packing of 10a with phenylenes on four intermeshed triptycenes highlighted.*
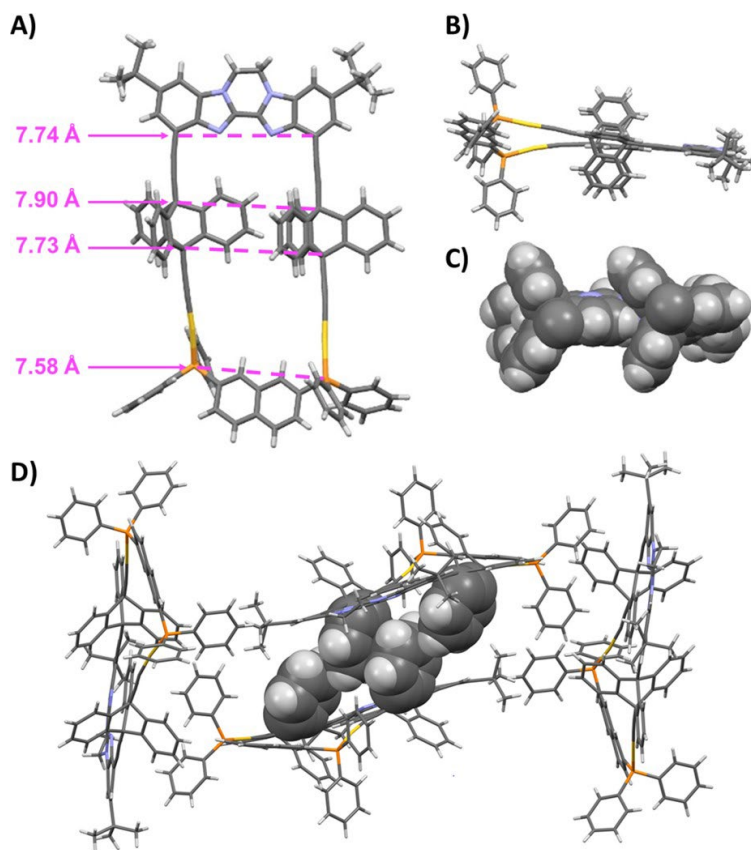


We discovered that removal of the boc- groups before TBAF was critical for maintaining a yield of 40% for these reactions. Presumably, the bibenzimidazole stator was decomposed by the presence of ammonium hydroxide in our TBAF solution if we attempted to deprotect the alkynes first. Finally, **8a** was dissolved in $CH_2Cl_2$ with a single drop of triethyl amine (TEA) and treated with 2 equiv of (dimethylthiol)gold(I) chloride to forge a covalently linked organogold template for macrocyclization.[20] Dropwise addition of **9** dissolved in $CH_2Cl_2$ produced the macrocyclic MSG **10a** in 60% yield after subsequent workup and trituration of the crude product. Molecular spur gear **10b** was synthesized using the same procedure with deuterated samples of **11b**, which proceeded with similar yields.

*Figure 7.4*. *Distinct sets of rotational gearing cycles (I, II, and III) of labeled triptycenes following the disrotatory interconversion of isomers by a gearing mechanism. Slippage requires conrotation and interconverts among isomers of the three sets. Three possible slippage transitions are shown. Enantiomeric conformers are denoted with prime symbols. Figure adapted from ref 10.*
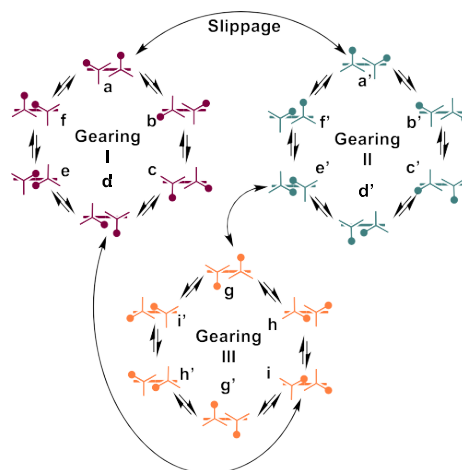


Once the solvent had been removed, the solubility of **10a** or **10b** became severely limited in all explored solvents, even at elevated temperatures. Despite their very low solubility, spectral characterization was possible by ^{1}H NMR, FTIR, and HRMS (SI section), but we were not able to obtain ^{2}H and ^{13}C NMR data within reasonable acquisition times as a result of sensitivity differences of $9.65 \times 10^{-3}$ (assuming 100% labeling) and $1.76 \times 10^{-4}$ (at natural abundance), respectively. Although large enough single crystals for X-ray diffraction could not be obtained, we were able to grow microcrystals suitable for electron diffraction by slow evaporation of **10a** from bromobenzene. Using continuous rotation electron diffraction, the structure was solved at 1.10 Å in space group $P2_1/n$.[21] Analysis of the crystal structure (Figure 7.3A) reveals that the bibenzimidazole stator takes on a somewhat puckered and twisted shape that forces two connecting points for each alkyne to be ca. 7.74 Å apart rather than the expected ca. 8.10 Å for the planar structure. Gratifyingly, the distance between each triptycene bridgehead carbons are ca. 7.90 and 7.73 Å apart for the bibenzimidazole and phosphine side of the molecular, respectively. The two phosphines on the coordinated stator are approximately ca. 7.58 Å apart, and 0.15 Å closer together than on the bibenzimidazole stator. This short distance may account for the puckering observed on the bibenzimidazole. Interestingly, the

tetrahedral geometry of the phosphines causes substantial stator twisting on the gold-coordinated side of the molecule (Figure 7.3B), which brings the two triptycenes slightly out of parallel alignment. Closer inspection of the triptycene cogs (Figure 7.3C) shows that one blade of the first triptycene neatly packs into the fold of the second one in a $C_s$ symmetric arrangement, indicating that the two triptycenes can engage in configurations conducive to gearing. Additionally, analysis of the crystal packing revealed that multiple molecules of **10a** arrange to intermesh their triptycene cogs (Figure 7.3D). This finding would likely preclude any solid-state dynamics and prompted us to focus solely on the solution-phased properties of **10a**.

### 7.2.2 Variable-Temperature NMR

The labeling of both triptycenes of the molecular spur gear with a suitable substituent, as indicated by a dot in two of the blades in Figure 7.4, results in desymmetrized rotators that lead to the formation of 18 different conformers (a-i') distributed in three distinct, isomeric cycles (I, II, and III).[22, 23] Close analysis of these cycles reveals that gearing cycles I and II are related by a mirror plane, and thus can be classified as *dl* isomers, while gearing cycle III has an internal mirror plane, leading to its classification as the *meso* cycle. Conformers within a single cycle can interconvert via a concerted, disrotatory (gearing) motion of each triptycene, while conrotatory rotation or independent rotation leads to slippage, interconverting the cycles. If gearing occurs with high fidelity, the time average solution NMR spectrum of an ideally labeled gear will reveal two sets of signals for each of the four triptycene protons in a 2:1 ratio that corresponds to isomers a-f and a'-f", and conformers g-i' in the *meso* cycle. In a situation where gearing fidelity is low, these isomeric cycles will interconvert, leading to a single set of four proton signals that represent the timeaveraged spectrum of all the individual conformers a-i'. The first experimental test of our design was aimed at exploring the dynamics of the blades by variable-temperature ^{1}H NMR, knowing that without proper labeling we can only ascertain whether rotational exchange between the three nonequivalent blade site occurs faster or slower than the NMR time scale. We expected to gain an additional insight into the energetics of the gearing and slippage processes by taking advantage of computational methods, which

could eventually be used to decide the type(s) of substituents that could make the two cycles experimentally observable.

*Figure 7.5. Variable-temperature $^1$H spectra of MSG 10b at temperatures ranging from 295 to 187 K. The α- and β-protons are marked with blue and red arrows, respectively. Signals indicated by the black arrow correspond to the phosphine ligand.*
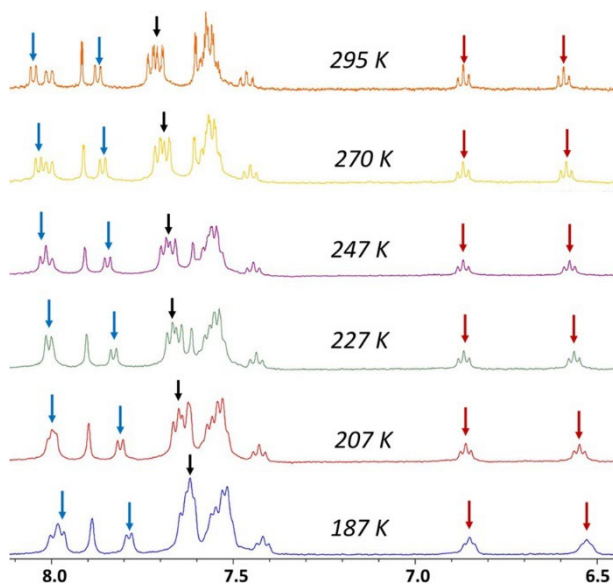


As shown in Figure 7.5, VT $^1$H NMR measurements with MSG **10b** were carried out in CD$_2$Cl$_2$ solutions with temperatures ranging from 295 to 187 K, which is close to the freezing point of the solvent and the limit for our spectrometer. Similar results obtained with **10a** between 298 and 212 K are shown included Figure F.26. Triptycene protons parallel to the axis of rotation and *ortho-* to the bridgehead carbon (α-protons) are labeled with blue arrows while protons *meta-* to the bridgehead carbon (β-protons) are indicated with red arrows. While the spectra are relatively complicated, chemical shift changes of both the triptycene α- and β-protons are easy to follow. The β-protons are highly shielded due to interactions with the neighboring triptycene blades and are easily identified by their coupling pattern as two sets of apparent triplets between 6.9 and 6.5 ppm. By comparison, the α-protons pointing toward the two different stator components occur as apparent doublets between 8.1 and 7.75 ppm. A number of changes were observed for the four triptycene blade signals. The β-protons observed at 6.60 ppm at 295 K shifted upfield by 32 Hz,

while the signal at 6.87 ppm shifted upfield by only 8.7 Hz. In contrast to this asymmetric change, both $\alpha$-protons shifted upfield by approximately 40 Hz as the temperature was lowered within the same range. As the temperature is lowered, the downfield signal experiences a 40 Hz upfield shift, similar to the two $\alpha$-protons and the upfield $\beta$-proton. Notably, the phosphine phenyl groups that are marked with a black arrow start as two sets of complex signals, one at approximately 7.55 ppm and another around 7.65 ppm, and they both shift upfield and merge as the temperature reaches 187 K. A similar broadening for all signals suggests that there are no internal dynamic processes in the $^1$H NMR time scale indicative of signal coalescence resulting from a slow site exchange. In fact, chemical shift changes might arise due to changes in the macrocycle structure, potentially mediated by hydrogen-bonding interaction between the bibenzidimazole stator and the $\alpha$-protons in the triptycene gear with broadening caused by an increase in the viscosity of CD$_2$Cl$_2$ as it nears its freezing point (Figure F.27).

One may conclude from the above experimental observations that the rotational dynamics of MSG **10**, whether gearing or slippage, are determined by free energy barriers that are easy to surmount even at 187 K. However, it is possible that differences in chemical shifts in the three nonequivalent blade position of each triptycene gear are not enough to elicit a noticeable effect in the NMR spectra. A simple estimate of the conditions that are needed to make rotational dynamics observable in solution by VT NMR can be obtained by analyzing the combined effect of the activation energy ($\Delta G^{\ddagger}$) and the difference in chemical shift between different exchange sites ($\Delta v$), on the observed coalescence temperature (T$_C$), as determined by the following equation

$$\Delta G^{\ddagger} = 4.55 * 10^{-3} * T_c * (9.97 * \log T_c - \log (500 * \Delta v))$$

For coalescence to be experimentally observable near the temperature limit of ca. T$c \approx$ 180 K of CD$_2$Cl$_2$, gearing dynamics would require activation free energy values ($\Delta G^{\ddagger}$) in the range of ca. 8.5 to 5.5 kcal mol$^{-1}$ for chemical shift differences between exchange sites ($\Delta v$) that differ from ca. 200 to 1500 Hz, respectively. This suggests that in addition to high barriers, different sites would require substantially different shielding environments ($\Delta v$) for gearing cycles to be unambiguously detected by VT NMR. With

this information at hand, we turned to density functional theory (DFT) and performed NMR calculations to obtain the isotropic shift values for hydrogen atoms of the three different triptycene blades. Calculated isotropic shielding values of the most stable gear structure revealed frequency variations in the range of 500 to 1500 Hz at a spectrometer frequency of 500 MHz, as the one used in our experiments (Appendix F Table F.1). On the basis of these values, we can conclude that an experimentally measurable rotational barrier at or above 187 K would need activation free energies greater than ca. 7−8 kcal mol$^{-1}$. However, it should be noted that this result is not an indication of gearing and/or slippage, as both can occur with high exchange rates over low barriers. In fact, for distinct gearing cycles to be experimentally observed in solution by VT $^1$H NMR, it is not enough to have optimal gearing barriers, but it would be also essential that slippage has a barrier that is substantially higher than 7−8 kcal mol$^{-1}$ as lower values will interconvert structures of the two types of cycles with corresponding NMR time scale.

**Figure 7.6**. *Interaxle distances between bridgehead carbons in intermeshed triptycenes for half-open gear (green) and locked macrocyclic gear (blue) as simulated in DCM at 300 K. The distribution of interaxle distances is wider for the half-open gear systems.*
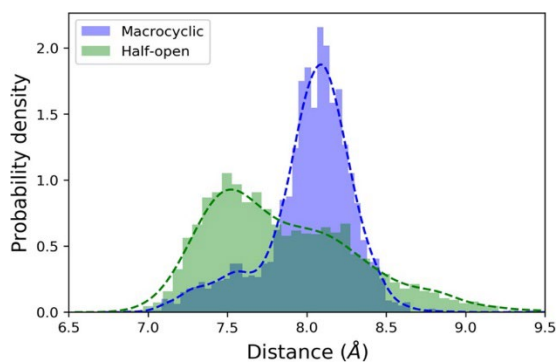


### 7.2.3 Computational Studies

To analyze gearing dynamics by computational methods,[24] we sought to assess how well the two triptycenes stay intermeshed in the macrocyclic architecture as compared to the half-open gear with a bibenzimidazole stator previously reported by Siegel *et al*.[11] We performed molecular dynamics (MD) simulations at 300 K for 1 $\mu$s for the two molecular gear systems immersed in a DCM solvent box and

tracked the distances between the bridgehead carbons in intermeshed triptycenes. MD simulations were performed using the GPU code (pmemd.cuda)[25] of the AMBER 16 package.[26] Parameters for all nonmetal atoms were generated within the antechamber module using the general AMBER force field (*gaff*).[27] Parameters for the $Au^{1+}$ ions were generated using metal center parameter builder (MCPB.py).[28] Further computational details are described in Appendix F and in a recent publication from our group.[24] Figure 7.6 depicts the range of distances that the intermeshed triptycenes are able to explore while undergoing their correlated motion. Triptycenes in the half-open gear (colored in green) spanned the range of ca. 7.0 to 9.5 Å with two broad peaks observed at ca. 7.4 Å and ca. 8.2 Å consistent with distances that are favorable for the slippage and gearing transition states, respectively. Notably, more conformations were found at distances suitable for the slippage transition state than for gearing. The distance range between triptycenes in the macrocyclic gear (colored in blue) was smaller varying from ca. 7.0 Å to ca. 8.6 Å with the highest probability density observed at ca. 8.1 Å, which suggests that triptycenes undergo their dynamics at a distance that is expected to favor the transition state for gearing. These theoretical observations support the use of macrocyclization in order to keep triptycene gears tightly intermeshed as a strategy to enhance the gearing fidelity.

Having gained insight into the positive impact of macrocyclization on the gearing process, we performed MD simulations in the temperature range used in the VT-NMR experiments in dichloromethane, from 207 to 300 K. The simulations were run for 1 $\mu$s to allow the system to visit all the energetically relevant configurations. Rotational trajectories were analyzed by tracing the motion of each triptycene gear via dihedral angle changes that vary from $-180°$ to $180°$. The dihedral angle for each triptycene is defined as the angle between the plane of the bibenzimidazole stator and the plane of one of the triptycene blades. For a meshed triptycene system undergoing correlated rotation, gearing is observed when dihedral angles associated with different triptycenes turn in opposite directions by $60°$. The MD trajectories performed at 207 K for 1 $\mu$s showed multiple gearing events (Figure 7.7A). Plotting the dihedral angle evolution in time shows that as one triptycene gear is changing its dihedral angle in one direction by $60°$, the other

simultaneously responds in the opposite direction, as required for geared rotation. As shown in the bottom frames in Figure 7.7, the extent of correlated behavior between the two gears can be appreciated by plotting one dihedral as a function of the other. At 207 K the occupied sites are consistent with the three symmetry-related ground state configurations achieved via gearing (Figure 7.7A, bottom frame). As the MD simulations temperature increases, more gearing events are observed. At 247 K (Figure 7.7B) and 300 K (Figure 7.7C), multiple symmetry-related gearing trajectories each offset by a ca. 60° are populated. Configurations outside the diagonal gearing trajectories indicate slippage events.

*Figure 7.7. Dynamic simulations of triptycene gearing carried out for 1 μs at (A) 207 K, (B) 247 K, and (C) at 300 K in a locked macrocyclic gear immersed in DCM solvent box. Different colors in each plot represent dihedral angle values for the two intermeshed triptycene gears. A gearing event is observed when a dihedral angle for each gear is changing by 60° in opposite directions. Correlated maps show how the two dihedral angles are simultaneously changing in opposite directions; as one dihedral is increasing, the other is simultaneously decreasing. As the simulation temperature increases, more correlated motion events are observed and more symmetry-related gearing trajectories are generated.*
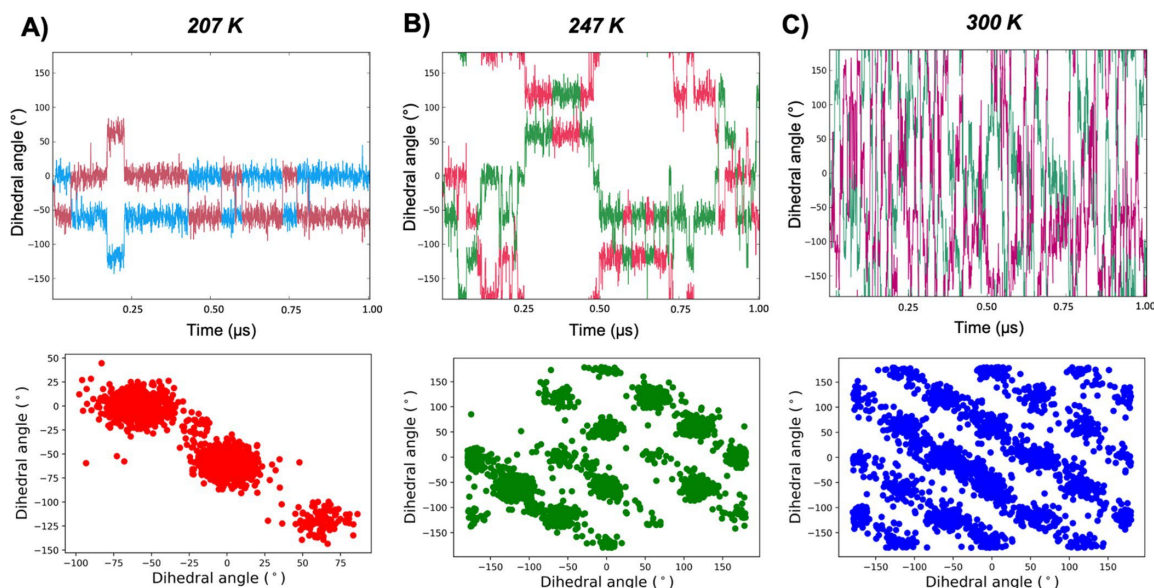


In order to evaluate the activation barrier to gearing and map the energy landscape, we utilized an accelerated sampling technique via well-tempered metadynamics simulations. Metadynamics simulation

were performed using the NAMD 3.0 program.[29] The free energy surface was reconstructed as a function of the dihedral angles describing each triptycene (Figure 7.8A). By introducing a bias potential (or force) that acts on the selected variables, the potential mean force (PMF) plot along the chosen coordinates was generated (Figure 7.8B). The lowest energy trajectories match the ones obtained with MD simulations (Figure 7.7C) and indicate efficient gearing. The energy barriers for gearing and slippage were calculated to be ca. 4 kcal mol$^{-1}$ and ca. 9 kcal mol$^{-1}$, respectively. Notably, the energy barrier for gearing is smaller than the 7.3 kcal mol$^{-1}$ barrier calculated by Siegel *et al.* for the half-open gear with bibenzimidazole stator in the gas phase.[11] The slight asymmetry in the PMF plot is attributed to the asymmetric structure of the molecular spur gear and its twisted framework.

***Figure 7.8**. (A) Dihedral angles (atoms circled in red and blue) used to define triptycene rotation in the macrocyclic gear. (B) Potential mean force plot for triptycene rotation generated using well-tempered metadynamics simulations. The top-left to bottom-right diagonals represent the lowest energy trajectory for gearing, with dihedral angles changing in opposite directions. Energy scale is in kcal mol$^{-1}$.*
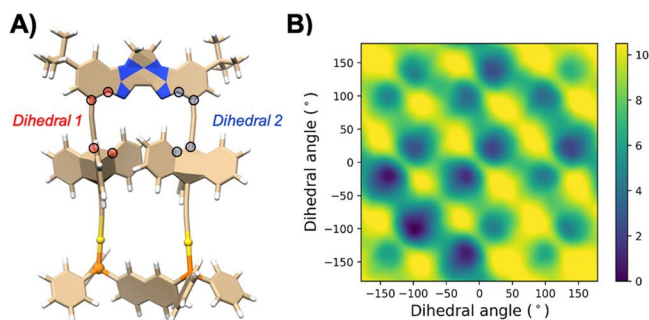


Similar metadynamics studies were previously done by our group on Siegel's half-open molecular spur gear with an ethenyl bridged bibenzimidazole stator. For that system, we confirmed low rotational barriers for gearing and slippage (2.4 and 3.5 kcal mol$^{-1}$, respectively) and showed perfectly symmetric PMF plot.[12] We believe that the locking of triptycenes in a meshed configuration, at suitable interaxle distance for gearing, stabilizes the gearing transition state and allows the system to efficiently undergo

gearing dynamics. These computational observations suggest that gearing dynamics are outside the experimental NMR time scales, and the calculated barriers for gearing and slippage are too low for the motion to be observed experimentally via phase isomer formation.

*Figure 7.9. Ground state and key transition states for 10a, and other triptycene-based spur gears, as well as key intermolecular interactions for tuning energetic barriers.*
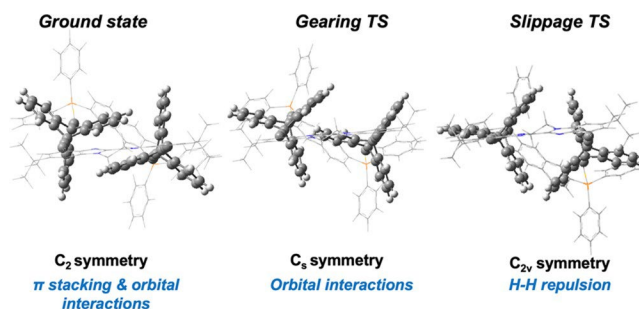


## 7.3 CONCLUSIONS

Our results suggest that macrocyclization is a valuable strategy for enhancing gearing fidelity in molecular spur gear systems in solution by locking the triptycene cogs into the correct position and orientation for gearing. Using a convenient convergent synthesis, we were able to create a rigid organogold complex with triptycenes aligned in parallel and at a proper gearing distance. The MD simulations showed that macrocyclization prevents **10a** from accessing slippage transition states and reverses the preference for slippage observed with MSG **5** by limiting the bending modes that would otherwise be accessible to the gear. Metadynamics simulations of the energetic profile for gearing indicated that macrocyclization did not change the relative barriers of **10a** significantly as compared to those of the half-open gear **5**. In the macrocyclic gear, the barriers for gearing and slippage were ca. 4 kcal mol$^{-1}$ and ca. 9 kcal mol$^{-1}$, respectively, while in the half-open gear **5**, as previously studied by Siegel *et al.*, they were ca. 7.3 kcal mol$^{-1}$ and ca. 11.6 kcal mol$^{-1}$, respectively. While bevel gears only required tight meshing to create experimentally visible dynamics, spur gears also require finely tuned energy barriers that bring the barrier

to slippage above 11 kcal mol$^{-1}$ such that the gearing dynamics will be observable in solution using variable-temperature NMR.

These findings suggest that future iterations of triptycene-based spur gears should utilize macrocyclic stators that position triptycenes ca. 8.1 Å apart in a rigid structure to prevent slippage and then alter the slippage barrier using asymmetric triptycenes containing a combination of electron-poor and electron-rich phenylenes. In this system, favorable orbital interactions would stabilize the ground state and gearing transition state but would be lost in the slippage transition state (Figure 7.9), widening the energetic gap between gearing and slipping.

## 7.4 REFERENCES

(1) Feynman, R. P.; Leighton, R.; Sands, M. The Feynman Lectures on Physics Addison-Wesley. *Reading, MA* **1963**, *1*, 1-9.

(2) Balzani, V.; Credi, A.; Raymo, F. M.; Stoddart, J. F. Artificial molecular machines. *Angewandte Chemie International Edition* **2000**, *39* (19), 3348-3391.

(3) Dattler, D.; Fuks, G.; Heiser, J.; Moulin, E.; Perrot, A.; Yao, X.; Giuseppone, N. Design of collective motions from synthetic molecular switches, rotors, and motors. *Chemical reviews* **2019**, *120* (1), 310-433.

(4) Krause, S.; Feringa, B. Towards artificial molecular factories from framework-embedded molecular machines. *Nature Reviews Chemistry* **2020**, *4* (10), 550-562.

(5) Kawada, Y.; Iwamura, H. UNCONVENTIONAL SYNTHESIS AND CONFORMATIONAL FLEXIBILITY OF BIS(1-TRIPTYCYL) ETHER. *Journal of Organic Chemistry* **1980**, *45* (12), 2547-2548.

(6) Hounshell, W. D.; Johnson, C. A.; Guenzi, A.; Cozzi, F.; Mislow, K. STEREOCHEMICAL CONSEQUENCES OF DYNAMIC GEARING IN SUBSTITUTED BIS(9 TRIPTYCYL)METHANES AND RELATED MOLECULES. *Proceedings of the National Academy of Sciences of the United States of America-Physical Sciences* **1980**, *77* (12), 6961-6964.

(7) Koga, N.; Kawada, Y.; Iwamura, H. RECOGNITION OF THE PHASE RELATIONSHIP BETWEEN REMOTE SUBSTITUENTS IN 9,10-BIS(3-CHLORO-9-TRIPTYCYLOXY)TRIPTYCENE MOLECULES UNDERGOING RAPID INTERNAL-ROTATION COOPERATIVELY. *Journal of the American Chemical Society* **1983**, *105* (16), 5498-5499.

(8) Ube, H.; Yamada, R.; Ishida, J.; Sato, H.; Shiro, M.; Shionoya, M. A Circularly Arranged Sextuple Triptycene Gear Molecule. *Journal of the American Chemical Society* **2017**, *139* (46), 16470-16473.

(9) Setaka, W.; Nirengi, T.; Kabuto, C.; Kira, M. Introduction of Clutch Function into a Molecular Gear System by Silane-Silicate Interconversion. *Journal of the American Chemical Society* **2008**, *130* (47), 15762.

(10) Sanada, K.; Ube, H.; Shionoya, M. Rotational Control of a Dirhodium-Centered Supramolecular Four Gear System by Ligand Exchange. *Journal of the American Chemical Society* **2016**, *138* (9), 2945-2948.

(11) Frantz, D. K.; Linden, A.; Baldridge, K. K.; Siegel, J. S. Molecular Spur Gears Comprising Triptycene Rotators and Bibenzimidazole-Based Stators. *Journal of the American Chemical Society* **2012**, *134* (3), 1528-1535.

(12) Jiang, X.; Yang, S.; Jellen, M. J.; Houk, K. N.; Garcia-Garibay, M. Molecular Spur Gears with Triptycene Rotators and a Norbornane-Based Stator. *Organic Letters* **2020**, *22* (11), 4049-4052.

(13) Toyota, S.; Shimizu, T.; Iwanaga, T.; Wakamatsu, K. Structures and Conformational Analysis of 1,8 Bis(9-triptycylethynyl)anthracene and Its Derivatives as Prototypes of Molecular Spur Gears. *Chemistry Letters* **2011**, *40* (3), 312-314.

(14) Liepuoniute, I.; Jellen, M. J.; Garcia-Garibay, M. A. Correlated motion and mechanical gearing in amphidynamic crystalline molecular machines. *Chemical Science* **2020**, *11* (48), 12994-13007.

(15) Marti-Centelles, V.; Pandey, M. D.; Burguete, M. I.; Luis, S. V. Macrocyclization Reactions: The Importance of Conformational, Configurational, and Template-Induced Preorganization. *Chemical Reviews* **2015**, *115* (16), 8736-8834.

(16) Bryan, J. C.; Sachleben, R. A.; Gakh, A. A.; Bunick, G. J. Molecular gears: Structures of (9,10-triptyceno) crown ethers. *Journal of Chemical Crystallography* **1999**, *29* (5), 513-521.

(17) Toyota, S.; Kawahata, K.; Sugahara, K.; Wakamatsu, K.; Iwanaga, T. Triple and Quadruple Triptycene Gears in Rigid Macrocyclic Frameworks. *European Journal of Organic Chemistry* **2017**, *2017* (37), 5696-5707.

(18) Jiang, X.; Rodriguez-Molina, B.; Nazarian, N.; Garcia-Garibay, M. A. Rotation of a Bulky Triptycene in the Solid State: Toward Engineered Nanoscale Artificial Molecular Machines. *Journal of the American Chemical Society* **2014**, *136* (25), 8871-8874.

(19) Jin, M.; Chung, T. S.; Seki, T.; Ito, H.; Garcia-Garibay, M. A. Phosphorescence Control Mediated by Molecular Rotation and Aurophilic Interactions in Amphidynamic Crystals of 1,4-Bis tri-(p-fluorophenyl)phosphane-gold(I)-ethynyl benzene. *Journal of the American Chemical Society* **2017**, *139* (49), 18115-18121.

(20) Vicente, J.; Chicote, M. T.; Alvarez-Falcon, M. M.; Jones, P. G. Gold(I) and silver(I)/gold(I) complexes derived from C6Me4(C CH)(2)-1,2. *Organometallics* **2005**, *24* (19), 4666-4675.

(21) Jones, C. G.; Asay, M.; Kim, L. J.; Kleinsasser, J. F.; Saha, A.; Fulton, T. J.; Berkley, K. R.; Cascio, D.; Malyutin, A. G.; Conley, M. P.; et al. Characterization of Reactive Organometallic Species via MicroED. *Acs Central Science* **2019**, *5* (9), 1507-1513.

(22) Kawada, Y.; Iwamura, H. PHASE ISOMERISM IN GEAR-SHAPED MOLECULES. *Tetrahedron Letters* **1981**, *22* (16), 1533-1536.

(23) Iwamura, H.; Mislow, K. STEREOCHEMICAL CONSEQUENCES OF DYNAMIC GEARING. *Accounts of Chemical Research* **1988**, *21* (4), 175-182.

(24) Liepuoniute, I.; Sanders, J. N.; Garcia-Garibay, M. A.; Houk, K. N. Computational Investigation into Ligand Effects on Correlated Geared Dynamics in Dirhodium Supramolecular Gears-Insights Beyond the NMR Experimental Window. *Journal of Organic Chemistry* **2020**, *85* (13), 8695-8701.

(25) Salomon-Ferrer, R.; Gotz, A. W.; Poole, D.; Le Grand, S.; Walker, R. C. Routine Microsecond Molecular Dynamics Simulations with AMBER on GPUs. 2. Explicit Solvent Particle Mesh Ewald. *Journal of Chemical Theory and Computation* **2013**, *9* (9), 3878-3888.

(26) Case, D.; Cerutti, D.; Cheatham III, T.; Darden, T.; Duke, R.; Giese, T.; Gohlke, H.; Goetz, A.; Greene, D.; Homeyer, N. H., DMY and PAK AMBER2017. *University of Calafornia: San Francisco* **2017**.

(27) Wang, J. M.; Wolf, R. M.; Caldwell, J. W.; Kollman, P. A.; Case, D. A. Development and testing of a general amber force field. *Journal of Computational Chemistry* **2004**, *25* (9), 1157-1174.

(28) Li, P. F.; Merz, K. M. MCPB.py: A Python Based Metal Center Parameter Builder. *Journal of Chemical Information and Modeling* **2016**, *56* (4), 599-604.

(29) Phillips, J. C.; Braun, R.; Wang, W.; Gumbart, J.; Tajkhorshid, E.; Villa, E.; Chipot, C.; Skeel, R. D.; Kale, L.; Schulten, K. Scalable molecular dynamics with NAMD. *Journal of Computational Chemistry* **2005**, *26* (16), 1781-1802.

*Chapter 8*

*Sterically Invariant Carborane-Based Ligands for the Morphological and Electronic Control of Metal−Organic Chalcogenolate Assemblies[1]*

## 8.1 INTRODUCTION

Transition-metal chalcogenides represent a large class of hybrid materials that have been extensively studied in both academic and nonacademic research areas due to their promise as materials for a variety of applications, including photoluminescence,[1-3] electronic devices,[4-6] and electrochemical reactions.[7-9] Practitioners have often employed dimensional reduction of bulk materials as a facile strategy to tune and diversify material properties.[10] This strategy of dimensional reduction may utilize either a top-down[11-13] or bottom-up[14-19] synthetic approach, resulting in the formation of low-dimensional (zero-, one-, or two-dimensional) materials with a variety of architectures and surface compositions. One established method for the bottom-up dimensional control of metal chalcogenides has made use of the inherent reactivity between organic chalcogenols and metal cation-based precursors. The formed structures, more recently referred to as metal−organic chalcogenolate assemblies (MOCHAs, Figure 8.1a), have shown great promise in the preparation of low-dimensional metal chalcogenide materials.[20-34] More specifically, some MOCHAs have been synthesized using a biphasic approach from aqueous metal cations (e.g., copper-(I),[20] silver(I)[24]) layered with chalcogenols (e.g., alkyl thiols, aryl selenols) dissolved in an organic solvent. At

---

the solvent−solvent interface, the organic chalcogenols react with the metal cations forming intermediary metal complexes, which then nucleate and propagate the growth of small crystallites. Recently, this approach to MOCHA growth has also been extended to methods utilizing metal surfaces and gaseous benzene selenol or diphenyl diselenide reagents, where nucleation and growth of the material occurs at the solid−vapor interface.[26, 32] In all cases, while the metal of choice serves as a general framework for MOCHA properties, the overall morphological, physical, and electronic properties are largely dictated by the chalcogenolate-based ligand chosen to template the material formation. It has been further hypothesized, and shown with adamantane and diamantine thiol reagents, that the steric environment of the organic chalcogenols plays an important role in the crystallite propagation and is a determining factor of the overall material morphology.[20] Furthermore, the intermolecular forces between adjacent chalcogenolate ligands are also expected to regulate the growth of the crystallites. Critically, with the current ligand scaffolds studied with MOCHAs, it is often impossible to isolate the effect of ligand electronics on MOCHA properties without also altering their steric profile in some way, thereby inadvertently changing the steric interactions between the chalcogenolate ligands while also varying the electrostatic interaction between ligands.

One unique class of chalcogen-containing ligands that have not yet been widely explored in the context of MOCHAs are functionalized boron clusters. This is surprising, considering that boron cluster ligands (thiolates or carboxylic acids) have been extensively studied on bulk surfaces for the past two decades[35-52] and more recently with metal chalcogenide nanoparticles[53, 54] as well as metallic super atoms.[55-57] The attractiveness of boron clusters in these applications is due in large part to their propensity to form "defect-free" monolayers as a function of both the steric bulk provided by the boron cluster and, in the case of neutral boron clusters (i.e., carboranes), their inherent molecular dipole that enables long-range order (Figure 8.1b). Carboranes, with the molecular formula of $C_2B_{10}H_{12}$, exist as three distinct isomers (*ortho*-, *meta*-, *para*-) distinguished by the relative orientation of the two carbon vertices. Importantly, the electronic nonuniformity of *ortho*- and *meta*-carboranes, resulting from the asymmetry introduced by the carbon vertices, has allowed for the precise modulation of metal surface[35-57] and metal center properties,[9, 58-64] as

determined by the relative positioning of ligating substituents on the sterically invariant boron clusters (Figure 8.1b). This electronic nonuniformity is further exemplified by the regioselective chemistry of carboranes that has permitted selective introduction of functional groups to the carbon-based vertices and various boron-based vertices of carboranes.[65-67]

*Figure 8.1. (a) Selected examples of metal−organic chalcogenolate assemblies (MOCHAs) composed of either copper(I) diamondoid thiolates or silver(I) benzene selenolates. (b) History of functionalized boron clusters (dodecaborates, carboranes) as self-assembled monolayers on bulk metal, metal chalcogenide, or super atom surfaces. The approximate dipoles of carborane-based ligands are depicted to the right of the respective ligand. (c) This work, utilizing sterically invariant carborane-based chalcogenolates to modulate morphology and photophysical properties of carborane- containing MOCHAs.*



a. previously studied metal-organic chalcogenolate assemblies (MOCHAs)

1D extended lattice    Cuᴵ-SAd unit    2D layered crystals

b. boron clusters as self-assembled monolayers    c. this work

[35]    [36-39,42-44,46]    [47]    [48]
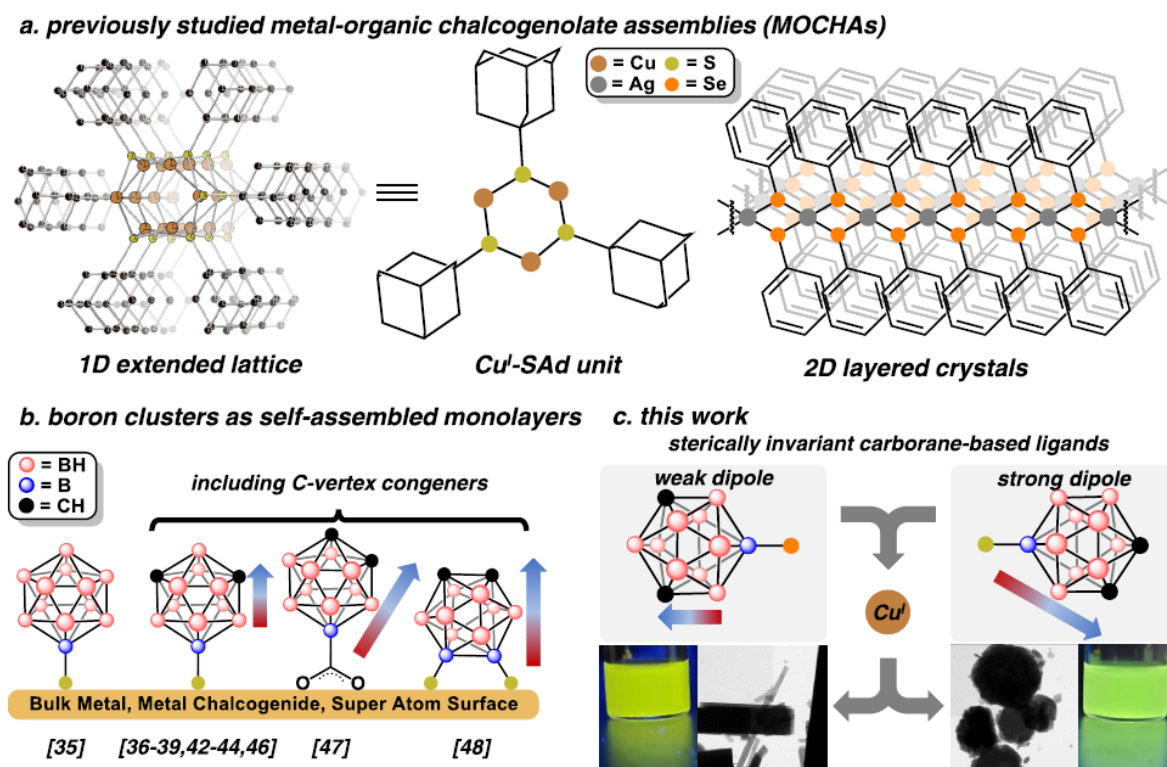
Despite the potential for carborane-based ligands to tune MOCHA properties, only two recent studies have reported the use of 9-*meta*-carboranyl thiolates to generate MOCHA-like structures with cadmium(I)[20] and copper(I).[22] In the case of the cadmium(I)-based MOCHA, the prepared materials were

preliminarily visualized by scanning electron microscopy with no additional characterization provided. Conversely, structural characterization of the copper(I)-based MOCHA was reported, though the study focused solely on the mechanical properties of the resulting materials. To further develop the understanding of structure−function relationships in the context of MOCHAs and, more specifically, the impact a molecular dipole might have on MOCHA morphology and electronic properties, we report our investigation on the formation of copper(I)-based MOCHA materials with sulfur and selenium-containing electron-rich carborane chalcogenolates (Figure 8.1c). Specifically, we show how sterically invariant carborane-based chalcogenolate ligands can control the morphology and electronic properties of copper(I)-based MOCHAs through differences in the carborane dipole between the *ortho-* and *meta-*isomers. The morphology, composition, and stability of all reported materials have been determined using scanning electron microscopy (SEM), transmission electron microscopy (TEM), powder X-ray diffraction (PXRD), Fourier transform infrared (FTIR) spectroscopy, thermogravimetric analysis (TGA), and X-ray photoelectron spectroscopy (XPS). Furthermore, critical structural characterization was obtained by applying emerging microcrystal electron diffraction (MicroED) techniques to determine the unique bonding arrangement between copper(I) and 9-*meta*carboranyl selenolate for the key MOCHA structure synthesized. All prepared materials exhibit photoluminescence that further exemplify control of MOCHA properties by tuning key photophysical properties, such as quantum yield and emission lifetimes, as a function of both the carborane dipole and the chalcogenolate (Se, S) used.

## 8.2 SYNTHESIS, CHARACTERIZATION AND ANALYSIS OF MOCHA SYSTEM

To understand whether one can form MOCHAs with sterically encumbering carborane ligands, we first opted to study the reaction between a copper(I) precursor and 9-*meta*-carboranyl selenol (SeH-mCB, **A'**). Copper(I) was chosen due to the previously reported reactivity between copper(I) precursors and sterically encumbered adamantane thiol[20] or *meta*-carboranyl thiol[22] ligands. Conversely, SeH-mCB was selected as our first ligand of study due to the known stability of exopolyhedral B−Se bonds,[68, 69] the established body of work utilizing *meta*-carborane ligands in self-assembled materials, [35-57] and, lastly, the

anticipated reactivity between the selenolate and copper(I). SeH-mCB was synthesized according to literature procedures[68, 69] (Figure 8.2a, see Appendix G for full experimental details) and isolated as an air-stable solid that showed little to no oxidation after several months when stored at 5 °C in laboratory air, in contrast to oxidatively unstable carbon-based selenols. To begin our studies regarding the self-assembly behavior of carborane chalcogenols in the presence of copper(I) salts, SeH-mCB and copper(I) acetate were mixed together as powders in a 4 mL dram vial equipped with a stir bar in a nitrogen-filled glovebox. Subsequently, anhydrous isopropanol was added via a syringe, and the reaction mixture was immediately stirred at 700 rpm in the dark (Figure 8.2b). This approach takes advantage of gradual etching of the copper(I) acetate particles by the dissolved selenol, decreasing the reaction rate that has previously resulted in noncrystalline MOCHA phases when using benzene selenol.[24] Within minutes, an off-white precipitate began to form, ultimately resulting in a milky suspension after stirring overnight. To separate the formed precipitate, the suspension was centrifuged, and the resulting pellet was collected and dried *in vacuo* to remove all volatiles, affording Cu−[Se-mCB] (**A**) in 76% yield as an analytically pure powder.

***Figure 8.2***. *(a) Synthesis of B(9)-substituted meta- and ortho-carborane selenols and thiols following literature procedures. Representative characterization ($^1H$, $^{77}Se$ NMR) of 9-SeH-mCB in THF-$d_6$. (b) General synthesis of carborane chalcogenolate-containing MOCHAs **A−D**.*
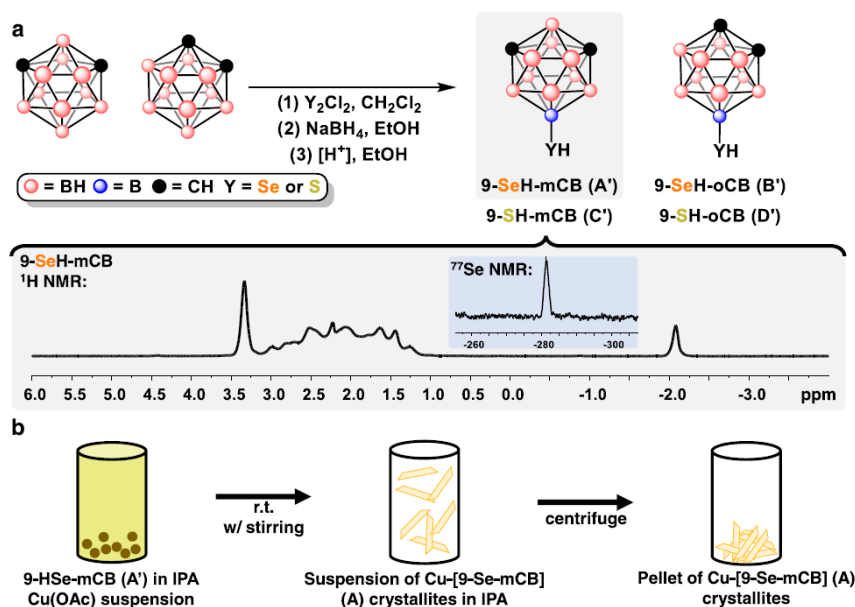
***Figure 8.3***. *(a) Representative bright-field TEM image of **A** crystallite used for MicroED experiments. (b) Representative frames of MicroED performed of **A** used for refinement. (c) MicroED-derived structure of **A** revealing a tetrameric Cu−Se core sterically protected by meta-carboranyl ligands. The table provides average bond lengths for relevant bonds. The packing of two clusters is also depicted, showing the proximity of the meta-carborane cluster to an adjacent selenolate. (d) PXRD pattern of bulk **A** at 293 K and 100 K, as well as the simulated[71] PXRD pattern from the MicroED-derived structure. Hydrogens have been omitted for clarity.*



| Bond | Length |
|------|--------|
| Cu-Se$_{avg}$ | 2.20(3) Å |
| Cu-Cu$_{avg}$ | 2.60(3) Å |
| B(9)-Se$_{avg}$ | 1.91(3) Å |
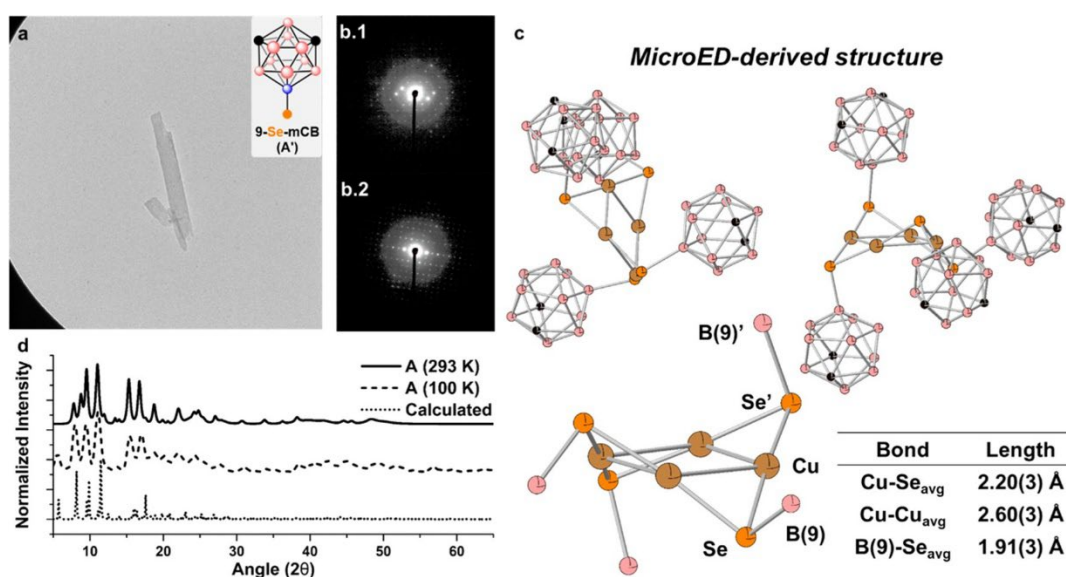
When visualizing powders of **A** through electron microscopy (TEM, SEM), the morphology of the crystallites was revealed to be square rods, approximately 5−10 $\mu$m in length and 1−2 $\mu$m in width (Figures 8.3a and 8.4a), somewhat reminiscent of previously imaged MOCHAs composed of Cd−[S-mCB].[20] The crystallinity of the **A** microcrystals present on the TEM sample grid was confirmed using selected area electron diffraction (SAED) (Figure 8.3b). After observing single-crystal diffraction using SAED, MicroED methods were applied for crystallographic analysis of **A**. Despite being highly crystalline, the crystal morphology of **A** microcrystals (square rods) and low symmetry presented a particular challenge as sampling the entirety of reciprocal space was limited due to the range of the TEM sample holder tilt axis. However, by combining data sets from five different microcrystals, sufficient unique reflections were

obtained for an *ab initio* solution, resulting in successful structural determination (see Appendix G for full experimental details). In contrast to previously reported materials with copper(I) diamondoid thiolates[20] or silver(I) benzene selenolates[24] containing an extended metal chalcogenolate network ([M−SR/SeR]$_\infty$), **A** crystallites are comprised entirely of isolated tetrameric copper carborane selenolate clusters with a $Cu_4Se_4$ core surrounded by four *meta*-carboranyl ligands, indicating a zero-dimensional morphology (Figure 8.3c). Surprisingly, the experimentally determined structure of **A** is highly reminiscent of that observed in the previously reported copper(I) *meta*-carboranyl thiolate material that adopted a $Cu_4S_4$ structure.[22] While the C−H vertices of the *meta*-carboranyl ligands cannot be immediately distinguished, the positioning of the exopolyhedral B(9)−Se bond and anticipated dipole−Se interactions between adjacent *meta*-carboranyl selenolates have been used to determine the exact positioning of the carbon-based vertices (Figure 8.3c). Notably, the $Cu_4Se_4$ core in **A** is the first structurally characterized copper(I) selenide tetramer with a planar $Cu_4$ geometry, the formation of which can likely be correlated to the steric bulk of the carboranyl ligands (see Appendix G for details). To confirm the validity of the crystal structure obtained via MicroED, experimental PXRD data of **A** was compared to the simulated[69] PXRD data generated from the single-crystal MicroED structure (Figure 8.3d). We observed good agreement between the experimental and simulated PXRD patterns despite some minor deviations that could likely be attributed to thermal contraction of the crystallites while performing MicroED. To confirm that this is the case, PXRD experiments were performed while cooling the crystallites to 100 K with liquid nitrogen (Figure 8.3d). Importantly, the cryogenic PXRD pattern more closely matches the simulated PXRD pattern, suggesting that the single-crystal structure obtained via MicroED is characteristic of the bulk material.

Based on the crystallographic data, all copper atoms in **A** are assigned to be in a formal oxidation state of +1. To further corroborate this, XPS measurements of **A** were performed. The XPS measurements of **A** were then compared with those of the copper(I) acetate starting material and (Se-mCB)$_2$ as an analogue of SeH-mCB due to the propensity of carborane chalcogenols to sublime under vacuum (Figure 8.4b). The Cu $2p_{1/2}$ and Cu $2p_{3/2}$ peaks of **A**, 952.7 and 932.8 eV, respectively, are shifted to a lower binding energy

relative to copper(I) acetate and are consistent with the more electronrich[68, 69] environment experienced by the copper(I) nuclei when interacting with the *meta*-carborane selenolate. There are no satellite peaks present adjacent to the Cu $2p_{1/2}$ peak, which are commonly found in XPS measurements of copper(II)-containing materials,[70] indicating that the copper(I) oxidation state is conserved during the course of the reaction. Peak fitting of the Cu 2p XPS signals further indicates the presence of a singular copper(I) environment, in agreement with the MicroED-derived structure (see Appendix G for details). Between (SemCB) 2 and **A**, there is no significant change in the Se 3d peak binding energies, and peak-fitting again confirms only one selenium environment (see Appendix G for details). The XPS measurements further allude to the resistance of the copper(I) centers in **A** to oxidation by atmospheric oxygen despite the electronrich environment imparted by the carborane selenolate,[68, 69] likely a result of the steric protection provided by the *meta*-carboranyl ligands as illustrated by the MicroED-derived single-crystal structure.

*Figure 8.4. (a) SEM images of A. The inset shows a more general overview of the crystallite morphology. Scale bar is applied to both SEM images. (b) XPS measurements of A, Cu(OAc), and (Se-mCB)₂. (c) FTIR spectra of 9-SeH-mCB (dotted trace) and A (solid trace). (d) TGA of A.*
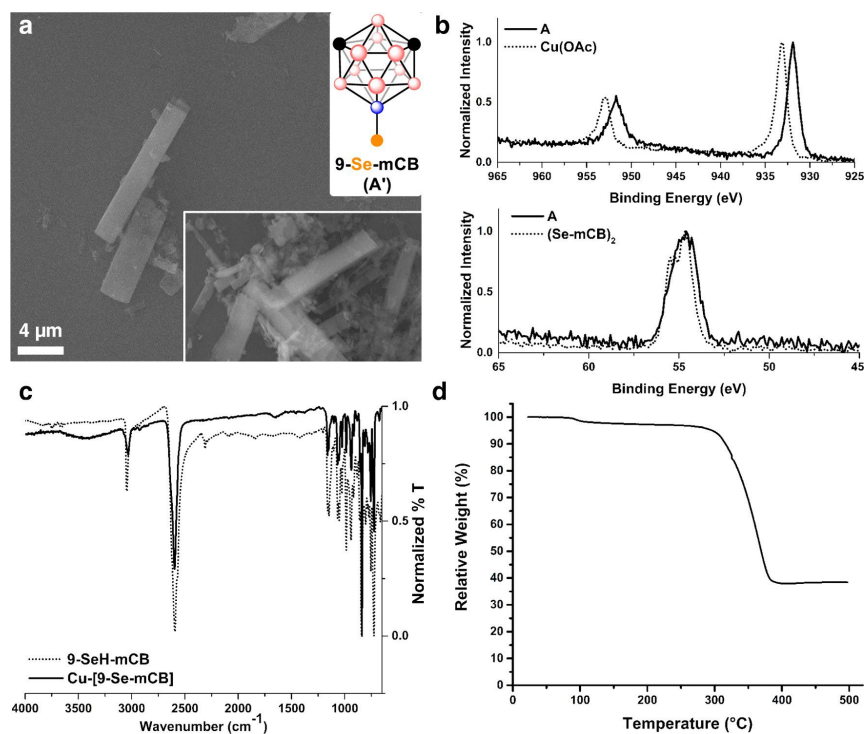
In addition to XPS measurements, FTIR spectroscopy of **A** was used to confirm the absence of any residual starting materials. Specifically, the FTIR spectrum of **A** revealed a distinct loss of signal associated with the Se−H stretch present in the FTIR spectrum of SeH-mCB at 2400 cm$^{-1}$ (Figure 8.4c); however, the remaining cluster structure appears to be intact with only slight deviations in signals present in the fingerprint region (1250−600 cm$^{-1}$). The presence of intact boron clusters in the powder of **A** is further confirmed by diagnostic B−H resonances (2600 cm$^{-1}$) in the spectrum. Furthermore, when comparing the FTIR spectrum of **A** with that of the copper(I) acetate starting material, there are no signals present in the formed material that could be correlated to the carbon−oxygen double bond in copper(I) acetate, indicating that the acetate ligand is not present in the resulting hybrid material. Consistent with FTIR, TGA (Figure 8.4d) also revealed that there are no substantial solvent adducts in the **A** crystallites, as indicated by no significant mass loss until 300 °C, which is most likely associated with the decomposition of the *meta*-carborane selenolate and agrees with the single-crystal MicroED structure.

***Figure 8.5***. *(a) Comparison of Cu 2p$_{1/2}$ and Cu 2p$_{3/2}$ XPS measurements for materials **A−D**. (b) Stacked PXRD patterns of materials **A−D**. (c) Overlaid peak patterns for materials **A** and **B**, **A** and **C**, and **B** and **D**. d−f. SEM and TEM (insets) images of **B−D**, respectively.*
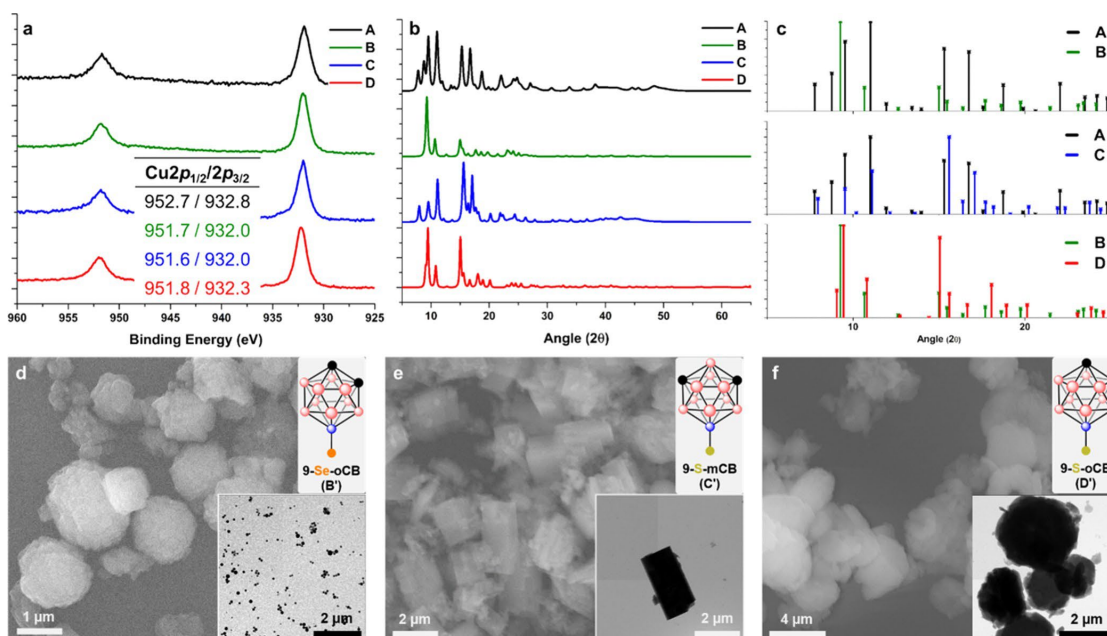
To determine any effects the carborane dipole might impart on the structural behavior of the isolated microcrystals as well as the impact of chalcogenide (Se *vs* S), we then studied the reaction of copper(I) acetate with 9-*ortho*-carborane selenol (9-SeH-oCB, **B'**), 9-*meta*-carborane thiol (9-SH-mCB, **C'**), and 9-*ortho*-carborane thiol (9-SH-oCB, **D′**). Notably, the molecular dipole in *ortho*-carborane is significantly larger in magnitude compared to that of *meta*-carborane.[44, 48] Following similar procedures used in the synthesis of **A**, crystalline powders of Cu−[Se-oCB] (**B**), Cu−[S-mCB] (**C**), and Cu−[S-oCB] (**D**) were isolated as white/tan powders in 65, 84, and 69% isolated yields, respectively (see Appendix G for details), and characterized in a similar fashion to **A**. Despite the use of different carborane-based chalcogenols, FTIR, TGA, and XPS data of powders **B**, **C**, and **D** closely resemble the data obtained for **A** (see Appendix G for details), suggesting a molecular similarity. FTIR, for example, revealed that there is no starting carborane chalcogenol or copper(I) acetate present in the isolated powders **B−D**, with all materials exhibiting comparable thermal stabilities by TGA, while XPS indicates that the copper(I) oxidation state is maintained during the formation of **B−D** with similar binding energy for the copper centers measured in **A** (Figure 8.5a). Additionally, solution-state $^1$H and $^{11}$B NMR spectroscopic measurements of materials **A−D** in dichloromethane further suggested similarities in the molecular structures of the materials and were consistent with FTIR and TGA measurements (SI Section 10).

When comparing the PXRD data (see Appendix G for details) of all four materials, there are clear similarities in the molecular structures of **A−D** due to the closely matching diffractions from 5 to 25 2$\theta$, regardless of the chalcogen or carborane isomer (Figure 8.5b). When comparing the PXRD patterns of materials **A** and **B** (same chalcogen, different carborane isomers), there are some deviations, though they can be explained by the expected differences in molecular packing as a result of differing dipole−dipole interactions within the crystal (Figure 8.5c). In contrast, a closer inspection of PXRD patterns (Figure 8.5c) for materials containing the same carborane isomer (*meta*: **A**, **C**; *ortho*: **B**, **D**) reveals nearly identical diffractions with negligible deviations between the data sets (<±0.5 2$\theta$) that can be explained by the slight changes in *d*-spacing when the chalcogen is changed from selenium to sulfur (see Appendix G for details).

As expected, this data indicates that the carborane dipole plays a critical role in determining molecular packing of the material while the choice of chalcogen has a minor impact.

*Figure 8.6. (a, b) Emission (solid trace) and absorption (dotted trace) spectra of materials **A−D**. Due to the excitation wavelength used to obtain emission spectra (280 nm) for **A−D**, a peak is present at ~560 nm in all emission spectra that is not part of the emission of materials **A−D**. (c) Images of emissive isopropanol suspensions of **A−D** along with their respective emission wavelengths (λ_max), quantum yields (ϕ_high, ϕ_low), lifetimes (τ), and calculated radiative (k_r) and nonradiative (k_nr) rate constants. (d) Highest occupied molecular orbital (HOMO) (red, blue) and lowest unoccupied molecular orbital (LUMO) (orange, teal) of **A**, calculated on the crystallographically derived structure using the B3LYP functional DZP basis set. The calculated HOMO−LUMO gap is 4.35 eV, corresponding to 285 nm. ᵃϕ_high and ϕ_low are calculated based on the relative emission peak integrations for the high-energy (low wavelength) and low-energy (high wavelength) bands, respectively. ᵇCalculated using ϕ_low. ᶜCalculated using ϕ_high.*



| Mat. | Emission $\lambda_{max}$ | $\varphi_{high}^a$ | $\varphi_{low}^a$ | $\tau$ (µs) | $k_r$ (s⁻¹) | $k_{nr}$ (s⁻¹) |
|---|---|---|---|---|---|---|
| A | 340, 550 | 0.09 | 0.11 | 14 | 7900[b] | 64000[b] |
| B | 340, 540 | 0.43 | - | 34 | 13000[c] | 17000[c] |
| C | 335, 515 | 0.09 | 0.64 | 46 | 14000[b] | 7800[b] |
| D | 335, 520 | 0.33 | 0.60 | 44 | 14000[b] | 9100[b] |
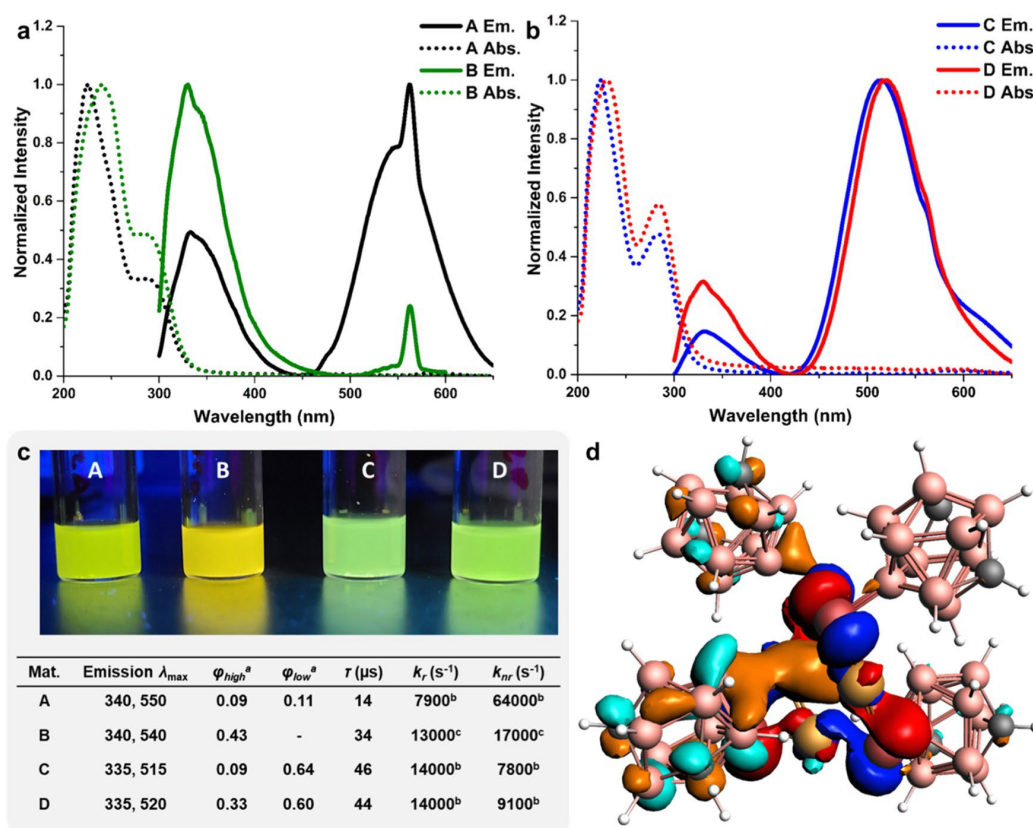
While FTIR, TGA, XPS, and PXRD suggested a molecular similarity between materials **A−D**, electron microscopy (SEM, TEM, Figure 8.5d−f) revealed a distinct difference in crystallite morphology, largely as a function of carborane isomer while also affected by which chalcogen was present. **C** crystallites (Figure 8.5e) were similar in morphology to **A**, though would be more accurately described as square prisms, being generally thicker (2−3 $\mu$m) and significantly shorter (3−5 $\mu$m) in length. In contrast, materials **B** and **D**, which contain *ortho*-carborane-based chalcogenolates, favored the formation of spherical particles with two major phases present. In the case of **B**, while some larger particle aggregates (1.10 $\mu$m ± 0.31) were present (Figure 8.5d), TEM revealed that a significant portion of the material consists of nanoscale particles (92 nm ± 25, Figure 8.5D inset); in contrast, **D** predominantly favored the formation of larger microscale particles (3.47 $\mu$m ± 0.72, Figure 8.5F). MicroED measurements of **B** and **C** were attempted (see Appendix G for details), though the crystal morphologies were not easily amenable to electron diffraction. In the case of material **B**, the spherical nature of the particles ultimately resulted in polycrystalline diffractions, while for material **C**, the thickness of the crystallites inhibited electron diffraction, resulting in low-intensity diffractions.[71] The difference in morphologies (rods *vs* spheres) between materials **A−D** can primarily be explained by the inductive effect of the carborane cluster imparted onto the chalcogenolates, as well as the magnitude of the carborane dipole. In other words, the weaker dipole of the *meta*-carborane-containing ligands present in materials **A** and **C** unequivocally favors the formation of cubic, rod-like microcrystals, whereas the stronger dipole of the *ortho*-carborane−containing ligands present in materials **B** and **D** appears to limit long-range crystal growth and results in spherical microcrystals.

Materials consisting of metal chalcogenolates, particularly those that are copper-based, often exhibit photoluminescence.[72-75] Similar properties are therefore expected for materials **A−D**. Differences in the electronic environment experienced by the copper chalcogenide core are expected to arise as a function of both the carborane isomer (*meta*-, *ortho*-) and chalcogenide (Se, S). Consequently, variations in the photophysical properties of each structure are expected. The normalized UV−vis absorption spectra for

uniform suspensions of **A**−**D** in isopropanol all show two strong absorptions located at 220−240 nm and 280 nm (Figure 8.6a,b, dotted tracs). While the wavelengths of absorption do not vary greatly between compounds, differences in relative peak intensity are evident. Using the excitation wavelengths, as indicated by UV−vis spectroscopy (220 nm and 280 nm), fluorescence measurements were subsequently obtained from the prepared isopropanol suspensions. While the higher-energy absorption (220 nm) was the most intense for all materials, no significant emission was associated with this excitation (see Appendix G for details). Notably, only the lower-energy transition (280 nm) yielded any measurable emission (Figure 8.6a,b, solid traces). For all four materials, emission was observed at 340 nm and at 450−650 nm, with the latter being significantly broader than the former and distinctly weaker in the case of **B**. Interestingly, when these materials are dissolved in polar aprotic organic solvents, all emissive properties are no longer present (see Appendix G for details). To confirm the copper(I) selenide core in **A** was still intact upon dissolution, **A** was precipitated from solution by trituration with pentane and the emission of the as-synthesized crystals was fully regained (see Appendix G for details), suggesting that luminescence is contingent upon restricted molecular motion that can be achieved in the solid state. This is further supported by the observation of luminescence in frozen solutions and in polymer matrices embedded with the materials. Notably, while the emission properties can be regained through these methods, they are red-shifted relative to the emission of the as-synthesized or triturated crystals (see Appendix G for details). Such effects of temperature and aggregation/crystallization on emissive properties are commonly observed phenomena.[76-78]

To further understand the photophysical properties of these materials, quantum yield ($\varphi_{high}/\varphi_{low}$) and lifetime ($\tau$) measurements were performed on **A**−**D** as crystalline powders (see Appendix G for full details). The quantum yields associated with the high- and low-energy emissions ($\varphi_{high}/\varphi_{low}$) were 0.09/0.11, 0.43/0.00, 0.09/0.64, and 0.33/0.60 for materials **A**−**D**, respectively (Figure 8.6c). Furthermore, the long lifetimes associated with the emissions (14, 34, 46, and 44 $\mu$s for **A**−**D**, respectively) indicate that the luminescence is phosphorescent in nature, which is caused by the presence of the heavier copper, selenium, and sulfur atoms. Materials **A** and **B** exhibited overall weaker emission compared to **C** and **D**, favoring

nonradiative relaxation from the excited state (Figure 8.6c). Furthermore, DFT calculations of **A** indicate that the emission most likely originates from a metal-to-ligand charge transfer (MLCT) between a copper(I) selenide-centered HOMO and a carborane selenolate-centered LUMO (Figure 8.6d). While the differences in these photophysical properties are most closely correlated to the chalcogen present in the material (Se: **A**, **B**; S: **C**, **D**), there is a noticeable trend between materials within the same morphology category (rods, spheres) and thus contain the same carborane isomer. Notably, materials containing *ortho*-carborane-based chalcogenolates (**B** and **D**), exhibited higher quantum yields compared to their *meta*-carborane-containing counterparts (**A** and **C**). These results suggest that the tunable inductive effect[7] afforded by the carborane-based ligands using different isomers can be used to fine-tune the electronic properties of copper(I) MOCHAs as demonstrated by the precise control over photophysical properties. This is consistent with what has been generally observed with other tunable carborane-based ligands in the context of organometallic Pt(II)-based luminescent emitters.[59]

## 8.3 CONCLUSIONS

In summary, we demonstrate the synthesis and characterization of zero-dimensional carborane chalcogenolate-containing microcrystalline MOCHAs with tunable photoluminescent properties. We show that the nature of the carborane ligand dictates the crystallite morphology of the resulting MOCHA and is able to fine-tune photophysical properties, such as quantum yield and emission lifetimes, without affecting the fundamental emission characteristics (Figure 8.6). Furthermore, MicroED has been used for the first time to structurally characterize this class of materials and has provided significant insight into the bonding arrangement between copper(I) and *meta*-carboranyl selenolate. In contrast to other MOCHA materials with an extended metal chalcogenide core, MicroED has revealed that the synthesized carborane-structured MOCHAs consist of an unprecedented zero-dimensional $Cu_4Se_4$ cluster that is representative of the smallest building block of bulk CuSe materials. This work therefore further establishes the utility of MicroED for hybrid material structure elucidation when reaching the limitations of more traditional structural

determination methods.[79-82] This study furthermore highlights how the use of bulky, organomimetic, boron cluster ligands can lead to the formation of hybrid materials with unique structures and properties.

## 8.4 REFERENCES

(1) Rismaningsih, N.; Yamauchi, H.; Kameyama, T.; Yamamoto, T.; Morita, S.; Yukawa, H.; Uematsu, T.; Baba, Y.; Kuwabata, S.; Torimoto, T. Photoluminescence properties of quinary Ag-(In,Ga)-(S,Se) quantum dots with a gradient alloy structure for in vivo bioimaging. *Journal of Materials Chemistry C* **2021**, *9* (37), 12791-12801.

(2) Kanatzidis, M. G. Discovery-Synthesis, Design, and Prediction of Chalcogenide Phases. *Inorganic Chemistry* **2017**, *56* (6), 3158-3173.

(3) Naskar, S.; Miethe, J. F.; Sanchez-Paradinas, S.; Schmidt, N.; Kanthasamy, K.; Behrens, P.; Pfnur, H.; Bigall, N. C. Photoluminescent Aerogels from Quantum Wells. *Chemistry of Materials* **2016**, *28* (7), 2089-2099.

(4) Liu, Y.; Weiss, N. O.; Duan, X. D.; Cheng, H. C.; Huang, Y.; Duan, X. F. Van der Waals heterostructures and devices. *Nature Reviews Materials* **2016**, *1* (9).

(5) Matthews, P. D.; McNaughter, P. D.; Lewis, D. J.; O'Brien, P. Shining a light on transition metal chalcogenides for sustainable photovoltaics. *Chemical Science* **2017**, *8* (6), 4177-4187.

(6) Maruyama, M.; Nagashio, K.; Okada, S. Influence of Interlayer Stacking on Gate-Induced Carrier Accumulation in Bilayer MoS2. *Acs Applied Electronic Materials* **2020**, *2* (5), 1352-1357.

(7) Giuffredi, G.; Asset, T.; Liu, Y. C.; Atanassov, P.; Di Fonzo, F. Transition Metal Chalcogenides as a Versatile and Tunable Platform for Catalytic CO2 and N-2 Electroreduction. *Acs Materials Au* **2021**, *1* (1), 6-36.

(8) Eng, A. Y. S.; Ambrosi, A.; Sofer, Z.; Simek, P.; Pumera, M. Electrochemistry of Transition Metal Dichalcogenides: Strong Dependence on the Metal-to-Chalcogen Composition and Exfoliation Method. *Acs Nano* **2014**, *8* (12), 12185-12198.

(9) Zhang, J.; Cao, B. L.; Ding, Y. Z.; Chang, J. R.; Li, S. J.; Chen, X. N. Syntheses and Structures of Group 10 Metal POCOP Pincer Complexes Bearing A Mercapto-o-carborane Auxiliary Ligand. *Chemistryselect* **2019**, *4* (4), 1292-1297.

(10) Tulsky, E. G.; Long, J. R. Dimensional reduction: A practical formalism for manipulating solid structures. *Chemistry of Materials* **2001**, *13* (4), 1149-1166.

(11) Coleman, J. N.; Lotya, M.; O'Neill, A.; Bergin, S. D.; King, P. J.; Khan, U.; Young, K.; Gaucher, A.; De, S.; Smith, R. J.; et al. Two-Dimensional Nanosheets Produced by Liquid Exfoliation of Layered Materials. *Science* **2011**, *331* (6017), 568-571.

(12) Backes, C.; Szydlowska, B. M.; Harvey, A.; Yuan, S. J.; Vega-Mayoral, V.; Davies, B. R.; Zhao, P. L.; Hanlon, D.; Santos, E. J. G.; Katsnelson, M. I.; et al. Production of Highly Monolayer Enriched Dispersions of Liquid-Exfoliated Nanosheets by Liquid Cascade Centrifugation. *Acs Nano* **2016**, *10* (1), 1589-1601.

(13) Bodik, M.; Annusova, A.; Hagara, J.; Micusik, M.; Omastova, M.; Kotlar, M.; Chlpik, J.; Cirak, J.; Svajdlenkova, H.; Angus, M.; et al. An elevated concentration of MoS2 lowers the efficacy of liquid-phase exfoliation and triggers the production of MoOx nanoparticles. *Physical Chemistry Chemical Physics* **2019**, *21* (23), 12396-12405.

(14) Manzeli, S.; Ovchinnikov, D.; Pasquier, D.; Yazyev, O. V.; Kis, A. 2D transition metal dichalcogenides. *Nature Reviews Materials* **2017**, *2* (8).

(15) Jia, C. C.; Lin, Z. Y.; Huang, Y.; Duan, X. F. Nanowire Electronics: From Nanoscale to Macroscale. *Chemical Reviews* **2019**, *119* (15), 9074-9135.

(16) Enright, M. J.; Dou, F. Y.; Wu, S. W.; Rabe, E. J.; Monahan, M.; Friedfeld, M. R.; Schlenker, C. W.; Cossairt, B. M. Seeded Growth of Nanoscale Semiconductor Tetrapods: Generality and the Role of Cation Exchange. *Chemistry of Materials* **2020**, *32* (11), 4774-4784.

(17) Li, T. Y.; Liu, Y. H.; Porter, S.; Goldberger, J. E. Dimensionally Reduced One-Dimensional Chains of TiSe2. *Chemistry of Materials* **2013**, *25* (9), 1477-1479.

(18) Chareev, D. A.; Evstigneeva, P.; Phuyal, D.; Man, G. J.; Rensmo, H.; Vasiliev, A. N.; Abdel-Hafiez, M. Growth of Transition-Metal Dichalcogenides by Solvent Evaporation Technique. *Crystal Growth & Design* **2020**, *20* (10), 6930-6938.

(19) Ding, K. L.; Lu, H.; Zhang, Y. C.; Snedaker, M. L.; Liu, D. Y.; Macia-Agullo, J. A.; Stucky, G. D. Microwave Synthesis of Microstructured and Nanostructured Metal Chalcogenides from Elemental Precursors in Phosphonium Ionic Liquids. *Journal of the American Chemical Society* **2014**, *136* (44), 15465-15468.

(20) Yan, H.; Hohman, J. N.; Li, F. H.; Jia, C. J.; Solis-Ibarra, D.; Wu, B.; Dahl, J. E. P.; Carlson, R. M. K.; Tkachenko, B. A.; Fokin, A. A.; et al. Hybrid metal-organic chalcogenide nanowires with electrically conductive inorganic core through diamondoid-directed assembly. *Nature Materials* **2017**, *16* (3), 349.

(21) Veselska, O.; Podbevsek, D.; Ledoux, G.; Fateeva, A.; Demessence, A. Intrinsic triple-emitting 2D copper thiolate coordination polymer as a ratiometric thermometer working over 400 K range. *Chemical Communications* **2017**, *53* (90), 12225-12228.

(22) Yan, H.; Yang, F.; Pan, D.; Lin, Y.; Hohman, J. N.; Solis-Ibarra, D.; Li, F. H.; Dahl, J. E. P.; Carlson, R. M. K.; Tkachenko, B. A.; et al. Sterically controlled mechanochemistry under hydrostatic pressure. *Nature* **2018**, *554* (7693), 505-510.

(23) Veselska, O.; Demessence, A. d(10) coinage metal organic chalcogenolates: From oligomers to coordination polymers. *Coordination Chemistry Reviews* **2018**, *355*, 240-270.

(24) Schriber, E. A.; Popple, D. C.; Yeung, M.; Brady, M. A.; Corlett, S. A.; Hohman, J. N. Mithrene Is a Self-Assembling Robustly Blue Luminescent Metal-Organic Chalcogenolate Assembly for 2D Optoelectronic Applications. *Acs Applied Nano Materials* **2018**, *1* (7), 3498-3508.

(25) Eichhofer, A.; Lebedkin, S. 1D and 3D Polymeric Manganese(II) Thiolato Complexes: Synthesis, Structure, and Properties of (3)(infinity) Mn-4(SPh)(8) and (1)(infinity) Mn(SMes)(2). *Inorganic Chemistry* **2018**, *57* (2), 602-608.

(26) Trang, B.; Yeung, M.; Popple, D. C.; Schriber, E. A.; Brady, M. A.; Kuykendall, T. R.; Hohman, J. N. Tarnishing Silver Metal into Mithrene. *Journal of the American Chemical Society* **2018**, *140* (42), 13892-13903.

(27) Popple, D. C.; Schriber, E. A.; Yeung, M.; Hohman, J. N. Competing Roles of Crystallization and Degradation of a Metal Organic Chalcogenolate Assembly under Biphasic Solvothermal Conditions. *Langmuir* **2018**, *34* (47), 14265-14273.

(28) Royappa, A. T.; Tran, C. M.; Papoular, R. J.; Khan, M.; Marbella, L. E.; Millstone, J. E.; Gembicky, M.; Chen, B. H.; Shepard, W.; Elkaim, E. Copper(I) and gold(I) thiolate precursors to bimetallic nanoparticles. *Polyhedron* **2018**, *155*, 359-365.

(29) Xiao, Q. R.; Burg, J. A.; Zhou, Y.; Yan, H.; Wang, C.; Ding, Y. C.; Reed, E.; Miller, R. D.; Dauskardt, R. H. Electrically Conductive Copper Core-Shell Nanowires through Benzenethiol-Directed Assembly. *Nano Letters* **2018**, *18* (8), 4900-4907.

(30) Wang, J.; Li, Y. L.; Wang, Z. Y.; Zang, S. Q. A robust wave- like silver- thiolate chain based metal-organic network: synthesis, structure and luminescence. *Crystengcomm* **2019**, *21* (14), 2264-2267.

(31) Veselska, O.; Dessal, C.; Melizi, S.; Guillou, N.; Podbevsek, D.; Ledoux, G.; Elkaim, E.; Fateeva, A.; Demessence, A. New Lamellar Silver Thiolate Coordination Polymers with Tunable Photoluminescence Energies by Metal Substitution. *Inorganic Chemistry* **2019**, *58* (1), 99-105.

(32) Yeung, M.; Popple, D. C.; Schriber, E. A.; Teat, S. J.; Beavers, C. M.; Demessence, A.; Kuykendall, T. R.; Hohman, J. N. Corrosion of Late- and Post-Transition Metals into Metal-Organic Chalcogenolates and Implications for Nanodevice Architectures. *Acs Applied Nano Materials* **2020**, *3* (4), 3568-3577.

(33) Vaidya, S.; Veselska, O.; Zhadan, A.; Diaz-Lopez, M.; Joly, Y.; Bordet, P.; Guillou, N.; Dujardin, C.; Ledoux, G.; Toche, F.; et al. Transparent and luminescent glasses of gold thiolate coordination polymers. *Chemical Science* **2020**, *11* (26), 6815-6823.

(34) Paritmongkol, W.; Sakurada, T.; Lee, W. S.; Wan, R.; Muller, P.; Tisdale, W. A. Size and Quality Enhancement of 2D Semiconducting Metal-Organic Chalcogenolates by Amine Addition. *Journal of the American Chemical Society* **2021**, *143* (48), 20256-20263.

(35) Yeager, L. J.; Saeki, F.; Shelly, K.; Hawthorne, M. F.; Garrell, R. L. A new class of self-assembled monolayers: closo-B12H11S3- on gold. *Journal of the American Chemical Society* **1998**, *120* (38), 9961-9962.

(36) Base, T.; Bastl, Z.; Plzak, Z.; Grygar, T.; Plesek, J.; Carr, M. J.; Malina, V.; Subrt, J.; Bohacek, J.; Vecernikova, E.; et al. Carboranethiol-modified gold surfaces. A study and comparison of modified cluster and flat surfaces. *Langmuir* **2005**, *21* (17), 7776-7785.

(37) Base, T.; Bastl, Z.; Slouf, M.; Klementova, M.; Subrt, J.; Vetushka, A.; Ledinsky, M.; Fejfar, A.; Machacek, J.; Carr, M. J.; et al. Gold micrometer crystals modified with carboranethiol derivatives. *Journal of Physical Chemistry C* **2008**, *112* (37), 14446-14455.

(38) Hohman, J. N.; Zhang, P. P.; Morin, E. I.; Han, P.; Kim, M.; Kurland, A. R.; McClanahan, P. D.; Balema, V. P.; Weiss, P. S. Self-Assembly of Carboranethiol Isomers on Au{111}: Intermolecular Interactions Determined by Molecular Dipole Orientations. *Acs Nano* **2009**, *3* (3), 527-536.

(39) Base, T.; Bastl, Z.; Havranek, V.; Lang, K.; Bould, J.; Londesborough, M. G. S.; Machacek, J.; Plesek, J. Carborane-thiol-silver interactions. A comparative study of the molecular protection of silver surfaces. *Surface & Coatings Technology* **2010**, *204* (16-17), 2639-2646.

(40) Hohman, J. N.; Claridge, S. A.; Kim, M.; Weiss, P. S. Cage molecules for self-assembly. *Materials Science & Engineering R-Reports* **2010**, *70* (3-6), 188-208.

(41) Lübben, J. F.; Baše, T.; Rupper, P.; Künniger, T.; Macháček, J.; Guimond, S. Tuning the surface potential of Ag surfaces by chemisorption of oppositely-oriented thiolated carborane dipoles. *Journal of Colloid and Interface Science* **2011**, *354* (1), 168-174.

(42) Bould, J.; Machacek, J.; Londesborough, M. G. S.; Macias, R.; Kennedy, J. D.; Bastl, Z.; Rupper, P.; Base, T. Decaborane Thiols as Building Blocks for Self-Assembled Monolayers on Metal Surfaces. *Inorganic Chemistry* **2012**, *51* (3), 1685-1694.

(43) Base, T.; Bastl, Z.; Havranek, V.; Machacek, J.; Langecker, J.; Malina, V. Carboranedithiols: Building Blocks for Self-Assembled Monolayers on Copper Surfaces. *Langmuir* **2012**, *28* (34), 12518-12526.

(44) Kim, J.; Rim, Y. S.; Liu, Y. S.; Serino, A. C.; Thomas, J. C.; Chen, H. J.; Yang, Y.; Weiss, P. S. Interface Control in Organic Electronics Using Mixed Monolayers of Carboranethiol Isomers. *Nano Letters* **2014**, *14* (5), 2946-2951.

(45) Vetushka, A.; Bernard, L.; Guseva, O.; Bastl, Z.; Plocek, J.; Tomandl, I.; Fejfar, A.; Base, T.; Schmutz, P. Adsorption of oriented carborane dipoles on a silver surface. *Physica Status Solidi B-Basic Solid State Physics* **2016**, *253* (3), 591-600.

(46) Thomas, J. C.; Boldog, I.; Auluck, H. S.; Bereciartua, P. J.; Dusek, M.; Machacek, J.; Bastl, Z.; Weiss, P. S.; Base, T. Self-Assembled p-Carborane Analogue of p-Mercaptobenzoic Acid on Au{111}. *Chemistry of Materials* **2015**, *27* (15), 5425-5435.

(47) Schwartz, J. J.; Mendoza, A. M.; Wattanatorn, N.; Zhao, Y. X.; Nguyen, V. T.; Spokoyny, A. M.; Mirkin, C. A.; Base, T.; Weiss, P. S. Surface Dipole Control of Liquid Crystal Alignment. *Journal of the American Chemical Society* **2016**, *138* (18), 5957-5967.

(48) Serino, A. C.; Anderson, M. E.; Saleh, L. M. A.; Dziedzic, R. M.; Mills, H.; Heidenreich, L. K.; Spokoyny, A. M.; Weiss, P. S. Work Function Control of Germanium through Carborane Carboxylic Acid Surface Passivation. *Acs Applied Materials & Interfaces* **2017**, *9* (40), 34592-34596.

(49) Thomas, J. C.; Goronzy, D. P.; Serino, A. C.; Auluck, H. S.; Irving, O. R.; Jimenez-Izal, E.; Deirmenjian, J. M.; Machacek, J.; Sautet, P.; Alexandrova, A. N.; et al. Acid-Base Control of Valency within Carboranedithiol Self-Assembled Monolayers: Molecules Do the Can-Can. *Acs Nano* **2018**, *12* (3), 2211-2221.

(50) Wang, S. K.; Goronzy, D. P.; Young, T. D.; Wattanatorn, N.; Stewart, L.; Base, T.; Weiss, P. S. Formation of Highly Ordered Terminal Alkyne Self-Assembled Monolayers on the Au{111}

Surface through Substitution of 1-Decaboranethiolate. *Journal of Physical Chemistry C* **2019**, *123* (2), 1348-1353.

(51) Hladík, M.; Vetushka, A.; Fejfar, A.; Vázquez, H. Tuning of the gold work function by carborane films studied using density functional theory. *Physical Chemistry Chemical Physics* **2019**, *21* (11), 6178-6185.

(52) Goronzy, D. P.; Stanek, J.; Avery, E.; Guo, H.; Bastl, Z.; Dusek, M.; Gallup, N. M.; Gun, S.; Kucerakova, M.; Levandowski, B. J.; et al. Influence of Terminal Carboxyl Groups on the Structure and Reactivity of Functionalized m-Carboranethiolate Self-Assembled Monolayers. *Chemistry of Materials* **2020**, *32* (15), 6800-6809.

(53) Li, Y. L.; Wang, Z. Y.; Ma, X. H.; Luo, P.; Du, C. X.; Zang, S. Q. Distinct photophysical properties in atom-precise silver and copper nanocluster analogues. *Nanoscale* **2019**, *11* (12), 5151-5157.

(54) Saini, A.; Saha, A.; Vinas, C.; Teixidor, F. The key to controlling the morphologies of quantum nanocrystals: spherical carborane ligands. *Chemical Communications* **2019**, *55* (66), 9817-9820.

(55) Wang, Q. Y.; Wang, J.; Wang, S.; Wang, Z. Y.; Cao, M.; He, C. L.; Yang, J. Q.; Zang, S. Q.; Mak, T. C. W. o-Carborane-Based and Atomically Precise Metal Clusters as Hypergolic Materials. *Journal of the American Chemical Society* **2020**, *142* (28), 12010-12014.

(56) Valusova, E.; Kanuchova, M.; Base, T.; Viglasky, V.; Antalik, M. The Au-25(SR)(18) cluster carrying icosahedral dodecaborate and glutathione ligands: A spectroscopic view. *Journal of Physics and Chemistry of Solids* **2021**, *150*.

(57) Jana, A.; Jash, M.; Poonia, A. K.; Paramasivam, G.; Islam, M. R.; Chakraborty, P.; Antharjanam, S.; Machacek, J.; Ghosh, S.; Adarsh, K.; et al. Light-Activated Intercluster Conversion of an Atomically Precise Silver Nanocluster. *Acs Nano* **2021**, *15* (10), 15781-15793.

(58) Eleazer, B. J.; Peryshkov, D. V. Coordination Chemistry of Carborane Clusters: Metal-Boron Bonds in Carborane, Carboranyl, and Carboryne Complexes. *Comments on Inorganic Chemistry* **2018**, *38* (3), 79-109.

(59) Kirlikovali, K. O.; Axtell, J. C.; Anderson, K.; Djurovich, P. I.; Rheingold, A. L.; Spokoyny, A. M. Fine-Tuning Electronic Properties of Luminescent Pt(II) Complexes via Vertex-Differentiated Coordination of Sterically Invariant Carborane-Based Ligands. *Organometallics* **2018**, *37* (18), 3122-3131.

(60) Eleazer, B. J.; Smith, M. D.; Popov, A. A.; Peryshkov, D. V. Expansion of the (BB) Ru metallacycle with coinage metal cations: formation of B-M-Ru-B (M = Cu, Ag, Au) dimetalacyclodiboryls. *Chemical Science* **2018**, *9* (9), 2601-2608.

(61) Zhang, J.; Cao, B.; Ding, Y.; Chang, J.; Li, S.; Chen, X. Syntheses and Structures of Group 10 Metal POCOP Pincer Complexes Bearing A Mercapto-o–carborane Auxiliary Ligand. *ChemistrySelect* **2019**, *4* (4), 1292-1297.

(62) Eleazer, B. J.; Smith, M. D.; Peryshkov, D. V. Reaction of a ruthenium B-carboranyl hydride complex and BH3(SMe2): Selective formation of a pincer-supported metallaborane LRu(B3H8). *Tetrahedron* **2019**, *75* (11), 1471-1474.

(63) Zhang, K.; Shen, Y. J.; Yang, X. L.; Liu, J. Y.; Jiang, T.; Finney, N.; Spingler, B.; Duttwyler, S. Atomically Defined Monocarborane Copper(I) Acetylides with Structural and Luminescence Properties Tuned by Ligand Sterics. *Chemistry-a European Journal* **2019**, *25* (37), 8754-8759.

(64) Mandal, D.; Rosair, G. Exploration of Bis (nickelation) of 1, 1-Bis (o-carborane). Crystals 2021, 11, 16. *Carborane* **2020**, 67.

(65) Dziedzic, R. M.; Spokoyny, A. M. Metal-catalyzed cross-coupling chemistry with polyhedral boranes. *Chemical Communications* **2019**, *55* (4), 430-442.

(66) Quan, Y. J.; Tang, C.; Xie, Z. W. Nucleophilic substitution: a facile strategy for selective B-H functionalization of carboranes. *Dalton Transactions* **2019**, *48* (22), 7494-7498.

(67) Quan, Y. J.; Xie, Z. W. Controlled functionalization of o-carborane via transition metal catalyzed B-H activation. *Chemical Society Reviews* **2019**, *48* (13), 3660-3673.

(68) Spokoyny, A. M.; Machan, C. W.; Clingerman, D. J.; Rosen, M. S.; Wiester, M. J.; Kennedy, R. D.; Stern, C. L.; Sarjeant, A. A.; Mirkin, C. A. A coordination chemistry dichotomy for icosahedral carborane-based ligands. *Nature Chemistry* **2011**, *3* (8), 590-596.

(69) Mills, H. A.; Alsarhan, F.; Ong, T. C.; Gembicky, M.; Rheingold, A. L.; Spokoyny, A. M. Icosahedral m-Carboranes Containing Exopolyhedral B-Se and B-Te Bonds. *Inorganic Chemistry* **2021**, *60* (24), 19165-19174.

(70) Biesinger, M. C. Advanced analysis of copper X-ray photoelectron spectra. *Surface and Interface Analysis* **2017**, *49* (13), 1325-1334.

(71) Zou, X.; Hovmöller, S.; Oleynikov, P. *Electron crystallography: electron microscopy and electron diffraction*; Oxford University Press, 2011.

(72) Crespo, O.; Gimeno, M. C.; Laguna, A.; Larraz, C.; Villacampa, M. D. Highly luminescent gold (I) silver(I) and gold(I)-copper(I) chalcogenide clusters. *Chemistry-a European Journal* **2007**, *13* (1), 235-246.

(73) Kriegel, I.; Jiang, C. Y.; Rodriguez-Fernandez, J.; Schaller, R. D.; Talapin, D. V.; da Como, E.; Feldmann, J. Tuning the Excitonic and Plasmonic Properties of Copper Chalcogenide Nanocrystals. *Journal of the American Chemical Society* **2012**, *134* (3), 1583-1590.

(74) Singh, A.; Singh, S.; Levcenko, S.; Unold, T.; Laffir, F.; Ryan, K. M. Compositionally Tunable Photoluminescence Emission in Cu2ZnSn(S1-xSex)(4) Nanocrystals. *Angewandte Chemie International Edition* **2013**, *52* (35), 9120-9124.

(75) Polgar, A. M.; Zhang, A.; Mack, F.; Weigend, F.; Lebedkin, S.; Stillman, M. J.; Corrigan, J. F. Tuning the Metal/Chalcogen Composition in Copper(I)-Chalcogenide Clusters with Cyclic (Alkyl)(amino)carbene Ligands. *Inorganic Chemistry* **2019**, *58* (5), 3338-3348.

(76) Mei, J.; Leung, N. L. C.; Kwok, R. T. K.; Lam, J. W. Y.; Tang, B. Z. Aggregation-Induced Emission: Together We Shine, United We Soar! *Chemical Reviews* **2015**, *115* (21), 11718-11940.

(77) Chin, P. T. K.; Donega, C. D. M.; Bavel, S. S.; Meskers, S. C. J.; Sommerdijk, N.; Janssen, R. A. J. Highly luminescent CdTe/CdSe colloidal heteronanocrystals with temperature-dependent emission color. *Journal of the American Chemical Society* **2007**, *129* (48), 14880-14886.

(78) Lu, W. F.; Tarekegne, A. T.; Ou, Y. Y.; Kamiyama, S.; Ou, H. Y. Temperature-dependent photoluminescence properties of porous fluorescent SiC. *Scientific Reports* **2019**, *9*.

(79) Jones, C. G.; Asay, M.; Kim, L. J.; Kleinsasser, J. F.; Saha, A.; Fulton, T. J.; Berkley, K. R.; Cascio, D.; Malyutin, A. G.; Conley, M. P.; et al. Characterization of Reactive Organometallic Species via MicroED. *Acs Central Science* **2019**, *5* (9), 1507-1513.

(80) Samkian, A. E.; Kiel, G. R.; Jones, C. G.; Bergman, H. M.; Oktawiec, J.; Nelson, H. M.; Tilley, T. D. Elucidation of Diverse Solid-State Packing in a Family of Electron-Deficient Expanded Helicenes via Microcrystal Electron Diffraction (MicroED)\*\*. *Angewandte Chemie-International Edition* **2021**, *60* (5), 2493-2499.

(81) Meng, Z.; Jones, C. G.; Farid, S.; Khan, I. U.; Nelson, H. M.; Mirica, K. A. Unraveling the Electrical and Magnetic Properties of Layered Conductive Metal-Organic Framework With Atomic Precision. *Angewandte Chemie* **2022**, *134* (6), e202113569.

(82) Doyle, L. R.; Thompson, E. A.; Burnage, A. L.; Whitwood, A. C.; Jenkins, H. T.; Macgregor, S. A.; Weller, A. S. MicroED characterization of a robust cationic σ-alkane complex stabilized by the [B (3, 5-(SF 5) 2 C 6 H 3) 4]− anion, via on-grid solid/gas single-crystal to single-crystal reactivity. *Dalton Transactions* **2022**, *51* (9), 3661-3665.

*Chapter 9*

*Elucidation of Diverse Solid-State Packing in a Family of Electron-Deficient Expanded Helicenes via Microcrystal Electron Diffraction*[1]

## 9.1 INTRODUCTION

There is growing interest in chirality as an orthogonal design element for next-generation molecular organic materials.[1-7] This parameter gives rise to new properties as a result of its impact on electronic structure, including circularly polarized absorption and emission,[8-10] nonlinear optical behavior,[11] and spin polarization.[12] While the impact of chirality on *molecular* properties is important, its impact on *supramolecular and solid-state* behavior is especially relevant if the molecule is to be integrated into a material or device.[13-16] The low symmetry and diverse geometries of chiral molecules have profound implications for the properties of their aggregates, but the complexities of such structures severely complicate efforts toward rational design.[17]

As the prototypical chiral aromatic molecules, helicenes—helical arrays of fused aromatic rings— have been at the forefront of efforts to exploit chirality in organic (opto)electronic applications.[4-6] The structural diversity of these compounds has recently grown at a rapid rate, with a particular surge of structures containing multiple helicenes embedded into larger polyaromatic frameworks.[18-28] Helicenes exhibit remarkable supramolecular and solid-state chemistry promoted by $\pi$-stacking interactions, which can result in enhanced or emergent properties.[11, 20, 29-33] For example, using a versatile helicene quinone

---

scaffold, Nuckolls, Katz, and Verbiest demonstrated significant enhancements of specific rotation, circular dichroism, and second-order nonlinear optical susceptibility due to aggregation.[11, 29] More recently, Itami and co-workers reported a double helicene that exhibits $\pi$-stacking in all three crystallographic dimensions, a rare phenomenon that may give rise to isotropic charge transport.[20] Along these lines, the unique solid-state behavior of helicenes has been exploited in a device setting. For example, in an organic field effect transistor, the enantiopurity of the helicene-based active layer can have dramatic or unexpected effects on performance.[9, 30-32] Nakamura demonstrated that a charge carrier inversion (switch from p- to n-type) can occur on going from a racemic to an enantiopure helicene[30] and Fuchter observed an 80-fold increase in charge carrier mobility for a racemic active layer (vs. an enantiopure analogue).[31] These results motivate further research related to helicene solid-state structure and highlight the important role of chirality.

In 2017, the Tilley group introduced a new class of chiral nanocarbons, "expanded helicenes," which possess internal cavities and large diameters due to alternating angular and linear ring fusion (e.g. **1a,b**, Scheme 9.1a).[34-37] One exciting feature of these compounds is their unique self-assembly and solid-state packing, facilitated in part by their structural flexibility. For example, expanded [13]helicene **1b** dimerizes via $\pi$-stacking to form the unusual double helix **1b-Dim**, both in chloroform-$d$ solution and in the solid-state, which is accompanied by a large (>2 x) increase in the pitch of the constituent helicenes.[34] In contrast, no aggregation was apparent for the [11]helicene analogue (**1a**). Subsequently, the covalent linkage of two expanded helicenes afforded a configurationally labile "Figure-eight" dimer that crystallized into an intricate homochiral network containing two distinct yet interconnected helical superstructures.[36]

Single crystal X-ray diffraction is the gold standard for solid-state structure elucidation since it can provide structural parameters with a high level of precision; however, even for crystalline compounds, it can be difficult or impossible to obtain suitable single crystals for analysis, which can preclude valuable insights. For example, our inability to obtain suitable crystals of **1a** prevented comparisons with its apparently more interesting analogue **1b**.[34] Microcrystal electron diffraction (MicroED) has recently

emerged as a way to circumvent limitations related to crystal growth since it can allow high-resolution structural data to be acquired on nanocrystalline samples.[38-40]

*Scheme 9.1. a) Previous Work: Expanded [11]- and [13]helicenes **1a** and **1b**, and the observation of π-stacked double helix **1b-Dim** (both in solution and the solid-state). Compound **1a** could not be analyzed by X-ray crystallography owing to the difficulty in obtaining suitable single crystals; b) This work: A simple post-synthetic oxidation of electron- rich and non-aggregating **1a** provided rapid, divergent access to electron-deficient analogues **2-di** and **3-di** and donor–acceptor analogues **2-mon** and **3-mon**. Conditions: i) CAN (6 equiv), CH₂Cl₂, MeCN, H₂O, 22 °C; ii) CAN (15 equiv), CH₂Cl₂, MeCN, H₂O, 22 °C; iii) 1,2-diaminobenzene (5 and 20 equiv for **3-mon** and **3-di**, respectively), DCE, 70 °C.*
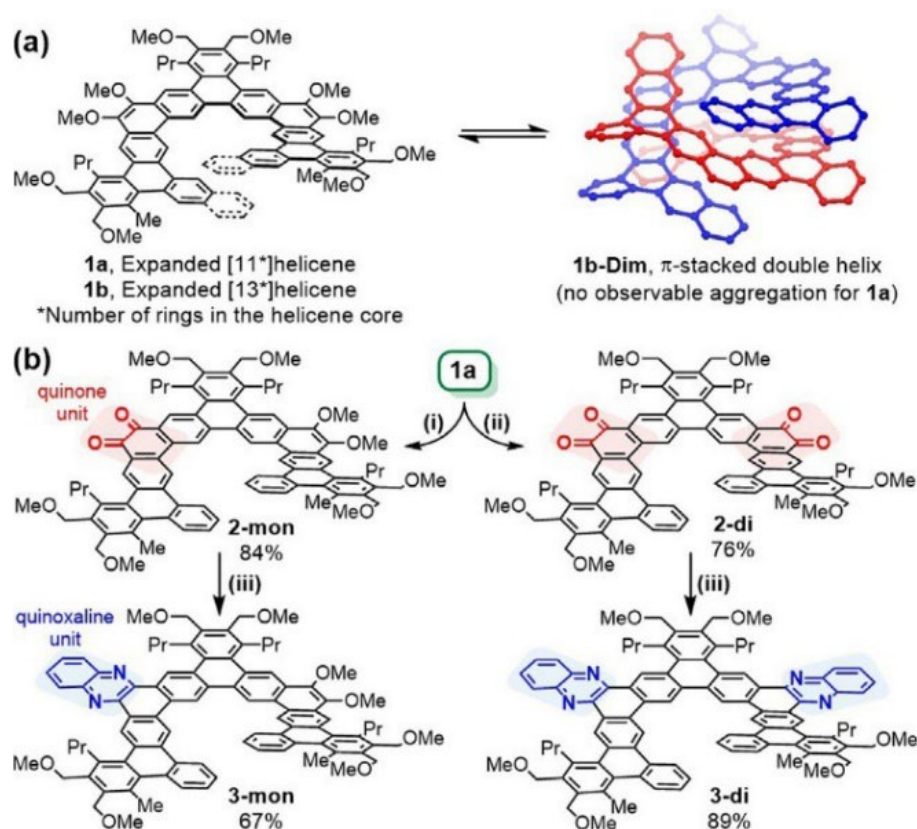


In this contribution, we use a combination of divergent synthesis and MicroED to interrogate solid-state behavior in a new family of expanded helicenes. The quinone- and quinoxiline-containing helicenes **2-mon**, **2-di**, **3-mon**, and **3-di** (Scheme 1b) were targeted due to their electron deficiency, which tends to

promote strong intermolecular interactions between $\pi$-systems.[29, 41] The new compounds were accessed via a highly selective oxidative dearomatization of electron-rich **1a**, which provided derivatives of the same or reduced symmetry. While uncontrollable crystallization kinetics consistently resulted in the formation of microcrystals that were unsuitable for single crystal X-ray diffraction, the application of MicroED enabled the rapid acquisition of high-resolution data for all five helicenes. This data revealed three different packing motifs, representing four different space groups. Three of the structures feature large (1.3–2.0 nm) channels, enforced by the ability of the helicenes to accommodate large distortions in molecular geometry.

***Figure 9.1****. UV/Vis a) absorption and b) emission spectra in CH Cl; c) Cyclic voltammograms in CH₂Cl₂ (1.0 mM) with 0.1 M ⁿBu₄NPF₆ as the supporting electrolyte, scanned at 100 mVs⁻¹.*
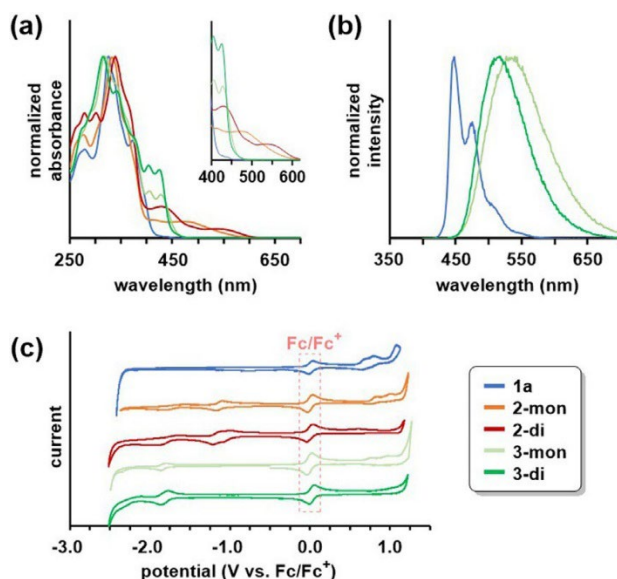


## 9.2 CHARACTERIZATION AND ANALYSIS OF HELICENE SYSTEMS

Quinone-containing helicenes display desirable properties due to their low LUMO levels, including red-shifted absorption, reversible redox behavior, and strong aggregation.[29, 42-44] Furthermore, polycyclic aromatic hydrocarbons (PAHs) with quinone functionalities are well-established synthons for a range of derivatives, including $\pi$-extended cyclopentadienones,[45-47] imidazoles,[48] and pyrazines,[49-51] which facilitates divergent manipulation of properties.[52, 53] An expedient way to install quinone units is via the oxidation of

a PAH with a 1,2-dimethoxy substitution pattern.[52, 54, 55] Since compound **1a** is available using a scalable procedure,[34] this strategy seemed to represent an opportunity to significantly increase functional diversity in expanded helicenes. Thus, in an attempt to fully oxidize **1a** to its diquinone derivative **2-di** (Scheme 1b), this compound was treated with an excess (6 equiv) of cerium ammonium nitrate (CAN) in a $CH_2Cl_2$/MeCN/$H_2O$ solvent system. Remarkably, this instead resulted in the selective formation of monoquinone **2-mon**, isolated in 84% yield. The exceptional selectivity for **2-mon** over **2-di** is surprising given the highly benzenoid nature of **1a** and its quinone derivatives, which is expected to limit electronic communication across the $\pi$-system.[56] This suggests that inductive effects play an important role in slowing down the oxidation of the second 1,2-dimethoxyarene unit even though the two reaction sites are physically distant. Importantly, diquinone **2-di** was also accessed, in 76% yield, simply with use of a larger excess of CAN (15 equiv).

The condensation of a 1,2-diamine onto a quinone-containing PAH is a reliable and general transformation that provides a means to install functionally-valuable nitrogen atoms and extend the p-system,[49-51] which could lead to stronger $\pi$-stacking interactions between molecules.[41] Thus, **2-mon** and **2-di** were treated with excess 1,2-phenylenediamine in 1,2-dichloroethane (DCE) at 70 °C, which afforded quinoxaline-containing helicenes **3-mon** and **3-di** in 67% and 89% isolated yields, respectively, after a simple workup/purification procedure consisting of precipitation followed by recrystallization from toluene. The identities of all new helicenes were initially confirmed with ^{1}H and ^{13}C NMR spectroscopies and high-resolution mass spectrometry (HRMS-ESI). Furthermore, the structures for all five helicenes were unambiguously confirmed by MicroED (see below).

The substitution of PAHs with quinone units often results in solubility problems,[55, 57] but the new helicenes **2-mon** and **2-di** are highly soluble (>100 mg mL$^{-1}$ in $CHCl_3$ and $CH_2Cl_2$). This is especially notable given their large size (14 fused rings). The solubility may be attributed to two different forms of non-planarity: 1) the helical distortion that is present in all helicenes and 2) a bending of the benzannulated rings away from the contour of the helix, which results from alkyl substituents in six different bay positions.

While the quinoxaline-annulated helicenes **3-mon** and **3-di** are similarly soluble to the quinone analogs in a thermodynamic sense, their kinetic solubility is low when isolated as a crystalline solid.

*Figure 9.2. Solid-state MicroED structures of a) **1a**, b) **2-di**, c) **2-mon**, d) **3-mon**, and e) **3-di**. *The starred distances represent helical pitch values for the associated helicene, which were estimated as described in Figure 9.3. †The crystals of **2-di** feature helicenes with two different pitch values.*
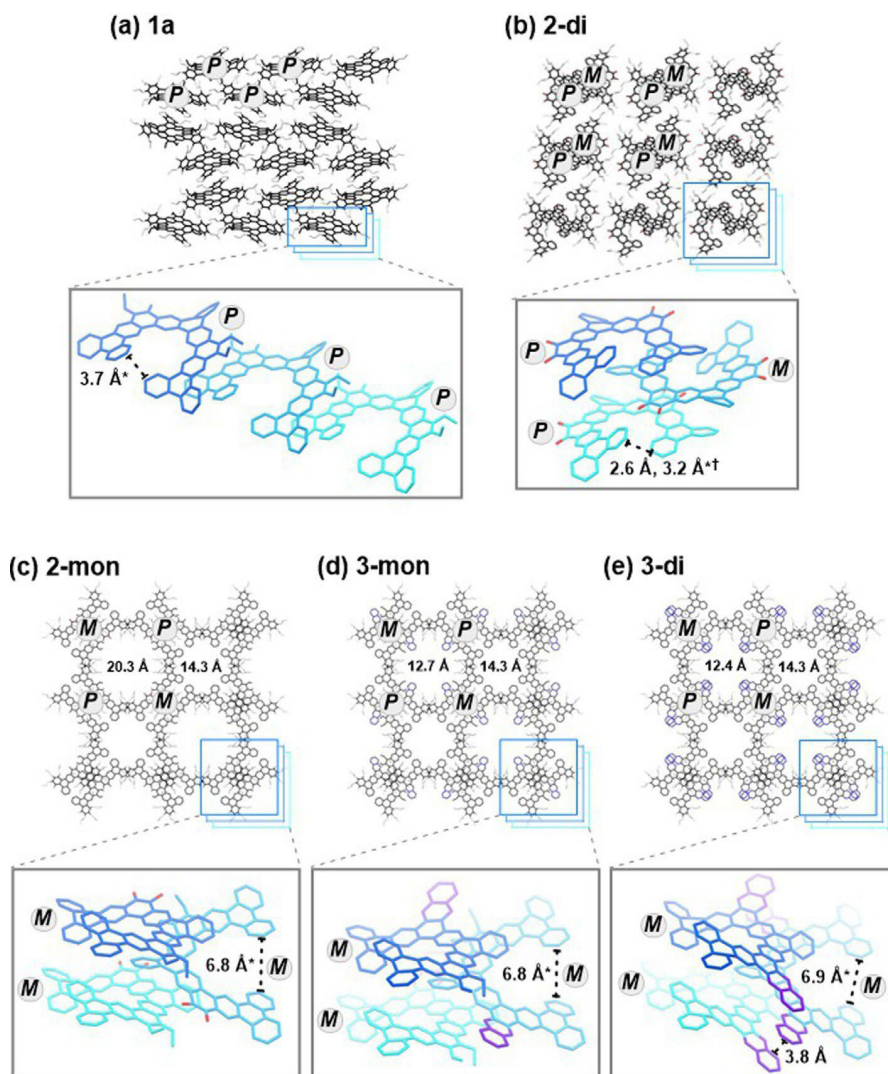


The photophysical properties of the new helicenes were probed by UV/Vis absorption and emission spectroscopies (Figure 9.1a,b). Most notable are the sizable decreases in photophysical HOMO–LUMO gaps (calculated from their absorption onset values) for quinone-containing helicenes **2-mon** (2.08 eV) and

**2-di** (2.05 eV) relative to that for their synthetic precursor **1a** (2.79 eV). In contrast, the quinoxaline units have only a small effect on this value (2.63 eV for both **3-mon** and **3-di**). Relative to the absorption maxima for **1a** (324 nm), small red shifts of 9 and 15 nm are observed for the mono- and diquinones **2-mon** and **2-di**, respectively, whereas blue shifts of comparable magnitude (5 and 9 nm) are observed for the mono- and diquinoxalines **3-mon** and **3-di**. Despite limited perturbation of their absorption maxima and onset values, **3-mon** and **3-di** display relatively large bathochromic shifts in emission maxima relative to that for **1a** (from 446 nm to 533 and 517 nm, respectively). As is typical for PAHs containing quinone units,[58] **2-mon** and **2-di** are nonemissive.

The electrochemical behavior of the helicenes was investigated by cyclic voltammetry (CV) in CH$_2$Cl$_2$ solution (Figure 9.1c). Only **1a**, **2-mon**, and **3-mon** display oxidation events (one per 1,2-dimethoxy substituent), which were quasireversible or irreversible. The four new compounds with quinone or quinoxaline units display one reversible reduction event per unit (e.g. the presence of two quinones in **2-di** gives rise to two reversible reduction events). The electrochemical HOMO–LUMO gaps for **2-mon** and **3-mon** (1.94 and 2.57 eV, respectively) are slightly smaller than those calculated from the absorption onset (see above). Replacement of the 1,2-dimethoxyarene units with quinone or quinoxaline units does not significantly affect HOMO energy levels. Compared to the HOMO level for **1a** (–5.46 eV), only slight decreases were observed for each additional quinone ($\approx 0.15$ eV) or quinoxaline ($\approx 0.06$ eV) unit. The large changes in HOMO/LUMO gaps result primarily from changes in LUMO levels ($\approx 1.0$ eV decreases for **2-mon** and **2-di** and $\approx 0.3$ eV decreases for **3-mon** and **3-di**).

One of the primary motivations for structural modifications of compound 1a was its limited aggregation via $\pi$-stacking. Aggregation behavior was initially probed by variable concentration ^{1}HNMR spectroscopy in chloroform-*d* solution. Like its precursor **1a**, monoquinone **2-mon** does not appear to aggregate to an appreciable extent in this solvent, as evidenced by the invariance of its ^{1}H NMR spectrum to concentration (Figures H.9 and H.10). In contrast, the ^{1}H NMR spectra of **2-di**, **3-mon**, and **3-di** all exhibit concentration dependence (Figures H.11-H.13). The most dramatic effects are observed for **3-di**,

whose chemical shifts are shielded by up to 1.3 ppm upon concentration from 0.024 mM to 80 mM. In contrast, the chemical shifts of monoquinoxaline **3-mon** and diquinone **2-di** exhibit a combination of shielding and de-shielding, and of a smaller magnitude. Compounds **2-di**, **3-mon**, and **3-di** are rare in that they simultaneously aggregate and exhibit high solubility, without the need for long alkyl chains on the periphery. Since these two properties are usually at odds with one another, and since both are of critical importance for applications (e.g. in organic electronics), further elucidation of the nature of the aggregation was of interest.

Dynamic light scattering (DLS) experiments were conducted to probe aggregate size in chloroform solution (Figure H.24). Measurements were made for diquinone **2-di** and diquinoxaline **3-di** since their variable concentration $^1$H NMR spectra suggest notable aggregation, and the non-aggregating parent helicene **1a** was analyzed for comparison. As expected, the DLS measurements suggest that **1a** is monomeric regardless of concentration, at an average size of $\approx 1.0$ nm. In contrast, the size of **2-di** exhibits strong concentration dependence, from 1.0 nm at 0.24 mM (consistent with monomeric **2-di**) to 271 nm at 24 mM (consistent with supramolecular polymers). For diquinoxaline **3-di**, the size approaches 1.7 nm at high concentration, which suggests that the large upfield shifts observed in the $^1$H NMR spectra of concentrated solutions result from small aggregates.

The observation of small aggregates for **3-di** via DLS prompted the use of the Horman/Dreux model for quantitative assessment of dimeric aggregation equilibria.[59] Using the aromatic chemical shifts from the variable concentration $^1$H NMR spectra, this model provided an excellent fit and an average association constant for dimerization ($K_a$) of 13 M$^{-1}$ at 298 K. Thus, these data are consistent with those from DLS, suggesting that higher-order aggregates of **3-di** do not play a significant role in the concentration range studied. The $K_a$ value is slightly lower than that for expanded [13]helicene **1b** (23 M$^{-1}$),[34] but these values may not be directly comparable since **1b** forms well-defined dimers (**1b-Dim**), whereas **3-di** may form aggregates with different molecularity.

Previously obtained crystal structures of expanded helicenes have revealed unique packing architectures and provided insight into their supramolecular interactions.[34-37] In pursuit of this information, significant effort was devoted to growing single crystals suitable for X-ray diffraction, but these efforts consistently provided microcrystals[60, 61] that were unsuitable (even with the aid of synchrotron radiation) for all compounds except **3-mon**. Thus, we turned to MicroED, and with this technique the structures of all five helicenes were elucidated with ease (Figure 9.2). The crystals used for analysis were grown as follows. For **1a**, the bulk, microcrystalline material obtained during its synthesis proved to be of sufficient quality. For **2-mon** and **2-di**, diffusion of pentane into an EtOAc solution yielded orange needles. For **3-mon** and **3-di**, slow evaporation of a benzene solution provided yellow rods.

The parent, electron-rich helicene **1a** crystallized in the chiral $P2_12_12_1$ space group, wherein the constituent molecules are homochiral and form weakly bound columns (Figure 9.2a). This is the second example of a homochiral expanded helicene crystal structure,[36] and it is notable since 1a is expected to have an extremely low enantiomerization barrier in solution.[34-36] The closest $\pi$-stacking distance is 3.8 Å, and there are only two overlapping rings. These weak interactions are consistent with the absence of observable aggregation in chloroform-*d* solution.[34] Notably, the packing is quite different than that of the isolated double helical dimers observed in the longer analogue **1b** (Figure 9.1a), which differs by only two rings at the terminus.

While the quinone-containing helicenes **2-di** and **2-mon** differ from **1a** only with respect to their oxidation state and associated methyl groups, all three compounds exhibit unique crystal packing. Compounds **2-di** and **2-mon** crystallized in the $P\bar{1}$ and *Iba*2 space groups, respectively (Figures 9.2b and 9.2c). In contrast to that of **1a**, these space groups are achiral. All three crystal structures feature columns driven by long-range $\pi$-stacking; however, in contrast to **1a** and **2-mon**, the columns of **2-di** are heterochiral (i.e. the helicenes within a given column alternate handedness), which leads to an achiral crystal. Individual columns for **2-mon** are homochiral, with alternation of chiralities between columns to make the overall structure achiral.

Compared to **1a**, the molecules of both quinone-containing helicenes exhibit more pronounced intermolecular interactions. This is especially true for **2-di**, which features eight overlapping rings per helicene and a closest $\pi$-contact of 3.4 Å. This close-packing appears to be driven by interactions between electron-deficient quinone units and relatively electron-rich benzannulated rings (two per molecule). The intermolecular interactions in **2-mon** support a complex framework with emergent macroscopic features, including the existence of two large cavities.

**Figure 9.3**. *MicroED (black) and calculated (blue) structures of helicenes a)* **2-mon**, *b)* **3-mon**, *and c)* **3-di**. *The noted distances represent the pitches of the helices that are defined by the centroids of the inner 11 rings*.
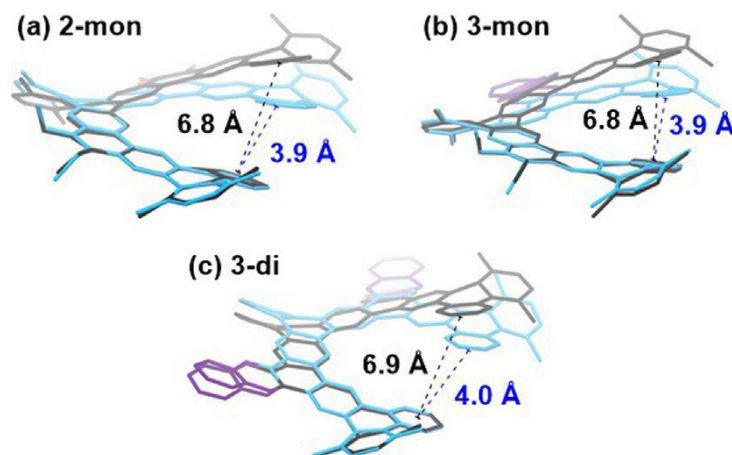


The crystal packings of **3-mon** and **3-di** (Figure 9.2d and e, respectively) are similar to that for **2-mon** in that all three exhibit a combination of one intrinsic and two extrinsic cavities. The intrinsic cavity ( $\approx 4$ Å in diameter) is consistent across all compounds since it is enforced by the alternating linear and angular ring fusion pattern that defines expanded helicenes. In all three cases, such cavities are occupied by the central methoxymethyl sidechains of neighboring molecules. There are two extrinsic cavities that emerge in each structure due to the packing arrangement. One is bordered by the terminal rings of the helicenes and is identical in all three structures (14.3 Å in diameter). The other differs for each helicene, and its size is dictated by the peripheral functionality (20.3 Å for **2-mon**, 12.7 Å for **3-mon**, 12.4 Å for **3-di**). While further examination of these cavities through the Fourier difference map shows some residual

density, there is likely substantial disordered solvent present as this is generally accepted for a wide range of porous and macromolecular structures.[60, 61] Like **2-mon**, compound **3-mon** also crystallized in the *Iba*2 space group, but compound **3-di** occupies the higher symmetry $I\bar{4}c2$ space group since it has a molecular $C_2$ axis. Each of these three helicenes has only one overlapping backbone ring with similar centroid-centroid distances (4.2 Å for **3-mon**, 4.0 Å for **3-di**, and 4.1 Å for **2-mon**) indicating weak interactions. In addition, **3-di** has overlapping quinoxaline units that may contribute to its strong aggregation in solution.

A striking feature of the MicroED structures is the large helical pitches for **2-mon**, **3-mon**, and **3-di** (6.8, 6.8, and 6.9 Å, respectively).[62] Previously reported expanded helicenes, and compounds **1a** and **2-di** described herein, have pitches in the range of 2.6–3.7 Å.[34-37] One exception is dimeric [13]helicene **1b-Dim** (Figure 9.1a),[34] wherein each helicene displays a large pitch (7.4 Å) to accommodate extensive $\pi$-stacking. Another case where a notable molecular distortion was observed in the crystal structure was for the recently-reported Figure-eight expanded helicene dimer.[36] There, an intricate network of $\pi$-stacking interactions appears to be the driving force for the distortion. In contrast to that for **1b-Dim** and the Figure-eight helicene, the driving forces for the observed, large molecular distortions are unclear.

The distorted molecular structures of **2-mon**, **3-mon**, and **3-di** in the solid-state suggest a high level of structural flexibility for these compounds, especially given the absence of notable intermolecular interactions. This motivated a computational study in an attempt to quantify the energy costs for these distortions. First, gas phase geometry optimizations were performed using density functional theory (DFT) at the B3LYP-6311 g(2d,p) level of theory (Figure 9.3). As expected, the calculated structures display only modest pitches of 3.9 Å (**2-mon**), 3.9 Å (**3-mon**), and 4.0 Å (**3-di**), which are in much better agreement with those from previously-reported expanded helicenes (vide supra). Next, the structures were optimized with geometry constraints to approximate the pitches observed in their respective crystal structures, and the energies were compared with those from the unconstrained geometries. The energy cost for the observed molecular distortion was estimated to be 3.2, 3.2, and 3.8 kcal mol$^{-1}$ for **2-mon**, **3-mon**, and **3-di**,

respectively (see Appendix H for details). These relatively small values provide rationale for the remarkable ability of these helicenes to "flex" in order to accommodate novel crystal packings.

## 9.3 CONCLUSION

In conclusion, the discovery of a selective oxidative dearomatization of a readily available, electron-rich expanded helicene provided access to a series of four electron deficient analogues. The five helicenes displayed variations in a range of properties, but the most notable differences were related to their solid-state structures. Despite difficulties with crystal growth and the associated failures of X-ray crystallography, the acquisition of high-resolution structural data for all helicenes was easily accomplished with MicroED. A range of unique solid-state packing behavior was observed, including four different space groups, homochirality in a crystal for a helicene with an extremely low enantiomerization barrier, nanometer scale cavities, and large molecular distortions without an obvious driving force. The latter suggests that expanded helicene flexibility may manifest in non-intuitive ways to afford unprecedented solid-state packing. Perhaps most importantly, the results of this study provide an initial indication of MicroED's potential utility for high-throughput crystallization to aid the discovery of novel organic materials.

## 9.4 REFERENCES

(1) Brandt, J. R.; Salerno, F.; Fuchter, M. J. The added value of small-molecule chirality in technological applications. *Nature Reviews Chemistry* **2017**, *1* (6).

(2) Fernandez-Garcia, J. M.; Evans, P. J.; Filippone, S.; Herranz, M. A.; Martin, N. Chiral Molecular Carbon Nanostructures. *Accounts of Chemical Research* **2019**, *52* (6), 1565-1574.

(3) Rickhaus, M.; Mayor, M.; Juricek, M. Strain-induced helical chirality in polyaromatic systems. *Chemical Society Reviews* **2016**, *45* (6), 1542-1556.

(4) Shen, Y.; Chen, C. F. Helicenes: Synthesis and Applications. *Chemical Reviews* **2012**, *112* (3), 1463-1535.

(5) Gingras, M. One hundred years of helicene chemistry. Part 1: non-stereoselective syntheses of carbohelicenes. *Chemical Society Reviews* **2013**, *42* (3), 968-1006.

(6) Gingras, M. One hundred years of helicene chemistry. Part 3: applications and properties of carbohelicenes. *Chemical Society Reviews* **2013**, *42* (3), 1051-1095.

(7) Dhbaibi, K.; Favereau, L.; Crassous, J. Enantioenriched Helicenes and Helicenoids Containing Main Group Elements (B, Si, N, P). *Chemical Reviews* **2019**, *119* (14), 8846-8953.

(8) Field, J. E.; Muller, G.; Riehl, J. P.; Venkataraman, D. Circularly polarized luminescence from bridged triarylamine helicenes. *Journal of the American Chemical Society* **2003**, *125* (39), 11808-11809.

(9) Yang, Y.; da Costa, R. C.; Fuchter, M. J.; Campbell, A. J. Circularly polarized light detection by a chiral organic semiconductor transistor. *Nature Photonics* **2013**, *7* (8), 634-638.

(10) Tanaka, H.; Inoue, Y.; Mori, T. Circularly Polarized Luminescence and Circular Dichroisms in Small Organic Molecules: Correlation between Excitation and Emission Dissymmetry Factors. *Chemphotochem* **2018**, *2* (5), 386-402.

(11) Verbiest, T.; Van Elshocht, S.; Kauranen, M.; Hellemans, L.; Snauwaert, J.; Nuckolls, C.; Katz, T. J.; Persoons, A. Strong enhancement of nonlinear optical properties through supramolecular chirality. *Science* **1998**, *282* (5390), 913-915.

(12) Kiran, V.; Mathew, S. P.; Cohen, S. R.; Delgado, I. H.; Lacour, J.; Naaman, R. Helicenes-A New Class of Organic Spin Filter. *Advanced Materials* **2016**, *28* (10), 1957.

(13) Palmans, A. R. A.; Meijer, E. W. Amplification of chirality in dynamic supramolecular aggregates. *Angewandte Chemie-International Edition* **2007**, *46* (47), 8948-8968.

(14) Yang, Y.; Zhang, Y. J.; Wei, Z. X. Supramolecular Helices: Chirality Transfer from Conjugated Molecules to Structures. *Advanced Materials* **2013**, *25* (42), 6039-6049.

(15) Liu, M. H.; Zhang, L.; Wang, T. Y. Supramolecular Chirality in Self-Assembled Systems. *Chemical Reviews* **2015**, *115* (15), 7304-7397.

(16) Yashima, E.; Ousaka, N.; Taura, D.; Shimomura, K.; Ikai, T.; Maeda, K. Supramolecular Helical Systems: Helical Assemblies of Small Molecules, Foldamers, and Polymers with Chiral Amplification and Their Functions. *Chemical Reviews* **2016**, *116* (22), 13752-13990.

(17) Schmidt, J. A.; Weatherby, J. A.; Sugden, I.; Santana-Bonilla, A.; Salerno, F.; Fuchter, M.; Johnson, E.; Nelson, J.; Jelfs, K. Computational screening of organic semiconductors: exploring side-group functionalisation and assembly to optimise charge transport in chiral molecules. **2021**.

(18) Barnett, L.; Ho, D. M.; Baldridge, K. K.; Pascal, R. A. The structure of hexabenzotriphenylene and the problem of overcrowded "D-3h" polycyclic aromatic compounds. *Journal of the American Chemical Society* **1999**, *121* (4), 727-733.

(19) Wang, X. Y.; Wang, X. C.; Narita, A.; Wagner, M.; Cao, X. Y.; Feng, X. L.; Mullen, K. Synthesis, Structure, and Chiroptical Properties of a Double 7 Heterohelicene. *Journal of the American Chemical Society* **2016**, *138* (39), 12783-12786.

(20) Fujikawa, T.; Segawa, Y.; Itami, K. Synthesis, Structures, and Properties of pi-Extended Double Helicene: A Combination of Planar and Nonplanar pi-Systems. *Journal of the American Chemical Society* **2015**, *137* (24), 7763-7768.

(21) Pradhan, A.; Dechannbenoit, P.; Bock, H.; Durola, F. Fused Helicene Chains: Towards Twisted Graphene Nanoribbons. *Chemistry-a European Journal* **2016**, *22* (50), 18227-18235.

(22) Hu, Y. B.; Wang, X. Y.; Peng, P. X.; Wang, X. C.; Cao, X. Y.; Feng, X. L.; Mullen, K.; Narita, A. Benzo Fused Double 7 Carbohelicene: Synthesis, Structures, and Physicochemical Properties. *Angewandte Chemie-International Edition* **2017**, *56* (12), 3374-3378.

(23) Hosokawa, T.; Takahashi, Y.; Matsushima, T.; Watanabe, S.; Kikkawa, S.; Azumaya, I.; Tsurusaki, A.; Kamikawa, K. Synthesis, Structures, and Properties of Hexapole Helicenes: Assembling Six 5 Helicene Substructures into Highly Twisted Aromatic Systems. *Journal of the American Chemical Society* **2017**, *139* (51), 18512-18521.

(24) Ball, M.; Zhong, Y.; Wu, Y.; Schenck, C.; Ng, F.; Steigerwald, M.; Xiao, S. X.; Nuckolls, C. Contorted Polycyclic Aromatics. *Accounts of Chemical Research* **2015**, *48* (2), 267-276.

(25) Li, C. Q.; Yang, Y.; Miao, Q. Recent Progress in Chemistry of Multiple Helicenes. *Chemistry-an Asian Journal* **2018**, *13* (8), 884-894.

(26) Schuster, N. J.; Paley, D. W.; Jockusch, S.; Ng, F.; Steigerwald, M. L.; Nuckolls, C. Electron Delocalization in Perylene Diimide Helicenes. *Angewandte Chemie-International Edition* **2016**, *55* (43), 13519-13523.

(27) Evans, P. J.; Ouyang, J. K.; Favereau, L.; Crassous, J.; Fernandez, I.; Perles, J.; Martin, N. Synthesis of a Helical Bilayer Nanographene. *Angewandte Chemie-International Edition* **2018**, *57* (23), 6774-6779.

(28) Schuster, N. J.; Joyce, L. A.; Paley, D. W.; Ng, F.; Steigerwald, M. L.; Nuckolls, C. The Structural Origins of Intense Circular Dichroism in a Waggling Helicene Nanoribbon. *Journal of the American Chemical Society* **2020**, *142* (15), 7066-7074.

(29) Nuckolls, C.; Katz, T. J.; Castellanos, L. Aggregation of conjugated helical molecules. *Journal of the American Chemical Society* **1996**, *118* (15), 3767-3768.

(30) Hatakeyama, T.; Hashimoto, S.; Oba, T.; Nakamura, M. Azaboradibenzo 6 helicene: Carrier Inversion Induced by Helical Homochirality. *Journal of the American Chemical Society* **2012**, *134* (48), 19600-19603.

(31) Yang, Y.; Rice, B.; Shi, X. Y.; Brandt, J. R.; da Costa, R. C.; Hedley, G. J.; Smilgies, D. M.; Frost, J. M.; Samuel, I. D. W.; Otero-De-La-Roza, A.; et al. Emergent Properties of an Organic Semiconductor Driven by its Molecular Chirality. *Acs Nano* **2017**, *11* (8), 8329-8338.

(32) Josse, P.; Favereau, L.; Shen, C.; Dabos-Seignon, S.; Blanchard, P.; Cabanetos, C.; Crassous, J. Enantiopure versus Racemic Naphthalimide End-Capped Helicenic Non-fullerene Electron Acceptors: Impact on Organic Photovoltaics Performance. *Chemistry-a European Journal* **2017**, *23* (26), 6277-6281.

(33) Shcherbina, M. A.; Zeng, X. B.; Tadjiev, T.; Ungar, G.; Eichhorn, S. H.; Phillips, K. E. S.; Katz, T. J. Hollow Six-Stranded Helical Columns of a Helicene. *Angewandte Chemie-International Edition* **2009**, *48* (42), 7837-7840.

(34) Kiel, G. R.; Patel, S. C.; Smith, P. W.; Levine, D. S.; Tilley, T. D. Expanded Helicenes: A General Synthetic Strategy and Remarkable Supramolecular and Solid-State Behavior. *Journal of the American Chemical Society* **2017**, *139* (51), 18456-18459.

(35) Nakakuki, Y.; Hirose, T.; Matsuda, K. Synthesis of a Helical Analogue of Kekulene: A Flexible pi Expanded Helicene with Large Helical Diameter Acting as a Soft Molecular Spring. *Journal of the American Chemical Society* **2018**, *140* (45), 15461-15469.

(36) Kiel, G. R.; Bay, K. L.; Samkian, A. E.; Schuster, N. J.; Lin, J. B.; Handford, R. C.; Nuckolls, C.; Houk, K. N.; Tilley, T. D. Expanded Helicenes as Synthons for Chiral Macrocyclic Nanocarbons. *Journal of the American Chemical Society* **2020**, *142* (25), 11084-11091.

(37) Fujise, K.; Tsurumaki, E.; Fukuhara, G.; Hara, N.; Imai, Y.; Toyota, S. Multiple Fused Anthracenes as Helical Polycyclic Aromatic Hydrocarbon Motif for Chiroptical Performance Enhancement. *Chemistry-an Asian Journal* **2020**, *15* (16), 2456-2461.

(38) Jones, C. G.; Martynowycz, M. W.; Hattne, J.; Fulton, T. J.; Stoltz, B. M.; Rodriguez, J. A.; Nelson, H. M.; Gonen, T. The CryoEM Method MicroED as a Powerful Tool for Small Molecule Structure Determination. *Acs Central Science* **2018**, *4* (11), 1587-1592.

(39) Jones, C. G.; Asay, M.; Kim, L. J.; Kleinsasser, J. F.; Saha, A.; Fulton, T. J.; Berkley, K. R.; Cascio, D.; Malyutin, A. G.; Conley, M. P.; et al. Characterization of Reactive Organometallic Species via MicroED. *Acs Central Science* **2019**, *5* (9), 1507-1513.

(40) Nannenga, B. L. MicroED methodology and development. *Structural Dynamics-Us* **2020**, *7* (1).

(41) Chen, Z. J.; Lohr, A.; Saha-Moller, C. R.; Wurthner, F. Self-assembled pi-stacks of functional dyes in solution: structural and thermodynamic features. *Chemical Society Reviews* **2009**, *38* (2), 564-584.

(42) Liberko, C. A.; Miller, L. L.; Katz, T. J.; Liu, L. B. THE ELECTRONIC-STRUCTURE OF HELICENE BISQUINONE ANION RADICALS. *Journal of the American Chemical Society* **1993**, *115* (6), 2478-2482.

(43) Schweinfurth, D.; Zalibera, M.; Kathan, M.; Shen, C. S.; Mazzolini, M.; Trapp, N.; Crassous, J.; Gescheidt, G.; Diederich, F. Helicene Quinones: Redox-Triggered Chiroptical Switching and

Chiral Recognition of the Semiquinone Radical Anion Lithium Salt by Electron Nuclear Double Resonance Spectroscopy. *Journal of the American Chemical Society* **2014**, *136* (37), 13045-13052.

(44) Schweinfurth, D.; Mazzolini, M.; Neshchadin, D.; Hoyer, C.; Geier, R.; Gatterer, K.; Trapp, N.; Gescheidt, G.; Diederich, F. Electronic Structures and Chiroptical Properties of Post-functionalized Helicene Quinones. *Chemistry-a European Journal* **2016**, *22* (21), 7152-7157.

(45) Pascal, R. A.; McMillan, W. D.; Vanengen, D.; Eason, R. G. SYNTHESIS AND STRUCTURE OF LONGITUDINALLY TWISTED POLYCYCLIC AROMATIC-HYDROCARBONS. *Journal of the American Chemical Society* **1987**, *109* (15), 4660-4665.

(46) Wang, Z. H.; Tomovic, E.; Kastler, M.; Pretsch, R.; Negri, F.; Enkelmann, V.; Mullen, K. Graphitic molecules with partial "Zig/Zag" periphery. *Journal of the American Chemical Society* **2004**, *126* (25), 7794-7795.

(47) Wasserfallen, D.; Kastler, M.; Pisula, W.; Hofer, W. A.; Fogel, Y.; Wang, Z. H.; Mullen, K. Suppressing aggregation in a large polycyclic aromatic hydrocarbon. *Journal of the American Chemical Society* **2006**, *128* (4), 1334-1339.

(48) Wang, Z. M.; Lu, P.; Chen, S. M.; Gao, Z.; Shen, F. Z.; Zhang, W. S.; Xu, Y. X.; Kwok, H. S.; Ma, Y. G. Phenanthro 9,10-d imidazole as a new building block for blue light emitting materials. *Journal of Materials Chemistry* **2011**, *21* (14), 5451-5456.

(49) Fogel, Y.; Kastler, M.; Wang, Z. H.; Andrienko, D.; Bodwell, G. J.; Mullen, K. Electron-deficient N heteroaromatic linkers for the elaboration of large, soluble polycyclic aromatic hydrocarbons and their use in the synthesis of some very large transition metal complexes. *Journal of the American Chemical Society* **2007**, *129* (38), 11743-11749.

(50) Bunz, U. H. F.; Engelhart, J. U.; Lindner, B. D.; Schaffroth, M. Large N-Heteroacenes: New Tricks for Very Old Dogs? *Angewandte Chemie-International Edition* **2013**, *52* (14), 3810-3821.

(51) Mateo-Alonso, A. Pyrene-fused pyrazaacenes: from small molecules to nanoribbons. *Chemical Society Reviews* **2014**, *43* (17), 6311-6324.

(52) Sakai, H.; Shinto, S.; Araki, Y.; Wada, T.; Sakanoue, T.; Takenobu, T.; Hasobe, T. Formation of One Dimensional Helical Columns and Excimerlike Excited States by Racemic Quinoxaline-Fused 7 Carbohelicenes in the Crystal. *Chemistry-a European Journal* **2014**, *20* (32), 10099-10109.

(53) Sun, Y. T.; Li, X. X.; Sun, C. L.; Shen, H. G.; Hou, X. Q.; Lin, D. X.; Zhang, H. L.; Di, C. A.; Zhu, D. B.; Shao, X. F. Trichalcogenasumanene ortho-Quinones: Synthesis, Properties, and Transformation into Various Heteropolycycles. *Angewandte Chemie-International Edition* **2017**, *56* (43), 13470-13474.

(54) Boden, B. N.; Jardine, K. J.; Leung, A. C. W.; MacLachlan, M. J. Tetraalkoxyphenanthrene: A new precursor for luminescent conjugated polymers. *Organic Letters* **2006**, *8* (9), 1855-1858.

(55) Rieger, R.; Kastler, M.; Enkelmann, V.; Mullen, K. Entry to coronene chemistry - Making large electron donors and acceptors. *Chemistry-a European Journal* **2008**, *14* (21), 6322-6325.

(56) Sola, M. Forty years of Clar's aromatic pi-sextet rule. *Frontiers in Chemistry* **2013**, *1*.

(57) Moriconi, E. J.; Oconnor, W. F.; Rakoczy, B. OXIDATION-REDUCTION POTENTIALS AND ABSORPTION SPECTRA OF POLYCYCLIC AROMATIC QUINONES. *Journal of Organic Chemistry* **1962**, *27* (8), 2772-&.

(58) Togashi, D. M.; Nicodem, D. E. Photophysical studies of 9,10-phenanthrenequinones. *Spectrochimica Acta Part a-Molecular and Biomolecular Spectroscopy* **2004**, *60* (13), 3205-3212.

(59) Shetty, A. S.; Zhang, J. S.; Moore, J. S. Aromatic pi-stacking in solution as revealed through the aggregation of phenylacetylene macrocycles. *Journal of the American Chemical Society* **1996**, *118* (5), 1019-1027.

(60) Oien-Odegaard, S.; Shearer, G. C.; Wragg, D. S.; Lillerud, K. P. Pitfalls in metal-organic framework crystallography: towards more accurate crystal structures. *Chemical Society Reviews* **2017**, *46* (16), 4867-4876.

(61) Weichenberger, C. X.; Afonine, P. V.; Kantardjieff, K.; Rupp, B. The solvent component of macromolecular crystals. *Acta Crystallographica Section D-Structural Biology* **2015**, *71*, 1023-1038.

(62) Enkhbayar, P.; Damdinsuren, S.; Osaki, M.; Matsushima, N. HELFIT: Helix fitting by a total least squares method. *Computational Biology and Chemistry* **2008**, *32* (4), 307-310.

*Chapter 10*

*A heterologous expression platform in Aspergillus nidulans for the elucidation of cryptic secondary metabolism biosynthetic gene clusters: discovery of the Aspergillus fumigatus sartorypyrone biosynthetic pathway[1]*

## 10.1 INTRODUCTION

Aspergillosis is the spectrum of diseases caused by *Aspergillus* species that colonize the bronchial trees of patients.[1] It is estimated that there are over 300,000 cases of life-threatening Aspergillosis in humans annually, with a mortality rate of 30–80%.[2-5] Invasive Aspergillosis (IA) is one of the most common causes of death in severely immunocompromised patients, with mortality rates up to 40% to 50% in patients with acute leukemia and recipients of hematopoietic stem cell transplantations.

*Aspergillus fumigatus* is by far the most common species causing IA (70%).[5] The World Health Organization "WHO fungal priority pathogens list to guide research, development and public health action 2022" classified *A. fumigatus* as one of four species in the critical priority group, the most urgent need category.[6] Secondary metabolites (SMs) in *A. fumigatus* contribute to its unique ability to survive in the environment and establish itself in human hosts.[7, 8] SMs are small molecules produced by fungi, prokaryotes and plants that are not strictly required for growth or reproduction, but they confer a selective advantage to the producing organism. In *A. fumigatus*, SMs play important roles in iron and copper uptake and

---

homeostasis, for example.[8, 9] *A. fumigatus* also produces SMs that kill or inhibit competitors and these activities are often important to pathogenesis. Gliotoxin, for one example of several, protects *A. fumigatus* against amoebae in the environment and against T lymphocytes and the macrophage immune response in pathogenesis. Genetic elimination of gliotoxin production results in attenuation of virulence.[10-12]

SMs in filamentous fungi are synthesized by enzymes encoded by genes organized in contiguous biosynthetic gene clusters (BGCs).[13] The genes of the BGCs are coordinately regulated, and the BGCs often contain genes encoding transcription factors that drive the expression of the other genes of the BGC. SM BGCs vary significantly across species and strains of *Aspergillus*.[14] The two most studied isolates of *A. fumigatus* are Af293 and CEA10.[15, 16] Bioinformatics indicate that the *A. fumigatus* Af293 strain contains 34 predicted SM BGCs, and the CEA10 derivative strain A1163 has 33 predicted SM BGCs. The SM BGCs of the two strains are largely but not completely overlapping, with three BGCs unique to Af293 and two unique to CEA10 making a total of 36 BGCs. The products of only 19 of these BGCs have been determined, leaving, prior to this study, 17 to be determined.[17-19]

In fungi, many SM BGCs are not expressed under normal laboratory growth conditions, whereas others are expressed at high levels, resulting in a "forest" of SM peaks in LC/MS traces. To determine the SMs produced by cryptic BGCs, one needs to find a way to activate their expression. Once they are expressed, the SMs they produce must be identified and purified from among the forest of metabolites produced by the fungus. Various approaches have been developed in the model fungus *Aspergillus nidulans* to activate SM production.[20-31] In principle, some of these approaches could be transferred to *A. fumigatus* to elucidate its secondary metabolome, but it would require a great deal of time and effort to develop them. Perhaps more seriously, metabolite profiles from *A. fumigatus* grown under laboratory conditions are quite complex due to high levels of production of many compounds such as fumigaclavine C, fumiquinazoline, and monomethyl-sulochrin and their pathway intermediates.[32-38] Therefore, identifying minor compounds is difficult due to the interference of these major metabolites, and determining the BGC responsible for any minor compound is equally difficult. In *A. nidulans*, we have developed a strategy we call "genetic

dereplication" that facilitates new compound discovery. We have deleted eight BGCs, in their entirety, that produce abundant SMs (>244,000 bp deleted), thereby reducing the complexity of SM profiles such that novel compounds are more easily detected.[26] Eliminating highly expressed biosynthetic pathways may also increase pools of SM precursors such as acetyl-CoA and malonyl-CoA for pathways expressed at low levels. Because developing the genetic dereplication approach for *A. fumigatus* would be a lengthy process, we are developing methods to express *A. fumigatus* BGCs in *A. nidulans* and determine their products.

**Table 10.1.** *Putative function of genes within the A. fumigatus spy cluster (the percentages represent the aligned regions in BLASTp searches)*

| *A. fumigatus spy* cluster | *A. felis sre* cluster | Similarity/identity (%) | *A. versicolor cle* cluster | Similarity/identity (%) | Putative function |
|---|---|---|---|---|---|
| Afu8g02350 (*spyA*) | *sre6* | 89/82 | *cle1* | 59/43 | Polyketide synthase |
| Afu8g02360 (*spyB*) | *sre5* | 86/79 | — | — | Acetyltransferase |
| Afu8g02380 (*spyC*) | *sre4* | 90/83 | *cle3* | 73/59 | FAD-dependent monooxygenase |
| Afu8g02390 (*spyD*) | *sre3* | 77/63 | *cle7* | 56/37 | Terpene cyclase |
| Afu8g02400 (*spyE*) | *sre2* | 91/87 | *cle6* | 81/70 | Geranylgeranyl pyrophosphate synthase |
| Afu8g02410 (*spyF*) | *sre1* | 83/76 | *cle5* | 68/57 | Prenyltransferase |
| Afu8g02420 | — | — | — | — | Hypothetical protein |
| Afu8g02430 | — | — | — | — | Alcohol dehydrogenase |
| Afu8g02440 | — | — | — | — | C-4 methyl sterol oxidase |
| No homolog | — | — | *cle2* | — | P450 monooxygenase |
| No homolog | — | — | *cle4* | — | P450 monooxygenase |

In this study, we report the expression of a heretofore cryptic *A. fumigatus* secondary metabolite biosynthesis pathway in *A. nidulans* and the determination of the products of the BGC. Using a genetic dereplication strain to reduce the SM background, we refactored the target BGC genes into *A. nidulans*, placing each gene under the control of an inducible promoter. The heterologously expressed SMs were purified, and the structures were determined by NMR and electron cryomicroscopy (cryoEM) microcrystal electron diffraction (MicroED). We found that the BGC encodes a family of meroterpenoids called sartorypyrones that have never been reported in *A. fumigatus*. Two of the compounds are novel while two have been found in the closely related nonpathogenic fungus *Neosartorya fischeri* (KUFC 6344 and FO-

5897).[39, 40] We generated deletant strains that were each missing one gene of the biosynthetic pathway. Some of these strains accumulated chemically stable intermediates and shunt products in sufficient amounts for complete structural characterization, resulting in the identification of a total of eight additional, related compounds. We also individually expressed the non-reducing polyketide synthase (NR-PKS) gene of the BGC and demonstrated that triacetic acid lactone (TAL) is the product of the PKS. TAL is a potentially important biorenewable platform chemical.[41] Combining these data with further bioinformatic analysis, we propose a biosynthetic pathway for sartorypyrones. Importantly, the approach reported in this study, and variations thereof, can be used to elucidate other *A. fumigatus* cryptic secondary metabolism BGCs.

**10.2 RESULTS**

**10.2.1 Analysis of a potential gene cluster for production of polyketide diterpenoids (PK-DT) in *A. fumigatus***

One of the *A. fumigatus* Af293 SM BGCs with unknown products attracted our interest because it contains a non-reducing polyketide synthase (NR-PKS) gene (Afu8g02350), a prenyltransferase gene (Afu8g02410) and a terpene cyclase (TC) gene (Afu8g02390), suggesting that the SM product of this gene cluster is an unidentified meroterpenoid. As annotated by Inglis *et al*., this BGC also contains an acetyltransferase gene (Afu8g02360), a flavin-containing monooxygenase (FMO) gene (Afu8g02380), a geranylgeranyl pyrophosphate synthase (GGPPS) gene (Afu8g02400), a hypothetical protein (Afu8g02420), and an alcohol dehydrogenase (Afu8g02430).[42] A C-4 methyl sterol oxidase (Afu8g02440) is adjacent. In all, the putative BGC is greater than 24 kbp in length. Synteny analysis in FungiDB reveals that the genes within the putative BGC are conserved and collinear between *A. fumigatus* isolates Af293 (Afu8g02350–Afu8g02440) and A1163 (AFUB_084240–AFUB_084150).[43] Bioinformatic analysis of this BGC using BLASTp showed that genes Afu8g02350–Afu8g02410 are homologous to genes in the *sre* cluster, which encodes the biosynthetic pathway for sartorypyrone A and D in *Aspergillus felis* 0260, and the *cle* cluster, which encodes the biosynthetic pathway for chevalone E in *Aspergillus versicolor* 0312 (Table 10.1).[44]

*Figure 10.1*. *(A) The spy BGC from A. fumigatus. (B) Refactoring the spyA, spyE, spyC, Afu8g02430 and Afu8g02440 genes at the yA locus in A. nidulans. (C) HPLC profiles of culture medium and mycelium extracts from A. nidulans transformants. (D) Structures of compounds 1–4. Afu8g02440 (putative C-4 methyl sterol oxidase) and Afu8g02430 (putative alcohol dehydrogenase) were also refactored at yA as shown, but deletion experiments proved them not to be components of the spy BGC.*
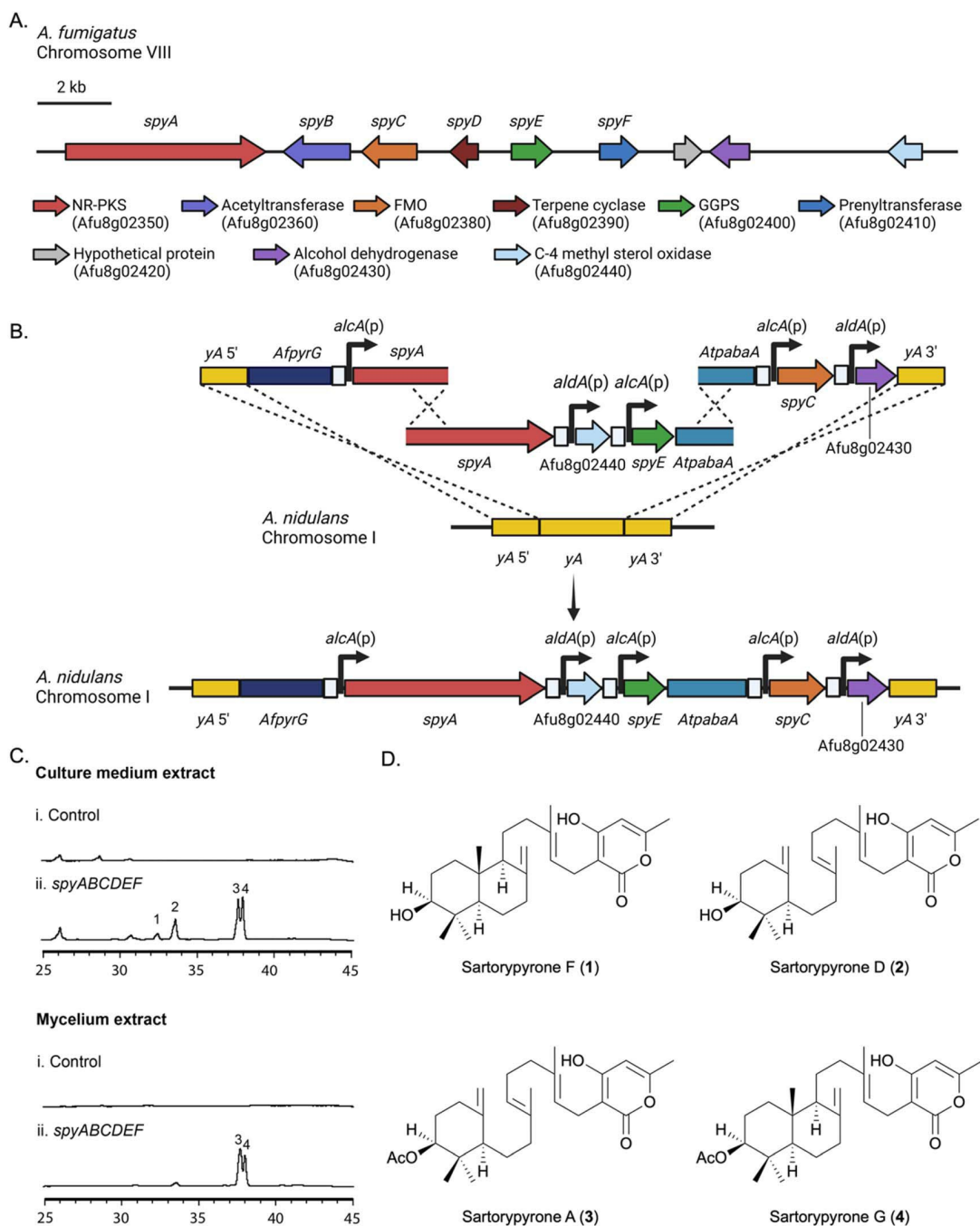
**10.2.2 Heterologous expression strategy of the Afu8g02350 BGC in *A. nidulans***

Our heterologous expression platform has two major elements. One is the use of an updated genetic dereplication strain we have developed, LO11098, and related strains for expression. We have engineered this strain for heterologous SM expression by removing eight of the most highly expressed BGCs which lowers the SM background, making expressed metabolites easier to identify and purify. We have also incorporated seven selectable markers in the strain to facilitate multiple sequential gene transfers. The strain also carries a deletion of the *nkuA* gene which dramatically reduces non-homologous recombination. The second element is an elaboration of multiplex fusion PCR procedures we have developed[45] to rapidly create large linear molecules for transformation with multiple genes under control of inducible promoters.

To express our target BGC we used two approaches. In the first approach, we refactored the entire target BGC in *A. nidulans*, placing each gene under control of the inducible *alcA* or *aldA* promoter (Figure 10.1A, B and I.1†). The *alcA* and *aldA* promoters are short (300–400 bp), strongly induced by a variety of alcohols, aldehydes and ketones, and repressed by glucose and certain other carbon sources.[46-48] Their shortness and relatively low homology reduce the probability of recombination of these promoters with each other or the native *alcA* or *aldA* loci during transformation. Our second approach was to reconstruct the entire BGC intact in *A. nidulans* and use global regulators of secondary metabolism to activate expression of the BGC. The BGC as predicted by Inglis *et al.* consisted of Afu8g2350–Afu8g02430.[42] We also included Afu8g02440 in case the BGC was larger than predicted (Figure 10.1A).

**10.2.3 Heterologous expression of the Afu8g02350 (*spy*) BGC in *A. nidulans* reveals that it produces sartorypyrones**

A key in correctly refactoring BGCs is identification of the correct start codon for each gene. BLASTp searches with the amino acid sequence of the putative acetyl transferase, Afu8g02360, as predicted from the FungiDB annotation (https://fungidb.org/fungidb/app),[43] suggested that the annotation of this gene might be incorrect, and the correct start site might be 593 base pairs downstream. The second

start site also had a better Kozak consensus sequence. We, therefore, refactored this gene in two ways inserting the *alcA* promoter upstream of the FungiDB annotated start codon (start site 1) and, separately, in front of the downstream putative start codon (start site 2).

The putative BGC genes were refactored in two steps. Five genes were refactored at the *yA* locus (Figure 10.1B). Three transforming fragments were first created by fusion PCR. A fragment carrying ~1 kb of DNA flanking the *yA* gene as well as the *pyrG* gene from *A. fumigatus* (*AfpyrG*) was fused to the *alcA* promoter [*alcA*(p)] and a portion of the Afu8g02350 gene from *A. fumigatus*. A second fragment constructed by fusion PCR contained an overlapping region of Afu8g02350 as well as two additional genes under control of the *aldA* promoter [*aldA*(p)] and *alcA*(p) and a portion of the *Aspergillus terreus pabaA* gene (*AtpabaA*), which was used as a selectable marker. The third fragment contained an overlapping fragment of *AtpabaA*, two additional genes under control of *alcA*(p) and *aldA*(p) and ~1 kb of *yA* 3′ flank. Upon transformation with the three fragments, homologous recombination resulted in the replacement of the *yA* locus with five genes, each under control of *alcA*(p) or *aldA*(p). Note that a functional copy of *AtpabaA* is not formed unless fragments 2 and 3 recombine correctly. Four additional genes were placed under control of *alcA* or *aldA* promoters and inserted at the *wA* locus using essentially the same procedure (Figure I.1†). Using fusion PCR to make transforming fragments, we were, thus, able to refactor the entire >24 kb BGC in two transformations.

Refactored strains were cultivated in lactose minimal medium (LMM), which is non-repressing for the *alcA* and *aldA* promoters and induced with methyl-ethyl-ketone (MEK). Extracts from the culture medium and mycelia were analyzed separately by LC/MS for the presence of new metabolites. In comparison with the *A. nidulans* control strain, which lacked the *A. fumigatus* BGC genes, compounds **1**–**4** were detected specifically in the refactored strains (Figure 10.1C). The strains in which Afu8g02360 was refactored by fusing *alcA*(p) at start site 1 (LO11784–LO11793), were not able to produce compounds **3** and **4**, however, in comparison with the start site 2 refactored strains (LO11794–LO11803) (Figure I.2†). This indicated to us that the FungiDB annotation of the acetyl transferase is incorrect. Refactoring

Afu8g02360 at start site 2 results in a functional acetyl transferase and production of **3** and **4**, the acetylated final products of the BGC. Data with deletion strains (below) support this conclusion.

*Figure 10.2. MicroED structure of compound 1. The relative stereochemistry of compound 1 was confirmed by MicroED.*
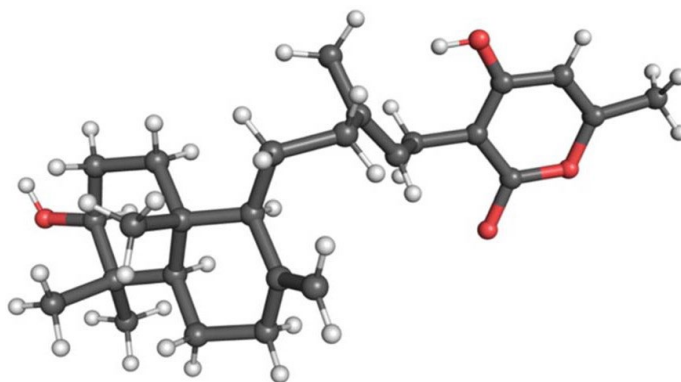


Yields of compounds from the initial strains were inadequate to allow determination of the structures of **1**–**4**. To increase yields, we deleted the *A. nidulans agsB* gene. *agsB* encodes α-1,3-glucan synthase and *agsB* deletants cause hyphae to disperse in liquid culture.[49] We hypothesized that deleting *agsB* would allow denser growth and increased metabolite yields, and this proved to be the case. An *agsB*Δ, Afu8g02360 start site 2 refactored strain (LO11839) was subjected to largescale cultivation and compounds **1**–**4** were isolated by flash chromatography and semi-preparative HPLC. Spectroscopic analysis (NMR, MS, and UV-Vis data) allowed us to determine that compounds **2** and **3** are sartorypyrone D and sartorypyrone A, respectively, which were previously identified in *Neosartorya fischeri* strains KUFC-6344 and FO-5897 (Figure 10.1D and Tables I.3and I.4†).[39, 40] (Note: *N. fischeri* is a homotypic synonym of *Aspergillus fischeri* and both designations are used in the scientific literature.) Sartorypyrone D has also been produced synthetically in *Aspergillus oryzae* by expressing chevalone E BGC genes from *A. versicolor* along with a terpene cyclase from *A. felis*.[44] Because it produces sartorypyrones we have designated the Afu8g02350 SM BGC as the *spy* BGC. Compounds **1** and **4** are new to science and were structurally elucidated by 1D and 2D NMR spectra (Figure 10.1D, for detailed structural elucidation, see Appendix I† – detailed structural characterizations of new compounds). Furthermore, the relative configuration was

confirmed by MicroED analysis on compound **1** (Figure 10.2, I.53 and Table I.13†). Taking the above spectroscopic analyses together, compounds **1** and **4** are new bicyclic meroditerpenoids, which we have named sartorypyrone F and sartorypyrone G, respectively.

*Figure 10.3. (A) HPLC profiles of culture medium and mycelium extracts from A. nidulans transformants, which carry individual gene deletions from the completely refactored spy strain LO11911 (Afu8g02420, Afu8g02430, Afu8g02440 were included). (B) Structures of compounds 5–11.*
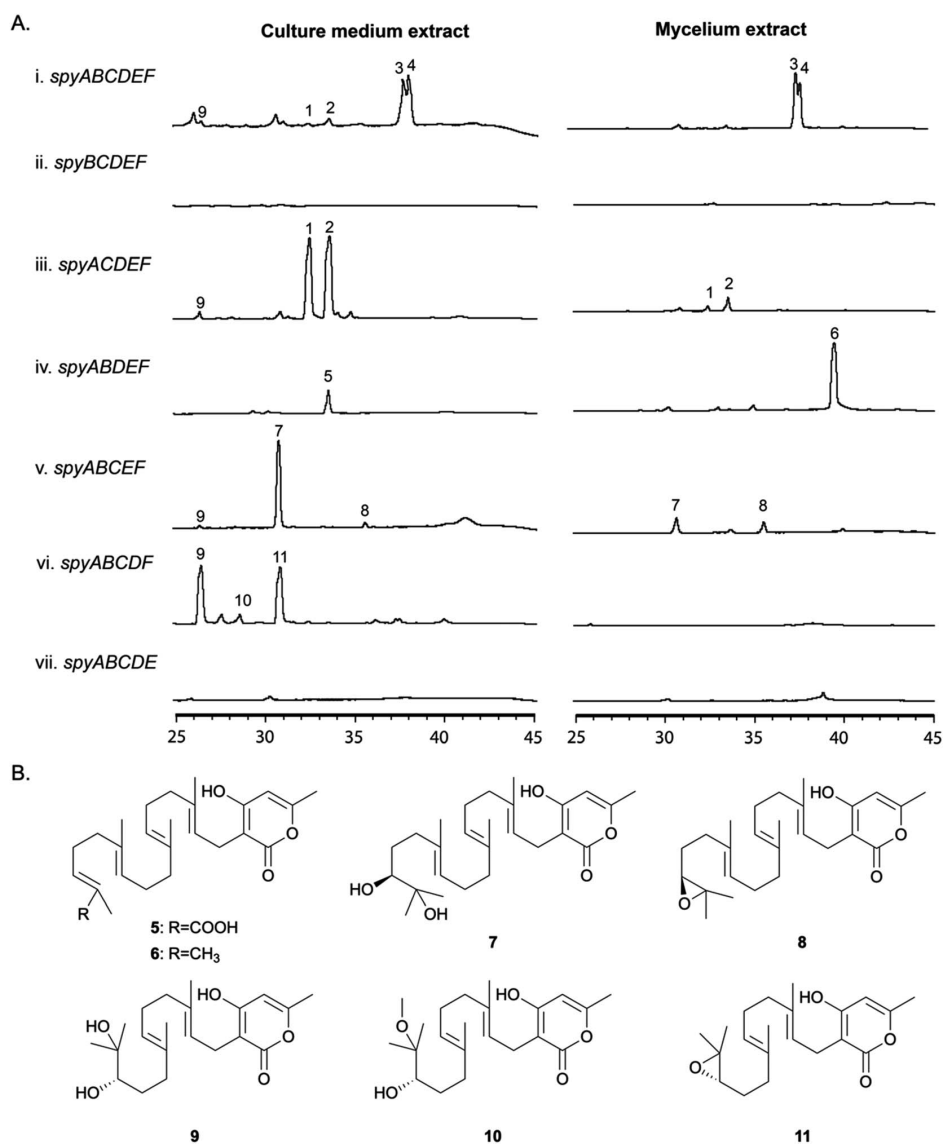
In our second heterologous expression approach, we reconstructed the entire target BGC in *A. nidulans* and attempted to use global regulators of secondary metabolism to activate its expression. We amplified portions of the target BGC and used PCR to fuse them to sequences flanking the *yA* (yellow spore color) gene and to selectable markers (*A. terreus pyrG* [*AtpyrG*] and *A. fumigatus pyroA* [*AfpyroA*]) (Figure I.3†). This created two fragments carrying a total of six genes. Afu8g02420 was on both fragments. Upon co-transformation (Figure I.3A–D†), the two fragments recombined homologously with the *yA* flanking sequences and the Afu8g02420 sequence on the two fragments recombined homologously with each other. The result is a replacement of the *yA* coding sequence with six genes from the target cluster. A second transformation with two additional fragments (Figure I.3A and E–G†) resulted in the reconstruction of the entire target BGC in *A. nidulans.* The second transformation also removes the *AfpyroA* selectable marker. Including primers, the entire sequence transferred into *A. nidulans* was 25 832 bp.

To potentially upregulate expression of the BGC in the reconstructed BCG strain, we separately deleted *mcrA*, a negative regulator of secondary metabolism,[29] and we placed two positive regulators of secondary metabolism, *laeA* and *llmG* under control of the inducible *alcA* promoter [*alcA*(p)*laeA* and *alcA*(p)*llmG*].[50, 51] We also created pairwise combinations of the *mcrA* deletion (*mcrA*Δ), *alcA*(p)*laeA* and *alcA*(p)*llmG*. Initial metabolite profiles (not shown) revealed that while deletion of *mcrA* upregulated secondary metabolite production, it created a sufficiently high background that identification of products of the target BGC wasn't feasible. Overexpression of *laeA* or *llmG*, however, did not create an excessive background, nor did overexpression of these two positive regulators in tandem. Overexpression of *laeA* and *llmG* did not yield strong new peaks that could easily be ascribed to the reconstructed BGC. However, knowing the masses of the sartorypyrones produced by the refactored cluster allowed us to unambiguously detect sartorypyrone A (**3**) and sartorypyrone G (**4**) in the *laeA*, *llmG* overexpressing strain by mass spectrometry in extracted ion chromatogram (EIC) mode (Figure I.3B†), while they were not detectable in control strains. This result provides a useful confirmation that **3** and **4** are the final products of the BGC.

**10.2.4 Identification, purification, and structural elucidation of the intermediates and shunt products from single-gene-deleted mutant strains**

In order to determine the roles of the individual genes in the BGC, we generated a series of single gene deletion strains (Table I.1†) from the completely refactored strain LO11911. LO11911 is LO11839 engineered to give even higher yields by replacing the promoter of the *alcR* gene with the strong constitutive *gpdA* promoter.[52] The deletant strains were verified by multiple diagnostic PCR reactions. They were cultivated under the same conditions as were used to produce sartorypyrones in the refactored strain (*i.e.*, under inducing conditions) and their SM profiles were examined by LC/MS. The results showed that the final products, **3** and **4**, were not produced in the *spyA–F* single gene deletion strains (Figure 10.3). Detectable intermediates or shunt products accumulated, however, in *spyB–E* single gene deletion strains (Figure 10.3). The metabolite profiles of mutants missing Afu8g02420, Afu8g02430, or Afu8g02440 did not show significant differences from their parent strain indicating that they were not involved in the biosynthesis of sartorypyrones (Figure I.4†). These data are consistent with transcription data available at FungiDB indicating that these three genes are regulated independently of the *spy* genes.

Deleting the PKS gene, *spyA* (Afu8g02350), which is expected to catalyze the first metabolic step in the pathway, dramatically reduced production of the products of the pathway. However, compounds **3** and **4** were produced in very small amounts (more than a 100-fold reduction relative to the strain with *spyA* present, as determined by EIC), suggesting that an alternative mechanism exists in *A. nidulans* for the production of small amounts of the polyketide produced by *SpyA* (Figure I.5†). Based on their domain structures, two *A. nidulans* PKS genes were candidates for producing the same compound as *SpyA*, AN6448, the PKS in the cichorine BGC and AN12440, the product of which is unknown.[53] However, deletion of these genes along with *spyA* left a very small residuum of **3** and **4**. These PKSs, therefore are not responsible for the production of trace amounts of **3** and **4** in the absence of *spyA* (Figure I.5†).

The *spyB* (Afu8g02360) gene is predicted to encode an acetyltransferase, and the mutant missing the *spyB* gene was unable to produce the acetylated compounds **3** and **4**. Instead, the unacetylated

derivatives, compounds **2** and **1**, respectively, accumulated in the culture medium and, at lower concentrations, in mycelia. We detected substantially more of compounds **1** and **2** than in the parental strain with the intact refactored BGC (more than a 100-fold increase as determined by EIC). These data confirm that the protein encoded by *spyB* is an acetyl transferase and, as indicated above, that start site 2 is correct.

***Figure 10.4***. *HPLC profiles of acidified induced culture medium extracts from an A. nidulans strain lacking spyA, and transformants which carry inducible spyA alone or carry the entire inducible spy BGC with spyF deleted (spyABCDE). An authentic TAL standard HPLC profile was included for comparison.*
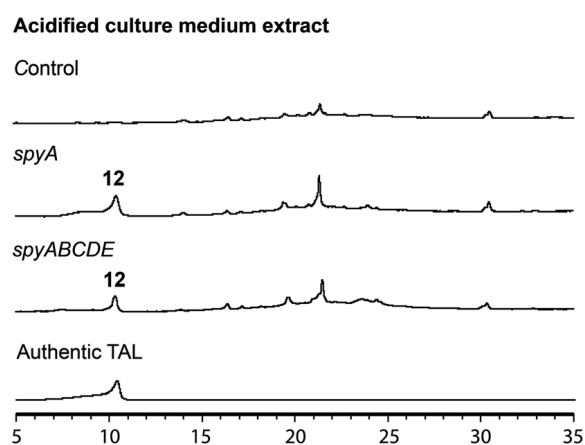


In the mutant missing the *spyC* (Afu8g02380) gene, we isolated two prenylated polyketides **5** and **6**, suggesting that the *spyC* gene codes for an FAD-dependent monooxygenase as the terminal olefin in the diterpene moiety was incapable of epoxidation. The analysis of $^1$H, $^{13}$C, and 2D NMR confirm compound **6** is a known intermediate, geranylgeranyl-triacetate lactone (Table I.7†),[44] while compound **5** is a new carboxylate shunt product of **6** (Figure 10.3B, for detailed structural elucidation see Appendix I†).

The *spyD* (Afu8g02390) gene is predicted to encode a terpene cyclase. In the mutant lacking the *spyD* gene, we detected two uncyclized prenylated polyketides **7** and **8**. The $^1$H, $^{13}$C, and 2D NMR analysis confirmed compound **7** is sartorypyrone E, which has been previously characterized in the literature (Table I.8†),[54] while compound **8** is the epoxide-containing intermediate in the biosynthetic pathway of sartorypyrones (Table I.9 and Figure I.33–I.37†). Although other studies have proposed the hypothetical biosynthetic intermediate structure of compound 8,[44, 55] our study provides the first evidence of its existence

as a metabolite of the producing fungus. We named this new compound epoxygeranylgeranyl-triacetate lactone. The epoxide in compound **8** is relatively unstable and thus significantly more of the hydroxylated shunt product compound **7** is generated.

***Figure 10.5***. *Proposed biosynthetic pathway for **3**, **4**, and related shunt products. The pathway bifurcates to **3**–**4** and related shunt products, which are separated by a dashed line. Brackets indicate hypothetical parts of the pathway. The following domains in the NR-PKS SpyA are indicated: SAT: starter unit-ACP transacylase; KS: ketosynthase; AT: acyl transferase; PT: product template; ACP: acyl carrier protein. SpyA is shown with acetyl- CoA conjugated to the SAT domain.*
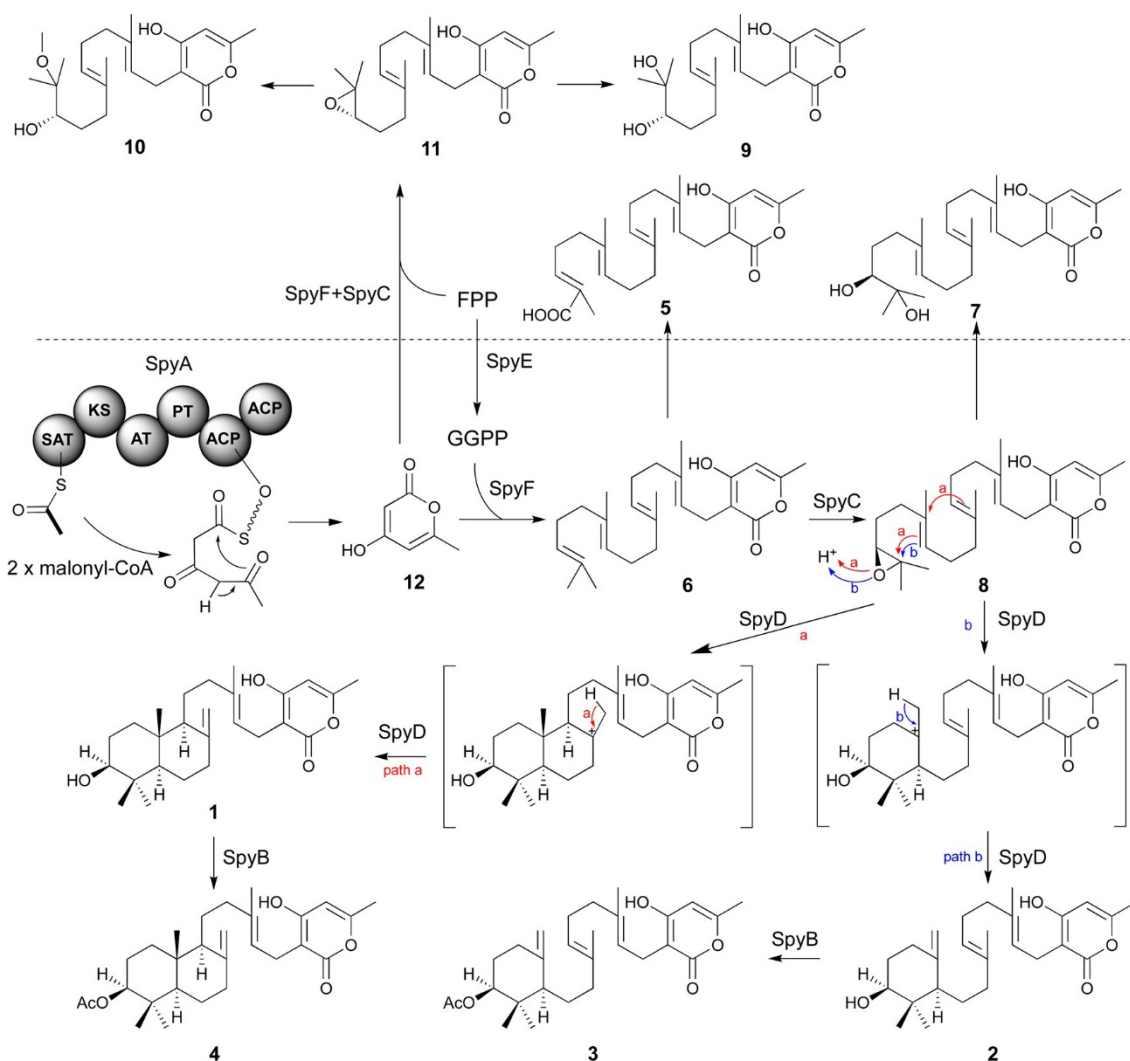
Compound **9** was present at low levels in the culture medium of the strain with the full refactored BGC and in the *spyB* and *spyD* deletants, but it accumulated at much higher levels in the *spyE* (Afu8g02400) deletant. **10** and **11** also accumulated in the *spyE* deletant but were not detected by LC/MS in other strains. Large scale isolation and characterization *via* NMR spectroscopy showed that metabolites **9–11** were produced by utilizing farnesyl pyrophosphate (FPP) instead of geranylgeranyl pyrophosphate (GGPP) (Table I.10–I.12 and Figure I.38–I.52†), consistent with *spyE* encoding a GGPS that converts FPP to GGPP. The production of these compounds suggests that the prenyltransferase and FMO have a broad substrate tolerance and can utilize both GGPP and FPP as substrates. Furthermore, the relative configurations of these compounds were deduced to be identical to their analogs with the GGPP moiety because of their biosynthetic relationships. We named these new compounds dihydroxyfarnesyl-triacetate lactone (**9**), 17-methoxy-16-hydroxyfarnesyl-triacetate lactone (**10**) and epoxyfarnesyltriacetate lactone (**11**).

In the mutant missing the *spyF* (Afu8g02410) gene, which encodes a putative prenyltransferase, all the peaks were abolished, as expected if *SpyF* is required for prenylation of triacetic acid lactone (TAL) for production of compounds **6** and **11**, but we did not detect the polyketide products. Matsuda *et al*. showed that co-expression in *A. oryzae* of the *A. felis sre3* terpene cyclase with the *A. versicolor* chevalone E BGC genes encoding the PKS, prenyl transferase, geranylgeranyl pyrophosphate synthase and FAD-dependent monooxygenase produced sartorypyrone D. The proposed biosynthetic pathway suggested that the polyketide TAL was the likely product of the chevalone E BGC PKS. TAL was not detected, however, when the chevalone E BGC NR-PKS Cle1 was expressed in *A. oryzae*.[44] Similarly, we deduced that TAL is the likely polyketide product of the *SpyA* NR-PKS, because compound **6** is a geranylgeranylated derivative of TAL. Our proposed biosynthetic pathway predicts that TAL should accumulate in the *spyF* deletion strain, but we did not initially detect TAL in this deletant. We therefore constructed an *A. nidulans* strain (LO12091) in which the *SpyA* NR-PKS, alone, is expressed under control of the inducible *alcA* promoter. Cultivation and direct analysis of the induced culture medium of the *spyA*-expressing strain compared with that of a control strain lacking *spyA* did not initially reveal any polyketide products of *SpyA*. In order to

extract acidic phenolic polyketide compounds, we lowered the pH value of the culture medium filtrate and subsequently extracted the acidified medium by ethyl acetate. Acidification of the culture medium from the *sypA*-expressing strain, but not the control strain lacking *spyA*, revealed a new peak, and we were able to confirm that the peak is TAL (**12**) by comparing it to a TAL standard (Figure 10.4). Therefore, *SpyA* is a TAL synthase. Armed with this information, we acidified culture medium from a *spyF* deletant and were able to detect **12**. The deletant strains in addition to the complete refactored strain allowed us to isolate, and characterize by NMR, all the intermediates in the sartorypyrone biosynthetic pathway (Figure 10.5).

## 10.3 DISCUSSION

Secondary metabolites contribute to the reproductive success and pathogenicity of fungi, but many of the secondary metabolites produced by the BGCs of the serious fungal pathogen *A. fumigatus* are unknown. We have used a combination of heterologous expression and natural products chemistry to determine the products of a heretofore cryptic *A. fumigatus* meroterpenoid BGC, which we have named the *spy* BGC. The *spy* BGC harbors homologs of all the genes in the sartorypyrone A (*sre*) BGC in *A. felis*. Several sartorypyrones have been isolated from *Aspergillus* species, but this study is, to our knowledge, the first to show the biosynthesis of this class of compounds from an *A. fumigatus* BGC. The isolation of compounds **1**–**4** from the refactored strain and the cluster reconstructed strain suggested that a single terpene cyclase in the pathway is able to produce both trans-decalin meroterpenoids and monocyclic meroterpenoids. Promiscuous behaviors of terpene cyclases have been reported in other studies.[56, 57]

We created a set of targeted gene deletions that have allowed us to elucidate roles of the *spy* genes in the biosynthesis of compounds **3** and **4**. Cultivation of deletant strains allowed us to identify and fully characterize twelve compounds from the pathway, seven of which have not been reported previously. Based on the intermediates and shunt products isolated from the mutant strains, we were able to propose a biosynthetic pathway for the sartorypyrones produced by the *spy* BGC (Figure 10.5). First, compound **12** is generated by the NR-PKS *SpyA* using one molecule of acetyl-CoA and two molecules of malonyl-CoA. As *SpyA* lacks a thioesterase (TE) domain, **12** is likely generated through self-release from *SpyA* by

spontaneous lactonization. The prenyltransferase *SpyF* then conjugates GGPP to **12** to form compound **6**, for which the pathway-specific GGPS *SpyE* is required to provide GGPP. Subsequently, compound **6** is epoxidized at the terminal olefin by the FMO *SpyC*, followed by cyclization of the terpenoid component catalyzed by the terpene cyclase *SpyD*. *SpyD* exhibits promiscuous activity, resulting in the formation of bicyclic sartorypyrone F (**1**) and monocyclic sartorypyrone D (**2**). While both compounds are generated by direct terminating deprotonation, the degrees of polyene cyclization are different (path a and b). Finally, the last step of the biosynthesis involves the acetylation of the meroterpenoids by the acetyltransferase *SpyB* to produce compound **3** and compound **4**. In the absence of GGPP (i.e. in the mutant lacking *spyE*), *SpyF* is able to catalyze addition of FPP to **12** to produce shunt products **9**–**11**. If *spyE* is intact, GGPP is produced, and we hypothesize that *SpyF* favors the addition of GGPP over addition of FPP such that little of the shunt products accumulate (although a small amount of 9 was detected). In addition, by driving conversion of FPP to GGPP, *SpyE* may reduce the available levels of FPP, thereby further reducing production of **9**–**11**. As to why **9** is detected in strains with *SpyE* but **10** and **11** are not, **11** is likely to be somewhat unstable which may reduce its levels and **11** appears to break down to **9** in preference to **10** such that little **10** is produced even in *spyE* deletants. A very small amount of **3** and **4** are produced in the *spyA* deletant, which indicates that **12** is also produced by an unknown minor mechanism. Note, however, that **12** is one of four products produced when the *A. terreus* PKS gene ATEG_00145.1 is expressed in *A. nidulans*.[58] The major product of ATEG_00145.1 is a pentaketide, but some triketide (**12**) and tetraketide is produced. It is likely that the PT domain in ATEG_00145.1 that controls product length is not stringent, allowing release of shorter products in addition to the main product. It is possible that an endogenous *A. nidulans* PKS produces a small amount of **12** as an early release product similar to ATEG_00145.1.

Several additional points are worth making. First, we were able to refactor the entire *A. fumigatus* BGC as annotated by Inglis *et al.*,[42] and an additional gene, in two transformations using transforming fragments created by fusion PCR, and we were easily able to detect metabolites produced by the BGC in our reduced SM background *A. nidulans* genetic dereplication strain. This demonstrates the efficiency and

practicality of our heterologous expression system for elucidating the products of cryptic BGCs from *A. fumigatus* and potentially from other fungi. Second, in the native BGC, promoters are likely of different strengths, optimized by evolution to produce the final products of the biosynthetic pathway. In our refactored BGC, all promoters are strong and this likely results in the accumulation of intermediate compounds such as **1** and **2**. This can be advantageous in elucidating the biosynthetic pathway. Furthermore, we demonstrated the feasibility of MicroED for elucidating structures of SMs produced in our heterologous expression system. Our strategy of reconstructing the target BGC in *A. nidulans* and up-regulating by manipulating global regulators of secondary metabolism, while very feasible, was of minor value with the sartorypyrone BGC, only providing a confirmation of the final products of the BGC. However, nearly all of the remaining cryptic BGCs of *A. fumigatus* harbor putative transcription factors that are predicted to drive expression of the genes of the BGCs. Reconstructing *A. fumigatus* BGCs in *A. nidulans* and upregulating the transcription factors of the BGCs could prove to be a very efficient approach toward elucidating the remaining *A. fumigatus* BGCs.

Finally, TAL is a potentially very valuable biorenewable platform chemical, and efforts are underway to produce it efficiently by a number of routes. The most well-known route is *via* type III PKSs, such as 2-pyrone synthase (2-PS), which catalyze decarboxylative Claisen condensation with one acetyl-CoA molecule as the initial unit and two malonyl-CoA molecules as extension units, followed by spontaneous lactonization to generate TAL.[59, 60] Some research has employed heterologous expression of 2-PS in various organisms, such as *Escherichia coli*, *Yarrowia lipolytica*, and *Saccharomyces cerevisiae* to achieve a higher production yield.[61-64] Alternatively, polyketoacyl-CoA thiolases (PKTs) were shown to be capable of producing TAL using acetyl-CoA as both initial and extension units.[65] In this study, we have now demonstrated that the NR-PKS *SpyA* is also able to form TAL. Although our yields of TAL are not large, our systemhas not been optimized for TAL production, and there are many routes to much higher yields. Unambiguous identification of a type I NRPKS that makes TAL herein potentially opens the way to more efficient and commercially viable TAL production.

## 10.4 CONCLUSION

In summary, we have deciphered an unknown SM BGC in the human pathogen *A. fumigatus* using a heterologous expression approach. The *spy* BGC consists of six contiguous genes involved in the biosynthesis of the sartorypyrones. By integrating data obtained from bioinformatic analysis and intermediates or shunt products isolated from the individual gene deletion mutants, we were able to propose a biosynthetic pathway for this family of compounds. Our approach of refactoring the entire gene cluster in the dereplicated *A. nidulans* host system provides us with a straightforward way to dissect the biosynthetic pathway. This work provides an appealing demonstration that the *A. nidulans* heterologous expression platform can be used for the elucidation of cryptic BGCs in *A. fumigatus* and other species.

## 10.5 REFERENCES

(1) Stevens, D. A.; Moss, R. B.; Kurup, V. P.; Knutsen, A. P.; Greenberger, P.; Judson, M. A.; Denning, D. W.; Crameri, R.; Brody, A. S.; Light, M.; et al. Allergic bronchopulmonary aspergillosis in cystic fibrosis - State of the art: Cystic Fibrosis Foundation Consensus Conference. *Clinical Infectious Diseases* **2003**, *37*, S225-S264.

(2) Pianalto, K. M.; Alspaugh, J. A. New Horizons in Antifungal Therapy. *Journal of Fungi* **2016**, *2* (4).

(3) Bongomin, F.; Gago, S.; Oladele, R. O.; Denning, D. W. Global and Multi-National Prevalence of Fungal Diseases-Estimate Precision. *Journal of Fungi* **2017**, *3* (4).

(4) Dagenais, T. R. T.; Keller, N. P. Pathogenesis of Aspergillus fumigatus in Invasive Aspergillosis. *Clinical Microbiology Reviews* **2009**, *22* (3), 447-465.

(5) Latge, J. P.; Chamilos, G. Aspergillus fumigatus and Aspergillosis in 2019. *Clinical Microbiology Reviews* **2020**, *33* (1).

(6) Rodrigues, M. L.; Nosanchuk, J. D. Recognition of fungal priority pathogens: What next? *PLoS neglected tropical diseases* **2023**, *17* (3), e0011136.

(7) Steenwyk, J. L.; Mead, M. E.; Knowles, S. L.; Raja, H. A.; Roberts, C. D.; Bader, O.; Houbraken, J.; Goldman, G. H.; Oberlies, N. H.; Rokas, A. Variation Among Biosynthetic Gene Clusters,

Secondary Metabolite Profiles, and Cards of Virulence AcrossAspergillusSpecies. *Genetics* **2020**, *216* (2), 481-497.

(8) Raffa, N.; Keller, N. P. A call to arms: Mustering secondary metabolites for success and survival of an opportunistic pathogen. *Plos Pathogens* **2019**, *15* (4).

(9) Leal, S. M.; Roy, S.; Vareechon, C.; Carrion, S. D.; Clark, H.; Lopez-Berges, M. S.; diPietro, A.; Schrettl, M.; Beckmann, N.; Redl, B.; et al. Targeting Iron Acquisition Blocks Infection with the Fungal Pathogens Aspergillus fumigatus and Fusarium oxysporum. *Plos Pathogens* **2013**, *9* (7).

(10) Sugui, J. A.; Pardo, J.; Chang, Y. C.; Zarember, K. A.; Nardone, G.; Galvez, E. M.; Muellbacher, A.; Gallin, J. I.; Simon, M. M.; Kwon-Chung, K. J. Gliotoxin is a virulence factor of Aspergillus fumigatus: gliP deletion attenuates virulence in mice Immunosuppressed with hydrocortisone. *Eukaryotic Cell* **2007**, *6* (9), 1562-1569.

(11) Spikes, S.; Xu, R.; Nguyen, C. K.; Chamilos, G.; Kontoyiannis, D. P.; Jacobson, R. H.; Ejzykowicz, D. E.; Chiang, L. Y.; Filler, S. G.; May, G. S. Gliotoxin production in Aspergillus fumigatus contributes to host-specific differences in virulence. *Journal of Infectious Diseases* **2008**, *197* (3), 479-486.

(12) Cramer, R. A.; Gamcsik, M. P.; Brooking, R. M.; Najvar, L. K.; Kirkpatrick, W. R.; Patterson, T. F.; Balibar, C. J.; Graybill, J. R.; Perfect, J. R.; Abraham, S. N.; et al. Disruption of a nonribosomal peptide synthetase in Aspergillus fumigatus eliminates gliotoxin production. *Eukaryotic Cell* **2006**, *5* (6), 972-980.

(13) Keller, N. P.; Turner, G.; Bennett, J. W. Fungal secondary metabolism - From biochemistry to genomics. *Nature Reviews Microbiology* **2005**, *3* (12), 937-947.

(14) Barber, A. E.; Sae-Ong, T.; Kang, K.; Seelbinder, B.; Li, J.; Walther, G.; Panagiotou, G.; Kurzai, O. Aspergillus fumigatus pan-genome analysis identifies genetic variants associated with human infection. *Nature Microbiology* **2021**, *6* (12), 1526.

(15) Nierman, W. C.; Pain, A.; Anderson, M. J.; Wortman, J. R.; Kim, H. S.; Arroyo, J.; Berriman, M.; Abe, K.; Archer, D. B.; Bermejo, C.; et al. Genomic sequence of the pathogenic and allergenic filamentous fungus Aspergillus fumigatus. *Nature* **2005**, *438* (7071), 1151-1156.

(16) Fedorova, N. D.; Khaldi, N.; Joardar, V. S.; Maiti, R.; Amedeo, P.; Anderson, M. J.; Crabtree, J.; Silva, J. C.; Badger, J. H.; Albarraq, A.; et al. Genomic islands in the pathogenic filamentous fungus Aspergillus fumigatus. *Plos Genetics* **2008**, *4* (4).

(17) Romsdahl, J.; Wang, C. C. C. Recent advances in the genome mining of Aspergillus secondary metabolites (covering 2012-2018). *Medchemcomm* **2019**, *10* (6), 840-866.

(18) Stroe, M. C.; Netzker, T.; Scherlach, K.; Kruger, T.; Hertweck, C.; Valiante, V.; Brakhage, A. A. Targeted induction of a silent fungal gene cluster encoding the bacteria-specific germination inhibitor fumigermin. *Elife* **2020**, *9*. DOI: 10.7554/eLife.52541.

(19) Kalb, D.; Heinekamp, T.; Lackner, G.; Scharf, D. H.; Dahse, H. M.; Brakhage, A. A.; Hoffmeister, D. Genetic Engineering Activates Biosynthesis of Aromatic Fumaric Acid Amides in the Human Pathogen Aspergillus fumigatus. *Applied and Environmental Microbiology* **2015**, *81* (5), 1594-1600.

(20) Bok, J. W.; Chiang, Y. M.; Szewczyk, E.; Reyes-Domingez, Y.; Davidson, A. D.; Sanchez, J. F.; Lo, H. C.; Watanabe, K.; Strauss, J.; Oakley, B. R.; et al. Chromatin-level regulation of biosynthetic gene clusters. *Nature Chemical Biology* **2009**, *5* (7), 462-464.

(21) Brakhage, A. A.; Schroeckh, V. Fungal secondary metabolites - Strategies to activate silent gene clusters. *Fungal Genetics and Biology* **2011**, *48* (1), 15-22.

(22) Chiang, Y. M.; Chang, S. L.; Oakley, B. R.; Wang, C. C. C. Recent advances in awakening silent biosynthetic gene clusters and linking orphan clusters to natural products in microorganisms. *Current Opinion in Chemical Biology* **2011**, *15* (1), 137-143.

(23) Ahuja, M.; Chiang, Y. M.; Chang, S. L.; Praseuth, M. B.; Entwistle, R.; Sanchez, J. F.; Lo, H. C.; Yeh, H. H.; Oakley, B. R.; Wang, C. C. C. Illuminating the Diversity of Aromatic Polyketide

Synthases in Aspergillus nidulans. *Journal of the American Chemical Society* **2012**, *134* (19), 8212-8221.

(24) Soukup, A. A.; Chiang, Y. M.; Bok, J. W.; Reyes-Dominguez, Y.; Oakley, B. R.; Wang, C. C. C.; Strauss, J.; Keller, N. P. Overexpression of the Aspergillus nidulans histone 4 acetyltransferase EsaA increases activation of secondary metabolite production. *Molecular Microbiology* **2012**, *86* (2), 314-330.

(25) Yaegashi, J.; Oakley, B. R.; Wang, C. C. C. Recent advances in genome mining of secondary metabolite biosynthetic gene clusters and the development of heterologous expression systems in Aspergillus nidulans. *Journal of Industrial Microbiology & Biotechnology* **2014**, *41* (2), 433-442.

(26) Chiang, Y. M.; Ahuja, M.; Oakley, C. E.; Entwistle, R.; Asokan, A.; Zutz, C.; Wang, C. C. C.;Oakley, B. R. Development of Genetic Dereplication Strains in Aspergillus nidulans Results in the Discovery of Aspercryptin. *Angewandte Chemie-International Edition* **2016**, *55* (5), 1662-1665.

(27) Yeh, H. H.; Ahuja, M.; Chiang, Y. M.; Oakley, C. E.; Moore, S.; Yoon, O.; Hajoysky, H.; Bok, J. W.; Keller, N. P.; Wang, C. C. C.; et al. Resistance Gene-Guided Genome Mining: Serial Promoter Exchanges in Aspergillus nidulans Reveal the Biosynthetic Pathway for Fellutamide B, a Proteasome Inhibitor. *Acs Chemical Biology* **2016**, *11* (8), 2275-2284.

(28) Macheleidt, J.; Mattern, D. J.; Fischer, J.; Netzker, T.; Weber, J.; Schroeckh, V.; Valiante, V.; Brakhage, A. A. Regulation and Role of Fungal Secondary Metabolites. In *Annual Review of Genetics, Vol 50*, Bonini, N. M. Ed.; Annual Review of Genetics, Vol. 50; 2016; pp 371-392.

(29) Oakley, C. E.; Ahuja, M.; Sun, W. W.; Entwistle, R.; Akashi, T.; Yaegashi, J.; Guo, C. J.; Cerqueira, G. C.; Wortman, J. R.; Wang, C. C. C.; et al. Discovery of McrA, a master regulator of Aspergillus secondary metabolism. *Molecular Microbiology* **2017**, *103* (2), 347-365.

(30) Grau, M. F.; Entwistle, R.; Chiang, Y. M.; Ahuja, M.; Oakley, C. E.; Akashi, T.; Wang, C. C. C.; Todd, R. B.; Oaldey, B. R. Hybrid Transcription Factor Engineering Activates the Silent Secondary Metabolite Gene Cluster for (+)-Asperlin in Aspergillus nidulans. *Acs Chemical Biology* **2018**, *13* (11), 3193-3205.

(31) Caesar, L. K.; Kelleher, N. L.; Keller, N. P. In the fungus where it happens: History and future propelling Aspergillus nidulans as the archetype of natural products research. *Fungal Genetics and Biology* **2020**, *144*.

(32) O'Hanlon, K. A.; Gallagher, L.; Schrettl, M.; Jochl, C.; Kavanagh, K.; Larsen, T. O.; Doyle, S. Nonribosomal Peptide Synthetase Genes pesL and pes1 Are Essential for Fumigaclavine C Production in Aspergillus fumigatus. *Applied and Environmental Microbiology* **2012**, *78* (9), 3166-3176.

(33) Unsold, I. A.; Li, S. M. Reverse prenyltransferase in the biosynthesis of fumigaclavine C in Aspergillus fumigatus: Gene expression, purification, and characterization of fumigaclavine C synthase FGAPT1. *Chembiochem* **2006**, *7* (1), 158-164.

(34) Wiemann, P.; Lechner, B. E.; Baccile, J. A.; Velk, T. A.; Yin, W. B.; Bok, J. W.; Pakala, S.; Losada, L.; Nierman, W. C.; Schroeder, F. C.; et al. Perturbations in small molecule synthesis uncovers an iron-responsive secondary metabolite network in Aspergillus fumigatus. *Frontiers in Microbiology* **2014**, *5*.

(35) Ames, B. D.; Liu, X. Y.; Walsh, C. T. Enzymatic Processing of Fumiquinazoline F: A Tandem Oxidative-Acylation Strategy for the Generation of Multicyclic Scaffolds in Fungal Indole Alkaloid Biosynthesis. *Biochemistry* **2010**, *49* (39), 8564-8576.

(36) Ames, B. D.; Walsh, C. T. Anthranilate-Activating Modules from Fungal Nonribosomal Peptide Assembly Lines. *Biochemistry* **2010**, *49* (15), 3351-3365.

(37) Throckmorton, K.; Lim, F. Y.; Kontoyiannis, D. P.; Zheng, W. F.; Keller, N. P. Redundant synthesis of a conidial polyketide by two distinct secondary metabolite clusters in Aspergillus fumigatus. *Environmental Microbiology* **2016**, *18* (1), 246-259.

(38) Blachowicz, A.; Raffa, N.; Bok, J. W.; Choera, T.; Knox, B.; Lim, F. Y.; Huttenlocher, A.; Wang, C. C. C.; Venkateswaran, K.; Keller, N. P. Contributions of Spore Secondary Metabolites to UV-C Protection and Virulence Vary in Different Aspergillus fumigatus Strains. *Mbio* **2020**, *11* (1).

(39) Eamvijarn, A.; Gomes, N. M.; Dethoup, T.; Buaruang, J.; Manoch, L.; Silva, A.; Pedro, M.; Marini, I.; Roussis, V.; Kijjoa, A. Bioactive meroditerpenes and indole alkaloids from the soil fungus Neosartorya fischeri (KUFC 6344), and the marine-derived fungi Neosartorya laciniosa (KUFC 7896) and Neosartorya tsunodae (KUFC 9213). *Tetrahedron* **2013**, *69* (40), 8583-8591.

(40) Kaifuchi, S.; Mori, M.; Nonaka, K.; Masuma, R.; Omura, S.; Shiomi, K. Sartorypyrone D: a new NADH-fumarate reductase inhibitor produced by Neosartorya fischeri FO-5897. *Journal of Antibiotics* **2015**, *68* (6), 403-405.

(41) Chia, M.; Schwartz, T. J.; Shanks, B. H.; Dumesic, J. A. Triacetic acid lactone as a potential biorenewable platform chemical. *Green Chemistry* **2012**, *14* (7), 1850-1853.

(42) Inglis, D. O.; Binkley, J.; Skrzypek, M. S.; Arnaud, M. B.; Cerqueira, G. C.; Shah, P.; Wymore, F.; Wortman, J. R.; Sherlock, G. Comprehensive annotation of secondary metabolite biosynthetic genes and gene clusters of Aspergillus nidulans, A. fumigatus, A. niger and A. oryzae. *Bmc Microbiology* **2013**, *13*.

(43) Amos, B.; Aurrecoechea, C.; Barba, M.; Barreto, A.; Basenko, E. Y.; Bazant, W.; Belnap, R.; Blevins, A. S.; Bohme, U.; Brestelli, J.; et al. VEuPathDB: the eukaryotic pathogen, vector and host bioinformatics resource center. *Nucleic Acids Research* **2022**, *50* (D1), D898-D911.

(44) Wang, W. G.; Du, L. Q.; Sheng, S. L.; Li, A.; Li, Y. P.; Cheng, G. G.; Li, G. P.; Sun, G. L.; Hu, Q. F.; Matsuda, Y. Genome mining for fungal polyketide-diterpenoid hybrids: discovery of key terpene cyclases and multifunctional P450s for structural diversification. *Organic Chemistry Frontiers* **2019**, *6* (5), 571-578.

(45) Szewczyk, E.; Nayak, T.; Oakley, C. E.; Edgerton, H.; Xiong, Y.; Taheri-Talesh, N.; Osmani, S. A.; Oakley, B. R. Fusion PCR and gene targeting in Aspergillus nidulans. *Nature Protocols* **2006**, *1* (6), 3111-3120.

(46) Flipphi, M.; Mathieu, M.; Cirpus, I.; Panozzo, C.; Felenbok, B. Regulation of the aldehyde dehydrogenase gene (aldA) and its role in the control of the coinducer level necessary for induction

of the ethanol utilization pathway in Aspergillus nidulans. *Journal of Biological Chemistry* **2001**, *276* (10), 6950-6958.

(47) Waring, R. B.; May, G. S.; Morris, N. R. CHARACTERIZATION OF AN INDUCIBLE EXPRESSION SYSTEM IN ASPERGILLUS-NIDULANS USING ALCA AND TUBULIN CODING GENES. *Gene* **1989**, *79* (1), 119-130.

(48) Felenbok, B. THE ETHANOL UTILIZATION REGULON OF ASPERGILLUS-NIDULANS - THE ALCA-ALCR SYSTEM AS A TOOL FOR THE EXPRESSION OF RECOMBINANT PROTEINS. *Journal of Biotechnology* **1991**, *17* (1), 11-17.

(49) Yoshimi, A.; Sano, M.; Inaba, A.; Kokubun, Y.; Fujioka, T.; Mizutani, O.; Hagiwara, D.; Fujikawa, T.; Nishimura, M.; Yano, S.; et al. Functional Analysis of the alpha-1,3-Glucan Synthase Genes agsA and agsB in Aspergillus nidulans: AgsB Is the Major alpha-1,3-Glucan Synthase in This Fungus. *Plos One* **2013**, *8* (1).

(50) Keller, N.; Bok, J.; Chung, D.; Perrin, R. M.; Shwab, E. K. LaeA, a global regulator of Aspergillus toxins. *Medical Mycology* **2006**, *44*, S83-S85.

(51) Grau, M. F.; Entwistle, R.; Oakley, C. E.; Wang, C. C. C.; Oakley, B. R. Overexpression of an LaeA like Methyltransferase Upregulates Secondary Metabolite Production in Aspergillus nidulans. *Acs Chemical Biology* **2019**, *14* (7), 1643-1651.

(52) Punt, P. J.; Zegers, N. D.; Busscher, M.; Pouwels, P. H.; Vandenhondel, C. INTRACELLULAR AND EXTRACELLULAR PRODUCTION OF PROTEINS IN ASPERGILLUS UNDER THE CONTROL OF EXPRESSION SIGNALS OF THE HIGHLY EXPRESSED ASPERGILLUS NIDULANS GPDA GENE. *Journal of Biotechnology* **1991**, *17* (1), 19-33.

(53) Sanchez, J. F.; Entwistle, R.; Corcoran, D.; Oakley, B. R.; Wang, C. C. C. Identification and molecular genetic analysis of the cichorine gene cluster in Aspergillus nidulans. *Medchemcomm* **2012**, *3* (8), 997-1002.

(54) Bang, S.; Song, J. H.; Lee, D.; Lee, C.; Kim, S.; Kang, K. S.; Lee, J. H.; Shim, S. H. Neuroprotective Secondary Metabolite Produced by an Endophytic Fungus, Neosartorya fischeri JS0553, Isolated from Glehnia littoralis. *Journal of Agricultural and Food Chemistry* **2019**, *67* (7), 1831-1838.

(55) Kanokmedhakul, K.; Kanokmedhakul, S.; Suwannatrai, R.; Soytong, K.; Prabpai, S.; Kongsaeree, P. Bioactive meroterpenoids and alkaloids from the fungus Eurotium chevalieri. *Tetrahedron* **2011**, *67* (30), 5461-5468.

(56) Tang, M. C.; Lin, H. C.; Li, D. H.; Zou, Y.; Li, J.; Xu, W.; Cacho, R. A.; Hillenmeyer, M. E.; Garg, N. K.; Tang, Y. Discovery of Unclustered Fungal Indole Diterpene Biosynthetic Pathways through Combinatorial Pathway Reassembly in Engineered Yeast. *Journal of the American Chemical Society* **2015**, *137* (43), 13724-13727.

(57) Barra, L.; Abe, I. Chemistry of fungal meroterpenoid cyclases. *Natural Product Reports* **2021**, *38* (3), 566-585.

(58) Chiang, Y. M.; Oakley, C. E.; Ahuja, M.; Entwistle, R.; Schultz, A.; Chang, S. L.; Sung, C. T.; Wang, C. C. C.; Oakley, B. R. An Efficient System for Heterologous Expression of Secondary Metabolite Genes in Aspergillus nidulans. *Journal of the American Chemical Society* **2013**, *135* (20), 7720-7731.

(59) Eckermann, S.; Schroder, G.; Schmidt, J.; Strack, D.; Edrada, R. A.; Helariutta, Y.; Elomaa, P.; Kotilainen, M.; Kilpelainen, I.; Proksch, P.; et al. New pathway to polyketides in plants. *Nature* **1998**, *396* (6709), 387-390.

(60) Zhu, L. P.; Pietiainen, M.; Kontturi, J.; Turkkelin, A.; Elomaa, P.; Teeri, T. H. Polyketide reductases in defense-related parasorboside biosynthesis in Gerbera hybrida share processing strategies with microbial polyketide synthase systems. *New Phytologist* **2022**, *236* (1), 296-308.

(61) Li, Y.; Qian, S. A.; Dunn, R.; Cirino, P. C. Engineering Escherichia coli to increase triacetic acid lactone (TAL) production using an optimized TAL sensor-reporter system. *Journal of Industrial Microbiology & Biotechnology* **2018**, *45* (9), 789-793.

(62) Yu, J.; Landberg, J.; Shavarebi, F.; Bilanchone, V.; Okerlund, A.; Wanninayake, U.; Zhao, L.; Kraus,.; Sandmeyer, S. Bioengineering triacetic acid lactone production in Yarrowia lipolytica for pogostone synthesis. *Biotechnology and Bioengineering* **2018**, *115* (9), 2383-2388.

(63) Markham, K. A.; Palmer, C. M.; Chwatko, M.; Wagner, J. M.; Murray, C.; Vazquez, S.; Swaminathan, A.; Chakravarty, I.; Lynd, N. A.; Alper, H. S. Rewiring Yarrowia lipolytica toward triacetic acid lactone for materials generation. *Proceedings of the National Academy of Sciences of the United States of America* **2018**, *115* (9), 2096-2101.

(64) Cardenas, J.; Da Silva, N. A. Metabolic engineering of Saccharomyces cerevisiae for the production of triacetic acid lactone. *Metabolic Engineering* **2014**, *25*, 194-203.

(65) Tan, Z. G.; Clomburg, J. M.; Cheong, S.; Qian, S.; Gonzalez, R. A polyketoacyl-CoA thiolase dependent pathway for the synthesis of polyketide backbones. *Nature Catalysis* **2020**, *3* (7), 593.

*Appendix A*

*Supporting Information for Chapter 2: The CryoEM Method MicroED as a*

*Powerful Tool for Small Molecule Structure Determination*

## A1.   Materials and methods

All commercial samples were used as received with no additional crystallization or chemical modification. Ethisterone, cinchonine, carbamazepine, and biotin were purchased from Sigma-Aldrich. Brucine was purchased from the The Matheson Company, Inc. Progesterone was purchased from Preparations Laboratories Inc. Thiostrepton was purchased from EMD Millipore. CVS®-brand acetaminophen and Kroger® brand ibuprofen were used as over-the-counter medications. (+)-Limaspermadine and HKL-I-029 were synthesized according to previously reported literature procedures (*1*, *2*).

### A1.1 Sample Preparation

To prepare commercial compounds for MicroED, approximately 1 mg of product as received was placed between two microscope slides and ground to a fine powder. The ground powder was placed into an Eppendorf tube along with a pre-clipped Quantifoil R2/2 Cu300 or Quantifoil R1/4 Cu300 mesh grid. The TEM grid was then removed from the Eppendorf tube and gently tapped against a filter paper to remove excess powder. Non-commercial samples of HKL-I-029 and (+)-limaspermadine were concentrated under vacuum to yield a dry film and solid powder respectively. Sample grids of HKL-I-029 were prepared by adding a TEM grid directly to a 20 mL scintillation vial with gentle shaking. (+)-Limaspermadine grids were prepared by scraping the residue off the side of a 20 mL scintillation vial over a TEM grid. Once sample grids were prepared, they were subsequently plunged into liquid nitrogen, placed into the sample cartridge, and loaded into the microscope for analysis. Heterogenous sample mixtures were prepared by adding ~1 mg of biotin, carbamazepine, cinchonine, and brucine to a glass cover slide and grinding to a fine powder. The heterogenous powder was then added to an Eppendorf tube and the grid was prepared in the same manner as the homogeneous samples.

### 1.2 Instrument Parameters

All data were collected on a Thermo-Fischer Talos Artica electron cryomicroscope operating at an acceleration voltage of 200keV, corresponding to a wavelength of ~0.0251 Å. Screening of the TEM grids for micro crystals was done by operating the microscope in over focused diffraction mode to minimize diffraction and hysteresis between screening and diffraction operational modes.

## A1.3 Data Collection Procedure

MicroED data collection was collected in rolling shutter using a Thermo-Fischer CetaD CMOS 4k x 4k camera. Images were collected as a movie as the crystal was continuously rotated in the electron beam (*3*). Typical data collection was performed using a constant tilt rate of ~0.6 ° s$^{-1}$ d over an angular wedge of ~60° between the minimum and maximum tilt ranges of -72° to +72° degrees, respectively. During continuous rotation the camera integrated frames continuously at a rate of 1-3s per frame. The dose rate was calibrated to <0.03 e$^-$ Å$^{-2}$ s$^{-1}$. Crystals selected for data collection were isolated by a selected area aperture to reduce the background noise contributions, and calibrated to eucentric height to stay in the aperture over the entire tilt range.

Diffraction movies saved as SER files were converted to SMV format using in-house software developed for the CetaD and made freely available online (https://cryoem.ucla.edu/pages/MicroED). Frames were indexed and integrated in XDS, and multiple datasets were scaled and merged using XSCALE (*4*, *5*). The intensities were converted to SHELX format using XDSCONV(*5*). All structures except thiostrepton (see below) were solved by *ab initio* direct methods in SHELXT, and refined in SHELXL as previously described (*6*, *7*).

Four datasets from thiostrepton were indexed and integrated in MOSFLM through its graphical user interface, iMosflm (*8*, *9*). Data were merged in AIMLESS, and phased by molecular replacement in MOLREP using 1E9W as a search model (*10*, *11*). The solution was refined using REFMAC5 with electron scattering factors to a resolution of 1.9Å with the free *R* set copied from the initial search model (*12*).

## A.2 Compound Data and Statistics
Individual integration and refinement statistics can be found for each compound in SI Figures 1-11 along with corresponding densities.

| acetaminophen | |
| --- | --- |
| Stoichiometric formula | $C_8 N_1 O_2$ |
| Temperature (K) | 100 |
| Space group | $P\,2_1/n$ |
| Unit cell lengths a, b, c (Å) | 6.630(2), 8.620(2), 10.790(2) |
| angles α, β, γ (°) | 90.00(3), 97.56(3), 90.00(3) |
| Reflections (#) | 2300 (380) |
| Unique reflections (#) | 874 (141) |
| $R_{obs}$ | 18.3 (34.7) |
| $R_{meas}$ | 22.8 (43.2) |
| $CC_{1/2}$ | 95.2 (83.6) |
| Resolution (Å) | 0.8 |
| Completeness (%) | 69.9 (70.1) |
| Total exposure ($e^- Å^{-2}$) | ~3 |
| $R$ | 0.22 |
| $wR2$ | 0.4462 |
| $GooF$ | 2.003 |
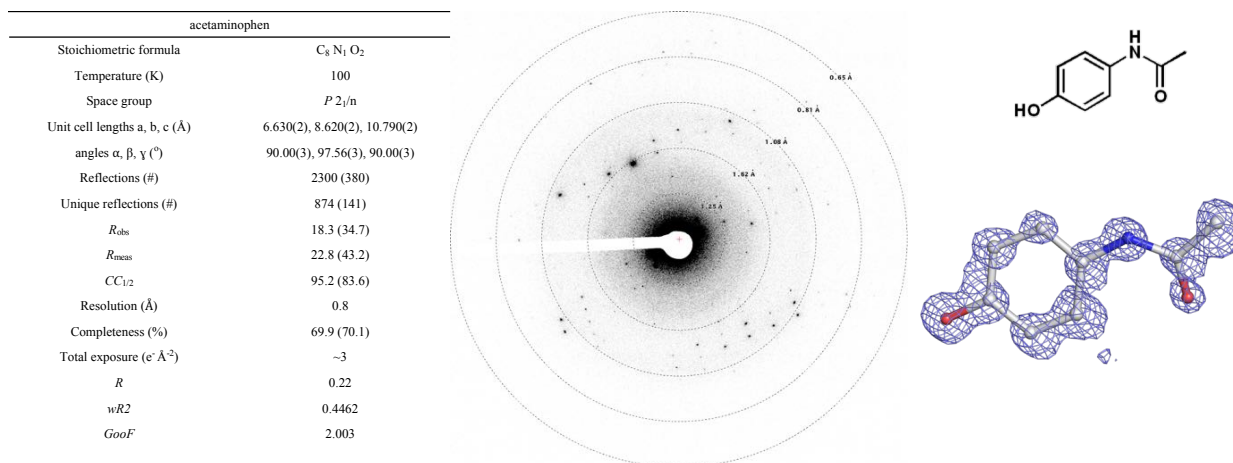
**Figure A.1.** Data processing statistics and final structure of acetaminophen.

| biotin | |
| --- | --- |
| Stoichiometric formula | $C_{10} N_2 O_3 S$ |
| Temperature (K) | 100 |
| Space group | $P\,2_1 2_1 2_1$ |
| Unit cell lengths a, b, c (Å) | 5.200(2), 10.310(2), 20.910(4) |
| angles α, β, γ (°) | 90.00(3), 90.00(3), 90.00(3) |
| Reflections (#) | 5498 (1081) |
| Unique reflections (#) | 1323 (246) |
| $R_{obs}$ | 20.3 (37.1) |
| $R_{meas}$ | 23.3 (42.1) |
| $CC_{1/2}$ | 95.5 (78.4) |
| Resolution (Å) | 0.9 |
| Completeness (%) | 82.6 (84.8) |
| Total exposure ($e^- Å^{-2}$) | ~3 |
| $R$ | 0.186 |
| $wR2$ | 0.3458 |
| $GooF$ | 1.818 |
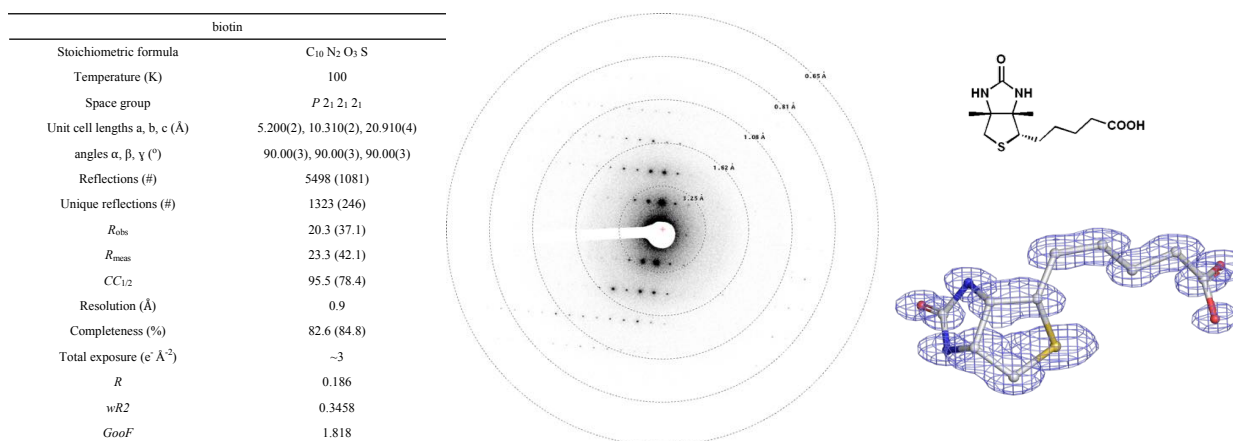
**Figure A.2.** Data processing statistics and final structure of biotin.

| brucine | |
| --- | --- |
| Stoichiometric formula | $C_{23} N_2 O_4$ |
| Temperature (K) | 100 |
| Space group | $P\,2_1$ |
| Unit cell lengths a, b, c (Å) | 15.340(3), 7.540(2), 20.010(4) |
| angles α, β, γ (°) | 90.00(3), 112.49(3), 90.00(3) |
| Reflections (#) | 12427 (814) |
| Unique reflections (#) | 5858 (416) |
| $R_{obs}$ | 18.2 (56.1) |
| $R_{meas}$ | 24.2 (74.9) |
| $CC_{1/2}$ | 95.1 (25.9) |
| Resolution (Å) | 0.9 |
| Completeness (%) | 95.3 (96.1) |
| Total exposure ($e^- Å^{-2}$) | ~3 |
| $R$ | 0.2244 |
| $wR2$ | 0.4468 |
| $GooF$ | 1.711 |
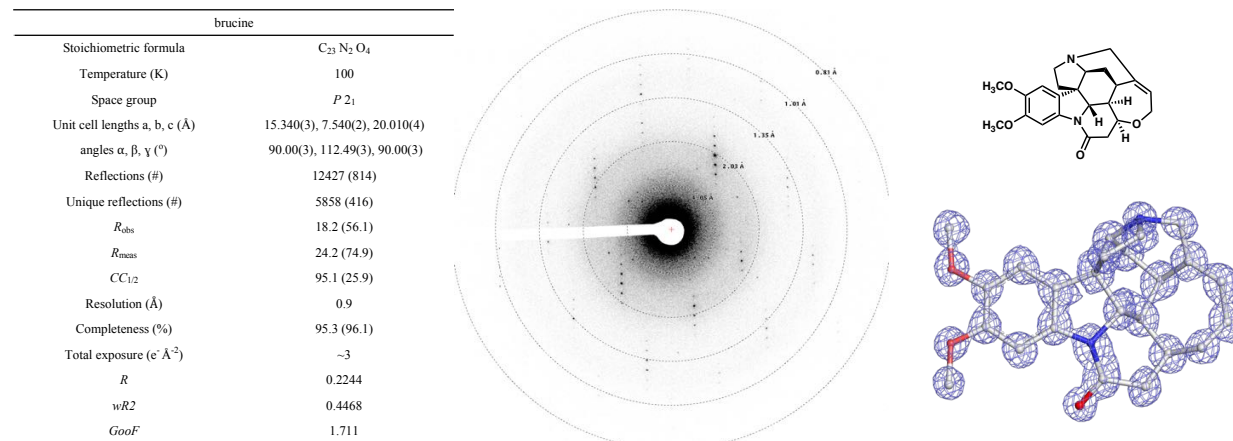
**Figure A.3.** Data processing statistics and final structure of brucine.

| carbamazepine | |
|---|---|
| Stoichiometric formula | $C_{15} N_2 O$ |
| Temperature (K) | 100 |
| Space group | $P 2_1/n$ |
| Unit cell lengths a, b, c (Å) | 7.460(2), 11.040(2), 13.760(3) |
| angles $\alpha$, $\beta$, $\gamma$ (°) | 90.00(3), 92.61(3), 90.00(3) |
| Reflections (#) | 4682 (678) |
| Unique reflections (#) | 1044 (146) |
| $R_{obs}$ | 17.3 (22.1) |
| $R_{meas}$ | 19.5 (24.7) |
| $CC_{1/2}$ | 97.3 (93.8) |
| Resolution (Å) | 1.0 |
| Completeness (%) | 88.3 (84.9) |
| Total exposure (e⁻ Å⁻²) | ~3 |
| $R$ | 0.1931 |
| $wR2$ | 0.3902 |
| $GooF$ | 2.398 |
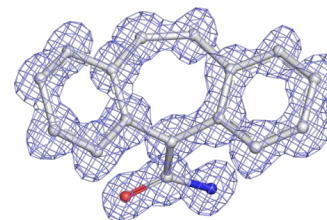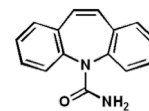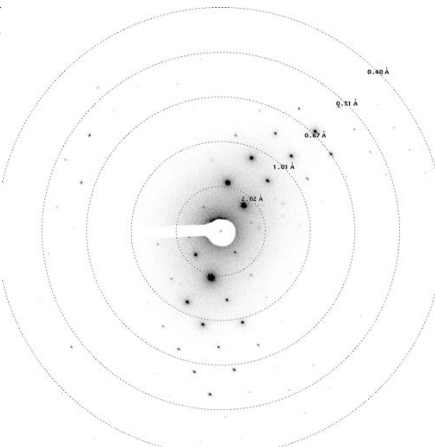
**Figure A.4.** Data processing statistics and final structure of carbamazepine.

| cinchonine | |
|---|---|
| Stoichiometric formula | $C_{19} N_2 O$ |
| Temperature (K) | 100 |
| Space group | $P 2_1/n$ |
| Unit cell lengths a, b, c (Å) | 10.710(2), 7.060(2), 11.150(2) |
| angles $\alpha$, $\beta$, $\gamma$ (°) | 90.00(3), 109.66(3), 90.00(3) |
| Reflections (#) | 1933 (399) |
| Unique reflections (#) | 1289 (262) |
| $R_{obs}$ | 11.0 (14.8) |
| $R_{meas}$ | 15.6 (21.0) |
| $CC_{1/2}$ | 95.0 (89.2) |
| Resolution (Å) | 1.0 |
| Completeness (%) | 77.4 (78.9) |
| Total exposure (e⁻ Å⁻²) | ~3 |
| $R$ | 0.1793 |
| $wR2$ | 0.3907 |
| $GooF$ | 1.831 |
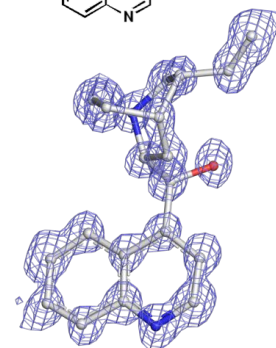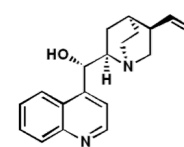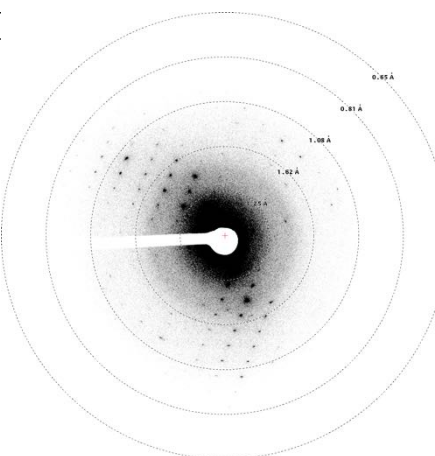
**Figure A.5.** Data processing statistics and final structure of cinchonine.

| ethisterone | |
|---|---|
| Stoichiometric formula | $C_{21} O_2$ |
| Temperature (K) | 100 |
| Space group | $P 2_1$ |
| Unit cell lengths a, b, c (Å) | 6.43(2), 21.17(4), 6.48(2) |
| angles $\alpha$, $\beta$, $\gamma$ (°) | 90.00(3), 105.6(3), 90.00(3) |
| Reflections (#) | 1811 (231) |
| Unique reflections (#) | 1506 (197) |
| $R_{obs}$ | 10.0 (25.4) |
| $R_{meas}$ | 14.1 (35.9) |
| $CC_{1/2}$ | 97.3 (56.1) |
| Resolution (Å) | 0.9 |
| Completeness (%) | 60.8 (54.6) |
| Total exposure (e⁻ Å⁻²) | ~3 |
| $R$ | 0.2481 |
| $wR2$ | 0.5109 |
| $GooF$ | 2.087 |
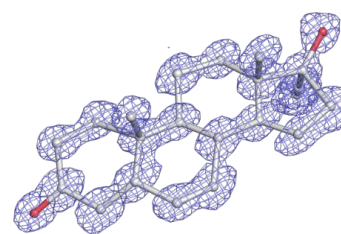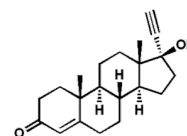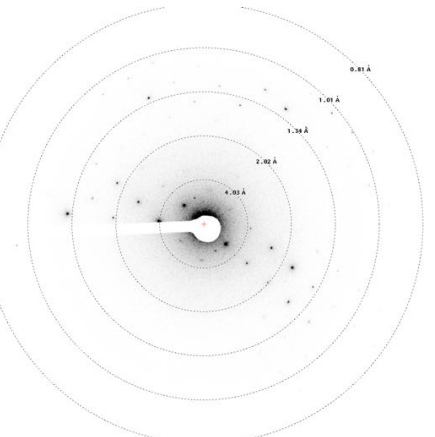
**Figure A.6.** Data processing statistics and final structure of ethisterone.

| HKL-I-029 | |
|---|---|
| Stoichiometric formula | $C_{21} N O_3$ |
| Temperature (K) | 100 |
| Space group | $P\,2_1/n$ |
| Unit cell lengths a, b, c (Å) | 8.280(2), 24.370(5), 8.810(2) |
| angles α, β, γ (°) | 90.00(3), 108.80(3), 90.00(3) |
| Reflections (#) | 3369 (446) |
| Unique reflections (#) | 1970 (262) |
| $R_{obs}$ | 14.1 (22.8) |
| $R_{meas}$ | 18.4 (29.5) |
| $CC_{1/2}$ | 94.5 (84.8) |
| Resolution (Å) | 1.0 |
| Completeness (%) | 55.3 (55.7)* |
| Total exposure (e⁻ Å⁻²) | ~3 |
| $R$ | 0.2366 |
| $wR2$ | 0.4762 |
| $GooF$ | 2.656 |
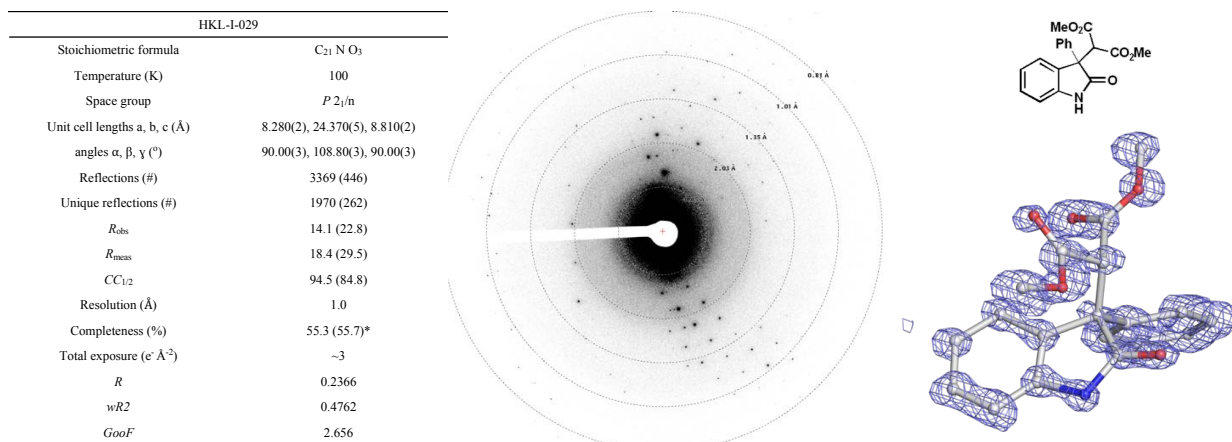


**Figure A.7.** Data processing statistics and final structure of HKL-I-029.
*The completeness of this compound was limited due to preferred orientation.

| ibuprofen | |
|---|---|
| Stoichiometric formula | $C_{13} O_2$ |
| Temperature (K) | 100 |
| Space group | $P\,2_1/c$ |
| Unit cell lengths a, b, c (Å) | 14.65(3), 7.88(2), 10.73(2) |
| angles α, β, γ (°) | 90.00(3), 99.7(3), 90.00(3) |
| Reflections (#) | 1452 (402) |
| Unique reflections (#) | 506 (138) |
| $R_{obs}$ | 14.7 (20.8) |
| $R_{meas}$ | 17.8 (25.2) |
| $CC_{1/2}$ | 97.8 (89.9) |
| Resolution (Å) | 1.1 |
| Completeness (%) | 54.3 (53.1)* |
| Total exposure (e⁻ Å⁻²) | ~3 |
| $R$ | 0.2559 |
| $wR2$ | 0.5282 |
| $GooF$ | 2.686 |
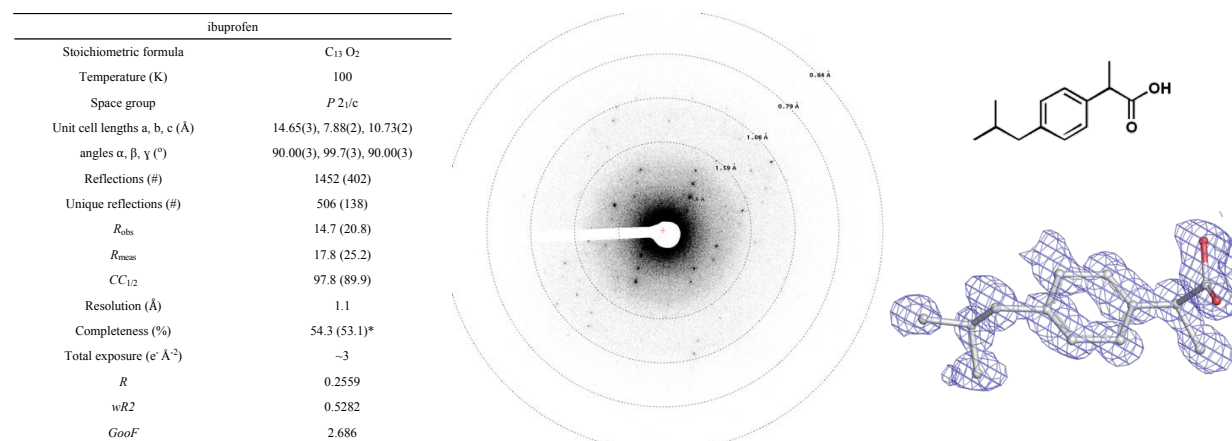


**Figure A.8.** Data processing statistics and final structure of ibuprofen.
*The completeness of this compound was limited due to preferred orientation.

| (+)-limaspermidine | |
|---|---|
| Stoichiometric formula | $C_{19} N_2 O$ |
| Temperature (K) | 100 |
| Space group | $P\,2_1 2_1 2_1$ |
| Unit cell lengths a, b, c (Å) | 7.620(2), 13.880(3), 15.200(3) |
| angles α, β, γ (°) | 90.00(3), 90.00(3), 90.00(3) |
| Reflections (#) | 8252 (387) |
| Unique reflections (#) | 3430 (185) |
| $R_{obs}$ | 16.7 (68.2) |
| $R_{meas}$ | 21.6 (88.6) |
| $CC_{1/2}$ | 97.0 (34.2) |
| Resolution (Å) | 0.77 |
| Completeness (%) | 93.0 (69.3) |
| Total exposure (e⁻ Å⁻²) | ~3 |
| $R$ | 0.2422 |
| $wR2$ | 0.4309 |
| $GooF$ | 1.541 |
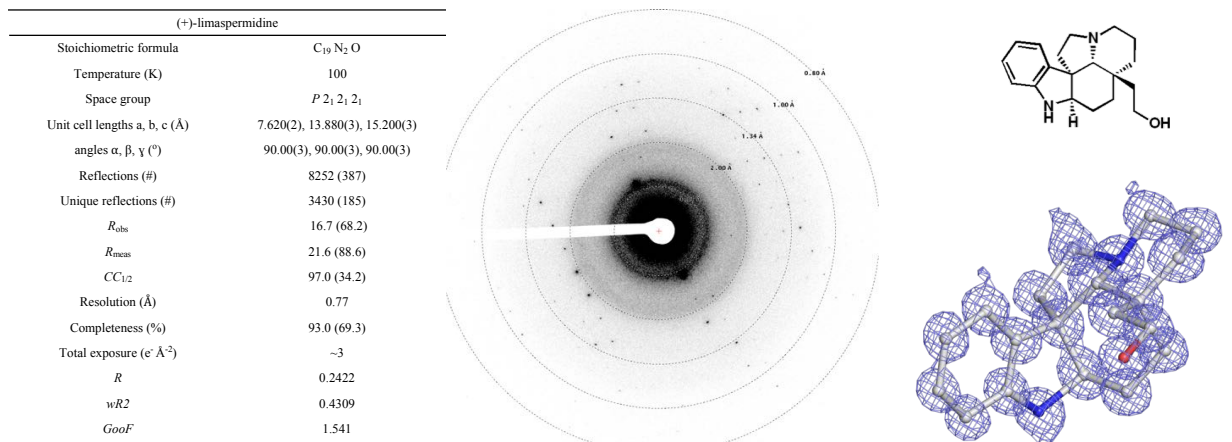


**Figure A.9.** Data processing statistics and final structure of (+)-limaspermidine.

| progesterone | |
|---|---|
| Stoichiometric formula | $C_{21} O_2$ |
| Temperature (K) | 100 |
| Space group | $P\,2_1 2_1 2_1$ |
| Unit cell lengths a, b, c (Å) | 10.380(2), 12.810(3), 13.890(3) |
| angles α, β, γ (°) | 90.00(3), 90.00(3), 90.00(3) |
| Reflections (#) | 4487(577) |
| Unique reflections (#) | 1871 (238) |
| $R_{obs}$ | 14.7 (44.6) |
| $R_{meas}$ | 18.0 (53.9) |
| $CC_{1/2}$ | 98.0 (66.1) |
| Resolution (Å) | 0.9 |
| Completeness (%) | 72.1 (68.6) |
| Total exposure (e⁻ Å⁻²) | ~3 |
| $R$ | 0.2045 |
| $wR2$ | 0.4155 |
| $GooF$ | 1.888 |
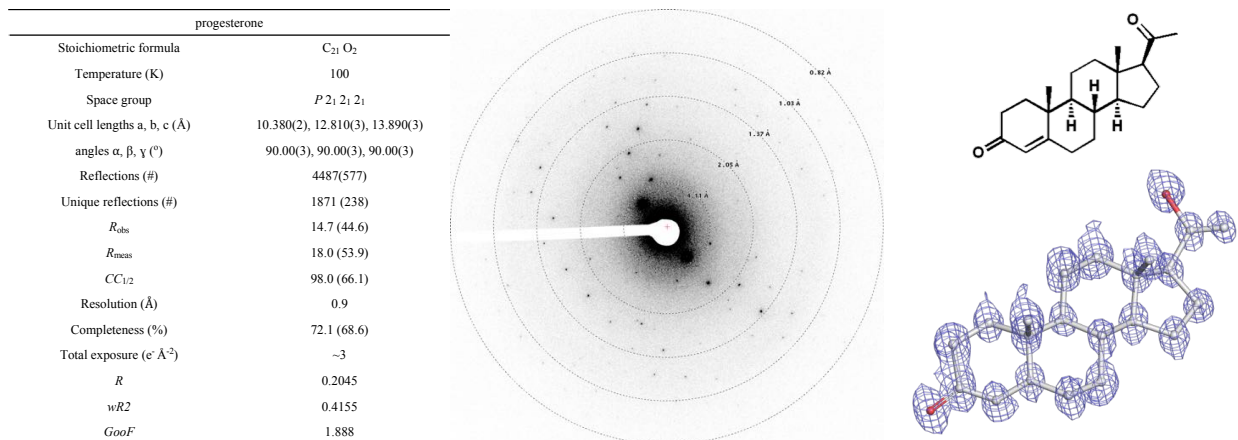
**Figure A.10.** Data processing statistics and final structure of progesterone.

| thiostrepton | |
|---|---|
| Resolution range (Å) | 18.99–1.91 (2.13–1.91) |
| Space group | $P\,4_3 2_1 2$ |
| Unit cell lengths a, b, c (Å) | 26.219, 26.219, 27.534 |
| angles α, β, γ (°) | 90, 90, 90 |
| Total reflections | 5578 (458) |
| Unique reflections | 686 (93) |
| Multiplicity | 8.1 (4.9) |
| Completeness (%) | 78.6 (40.3) |
| Mean $I/\sigma(I)$ | 5.1 (3.4) |
| Wilson $B$-factor | 2.6 |
| $R_{merge}$ | 0.236 (0.320) |
| $R_{meas}$ | 0.251 (0.353) |
| $CC_{1/2}$ | 0.985 (0.813) |
| Reflections used in refinement | 620 (92) |
| $R_{work}$ | 0.1818 (0.2191) |
| $R_{free}$ | 0.2396 (0.1766) |

**Figure A.11.** Data processing statistics and final structure of thiostrepton.

## References

1. Y. Liu, S.-J. Han, W.-B. Liu, B. M. Stoltz, Catalytic Enantioselective Construction of Quaternary Stereocenters: Assembly of Key Building Blocks for the Synthesis of Biologically Active Molecules. *Acc. Chem. Res.* **48**, 740–751 (2015).

2. B. P. Pritchett, E. J. Donckele, B. M. Stoltz, Enantioselective Catalysis Coupled with Stereodivergent Cyclization Strategies Enables Rapid Syntheses of (+)-Limaspermidine and (+)-Kopsihainanine A. *Angew. Chemie Int. Ed.* **56**, 12624–12627 (2017).

3. B. L. Nannenga, D. Shi, A. G. W. Leslie, T. Gonen, High-resolution structure determination by continuous-rotation data collection in MicroED. *Nat. Methods.* **11**, 927–930 (2014).

4. W. Kabsch, Xds. *Acta Crystallogr. Sect. D Biol. Crystallogr.* **66**, 125–132 (2010).

5. W. Kabsch, Integration, scaling, space-group assignment and post-refinement. *Acta Crystallogr. Sect. D Biol. Crystallogr.* **66**, 133–144 (2010).

6. G. M. Sheldrick, SHELXT - Integrated space-group and crystal-structure determination.

*Acta Crystallogr. Sect. A Found. Crystallogr.* **71**, 3–8 (2015).

7. G. M. Sheldrick, Crystal structure refinement with SHELXL. *Acta Crystallogr. Sect. C Struct. Chem.* **71**, 3–8 (2015).

8. A. G. W. Leslie, H. R. Powell, (2007; http://link.springer.com/10.1007/978-1-4020-6316-9_4), pp. 41–51.

9. T. G. G. Battye, L. Kontogiannis, O. Johnson, H. R. Powell, A. G. W. Leslie, iMOSFLM: A new graphical interface for diffraction-image processing with MOSFLM. *Acta Crystallogr. Sect. D Biol. Crystallogr.* **67**, 271–281 (2011).

10. P. R. Evans, G. N. Murshudov, How good are my data and what is the resolution? *Acta Crystallogr. Sect. D Biol. Crystallogr.* **69**, 1204–1214 (2013).

11. A. Vagin, A. Teplyakov, MOLREP : an Automated Program for Molecular Replacement. *J. Appl. Crystallogr.* **30**, 1022–1025 (1997).

12. G. N. Murshudov *et al.*, REFMAC 5 for the refinement of macromolecular crystal structures. *Acta Crystallogr. Sect. D Biol. Crystallogr.* **67**, 355–367 (2011).

*Appendix B*

*Supporting Information for Chapter 3: Characterization of Reactive*

*Organometallic Species via MicroED*

## B1. Materials and Methods

### B1.1 General Considerations

Grubbs Catalyst® 1st Generation and Schwartz's reagent were purchased from Sigma-Aldrich. Carbonyl(hydrido)tris(triphenylphosphane)rhodium(I) was purchased from Strem Chemicals. All commercial samples were used as received from the supplier. Pd(dba)(PHOX), Fe(acac)$_3$, and Ni(dppf)Cl$_2$ were prepared according to the reported literature procedures (1–3). Synthetic samples were precipitated from solution and used as prepared with no formal recrystallization. Unless otherwise stated, all manipulations were carried out using standard Schlenk or glovebox techniques (O$_2$, H$_2$O < 1ppm) under a dinitrogen or argon atmosphere. Solvents were dried on K or CaH$_2$ and distilled under argon before use. ($\kappa^2$-P,Cl-PPh$_2$CB$_9$Cl$_9$)PdMe(THF) was prepared according to the literature procedure (4). Solution state NMR spectra were recorded at room temperature on Bruker Avance 300MHz, Bruker Avance 400MHz, or Bruker Avance 600MHz spectrometers. NMR chemical shifts are reported in parts per million (ppm). $^1$H NMR and $^{13}$C NMR chemical shifts were referenced to residual protio solvent. $^{11}$B NMR chemical shifts were externally referenced to BF$_3$OEt$_2$. $^{31}$P NMR chemical shifts were externally referenced to 80% H$_3$PO$_4$ in H$_2$O. The $^{13}$C{$^1$H} Cross Polarization Magic Angle Spinning (CPMAS) NMR spectrum of compound **3** was acquired on a Bruker NEO600 operating at an $^1$H frequency of 600 MHz. The analyte was packed in a 4 mm zirconia rotor packed in an Argon filled glovebox. The spinning speed was 10 kHz at the magic angle, and contact time was 2 ms for both $^{13}$C{$^1$H} and $^{31}$P{$^1$H} CPMAS NMR spectra. $^{13}$C{$^1$H} spectra were referenced to external adamantane, $^{31}$P{$^1$H} spectra were referenced to external H$_3$PO$_4$, and $^{11}$B{$^1$H} spectra were referenced to NaBH$_4$. FT-IR spectra were recorded as pressed pellets using a Bruker Alpha IR spectrometer in an argon-filled glovebox.

### B1.2 Safety Statement

No unexpected or unusually high safety hazards were encountered.

### B1.3 Sample Preparation

Samples were prepped using Quantifoil R1/2 Cu200 mesh grids. For preparation of Fe(acac)$_3$ **4**, Ni(dppf)Cl$_2$ **6**, and Pd(dba)(PHOX) **7** samples, grids were placed in a dram vial with ~1 mg of compound and shaken lightly. The samples were tapped against the surface of a filter paper to remove residual compound and the TEM grid was subsequently transferred to a clean vial. Schwartz's reagent **1**, compound **3**, Grubbs Catalyst **5** and Carbonyl(hydrido)tris (triphenylphosphane)rhodium(I) **8** samples were prepared in a similar fashion within a glove box under N$_2$ as received from the supplier. All samples were transferred from sealed vials to the sample holder under ambient conditions with no additional experimental setup.

### B1.4 Instrument Parameters

All data was collected on a FEI Tecnai TF-30 electron microscope operating at ambient temperature with an operating voltage of 300 keV, corresponding to a wavelength of ~0.0196 Å

using a single-tilt sample holder. TEM grids were screened by operating the microscope in over focused diffraction mode.

## B1.5 Data Collection Procedure

Diffraction data was collected using rolling shutter mode with a TVIPS TemCam-XF416 CMOS 4k x 4k camera. Images were collected as movies by continuous rotation of crystals under a parallel electron beam using a constant tilt rate of ~0.3 deg s$^{-1}$ over an angular wedge of ~50° between the minimum and maximum tilt ranges of –72° to +72° respectively (5). During data collection, the camera integrated continuously at a rate of 3 s per frame. Crystals were isolated using a selected area aperture to reduce background noise and calibrated to eucentric height to remain within the aperture during continuous rotation over the tilt range.

Diffraction movies were saved as TVIPS files and were converted to SMV format using open source software freely available online (https://cryoem.ucla.edu/pages/MicroED). Frames were indexed and integrated in XDS and multiple datasets were scaled and merged using XSCALE (6, 7). Intensities were converted to SHELX format using XDSCONV (7).

## B2. Diffraction Data and Statistics

Electron diffraction data of compounds **1**, **3-8** were collected and treated in the above manner. All structures were solved *ab initio* using direct methods in SHELXT and refined with SHELXL using ShelXle (8, 9,10). All non-hydrogen atoms were refined anisotropically and all hydrogen atoms, aside from the metal hydrides in compound **1** and **8**, were refined using the riding model. X-ray diffraction data for **2** was collected on a Bruker-AXS Apex II diffractometer with an Apex II CCD detector using Mo $K_a$ radiation ($\lambda = 0.71073$ Å) from a fine-focus sealed tube source. Data were collected at 100 K by performing 0.5° $\omega$-scans, integrated using SAINT (11), and absorption corrected using SADABS (12). The structure was solved by direct methods using SHELXT (8) and refined against $F^2$ on all data by full-matrix least squares with SHELXL-2018/3 (9) following established refinement strategies (13). All non-hydrogen atoms were refined anisotropically. All hydrogen atoms were included into the model at geometrically calculated positions and refined using a riding model. The isotropic displacement parameters of all hydrogen atoms were fixed to 1.2 times the $U$ value of the atoms they are linked to (1.5 times for methyl groups). Crystal and data quality details, as well as a summary of the residual refinement values, are listed in the accompanying table.

Compound **2** crystallizes in the monoclinic centrosymmetric space group *P2₁/c* with one molecule of **2**, two molecules of tetrahydrofuran, and one molecule that was a mixture of pentane and tetrahydrofuran per asymmetric unit. The ratio of pentane: tetrahydrofuran was refined freely and converged at 51:49. The solvent molecules were refined with the help of similarity restraints on 1,2- and 1,3- distances as well as similarity and rigid-bond restraints for anisotropic displacement parameters. The mixture of solvents results in an empirical formula with non-integer numbers of atoms for C, H, and O.

Table S1. Crystal data and structure refinement for Compound **2**.

| Identification code | vl334jk |

| | |
|---|---|
| Empirical formula | C38.51 H46.04 B18 Cl18 O2.49 P2 Pd2 |
| Formula weight | 1656.17 |
| Temperature | 100(2) K |
| Wavelength | 0.71073 Å |
| Crystal system | Monoclinic |
| Space group | $P2_1/c$ |
| Unit cell dimensions | a = 15.4952(4) Å $\quad\quad$ α = 90°. |
| | b = 15.2588(4) Å $\quad\quad$ β = 91.4479(12)°. |
| | c = 27.3371(7) Å $\quad\quad$ γ = 90°. |
| Volume | 6461.5(3) Å$^3$ |
| Z | 4 |
| Density (calculated) | 1.702 Mg/m$^3$ |
| Absorption coefficient | 1.388 mm$^{-1}$ |
| F(000) | 3260 |
| Crystal color | red |
| Crystal size | 0.346 x 0.185 x 0.174 mm$^3$ |
| Theta range for data collection | 1.873 to 30.999° |
| Index ranges | -22 <= h <= 22, -22 <= k <= 21, -39 <= l <= 39 |
| Reflections collected | 148833 |
| Independent reflections | 20596 [R(int) = 0.0457] |
| Completeness to theta = 25.242° | 100.0 % |
| Absorption correction | Semi-empirical from equivalents |
| Refinement method | Full-matrix least-squares on F$^2$ |
| Data / restraints / parameters | 20596 / 130 / 776 |
| Goodness-of-fit on F$^2$ | 1.029 |
| Final R indices [I>2sigma(I) = 16909 data] | R1 = 0.0313, wR2 = 0.0644 |
| R indices (all data, ? Å) | R1 = 0.0438, wR2 = 0.0702 |
| Extinction coefficient | n/a |
| Largest diff. peak and hole | 0.732 and -0.676 e.Å$^{-3}$ |

Crystallographic information files (CIF) for compounds **1**–**8** have been deposited at the Cambridge Crystallographic Data Center and are available free of charge under reference numbers 1908168-1908175 at:
http://www.ccdc.cam.ac.uk/Community/Requestastructure/Pages/DataRequest.aspx.

| Schwartz's Reagent | |
|---|---|
| Stoichiometric Formula | $C_{24}H_{34}Cl_2Zr_2$ |
| Temperature (K) | ~293 |
| Space Group | Pnnm |
| Unit cell lengths a, b, c (Å) | a = 7.21 Å, b = 9.20 Å, c = 13.84 Å |
| angles α, β, γ | α = 90.000°, β = 90.000°, γ = 90.000° |
| Reflections (#) | 2139 |
| Unique reflections (#) | 307 |
| Robs | 17.8% |
| Rmeas | 19.5% |
| CC1/2 | 97.8 |
| Resolution (Å) | 1.15 |
| Completeness (%) | 90.6% |
| Total exposure (e Å-2 ) | ~3 |
| R | 0.1495 |
| wR2 | 0.3785 |
| GooF | 2.254 |
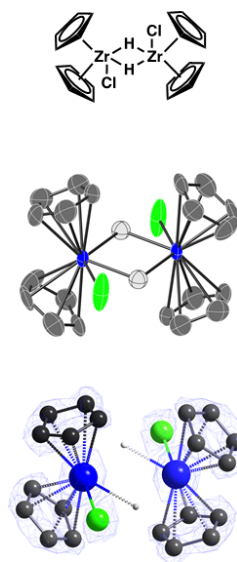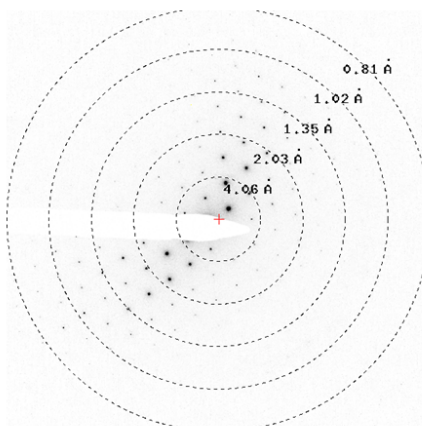
**Figure B.1.** Data, statistics, sample diffraction pattern and structures for compound **1**

**Figure B.2.** Data, statistics, sample diffraction pattern and structures for compound **3**



| Compound 3 | |
|---|---|
| Stoichiometric Formula | $C_{36}H_{40}B_{18}O_2P_2Cl_{18}Pd_2$ |
| Temperature (K) | ~293 |
| Space Group | P-1 |
| Unit cell lengths a, b, c (Å) | 13.050 12.040 13.060 |
| angles α, β, γ | 107.566 91.152 123.194 |
| Reflections (#) | 23883 |
| Unique reflections (#) | 3713 |
| Robs | 22.5% |
| Rmeas | 23.8% |
| CC1/2 | 98.0 |
| Resolution (Å) | 0.90 |
| Completeness (%) | 80.5% |
| Total exposure (e Å-2 ) | ~3 |
| R | 0.1808 |
| wR2 | 0.4000 |
| GooF | 1.803 |

| Fe(acac)$_3$ | |
|---|---|
| Stoichiometric Formula | C$_{15}$H$_{24}$FeO$_6$ |
| Temperature (K) | ~293 |
| Space Group | Pbca |
| Unit cell lengths a, b, c (Å) | 15.5200 13.4100 16.4900 |
| angles α, β, γ | 90.000 90.000 90.000 |
| Reflections (#) | 14159 |
| Unique reflections (#) | 2269 |
| Robs | 16.40% |
| Rmeas | 17.90% |
| CC1/2 | 99 |
| Resolution (Å) | 0.9 |
| Completeness (%) | 92.10% |
| Total exposure (e Å-2 ) | ~3 |
| R | 0.1607 |
| wR2 | 0.3941 |
| GooF | 1.826 |
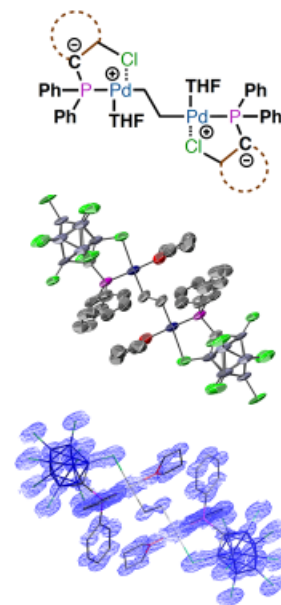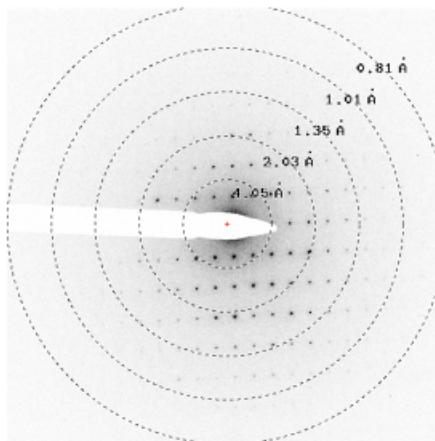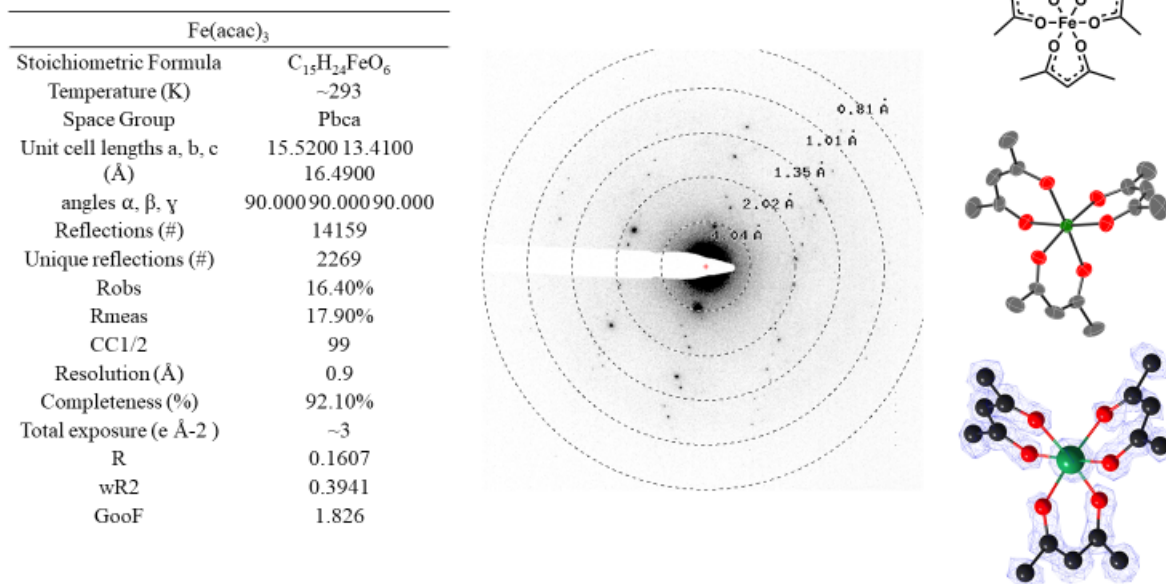


**Figure B.3.** Data, statistics, sample diffraction pattern and structures for compound **4**

| Grubbs Catalyst 1$^{st}$ Generation | |
|---|---|
| Stoichiometric Formula | C$_{43}$H$_{72}$Cl$_2$P$_2$Ru |
| Temperature (K) | ~293 |
| Space Group | P2(1)/n |
| Unit cell lengths a, b, c (Å) | 9.9700 26.0500 16.3400 |
| angles α, β, γ | 90.000 94.185 90.000 |
| Reflections (#) | 31201 |
| Unique reflections (#) | 6768 |
| Robs | 17.4% |
| Rmeas | 19.6% |
| CC1/2 | 98.5 |
| Resolution (Å) | 0.85 |
| Completeness (%) | 99.3% |
| Total exposure (e Å-2 ) | ~3 |
| R | 0.1595 |
| wR2 | 0.3997 |
| GooF | 1.802 |
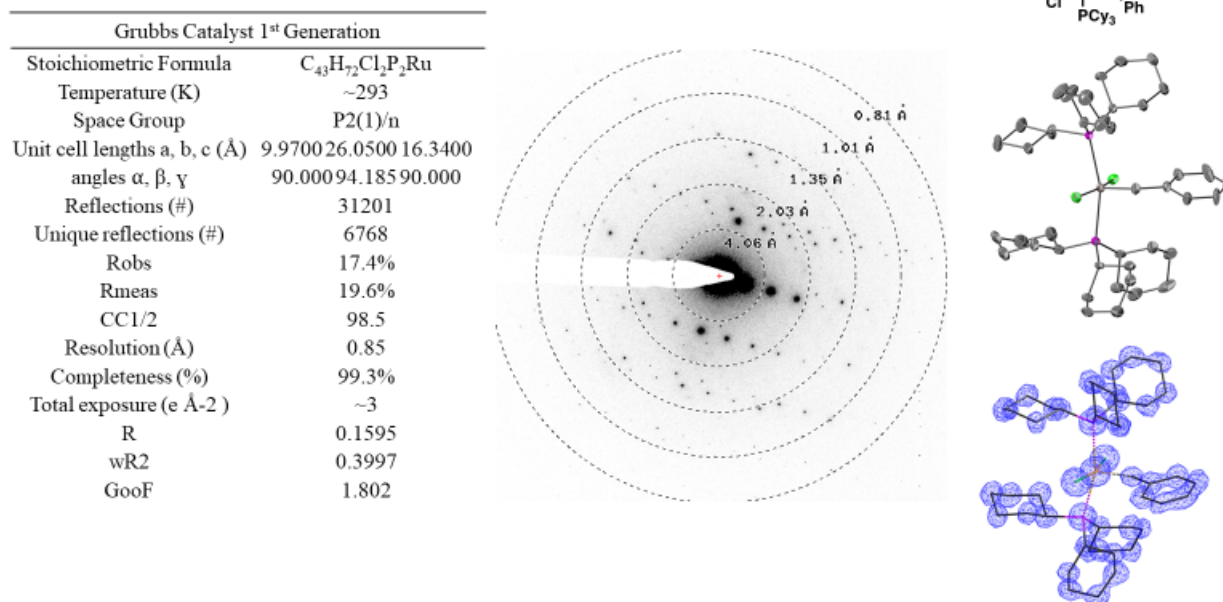


**Figure B.4.** Data, statistics, sample diffraction pattern and structures for compound **5**

**Figure B.5.** Data, statistics, sample diffraction pattern and structures for compound **6**

| Ni(dppf)Cl$_2$ | |
|---|---|
| Stoichiometric Formula | C$_{34}$H$_{28}$Cl$_2$FeNiP$_2$ |
| Temperature (K) | ~293 |
| Space Group | Pna2(1) |
| Unit cell lengths a, b, c (Å) | 19.7600 10.1000 14.5800 |
| angles α, β, γ | 90.000 90.000 90.000 |
| Reflections (#) | 18929 |
| Unique reflections (#) | 1379 |
| Robs | 21.2% |
| Rmeas | 22.1% |
| CC1/2 | 98.5 |
| Resolution (Å) | 1.00 |
| Completeness (%) | 86.3% |
| Total exposure (e Å-2 ) | ~3 |
| R | 0.1126 |
| wR2 | 0.2739 |
| GooF | 1.468 |



| Pd(dba)(PHOX) | |
|---|---|
| Stoichiometric Formula | C$_{43}$H$_{43}$NO$_2$PPd |
| Temperature (K) | ~293 |
| Space Group | P2(1)2(1)2(1) |
| Unit cell lengths a, b, c (Å) | 10.2800 14.2700 26.5500 |
| angles α, β, γ | 90.000 90.000 90.000 |
| Reflections (#) | 12385 |
| Unique reflections (#) | 2102 |
| Robs | 26.0% |
| Rmeas | 28.8% |
| CC1/2 | 93.5 |
| Resolution (Å) | 1.00 |
| Completeness (%) | 99.1% |
| Total exposure (e Å-2 ) | ~3 |
| R | 0.1432 |
| wR2 | 0.3504 |
| GooF | 1.249 |



**Figure B.6.** Data, statistics, sample diffraction pattern and structures for compound **7**

| HRh(CO)(PPh₃)₃ | |
|---|---|
| Stoichiometric Formula | C₅₅H₄₆OP₃Rh |
| Temperature (K) | ~293 |
| Space Group | P2(1)/n |
| Unit cell lengths a, b, c (Å) | 10.0100 31.7800 13.3400 |
| angles α, β, γ | 90.000 90.155 90.000 |
| Reflections (#) | 19748 |
| Unique reflections (#) | 3400 |
| Robs | 19.40% |
| Rmeas | 21.30% |
| CC1/2 | 98.5 |
| Resolution (Å) | 1 |
| Completeness (%) | 76.70% |
| Total exposure (e Å-2 ) | ~3 |
| R | 0.1324 |
| wR2 | 0.3401 |
| GooF | 1.665 |
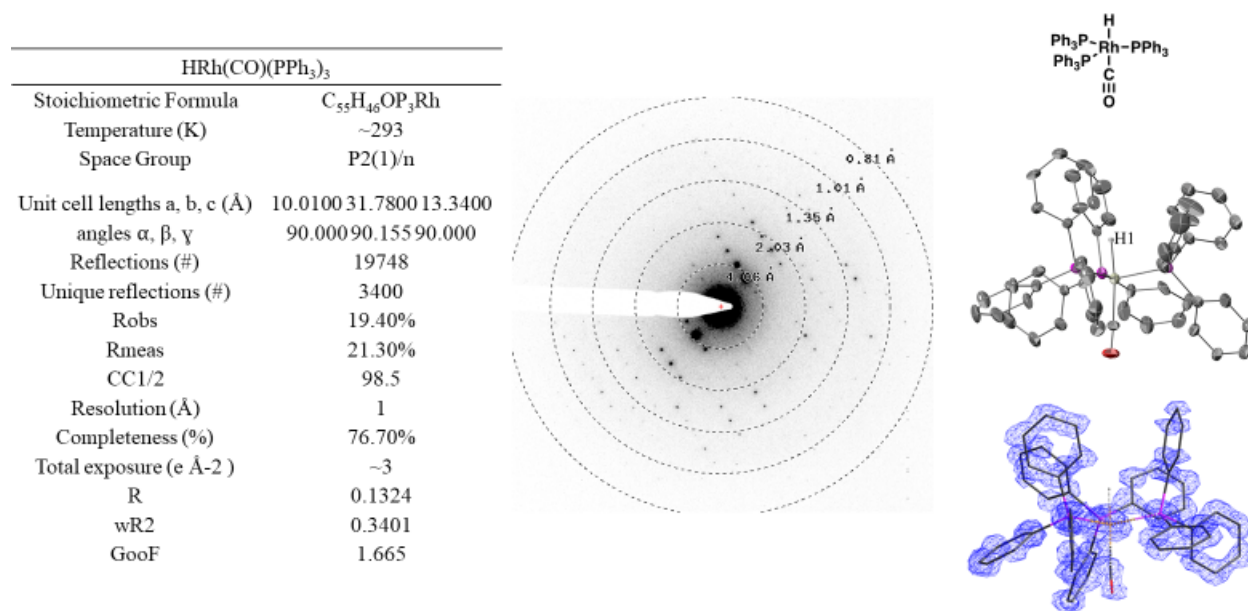


**Figure B.7.** Data, statistics, sample diffraction pattern and structures for compound **8**
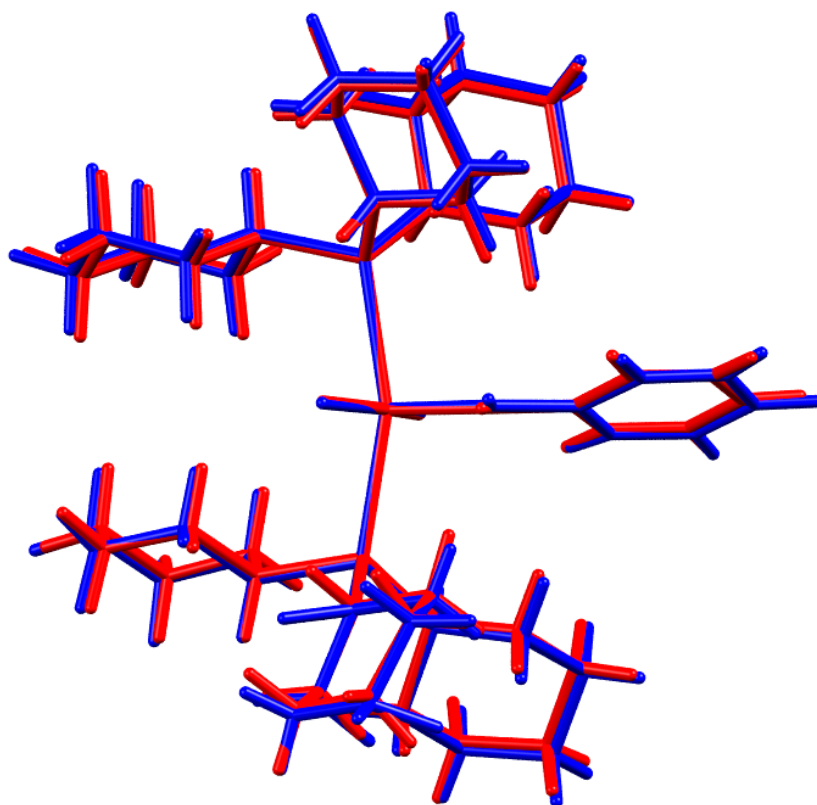
**Figure B.8. Overlay of electron diffraction structure obtained from Grubb's Catalyst (red) with previously reported X-ray structure (blue) (14). Root mean square (RMS) = 0.1311 Å, Max. Deviation = 0.2270 Å.**

**B3. Screened Coulombic potential computational analysis and isolation of hydrides**

The ShelXle-refined structure was loaded into MATLAB using the `tom_mrcread` function from the Max Planck Institute of Biochemistry's tomography toolbox (15). Since `tom_mrcread` does not accommodate .res files, the `shelx2map` conversion tool was used to generate .map files directly from the ShelXle output (http://shelx.uni-ac.gwdg.de/~tg/research/programs/conv/shelx2map/). This gave two daughter files, a difference Fourier map of the asymmetric unit and a standard map. Both of these .map files could be loaded without modification into MATLAB using `tom_mrcread`. The output from `tom_mrcread` was stored in a temporary variable which materialized as a 40x20x24 single. These arbitrary dimensional values scale to the corresponding unit cell vectors (i.e., $a$ = 7.21, $b$ = 9.20, $c$ = 13.84). To facilitate further manipulation, each of these dimensions was multiplied by a factor of 4; the variable was thus resized into a 160x80x96 double `vol` using the `imresize` command. To take consecutive real-space slices of screened Coulombic potential along the $a$-axis, a loop of this general template was employed:

```
for x=2:159
imagesc(squeeze(sum(vol(x-1:x+1,:,:),1))), axis image tight manual, colormap jet;
```

```
set(gca, 'YTickLabel',(10:10:80)./80);
set(gca, 'XTickLabel',(10:10:90)./96);
pause();
end
```

These lines of code generate screened Coulombic potential maps along the *a*-Axis like that found in Figure B.9.
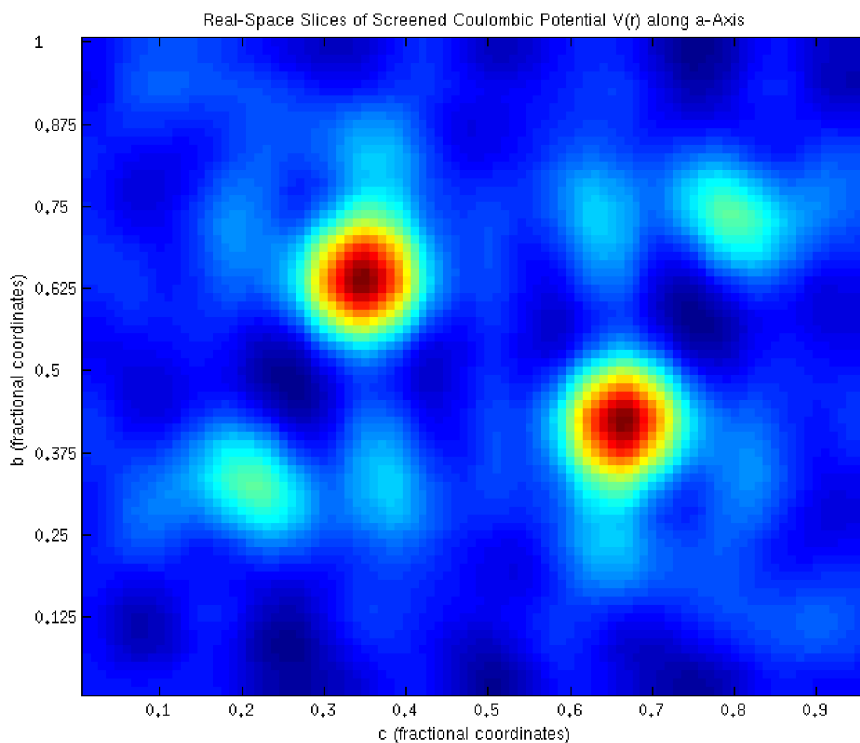


**Figure B.9**. Diagnostic frame showing clear screened Coulombic potential for the two hydrides, which materialize at (0.378, 0.291) and (0.622, 0.709). These values correspond precisely to the fractional coordinates predicted by the .cif file generated from ShelXle.

To confirm the presence of the hydrides, the diagnostic areas of Yukawa potential were cross-referenced to the fractional coordinates of the .cif file generated from ShelXle (Figure S9).

| | Number ⌄ | Label | Charge | SybylType | Xfrac + ESD | Yfrac + ESD | Zfrac + ESD | Symm. op. | Xorth | Yorth | Zor |
|---|---|---|---|---|---|---|---|---|---|---|---|
| 1 | 1 | ZR01 | 0 | Zr | 0.601955 | 0.331931 | 0.5 | x,y,z | 4.340 | 3.054 | 6.920 |
| 2 | 2 | u7H1 | 0 | U | 0.290731 | 0.378099 | 0.5 | x,y,z | 2.096 | 3.479 | 6.920 |
| 3 | 3 | CL02 | 0 | Cl | 0.299978 | 0.186119 | 0.5 | x,y,z | 2.163 | 1.712 | 6.920 |
| 4 | 4 | C003 | 0 | C.3 | 0.586721 | 0.332806 | 0.317518 | x,y,z | 4.230 | 3.062 | 4.394 |
| 5 | 5 | H003 | 0 | H | 0.486643 | 0.377957 | 0.287578 | x,y,z | 3.509 | 3.477 | 3.980 |
| 6 | 6 | C004 | 0 | C.3 | 0.755061 | 0.398773 | 0.340803 | x,y,z | 5.444 | 3.669 | 4.717 |
| 7 | 7 | H004 | 0 | H | 0.786538 | 0.494611 | 0.327099 | x,y,z | 5.671 | 4.550 | 4.527 |
| 8 | 8 | C005 | 0 | C.3 | 0.756601 | 0.181388 | 0.384917 | x,y,z | 5.455 | 1.669 | 5.327 |
| 9 | 9 | H005 | 0 | H | 0.793408 | 0.092424 | 0.410421 | x,y,z | 5.720 | 0.850 | 5.680 |
| 10 | 10 | C006 | 0 | C.3 | 0.865728 | 0.3014 | 0.386548 | x,y,z | 6.242 | 2.773 | 5.350 |
| 11 | 11 | H006 | 0 | H | 0.984048 | 0.313608 | 0.412046 | x,y,z | 7.095 | 2.885 | 5.703 |
| 12 | 12 | C007 | 0 | C.3 | 0.592935 | 0.202187 | 0.343764 | x,y,z | 4.275 | 1.860 | 4.758 |
| 13 | 13 | H007 | 0 | H | 0.500048 | 0.133082 | 0.33579 | x,y,z | 3.605 | 1.224 | 4.647 |
| 14 | 14 | ZR01 | 0 | Zr | 0.398045 | 0.668069 | 0.5 | 1-x,1-y,z | 2.870 | 6.146 | 6.920 |
| 15 | 15 | u7H1 | 0 | U | 0.709269 | 0.621901 | 0.5 | 1-x,1-y,z | 5.114 | 5.721 | 6.920 |
| 16 | 16 | CL02 | 0 | Cl | 0.700022 | 0.813881 | 0.5 | 1-x,1-y,z | 5.047 | 7.488 | 6.920 |
| 17 | 17 | C003 | 0 | C.3 | 0.413279 | 0.667194 | 0.317518 | 1-x,1-y,z | 2.980 | 6.138 | 4.394 |

**Figure B.10**. Fractional coordinates of the two hydrides as predicted by the refined solution generated by ShelXle.

The upper and lower bounds of the loop correspond to the minimum and maximum values possible for the *a*-axis adjusted by 1 (i.e., 1+1, 160-1). This is because the first argument of `vol` visualizes a single slice by isolating one frame (i.e., the frame between `x-1` and `x+1`). To display an average of several frames in lieu of a single frame (i.e., to thicken the width of one slice), the `x-1` and `x+1` parameters can be adjusted accordingly. To display a series of slices taken along a different axis, the bounds of the loop and the position of the variable argument were adjusted accordingly. The `set` commands provide increments for the axes. Supplying a numerical argument for `pause` will auto-cycle through the frames.

To generate .gif files containing all of the individual slices taken along the *a*-axis, each image generated was saved as a .png file using the `imwrite` function and horizontally concatenated using `strcat`, as follows:

```
for x=1:159
imwrite(uint8(squeeze((255/5.3)*vol(x,:,:))),strcat('./filepath',int2str(x),'.png'),'p
ng');
end
```

The resulting stack of .png images was loaded into the image processing software ImageJ, fused into a .gif file, and finally converted to .mp4 format.

**B5. Synthetic procedure and spectroscopic data for Compounds 2 and 3.**
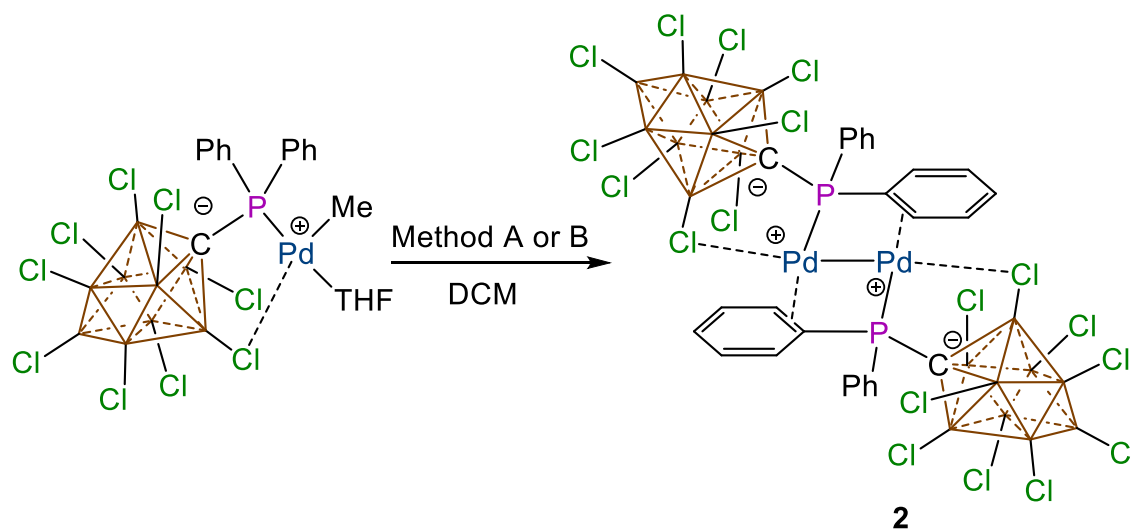


### B5.1 Synthesis of Complex 2.

Complex ($\kappa^2$-P,Cl-PPh$_2$CB$_9$Cl$_9$)PdMe(THF)(4) (500 mg, 619 μmol) was placed in a 200mL flame dried Schlenk flask and was subsequently dissolved in DCM (80 mL). The flask was placed on the Schlenk line and placed under UV radiation (Method A) or heated to 40°C (Method B) for 4 days without stirring. After 4 days, the reaction was taken into the glovebox and filtered through a Hirsch funnel fitted with a glass microfiber filter and washed with DCM (5 x 20 mL). The washings were discarded. The red solid was then passed through the filter with copious amounts of THF. The THF was then removed in vacuo give **2** as a red solid. (Method A: 309 mg, 215 μmol, 66% yield; Method B: 178 mg, 124 μmol, 35% yield). Crystals suitable for an X-ray diffraction study were obtained by layering a THF solution of **2** with pentane. m.p. = 221°C (dec.); $^1$H NMR (600 MHz, THF-$d_8$, 25°C): δ = 8.12 (t, 4H, $^3J(H,H)$ = 9.0 Hz), δ = 8.00 (t, 2H, $^3J(H,H)$ = 7.4 Hz), δ = 7.89-7.86 (dt, 4H, $^3J(H,H)$ = 7.5 Hz, $^4J(H,H)$ = 2.5 Hz); $^{13}$C NMR (151 MHz, THF-$d_8$, 25°C): δ = 137.4, 134.3, 132.3, 117.7; $^{31}$P[$^1$H] NMR (243 MHz, THF-$d_8$, 25°C): δ = 25.1; $^{11}$B[$^1$H] NMR (192 MHz, THF-$d_8$, 25°C): δ = 24.0, −4.2, −7.4.
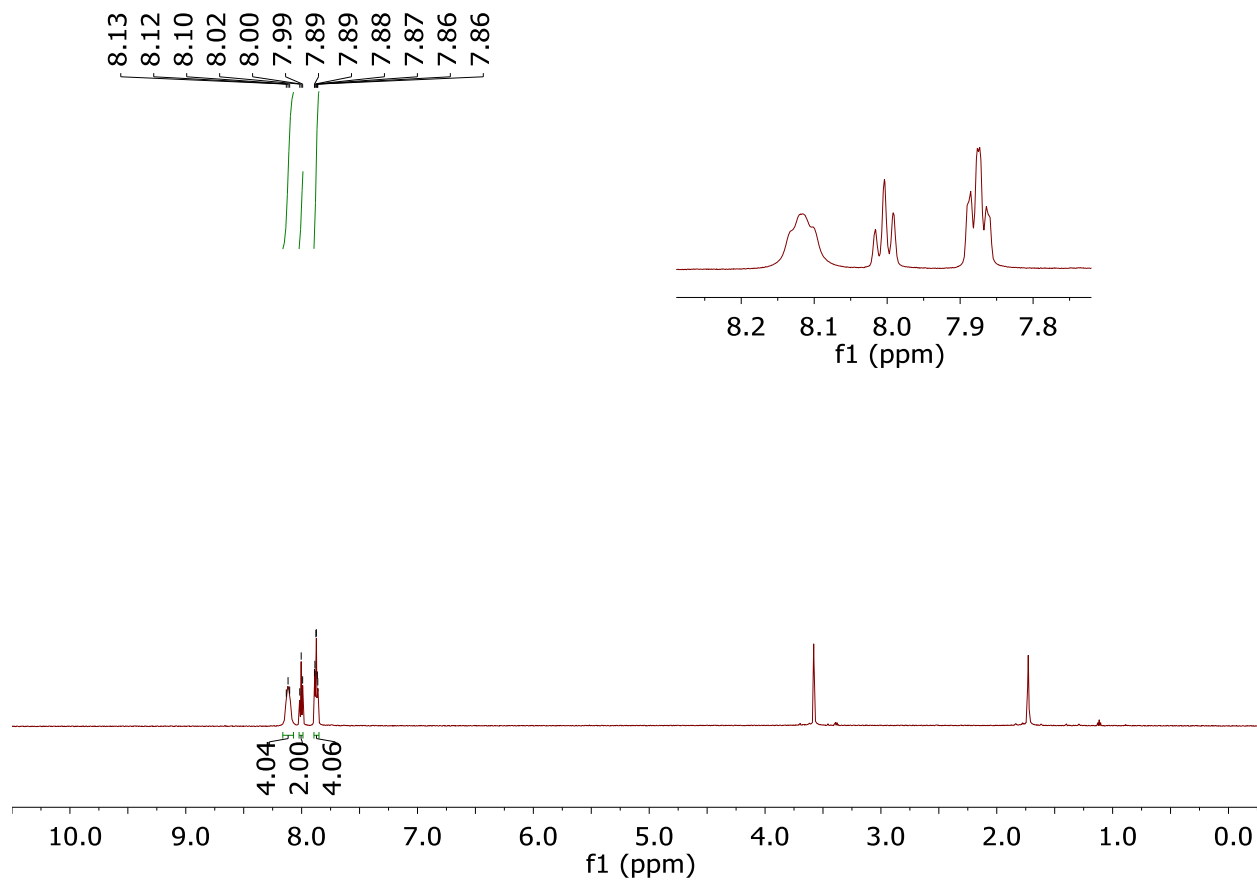
**Figure B.11**. $^1$H NMR of compound **2** (THF-$d_8$, 600MHz).
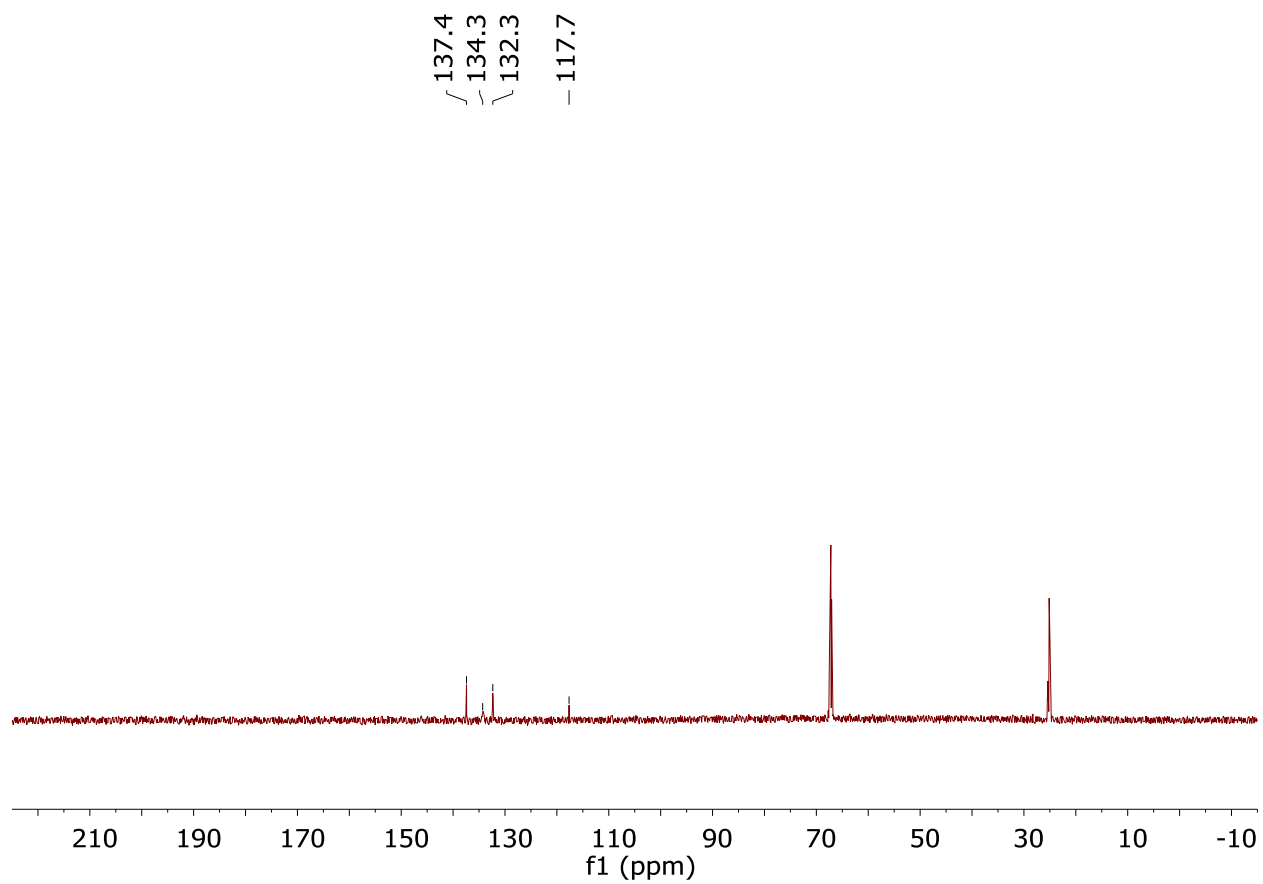
**Figure B.12**. $^{13}$C NMR of compound **2** (THF-$d_8$, 151MHz).

— 25.1
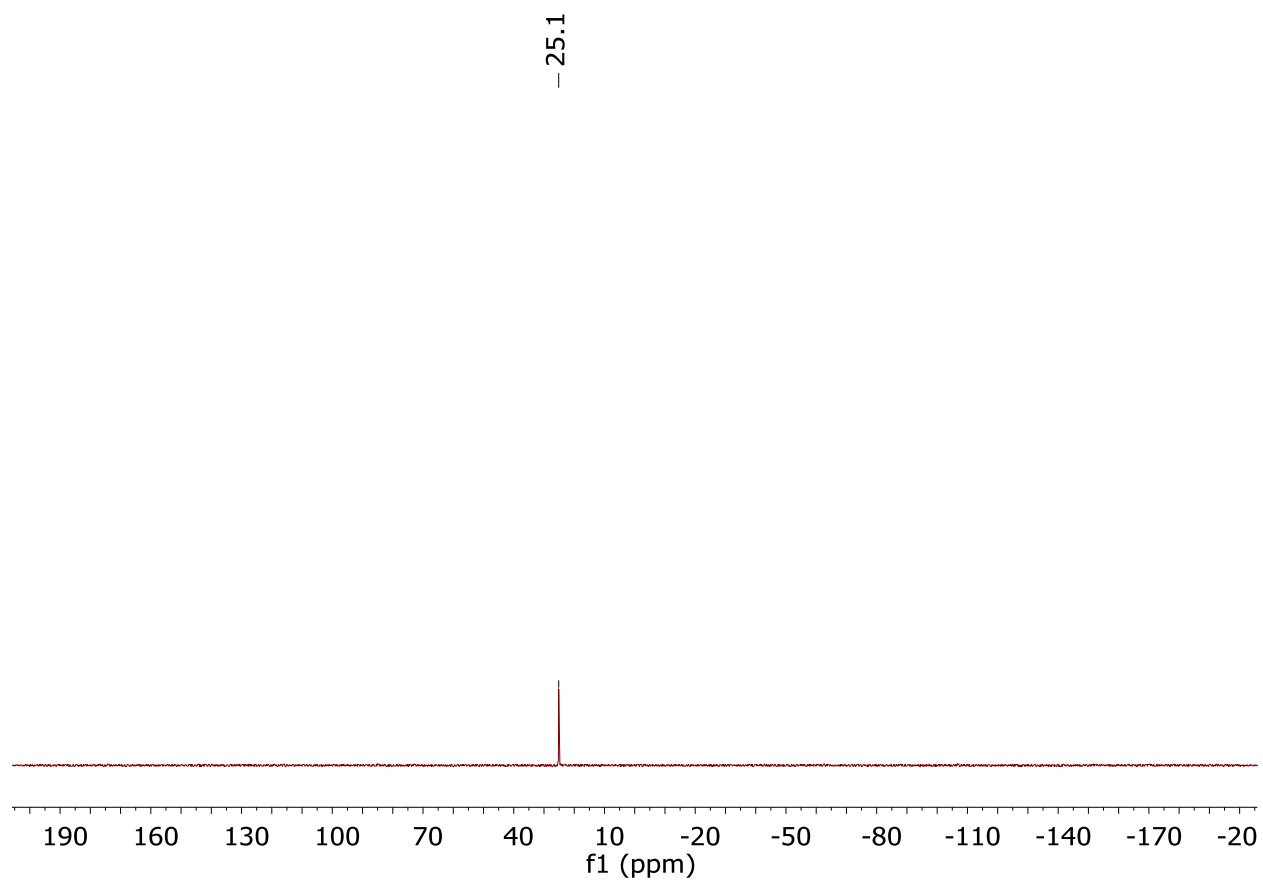


**Figure B.13**. $^{31}$P[$^1$H] NMR of compound **2** (THF-$d_8$, 243MHz).
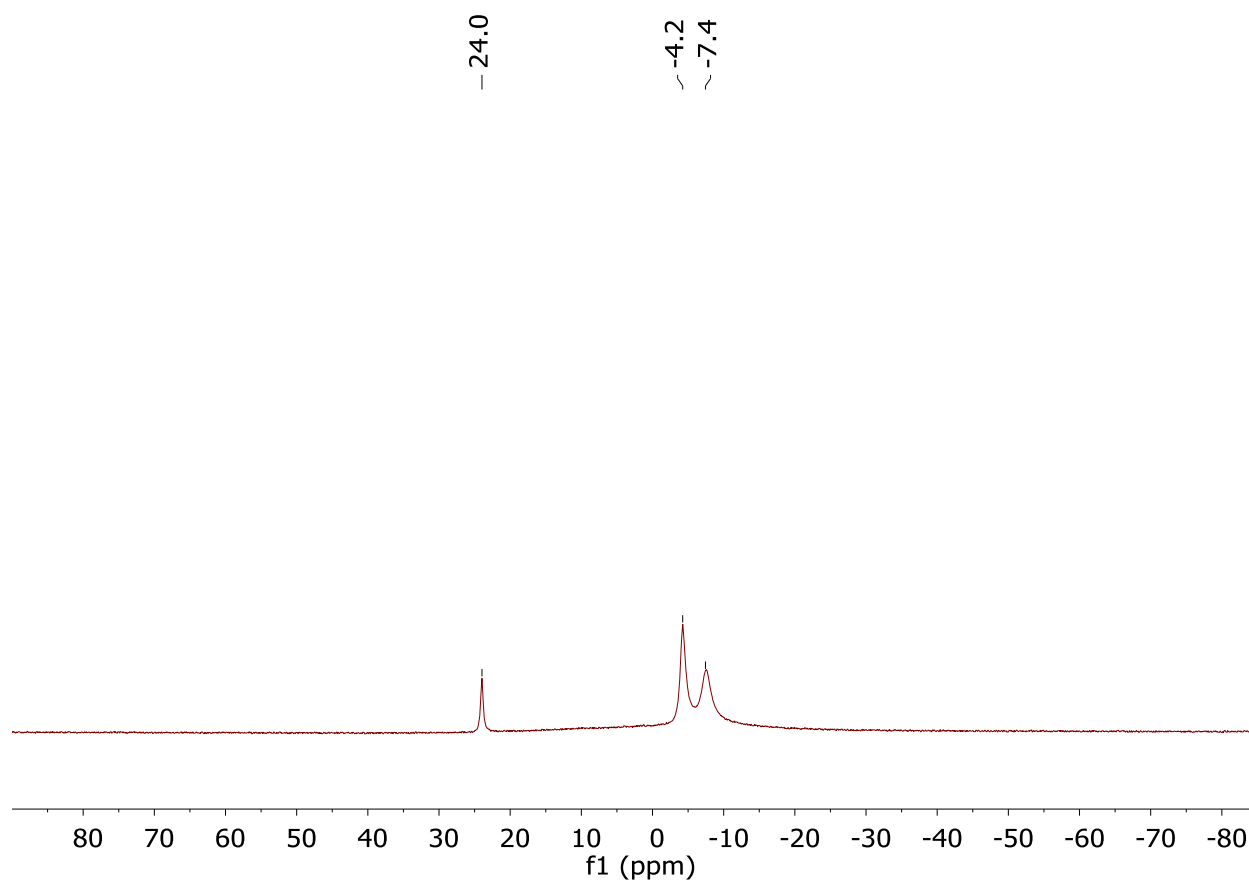
**Figure B.14**. $^{11}$B[$^{1}$H] NMR of compound **2** (THF-$d_8$, 192MHz).
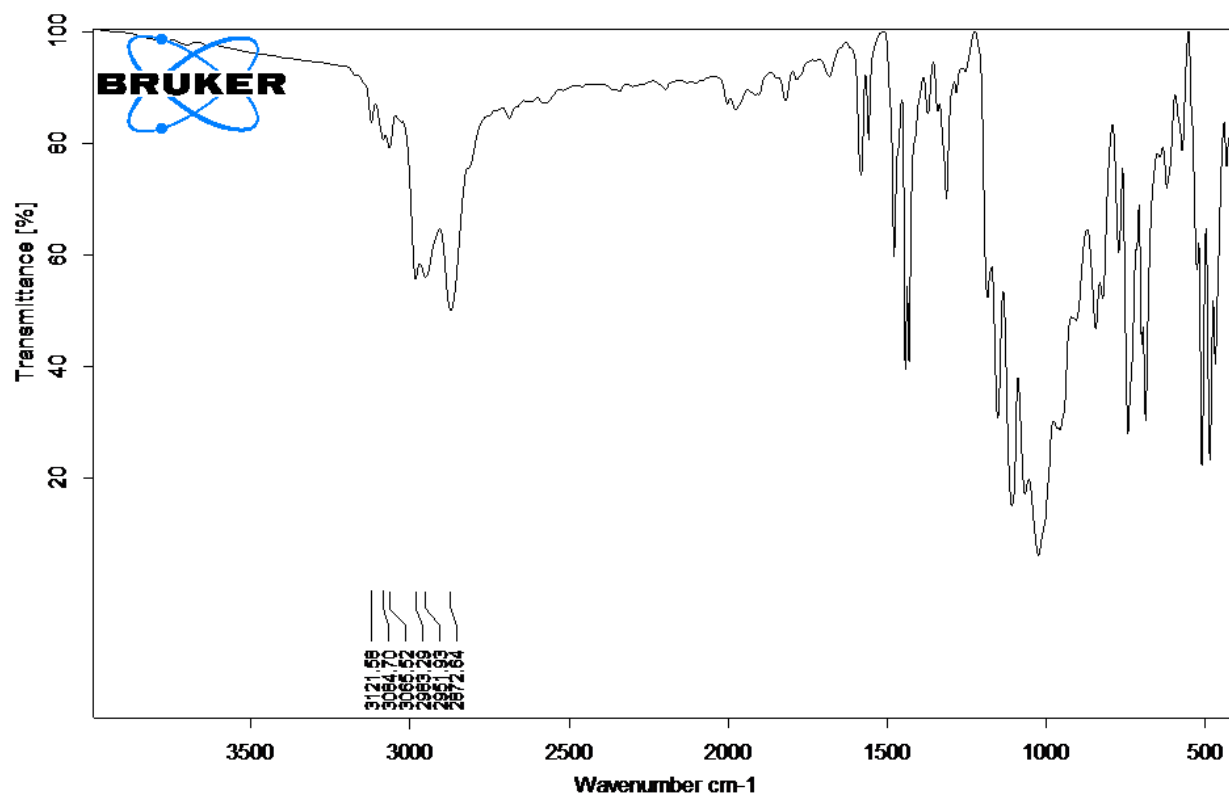
**Figure B.15**. FTIR spectrum of compound **2**.

Synthesis of Complex **3**:
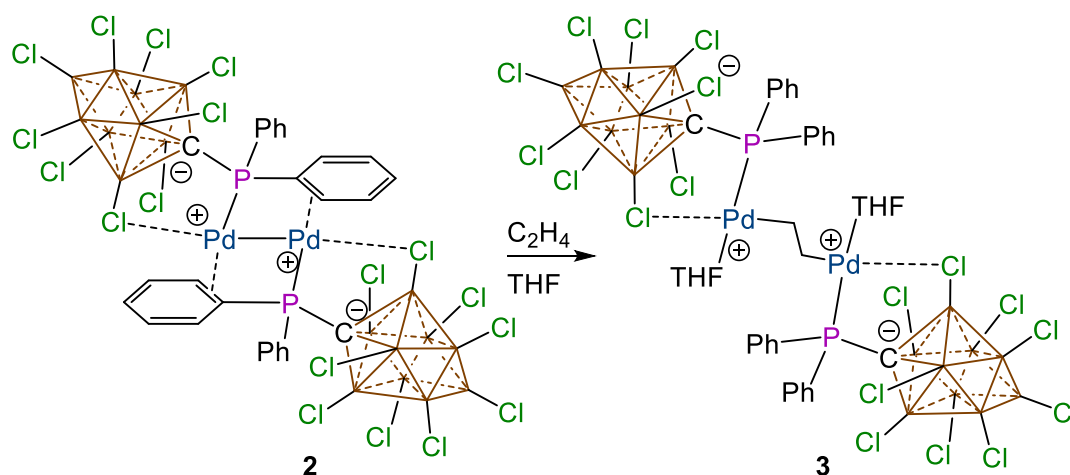


Complex **2** (80 mg, 56 μmol) was added to a 20 mL glass scintillation vial and THF (10 mL) was added. The THF solution was then placed in a dried 25 mL thick-walled Teflon Schlenk tube. The vial was washed with THF (5mL) and added to the Schlenk tube. The tube was sealed and then a regimen of free-pump-thaw was carried out with liquid $N_2$. Once at room temperature, the Schlenk tube was then back-filled with an ethylene atmosphere and then submerged in liquid $N_2$ to condense roughly 1cm of liquid ethylene. After sealing the Schlenk, the reaction was allowed to warm to room temperature with the ethylene slowly diffusing into the rest of the THF solution. After 6 hours, the reaction turned clear with a yellow powder settled at the bottom. With constant positive ethylene pressure, the THF was removed via syringe and then the Schlenk was placed under vacuum to remove residual solvent, giving **3** (64 mg, 44 μmol, 72% yield).
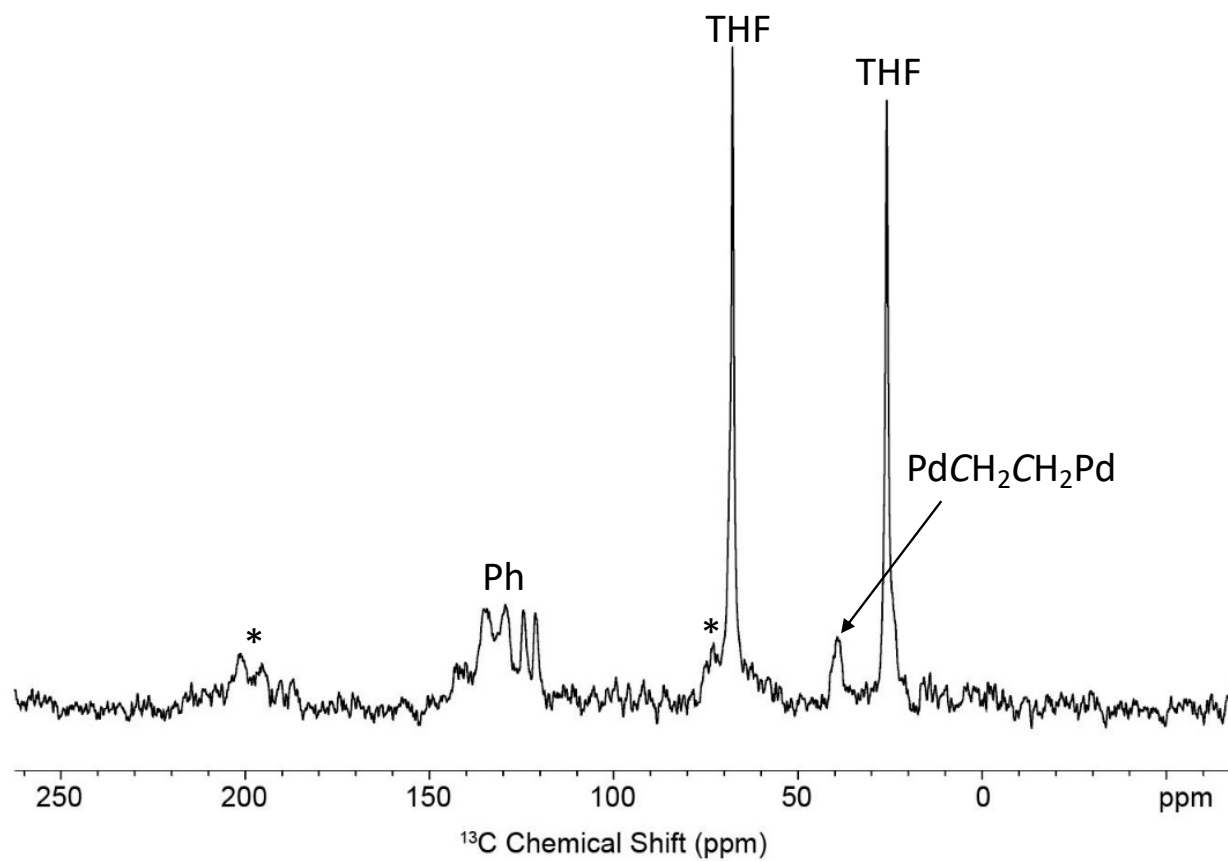
**Figure B.16.** Solid-state $^{13}$C NMR of complex **3**. The $^{13}$C chemical shift for the PdCH$_2$CH$_2$Pd carbons is at 37 ppm (* spinning side bands).
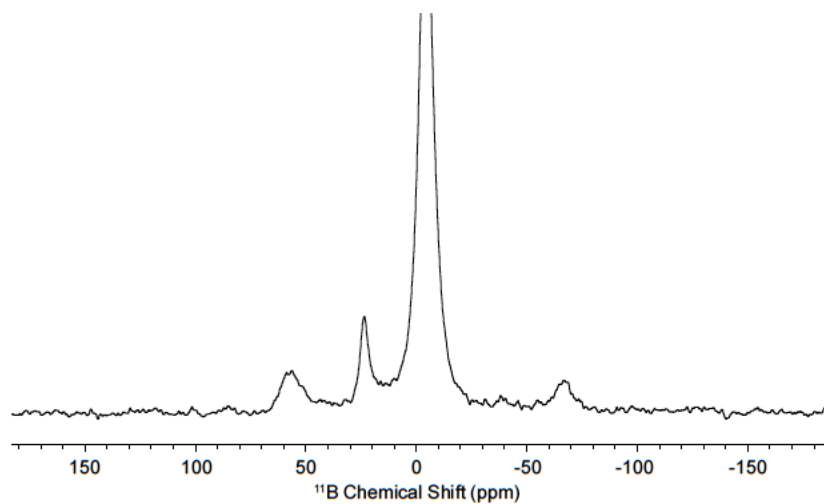


**Figure B.17**. Solid-state $^{11}$B NMR of compound **3**.
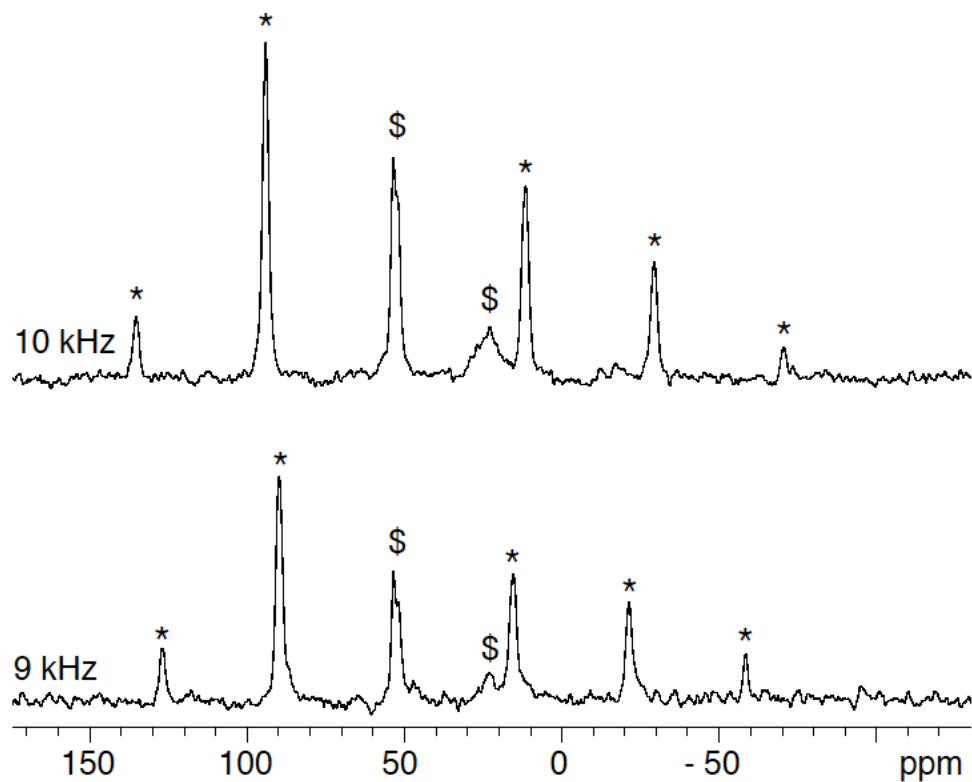
**Figure B.18**. Solid-state CPMAS $^{31}$P NMR of compound **3**. The two spectra (at spinning rates of 10 kHz and 9 kHz, respectively) were used to differentiate the spinning sidebands (*) from the three isotropic shifts ($ = 53.4, 51.8 and 23.0 ppm).
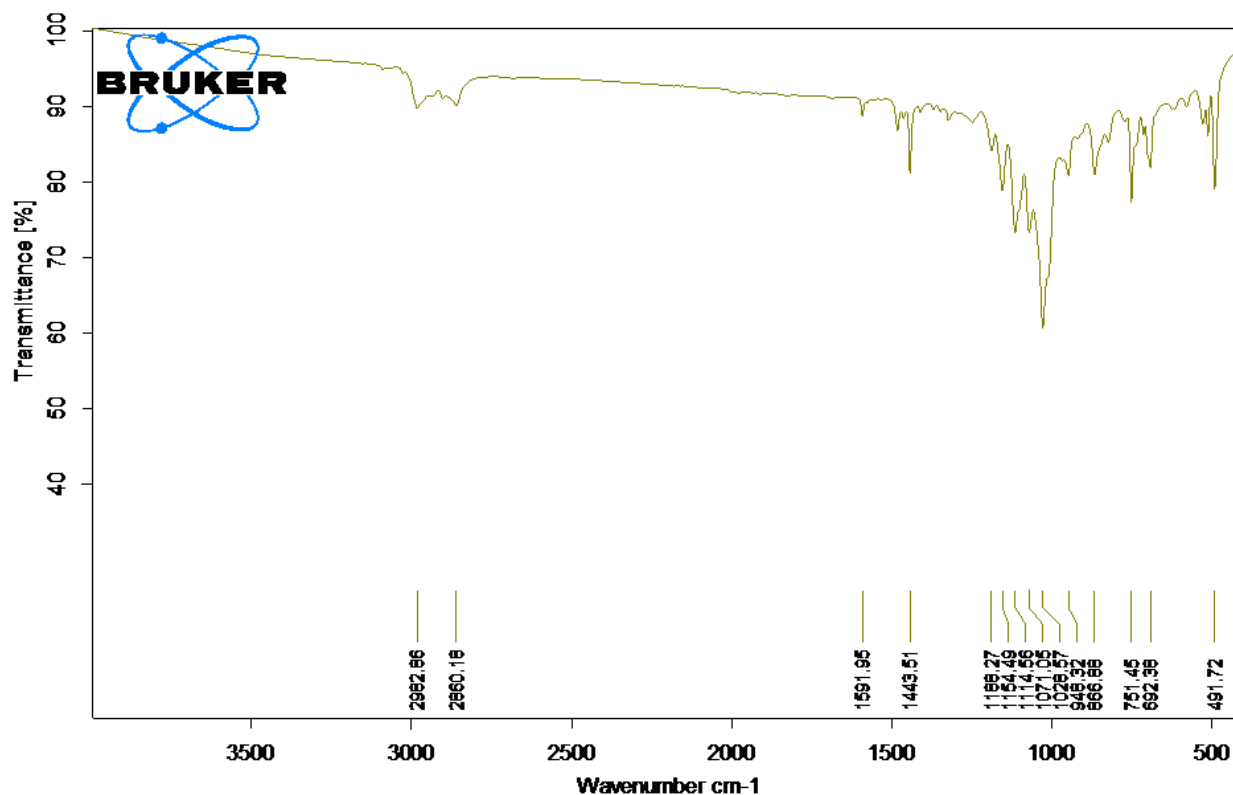
**Figure B.19**: FTIR spectrum for compound **3** with C-H peaks observable at 2982.86 cm$^{-1}$ and 2880.18 cm$^{-1}$.

## B6. References

1. Behenna, D. C.; Mohr, J. T.; Sherden, N. H.; Marinescu, S. C.; Harned, A. M.; Tani, K.; Seto, M.; Ma, S.; Novák, Z.; Krout, M. R.; McFadden, R. M.; Roizen, J. L.; Enquist, J. A.; White, D. E.; Levine, S. R.; Petrova, K. V.; Iwashita, A.; Virgil, S. C.; Stoltz, B. M. Enantioselective decarboxylative alkylation reactions: Catalyst development, substrate scope, and mechanistic studies. *Science*, **2011**, *17*, 14199–14223.

2. Chaudhuri, M. K.; Ghosh, S. K.; Novel synthesis of tris(acetylacetonato)iron(III). *Dalton Trans.* **1983**, 839–840.

3. Pilloni, G.; Toffoletti, A.; Bandoli, G.; Longato, B. Homoleptic complexes of cobalt(0) and nickel(0,I) with 1,1'-Bis(diphenylphosphino)ferrocene (dppf): Synthesis and characterization. *Inorg. Chem.* **2006**, *45*, 10321–10328.

4. Kleinsasser, J. F.; Reinhart, E. D.; Estrada, J.; Jordan, R. F.; Lavallo, V. Ethylene oligomerization and polymerization by palladium(II) methyl complexes supported by phosphines bearing a perchlorinated 10-vertex closo-carborane anion substituent. Organometallics 2018, 37, 4773–4783.

5.      Nannenga, B. L.; Shi, D.; Leslie, A. G. W.; Gonen, T. High-resolution structure determination by continuous-rotation data collection in MicroED. *Nat. Methods*. **2014**, *11*, 927–930

6.      Kabsch, W. Xds. *Acta Crystallogr. Sect. D Biol. Crystallogr.* **2010**, *66*, 125–132.

7.      Kabsch, W. Integration, scaling, space-group assignment and post-refinement. *Acta Crystallogr. Sect. D Biol. Crystallogr.* **2010**, *66*, 133–144.

8.      Sheldrick, G. M. SHELXT - Integrated space-group and crystal-structure determination. *Acta Crystallogr. Sect. A Found. Crystallogr.* **2015**, *71*, 3–8.

9.      Sheldrick, G. M. Crystal structure refinement with SHELXL. *Acta Crystallogr. Sect. C Struct. Chem.* **2015**, *71*, 3–8.

10.     Hübschle, C. B.; Sheldrick, G. M.; Dittrich, B. *ShelXle*: A Qt graphical user interface for *SHELXL J. Appl. Cryst.*, **2011**, *44*, 1281–1284.

11.     SAINT, version 8.34A, Bruker (2012), Bruker AXS Inc., Madison, Wisconsin, USA.

12.     SADABS, version 2012/1, Bruker (2012), Bruker AXS Inc., Madison, Wisconsin, USA.

13.     Müller, P. Practical suggestions for better crystal structures. *Crystallogr. Rev.* **2009**, *15*, 57–83.

14.     Trnka, T. M. Catalyst for olefin metathesis: ruthenium alkylidene complexes with phosphine and N-heterocyclic ligands. Ph.D. Dissertation [Online], California Institute of Technology, Pasadena, CA, December 2002.15.      Nickell, S.; Förster, F.; Linaroudis, A.; Del Net, W.; Beck, F.; Hegerl, R.; Baumeister, W.; Plitzko J. M. TOM software toolbox: acquisition and analysis for electron tomography. *J. Struct. Biol.* **2005**, *149*, 227–234.

*Appendix C*

*Supporting Information for Chapter 4: Solution-processable and functionalizable*

*ultrahigh molecular weight polymers via topochemical synthesis*

## Supplementary Methods

### General

All reactions were carried out in oven-dried glassware sealed with rubber septa under an atmosphere of nitrogen unless otherwise noted and were stirred using Teflon-coated magnetic stir bars. Large volumes of volatile solvents were removed using rotary evaporation, and small volumes of volatile solvents were removed using nitrogen gas flow. All commercially available chemicals were purchased from Alfa Aesar, Spectrum Chemicals, Acros Organics, TCI America, or Sigma-Aldrich, and were used without further purification. Deuterated solvents were purchased from Cambridge Isotope Laboratories and used as received. Solid-state $^{13}C$ NMR spectra were carried out at 500.12 MHz (11.7 T) on a Bruker Avance spectrometer with a Bruker 4 mm narrow bore H/C/N magic angle spinning probe. Solid state $^{13}C$ NMR spectra were in general acquired by cross-polarization from $^1H$ with a contact time of 5 ms at a spinning rate of 10 kHz. All solution NMR spectra were recorded at 298 K on a Bruker 500 MHz Avance instrument unless otherwise specified. All chemical shifts are quoted using the δ scale, and all coupling constants (J) are expressed in Hertz (Hz). Solution $^1H$ and $^{13}C$ NMR spectra chemical shifts are reported relative to the residual solvent signal ($^1H$ NMR: $CDCl_3$ δ = 7.26 ppm, acetone-$d_6$ δ = 2.05 ppm, THF-$d_8$ δ = 1.72/3.58 ppm, and DMSO-$d_6$ δ = 2.50 ppm; $^{13}C$ NMR: $CDCl_3$ δ = 77.16 ppm, acetone-$d_6$ δ = 29.84/206.26 ppm, THF-$d_8$ δ = 67.21/25.31 ppm, and DMSO-$d_6$ δ = 39.52 ppm). NMR data are reported as follows: chemical shift (multiplicity, coupling constants where applicable, number of hydrogens where applicable). Splitting is reported with the following symbols: s = singlet, d = doublet, t = triplet, dd = doublet of doublets, td = triplet of doublets, ddd = doublet of doublet of doublets, sept = septet, m = multiplet, bs = broad singlet. MALDI-TOF mass spectrometry experiments were performed on an Applied Biosystems 4800 MALDI TOF/TOF instrument in reflector mode using super-DHB (purchased from Sigma-Aldrich) as matrix. UV-Vis-NIR

spectra were recorded using a Cary 5000 UV-Vis-NIR spectrometer. Films for UV-Vis spectroscopy were prepared via spin-coating 100 µL of 10 mg mL$^{-1}$ solutions on substrates spinning at 1000 rpm for 40 seconds protected from significant exposure to light. Solution UV-Vis spectra were taken in dilute solutions in dichloromethane or in films on quartz substrates, and optical band gaps were determined based on the onset of the highest-wavelength absorbance feature. Scanning electron microscope (SEM) images were obtained using a ZEISS Ultra-55 field emission scanning electron microscope (FESEM). Size exclusion chromatography (SEC) was performed on a Malvern OMNISEC equipped with refractive index, light scattering, and intrinsic viscosity detectors calibrated with a single poly(styrene) standard. Analysis was performed in tetrahydrofuran running at 1 mL min$^{-1}$ and 35 ºC. Computations were run on the Etna partition of the Lawrencium Supercluster at Lawrence Berkeley National Labs using Qchem 5.1.[1] Molecular geometries were optimized starting from structures generated in the IQmol software and relaxed using the UFF molecular mechanics force field.[2] Molecular geometries were then optimized and single-point energies were determined at the 6-311++G** level using the B3LYP functional. Orbital density maps were visualized using the IQmol software with an isovalue of 0.02.

## X-ray Crystallography

Monomers **1**, **2**, and **4** were crystallized via slow evaporation from toluene, and monomer **3** was crystallized via slow evaporation from chloroform (see crystallization section below for details). After 1-3 weeks undisturbed, all of the monomers had formed yellow needle-like crystals roughly 5 mm in size of suitable quality to obtain x-ray structures. Single crystals of **1**-**4** were selected and mounted on Mitegen® loops with Paratone oil, and data were collected on beamline 12.2.1 at the Advanced Light Source with λ = 0.7749 Å at 100 K using an Oxford Cryosystems Cryostream 800 plus. The x-ray structures of monomers **1**-**4** were collected on a Bruker D8 diffractometer with a Bruker PHOTON100 CMOS detector. Data reduction was performed and corrected for Lorentz and polarization effects using SAINT[3] v8.38a and were corrected for absorption effects using SADABS v2016/2.[4] Structures were solved using SHELXT[4] and were refined by least-square refinement against F$^2$ by SHELXL.[5]

## Electron Cryomicroscopy (CryoEM)

Microcrystals of polymer **P2** were deposited on TEM grids by preparing 10 mg mL$^{-1}$ solutions of monomer **2** in chloroform, tetrahydrofuran, and dichloromethane. TEM grids were dipped into the solutions, removed, and allowed to air dry for a few seconds (Supplementary Figure 1). Afterwards, the TEM grids were placed in clean vials, and the vials were placed on a windowsill that receives direct sunlight. After three days on the windowsill, the polymerization was complete.

Coated TEM grids were loaded in a Gatan 626 single-tilt cryo holder and cooled with liquid nitrogen. Screening and data collection was performed using a Thermo-Fisher F200C transmission

electron microscope operating at 200 kV and equipped with a Thermo-Fisher Ceta-D detector. Screening was done in low-dose mode and diffraction was identified through condensing of the electron beam. After selection of a crystal on the grid, the crystal was centered, the eucentric height adjusted by tilting the crystal through the desired rotation range, and the selected area aperture and beam stop were inserted.[6]

Images were collected in a movie format as crystals were continuously rotated in the electron beam. Typical data collection was performed using a constant tilt rate of 0.3°/s between the minimum and maximum tilt ranges of -72° to +72°, respectively. During continuous rotation, the camera integrated frames continuously at a rate of 3 seconds per frame. The dose rate was calibrated to <0.03 e-/$Å^2$ s. Crystals selected for data collection were isolated by a selected area aperture to reduce the background noise contributions and calibrated to eucentric height to stay in the aperture over the entire tilt range. All diffraction data were processed using the XDS suite of programs.[7] The resulting crystal structure was solved ab initio using direct methods in SHELXT[4] and refined with SHELXL[8] using ShelXle.[9] Structure refinement was performed using electron scattering factors reported by Peng.[10] Thermal parameters were refined anisotropically for all non-hydrogen atoms.
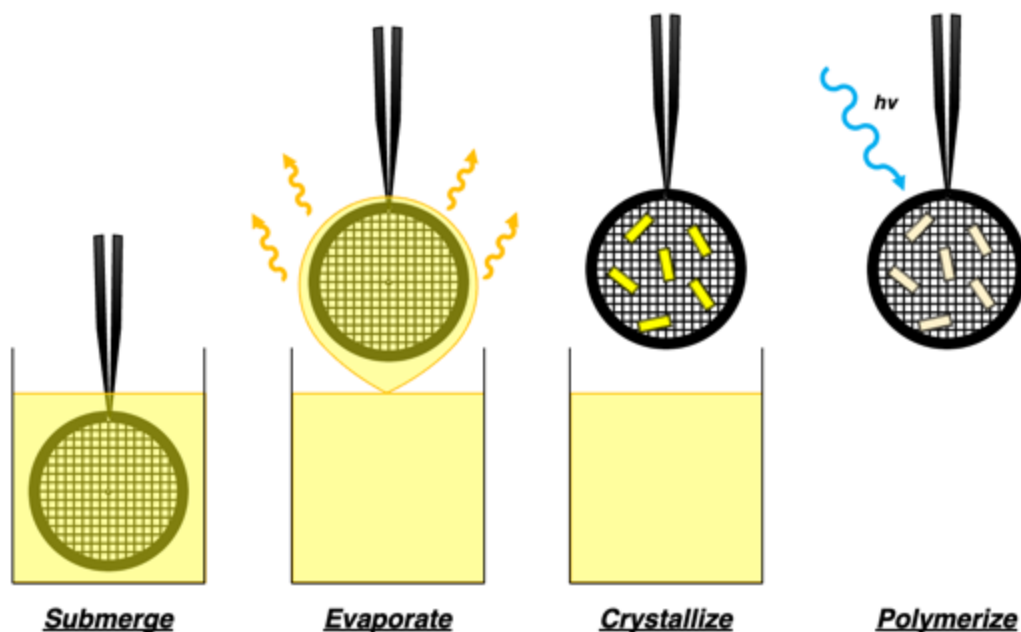


**Supplementary Figure C.1.** A schematic representation of the preparation of polymer **P2** microcrystals on TEM grids for cryoEM.

## Dielectric Measurements

Indium tin oxide (ITO) coated glass substrates (2-3 $\Omega$ sq$^{-1}$, Thin Film Devices Inc., USA) were pre-cleaned using soapy water, deionized (DI) water, acetone, and isopropanol, sequentially. The substrates were then heated at 100 ºC for at least four hours, followed by ultraviolet/ozone (UV/O$_3$) treatment for 20 min prior to use.

### Parylene-C Films

A ~1.5 μm thick layer of Parylene-C was deposited on ITO-coated glass substrates using chemical vapor deposition (PDS 2010 Labcoter, SCS) as follows. Parylene-C Dimer (2 g) was placed in the sublimation chamber, which was heated to 175 ºC under high vacuum. The dimer vapor was cleaved to monomer vapor at 690 ºC and flowed into the unheated deposition chamber, which contained the ITO coated glass substrates. The thickness was checked using a Dektak 3030ST profilometer to be between 1.4 μm and 1.6 μm. A gold electrode (4 mm$^2$ area with 30 nm thickness) was deposited on the top surface of the polymer film using a thermal evaporator (MBRAUN, Germany) for dielectric characterization.

### Polymer P3 Films

Polymer **P3** (20 mg) was dissolved in 3 mL tetrahydrofuran (THF) and magnetically stirred for 24 h to yield a transparent solution. Afterwards the solution was drop-cast on ITO substrates and they were placed in a covered petri dish to slow down the solvent evaporation process. The coated substrates were then thermally treated at 105 ºC for 24 h in a vacuum oven to remove solvent residual. The thickness was checked using a Dektak 150 profilometer to be between 2.6 μm and 4.4 μm. A gold electrode (4 mm$^2$ area with 30 nm thickness) was deposited on the top surface of the polymer film using a thermal evaporator (MBRAUN, Germany) for dielectric characterization.

### Other Dielectric Polymer Films

Free-standing polymer films of biaxially-oriented polypropylene (BOPP, capacitor grade, ~3.8 μm) ethylene tetrafluoroethylene (ETFE, ~12 μm), polycarbonate (PC, ~10 μm), poly(ethylene 2,6-naphthalate (PEN, ~8 μm), polyimide (PI, Upilex-S, ~8.8 μm), poly(ether imide) (PEI, ~12 μm), poly(vinylidene fluoride) (PVDF, 8 μm), and Poly(vinylidene fluoride-*co*-hexafluoropropylene) (PVDF-HFP, 10 wt% HFP, 5 μm) were obtained from PolyK Technologies, LLC, USA. Gold electrodes (4 mm$^2$ area with 30 nm thickness) were deposited on both sides of the dielectric polymer films using a thermal evaporator (MBRAUN, Germany) for dielectric characterization.

Polystyrene (PS, Sigma Aldrich, 280,000 molecular weight (SEC)) and poly(vinylidene fluoride-*co*-chlorotrifluoroethylene) (PVDF-CTFE, 15 wt% CTFE, PolyK Technologies) polymer powders (60 mg) were each dissolved in 3 mL dimethyl formamide (DMF), and magnetically stirred for 24 h to yield

clear solutions. Afterwards the solution was drop-cast onto ITO substrates in an air-circulating oven at 65 °C, followed by a thermal treatment step at 105 °C for 24 h in a vacuum oven to remove residual solvent. The thickness of the cast films was controlled between 2.5 μm and 5 μm. A gold electrode (4 mm$^2$ area with 30 nm thickness) was deposited on the top surface of the polymer film using a thermal evaporator (MBRAUN, Germany) for dielectric characterization.

To avoid creeping discharge, the samples for all of the dielectric measurements were immersed in a Galden HT-270 PFPE fluorinated fluid. Electric displacement–electric field (*D–E*) loops were collected under varied applied electric fields using a PK-CPE1801 high-voltage test system containing a high voltage amplifier (Trek 610D, PolyK Technologies, LLC, USA). The voltages with a unipolar triangular waveform were applied at a frequency of 100 Hz. The electric field of 200 MV m$^{-1}$ was chosen as it is the field of interest for power inverters in hybrid electric vehicles.[11,12] The charge–discharge cyclic tests were performed under a repeatedly applied electric field of 200 MV m$^{-1}$ using on the same high-voltage test system using the Fatigue mode. Discharged energy density ($U_d$) and charge–discharge efficiency ($\eta$) were calculated from the *D–E* loops using the method illustrated in Supplementary Figure 27. Dielectric breakdown strength measurements were performed using the same Trek 610D high voltage amplifier using the electrostatic pull-down method, where a DC voltage ramp of 200 V s$^{-1}$ was applied to the polymer film samples until dielectric failure.

## Synthesis
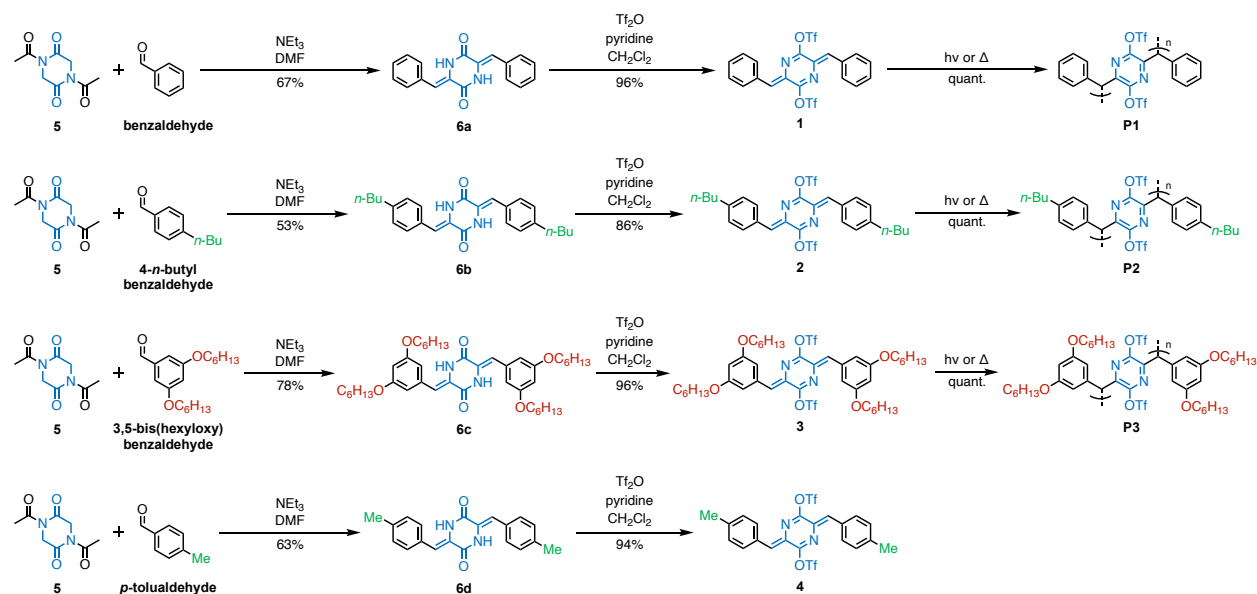


**Supplementary Figure C.2.** The syntheses of monomers **1**-**4** and polymers **P1**-**P3**.

1,4-Diacetylpiperazine-2,5-ione (**5**)

1,4-Diacetylpiperazine-2,5-dione was synthesized from glycine anhydride according to a previously reported procedure.[13]
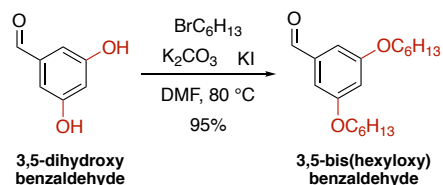


### 3,5-bis(hexyloxy)benzaldehyde

A 250 mL round-bottom flask with a stir bar and air-condenser was charged with 3,5-dihydroxybenzaldehyde (1.00 g, 7.24 mmol) and dry DMF (100 mL). Potassium carbonate (2.50 g, 18.10 mmol), potassium iodide (120.19 mg, 724.00 mmol), and 1-bromohexane (2.24 mL, 15.93 mmol) were added. The mixture was heated to 80 °C and continually stirred for 15 hrs at this temperature. After cooling to room temperature, the solvent was removed via rotary evaporation. The mixture was subjected to column chromatography (hexanes to ethyl acetate gradient) to yield analytically pure 3,5-bis(hexyloxy)benzaldehyde as a very faintly brown liquid (95% yield). $^1$H NMR (500 MHz, CDCl$_3$) δ 9.88 (s, 1H), 6.98 (d, $J$ = 2.4 Hz, 2H), 6.69 (t, $J$ = 2.3 Hz, 1H), 3.97 (t, $J$ = 6.6 Hz, 4H), 1.80 (dt, $J$ = 15.3, 6.7 Hz, 4H), 1.49 – 1.42 (m, 4H), 1.36 – 1.32 (m, 8H), 0.91 (t, $J$ = 6.9 Hz, 6H). $^{13}$C NMR (126

MHz, CDCl$_3$) δ 192.08, 160.70, 138.25, 107.88, 107.48, 68.35, 31.57, 29.10, 25.70, 22.67, 14.07. MS (ESI) for C$_{19}$H$_{30}$O$_3$ [M+1]$^+$: calcd., 307.2195; found, 307.2338.
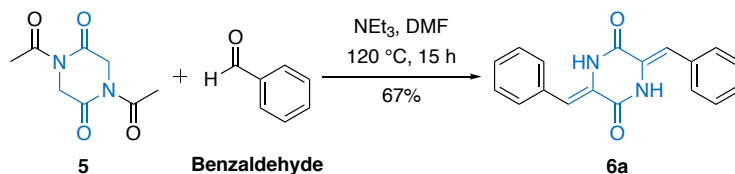


## Compound 6a

1,4-Diacetylpiperazine-2,5-dione (5) (5.00 g, 25.23 mmol), triethylamine (14.08 mL, 100.92 mmol), and benzaldehyde (5.46 mL, 63.08 mmol) were dissolved in DMF (50 mL), and the resulting solution was stirred in a 120 °C sand bath for 15 h. The reaction mixture was then cooled to room temperature and diluted with water (40 mL). The precipitated solid was filtered and washed with roughly 10 mL each of water, ethyl acetate, and finally methanol to afford 6a as a light-yellow powder (67%). $^1$H NMR (500 MHz, DMSO-$d_6$) δ 10.31 (s, 1H), 7.55 (d, $J$ = 7.3 Hz, 2H), 7.42 (t, $J$ = 7.6 Hz, 2H), 7.33 (t, $J$ = 7.4 Hz, 1H), 6.78 (s, 1H). $^{13}$C NMR (126 MHz, DMSO-d$_6$) δ 158.04, 133.11, 129.37, 128.72, 128.23, 126.39, 115.06. MS (MALDI-TOF) for C$_{18}$H$_{14}$N$_2$O$_2$ [M]$^+$: calcd., 290.1055; found, 290.1117.
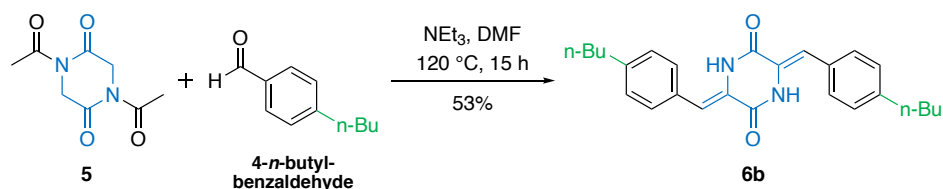
## Compound 6b

1,4-Diacetylpiperazine-2,5-dione (**5**) (596.00 mg, 3.01 mmol), triethylamine (1.68 mL, 12.03 mmol), and 4-*n*-butyl-benzaldehyde (1.03 mL, 6.16 mmol) were dissolved in DMF (6 mL), and the resulting solution was stirred in a 120 °C sand bath for 15 h. The reaction mixture was then cooled to room temperature and diluted with water (10 mL). The precipitated solid was filtered and washed with roughly 10 mL each of water, ethyl acetate, and finally methanol to afford **6b** as a light-yellow powder (53%). $^{1}$H NMR (500 MHz, DMSO-$d_6$) δ 9.64 (s, 1H), 7.46 (d, $J$ = 7.9 Hz, 2H), 7.27 (d, $J$ = 7.8 Hz, 2H), 6.79 (s, 1H), 2.64 (t, $J$ = 7.6 Hz, 2H), 1.62 (p, $J$ = 7.2 Hz, 2H), 1.37 (h, $J$ = 7.3 Hz, 2H), 0.94 (t, $J$ = 7.3 Hz, 4H). $^{13}$C NMR (126 MHz, DMSO-$d_6$) δ 158.16, 143.29, 131.03, 129.56, 129.18, 126.38, 115.48, 35.09, 33.12, 22.07, 13.97. MS (ESI) for $C_{26}H_{30}N_2O_2$ [M+1]$^+$: calcd., 403.2307; found, 403.2433.
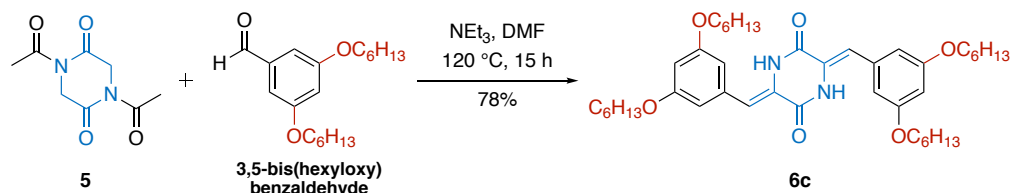


## Compound 6c

1,4-Diacetylpiperazine-2,5-dione (**5**) (100.00 mg, 504.60 µmol), triethylamine (281.53 µL, 2.02 mmol), and 3,5-bis(hexyloxy)benzaldehyde (324.73 mg, 1.06 mmol) were dissolved in DMF (1 mL), and the resulting solution was stirred in a 120 °C sand bath for 15 h. The reaction mixture was then cooled to room temperature and diluted with water (5 mL). The precipitated solid was filtered and washed with roughly 10 mL each of water and methanol (Note: do not wash with ethyl acetate) to afford **6c** as a light-yellow powder (78%). $^{1}$H NMR (500 MHz, CDCl$_3$) δ 8.28 (s, 1H), 6.96 (s, 1H), 6.49 (dd, $J$ = 2.3, 0.6 Hz, 2H), 6.46 (t, $J$ = 2.2 Hz, 1H), 3.96 (t, $J$ = 6.6 Hz, 4H), 1.80 (dt, $J$ = 15.3, 6.6 Hz, 4H), 1.53 – 1.43 (m, 4H), 1.43 – 1.31 (m, 8H), 0.94 (t, $J$ = 7.0 Hz, 6H). $^{13}$C NMR (126 MHz, CDCl$_3$) δ 161.10, 156.81, 125.76, 116.97, 106.62, 101.53, 68.24, 31.60, 29.17, 25.74, 22.64, 14.11. MS (ESI) for $C_{42}H_{62}N_2O_6$ [M+1]$^+$: calcd., 691.4608; found, 691.4719.
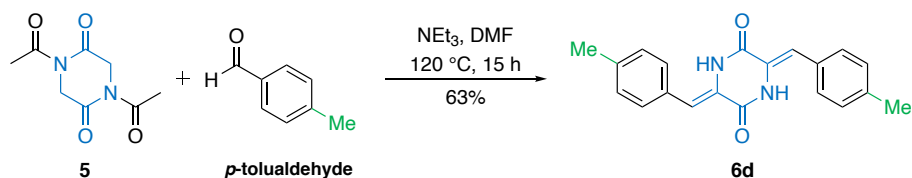
**Compound 6d**

1,4-Diacetylpiperazine-2,5-dione (**5**) (804.59 mg, 4.06 mmol), triethylamine (2.27 mL, 16.24 mmol), and *p*-tolualdehyde (981.35 µL, 8.32 mmol) were dissolved in DMF (8 mL), and the resulting solution was stirred in a 120 °C sand bath for 15 h. The reaction mixture was then cooled to room temperature and diluted with water (10 mL). The precipitated solid was filtered and washed with roughly 10 mL each of water, ethyl acetate, and finally methanol to afford **6d** as a light-yellow powder (63%). $^1$H NMR (500 MHz, DMSO-$d_6$) δ 9.67 (s, 1H), 7.44 (d, $J$ = 8.2 Hz, 2H), 7.25 (d, $J$ = 7.8 Hz, 2H), 6.77 (s, 1H), 2.35 (s, 3H). $^{13}$C NMR (126 MHz, DMSO-$d_6$) δ 157.24, 137.43, 129.85, 128.93, 128.61, 125.42, 114.54, 20.32. MS (ESI) for $C_{20}H_{18}N_2O_2$ [M+1]$^+$: calcd., 319.1368; found, 319.1506.
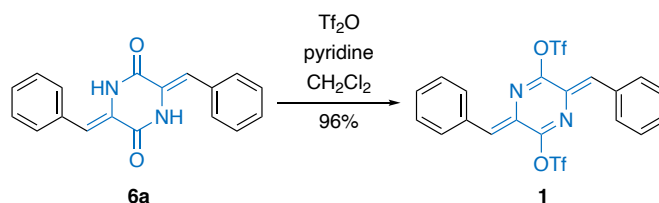


**Monomer 1**

Trifluoromethanesulfonic anhydride (607.4 µL, 3.62 mmol) was added dropwise to a solution of **6a** (500.00 mg, 1.72 mmol) and pyridine (3.62 mmol, 291.36 µL) in dichloromethane (10 mL) at -78 °C (dry ice/acetone bath). The reaction was stirred at -78 °C for 30 mins and then slowly warmed to room temperature and stirred over 16 hrs. Hexanes was added to the crude reaction mixture, the precipitate was filtered, and the solid was washed with roughly 10 mL each of hexanes, water, and finally methanol to give analytically pure **1** as yellow needles (96%). Note: the product should be protected from ambient light and heating above 40 °C as much as possible. It is advisable to store the product in a refrigerator or freezer within aluminum-foil wrapped and/or darkened glass vessels. $^1$H NMR (500 MHz, CDCl$_3$) δ 8.06 – 7.99 (m, 2H), 7.47 – 7.42 (m, 3H), 6.98 (s, 1H). $^{13}$C NMR (126 MHz, CDCl$_3$) δ 151.51, 133.10, 132.69, 131.62, 131.58, 128.98, 126.22, 119.80, 117.24. MS (ESI) for $C_{20}H_{12}F_6N_2O_6S_2$ [M+1]$^+$: calcd., 555.0041; found, 555.0188.
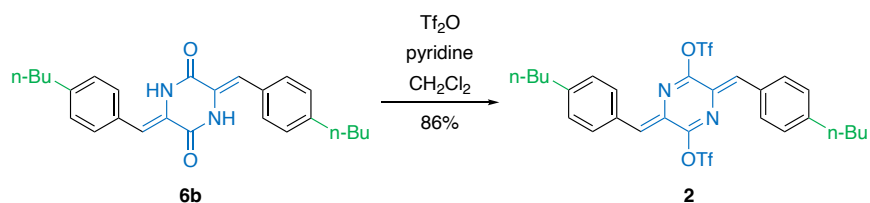
**Monomer 2**

Trifluoromethanesulfonic anhydride (299.87 µL, 1.78 mmol) was added dropwise to a solution of **6b** (350.00 mg, 869.48 µmol) and pyridine (147.10 µL, 1.83 mmol) in dichloromethane (14 mL) at -78 °C (dry ice/acetone bath). The reaction was stirred at -78 °C for 30 mins and then slowly warmed to room temperature and stirred over 16 h. Hexanes was added to the crude reaction mixture, the precipitate was filtered, and the solid was washed with roughly 10 mL each of hexanes, water, and finally methanol to give analytically pure **2** as yellow needles (86%). Note: the product should be protected from ambient light and heating above 40 °C as much as possible. It is advisable to store the product in a refrigerator or freezer within aluminum-foil wrapped and/or darkened glass vessels. $^1$H NMR (500 MHz, CDCl$_3$) δ 7.98 (d, $J$ = 8.4 Hz, 2H), 7.30 (d, $J$ = 8.5 Hz, 2H), 6.95 (s, 1H), 2.68 (t, $J$ = 7.7 Hz, 2H), 1.70 – 1.60 (m, 2H), 1.39 (h, $J$ = 7.4 Hz, 2H), 0.96 (t, $J$ = 7.3 Hz, 3H). $^{13}$C NMR (126 MHz, CDCl$_3$) δ 151.16, 147.35, 132.58, 130.89, 129.65, 129.04, 125.48, 119.65, 117.10, 35.84, 33.25, 22.41, 13.96. MS (MALDI-TOF) for C$_{28}$H$_{28}$F$_6$N$_2$O$_6$S$_2$ [M]$^+$: calcd., 666.1293; found, 666.1204.
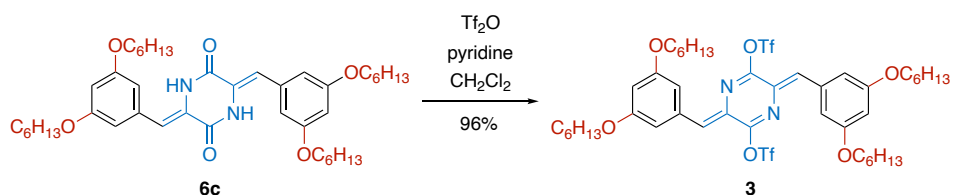


**Monomer 3**

1M Trifluoromethanesulfonic anhydride solution in DCM (2.97 mL, 2.97 mmol) was added dropwise to a solution of **6c** (1.00 g, 1.45 mmol) and pyridine (244.84 µL, 3.04 mmol) in dichloromethane (50 mL) at -78 °C (dry ice/acetone bath). The reaction was stirred at -78 °C for 30 mins and then slowly warmed to room temperature and stirred over 16 h. Hexanes was added to the crude reaction mixture, the precipitate was filtered, and the solid was washed with roughly 20 mL each of hexanes, water, and finally methanol to give analytically pure **3** as yellow needles (96%). Note: the product should be protected from ambient light and heating above 40 °C as much as possible. It is advisable to store the product in a refrigerator or freezer within aluminum-foil wrapped and/or brown glass vessels. $^1$H NMR (500 MHz, CDCl$_3$) δ 7.17 (d, $J$ = 2.1 Hz, 2H), 6.85 (s, 1H), 6.59 (t, $J$ = 2.2 Hz, 1H), 4.01 (t, $J$ = 6.6 Hz, 4H), 1.80 (p, $J$ = 6.9 Hz, 4H), 1.52 – 1.45 (m, 4H), 1.41 – 1.33 (m, 8H), 0.93

(t, $J$ = 7.0 Hz, 6H). $^{13}$C NMR (126 MHz, CDCl$_3$) δ 160.35, 151.12, 134.41, 131.65, 125.67, 110.62, 105.84, 68.42, 31.60, 29.24, 25.64, 22.64, 14.07. MS (ESI) for C$_{44}$H$_{60}$F$_6$N$_2$O$_{10}$S$_2$ [M+1]$^+$: calcd., 955.3594; found, 955.3640.
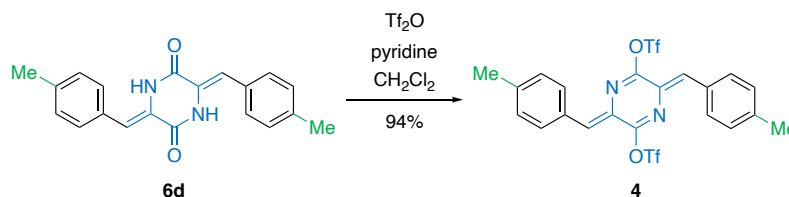


### Monomer 4

Trifluoromethanesulfonic anhydride (neat, 711.69 µL, 4.23 mmol) was added dropwise to a solution of **6d** (657.00 mg, 2.06 mmol) and pyridine (349.11 µL, 4.33 mmol) in dichloromethane (30 mL) at -78 ºC (dry ice/acetone bath). The reaction was stirred at -78 ºC for 30 mins and then slowly warmed to room temperature and stirred over 16 h. Hexanes was added to the crude reaction mixture, the precipitate was filtered, and the solid was washed with roughly 10 mL each of hexanes, water, and finally methanol to give analytically pure **4** as yellow needles (94%). $^1$H NMR (500 MHz, CDCl$_3$) δ 7.93 (d, $J$ = 8.1 Hz, 2H), 7.23 (d, $J$ = 11.7 Hz, 2H), 6.92 (s, 1H), 1.25 (s, 3H). $^{13}$C NMR (126 MHz, CDCl$_3$) δ 151.29, 142.49, 132.65, 131.02, 130.59, 129.82, 125.60, 21.92. MS (ESI) for C$_{22}$H$_{16}$F$_6$N$_2$O$_6$S$_2$ [M+1]$^+$: calcd., 583.0354; found, 583.0500.

### Crystallizations of Monomers 1-4

Nearly all crystallization conditions attempted on monomers **1-4** presented herein formed similar long aspect-ratio needle or hair-like crystals (Figure 1, Supplementary Figures 3 and 4). This consistency presents a trade-off, in that it both allows for flexibility in the chosen method of crystallization, while also restricting the morphology of the obtained crystal to a single type. A typical slow evaporation crystallization is detailed as follows. A small amount of the monomer compound was dissolved in a solvent (most commonly CH$_2$Cl$_2$, CHCl$_3$, tetrahydrofuran, or toluene) or combination thereof and filtered through a syringe filter into an aluminum foil-wrapped vial. The vial cap was slightly unscrewed and the solvent was allowed to evaporate over the course of days to weeks in the dark and protected from excessive vibrations. In general, number-averaged molecular weights and crystallinity in the polymer crystals produced from these monomer crystals both increased with higher boiling-point solvents.
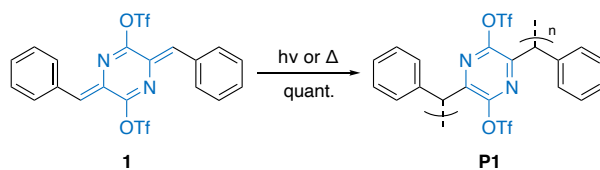
**Polymer P1**

After generating crystals of **1** via the method detailed above, the vial of crystals was sparged with N₂, recapped, the aluminum foil wrapping was removed, and the vial was placed on a sunny windowsill or under a controlled light source. After roughly three days, the crystals had converted from yellow to transparent-white, indicating the conversion to **P1**. Solid-state (CP-MAS) $^{13}$C NMR (126 MHz) δ 149.02, 146.45, 135.61, 128.95, 120.35, 117.81, 49.53.
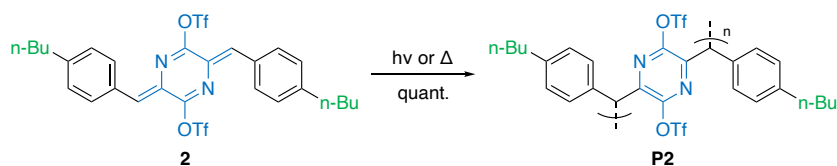


**Polymer P2**

After generating crystals of **2** via the method detailed above, the vial of crystals was sparged with N₂, recapped, the aluminum foil wrapping was removed, and the vial was placed on a sunny windowsill or under a controlled light source. After the formation of crystals, the vial was sealed, the aluminum foil was removed, and the vial was placed on a sunny windowsill. After roughly three days, the crystals had converted from yellow to transparent-white, indicating the conversion to **P2**. Solid-state (CP-MAS) $^{13}$C NMR (126 MHz) δ 148.82, 143.63, 133.64, 129.04, 120.16, 117.63, 52.16, 35.49, 22.74, 13.76.
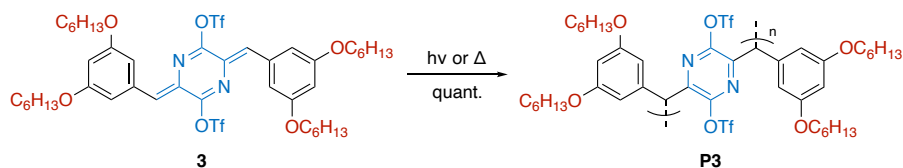


**Polymer P3**

After generating crystals of **3** via the method detailed above, the vial of crystals was sparged with N₂, recappd, the aluminum foil wrapping was removed, and the vial was placed on a sunny windowsill or under a controlled light source. After roughly three days, the crystals had converted from yellow to transparent-white, indicating the conversion to **P3**. The highest molecular weight polymer crystals of **P3** were obtained via slow evaporation from toluene of **3**, with lower molecular weight distributions produced by slow evaporation from tetrahydrofuran, chloroform, and CH₂Cl₂ (Supplementary Figure

7). In order to provide a more accurate comparison to the molecular weight distributions of **P3-A** and **P3-B**, a small amount of poly(4c) was stirred in 1,4-dioxane at 100 °C for 5 days. Afterwards, the solvent was evaporated and the polymeric product was resuspended in acetone and precipitated with water. The precipitated solution was filtered, and washed with water, methanol, hexanes, diethyl ether, and acetone before being washed through with dichloromethane (78% recovery). $^1$H NMR (500 MHz, CDCl$_3$) δ 6.60 – 5.80 (m, 3H), 4.95 (s, 1H), 3.94 – 2.99 (m, 4H), 1.78 – 1.50 (m, 4H), 1.28 (s, 12H), 0.88 (s, 6H). $^{13}$C NMR (126 MHz, CDCl$_3$) δ 160.65, 148.24, 143.55, 137.39, 119.65, 117.10, 105.64, 102.64, 67.74, 49.63, 31.70, 29.28, 25.63, 22.74, 14.10.
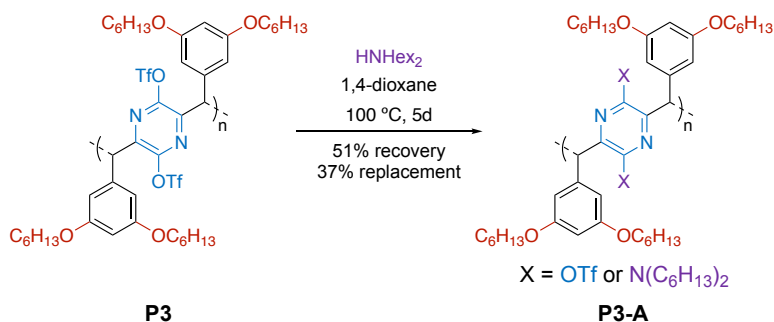


Polymer **P3-A**

Polymer **P3** (39.82 mg, 39.39 µmol) and dihexylamine (422.74 µL, 1.58 mmol) were stirred in 1,4-dioxane (5 mL) n a 1-dram vial at 100 °C for 5 days. Afterwards, the solvent was evaporated and the polymeric product was resuspended in acetone and precipitated with water. The precipitated solution was filtered, and washed with water, methanol, hexanes, diethyl ether, and acetone before being washed through with dichloromethane (51% recovery). $^1$H NMR (500 MHz, CDCl$_3$) δ 6.44 – 5.73 (m), 4.82 (m), 3.92 – 2.55 (m), 1.55 (m), 1.40 – 0.96 (m), 0.95 – 0.69 (m).
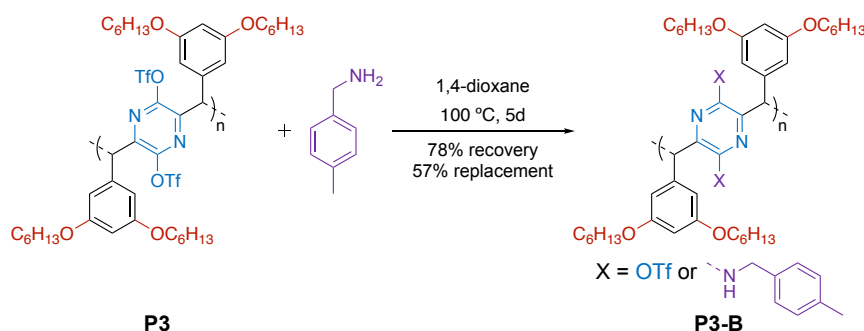


Polymer **P3-B**

Polymer **P3** (41.89 mg, 41.43 µmol) and 4-methylbenzylamine (210.97 µL, 1.66 mmol) were stirred in 1,4-dioxane (5 mL) in a 1-dram vial at 100 °C for 5 days. Afterwards, the solvent was

evaporated and the polymeric product was resuspended in acetone and precipitated with water. The precipitated solution was filtered, and washed with water, methanol, hexanes, diethyl ether, and acetone before being washed through with dichloromethane (78% recovery). ^{1}H NMR (500 MHz, CDCl$_3$) δ 7.02 (m), 6.41 – 5.88 (m), 4.70 (m), 3.51 (m), 2.45 – 2.13 (m), 1.59 (m), 1.29 (m), 1.02 – 0.74 (m).
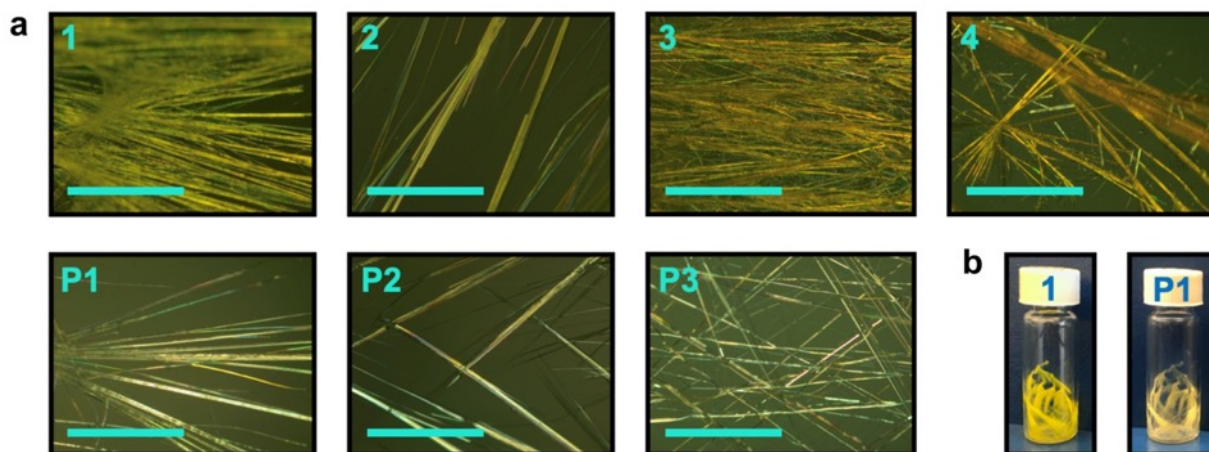
**Supplementary Figure C.3.** (**a**) Optical microscope images under 90° polarization showing the typical morphology of crystals of monomers **1**-**4** (top row) and polymers **P1**-**P3** (bottom row). Scale bar: 1 mm. (**b**) Photographs of vials containing crystals of **1** and **P1**.
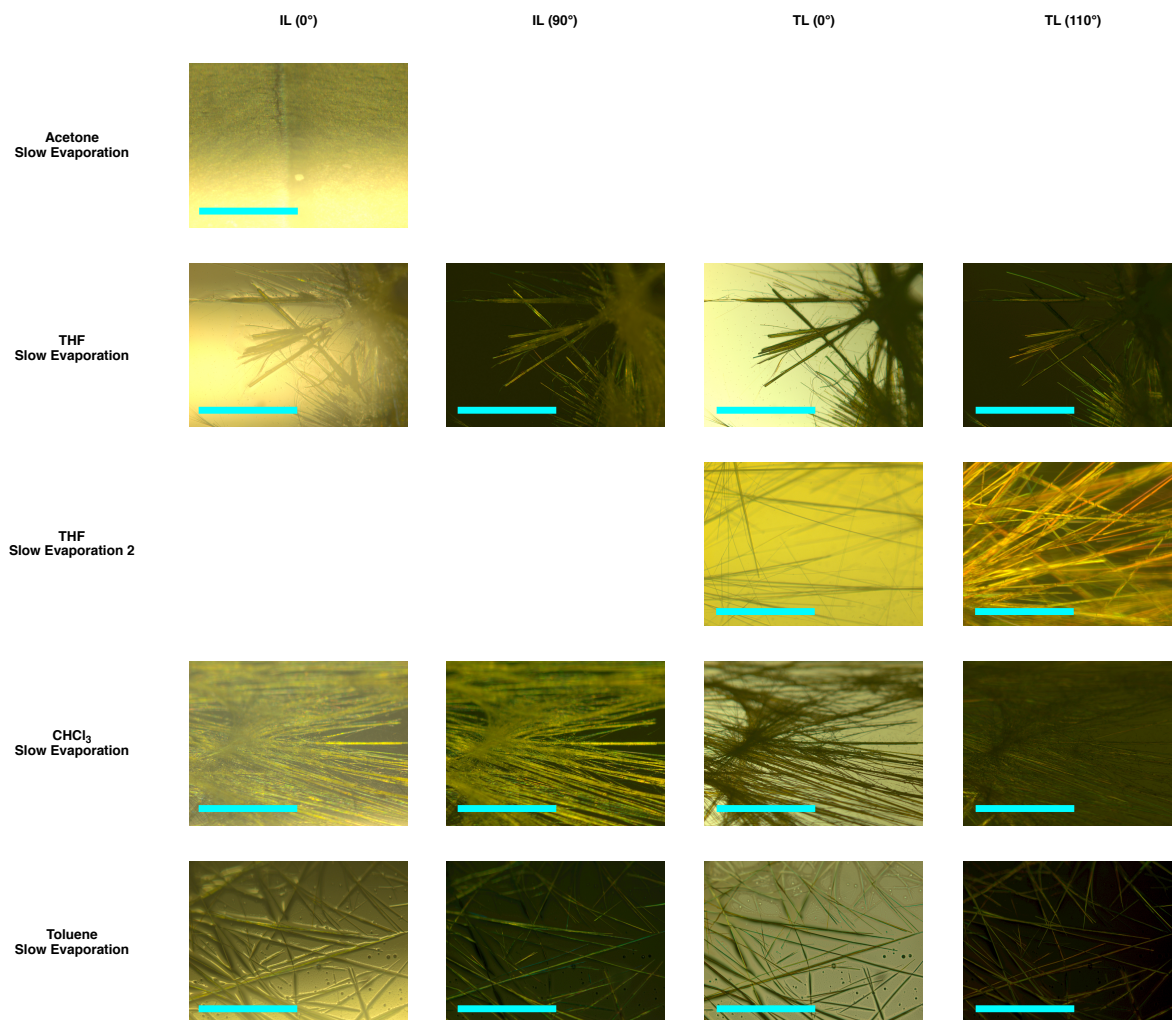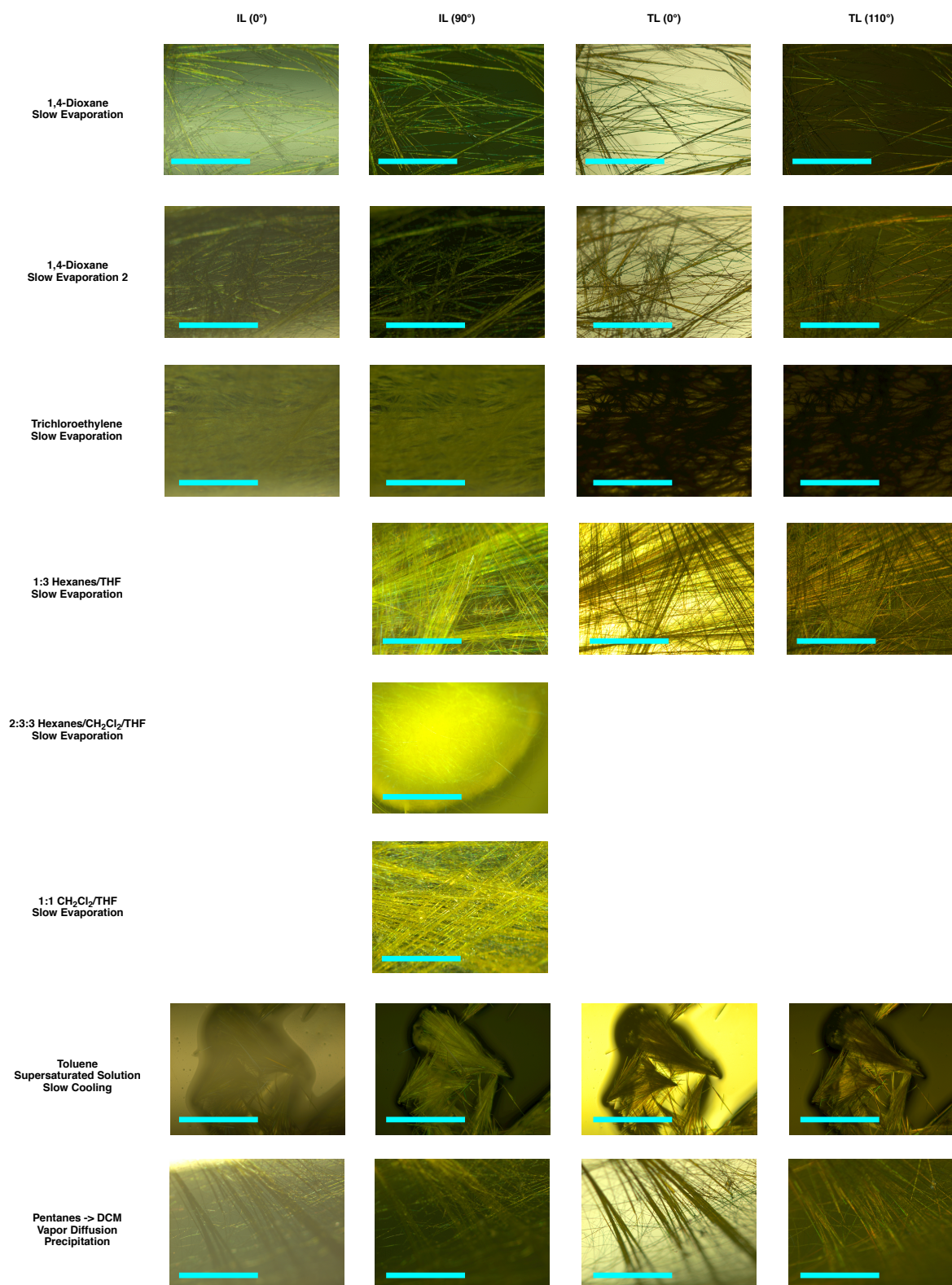
**Supplementary Figure C.4.** Optical microscope images of monomeric crystals of **1** grown under different conditions (left) obtained with either transmitted light (TL) or incident light (IL) of the given polarization. Scale bar: 1 mm
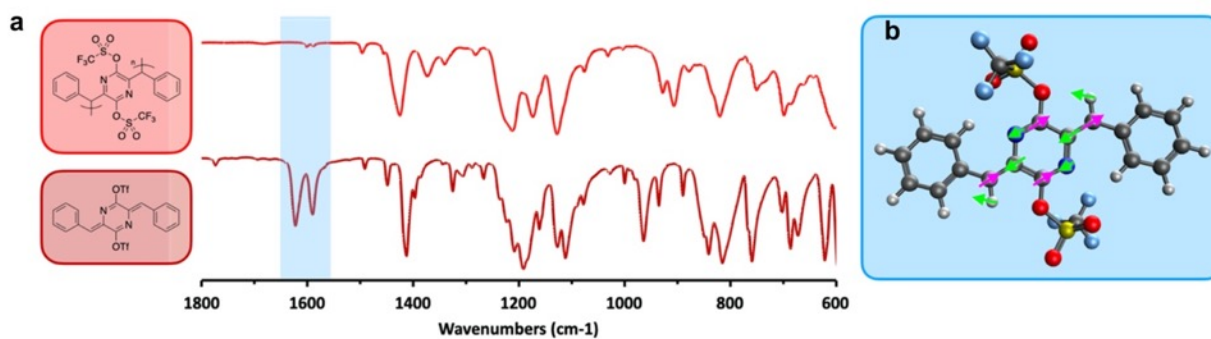
**Supplementary Figure C . 5:** Fourier-Transform Infrared Spectroscopy (FTIR) characterization  of monomer **1** and polymer **P1**. (**a**) The fingerprint regions of the FTIR traces of **1** and **P1** highlighting the disappearance of the quinoidal ring exocyclic methylene feature upon polymerization. (**b**) Computed vibrations of the quinoidal ring exocyclic methylene corresponding to the feature at 1570–1635 cm$^{-1}$ in **1** (B3LYP/6-311++G**).
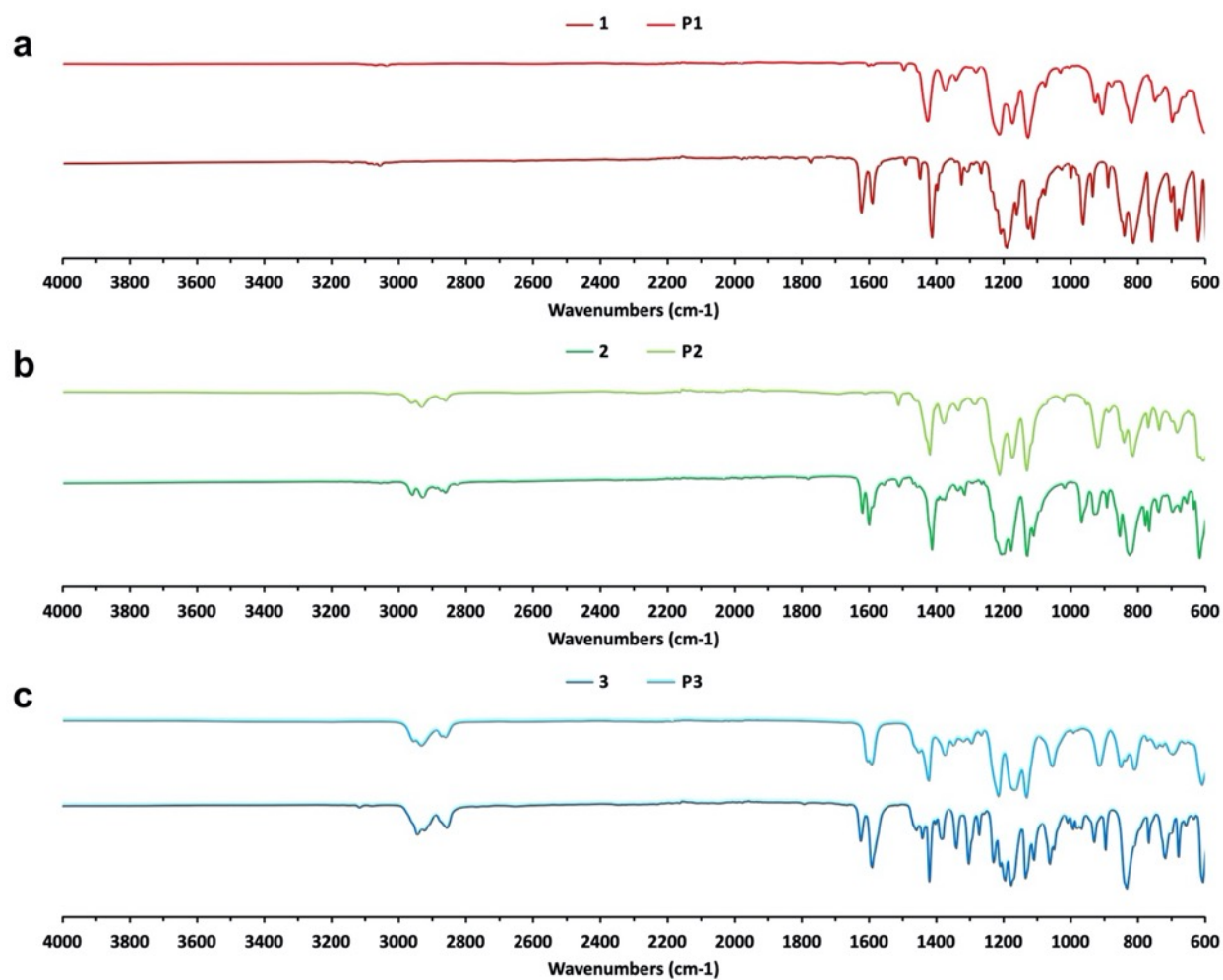
**Supplementary Figure C.6.** FTIR spectra of monomers **1**-**3** and polymers **P1**-**P3**. (**a**) FTIR of **1** vs. **P1**. (**b**) FTIR of **2** vs. **P2**. (**c**) FTIR of **3** vs. **P3**. The peak at 1600 cm$^{-1}$ in **P3** corresponds to the phenolic stretching vibration which overlaps with the exocyclic methylene vibration.
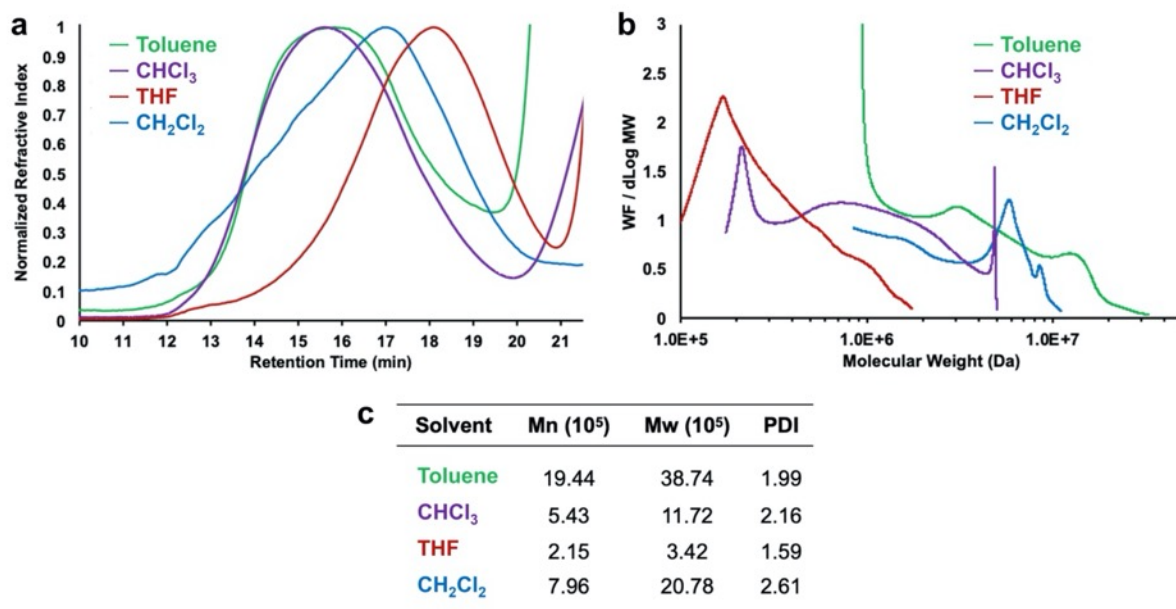
**Supplementary Figure C.7.** Molecular weight distributions of **P3** generated via crystallization from different solvents. (**a**) Size-exclusion chromatography (SEC) traces. (**b**) SEC-derived molecular weight distributions displayed on a logarithmic scale. (**c**) Molecular weight data derived from the SEC traces shown in **a**.
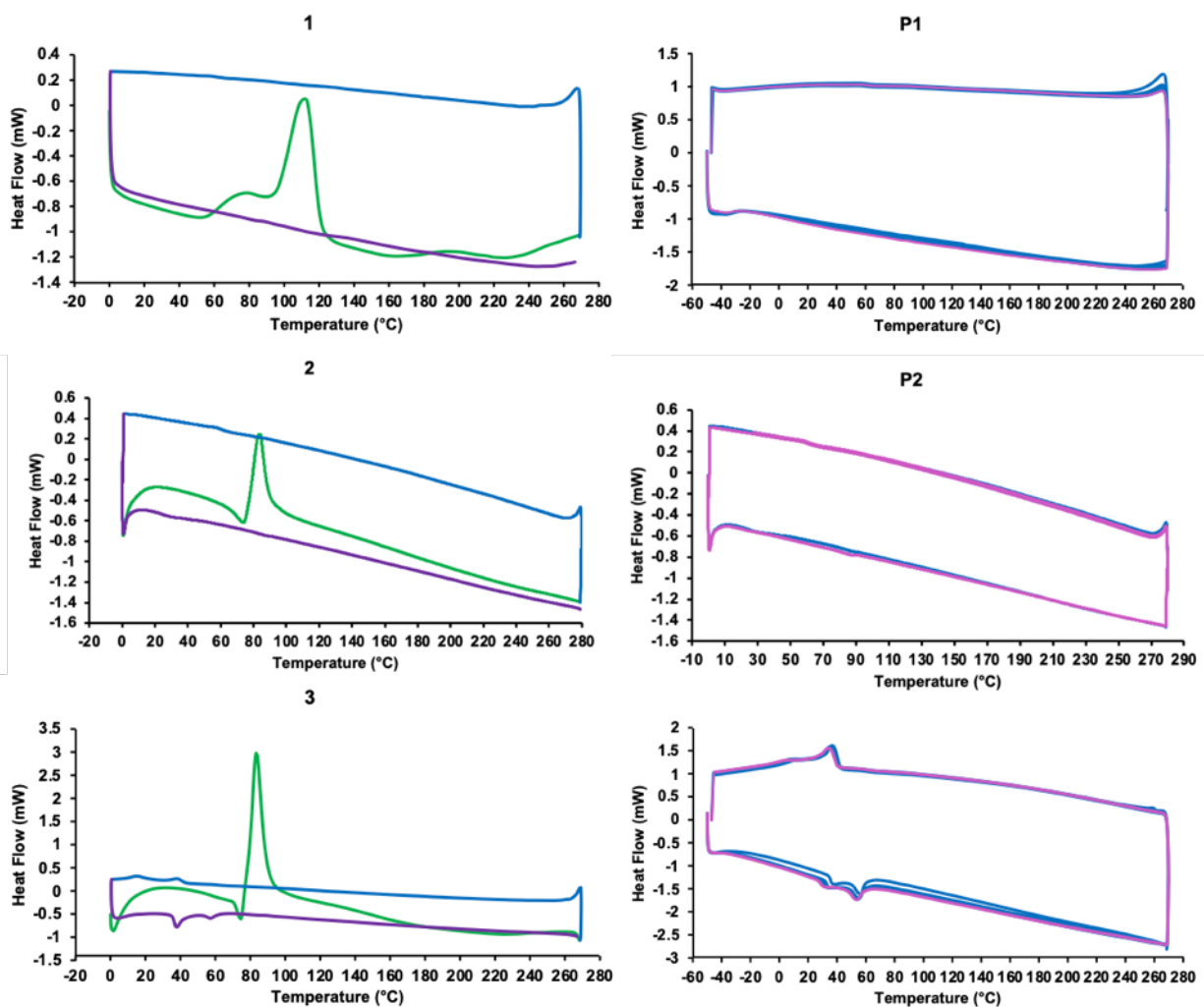
**Supplementary Figure C.8.** Differential Scanning Calorimetry (DSC) traces. The left column shows the first heating (green), first cooling (blue), and second heating (purple) scans of monomers **1**-**3**. The right column shows multiple heating and cooling cycles (blue = first four cycles, pink = final cycle) of **P1**-**P3**.
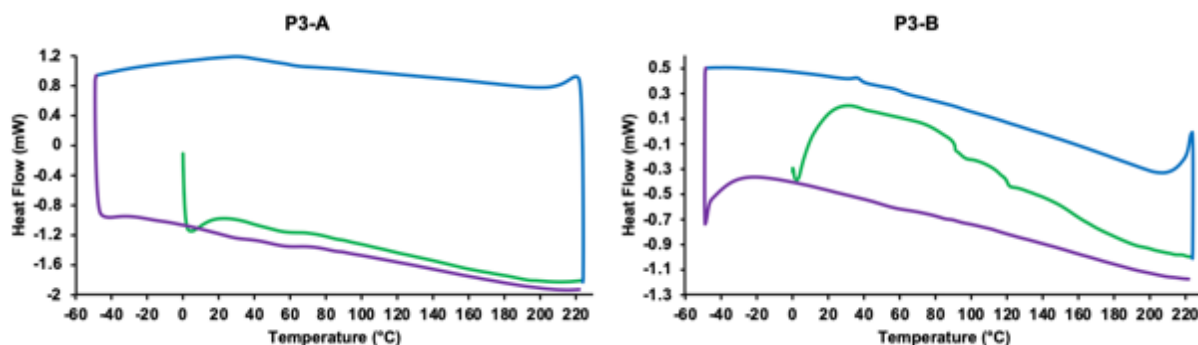
**Supplementary Figure C.9.** Differential Scanning Calorimetry (DSC) traces of post-polymerization functionalization products **P3-A** and **P3-B** showing the first heating (green), first cooling (blue), and second heating (purple) scans.
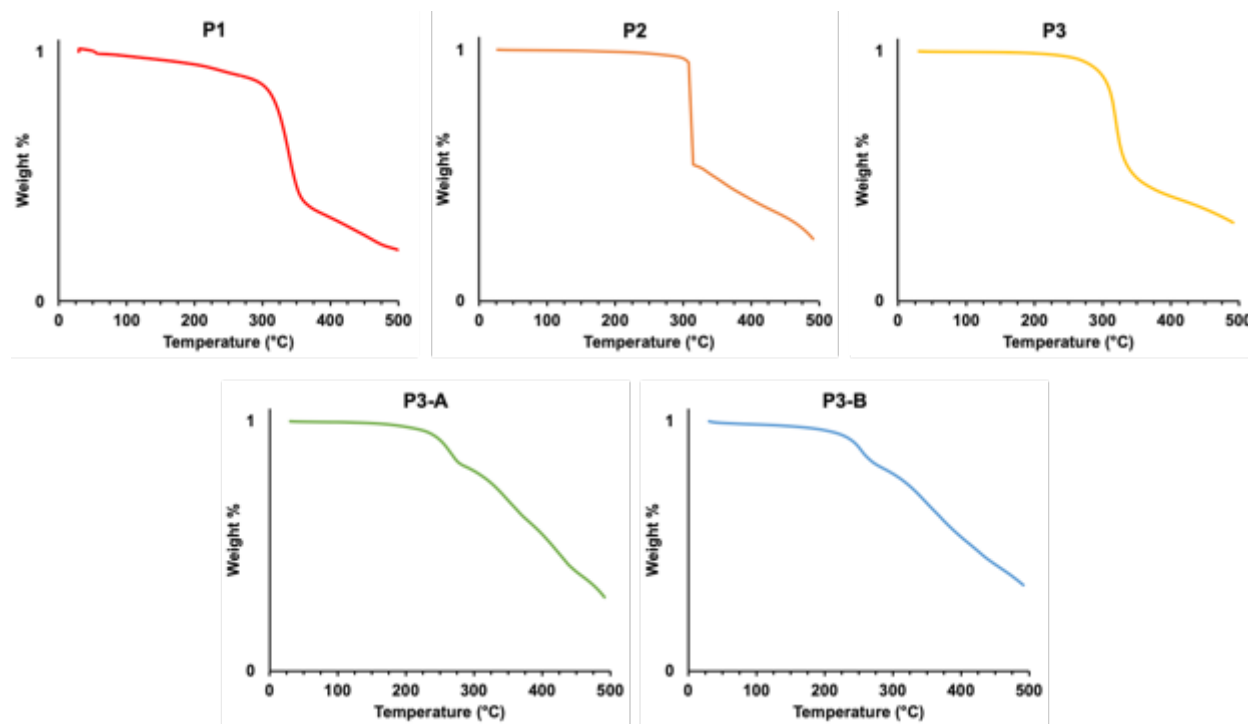


**Supplementary Figure C.10.** Thermogravimetric analysis (TGA) traces of polymers **P1**-**P3** and post-polymerization functionalized **P3-A** and **P3-B**. Note: separate TGA traces were not taken for **1**-**3** as they were expected to have polymerized during the course of temperature ramping.
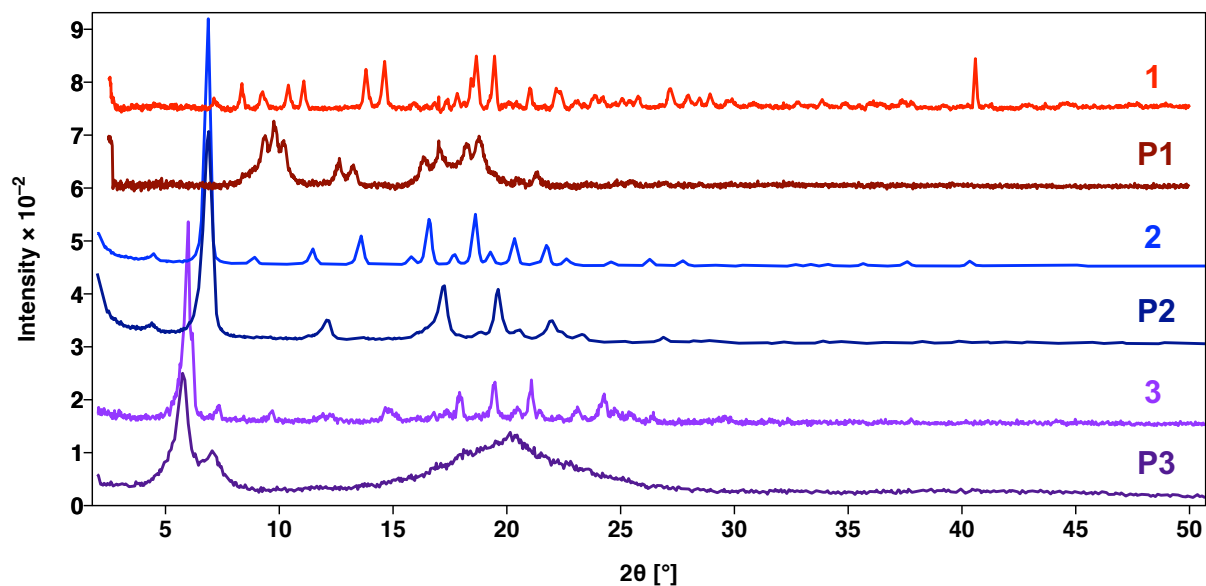
**Supplementary Figure C.11.** Powder X-ray diffraction (PXRD) traces of monomers **1-3** and polymers **P1**-**P3**. Intensity axis is scaled for each trace so as to allow for comparison of the data.
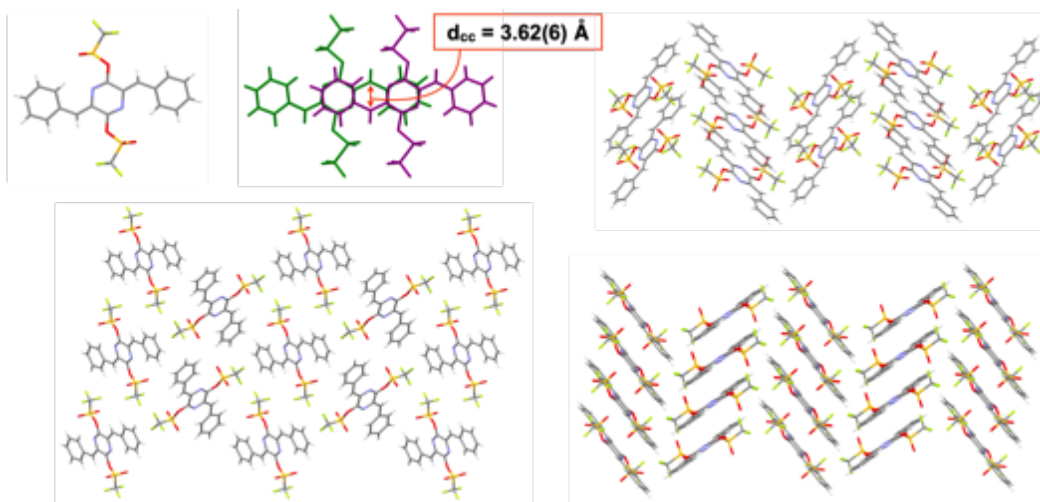


**Supplementary Figure C.12.** Stick representations of X-ray crystallographic structure of monomer **1**, showing molecular structure (top left), $d_{CC}$ distance (top middle), and three different views of molecular packing.
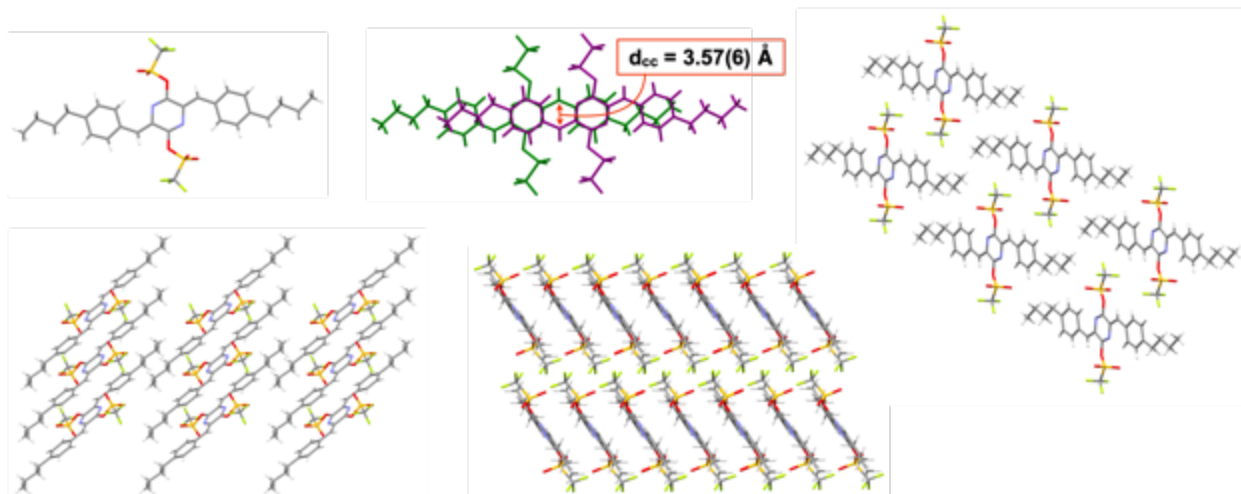
**Supplementary Figure C.13.** Stick representations of X-ray crystallographic structure of monomer **2**, showing molecular structure (top left), $d_{CC}$ distance (top middle), and three different views of molecular packing.
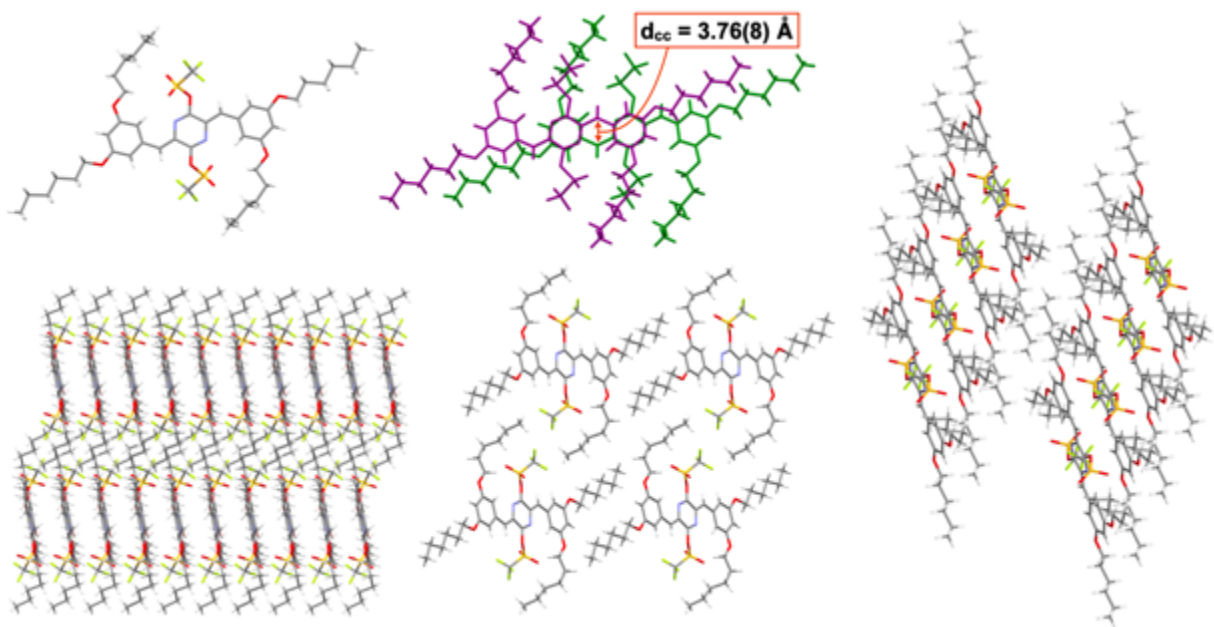


**Supplementary Figure C.14.** Stick representations of X-ray crystallographic structure of monomer **3**, showing molecular structure (top left), $d_{CC}$ distance (top middle), and three different views of molecular packing.
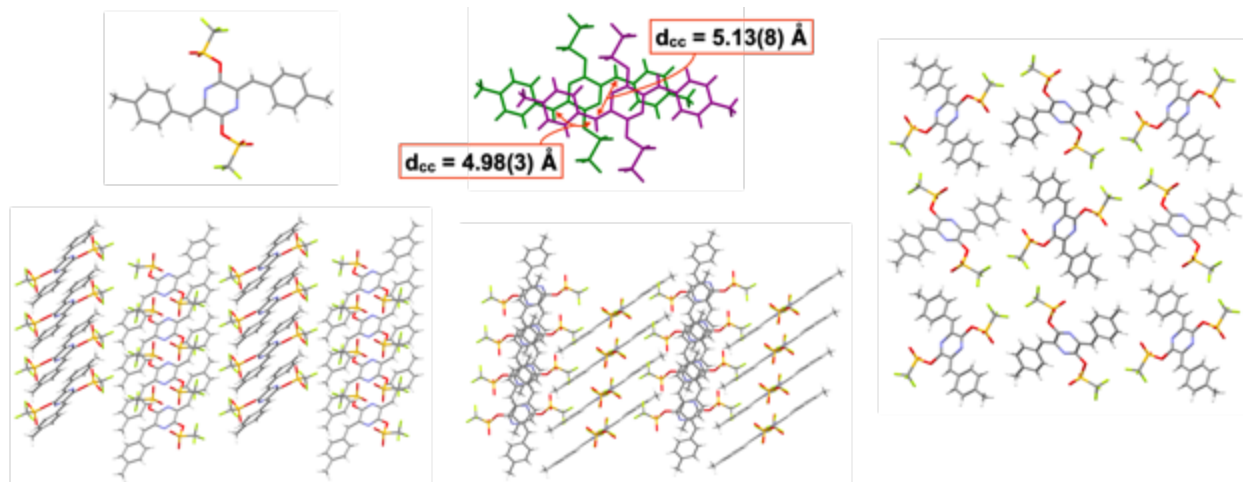
**Supplementary Figure C.15.** Stick representations of X-ray crystallographic structure of monomer **4**, showing molecular structure (top left), two possible $d_{CC}$ distances (top middle), and three different views of molecular packing.
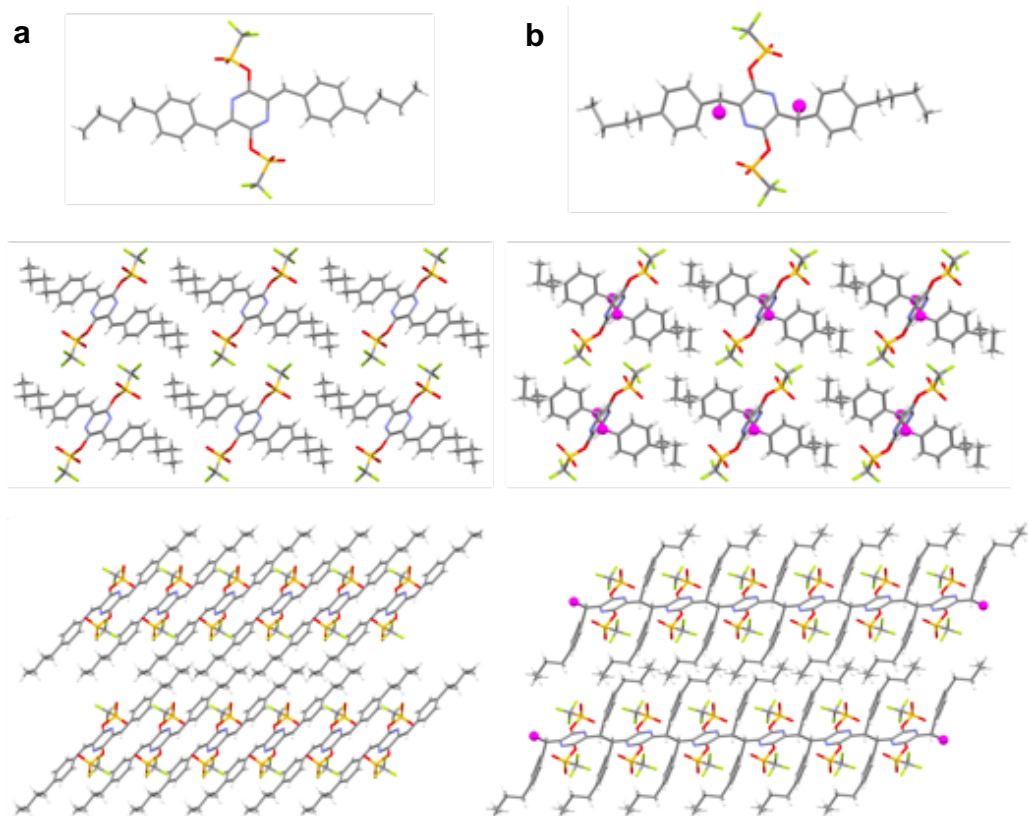


**Supplementary Figure C.16.** Stick representations of crystallographic structure of (**a**) monomer **2** (via X-ray diffraction), and (**b**) polymer **P2** (via cryoEM) showing molecular structure (left) and different views of molecular packing (right).
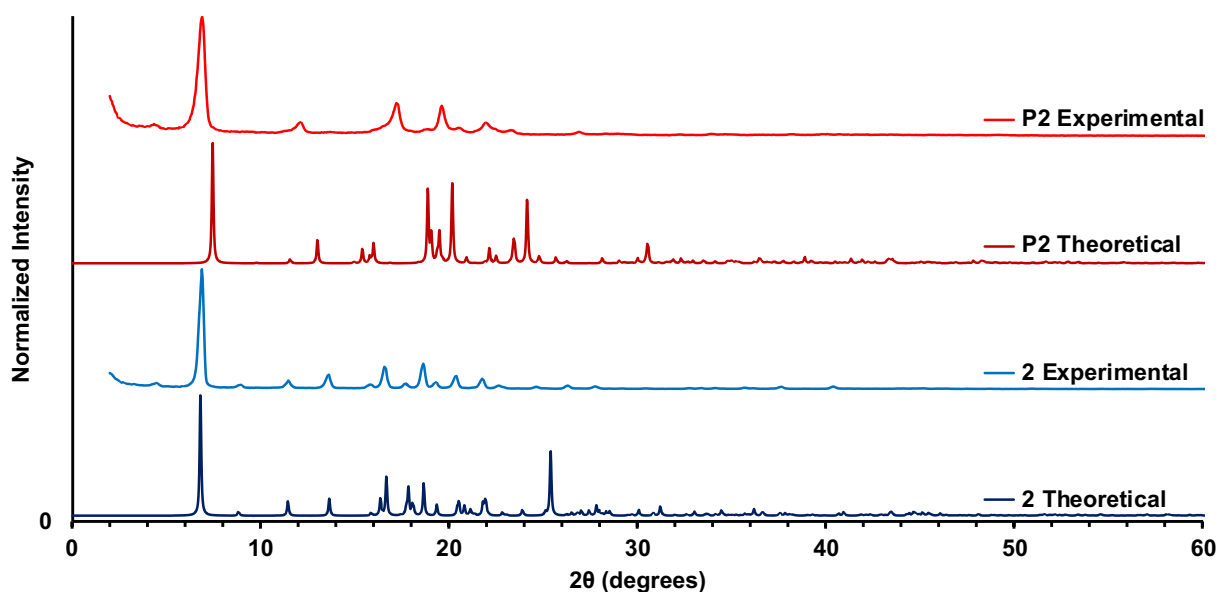
**Supplementary Figure C.17.** Experimental PXRD traces (Experimental) and PXRD traces predicted based on the obtained crystal structure of monomer **2** and cryoEM structure of polymer **P2** (Theoretical). Intensity axis is scaled for each trace so as to allow for comparison of the data. Note: The peak shifts between P2 experimental and P2 theoretical are ascribed to a temperature effect, since P2 experimental was acquired at 25 ºC while the theoretical trace was based on data acquired at –196 ºC. This temperature effect was supported by variable temperature PXRD results shown in Supplementary Figures 18 and 19.
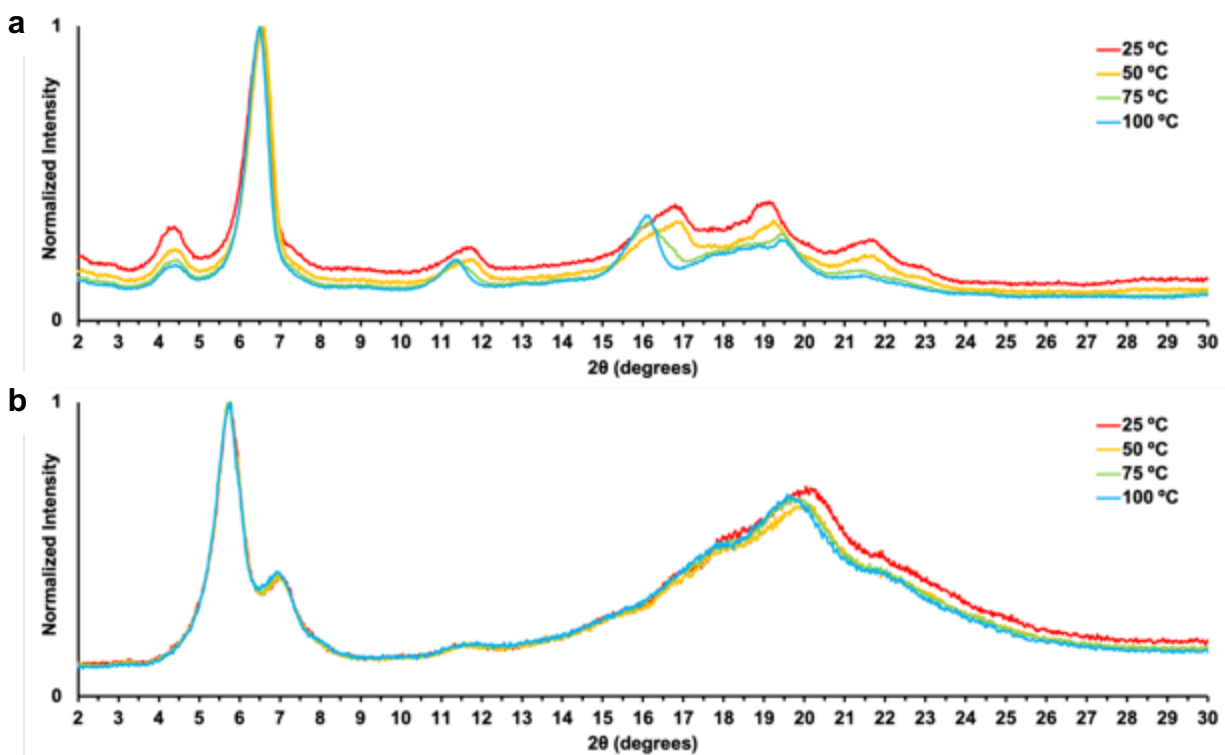
**Supplementary Figure C.18.** Effects of temperature on PXRD traces of polymers (**a**) **P2** and (**b**) **P3** showing the changes in the normalized PXRD traces of each at 25, 50, 75, and 100 °C.
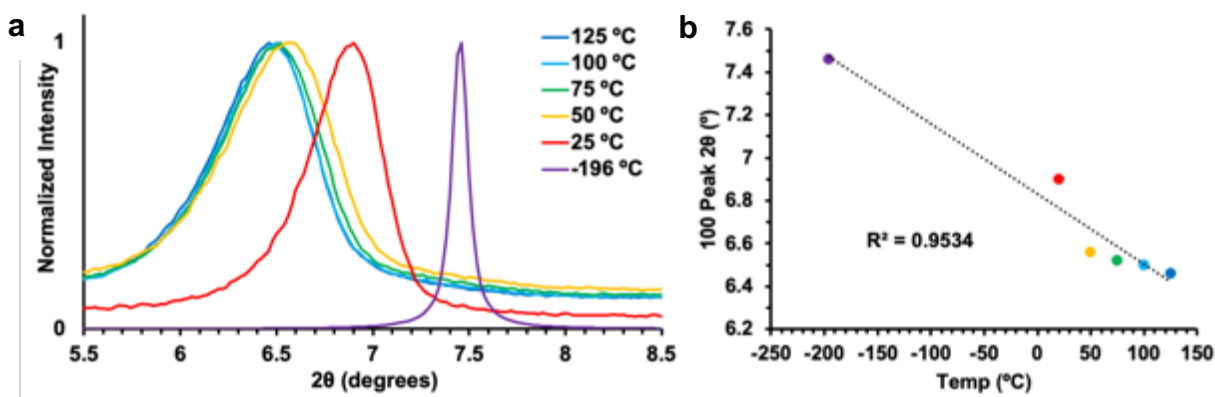


**Supplementary Figure C.19.** Effects of temperature on PXRD traces of polymer **P2**. (**a**) The 100 peak in PXRD traces taken at various different temperatures (traces at 25–125 °C are experimental, the -196 °C trace is predicted from the cryoEM structure). (**b**) The correlation between temperature and the 100 peak maximum value, showing a consistent increase of d spacing at higher temperature. A linear line is shown to indicate the trend.

**Supplementary Table C.1.** Numerical summary of X-ray crystallographic and cryoEM results for monomers **1-4** and polymer **P2**

| Compound | Space Group | Cell Lengths (Å) | Cell Angles (°) | Cell Volume (Å) | $d_{CC}$ (Å) | R factor (%) |
|---|---|---|---|---|---|---|
| **1** | P-1 | a: 5.5195(3)<br>b: 10.6780(5)<br>c: 19.1750(9) | α: 101.861(2)<br>β: 94.954(2)<br>γ: 95.245(2) | 1094.93(9) | 3.62(6) | 4.30 |
| **2** | P-1 | a: 5.5851(5)<br>b: 10.319(1)<br>c: 13.0045(13) | α: 92.459(4)<br>β: 92.246(4)<br>γ: 103.837(4) | 726.12(12) | 3.57(6) | 6.25 |
| **P2** | P-1 | a: 6.080(5)<br>b: 9.450(4)<br>c: 12.390(12) | α: 92.35(7)<br>β: 105.49(16)<br>γ: 105.58(11) | 655.9(11) | 1.50(2) | 18.62 |
| **3** | P-1 | a: 5.4708(7)<br>b: 14.4268(18)<br>c: 15.2986(19) | α: 73.767(5)<br>β: 85.910(5)<br>γ: 87.203(5) | 1155.8(3) | 3.76(8) | 6.36 |
| **4** | P 42/n | a: 22.0352(13)<br>b: 22.0352(13)<br>c: 4.8929(4) | α: 90<br>β: 90<br>γ: 90 | 2375.8(3) | 4.89(3)[a]<br>5.13(8)[a] | 3.85 |

[a]Different $d_{CC}$ values can be obtained depending on which methylene carbons are assumed to react with each other
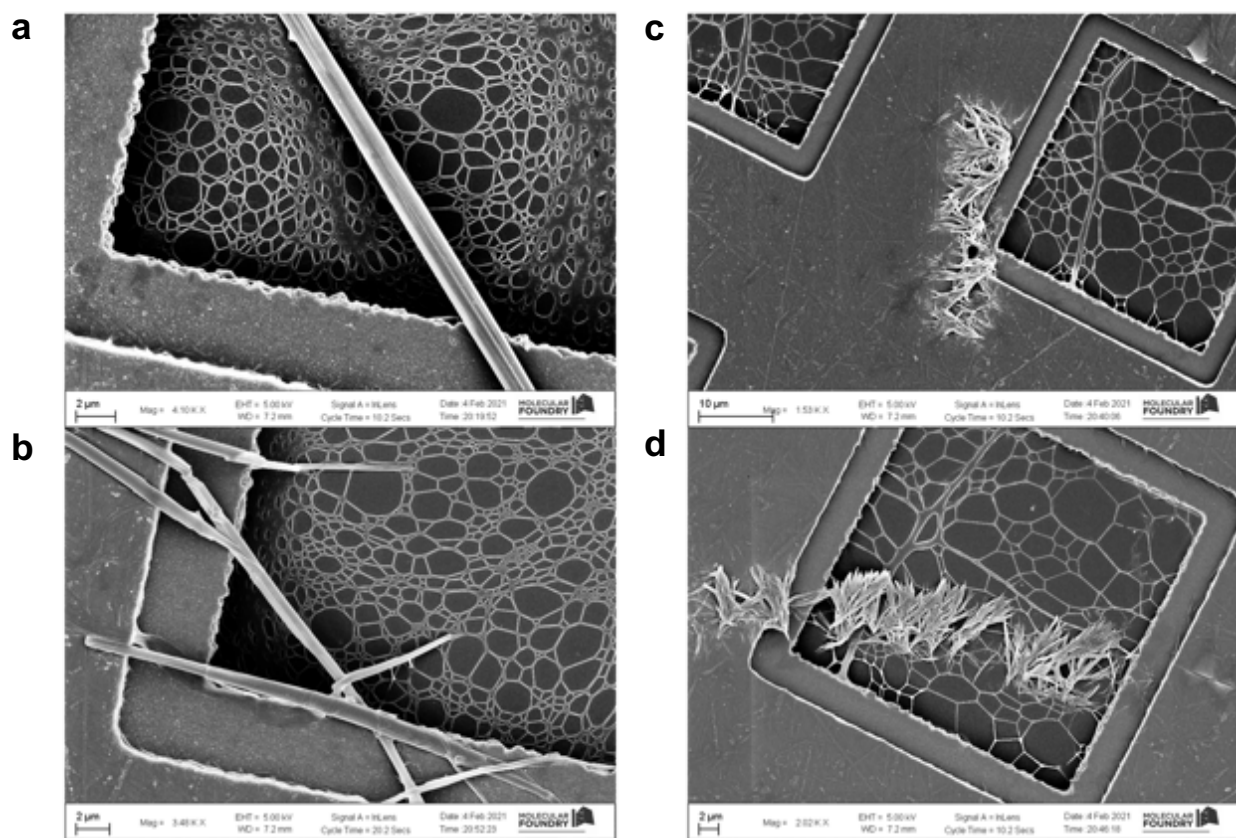
**Supplementary Figure C.20.** Scanning electron microscopy (SEM) images of crystals of **P2**, generated from crystals of monomer **2** deposited on TEM grids via dip-coating from (**a**, **b**) chloroform, and (**c**, **d**) dichloromethane and polymerized on the grids. See Supplementary Figure 1 for microcrystal deposition process.

**CH₂Cl₂**  **THF**  **CHCl₃**
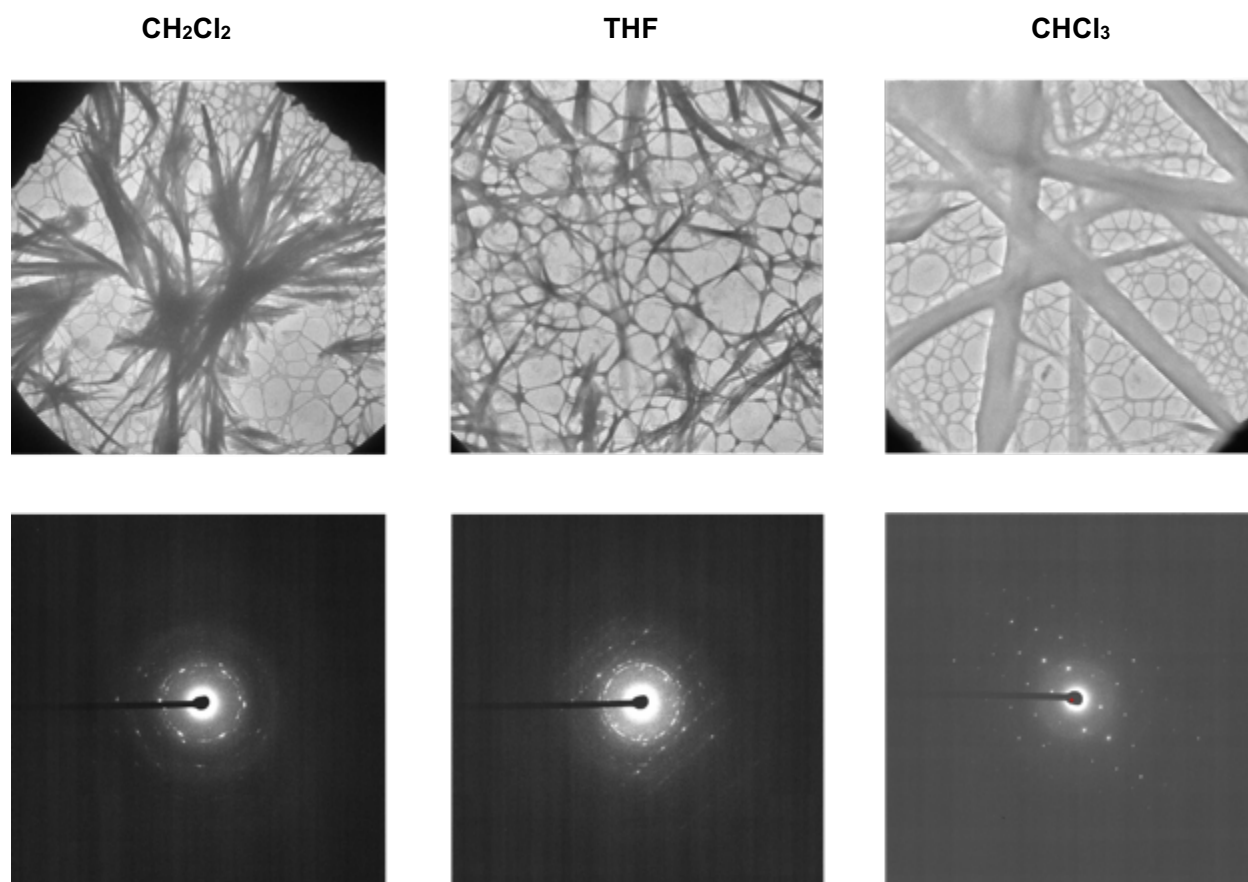


**Supplementary Figure C.21.** Transmission electron microscopy (TEM) images of crystals of **P2** (top) and representative electron diffraction patterns from each (bottom). **P2** crystals were generated from crystals of monomer **2** deposited on TEM grids via dip-coating from dichloromethane (CH₂Cl₂), tetrahydrofuran (THF), and chloroform (CHCl₃). See Supplementary Figure 1 for microcrystal deposition process.
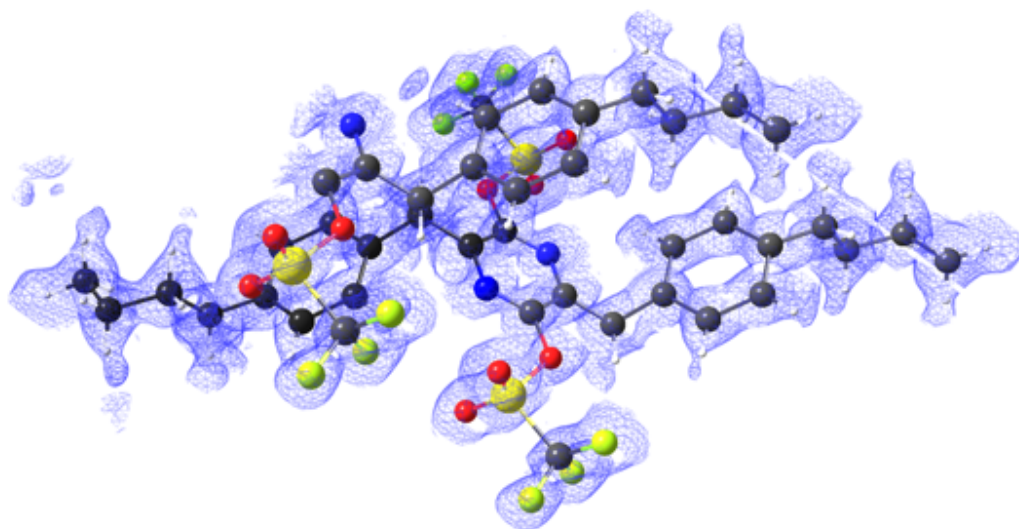
**Supplementary Figure C.22.** CryoEM-derived 3D electron density map with the unit cell of the polymeric **P2** structure obtained therefrom shown within it.
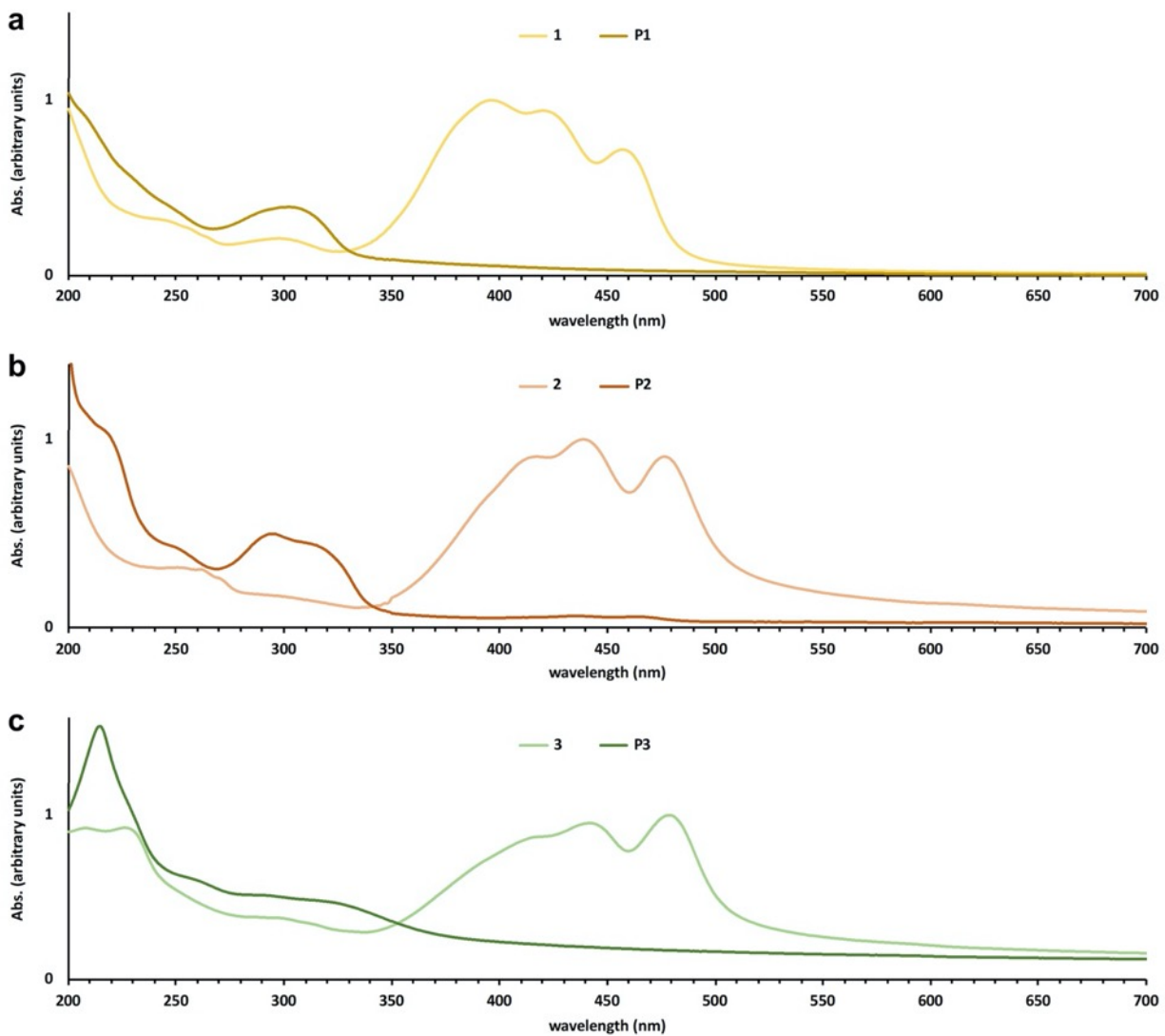
**Supplementary Figure C.23.** UV-Visible absorption spectra of films of (**a**) **1** and **P2**, (**b**) **2** and **P2**, and (**c**) **3** and **P3** on quartz substrates.
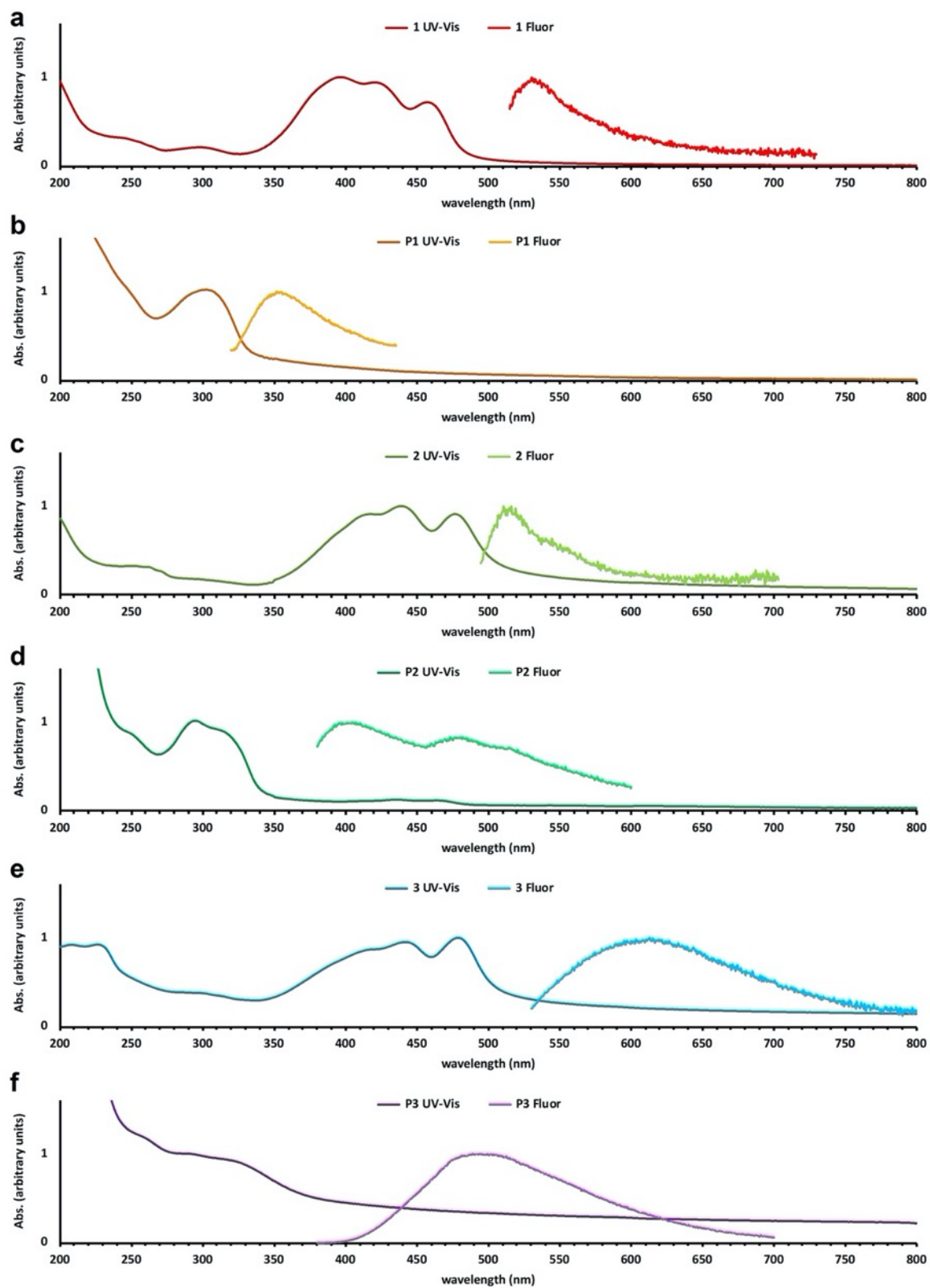
**Supplementary Figure C.24.** UV-Visible absorption and fluorescence spectra of solutions of (**a**) **1**, (**c**) **2**, (**e**) **3** (solvent: CH₂Cl₂) and films of (**b**) **P1**, (**d**) **P2**, and (**f**) **P3**.
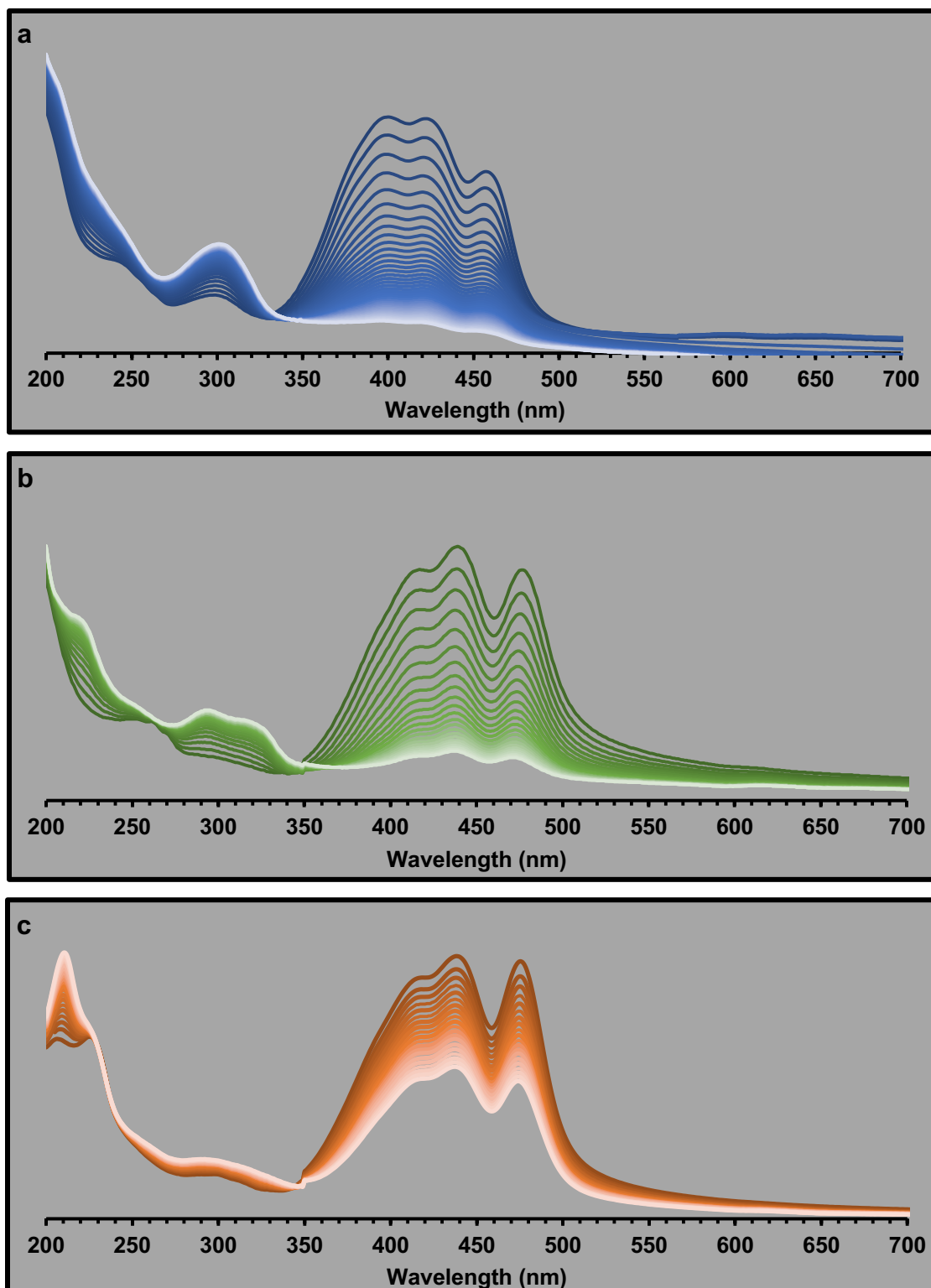
**Supplementary Figure C.25.** UV-Vis scanning kinetics experiment run on films of (**a**) **1**, (**b**) **2**, and (**c**) **3** on quartz substrates showing the (partial) conversion from monomer (blue, green, or orange) to polymer (white) over roughly 8 hours at room temperature and protected from ambient light.
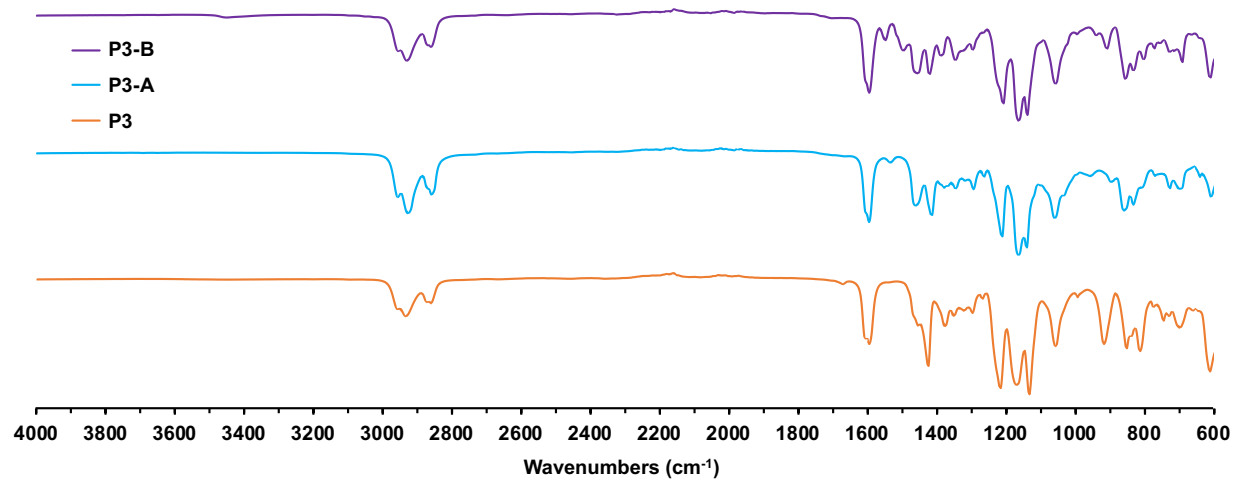
**Supplementary Figure C.26.** FTIR spectra of **P3**, **P3-A**, and **P3-B**.
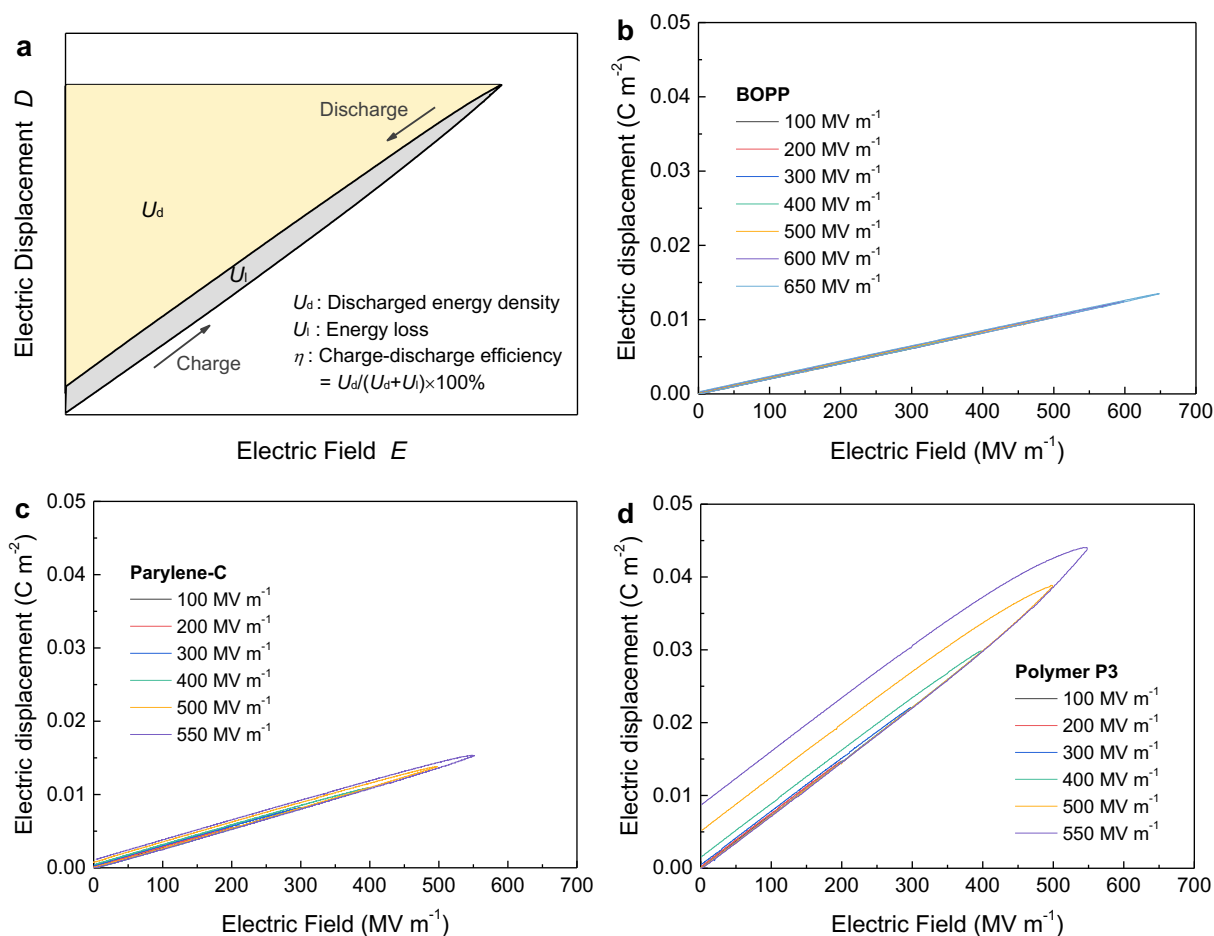
**Supplementary Figure C.27.** Electric displacement–electric field ($D$–$E$) loops of dielectric polymers described herein (**a**) Schematic $D$–$E$ loop of a linear dielectric material with the discharged energy density ($U_d$) represented by the yellow region and energy loss ($U_l$) indicated by the gray region. The total charged energy density equals $U_e$ plus $U_l$, and the charge–discharge efficiency ($\eta$) can be calculated by $\eta = U_d/(U_d+U_l) \times 100\%$.[14] Unipolar $D$–$E$ loops of (**b**) BOPP, (**c**) parylene-C, and (**d**) polymer **P3**. The effective $K$ values were determined from the slope in the linear range of the $D$–$E$ loops (*i.e.*, at 200 MV m$^{-1}$), which amounted to 2.29, 2.87 and 8.14 for BOPP, parylene-C and polymer **P3**, respectively.[15]
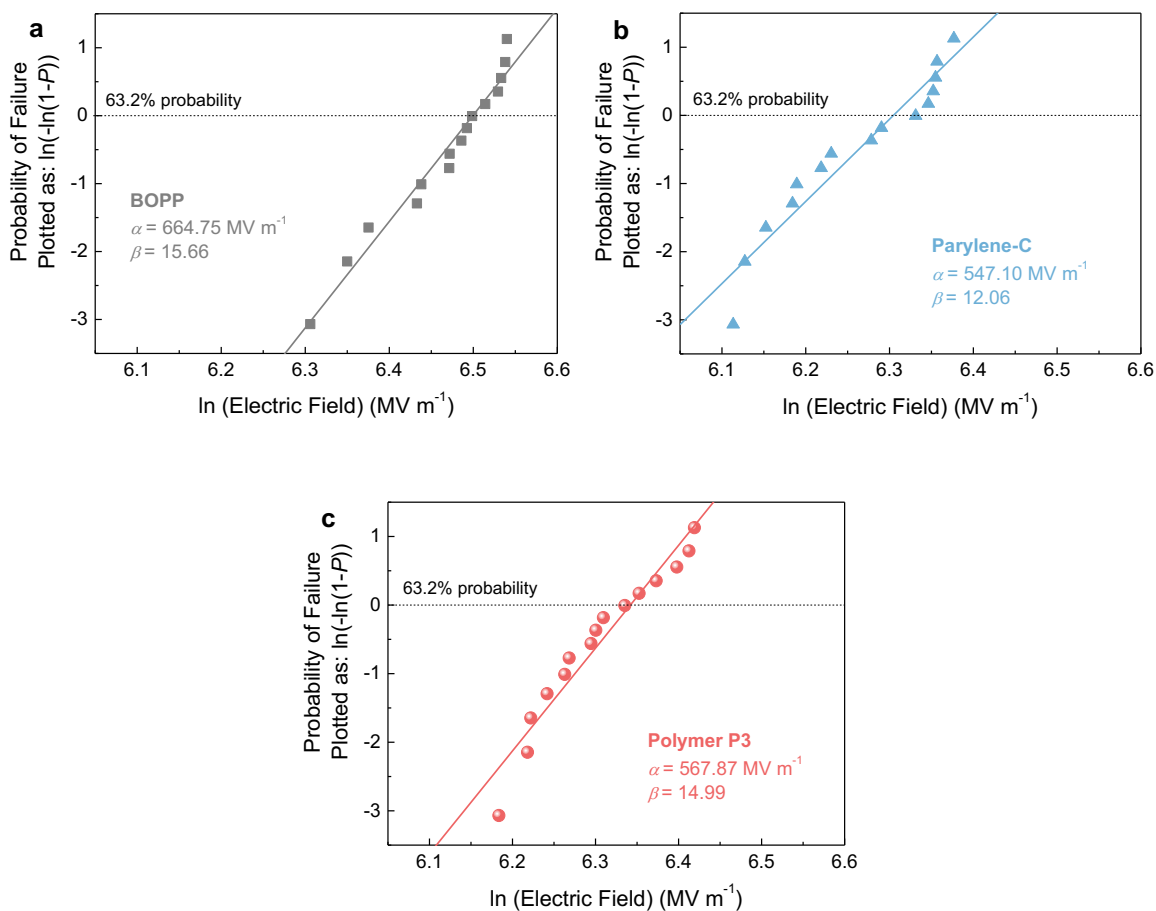
**Supplementary Figure C.28.** Weibull plots of dielectric breakdown strength for (**a**) BOPP, (**b**) parylene-C, and (**c**) polymer **P3**. The fitting model is based on a two-parameter Weibull statistic that can be described as

$$P(E) = 1 - \exp(-(E/\alpha)^{\beta}) \tag{S1}$$

where $P(E)$ is the cumulative probability of dielectric failure, $E$ is the measured dielectric breakdown field, the scale parameter $\alpha$ is the characteristic breakdown strength which corresponds to a failure probability of 63.2%, the shape parameter $\beta$ is associated with the scatter of data. A higher $\beta$ value refers to a narrower data spread. The $\beta$ values of BOPP, parylene-C, and polymer **P3** range from 12 to 16, signifying the relatively high dielectric reliability of these polymers. At least 15 measurements were performed for each Weibull fitting.
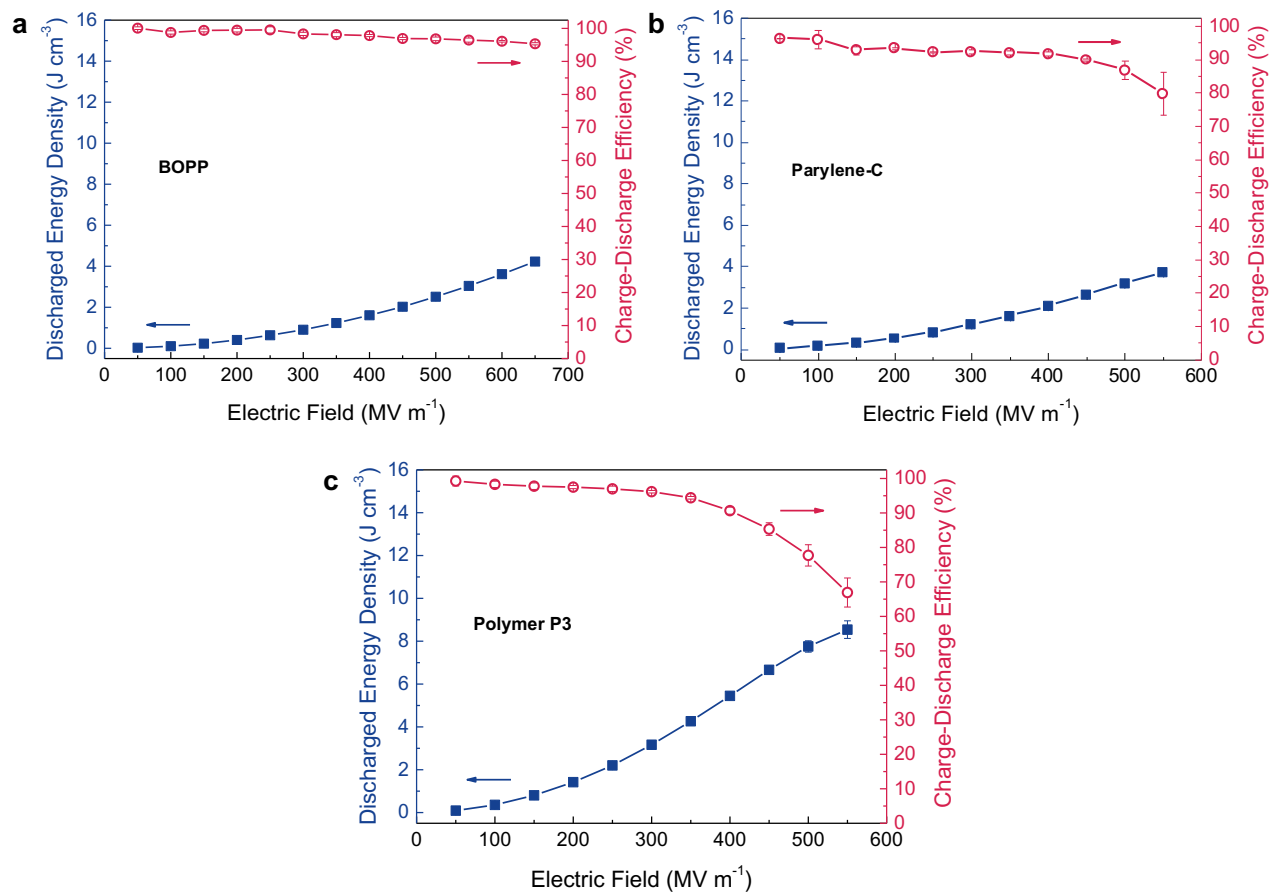
**Supplementary Figure C.29.** Discharged energy density and charge–discharge efficiency plots as a function of electric field for (**a**) BOPP, (**b**) parylene-C, and (**c**) polymer **P3**.
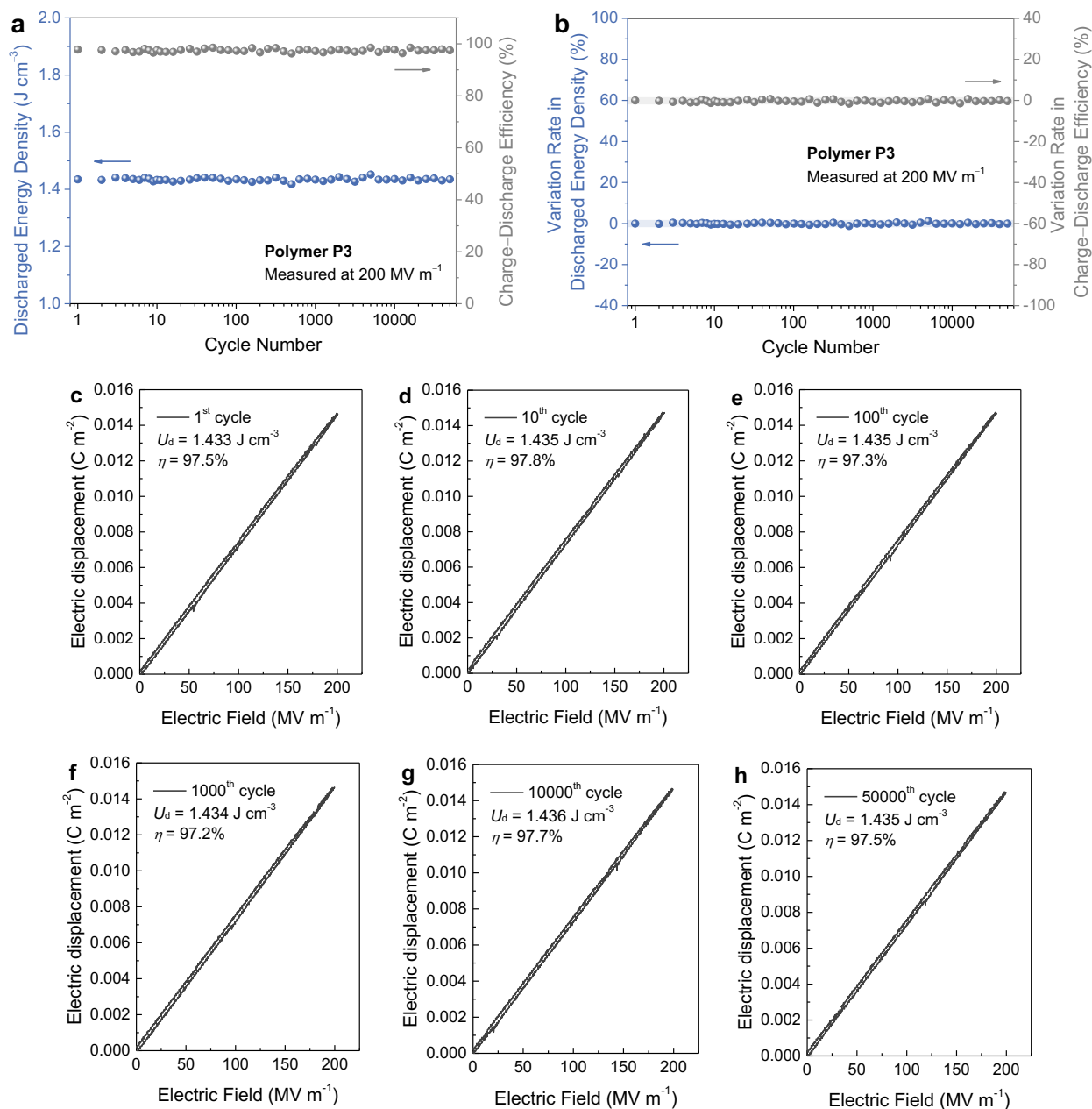
**Supplementary Figure C . 30.** Cyclability studies on polymer **P3**-based thin-film capacitors. (**a**) Discharged energy density and charge–discharge efficiency. (**b**) Variation rate in discharged energy density and charge–discharge efficiency of polymer **P3** as a function of cycle numbers obtained from 50,000 consecutive charge–discharge cycles. (**c-h**) *D–E* loops of polymer **P3** at 200 MV m$^{-1}$ for the 1$^{st}$, 10$^{th}$, 100$^{th}$, 1,000$^{th}$, 10,000$^{th}$, and 50,000$^{th}$ cycles, respectively.

The variation rate ($R_v$) of discharged energy density or charge–discharge efficiency is described as

$$R_v = |(U_{di} - U_{d1}) / U_{d1}| \tag{C.2}$$

or

$$R_v = |(\eta_i - \eta_1) / \eta_1| \tag{C.3}$$

where $U_{d1}$ is the discharged energy density and $\eta_1$ is the charge–discharge efficiency of the 1$^{st}$ cycle, $U_{di}$ is the discharged energy density and $\eta_i$ is the charge–discharge efficiency of the $i^{th}$ cycle, $i$ refers to the number of charge-discharge cycles. The variation rate in discharged energy density is < 1.2% while that in charge–discharge efficiency is < 1.6%, corresponding to outstanding device cyclability under a high electric field.
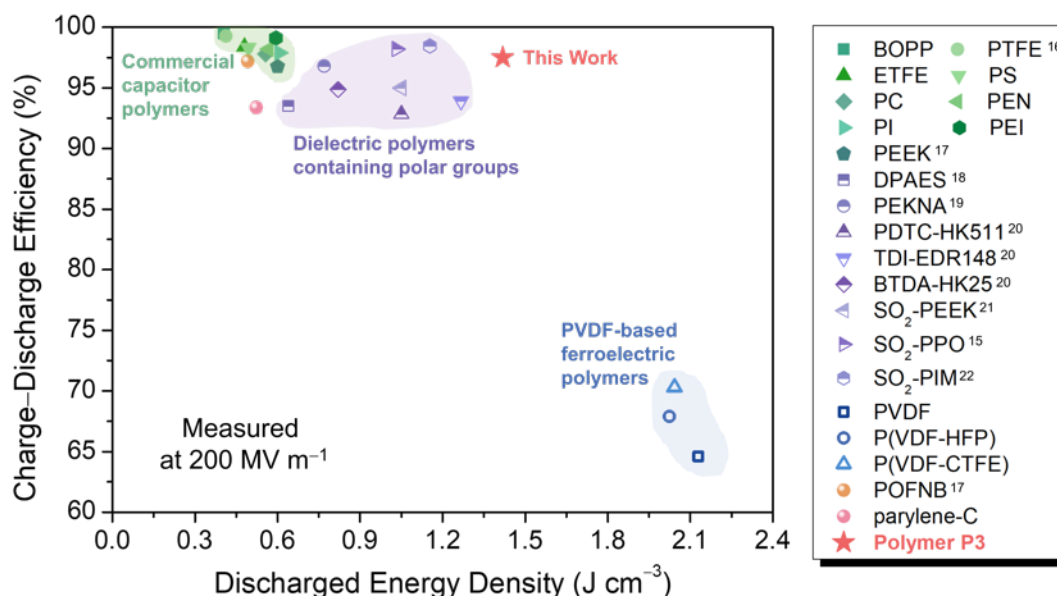
**Supplementary Figure C.31.** Capacitive performance comparison amongst dielectric polymers at 200

MV m$^{-1}$. Note that all the dielectric polymers are measured at 200 MV m$^{-1}$ with a frequency of 100 Hz except for SO$_2$-PEEK (10 Hz), SO$_2$-PPO and SO$_2$-PIM (1000 Hz).

BOPP: biaxially-oriented polypropylene
PTFE: polytetrafluoroethylene[16]
ETFE: ethylene tetrafluoroethylene
PS: polystyrene
PC: polycarbonate
PEN: poly(ethylene 2,6-naphthalate)
PI: polyimide
PEI: poly(ether imide)
PEEK: polyether ether ketone[17]
DPAES: poly(aryl ether sulfone)[18]
PEKNA: poly(naphthalene ether ketone amide)[19]
PDTC-HK511: polythiourea synthesized from *para*-phenylene diisothiocyanate (PDTC) and Jeffamine HK511[20]
TDI-EDR148: polyurea synthesized from toluene-2,4-diisocyanate (TDI) and Jeffamine EDR148[20]
BTDA-HK25: polyimide synthesized from 3,3',4,4'-benzophenone tetracarboxylic dianhydride (BTDA), Jeffamine HK511 and hexane-1,6-diamine (HDA)[20]
SO$_2$-PEEK: sulfonylated poly(ether ether ketone)[21]
SO$_2$-PPO: sulfonylated poly(2,6-dimethyl-1,4-phenylene oxide)[15]
SO$_2$-PIM: sulfonylated polymers of intrinsic microporosity[22]
PVDF: poly(vinylidene fluoride)
PVDF-HFP: poly(vinylidene fluoride-*co*-hexafluoropropylene)
PVDF-CTFE: poly(vinylidene fluoride-*co*-chlorotrifluoroethylene)
POFNB: polyoxafluoronorbornene[17]
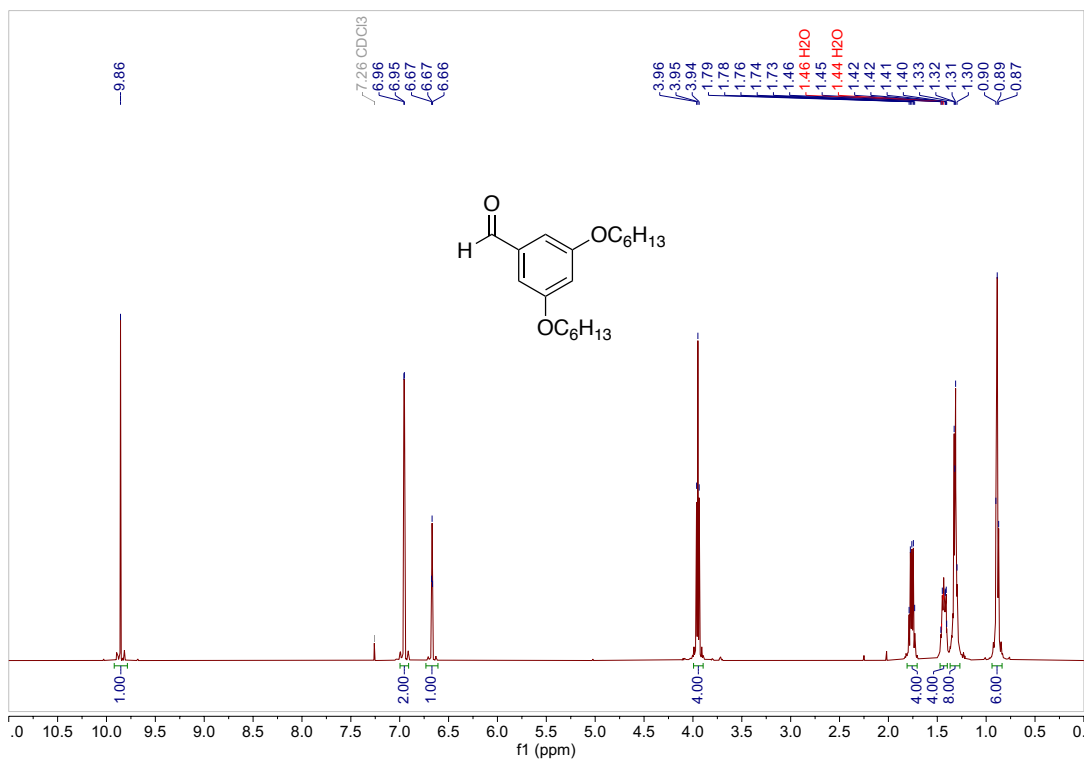
**Supplementary Figure C.32.** $^1$H NMR Spectrum of 3,5-bis(hexyloxy)benzaldehyde (CDCl$_3$, 298K).
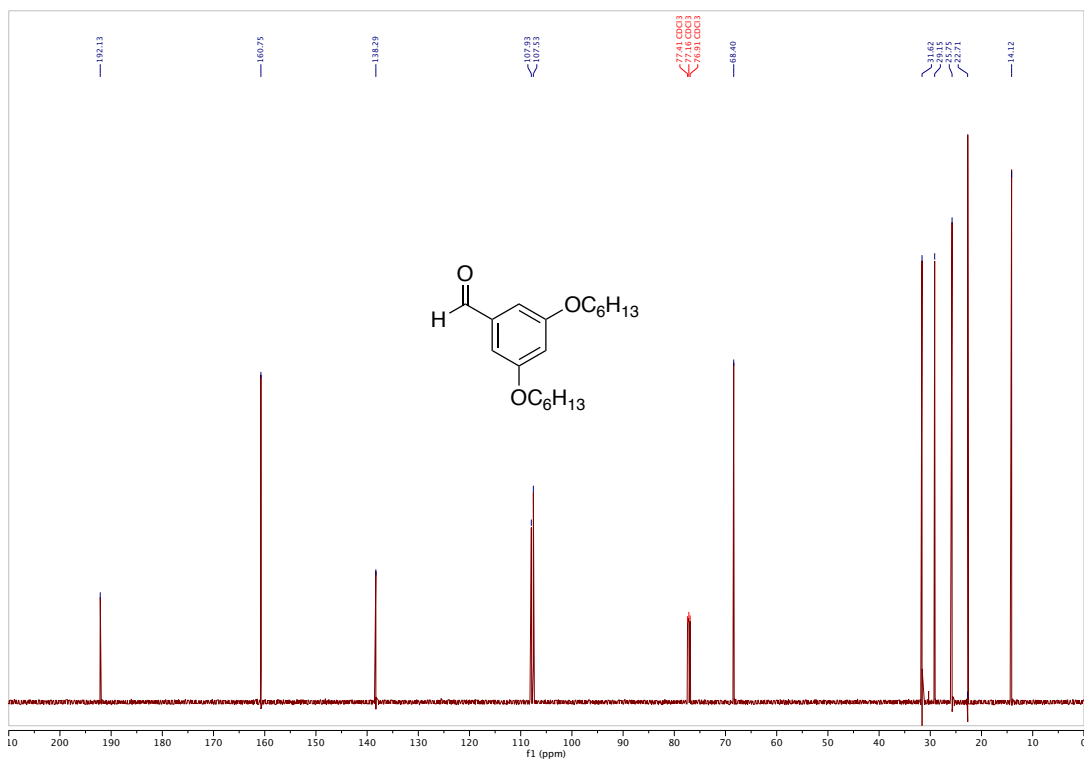


**Supplementary Figure C.33.** $^{13}$C NMR Spectrum of 3,5-bis(hexyloxy)benzaldehyde (CDCl$_3$, 298K).
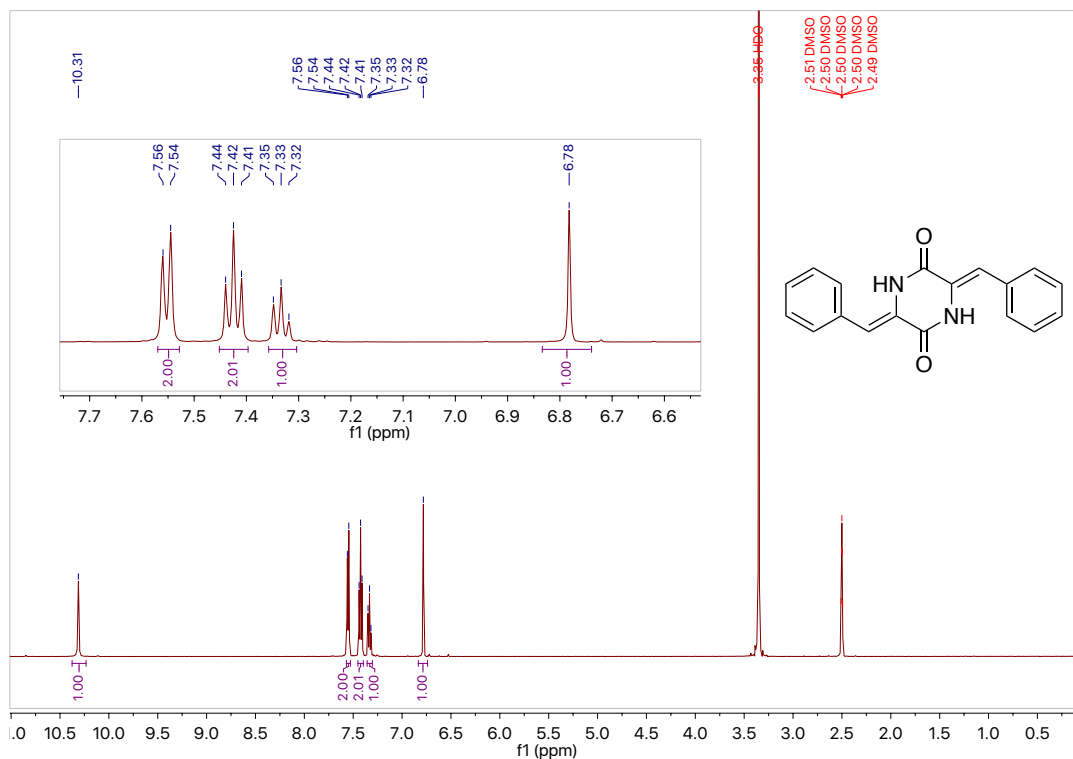
**Supplementary Figure C.34.** $^1$H NMR Spectrum of compound **6a** (DMSO-d$_6$, 298K).
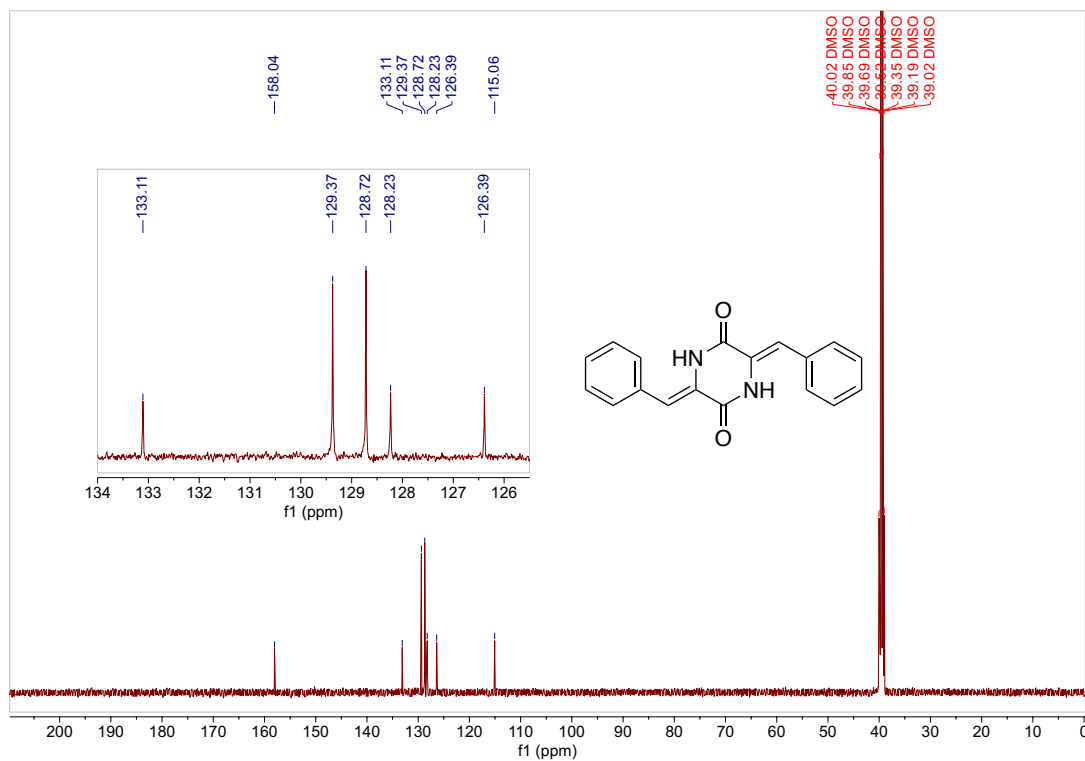


**Supplementary Figure C.35.** $^{13}$C NMR Spectrum of compound **6a** (DMSO-d$_6$, 298K).
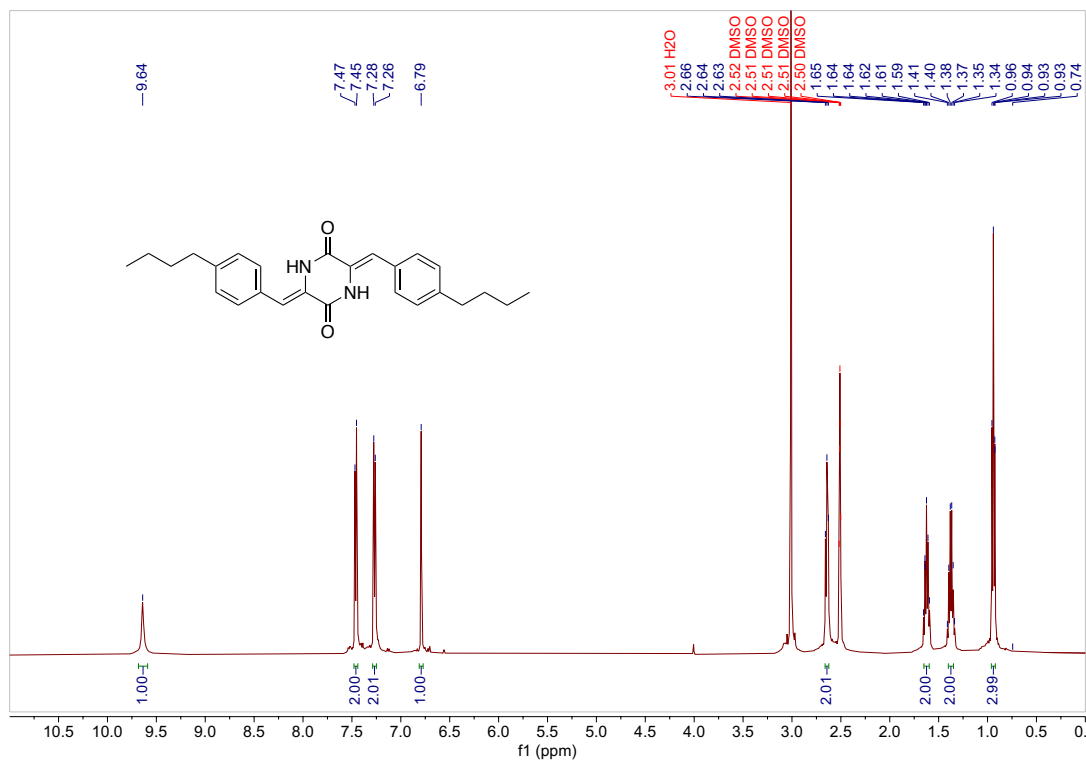
**Supplementary Figure C.36.** $^1$H NMR Spectrum of compound **6b** (DMSO-d$_6$, 298K).
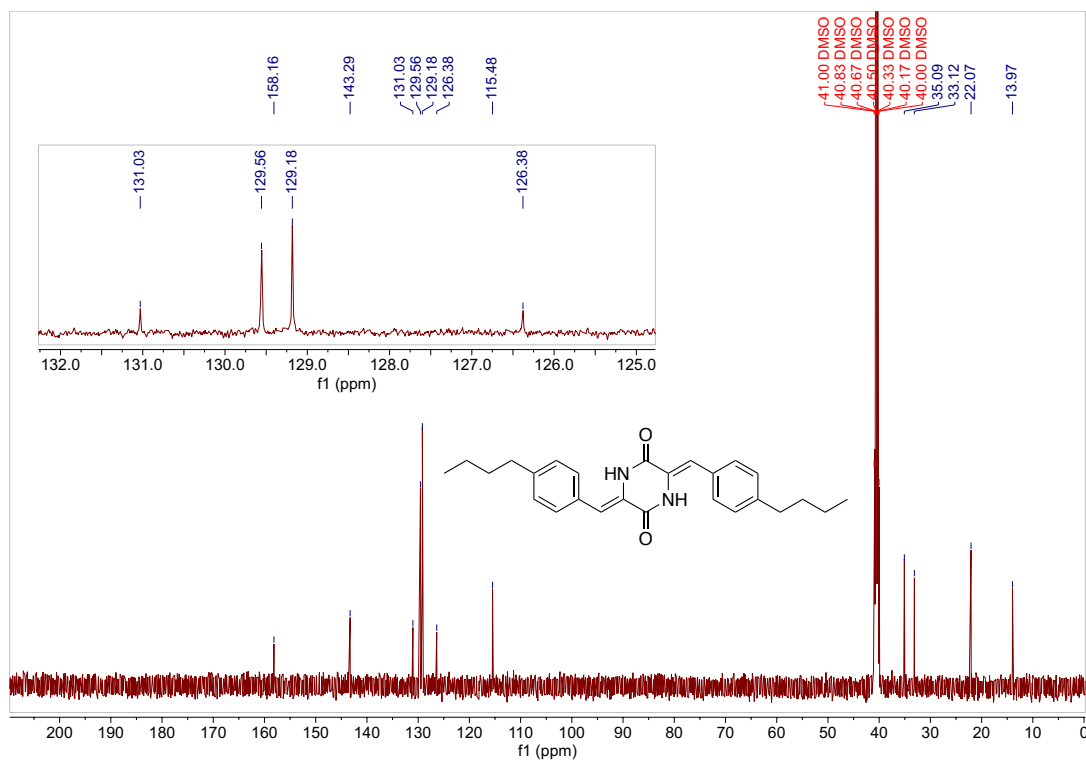


**Supplementary Figure C.37.** $^{13}$C NMR Spectrum of compound **6b** (DMSO-d$_6$, 298K).
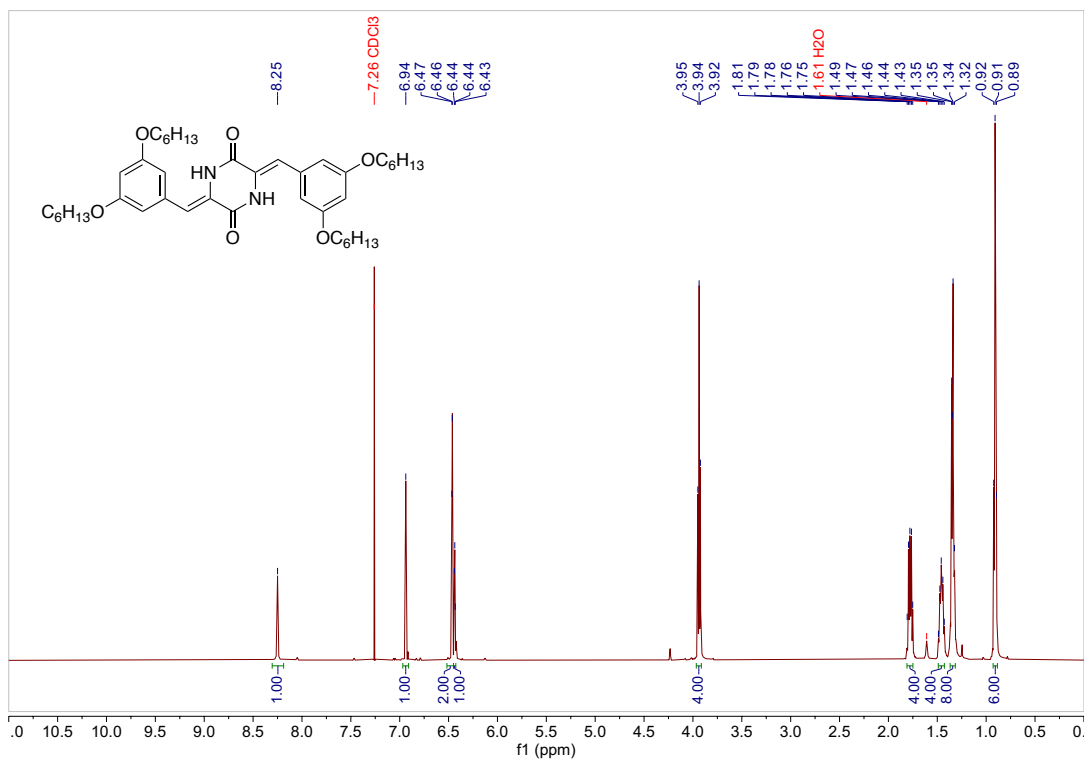
**Supplementary Figure C.38.** ¹H NMR Spectrum of compound **6c** (CDCl₃, 298K).
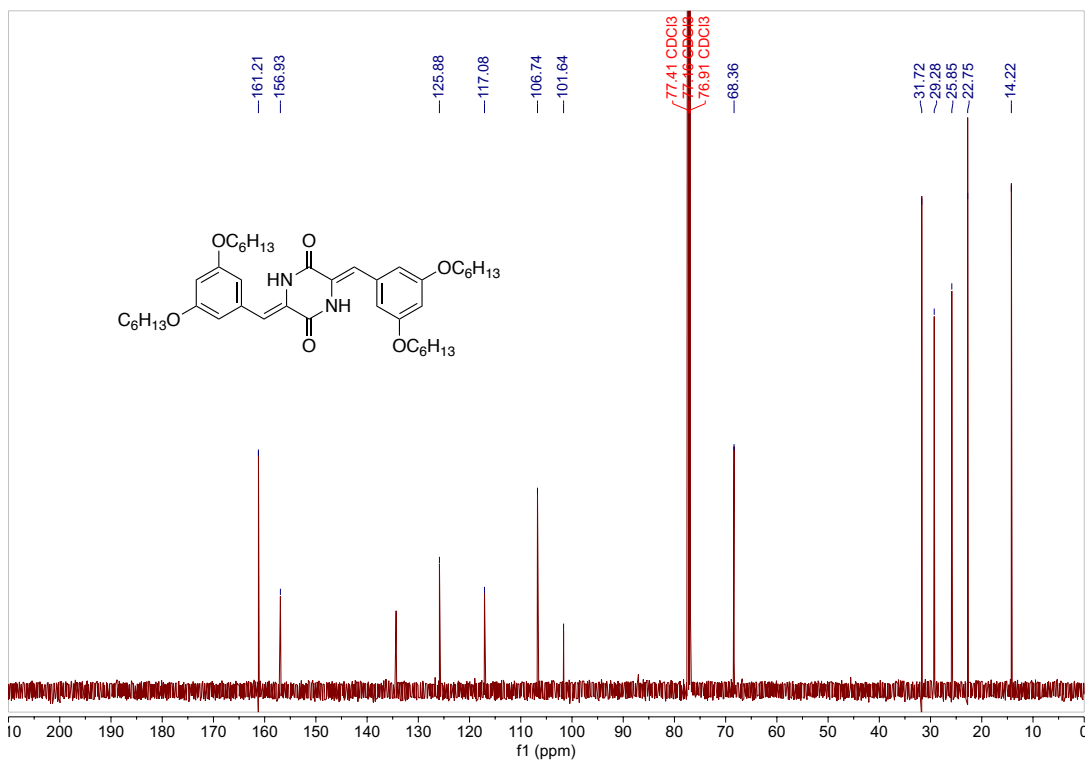


**Supplementary Figure C.39.** ¹³C NMR Spectrum of compound **6c** (CDCl₃, 298K).

**Supplementary Figure C.40.** $^1$H NMR Spectrum of compound **6d** (DMSO-d$_6$, 398K).



**Supplementary Figure C.41.** $^{13}$C NMR Spectrum of compound **6d** (DMSO-d$_6$, 398K).
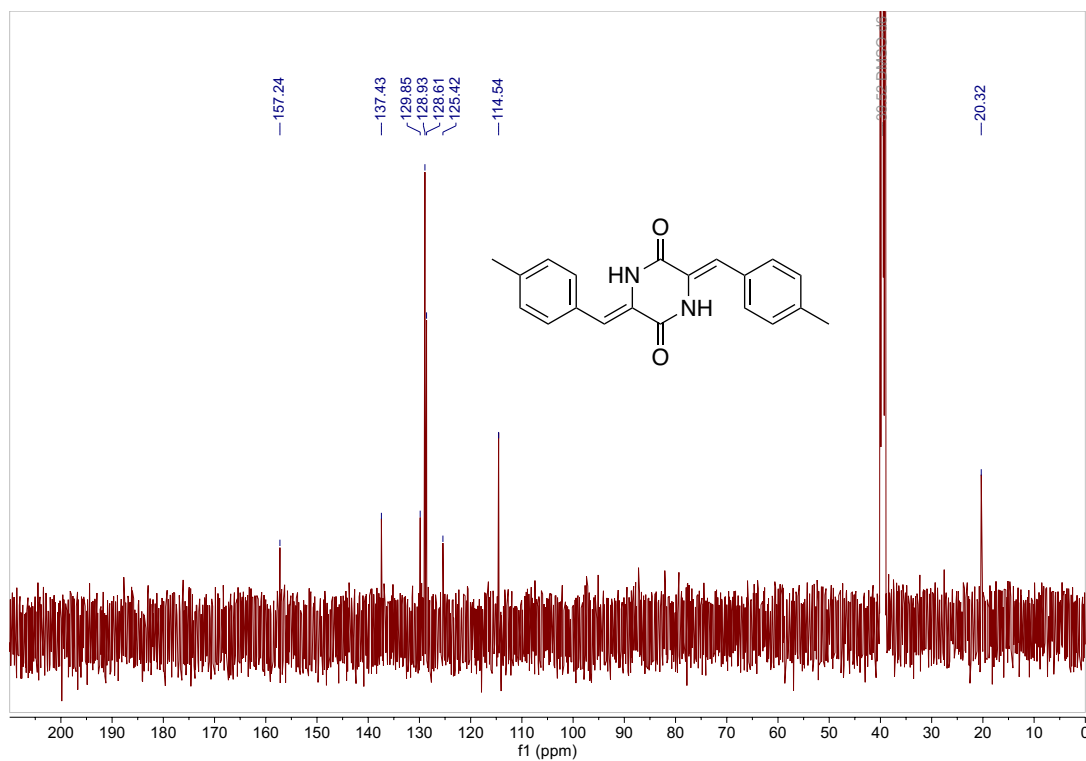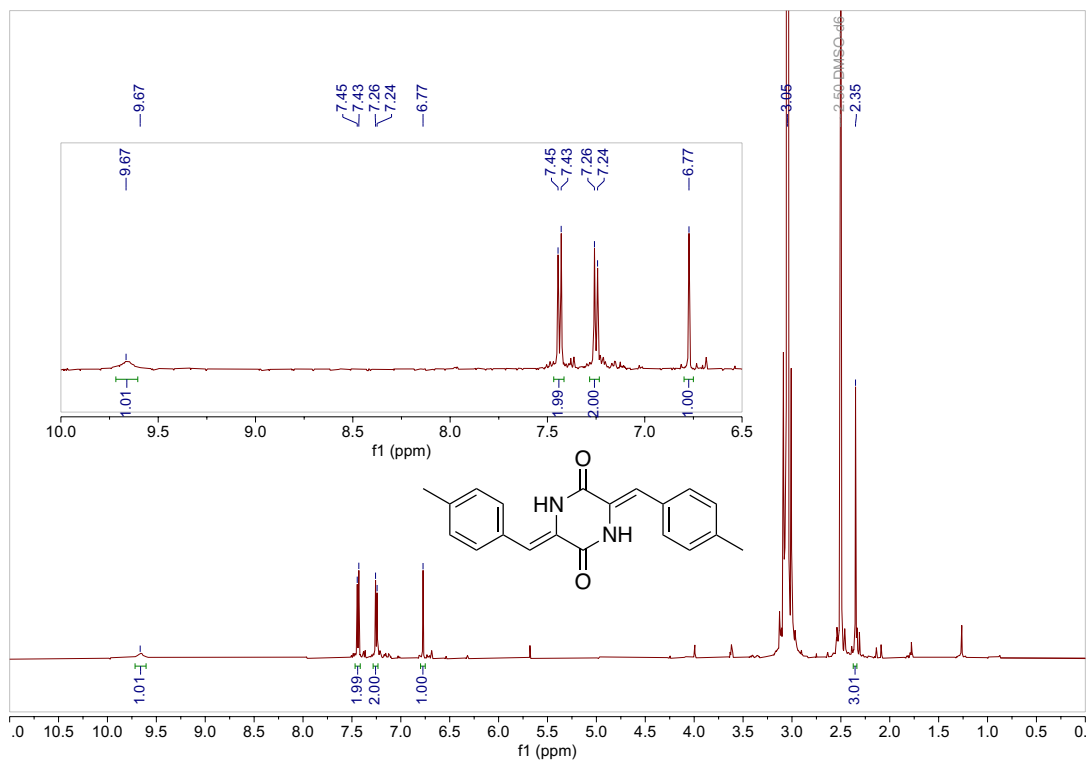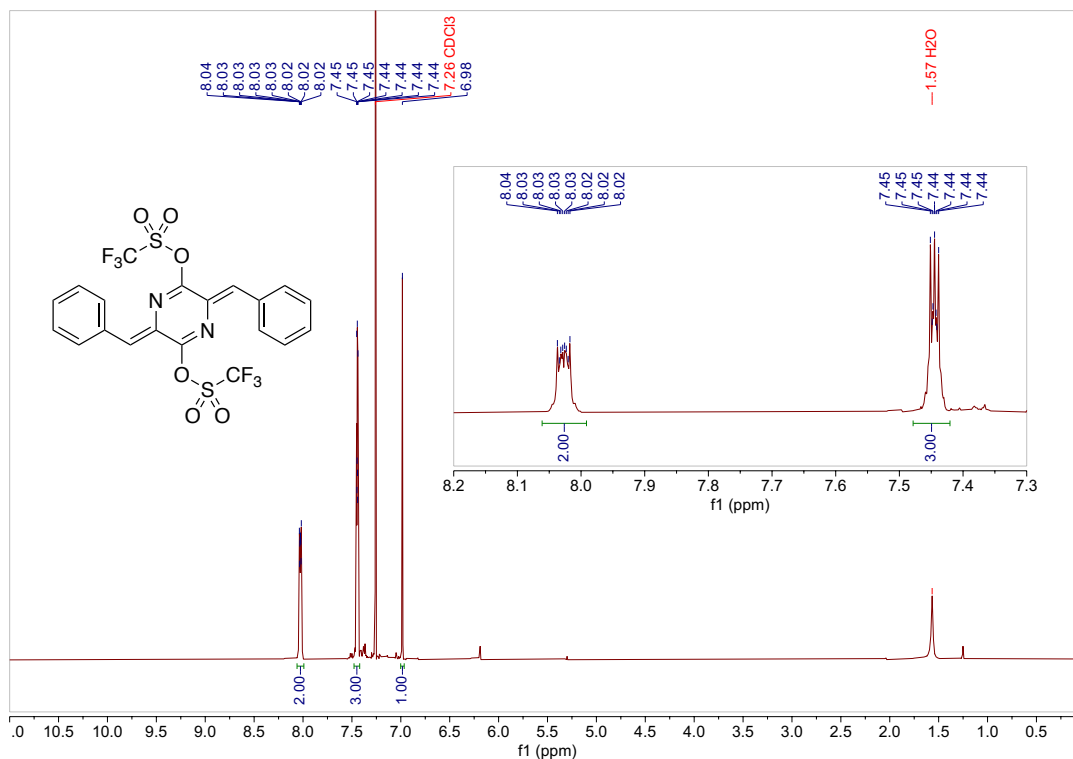
**Supplementary Figure C.42.** $^1$H NMR Spectrum of monomer **1** (CDCl$_3$, 298K).
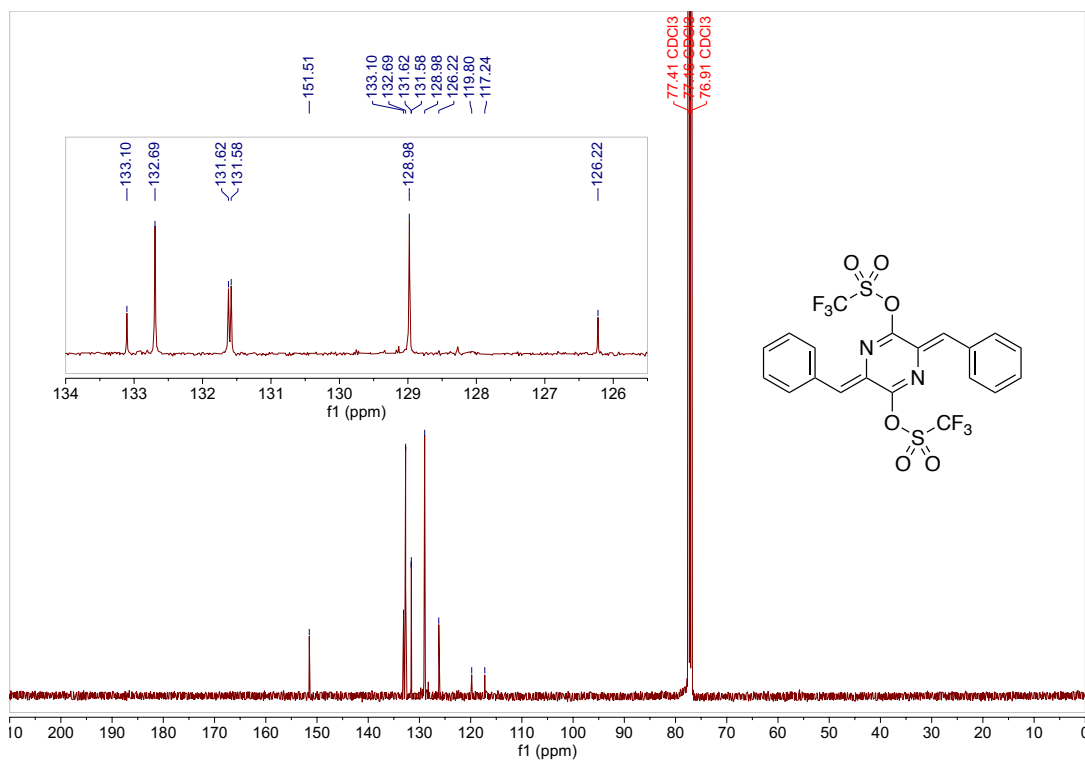


**Supplementary Figure C.43.** $^{13}$C NMR Spectrum of monomer **1** (CDCl$_3$, 298K).
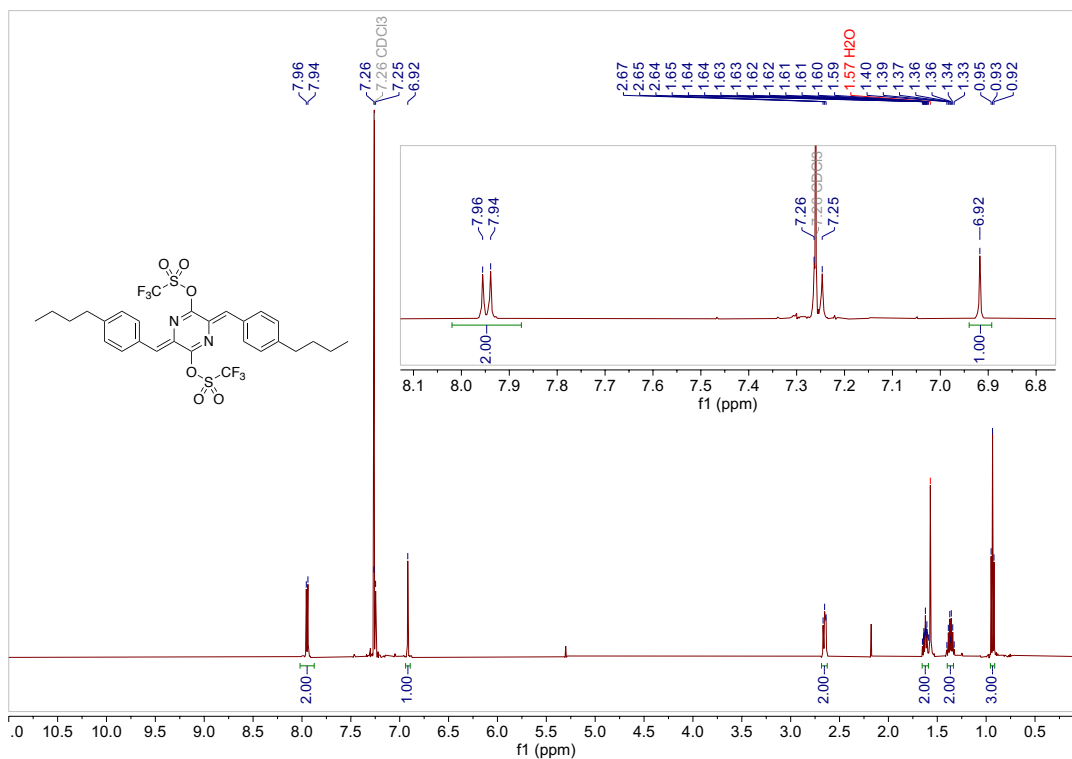
**Supplementary Figure C.44.** $^1$H NMR Spectrum of monomer **2** (CDCl$_3$, 298K).
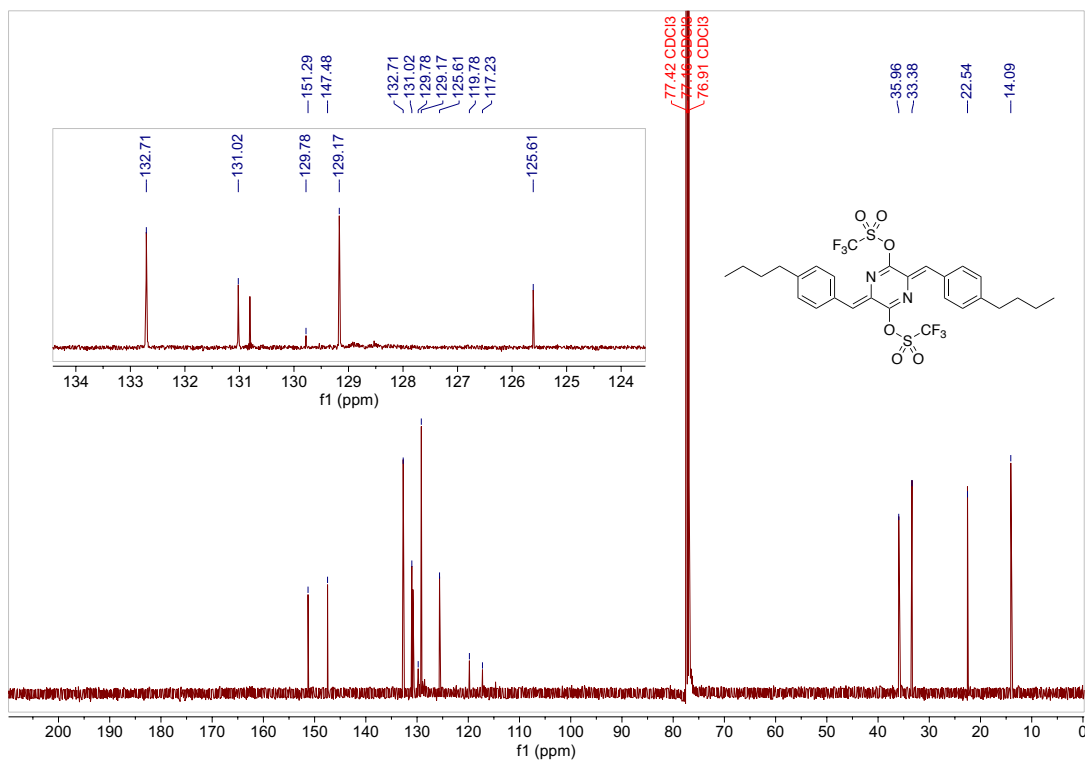


**Supplementary Figure C.45.** $^{13}$C NMR Spectrum of monomer **2** (CDCl$_3$, 298K).
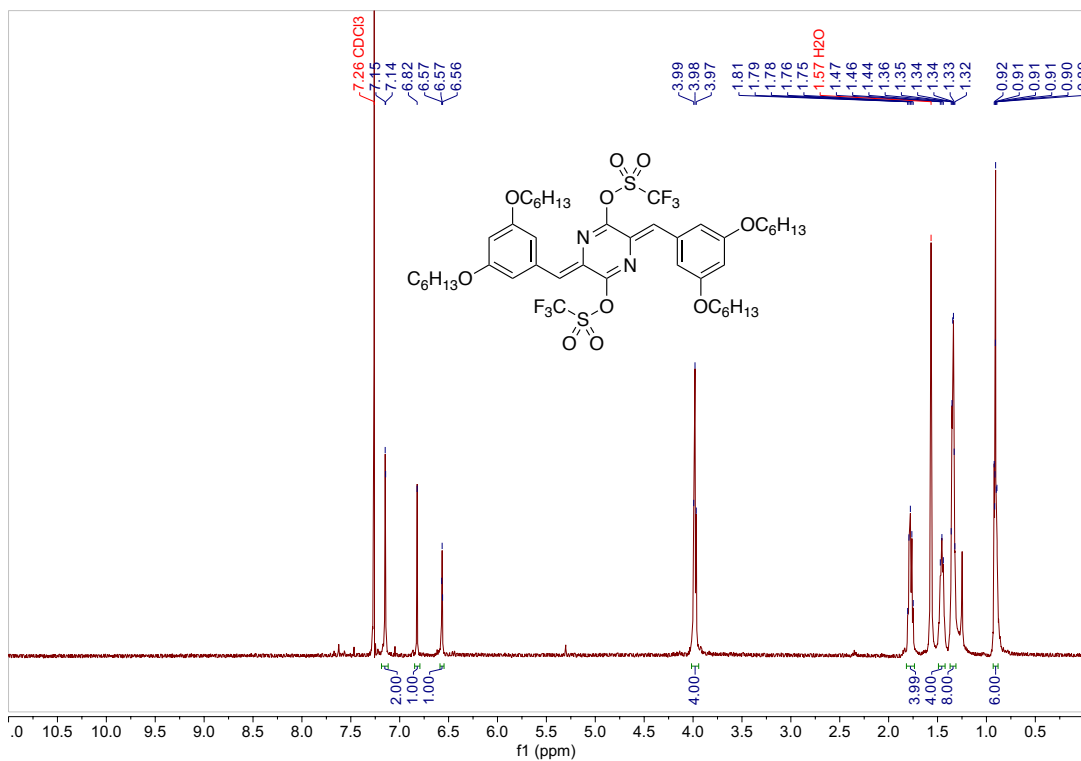
**Supplementary Figure C.46.** $^1$H NMR Spectrum of monomer **3** (CDCl$_3$, 298K).
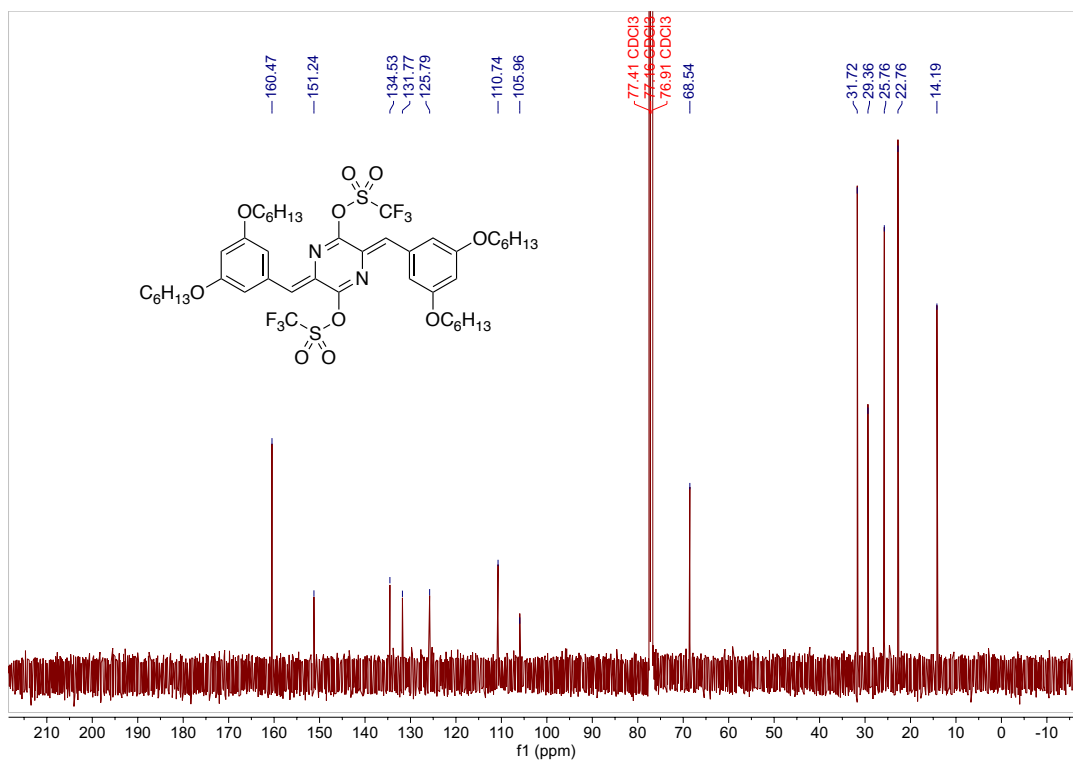


**Supplementary Figure C.47.** $^{13}$C NMR Spectrum of monomer **3** (CDCl$_3$, 298K).
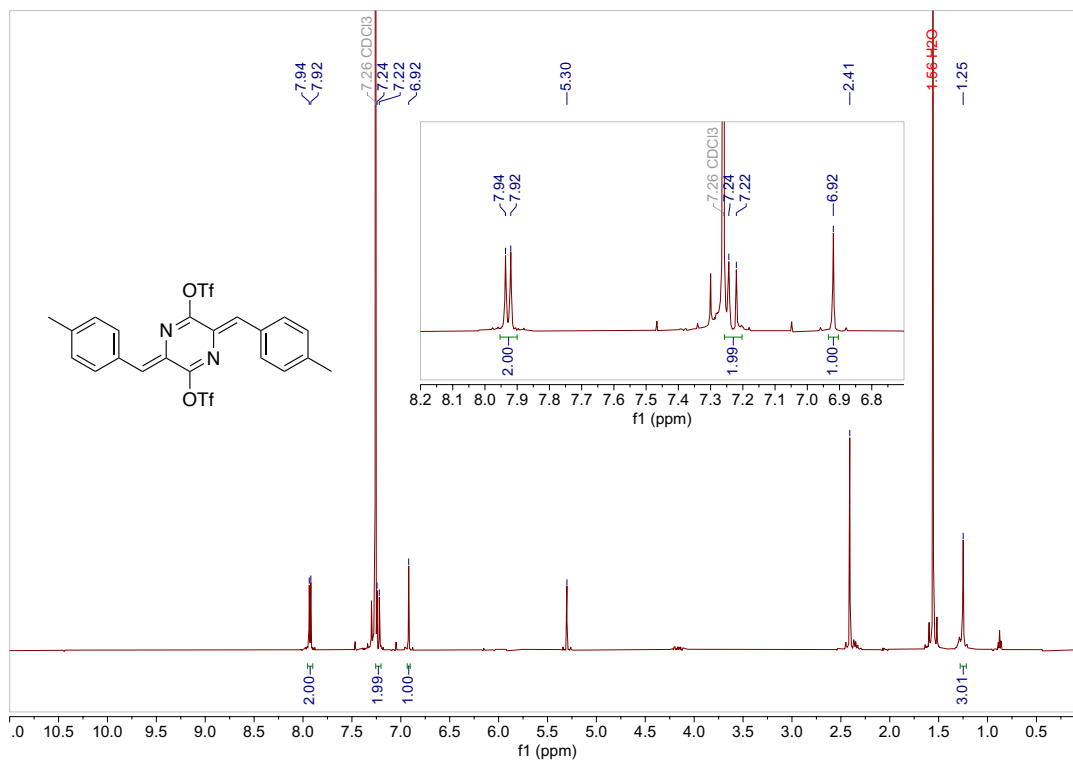
**Supplementary Figure C.48.** $^1$H NMR Spectrum of monomer **4** (CDCl$_3$, 298K).
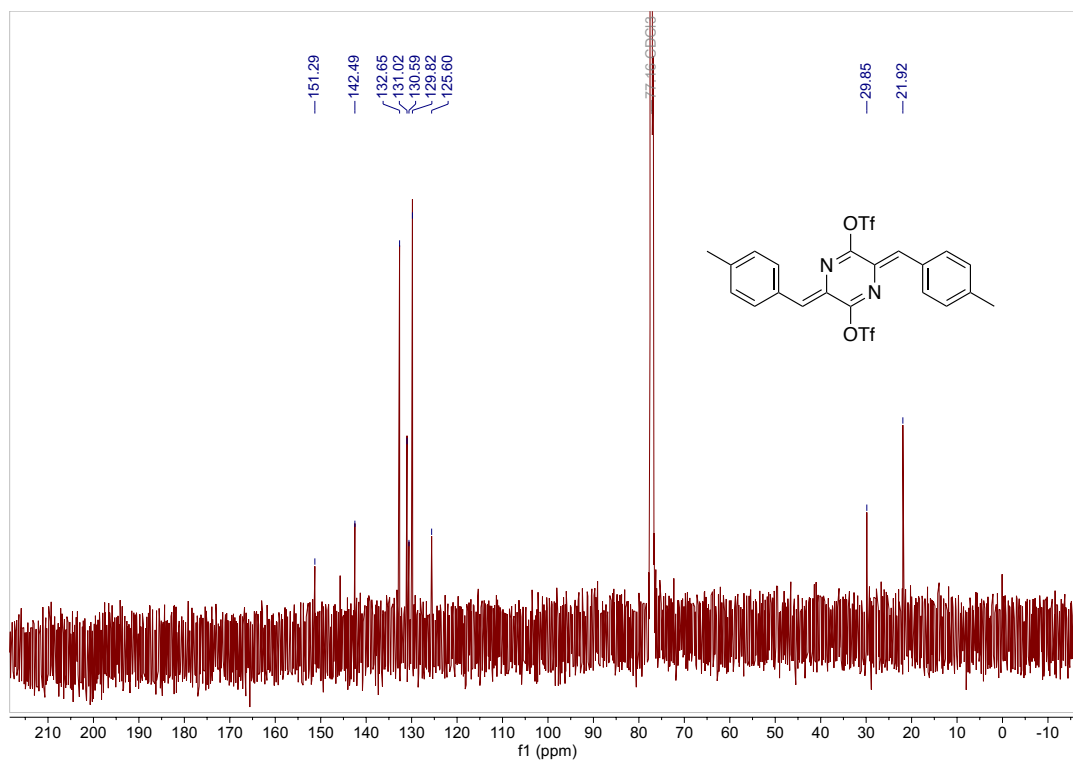


**Supplementary Figure C.49.** $^{13}$C NMR Spectrum of monomer **4** (CDCl$_3$, 298K).
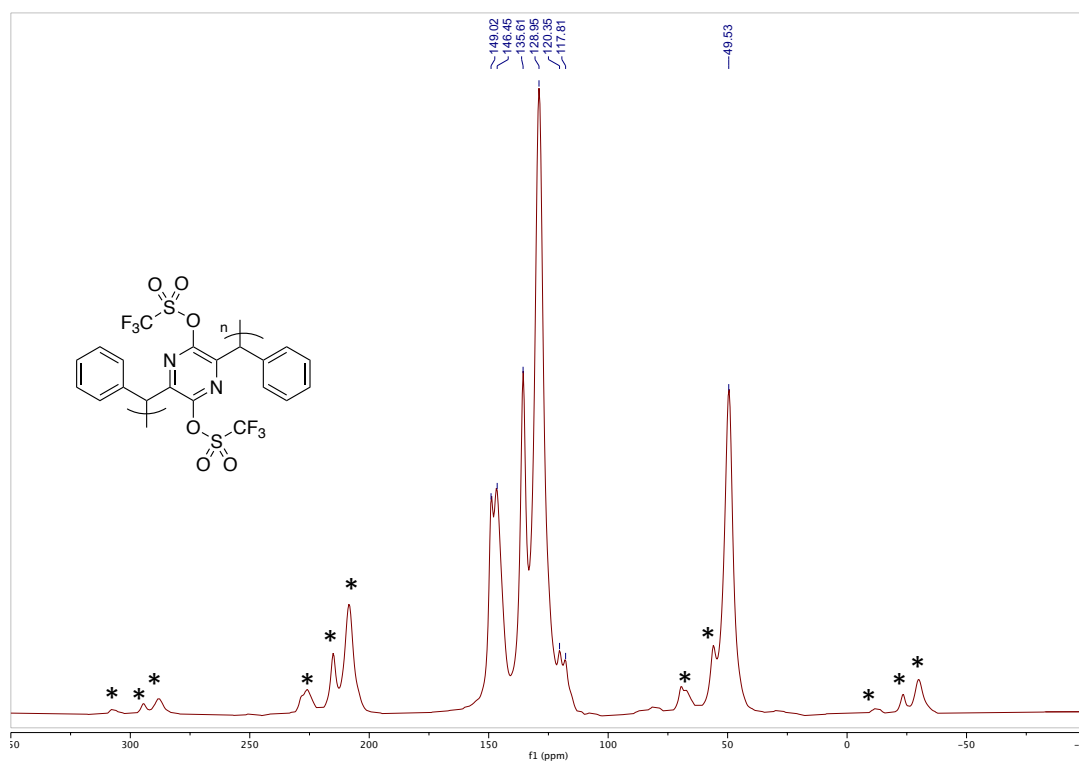
**Supplementary Figure C.50.** Solid-state $^{13}$C NMR (CP-MAS) Spectrum of polymer **P1** (298K).

Note: Asterisked peaks denote spinning-side bands of the cluster of peaks between 100-175 ppm.
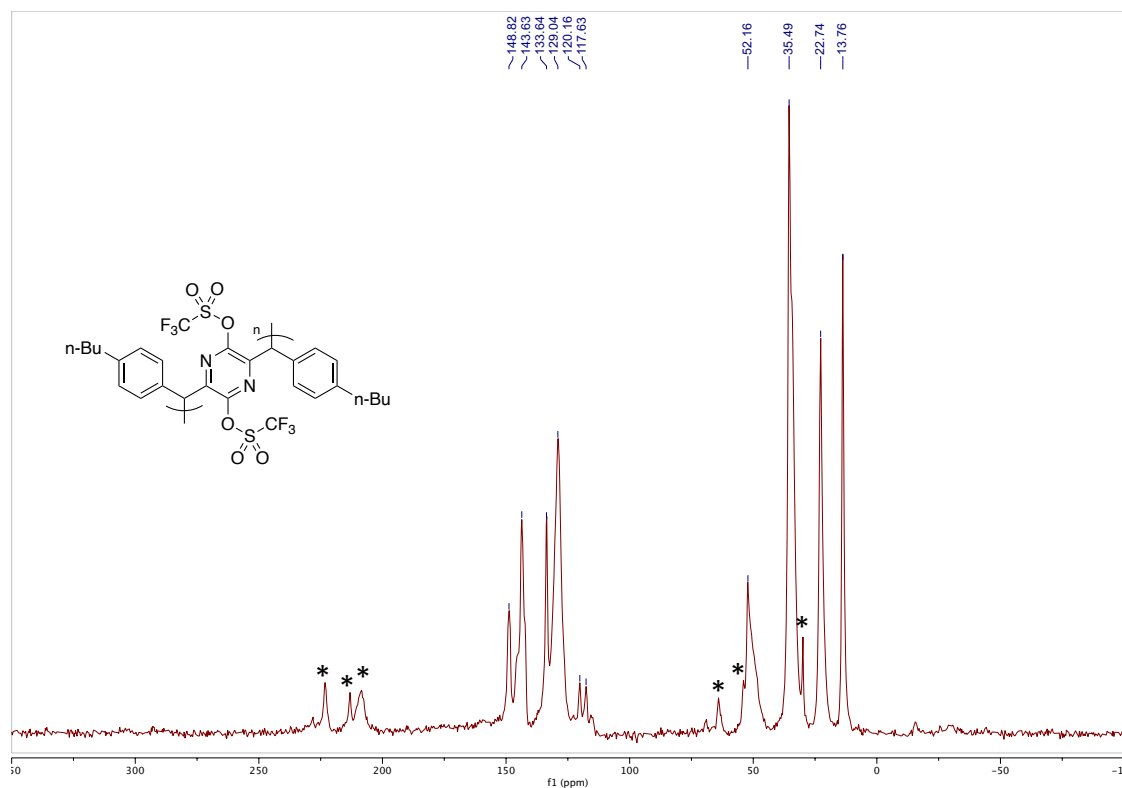
**Supplementary Figure C.51.** Solid-state $^{13}$C NMR (CP-MAS) Spectrum of polymer **P2** (298K).

Note: Asterisked peaks denote spinning-side bands of the cluster of peaks between 100-175 ppm.
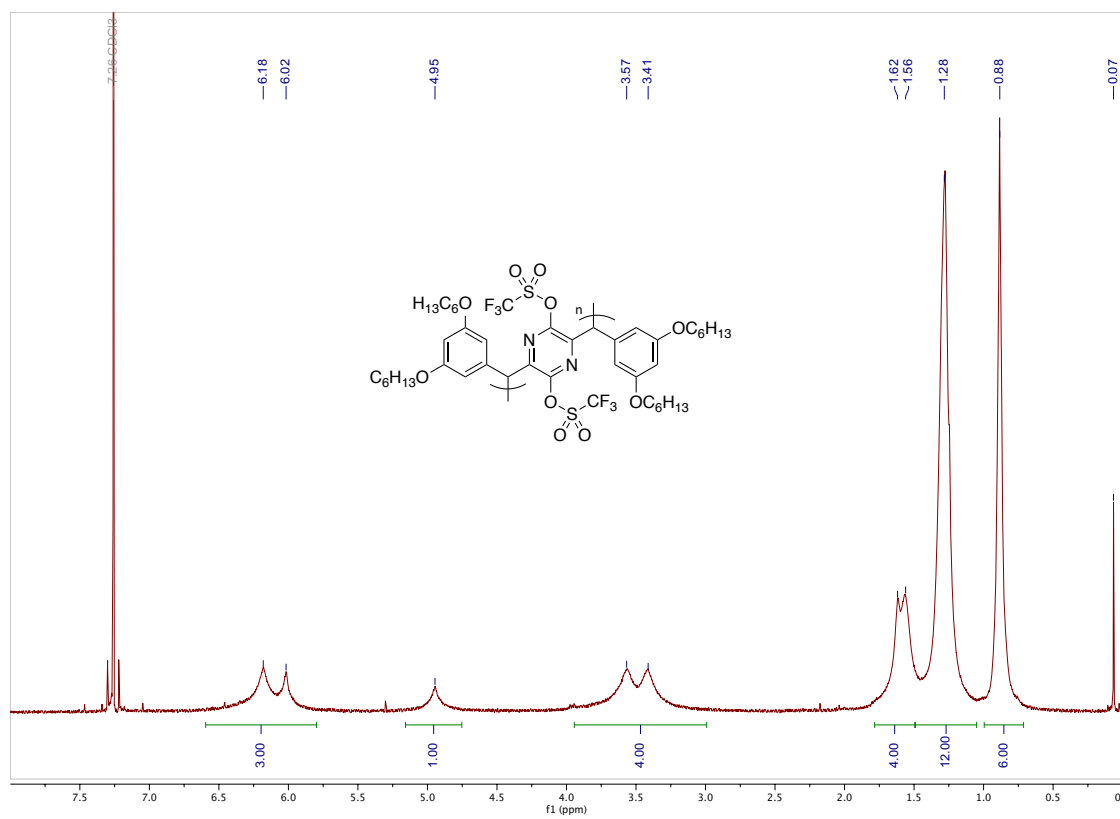
**Supplementary Figure C.52.** $^1$H NMR Spectrum of polymer **P3** (CDCl$_3$, 298K).
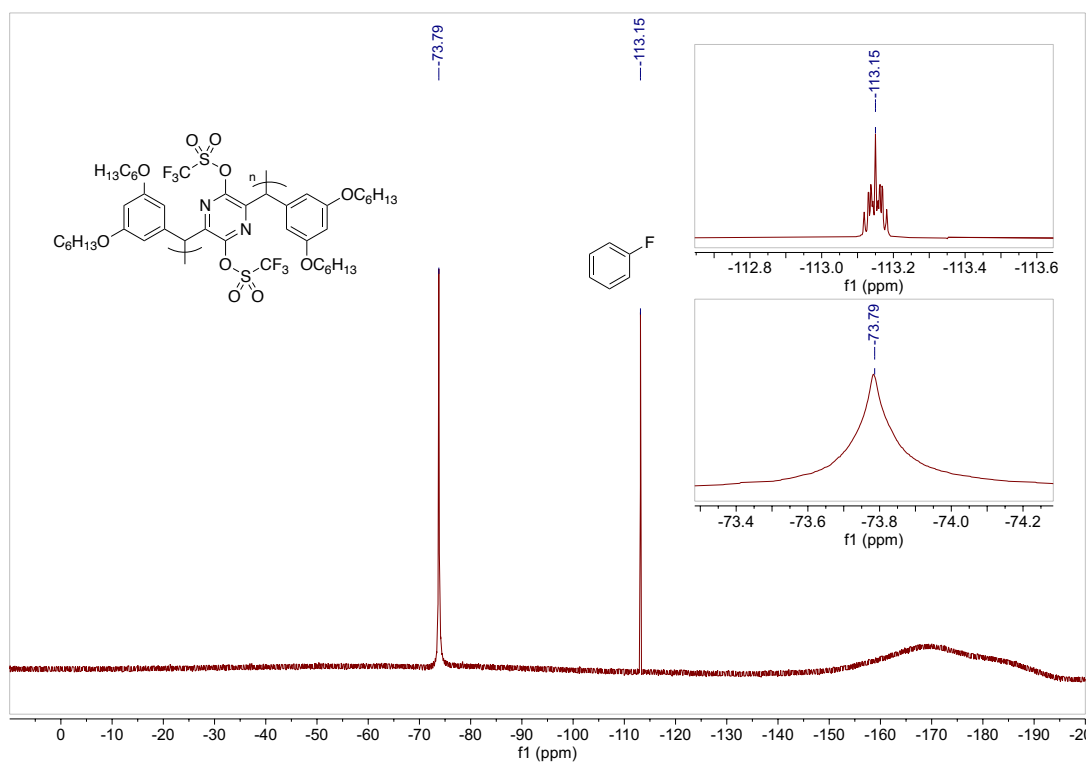
**Supplementary Figure C.53.** $^{19}$F NMR Spectrum of polymer **P3** (CDCl$_3$, 298K). Insets: zoomed-in subspectra of each peak to show broadening of the triflate peak. Note: spiked with 30 mM fluorobenzene as an internal standard at -113.15 ppm.
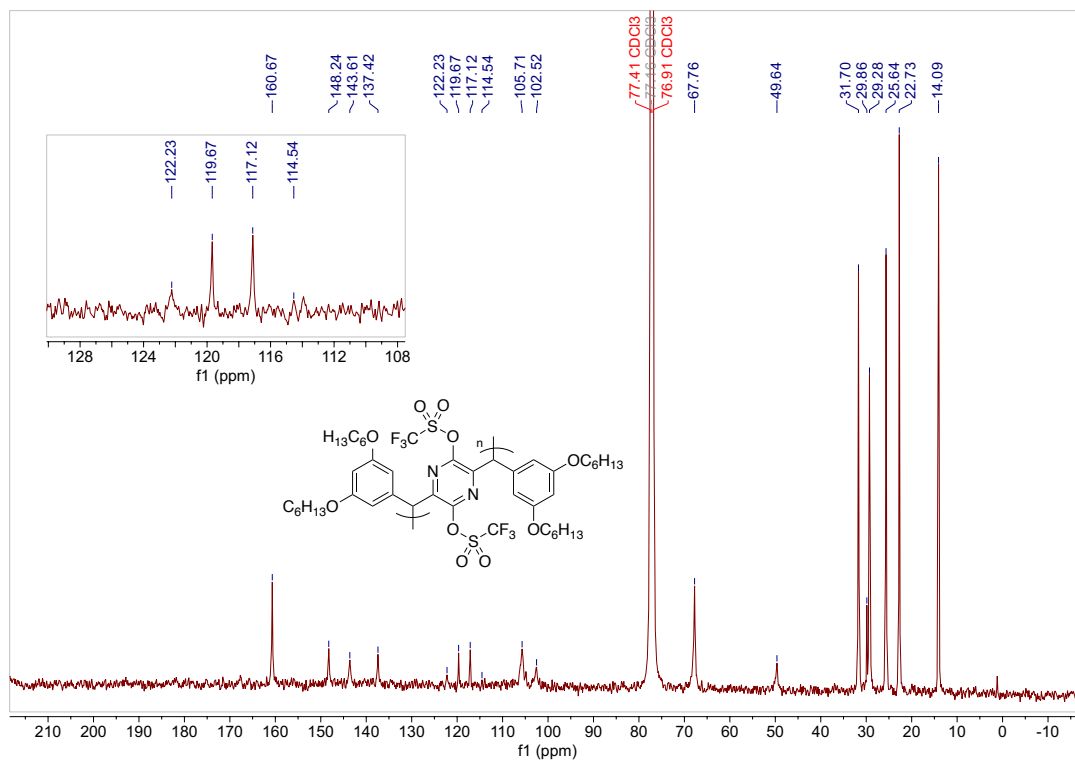
**Supplementary Figure C.54.** $^{13}$C NMR Spectrum of polymer **P3** (CDCl$_3$, 298K).
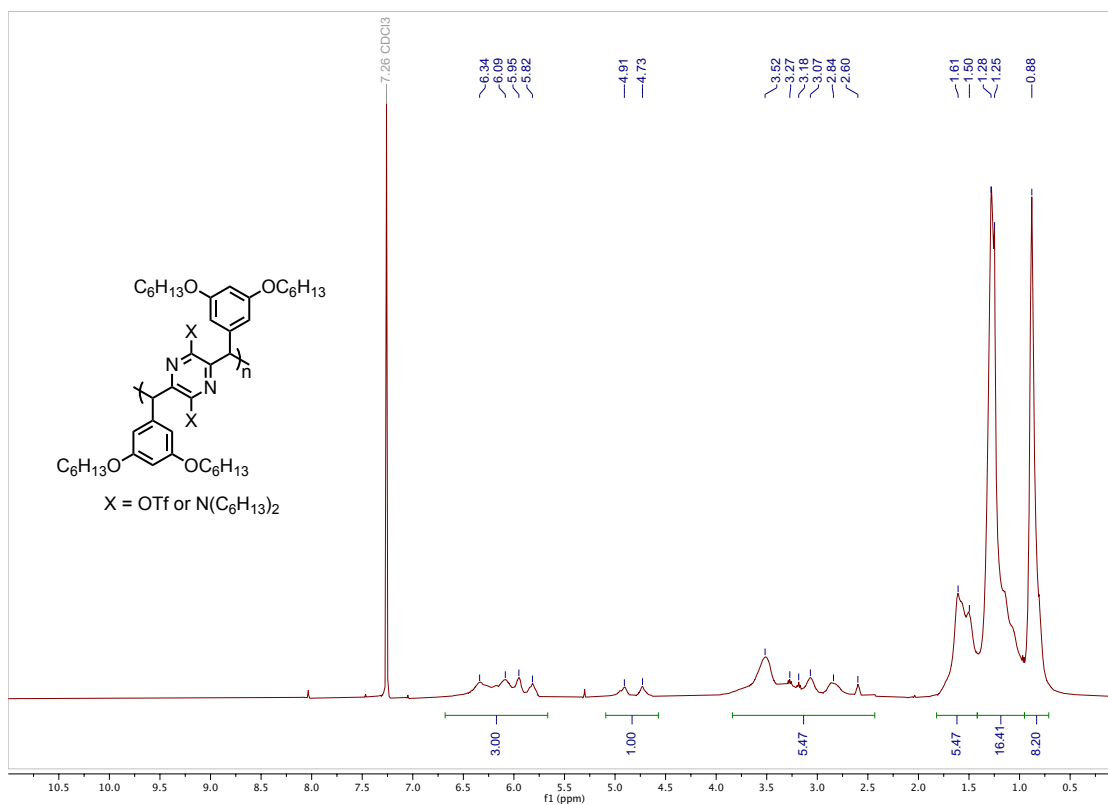


**Supplementary Figure C.55.** $^1$H NMR Spectrum of polymer **P3-A** (CDCl$_3$, 298K).
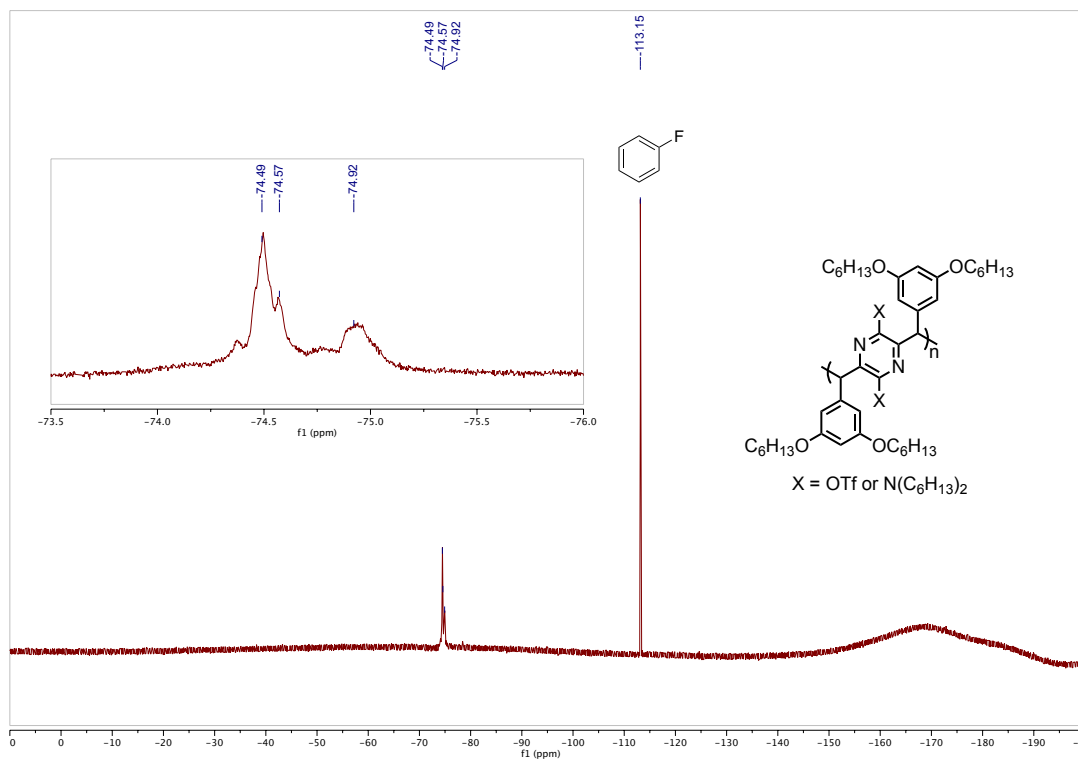
**Supplementary Figure C.56.** $^{19}$F NMR Spectrum of polymer **P3-A** (CDCl$_3$, 298K). Spiked with 30 mM fluorobenzene as an internal standard. Fluorobenzene $^{19}$F signal set to -113.15 ppm.
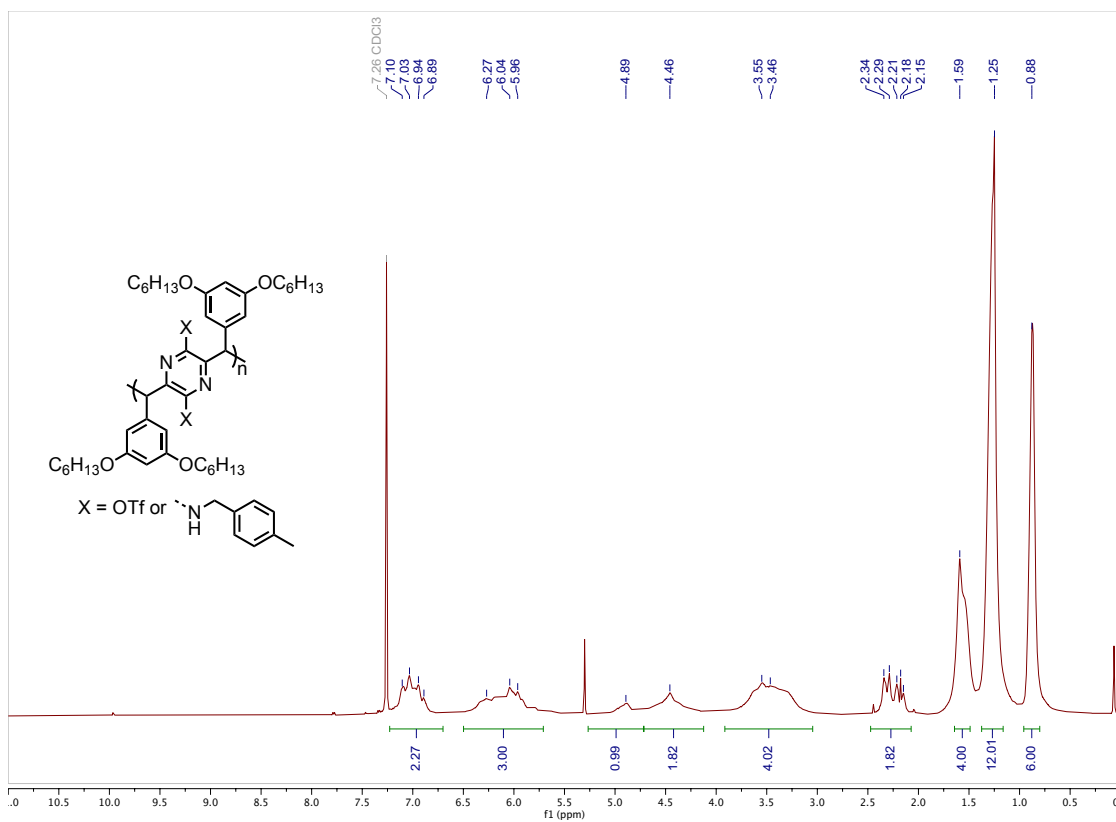
**Supplementary Figure C.57.** $^1$H NMR Spectrum of polymer **P3-B** (CDCl$_3$, 298K).
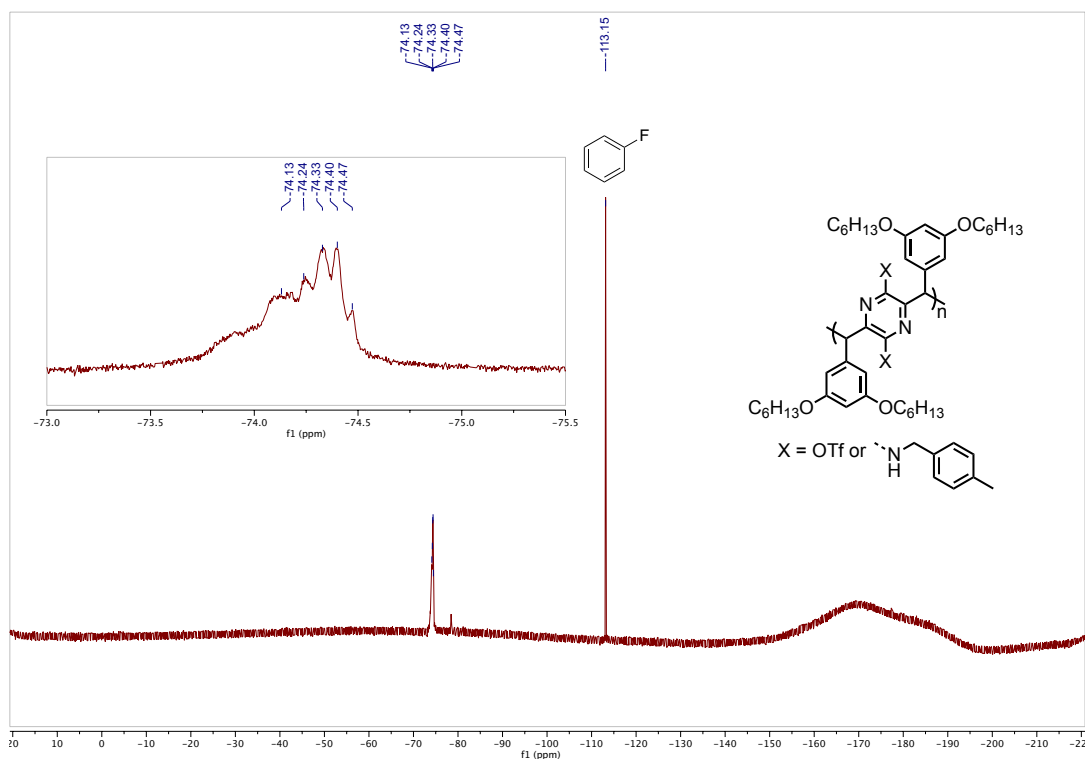
**Supplementary Figure C.58.** $^{19}$F NMR Spectrum of polymer **P3-B** (CDCl$_3$, 298K). Spiked with 30 mM fluorobenzene as an internal standard. Fluorobenzene $^{19}$F signal set to -113.15 ppm.
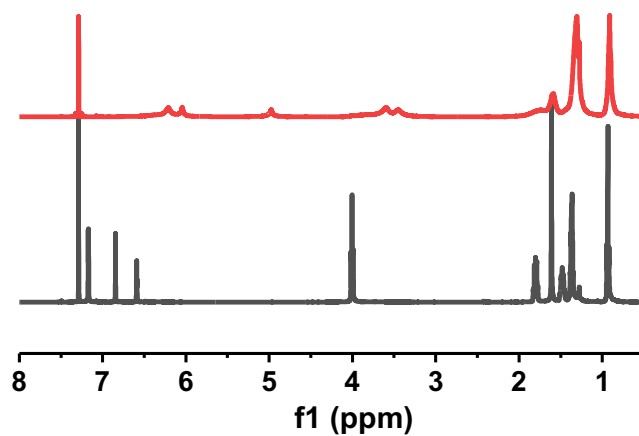


**Supplementary Figure C.59.** Overlay of $^{1}$H NMR spectra (CDCl$_3$, 298K) of monomer **3** (bottom) and polymer **P3** (top).

## Supplementary References

1 Shao, Y. et al. Advances in molecular quantum chemistry contained in the Q-Chem 4 program package. *Mol. Phys.* **113,** 184–215 (2015).
2 Rappe, A. K., Casewit, C. J., Colwell, K. S., Goddard, W. A. & Skiff, W. M. UFF, a full periodic table force field for molecular mechanics and molecular dynamics simulations. *J. Am. Chem. Soc.* **114,** 10024–10035 (1992).
3 Sheldrick, G. M. SADABS, Bruker Analytical X-ray Systems, Inc., Madison, WI, 2000.
4 Sheldrick, G. M. SHELXT—Integrated space-group and crystal-structure determination. *Acta Crystallogr. A* **71,** 3–8 (2015).
5 Sheldrick, G. M. A short history of SHELX. *Acta Crystallogr. A* **64,** 112–122 (2008).
6 Hattne, J. et al. MicroED data collection and processing. *Acta Crystallogr. A* **71,** 353–360 (2015).
7 Kabsch, W. XDS. *Acta Crystallogr. D* **66,** 125–132 (2010).
8 Sheldrick, G. Crystal structure refinement with SHELXL. *Acta Crystallogr. C* **71,** 3–8 (2015).
9 Hubschle, C. B., Sheldrick, G. M. & Dittrich, B. ShelXle: A Qt graphical user interface for SHELXL. *J. Appl. Crystallogr.* **44,** 1281–1284 (2011).
10 Peng, L. M. Electron atomic scattering factors and scattering potentials of crystals. *Micron* **30,** 625–648 (1999).
11 Zhou, Y. & Wang, Q. Advanced polymer dielectrics for high temperature capacitive energy storage. *J. Appl. Phys.* **127,** 240902 (2020).
12 Montanari, D. et al. Film capacitors for automotive and industrial applications. Vol. 29 (2009).
13 Yang, L.-M., Rong-Yang, W., McPhail, A. T., Yokoi, T. & Lee, K.-H. Neihumicin, a new cytotoxic antibiotic from micromonospora neihuensis II. Structural determination and total synthesis. *J. Antibiot.* **41,** 488–493 (1988).
14 Zhu, L. & Wang, Q. Novel ferroelectric polymers for high energy density and low loss dielectrics. *Macromolecules* **45,** 2937–2954 (2012).
15 Zhang, Z., Wang, D. H., Litt, M. H., Tan, L.-S. & Zhu, L. High-temperature and high-energy-density dipolar glass polymers based on sulfonylated poly(2,6-dimethyl-1,4-phenylene oxide). *Angew. Chem. Int. Ed.* **57,** 1528–1531 (2018).
16 Luo, S. et al. Elaborately fabricated polytetrafluoroethylene film exhibiting superior high-temperature energy storage performance. *Appl. Mater. Today* **21,** 100882 (2020).
17 Wu, C. et al. Flexible temperature-invariant polymer dielectrics with large bandgap. *Adv. Mater.* **32,** 2000499 (2020).
18 Xu, W. et al. Bioinspired polymer nanocomposites exhibit giant energy density and high efficiency at high temperature. *Small* **15,** 1901582 (2019).
19 Xu, D. et al. Rational design of soluble polyaramid for high-efficiency energy storage dielectric materials at elevated temperatures. *Macromol. Mater. Eng.* **305,** 1900820 (2020).
20 Li, Z. et al. High energy density and high efficiency all-organic polymers with enhanced dipolar polarization. *J. Mater. Chem. A* **7,** 15026–15030 (2019).
21 Wei, J. et al. High dielectric constant dipolar glass polymer based on sulfonylated poly(ether ether ketone). *Polymer* **178,** 121688 (2019).
22 Zhang, Z. et al. High-κ polymers of intrinsic microporosity: a new class of high temperature and low loss dielectrics for printed electronics. *Mater. Horiz.* **7,** 592–597 (2020).

*Appendix D*

*Supporting Information for Chapter 5: Unraveling the Electrical and Magnetic*

*Properties of Layered Conductive Metal-Organic Framework with Atomic*

*Precision*

### D1.    Materials and Methods

Copper(II) nitrate hemi(pentahydrate) (CAS N.O.: 19004-19-4) and ammonium acetate (CAS N.O.: 631-61-8) were purchased from Alfa Aesar. Tetrahydroxy-1,4-quinone hydrate (THQ, CAS N.O.: 123334-16-7), ethylenediamine (en, CAS N.O.: 107-15-3), and trifluoroacetic acid (TFA, CAS N.O.: 76-05-1) were purchased from Sigma Aldrich. Acetone (CAS N.O.: 67-64-1), methanol (MeOH, CAS N.O.: 67-56-1), ethanol (EtOH, CAS N.O.: 64-17-5), isopropyl alcohol (iPrOH, CAS N.O.: 67-63-0) tetrahydrofuran (THF, CAS N.O.: 109-99-9), and ammonia water (CAS N.O.: 1336-21-6) were purchased from BDH Chemicals. 1,3-Dimethyl-2-imidazolidinone (DMI, CAS N.O.: 80-73-9) was purchased from TCI chemicals.

Scanning Electron Microscopy (SEM) and Energy Dispersive X-ray Spectroscopy (EDX) were performed using a Hitachi TM3000 SEM (Tokyo, Japan) equipped for X-ray microanalysis with a Bruker Edax light element Si(Li) detector (Billerica, MA). Transmission electron microscopy was carried out at a Tecnai F20ST FEG TEM instrument. In-house powder X-ray diffraction (pXRD) measurements were performed with a Rigaku sixth generation MiniFlex X-ray diffractometer with a 600 W (40 kV, 15 mA) $CuK_\alpha$ ($\lambda$= 1.5406 Å) radiation source. High-resolution pXRD data were collected at beamline 11-BM of the Advanced Photon Source using a wavelength of 0.458068 Å at the temperature of 100 K. Nitrogen adsorption experiments were performed with 3Flex (Mircromeritics, Norcross, Georgia) instrument. pH was measured using edge® Wine pH Meter. X-ray photoelectron spectroscopy experiments were conducted on Kratos Analytical AXIS Supra X-ray Photoelectron Spectrometer under ultrahigh vacuum (base pressure $10^{-7}$ Torr). The measurement chamber was equipped with a monochromatic Al ($K_\alpha$) X-ray source. Both survey and high-resolution spectra were obtained using a beam diameter of 200 μm. Magnetic measurements were performed on a Quantum Design magnetic properties measurement system (MPMS3).

### D2.    Synthesis of $Cu_3(C_6O_6)_2$

*N.O. 1*: $Cu(NO_3)_2 \cdot 2.5H_2O$ (93 mg, 0.4 mmol, 2.0 eq) and ammonium acetate (308 mg, 4 mmol, 20.0 eq) were dissolved in 5 mL $N_2$ degassed $H_2O$ to form a light blue solution. A solution of 42 mg (0.2 mmol) of tetrahydroxyquinone (THQ) in 5 mL degassed $H_2O$ was then poured into the solution of $Cu(NO_3)_2 \cdot 2.5H_2O$ and ammonium acetate. The reaction mixture was sealed after bubbling with $N_2$ for 5 min. After the reaction sample was placed at room temperature for 20 h without stirring, the dark blue precipitate was filtered and washed with water (50 mL × 3) and acetone (20 mL × 5). The product was dried under vacuum desiccator at room temperature by using an oil pump for 18 hours to a dark-blue powder (41 mg, yield 65% based on the formula $Cu_3(C_6O_6)_2 \cdot 6H_2O$).

Different organic solvents were used systematically in combination with water (1:1) to examine their influence on the nucleation process and size of the crystal. Reactions were performed by pouring the THQ solution in MeOH, EtOH, DMF, DMSO, THF, NMP, ACN, DMA (*N.O. 2-9*)

into an aqueous solution of $Cu(NO_3)_2 \cdot 2.5H_2O$ and ammonium acetate with all the other conditions the same with that in ***N.O. 1***.

The ammonium acetate was also replaced by $NH_4F$, $CH_3COOK$, $K_2CO_3$, $CH_3COONa$, corresponding to ***N.O. 10-13***, respectively, to examine the effect of salt additives. The reactions were carried out by pouring a solution of THQ in DMF into a $Cu(NO_3)_2 \cdot 2.5H_2O$ and salt additives (20 e.q.) in water with other conditions the same with ***N.O. 1.***

***N.O. 14***: $Cu(NO_3)_2 \cdot 2.5H_2O$ (93 mg, 0.4 mmol, 2.0 eq) and ammonium acetate (308 mg, 4 mmol, 20.0 eq) were dissolved in 3 mL degassed $H_2O$ in a 5 mL glass vial to form a light blue solution, then 42 mg (0.2 mmol) of tetrahydroxyquinone solid was added. The vial was sealed after bubbling with $N_2$ for 5 min. After the reaction was placed at room temperature for 20 h without stirring, the dark blue precipitate was filtered and washed with water (50 mL× 3) and acetone (20 mL × 5).

***N.O. 15-18***: $Cu(NO_3)_2 \cdot 2.5H_2O$ (93 mg, 0.4 mmol, 2.0 eq) and ammonium acetate (308 mg, 4 mmol, 20.0 eq), 0.83 mmol modulator acid (acetic acid, formic acid, malonic acid, and trifluoroacetic acid, respectively corresponding to ***N.O. 15-18***) were dissolved in 3 mL degassed $H_2O$ to form a light blue solution, then 42 mg (0.2 mmol) of tetrahydroxyquinone solid was added. The reaction mixture was sealed after bubbling with $N_2$ for 5 min. After the reaction was placed at room temperature for 20 h without stirring, the dark blue precipitate was filtered and washed with water (50 mL× 3) and acetone (20 mL × 5).

***N.O. 19.*** $Cu(NO_3)_2 \cdot 2.5H_2O$ (93 mg, 0.4 mmol, 2.0 eq) and ammonium acetate (308 mg, 4 mmol, 20.0 eq) were dissolved in 3 mL degassed $H_2O$ in a 5 mL glass vial to form a light blue solution, then 42 mg (0.2 mmol) of tetrahydroxyquinone solid was added. The reaction mixture was gently bubbled with air (~4 bubbles/second) without stirring at room temperature. In condiction ***N.O. 20.***, a reaction temperature of 45 °C was used with other conditions same as those in ***N.O. 19***.

***N.O. 21.*** $Cu(NO_3)_2 \cdot 2.5H_2O$ (93 mg, 0.4 mmol, 2.0 eq) and ammonium acetate (308 mg, 4 mmol, 20.0 eq) were dissolved in 3 mL degassed $H_2O$ in a 5 mL glass vial to form a light blue solution, then 42 mg (0.2 mmol) of tetrahydroxyquinone solid was added. The reaction vial was sealed after bubbling with $N_2$ for 5 min. After the reaction was placed at 65 °C for 20 h without stirring, the precipitate was filtered and washed with water (50 mL× 3) and acetone (20 mL × 5).

***N.O. 22.*** (**optimized synthetic condition**): $Cu(NO_3)_2 \cdot 2.5H_2O$ (93 mg, 0.4 mmol, 2.0 eq) and ammonium acetate (308 mg, 4 mmol, 20.0 eq) were dissolved in 3 mL degassed $H_2O$ to form a light blue solution (pH=5.98), then 42 mg (0.2 mmol) of tetrahydroxyquinone solid was added. The reaction mixture was then heated at 65 °C and gently bubbled with air (~4 bubbles/second) without stirring. After the reaction was run for 20 h, the dark blue precipitate formed in the reaction mixture (pH=5.83) was filtered and washed with water (50 mL× 3) and acetone (20 mL × 5). The product was dried under vacuum system equipped with an oil pump at room temperature for 20 hours to give a dark-blue powder (47 mg, yield 74% based on the formula $Cu_3(C_6O_6)_2 \cdot 6H_2O$).

**Table D.1.** Summary of the synthetic conditions of $Cu_3(C_6O_6)_2$.

| N.O. | solvent (v/v) | ligand conc. | additive (e.q.) | CuL$_2$ (e.q.) | modulator | $T$ | atm. |
|---|---|---|---|---|---|---|---|
| 1 | H$_2$O | 20 mM | CH$_3$COONH$_4$ (20) | Cu(NO$_3$)$_2$ (2) | N/A | r.t. | N$_2$ |
| 2 | H$_2$O/DMAC 1/1) | 20 mM | CH$_3$COONH$_4$ (20) | Cu(NO$_3$)$_2$ (2) | N/A | r.t. | N$_2$ |
| 3 | H$_2$O/ACN (1/1) | 20 mM | CH$_3$COONH$_4$ (20) | Cu(NO$_3$)$_2$ (2) | N/A | r.t. | N$_2$ |
| 4 | H$_2$O/DMSO (1/1) | 20 mM | CH$_3$COONH$_4$ (20) | Cu(NO$_3$)$_2$ (2) | N/A | r.t. | N$_2$ |
| 5 | H$_2$O/DMF (1/1) | 20 mM | CH$_3$COONH$_4$ (20) | Cu(NO$_3$)$_2$ (2) | N/A | r.t. | N$_2$ |
| 6 | H$_2$O/NMP (1/1) | 20 mM | CH$_3$COONH$_4$ (20) | Cu(NO$_3$)$_2$ (2) | N/A | r.t. | N$_2$ |
| 7 | H$_2$O/MeOH(1/1) | 20 mM | CH$_3$COONH$_4$ (20) | Cu(NO$_3$)$_2$ (2) | N/A | r.t. | N$_2$ |
| 8 | H$_2$O/EtOH (1/1) | 20 mM | CH$_3$COONH$_4$ (20) | Cu(NO$_3$)$_2$ (2) | N/A | r.t. | N$_2$ |
| 9 | H$_2$O/THF (1/1) | 20 mM | CH$_3$COONH$_4$ (20) | Cu(NO$_3$)$_2$ (2) | N/A | r.t. | N$_2$ |
| 10 | H$_2$O/DMF (1/1) | 20 mM | NH$_4$F (20) | Cu(NO$_3$)$_2$ (2) | N/A | r.t. | N$_2$ |
| 11 | H$_2$O/DMF (1/1) | 20 mM | CH$_3$COOK (20) | Cu(NO$_3$)$_2$ (2) | N/A | r.t. | N$_2$ |
| 12 | H$_2$O/DMF (1/1) | 20 mM | K$_2$CO$_3$ (20) | Cu(NO$_3$)$_2$ (2) | N/A | r.t. | N$_2$ |
| 13 | H$_2$O/DMF (1/1) | 20 mM | CH$_3$COONa (20) | Cu(NO$_3$)$_2$ (2) | N/A | r.t. | N$_2$ |
| 14 | H$_2$O | 42 mg/3 mL | CH$_3$COONH$_4$ (20) | Cu(NO$_3$)$_2$ (2) | N/A | r.t. | N$_2$ |
| 15 | H$_2$O | 42 mg/3 mL | CH$_3$COONH$_4$ (20) | Cu(NO$_3$)$_2$ (2) | acetic acid | r.t. | N$_2$ |
| 16 | H$_2$O | 42 mg/3 mL | CH$_3$COONH$_4$ (20) | Cu(NO$_3$)$_2$ (2) | formic acid | r.t. | N$_2$ |
| 17 | H$_2$O | 42 mg/3 mL | CH$_3$COONH$_4$ (20) | Cu(NO$_3$)$_2$ (2) | malonic acid | r.t. | N$_2$ |
| 18 | H$_2$O | 42 mg/3 mL | CH$_3$COONH$_4$ (20) | Cu(NO$_3$)$_2$ (2) | trifluoroacetic acid | r.t. | N$_2$ |
| 19 | H$_2$O | 42 mg/3 mL | CH$_3$COONH$_4$ (20) | Cu(NO$_3$)$_2$ (2) | N/A | r.t. | air bubbling |
| 20 | H$_2$O | 42 mg/3 mL | CH$_3$COONH$_4$ (20) | Cu(NO$_3$)$_2$ (2) | N/A | 45 °C | air bubbling |
| 21 | H$_2$O | 42 mg/3 mL | CH$_3$COONH$_4$ (20) | Cu(NO$_3$)$_2$ (2) | N/A | 65 °C | N$_2$ |
| 22 | H$_2$O | 42 mg/3 mL | CH$_3$COONH$_4$ (20) | Cu(NO$_3$)$_2$ (2) | N/A | 65 °C | air bubbling |
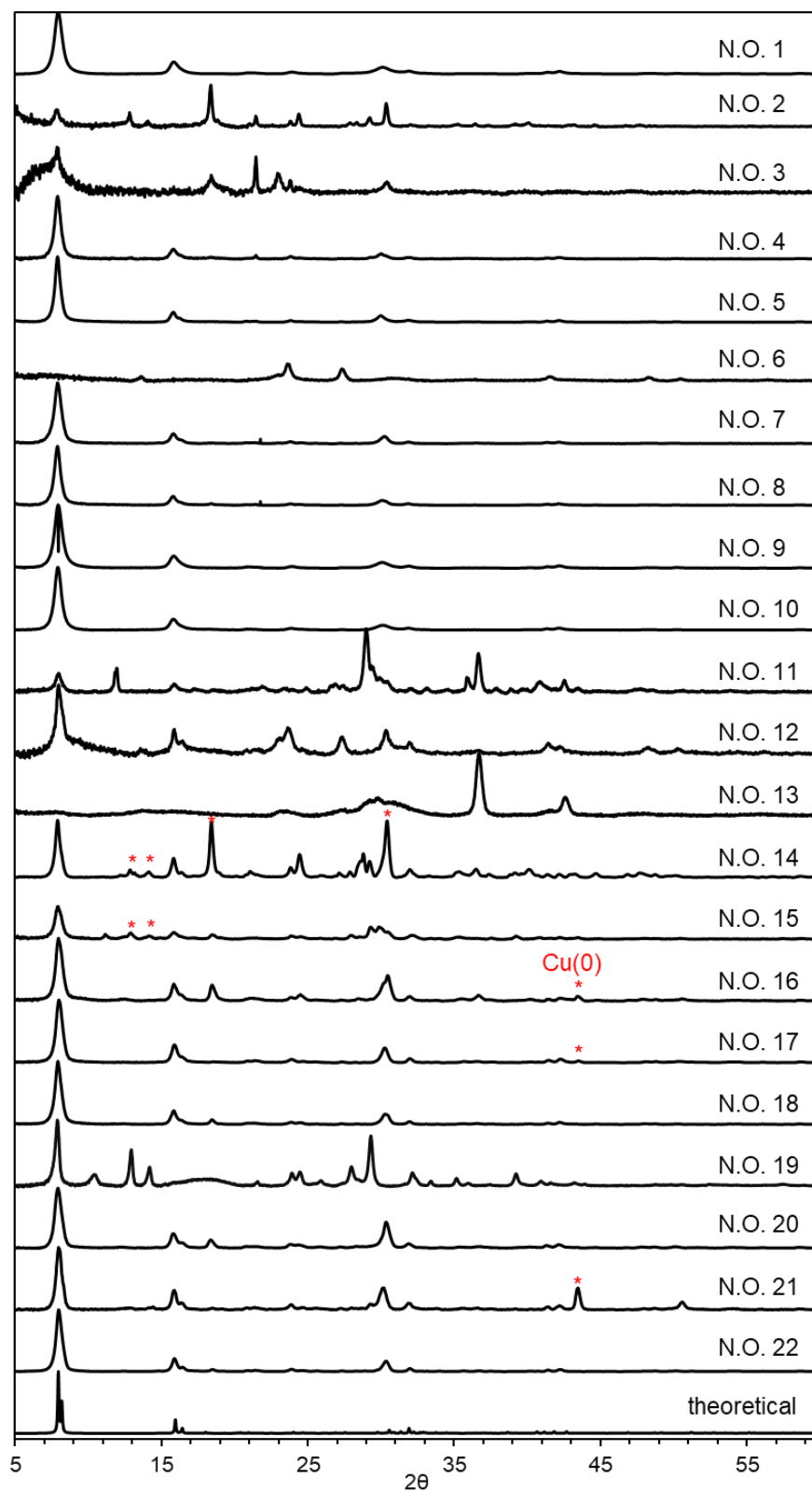
**Figure D.1.** Comparison of pXRD ($\lambda = 1.5406$ Å) of $Cu_3(C_6O_6)_2$ synthesized from conditions in **Table D.1** and theoretical pXRD from the MicroED resolved structure of $Cu_3(C_6O_6)_2$.
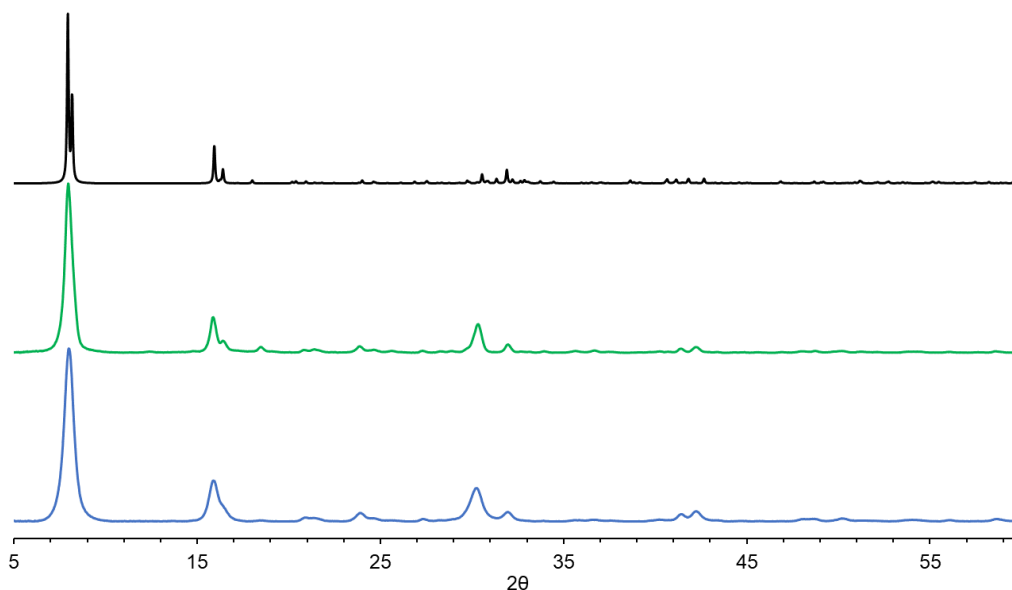
**Figure D.2.** Comparison of experimental pXRD of $Cu_3(C_6O_6)_2$ synthesized using condition from the previous report[1] (blue line) and the optimized condition (green line, **entry 22** in **Table D.1**) in this work and the theoretical pXRD ($\lambda$ = 1.5406 Å) from the MicroED resolved structure of $Cu_3(C_6O_6)_2$ (black line).

Our findings through these optimizations are summarized as follows. (1) Directly mixing the solution of the THQ and water solution of $Cu(NO_3)_2$ with the buffer salt ammonium salt can generate $Cu_3(C_6O_6)_2$ (**N.O. 1, 4, 5, 9** in **Table D.1**), however, can only give material with very small crystallites at nanometer scale (**Figure D.3b-3e**) (2) Additive salts, including $NH_4F$, $CH_3COOK$, $K_2CO_3$ can be used to also generate $Cu_3(C_6O_6)_2$ with comparable (**N.O. 10, 12** in **Table D.1**) or slightly diminished (**N.O. 11** in **Table D.1**) crystallinity as that using $CH_3COONH_4$. (3) Compared with adding THQ as a solution, adding THQ in the solid form in $N_2$ atmosphere and at room temperature can produce $Cu_3(C_6O_6)_2$ in good crystallinity (**N.O. 14-18** in **Table D.1**) and significant improved crystalline size (**Figure D.3f-g**). However, without using acidic modulator (**N.O. 14** in **Table D.1**) or using weak acid as the modulator (**N.O. 15** in **Table D.1**), the formation of other unspecified species with extra peaks shown in pXRD (marked with * in **Figure D.1**) were observed. Using trifluoroacetic acid as acidic modulator although gave fair crystallinity (**N.O. 18** in **Table D.1**), generated materials with much smaller crystallites compared with using no acidic modulator (**Figure D.3h**). (5) Adding THQ in the solid form, meanwhile, gently bubbling air into the reaction system under 65 °C (**N.O. 19-22** in **Table D.1**) generated $Cu_3(C_6O_6)_2$ with high crystallinity with better resolved pXRD peaks (e.g. peaks at $2\theta$=15-17°) and cleaner spectrum compared materials obtained from all the other conductions being tried. In addition, this condition (**N.O. 22** in **Table D.1**) generated crystals up to micrometer scales compared (**Figure D.3i**), which is significantly large than the material obtained using the literature procedure (**Figure D.3a** *vs* **Figure D.3i**).

Therefore, we adopted *condition N.O. 22* (**N.O. 22** in **Table D.1**) as our optimized synthetic condition for $Cu_3(C_6O_6)_2$. In the following characterizations and tests, including MicroED, FTIR, Raman, XPS, EPR, TGA, conductivity tests, and magnetic measurements, the materials synthesized from condition *N.O. 22* was used without further treatment.

This optimized synthetic condition was inspired by the initial work from Bao and coworkers,[1] which showed the synthesis of MOF $Cu_3(C_6O_6)_2$ from copper nitrite and THQ or hexahydroxybenzene. This previous study showed that precise control of the molar ratio of the ligand to the coordinative base ethylenediamine was important in mediating the competing kinetic and thermodynamic effects during framework formation to yield a crystalline product. We hypothesized that controlling and optimizing the acidity of solution would be beneficial for this chemical transformation, as a moderately lower level of basicity can slow down the deprotonation of the ligand resulting in a slower rate of framework formation. Furthermore, considering the redox chemistry of THQ, which needs to be oxidized (at least partially) as it is being incorporated into the MOF,[1-2] we reasoned that an $O_2$-rich environment can facilitate the oxidation of the ligand to promote the formation of the charge-neutral framework, while avoiding the formation of reduced metallic Cu(0) impurity. To improve the outcome of this chemical transformation, we made three strategic modifications to the previously reported conditions.[1, 3] *First*, for optimizing the acidity of this reaction media, we adopted a commonly used buffer salt, ammonium acetate, that gave a moderate acidity (pH = 5.98) for the reaction system. *Second*, THQ was added into the reaction mixture directly in the solid form rather than as a solution utilized in a previous report; this approach can provide control over the rate of growth of the framework through slow dissolution of the ligand. *Third*, the air was bubbled into the reaction mixture to promote rapid oxidation of the dissolved THQ ligand, thereby promoting coordination-polymerization.

**D3.        SEM and TEM**

Scanning electron microscopy of $Cu_3(C_6O_6)_2$ was obtained using a Hitachi TM3000 SEM. The material was pressed onto carbon conductive tape that was attached to the aluminum plate. The images were taken at a 7 mm working distance using a 5-30 kV beamline in a $10^{-6}$ torr vacuum chamber.

Transmission electron microscopy was carried out in a Tecnai F20ST FEG TEM instrument. The sample was prepared by sonicating the MOF sample in $H_2O$ (0.5 mg in 1 mL) for two hours. 5 μL of the suspension was then drop-casted onto a copper grid (300 mesh, 3.0 mm O.D), which was then dried under vacuum for 24 hours at room temperature before TEM imaging. An operating voltage of 120 kV was used for imaging.
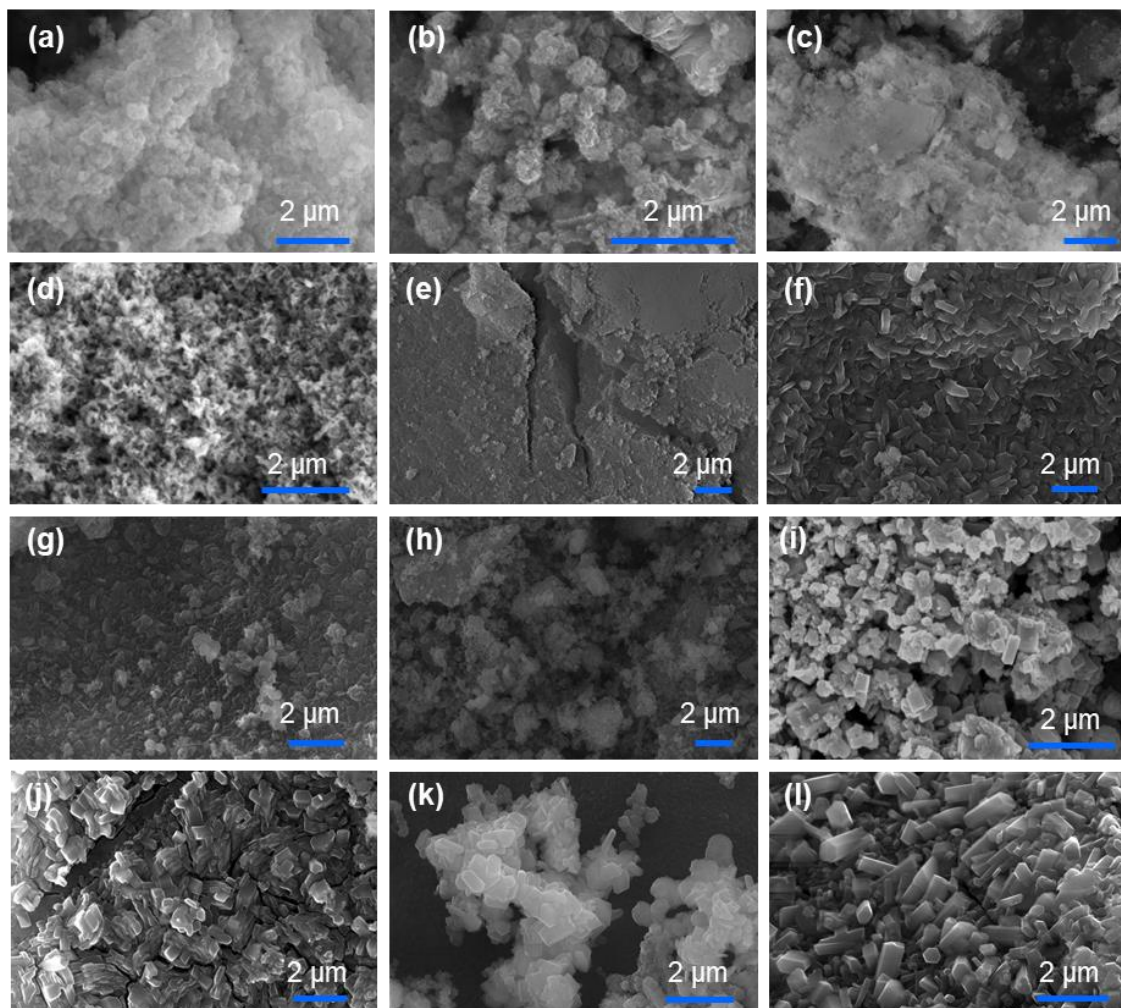
**Figure D.3.** SEM images of $Cu_3(C_6O_6)_2$ synthesized using (a) condition from the previous report[1] and (b)-(l) conditions in *N.O. 1, 4, 5, 9, 14, 16, 18, 19, 20, 21, 22* as summarized in **Table D.1** in which condiction **N.O. 22** showed the significantly improved size of crystallite
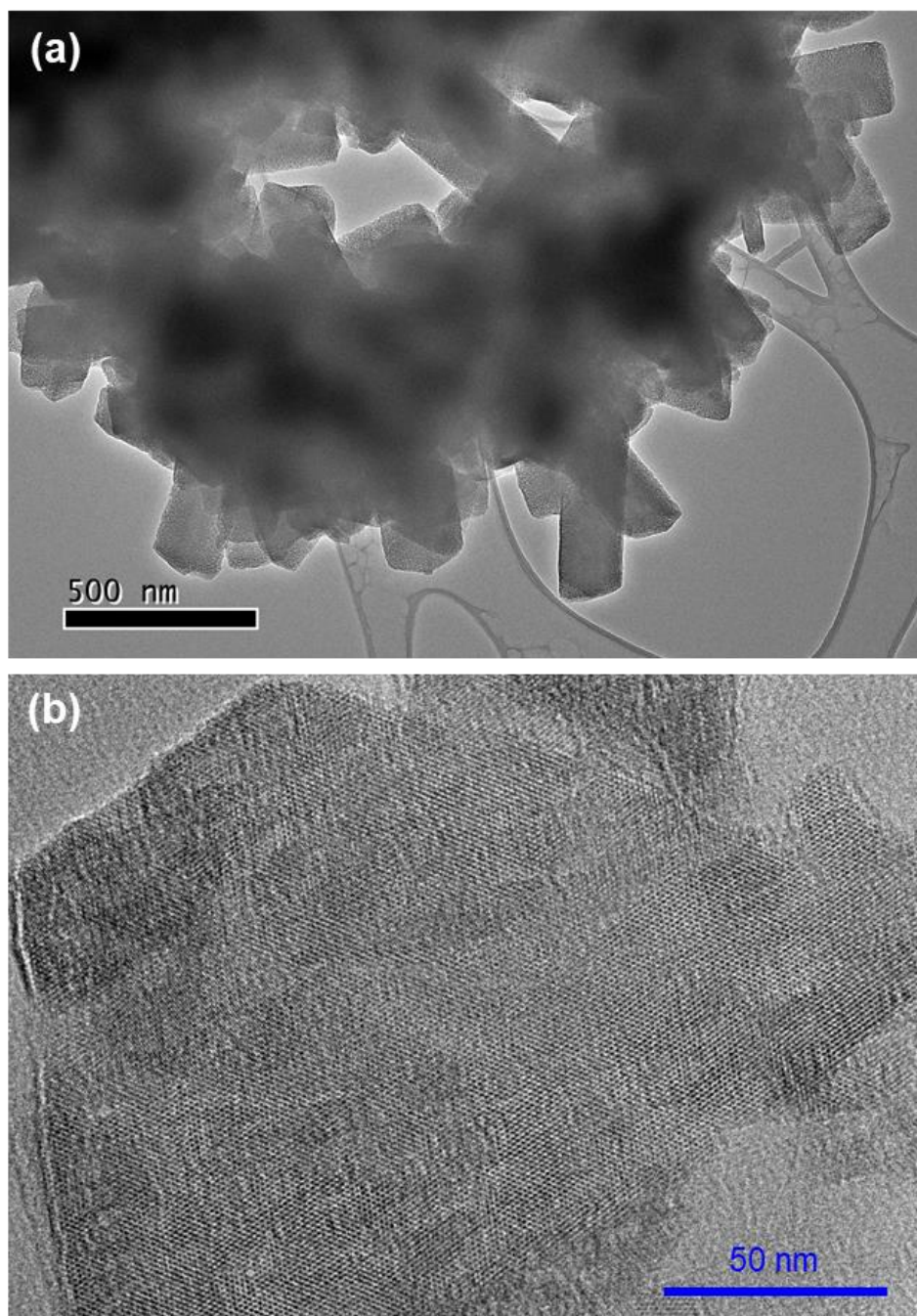
**Figure D.4**. (a) and (b) TEM images in different magnifications of $Cu_3(C_6O_6)_2$ synthesized under condition *N.O. 22* as listed in **Table D.1**.
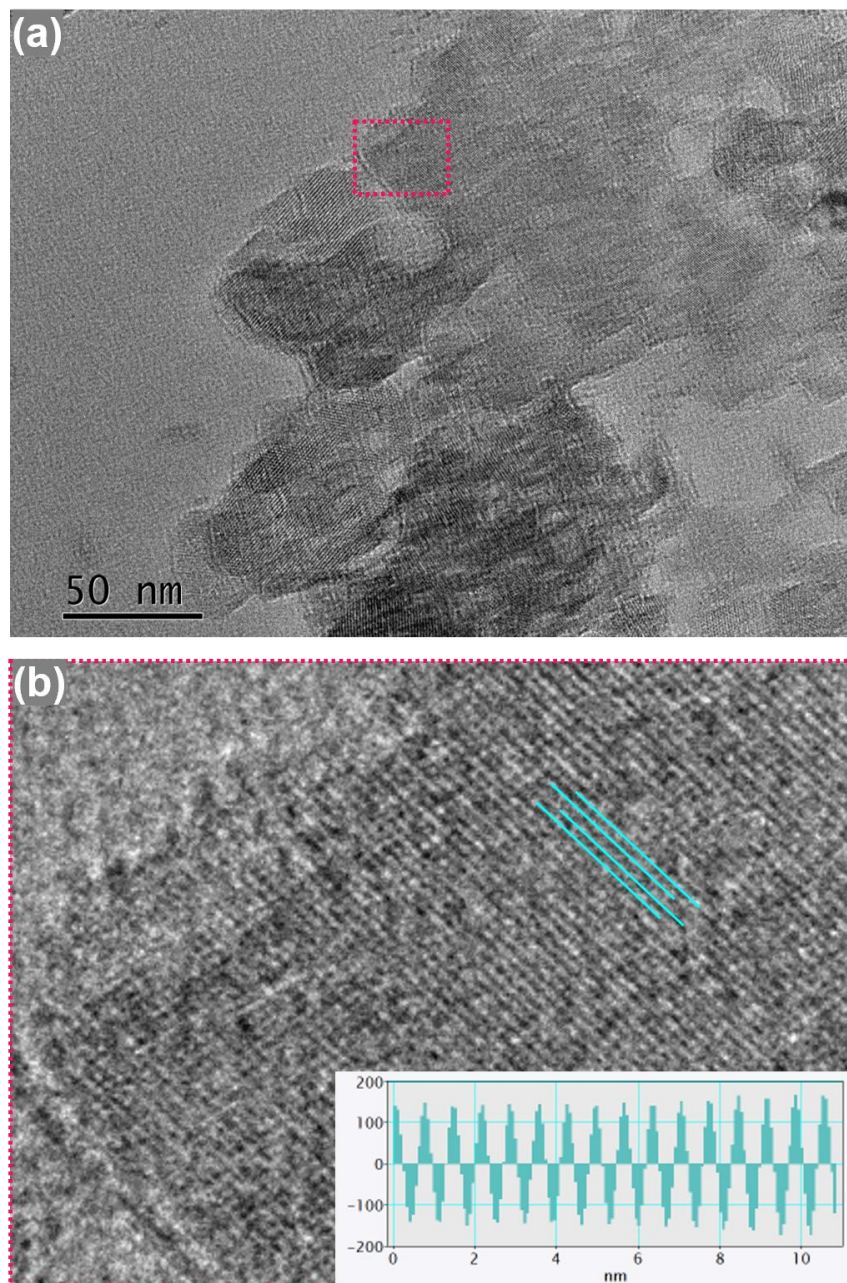
**Figure D.5**. (a) and (b) TEM images of $Cu_3(C_6O_6)_2$ that show the ordered layer stacking in this material. The regular spacing between the lines as indicated in the TEM image was analyzed using the software DigitalMicrograph, which gave a spacing distance of ~3.1 nm (inset in b).

## D4.      Fourier-Transform Infrared (FTIR) Spectroscopy and Raman Spectroscopy

Infrared spectra were collected using a JASCO model FT IR-6100 Fourier transform infrared spectrophotometer. Raman spectra were measured at room temperature in LabRAM HR

Evolution Raman microscopy with the laser in the wavelength of 633 nm was used for excitation. Raman scattering radiation was collected in a back–scattering configuration with a standard spectral resolution of 4 cm$^{-1}$. The Cu$_3$(C$_6$O$_6$)$_2$ powder was dusted on a gold substrate for Raman measurement.
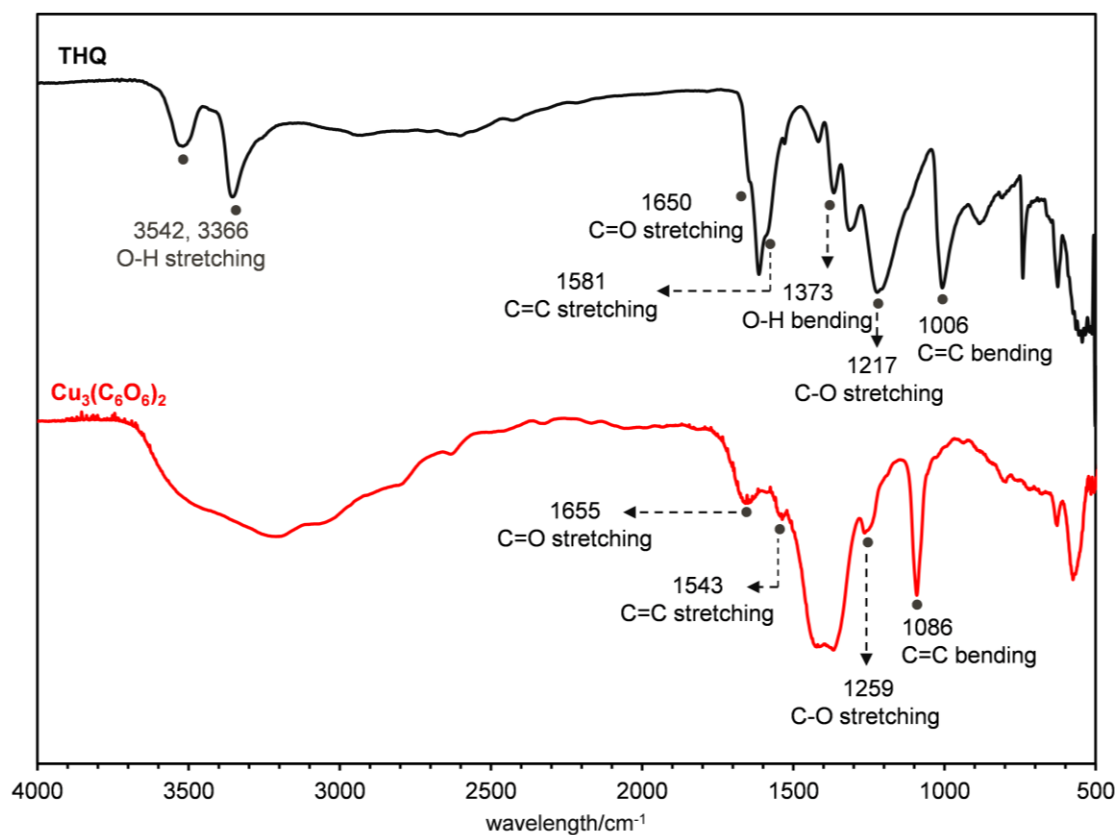


**Figure D.6**. Comparison of FTIR spectra of THQ and Cu$_3$(C$_6$O$_6$)$_2$.
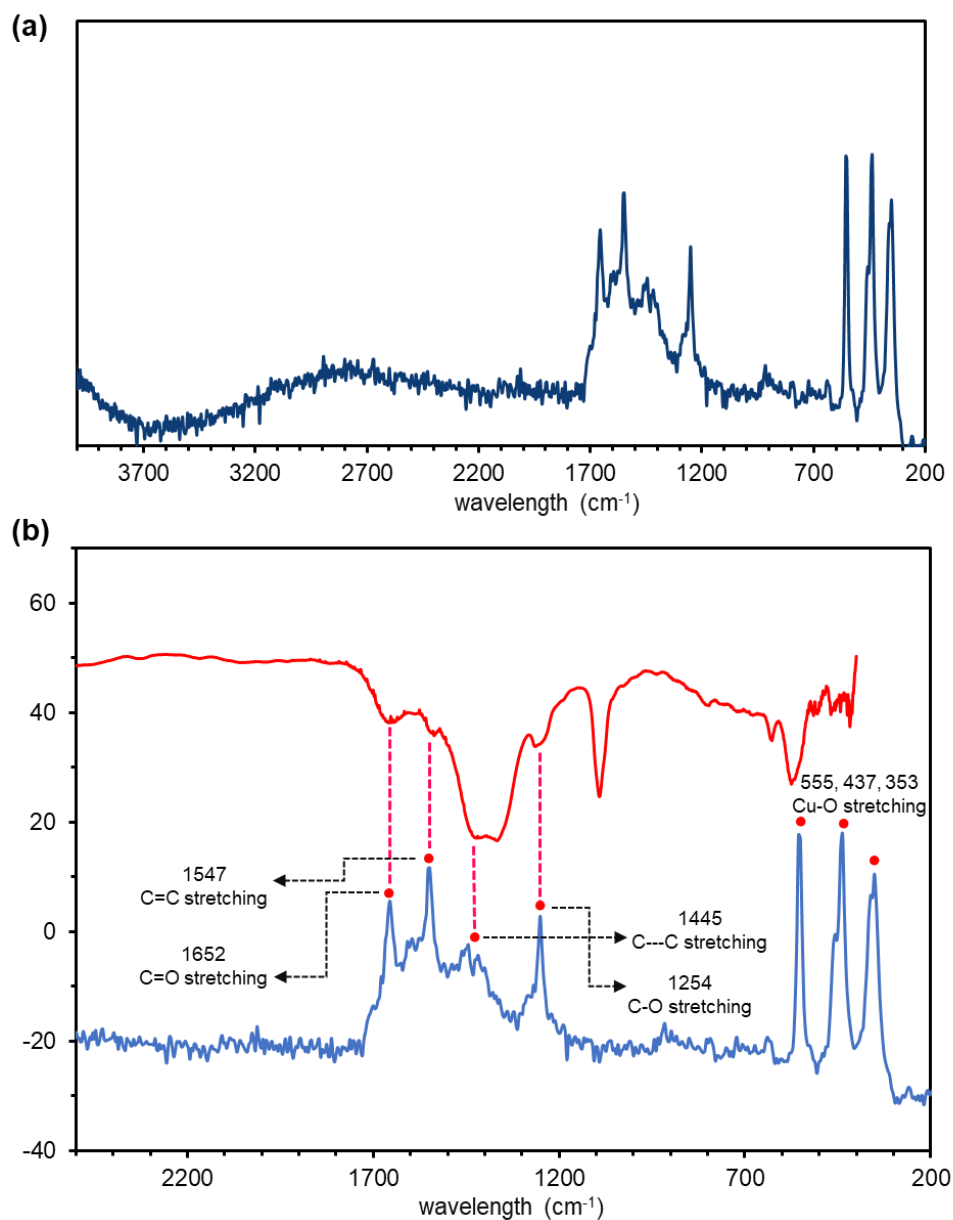
**Figure D.7**. (a) Raman spectrum of $Cu_3(C_6O_6)_2$ at the range of 200-5000 cm$^{-1}$. (b) Comparison of the Raman at the range of 200-2500 cm$^{-1}$ (blue) and FTIR spectrum at the range of 500-2500 cm$^{-1}$ (red) with a few critical peaks indicated.

## D5.  Diffuse Reflectance UV-vis-NIR spectra

To measure the UV-vis-NIR spectra of $Cu_3(C_6O_6)_2$, its thin films were grown in-situ on the quartz by putting quartz slides into reaction solutions as described in the condition ***N.O. 22*** in section **D2**. UV–vis–NIR between 250 and 2500 nm were collected on a JASCOV-570

spectrophotometer at the scan rate of 200 nm/min under ambient conditions. A blank quartz baseline and a zero background correction were collected prior to the sample measurement.
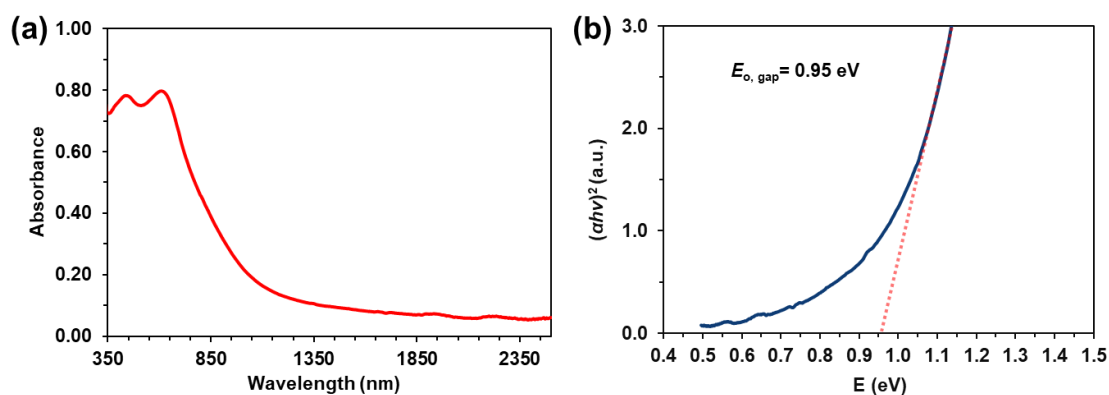


**Figure D.8.** (a) UV -vis-NIR of $Cu_3(C_6O_6)_2$ MOF thin films deposited on quartz slides. (b) NormalizedTauc plots from the spectra in (a).

Tauc method was initially proposed for estimating the band gap energy of amorphous semiconductors using optical absorption spectra,[4] which is based on the assumption that the energy-dependent absorption coefficient $\alpha$ can be expressed by the following equation (**D.1**):

$$(\alpha \cdot hv)^{\frac{1}{\gamma}} = B(hv - E_g) \qquad \text{(\textbf{D.1})}$$

In the equation, $h$ is the Planck constant, $v$ is the photon's frequency, $E_g$ is the optical band gap energy, and $B$ is a constant. Depending on the nature of the electron transition, the $\gamma$ factor can be 1/2 or 2 for the direct and indirect transition band gaps, respectively.[5] This approach can be applied for many semiconducting materials that do not absorb light of the sub-band gap energy and has been used for the estimation of optical band gaps of semiconductive/conductive MOFs[6] However, materials that are defected, doped, or surface modified may introduce intraband gap states that reflect in the absorption spectrum as an Urbach tail, i.e., an additional, broad absorption band.[7] Their presence influences the Tauc plot and therefore should be taken into account to determine the band gap energy. In our case, the defects and presence of slight amount of impurities might affect the estimation of the optical band-gap using the Tauc method.

## D6.     Elemental Analysis

Elemental analyses, including C, H, and N were performed by Atlntic Microlab inc. using the combustion method by automatic analyzers. Cu content was analyzed by ICP -MS. The results are listed below.

**Table D.2.** Elemental analysis of **$Cu_3(C_6O_6)_2$**.

| $Cu_3(C_6O_6)_2$ | theoretical 1 [$Cu_3(C_6O_6)_2$] | theoretical 2 [$Cu_3(C_6O_6)_2 \cdot 6H_2O$] | experimental |
|---|---|---|---|
| C | 27.36% | 22.70% | 22.65% |
| H | 0 | 1.91% | 2.16% |
| N | 0 | 0 | 0.36% |
| O | 36.45% | 45.36% | N/A |
| Cu | 36.19% | 30.03% | 30.09% |

### D7. X-ray Photoelectron Spectroscopy

X-ray photoelectron spectroscopy (XPS) experiments were conducted on a Kratos Analytical

AXIS Supra X-ray photoelectron spectrometer under ultrahigh vacuum (base pressure $10^{-7}$ Torr). The measurement chamber was equipped with a monochromatic Al ($K_\alpha$) X-ray source. The material was mounted by lightly pressing onto a copper tape which was mounted on a Dual-Height (Kratos) sample holder. A survey spectrum was obtained from 0 eV–1400 eV to obtain elemental surface composition. High-resolution spectra were then obtained at energy regions specific to elements observed in the survey spectrum. XPS was performed under a pressure of ~$10^{-7}$ Torr. Both survey and high-resolution spectra were obtained using a beam diameter of 200 μm. The spectra were processed with CasaXPS.
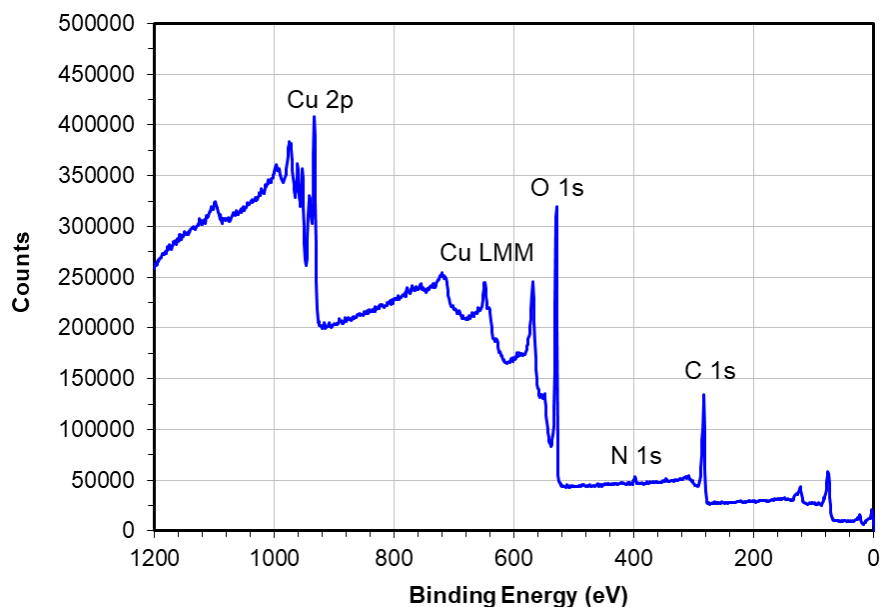


**Figure D.9.** XPS survey spectrum showing C, O, Cu, and a slight amount of N in $Cu_3(C_6O_6)_2$.
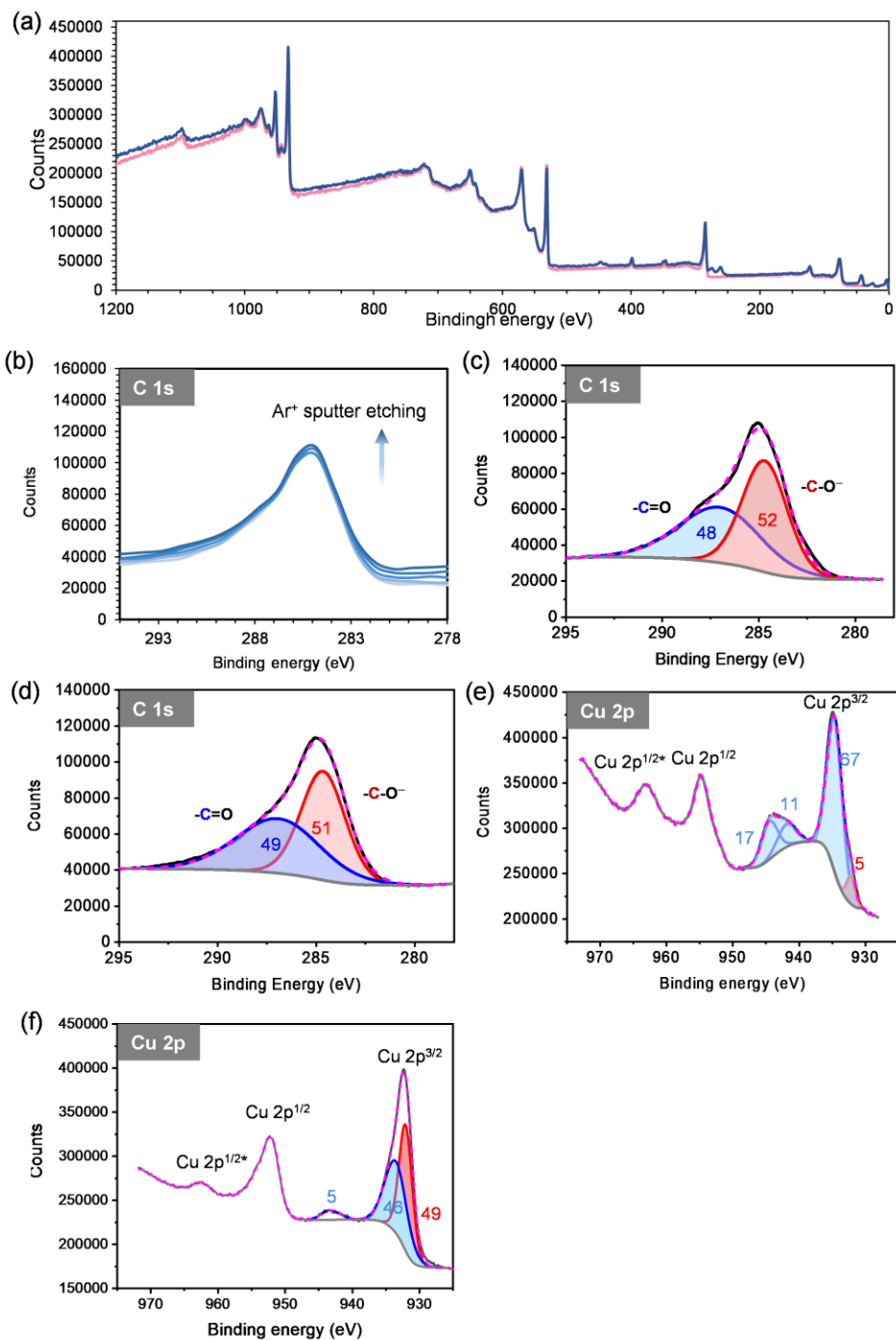
**Figure D.10**. (a) XPS survey spectrum of $Cu_3(C_6O_6)_2$ before and after $Ar^+$ sputtering. (b) High-resolution spectra of C 1s with a gradual $Ar^+$ sputter etching process. The deconvoluted C 1s XPS spectra (c) before and (d) after five cycles of $Ar^+$ sputter etching process. The deconvoluted Cu 2p spectra of $Cu_3(C_6O_6)_2$ (e) before and (f) after five cycles of $Ar^+$ sputtering. Deconvoluted peaks are color-coded and their corresponding ratios are given.

The XPS binding energy values were calibrated with C 1s core level signal, which was assumed to have the binding energy of 284.8 eV.[8] The scan spectra showed the presence of C, O, and Cu, as well as a trace amount of N in $Cu_3(C_6O_6)_2$ (**Figure D.9**). The presence of a trace amount (0.98%, directly quantified by XPS) of the N element indicated that $NH_4^+$ or $NO_3^-$ ions may reside on the edges of the MOF crystals for the compensation of the charged ends.

Considering that the presence of adventitious carbon that is usually present on most air-exposed samples may affect the quantification, we performed a gradual $Ar^+$ sputter etching process to remove the adventitious carbon.[8-9] The $Ar^+$ sputter etching process consisted of five consecutive cycles. Each etching cycle lasted for 2 min and was performed at the voltage of 500 eV. After each cycle, a spectrum was recorded to monitor any possible change. After 5 cycles of $Ar^+$ sputter etching, we did not observe significant changes of the C1s range of the $Cu_3(C_6O_6)_2$ (**Figure D.10b**), which indicated that the adventitious carbon may only play a very minor contribution to the C 1s range of the spectrum. The deconvolution of the C 1s region showed two components at the binding energies of 284.7 and 287.1eV, which we ascribed to -C-O, and -C=O, respectively (**Figures D.10c-d**).[8-9] The area ratios of peaks at these two binding energies before and after the $Ar^+$ sputter etching were respectively 48:52 and 49:51 (**Figures D.10c-d**). The ratios of -C-O and -C=O were close to 1:1, indicating that the ligand in MOF $Cu_3(C_6O_6)_2$ was in tris(semiquinone) state.

In practice, the established methods for the quantification of different Cu species by XPS include two styles. One style only considers the main Cu 2p3/2 line, the other style considers both the main Cu 2p3/2 region and satellite structure.[10] The quantification of the Cu(I) and Cu(II) species in this work was followed by the method suggested by Biesinger and coworkers[11] and others,[10, 12] in which the satellite peaks in the binding energy range of ~935-945 eV were taking into account for accuracy. The reason for this consideration was discussed in detail in the cited publication.[10-11] Shake-up peaks are present in the spectra of Cu(II)-containing samples but are nearly absent in Cu(0) or Cu(I) spectra. Shake-up peaks occur when the outgoing photoelectron simultaneously interacts with a valence electron and excites it to a higher energy level, thus giving satellite structure a few eV below the core level position. Hence, these electrons are part of the total Cu 2p emission and should be included in both total Cu and relative chemical state speciation. The deconvolution of the Cu 2p3/2 range of $Cu_3(C_6O_6)_2$ showed a main component at the binding energy of 933.8 eV and a minor component at a binding energy of 932.2 eV (**Figure D.10e**), the latter of which was ascribed to Cu(I). Using the method given,[11] the Cu(II): sputtering is known to cause metal reduction (e.g., CuO, $Fe_2O_3$, and other metal oxides),[13] after) the argon sputtering, an increase in the ratio of Cu(I) to 49% was observed (**Figure D.10f**).

In the previous work[1] from Prof. Bao's group for the synthesis of the Cu-HHB (the name given for $Cu_3(C_6O_6)_2$ in the cited work), Cu(II) was also found as a dominant species for the MOF even through an inert atmosphere environment was used during the synthesis. The use of oxygen-rich conditions in our work likely produces higher content of Cu(II) in $Cu_3(C_6O_6)_2$. The dominant

presence of Cu(II) in the bulk phase is also consistent with our magnetic characterization, as discussed in the manuscript. With the resolved single crystal structure for $Cu_3(C_6O_6)_2$ (see section 10) in our hands, another robust method for the analysis of the oxidation state of Cu in MOF $Cu_3(C_6O_6)_2$ can be performed using the new method developed by Smit and coworkers, which is specifically designed for oxidation state analysis of metals in MOFs based on machine learning and single crystal structure.[14] Using this method,[14] we determined the oxidation state of Cu in $Cu_3(C_6O_6)_2$ to be Cu(II) with a predicted probability of 0.994.

**D8.  Electron Paramagnetic Resonance (EPR) Spectroscopy**

EPR spectra were collected on a Bruker BioSpin Gmbh spectrometer equipped with a standard mode cavity. For each sample, about 2 mg of material was used. The samples were flushing with $N_2$ for 1 hour and then sealed in the EPR tube under $N_2$ atmosphere. The EPR spectrum was collected under room temperature (298 K), liquid nitrogen temperature (77 K), and 5 K (cooled with liquid helium) with the parameters listed in **Table D.3**. THQ showed a very intense peak at $g$ = 1.991, which is likely due to the existence of partially oxidized species or intramolecular charge transfer. $Cu_3(C_6O_6)_2$ showed a strong EPR signal at $g$=2.085 from the metal-centered radical. This observation is consistent with XPS results, which indicated that Cu ions in $Cu_3(C_6O_6)_2$ exist as Cu(II).

**Table D.3.** Parameters of EPR.

| Sample | Temperature/K | sweep width/G | center field/G | modulation amplitude/G | microwave frequency/GHz | microwave power/mW |
|---|---|---|---|---|---|---|
| THQ | 298 | 2000 | 3500 | 4 | 9.688 | 3.414 |
| $Cu_3(C_6O_6)_2$ | 298 | 2000 | 3500 | 4 | 9.653 | 3.414 |
| $Cu_3(C_6O_6)_2$ | 77 | 2000 | 3500 | 4 | 9.655 | 3.413 |
| $Cu_3(C_6O_6)_2$ | 5 | 2000 | 3500 | 4 | 9.524 | 3.419 |
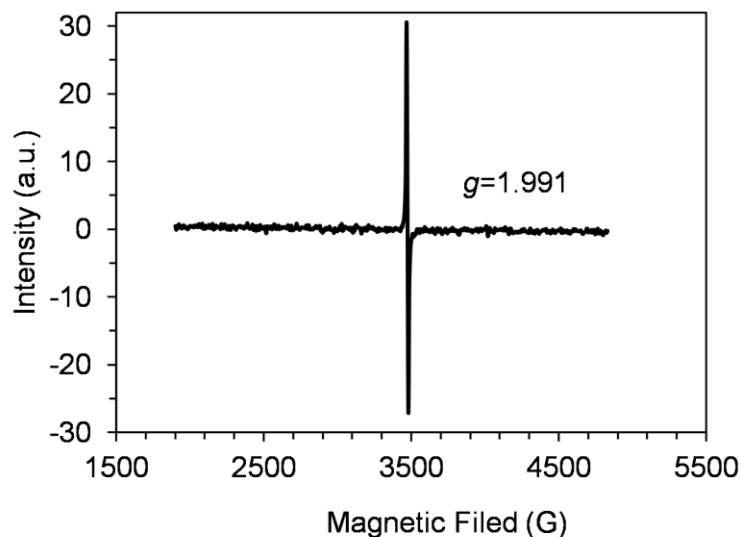
**Figure D.11.** EPR spectra of THQ (solid state) under liquid nitrogen temperature.
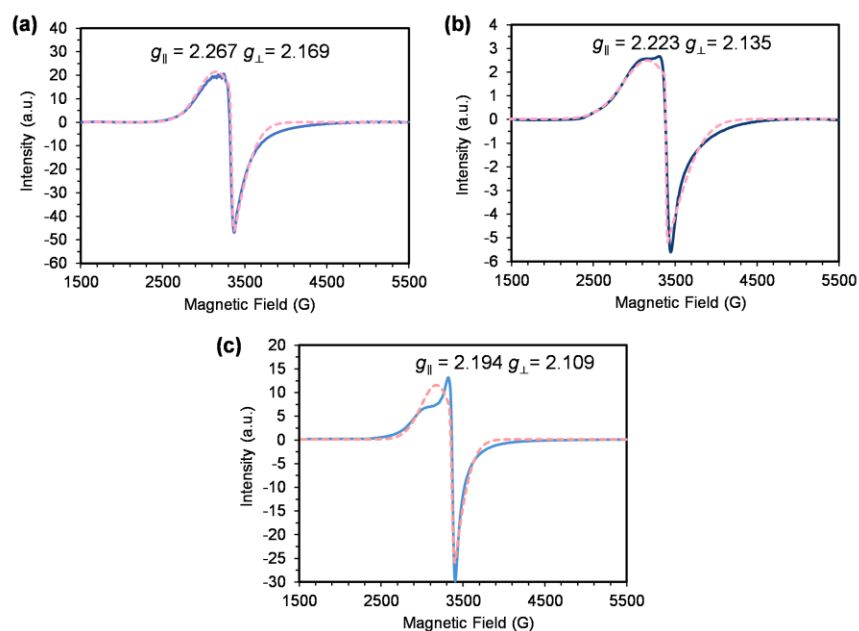


**Figure D.12.** EPR spectra of $Cu_3(C_6O_6)_2$ at (a) 298 K, (b)77 K, and (c) 5 K. The dashed lines are the simulated traces with the EasySpin 5.2.33 in Matlab (R2020b).

The ligand THQ showed a sharp signal at $g=1.991$. THQ should have no formal radical. The observed signal may be due to the partial oxidation of THQ or the surface adsorbed oxygen molecule. Nevertheless, in sharp contrast with that of the ligand, $Cu_3(C_6O_6)_2$ exhibited a broad and unsymmetrical signal in the range of 2500–4500 G. The simulation of the EPR peak of $Cu_3(C_6O_6)_2$ at room temperature revealed $g_\parallel = 2.223$, $g_\perp = 2.135$. The simulated EPR peak of $Cu_3(C_6O_6)_2$ at 77

K revealed $g_∥ = 2.267$ and $g_⊥ = 2.169$. These values agree with the signal expected for a $Cu^{2+}$-based $S = 1/2$ spin.[2, 15] The asymmetric shapes of the EPR spectra may result from the pseudo-square planar coordination of Cu, in which in-plane Cu•••O coordination bonds are much longer than Cu to O and Cu to Cu distances along the axial direction (see Figure D.33 in section D16).[16]

## D9. Structural Determination of $Cu_3(C_6O_6)_2$ by MicroED

Samples were prepared by placing a TEM grid in a vial of dry powder of the MOF materials and gently shaking. The prepared TEM grid was loaded in a Gatan 626 single-tilt cryo holder and cooled with liquid nitrogen. Screening and data collection were performed using a Thermo-Fisher F200C transmission electron microscope operating at 200 kV corresponding to a wavelength of 0.0251 Å. Electron diffraction data were collected using a Thermo-Fischer Ceta-D CMOS 4k × 4k camera. The screening of crystal was done in low-dose mode and diffraction was identified through condensing of the electron beam. After the selection of a crystal on the grid, the crystal was centered, the eucentric height adjusted by tilting the crystal through the desired rotation range, and the selected area aperture and beam stop were inserted.[17]

Images were collected in a movie format as crystals were continuously rotated in the electron beam.[18] Typical data collection was performed using a constant tilt rate of 0.3°/s between the minimum and maximum tilt ranges of −72° to +72°, respectively. During continuous rotation, the camera integrated frames continuously at a rate of 3 seconds per frame. The dose rate was calibrated to <0.03 e$^-$/Å$^2$ s. Crystals selected for data collection were isolated by a selected area aperture to reduce the background noise contributions and calibrated to eucentric height to stay in the aperture over the entire tilt range. The electron diffraction data were processed using the XDS suite of programs.[19] The structure was solved *ab initio* using direct methods in SHELXT[20] using ShelXle.[21] Structure refinement was performed using electron scattering factors reported by Peng.[22] Thermal parameters were refined anisotropically for all non-hydrogen atoms. The data processing statistics and refinement results were shown in **Table D.4** and the resolved structure was shown in **Figure D.14**.

As shown in **Figure D.14a**, in the MicroED resolved structure of $Cu_3(C_6O_6)_2$, the positions of the O atoms of the water molecules in the pores were successfully determined. Since the positions of H atoms of the water molecules in the channel of the MOF $Cu_3(C_6O_6)_2$ could not be determined by MicroED, we generated the position of the H atoms by DFT calculations using the CASTEP module[23] embedded in Material Studio 2019. The positions of C, O, and Cu in the structure resolved by MicroED were fixed during the optimization. H atoms were added to the O atoms of water molecules and the positions of H atoms were optimized. Perdew−Burke−Ernzerhof (PBE) functional with generalized gradient approximation (GGA) was applied with the application of

DFT-D dispersion correction method of Grimme for the long-range van der Waals interaction.[24] The energy cut-off was set at 800 eV. The Brillouin zone was sampled with the gamma-centered Monkhorst-Pack k-point grid of $2 \times 2 \times 4$. The convergence criterion for the self-consistent field calculation was set to $1 \times 10^{-6}$ eV/atom. The MicroED structure of MOF $Cu_3(C_6O_6)_2$ with H atoms of water molecules regenerated was shown in **Figure D.15**.

Despite the good quality of data collected, it is difficult to directly compare electron diffraction statistics to those of traditional X-ray crystallography as current electron structures display much higher R-values. This is a result of a number of factors, including low signal-to-noise, scattering factor accuracy, and unaccounted dynamical scattering effects.[18, 25] Newly emerging techniques such as dynamical refinement have been used to generate structures with statistics on par with that of X-rays.[26] However, these techniques are not yet routine and require specialized knowledge. It is likely that these techniques will be more widely available in the coming years and produce results more consistent with traditional crystallography. Another limitation of electron diffraction is the tilt range achievable with a standard TEM, which can make sampling all of the reciprocal space difficult.[25] In this case, despite the bulk material being crystalline, finding sufficiently many pristine microcrystals needed to generate a structure was challenging as most particles were polycrystalline. Despite this limitation, we were still able to generate a structure that corroborates with other experimental evidence and PXRD data (Section 10 in Supporting Information). While these limitations can make electron diffraction challenging, it is still the only method capable of extracting accurate solid-state information from micro and nanoscale crystals, especially for compounds such as MOFs whose crystallinity is often dictated through the synthesis procedure and therefore cannot readily be recrystallized.
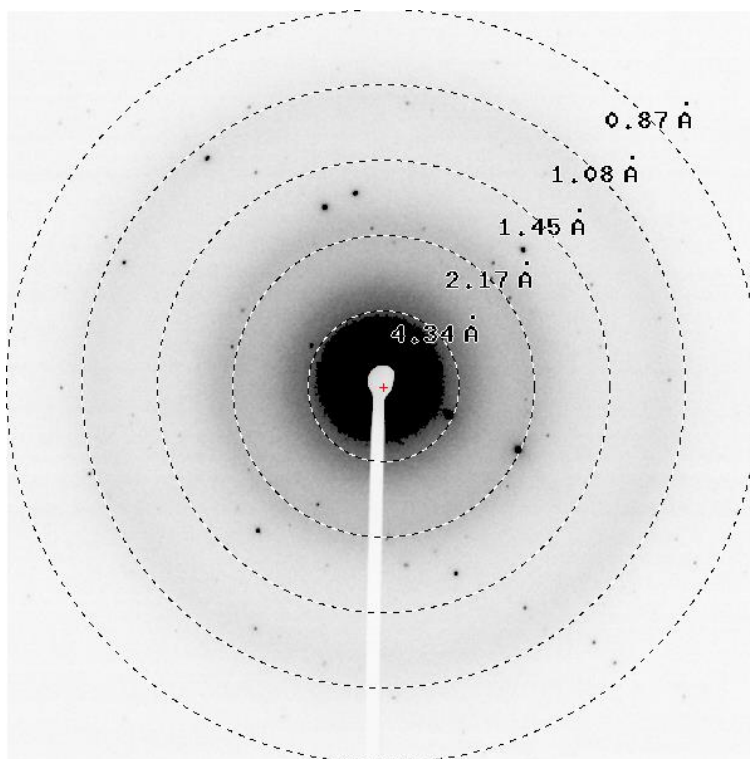
**Figure D.13.** Electron diffraction pattern obtained for the crystal of $Cu_3(C_6O_6)_2$.

**Table D.4**. Data processing statistics and refinement results of $Cu_3(C_6O_6)_2$ by MicroED.

| name | $Cu_3(C_6O_6)_2$ |
|---|---|
| Chemical Formula | $C_{12}O_{12}Cu_3$ |
| Temperature (K) | 100 |
| Space Group | C2/m |
| a/Å | 21.86(3) |
| b/Å | 12.950(5) |
| c/Å | 6.120(7) |
| angles $\alpha, \beta, \gamma$ | $\alpha = 90.000°, \beta = 102.12(8)°, \gamma = 90.000°$ |
| Reflections (#) | 3804 |
| Unique reflections (#) | 1262 |
| $R_{obs}$ | 12.4% |
| $R_{meas}$ | 14.9% |
| CC1/2 | 98.8 |
| Resolution (Å) | 0.80 |

| | |
|---|---|
| Completeness (%) | 70% |
| Total exposure (e Å$^{-2}$ ) | ~3 |
| R | 0.1987 |
| wR2 | 0.4553 |
| GoF | 2.262 |
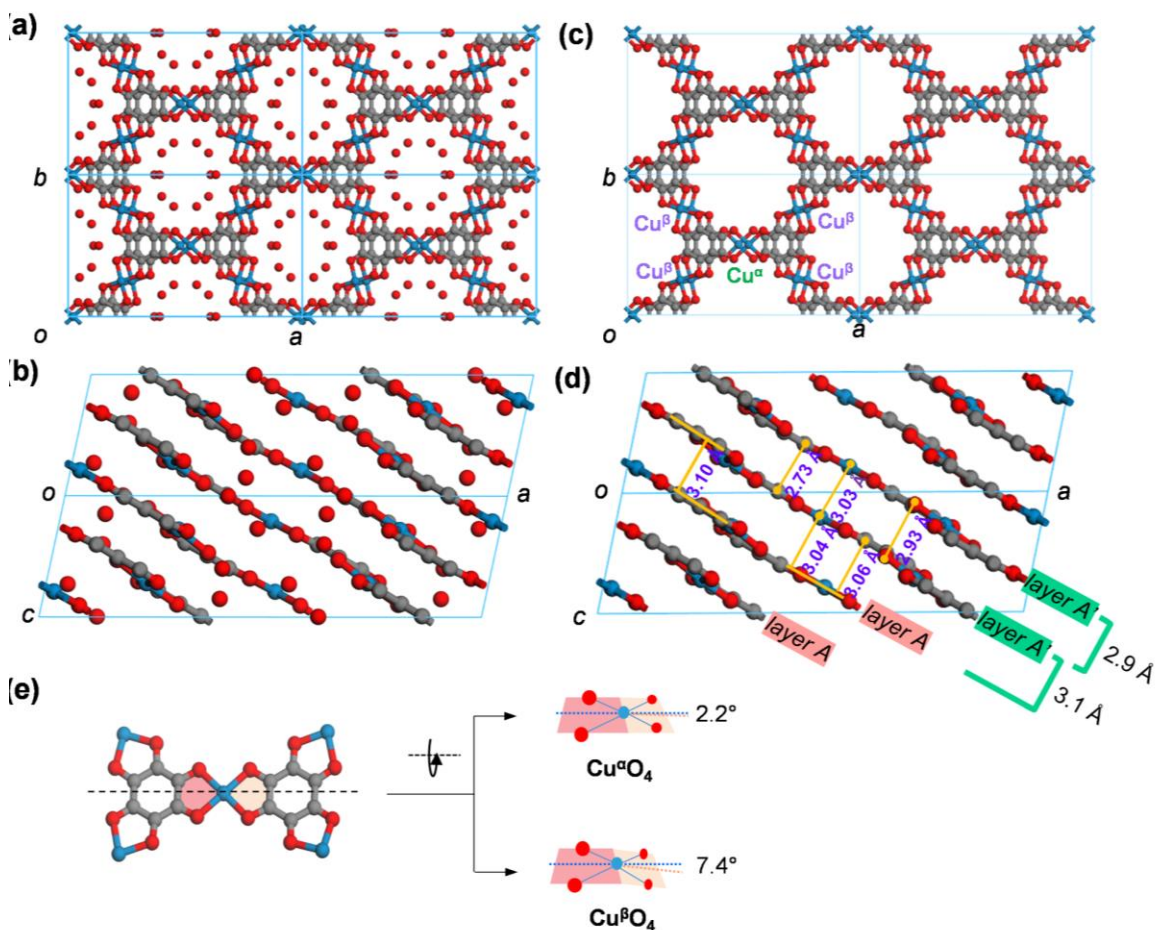


**Figure D.14**. (a)-(b) Crystal structure of $Cu_3(C_6O_6)_2$ resolved by MicroED in front and side views with water molecules shown inside the open channel. In the MicroED resolved structure of $Cu_3(C_6O_6)_2$, the positions of the O atoms of the water molecules in the pores were successfully determined. (c)-(d) Crystal structure of $Cu_3(C_6O_6)_2$ resolved by MicroED in front and side views with water molecule inside the channel omitted. The AAA′A′ attacking of $Cu_3(C_6O_6)_2$ is indicated in **Figure D.14d**. Because the layers in $Cu_3(C_6O_6)_2$ are not flat, it is difficult to directly give an exact value of the interlayer distance. To describe the interlayer distance as accurately as possible, we employed the term "average interlayer distance" by averaging multiple representative interatomic distances between the two adjacent layers. As shown in **Figure D.14d**, we defined the averaged

interlayer distance for the fully-eclipsed layers (AA or A′A′) as the averaged distance values of C to C, O to O, and Cu to Cu distances in the adjacent layers, which are 2.70 Å, 2.92 Å, and 3.01 Å, respectively, that gives an average interlayer distance of 2.9 Å for AA or A′A′ layers. We defined the average interlayer distance for the slipped-parallel (A′A or AA′) layers as average distance values of $C_6$ to $C_6$ ring, Cu to O-Cu-O plane, and C to O-Cu-O plane in the adjacent layers, which are 3.13 Å, 3.04, and 3.06 Å, respectively, that gives an average interlayer distance of 3.1 Å for A′A or AA′ layers. (e) The slightly distorted conformations of the $CuO_4$ units formed by $Cu^\alpha$ and $Cu^\beta$. Dihedral angles of 2.2° and 7.4° were respectively found between the planes (blue and orange) determined by O-$Cu^\alpha$-O atoms and O-$Cu^\beta$-O atoms.

By comparing the structural information of the MOF in the previous report [1] by Prof. Bao's group with that in our work, we have noted two differences. **(1)** The resolved structure by pXRD in the previous work[1] indicated that Cu-HHB (the name given for $Cu_3(C_6O_6)_2$ in the cited work) exhibits a C-centered orthorhombic unit cell with cell parameters of $a = 13.108$ Å, $b = 21.592$ Å, $c = 5.924$ Å. In our work, MicroED analysis on single crystal of the MOF showed that $Cu_3(C_6O_6)_2$ crystalized as a C2/M space group with cell parameters of $a = 21.86(3)$ Å, $b = 12.950(5)$ Å, $c = 6.120(7)$ Å, $\alpha=\gamma=90°$, and $\beta=102.12(8)°$. These values suggested that resolved cell parameters in the previous work and our work resemble but do show appreciable differences (e.g. 13.108 vs 12.950 Å, 21.592 vs 21.86 Å). **(2)** In the previous work[1], the calculated pXRD for Cu-HHB with a slipped-parallel packing model showed a difference with the experimental pXRD at $2\theta$=~4.78° ($\lambda = 0.45236$ Å, Q=1.19 Å$^{-1}$), in which a shoulder peak is shown $2\theta$=~4.78° ($\lambda = 0.45236$ Å) in the experimental pXRD but is absent in the calculated pXRD. In our work, the shoulder peak at Q=1.19 Å$^{-1}$ is clearly resolved from other peak(s) (**Figure D.19** in Supporting Information) and it agrees well with both the MicroED and calculated pXRD of $Cu_3(C_6O_6)_2$ with a AAA′A′ attacking as discussed in our manuscript.

However, as we have mentioned in the manuscript, the MOF Cu-HHB in the previous work[1] had a negatively charged scaffold with protonated ethylenediamine as the positive counter ions. Due to the different synthetic procedures, $Cu_3(C_6O_6)_2$ in our work has a neutral skeleton without counter ions. Therefore, the materials made from the previous report and our work are chemically distinct, which may have different crystal structures, albeit the difference can be very slight. Nevertheless, the direct access to the crystal structure by MicroED analysis in our work led to the ambiguous elucidation of the packing structure of the 2D MOFs. In contrast, the method relying on pXRD in combination with quantum calculation is not yet able to provide exact information for the stacking structure, especially when the stacking structure is nontrivial.
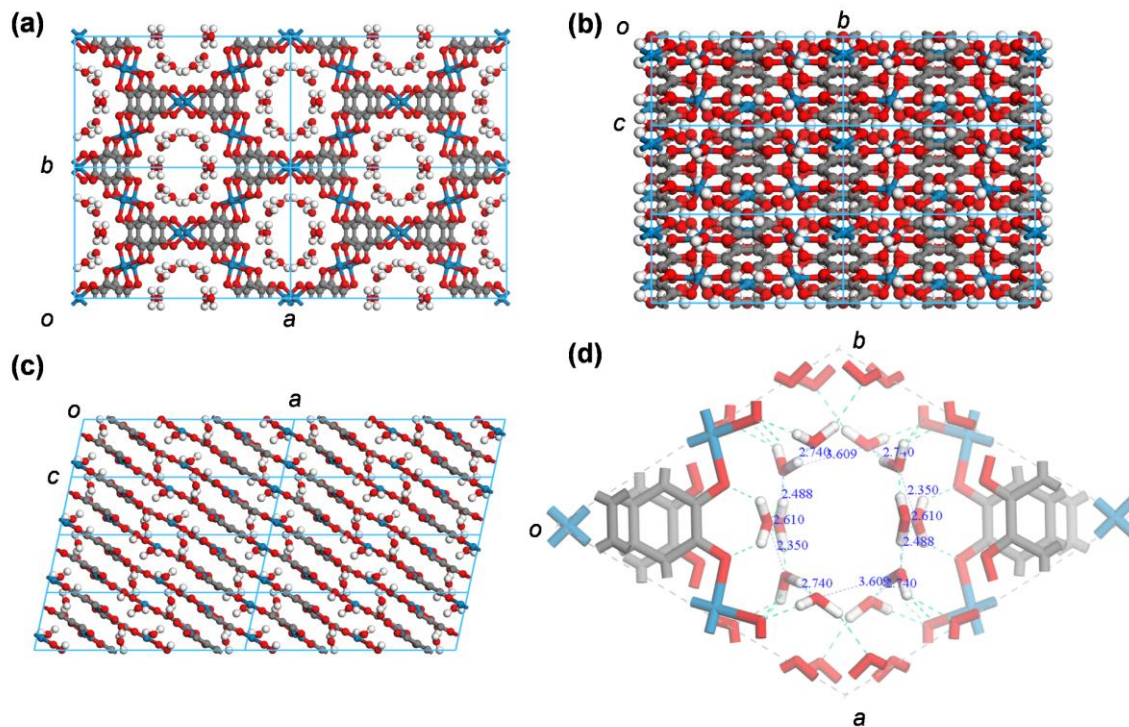
**Figure D.15**. Crystal structure of $Cu_3(C_6O_6)_2$ resolved by MicroED (positions of the O atoms of the water molecules in the pores were successfully determined by MicroED) viewing from (a) $c$, (b) $a$, and (c) $b$ axis. (d) Hydrogen bonding interactions between adjacent water molecules in $(H_2O)_{12}$ cluster and hydrogen bonding interactions between $(H_2O)_{12}$ cluster and scaffold of the MOF. The structure in (d) was shown as the primitive cell to highlight a single-channel structure. The hydrogen bonds are denoted by green dash lines. The O-O distances are labeled with blue. H atoms of water molecules regenerated by DFT calculations.
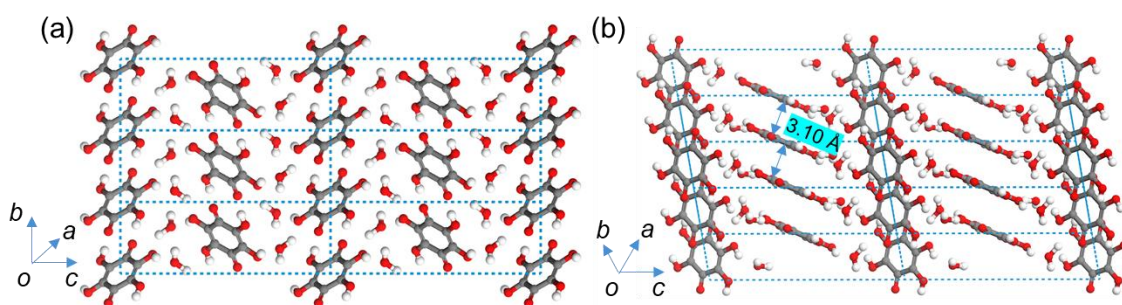


**Figure D.16.** Single crystal X-ray structure of THQ from different point of view (CCDC #: 1274764). In the crystal of THQ, the THQ molecules are stacked into two directions with a fishbone style. In each direction, the packing of THQ molecule is in a staggered mode with a face-to-face distance of 3.10 Å.

**D10.**     **Structural Analysis of $Cu_3(C_6O_6)_2$ by pXRD**

In-house pXRD data were collected using a Rigaku sixth generation MiniFlex X-ray diffractometer at room temperature (298 K). Cu Kα radiation ($\lambda$ = 1.5406 Å, 600 W, tube voltage 40 kV, and current 15 mA) was focused using a planar Göbel mirror riding the Kα line. The scan rate was 1°/min and data points were collected every 0.02° in the range of $2\theta$=2 to 60°.

High-resolution synchrotron pXRD data were collected at beamline 11-BM of the Advanced Photon Source using a wavelength of 0.458068 Å at the temperature of 100 K. Data points were collected in a range from $2\theta$=0.5 to 50° with data points collected every 0.001° (actual $2\theta$/step 0.0009984375°) and a scan speed of 0.1 s/step.

To generate the initial cell parameters for $Cu_3(C_6O_6)_2$ for pXRD analysis, the structure determined from MicroED (**Figure D.14**) was used. The unit cell parameters were refined against the experimental in-house pXRD pattern with a Pawley method (**Figure D.17**). The refined cell parameters were found in a space group of *P2/m* with $a$=21.83 Å, $b$=13.01 Å, $c$=6.16 Å, $\alpha$=$\gamma$=90.0°, and $\beta$=101.8°. The refined crystallographic data, pXRD condition, and Pawley refinement results of $Cu_3(C_6O_6)_2$ are shown in **Table D.4.**
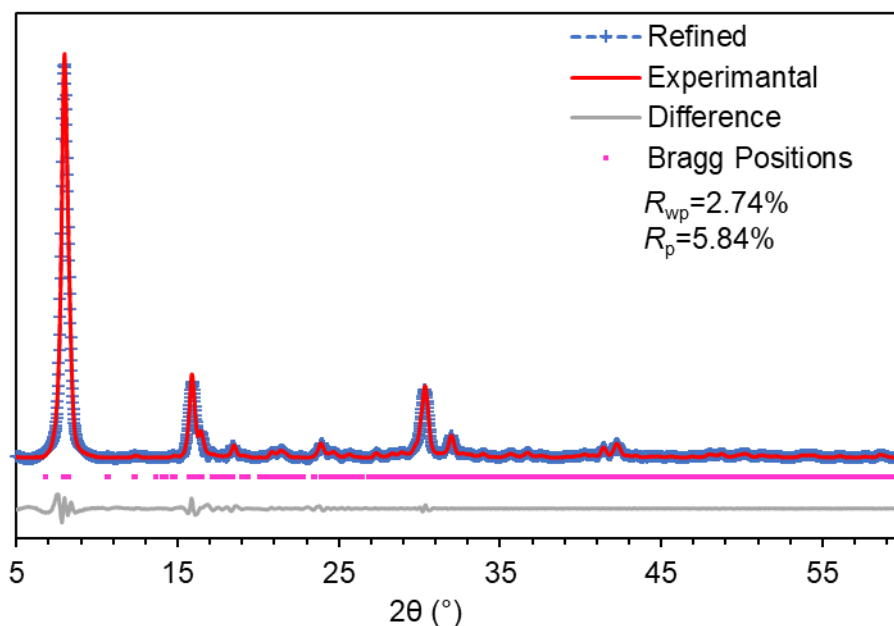


**Figure D.17**. Indexed pXRD pattern (red) and Pawley refinement (blue) of the unit cell from $Cu_3(C_6O_6)_2$.

**Table D.5**. Crystallographic data, powder X-ray collection conditions, and Rietveld refinement results of $Cu_3(C_6O_6)_2$.

| Name | $Cu_3(C_6O_6)_2$ |
|---|---|
| Chemical formula | $C_{12}Cu_3O_{14}$ |
| Formula weight | 558.8 |

| Crystal system | Monoclinic |
|---|---|
| Space group | *P2/M* |
| a/Å | 21.83284 ± 0.00168 |
| b/Å | 13.00587 ± 0.00337 |
| c/Å | 6.16085 ± 0.00124 |
| angles α, β, γ | α = 90.000°, β = 101.80487 ± 0.00172°, γ = 90.000° |
| Temperature/K | 298 |
| Wavelength/Å | 1.5406 |
| $2\theta$ range/° | 5-60 |
| Number of reflections | 65 |
| Number of structural variables | 36 |
| $R_p$ | 0.0584 |
| $R_{wp}$ | 0.0274 |
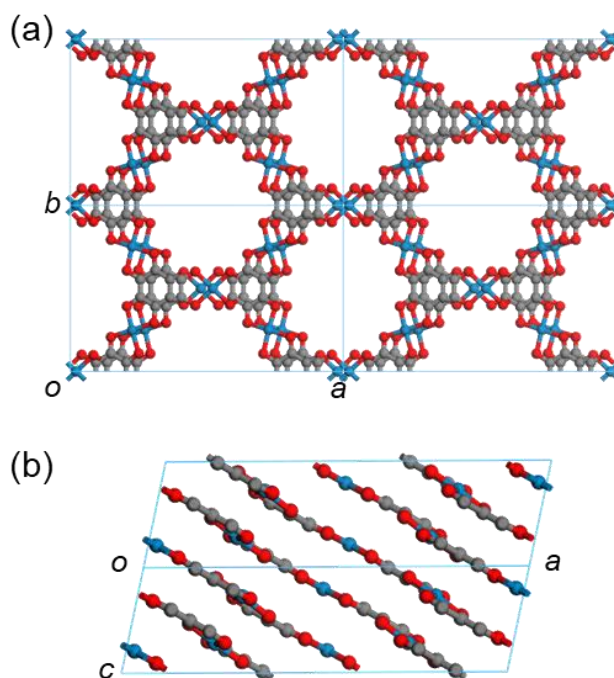


**Figure D.18.** Refined structure of $Cu_3(C_6O_6)_2$ (water molecules are omitted for clarity).
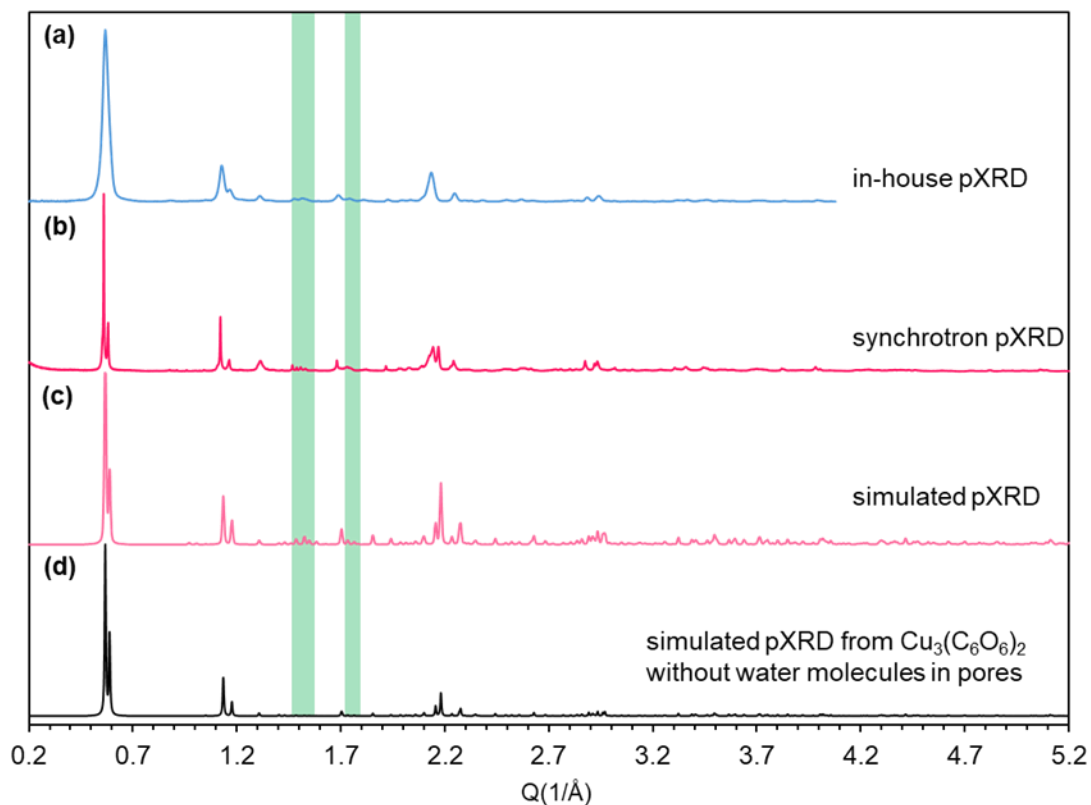
**Figure D.19.** Overlay of (a) in-house pXRD ($\lambda$ = 1.5406 Å, Rigaku MiniFlex), (b) synchrotron pXRD ($\lambda$ = 0.458068 Å, 11-BM of the Advanced Photon Source), (c) simulated pXRD from the structure of $Cu_3(C_6O_6)_2$ resolved MicroED, and (d) simulated pXRD from the structure of $Cu_3(C_6O_6)_2$ without water molecules in the pores ($Q=4\pi\sin(\theta)/\lambda$, Å). The green bars highlight the differences of the pXRD patterns from the structures of $Cu_3(C_6O_6)_2$ with and without water clusters in the pores: the structure without water clusters in the pores don't have obvious diffractions at Q=1.50 and 1.75 Å (**Figure D.19d**); the experimental (**Figures D.19a, b**) and simulated pXRD (**Figure D.19c**) from the MicroED resolved structure have clear diffractions at Q=1.50 and 1.75 Å
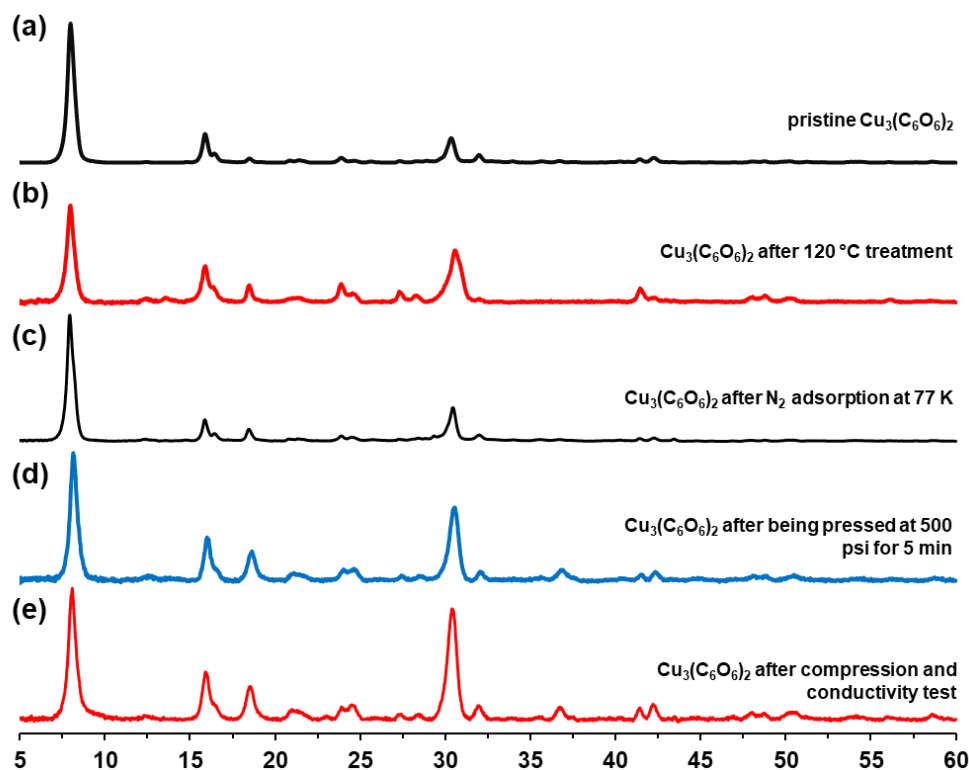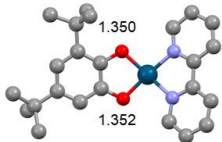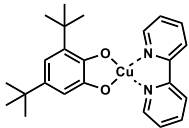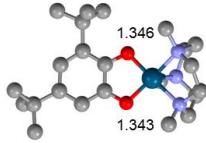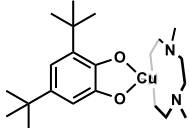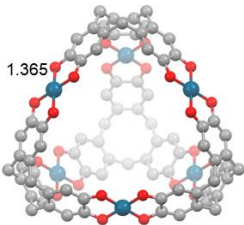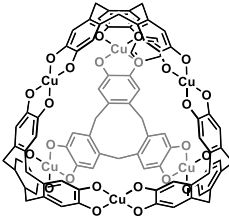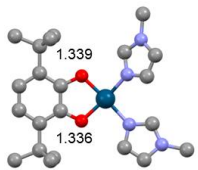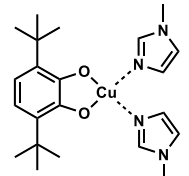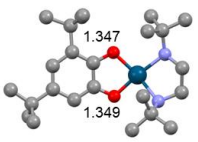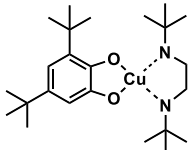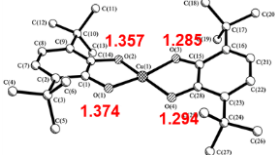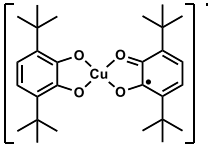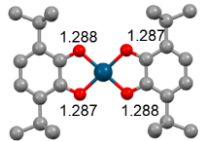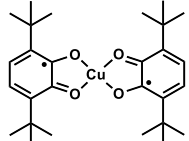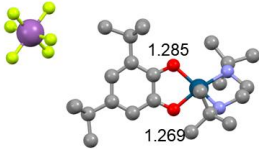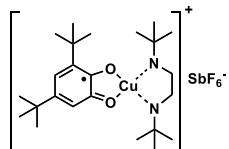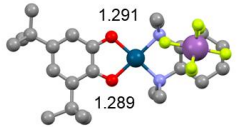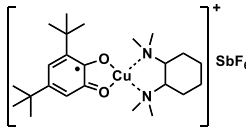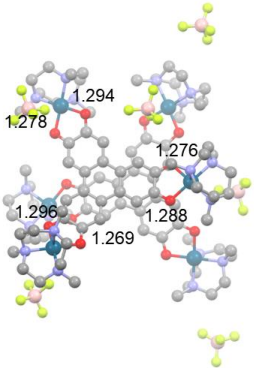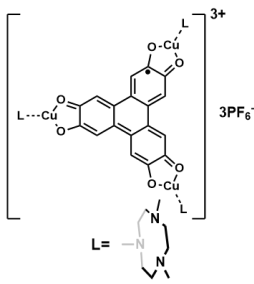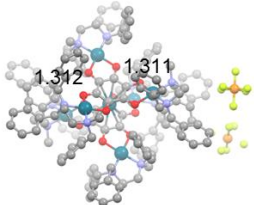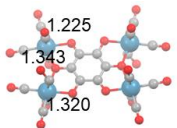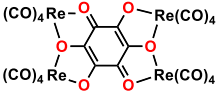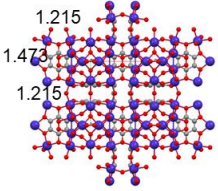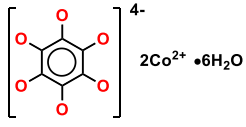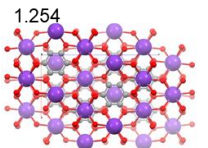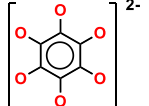
**Figure D.20** . pXRD of (a) pristine Cu₃(C₆O₆)₂, (b) Cu₃(C₆O₆)₂ after heating under 120 °C under vacuum for 3 hours, (c) Cu₃(C₆O₆)₂ after N₂ sorption test at 77 K; (d) Cu₃(C₆O₆)₂ after compression into a pellet at 500 psi for 5 min, (e) Cu₃(C₆O₆)₂ conductivity test (see section 14). After heating treatment, activation for N₂ sorption, and conductivity test, the diffractions of materials were still strong and diffraction peaks still maintained their original positions. These results demonstrated that after these treatments the materials remained highly crystalline and retained the same structural parameters of the pristine MOF. We noticed that after compression and compression followed by the conductivity test, the relative intensity of peak at $2\theta=30.5°$ increased compared with the pristine Cu₃(C₆O₆)₂; we attribute this observation to the possibility of pressure-induced reorientation or preferential alignment of the crystallites within the compressed pellet.

## D11.  Analysis of C-O Bond Lengths of Cu₃(C₆O₆)₂

**Table D.6.** Single-crystal X-ray structures and C-O bond lengths of Cu(II) catecholate complexes with catecholate ligands in different oxidation states and representative single crystal X-ray structures of C₆O₆ ligand-based compounds.

| crystal structure (C-O bond length labeled/Å) | chemical structure | oxidation state of the ligand | formal charge on the ligand | average C-O bond | ref/CCDC # |
|---|---|---|---|---|---|

| | | | | length | |
|---|---|---|---|---|---|
|  |  | *cat*[a] | -2 | 1.351 | [27]/ 1146938 |
|  |  | *cat* | -2 | 1.344 | [28]/ 105988 |
|  |  | *cat* | -2 | 1.365 | [29]/ 803735 |
|  |  | *cat* | -2 | 1.338 | [30]/ 665898 |
|  |  | *cat* | -2 | 1.348 | [31]/ 856841 |
|  |  | *cat; sq*[b] | -2; -1 | 1.365; 1.289 | [32]/ n.a. |
|  |  | *sq* | -1 | 1.288 | [30]/ 665892 |

| | | | | | |
|---|---|---|---|---|---|
|  1.285 1.269 |  | *sq* | -1 | 1.277 | [31]/ 856842 |
|  1.291 1.289 |  | *sq* | -1 | 1.290 | [31]/ 856843 |
|  1.294 1.278 1.276 1.296 1.288 1.269 |  | *(sq,sq,sq)* | -3 | 1.284 | [2]/ 1936666 |
|  1.312 1.311 |  | *(cat,sq,sq)* | -4 | 1.312 | [33]/ 748926 |
|  1.225 1.343 1.320 |  | *(cat, sq,sq)* | -4 | 1.300 | [34]/ 872909 |
|  1.215 1.473 1.215 |  | *(cat, sq,sq)* | -4 | 1.301 | [35]/ 1996631$^d$ |
|  1.254 |  | *(sq,sq,q)$^c$* | -2 | 1.254 | [36]/ 238687 |

| | | | | | | |
|---|---|---|---|---|---|---|
| 1.254  |  2Rb⁺ | | *(sq,sq,q)* | -2 | 1.254 | [37]/ 163619 |
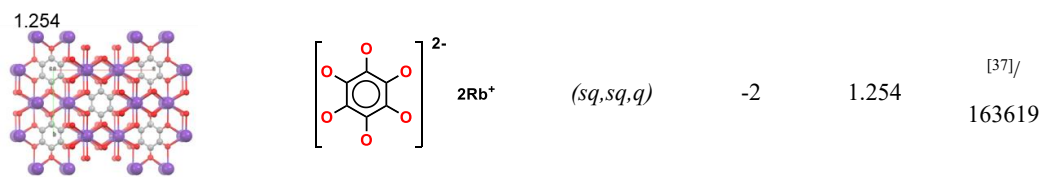
*ᵃ cat*, catecholate. *ᵇsq*, semiquinone. *ᶜq,* quinone. n.a., not available. *ᵈ* electron diffraction data.
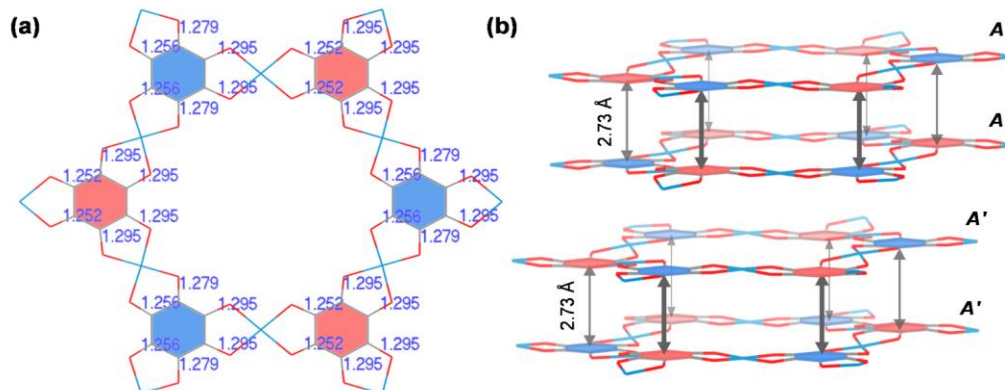


**Figure D.21. (a)** The C-O bond lengths in the two structurally slightly different $C_6O_6$ ligands (color in pink and blue, respectively) in $Cu_3(C_6O_6)_2$ MOF. **(b)** The stacking of the two types of $C_6O_6$ ligand in MOF layers. The interplanar distance of the two cofacially stacked $C_6O_6$ ligands, define as the average C to C distance of two ligands, is 2.73 Å
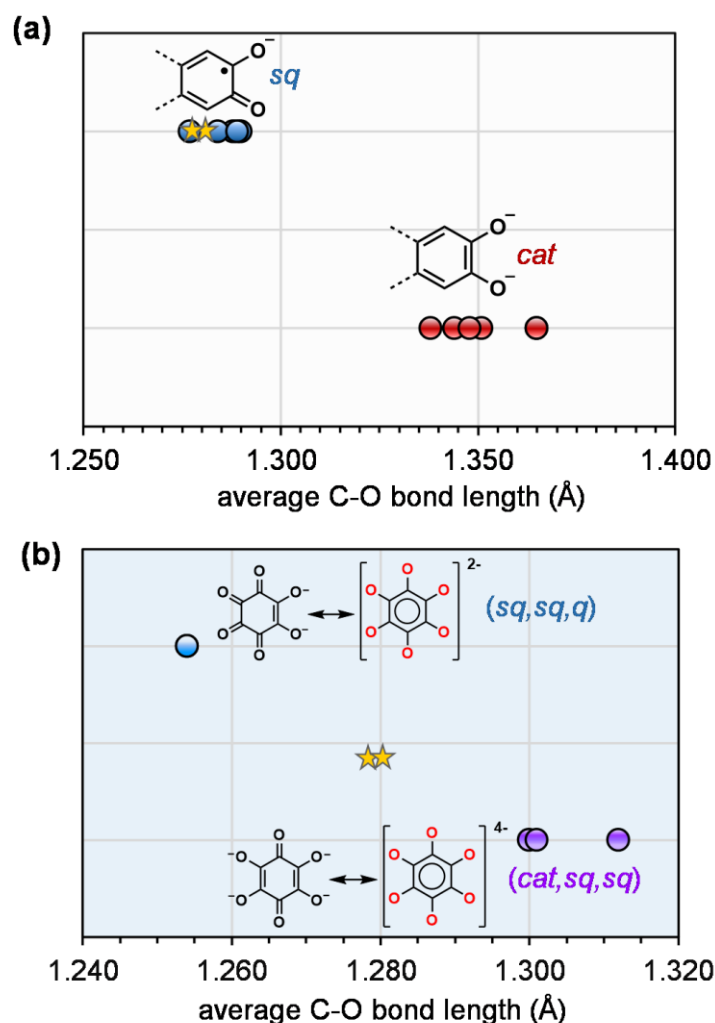
**Figure D.22.** Summary of the average C-O bond lengths in (a) Cu(II) complexes with catecholate ligands in catecholate (equivalent to −2) and semiquinone (equivalent to −1) state and (b) in $C_6O_6$ based metal complexes with $C_6O_6$ in (cat,sq,sq) (equivalent to −4) and (sq,sq,q) (equivalent to −2) state from the data list in **Table D.6** (round data points). The star data points represent the average C-O bond lengths in the two structurally slightly different $C_6O_6$ ligands in $Cu_3(C_6O_6)_2$ MOF.

In the catecholate-based Cu(II) complexes, the C-O bond lengths of the ligand exhibited an obvious dependence of the oxidation states of the ligand. As shown in **Table D.6** and **Figure D.22a,** when the ligands are in a catecholate state (−2), the average lengths of the two C-O bonds in the ligands are in the range of 1.338 to 1.365 Å. The average C-O bond lengths of the ligands in catecholate state are much longer than those in the semiquinone state (−1), which are in the range of 1.277 to 1.290  ÅIn MOF $Cu_3(C_6O_6)_2$, the average C-O bond lengths in the two structurally slightly different $C_6O_6$ ligands were 1.277 and 1.281Å **Figure D.21a**). Both of the two values are far beyond the range of the C-O bond lengths in ligands in catecholate state, instead, they fell into

the range of the C-O bond lengths in semiquinone state.

For $C_6O_6$ containing compounds, the average C-O bond length of $C_6O_6$ ligand is also oxidation state-dependent (**Table D.6** and **Figure D.22b**). For the $C_6O_6$ ligand in (cat,sq,sq) state, corresponding to −4 state, the averaged C-O bond lengths are 1.300-1.312 Å, with an influence from the type of the metal ions. For the $C_6O_6$ ligand in (sq,sq,q) state, corresponding to −2 state, the averaged C-O bond length is 1.254 Å regardless of the counter metal ions ($K^+$ or $Rb^+$). Compared with these values, the average C-O bond lengths of 1.277 and 1.281 Å in MOF $Cu_3(C_6O_6)_2$ are smaller than those in $C_6O_6$ ligand with −4 oxidation state. Meanwhile, both the values 1.277 and 1.281 Å are significantly larger than average C-O bond lengths in $C_6O_6$ ligand with −2 oxidation state. Therefore, the possibility of $C_6O_6$ ligand in −2 oxidation state in MOF $Cu_3(C_6O_6)_2$ can be safely excluded. As we have demonstrated by MicroED (**section D9**), elemental (**section D6**), and XPS (**section D7**) analysis that MOF $Cu_3(C_6O_6)_2$ is charge neutral, the absence of $C_6O_6$ ligand in −2 oxidation state means the absence of $C_6O_6$ −4 oxidation state as well.

In summary, the C-O bond length analysis by the comparison with Cu(II) catecholate complexes and $C_6O_6$ containing metal compounds both pointed to the conclusion that the two structurally slightly different $C_6O_6$ ligands in MOF $Cu_3(C_6O_6)_2$ were in tris(semiquinone) form, equivalent to −3 state. As we have demonstrated in section 7 that Cu ions in $Cu_3(C_6O_6)_2$ predominately exited as Cu(II), the combination of Cu ions and $C_6O_6$ ligands in a 3:2 ratio should give a charge-neutral framework. We hypothesized that the oxidation state of Cu and $C_6O_6$ present in $Cu_3(C_6O_6)_2$ in this work was related to the redox potentials of these building blocks and the synthetic condictions. The use of redox-active building blocks, including inorganic species (e.g., Cu and Fe ions) and organic species (e.g., Cu and Fe ions) and organic species (e.g., hexasubstituted benzene[38] and hexasubstituted triphenylene[39]) may lead to their presence in multiple possible oxidation states in conjugated MOFs. $C_6O_6$ ligand is a type of redox noninnocent ligand with up to seven oxidation states.[38] Previous studies based on the $C_6O_6$-containing MOFs and metal complex have shown that the oxidation state of $C_6O_6$ in these materials can be modulated by using external potentials or oxidizing/reducing reagent, in which the oxidation state of $C_6O_6$ ligand can exist as −4,− 3, or −2 states.[3a, 40] To realize a more oxidized state than semiquinone state (−3) in $C_6O_6$ ligand, such as −2 state, a higher potential needs to be provided. Through the control of the reaction conditions, such as through the addition of the oxidant, the coexistence of $Cu^{2+}$ and the semiquinone state can be realized, which have already been found in multiple coordination complexes.[2, 30-31] In this work, $O_2$ likely acts as the oxidant that promotes the oxidation of the $C_6O_6$ the ligand from the −4 to a −3 state. We hypothesize that the combination of moderately acidic condition (pH=5.98) with large access of the buffer salt (20 equivalents with respect to the ligand), as well as the formation of solid-state framework that results in a heterogeneous reaction conditions, the oxidization of the ligand beyond −3 states may be not achievable by $O_2$. We note, however, that the presence of equal amounts of −2 and −4 oxidation states of ligand in $Cu_3(C_6O_6)_2$ cannot be fully

excluded.

## D12.    Brunauer–Emmett–Teller (BET) Analysis

In order to assess the porosity of $Cu_3(C_6O_6)_2$, gas adsorption measurements were performed on 3Flex (Micromeritics, Norcross, Georgia) with $N_2$ at 77K. The sample of $Cu_3(C_6O_6)_2$ synthesized from condition N.O. 22 was activated by soaking in methanol at 65 °C for 3 days during which the methanol was exchanged every 12 hours. The samples were then dried in the oven under a vacuum (20 mTorr, 65 °C for 24 hours). Before gas adsorption measurements, the samples were further degassed under vacuum at 80 °C for 4 hours. For BET surface area calculations, a full isotherm with a fitting range of 0 to 0.3 $P/P_0$ was used (**Figure D.23**). The BET surface area by the gas adsorption analysis is 196.7 $m^2/g$. This BET value is higher than the previous reports.[1, 3]
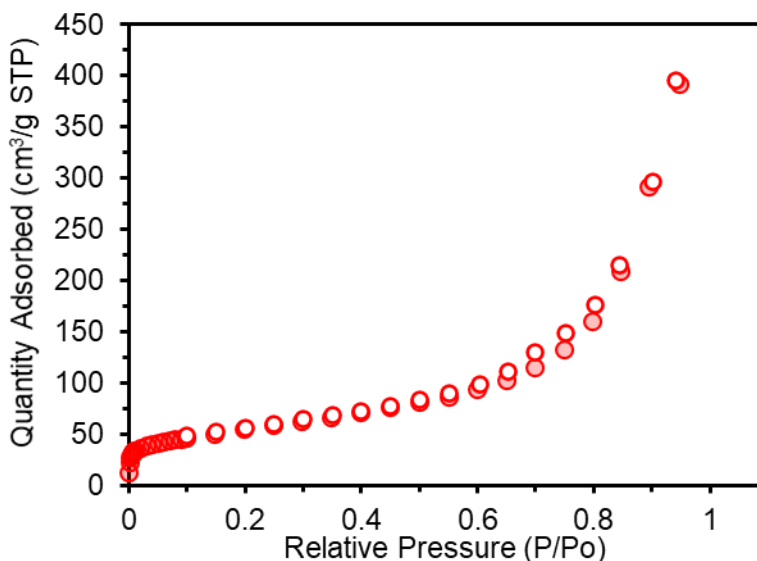


**Figure D.23.** Nitrogen sorption curves (filled circles: adsorption, open circles: desorption,
STP=standard temperature pressure) for activated $Cu_3(C_6O_6)_2$ at 77 K.

## D13.    Thermal Gravimetric Analyses (TGA)

Thermal gravimetric analysis was performed using a TA Instruments TGA Q150 with a 20 °C/min ramp from room temperature to 850 °C under $N_2$ using the materials synthesized from condition **N.O. 22** as described in section 2. When the temperature raised from room temperature to 215 °C, a mass loss stage can be clearly identified. The mass loss percentage of 16.58% was in excellent agreement with the loss of the six associated water molecules per $Cu_3(C_6O_6)_2$ unit.
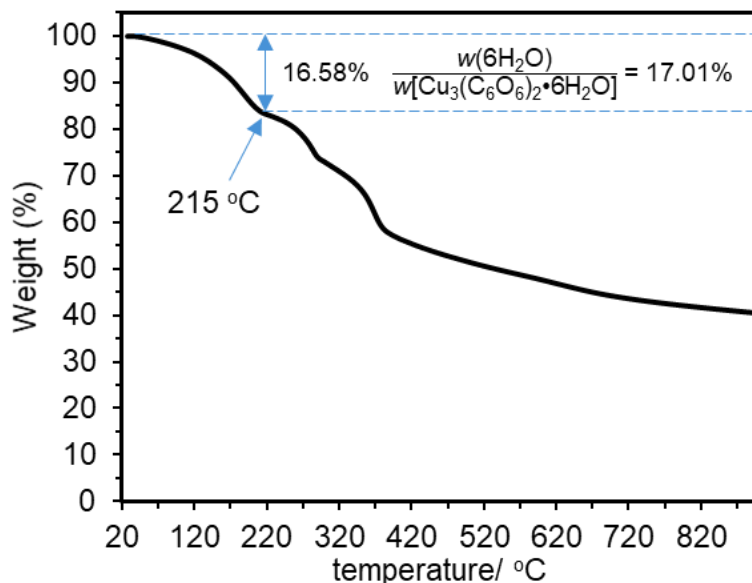
**Figure D.24**. TGA curve of $Cu_3(C_6O_6)_2$.

### D14.    Conductivity Measurements and Determination of Activation Energy

To make a pressed pellet, ~45 mg of $Cu_3(C_6O_6)_2$ was put into a split sleeve pressing die with an inner diameter of 6 mm and pressed for 5 min under a pressure of 500 psi. A two-contact probe method was employed to measure the conductivity. The *I-V* curves were collected using a GAMRY Interface 1010E™ potentiostat with an applied voltage from −0.5 V to 0.5 V. For parallel measurements, tests on four pellets were performed. We calculated the bulk conductivity measurements (S/cm) using **Equation D.2**.[41] Herein, $I$ (A) is current, $V$ (V) is the voltage of cross the pellet, $d$ (cm) is the thickness of the pellet, $S$ (cm$^2$) is the contact area of the pellet. $I/V$ values were the slope extracted from the *I-V* curves. The calculated conductivity of $Cu_3(C_6O_6)_2$ is $1.2 \times 10^{-6}$ S cm$^{-1}$ at room temperature (~298 K). To investigate the activation energy for electrical conductivity of the material and charge transport feature, *I-V* curves were measured from 298 K to 393 K (**Figure D.25**) to afford the conductivities under different temperatures.

$$\sigma = \frac{I}{V}\frac{d}{S} \qquad\qquad \textbf{(D.2)}$$
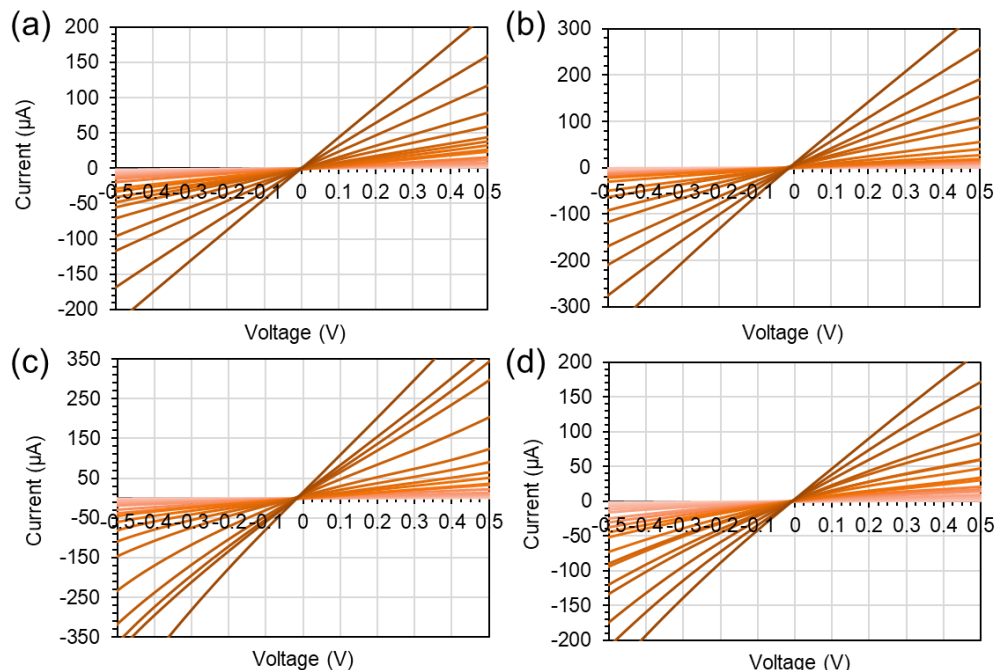
**Figure D.25**. (a-d) *I-V* curves of four pellets made of $Cu_3(C_6O_6)_2$ at the temperature of 298-393 K.

To probe the potential dynamics of charge transport, we fitted the conductivity-temperature data using three models, including Arrhenius model, polaronic nearest-neighbor hopping model, and three-dimensional Mott variable range hopping model. Typically, the Arrhenius **equation D.23**,

$$\sigma = \sigma_0 e^{-\frac{E_a}{k_B T}} \quad \textbf{(D.3)}$$

can be used to access the Arrhenius activation energy.[42] In this equation, $\sigma$ is the conductivity, $\sigma_0$ is the pre-exponential factor and is constant, $E_a$ is the Arrhenius activation energy, $k_B$ is the Boltzmann constant, and $T$ is the temperature. **Equation D.3** can also be written as:

$$ln(\sigma) = ln(\sigma_0) - \frac{1}{T}\frac{E_a}{k_B} \quad \textbf{(D.4)}$$

The plot of the natural log of conductivity ($ln(\sigma)$) to reciprocal temperature (1/T, in K⁻¹) generates the value $-\frac{E_a}{k_B}$.

Polaronic nearest-neighbor hopping model describes conduction via carrier hopping to the nearest neighbor empty site, and can be described as **equation D.5,**

$$\sigma T = \sigma_0 e^{-\frac{E_a}{k_B T}} \quad \textbf{(D.5)}$$

In the polaronic nearest-neighbor hopping model, carriers hop to the nearest neighbor empty site which also needs activation energy but it is usually smaller as compared to the energy required for thermally activated band conduction. **Equation D.5** can also be written as:

$$\ln(\frac{\sigma}{T}) = ln(\sigma_0) - \frac{1}{T}\frac{E_a}{k_B} \quad \textbf{(D.6)},$$

Therefore, the linear plot of the natural log of $(\ln(\sigma/T))$ to reciprocal temperature $(1/T, \text{ in } K^{-1})$ will generate the value $-\frac{E_a}{k_B}$.

Three-dimensional Mott variable range hopping model usually describes low-temperature conduction in disordered systems with localized charge-carrier states, and can be characterized as **equation D.7,**

$$\sigma = C(\frac{1}{T})^{\frac{1}{2}}e^{-(\frac{T_0}{T})^{\frac{1}{4}}} \qquad \textbf{(D.7)}$$

which is equivalent to

$$\ln\left(\sigma T^{\frac{1}{2}}\right) = \ln(\sigma_0) - (T_0)^{\frac{1}{4}}(\frac{1}{T})^{\frac{1}{4}} \qquad \textbf{(D.8)}$$

In **equation D.7**, $T_0$ is a characteristic temperature, $C$ is a constant. If one system can be described by three-dimensional Mott variable range hopping model, the plot of the natural log of conductivity $(\ln(\sigma T^{\frac{1}{2}}))$ to $(\frac{1}{T})^{\frac{1}{4}}$ should give a linear relationship.
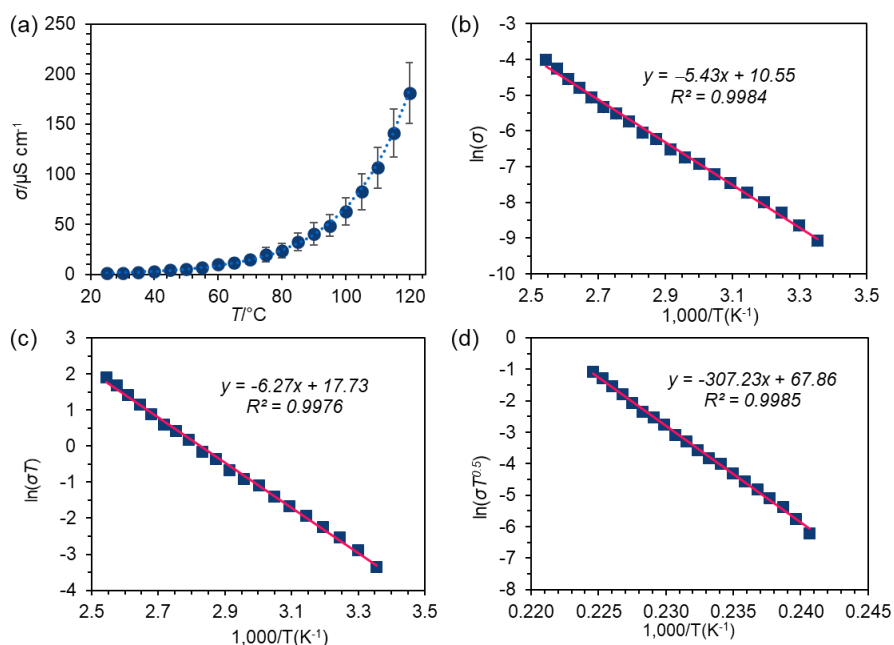


**Figure D.26.** (a) Electrical conductivity of $Cu_3(C_6O_6)_2$ at different temperatures. Fitting of conductivity to temperature using (b) Arrhenius model, (c) polaronic nearest-neighbor hopping model, (d) three-dimensional Mott variable range hopping model.

The conductivity-temperature relationship exhibited a good Arrhenius-type dependence at the whole tested temperature range of 298-393 K (**Figure D.26b**), which indicated that thermally activated type of conduction is dominating in the tested temperature range. The Arrhenius fitting gave activation energy of 468 meV based on the slope of $\ln(\sigma)$ vs $1/T$ plot. This value was lower than that determined by the polaronic nearest-neighbor hopping model (540 meV, **Figure D.26c**). The plot of $\ln(\sigma)$ versus $T^{-0.25}$ at the temperature range of 298-393 K was also found well fitted to

the 3D Mott variable range hopping model (**Figure D.26d**). Although some literature reported that 3D Mott VRH can occur above room temperature,[43] carrier dynamics in 3D variable range hopping model typically occurs at temperatures below 80 K.[44] We noted that the fitting of $\ln(\sigma)$ versus $T^{-0.25}$ in our case was based on a relatively small temperature window of data points (298-393 K), which may increase the chance of overestimating the goodness of fitting compared with the situation where a wider temperature window of data points is used.

Therefore, the conductivity-temperature fitting using different models suggested that that the thermally activated charge hopping processes between localized states and different grains boundaries of the material may be responsible for the electrical conducting process in $Cu_3(C_6O_6)_2$.

## D15.    Computational Study of Electronic Properties

Spin-polarized density-functional theory calculations of the band structure, density of state, orbitals were carried out using the DMol$^3$ module[45] embedded in Material Studio 2019. The equivalent primitive unit cell of the original unit cell in P2/M space group of the crystal structure of $Cu_3(C_6O_6)_2$ MOF was utilized for the band structure and orbital calculation. The GGA-PBE can usually yield good lattice constants but poor atomization energies.[46] The meta-generalized gradient approximation functional (m-GGA) has been applied for the prediction of bandgaps for the semiconductors having narrow and moderate band gaps with accuracy comparable to the expensive hybrid functional.[47] Here, m-GGA-revTPSS was applied with double-numerical + d (DND) basis.[46] In the calculations, the smearing value was set at 0.01 Hartee. The Brillouin zone was sampled with the gamma-centered Monkhorst-Pack k-point grid of $2 \times 2 \times 4$. The convergence criterion for the self-consistent field calculation was set to $1 \times 10^{-6}$ eV/atom.
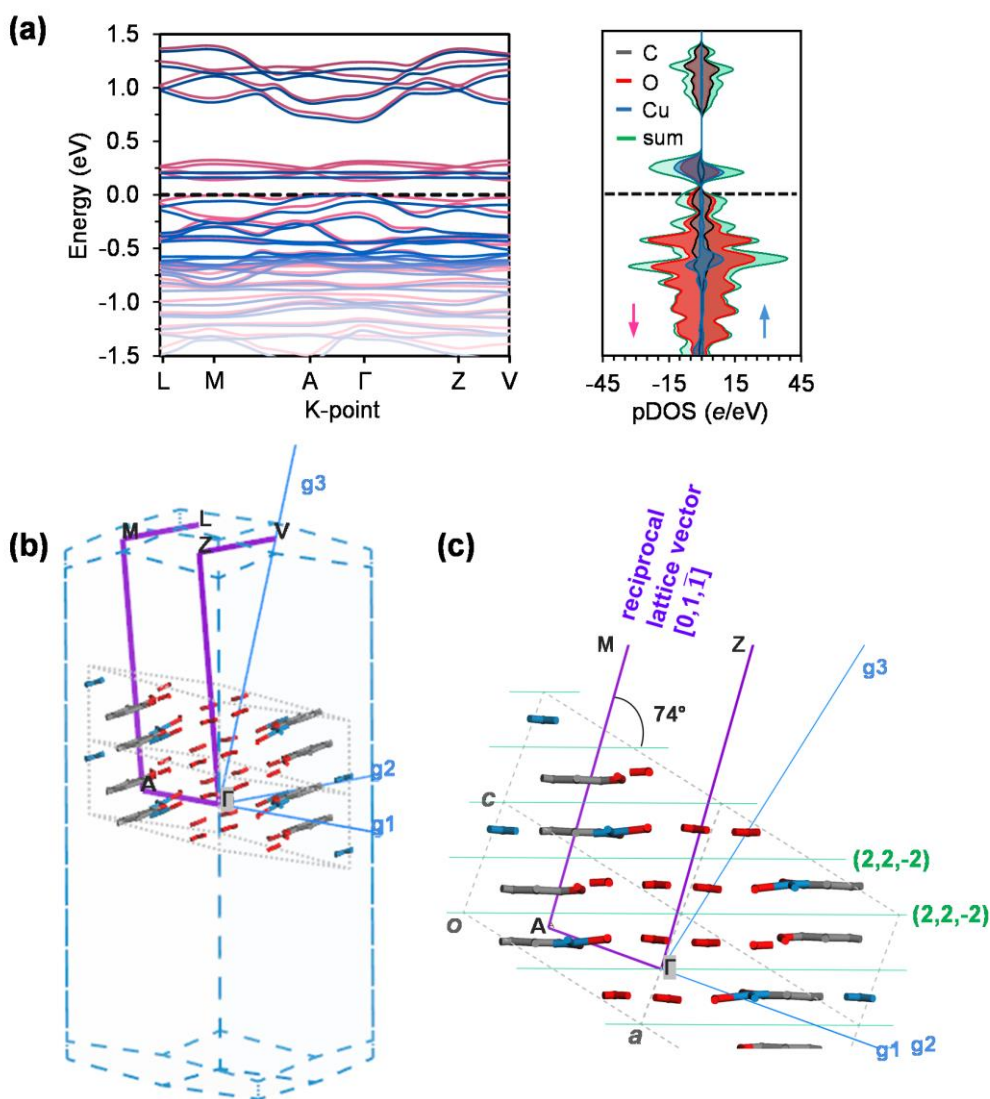
**Figure D.27**. (a) Calculated electronic band structure (blue and red lines for spin-up and spin-down electron associated bands, respectively) and density of state for $Cu_3(C_6O_6)_2$. (b) The corresponding first Brillouin zone (box with dashed blue lines) and high-symmetry K-points (L, M, A, Γ, Z, and V). (c) The position of K-point paths (purples lines) relative to the real space viewing from the *b* axis of the cell lattice (grey dashed lines). The K-point path *M-A* (reciprocal lattice vector, $[0,1,\bar{1}]$) formed a 74° angle with $(2,2,\bar{2})$ plane when viewing from the *b* axis of the cell lattice. Water molecules in the structure are omitted for clarity.

Because of the specific cell parameters of $Cu_3(C_6O_6)_2$ MOF, the 2D layers of the MOF were not parallel to any axis of the cell lattice. It consequently causes the correlation between the K-point path and the real space hard to describe. The K-point path *M-A* is neither perpendicular to the 2D layers of $Cu_3(C_6O_6)_2$ MOF nor parallel to the *c* axis. In order to give a descriptive demonstration of the K-point path *M-A*, its position relative to the real space viewing from the *b* axis of the cell

lattice (grey dashed lines) was given in Figure D.27c.

The carrier effective mass was calculated through the curvature of the band dispersion by following the literature procedure. According to the definition of the carrier effective mass in equation (**D.9**)

$$\frac{1}{m^*} = \frac{1}{\hbar^2} \frac{\partial^2 E(k)}{\partial k^2} \quad \textbf{(D.9)}$$

where E($k$) is the energy (in the unit of J) of an electron at wavevector $k$ (in the unit of m$^{-1}$), $\hbar$ is the reduced Planck constant (1.054571817×10$^{-34}$ J·s), and m* is the carrier effective mass (relative to the mass of one electron $m_e$. To calculate the curvature ($\partial^2 E(k)/\partial k^2$) of a band along a wavevector, the band was fitted to a quadratic polynomial with $E(k) = ak^2 + bk + c$. The value of 2a was obtained through the second derivative and substituted into the equation **D.9** to obtain a carrier effective mass m*. The calculated minimum carrier effective of valency band maximum along the L-M, M-A, A-Γ, Γ-Z, and Z-V directions were 0.15, 0.05, 2.01, 0.18, and 0.40 $m_e$, respectively.
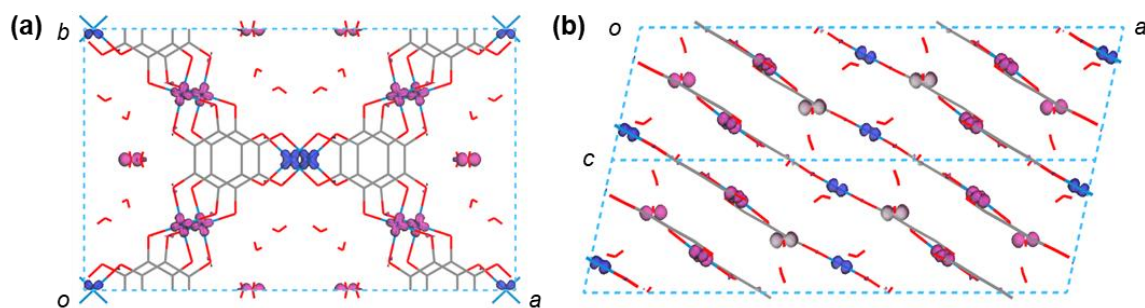


**Figure D.28**. (a) and (b) Calculated spin density of $Cu_3(C_6O_6)_2$. Red and blue represent spin-up and spin-down densities.
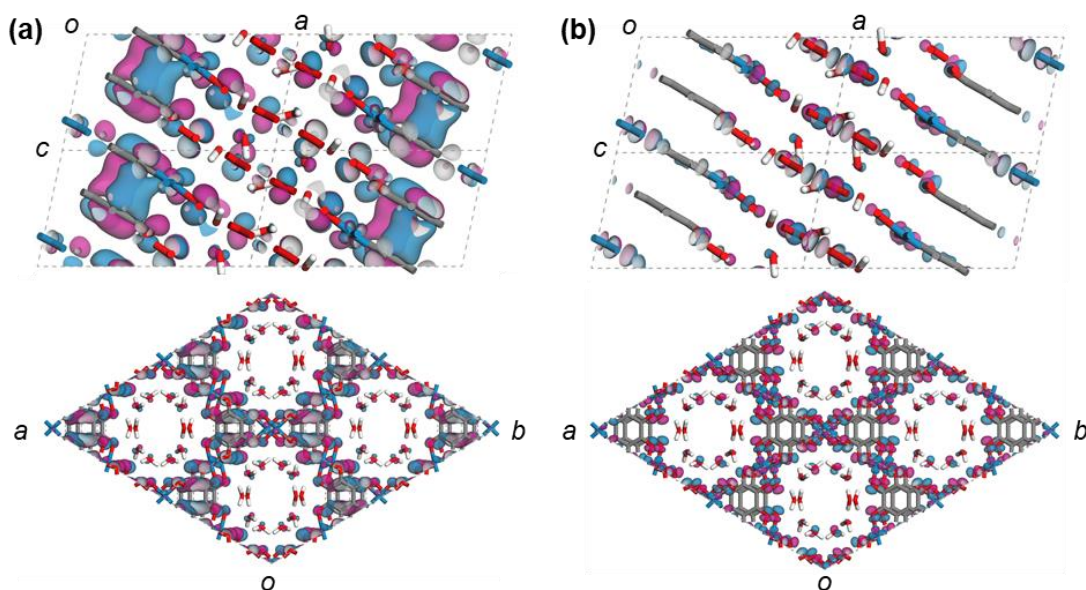
**Figure D.29**. Calculated orbitals near the (e) valence band maximum and (f) conduction band minimum view from *b* (upper row) and *c* (lower row) axis.

## D16. Measurement and Analysis of Magnetic Properties

The measurements were performed on a Quantum Design magnetic properties measurement system (MPMS3) using a brass-half tube sample holder with a vibrating sample magnetometer (VSM) powder sample holder made of injecton molded polypropylene. The empty plastic powder holder was weighed (184.34 mg). The power of the sample was transferred to the holder using a plastic tool and was compressed. The holder plus sample was weighed again (191.59 mg, net mass of the sample, 7.25 mg). The VSM powder sample holder was then pressed into the brass half-tube and loaded into the MPMS3. Three measurements were run on the empty holder to measure the background and then on the sample.

For the zero-filed cooled test, the magnet was first reset to remove the possible remnant field. Then the sample was cooled in zero field to 1.8 K at a rate of 30 K/min. A chosen field was set, and a moment vs temperature measurement was performed while the temperature was swept continuously from 1.8-30 K with a sweep rate of 0.2 K/min, from 30-150 K with a sweep rate of 1 K/min, and from 150-300 K with a sweep rate of 2 K/min. The VSM peak Amplitude was 5 mm and the averaging time was 5 s. Sticky autorange and auto tracking were selected.

For the field cooled test, the temperature was swept continuously from 300-150 K with a sweep rate of 2 K/min, from 150-30 K with a sweep rate of 1 K/min, and from 30-1.8 K with a sweep rate of 0.2 K/min. The rest of the settings were the same as the previous measurements.

For magnetic hysteresis measurement, a four-quadrant moment vs field measurement was performed at 5 K and 2 K. The field was initially set at 70,000 Oe. The field was then swept from 70,000 Oe → 0 Oe → -70,000 Oe → 0 Oe → 70,000 Oe. The sweep rate was 50 Oe/s, stabilizing at each field. The measurement increment was 500 Oe. The rest of the settings were the same as the previous measurements.

To calculated the molar paramagnetic susceptibility ($\chi_{m,p}$), the measured molar susceptibility $\chi_{measured}$ (background subtracted) of the material was corrected by considering diamagnetic susceptibility values from atoms/molecules ($\chi_{D,\ i}$) and bonds ($\lambda_{bond,\ i}$). The molar paramagnetic susceptibility ($\chi_{m,p}$) was calculated using equation (**D.10**):

$$\chi_{m,p} = \chi_{measured} - \left( \Sigma\ \chi_{D,i} + \Sigma\ \lambda_{bond,i} \right)\quad \textbf{(D.10)}$$

The following values (**Table D.7**) as suggested by literature values[48] have been used for diamagnetic corrections for formula $Cu_3(C_6O_6)_2 \cdot 6H_2O$. The bond types of the ligand were considered using the structure with a tris(semiquinone) state as discussed in the main text (see **Figure D.3c**).

**Table D.7**. Values used for diamagnetic corrections for formula $Cu_3(C_6O_6)_2 \cdot 6H_2O$.

| items | $\chi_{D,i}/\lambda_{bond,i}$ (emu mol$^{-1}$) | numbers in formula $Cu_3(C_6O_6)_2 \cdot 6H_2O$ |
|---|---|---|
| $Cu^{2+}$ | $-11.0 \times 10^{-6}$ | 3 |
| $H_2O$ | $-13.0 \times 10^{-6}$ | 6 |
| C | $-6.0 \times 10^{-6}$ | 12 |
| O in the ligand | $-4.6 \times 10^{-6}$ | 12 |
| C=C bond | $5.5 \times 10^{-6}$ | 2 |
| C=O bond | $6.3 \times 10^{-6}$ | 6 |

The sum of diamagnetic corrections ($\sum \chi_{D,i} + \sum \lambda_{bond,i}$) for formula $Cu_3(C_6O_6)_2 \cdot 6H_2O$ was $-1.89 \times 10^{-4}$ emu mol$^{-1}$. We noticed that the diamagnetic corrections can also be performed by considering the exact type of the atoms or using slightly different diamagnetic correction values reported for some of the atoms (e.g., $-12.8$ vs $-11.0 \times 10^{-6}$ emu mol$^{-1}$ for $Cu^{2+}$). These different treatments only lead to less than 10% variations of the sum of diamagnetic corrections, thus were not further discussed.
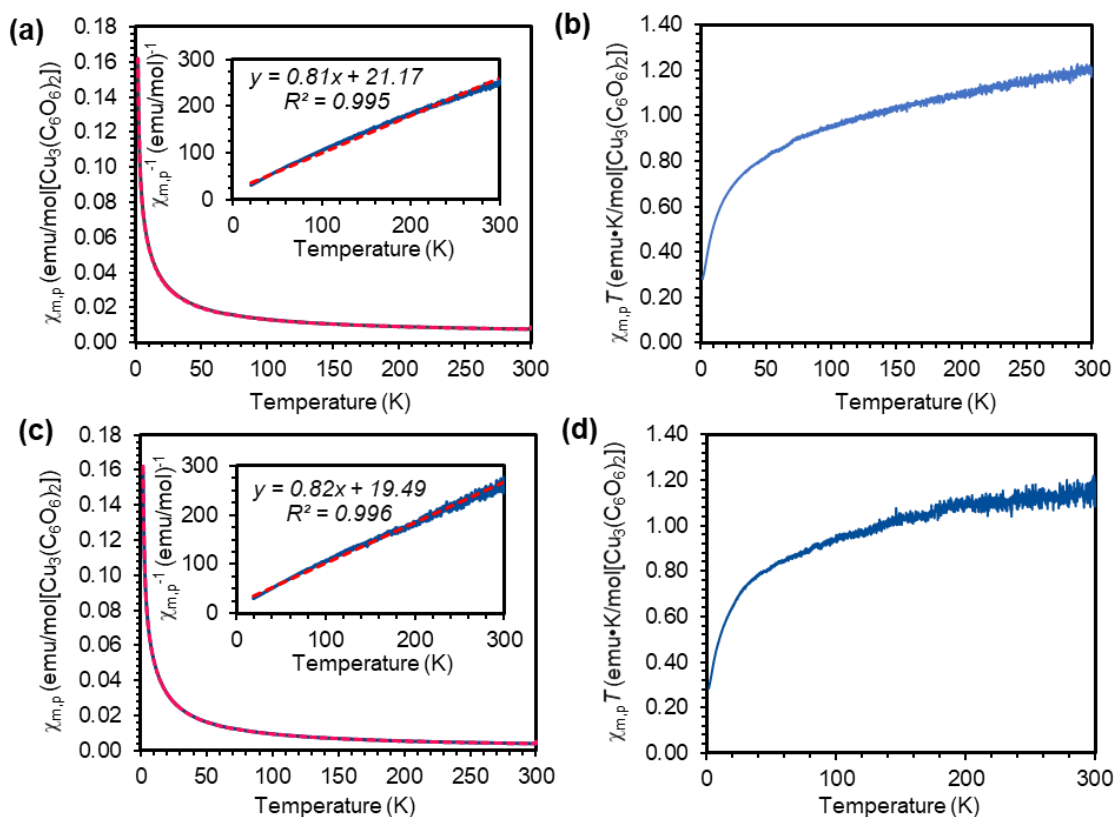


**Figure D.30.** (a) ZFC (solid blue line) and FC (dashed red line) magnetization for $Cu_3(C_6O_6)_2$ MOF and (b) temperature dependence of the product of the magnetic susceptibility and temperature ($\chi_m T$) in an applied magnetic field of 100 Oe. (c) ZFC (solid blue line) and FC (dashed red line) magnetization for $Cu_3(C_6O_6)_2$ MOF e and (d) temperature dependence of $\chi_m T$ in an applied magnetic field of 500 Oe. At the high-temperature range, the product of the magnetic susceptibility

and temperature ($\chi_m T$) showed linearity with the applied field of 100 Oe. We ascribed such linearity to temperature-independent paramagnetism. With a higher field of 500 Oe, the slope of $\chi_m T$ *vs* $T$ at high-temperature range is similar to that under an applied field of 100 Oe. This comparison ruled out the presence of ferromagnetic impurity in $Cu_3(C_6O_6)_2$ and supported the assignment of the linearity to temperature-independent paramagnetism.[2]
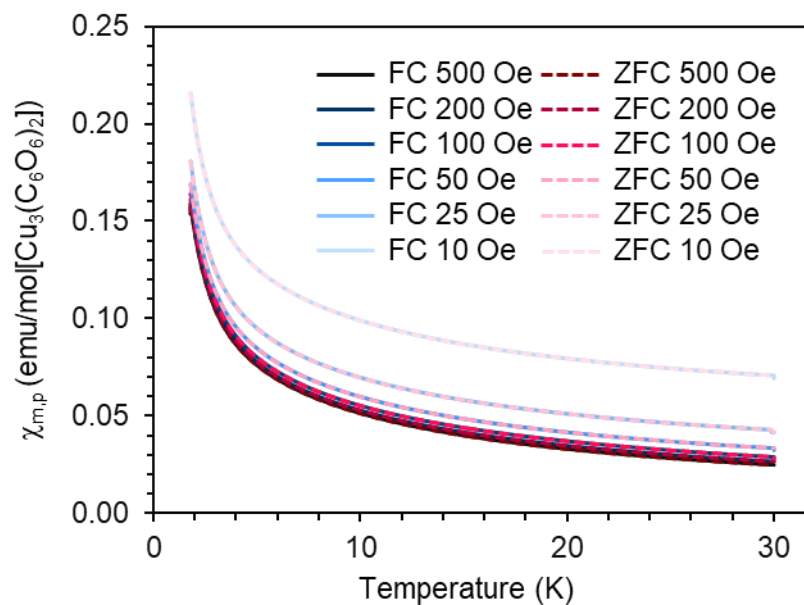


**Figure D.31.** FC and ZFC magnetization for $Cu_3(C_6O_6)_2$ MOF in an applied magnetic field of 10, 25, 50, 100, 200, and 500 Oe.
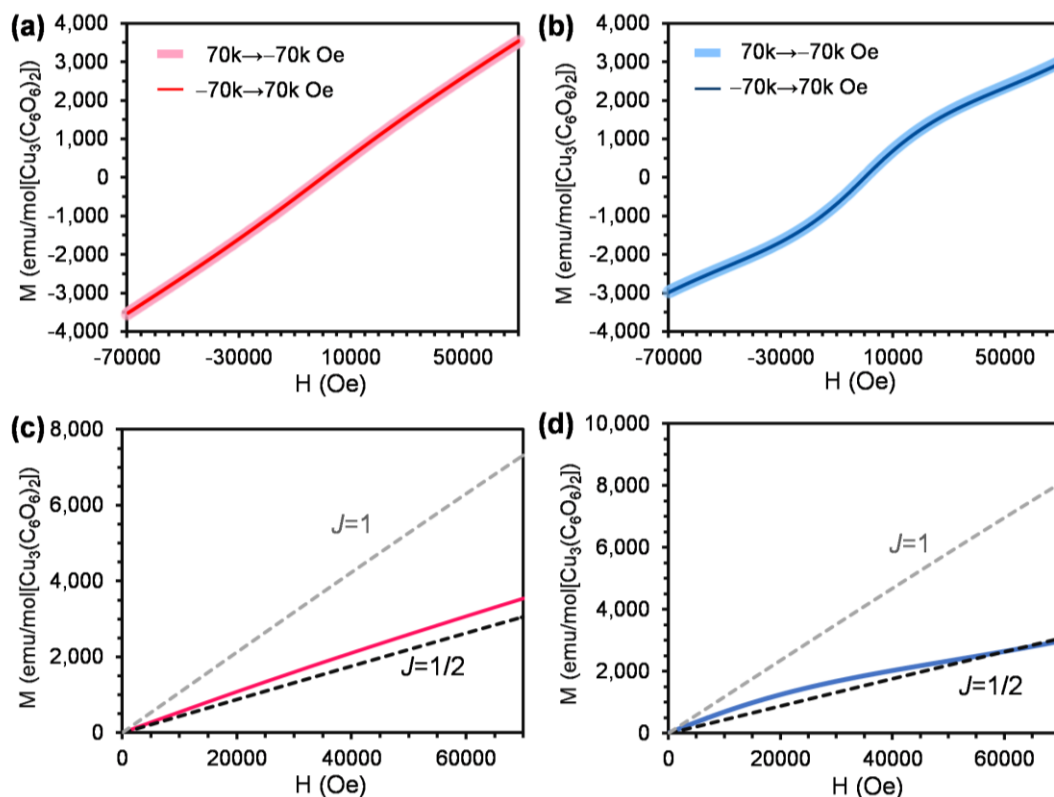
**Figure D.32.** Magnetic hysteresis of $Cu_3(C_6O_6)_2$ MOF at (a) 5 K and (b) 2 K. The M-H plot at (c) 5 K and (d) 2K fitting according to the Brillouin function with $J$=1/2, 1. For both the M-H plots under 5 K and 2 K, the experimental data fits better when $J$=1/2, indicating that $Cu_3(C_6O_6)_2$ MOF was reasonably close to $S$ =1/2 paramagnetic system.

To further verify the paramagnetism of $Cu_3(C_6O_6)_2$, the M (emu/mol) *vs* H (Oe) plots at 2K and 5K were fitted using Brillouin function expected for $S$=1/2 systems, which was given by equations **D.11-D.12**.[49]

$$M = 3N_A g u_B J [\frac{2J+1}{2J} \coth\left(\frac{2J+1}{2J} y\right) - \frac{1}{2J} \coth\left(\frac{1}{2J} y\right)] \quad \text{(S11)}$$

$$y = g u_B \mu_o J H / [k_B (T - \theta)] \quad \text{D.12}$$

In those equations, $N_A$ is the Avogadro's number ($6.022141793 \times 10^{23}$ mol$^{-1}$), $g$ is the $g$-factor value (2.085), $\mu_0$ is vacuum permittivity ($1.2566370614 \times 10^{-6}$ N A$^{-2}$), $\mu_B$ is Bohr magneton ($9.274009994 \times 10^{-24}$ A m$^2$), $k_B$ is Boltzmann constant ($1.380649 \times 10^{-23}$ J K$^{-1}$), $T$ is the temperature (K), and $J$ is total angular momentum quantum number.

A full understanding of the magnetic coupling in 2D layered MOFs is complex because of the possible participation of the intralayer and interlayer spin coupling. In $Cu_3(C_6O_6)_2$ MOF, the distance of the adjacent Cu(II) ions in each layer (intralayer Cu distance) is 6.5 Å and the distances

of Cu(II) ions in the adjacent layers (interlayer Cu distance) are 2.9 Å (fully-eclipsed layers) and 3.5 Å (slipped-parallel layers). Even though the interlayer Cu-Cu distance is shorter than the intralayer Cu-Cu distance, we suggested that the intralayer Cu coupling could dominate the magnetism of $Cu_3(C_6O_6)_2$. Our hypothesis is for the following considerations.

*First,* based on the crystal structure of $Cu_3(C_6O_6)_2$, the length of the coordination bonds between Cu and O within each layer is about 1.91 Å, and the distances of a Cu ion to its surrounding Cu and O atoms along the axial direction in the adjacent layers are 3.03 Å (to Cu ions in the adjacent layer) and 2.64 Å (to O atoms in the other adjacent layer, **Figure D.33a**), respectively. The values of these bond lengths clarified that Cu ions in the MOFs adopt pseudo-square planar coordination modes. Consistently, in the calculated spin density map (**Figure D.28**), the spin density resides mostly on the $d_{x^2-y^2}$ orbital of Cu(II) ions. The four lobes of $d_{x^2-y^2}$ orient toward the four O atoms in a nearly square-planar environment (**Figure D.33b**). Meanwhile, the interlayer Cu-Cu distance of 3.01 Å is too large for the two $d_{x^2-y^2}$ orbitals to overlap to form effective interactions.[50] Therefore, in the extended conjugated 2D layer, the "through-bond" magnetic spin interaction would be much more effective than the "through-space" type magnetic interactions.
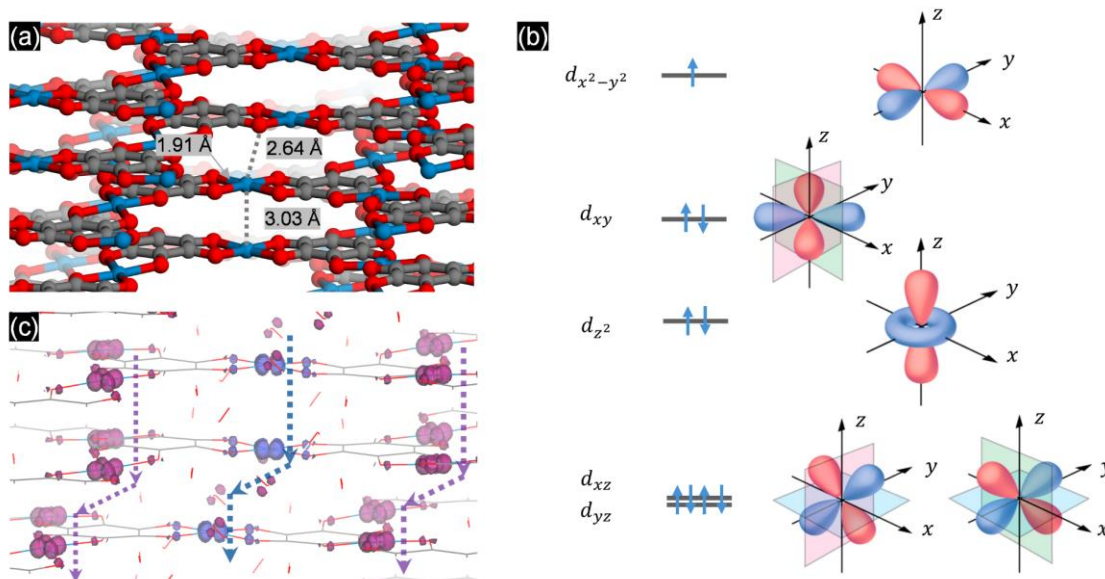


**Figure D.33.** (a) The pseudo-square planar coordination modes of Cu ions in MFO layers. (b) The general representation of *d* orbitals and electron configuration of Cu(II) with a square-planar coordination environment. (c) Calculated spin density on $Cu^\alpha$ and $Cu^\beta$ and the assumed ferromagnetic coupling interactions between interlayer Cu(II) ions.

*Second*, based on the calculated spin density map, the spins on $Cu^\alpha$ and $Cu^\beta$, which have a molar ratio of 1:2 in $Cu_3(C_6O_6)_2$ with opposite signs. If there are ferromagnetic coupling

interactions between interlayer Cu(II) ions, as schematically shown in **Figure D.33c**, such magnetic coupling interactions would lead to ferrimagnetism or ferromagnetism. However, the magnetic characterization of $Cu_3(C_6O_6)_2$ revealed a paramagnetic behavior for $Cu_3(C_6O_6)_2$ without magnetic ordering down to the temperature of 1.8 K. Therefore, ferromagnetic coupling interactions between interlayer Cu(II) ions are not likely. In fact, other related 2D Cu-based coordination polymers with layered structures, including $Cu_3(HHTP)_2$ and Cu-BHT (**Figure D.34**), have been found to be paramagnetic with strong antiferromagnetic interaction between the adjacent intralayer Cu ions.[51]
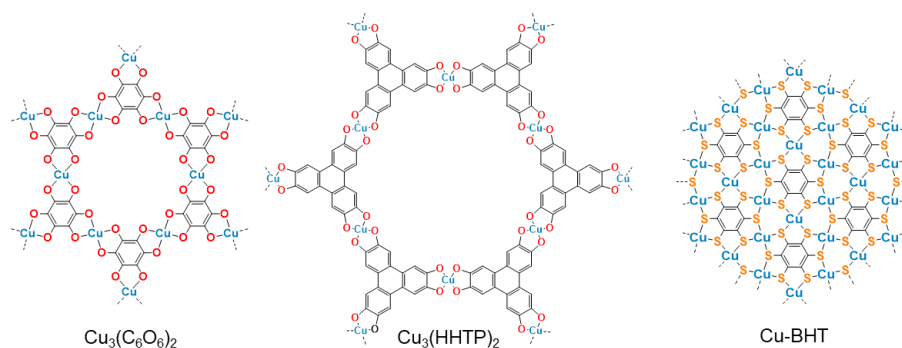


**Figure D.34**. Chemical structure of $Cu_3(C_6O_6)_2$, $Cu_3(HHTP)_2$, and Cu-BHT.

In short, we hypothesize that the intralayer Cu couplings are the key factor towards the understanding of the magnetic property of $Cu_3(C_6O_6)_2$. Since the magnetic spin for $Cu^\alpha$ and $Cu^\beta$ both likely reside on $d_{x^2-y^2}$ orbitals and Cu(II) ions in each layer have a Kogamé arrangement in $Cu_3(C_6O_6)_2$, the magnetic system of $Cu_3(C_6O_6)_2$ is supposed to be similar to spin-1/2 Kogamé lattice,[51a, 52] we adopted the model in **Figure D.35** for the analysis of the exchange couplings. The spin Hamiltonian of the model is then given by[52a, 52b]

$$H = J \sum_{<i,j>} S_i S_j \qquad (\textbf{D.11})$$

where *J* is the magnitude of coupling constant between these two spins., *<i, j>* stands for the summation over nearest neighbors, $S_i$ is the spin operator on the *i*th site.
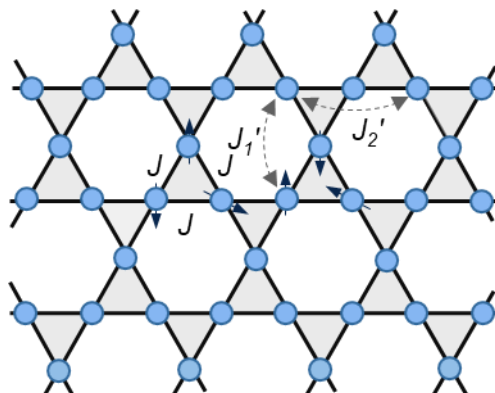
**Figure D.35**. Schematic representation of the antiferromagnetic coupling interactions in $Cu_3(C_6O_6)_2$ MOF. The circles and triangles represent Cu ions and ligands in the MOF.

To estimate the magnitude of the antiferromagnetic coupling, we used the tenth-order high-temperature series expansion (HTSE) which is a straightforward and well-established approach to calculate thermodynamic quantities for unfrustrated and frustrated magnetic systems.[53] The magnetic susceptibility was fitted to the following equation:

$$\chi_{m,p} = \frac{N_A g^2 \mu_0 \mu_B^2}{J} \sum_{n=1}^{10} c_n \left(\frac{J}{k_B T}\right)^n \qquad \textbf{(D.12)}$$

In the equation **D.12**, $N_A$ is the Avogadro's number ($6.022141793 \times 10^{23}$ mol$^{-1}$), $g$ is the $g$-factor value (2.085), $\mu_0$ is vacuum permittivity ($1.2566370614 \times 10^{-6}$ N A$^{-2}$), $\mu_B$ is Bohr magneton ($9.274009994 \times 10^{-24}$ A m$^2$), $k_B$ is Boltzmann constant ($1.380649 \times 10^{-23}$ J K$^{-1}$), $T$ is the temperature (K), $\chi_{m,p}$ is molar paramagnetic susceptibility in the unit of emu mol$^{-1}$, and $c_n$ is the coefficient whose detailed calculations are given in ref [54] for spin-1/2 Kogamé lattice. It should be noted that the HTSE approach represents a minimal model to fit the experimental susceptibility with a Kogamé lattice model and only gives an idea of the magnitude of the magnetic interactions in the investigated compound.
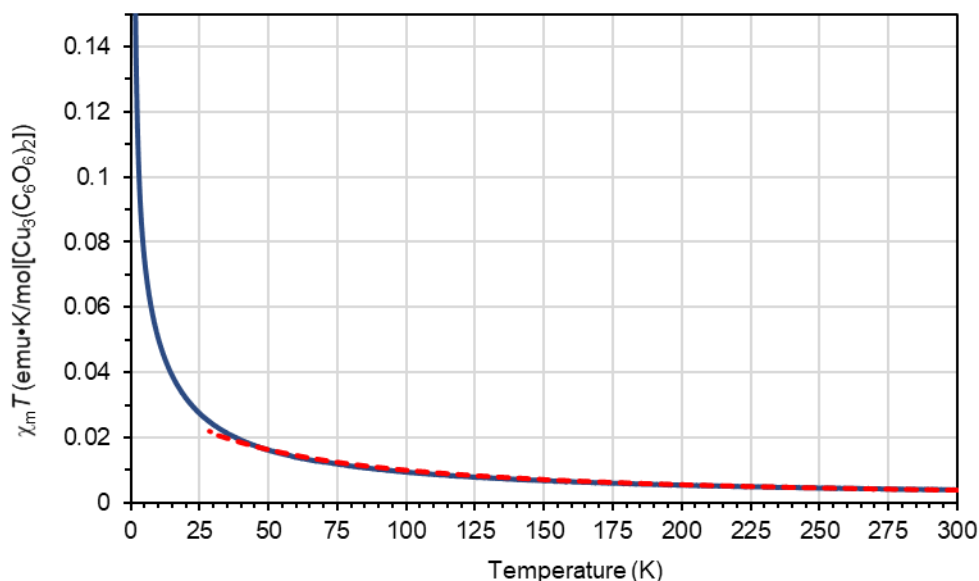


**Figure D.36.** The molar magnetic susceptibility data (dark blue) and the fitted curve the uniform Kogamé lattice model by high-temperature series expansions. The HTSE fitting at high temperatures range yielded $|J|/k_B = 20$ K.

# References

[1]    J. Park, A. C. Hinckley, Z. Huang, D. Feng, A. A. Yakovenko, M. Lee, S. Chen, X. Zou, Z. Bao, *J. Am. Chem. Soc.* **2018**, *140*, 14533-14537.

[2]    L. Yang, X. He, M. Dincă, *J. Am. Chem. Soc.* **2019**, *141*, 10475-10480.

[3]     a) Q. Jiang, P. Xiong, J. Liu, Z. Xie, Q. Wang, X. Q. Yang, E. Hu, Y. Cao, J. Sun, Y. Xu, L. Chen, *Angew. Chem. Int. Ed.* **2020**, *59*, 5273-5277; b) J. Nyakuchena, S. Ostresh, D. Streater, B. Pattengale, J. Neu, C. Fiankor, W. Hu, E. D. Kinigstein, J. Zhang, X. Zhang, C. A. Schmuttenmaer, J. Huang, *J. Am. Chem. Soc.* **2020**, *142*, 21050-21058.

[4]     J. Tauc, R. Grigorovici, A. Vancu, *Phys. Status Solidi B* **1966**, *15*, 627-637.

[5]     J. I. Pankove, *Optical Processes in Semiconductors*, Courier Corporation, **1971**.

[6]     a) A. Mahringer, A. C. Jakowetz, J. M. Rotter, B. J. Bohn, J. K. Stolarczyk, J. Feldmann, T. Bein, D. D. Medina, *ACS Nano* **2019**, *13*, 6711-6719; b) T. Chen, J. H. Dou, L. Yang, C. Sun, N. J. Libretto, G. Skorupskii, J. T. Miller, M. Dinca, *J. Am. Chem. Soc.* **2020**, *142*, 12367-12373; c) G. Skorupskii, B. A. Trump, T. W. Kasel, C. M. Brown, C. H. Hendon, M. Dinca, *Nat. Chem.* **2020**, *12*, 131-136.

[7]     P. Makula, M. Pacia, W. Macyk, *J. Phys. Chem. Lett.* **2018**, *9*, 6814-6817.

[8]     G. Greczynski, L. Hultman, *Prog. Mater. Sci.* **2020**, *107*, 100591.

[9]     a) C. D. Easton, C. Kinnear, S. L. McArthur, T. R. Gengenbach, *J. Vac. Sci. Technol. A* **2020**, *38*, 023207; b) T. L. Barr, S. Seal, *J. Vac. Sci. Technol.* **1995**, *13*, 1239-1246.

[10]    C. R. Brundle, B. V. Crist, *J. Vac. Sci. Technol. A* **2020**, *38*, 041001.

[11]    a) M. C. Biesinger, L. W. M. Lau, A. R. Gerson, R. S. C. Smart, *Appl. Surf. Sci.* **2010**, *257*, 887-898; b) M. C. Biesinger, B. R. Hart, R. Polack, B. A. Kobe, R. S. C. Smart, *Miner. Eng.* **2007**, *20*, 152-162.

[12]    C.-K. Wu, M. Yin, S. O'Brien, J. T. Koberstein, *Chem. Mater.* **2006**, *18*, 6054-6058.

[13]    a) G. Panzner, B. Egert, H. P. Schmidt, *Surf. Sci.* **1985**, *151*, 400-408; b) T. Yamashita, P. Hayes, *Appl. Surf. Sci.* **2008**, *254*, 2441-2449; c) R. Simpson, R. G. White, J. F. Watts, M. A. Baker, *Appl. Surf. Sci.* **2017**, *405*, 79-87.

[14]    K. M. Jablonka, D. Ongari, S. M. Moosavi, B. Smit, *Nat. Chem.* **2021**, *13*, 771-777.

[15]    a) M. Tachibana, *J. Inorg. Biochem.* **1987**, *30*, 133-140; b) R. M. Stolz, A. Mahdavi-Shakib, B. G. Frederick, K. A. Mirica, *Chem. Mater.* **2020**, *32*, 7639-7652; c) J. H. Dou, M. Q. Arguilla, Y. Luo, J. Li, W. Zhang, L. Sun, J. L. Mancuso, L. Yang, T. Chen, L. R. Parent, G. Skorupskii, N. J. Libretto, C. Sun, M. C. Yang, P. V. Dip, E. J. Brignole, J. T. Miller, J. Kong, C. H. Hendon, J. Sun, M. Dinca, *Nat. Mater.* **2021**, *20*, 222-228.

[16]    E. Garribba, G. Micera, *J. Chem. Educ.* **2006**, *83*.

[17]    J. Hattne, F. E. Reyes, B. L. Nannenga, D. Shi, M. J. de la Cruz, A. G. Leslie, T. Gonen, *Acta Crystallogr. A Found. Adv.* **2015**, *71*, 353-360.

[18]    B. L. Nannenga, D. Shi, A. G. W. Leslie, T. Gonen, *Nat. Methods* **2014**, *11*, 927-930.

[19]    W. Kabsch, *Acta Crystallogr. D Biol. Crystallogr.* **2010**, *66*, 125-132.

[20]    G. M. Sheldrick, *Acta Crystallogr. A Found. Adv.* **2015**, *71*, 3-8.

[21]    C. B. Hubschle, G. M. Sheldrick, B. Dittrich, *J. Appl. Crystallogr.* **2011**, *44*, 1281-1284.

[22]    L. M. Peng, *Micron* **1999**, *30*, 625-648.

[23]    S. J. Clark, M. D. Segall, C. J. Pickard, P. J. Hasnip, M. J. Probert, K. Refson, M. C. Payne, *Z. Kristallogr. Krist.* **2005**, *220*, 567-570.

[24]    S. Grimme, *J. Comput. Chem.* **2006**, *27*, 1787-1799.

[25]    T. Kunde, B. M. Schmidt, *Angew. Chem. Int. Ed.* **2019**, *58*, 666-668.

[26] a) B. L. Nannenga, *Struct. Dyn.* **2020**, *7*, 014304; b) T. B. Blum, D. Housset, M. T. B. Clabbers, E. van Genderen, M. Bacia-Verloop, U. Zander, A. A. McCarthy, G. Schoehn, W. L. Ling, J. P. Abrahams, *Acta Cryst.* **2021**, *77*, 75-85.

[27] R. M. Buchanan, C. Wilson-Blumenberg, C. Trapp, S. K. Larsen, D. L. Greene, C. G. Pierpont, *Inorg. Chem.* **1986**, *25*, 3070-3076.

[28] J. Rall, M. Wanner, M. Albrecht, F. M. Hornung, W. Kaim, *Chem. Eur. J.* **1999**, *5*, 2802-2809.

[29] B. F. Abrahams, B. A. Boughton, N. J. FitzGerald, J. L. Holmes, R. Robson, *Chem. Commun.* **2011**, *47*.

[30] V. I. Ovcharenko, E. V. Gorelik, S. V. Fokin, G. V. Romanenko, V. N. Ikorskii, A. V. Krashilina, V. K. Cherkasov, G. A. Abakumov, *J. Am. Chem. Soc.* **2007**, *129*, 10512-10521.

[31] P. Verma, J. Weir, L. Mirica, T. D. P. Stack, *Inorg. Chem.* **2011**, *50*, 9816-9825.

[32] G. A. Abakumov, A. V. Krashilina, V. K. Cherkasov, I. L. Eremenko, S. E. Nefedov, *Russ. Chem. Bull.* **2001**, *50*, 2193-2199.

[33] E. Asato, A. Kyan, T. Madanbashi, T. Tamura, M. Tadokoro, M. Mizuno, *Chem. Commun.* **2010**, *46*.

[34] D. Gupta, B. Shankar, P. Elumalai, R. Shanmugam, S. M. Mobin, F. Weisser, B. Sarkar, M. Sathiyendiran, *J. Organomet. Chem.* **2014**, *754*, 59-62.

[35] X. Wu, Y. Qiu, Z. Chen, B. Guan, X. Hao, A. I. Rykov, Y. Sun, L. Liu, Y. Zou, J. Sun, W. Xu, D. Zhu, *Angew. Chem. Int. Ed.* **2020**, *59*, 20873-20878.

[36] J. A. Cowan, J. A. K. Howard, *Acta Cryst.* **2004**, *60*, m511-m513.

[37] D. Braga, G. Cojazzi, L. Maini, F. Grepioni, *New J. Chem.* **2001**, *25*, 1221-1223.

[38] M. Lee, J. Hong, J. Lopez, Y. M. Sun, D. W. Feng, K. Lim, W. C. Chueh, M. F. Toney, Y. Cui, Z. N. Bao, *Nat. Energy* **2017**, *2*, 861-868.

[39] A. M. Barthram, R. L. Cleary, R. Kowallick, M. D. Ward, *Chem. Commun.* **1998**, 2695-2696.

[40] H. Chen, M. Armand, M. Courty, M. Jiang, C. P. Grey, F. Dolhem, J. M. Tarascon, P. Poizot, *J. Am. Chem. Soc.* **2009**, *131*, 8984-8988.

[41] L. Sun, S. S. Park, D. Sheberla, M. Dinca, *Journal of the American Chemical Society* **2016**, *138*, 14772-14782.

[42] L. E. Darago, M. L. Aubrey, C. J. Yu, M. I. Gonzalez, J. R. Long, *J. Am. Chem. Soc.* **2015**, *137*, 15703-15711.

[43] a) M. Rudra, S. Halder, S. Saha, A. Dutta, T. P. Sinha, *Mater. Chem. Phys.* **2019**, *230*, 277-286; b) M. Rudra, H. S. Tripathi, A. Dutta, T. P. Sinha, *Mater. Chem. Phys.* **2021**, *258*.

[44] a) R. M. Hill, *Phys. Status Solidi* **1976**, *34*, 601-613; b) B. I. Shklovskii, A. L. Efros, *Electronic Properties of Doped Semiconductors*, **1984**.

[45] B. Delley, *J. Chem. Phys.* **2000**, *113*, 7756-7764.

[46] S. Grimme, J. Antony, S. Ehrlich, H. Krieg, *J. Chem. Phys.* **2010**, *132*, 154104.

[47] B. Patra, S. Jana, L. A. Constantin, P. Samal, *Phys. Rev. B* **2019**, *100*, 045147.

[48] G. A. Bain, J. F. Berry, *J. Chem. Educ.* **2008**, *85*.

[49] a) M. I. Darby, *British Journal of Applied Physics* **1967**, *18*, 1415-1417; b) Z. Wang, L. Pi,

M. S. Seehra, J. Bindra, H. van Tol, N. S. Dalal, *Journal of Magnetism and Magnetic Materials* **2017**, *422*, 386-390.

[50]   a) F. Bertolotti, A. Forni, G. Gervasio, D. Marabello, E. Diana, *Polyhedron* **2012**, *42*, 118-127; b) R. D. Cannon, *Inorg. Chem.* **2002**, *20*, 2341-2342.

[51]   a) Y. Misumi, A. Yamaguchi, Z. Zhang, T. Matsushita, N. Wada, M. Tsuchiizu, K. Awaga, *J. Am. Chem. Soc.* **2020**, *142*, 16513-16517; b) X. Huang, S. Zhang, L. Liu, L. Yu, G. Chen, W. Xu, D. Zhu, *Angew. Chem. Int. Ed.* **2018**, *57*, 146-150.

[52]   a) N. Elstner, A. P. Young, *Phys. Rev. B* **1994**, *50*, 6871-6876; b) Z. Hiroi, H. Yoshida, Y. Okamoto, M. Takigawa, *J. Phys.: Conf. Ser.* **2009**, *145*, 012002; c) S. Yan, D. A. Huse, S. R. White, *Science* **2011**, *332*, 1173-1176; d) H. J. Liao, Z. Y. Xie, J. Chen, Z. Y. Liu, H. D. Xie, R. Z. Huang, B. Normand, T. Xiang, *Phys. Rev. Lett.* **2017**, *118*, 137202.

[53]   J. Oitmaa, C. Hamer, W. Zheng, *Series Expansion Methods for Strongly Interacting Lattice Models*, Cambridge University Press, **2006**.

[54]   A. Lohmann, H.-J. Schmidt, J. Richter, *Phys. Rev. B* **2014**, *89*, 014415.

*Appendix E*

*Supporting Information for Chapter 6: Conductive Stimuli-Responsive*

*Coordination Network Linked with Bismuth for Chemiresistive Gas Sensing*

**Section E1.**

E1. Materials and methods

Powder X-ray diffraction (PXRD) measurements were performed with a Rigaku sixth generation MiniFlex X-ray diffractometer with a 600 W (40 kV, 15 mA) CuKα (λ = 1.54 Å) radiation source. Nitrogen adsorption experiments were performed with 3Flex (Mircromeritics, Norcross, Georgia) instrument. Elemental analyses were performed by *Atlantic Microlab, inc.* X-ray photoelectron spectroscopy (XPS) experiments were conducted on Kratos Analytical AXIS Supra X-ray Photoelectron Spectrometer under ultrahigh vacuum (base pressure $10^{-7}$ Torr) equipped with a monochromatic Al (Kα) X-ray source. Both survey and high-resolution spectra were obtained using a beam diameter of 200 μm. FT-IR was performed on a JASCO FT-IT 6200 type A serial number: A008261022 equipped with a TGS detector. For MicroED analysis, data was acquired on a Thermo Fisher Talos F200C electron microscope operating at an acceleration voltage of 200 KeV, corresponding to a wavelength of 0.0251 Å. Screening of the TEM grids for micro crystals was done by operating the microscope in over focused diffraction mode to minimize diffraction and hysteresis between screening and diffraction operational modes. Infrared (IR) data was collected on a Thermoscientific Nicolet iS50 FT-IR spectrometer in a DRIFTS configuration.
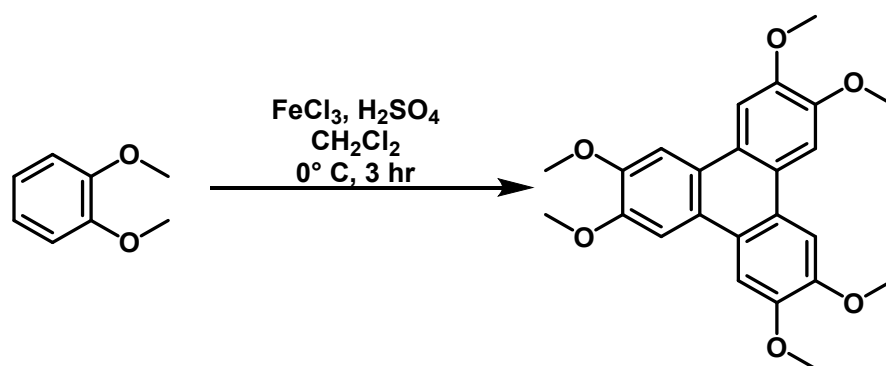


**Figure E.1.** Reaction scheme for the synthesis of 2,3,6,7,10,11-hexamethoxytriphenylene (HMTP).

1.1 Synthesis of 2,3,6,7,10,11-hexamethoxytriphenylene (HMTP): The synthesis of HHTP was carried out according to previously reported conditions.[1] 9.2 mL of veratrole (72.4 mmol) was suspended in 50 mL of dichloromethane. Subsequently, 35.2 g (217.2 mmol) of $FeCl_3$ was suspended in dichloromethane (100 mL), and concentrated sulfuric acid (0.75 mL) was added dropwise at 0 °C. The veratrole solution was added dropwise to the iron (III) chloride solution at 0 °C over 15 minutes. The resulting solution was returned to room temperature over the course of 3 hours with stirring. At this stage, methanol was added slowly to quench the reaction (150

mL). The first portion (50 mL) of methanol was added a milliliter at a time (dropwise) until the reaction was transformed from a thick, tarry black slurry to a smooth, opaque, yellow suspension. Once the methanol had been fully added, the reaction was stirred for 30 minutes then filtered. The white solid was washed thoroughly with methanol (5 x 50 mL), then dried under reduced pressure at 52 $^0$C, affording pure compound (64.3 g, yield = 64%).
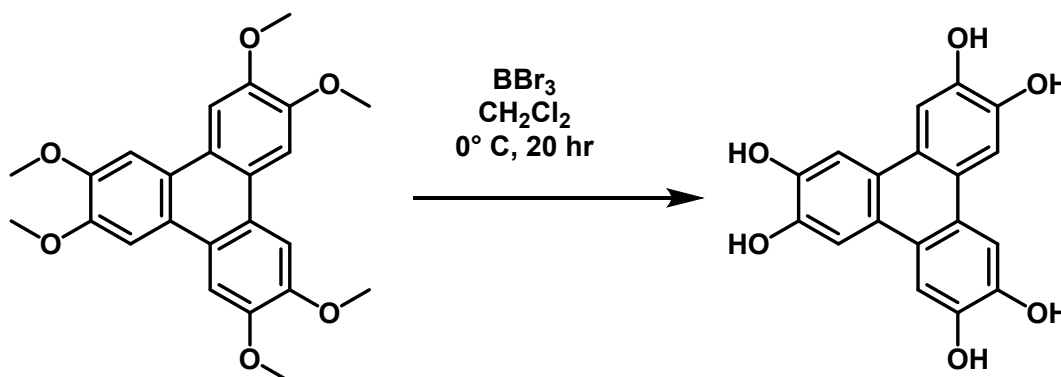


**Figure E.2.** Reaction scheme for the synthesis of 2,3,6,7,10,11-hexahdroxytriphenylene (HHTP).

1.2 Synthesis of 2,3,6,7,10,11-hexahydroxytriphenylene (HHTP): 3.01 g (7.35 mmol) of HMTP was dissolved in dichloromethane (25 mL) within the reaction vessel at 0 $^0$C. The resulting solution turned milky-grey, and after 30 minutes of stirring 5.2 mL of boron tribromide (51.45 mmol) was added dropwise under inert atmosphere, forming a light blue mixture. The reaction mixture returned to room temperature and stirred overnight (20 hrs). The resulting blue mixture was slowly quenched with 30 mL of DI water. 25 mL of brine was added to the blue-grey reaction mixture and stirred for 5 minutes. 100 mL of ethyl acetate was then added to the reaction mixture, wherein the product remained in the aqueous phase. The biphasic solution of ethyl acetate and water was heated (75$^0$C) and stirred for 12 hrs to afford a purple solution. To the purple solution, dilute sulfuric acid was added, and the acidic solution stirred at 50 $^0$C for 8 hrs. Finally, the solution was filtered, and the deep purple powder was dried under reduced pressure at 52 $^0$C, affording pure HHTP (1.81 g, yield = 76%). Characterization matched reported analysis.
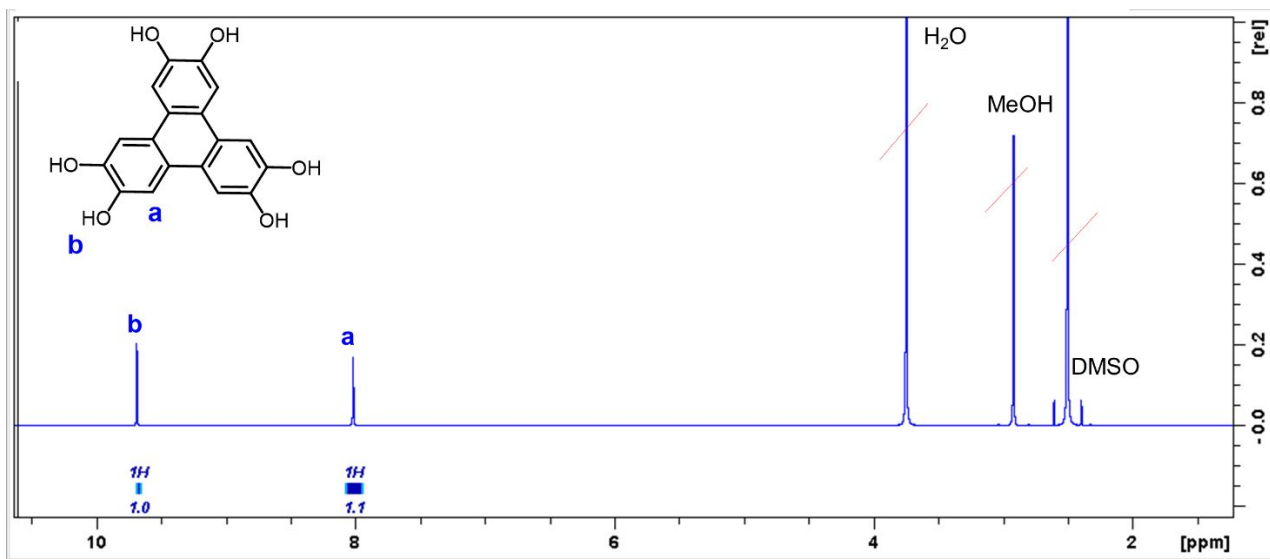
**Figure E.3**. H$^1$NMR of HHTP taken in deuterated DMSO.
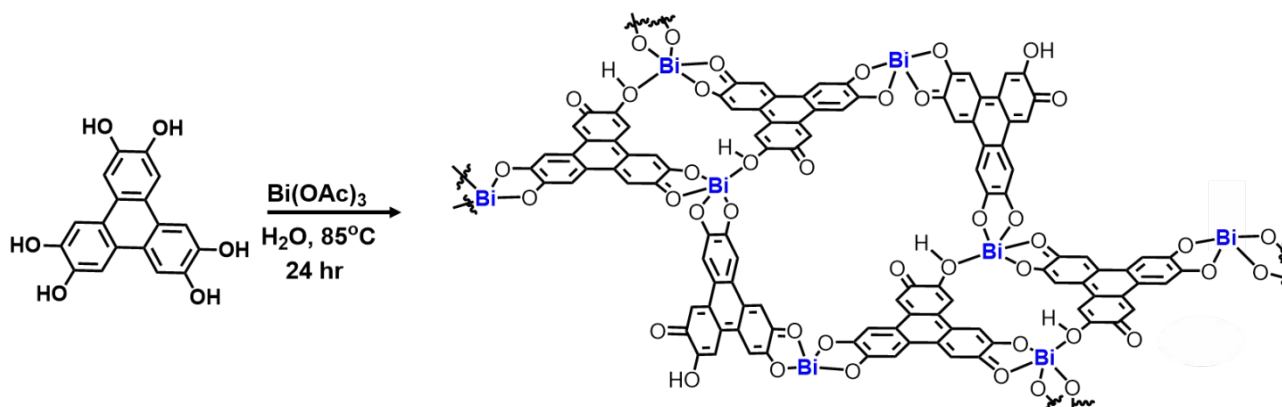


**Figure E.4.** Reaction scheme for the synthesis of Bi(HHTP).

1.3 Procedure 1: Synthesis of Bi(HHTP) at 2:1 molar ratio of metal to ligand ratio: To a 250 mL round bottom flask was added 100 mg (0.308 mmol) of HHTP and 200 mL of $H_2O$. The suspension was sonicated for 5 minutes until homogenous. 238 mg (0.616 mmol) of Bi(OAc)$_3$ was then added and the suspension was sonicated for an additional 5 minutes. The mixture was heated at 85ºC for 24 hours under open atmosphere with stirring, then cooled to room temperature. The suspension was centrifuged at 6000 RPM for 5 minutes and decanted. The dark green solid was suspended in 200 mL DI $H_2O$ and heated with stirring at 50 ºC for 24 hours (water exchanged after 6 hours). The suspension was then cooled to room temperature and subsequently centrifuged (6000 RPM for 5 minutes) and decanted. The material was then dried overnight in a vacuum desiccator. The next day, the green/blue solid was placed in 40 mL EtOAc and vortexed for 30 seconds. The material was left in EtOAc for 3 days for activation (solvent exchanged each

day and vortexed for 30 seconds in between exchanges). The material was dried in a vacuum oven for 24 hours before sensing.

1.4 Procedure 2: Synthesis of Bi(HHTP) at 1:1 molar ratio of metal to ligand ratio: To a 250 mL round bottom flask was added 100 mg (0.308 mmol) of HHTP and 200 mL of $H_2O$. The suspension was sonicated for 5 minutes until homogenous. 119 mg (0.308 mmol) of Bi(OAc)$_3$ was then added and the suspension was sonicated for an additional 5 minutes. The mixture was heated at 85 ºC for 24 hours under open atmosphere with stirring, then cooled to room temperature. The suspension was centrifuged at 6000 RPM for 5 minutes and decanted. The dark green solid was suspended in 100 mL DI $H_2O$ and heated with stirring at 50 ºC for 24 hours (water exchanged after 6 hours). The suspension was then cooled to room temperature and subsequently centrifuged (6000 RPM for 5 minutes) and decanted. The material was then dried overnight in a vacuum desiccator. The next day, the green/blue solid was placed in 40 mL EtOAc and vortexed for 30 seconds. The material was left in EtOAc for 3 days for activation (solvent exchanged each day and vortexed for 30 seconds in between exchanges). The material was dried in a vacuum oven for 24 hours before sensing.

## E2.  Reaction Optimization Procedures

| # | Temp. (H₂O)/days | Concentration (of HHTP) | Scale of HHTP ligand | Purification | Metal to Ligand ratio |
|---|---|---|---|---|---|
| 1 | 85°C / 1 | 1.5 mM | 20 mg | Solid washed with 30 mL $H_2O$ (3x) | (2:1) |
| 2 | 85°C / 1 | 1.5 mM | 20 mg | 1-week Soxhlet extraction in EtOAc | (2:1) |
| 3 | 85°C / 1 | 1.5 mM | 80 mg | 1-week Soxhlet in EtOAc and stirred overnight in 50°C $H_2O$ (water exchanged 3x) | (2:1) |
| 4 | 85°C / 1 | 1.5 mM | 80 mg | Solid washed with 30 mL $H_2O$ and 30 mL EtOAc (2x) | (1:1) |
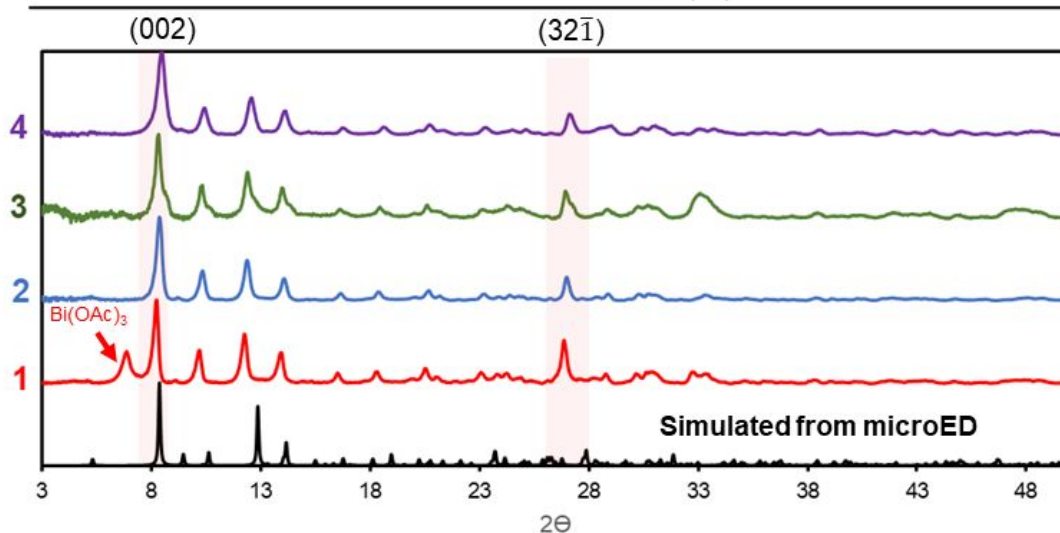


**Figure E.5.** Reaction optimization table depicting synthetic conditions and/or different purification procedures for Bi(HHTP) and corresponding pXRDs.

**Procedures used to carry out synthesis of materials in Figure E.1:**

**Synthetic procedure for trace 1**: 20 mg (0.062 mmol) of HHTP was added to a 100 mL round bottom flask with 40 mL of DI $H_2O$ [1.5 M]. The suspension was sonicated for 5 minutes. 46 mg (0.119 mmol) of $Bi(OAc)_3$ was added to the suspension and the suspension was sonicated for an additional 3 minutes. The mixture was then heated to 85 °C for 24 hours with stirring, stopped and cooled to room temperature. The material was dried in a vacuum desiccator overnight before the pXRD trace was taken (trace 1).

**Purification procedure for procedure 1 (trace 2)**: The material from procedure 1 was taken and place into Soxhlet extractor. Ethyl acetate was used for activation for one week at 165 °C. The

material was subsequently dried in a vacuum desiccator for 18 hours before pXRD, which indicated the absence of bismuth acetate.

**Synthetic procedure for trace 3**: 80 mg of HHTP (0.247 mmol) was added to a 250 mL round bottom flask with 160 mL of DI $H_2O$ [1.5 M].  The suspension was sonicated for 5 minutes. 184 mg (0.477 mmol) of $Bi(OAc)_3$ was added to the suspension and the suspension was sonicated for an additional 3 minutes. The mixture was then heated to 85 ºC for 24 hours with stirring, stopped and cooled to room temperature. The material was dried in a vacuum desiccator overnight before placed in a Soxhlet extractor for one week and dried. After pXRD indicated the presence of $Bi(OAc)_3$, the material was placed 100 mL of DI $H_2O$ and stirred at 50 ºC for two days (water exchanged on second day).

**Synthetic procedure for trace 4**: To a 250 mL round bottom flask was added 100 mg (0.308 mmol) of HHTP and 200 mL of $H_2O$ [1.5 M]. The suspension was sonicated for 5 minutes until homogenous. 119 mg (0.308 mmol) of $Bi(OAc)_3$ was then added and the suspension was sonicated for an additional 5 minutes. The mixture was heated at 85 ºC for 24 hours under open atmosphere with stirring, then cooled to room temperature. The suspension was centrifuged at 6000 RPM for 5 minutes and decanted. The dark green solid was suspended in 100 mL DI H2O and heated with stirring at 50 ºC for 24 hours (water exchanged after 6 hours).

## E3. pXRD patterns of Bi(HHTP) and HHTP polymorphs
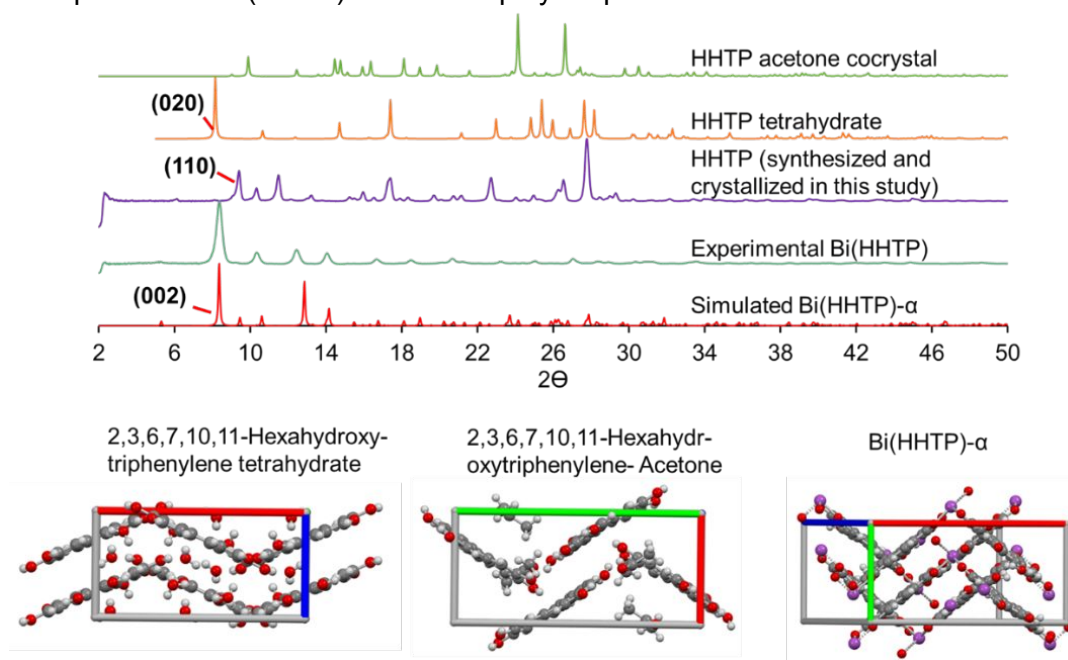


**Figure E.6.** pXRD patterns of (top to bottom) HHTP acetone cocrystal (resolved through this study), HHTP tetrahydrate,[2] in house synthesized HHTP, Experimental Bi(HHTP) and simulated Bi(HHTP).



| Cell Lengths | a 16.2 b 8.0 c 20.0 |
|---|---|
| Cell Angles | α 90 β 94.4 γ 90 |
| Cell Volume | 2599.9 |
| Space group | P 2₁/c |

| Cell Lengths | a 16.5 b 7.8 c 20.7 |
|---|---|
| Cell Angles | α 90 β 96.7 γ 90 |
| Cell Volume | 2624.4 |
| Space group | P 2₁/c |
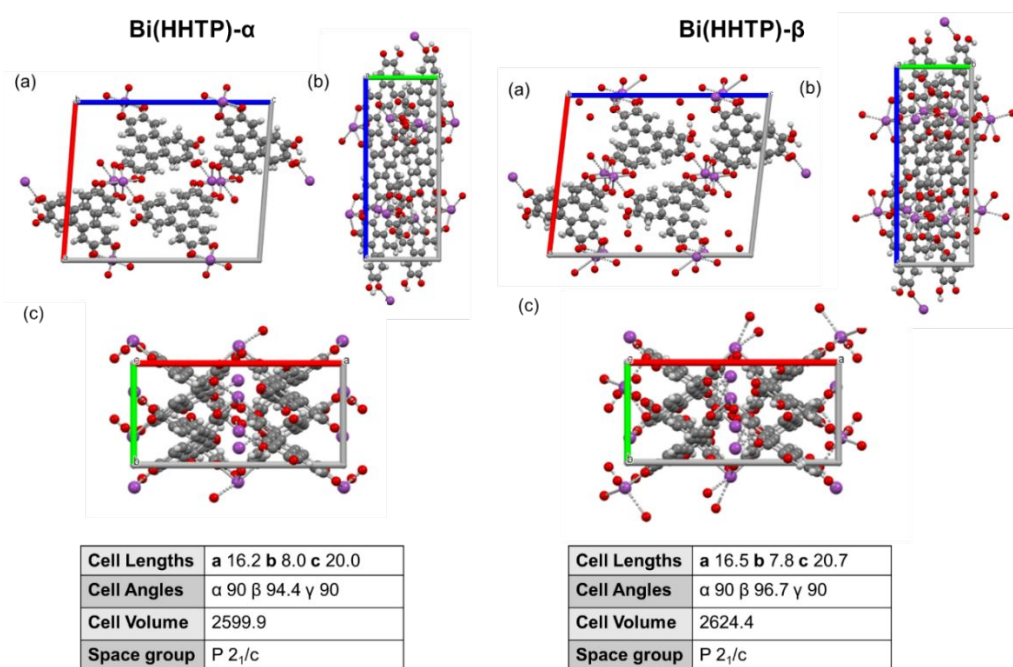
**Figure E.7.** View along the crystallographic (a) b- axis (b) a-axis and (c) and c-axis for Bi(HHTP)-α and Bi(HHTP)-β with cell parameters.

**Section E2. Morphological analysis, Crystallographic data, Network Topology Analysis and Description of Bi(HHTP)**

1. SEM and TEM Characterization
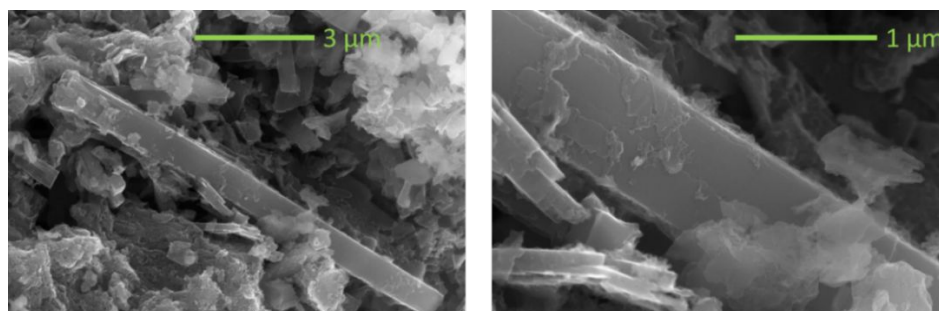


**Figure E.8.** SEM Micrographs of 2:1 Bi(HHTP) made using **Procedure 1** and taken with beam voltage of 15 kV at 35000x magnification and working distance of 4 mm.
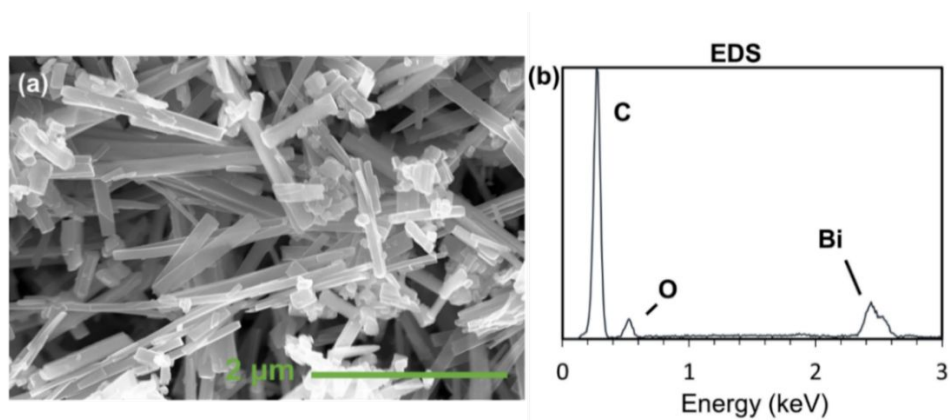


**Figure E.9. (a)** SEM Micrographs of 1:1 Bi(HHTP) made using **Procedure 2** and taken with beam voltage of 15 kV at 35000x magnification and working distance of 4 mm. (b) Energy Dispersive Spectroscopy (EDS) analysis of Bi(HHTP).
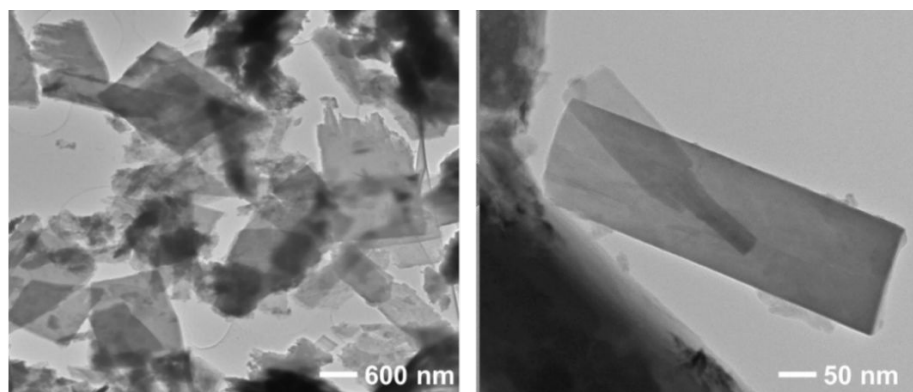


**Figure E.10.** TEM Micrographs of Bi(HHTP) made using **Procedure 1** and taken with beam voltage of 50 kV at 38000x magnification.

## Selected Area Diffraction Analysis (SAED) of Bi(HHTP)

The sample was prepared by drop casting an acetone suspension (1.0 mg in 5 mL sonicated for 16 hours) onto a copper grid (300 mesh, 3.0 mm O.D) for SAED on a TEM (Tecnai F20ST FEG instrument). The TEM was transitioned into diffraction mode and a beam stopper was position over the direct electron beam. The distances between lattices ($d_{hkl}$) and each diffraction spot were calculated using **Equation E.1**, where Lλ is a camera constant (λ at 200kV = 0.0027nm, Lλ= 0.664), and R is measured distance between diffraction spots. The data obtained from diffraction spots corresponded to the 2Θ peaks observed in powder X-ray diffraction patterns of Bi(HHTP).

$$Rd_{hkl}=L\lambda \qquad\qquad E.1$$
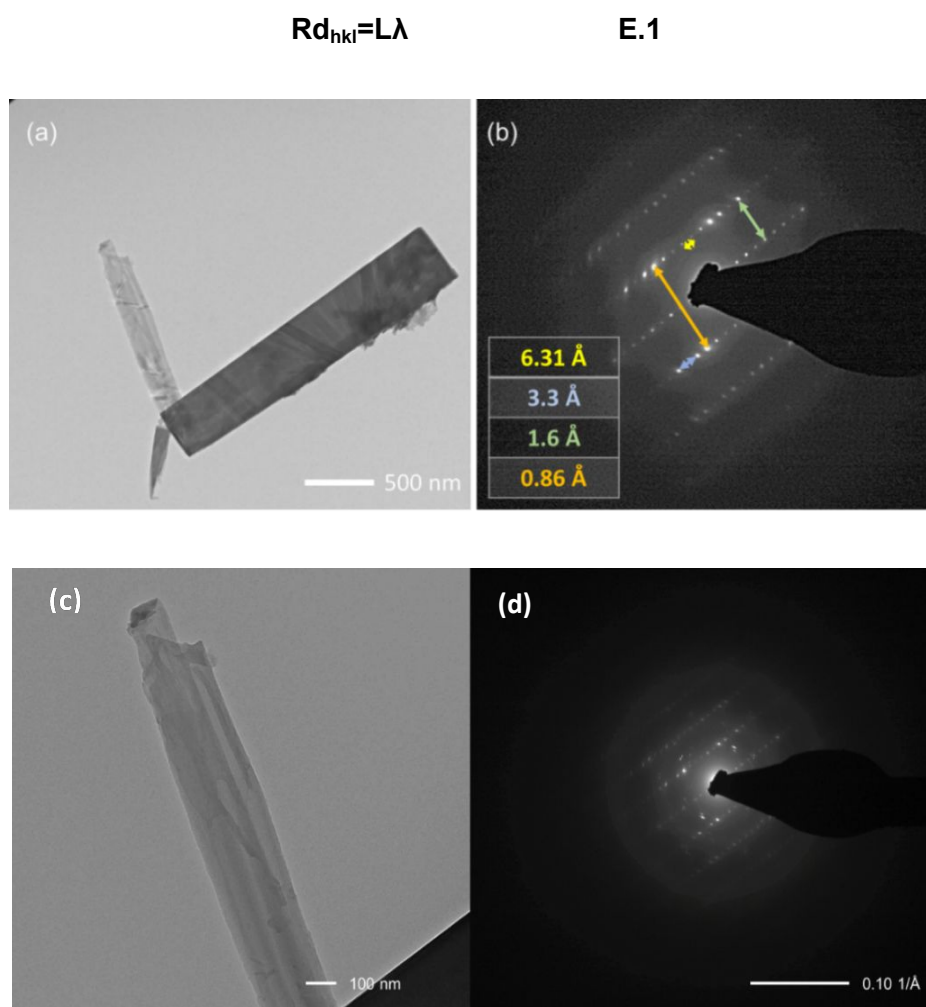


**Figure E.11.** **(a)** Nanocrystal of Bi(HHTP) and selected area diffraction (SAD) pattern obtained using diffraction mode in TEM (Tecnai F20ST FEG TEM instrument) (b) corresponding d-spacing ($d_{hkl}$).**(c)** Nanocrystal of Bi(HHTP) and **(d)** SAED pattern obtained using diffraction mode in TEM (Tecnai F20ST FEG TEM instrument).

The analysis was performed with the ToposPro program package[3], topcryst.com,[4] and the TTD collection of periodic network.[4] The reticular chemistry structure resource (RCSR)[5] symbols were used to describe the crystal nets and to designate the network topologies.
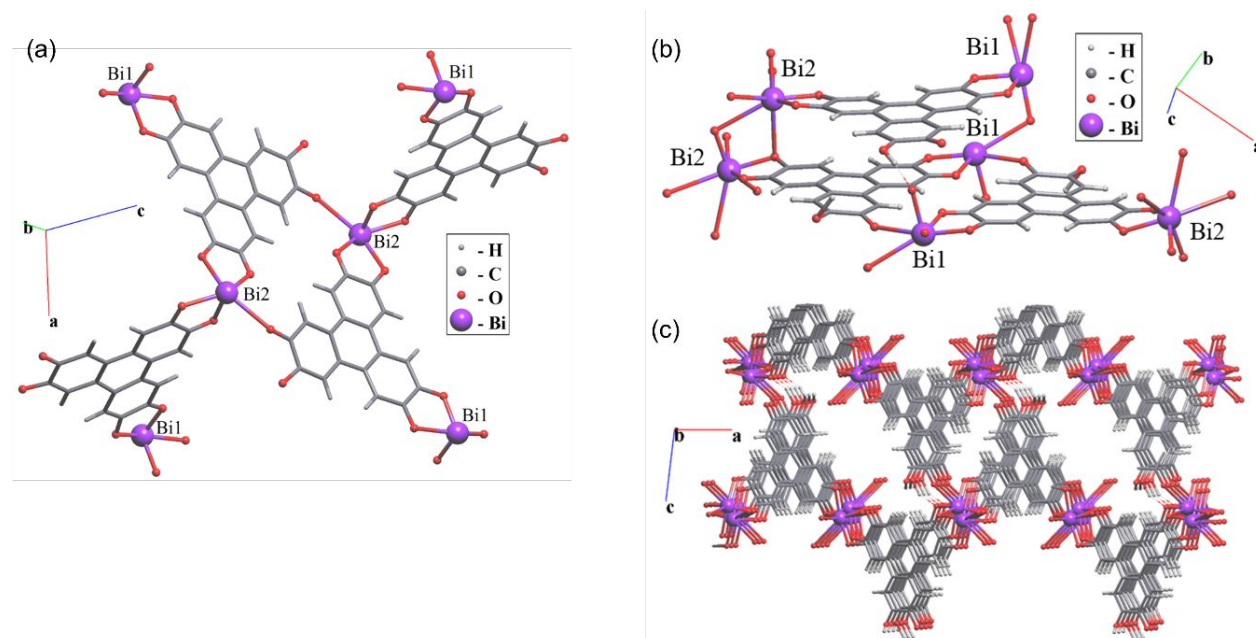


**Figure E.12. (a)** Structure of Bi(HHTP)-α displaying the interchain Bi-O bond of Bi2 and **(b)** the structure and **(c)** layering of Bi(HHTP)-β.

ToposPro © software , topcryst.com and the ToposPro analyst team decribed the two models of the adjacency matrix for Bi(HHTP)-α. In Bi(HHTP)-α, the coordination polyhedron of two nonequivalent Bi1 and Bi2 atoms are distorted quadrilateral (CN=4) and distorted tetragonal pyramid (CN=5), respectively. The structure of Bi(HHTP)-β displayed the coordination polyhedra of $Bi_1$ and $Bi_2$ as distorted pentagonal pyramid (CN=6) and distorted one-caped octahedron (CN=6), respectively (*vide infra*).
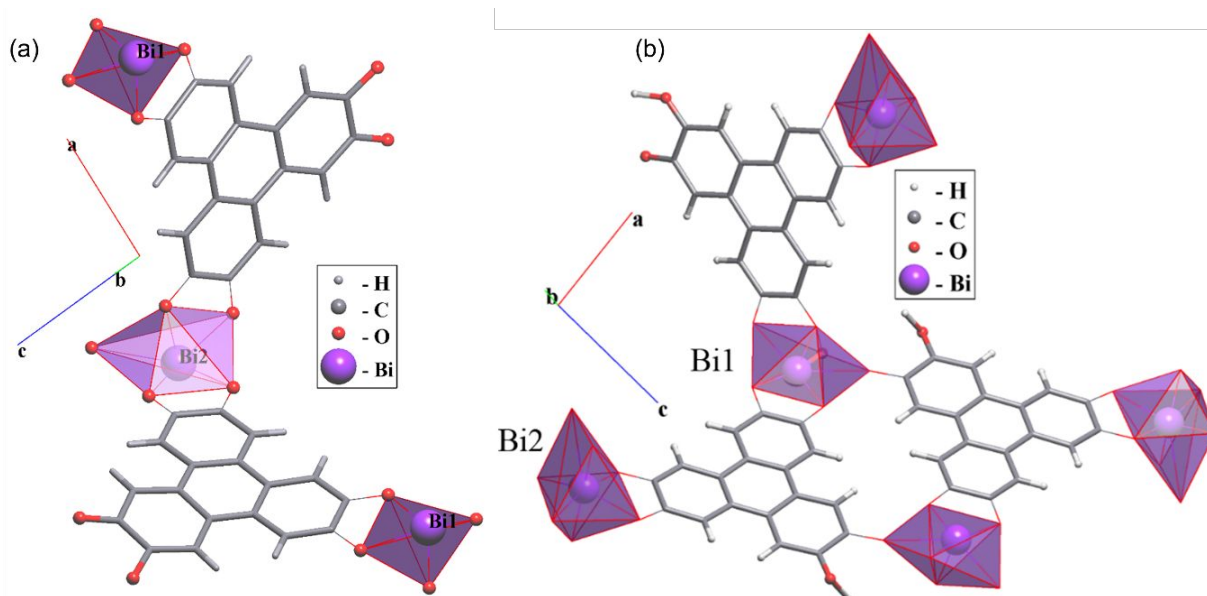
**Figure E.13. (a)** Structure of Bi(HHTP)-α displaying the coordination polyhedron of $Bi_1$ and $Bi_2$ atoms that are distorted quadrilateral (CN=4) and distorted tetragonal pyramid (CN=5), respectively. **(b)** Structure of Bi(HHTP)-β displaying the coordination polyhedra of $Bi_1$ and $Bi_2$ which are distorted pentagonal pyramid for Bi1 (CN=6) and distorted one-caped octahedron for $Bi_2$ (CN=6).
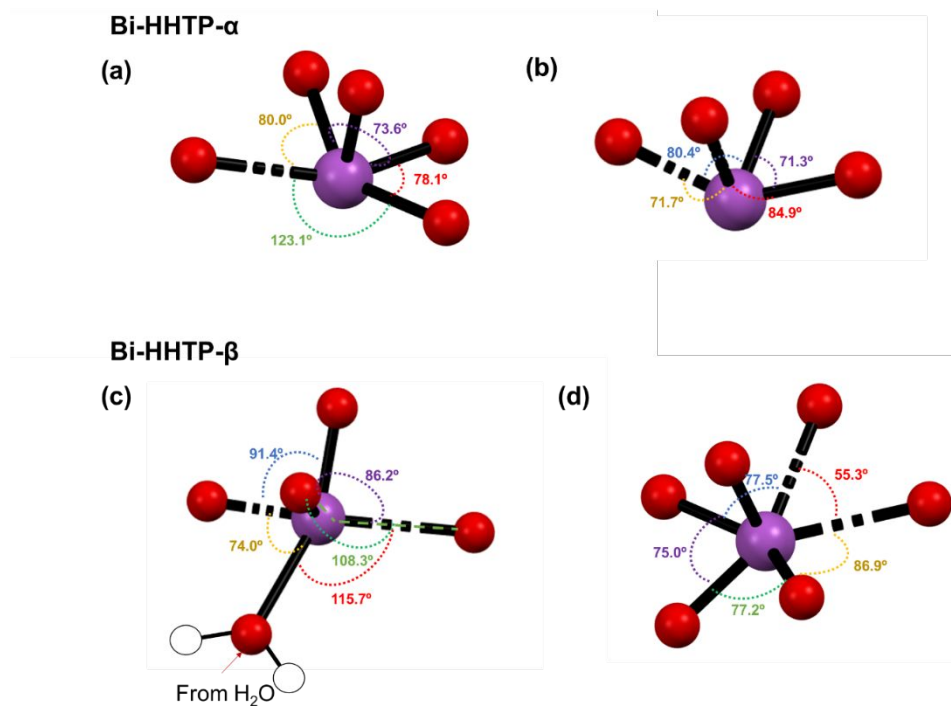


**Figure E.14.** Bi(HHTP)-α Coordination geometry and bond angles of (a) $Bi_2$ and (b) $Bi_1$. Bi(HHTP)-β Coordination geometry and bond angles of (c) $Bi_2$ and (d) $Bi_1$.

2. Standard representation

The topology may also be described using a simplification procedure, i.e. representation of a network in terms of the graph-theory approach[3, 6] Here the ligands are represented by their centers of mass and the obtained net includes removing of the 0- and 1-coordinated nodes and replacing the 2-coordinated nodes (bridge structural groups) by net edges.
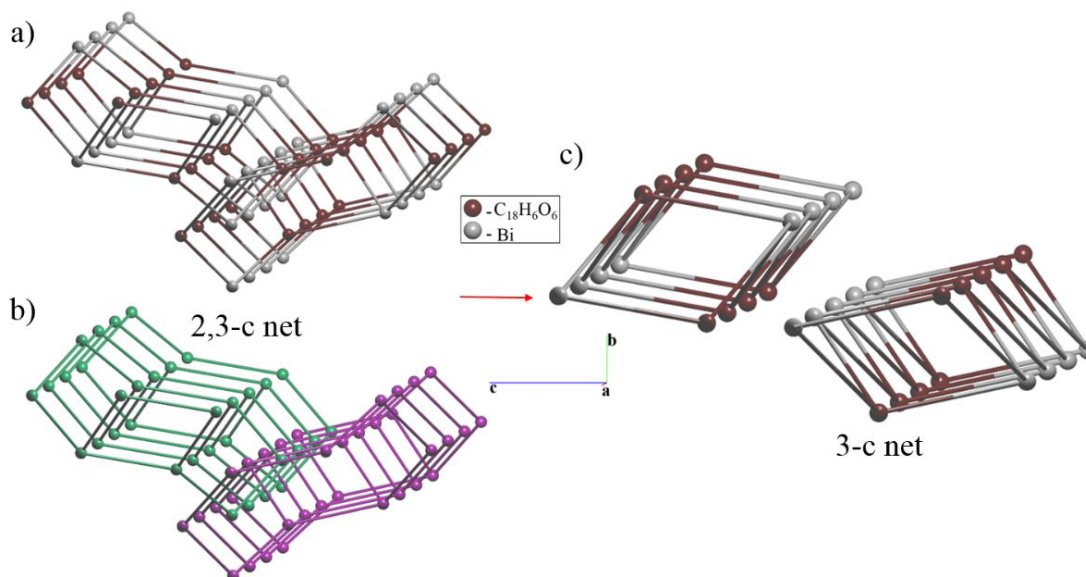


**Figure E.15. (a)** Bi(HHTP)-α displaying a 2,3-C4 uninodal net in standard representation of the valence-bonded MOFs. **(b)** The tightly packed chains are presented. **(c)** 3-c uninodal net after the contraction of the 2-coordinated nodes. Bi atoms are gray spheres. The centers of mass of the HHTP ligands are burgundy.[3]
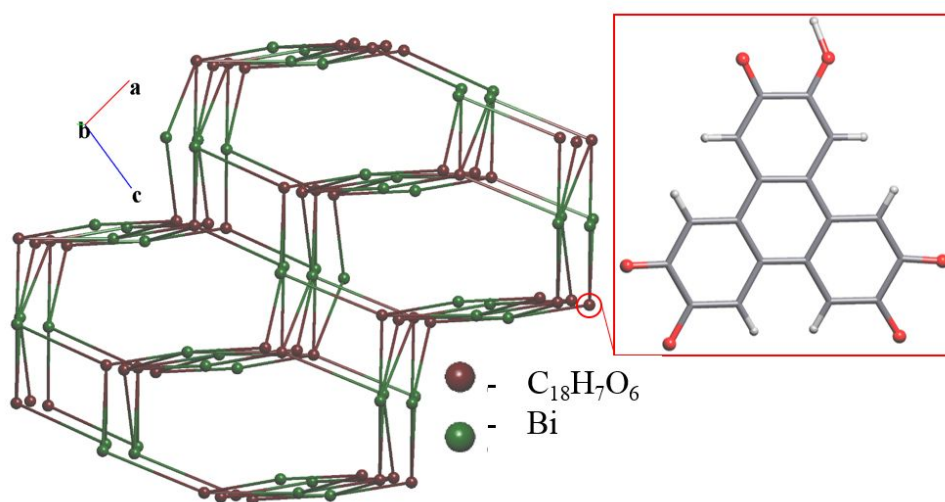


**Figure E.16.** The standard representation of Bi(HHTP)-β resulted in the 3,4,4,5-c nodal net of the new topological type with point symbol for net: {42.62.82} {42.6} {43.63.84} {43.63}

Considering the presence of a lone electron pair on the bismuth atom, through which the oxygen atom weakly interacts with it, we have performed the generation of representations for the Bi-O bonds of the initial structure. As a result, two topologies were obtained, which differ in the value of the solid angle ($\Omega i$): 10 % (**I generated representation**), 14 % (**II generated representation**). The I generated representation resulted in the 2,3-c nodal net of 2,3C4 topological type with point symbol for net: {4.8.10}{8}. The II generated representation resulted in the 2-c uninodal net of 2C1 topological type with point symbol for net: {0} (**Figure E.17**).
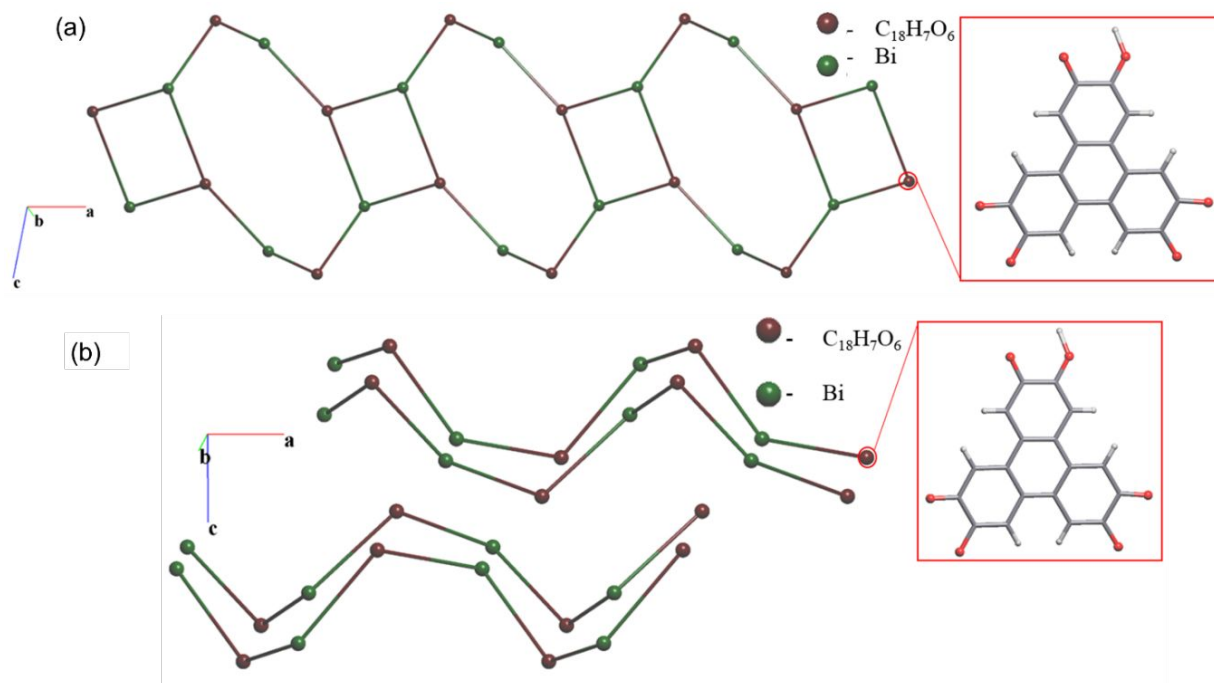


**Figure E.17. (a)** Bi(HHTP)-β displayed a 2,3-c binodal net obtained within I generated representation. **(b)** Bi(HHTP)-β 2-c uninodal net obtained within II generated representation.

**Generation of representations for the underlying net links**

Using the subroutine implemented in ToposPro,[4] different subnets can be obtained from the underlying net that contain the edges of a weight no less than a specified value. Having applied the multilevel analysis, we obtain the following order of the subnets that describe the packing of the structure of Bi(HHTP)-β on different levels of solid angle (**Table E.1**).

| № | Node degrees | $\Omega i$, % | Dimensionality of net | Topological type |
|---|---|---|---|---|
| 1 | 3,4,4,5-c | 8.39 | 3D | New topology with point symbol for net: {4².6².8²}{4².6}{4³.6³.8⁴}{4³.6³} |
| 2 | 3,4,5-c | 8.98 | 3D | New topology with point symbol for net: {4.5³.6.7}{4.5⁴.6.7².8²}{5³} |
| 3 | 4-c | 9.27 | 3D | **sra** |
| 4 | 2,3-c | 10.18 | 1D | 2,3C4 |

| 5 | 2-c | 12.36 | 1D | 2C1 |
|---|---|---|---|---|
| 6 | 1,2-c | 35.38 | 0D | 1,2M4-1 |
| 7 | 1,2-c | 37.28 | 0D | 1,2M3-1 |
| 8 | 1-c | 37.70 | 0D | 1M2-1 |

**Table E.1**. Multilevel analysis of the packing of structural building units (ligands and complexing atoms)
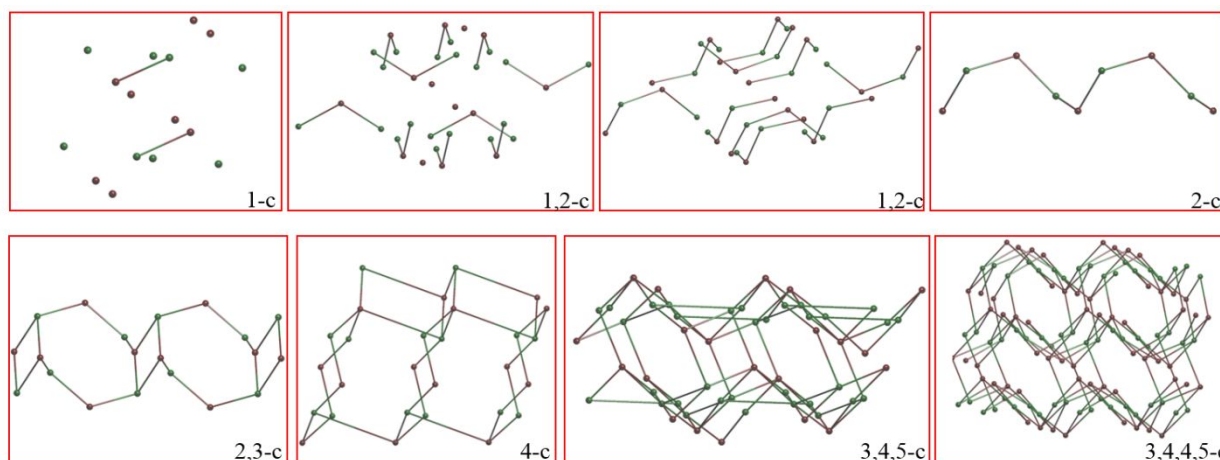


**Figure E.18.** Order of the subnets that describe the packing of the structure on different levels of $\Omega i$.

3. Cluster representation

The cluster simplification procedure implemented in ToposPro allows one to identify more complex building units of a structure and characterize their connection mode. Structural building units in this representation are periodic chains in the direction of [100]. Fragments of $C_{36}H_{12}O_{11}Bi_2$ (blue spheres) (**Figure E.19a**) form these infinite chains which are linked together through an oxygen atom (**Figure E.19b**). The rod packing with 2M4-1 topology and point symbol [7] is presented in **Figure 6.4a**.
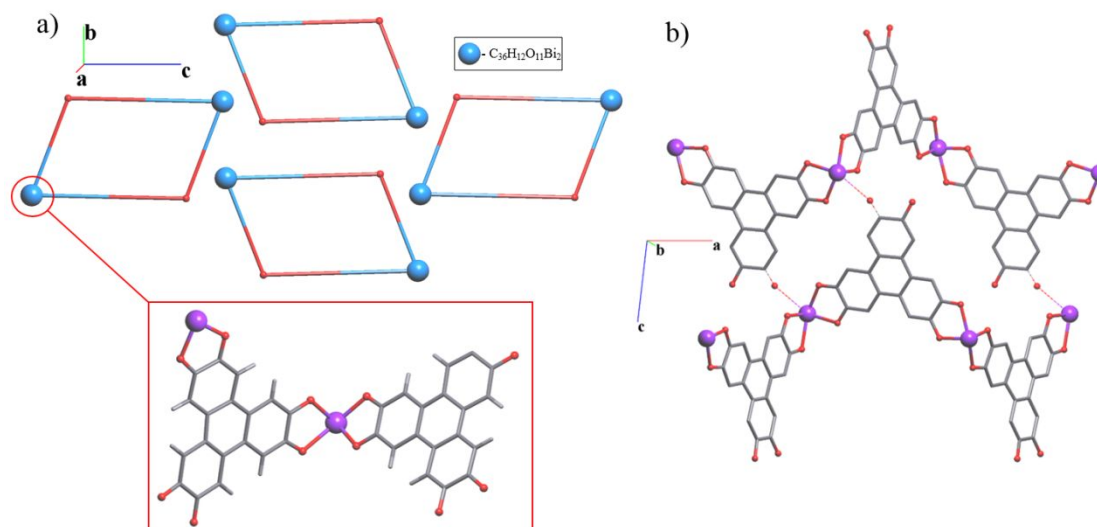
**Figure E.19.** **(a)** Packing of rods (or chains) with 2M4-1 topology. **(b)** The fragments $C_{36}H_{12}O_{11}Bi_2$ (blue spheres) form the chains that are linked to each other through the oxygen atoms.

**4.** Void Volume
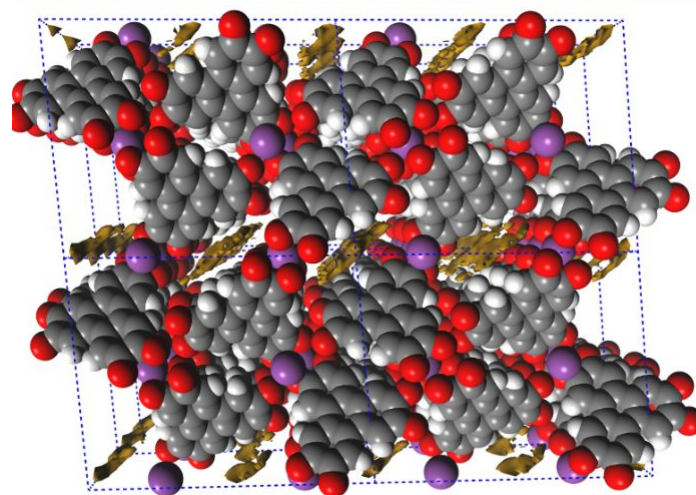


**Figure E.20.** Four unit cells of Bi(HHTP) displaying accessible solvent surface area (blue) calculated using Materials Studio© software using a probe radius of 1.2 Å and a calculated surface area 101.6 Å² and a free volume of 22.62 Å³

**Section E3. Characterization of Bi(HHTP)**
1. ATR-FTIR spectroscopy
Infrared spectra were collected using a JASCO model FT- IR-6100 Fourier transform infrared

spectrophotometer. IR spectrum obtained using a KBr pellet of Bi(HHTP) powder (3 mg) ground

with KBr (20 mg) and hand pressed (PIKE Technologies Hand Press) into a translucent 6 mm

pellet. The chamber was purged with $N_2$ for 10 minutes prior to measurement to remove $CO_2$.
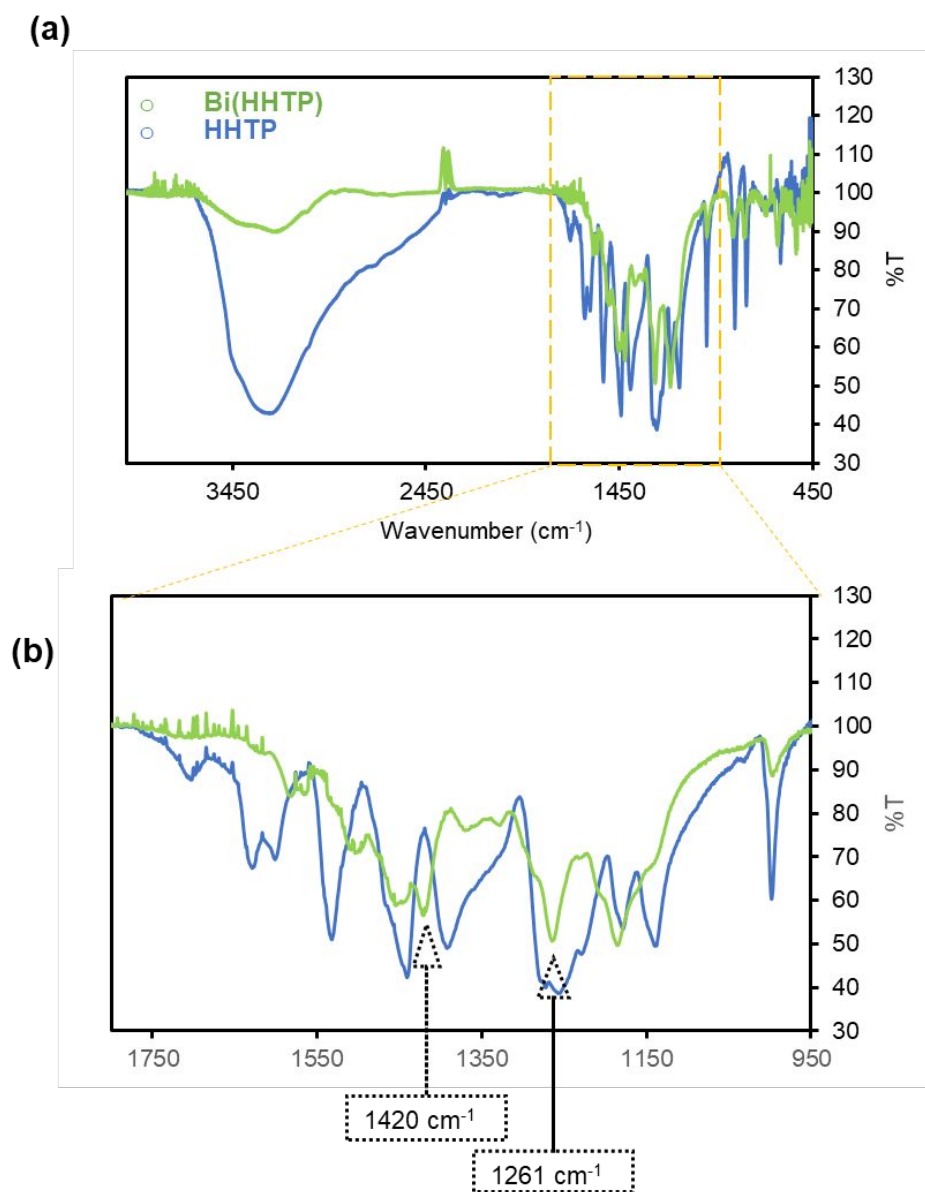


**Figure E.21**. (a) FT-IR of HHTP precursor (blue) and Bi(HHTP) (green). (b) Expanded (1700 – 950 cm$^{-1}$) section indicating presence of new peaks or peak shifts at 1420 and 1261 cm$^{-1}$ indicating bidentate catechol coordination event.[8]

## 2. Brauner-Emmet Teller (BET) surface analysis of Bi(HHTP)

For surface area analysis, the gas adsorption measurements were performed on a 3FLEX instrument (Mircromeritics, Norcross, Georgia) with $N_2$ at 77K. 120 mg of Bi(HHTP) prepared using **Procedure 1** was first activated through Soxhlet extraction in EtOAc for one week and dried in the oven under vacuum (20 mTorr, 85 °C) for 24 hours. Before gas adsorption measurements, the samples were degassed under vacuum at 95°C for 2 days. For BET calculations, a full isotherm with a fitting range of 0 to 1 $P/P^0$ was used.
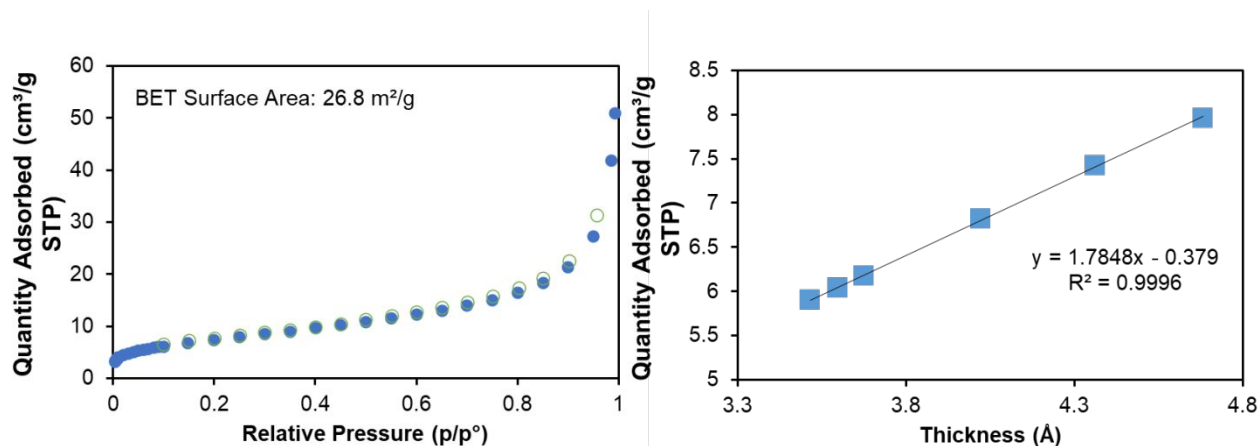


**Figure S22.** BET surface area analysis of Bi(HHTP) made using procedure 2.

## 3. Elemental Analysis of Bi(HHTP)

Before elemental analysis, Bi(HHTP) was activated in ethyl acetate for 2 days, dried and stored in a vacuum desiccator at room temperature for > 3 weeks. C and H analysis was performed by Atlantic Microlab Inc. using combustion method by automatic analyzers. The Bi(HHTP) sample for elemental analysis was prepared using **Procedure 1**. The metal bismuth was analyzed by ICP-MS at Dartmouth's elemental analysis facility. The sample for this was prepared by dissolving 1.0 mg of Bi(HHTP) in 10 mL of 10% $H_2O_2$ solution. The solution was then diluted again by 10% in deionized $H_2O$ and sent for analysis. The results are listed below.   The percent mass of carbon, hydrogen and bismuth observed experimentally within the coordination network (38.3%, 1.51%

and 33.1%, respectively) were comparable to theoretical calculations (39.0%, 1.62% and 37.7 %, respectively) based on the empirical formula of Bi(HHTP)-β ($C_{36}H_{12}O_{12}$)$Bi_2$-2($H_2O$).

| Element | Theory [Bi(HHTP)] | Found |
|---|---|---|
| Carbon | 39.0% | 38.3% |
| Hydrogen | 1.62 % | 1.73% |
| Bismuth | 37.7% | 33.1% |

**Table E.2.** Elemental analysis performed using both ICP-MS and Combustion techniques of Bi(HHTP).

The found carbon and hydrogen content of the Bi(HHTP) matched very well with the theoretical values for Bi(HHTP)-β. The observed bismuth content was slightly lower than theoretical values, which could also result from the presence of a small amount of residual metal salt impurities.

4. Thermogravimetric Analysis (TGA)

Thermal gravimetric analysis was performed using a TA Instruments TGA 55 with a 20°C/min ramp from 25°C to 900°C under $N_2$. TGA profile of Bi(HHTP) revealed a total of ~34% weight loss with the highest rate of decomposition occurring at 466°C (**Figure E.14**). There was an initial loss of ~8% from 100–200°C, potentially due to the loss of volatile solvent molecules such as acetone or $H_2O$. Bi(HHTP) also appeared to display slightly higher thermal stability than its precursors (HHTP and Bi(OAc)$_3$).
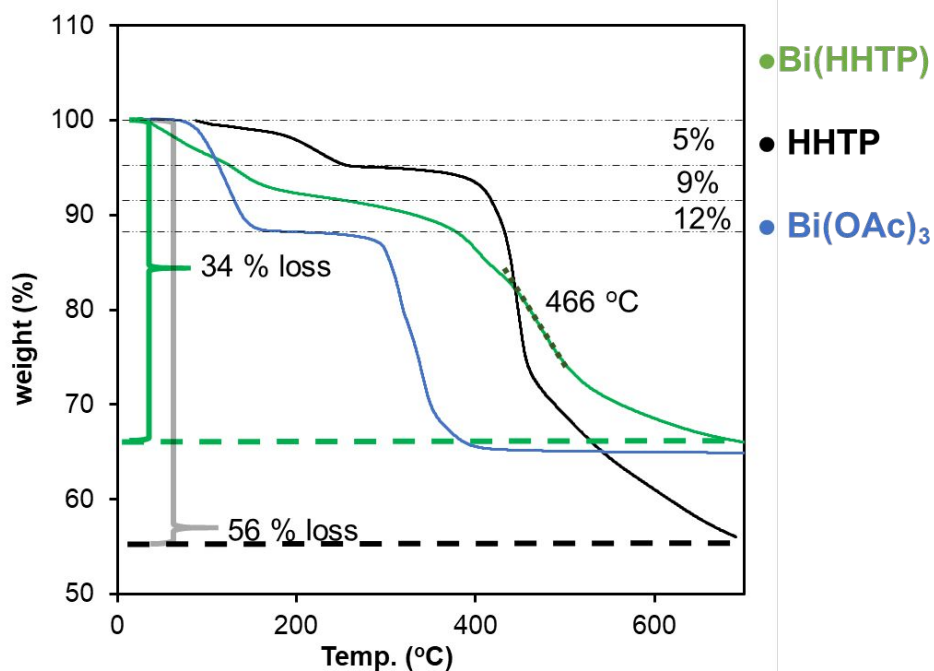
**Figure E.23.** Thermogravimetric analysis of HHTP, Bi(OAc)$_3$, and Bi(HHTP) coordination network prepared using **Procedure 2**. Thermal gravimetric analysis was performed using a TA Instruments TGA Q150 with a 20°C/min ramp from room temperature to 800°C under a nitrogen atmosphere.

5. Conductivity measurements on pressed pellets

      A pellet press (Desktop Pellet Press, Across International) was used to compress 0.100 g of Bi(HHTP) powder into a 6 mm pellet of 0.41 mm thickness. The measure of bulk conductivity of the pellet taken using a four-point probe with 1.25 mm space between the probes. We calculated the bulk conductivity in Siemens per centimeter using **Equation E.2**, where I(A) is current, V is the voltage, s(cm) is distance of between the probes (1.25 mm), F (unitless) is the

correction factor accounting for the diameter and thickness of the pellet. The bulk conductivity of the pellet was measured at 5.3 × 10$^{-3}$ S•cm$^{-1}$.

$$\sigma = \frac{I}{V}\frac{1}{2\pi sF}$$
          **E.2**

6. Investigation of Arrhenius Activation Energy using Temperature dependent I-V curves.

To investigate the Arrhenius activation energy for electrical conductivity of Bi(HHTP), a 2-point probe on a 100 mg pressed pellet (thickness was measured to be 0.54 mm) was employed to collect the current change under different temperature (293 K to 383 K) with a linear sweep voltage from -2.0 V to 2.0 V. The Arrhenius equation can be used to calculate the Arrhenius activation energy:
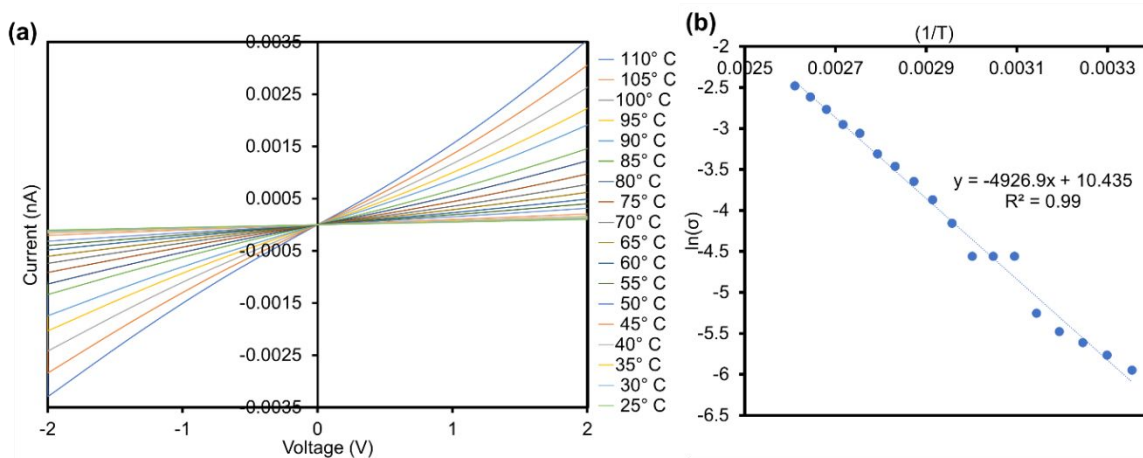


**Figure E.24. (a)** I-V curves collected from 25°C to 110°C display Ohmic response between +2 and −2 V. **(b)** plot of natural log of current I (ln(I)) to reciprocal temperature (1/T, in K$^{-1}$)

$$\sigma = \sigma_o \, e^{\frac{E_a}{k_B T}} \qquad \textbf{E.3}$$

In **Equation E.3**, σ is the conductivity, $\sigma_0$ is the pre-exponential factor and  is  constant, Ea is  the Arrhenius  activation  energy, $k_B$ is  the Boltzmann constant, and T is the temperature in Kelvin. Because the current (I) measured is proportional to the conductivity σ under the same temperature, the above equation can be further written as,

$$I = Ae^{-\frac{E_a}{k_B T}} \qquad \textbf{E.4}$$

which equals

$$\ln(I) = \ln(A) - \frac{1}{T}\frac{Ea}{k_B} \qquad \textbf{E.5}$$

where A is a constant. The plot of natural log of current I (ln(I)) to reciprocal temperature (1/T, in K$^{-1}$) generates the value $-Ea/kB$. The activation energy determined by this method was 425 meV.

## 7. X-Ray Photoelectron Spectroscopy (XPS)

X-ray photoelectron spectroscopy (XPS) experiments were conducted on a Kratos Analytical AXIS Supra X-ray Photoelectron Spectrometer under ultrahigh vacuum (base pressure $10^{-7}$ Torr). The measurement chamber was equipped with a monochromatic Al (Kα) X-ray source. Bi(HHTP) was stored under $N_2$ until needed. The material was pressed onto copper tape which was mounted on a Dual-Height (Kratos) sample holder. A survey spectrum was obtained from 0 eV–1400 eV to obtain elemental surface composition and high-resolution spectra were obtained at energy regions specific to elements observed in the survey spectrum (C 1s, Bi 4f, O 1s) under a pressure of ~$10^{-7}$ Torr.
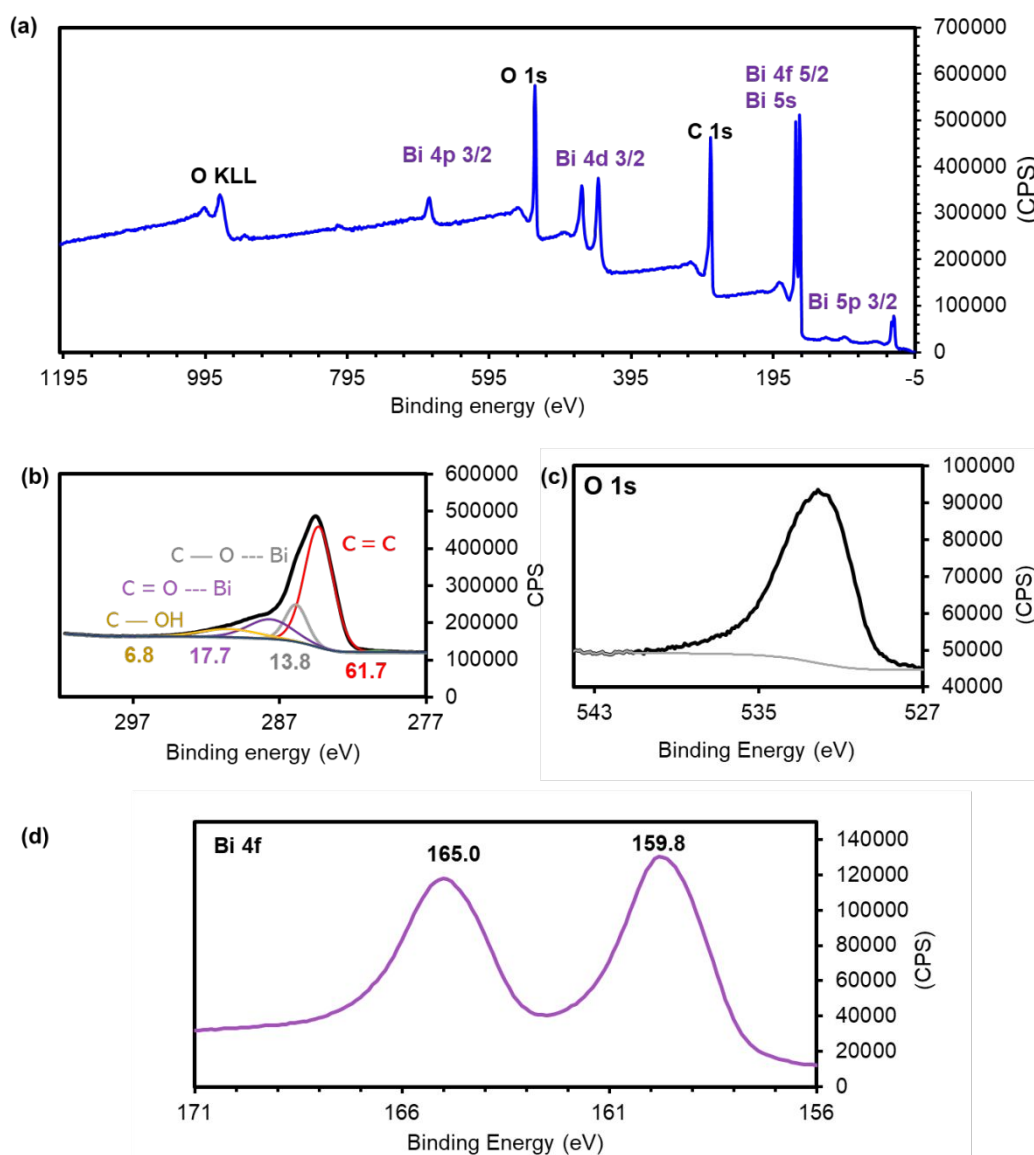


**Figure E.25.** XPS survey spectrum of Bi(HHTP) indicating the presence of C, Bi, and O, elements.

XPS spectra revealed the presence of C, O, and Bi in the wide scan spectrum (**Figure E.25**). High resolution scans of the C1s peak revealed the presence of multiple peaks centered around 284.9 eV, which were attributed to $sp^2$ aromatic C=C bonds, C-O--Bi, C=O--Bi, and C—OH bonds, respectively.[9] Bi in low valence oxidation states with peaks at binding energies of 159.8 eV and 165.0 eV, assigned to $Bi^{3+}$ $4f_{7/2}$ and Bi $4f_{5/2}$ levels. We were unable to deconvolute the region of the O1s peak present at 532 eV to assign the C-O and C=O bonds, due to the likely presence if $H_2O$ both within the pores of the network and within the coordination sphere of Bi(HHTP)-β creating uncertainty of the correct electronic state of the ligand. Based on the deconvoluted C 1s peaks (**Figure E.25b**) data and considering the presence of Bi(III), one possible oxidation state of the ligand to result in an overall neutral coordination network is a bis-semiquinone catechol state (sq, sq, cat) to generate Bi(III) within the network (**Figure E.26a**). The C 1s spectra is consistent with this oxidation state, as the deconvoluted peaks in this area present C-O, C=O, and C-OH bonds in 2:2.6:1 ratio.

Another possibility that renders a neutral framework is that all bismuth are in a ratio of $Bi^{3+}/Bi^{2+}$ oxidation states is HHTP generating an alternating (sq, sq, sq) and (sq, sq, cat) state (**Figure E.26b**). This would generate a -2.5-overall charge on the ligand. This structure would also create a radical ion on HHTP, which is plausibly what we are observing in Electron Paramagnetic Resonance (EPR) spectroscopy (**Figure E.45**). Both structures are simply proposed possibilities based on XPS data and bond length analysis using previously reported bismuth-catecholates (**Table E.3**). It is important to also note that errors in present in bond length measurements, due to normal deviations in electron density during diffraction analysis, can introduce a standard deviation of around 0.003 Å.
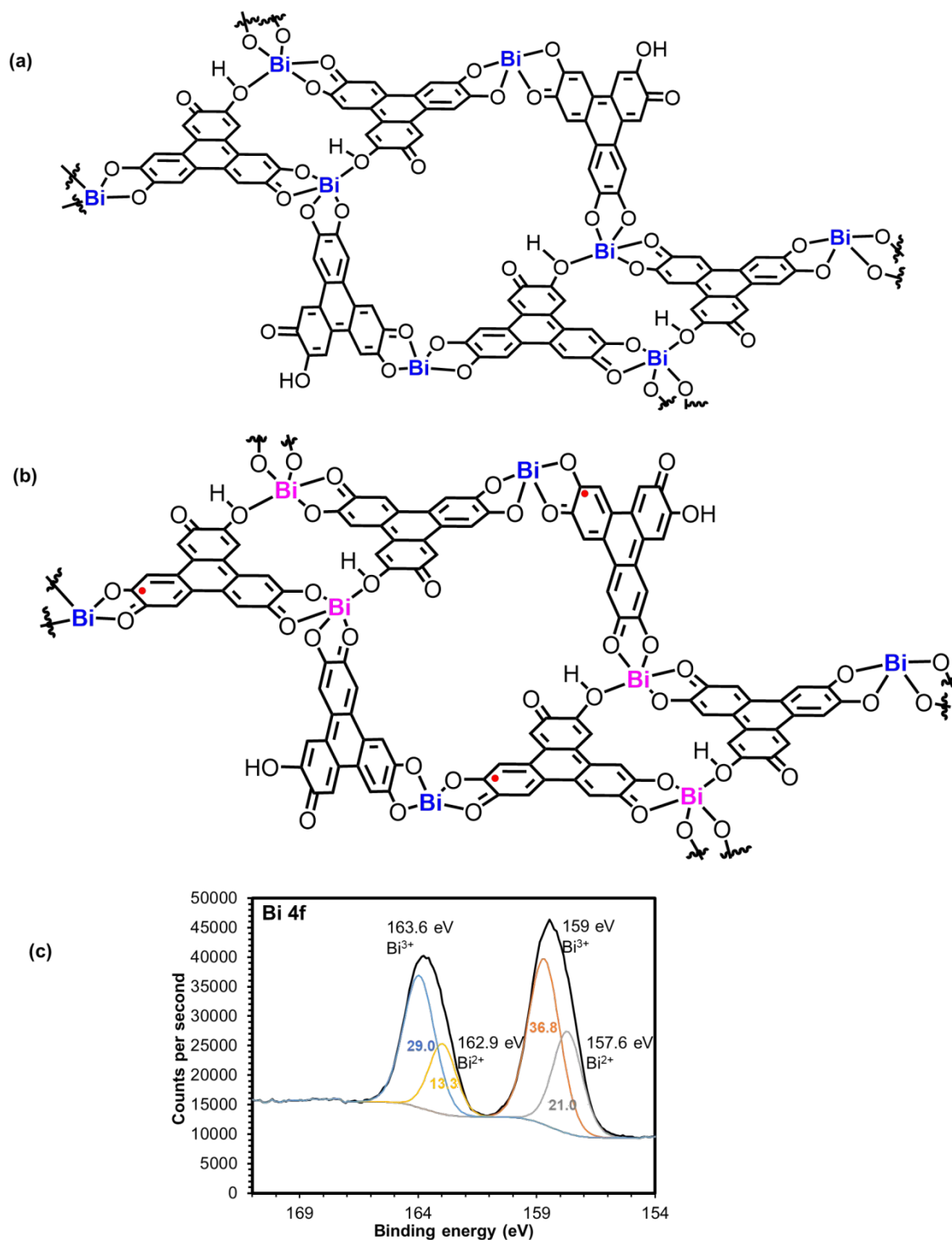
**Figure E.26. (a)** Oxidation state assignment of Bi(HHTP)-α displaying oxidation states of HHTP ligand as bis-semiquinone catechol oxidation state to generate Bi(III). **(b)** Oxidation state assignment of Bi(HHTP)-α displaying oxidation states of HHTP ligand as alternating bis-semiquinone catechol and tris-semiquinone state of HHTP to generate Bi(III)/Bi(II) state ratio. **(c)** XPS analysis of deconvoluted Bi 4f region indicating the possible presence of Bi$^{2+}$.

Comparison to Bismuth Catecholate Complex:
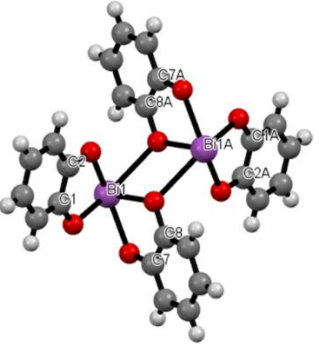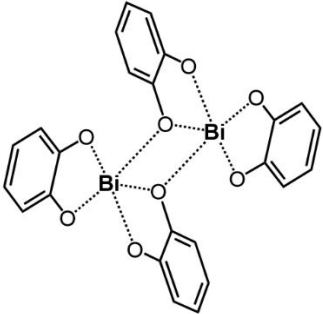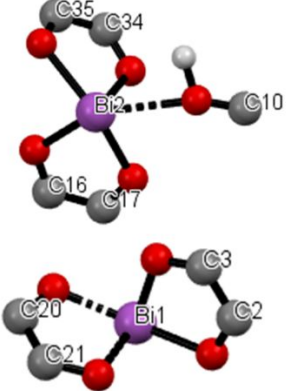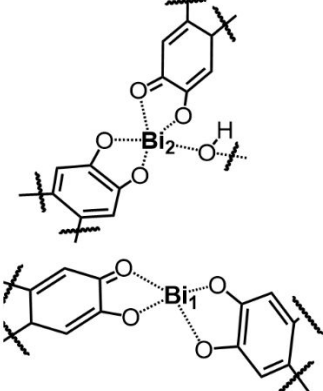
| [Bi$_2$(C$_6$H$_4$O$_2$)$_4$$^{2-}$] | Structure | Bond Length C-O | Ref. |
|---|---|---|---|
|  |  | Bond Length (Å)<br>C1-O   1.354<br>C2-O   1.348<br>C1A-O  1.354<br>C2A-O  1.348<br>C7-O   1.346<br>C8-O   1.366<br>C7A-O  1.346<br>C8A-O  1.366 | (5) |
| **Bi(HHTP)-α** | **Structure** | **Bond Length C-O** | **Ref.** |
|  |  | Bond Length (Å)<br>C10-O  1.226<br>C16-O  1.201<br>C17-O  1.205<br>C34-O  1.239<br>C35-O  1.181<br><br>C2-O   1.224<br>C3-O   1.269<br>C20-O  1.176<br>C21-O  1.275 | This work |

**Table S3**. Previously reported bismuth-catecholate molecular structure[10] comparing C-O bond lengths to aid in the oxidation state assignment.

**Figure E.27.** Bi with CN=4 displaying shift in position and coordination environment in the presence of water.

8. Optical absorbance Band Gap Calculation

The optical absorbance spectrum was measured by drop casting a 5-minute sonicated solution of Bi(HHTP) (10 mg in 2 mL) onto quartz cuvette to generate a transparent thin film. The spectrum was taken on a Jasco v570 at room temperature. Bi(HHTP) showed a measurable absorbance at 690 nm. The optical band gap was determined by plotting the absorbance squared vs energy(eV) and estimated to be 1.61 eV based on the value of absorption edge.

**Figure E.28. (a)** UV–vis–NIR spectrum of Bi(HHTP) at room temperature. **(b)** The plot of absorbance squared vs. energy in eV and calculated optical bandgap of 1.18 eV.

### 9. Computational Study of Electronic Properties

Computation of electronic properties of Bi(HHTP), including band structure, density of states, was calculated using BIOVIA Materials Studio with functional generalized gradient approximations (GGAs), which are formulas that use both the density and its gradient at each point. PBE[11] is a version of GGA that is recommended for studies of molecules interacting with metal surfaces and fairly reliable for bulk calculations. The SCF tolerance is set at fine level at $5.0 \times 10^{-7}$ eV/atom. The Brillouin zones were sampled using a 2 × 2 × 4 k-point mesh in the Monkhorst-Pack scheme.



**Figure E.29.** (a) Calculated electronic band structure (b) and partial and total density of states (right) for Bi(HHTP)-α. (c) Calculated electronic band structure (d) and partial and total density of states (right) for Bi(HHTP)-β.

Electronic band structure showed that Dirac bands near Fermi level in both Y-A and E−C directions, suggesting the intrinsically conductive nature of Bi(HHTP)-α. The high symmetry points in the first Brillouin zone showed that the Dirac bands approached the Fermi level through the Y-A and E-C (crystallographic c) directions where a low band gap of approximately 0.1 eV was observed for Bi(HHTP)-α. The electronic band structure for Bi(HHTP)-β showed Dirac bands near the Fermi level in the Z-G and B-D directions with a low band gap of 0.078 eV. The partial density

of states analysis showed that, compared with bismuth, the p orbitals from C and O atom contribute significantly to the Dirac bands.

10. Electron Diffraction Data Collection and Processing
**Sample Preparation for Electron Diffraction**

Samples were prepared using either Quantifoil or pure Carbon TEM grids. To prepare grids, a TEM grid was placed in a vial containing dry powder and gently shaken. The grid was then removed and placed in a single-tilt holder at room temperature. Grids were loaded in a Gatan 626 single-tilt cryo holder and then cooled with liquid nitrogen. After selection of a crystal on the grid, the crystal was centered, the eucentric height was adjusted by tilting the crystal through the desired rotation range, and the selected area aperture and beam stop were inserted.[12]

Electron diffraction data was collected using Thermo-Fischer CetaD detector. Images were collected in a movie format as crystals were continuously rotated in the electron beam. Typical data collection was performed using a constant tilt rate of 0.3°/s between the minimum and maximum tilt ranges of -72° to +72°, respectively. During continuous rotation, the camera integrated frames continuously at a rate of 3 seconds per frame. The dose rate was calibrated to <0.03 e-/Å$^2$ s. Crystals selected for data collection were isolated by a selected area aperture to reduce the background noise contributions and calibrated to eucentric height to stay in the aperture over the entire tilt range. All diffraction data were processed using the XDS suite of programs. All structures were solved ab initio using direct methods in SHELXT and refined with SHELXL using ShelXle. Thermal parameters refined anisotropically for all non-hydrogen atoms.



**Figure E.30.** Images of Bi(HHTP)-α and Bi(HHTP)-β taken through Coot software. The density

in the voids of Bi(HHTP)-β are postulated to be water molecules visualized in Coot for Windows (bernhardcl.github.io) software.

Checkcif report alerts encountered during refinement:

1.  THETM01_ALERT_3_A The value of sine(theta_max)/wavelength is less than 0.550 Calculated sin(theta_max)/wavelength = 0.4990

Response: The TEM sample stage has a limited range of rotation. The flat nature of the crystals yielded poor signal-to-noise ratio making data collection difficult at very high angles. Furthermore, disordered solvent within the void space contributed also contributed to lower crystal quality. The data collection was appropriate to the sample and conditions given instrument limitations. The derived crystal structure unambiguously establishes the chemical arrangement between Bi center and organic linker.

2.  PLAT355_ALERT_3_A Long O-H (X0.82,N0.98A) $O_3$ - $H_{1A}$ . 1.16 Ang.

Potential from the electron diffraction data suggests an -OH group where H1A is participating in hydrogen bonding with an O of another linker.

3.  PLAT430_ALERT_2_A Short Inter D...A Contact $O_4$ ..$O_5$ . 2.41 Ang.

There is likely additional hydrogen bonding occurring between these atoms due to the presence of highly disordered solvent in the void spaces of the crystal.

4.  PLAT430_ALERT_2_A Short Inter D...A Contact $O_8$ ..$O_{12}$ . 2.50 Ang.

There is likely additional hydrogen bonding occurring between these atoms due to the presence of highly disordered solvent in the void spaces of the crystal.

5.  PLAT082_ALERT_2_B High R1 Value ................................. 0.20 Report

Currently, crystallographic refinement of structures solved through electron diffraction yield significantly higher R1 values than that of X-rays. This is likely a result of a combination of factors including crystal quality, detector sensitivity, and scattering factor accuracy. Additionally, due to instrument limitations, data sets from multiple crystals must be merge which typically introduces disorder and diminishes the quality of the final structure. For this particular case, highly disordered solvent present within the void space of the crystal is likely contributing to the higher-than-average R1 value typically seen for most solved through electron diffraction. Better refinement techniques for electron diffraction data will likely arise in the future which will drastically decrease these values for similar quality structures.

6.  PLAT084_ALERT_3_B High wR2 Value (i.e. > 0.25) ................... 0.42 Report

See PLAT082_ALERT_2_B.

7.      PLAT149_ALERT_3_B s.u. on the   beta   Angle is Too Large .......      0.20 Degree

The error of the beta angle increases as a result of the slight difference between the merged datasets of multiple crystals. This is current limitation of electron diffraction as full set of reflections is difficult to obtain within a single movie.

8.      PLAT410_ALERT_2_B Short Intra H...H Contact  $H_1$     .. $H_8$     .      1.83 Ang.

Highly disordered solvent in the void space along with added disorder from merging of datasets from multiple crystals decreases the precision of bond lengths and angles. Given the current limitations in electron diffraction data processing and refinement the distance between atoms is reasonable.

9.      PLAT410_ALERT_2_B Short Intra H...H Contact  $H_4$     .. $H_{17}$     .      1.80 Ang.

Highly disordered solvent in the void space along with added disorder from merging of datasets from multiple crystals decreases the precision of bond lengths and angles. Given the current limitations in electron diffraction data processing and refinement the distance between atoms is reasonable.

10.     PLAT410_ALERT_2_B Short Intra H...H Contact  $H_{11}$     .. $H_{14}$     .      1.88 Ang.

Highly disordered solvent in the void space along with added disorder from merging of datasets from multiple crystals decreases the precision of bond lengths and angles. Given the current limitations in electron diffraction data processing and refinement the distance between atoms is reasonable.

11.     PLAT410_ALERT_2_B Short Intra H...H Contact  $H_{19}$     .. $H_{26}$     .      1.84 Ang.

Highly disordered solvent in the void space along with added disorder from merging of datasets from multiple crystals decreases the precision of bond lengths and angles. Given the current limitations in electron diffraction data processing and refinement the distance between atoms is reasonable.

12.     PLAT410_ALERT_2_B Short Intra H...H Contact  $H_{22}$     .. $H_{35}$     .      1.88 Ang.

Highly disordered solvent in the void space along with added disorder from merging of datasets from multiple crystals decreases the precision of bond lengths and angles. Given the current limitations in electron diffraction data processing and refinement the distance between atoms is reasonable.

13.     PLAT410_ALERT_2_B Short Intra H...H Contact $H_{29}$     .. $H_{32}$     .      1.86 Ang.

Highly disordered solvent in the void space along with added disorder from merging of datasets from multiple crystals decreases the precision of bond lengths and angles. Given the current limitations in electron diffraction data processing and refinement the distance between atoms is reasonable.

14.     PLAT415_ALERT_2_B Short Inter D-H..H-X      $H_{1A}$     ..$H_{17}$    .     1.97 Ang.

Highly disordered solvent in the void space along with added disorder from merging of datasets from multiple crystals decreases the precision of bond lengths and angles. Given the current limitations in electron diffraction data processing and refinement the distance between atoms is reasonable.

15.     PLAT430_ALERT_2_B Short Inter D...A Contact  $O_4$     ..$O_6$    .     2.79 Ang.

Highly disordered solvent in the void space along with added disorder from merging of datasets from multiple crystals decreases the precision of bond lengths and angles. Given the current limitations in electron diffraction data processing and refinement the distance between atoms is reasonable.

16.     PLAT601_ALERT_2_B Unit Cell Contains Solvent Accessible VOIDS of 133 Ang**3

Structure contains large voids with highly disordered solvent.  Using the SQUEEZE technique did not substantially improve the quality of the data and produced additional alerts.

## 11. Pawley Refinement

Pawley refinement was performed using BOVIVA Materials studio on the electron diffraction data. This method is useful to process the diffraction data to achieve valuable information on lattice parameters, the presence of background noise and subtractions, and reflection intensities.[13] The sample, pattern and lattice parameters were either refined or not to optimize crystallite size, lattice strain and unit cell sizes (see below). The results of this calculation presented a Rwp of 7.07% and an Rp of 12.54% (**Figure E.32**).

**Lattice Parameters**

Lattice Type:                                              Monoclinic

| Parameter | Value | Refined? |
|---|---|---|
| a | 16.74296 ± 0.00588 | Yes |
| b | 7.85657 ± 0.00113 | Yes |
| c | 21.24533 ± 0.00131 | Yes |
| α | 90.00000 | No |
| β | 95.62920 ± 0.02048 | Yes |
| γ | 90.00000 | No |

**Space Group: P 1 21/C 1**

**Sample Parameters**

**Lattice Strain**

| Parameter | Value | Refined? |
|---|---|---|
| A | 0.24090 ± 0.10219 | Yes |
| B | 0.01111 ± 0.24936 | Yes |
| C | 0.00411 ± 0.25824 | Yes |

**Pattern Parameters**

Profile Function:                                          Pseudo-Voigt

**FWHM**

| Parameter | Value | Refined? |
|---|---|---|
| U | 0.08472 ± 0.37069 | Yes |
| V | 0.22556 ± 0.11063 | Yes |
| W | 0.10995 ± 0.00663 | Yes |

**Profile**

| Parameter | Value | Refined? |
|---|---|---|
| NA | 0.50000 | No |
| NB | 0.00000 | No |

**Line Shift**

Instrument Geometry:                                       Bragg-Brentano

| Parameter | Value | Refined? |
|---|---|---|
| Zero Point | 0.00000 | No |
| Shift #1 | 0.00000 | No |
| Shift #2 | 0.00000 | No |



Powder Refinement: Rwp = 7.07%   Rwp(w/o bck) = 6.95%   Rp = 12.54%

**Figure E.32. (Top)** Parameters used for Pawley Refinement in Materials Studio © **(bottom)** Pawley refinement of the powder X-ray diffraction pattern of activated Bi(HHTP) demonstrating the experimental pattern (red dots), the simulated pattern from a computational model (blue line), the difference (black line), and the background positions (yellow). The inset in this graph demonstrates the optimized structure after refinement.

**Section E4. Gas Sensing**

1. Fabrication of sensing devices

To generate chemiresistive devices, 1.5 mg of Bi(HHTP) powder was sonicated in 1 mL of deionized water for one hour until the suspension was a homogenous dark green color. The suspension was dropcasted on 10 μm gap electrodes purchased from Metrohm (part NO. G-IDEAU10). The devices were left to dry in the dark in ambient atmosphere for approximately 16 – 18 hours before use. Typical devices resistances (using Bi(HHTP) generated from **Procedure 2**) ranged from 1.50 ∓ 1.0 kΩs (measurement on a total of 20 devices).



**Figure E.33.  (a)** Five devices made using 1.5 mg of Bi(HHTP) sonicated for one hour and subsequently dropcast 10 μL on the surface of 10 μm gap electrodes **(b)** Same devices within an edge connector connected to a breadboard.

2.  Sensing Experiments

The devices were placed into an edge connector where a voltage of 1.0 V was applied using a potentiostat (PalmSens) (**Figure E.34**). The edge connector was enclosed in a Teflon chamber which had gas-inlet and gas outlet ports connected to Sierra Micro-Trak and a Smart-Trak mass flow controller which were used to deliver controlled concentrations of gases (NO, $H_2S$ and $NH_3$) from pre-mixed gas tanks (purchased from AirGas tanks of 10,000 ppm of $NH_3$ in $N_2$, and 10,000 ppm of $H_2S$ or NO in $N_2$). The devices were generally equilibrated under $N_2$ for 1 hour before sensing experiments began.  The concentrations of the gaseous analytes were modified by adjusting flow rates ($N_2$ as the balance/purging gas). For sequential exposure experiments, 3-4 devices at a time were exposed to one or five minutes of a specified concentration (5 – 40 ppm or 0.25 - 2 mL/min) of the chosen analyte at a $N_2$ flow rate of 0.5 L/min and then purged with dry $N_2$ for 5 minutes to examine Bi(HHTP) recovery. For saturation exposure experiments, 3-4 devices were exposed to 15-20 minutes of the specific analyte (5 – 40 ppm or 0.25 - 2 mL/min) at a $N_2$ flow rate of 0.5 L/min, and then allowed to recover for at least 30 minutes. The sensing experiments were stopped after the traces reached 50 minutes.

**Figure E.34.** Schematic representation of sensing experiment setup.

**Data Processing:** Raw data was normalized in Microsoft Excel using **Equation E.6**. Here, Io is initial current, I = current at a specific time to generate normalized change in conductance (-$\Delta G/G_o$)

$$\frac{I_o - I}{I_o} \times 100 = \frac{\Delta G}{G_o} \qquad \textbf{E.6}$$

This value was plotted against time in minutes.



**Figure E.35.** Chemiresistive sensing responses sequential exposure toward **(a)** 80 ppm of NH$_3$ **(b)** 40 ppm of NO.

3.  Studies of Reproducibility Sensing NH$_3$ and NO



**Figure E.36.** Chemiresistive sensing responses of two batch of Bi((HTP) made using 10-Micron gap electrodes to **(a)** (5 - 80 ppm) of NO **(b)** (5 - 80 ppm) 40 ppm of NH$_3$.

4.  Initial Rates of Response

The initial rates of response toward gaseous analytes depend on several properties, both intrinsic to the material and related to the sensing apparatus such as electrode contacts and sensing chamber. In terms of Bi(HHTP), parameters such as thickness of film on device, orientation of crystallites, morphology, size of crystallites, and initial resistances likely play a role in the initial rates of response during the first minute of analyte exposure. Extrinsic characteristics of the sensing apparatus such as volume of sensing enclosure, rates of analyte delivery, fundamental nature of host-guest interactions, contact with gold electrode and their spacing also play a vital role.[14]  Thus, the kinetics of host-guest interactions depend on both the sensing material and the intrinsic characteristics of the sensing apparatus, which were kept constant.

The responses to the given analyte of each concentration during the first minute of exposure are shown below. After the first minute of exposure in which the response changes rabidly and there is generally a higher rate of response ($-\Delta G/G_o$/min), the rate generally decreases as the sensor approaches saturation and the initial active sites become occupied.



**Figure E.37. (a)** Chemiresistive responses of Bi(HHTP) to 40, 20, 10, and 5, ppm of $NH_3$ after 1 min exposure and the linear fitting of the response. **(b)** The slope of the fitting as a function of concentration. Error bars represent standard deviations from the mean after averaging values from 3 devices.



**Figure E.38. (a)** Chemiresistive responses of Bi(HHTP) to 40, 20, 10, and 5 ppm of NO after 1 min exposure and the linear fitting of the response. **(b)** The slope of the fitting as a function of concentration. Error bars represent standard deviations from the mean after averaging values from 3 devices.

5. I-V Curves Plots with Exposure to Ethanol

Data for current/voltage plots for Bi(HHTP) collected using EmSTAT potentiostats and PStrace software©. Bi(HHTP) was drop cast onto a 10 micron gap electrode device and left overnight to dry in ambient atm. The device was then connected to an EmSTAT potentiostat and equilibrated for approximately one hour. Linear sweep voltammetry (LSV) was collected by sweeping the voltage from -1.0 to 1.0 V at a scan rate of 0.1V/second. **Figure E.39b** displays the change in current during exposure of scans 3-5 (8 scans total) to 1000 ppm of ethanol at 35°C. **Figure E.39c** displays the I-V curve of Bi(HHTP) after full saturation with EtOH vapor (after approximately 5 minutes of exposure).



**Figure E.39. (a**) I-V plot for Bi(HHTP) demonstrating Ohmic nature of contacts when sweeping voltage from -1.0V to 1.0V **(b)** Cyclic voltammetry of 8 scans of Bi(HHTP) from -1.0V to 1.0V while exposing scans 3-5 to 1000 ppm of EtOH **(c)** LSV scan after saturation with EtOH vapor (5 minute exposure).

The I-V curves of Bi(HHTP) display ohmic contacts based on the linear relationship of current and voltage. The exposure of 1000 ppm of ethanol vapor also demonstrates ohmic contacts after saturation, indicating no Schottky barrier modulation during the sensing of VOCs.

6. Sensing in the Presence of Humidity

The generation of 5000 ppm humidified $N_2$ stream was followed by the procedure previously reported by our group.[15] By varying the flow rate parameter, we were able to maximize the deliverable ppm (lower flow rate = higher concentration). Typically, the gas generator permeation tube was heated to 80 °C using the embedded oven with temperature control and loaded with a vial of deionized water. Total span gas flow through the oven was set to 350 mL/min to deliver 5000 ppm of $H_2O$ vapor. The gas/vapor stream was mixed with the mass flow system

using a Y-connection, where one connection was to the vapor generator and the other to the mass flow controllers used for gas delivery. The dilution vapor (5000 ppm water) was mixed with the controlled stream from the mass flow controllers (2 mL/min) to deliver a humidified stream of a single gaseous analyte at 40 ppm.



**Figure E.40.** Comparison of response of Bi(HHTP) devices to (a) 40 ppm of $NH_3$ without presence of $H_2O$ and (b) 40 ppm of $NH_3$ in the presence of 5000 ppm of $H_2O$. Devices were used at an applied voltage of 1.0 V.



**Figure E.41.** Comparison of response of Bi(HHTP) devices to (a) 40 ppm of NO without presence of $H_2O$ and (b) 40 ppm of NO in the presence of 5000 ppm of $H_2O$. Devices were used at an applied voltage of 1.0 V.

**Figure E.42.** Comparison of response of Bi(HHTP) devices using bar chart to 40 ppm of NO and NH$_3$ without presence of H$_2$O and in the presence of 5000 ppm of H$_2$O. Devices were used at an applied voltage of 1.0 V.



**Figure E.43.** Response of Bi(HHTP) devices to (a) 5000 ppm of H$_2$O and (b) 1000 ppm of H$_2$O. Devices were used at an applied voltage of 1.0 V and exposed for approximately 20 minutes.

Bi(HHTP) displays a concentration dependent "turn-on" response to H$_2$O. At higher concentrations of humidity (5000 ppm), Bi(HHTP) demonstrates a decrease in normalized change in conductance while at lower concentrations (1000 ppm), Bi(HHTP) demonstrates a an increase in normalized change in conductance. This sensing mechanism has been reported before with other HHTP-based MOFs,[16] and may be indictive of multiple active sites and mechanisms of sensing at play.

**Figure E.44.** Response of Bi(HHTP) devices under an applied voltage of 1.0 V to (a) 40 ppm NO and NH$_3$ (b) Response of Bi(HHTP) devices under an applied voltage of 0.1 V to 40 ppm NO and NH$_3$ (c) Sensing responses of Bi(HHTP) to 1.0 V and 0.1 V to NO and NH$_3$.

7. Limits of Detection Calculation

The theoretical limits of detection (LOD) were calculated using the following equation First, the root mean squared (rms) value — representing the noise-based deviation in $-\Delta G/Go$ — was calculated using the baseline trace for 600 data points before exposure to analyte. We took 600

consecutive points (N = 600) and fit the data to a polynomial (5th order). We calculated $Vx^2$ from **Equation E.4**, where yi = measured $-\Delta G/G_o$ and y is the value calculated from the extracted polynomial fit. We plotted concentration of analyte versus largest measured $-\Delta G/G_o$ and isolated the range of values wherein this relationship was linear. The linear regression provided an equation of best-fit (slope = m) which we extracted from this concentration dependence analysis to be used in **Equation E.7**. With the values, we extrapolated the theoretical LOD from **Equations E.8** and **E.9**.

$$V_{X^2} = \Sigma(y - y_i)^2 \qquad \textbf{E.7}$$

$$Rms = \sqrt{\frac{V_{X^2}}{n}} \qquad \textbf{E.8}$$

$$LOD = 3 \times \frac{rms}{m} \qquad \textbf{E.9}$$

Comparison of material-based sensors:

| Class of Sensor | Material | Gaseous Analyte | Limit of Detection | Device | Voltage | Ref. |
|---|---|---|---|---|---|---|
| Coordination network | Bi(HHTP) | NH$_3$ | 0.29 ppm | Chemiresistor | 1.0 V | This Work |
| | | NO | 0.15 ppm | | | |
| | | Acetone | 41.2 ppm | | | |
| | | MeOH | 278 ppm | | | |
| | | EtOH | 185 ppm | | | |
| | | iPrOH | 50.2 ppm | | | |
| Metal–Organic Frameworks | Cu$_3$(HITP)$_2$ | NH$_3$ | 0.5 ppm | Chemiresistor | 0.1 V | [17] |
| | Cu$_3$(HHTP)$_2$ | NH$_3$ | 0.5 ppm | Chemiresistor | 5 V | [18] |
| | NDC-Y-fcu | NH$_3$ | 0.1 ppm | Chemiresistor | 1 V | [19] |
| | NiPc-Ni | NH$_3$; NO | 0.31 ppm; 0.06 ppb | Chemiresistor; Chemiresistor | 0.01 V | [20] |
| | NiPc-Cu | NH$_3$; NO | 0.33 ppm; 0.13 ppb | Chemiresistor; Chemiresistor | 0.01 V | |
| | ZnO@ZIF-8 | EtOH | 5 ppm | Chemiresistor | N/A | [21] |
| Conductive Polymers | Polypyrole (PPy) thin film | NH$_3$; Acetone; NO$_2$ | 1.5 ppm; 50 ppm; 10 ppm | Chemiresistor | 1 kHz AC Voltage; | [22] [23] [24] |

| | | | | | DC Volage; Varied | |
|---|---|---|---|---|---|---|
| | Polyaniline (PANI) thin film | $NH_3$; $NO_2$; EtOH | 1 ppm; 0.05 ppm; 32 ppm | Chemiresistor; Chemical FET; Chemiresistor | 1 V; 1 V; 0.1 V | 25 26 27 |
| | Polythiophene (PTh) | $NO_2$ | 10 ppm | Chemiresistor | 1 V | 28 |
| | Poly(3,4-ethylenedioxythiophene) (PEDOT) | $NH_3$; $NO_2$; NO; MeOH | 1 ppm; 0.2 ppm; 2.5 ppm; 1 ppm | Chemiresistor; Chemiresistor; Chemiresistor; Chemiresistor | 1 V; 1 V; 1 V; 1 V | 29 30 31 32 |
| Metal Oxides | $ZnFe_2O_4$ microspheres | EtOH | 0.5 ppm; | Chemical FET | N/A | 33 |
| | $Pt/SnO_2$ nanospheres | EtOH | 0.25 ppm | Chemical FET | N/A | 34 |
| | $SnO_2$ hierarchical Structures | Acetone; EtOH | 0.05 ppm; 5 ppm | Chemical FET Chemical FET | N/A | 35 |
| | Au/ZnO nanoparticles | Acetone | 0.05 ppm | Chemical FET | N/A | 36 |
| | $Pt/In_2O_3$ nanoparticles | Acetone | 0.01 ppm | Chemical FET | N/A | 37 |

**Table E.4.** Comparison metrics for sensing using MOFs, Conductive Polymers and Metal Oxides

8. Investigation of Sensing Mechanism of NO and $NH_3$ using ATR-IR, XPS and EPR

To investigate the sensing mechanism, attenuated total reflectance – infrared spectroscopy, (ATR-IR), XPS and electron paramagnetic resonance (EPR) spectroscopy were used. All three instruments were utilized to observe changes induced in the materials after analyte exposure and binding. First, pristine Bi(HHTP) was prepared for ATR-IR analysis by placing 20 mg of powder into a 2 mL vial and degassing with $N_2$ (1 L/min) for 2 hours. This sample was also stored under $N_2$. Analyte-exposed materials were prepared by purging the pristine Bi(HHTP) with NO or $NH_3$ (1% of 10000 ppm tank) for 1 hour. The samples were then sealed under an atmosphere of 1% analyte (balanced with $N_2$) and left overnight before testing. For ATR-IR, a ZnSe crystal (part number 6584-J331A) was utilized.

We used high concentrations of the analyte to ensure saturation of each sample to observe small detectable differences using XPS, in which samples are subjected to high vacuum conditions that may promote desorption of this analyte from Bi(HHTP). The samples were then sealed under an atmosphere of either $N_2$ or 1% analyte (balanced with $N_2$) and left overnight before measurement. ATR-IR revealed that after exposure to high concentrations of NO, the shifting of the peaks assigned to the bismuth-catechol vibrational frequencies at 1256 $cm^{-1}$ and 1426 $cm^{-1}$ (**Figure 7b**).[38] This result suggests that the analyte-material interaction is occurring near or at the bismuth metal center,

affecting the vibrational frequencies of the ligand near the semiquinone/catechol region. IR analysis also revealed new bands occurring near 1500 cm$^{-1}$ , which indicate the creation of some ionic nitrate ($NO_3^-$) species.[39] This nitrite species could be generated from NO reaction with surface-bound $O_2$ on the coordination network. IR analysis of $NH_3$-exposed Bi(HHTP) revealed the presence of new bands present at approximately 1564 cm$^{-1}$, 1438 cm$^{-1}$ and 1173 cm$^{-1}$ (**Figure 6.7a**), which may arise from the contribution of Lewis acid site (LAS) interaction at the bismuth center,[40] given Bi(III) complexes are known to have good affinity for nitrogen donor ligands[41] and Bi(III) borderline "hard" Lewis acidity.[7] The symmetric stretching mode of $NH_3$ gas was also observed at 950 cm$^{-1}$. There may also be an indication of hydrogen bonding or interaction using Brønsted acid sites (BAS)[40, 42] of ammonia with uncoordinated hydroxy groups suggestive of the bands arising near 1250 - 1050 cm$^{-1}$.

ATR-IR analysis of Pristine and $NH_3$-exposed Bi(HHTP)



**Figure E.45.** ATR-IR data analysis of (a) pristine and $NH_3$-doped Bi(HHTP) depicting the ranges
(a) 4000 – 500 cm$^{-1}$ (b) 2000 – 600 cm$^{-1}$ pristine and $NH_3$-doped Bi(HHTP).

ATR-IR spectroscopy on pristine and exposed samples revealed that after exposure to high concentrations of NO and $NH_3$, the shifting of bands and presence of several new bands was observed. For the ammonia exposed sample, the presence of new bands was observed, particularly at 3267 and 2959 $cm^{-1}$. There is also new bands present at approximately 1564 $cm^{-1}$, 1438 $cm^{-1}$ and 1173 $cm^{-1}$ which may arise from the contribution of Lewis acid site (LAS) interaction at the bismuth center,[40, 42] given that Bi(III) complexes are known to have good affinity for nitrogen donor ligands[41] and Bi(III) borderline "hard" Lewis acidity. The symmetric stretching mode of $NH_3$ gas was also observed at 950 $cm^{-1}$ (**Figure E.44**). There may also be an indication of hydrogen bonding or Brønsted acidity of ammonia with uncoordinated hydroxy groups suggestive of the new bands arising near 1250 - 1050 $cm^{-1}$, which may be Brønsted acid sites (BAS).[40, 42]



**Figure E.46.** FT-IR data analysis of (a) pristine and NO-doped Bi(HHTP) depicting the ranges (a) 4000 – 500 $cm^{-1}$ (b) 2000 – 600 $cm^{-1}$ pristine and NO-doped Bi(HHTP).

The presence of new bands occurring near 1426 $cm^{-1}$ indicate the creation of some ionic Nitrite ($NO^{-2}$) species. Analyte-material interaction occurring near or at the bismuth metal center

is also suggested by the shifting of the peaks assigned to the Bismuth-catechol vibrational frequencies at 1256 cm$^{-1}$ and 1426 cm$^{-1}$.[8] This suggests that the site of interaction with the analyte NO are likely occurring either at or near the Bi node.

XPS Analysis of Pristine and NO-exposed Bi(HHTP)



**Figure E.47.** Top: Survey spectrum of Bi(HHTP) exposed to NO and NH$_3$ **(a)** High resolution deconvoluted XPS spectra of carbon 1s peak of pristine Bi(HHTP) **(b)** C 1s peak of NO exposed Bi(HHTP). **(c)** NH$_3$ exposed Bi(HHTP) **(d)** Bi 4f of pristine Bi(HHTP) and after exposure to NO. High **(e)** Bi 4f region of pristine Bi(HHTP) and after exposure to NH$_3$ **(f)** deconvoluted spectrum of N 1s region after exposure of Bi(HHTP) to NH$_3$.

XPS analysis on both pristine and gas exposed materials were prepared using the same method as for IR analysis. 20 mg of Bi(HHTP) powder into a 2 mL vial and degassing with $N_2$ (1 L/min) for 2 hours. This sample was also stored under $N_2$. Analyte-exposed materials were prepared by purging the pristine Bi(HHTP) with NO (1% of 10000 ppm tank) for 1 hour. Both samples were then mounted on copper tape which was placed on a Dual-Height (Kratos) sample holder. A survey spectrum was first obtained to examine the elemental surface composition. Then high-resolution spectra were obtained (under ~$10^{-7}$ Torr pressure) at energy regions specific to the elements present in the sample (Bi, O, C).

High-resolution deconvoluted spectra of the carbon 1 region after NO dosing revealed an increase in the peak assigned to the C-O--Bi binding energy and decrease in the peak area corresponding to the C=O—Bi binding energy, which supports the hypothesis that the interaction is occurring at the Bi node is causing a shift in the chemical environment near the semiquinone region. Compared to the pristine Bi(HHTP), the deconvoluted region of Bi4$f_{7/2}$ and the Bi4$f_{5/2}$ in the NO-doped Bi(HHTP) displayed a slight shift toward higher binding energies (**Figure E.47d**). This shift may be attributed to electron density transferring from the bismuth center to the guest analyte, causing higher binding energies of more tightly bound emitted electrons. For $NH_3$ exposure, the C 1s spectrum displayed a slight increase in the area corresponding to the C=O--bismuth bond (**Figure E.47c**), and in the region corresponding to the C-O--Bi bond. The high-resolution spectrum of the Bi 4f orbitals also indicated a small shift of the Bi4$f_{7/2}$ and the Bi4$f_{5/2}$ peaks, indicating an increase in electron density near the Bi metal node (**Figure E.47e**).

EPR Analysis of Pristine and $NH_3$-dosed and NO-dosed Bi(HHTP)

EPR spectra were collected on a Bruker BioSpin Gmbh spectrometer equipped with a standard mode cavity. For each sample, about 2 mg material was used. The samples were flushed with $N_2$ overnight and then sealed in the EPR tube under $N_2$ atmosphere.



**Figure E.48.** EPR spectrum of (a) Pristine and Bi(HHTP)-NO and (b) Pristine and Bi(HHTP)-$NH_3$.

Electron paramagnetic resonance spectroscopy of the pristine Bi(HHTP) material revealed a broad absorbance band with low intensity centered at g= 2.0, which may indicate an unpaired electron residing primarily in a ligand-centered orbital or possibly oxygen located on defect sites within the material. Only a slight increase in the intensity of the resonant absorbance was observed with exposure to NO, which is consistent with our observations from sensing that the interaction of the material with NO is weak and reversible. This slight increase was also observed in a marginally higher intensity in $NH_3$-exosed Bi(HHTP) (**Figure E.48**) This result suggests that $NH_3$ induced a slight change in the coordination sphere around the EPR active centers.

MicroED analysis of $NH_3$ and NO exposed samples

To analyze the structural changes induced by analyte exposure, we utilized microED analysis on samples before and after exposure to 10,000 ppm of $NH_3$ and NO for one hour. The samples were capped, parafilmed and sent to UCLA for analysis.



**Figure E.49.** Images from microED analysis of BiHHTP-α and Bi(HHTP)-NO in Coot for Windows (bernhardcl.github.io) software.

**Figure E.50.** Images from microED analysis of BiHHTP-α and Bi(HHTP)-NH$_3$ in Coot for Windows (bernhardcl.github.io) software.

One distinct difference between unexposed Bi(HHTP)-α and the gas exposed samples is the presence of density within the void volume of the coordination network. We believe this density could be either the presence of water within the pores trapped during synthesis of the network or density resulting from the gas exposure treatment of the samples. We also hypothesize that the occupation of these pores cause deviation from unit cell parameters that we observed in Bi(HHTP)-α (**Figure E.50**)**.**

**Bi(HHTP)-NO**



| Cell Lengths | a 16.5 b 7.8 c 20.6 |
|---|---|
| Cell Angles | α 90 β 97.1 γ 90 |
| Cell Volume | 2677.7 |
| Space group | P 2$_1$/c |

**Bi(HHTP)-NH$_3$**



| Cell Lengths | a 16.7 b 7.78 c 20.8 |
|---|---|
| Cell Angles | α 90 β 97.6 γ 90 |
| Cell Volume | 2677.7 |
| Space group | P 2$_1$/c |

**Figure E.51.** View along the crystallographic (a) b- axis (b) a-axis and (c) and c-axis for Bi-(HHTP)-NO and Bi(HHTP)-NH$_3$ with cell parameters.

## pXRD analysis of NH$_3$ and NO exposed samples

To analyze the structural changes induced by analyte exposure, we utilized pXRD analysis on samples before and after exposure to 10,000 ppm of NH$_3$ and NO. To carry out this procedure, we placed approximately 10 mg of Bi(HHTP) on a zero diffraction plate and carried out pXRD analysis from 2 – 50 2Ө at a analysis rate of 5º per min. We then used a bell jar with a gas inlet port to exposure either NH$_3$ or NO for 1 hour before another analysis was taken at the same conditions. For recovery, the bell jar was used to recover the same zero diffraction plate for 2 hours.

**Figure E.52.** pXRD analysis of Bi(HHTP) before (blue trace) and after exposure to 10,000 ppm NH₃ for one hour (red trace) and recovered for 2 hours under nitrogen (yellow trace).



**Figure E.53.** pXRD analysis of Bi(HHTP) before (blue trace) and after exposure to 10,000 ppm NO for one hour (orange trace) and recovered for 2 hours under nitrogen (green trace).

After NH$_3$ exposure there was a significant shift in the peak corresponding the (32$\bar{1}$) plane. This plane is parallel to the π-π stacking layers, which indicates that ammonia exposure is resulting in the increasing of distances within these planes. This could result from ammonia occupying the available void volumes within Bi(HHTP), causing the expansion of these layers. After recovery in N$_2$ for two hours, this shift did not return to its original peak position, consistent with our observations in sensing that NH$_3$ binds irreversibly to Bi(HHTP). For NO exposure, we observed a slight shift in the (002), (200), (20$\bar{2}$) and (32$\bar{1}$) planes. This peak shift partially recovers after N$_2$ exposure for two hours (we believe partial recovery is due to exposure to extremely high concentrations of NO), which is consistent with our observation in sensing that NO binding is weak and reversible. These slight deviations in peak position could also indicate NO occupying the available volume within the pores of Bi(HHTP), causing increases in Bragg planes.

9.  Sensing of Volatile Organic Compounds: MeOH, EtOH, Acetone, iPrOH

A Kintek FlexStream gas generator was used to produce vapors of analyte (ethanol, methanol, acetone, or isopropanol) which was diluted in N$_2$ to the desired concentration (1000 ppm). Each organic vapor was calibrated before use in the generator by heating the internal permeation glass chamber/tube (90 °C) through loading a vial of the desired VOC and setting the span flow rate at 4 L/min. **Equation E.10**, seen below was used to calculate the concentration delivered of each vapor.[1] The mass loss of each vial was measured after approximately 16 hours and the equation below was used to determine the flow rates and concentrations (ppm). Here, MW = molecular weight of solvent (18.01 g/mol), m = solvent mass loss during calibration, t = calibration time (minutes), and f = flow rate of dry N$_2$ through the tube (mL/min) 90 °C.

$$\mathrm{ppm} = \frac{(m \times 10^{-9})}{t} \times \frac{22.41}{(f \times MW)} \qquad \textbf{E.10}$$
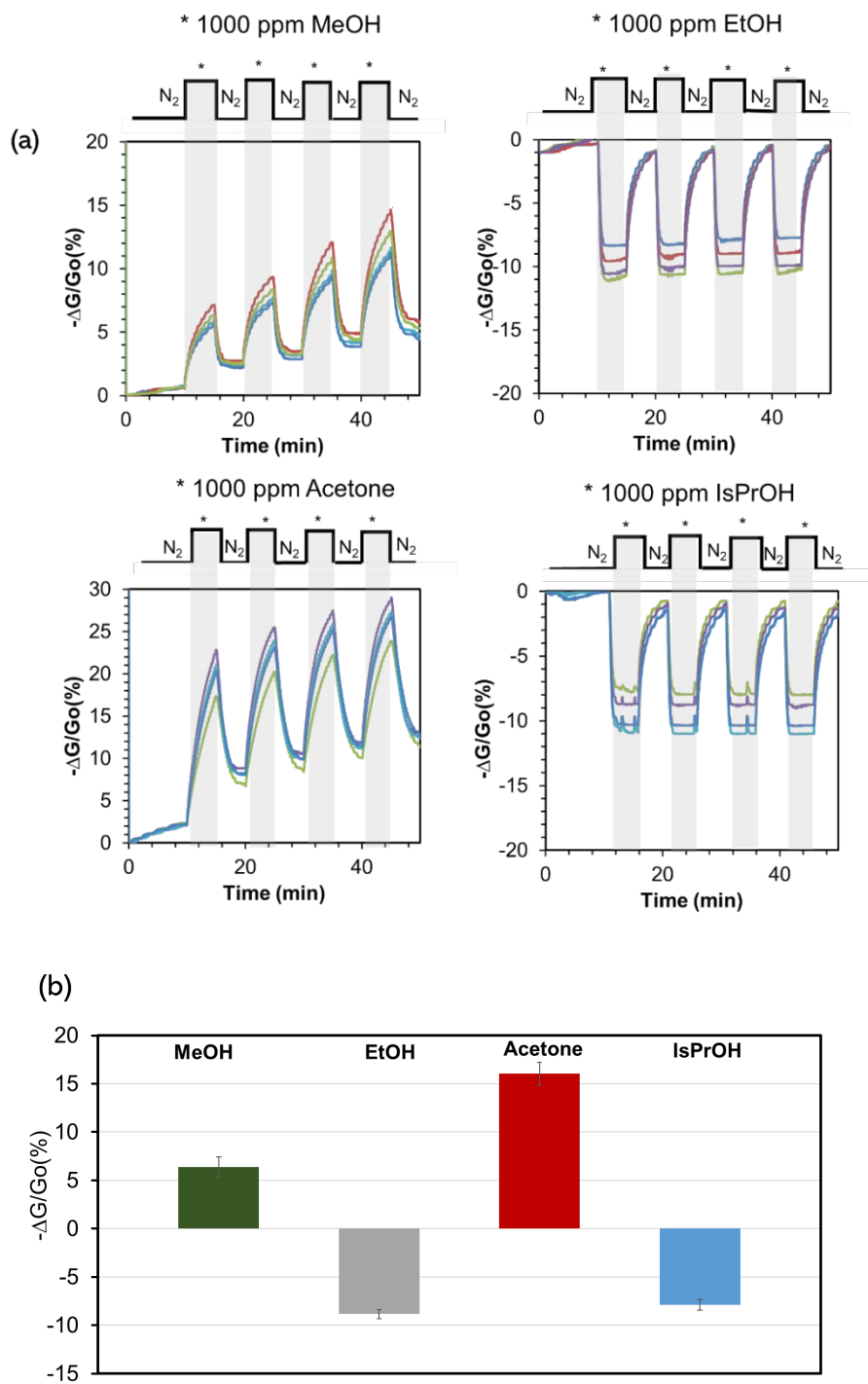
**Figure E.54.** Exposure to 1000 ppm of **(a)** MeOH, EtOH, Acetone, and iPrOH **(b)** Normalized change in conductance $-\Delta G/G_o(\%)$ for each vapor.

| Solvent | pKa (25°C) | Relative polarities | Dipole moment (25°C) | Dielectric constant ε |
|---------|-----------|---------------------|----------------------|------------------------|
| Methanol | 15.5 | 0.762 | 1.70 D | 33.0 |
| Ethanol | 16.0 | 0.654 | 1.66 D | 25.3 |
| Isopropanol | 17.1 | 0.389 | 1.66 D | 19.92 |
| Acetone | 19.3 | 0.355 | 2.87 D | 20.7 |

**Table E.5**. Reported pKa values (25 °C), relative polarities, dipole moments (25 °C) and dielectric constants of all VOCs used in sensing.

10.     Diffuse Reflectance Infrared Fourier Transform Spectroscopy – Investigation of sensing mechanism of VOCs and small reactive gases.

Infrared (IR) data was collected on a Thermo Fisher Scientific Nicolet iS50 FT-IR spectrometer equipped with a Harrick Praying Mantis DRIFTS accessory. Gas delivery for in-situ DRIFTS analysis was handled with a homemade manifold allowing delivery of vacuum, gas analytes, VOCs, and pure $N_2$ to purge samples. The Praying Mantis chamber consisted of an air-tight steel domed volume that housed a sample cup. A gas inlet and a gas outlet port were affixed to the chamber with a Schlenk flask that contained the desired VOC. Gaseous analytes ($NH_3$, NO) were delivered from premixed tanks containing 1% analyte in $N_2$. The IR beam path accessed the sample cup through KBr windows. Temperature was regulated by a thermocouple-controlled heating element.
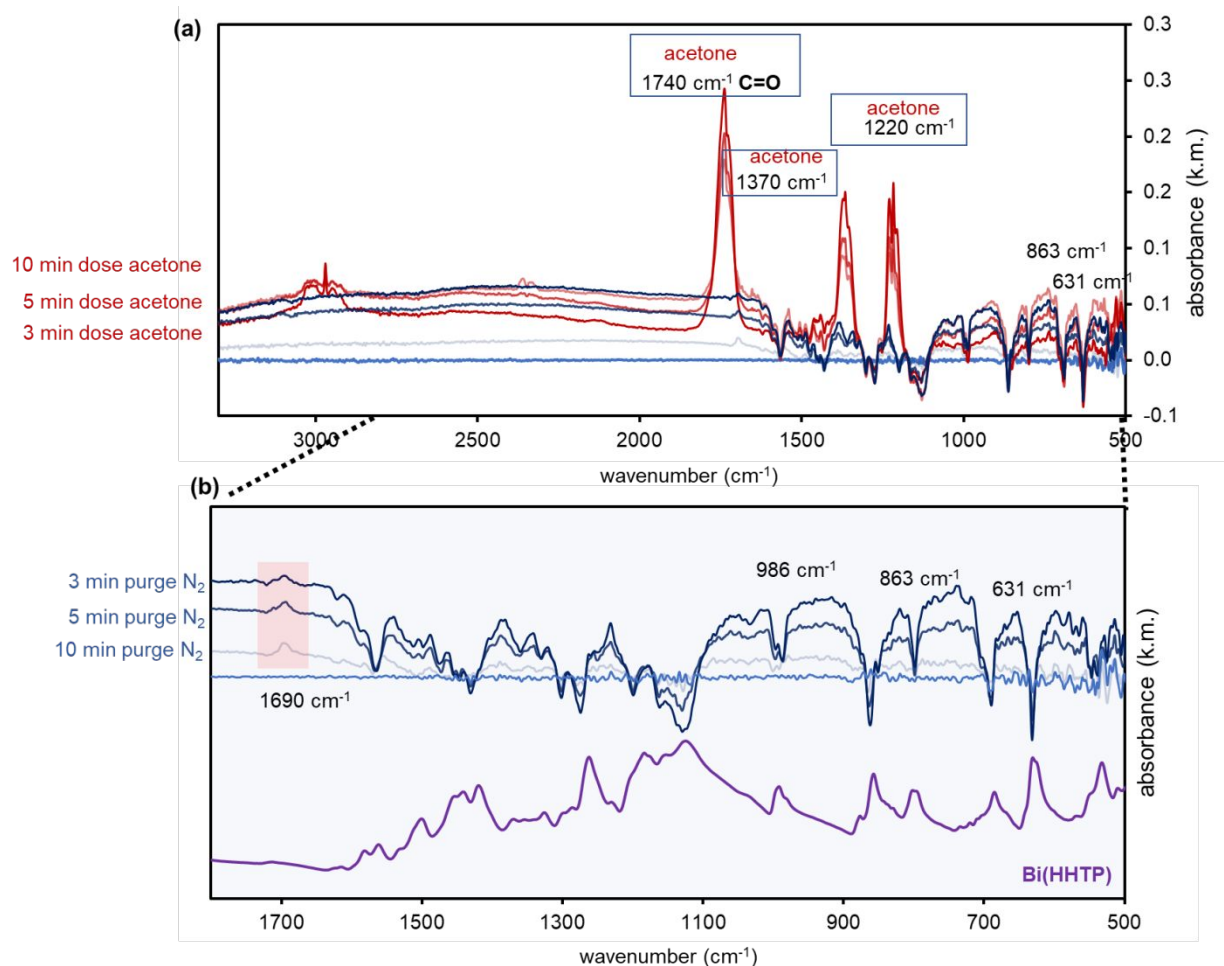
**Figure E.55. (a)** Exposure to 558000 ppm of acetone and recovery from acetone vapor. **(b)** Inset of top panel displaying the residual peak at 1690 cm$^{-1}$ after purging with vacuum.

Under an atmosphere of acetone, we observed negative-going absorbance bands that matched absorbance bands of pristine Bi(HHTP) (**Figure E.55**). After removal of acetone from the headspace, a remaining positive absorbance band was observed at 1690 cm$^{-1}$. The presence of new positive band was assigned to physiosorbed acetone species or possibly chemisorbed acetone species interacting with Lewis acid sites (LAS) at the Bi node.[40] The negative-going bands associated with pristine Bi(HHTP) diminished when acetone was removed with vacuum purging but did not fully recover over the course of 10 min.
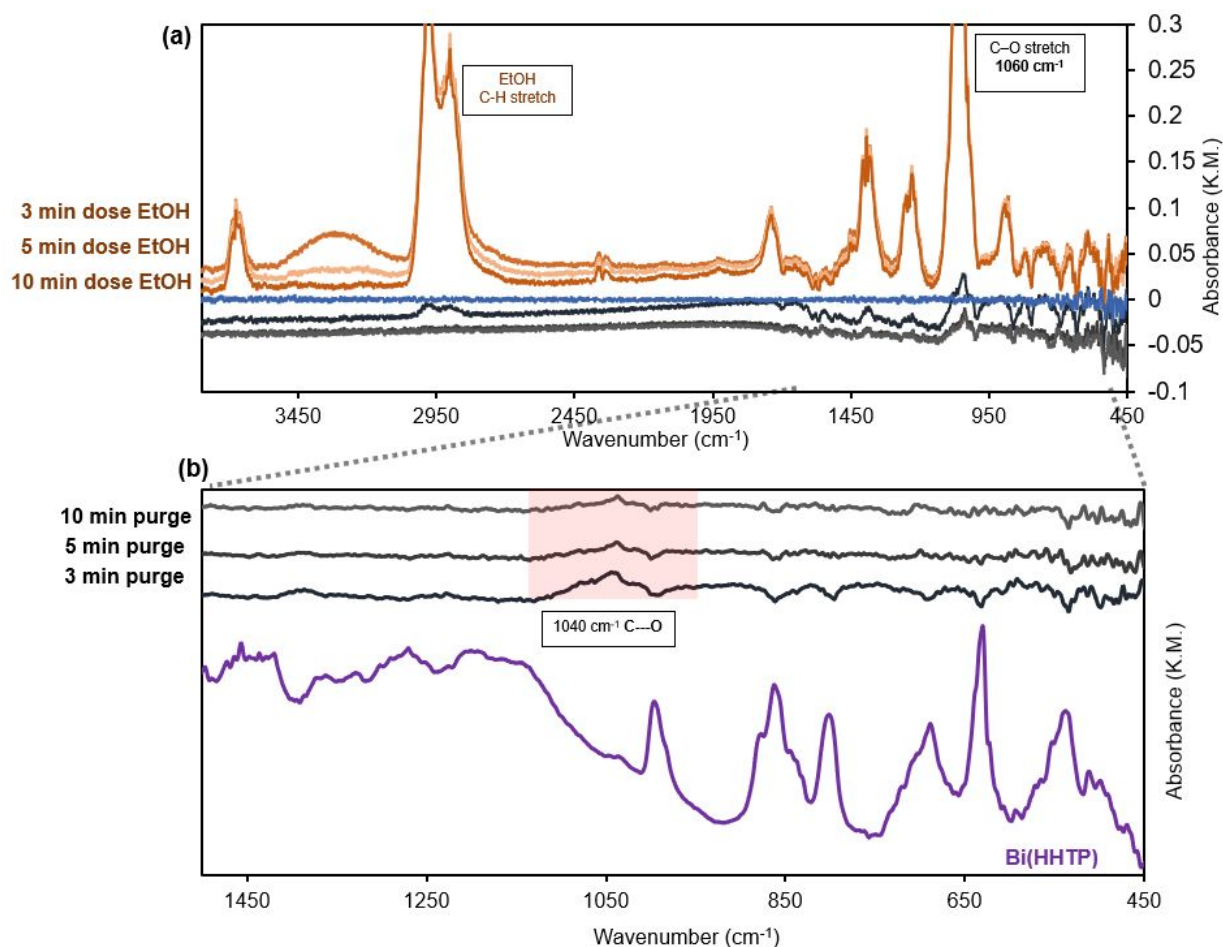
**Figure E.56. (a)** Exposure to 108000 ppm of ethanol and recovery from ethanol vapor. **(b)** Inset of top panel displaying the residual peak at 1040 cm$^{-1}$ after purging with vacuum.

Exposure of Bi(HHTP) to ethanol resulted in two primary spectroscopic features. First, we observed a set of negative-going bands that coincided with bands observed for pristine Bi(HHTP) (**Figure E.56**). Second, we observed absorbance bands assigned to gas-phase ethanol. When the sample and headspace were purged with vacuum, the gas-phase ethanol bands were removed revealing a band at 1040 cm$^{-1}$ which we assigned to the $v$(C-O) mode of ethanol interacting with LAS (**Figure E.56**).[68] The negative-going bands that coincided with absorbance bands of pristine Bi(HHTP) recovered slowly but did not fully return the initial baseline of the pristine sample.
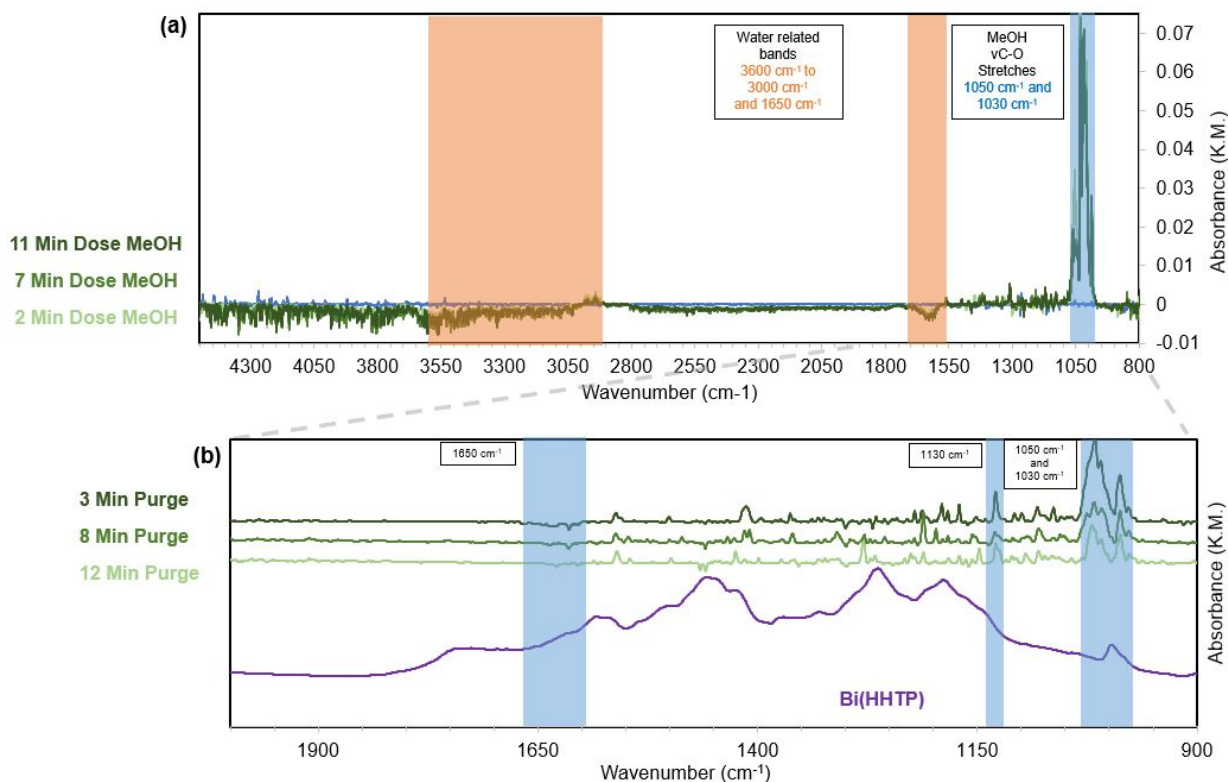
**Figure E.57. (a)** Exposure and recovery of Bi(HHTP) to 164000 ppm methanol vapor. **(b)** Inset of top panel displaying the residual peaks at 1600 cm$^{-1}$, 1460 cm$^{-1}$, 1130 cm$^{-1}$, 1050 cm$^{-1}$, and 1030 cm$^{-1}$ after purging with vacuum.

After exposure to methanol (MeOH), we observed the appearance of new positive-going absorbance bands at 1030 cm$^{-1}$ and 1050 cm$^{-1}$ as well as negative going bands in the 1650 cm$^{-1}$ and 3500 cm$^{-1}$ range (**Figure E.57**). After removal of MeOH with vacuum purging, we observed the bands at 1030 cm$^{-1}$ and 1050 cm$^{-1}$, as well as the negative-going bands at 1650 cm$^{-1}$ and 3500 cm$^{-1}$, remained after 12 minutes of vacuum purging. We also observed good background recovery of the baseline with extended vacuum purging.

Positive bands at 1030 cm$^{-1}$ and 1050 cm$^{-1}$ were observed after 12 minutes of vacuum purging. The new positive bands at 1030 cm$^{-1}$ and 1050 cm$^{-1}$ suggested possible chemisorbed methanol species interacting with Lewis acid sites (LAS) at the bismuth node.[43] The negative going bands at 1650 cm$^{-1}$ and 3500 cm$^{-1}$ were in regions associated with the $\delta$(HOH) and $v$(OH) modes of water, respectively. These negative bands suggested that exposure to MeOH disrupted these features as a result of either hydrogen bonding interactions or desorption of water from the network.
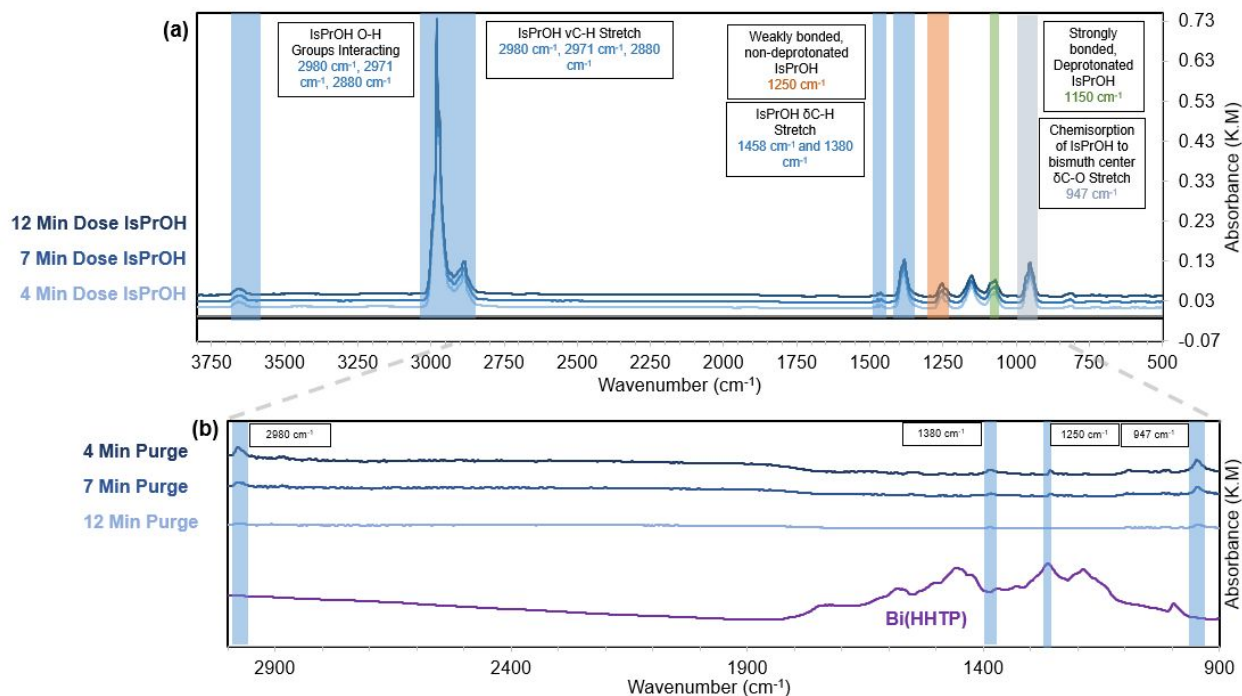
**Figure E.58 (a)** Exposure and recovery to 106,000 ppm isopropanol vapor. **(b)** Inset of top panel displaying the residual peaks at 2980, 1380, 1250, and 947 cm$^{-1}$ before disappearing after 12 minutes of purging with vacuum.

After exposure to isopropanol, we observed positive going absorbance bands at 2980 cm$^{-1}$, 1380 cm$^{-1}$, 1250 cm$^{-1}$ and 947 cm$^{-1}$. These bands decreased in intensity yet remained when the chamber was purged with vacuum for 12 min. We observed good recovery of the baseline upon exposure of Bi(HHTP) to isopropanol (iPrOH) and vacuum purging. The bands at 2980 cm$^{-1}$, 1380 cm$^{-1}$, 1250 cm$^{-1}$, and 947 cm$^{-1}$ were characterized as a $v$(C-H) mode, a non-deprotonated iPrOH interaction with the framework, a $\delta$(C-H) iPrOH interaction, and a Lewis-acid type interaction between iPrOH and the bismuth metal center, respectively. Unlike acetone and EtOH, iPrOH and MeOH did not elicit strong negative going bands corresponding to vibrational modes of pristine Bi(HHTP).
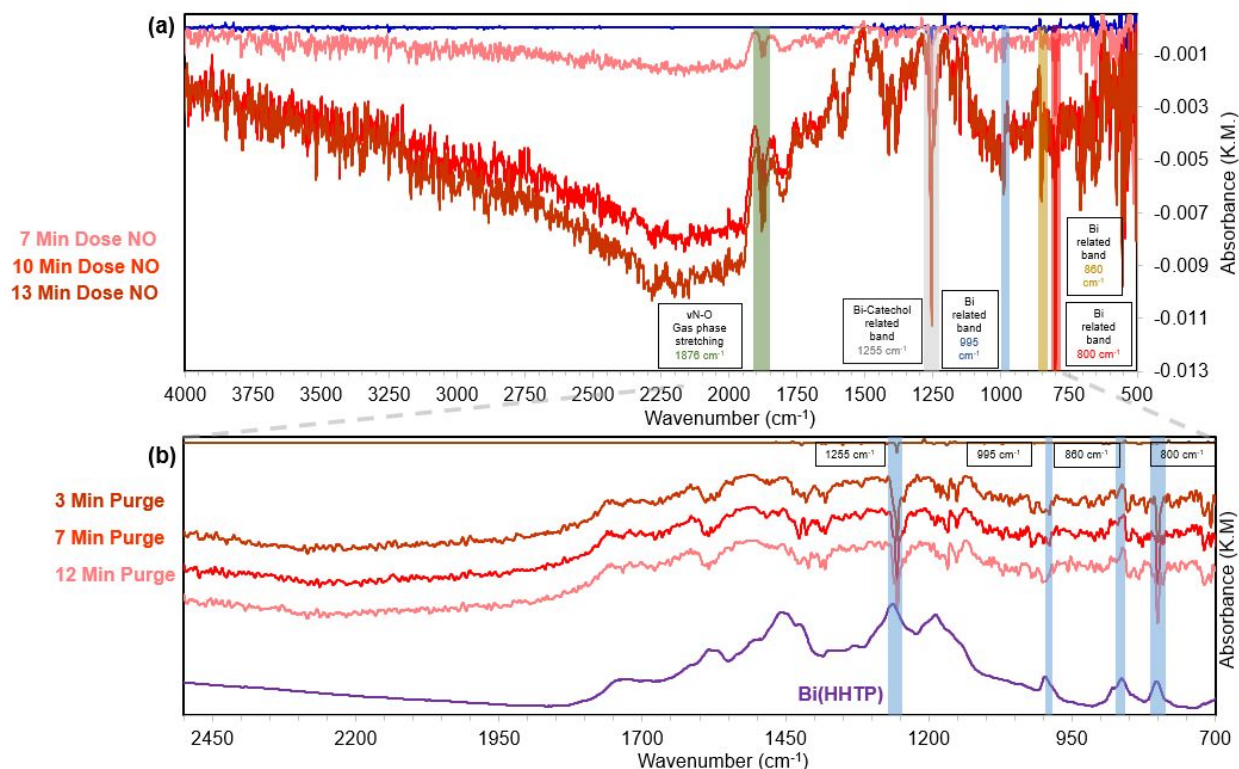
**Figure E.59 (a)** Exposure and recovery to 10,000 ppm nitric oxide gas. **(b)** Inset of top panel displaying the residual peaks at 1580, 1270, 1185, 995, 860, and 800 cm^{-1} after purging in $N_2$. Exposure to NO resulted in the appearance of sharp negative going bands at 1255 cm^{-1}, 995 cm^{-1}, 860 cm^{-1} and 800 cm^{-1}.

Upon exposure of Bi(HHTP) to NO, we observed two types of spectroscopic features. First, under and atmosphere containing 1% NO in $N_2$, the gas-phase spectral features of NO were clearly visible. Second, an immediate, strong, and broad negative band spanning from 3000 cm^{-1} to 2000 cm^{-1} was observed which continued to increase in intensity until NO was removed. We assigned this negative going broad feature to perturbations of the electronic structure of the framework resulting in changes to the electronic structure of the framework. Third, sharp negative bands at 1255 cm^{-1}, 995 cm^{-1}, 860 cm^{-1}, and 800 cm^{-1} were observed after 12 minutes of vacuum purging; they, as well as the other negative going bands, are possibly due to NO impacting the electronic structure of the Bi(HHTP) framework and bonds in an oxidative deleterious manner. One possible explanation of the 1255 cm^{-1} , 860 cm^{-1}, and 800 cm^{-1} bands were disappearance of a bismuth-catechol band and the disappearance of bismuth bonding related bands, respectively.[44]
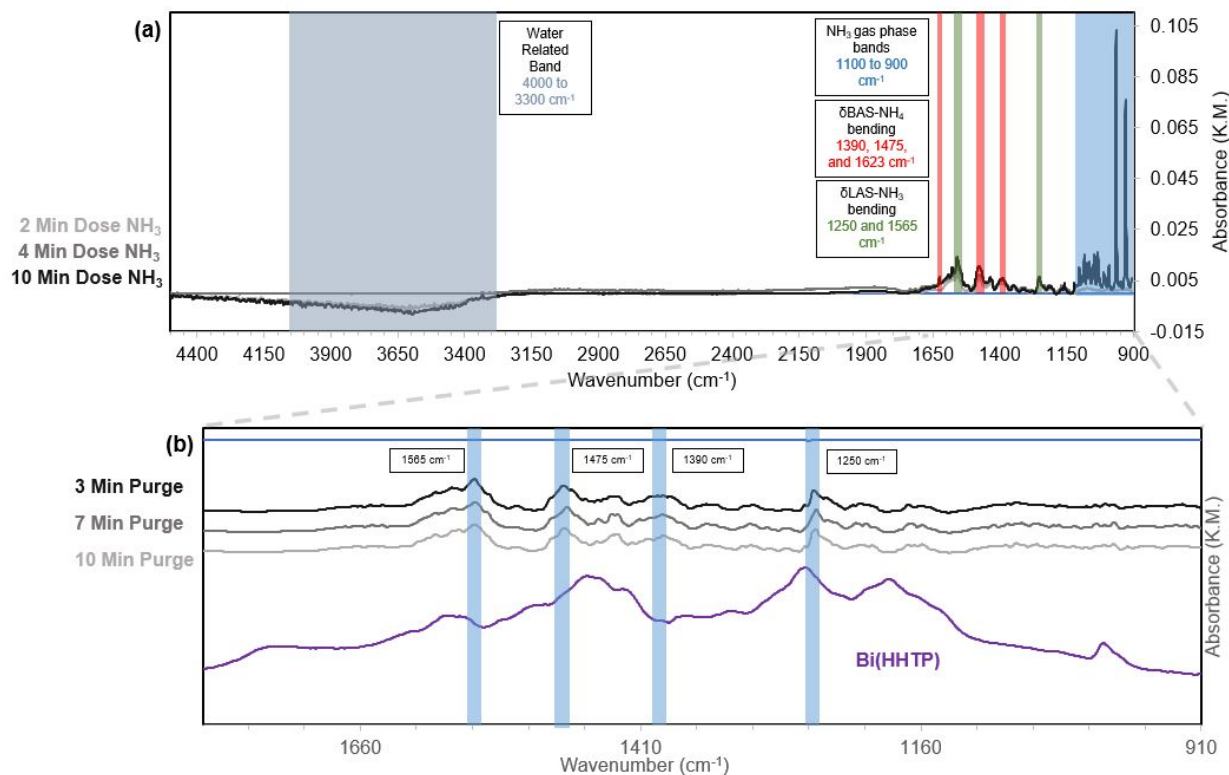
**Figure E.60. (a)** Exposure and recovery to 10,000 ppm ammonia gas. **(b)** Inset of top panel displaying the residual peaks at 1565, 1475, 1430, and 1250 cm$^{-1}$ after purging in N$_2$.

Upon exposure of Bi(HHTP) to ammonia (NH$_3$) we observed two primary spectral features. First, we observed positive-going bands near 1565 cm$^{-1}$, 1475 cm$^{-1}$, 1390 cm$^{-1}$, and 1250 cm$^{-1}$. Second, we observed negative-going bands in the 4000 cm$^{-1}$ to 3300 cm$^{-1}$ range and in the 1650 cm$^{-1}$ range. After purging with N$_2$ gas for 12 minutes, we observed that the set of positive going bands between 1565 cm$^{-1}$ and 1250 cm$^{-1}$ remained as did the negative going bands observed between 4000 cm$^{-1}$ to 3300 cm$^{-1}$ and at 1650 cm$^{-1}$. We assigned the bands at 1565 cm$^{-1}$ and 1250 cm$^{-1}$ to the $\delta_{asym}$ and $\delta_{sym}$ bands of NH$_3$+LAS, respectively. The bands at 1475 cm$^{-1}$ and 1390 cm$^{-1}$ were assigned to the $\delta_{asym}$ and $\delta_{sym}$ bands of (NH$_4^+$) which indicated NH$_3$ adsorbed to Brønsted acid sites (BAS) within the network.[43,45] The negative going bands 4000 cm$^{-1}$ to 3300 cm$^{-1}$ and at 1650 cm$^{-1}$ were assigned to the $v$(OH) mode and the $\delta$(HOH) mode of water, respectively. Their negative-going nature suggested that water was either desorbing from the framework or otherwise being altered by interactions with NH$_3$ (possibly at BAS).

References

1.      Smith, M. K.; Mirica, K. A., Self-Organized Frameworks on Textiles (SOFT): Conductive Fabrics for Simultaneous Sensing, Capture, and Filtration of Gases. *J. Am. Chem. Soc.* **2017,** *139,* 16759-16767.
2.      Thebault, F.; Ohrstrom, L.; Haukka, M., 2,3,6,7,10,11-Hexahydroxytriphenylene Tetrahydrate: a New Form of an Important Starting Material for Supramolecular Chemistry and Covalent Organic frameworks. *Acta. Crystallogr. C* **2011,** *67,* o143-5.

3.      Alexandrov, E. V.; Blatov, V. A.; Kochetkov, A. V.; Proserpio, D. M., Underlying Nets in Three-Periodic Coordination Polymers: Topology, Taxonomy and Prediction from a Computer-Aided Analysis of the Cambridge Structural Database. *CrystEngComm* **2011,** *13,* 3947-3958.

4.      Blatov, V. A.; Shevchenko, A. P.; Proserpio, D. M., Applied Topological Analysis of Crystal Structures with the Program Package ToposPro. *Crystal Growth & Design* **2014,** *14,* 3576-3586.

5.      O'Keeffe, M.; Peskov, M. A.; Ramsden, S. J.; Yaghi, O. M., The Reticular Chemistry Structure Resource (RCSR) Database of, and Symbols for, Crystal Nets. *Acc. Chem. Res.* **2008,** *41,* 1782-1789.

6.      Blatov, V. A., Search for Isotypism in Crystal Structures by Means of the Graph Theory. *Acta. Crystallogr. A* **2000,** *56 (Pt 2),* 178-88.

7.      Chapter 2 - Organobismuth(III) Compounds. In *Organobismuth Chemistry*, Suzuki, H.; Matano, Y., Eds. Elsevier Science: Amsterdam, 2001; pp 21-245.

8.      Guilhaume, N.; Postel, M., Easy Access to Bismuth Catecholates. *Heteroatom Chem.* **1990,** *1,* 233-235.

9.      Ciszewski, M.; Mianowski, A.; Szatkowski, P.; Nawrat, G.; Adamek, J., Reduced Graphene Oxide–Bismuth Oxide Composite as Electrode Material for Supercapacitors. *Ionics* **2015,** *21,* 557-563.

10.     Smith, G.; Reddy, A. N.; Byriel, K. A.; Kennard, C. H. L., The Preparation and Crystal Structure of the Bismuth(III) Catecholate Complex Adduct $(NH_4)_2[Bi_2(C_6H_4O_2)_4].(C_6H_6O_2)_2.2H_2O$. *Aust. J. Chem.* **1994,** *47,* 1413.

11.     Perdew, J. P.; Burke, K.; Ernzerhof, M., Generalized Gradient Approximation Made Simple. *Phys. Rev. Lett.* **1996,** *77,* 3865-3868.

12.     Hattne, J.; Reyes, F. E.; Nannenga, B. L.; Shi, D.; de la Cruz, M. J.; Leslie, A. G.; Gonen, T., MicroED Data Collection and Processing. *Acta. Crystallogr. A Found Adv.* **2015,** *71,* 353-60.

13.     Luo, Z.; Vasquez, Y.; Bondi, J. F.; Schaak, R. E., Pawley and Rietveld Refinements Using Electron Diffraction from $L1_2$-Type Intermetallic $Au_3Fe_1$-x Nanocrystals During Their In-Situ Order-Disorder Transition. *Ultramicroscopy* **2011,** *111,* 1295-304.

14.     Meng, Z.; Stolz, R. M.; Mirica, K. A., Two-Dimensional Chemiresistive Covalent Organic Framework with High Intrinsic Conductivity. *J. Am. Chem. Soc.* **2019,** *141,* 11929-11937.

15.     Meng, Z.; Aykanat, A.; Mirica, K. A., Welding Metallophthalocyanines into Bimetallic Molecular Meshes for Ultrasensitive, Low-Power Chemiresistive Detection of Gases. *J. Am. Chem. Soc.* **2019,** *141,* 2046-2053.

16.     Campbell, M. G.; Liu, S. F.; Swager, T. M.; Dincă, M., Chemiresistive Sensor Arrays from Conductive 2D Metal–Organic Frameworks. *J. Am. Chem. Soc.* **2015,** *137,* 13780-13783.

17.     Campbell, M. G.; Sheberla, D.; Liu, S. F.; Swager, T. M.; Dincă, M., Cu3(hexaiminotriphenylene)2: An Electrically Conductive 2D Metal–Organic Framework for Chemiresistive Sensing. *Angew.* **2015,** *54,* 4349-4352.

18.     Yao, M.-S.; Lv, X.-J.; Fu, Z.-H.; Li, W.-H.; Deng, W.-H.; Wu, G.-D.; Xu, G., Layer-by-Layer Assembled Conductive Metal-Organic Framework Nanofilms for Room-Temperature Chemiresistive Sensing. *Angew.* **2017,** *129,* 16737-16741.

19.     Assen, A. H.; Yassine, O.; Shekhah, O.; Eddaoudi, M.; Salama, K. N., MOFs for the Sensitive Detection of Ammonia: Deployment of FCU-MOF Thin Films as Effective Chemical Capacitive Sensors. *ACS Sens.* **2017,** *2,* 1294-1301.

20.     Meng, Z.; Aykanat, A.; Mirica, K. A., Welding Metallophthalocyanines into Bimetallic Molecular Meshes for Ultrasensitive, Low-Power Chemiresistive Detection of Gases. *J. Am. Chem. Soc* **2019,** *141,* 2046-2053.

21.     Ren, G.; Li, Z.; Yang, W.; Faheem, M.; Xing, J.; Zou, X.; Pan, Q.; Zhu, G.; Du, Y., ZnO@ZIF-8 Core-Shell Microspheres for Improved Ethanol Gas Sensing. *Sens. and Act.  B: Chem* **2019,** *284,* 421-427.

22.    Zhang, L.; Meng, F.; Chen, Y.; Liu, J.; Sun, Y.; Luo, T.; Li, M.; Liu, J., A Novel Ammonia Sensor Based on High Density, Small Diameter Polypyrrole Nanowire Arrays. *Sens. and Act.  B: Chem.* **2009,** *142,* 204-209.

23.    Yu, J.-B.; Byun, H.-G.; So, M.-S.; Huh, J.-S., Analysis of Diabetic Patient's Breath with Conducting Polymer Sensor Array. *Sens. and Act. B: Chem.* **2005,** *108,* 305-308.

24.    Navale, S. T.; Mane, A. T.; Chougule, M. A.; Sakhare, R. D.; Nalage, S. R.; Patil, V. B., Highly Selective and Sensitive Room Temperature $NO_2$ Gas Sensor Based on Polypyrrole Thin Films. *Synth. Met.* **2014,** *189,* 94-99.

25.    Sharma, A. L.; Kumar, K.; Deep, A., Nanostructured Polyaniline Films on Silicon for Sensitive Sensing of Ammonia. *Sens. and Act. A: Phys.* **2013,** *198,* 107-112.

26.    Srinives, S.; Sarkar, T.; Mulchandani, A., Nanothin Polyaniline Film for Highly Sensitive Chemiresistive Gas Sensing. *Electroan.* **2013,** *25,* 1439-1445.

27.    Li, Z.; Blum, F.; Bertino, M.; Kim, C.; Pillalamarri, S., One-Step Fabrication of a Polyaniline Nanofiber Vapor Sensor. *Sens. and Act. B: Chem* **2008,** *134,* 31-35.

28.    Navale, S. T.; Mane, A. T.; Khuspe, G. D.; Chougule, M. A.; Patil, V. B., Room Temperature $NO_2$ Sensing Properties of Polythiophene Films. *Synth. Met.* **2014,** *195,* 228-233.

29.    Sharma, S.; Hussain, S.; Singh, S.; Islam, S. S., MWCNT-Conducting Polymer Composite Based Ammonia Gas Sensors: A New Approach for Complete Recovery Process. *Sens. and Act. B: Chem.* **2014,** *194,* 213-219.

30.    Shaik, M.; Rao, V. K.; Sinha, A. K.; Murthy, K. S. R. C.; Jain, R., Sensitive Detection of Nitrogen Dioxide Gas at Room Temperature Using Poly(3,4-ethylenedioxythiophene) Nanotubes. *Journal of Environmental Chemical Engineering* **2015,** *3,* 1947-1952.

31.    Lin, C.-Y.; Chen, J.-G.; Hu, C.-W.; Tunney, J. J.; Ho, K.-C., Using a PEDOT:PSS Modified Electrode for Detecting Nitric Oxide Gas. *Sens. and Act.  B: Chem* **2009,** *140,* 402-406.

32.    Gavgani, J. N.; Dehsari, H. S.; Hasani, A.; Mahyari, M.; Shalamzari, E. K.; Salehi, A.; Taromi, F. A., A Room Temperature Volatile Organic Compound Sensor with Enhanced Performance, Fast Response and Recovery Based on N-Doped Graphene Quantum Dots and Poly(3,4-ethylenedioxythiophene)–Poly(styrenesulfonate) Nanocomposite. *RSC Advances* **2015,** *5,* 57559-57567.

33.    Liu, T.; Liu, J.; Liu, Q.; Rumin, L.; Zhang, H.; Jing, X.; Wang, J., Shape-Controlled Fabrication and Enhanced Gas Sensing Properties of Uniform Sphere-Like $ZnFe_2O_4$ Hierarchical Architectures. *Sens. and Act.  B: Chem* **2017,** *250,* 111-120.

34.    Kim, B.-Y.; Cho, J. S.; Yoon, J.-W.; Na, C. W.; Lee, C.-S.; Ahn, J. H.; Kang, Y. C.; Lee, J.-H., Extremely Sensitive Ethanol Sensor Using Pt-Doped $SnO_2$ Hollow Nanospheres Prepared by Kirkendall Diffusion. *Sens. and Act. B: Chem* **2016,** *234,* 353-360.

35.    Li, Y. X.; Guo, Z.; Su, Y.; Jin, X. B.; Tang, X. H.; Huang, J. R.; Huang, X. J.; Li, M. Q.; Liu, J. H., Hierarchical Morphology-Dependent Gas-Sensing Performances of Three-Dimensional $SnO_2$ Nanostructures. *ACS Sens.* **2017,** *2,* 102-110.

36.    Gu, F.; Chen, H.; Han, D.; Wang, Z., Metal–Organic Framework Derived Au@ZnO Yolk–Shell Nanostructures and Their Highly Sensitive Detection of Acetone. *RSC Advances* **2016,** *6,* 29727-29733.

37.    Karmaoui, M.; Leonardi, S. G.; Latino, M.; Tobaldi, D. M.; Donato, N.; Pullar, R. C.; Seabra, M. P.; Labrincha, J. A.; Neri, G., Pt-Decorated $In_2O_3$ Nanoparticles and Their Ability as a Highly Sensitive (<10 ppb) Acetone Sensor for Biomedical Applications. *Sens. and Act. B: Chem.* **2016,** *230,* 697-705.

38.    Guilhaume, N.; Postel, M., Easy Access to Bismuth Catecholates. *Heteroat. Chem.* **1990,** *1,* 233-235.

39.    Palleros, D. R., *Experimental Organic Chemistry*. Wiley: New York, February 2000; p p. 688.

40.     Stolz, R. M.; Mahdavi-Shakib, A.; Frederick, B. G.; Mirica, K. A., Host–Guest Interactions and Redox Activity in Layered Conductive Metal–Organic Frameworks. *Chem. Mater.* **2020,** *32,* 7639-7652.

41.     Hancock, R. D.; Cukrowski, I.; Baloyi, J.; Mashishi, J., The Affinity of Bismuth(III) for Nitrogen-Donor Ligands. *J. Chem. Soc., Dalton Trans.* **1993,**  2895-2899.

42.     Tsyganenko, A. A.; Pozdnyakov, D. V.; Filimonov, V. N., Infrared Study of Surface Species Arising from Ammonia Adsorption on Oxide Surfaces. *J. Mol. Struct.* **1975,** *29,* 299-318.

43.     Qi, Z.; Chen, L.; Zhang, S.; Su, J.; Somorjai, G. A., Mechanism of Methanol Decomposition over Single-Site $Pt_1/CeO_2$ Catalyst: A DRIFTS Study. *J. Am. Chem. Soc.* **2021,** *143,* 60-64.

44.     Hadjiivanov, K. I.; Panayotov, D. A.; Mihaylov, M. Y.; Ivanova, E. Z.; Chakarova, K. K.; Andonova, S. M.; Drenchev, N. L., Power of Infrared and Raman Spectroscopies to Characterize Metal-Organic Frameworks and Investigate Their Interaction with Guest Molecules. *Chem. Rev.* **2021,** *121,* 1286-1424.

45.     Larkin, P. J., Chapter 7 - General Outline for IR and Raman Spectral Interpretation. In *Infrared and Raman Spectroscopy (Second Edition)*, Larkin, P. J., Ed. Elsevier: 2018; pp 135-151.

*Appendix F*

*Supporting Information for Chapter 7: Enhanced Gearing Fidelity Achieved*

*Through Macrocyclization of a Solvated Molecular Spur Gear*

## Section F1. General Information

Unless otherwise notified all commercially available compounds were used as received without further purification. 9,10-diethynyl triptycene, **11a**, 9,10-diethynyl triptycene-$d_8$, **11b**, and naphthalene-2,7-ditriflyl, **S1** were prepared as reported in the literature.[1,2] Thin-layer chromatography (TLC) plates pre-coated with silica gel 60 F254 were purchased and were visualized using a UV lamp. Flash column chromatography was performed using silica gel (230−400 mesh) as the stationary phase. Anhydrous tetrahydrofuran (THF) was distilled from sodium-benzophenone in a continuous still under an atmosphere of argon. Melting points of solids were measured without calibration of the apparatus. ^{1}H NMR and ^{13}C NMR spectra in solution were recorded at 500 MHz and 126 MHz, respectively. Chemical shifts are reported in ppm and the (residual) solvent signals of CDCl$_3$ (^{1}H NMR: δ 7.26 ppm; ^{13}C NMR: δ 77.0 ppm) or CD$_2$Cl$_2$ (^{1}H NMR: δ 5.32 ppm; ^{13}C NMR: δ 53.8 ppm) were used as reference. Multiplicities of the peaks are reported as singlet (s), doublet (d), triplet (t), or multiplet (m). The coupling constants J are reported in Hz. Infrared spectra (IR) were recorded with a HATR-FTIR instrument. High-resolution mass spectra were acquired using APCI/MALDI ionization methods and the signal was detected with a TOF detector.

## Section F2. Synthesis and Characterization



**11a** → **12a**

TIPSCl
nBuLi

THF
reflux
overnight
40%
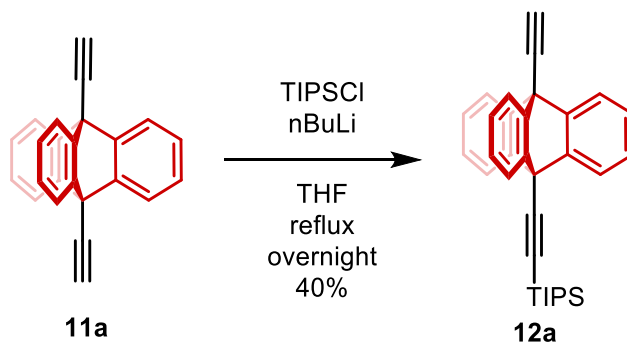
A 50 mL round bottom flask was charged with dialkyne **11a** (300 mg, 0.99 mmol) and placed under an inert argon atmosphere. 15 mL of THF were then added and the solution was cooled to -78 °C. n-butyllithium (0.6 mL, 0.99 mmol) was then added to the flask and the mixture was stirred for 30 minutes. Triisopropylsilyl chloride (0.24 mL, 1.14 mmol) was then added to the flask and the reaction mixture was first warmed to room temperature and then brought to reflux overnight. The mixture was then cooled to room temperature and quenched with saturated ammonium chloride solution. The resultant solution was extracted three times with DCM (10 mL), dried over MgSO$_4$, and concentrated to yield a white powder. Purification of the crude mixture was accomplished by flash chromatography (SiO$_2$, Hexanes) to yield 200 mg of pure monoprotected product (44% yield) as a white solid. Diprotected and unprotected products were combined, deprotected with tetrabutylammonium fluoride and purified with a hexane column to be reused in subsequent reactions.

Rf 0.37 (SiO$_2$, Hexane);

^{1}H NMR (500 MHz, CDCl$_3$) δ 7.83 – 7.79 (m, 3H), 7.79 – 7.74 (m, 3H), 7.20 – 7.07 (m, 6H), 3.31 (s, 1H), 1.43 – 1.26 (m, 21H);

$^{13}$C NMR (126 MHz, CDCl$_3$) δ 143.56, 143.20, 125.97, 125.87, 122.53, 122.23, 101.25, 94.28, 81.04, 78.27, 53.51, 52.34, 19.02, 11.59;

IR (Film) 3285.72, 2943.08, 2865.07, 2175.53, 1453.33, 1302.91, 1219.17, 1032.29, 881.61, 751.82, 745, 696.4, 674.13, 657.22, 639.94, 489.35 cm$^{-1}$;

HRMS (APCI) Calcd for C$_{33}$H$_{34}$Si (M+1) 458.24298, found 459.24859.
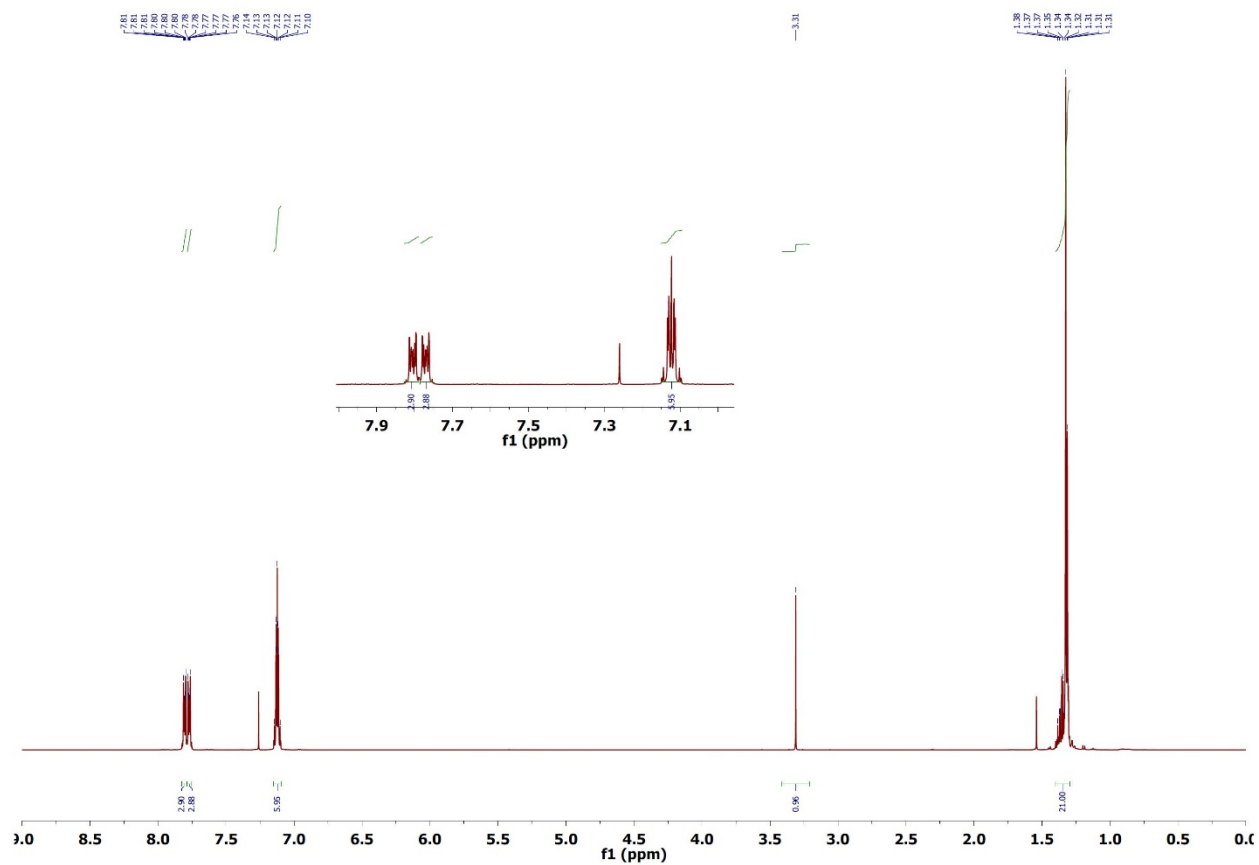


**Figure F.1.** $^1$H NMR spectrum of compound **12a** at 500 MHz in CDCl$_3$.
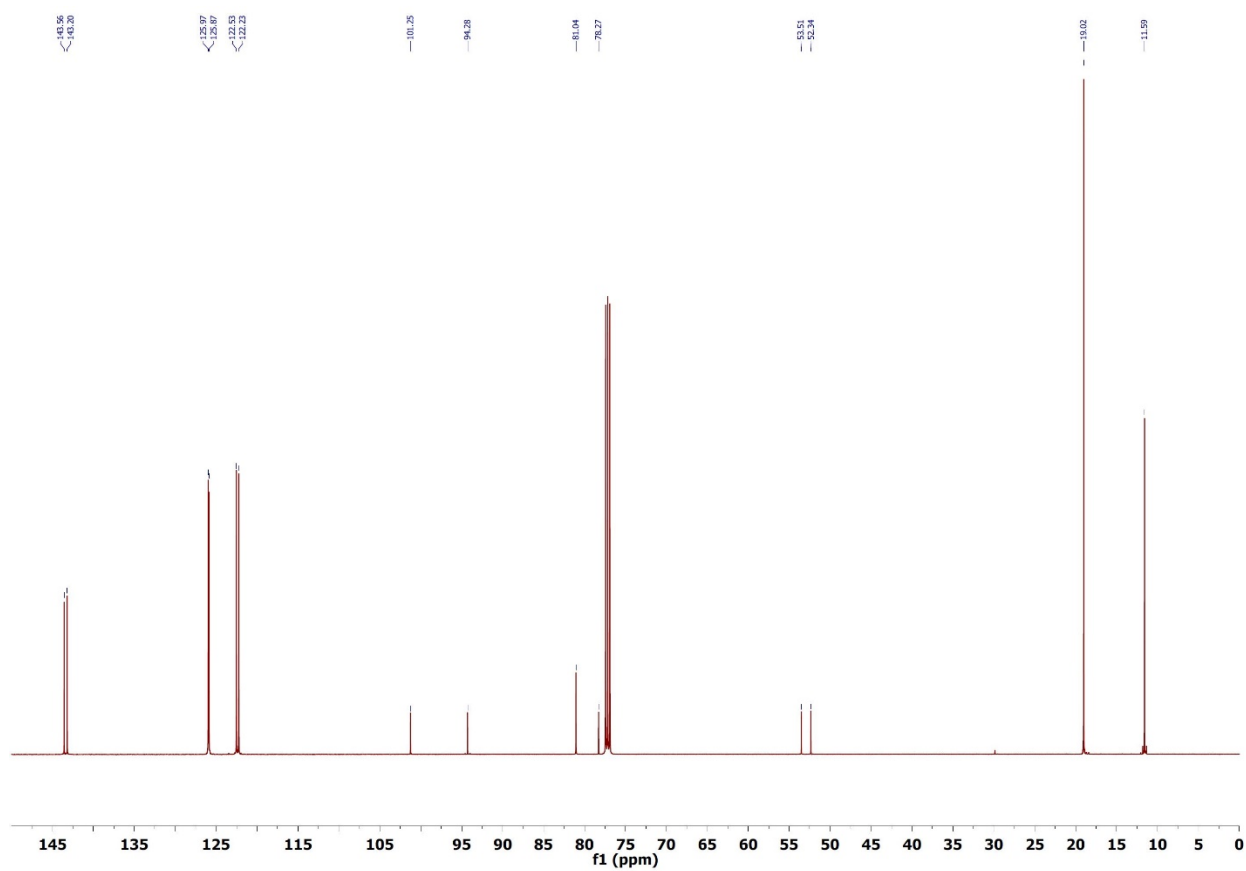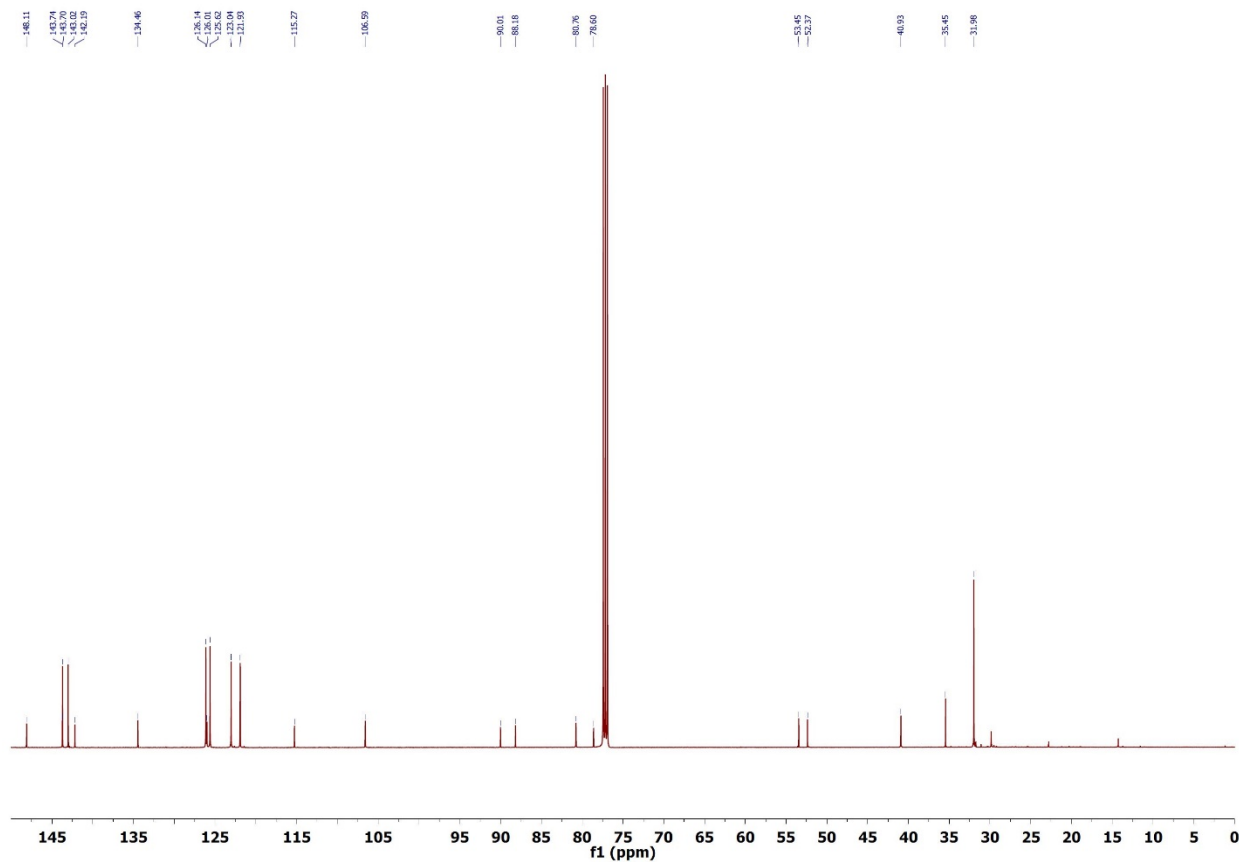
**Figure F.2.** $^{13}$C NMR spectrum of compound **12a** at 126 MHz in CDCl$_3$.
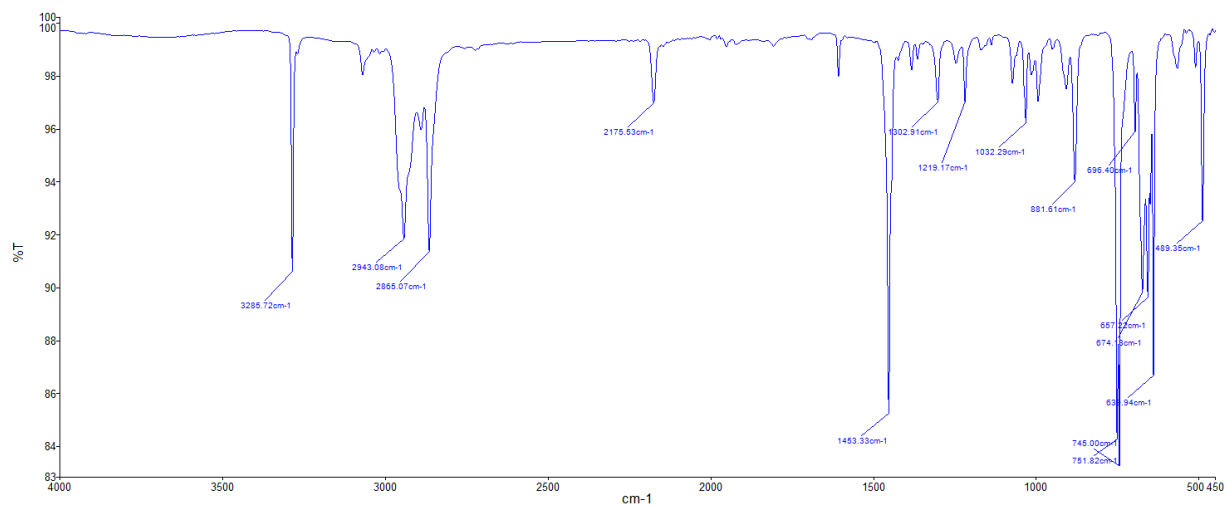


**Figure F.3.** FTIR Spectrum of compound **12a** taken as a powder.
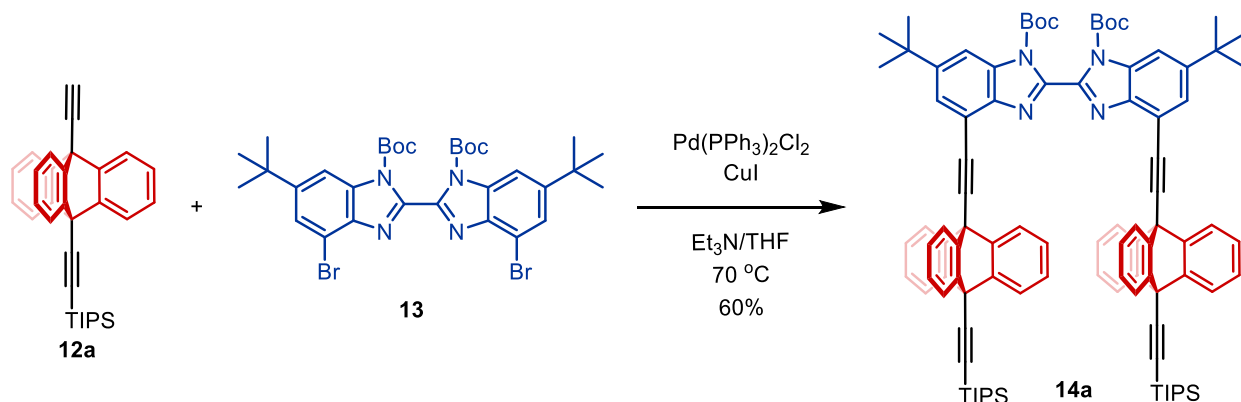
To an argon-flushed solid mixture of **12a** (400 mg, 0.872 mmol), **13** (292.5 mg, 0.415 mmol), CuI (15.8 mg, 83 $\mu$mol), and Pd(PPh$_3$)$_2$Cl$_2$ (29.2 mg, 41.5 $\mu$mol) were added. The flask was then charged with degassed, dry THF (10 mL) and degassed triethylamine (10 mL). The reaction mixture was stirred and heated to 70 °C. After 18 h, the solvents were removed from the reaction mixture and the remaining solid was subjected to column chromatography (alumina, hexane/CH$_2$Cl$_2$ = 9.5:0.5 - 9:1), giving **14a** as a white solid (360 mg, 60%).

Rf 0.6 (alumina, 2:8 CH$_2$Cl$_2$:Hexane);

$^1$H NMR (500 MHz, CDCl$_3$) δ 8.27 (d, $J$ = 1.8 Hz, 2H), 8.06 – 8.00 (m, 6H), 7.95 (d, $J$ = 1.8 Hz, 2H), 7.77 – 7.72 (m, 6H), 7.06 – 7.00 (m, 12H), 1.54 (s, 18H), 1.45 (s, 18H), 1.36 – 1.27 (m, 42H);

$^{13}$C NMR (126 MHz, CDCl$_3$) δ 149.77, 148.02, 144.60, 143.76, 143.54, 142.21, 133.13, 126.72, 125.89, 125.68, 122.97, 122.25, 114.98, 112.71, 101.61, 93.89, 89.67, 88.19, 85.80, 53.54, 53.37, 35.61, 31.95, 27.95, 19.01, 11.59;

IR (Film) 2952.09, 2864.88, 1750.49, 1606.98, 1454.51, 1403.52, 1357.15, 1305.99, 1293.24, 1250.44, 1234.33, 1129.21, 1048.77, 1031.73, 907.89, 878.92, 843.52, 752.16, 731.88, 697.08, 677.22, 667.15, 639.77, 582.03, 488.75 cm$^{-1}$;

HRMS (MALDI) Calcd for C$_{98}$H$_{106}$N$_4$O$_4$Si$_2$ with loss of 2 x Boc + Na$^+$ (1281.6602) Found: 1281.6366.
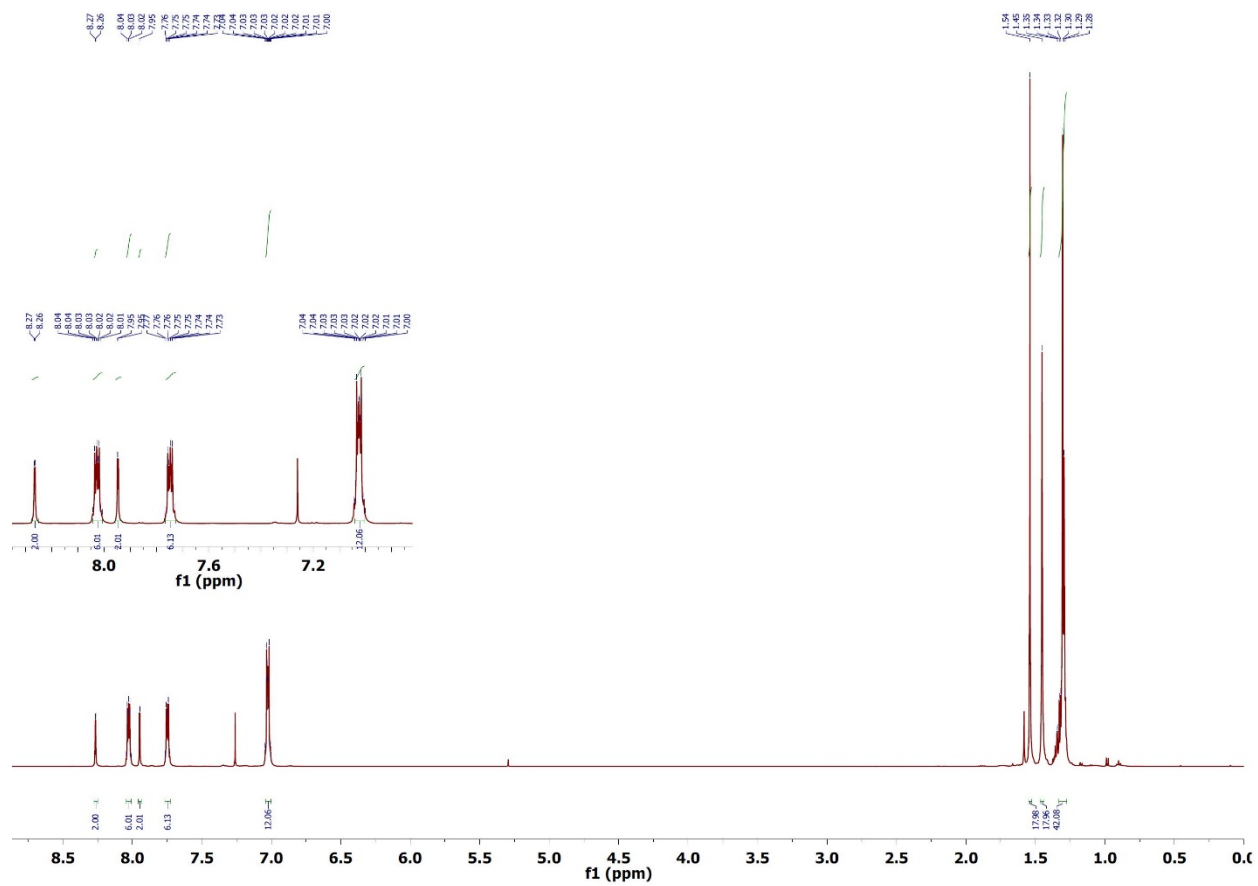
**Figure F.4.** $^1$H NMR spectrum of compound **14a** at 500 MHz in CDCl$_3$.

**Figure F.5.** $^{13}$C NMR specrtum of compound **14a** at 126 MHz in CDCl$_3$.



**Figure F.6.** FTIR Spectrum of compound **14a** taken as a powder.
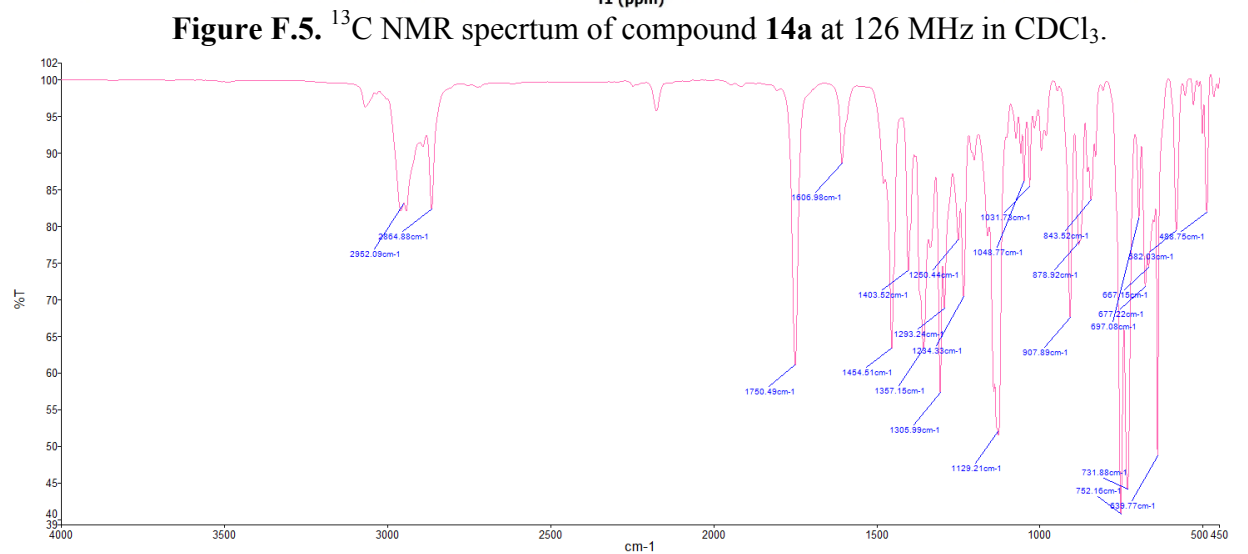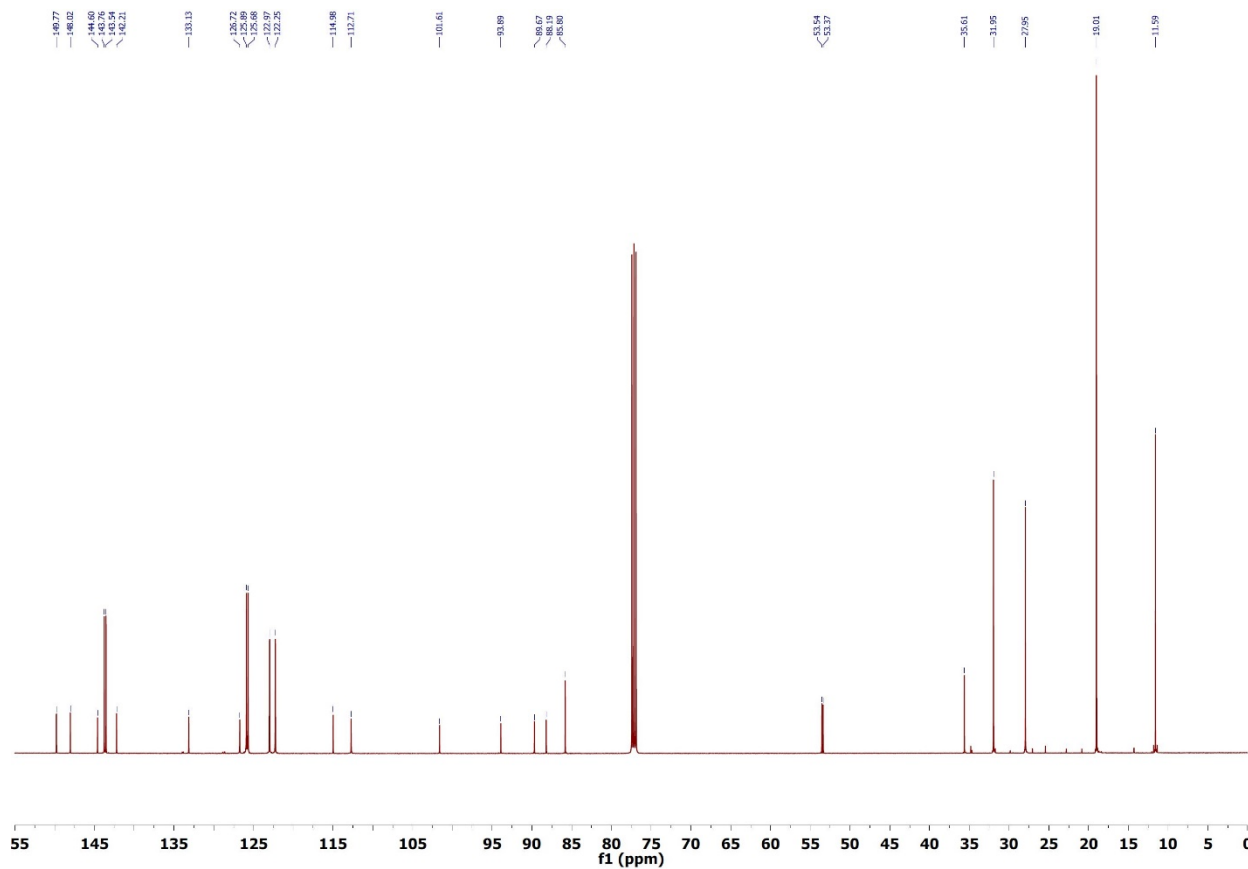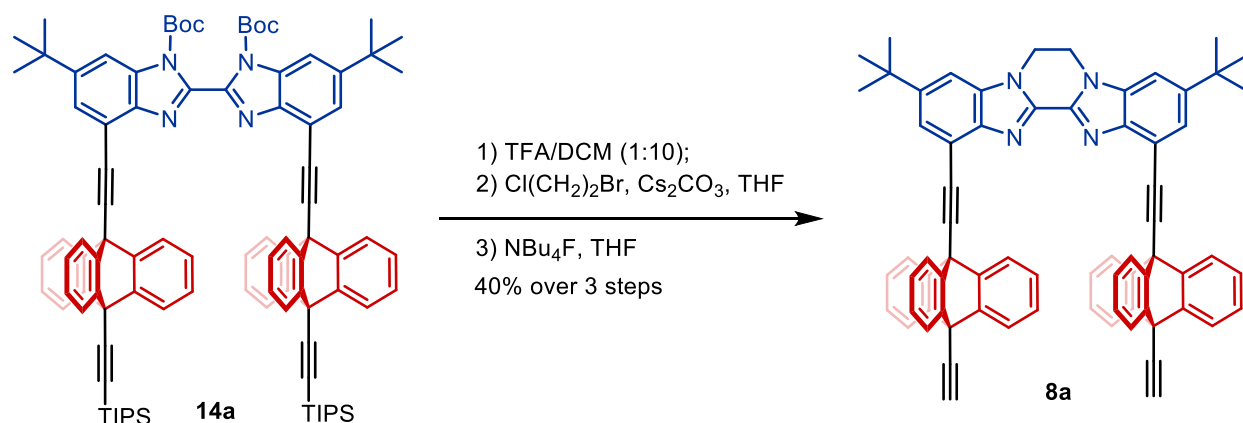
To a solution of **14a** (300 mg, 0.205 mmol) in CH₂Cl₂ (4 mL) under air was added trifluoroacetic acid (0.45 mL). The reaction mixture was stirred at room temperature for 3 h, after which water, sat. NaHCO₃ solution was added until the solution was neutralized. The layers were separated and the aqueous phase was extracted with CH₂Cl₂. The combined organic phases were washed with saturated NaCl solution and dried over MgSO₄, and concentrated, affording crude **4,4'-bis(triptycen-9-ylethynyl)-6,6'-di-tert-butyl-2,2'-bibenzimidazole** as a white solid (258 mg), which was used directly in the next step.

Crude **4,4'-bis(triptycen-9-ylethynyl)-6,6'-di-tertbutyl-2,2'-bibenzimidazol**e (260. mg, 21 $\mu$mol) was dissolved in THF (5 mL). To this solution, Cs₂CO₃ (201. mg, 617 $\mu$mol) and excess 1-bromo-2-chloroethane (5 mL) were added. The reaction mixture was stirred for 17 h at 60 ℃. Water and CH₂Cl₂ were added and the layers were separated. The aqueous phase was extracted with CH₂Cl₂ and the combined organic phases were washed with sat. NaCl, dried with MgSO₄ and concentrated in vacuo. The resulting residue was subjected to column chromatography (SiO₂, hexane/EtOAc = 7:3 – 1:1) giving 156 mg of white powder.

135 mg of the resultant compound was added to a 50 mL round bottom flask and placed under argon. 25 mL of dry THF was then added to the solution and the mixture was cooled to -78 ℃. Subsequently, 0.22 mL of 1M TBAF in THF was added to the solution and then the mixture was allowed to warm to 0 ℃. The mixture then stirred for 15 minutes before being quenched with a saturated NH₄Cl solution. The mixture was then extracted 3 times with 20 mL CH₂Cl₂ and the organic phase was dried over MgSO₄ and concentrated. The crude mixture was purified with column chromatography (SiO₂, hexane/EtOAc 1:1) to yield 75 mg of **8a** as a white, crystalline powder (44% yield over three steps).

Rf 0.38 (SiO₂, 1:2 EtOAc:Hexane);

¹H NMR (500 MHz, CDCl₃) δ 8.11 (d, $J$ = 7.3 Hz, 6H), 7.85 (d, $J$ = 1.5 Hz, 2H), 7.68 (d, $J$ = 7.3 Hz, 6H), 7.50 (d, $J$ = 1.5 Hz, 2H), 6.98 (td, $J$ = 7.4, 0.8 Hz, 6H), 6.78 (td, $J$ = 7.4, 0.8 Hz, 6H), 4.73 (s, 4H), 3.29 (s, 2H), 1.53 (s, 18H);

¹³C NMR (126 MHz, CDCl₃) δ 148.11, 143.74, 143.70, 143.02, 142.19, 134.46, 126.14, 126.01, 125.62, 123.04, 121.93, 115.27, 106.59, 90.01, 88.18, 80.76, 78.60, 53.45, 52.37, 40.93, 35.45, 31.98;

IR (film) 3298.91, 3067.63, 2959.62, 2925.25, 2866.75, 1727.8, 1608.51, 1454.17, 1420.65, 1379.59, 1363.8, 1337.83, 1326.83, 1306.01, 1255.35, 1233.56, 1202.06, 1155.91, 1079.35, 1031.93, 908.13, 879.05, 849.32, 803.65, 753.62, 732.48, 654.81, 640.02, 576.94, 486.8 cm⁻¹;

HRMS (APCI) Calcd for $C_{72}H_{52}N_4$ (M+1) 973.42647, found 973.4275.
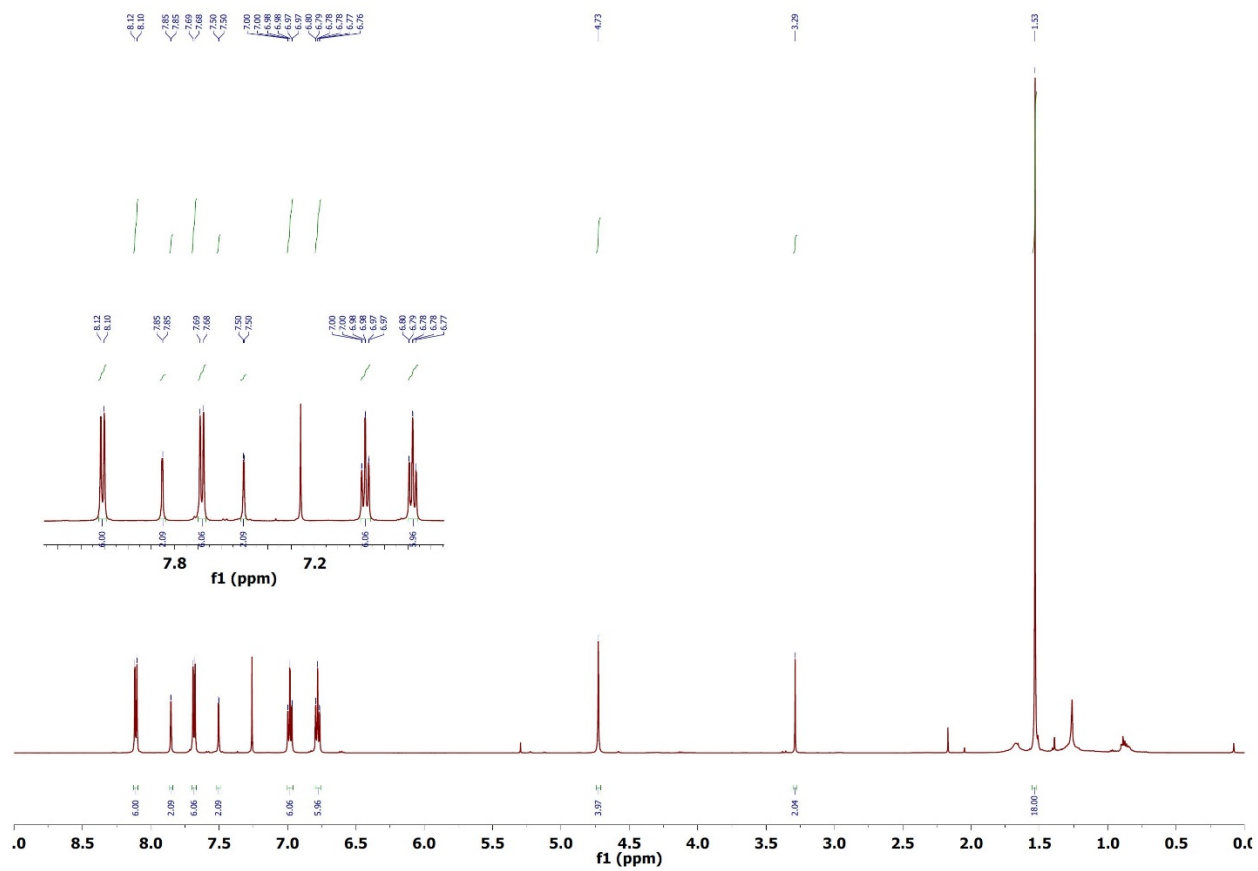


**Figure F.7.** $^1$H NMR spectrum of compound **8a** at 500 MHz in CDCl$_3$.

**Figure F.8.** $^{13}C$ NMR spectrum of compound **8a** at 126 MHz in CDCl$_3$.
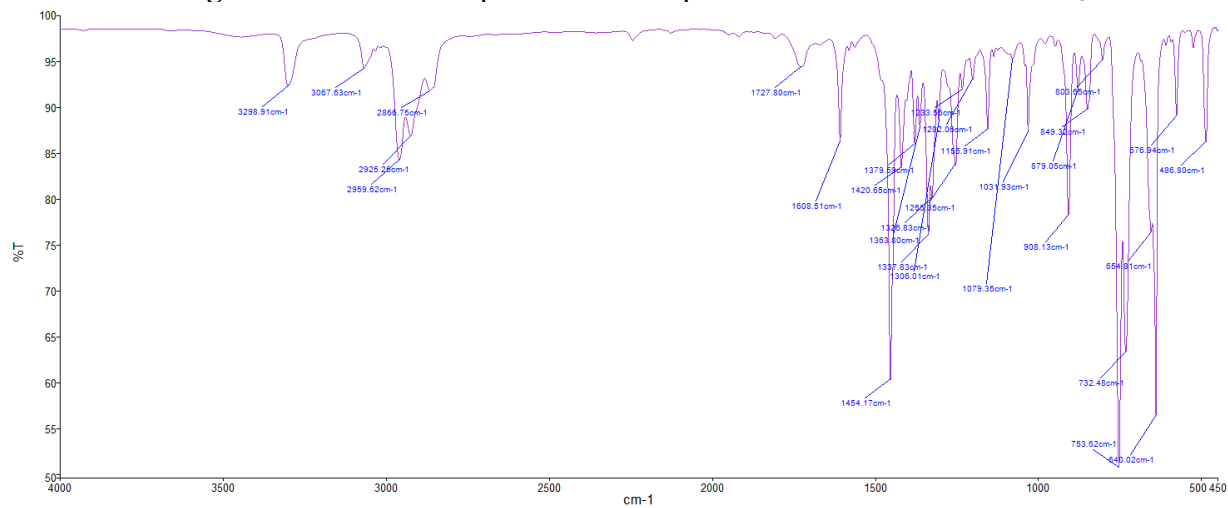


**Figure F.9.** FTIR Spectrum of compound **8a** taken as a powder.
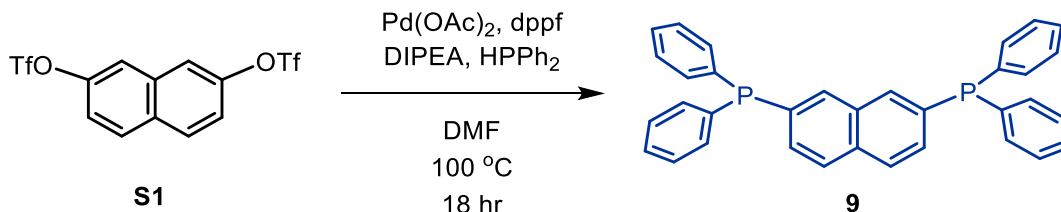
A 25 mL Schlenk flask was charged with dppf (33.17 mg, 0.077 mmol), Pd(OAc)$_2$ (15.9 mg, 0.071 mmol) and placed under an argon atmosphere. Subsequently, 3 mL of argon sparged DMF and 2 mL of argon sparged DIPEA were added to the flask and the solution was stirred for 1 hr. HPPh$_2$ (0.492 mL, 2.83 mmol) was then added and the mixture was stirred for an additional 5 minutes. Finally, **S1** (300 mg, 0.71 mmol) dissolved in 2 mL of argon sparged DMF was slowly syringed into the mixture and the mixture was stirred overnight at 100 °C. After this time, the crude solution was cooled to room temperature and 10mL of water was added. This mixture was then extracted 3 times with CH$_2$Cl$_2$ (20 mL), and the combined organic layers were dried over MgSO$_4$ then concentrated *in vacuo*. The crude compound was columned using silica as the stationary phase and a 1:2 mixture of CH$_2$Cl$_2$:Hexane to yield 300 mg of **9** (85% yield).

Rf 0.33 (SiO$_2$, 1:1 CH$_2$Cl$_2$:Hexane);

1H NMR (500 MHz, CDCl$_3$) δ 7.78 (t, J = 7.5 Hz, 4H), 7.43 – 7.40 (m, 2H), 7.39 – 7.34 (m, 20H);

13C NMR (126 MHz, CDCl3) δ 136.98, 136.90, 135.46, 135.37, 134.66, 134.46, 133.96, 133.81, 133.40, 133.25, 133.18, 131.03, 130.90, 128.98, 128.73, 128.68, 127.93, 127.88;

IR (film) 3050.95, 1584.51, 1477.6, 1433, 1316.28, 1272.23, 1183.22, 1087.18, 1069.26, 1026.36, 999.36, 946.92, 907.56, 842.81, 738.61, 694.06, 651.48, 565, 491.16, 477.2 cm$^{-1}$;

HRMS (APCI) Calcd for C$_{34}$H$_{26}$P$_2$ (M+1) 497.15996, found 497.15825.
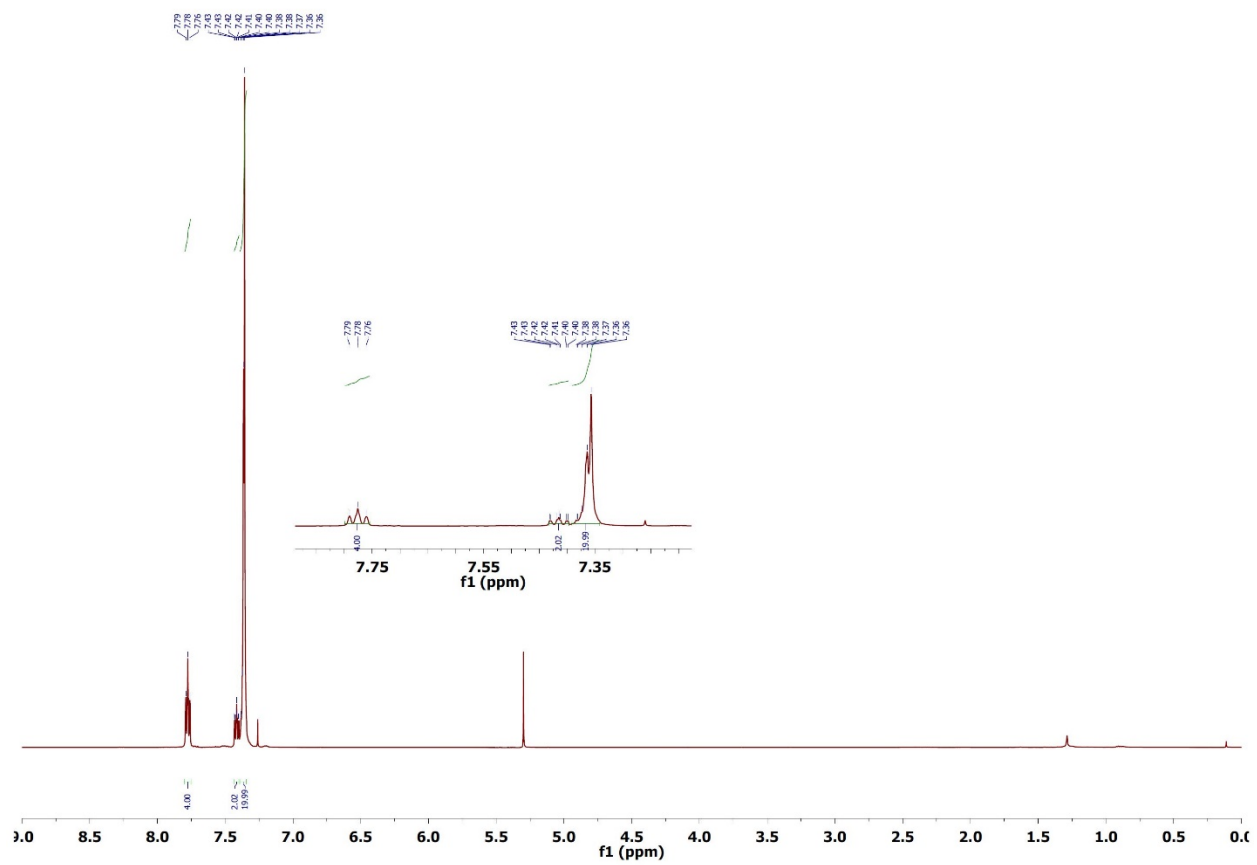
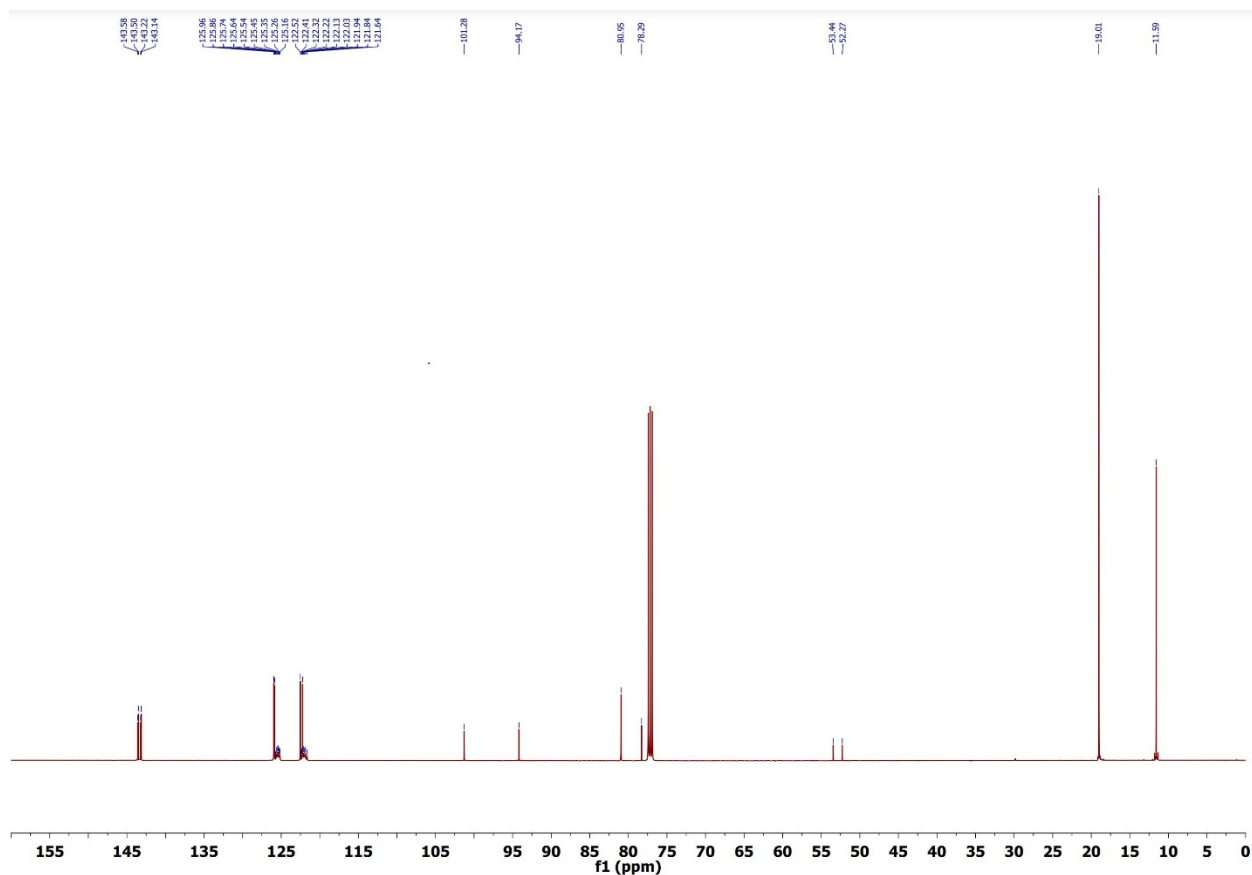**Figure F.10.** $^1$H NMR spectrum of compound **9** at 500 MHz in CDCl$_3$.
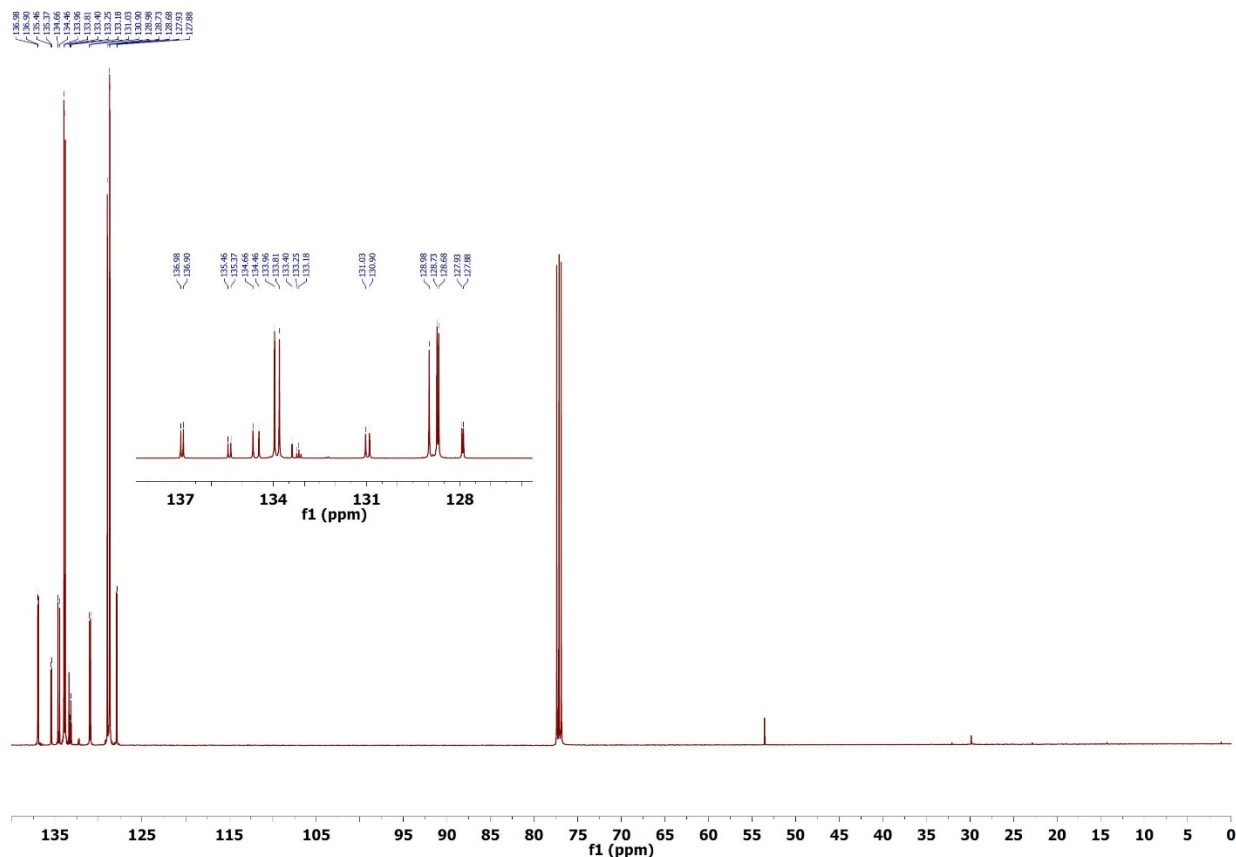
**Figure F.11.** $^{13}$C NMR spectrum of compound **9** at 126 MHz in CDCl$_3$.
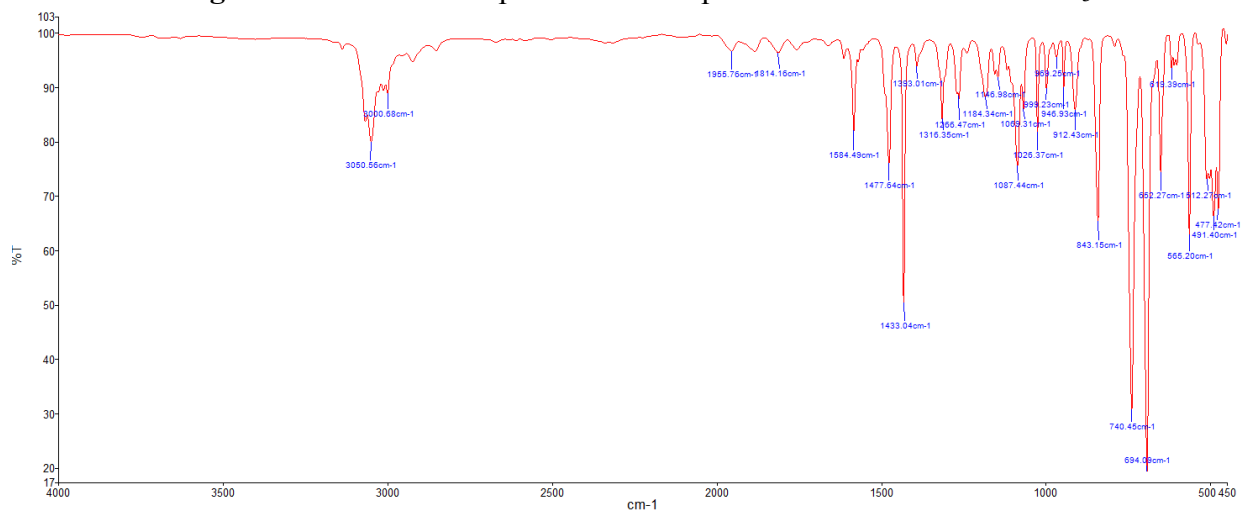


**Figure F.12.** FTIR Spectrum of compound **9** taken as a powder.
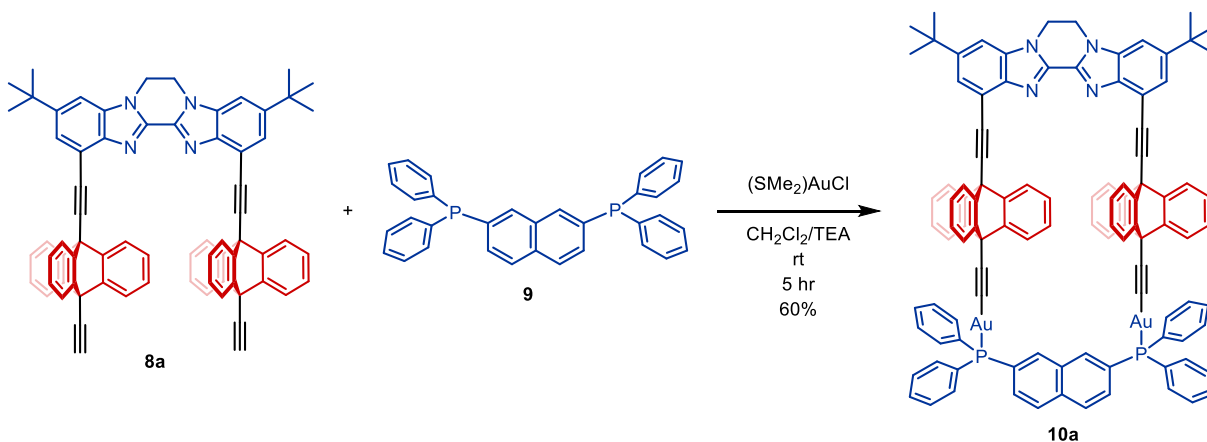
**8a** (10 mg, 0.010 mmol) was dissolved in 5 mL of CH₂Cl₂ and added to a 25 mL round bottomed flask. (SMe₂)AuCl (6.05 mg, 0.020 mmol) dissolved in 5 mL CH₂Cl₂ was then added followed by 1 drop of triethylamine. This mixture was stirred for 15 min to allow complexation to occur, which can be convenient monitored by the disappearance of **8a** on TLC. After this, **9** (5.10 mg, 0.01 mmol) dissolved in 5 mL of CH₂Cl₂ was added dropwise and the final mixture was stirred for 3 hrs. Additional **9** could be titrated into the mixture if complete conversion of **8a** into **10a** did not proceed efficiently. After completion of the reaction, the mixture was run through a small silica plug and rinsed multiple times with CH₂Cl₂. This mixture was then concentrated *in vacuo* to yield a crude yellow colored paste. This paste was then dissolved in 3 mL CH₂Cl₂ and then 5 mL of hexane and 1 mL of MeOH was added to crashed **10a** out of solution. This heterogeneous mixture was then centrifuged and the solvent mixture was removed. This powder was then washed with 3 mL of CH₂Cl₂ and 6 mL of hexane 3 more times with centrifugation between each step. After completion of these purifications, the white powder was dried to yield 11.6 mg of **10a** (60% yield).

Rf 0.25 (SiO₂, 4:1 CH₂Cl₂:Hexane);

mp 420°C (decomposition);

¹H NMR (500 MHz, CD₂Cl₂) δ 9.23 (d, *J* = 17.0 Hz, 2H), 8.06 (d, *J* = 7.3 Hz, 6H), 8.01 (d, *J* = 8.4 Hz, 2H), 7.92 (s, 2H), 7.88 (d, *J* = 7.3 Hz, 6H), 7.72 (dd, *J* = 11.8, 7.4 Hz, 8H), 7.61 (s, 2H), 7.58 (m, *J* = 7.6 Hz, 12H), 7.47 (t, *J* = 8.6 Hz, 2H), 6.87 (t, *J* = 7.3 Hz, 6H), 6.59 (t, *J* = 7.4 Hz, 6H), 4.80 (s, 4H), 1.55 (s, 18H);

IR (film) 2957.37, 1708.72, 1607.37, 1454.16, 1436.85, 1419.51  1379.36, 1362.69, 1332.35, 1253.49, 1155.56, 1099.04, 1029.69, 998.79, 916.45, 877.64, 845.43, 749.41, 692.21, 659.93, 639.66, 621.71, 565.91, 537.91, 489.27 cm⁻¹;

HRMS (ESI) Calcd for C₁₀₆H₇₆Au₂N₄P₂ (M+H) 1861.4955, found 1861.4944.
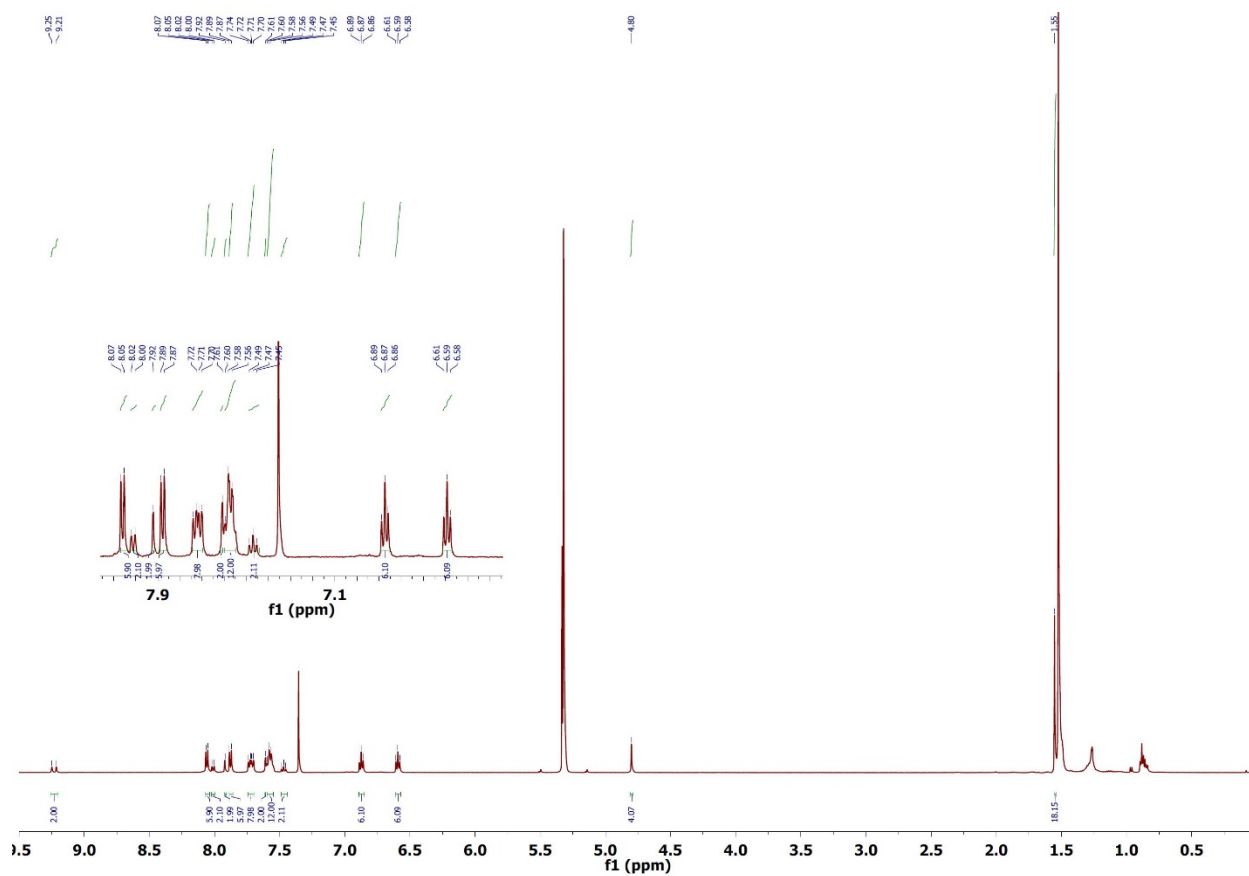
**Figure F.13.** $^1$H NMR spectrum of compound **10a** at 500 MHz in CD$_2$Cl$_2$.
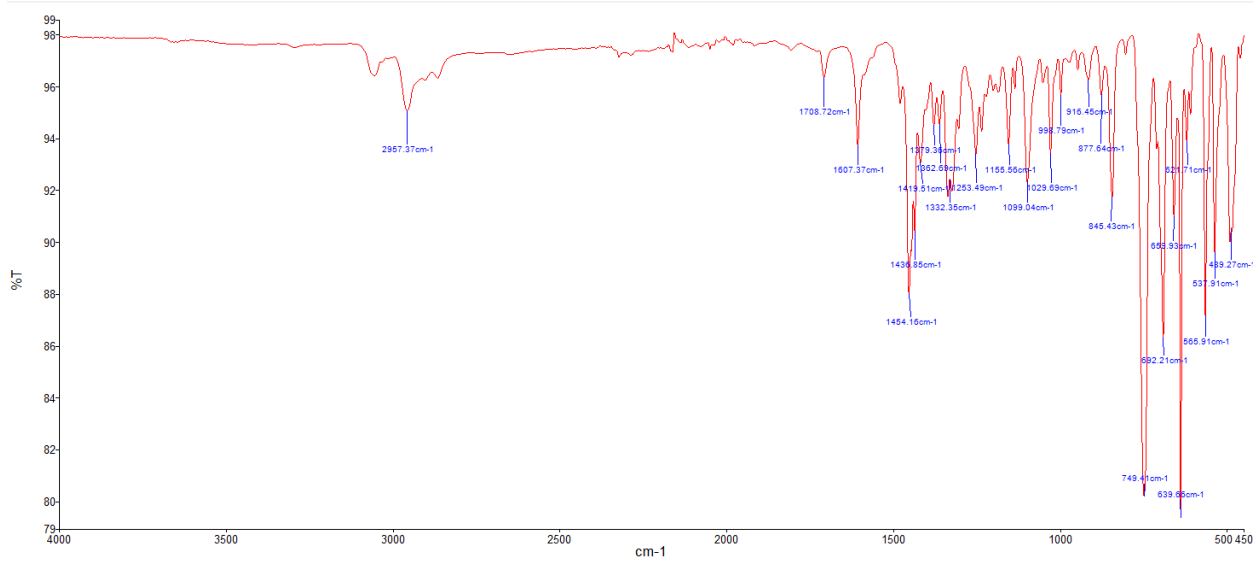


**Figure F.14.** FTIR Spectrum of compound **10a** taken as a powder.
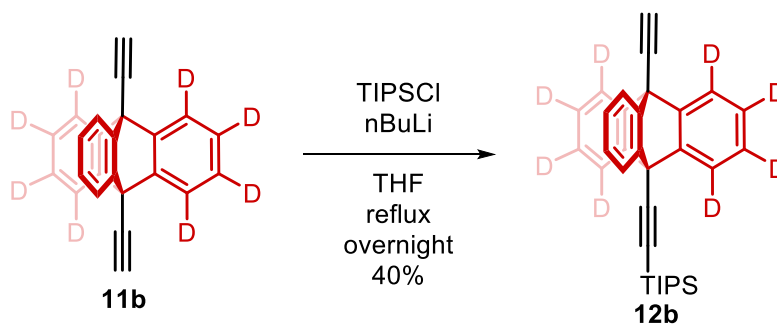
A 50 mL round bottom flask was charged with dialkyne **11b** (600 mg, 1.93 mmol) and placed under an inert argon atmosphere. 15 mL of THF were then added and the solution was cooled to -78 °C. n-butyllithium (0.775 mL, 1.93 mmol) was then added to the flask and the mixture was stirred for 30 minutes. Triisopropylsilyl chloride (0.42 mL, 2.20 mmol) was then added to the flask and the reaction mixture was first warmed to room temperature and then brought to reflux overnight. The mixture was then cooled to room temperature and quenched with saturated ammonium chloride solution. The resultant solution was extracted three times with DCM (10 mL), dried over MgSO$_4$, and concentrated to yield a white powder. Purification of the crude mixture was accomplished by flash chromatography (SiO$_2$, Hexanes) to yield 430 mg of pure monoprotected product (44% yield) as a white solid. Diprotected and unprotected products were combined, deprotected with tetrabutylammonium fluoride and purified with a hexane column to be reused in subsequent reactions.

Rf 0.37 (Silica, Hexane);

$^1$H NMR (500 MHz, CDCl$_3$) δ 8.62 (dd, $J$ = 9.5, 5.4 Hz, 2H), 8.20 (dd, $J$ = 10.5, 2.5 Hz, 2H), 7.43 (ddd, $J$ = 10.0, 7.8, 2.5 Hz, 2H), 1.36 – 1.21 (m, 42H);

$^{13}$C NMR (126 MHz, CDCl$_3$) 143.58, 143.50, 143.22, 143.14, 125.96, 125.86, 125.74, 125.64, 125.54, 125.45, 125.35, 125.26, 125.16, 122.52, 122.41, 122.32, 122.22, 122.13, 122.03, 121.94, 121.84, 121.64, 101.28, 94.17, 80.95, 78.29, 53.44, 52.27, 19.01, 11.59;

IR (Film) 3285.72, 2943.08, 2890.66, 2865.08, 2277.2, 2172.2, 1601.37, 1578.39, 1467.68, 1387.81, 1358.9, 1289.62, 1229.19, 1058.76, 1016.05, 992.16, 917.8, 882.46, 810.28, 744.47, 674.17, 657.05, 621.2, 583.76, 577, 509.82, 478.7, 455.83 cm$^{-1}$;

HRMS (APCI) Calcd for C$_{33}$H$_{26}$D$_8$Si (M) 466.29341, found 466.29264.
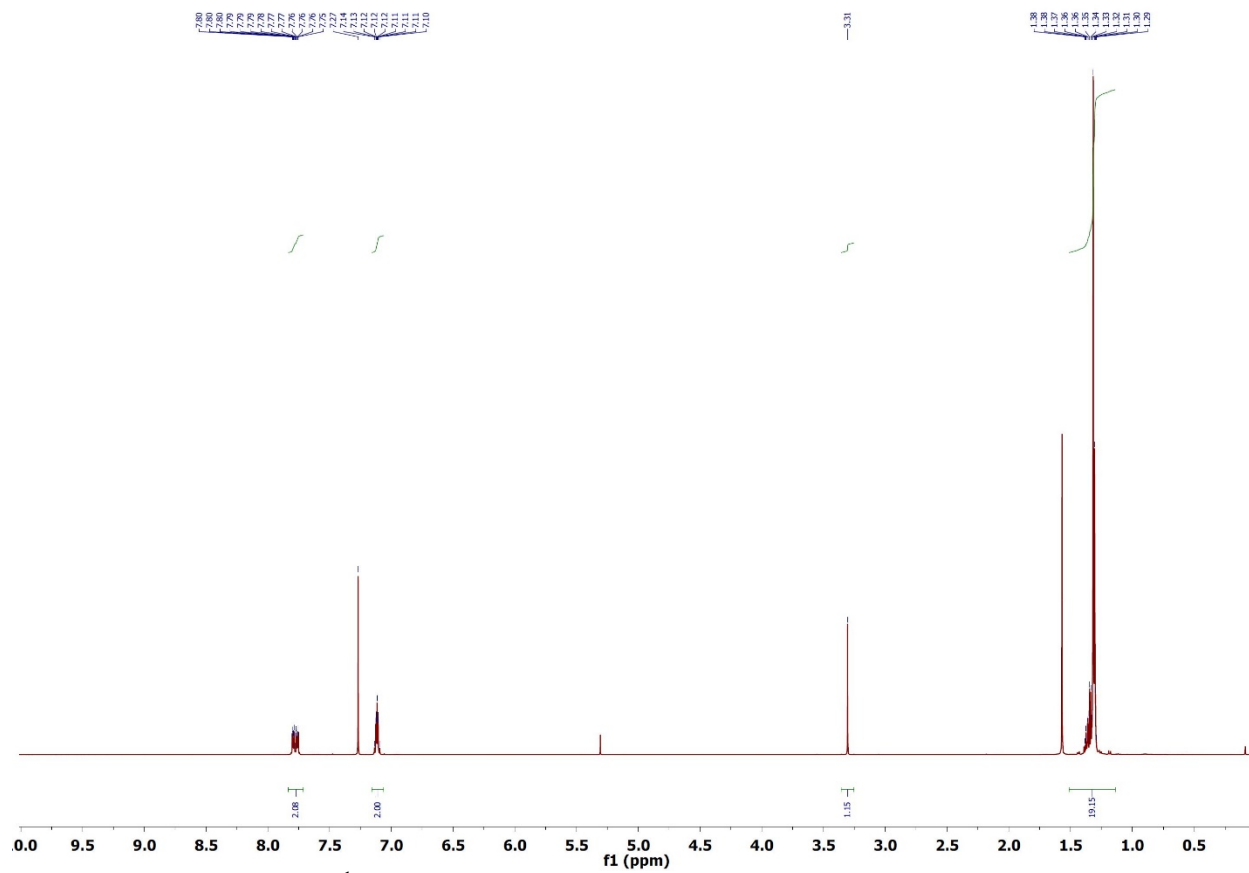
**Figure F.15.** $^{1}$H NMR spectrum of compound **12b** at 500 MHz in CDCl$_3$.

**Figure F.16.** $^{13}$C NMR spectrum of compound **12b** at 126 MHz in CDCl$_3$.
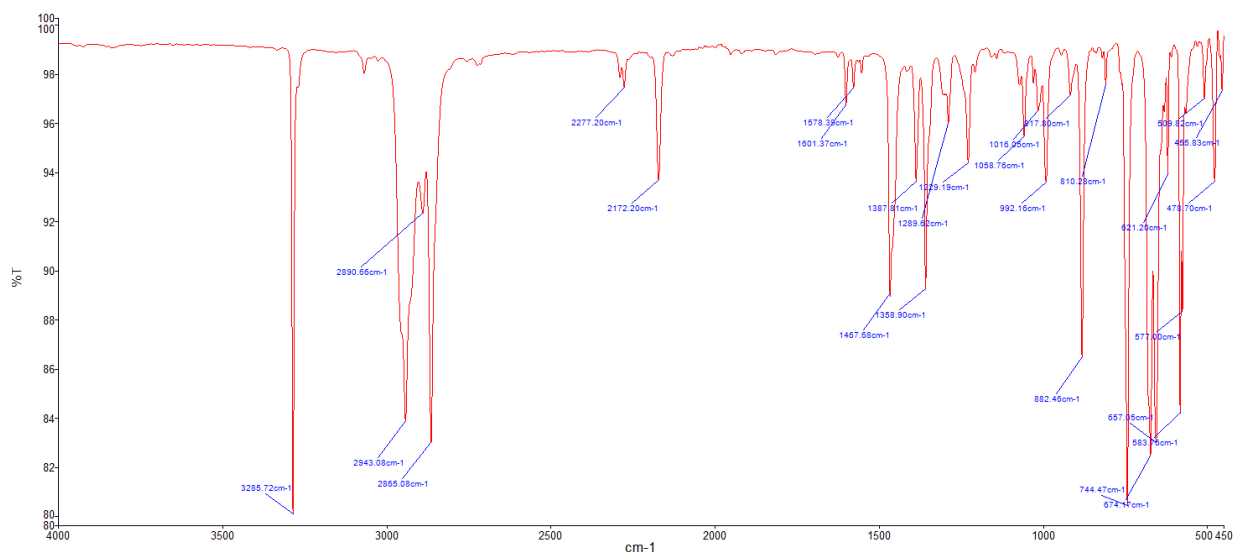


**Figure F.17.** FTIR Spectrum of compound **12b** taken as a powder.
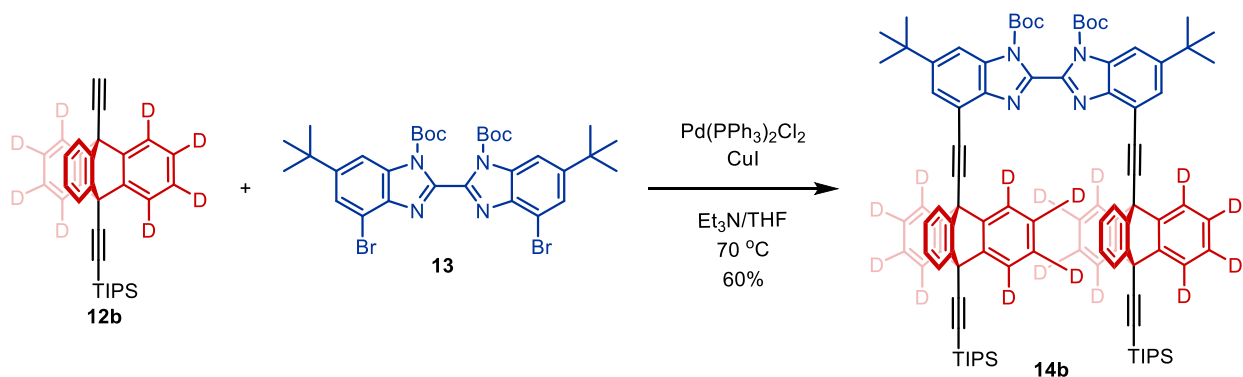
To an argon-flushed solid mixture of **12b** (275 mg, 0.590 mmol), **13** (197.6 mg, 0.28 mmol), CuI (10.70 mg, 56.11 $\mu$mol), and Pd(PPh$_3$)$_2$Cl$_2$ (19.7 mg, 28.06 $\mu$mol) were added. The flask was then charged with degassed, dry THF (8 mL) and degassed triethylamine (8 mL). The reaction mixture was stirred and heated to 70 °C. After 18 h, the solvents were removed from the reaction mixture and the remaining solid was subjected to column chromatography (alumina, hexane/CH$_2$Cl$_2$ = 9.5:0.5 - 9:1), giving **14b** as a white solid (248 mg, 60%).

Rf 0.6 (alumina, 2:8 CH$_2$Cl$_2$:Hexane);

$^1$H NMR (500 MHz, CDCl$_3$) δ 8.25 (d, J = 1.7 Hz, 2H), 8.01 (dd, J = 5.6, 3.1 Hz, 2H), 7.93 (d, J = 1.7 Hz, 2H), 7.73 (dd, J = 5.6, 3.1 Hz, 2H), 7.09 – 6.94 (m, 2H), 1.53 (s, 16H), 1.44 (s, 16H), 1.28 (d, J = 5.3 Hz, 42H);

$^{13}$C NMR (126 MHz, CDCl$_3$) δ 149.77, 148.02, 144.60, 143.78, 143.70, 143.56, 143.48, 142.20, 133.13, 126.73, 126.56, 125.88, 125.67, 125.37, 124.39, 122.96, 122.88, 122.60, 122.24, 122.08, 121.86, 114.98, 112.71, 101.64, 93.79, 89.57, 88.21, 85.80, 53.47, 53.30, 35.61, 31.95, 29.85, 28.66, 27.95, 19.01, 11.59;

IR (Film) 2959.33, 2942.81, 2865.17, 2287.75, 2173.48, 1751.44, 1692.74, 1601.62, 1462.37, 1404.16, 1352.17, 1300.61, 1247.94, 1233.78, 1206.86, 1144.19, 1121.33, 1056, 1005.14, 996.02, 974.64, 908.85, 881.99, 843.53, 810.17, 749.2, 735.78, 677.87, 661.16, 621.23, 582, 529.48, 500.67, 478.9 cm$^{-1}$;

HRMS (MALDI) Calcd for C$_{98}$H$_{90}$D$_{16}$N$_4$O$_4$Si$_2$ with loss of 2 x Boc + Na$^+$ (1297.7606) Found: 1297.7253.
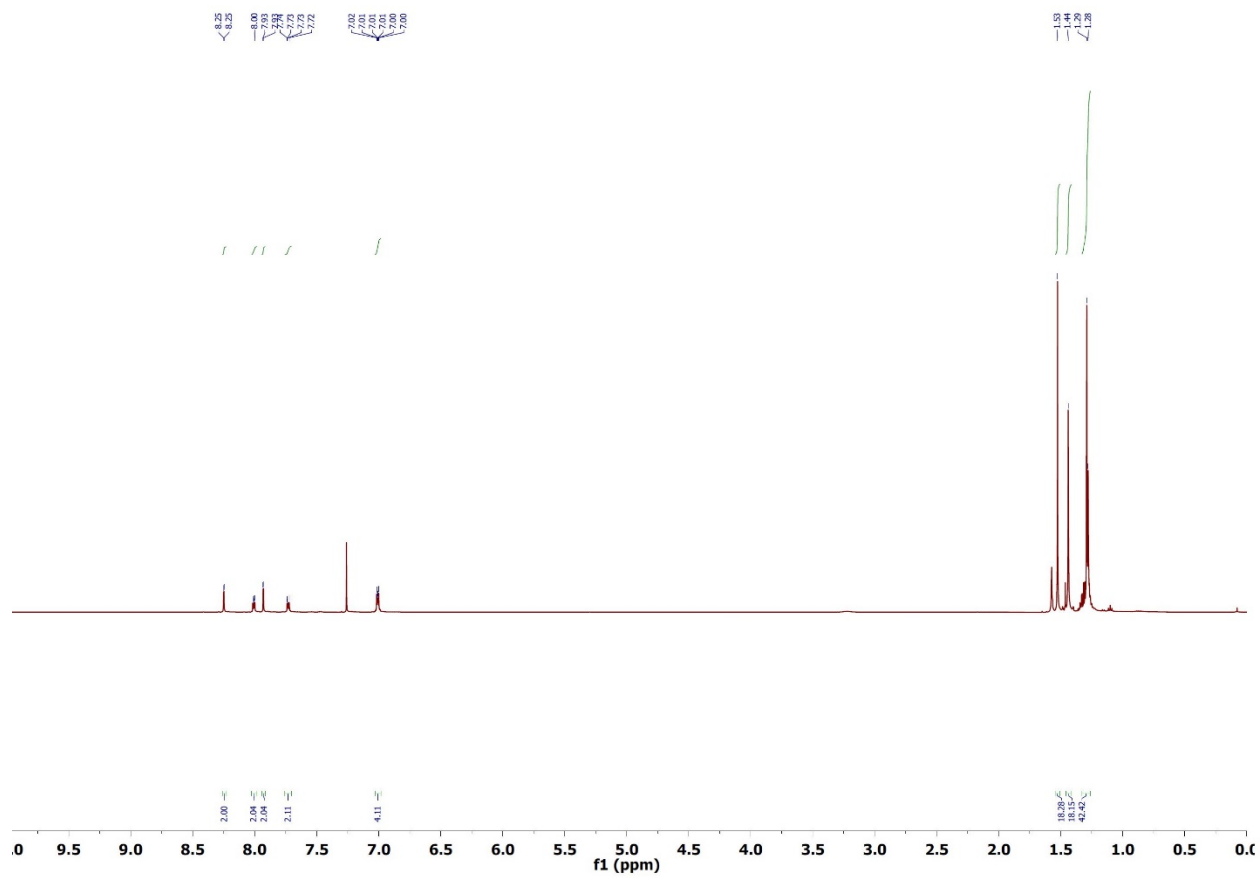
**Figure F.18.** $^1$H NMR spectrum of compound **14b** at 500 MHz in CDCl$_3$.

**Figure F.19.** $^{13}$C NMR spectrum of compound **14b** at 126 MHz in CDCl$_3$.



**Figure F.20** FTIR Spectrum of compound **14b** taken as a powder.
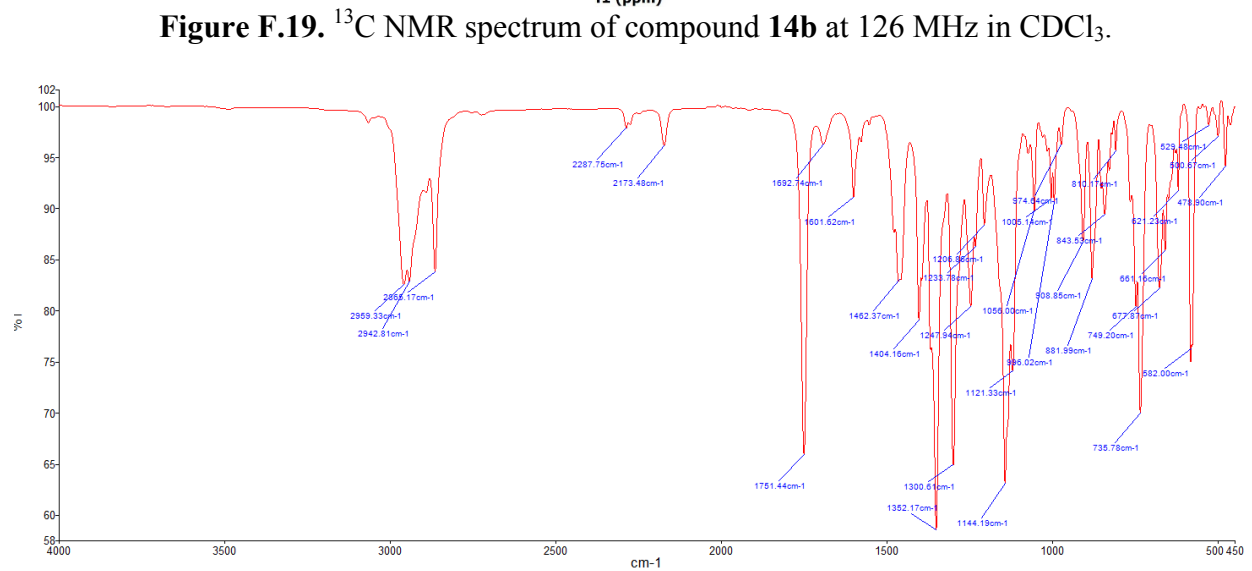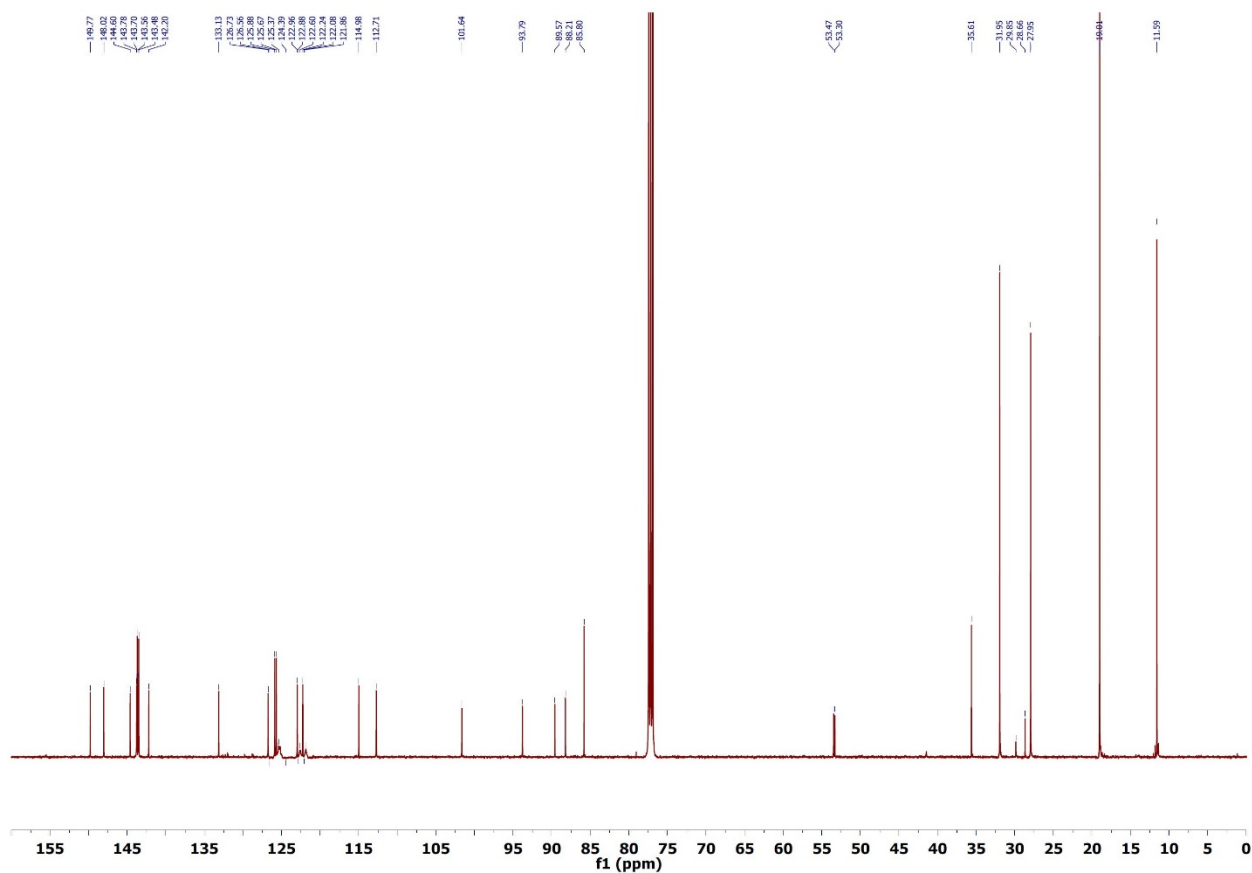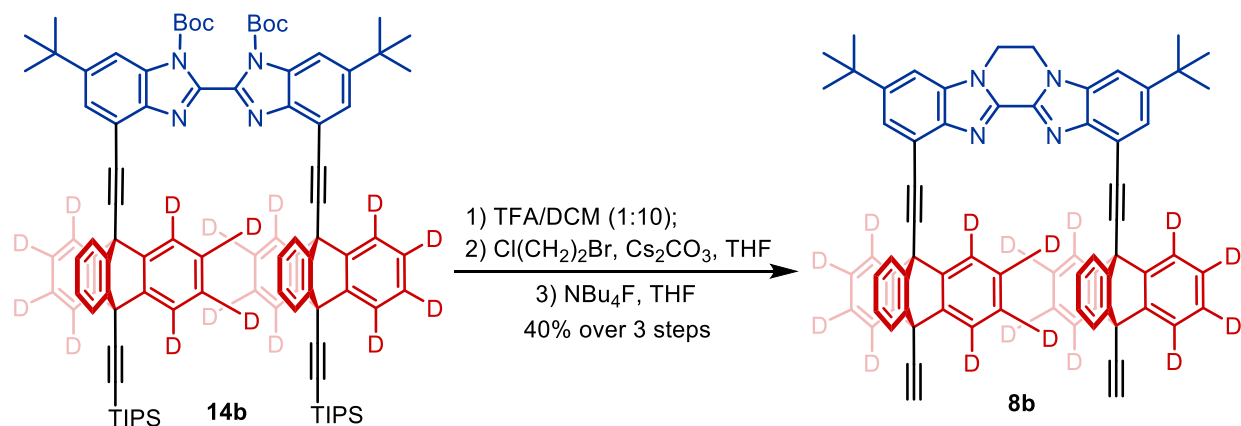
To a solution of **14b** (160 mg, 0.108 mmol) in CH₂Cl₂ (4 mL) under air was added trifluoroacetic acid (0.45 mL). The reaction mixture was stirred at room temperature for 3 h, after which water, sat. NaHCO₃ solution was added until the solution was neutralized. The layers were separated and the aqueous phase was extracted with CH₂Cl₂. The combined organic phases were washed with saturated NaCl solution and dried over MgSO₄, and concentrated, affording crude **4,4'-bis(triptycen-9-ylethynyl)-6,6'-di-tert-butyl-2,2'-bibenzimidazole-$d_{16}$** as a white solid (138 mg), which was used directly in the next step.

Crude **4,4'-bis(triptycen-9-ylethynyl)-6,6'-di-tertbutyl-2,2'-bibenzimidazole-$d_{16}$** (138 mg, 108 $\mu$mol) was dissolved in THF (5 mL). To this solution, Cs₂CO₃ (104.5 mg, 320 $\mu$mol) and excess 1-bromo-2-chloroethane (3 mL) were added. The reaction mixture was stirred for 17 h at 60 °C. Water and CH₂Cl₂ were added and the layers were separated. The aqueous phase was extracted with CH₂Cl₂ and the combined organic phases were washed with sat. NaCl, dried with MgSO₄ and concentrated in vacuo. The resulting residue was subjected to column chromatography (SiO₂, hexane/EtOAc = 7:3 – 1:1) giving 120 mg of white powder.

120 mg (0.085 mmol) of the resultant compound was added to a 25 mL round bottom flask and placed under argon. 10 mL of dry THF was then added to the solution and the mixture was cooled to -78 °C. Subsequently, 0.2 mL (.186 mmol) of 1M TBAF in THF was added to the solution and then the mixture was allowed to warm to 0 °C. The mixture then stirred for 15 minutes before being quenched with a saturated NH₄Cl solution. The mixture was then extracted 3 times with 20 mL CH₂Cl₂ and the organic phase was dried over MgSO₄ and concentrated. The crude mixture was purified with column chromatography (SiO₂, hexane/EtOAc 1:1) to yield 45 mg of **8b** as a white, crystalline powder (44% yield over three steps).

Rf 0.38 (SiO₂, 1:2 EtOAc:Hexane);

¹H NMR (600 MHz, CD₂Cl₂) δ 8.08 (dd, J = 7.5, 0.8 Hz, 1H), 7.89 (d, J = 1.7 Hz, 1H), 7.68 (dd, J = 7.5, 0.8 Hz, 1H), 7.52 (d, J = 1.7 Hz, 1H), 6.98 (td, J = 7.5, 1.2 Hz, 1H), 6.79 (td, J = 7.5, 1.2 Hz, 1H), 4.77 (s, 2H), 3.28 (s, 1H), 1.54 (s, 8H);

¹³C NMR (126 MHz, CD₂Cl₂) δ 148.78, 148.73, 144.24, 144.20, 144.11, 144.08, 143.50, 143.42, 143.39, 142.86, 135.04, 131.48, 129.29, 126.58, 126.19, 126.15, 123.24, 122.36, 121.98, 115.11, 107.64, 90.56, 88.07, 81.44, 78.51, 52.70, 41.53, 35.82, 32.09, 30.25;

IR (Film) 3282.11, 2964.29, 1602.83, 1466.91, 1417.54, 1376.49, 1355.6, 1337.45, 1323.24, 1266.59, 1156.76, 1031.03, 870, 857.1, 843.34, 811.6, 749.54, 664.99, 621.24, 580.88, 528.32, 477.16 cm⁻¹;

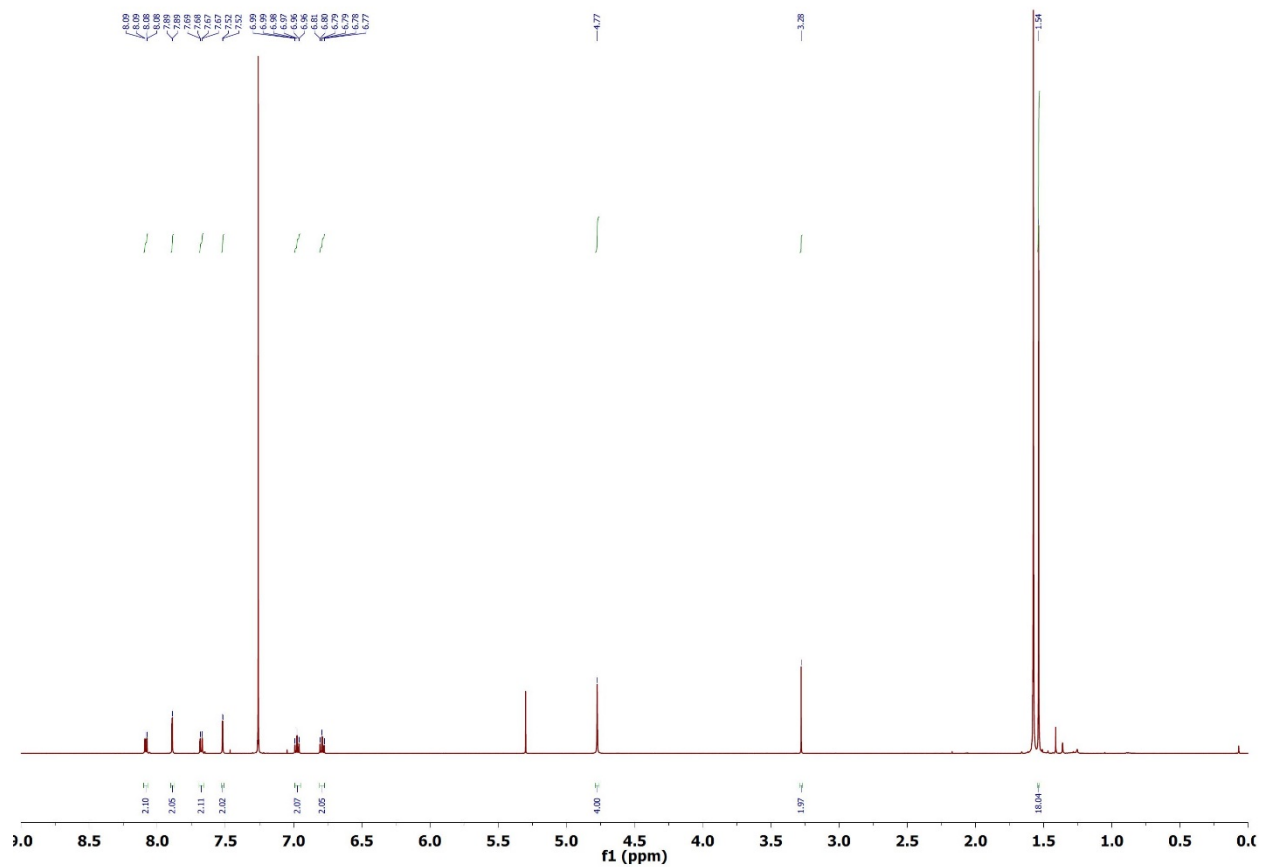HRMS (APCI) Calcd for $C_{72}H_{36}D_{16}N_4$ (M+1) 989.52690, found 989.52785.



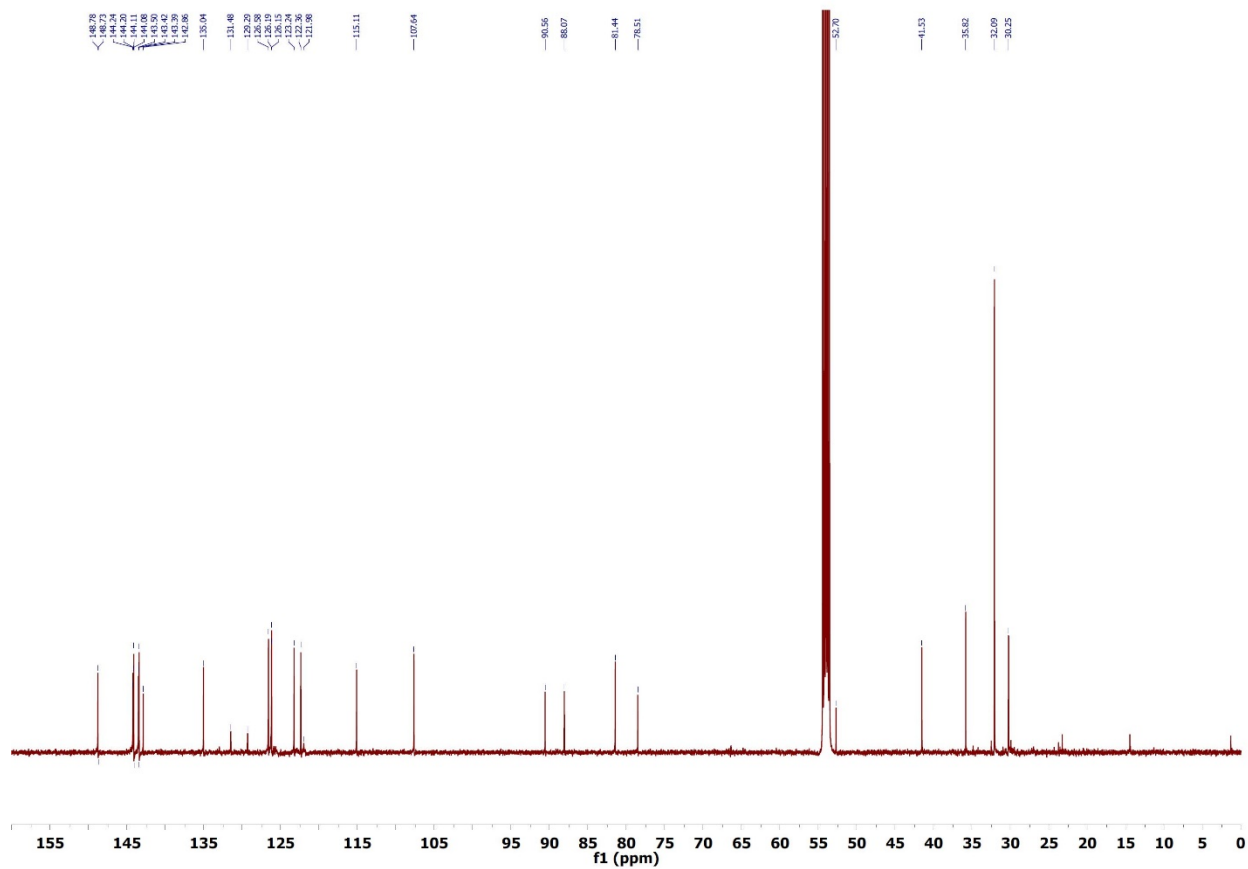**Figure F.21.** $^1$H NMR spectrum of compound **8b** at 500 MHz in CDCl$_3$.

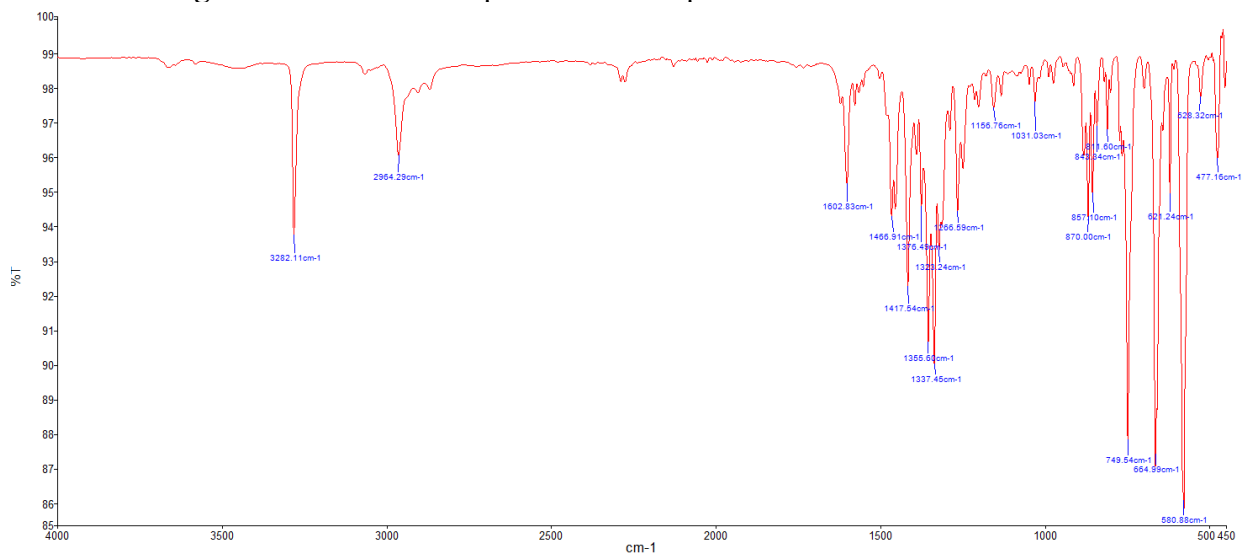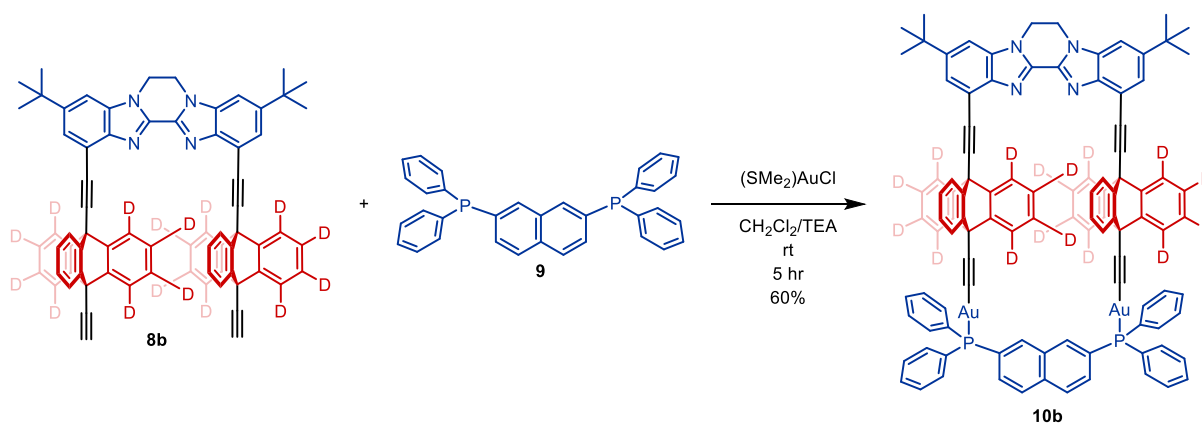**Figure F.22.** $^{13}$C NMR spectrum of compound **8b** at 126 MHz in CD$_2$Cl$_2$.



**Figure F.23.** FTIR Spectrum of compound **8b** taken as a powder.

**8b** (10 mg, 0.010 mmol) was dissolved in 5 mL of CH₂Cl₂ and added to a 25 mL round bottomed flask. (SMe₂)AuCl (6.05 mg, 0.020 mmol) dissolved in 5 mL CH₂Cl₂ was then added followed by 1 drop of triethylamine. This mixture was stirred for 15 min to allow complexation to occur, which can be convenient monitored by the disappearance of **8b** on TLC. After this, **9** (5.10 mg, 0.01 mmol) dissolved in 5 mL of CH₂Cl₂ was added dropwise and the final mixture was stirred for 3 hrs. Additional **9** could be titrated into the mixture if complete conversion of **8b** into **10b** did not proceed efficiently. After completion of the reaction, the mixture was run through a small silica plug and rinsed multiple times with CH₂Cl₂. This mixture was then concentrated *in vacuo* to yield a crude yellow colored paste. This paste was then dissolved in 3 mL CH₂Cl₂ and then 5 mL of hexane and 1 mL of MeOH was added to crashed **10b** out of solution. This heterogeneous mixture was then centrifuged and the solvent mixture was removed. This powder was then washed with 3 mL of CH₂Cl₂ and 6 mL of hexane 3 more times with centrifugation between each step. After completion of these purifications, the white powder was dried to yield 11.6 mg of **10b** (60% yield).

Rf 0.25 (SiO₂, 4:1 CH₂Cl₂:Hexane);

mp 420°C (decomposition);

¹H NMR (500 MHz, CD₂Cl₂) δ 9.23 (d, J = 17.2 Hz, 2H), 8.06 (dd, J = 7.5, 0.7 Hz, 2H), 8.01 (d, J = 7.0 Hz, 2H), 7.92 (d, J = 1.7 Hz, 2H), 7.88 (dd, J = 7.5, 0.8 Hz, 2H), 7.79 – 7.67 (m, 2H), 7.58 (dddd, J = 11.2, 6.5, 5.6, 2.0 Hz, 1H), 7.47 (td, J = 8.4, 1.5 Hz, 1H), 6.87 (td, J = 7.4, 1.2 Hz, 1H), 6.60 (td, J = 7.4, 1.2 Hz, 1H), 4.80 (s, 1H), 1.55 (s, 1H)

IR (Film) 2956.95, 1601, 1454.78, 1436.33, 1356.86, 1249.43, 1156.54, 1098.37, 1027.36, 998.52, 915.56, 880.56, 844.93, 808.54, 745.26, 692.18, 659.71, 621.48, 583.03, 565.71, 537.65, 493.64, 476.48 cm⁻¹;

HRMS (MALDI) Calcd for C₁₀₆H₆₀D₁₆Au₂N₄P₂ [M+Na]⁺ 1899.5778, found 1899.4804.
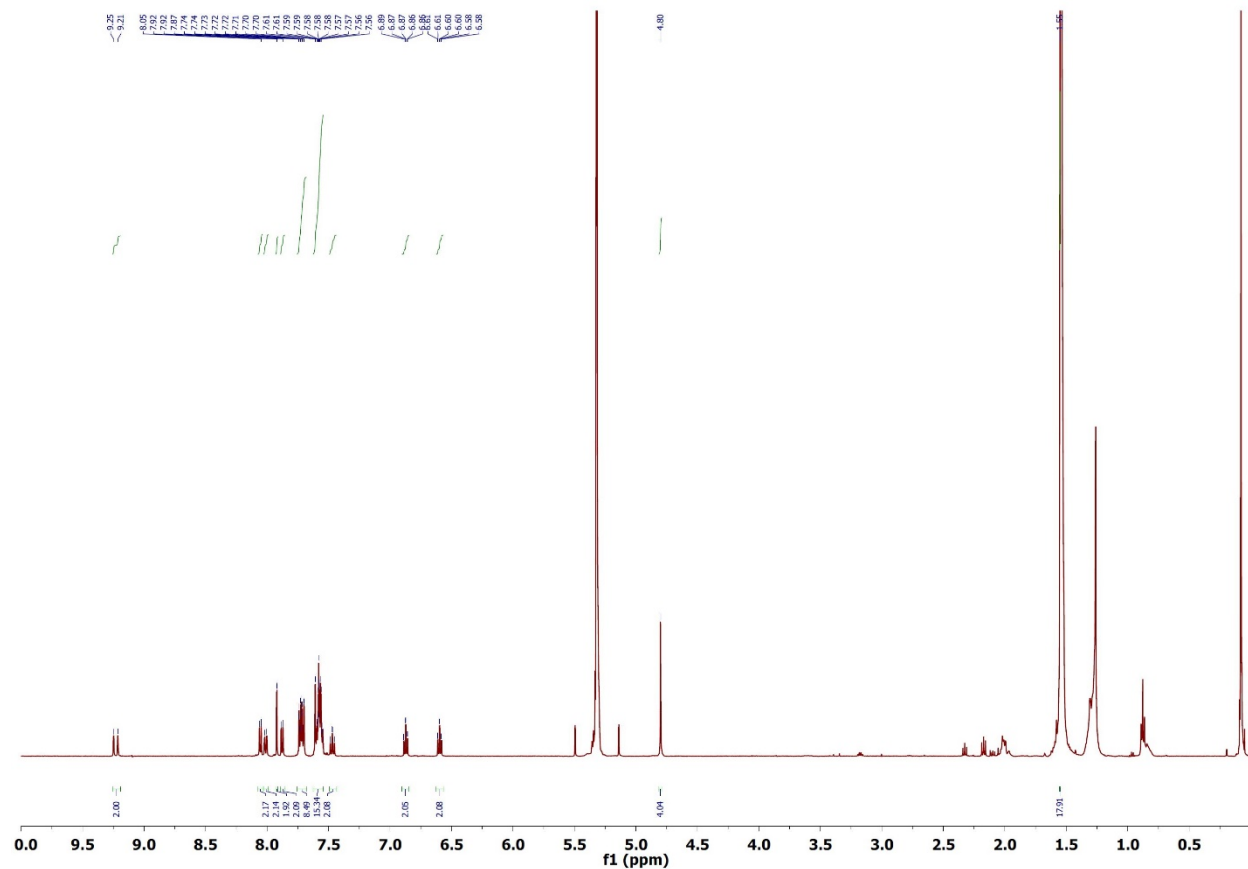
**Figure F.24.** $^1$H NMR spectrum of compound **10b** at 500 MHz in CD$_2$Cl$_2$.
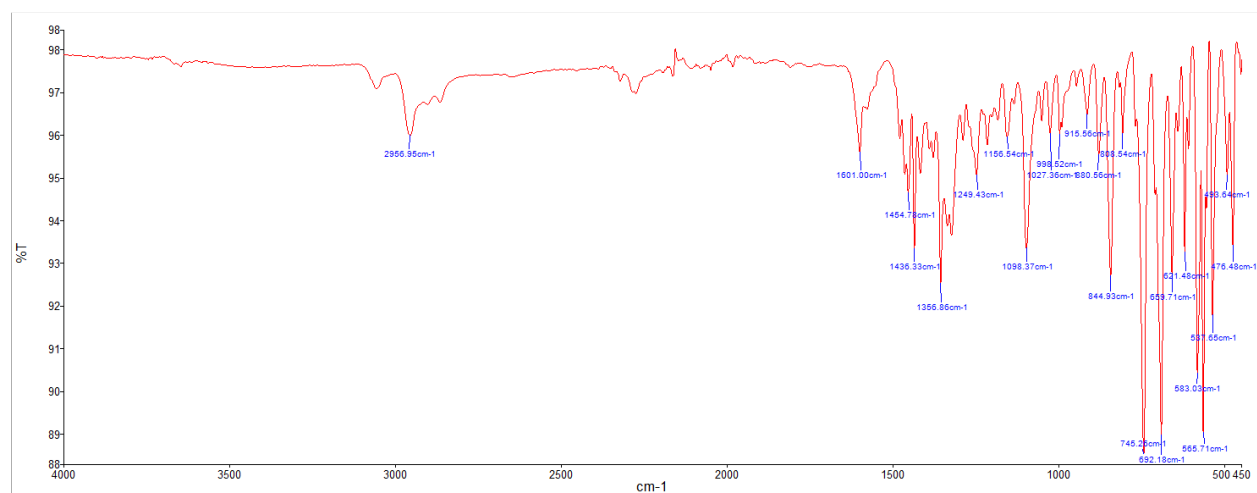


**Figure F.25.** FTIR Spectrum of compound **10b** taken as a powder.
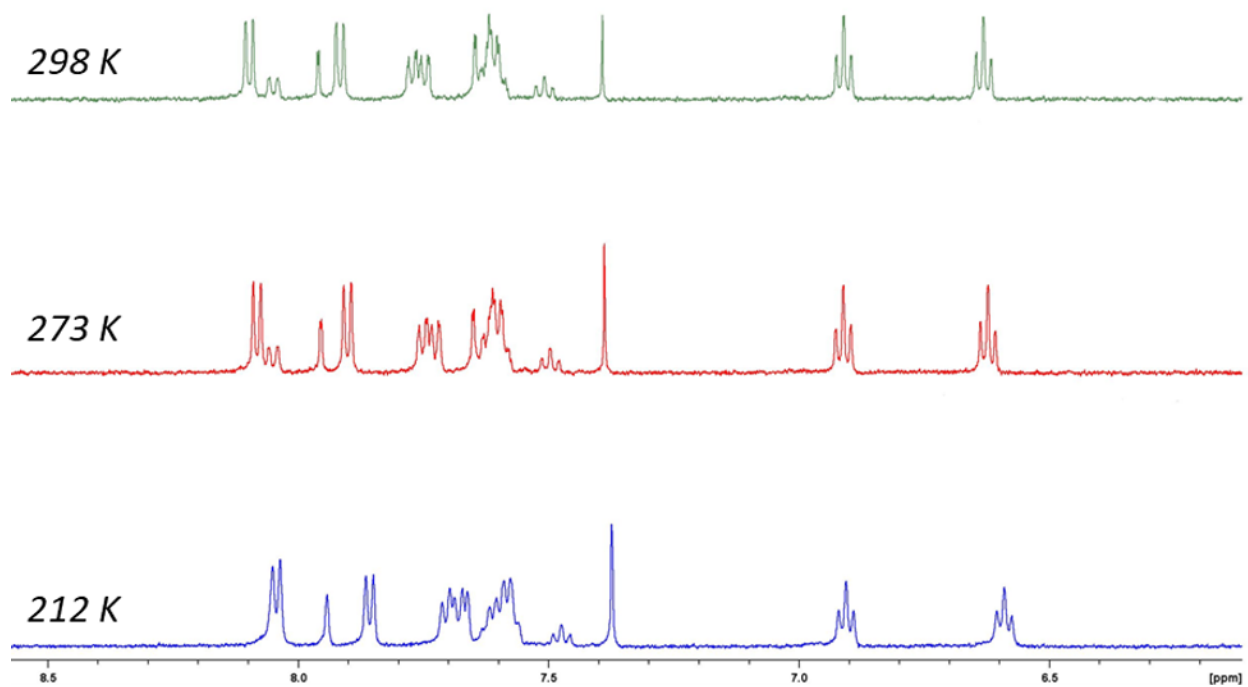
# Section C. Variable Temperature $^1$H NMR

**Figure F.26.** Variable-temperature 1H spectra of MSG **10a** at temperatures ranging from 298 to 212 K

## Section F4. Micro Electron-Diffraction

### Sample Preparation for Electron Diffraction

Samples were prepared using Quantifoil TEM grids. To prepare sample grids, a new TEM grid was placed in a vial with the sample as a dry powder and gently shaken. TEM grids were then placed in a standard single-tilt TEM holder at room temperature.

### Instrument Parameters

Data was acquired on an FEI Tecnai TF-30 electron microscope operating at ambient temperature with and operating voltage of 300 KeV, corresponding to a wavelength of 0.0196 Å. Screening of the TEM grids for micro crystals was done by operating the microscope in over focused diffraction mode to minimize diffraction and hysteresis between screening and diffraction operational modes.

### Electron Diffraction Data Collection Procedure

Electron diffraction data was collected using a TVIPS TemCam-XF416 CMOS 4k x 4k camera. Images were collected in a movie format as crystals were continuously rotated in the electron beam. Typical data collection was performed using a constant tilt rate of 0.3°/s between the

minimum and maximum tilt ranges of -72° to +72°, respectively. During continuous rotation the camera integrated frames continuously at a rate of 3 seconds per frame. The dose rate was calibrated to <0.03 e⁻/Å² s. Crystals selected for data collection were isolated by a selected area aperture to reduce the background noise contributions and calibrated to eucentric height to stay in the aperture over the entire tilt range.

## Crystallographic Data Processing

All diffraction data were processed using the XDS suite of programs [W. Kabsch, *Acta Cryst.* D**66**, 125-132 (2010)]. All structures were solved *ab initio* using direct methods in SHELXT [G.M. Sheldrick, *Acta Cryst.* A**71**, 3–8 (2015)] or SHELXD [G.M. Sheldrick, *Acta Cryst.* D**58**, 1772–1779 (2002)] and refined with SHELXL [G.M. Sheldrick, *Acta Cryst.* C**71**, 3–8 (2015).] using ShelXle [G.M. Sheldrick *J. Appl. Cryst.*, **44**, (2011) 1281-1284].

| | |
|---|---|
| Empirical formula | $C_{106}H_{76}N_4P_2Au_2$ |
| Formula weight (g/mol) | 1861.68 |
| Crystal system | Monoclinic |
| Space group | P2(1)/n (14) |
| Point group | 2 |
| Laue symmetry | 2/m |
| Temperature (K) | 293 |
| Unit cell lengths a, b, c (Å) | 15.240(5), 30.41(1), 23.080(16) |
| Unit cell angles α, β, γ (°) | 90.000, 88.04(6), 90.000 |
| Unit cell volume ($Å^3$) | 10690 |
| F(000) | 3711.2 |
| Z | 4 |
| Density (calculated) (g/cm$^3$) | 1.157 |
| Radiation source, wavelength (Å) | electron, 0.01969 |
| Resolution (Å) | 1.10 |
| Measured reflections | 27672 |
| Unique reflections | 6521 |
| Reflections with $I > 2\sigma(I)$ | 4262 |
| Completeness | 77.6% (3 merged datasets) |
| $I/\sigma$ | 4.68 |
| $\Theta_{max}$, $\Theta_{min}$ (°) | 0.513, 0.071 |
| Index ranges | $-13 \leq h \leq 13$, $-27 \leq k \leq 27$, $-18 \leq l \leq 18$ |
| Refinement method | Full-matrix least-squares on $F^2$ |
| H-atom treatment | H-atom parameters constrained |
| $R[F^2 > 2\sigma(F^2)]$ | 0.131 |
| $wR(F^2)$ | 0.369 |
| Goodness-of-fit on $F^2$ | 1.120 |
| $\Delta\rho_{max}$, $\Delta\rho_{min}$ (e/$Å^3$) | 0.12, -0.15 |
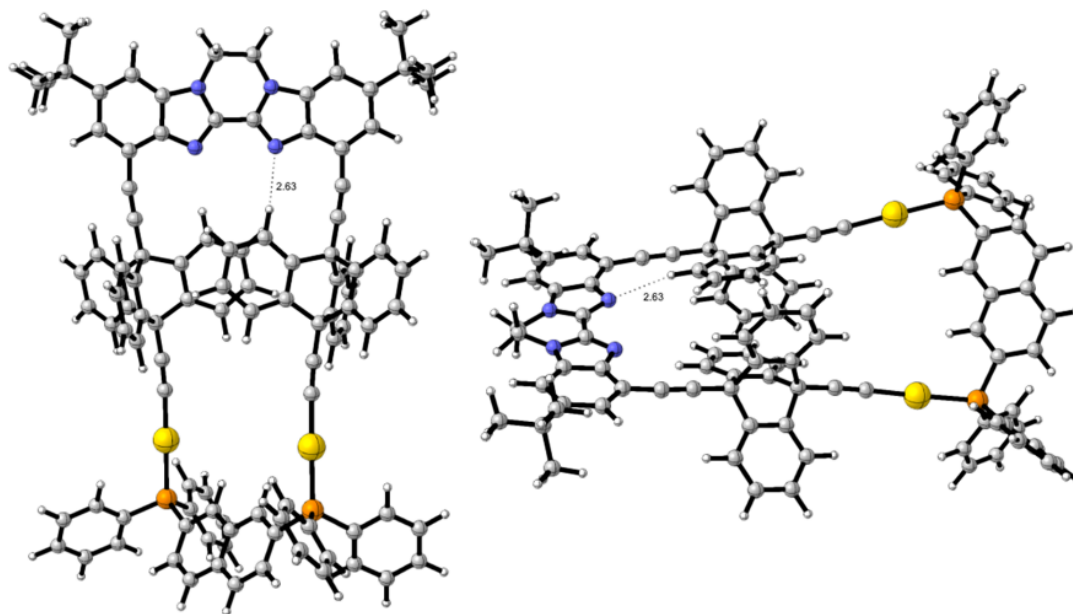
**Figure F.27.** Key hydrogen-bonding interaction in the crystal structure may stabilize the transition state for gearing.
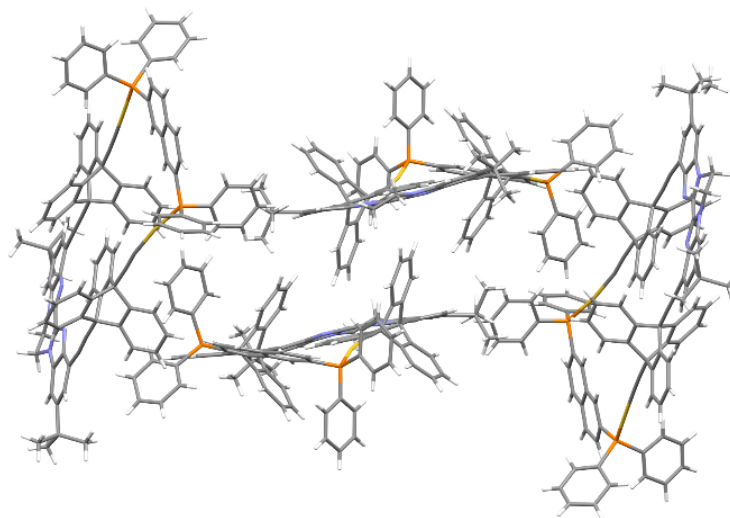


**Figure F.28.** Image detailing the packing arrangement of **10a**.

## Section F5. Computational Methods

**Molecular Dynamics Simulations**

Molecular dynamics simulations were performed using the GPU code (*pmemd*)[3] of the AMBER 16 package.[4] Parameters for the studied gear systems were generated within the *antechamber* module using the general AMBER force field (*gaff*).[5] Parameters involving the $Au^{2+}$ ions were generated with the Metal Center Parameter Builder (*MCPB.py*)[6,7] using optimization and frequency calculations performed in Gaussian 09[8] at the B3LYP[9,10]/6-31G(d) level, with the LANL2DZ basis set and pseudopotential being used for the $Au^{2+}$ ions. Partial charges were set to fit the electrostatic potential generated at the HF/6-31G(d) level by the RESP model,[11] with the LANL2DZ basis set and effective core potential[12] again being used for the $Au^{2+}$ ions. These partial charges were calculated according to the Merz–Singh–Kollman scheme[13,14] using Gaussian 09. Each molecular gear was immersed in a pre-equilibrated truncated octahedral box with a 15 Å buffer of DCM solvent molecules using the *leap* module. All subsequent calculations were done using the widely tested Stony Brook modification of the Amber14 force field (*ff14sb*).[15] DCM molecules were treated with the SHAKE algorithm such that the angle between the hydrogen atoms was kept fixed. Long-range electrostatic effects were modeled using the particle-mesh-Ewald method.[16] An 8 Å cutoff was applied to Lennard–Jones and electrostatic interactions. First, a geometry optimization was performed on each system to minimize the positions of solvent molecules while imposing positional restraints on the molecular gear using a harmonic potential with a force constant of 2 kcal·mol$^{-1}$·Å$^{-2}$. Second, each system was gently and continuously heated over 1 ns from 0 K to 207 K, 247 K and 300 K, respectively, under constant-volume and periodic-boundary conditions. Harmonic restraints of 2 kcal·mol$^{-1}$ were applied to the molecular gear and the Andersen equilibration scheme was used to control and equalize the temperature. The time step was kept at 1 fs during the heating stages, allowing potential inhomogeneities to self-adjust. Third, each system was then equilibrated for a total of 4 ns at constant pressure of 1 atm with a Berendson barostat with a 2 fs time step; harmonic restraints of 2 kcal·mol$^{-1}$ were applied for the first 2 ns and harmonic restraints of 1 kcal·mol$^{-1}$ were applied for the second 2 ns. Finally, production trajectories without harmonic restraints were run for an additional 1 μs under the same simulation conditions.

**Metadynamics**

Metadynamics simulations[17,18] were performed using NAMD v2.13[19] parallel, object-oriented molecular dynamics code. AMBER coordinate and parameter PARM files were used as an input for metadynamics simulations. Collective variables used to construct the free-energy surface[18] were chosen to be the dihedral angles that define each triptycene in the molecular gear. The dihedral angle was defined as an angle between the plane of bibenzimidazole stator and the plane of triptycene blade, and was constrained to change in the -180° to 180° range. Well-tempered metadynamics[20] in conjunction with multiple-walker algorithm was used to accelerate convergence of the free energy landscape. Collective variable space was sampled to a modified temperature T+ΔT, where T was 300 K and ΔT was 100 K. The Langevin thermostat[21] controlled the temperature at 300 K and Langevin barostat kept at the pressure at 1 atm under

periodic-boundary conditions. The system was first minimized for 500 steps and equilibrated for 10 ns to eliminate bad initial contacts. The velocities were then initialized to the desired target temperature, and the simulation was run for 2500000 steps per walker utilizing 10 walkers in total (500 ns). Free energies were calculated and the potential of mean force plot as a function of collective variables was generated.

**Density Functional Theory (NMR Calculations)**

DFT NMR calculations of ground state structure were carried out using Gaussian16. Single point NMR calculations (nmr=giao) with implicit solvent (PCM model) were performed using the B3LYP-D3 functional and the 6-311G(d,p) basis set for nonmetal atoms and the SDD basis set with effective core potential (ECP) for Au. Isotropic shift values were extracted for all hydrogen atoms on intermeshed triptycene gears and scaled accordingly using TMS as a reference. (Table S1).
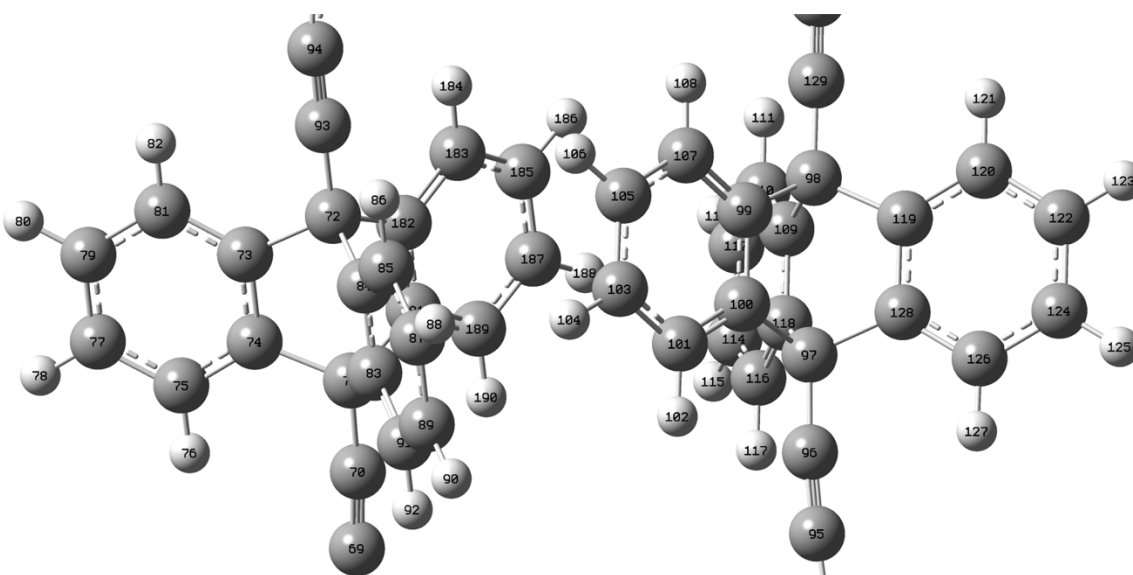


**Figure F.29.** Hydrogen and carbon atom ID numbers on triptycene gears from DFT NMR calculations.

**Table F.1.** Hydrogen atom ID numbers and isotropic shift values (ppm) from DFT NMR calculations of triptycene spur gears. Isotropic shift values were scaled using TMS as a reference. Several hydrogen atom pairs are highlighted in green (H80 and H186) and yellow (H82 and H184) for comparison.

| Triptycene 1 | | | | |
|---|---|---|---|---|
| ID | Atom type | Isotropic (ppm) | TMS Shielding | Scaled (ppm) |
| 76 | H | 23.5651 | 31.8821 | 8.317 |
| 78 | H | 24.5881 | 31.8821 | 7.294 |
| 80 | H | 24.603 | 31.8821 | 7.2791 |
| 82 | H | 23.8577 | 31.8821 | 8.0244 |
| 86 | H | 23.7735 | 31.8821 | 8.1086 |
| 88 | H | 24.5446 | 31.8821 | 7.3375 |
| 90 | H | 24.4752 | 31.8821 | 7.4069 |
| 92 | H | 23.5281 | 31.8821 | 8.354 |
| 184 | H | 22.7955 | 31.8821 | 9.0866 |
| 186 | H | 25.405 | 31.8821 | 6.4771 |
| 188 | H | 27.6923 | 31.8821 | 4.1898 |
| 190 | H | 24.6493 | 31.8821 | 7.2328 |

| Triptycene 2 | | | | |
|---|---|---|---|---|
| ID | Atom type | Isotropic (ppm) | TMS Shielding | Scaled (ppm) |
| 121 | H | 23.8517 | 31.8821 | 8.0304 |
| 123 | H | 24.6006 | 31.8821 | 7.2815 |
| 125 | H | 24.5923 | 31.8821 | 7.2898 |
| 127 | H | 23.566 | 31.8821 | 8.3161 |
| 111 | H | 23.7621 | 31.8821 | 8.12 |
| 113 | H | 24.5219 | 31.8821 | 7.3602 |
| 115 | H | 24.4413 | 31.8821 | 7.4408 |
| 117 | H | 23.5159 | 31.8821 | 8.3662 |
| 102 | H | 24.662 | 31.8821 | 7.2201 |
| 104 | H | 27.6864 | 31.8821 | 4.1957 |
| 106 | H | 25.3965 | 31.8821 | 6.4856 |
| 108 | H | 22.7871 | 31.8821 | 9.095 |

# Section F6. References

1)      Jiang, X.; Duan, H.-B.; Khan, S.I.; Garcia-Garibay, M.A. Diffusion-Controlled Rotation of Triptycene in a Metal-Organic Framework (MOF) Sheds Light on the Viscosity of MOF-Confined Solvent. *ACS Central Science*, **2016**, *2*, 608–613

2)      Wazeer, M. I. M.; Ali, Sk.A.; Arab, M. Synthesis and carbon-13 NMR study of some methanesulfonyloxy and trifluoroacetoxy derivatives of naphthalene. *Spectrochimica Acta, Part A: Molecular and Biomolecular Spectroscopy* **1987**, *6*, 843-847.

3)      Salomon-Ferrer, R.; Götz, A. W.; Poole, D.; Le Grand, S.; Walker, R. C. Routine Microsecond Molecular Dynamics Simulations with AMBER on GPUs. 2. Explicit Solvent Particle Mesh Ewald. *J. Chem. Theory Comput.* **2013**, *9*, 3878–3888.

4)      Case, D. A.; Cerutti, D. S.; Cheatham, III, T. E.; Darden, T. A.; Duke, R. E.; Giese, T. J.; Gohlke, H.; Goetz, A. W.; Greene, D.; Homeyer, N.; Izadi, S.; Kovalenko, A.; Lee, T. S.; LeGrand, S.; Li, P.; Lin, C.; Liu, J.; Luchko, T.; Luo, R.; Mermelstein, D.; Merz, K. M.; Monard, G.; Nguyen, H.; Omelyan, I.; Onufriev, A.; Pan, F.; Qi, R.; Roe, D. R.; Roitberg, A.; Sagui, C.; Simmerling, C. L.; Botello-Smith, W. M.; Swails, J.; Walker, R. C.; Wang, J.; Wolf, R. M.; Wu, X.; Xiao, L.; York, D. M.; Kollman, P. A. AMBER 2017, University of California, San Francisco.

5)      Wang, J. M.; Wolf, R. M.; Caldwell, J. W.; Kollman, P. A.; Case, D. A. Development and Testing of a General Amber Force Field. *J. Comput. Chem.* **2004**, *25*, 1157–1174.

6)      Peters, M. B.; Yang, Y.; Wang, B.; Füsti-Molnár, L.; Weaver, M. N.; Merz, K. M. Structural Survey of Zinc-Containing Proteins and Development of the Zinc AMBER Force Field (ZAFF). *J. Chem. Theory Comput.* **2010**, *6*, 2935–2947.

7)      Li, P.; Merz, K. M. MCPB.py: A Python Based Metal Center Parameter Builder. *J. Chem. Inf. Model.* **2016**, *56*, 599–604.

8)      Gaussian 09, Revision D.01, Frisch, M. J.; Trucks, G. W.; Schlegel, H. B.; Scuseria, G. E.; Robb, M. A.; Cheeseman, J. R.; Scalmani, G.; Barone, V.; Mennucci, B.; Petersson, G. A.; Nakatsuji, H.; Caricato, M.; Li, X.; Hratchian, H. P.; Izmaylov, A. F.; Bloino, J.; Zheng, G.; Sonnenberg, J. L.; Hada, M.; Ehara, M.; Toyota, K.; Fukuda, R.; Hasegawa, J.; Ishida, M.; Nakajima, T.; Honda, Y.; Kitao, O.; Nakai, H.; Vreven, T.; Montgomery, Jr., J. A.; Peralta, J. E.; Ogliaro, F.; Bearpark, M.; Heyd, J. J.; Brothers, E.; Kudin, K. N.; Staroverov, V. N.; Keith, T.; Kobayashi, R.; Normand, J.; Raghavachari, K.; Rendell, A.; Burant, J. C.; Iyengar, S. S.; Tomasi, J.; Cossi, M.; Rega, N.; Millam, J. M.; Klene, M.;

Knox, J. E.; Cross, J. B.; Bakken, V.; Adamo, C.; Jaramillo, J.; Gomperts, R.; Stratmann, R. E.; Yazyev, O.; Austin, A. J.; Cammi, R.; Pomelli, C.; Ochterski, J. W.; Martin, R. L.; Morokuma, K.; Zakrzewski, V. G.; Voth, G. A.; Salvador, P.; Dannenberg, J. J.; Dapprich, S.; Daniels, A. D.; Farkas, O.; Foresman, J. B.; Ortiz, J. V.; Cioslowski, J.; Fox, D. J. Gaussian, Inc., Wallingford CT, 2013.

9)      Becke, A. D. Density  functional Thermochemistry. III. The Role of Exact Exchange. *J. Chem. Phys.* **1993**, *98*, 5648–5652.

10)     Lee, C.; Yang, W.; Parr, R. G. Development of the Colle-Salvetti Correlation-Energy Formula into a Functional of the Electron Density. *Phys. Rev. B* **1988**, *37*, 785–789.

11)     Bayly, C. I.; Cieplak, P.; Cornell, W.; Kollman, P. a. A Well-Behaved Electrostatic Potential Based Method Using Charge Restraints for Deriving Atomic Charges: The RESP Model. *J. Phys. Chem.* **1993**, *97*, 10269–10280.

12)     Hay, P. J.; Wadt, W. R. Ab Initio Effective Core Potentials for Molecular Calculations. Potentials for the Transition Metal Atoms Sc to Hg. *J. Chem. Phys.* **1985**, *82*, 270–283.

13)     Besler, B. H.; Merz, K. M.; Kollman, P. A. Atomic Charges Derived from Semiempirical Methods. *J. Comput. Chem.* **1990**, *11*, 431–439.

14)     Singh, U. C.; Kollman, P. A. An Approach to Computing Electrostatic Charges for Molecules. *J. Comput. Chem.* **1984**, *5*, 129–145.

15)     Maier, J. A.; Martinez, C.; Kasavajhala, K.; Wickstrom, L.; Hauser, K. E.; Simmerling, C. ff14SB: Improving the Accuracy of Protein Side Chain and Backbone Parameters from ff99SB. *J. Chem. Theory Comput.* **2015**, *11*, 3696–3713.

16)     Darden, T.; York, D.; Pedersen, L. Particle Mesh Ewald: An N·log(N) Method for Ewald Sums in Large Systems. *J. Chem. Phys.* **1993**, *98*, 10089.

17)     Laio, A.; Parrinello, M. Escaping free-energy minima. *Proc. Natl. Acad. Sci. U.S.A.* **2002**, *99*, 12562–12566.

18)     Barducci, A.; Bonomi, M.; Parrinello, M. Metadynamics. *Wiley Interdiscip. Rev. Comput. Mol.* **2011**, *1*, 826–843.

19)     Phillips, J. C.; Hardy, D. J.; Maia, J. D. C.; Stone, J. E.; Ribeiro, J. V.; Bernardi, R. C.; Buch, R.; Fiorin, G.; Hénin, J.; Jiang, W.; McGreevy, R.; Melo, M. C. R.; Radak, B. K.; Skeel, R. D.; Singharoy, A.; Wang, Y.; Roux, B.; Aksimentiev, A.; Luthey-Schulten, Z.; Kalé, L. V.; Schulten, K.; Chipot, C.; Tajkhorshid, E. Scalable molecular dynamics on CPU and GPU architectures with NAMD. *J. Chem. Phys* **2020**, *153*, 044130–044163.

20)     Ilott, A. J.; Palucha, S.; Hodgkinson, P.; Wilson, M. R. Well-Tempered Metadynamics as a Tool for Characterizing Multi- Component, Crystalline Molecular Machines. *J. Phys. Chem. B* **2013**, *117*, 12286.

21)     Davidchack, R. L.; Handel, R.; Tretyakov, M. V. Langevin thermostat for rigid body dynamics. *J. Chem. Phys* **2009**, *130*, 234101–234116.

*Appendix G*

*Supporting Information for Chapter 8: Sterically Invariant Carborane-Based*

*Ligands for the Morphological and Electronic Control of Metal−Organic*

*Chalcogenolate Assemblies*

## G1. General Considerations

*Ortho*-$C_2B_{10}H_{12}$ (Boron Specialties) was sublimed prior to use. *Meta*-$C_2B_{10}H_{12}$ (Katchem or Alfa Aesar) was used as is. Anhydrous dichloromethane was obtained from a Grubbs column with activated alumina and copper catalyst. $Se_2Cl_2$ used in the synthesis of **9-HSe-mCB** and **9-HSe-oCB** was prepared according to the procedure found in reference 1 and subsequently stored in a PTFE-capped vial at -15 °C. *Iso*-propanol (200 proof) was purchased from Fisher Sci., Certified ACS quality. *Iso*-propanol used in the synthesis of materials **A-D** was dried by refluxing 100 mL of *iso*-propanol over 5g of elemental magnesium chips with vigorous stirring. After refluxing overnight, the anhydrous *iso*-propanol was distilled under an atmosphere of $N_2$ into a 100 mL Schlenk tube containing activated 3Å molecular sieves. The Schlenk tube was sealed with a Teflon stopper and stored in ambient conditions. Cu(OAc) of 97% purity was purchased from Strem Chemical Inc. and stored in an $N_2$-filled glovebox at -30 °C. All other reagents were purchased from commercial vendors and used as is. All synthesized chalcogenols were stored in an $N_2$-filled glovebox at -30 °C for long term storage. Unless otherwise stated, all reactions were performed under an inert atmosphere of $N_2$ either in a glovebox or using a Schlenk line, and all manipulations were performed under ambient laboratory air, exposed to ambient light.

## G2. Instrumentation

$^1H$, $^{11}B$, and $^{77}Se$ NMR spectra were recorded on either a Bruker DRX500 or Bruker AVIII HD 400 spectrometers in ambient conditions at room temperature. MestReNova v6.0.2-5475 software was used to process the FID data and visualize the spectra. $^1H$ NMR spectra were referenced to residual solvent resonances in deuterated solvents (note: due to high humidity $H_2O$ resonances are often present) and are reported relative to tetramethylsilane ($\delta = 0$ ppm). $^{11}B$ NMR spectra were referenced externally to $Et_2O \cdot BF_3$ ($\delta = 0$ ppm). $^{77}Se$ NMR spectra were referenced externally to diphenyldiselenide ($\delta = 463.15$ ppm). Exponential apodization (5-30 Hz) was applied through MestReNova to $^{77}Se$ spectra in order to enhance the signal to noise ratio.

Elemental analysis of materials **A-D** was performed by Atlantic Microlabs.

Transmission electron microscopy (TEM) was carried out using either an FEI T20 iCorr cryo TEM operated at 200 kV or an FEI T12 TEM operated at 120 kV. TEM samples were prepared by adding 5-10 µL of a colloidal suspension of nanoparticles in *iso*-propanol to a copper grid (200 mesh, Formvar/Carbon or Carbon Film only, Ted Pella, Redding, CA).

Samples prepared for TEM were additionally used for microcrystal electron diffraction (MicroED) experiments. The prepared TEM grid was loaded in a Gatan 626 single-tilt cryo holder and cooled with liquid nitrogen. Screening and data collection were performed using a Thermo-Fisher F200C transmission electron microscope operating at 200 kV corresponding to a wavelength of 0.0251 Å. Electron diffraction data were collected using a Thermo-Fischer Ceta-D CMOS 4k × 4k camera. The screening of crystals was done in low-dose mode and diffraction was identified through condensing of the electron beam. After the selection of a crystal on the grid, the crystal was centered, the eucentric height adjusted by tilting the crystal through the desired rotation range, and the selected area aperture and beam stop were inserted (reference 2). Images were collected in a movie format as crystals were continuously rotated in the electron beam (reference 3). Typical

data collection was performed using a constant tilt rate of 0.3°/s between the minimum and maximum tilt ranges of -72° to +72°, respectively. During continuous rotation, the camera integrated frames continuously at a rate of 3 seconds per frame. The dose rate was calibrated to <0.03 e$^-$/Å$^2$ s. Crystals selected for data collection were isolated by a selected area aperture to reduce the background noise contributions and calibrated to eucentric height to stay in the aperture over the entire tilt range. The electron diffraction data were processed using the XDS suite of programs (reference 4). To achieve a sufficient number of reflections datasets from five different crystals were merged and scaled with XSCALE. The structure was solved *ab initio* using direct methods in SHELXT (reference 5) using ShelXle (reference 6). Structure refinement was performed using electron scattering factors reported by Peng (reference 7). Thermal parameters were refined anisotropically for all non-hydrogen atoms.

Scanning electron microscopy (SEM) was carried out using a ZEISS SUPRAU 40VP Field Emission Scanning Electron Microscope operating at 30 kV. SEM samples were prepared by adding several drops of a colloidal suspension of nanocrystals in *iso*-propanol to a square-cut chip of silicon wafer.

X-ray photoelectron spectroscopy (XPS) measurements were performed on an AXIS Ultra DLD instrument (Kratos Analytical Inc.). Spectra were obtained using a monochromatic AI Kα X-ray source (Filament current: 1.8 A) with a 10 mA emission current and an anode voltage of 15 kV. Survey spectra were conducted with a pass energy of 160 eV, 1 eV step size, and 100 ms dwell time. High-resolution spectra were conducted with a pass energy of 20 eV, 1 eV step size, and 600 ms dwell time. All spectra were measured with automatic charge neutralization and referenced to the adventitious carbon 1s signal at 284.6 eV. XPS data was further processed and peak fitted using CasaXPS Version 2.3.24PR1.0 (reference 8).

Infrared absorption spectra (FTIR) were obtained using a PerkinElmer Spectrum One spectrometer equipped with a universal ATR assembly. Samples were deposited as dry powders.

Thermogravimetric analysis (TGA) was carried out on a PerkinElmer Pyris Diamond TG/DTA under a constant flow of argon gas (200 mL/min). Samples were heated in alumina oxide trays from 25 °C to 500 °C at a rate of 20 °C/min.

Powder X-ray diffraction (PXRD) was conducted using a Panalytical X'Pert Pro X-ray Powder Diffractometer. Samples were deposited as dry powders onto a zero-background sample holder as a level pellet. Samples were diffracted from 5 to 65 2θ with a step size of 0.016°.

UV-Vis absorption measurements were taken using an Ocean Optics Flame Miniature Spectrometer detector and Ocean Optics DH-2000 UV-Vis-NIR source. All samples were suspended in *iso*-propanol and measurements were taken in a 1 cm quartz cuvette.

Fluorescence emission scans were performed using a Horiba Instruments PTI QuantaMaster Series fluorometer equipped with a PMT detector operated under ambient conditions. Dilute suspensions of microcrystals were prepared in *iso*-propanol and measurements were taken in a 1 cm quartz cuvette.

Quantum yield measurements were carried out using a Hamamatsu C9920 system equipped with a xenon lamp, calibrated integrating sphere, and model C10027 photonic multichannel analyzer (PMA). Samples were deposited as dry powders on quartz plates and excited at 290 nm.

Photoluminescence lifetimes were measure by time-correlated single-photon counting using an IBH Fluorocube instrument equipped with an LED excitation source. Samples were deposited as dry powders on quartz plates and were excited at 372 nm and observed at 550 nm.

## G3.    Synthesis    of    Chalcogenols

### Synthesis of 9-SeH-mCB (A')

Synthetic procedures adapted from reference 9. *Meta*-$C_2B_{10}H_{12}$ (1.44 g, 10 mmol) and $AlCl_3$ (1.33 g, 10 mmol, 1 eq) were added to an oven-dried Schlenk flask equipped with a stir bar and rubber septum and evacuated/backfilled with $N_2$ three times. Anhydrous $CH_2Cl_2$ (25 ml), collected from a Grubb's column, was added to the Schlenk flask *via* cannula and the solids were allowed to dissolved. Subsequently, $Se_2Cl_2$ (0.42 mL, 5 mmol, 0.5 eq) was added dropwise to the stirring suspension *via* syringe, forming a dark red solution that was allowed to stir overnight at room temperature. Upon completion of the reaction, determined by TLC, the reaction was carefully quenched by the addition of distilled $H_2O$ (15 mL), yielding a dark yellow, cloudy suspension. The yellow organic layer was separated from the aqueous layer and the aqueous layer was extracted with $CH_2Cl_2$ (3 x 15 mL). The organic layers were combined and dried with $Na_2SO_4$, resulting in a clear yellow/orange solution. The solution was then decanted from the $Na_2SO_4$ and volatiles were removed under reduced pressure to yield the *meta*-carboranyl diselenide. The diselenide was then dissolved in a minimal amount of absolute EtOH (30-50 mL), resulting in a red-orange solution with some solids still suspended (sonication may be required). While stirring the solution of the diselenide, an excess of $NaBH_4$ (0.80 g) was carefully added over the course of several minutes. During the course of the addition, some heat and gas were generated, with the consumption of the diselenide indicated by the reaction mixture turning cloudy and colorless. The reduction was stirred for an additional 15 minutes before the dropwise addition of aqueous HCl (~2M, 10-20 mL) to quench any residual $NaBH_4$ and protonate the selenolate intermediate. Once no more gas was evolved upon addition of HCl, distilled $H_2O$ (200 mL) was added resulting in a foamy, pale yellow suspension. The product was then extracted from the aqueous solution with $CH_2Cl_2$ (4 x 30 mL) and the collected organic layers were dried over $Na_2SO_4$. The dried organic layers were decanted away from the $Na_2SO_4$ and all volatiles were removed under reduced pressure, leaving the crude product as a pale-yellow solid. The crude product was further purified *via* vacuum sublimation at 90 °C, affording the product as a white, crystalline solid in 58% yield with a mild odor.

Yield: 1.3 g (58%), white, odorous solid

All characterization matches literature data, and representative ^{1}H and ^{11}B NMR spectra recorded in $CDCl_3$ have been provided below:
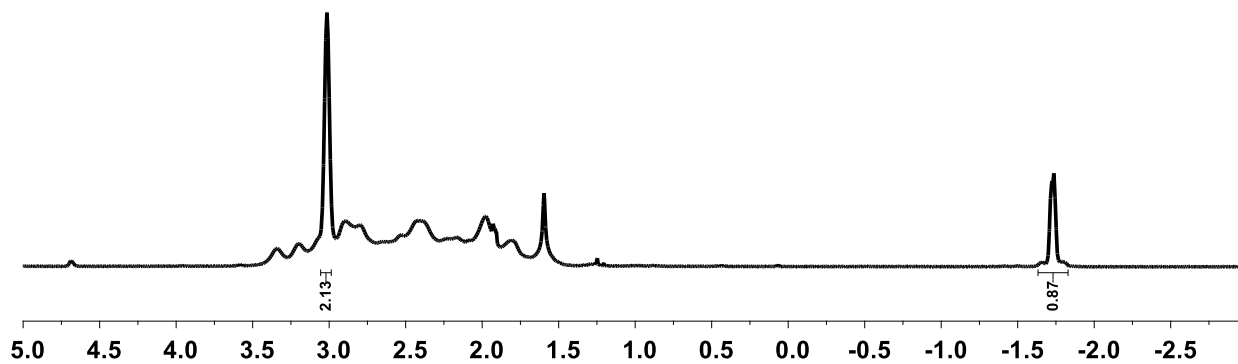
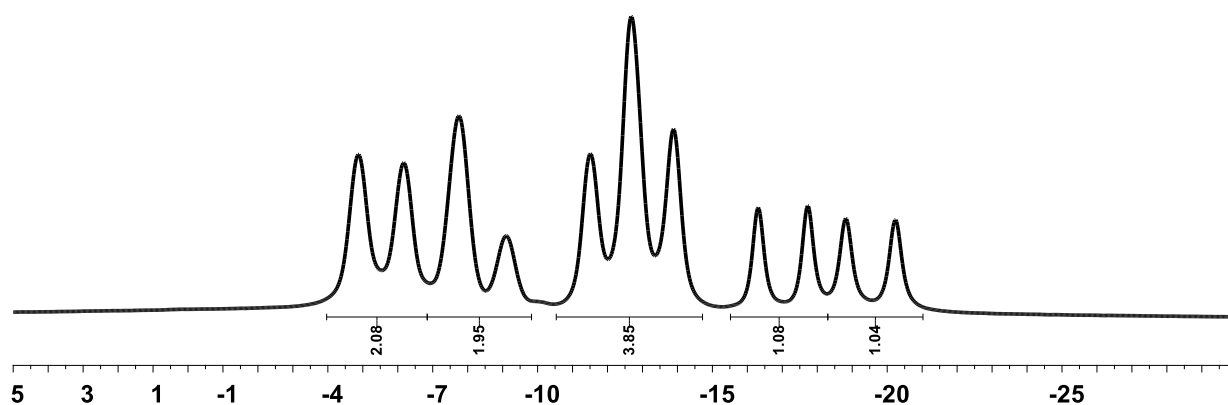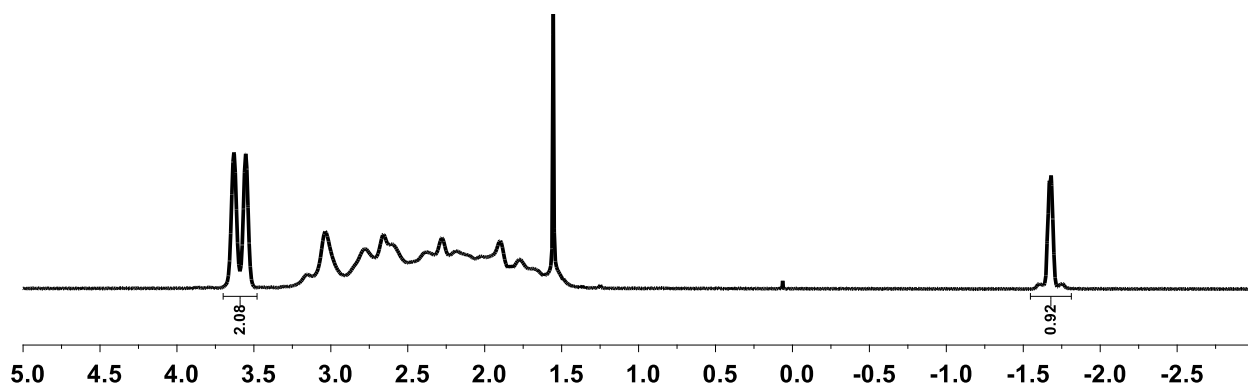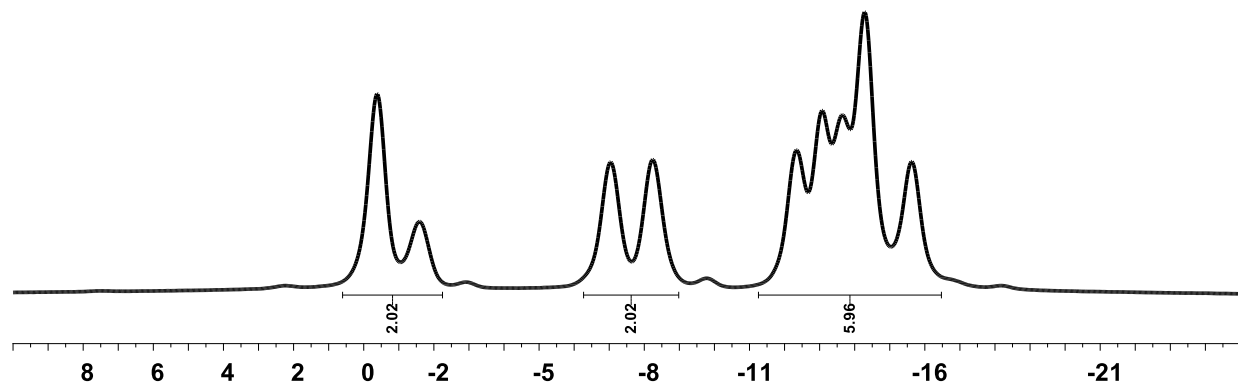**Figure G,1:** $^1$H NMR spectrum of 9-SeH-mCB (**A'**)



**Figure G.2:** $^{11}$B NMR spectrum of 9-SeH-mCB (**A'**)

## Synthesis of 9-SeH-oCB (B')

9-HSe-oCB was prepared in an analogous manner as 9-HSe-mCB, where *ortho*-$C_2B_{10}H_{12}$ was used instead of *meta*-$C_2B_{10}H_{12}$.

Yield: 720 mg (31%), white, odorous solid

All characterization matches literature data, and representative $^1$H and $^{11}$B NMR spectra recorded in CDCl$_3$ have been provided below:
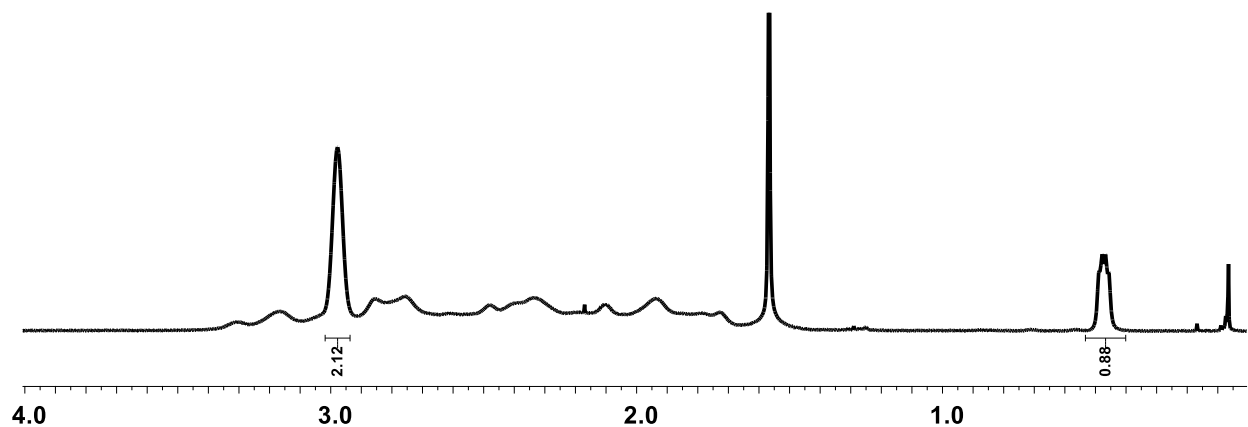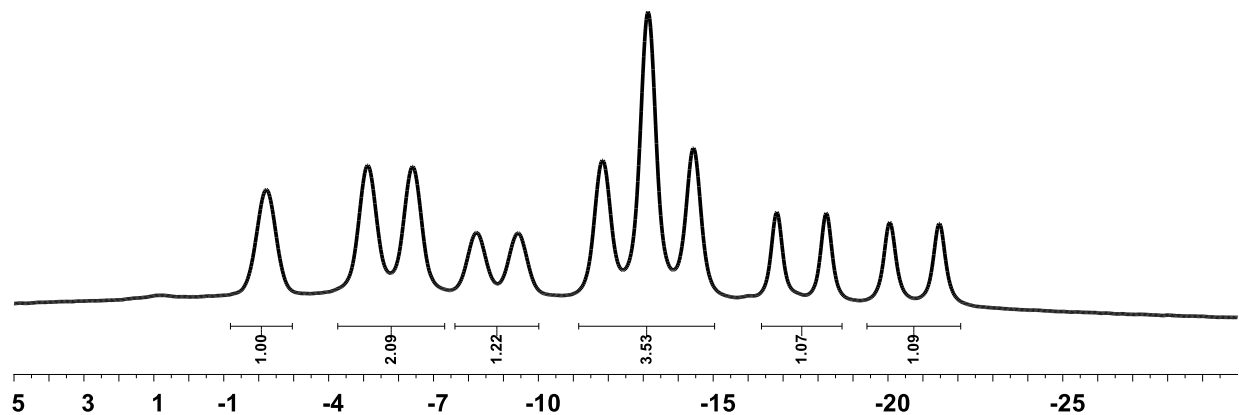
**Figure G.3:** $^1$H NMR spectrum of 9-SeH-oCB (**B'**)



**Figure G.4:** $^{11}$B NMR spectrum of 9-SeH-oCB (**B'**)

## Synthesis of 9-SH-mCB (C')

Synthetic procedures adapted from references 10 and 11. *Meta*-C$_2$B$_{10}$H$_{12}$ (1.44 g, 10 mmol) and AlCl$_3$ (1.33 g, 10 mmol, 1 eq) were added to an oven-dried Schlenk flask equipped with a stir bar and rubber septum and evacuated/backfilled with N$_2$ three times. Anhydrous CH$_2$Cl$_2$ (25 ml), collected from a Grubb's column, was added to the Schlenk flask *via* cannula and the solids were allowed to dissolved. Subsequently, S$_2$Cl$_2$ (0.42 mL, 5 mmol, 0.5 eq) in 2 mL of anhydrous CH$_2$Cl$_2$, was added dropwise to the stirring suspension *via* syringe, forming a red solution that was allowed to stir overnight at room temperature. Upon completion of the reaction, determined by TLC, the reaction was carefully quenched by the addition of distilled H$_2$O (15 mL), yielding a dark yellow, cloudy suspension. The yellow organic layer was separated from the aqueous layer and the aqueous layer was extracted with CH$_2$Cl$_2$ (3 x 15 mL). The organic layers were combined and dried with Na$_2$SO$_4$, resulting in a clear yellow/orange solution. The solution was then decanted from the Na$_2$SO$_4$ and volatiles were removed under reduced pressure to yield the *meta*-carboranyl disulfide. The disulfide was then dissolved in a minimal amount of absolute EtOH (30-50 mL), resulting in a yellow solution (sonication may be required). While stirring the solution of the disulfide, 1-2 chips of NaOH and excess of NaBH$_4$ (0.60 g) was carefully added over the course of several minutes. After completing the addition of NaOH and NaBH$_4$, the flask was capped with a septum and bleed needle before heating to 50 °C for 1 hour. After stirring for 1 hour, the reduction was allowed to cool to room temperature before the dropwise addition of aqueous HCl (~2M, 10-20 mL) to quench any residual NaBH$_4$ and protonate the thiolate intermediate. Once no more gas was evolved upon addition of HCl, distilled H$_2$O (200 mL) was added resulting in a foamy, pale yellow suspension. The product was then extracted from the aqueous solution with CH$_2$Cl$_2$ (4 x 30 mL) and the collected organic layers were dried over Na$_2$SO$_4$. The dried organic layers were decanted away from the Na$_2$SO$_4$ and all volatiles were removed under reduced pressure, leaving the crude product as a pale-yellow solid. The crude product was further purified *via* vacuum sublimation at 90 °C, affording the product as a white, crystalline solid in 78% yield with a mild odor.

Yield: 1.4 g (78%), white, odorous solid

All characterization matches literature data, and representative $^1$H and $^{11}$B NMR spectra recorded in CDCl$_3$ have been provided below:
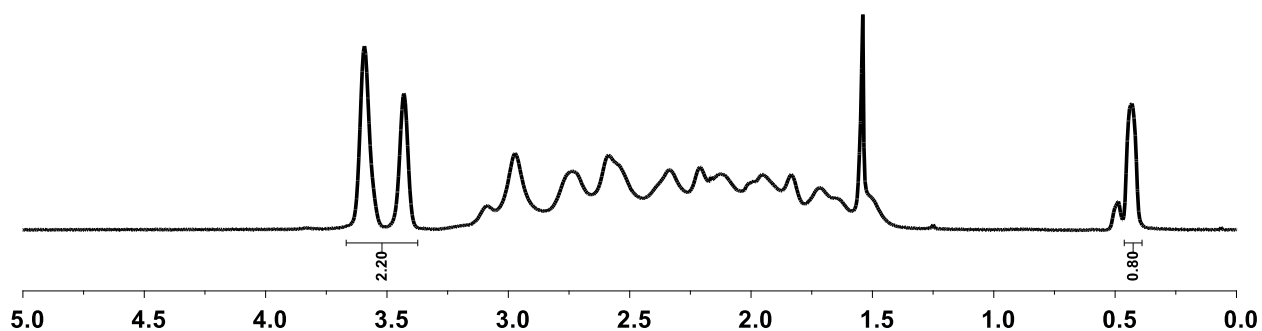


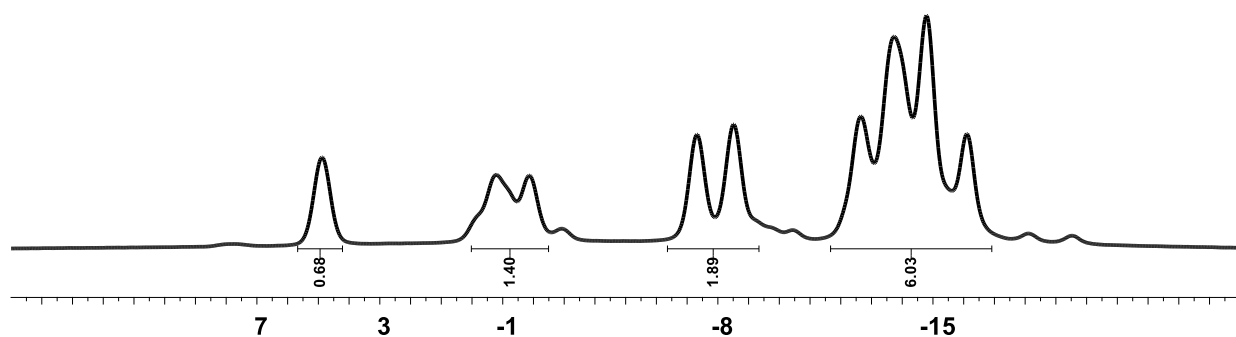**Figure G.5:** $^1$H NMR spectrum of 9-SH-mCB (**C'**)



**Figure G.6:** $^{11}$B NMR spectrum of 9-SH-mCB (**C'**)

**Synthesis of 9-SH-oCB (D')**

9-SH-oCB was prepared in an analogous manner as 9-SH-mCB, where *ortho*-C$_2$B$_{10}$H$_{12}$ was used instead of *meta*-C$_2$B$_{10}$H$_{12}$ and with minor alterations to the reduction procedure. Instead of heating for 1 hour equipped with a bleed needle, the reduction was instead left heating at 50 °C overnight under positive nitrogen pressure. All workup procedures were identical.

Yield: 700 mg (40%), white, odorous solid

All characterization matches literature data, and representative $^1$H and $^{11}$B NMR spectra recorded in CDCl$_3$ have been provided below:

**Figure G.7:** $^1$H NMR spectrum of 9-SH-oCB (**D'**)



**Figure G.8:** $^{11}$B NMR spectrum of 9-SH-oCB (**D'**)

## 4.  Synthesis of MOCHAs (A-D)

### General Procedures

An oven-dried 4 mL dram vial equipped with a stir bar and PTFE septa cap was transferred into a N$_2$-filled glovebox. In the glovebox, chalcogenol (0.11 mmol; 1.1 eq) and anhydrous copper(I) acetate (12 mg, 0.1 mmol; 1 eq) were subsequently added to the dram vial and sealed with the PTFE cap. The vial was then transferred out of the glove box and anhydrous *iso*-propanol (1 mL, see SI sec. 1 for drying and storage procedures) was quickly added *via* syringe and the resulting suspension was immediately stirred at ~700 rpm. The reaction vial was then covered to limit exposure to light and then left to stir for 24 hours.

After stirring for 24 hours, the reaction appeared as milky white, off-white, or pale-yellow suspension. The suspension mixture was then transferred to a pre-weighed screw-capped tube suitable for centrifugation. Additional *iso*-propanol (non-anhydrous) was added to the reaction vial to maximize transfer of product to the screw-capped tube. The suspension was then centrifuged at 2900xg until all material was pelleted at the bottom of the tube (10 minutes). Once pelleted, the supernatant (*iso*-propanol, excess chalcogenol) was decanted from the tube and additional *iso*-propanol (2 mL, non-anhydrous) was added. The screw-capped tube was then vortexed to resuspend all powder before centrifuging once more, and the supernatant decanted. The above

process was repeated once more before drying the pellet on a high-vacuum Schlenk line while in the screw-capped tube to remove all volatiles. After drying, materials **A-D** were afforded as free-flowing powders of varying fluffiness.

Yields:

Cu-[9-Se-mCB] (**A**), off-white/pale-yellow powder: 22 mg, 76%

> **Elemental Analysis**: Calculated for $CuSeC_2B_{10}H_{11}$: C, 8.41; H, 3.88; found: C, 8.87; H, 3.78 (average of two duplicate runs)

Cu-[9-Se-oCB] (**B**), off-white/pale-yellow powder: 19 mg, 65%

> **Elemental Analysis**: Calculated for $CuSeC_2B_{10}H_{11}$: C, 8.41; H, 3.88; found: C, 8.66; H, 3.79

Cu-[9-S-mCB] (**C**), off-white/light grey powder: 21 mg, 84%

> **Elemental Analysis**: Calculated for $CuSC_2B_{10}H_{11}$: C, 10.06; H, 4.64; found: C, 10.31; H, 4.63

Cu-[9-S-oCB] (**D**), off-white/light grey powder: 17 mg, 69%

> **Elemental Analysis**: Calculated for $CuSC_2B_{10}H_{11}$: C, 10.06; H, 4.63; found: C, 11.27; H, 4.86 (average of two duplicate runs). In the case of **D**, the experimental analysis deviates more significantly from the calculated values than the other three samples. However, when calculated with an impurity of *iso*-propanol (~10%), the calculated percent composition (C, 11.28; H, 4.86) matches the experimental data nearly exactly. These results suggest that the deviation between experimental and theoretical percent composition can be attributed to a small amount of *iso*-propanol impurity.

## G5.  Supplementary Characterization and Data of A
### a.  Additional Electron Microscopy Images

**Scanning Electron Microscopy**
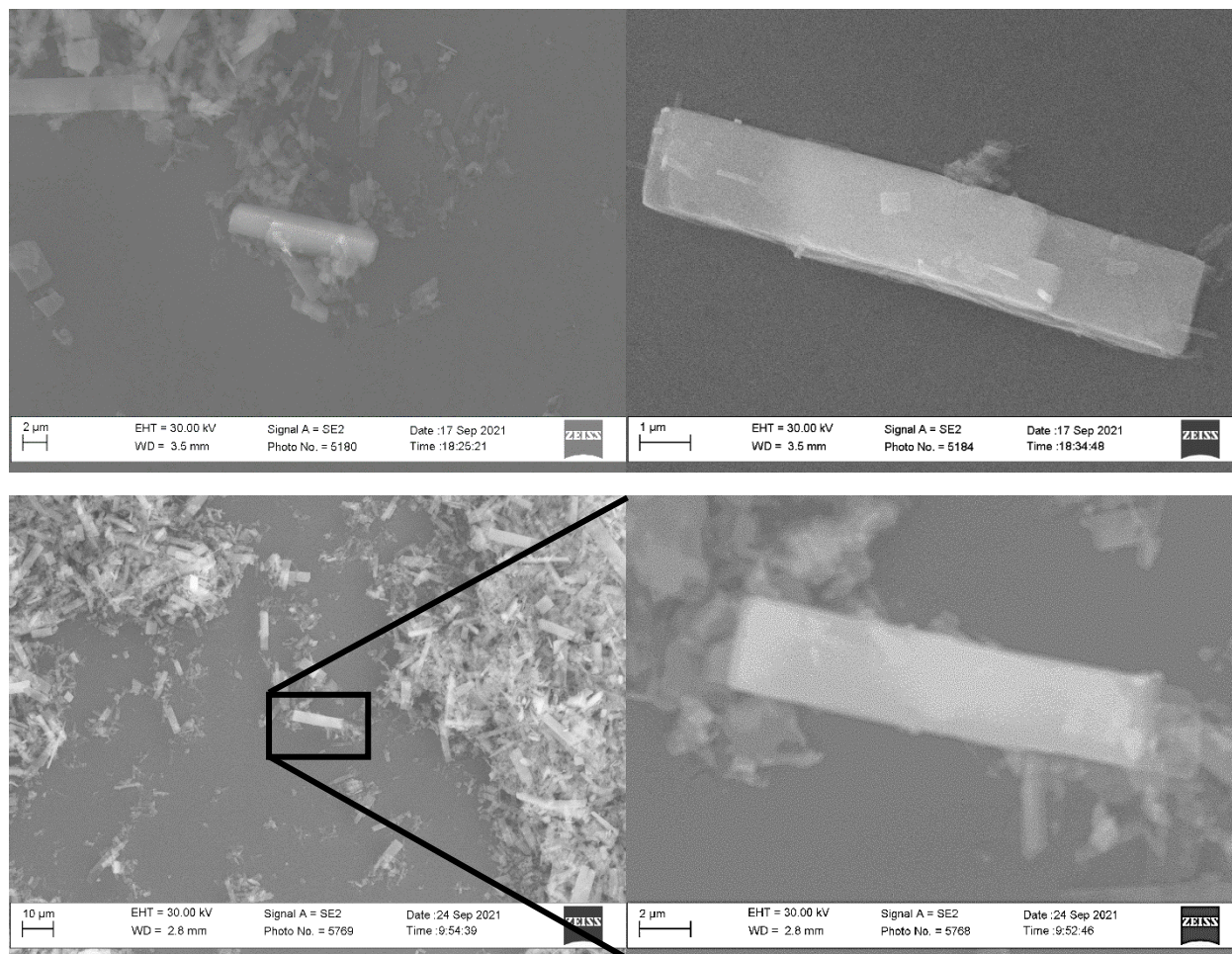


**Figure G.9:** SEM images of **A** microcrystals deposited on a silicon wafer chip. SEM images reveal a consist crystallite morphology throughout the bulk material. Crystallites are typically between 5-10 μm in length and 1-2 μm in width. While there are some crystallites that exceed these dimensions, they maintain a consistent morphology of square rods.

**Transmission Electron Microscopy**
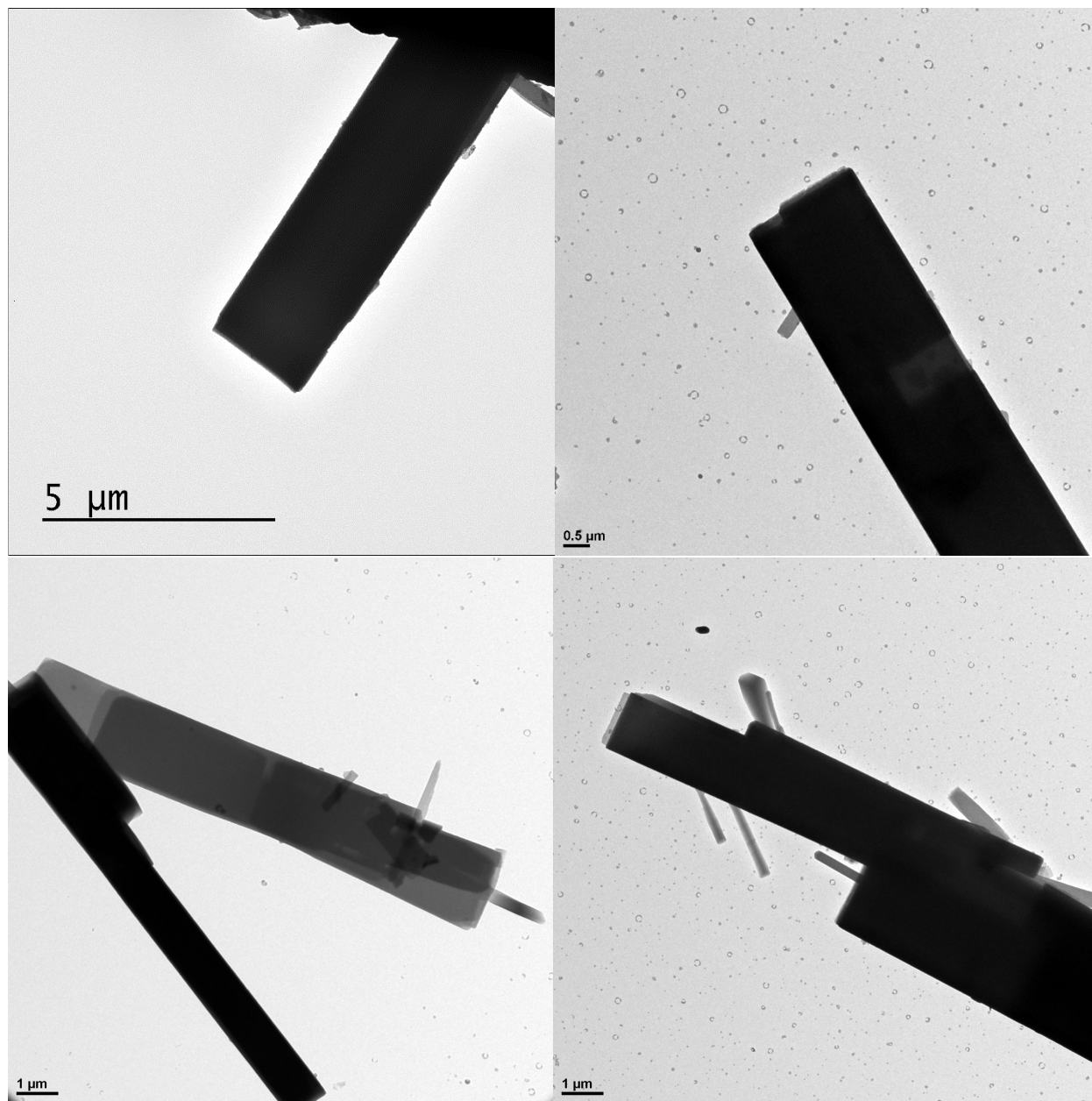


**Figure G.10:** TEM images of **A** microcrystals deposited a copper grid (200 mesh, Formvar/ Carbon or Carbon Film only). TEM images reveal the presence of rod-like microcrystals generally 5-10 µm in length and 1-2 µm in width. There is also evidence of smaller rods as shown in the bottom right TEM image.

**b. Powder X-ray Diffraction Pattern**
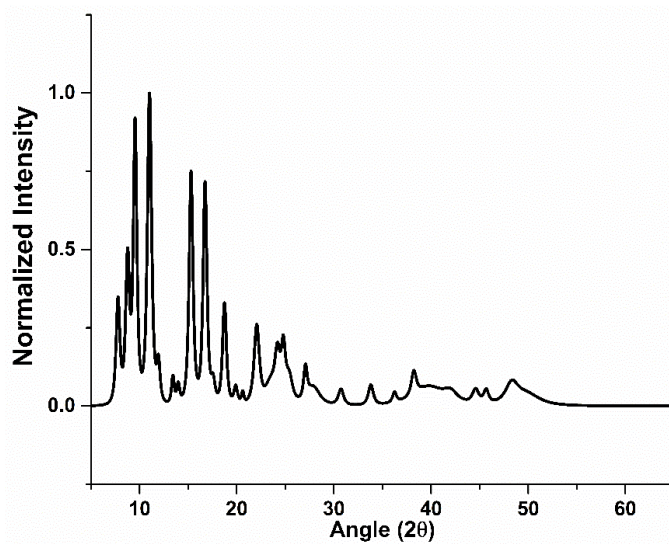


**Figure G.11:** Powder X-ray diffraction pattern of **A** microcrystals deposited on a zero-background plate. Sample was diffracted from 5.000° to 65.000° with a step size of 0.016°. See included spreadsheet for peak list and corresponding intensities.

**Cryo PXRD of A to Determine Effect of Thermal Contraction on PXRD Pattern**
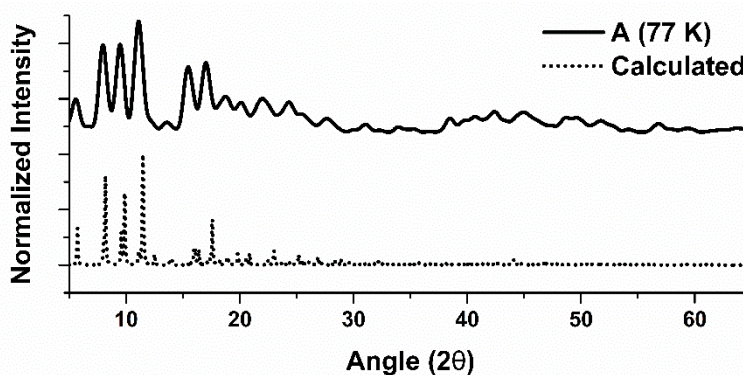


**Figure G.12:** Stacked cryo (100K) and calculated from MicroED PXRD patterns.

When comparing the ambient temperature PXRD pattern of **A** with the calculated PXRD pattern determined from the MicroED structure, some deviations between the diffraction peaks was evident. To confirm that these differences were a result of thermal contraction/expansion from the two pieces of data obtained at separate temperatures, Cryo PXRD (depicted above) experiments were performed. The powder diffraction data were measured at 100K(2) on a Bruker Smart Apex2 CCD-based X-ray diffractometer system equipped with a micro-focus Cu-Kα radiation (λ = 1.54 Å). A total of 5 frames were collected to cover the entire 2-theta range. The frames were integrated with the Bruker Pilot software package (Apex v2014) to obtain the raw data file to plot and analyze the data. Importantly, the diffractions peaks matched the calculated PXRD almost exactly, suggesting that the previously observed deviations are likely attributed to thermal contraction/expansion of the crystallites.

## c. Infrared Spectroscopy
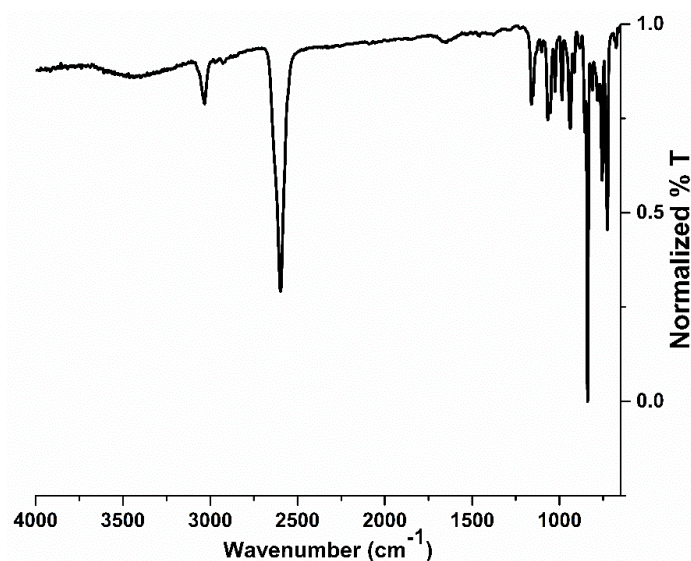


**Figure G.13:** FTIR spectrum of **A**.

FTIR spectrum of **A** reveals no signals that could be correlated to residual starting material (CuOAC (C=O: ~1500 cm$^{-1}$), HSe-mCB (H-Se: ~2250 cm$^{-1}$), *iso*-propanol (H-C: ~3000 cm$^{-1}$; H-O: ~3500 cm$^{-1}$)). Two diagnostic resonances attributed to the carborane cluster (H-C$_{carborane}$: 3000 cm$^{-1}$; H-B$_{carborane}$: 2700 cm$^{-1}$) are present and are expected to be symmetric as a function of the *meta*-carboranyl-selenolate symmetry.

## d. Thermogravimetric Analysis
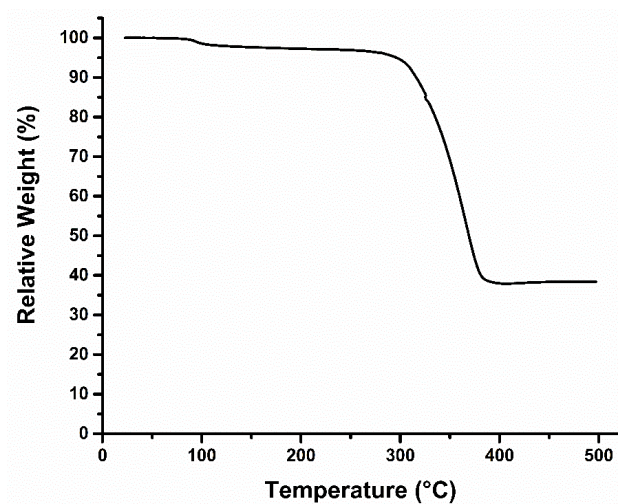


**Figure G.14:** TGA of **A**.

TGA of **A** indicates the material is thermally stable until 300 °C, after which, the material decomposes until reaching 40% relative weight at 375 °C. There is no evident desolvation step that would indicate the presence of solvent adducts within the material, which would be expected near 100 °C.

### e.   X-ray Photoelectron Spectroscopy
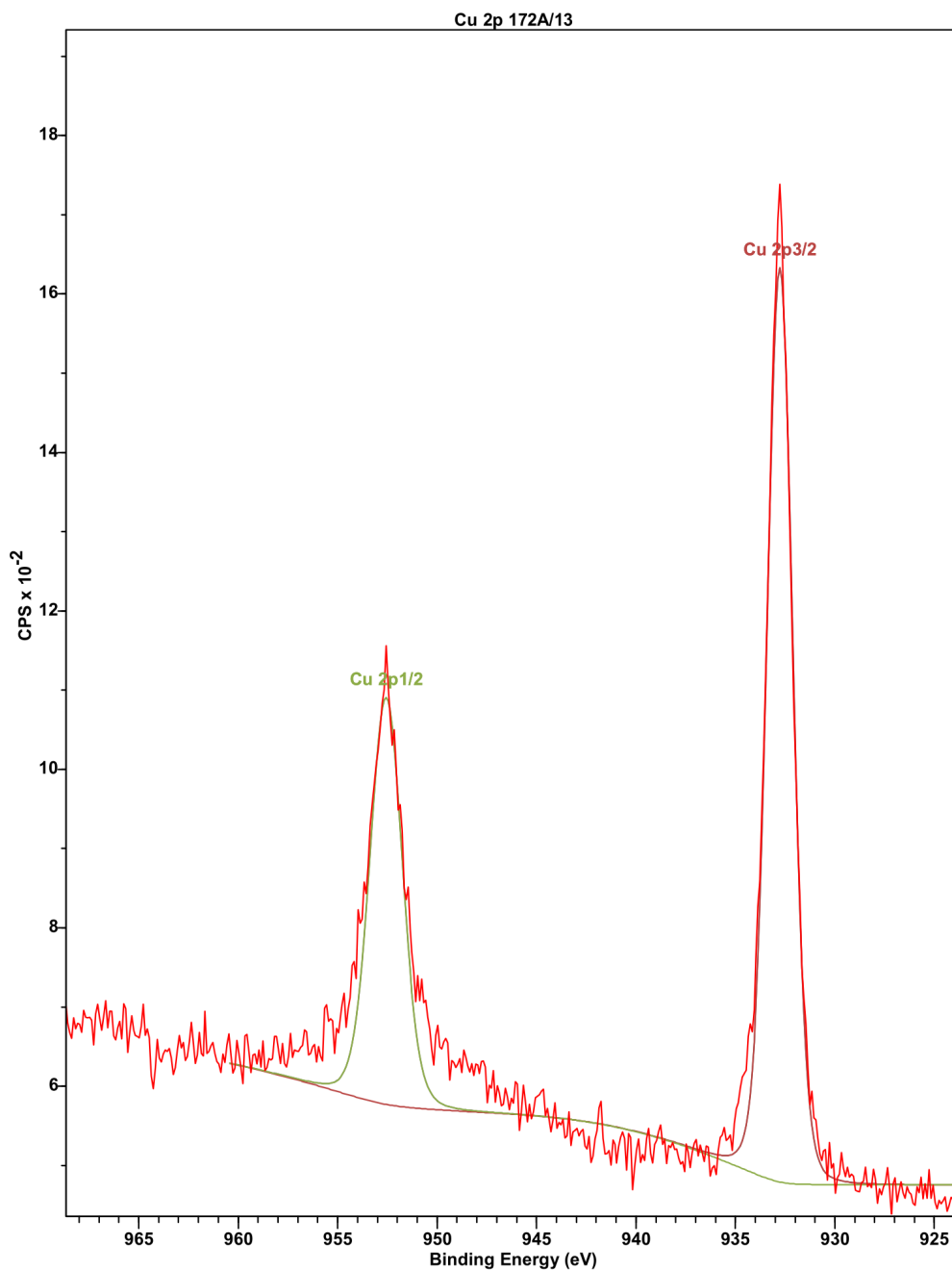


**Figure G.15:** Cu *2p* XPS region of **A**.

XPS data of **A** was processed and peak-fitted using CasaXPS. Peak fitting indicates the presence of only a single copper(I) environment, and is in agreement with all other structural characterization.
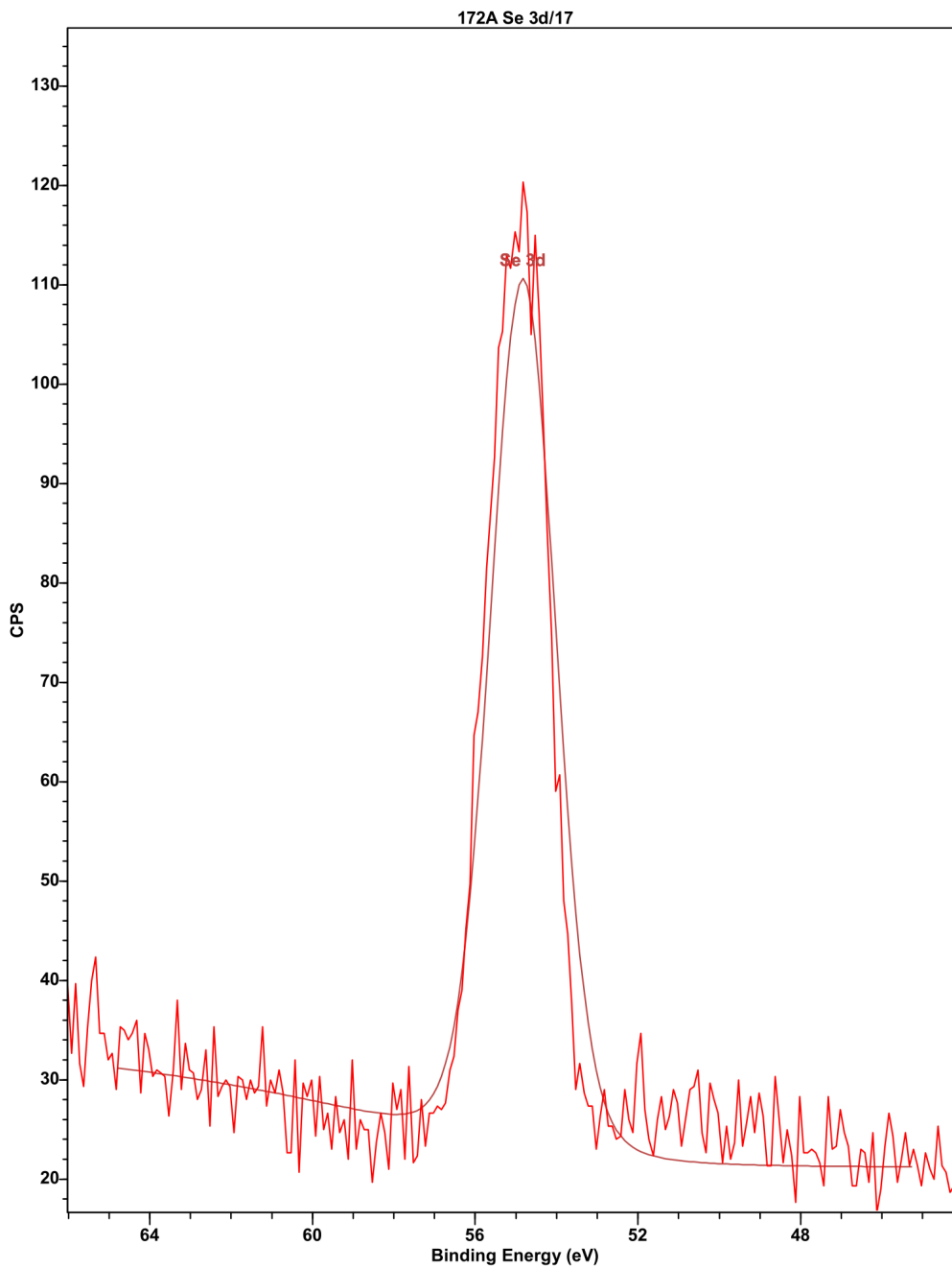
**Figure G.16:** Se *3d* XPS region of **A**.

XPS data of **A** was processed and peak-fitted using CasaXPS. Peak fitting indicates the presence of only a single selenolate environment, and is in agreement with all other structural characterization.

### f. Photophysical Measurements

**Absorption and Emission Measurements**
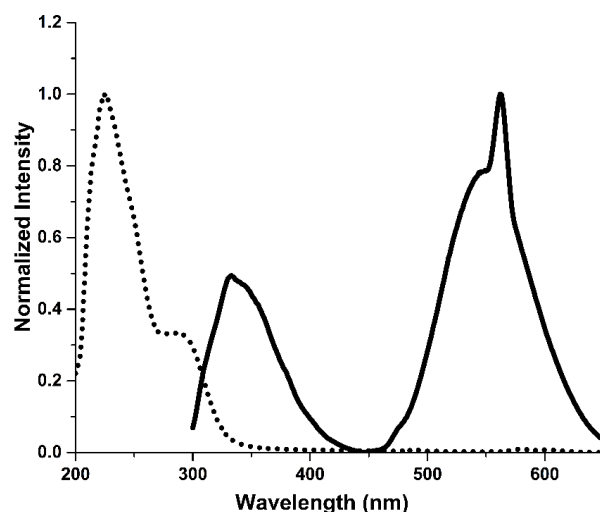


**Figure G.17:** Absorption (dotted trace) and emission (solid trace) spectra of **A**.

Absorption (dotted trace) and emission (solid trace) of **A** have been normalized and plotted on the same set of axes. Both measurements were performed on suspension of **A** in *iso*-propanol. Emission spectrum was obtained by exciting the suspension with 280 nm light, and the emission was monitored between 300-650 nm. The sharp peak at 560 nm is an artifact of the excitation wavelength (280 nm), and is not a result of emission from **A**.

**Comparison of Emission Intensity at Different Excitation Wavelengths**
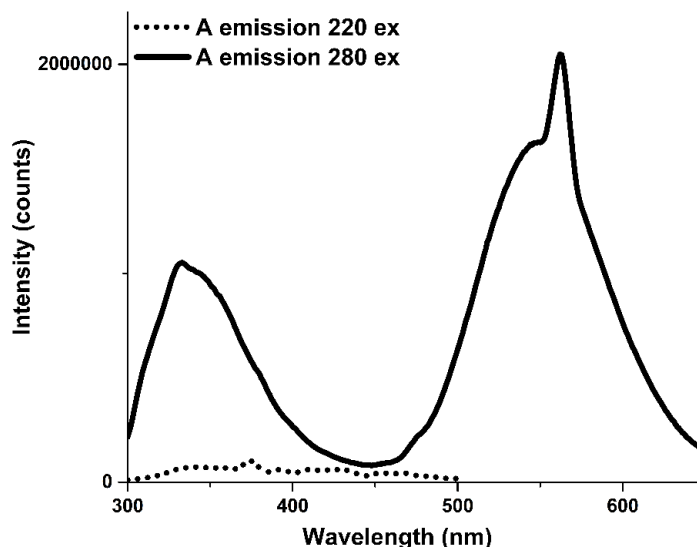


**Figure G.18:** Comparison of emission intensity at different excitation wavelengths.

Emission traces when exciting a suspension of **A** in *iso*-propanol at 220 nm (dotted trace) and 280 nm (solid trace). Negligible emission can be correlated to excitation at 220 nm.
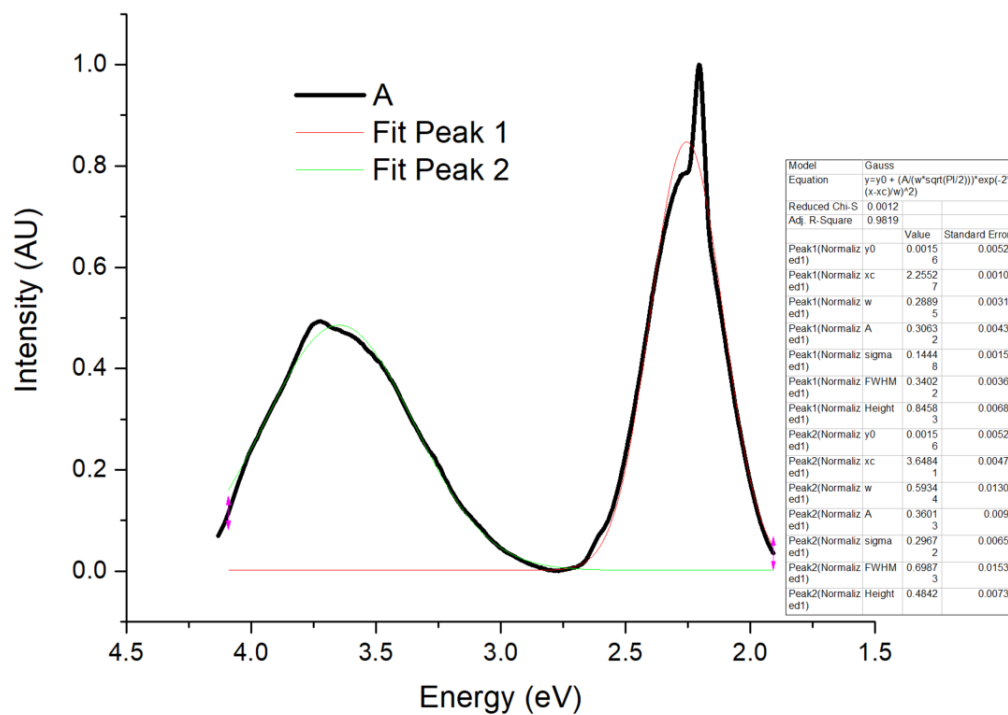
## Quantum Yields



**Figure G.19:** Peak fitting of **A** emission used to determine the relative peak integrations of the high (54%) and low (46%) energy transitions.
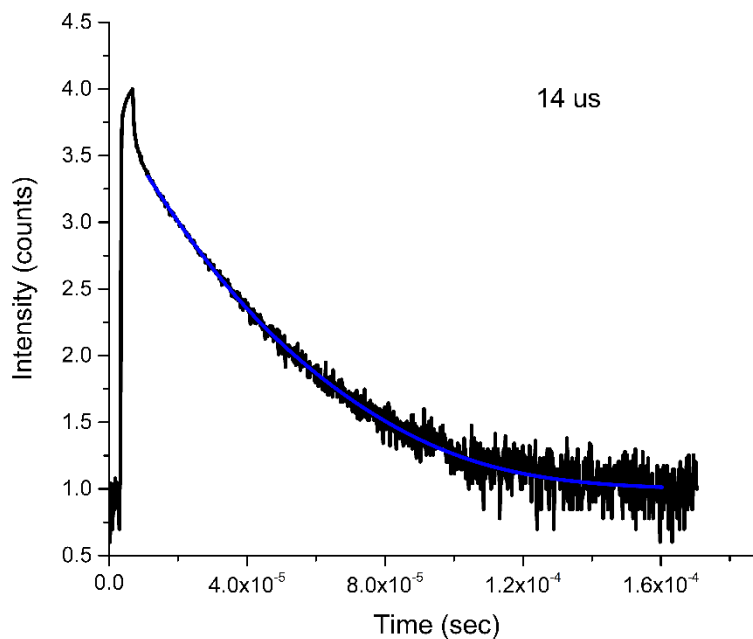
## Lifetime Measurements



**Figure G.20:** Lifetime plot of **A**, indicating a lifetime emission of 14 μs.

## g. DFT Calculations

DFT calculations of **A** were performed using B3LYP functional with DZP basis set. The crystallographically derived structure by MicroED was used for calculations of the molecular orbitals of **A**. The calculated HOMO-LUMO gap is 4.35 eV, corresponding to 285 nm.

Atomic Coordinates:

| | | | | | | | |
|---|---|---|---|---|---|---|---|
| B | -4.46822700 | 9.01069500 | 18.61489900 | B | 3.56649000 | 8.26239800 | 22.42978100 |
| B | 2.67677300 | 9.14329000 | 13.97659400 | B | -1.44958400 | 9.63446800 | 20.04894900 |
| C | 1.40147700 | 1.08382000 | 19.78681100 | C | 4.23724700 | 6.82576000 | 14.39293100 |
| B | 3.75695800 | 9.43154000 | 25.08508800 | B | 2.14388000 | 8.67056000 | 24.91546900 |
| Se | 3.12285800 | 8.50222200 | 18.31883700 | B | -3.52080000 | 7.72164100 | 19.42598600 |
| Se | -0.69886300 | 6.62975000 | 19.00656400 | C | -4.19295700 | 9.05450900 | 20.34192700 |
| Cu | 1.19179600 | 7.61441200 | 18.77218200 | B | 4.34832100 | 8.54373000 | 14.09995300 |
| B | 3.06332300 | 8.08253000 | 16.55480100 | B | 0.60838600 | 2.06617600 | 18.58405900 |
| B | 3.48353900 | 6.50292000 | 15.95034100 | C | 4.56008700 | 9.19517500 | 23.54926600 |
| B | 3.19123100 | 2.90440700 | 17.67120100 | H | 4.98652400 | 6.18008000 | 14.04444200 |
| C | -3.28887600 | 10.13487000 | 17.97343100 | H | 0.70864300 | 7.71357000 | 13.73912800 |
| C | 1.64189100 | 7.74816000 | 14.21714500 | H | 0.82702400 | 0.50732000 | 20.45603500 |
| B | 2.92167000 | 0.45428200 | 19.18851900 | H | 3.59027200 | 0.63415000 | 16.84161100 |
| C | 2.34608400 | 10.39198900 | 24.66875000 | H | 5.60412300 | 9.08564000 | 23.51225800 |
| B | -2.96256200 | 10.22480400 | 20.77985200 | H | 1.95299500 | 11.06880000 | 25.37498200 |
| B | 3.10836100 | 7.55215000 | 13.27036300 | H | -4.99397600 | 8.87810000 | 21.00189900 |
| B | 1.49566000 | 0.58803000 | 18.09987400 | H | -3.50563200 | 10.66525000 | 17.08832900 |
| B | 3.86260000 | 10.76556100 | 23.87308400 | H | 1.21329880 | 4.55124948 | 18.03426446 |
| B | -4.11272500 | 10.56263300 | 19.45990900 | H | 0.97645698 | 3.64404127 | 20.68729267 |
| B | 1.66406300 | 2.12152000 | 17.17159700 | H | -0.57788637 | 2.13620653 | 18.50576360 |
| B | 3.73986800 | 10.02994700 | 22.24474300 | H | 3.32730396 | 1.70452228 | 21.43648619 |
| B | -2.37503300 | 10.92236900 | 19.24403100 | H | 5.11632103 | 1.96134113 | 19.24200738 |
| B | 2.56511100 | 6.28385000 | 14.42993900 | H | 3.38467358 | -0.59713361 | 19.50125489 |
| C | 3.07051400 | 1.15300000 | 17.59410200 | H | 1.08300532 | -0.28661754 | 17.39941833 |
| B | 2.31381200 | 10.80130400 | 22.96947800 | H | 3.75676724 | 3.76550436 | 17.06947936 |
| B | 2.13885600 | 9.27012000 | 22.08437600 | H | 1.26563348 | 2.22851144 | 16.05513101 |
| B | -1.65209500 | 9.60449000 | 18.27874500 | H | -4.94569154 | 11.34103548 | 19.81427006 |
| Se | 4.07544500 | 4.64428400 | 20.12296500 | H | -3.90091593 | 6.59685371 | 19.52087693 |
| Cu | 3.46166800 | 6.50637900 | 19.21627500 | H | -5.39629337 | 8.84360624 | 17.88005707 |
| B | 3.01124800 | 3.25261300 | 19.35813800 | H | -3.41012589 | 8.10153648 | 16.85806986 |
| B | 1.81745700 | 7.10248000 | 15.83623400 | H | -2.08084574 | 7.84781518 | 21.64067151 |
| B | 3.96986500 | 1.87939000 | 18.91712900 | H | -0.38277667 | 9.82436143 | 20.53899804 |
| B | 1.25105000 | 9.51916800 | 23.61402900 | H | -2.99342150 | 10.84923110 | 21.79282831 |
| B | -2.94758200 | 8.42843000 | 17.89324800 | H | -0.74201764 | 9.80177943 | 17.53641460 |
| Se | 1.18177600 | 6.34495900 | 23.00648500 | H | -1.86410918 | 11.99125588 | 19.39687578 |
| Cu | 2.56444700 | 5.49404500 | 21.51383900 | H | 3.80896452 | 5.43441895 | 16.37450674 |
| B | 2.09148000 | 8.04217500 | 23.30563100 | H | 1.94917826 | 5.30598957 | 14.12810262 |
| B | 1.87898600 | 8.86657000 | 15.55559200 | H | 3.40587408 | 7.35456458 | 12.13103978 |
| B | 2.89547700 | 1.82174000 | 20.33267500 | H | 5.30797584 | 9.05590660 | 13.57226127 |
| Cu | 0.29477800 | 6.57210000 | 21.01423500 | H | 2.11920473 | 10.00854801 | 13.36473020 |
| B | -1.86125400 | 8.17131100 | 19.22244300 | H | 3.94015672 | 10.40617644 | 15.88537625 |
| B | 3.58421200 | 9.33930000 | 15.49391200 | H | 1.23402597 | 9.67514048 | 16.14998230 |
| B | 1.45583300 | 2.82485000 | 19.96259800 | H | 0.92888442 | 6.57742719 | 16.42525283 |
| B | 3.57325900 | 7.90266200 | 24.18456600 | H | 5.64474423 | 7.94354013 | 16.29567166 |
| B | -2.59289500 | 8.47339700 | 20.76134900 | H | 3.98832985 | 6.85339983 | 24.56834531 |
| B | 4.58868500 | 7.89805000 | 15.74679800 | H | 4.50354687 | 11.78241792 | 23.95253690 |
| B | 1.64885800 | 3.48321300 | 18.31883700 | H | 1.97357490 | 11.93316070 | 22.77050855 |

| | | | |
|---|---|---|---|
| H | 1.58025130 | 8.17737769 | 25.84094306 |
| H | 4.31110459 | 9.49062940 | 26.13875402 |
| H | 0.05096366 | 9.66278452 | 23.54141361 |

| | | | |
|---|---|---|---|
| H | 4.01843285 | 7.48395087 | 21.65332006 |
| H | 4.28522433 | 10.33224774 | 21.24294425 |
| H | 2.26418057 | 9.67616380 | 20.98354805 |

### G6. Supplementary Characterization and Data of B
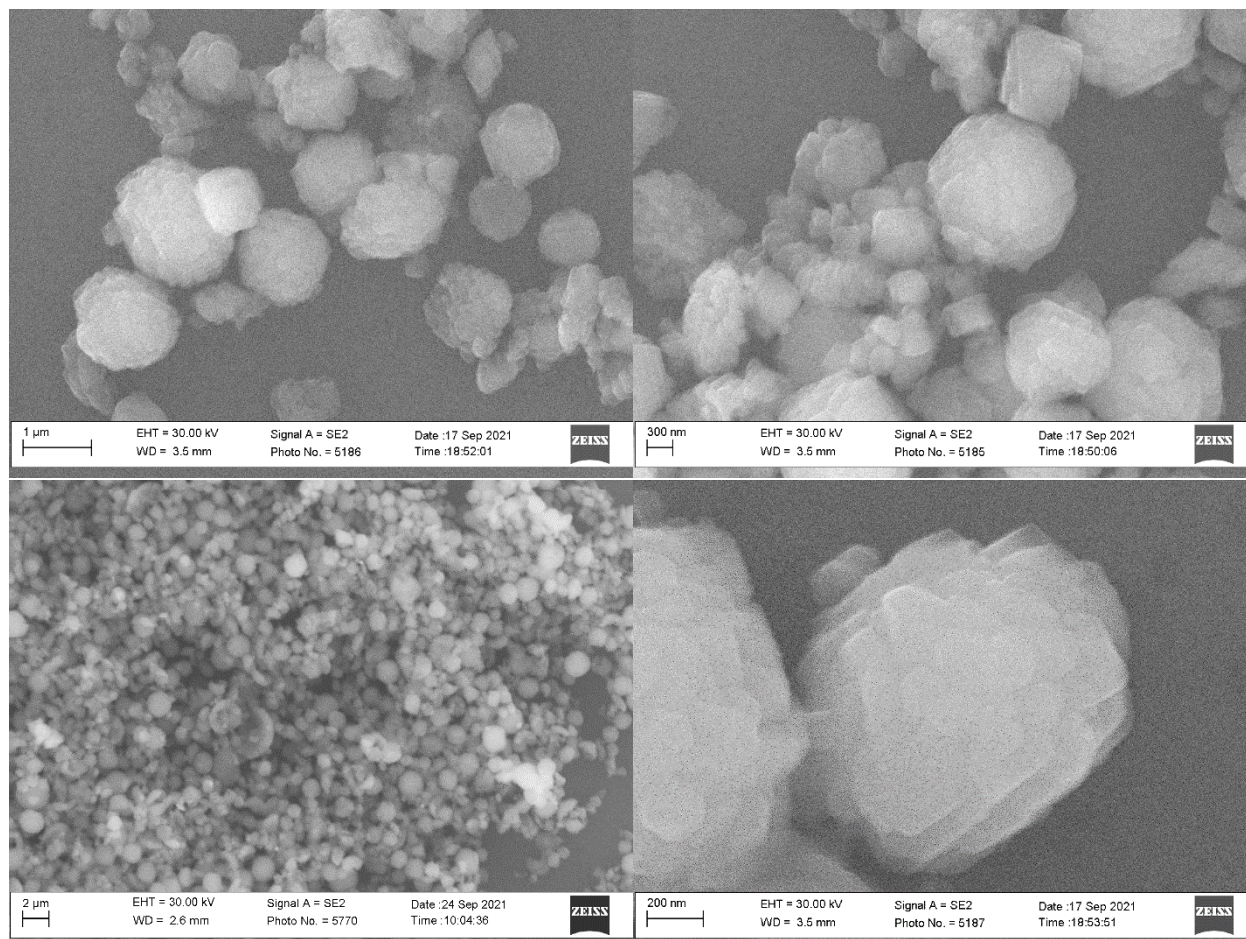### a. Additional Electron Microscopy Images

**Scanning Electron Microscopy**



**Figure G.21:** SEM images of **B** microcrystals deposited on a silicon wafer chip. SEM images reveal a microscale particle phase present in bulk **B**. The upper two images were used to determine the average microscale particle size to be 1.10 μm ± 0.31 in diameter. While spherical in nature, in higher magnification images (bottom right), the particles appear to be comprised of platelets stacked on top of one another.

**Transmission Electron Microscopy**
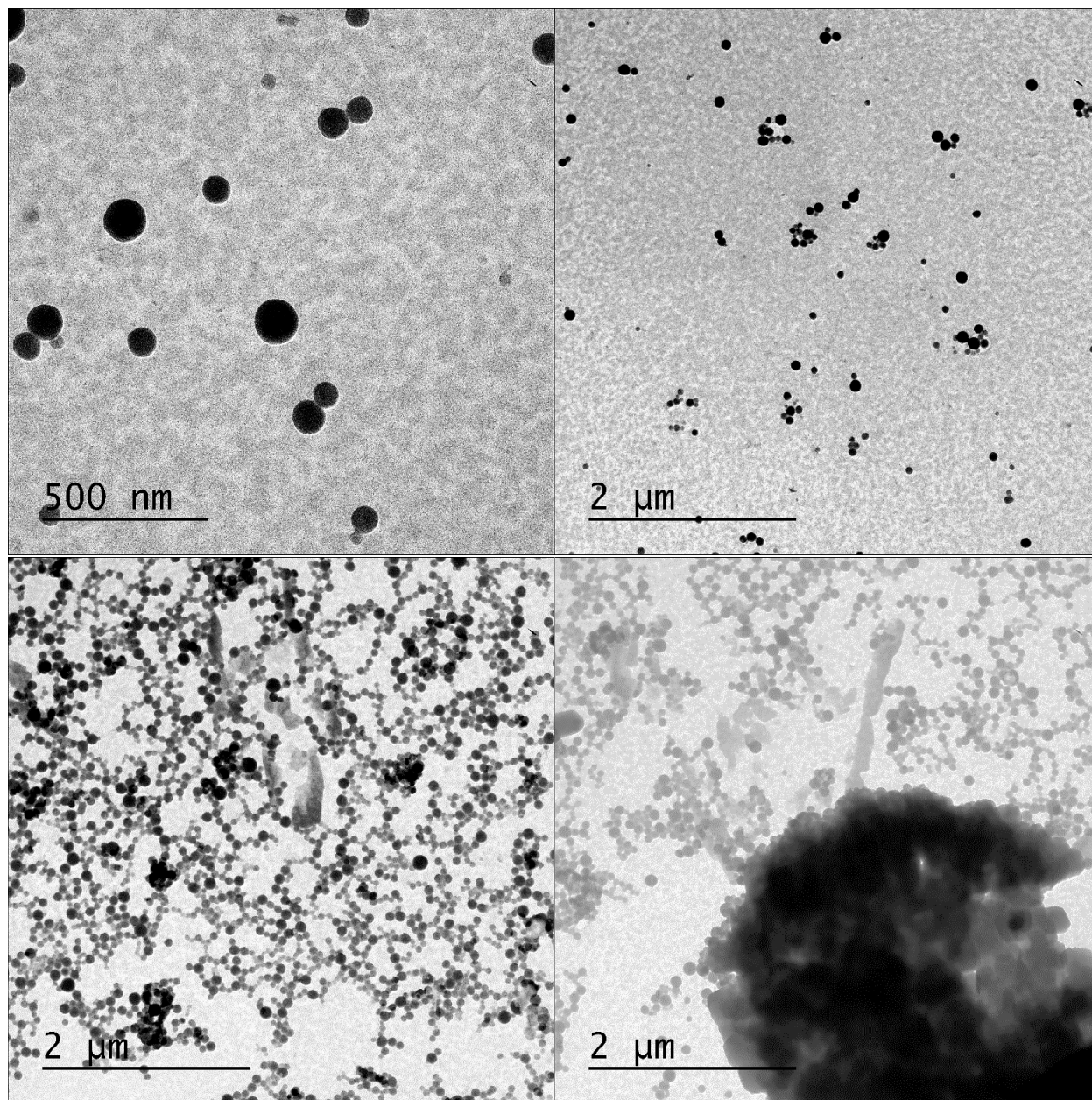


**Figure G.22:** TEM images of **B** microcrystals deposited a copper grid (200 mesh, Formvar/ Carbon or Carbon Film only). TEM images reveal the presence of spherical nanoparticles comingled with the larger aggregates observed by SEM (bottom right). The upper two images were used to determine the average nanoparticle size to be 92 nm ± 25 nm in diameter.

### b. Powder X-ray Diffraction Pattern
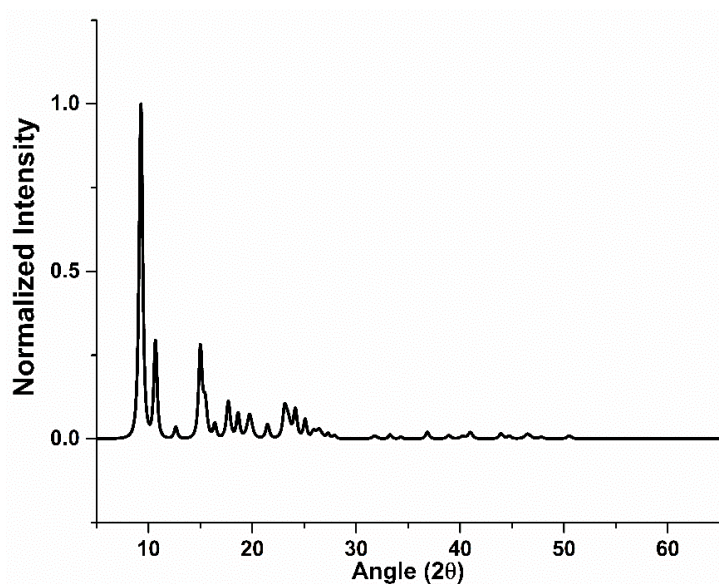


**Figure G.23:** Powder X-ray diffraction pattern of **B** microcrystals deposited on a zero-background plate. Sample was diffracted from 5.000° to 65.000° with a step size of 0.016°. See included spreadsheet for peak list and corresponding intensities.

### c. Infrared Spectroscopy
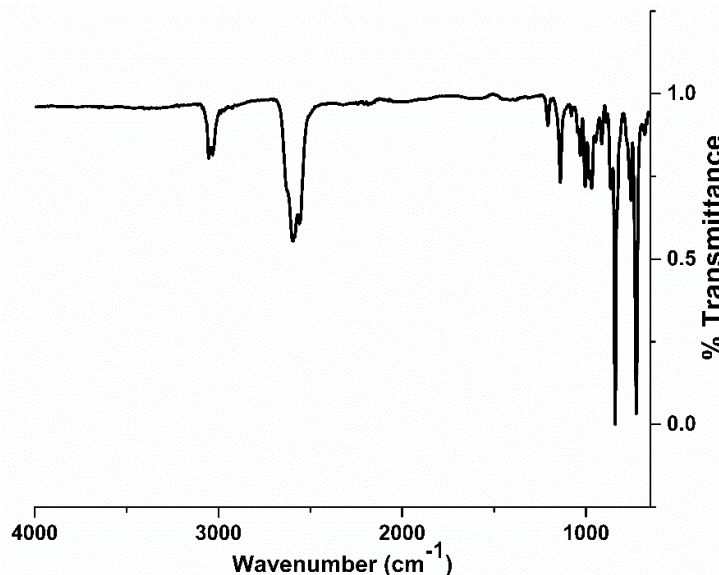


**Figure G.24:** FTIR spectrum of **B**.

FTIR spectrum of **B** reveals no signals that could be correlated to residual starting material (CuOAC (C=O: ~1500 cm$^{-1}$), HSe-oCB (H-Se: ~2250 cm$^{-1}$), *iso*-propanol (H-C: ~3000 cm$^{-1}$; H-O: ~3500 cm$^{-1}$)). Two diagnostic resonances attributed to the carborane cluster (H-C$_{carborane}$: 3000 cm$^{-1}$; H-B$_{carborane}$: 2500 cm$^{-1}$) are present and are expected to be slightly asymmetric as a function of the *ortho*-carboranyl-selenolate asymmetry.

### d. Thermogravimetric Analysis
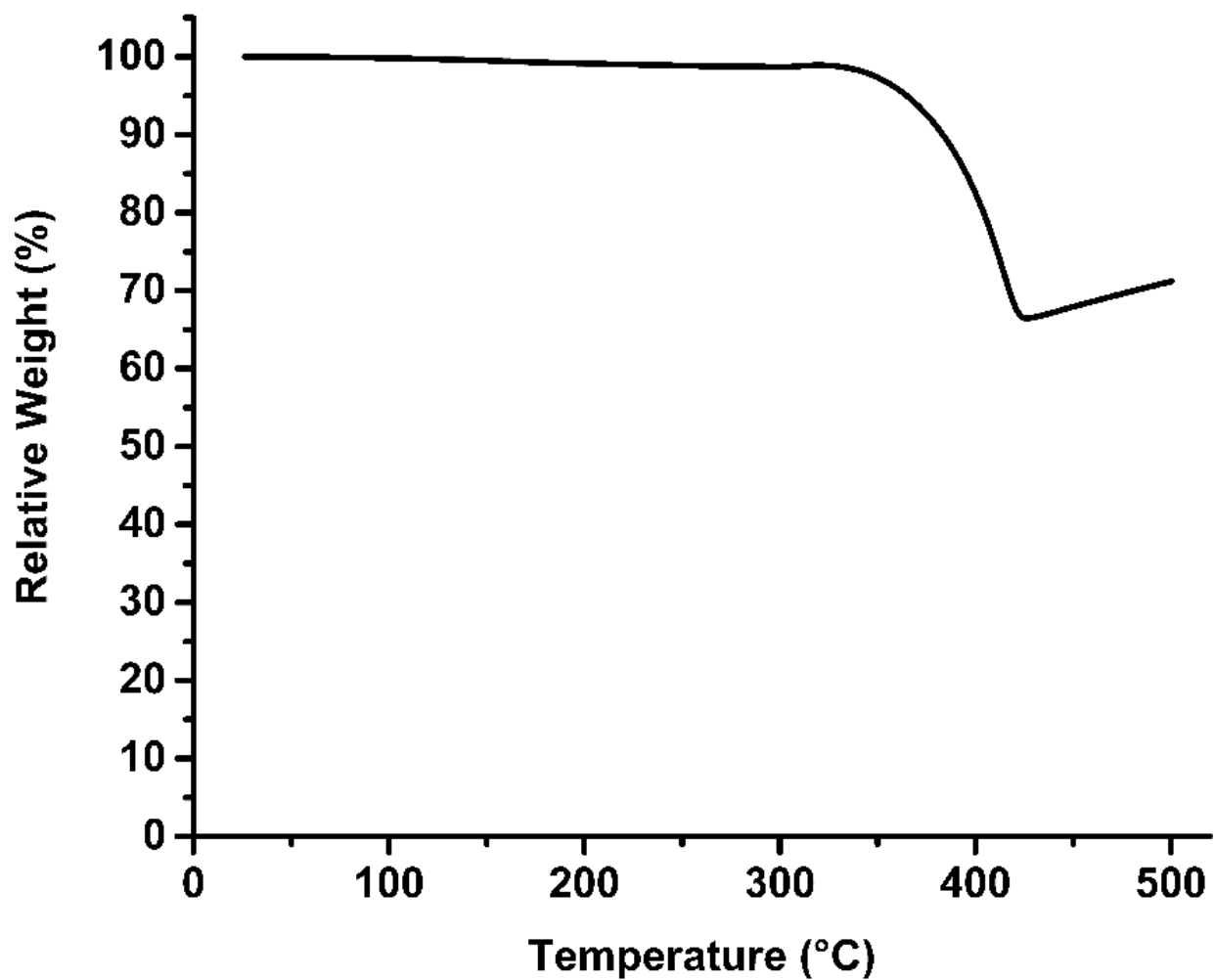


**Figure G.25:** TGA of **B**.

TGA of **B** indicates the material is thermally stable until 350 °C, after which, the material decomposes until reaching 65% relative weight at 400 °C. There is no evident desolvation step that would indicate the presence of solvent adducts within the material, which would be expected near 100 °C.

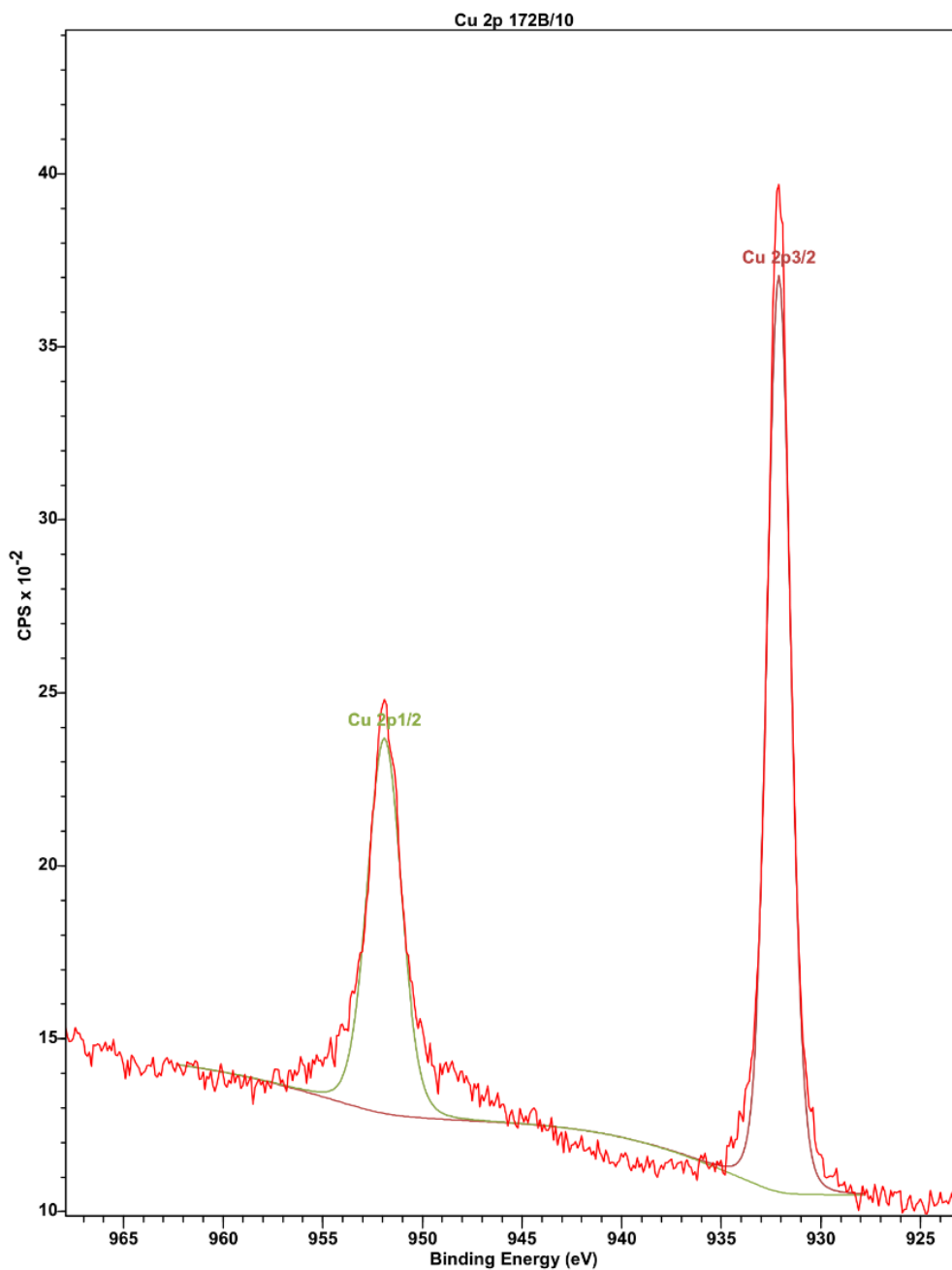**e.   X-ray Photoelectron Spectroscopy**



**Figure G.26:** Cu *2p* XPS region of **B**.

XPS data of **B** was processed and peak-fitted using CasaXPS. Peak fitting indicates the presence of only a single copper(I) environment, and is in agreement with all other structural characterization.
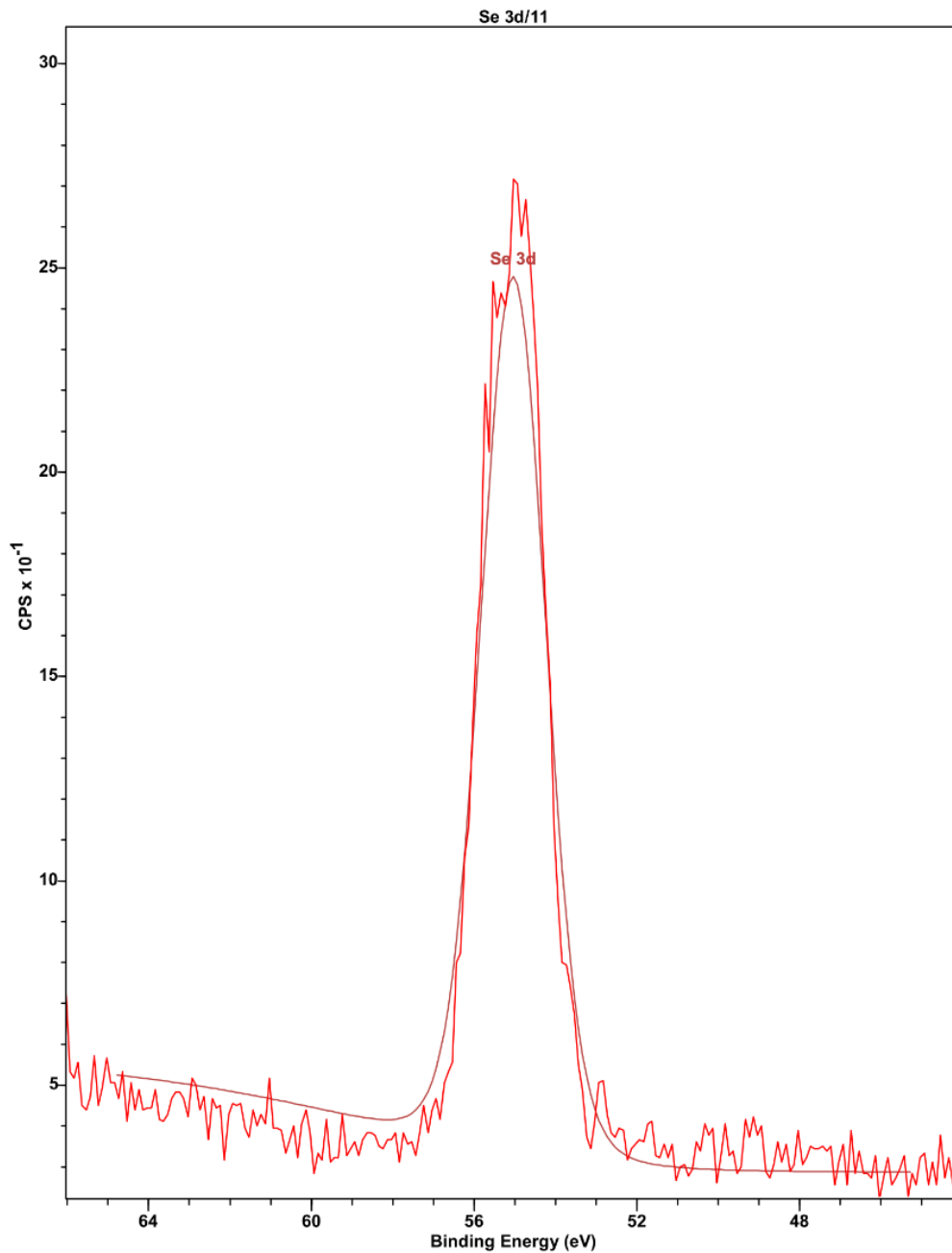
**Figure G.27:** Se *3d* XPS region of **B**.

XPS data of **B** was processed and peak-fitted using CasaXPS. Peak fitting indicates the presence of only a single selenolate environment, and is in agreement with all other structural characterization.

### f. Photophysical Measurements

### Absorption and Emission Measurements
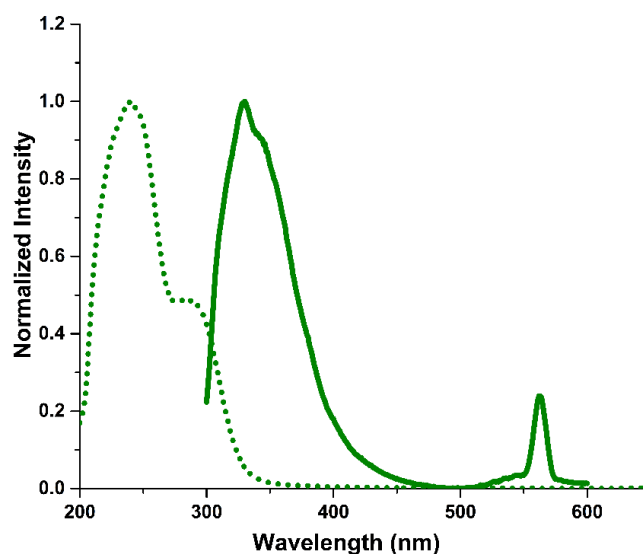


**Figure G.28:** Absorption (dotted trace) and emission (solid trace) spectra of **B**.

Absorption (dotted trace) and emission (solid trace) of **B** have been normalized and plotted on the same set of axes. Both measurements were performed on suspension of **B** in *iso*-propanol. Emission spectrum was obtained by exciting the suspension with 280 nm light, and the emission was monitored between 300-600 nm. The sharp peak at 560 nm is an artifact of the excitation wavelength (280 nm), and is not a result of emission from **B**.

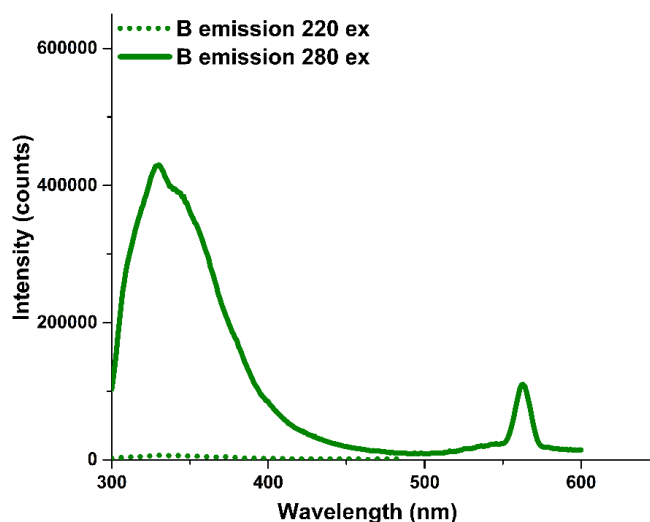### Comparison of Emission Intensity at Different Excitation Wavelengths



**Figure G.29:** Comparison of emission intensity at different excitation wavelengths.

Emission traces when exciting a suspension of **B** in *iso*-propanol at 220 nm (dotted trace) and 280 nm (solid trace). Negligible emission can be correlated to excitation at 220 nm.
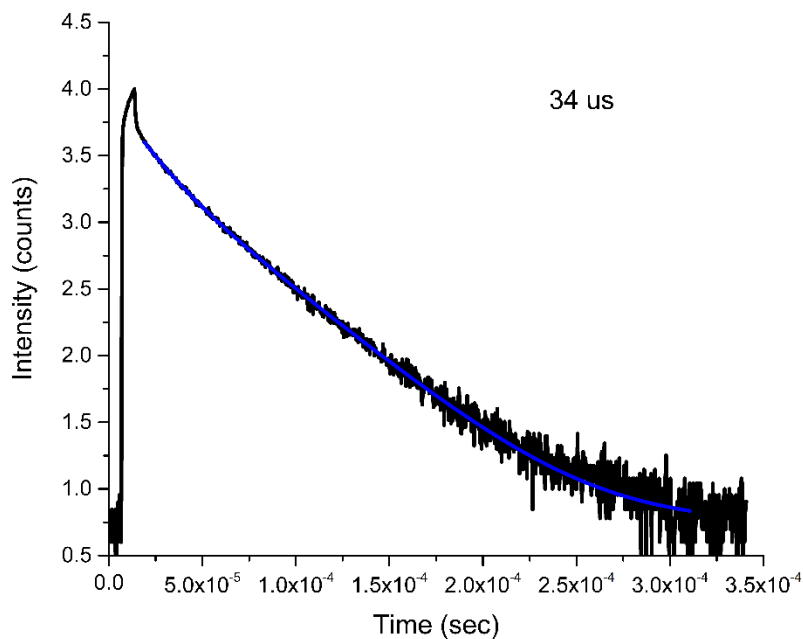
**Lifetime Measurements**



**Figure G.30:** Lifetime plot of **B**, indicating a lifetime emission of 34
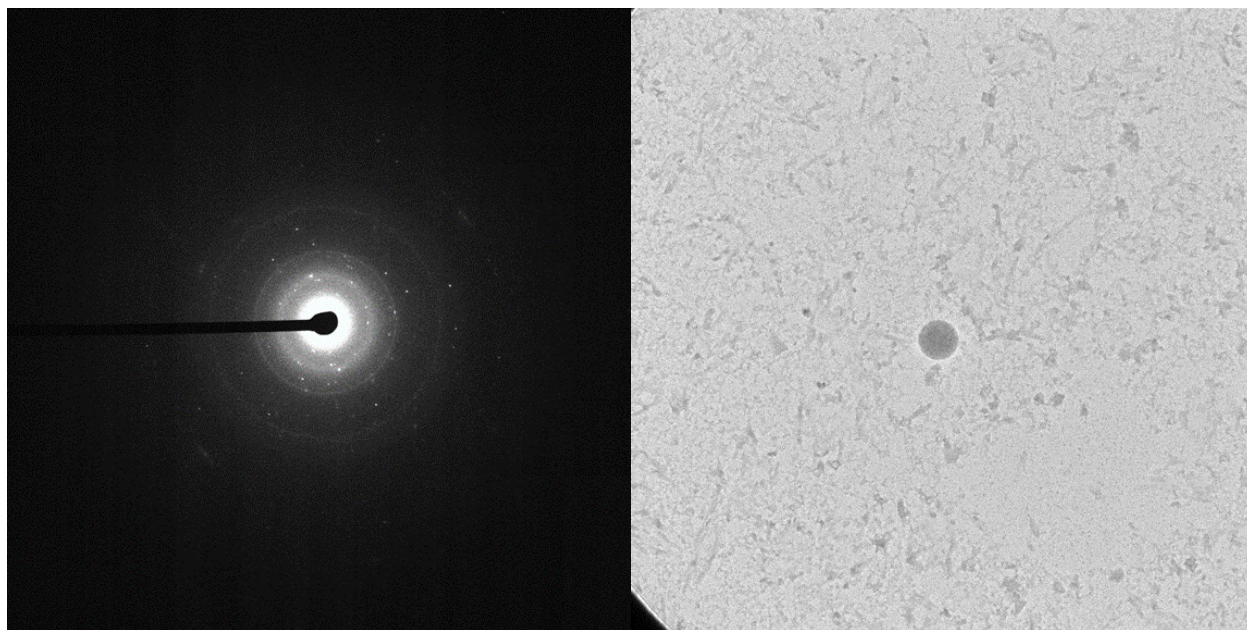
µs. **g.   Attempted MicroED**



**Figure G.31:** SAED and bright field image of **B** microcrystal on TEM grid.

MicroED was attempted using the previously described method outlined above. Selected Area Electron Diffraction (SAED, left image) confirmed the presence of crystalline material, however the majority of the observed diffractions were polycrystalline in nature and thus were not sufficient for single crystal analysis using MicroED.

## G7. Supplementary Characterization and Data of C
### a. Additional Electron Microscopy Images
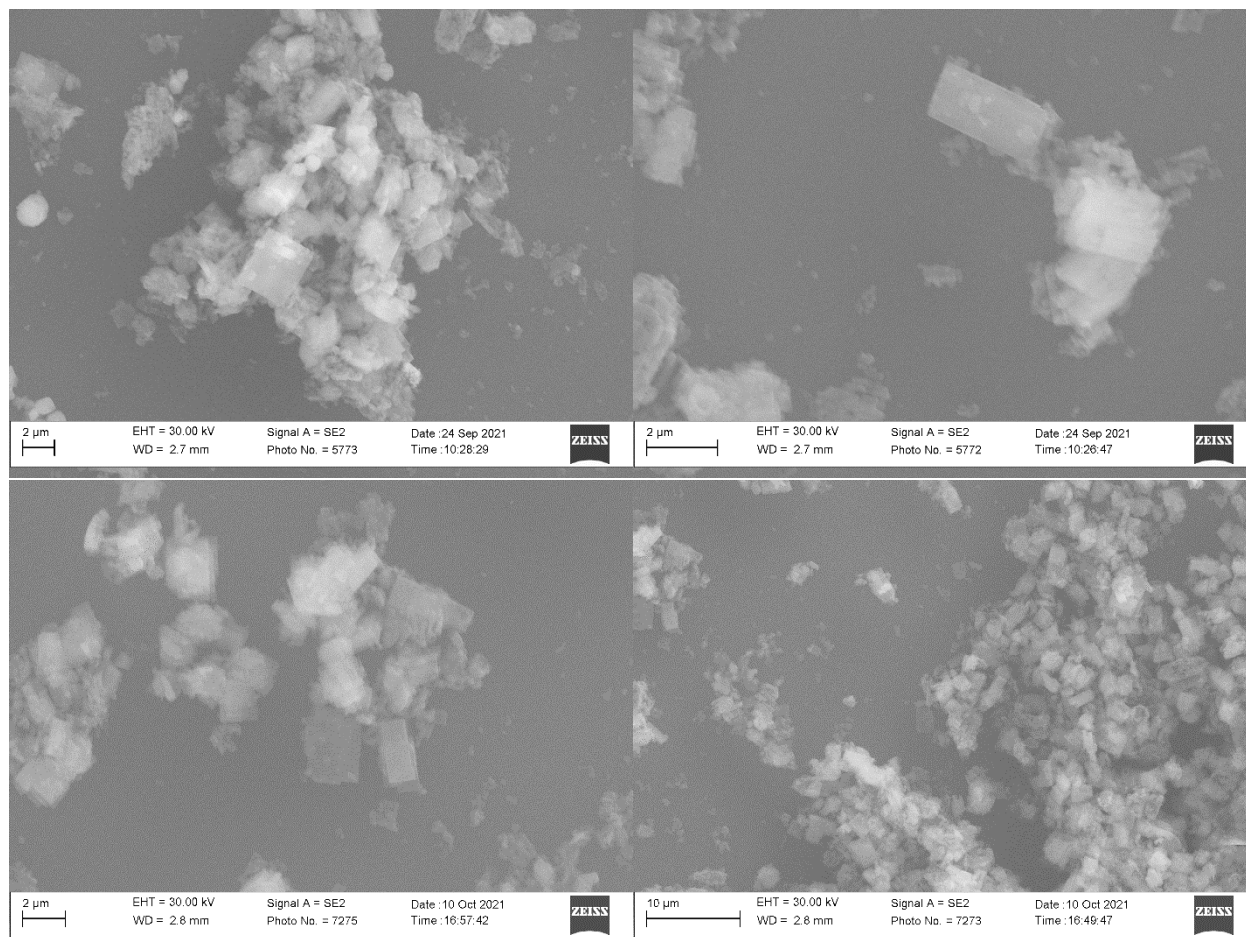
**Scanning Electron Microscopy**



**Figure G32:** SEM images of **C** microcrystals deposited on a silicon wafer chip. SEM images reveal a consistent crystallite morphology throughout the bulk material. Crystallites are typically between 3-5 µm in length and 2-3 µm in width. While there are some crystallites that exceed these dimensions, they maintain a consistent morphology of square prisms.
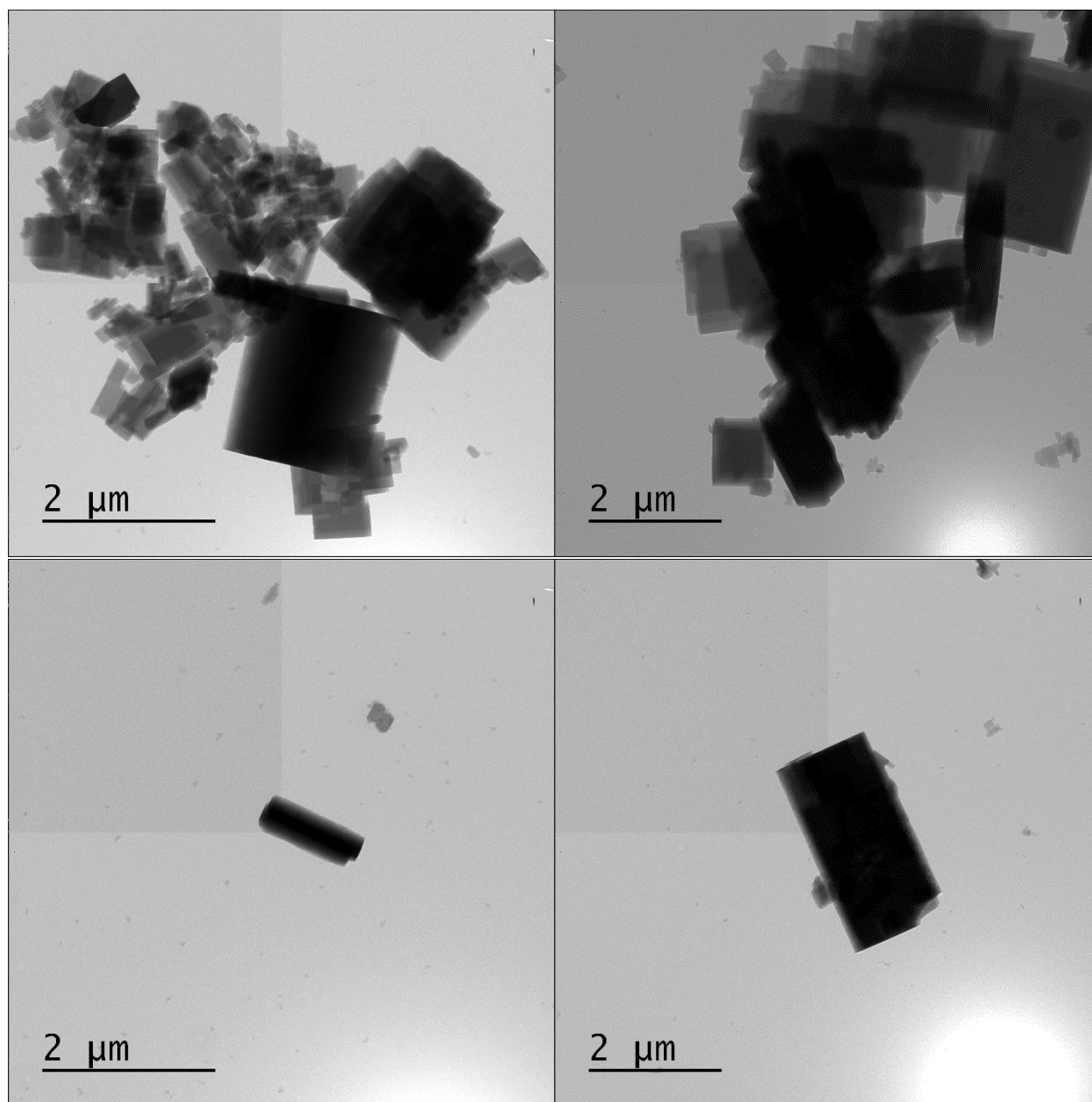
**Transmission Electron Microscopy**



**Figure G.33:** TEM images of **C** microcrystals deposited a copper grid (200 mesh, Formvar/ Carbon or Carbon Film only). TEM images reveal the presence of cubic crystallites, in agreement with morphology observed by SEM.
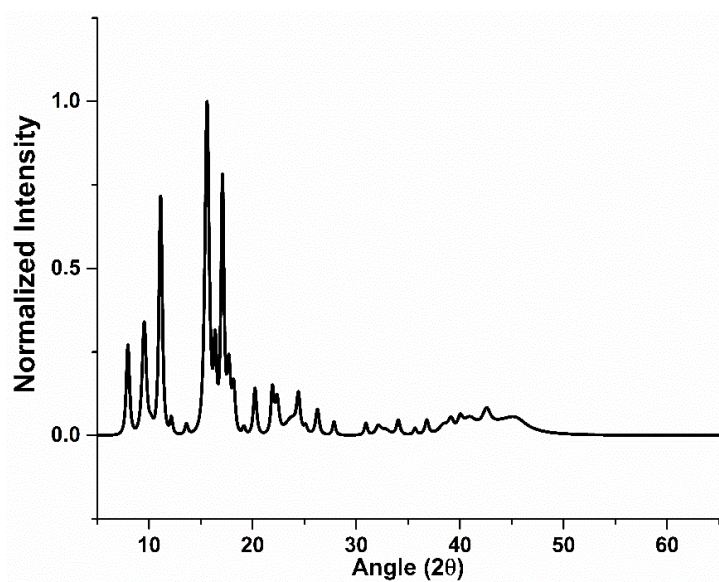
**b. Powder X-ray Diffraction Pattern**



**Figure G.34:** Powder X-ray diffraction pattern of **C** microcrystals deposited on a zero-background plate. Sample was diffracted from 5.000° to 65.000° with a step size of 0.016°. See included spreadsheet for peak list and corresponding intensities.
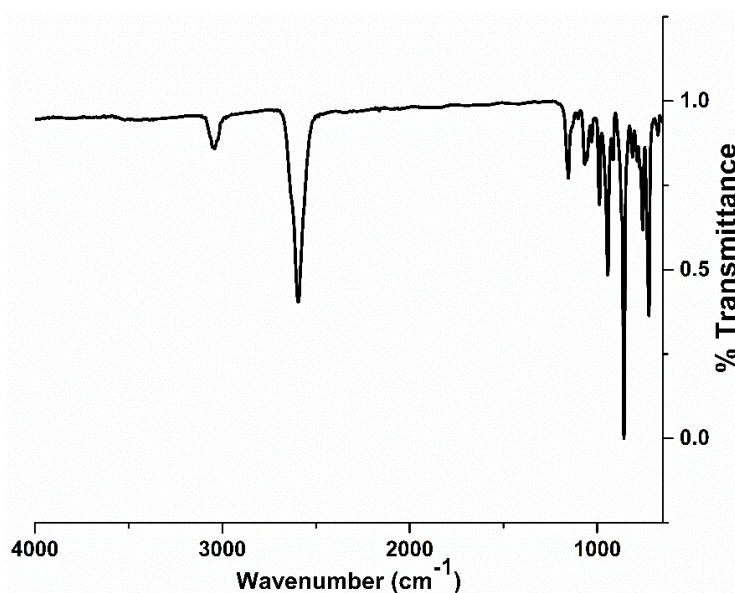
**c. Infrared Spectroscopy**



**Figure G.35:** FTIR spectrum of **C**.

FTIR spectrum of **C** reveals no signals that could be correlated to residual starting material (CuOAC (C=O: ~1500 cm$^{-1}$), HS-mCB (H-S: ~2500 cm$^{-1}$), *iso*-propanol (H-C: ~3000 cm$^{-1}$; H-O: ~3500 cm$^{-1}$)). Two diagnostic resonances attributed to the carborane cluster (H-C$_{carborane}$: 3000 cm$^{-1}$; H-B$_{carborane}$: 2600 cm$^{-1}$) are present and are expected to be symmetric as a function of the *meta*-carboranyl-thiolate symmetry.

## d. Thermogravimetric Analysis
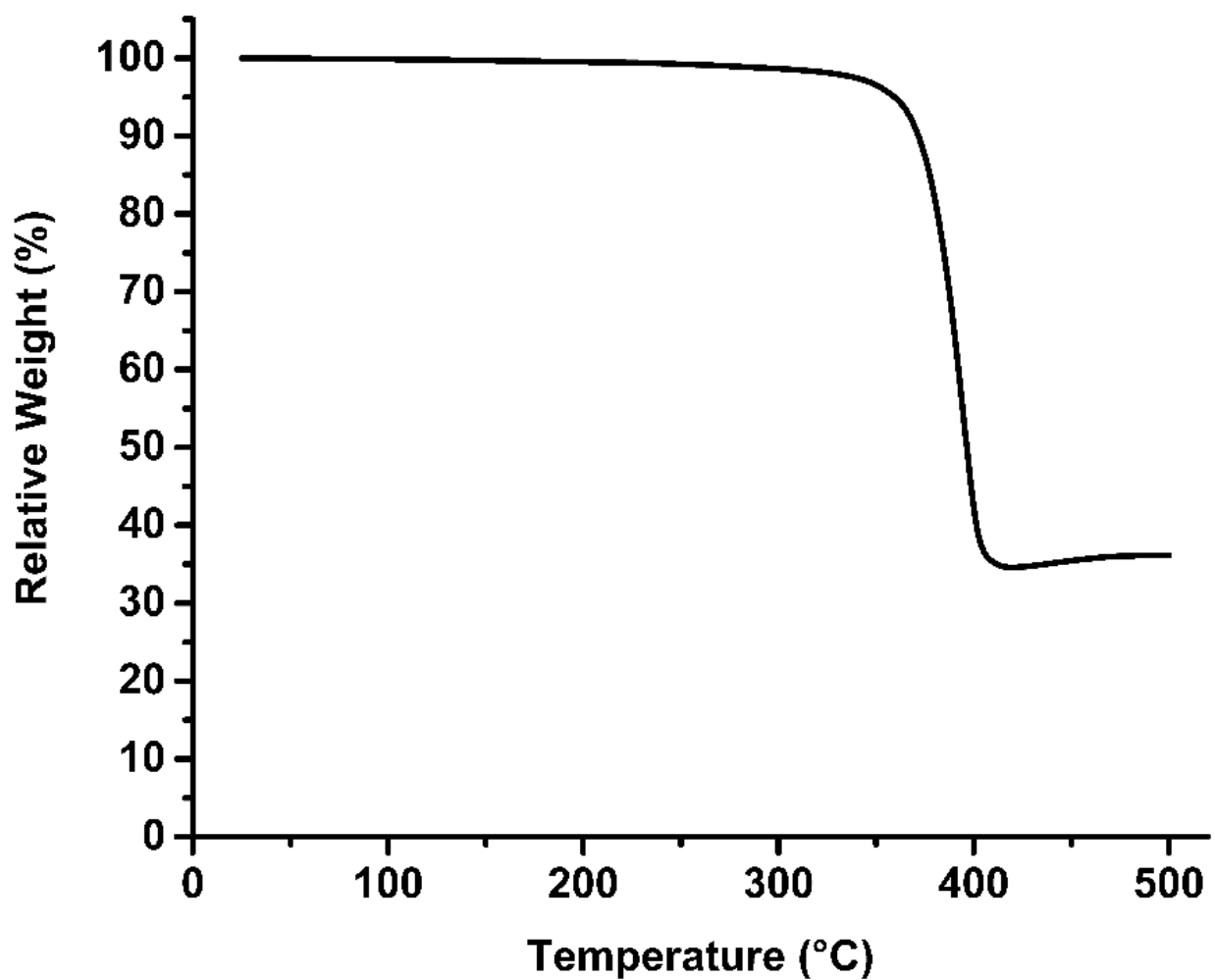


**Figure G.36:** TGA of **C**.

TGA of **C** indicates the material is thermally stable until 350 °C, after which, the material decomposes until reaching 40% relative weight at 400 °C. There is no evident desolvation step that would indicate the presence of solvent adducts within the material, which would be expected near 100 °C.

**e. X-ray Photoelectron Spectroscopy**



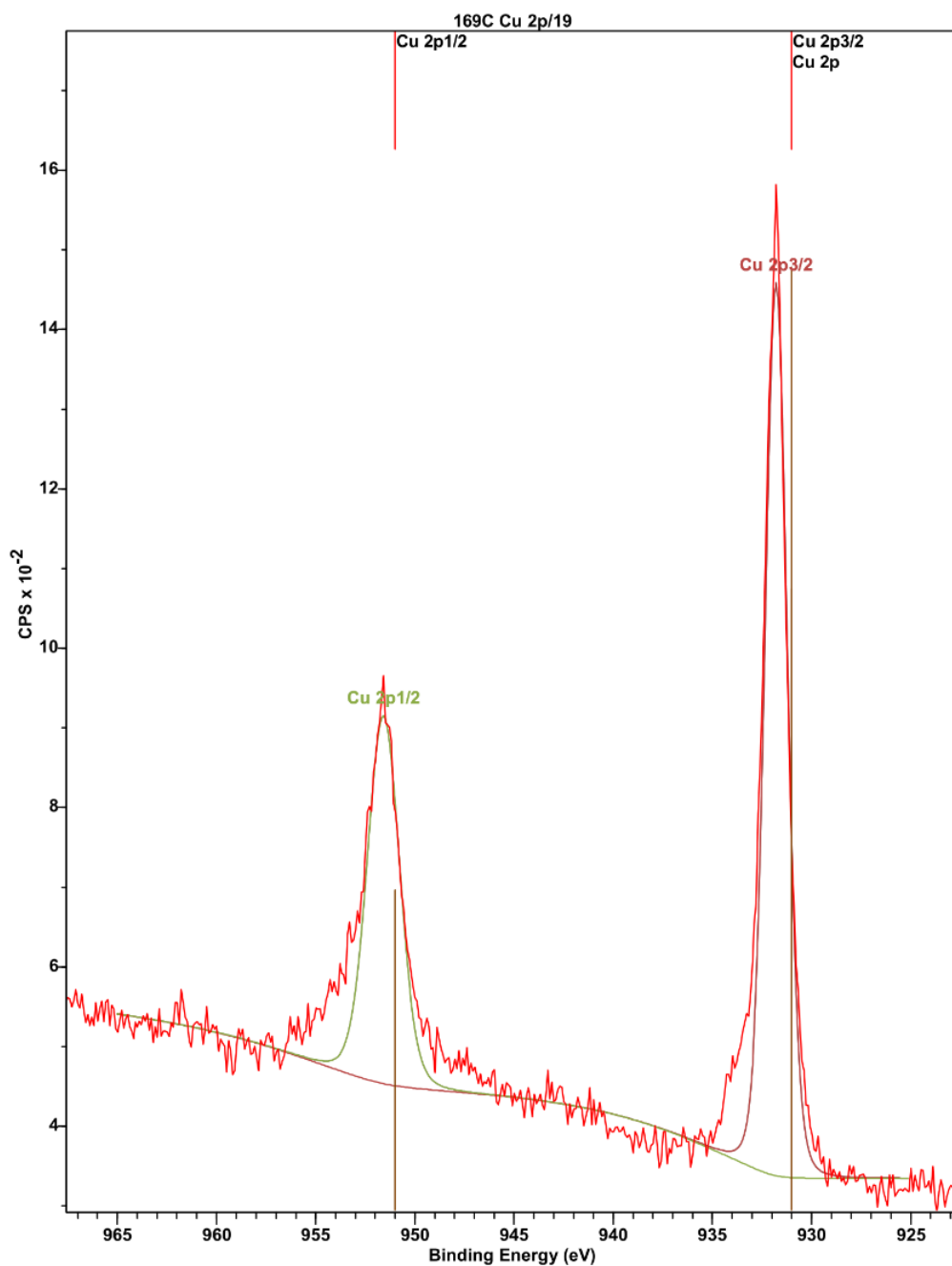**Figure G.37:** Cu *2p* XPS region of **C**.

XPS data of **C** was processed and peak-fitted using CasaXPS. Peak fitting indicates the presence of only a single copper(I) environment, and is in agreement with all other structural characterization.

**Figure G.38:** S *2p* XPS region of **C**.

XPS data of **C** was processed and peak-fitted using CasaXPS. Peak fitting indicates the presence of only a single thiolate environment, and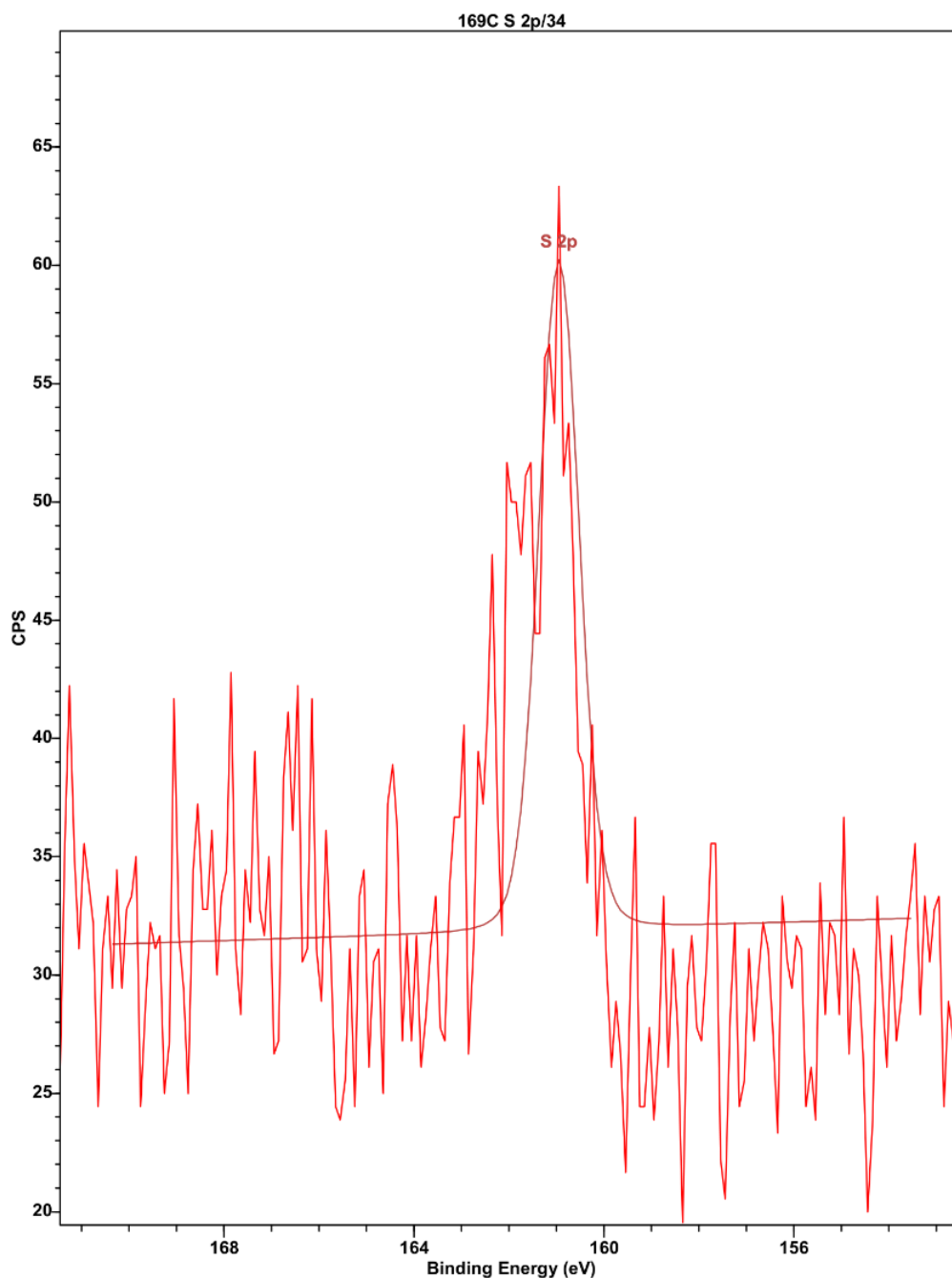 is in agreement with all other structural characterization. **Note:** The XPS instrument used to obtain measurements currently has decreased sensitivity in the S *2p* region, resulting in lower signal to noise ration.

### f. Photophysical Measurements

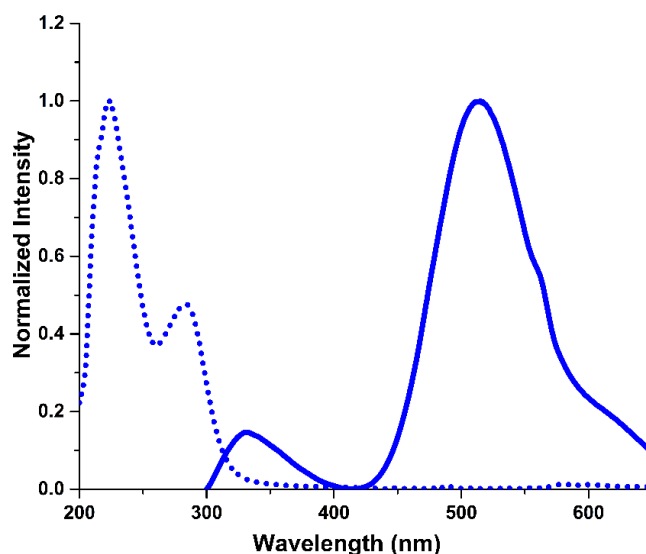### Absorption and Emission Measurements



**Figure G.39:** Absorption (dotted trace) and emission (solid trace) spectra of **C**.

Absorption (dotted trace) and emission (solid trace) of **C** have been normalized and plotted on the same set of axes. Both measurements were performed on suspension of **C** in *iso*-propanol. Emission spectrum was obtained by exciting the suspension with 280 nm light, and the emission was monitored between 300-650 nm. Although not as evident as in materials **A** and **B**, the artifact from the excitation wavelength (280 nm) is present as a slight shoulder at 560 nm.

### Comparison of Emission Intensity at Different Excitation Wavelengths
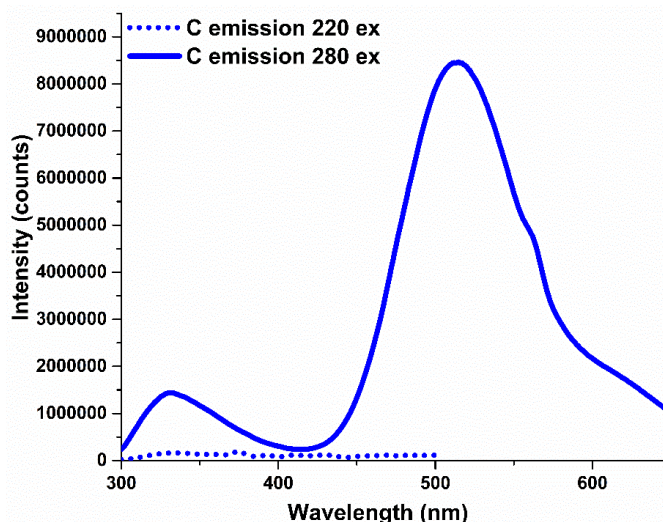


**Figure G.40:** Comparison of emission intensity at different excitation wavelengths.

Emission traces when exciting a suspension of **C** in *iso*-propanol at 220 nm (dotted trace) and 280 nm (solid trace). Negligible emission can be correlated to excitation at 220 nm.
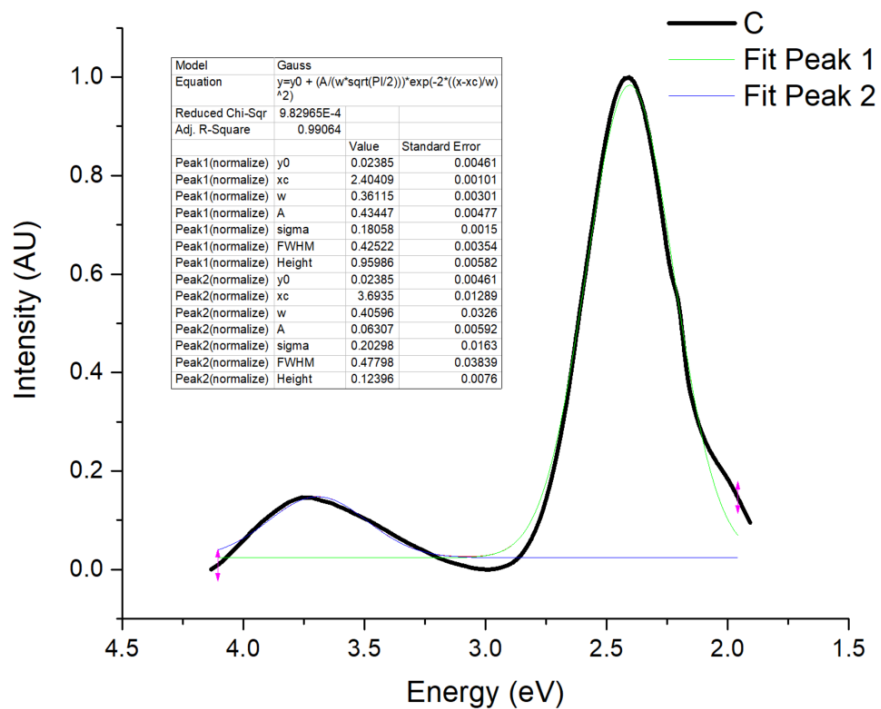
## Quantum Yields



| Model | Gauss | | |
|---|---|---|---|
| Equation | y=y0 + (A/(w*sqrt(PI/2)))*exp(-2*((x-xc)/w)^2) | | |
| Reduced Chi-Sqr | 9.82965E-4 | | |
| Adj. R-Square | 0.99064 | | |
| | | Value | Standard Error |
| Peak1(normalize) | y0 | 0.02385 | 0.00461 |
| Peak1(normalize) | xc | 2.40409 | 0.00101 |
| Peak1(normalize) | w | 0.36115 | 0.00301 |
| Peak1(normalize) | A | 0.43447 | 0.00477 |
| Peak1(normalize) | sigma | 0.18058 | 0.0015 |
| Peak1(normalize) | FWHM | 0.42522 | 0.00354 |
| Peak1(normalize) | Height | 0.95986 | 0.00582 |
| Peak2(normalize) | y0 | 0.02385 | 0.00461 |
| Peak2(normalize) | xc | 3.6935 | 0.01289 |
| Peak2(normalize) | w | 0.40596 | 0.0326 |
| Peak2(normalize) | A | 0.06307 | 0.00592 |
| Peak2(normalize) | sigma | 0.20298 | 0.0163 |
| Peak2(normalize) | FWHM | 0.47798 | 0.03839 |
| Peak2(normalize) | Height | 0.12396 | 0.0076 |

**Figure G.41:** Peak fitting of **C** emission to determine the relative peak integrations of the high (12%) and low (87%) energy transitions
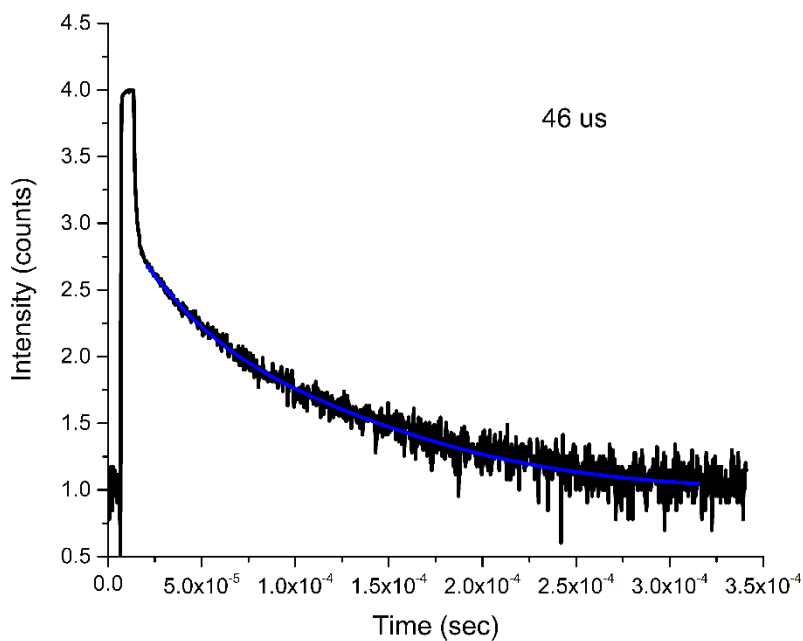
## Lifetime Measurements



**Figure G.42:** Lifetime plot of **C**, indicating a lifetime emission of 46 μs.
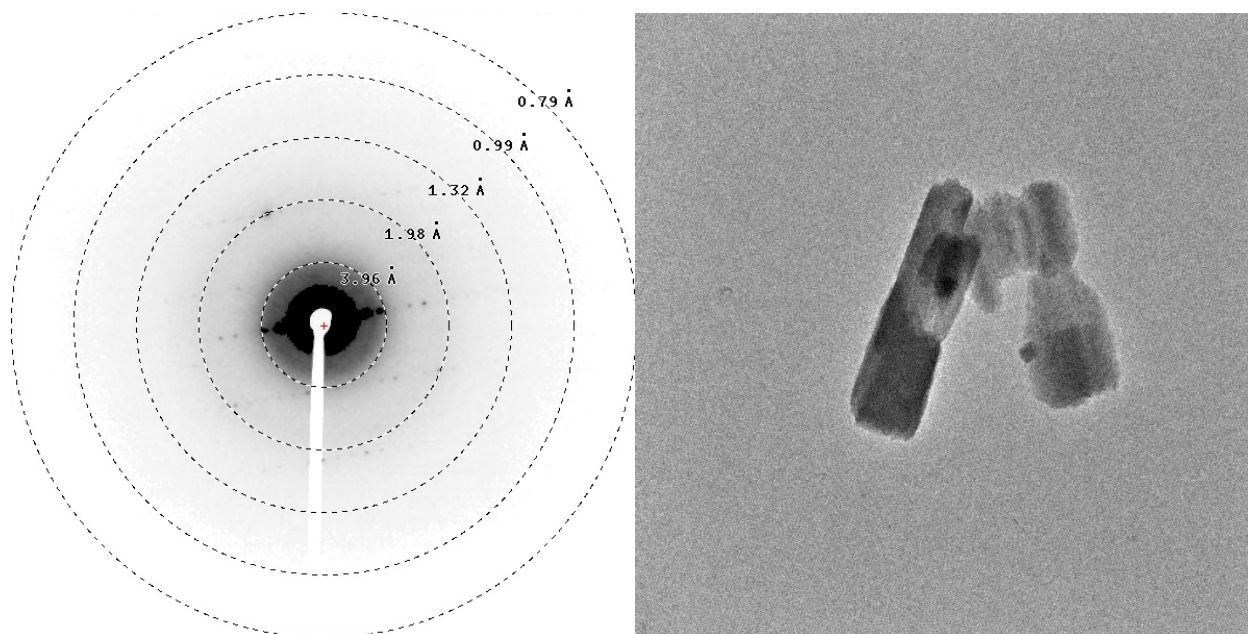
### g. Attempted MicroED



**Figure G.43:** SAED and bright field image of **C** microcrystal on TEM grid.

MicroED was attempted using the previously described method outlined above. Selected Area Electron Diffraction (SAED, left image) confirmed the presence of crystalline material and several tilt series could be collected. Despite the single-crystalline nature of the sample, the highest resolution reflections were observed at ~1.5 Å, which is insufficient resolution for an *ab initio* solution. However, the obtained diffraction data could be indexed yielding approximate unit cell parameters of a = 10.86, b = 18.71, c = 38.03, $\alpha$ = 90, $\beta$ = 90, $\gamma$ = 90 and a suggested space group of $P2_12_12_1$.

## G8.  Supplementary Characterization and Data of D
### a.  Additional Electron Microscopy Images

**Scanning Electron Microscopy**
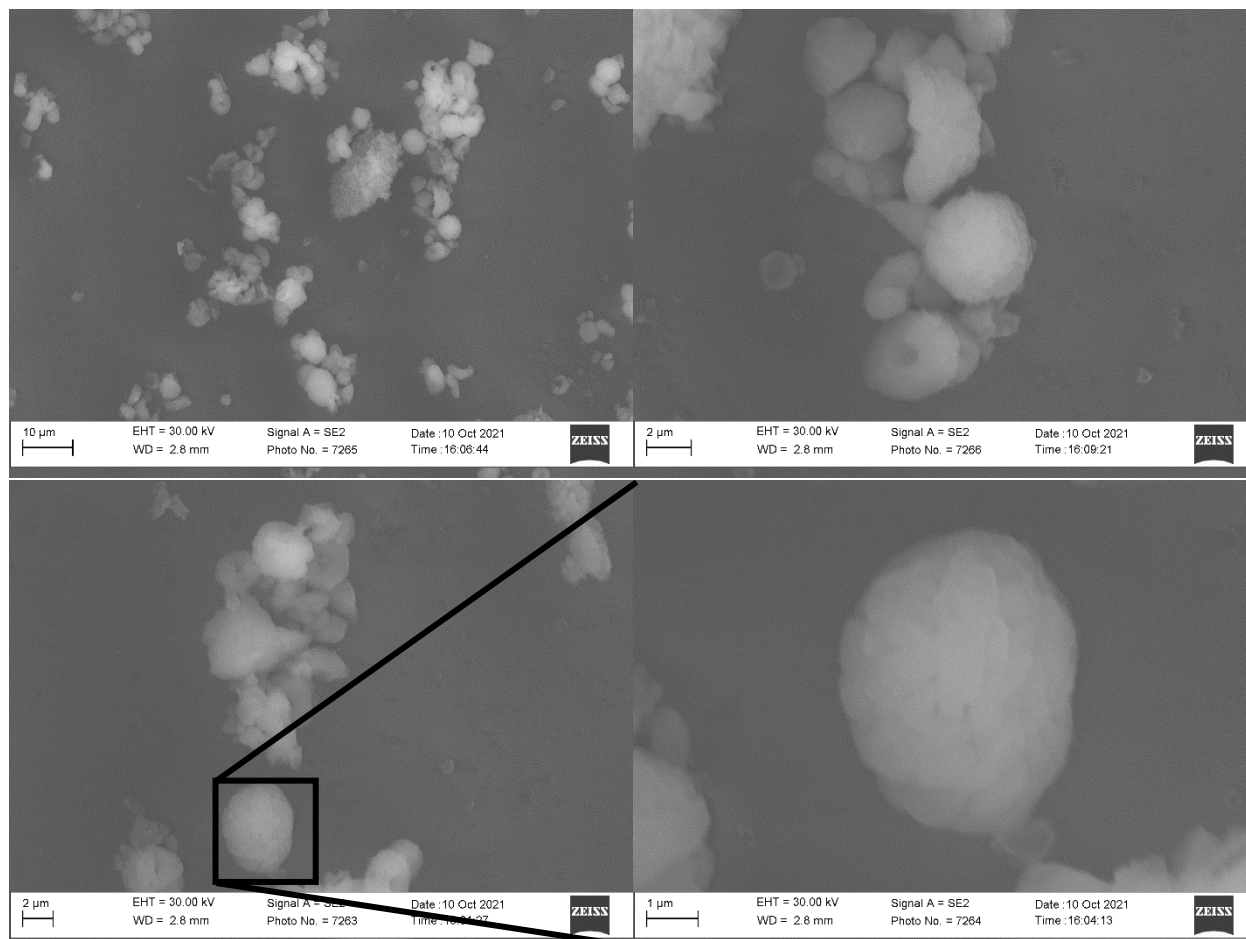


**Figure G.44:** SEM images of **D** microcrystals deposited on a silicon wafer chip. SEM images reveal a microscale particle phase present in bulk **D** with an average particle size diameter of 3.47 μm ± 0.72. While spherical in nature, in higher magnification images (bottom right), the particles appear to be comprised of platelets stacked on top of one another. There is also some evidence of "donut-like" morphologies as seen in the top right SEM image.
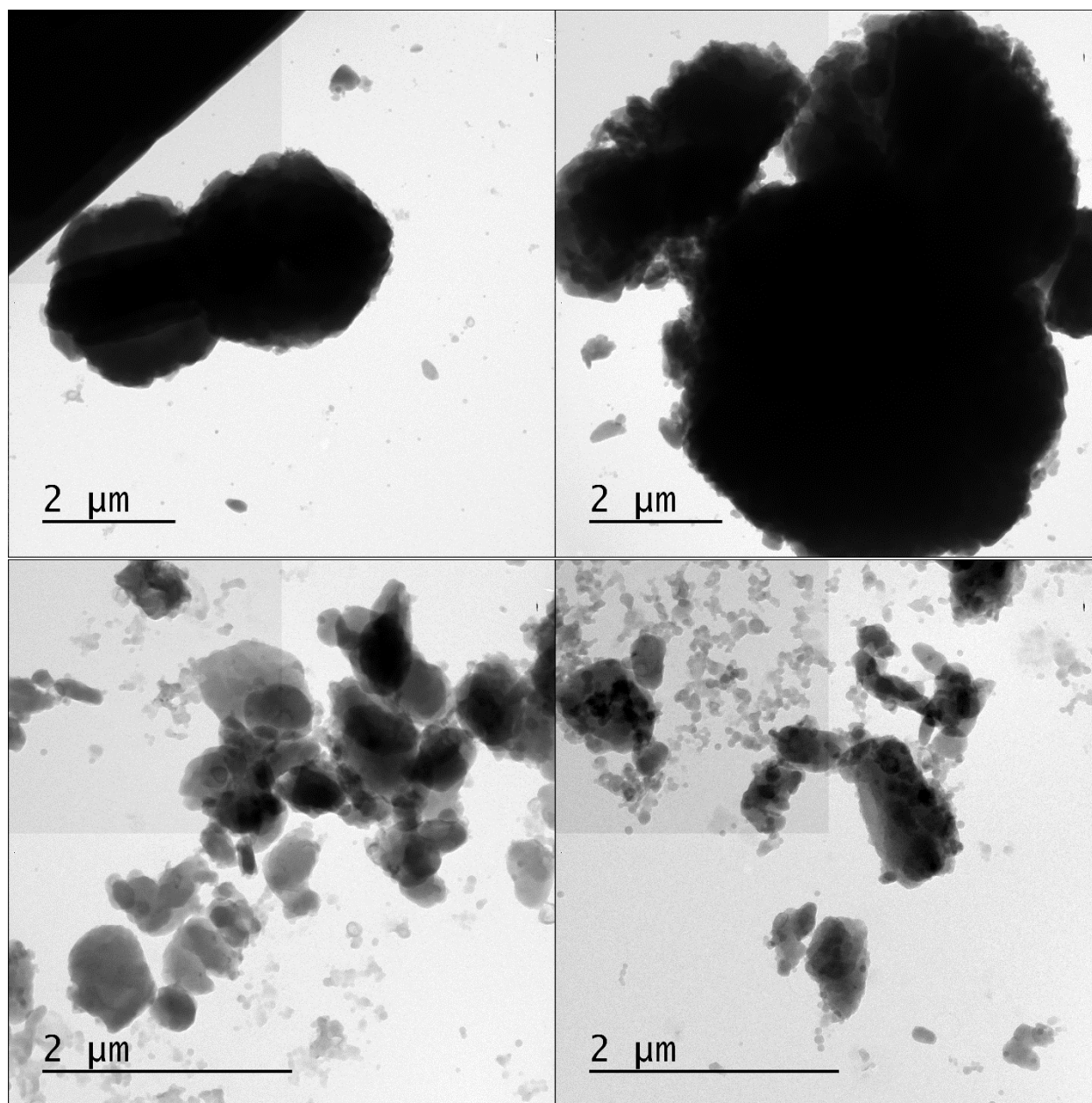
**Transmission Electron Microscopy**



**Figure G.45:** TEM images of **D** microcrystals deposited a copper grid (200 mesh, Formvar/Carbon or Carbon Film only). TEM images of **D** reveal the presence of spherical nanoparticles comingled with the larger aggregates observed by SEM, though significantly less prominent than in **B**.
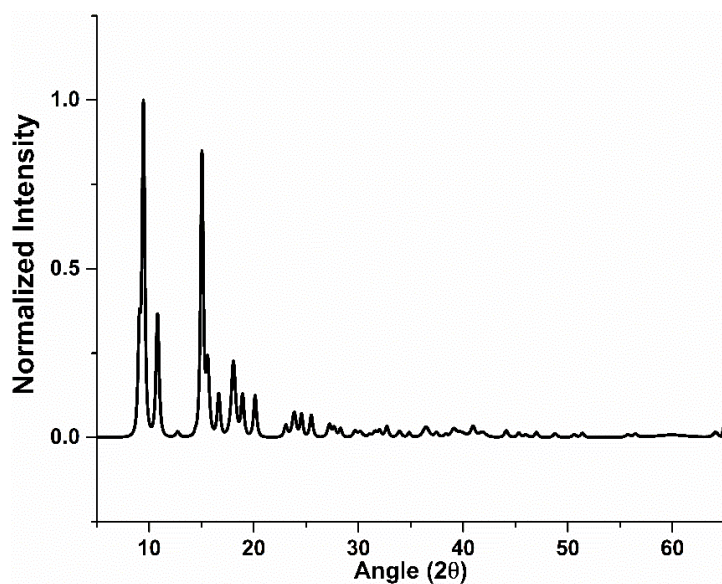
**b. Powder X-ray Diffraction Pattern**



**Figure G.46:** Powder X-ray diffraction pattern of **D** microcrystals deposited on a zero-background plate. Sample was diffracted from 5.000° to 65.000° with a step size of 0.016°. See included spreadsheet for peak list and corresponding intensities.

**c. Infrared Spectroscopy**
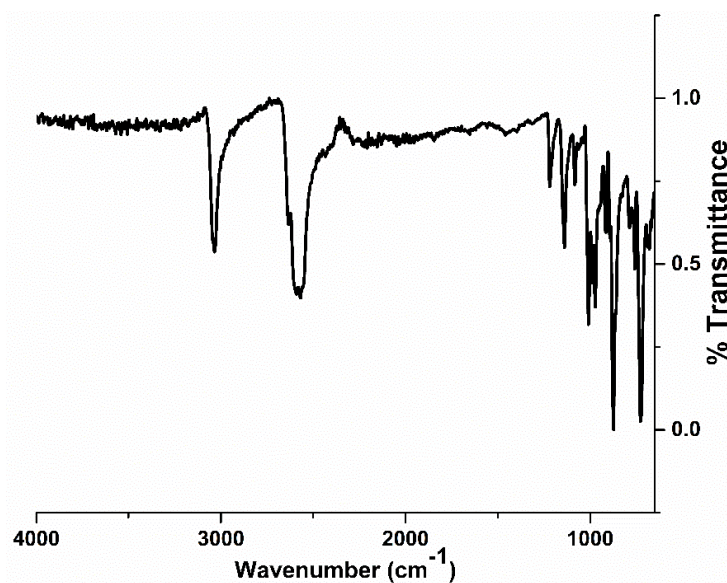


**Figure G.47:** FTIR spectrum of **D**.

FTIR spectrum of **D** reveals no signals that could be correlated to residual starting material (CuOAC (C=O: ~1500 cm$^{-1}$), HS-oCB (H-Se: ~2500 cm$^{-1}$), *iso*-propanol (H-C: ~3000 cm$^{-1}$; H-O: ~3500 cm$^{-1}$)). Two diagnostic resonances attributed to the carborane cluster (H-C$_{carborane}$: 3000 cm$^{-1}$; H-B$_{carborane}$: 2500 cm$^{-1}$) are present and are expected to be slightly asymmetric as a function of the *ortho*-carboranyl-selenolate asymmetry.

### d. Thermogravimetric Analysis
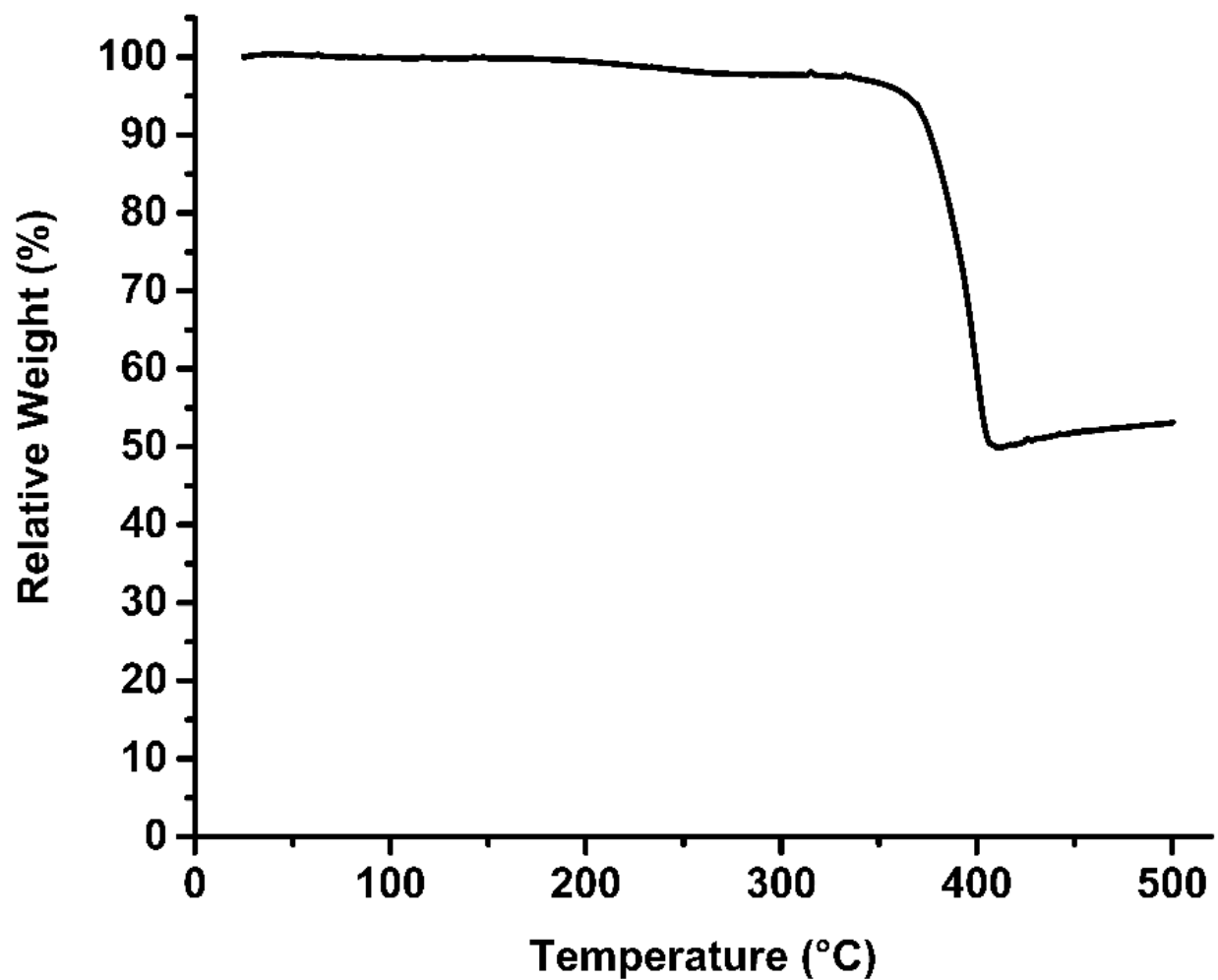


**Figure G.48:** TGA of **D**.

TGA of **D** indicates the material is thermally stable until 375 °C, after which, the material decomposes until reaching 50% relative weight at 400 °C. There is no evident desolvation step that would indicate the presence of solvent adducts within the material, which would be expected near 100 °C.

e.  **X-ray Photoelectron Spectroscopy**



**Figure G.49:** Cu *2p* XPS region of **D**.

XPS data of **D** was processed and peak-fitted using CasaXPS. Peak fitting indicates the presence of only a single copper(I) environment, and is in agreement with all other structural characterization.

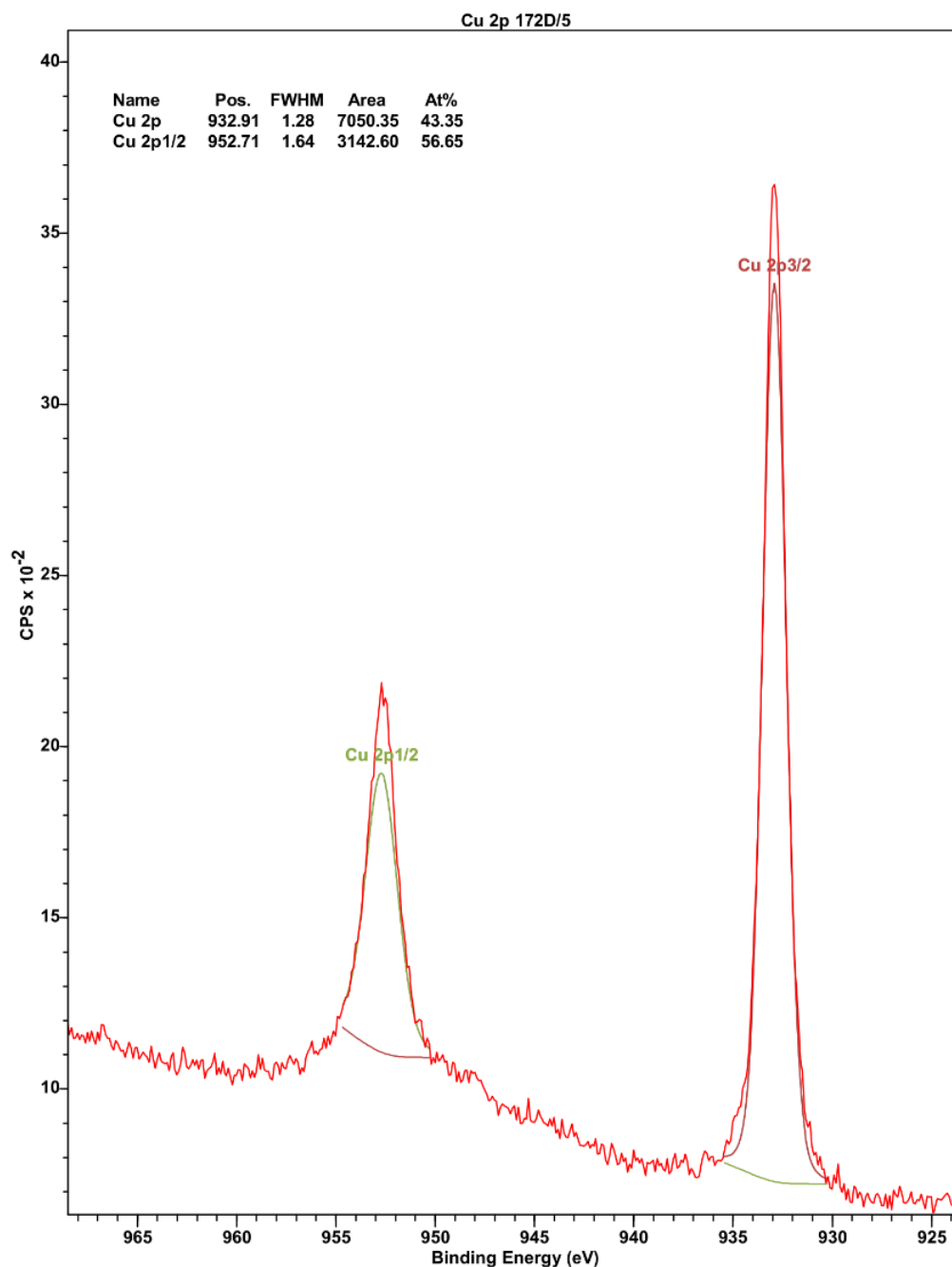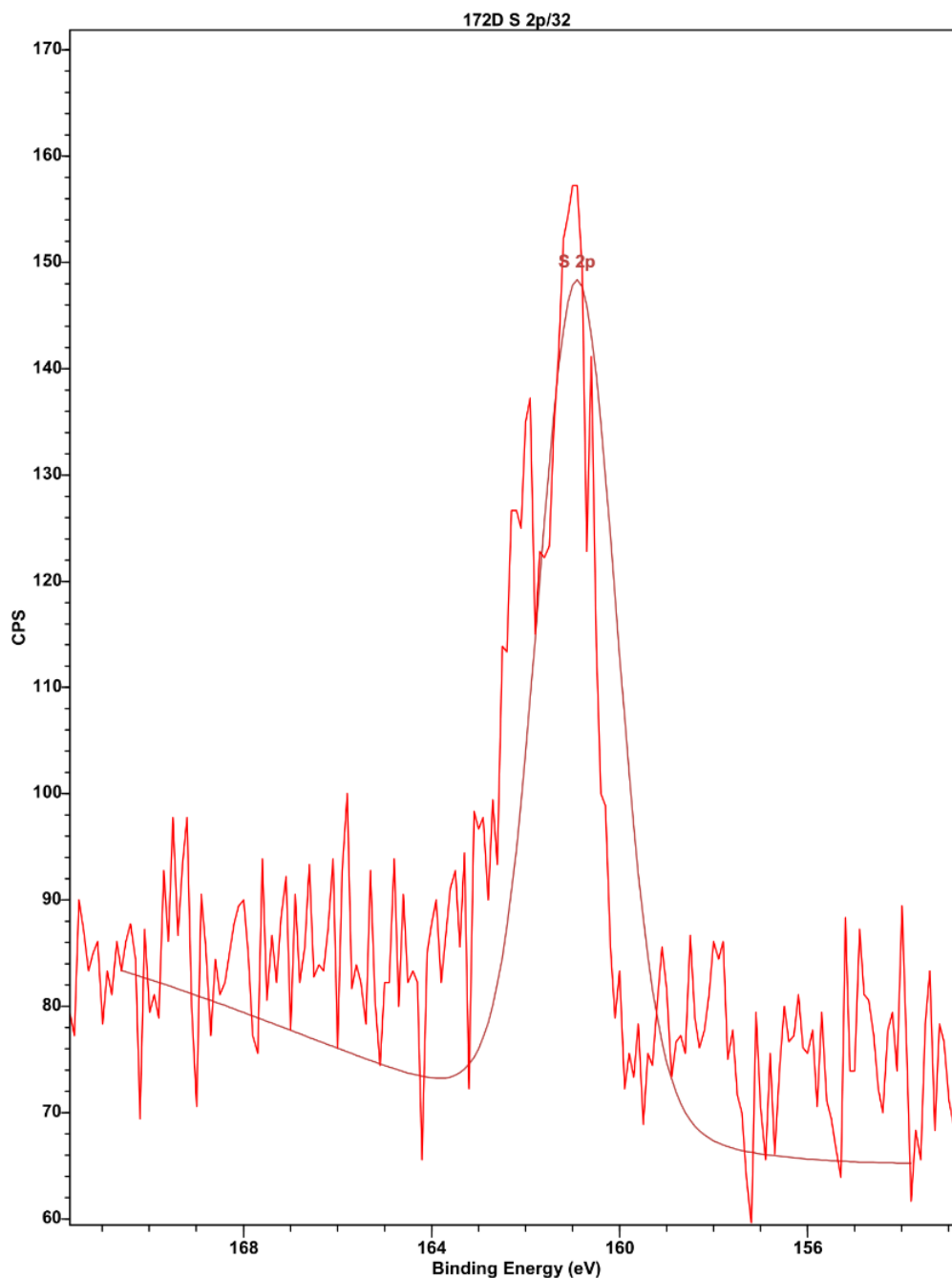**Figure G.50:** S *2p* XPS region of **D**.

XPS data of **D** was processed and peak-fitted using CasaXPS. Peak fitting indicates the presence of only a single thiolate environment, and is in agreement with all other structural characterization. **Note:** The XPS instrument used to obtain measurements currently has decreased sensitivity in the S *2p* region, resulting in lower signal to noise ration.

**f.  Photophysical Measurements**

**Absorption and Emission Measurements**
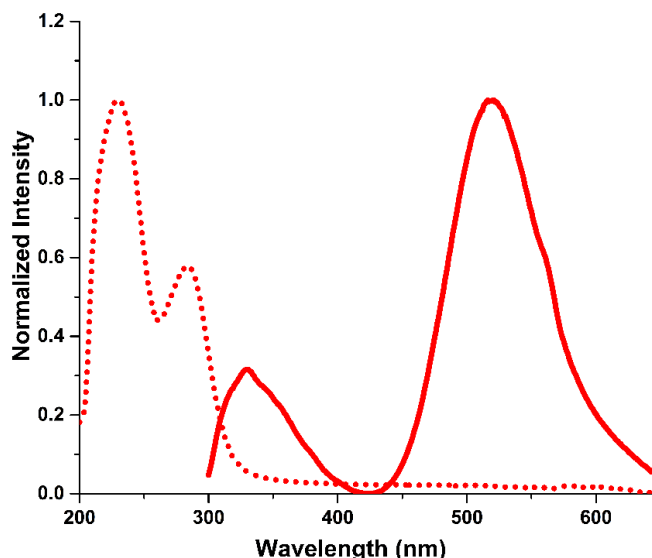


**Figure G.51:** Absorption (dotted trace) and emission (solid trace) spectra of **D**.

Absorption (dotted trace) and emission (solid trace) of **D** have been normalized and plotted on the same set of axes. Both measurements were performed on suspension of **D** in *iso*-propanol. Emission spectrum was obtained by exciting the suspension with 280 nm light, and the emission was monitored between 300-650 nm. Although not as evident as in materials **A** and **B**, the artifact from the excitation wavelength (280 nm) is present as a slight shoulder at 560 nm.

**Comparison of Emission Intensity at Different Excitation Wavelengths**
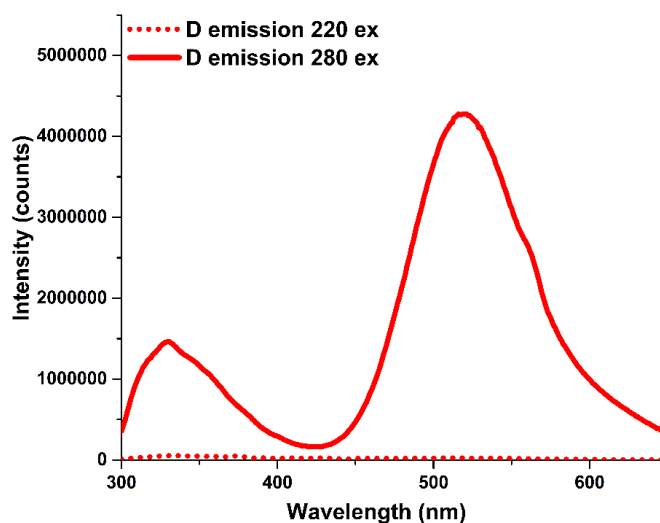


**Figure G.52:** Comparison of emission intensity at different excitation wavelengths.

Emission traces when exciting a suspension of **D** in *iso*-propanol at 220 nm (dotted trace) and 280 nm (solid trace). Negligible emission can be correlated to excitation at 220 nm.

## Quantum Yields
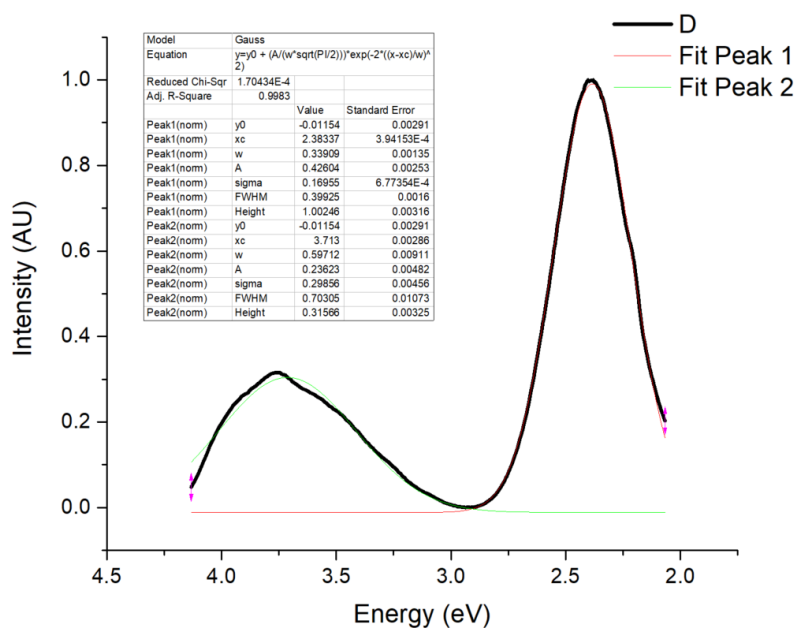


**Figure G.53:** Peak fitting of **D** emission to determine the relative peak integrations of the high (36%) and low (64%) energy transitions

## Lifetime Measurements
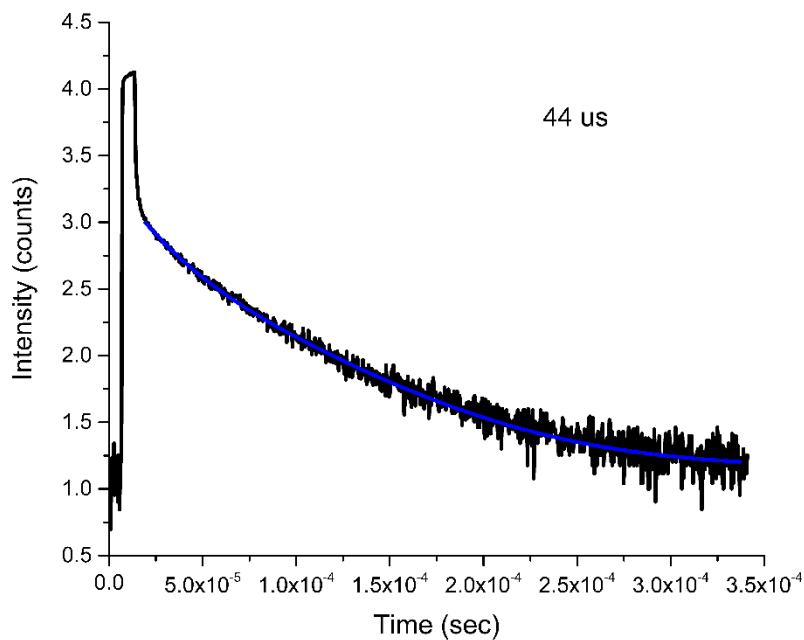


**Figure G.54:** Lifetime plot of **D**, indicating a lifetime emission of 44 μs.

## 9. Further Analysis of Literature Copper Selenide Clusters

To further understand the Cu-Se bonding arrangement, a search of the CCDC was performed, targeting the isolated $Cu_4Se_4$ observed by MicroED. Using ConQuest 2.0.4, a build query was developed using the below search parameters:
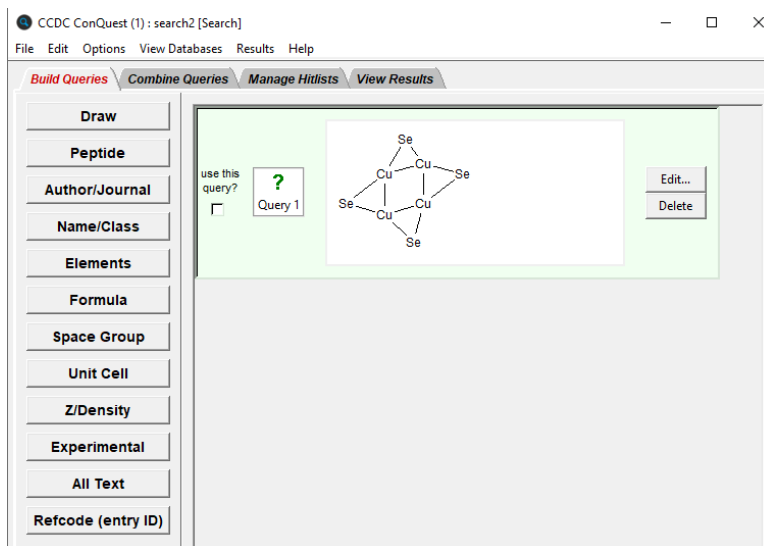


**Figure G.55:** CCDC ConQuest search window with $Cu_4Se_4$ bonding arrangement searched for.

Searching for this bonding arrangement yielded 39 results of crystallographically characterized $Cu_4Se_4$ bonding units, see below for tabulated RefCodes for each entry.
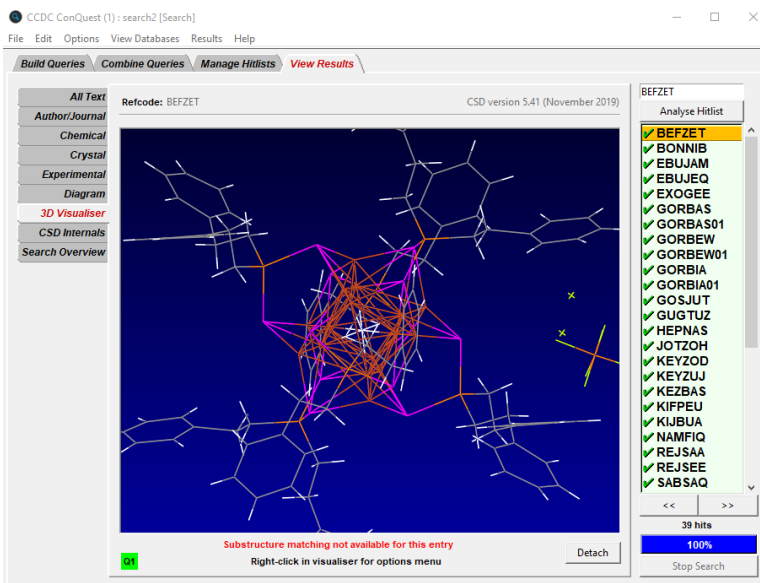


**Figure G.56:** ConQuest search result window.

| | | | | | | | |
|---|---|---|---|---|---|---|---|
| BEFZET | BONNIB | EBUJAM | EBUJEQ | EXOGEE | GORBAS | GORBAS01 | GORBEW |
| GORBEW01 | GORBIA | GORBIA01 | GOSJUT | GUGTUZ | HEPNAS | JOTZOH | KEYZOD |
| KEYZUJ | KEZBAS | KIFPEU | KIJBUA | NAMFIQ | REJSAA | REJSEE | SABSAQ |
| TAMYEL | TUNBIP | VEYROH | VEYRUN | WESQIV | WESQOB | WIXDUF | XAHMAU |
| XAHMAU01 | XAHMEY | XAHMEY01 | XAJGIZ | XUBKUA | XUBLAH | YUKBEL | |

Surprisingly, over half (21) of the entries consist of larger copper-selenide clusters with complex Cu-Cu and Cu-Se bonding arrangements. Meanwhile, some smaller, molecular, clusters have been crystallographically characterized and contain more analogous $Cu_4Se_4$ bonding arrangements to that found in **A**. A few selected examples have been rendered below accompanied by their RefCode (atoms comprising the ligands, other than the carbon atom bound to the selenolate have been hidden for clarity).
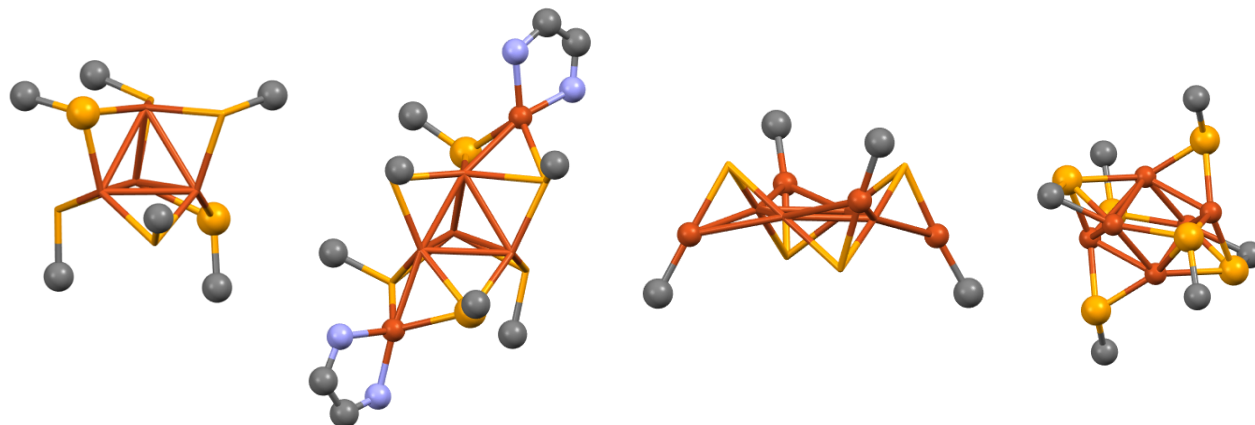


**Figure G.57:** RefCodes (left to right): BONNIB, GUGTUZ, WIXDUF, YUKBEL

Of the smaller clusters, the vast majority contain tetrahedral copper tetramers (see BONNIB, GUGTUZ, YUKBEL) with only one example (WIXDUF, reference 12) somewhat resembling the observed $Cu_4Se_4$ in material **A** with some notable differences. Unlike in **A**, there are no ligands attached to the selenolate and the cluster is instead structured by N-heterocyclic carbenes bound to the peripheral copper atoms (see below). Furthermore, the cluster in WIXDUF is substantial larger with an overall molecular formula of $Cu_8Se_4$.
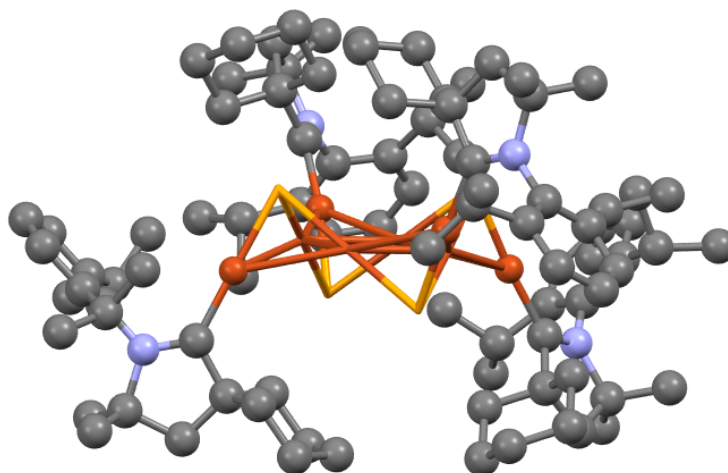


**Figure G.58:** Single crystal X-ray structure of WIXDUF.

## 10. $^1$H and $^{11}$B NMR Experiments of Dissolved Materials A-D

As a further assessment of both purity from starting materials (chalcogenols, *iso*-propanol) in addition to understanding potential intermolecular forces between the copper chalcogenides clusters. Approximately 10 mg of each material was added to an NMR tube and dissolved in 0.4 mL of CD$_2$Cl$_2$. Unexpectedly, the materials appear to be only partially soluble in dichloromethane, particularly those containing *ortho*-carborane (see right, samples are **A**, **B**, **C**, **D** from left to right).

In contrast to the purity of the materials suggested by TGA, $^1$H NMR of **A-D** suggested the presence of up to 20% *iso*-propanol. This apparent impurity is likely inflated from the real purity due to the poor solubility of materials **B** and **D**, and should be more closely associated with the lack of solvent adducts observed by TGA. In all $^1$H NMRs (see below), no chalcogenol resonance is observed.
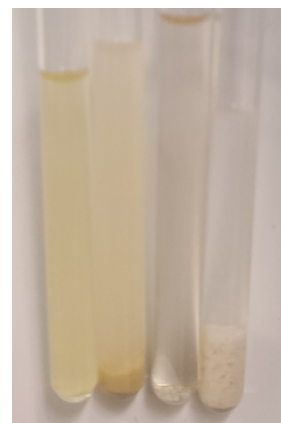
**Figure S59:** NMR samples of **A-D**
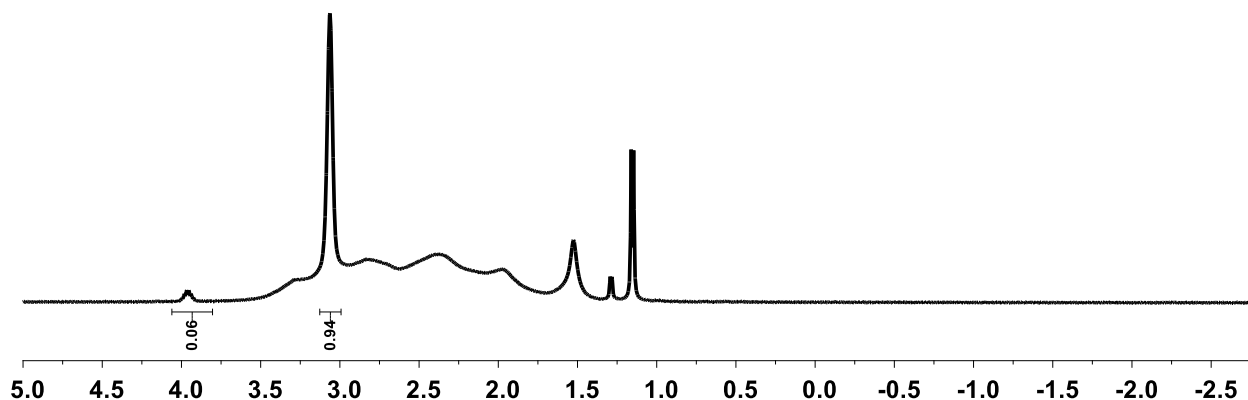
**Figure G.60:** $^1$H NMR of **A**
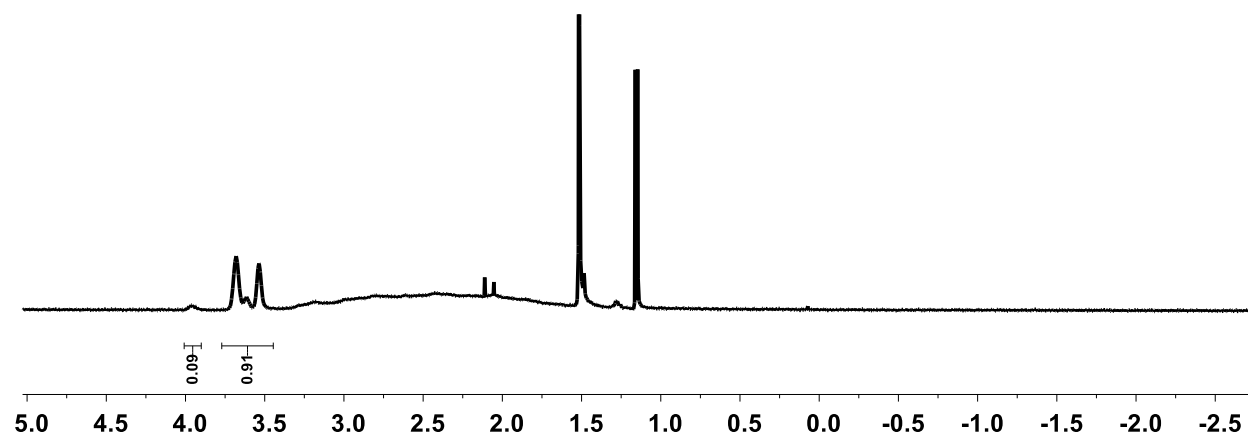
**Figure G.61:** $^1$H NMR of **B**
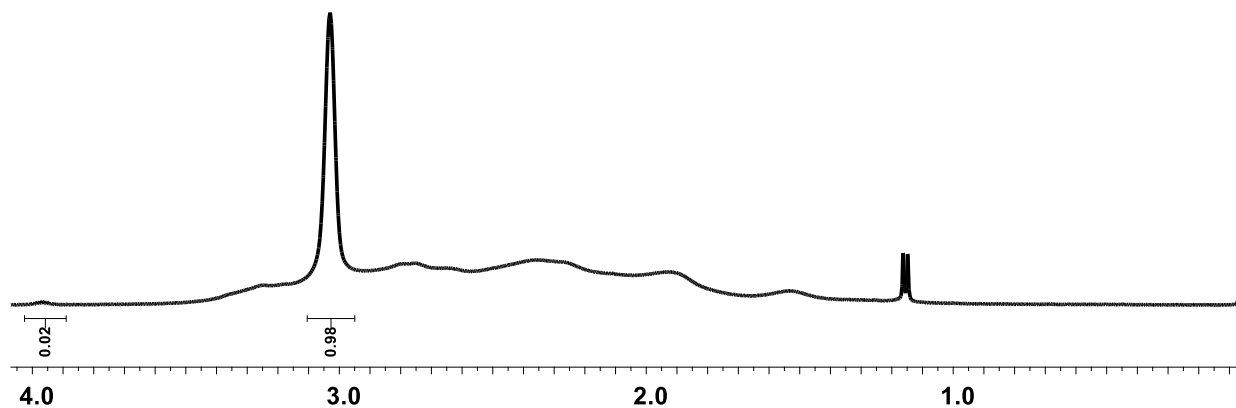
**Figure G.62:** $^1$H NMR of **C**
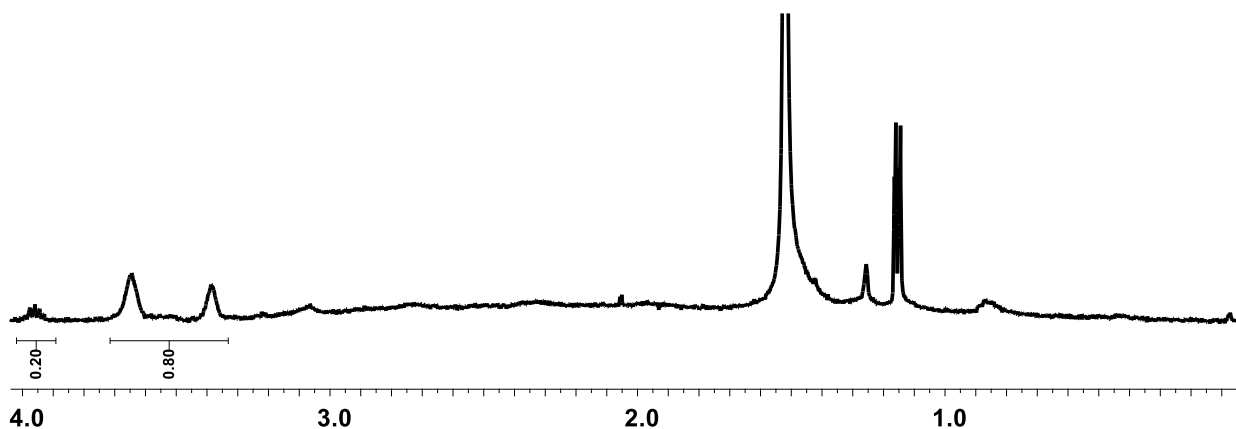


**Figure G.63:** $^1$H NMR of **D**

$^{11}$B NMR spectroscopy of materials **A-D** further corroborated the observations made by FTIR spectroscopy (see below). The NMR spectra indicate that the boron cluster cage is fully intact with no decomposition of the cluster observed. As expected, there are slight shifts in the $^{11}$B NMR resonances attributed to the boron nucleus bound to the exopolyhedral chalcogen-based substituent (Se, S). More noticeably, however, is the significant broadening of the $^{11}$B NMR resonance assigned to the B(3) boron vertex in a position distal to the exopolyhedral boron-chaclogen bond. While this is difficult to see in materials **B** and **D** due to overlapping resonances in the upfield region, it is quite prominent in materials **A** and **C**. This broadening is likely attributed to the rotation of the carborane cage relative to the exopolyhedral B-Se or B-S bond while the copper cluster is dissolved in solution.
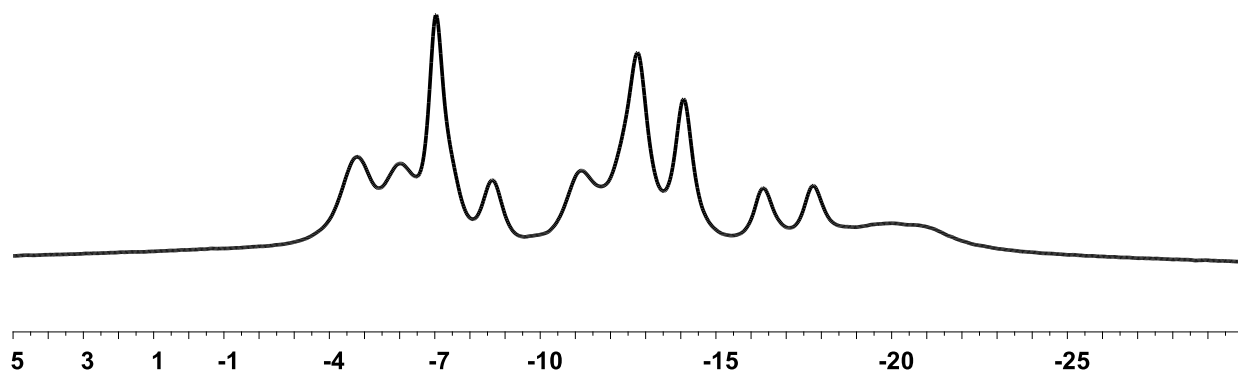
**Figure G.64:** $^{11}$B NMR of **A**
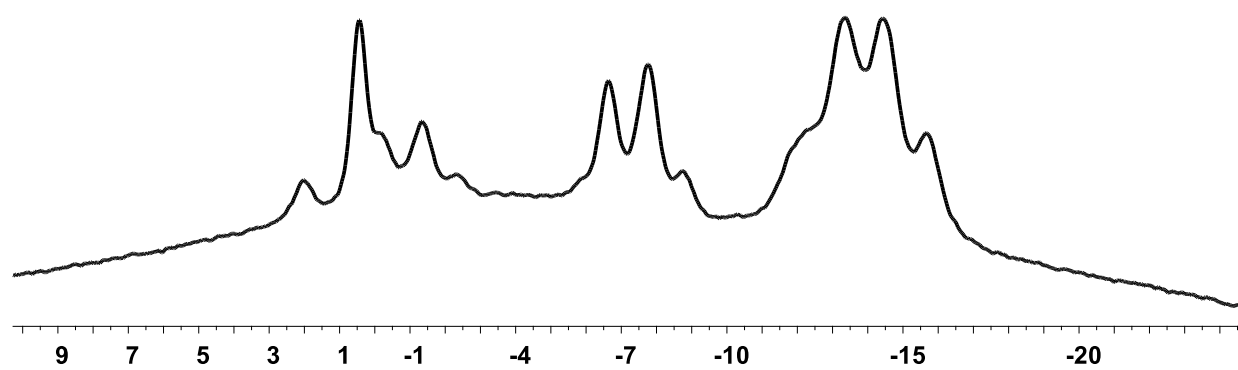


**Figure G.65:** $^{11}$B NMR of **B**
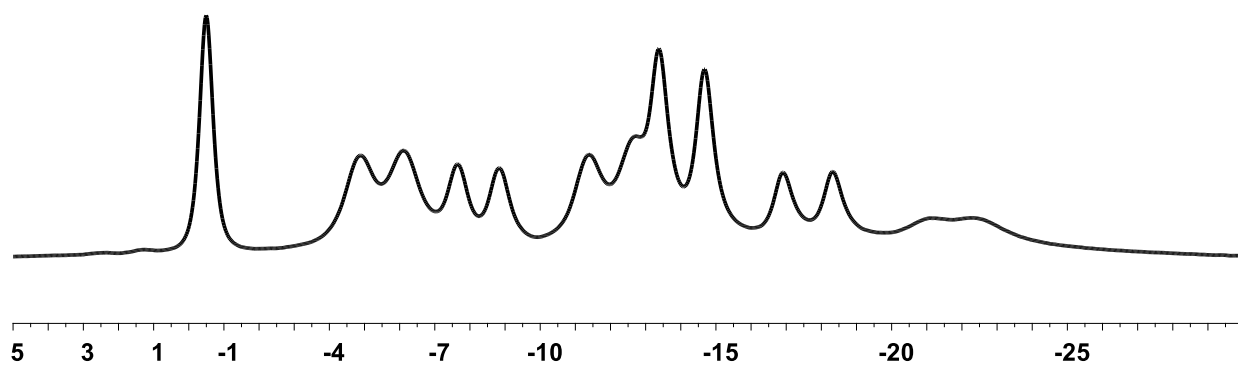


**Figure G.66:** $^{11}$B NMR of **C**
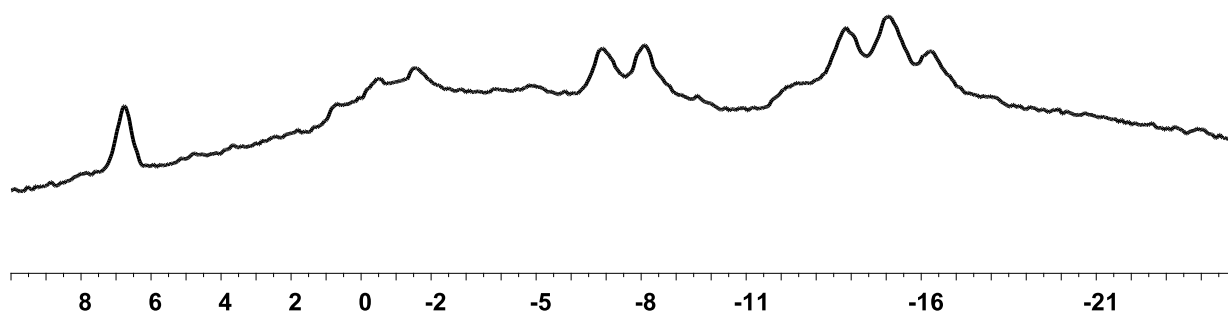
**Figure G.67:** $^{11}$B NMR of **D**

## 11. Study and Comparison of Literature PXRD Patterns with Varying Carborane Isomers and Chalcogens

To validate the observed differences in the PXRD patterns of materials **A** and **B**, **B** and **C**, and **C** and **D**, the comparison of simulated PXRD patterns of molecular carborane-based compounds with different carborane isomers and chalcogens was performed (references 9 and 13).

**Comparison of Simulated PXRD for 9-TEMPO-*Ortho*-Carborane (9-TEMPO-oCB) and 9-TEMPO-*Meta*-Carborane (9-TEMPO-mCB)**

Similar to the observed differences in the PXRD peaks between materials **A** and **B**, or **C** and **D**, minor deviations are expected as a result of different molecular packing in the solid state as a result of the carborane dipole. Below you will find the simulated PXRD peak patterns of 9-TEMPO-*ortho*-carborane (9-TEMPO-oCB, green) and 9-TEMPO-*meta*-carborane (9-TEMPO-mCB, black). Despite the molecular similarity between the two TEMPO adducts, the two PXRD patterns show differences on a similar magnitude as seen when comparing the PXRD patterns of materials containing separate carborane isomers.
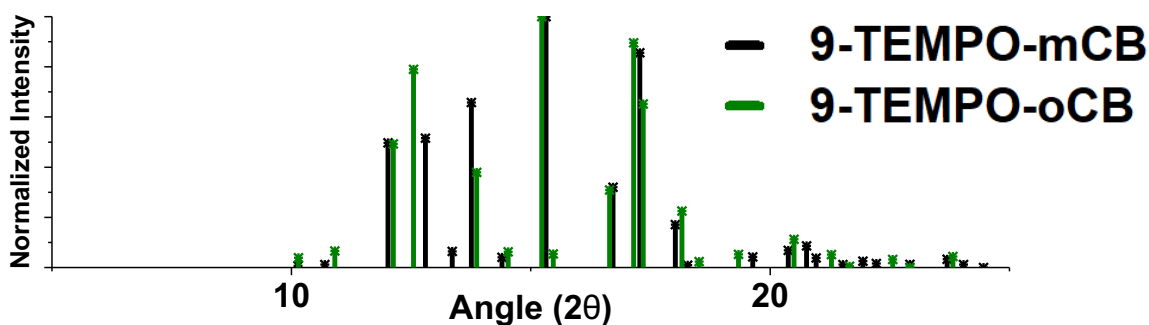


**Figure G.68:** Overlay of calculated PXRD patterns of 9-TEMPO-mCB (black) and 9-TEMPO-oCB (green)

**Comparison of Simulated PXRD for *Meta*-Carborane Diselenide ((Se-mCB)₂) and Ditelluride ((Te-mCB)₂)**

Similar to the observed differences in the PXRD peaks between materials **A** and **C**, or **B** and **D**, minor deviations are expected as a result of the presence of differently sized chalcogens present in the material. Below you will find the simulated PXRD peak patterns of *meta*-carborane diselenide ((Se-mCB)₂, black) and *meta*-carborane ditelluride ((Te-mCB)₂, green). As expected, by increasing the size of the chalcogen present in the crystal, a general shift to lower 2theta values is observed. This trend is also evident when comparing the PXRD patterns of material **A** and **C**, or **B** and **D**
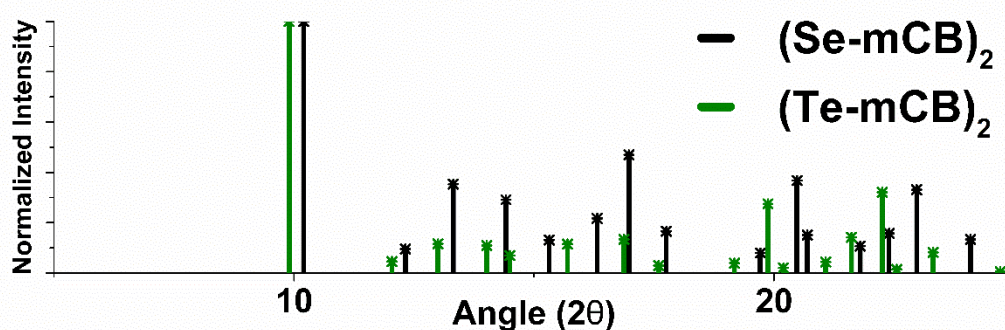


**Figure G.69:** Overlay of calculated PXRD patterns of (Se-mCB)₂ (black) and (Te-mCB)₂ (green)

## 12. Qualitative Assessment of Emission Properties in Various Solvents and Media

To further understand the emission properties and mechanism at play in materials **A-D** the emission of materials **A** and **B** were qualitatively assessed in several solvents and media.

**Emission of Soluble Solutions of A and B in Organic Solvents**

Surprisingly, all materials are partially soluble in several polar, aprotic organic solvents, and all emissive properties are no longer present after dissolution at room temperature (see below). Unexpectedly, the solubility of **B** in dichloromethane is significantly lower than that of **A**. This is likely a result of the stronger intermolecular forces present in the *ortho*-carborane-containing material hindering dissolution. Upon freezing the solutions of **A** and **B** to 77 K in liquid nitrogen, emission of the copper chalcogenide clusters in all cases return, albeit significantly red-shifted relative to the room temperature emission from the microcrystals as obtained from the reaction mixture (see below). This suggests that emission from the copper chalcogenide clusters occurs only when molecular movements are decreased either through decreasing the temperature of the molecule, as is the case in the below organic solutions, or by enforcing the clusters into a crystalline lattice, where motion would be limited by intermolecular interactions between adjacent clusters.
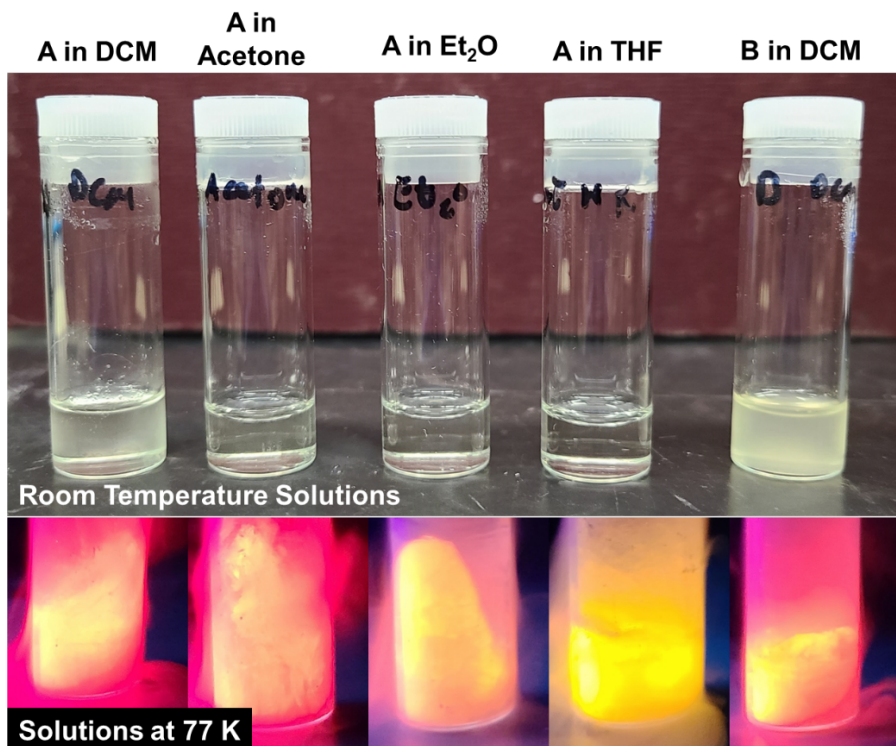
**Figure G.70:** Images of dissolved **A** and **B** in several solvents exhibiting emission at 77 K.

To confirm that the copper selenide clusters were still intact for material **A**, the dichloromethane solution was triturated with pentane, and the acetone solution was layered with *iso*-propanol. In both cases, **A** precipitated, and the initial green emission of the as synthesized microcrystals returned (see below).
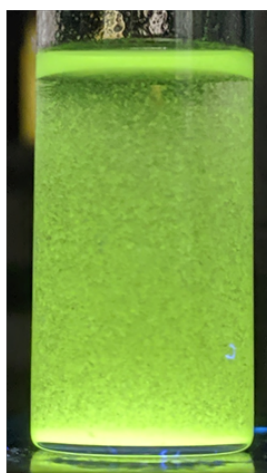


**Triturated by pentane from DCM (298 K)**
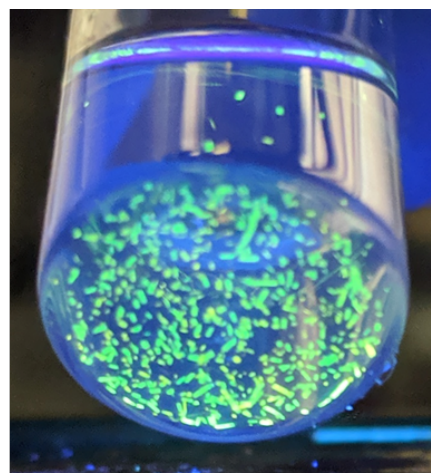
**Dissolved in acetone, layered by IPA (298 K)**

**Figure G.71:** Emission of triturated (left) and recrystallized (right) **A** at room temperature.

## Emission of A in Polymer Films

In addition to restricting molecular movement in the excited state by either freezing or crystallizing the copper selenide clusters, movement can also by restricted by a polymer matrix. In this situation, molecular movement would theoretically be limited by intermolecular interactions between the polymer matrix and copper selenide cluster, conceptually similar to crystallization. Solutions of PMMA (top) and polystyrene (bottom) were prepared in dichloromethane before the addition of several milligrams of **A**. Once fully dissolved, the solutions were cast onto quartz plates. Surprisingly, the as cast films exhibited similar luminescence to the frozen solutions though were still red-shifted relative to the pristine crystals (see below). This suggests that molecular movement is in fact somewhat limited while in the polymer matrix, but still less of that when in a crystalline matrix.
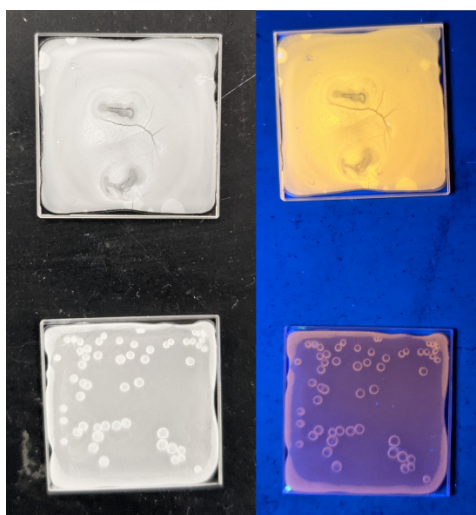


**Figure G.72:** Emission of **A** in polymer films.

## 13. References:

1. Lenher *et al. J. Am. Chem. Soc.* **1925** 47, 3, 772-774.
2. Hattne *et al. Acta Crystallogr. A Found. Adv.* **2015**, *71*, 353-360.
3. Nannenga *et al. Nat. Methods* **2014**, *11*, 927-930.
4. Kabsch *Acta Crystallogr. D Biol. Crystallogr.* **2010**, *66*, 125-132.
5. Sheldrick *et al. Acta Crystallogr. A Found. Adv.* **2015**, *71*, 3-8.
6. Hubschle *et al. J. Appl. Crystallogr.* **2011**, *44*, 1281-1284.
7. Peng *Micron* **1999**, *30*, 625-648.
8. Fairley *et al. Applied Surface Science Advances* **2021** doi.org/10.1016/j.apsadv.2021.100112
9. Mills *et al. Inorg. Chem.* **2021**, 60, 24, 19165-19174.
10. Plešek *et al. Coll. Czech. Chem. Commun.* **1981**, 46, 687-692.
11. Zakharkin *et al. Phosphorus and Sulfur* **1984**, 20, 357-370.
12. Polgar *et al. Inorg. Chem.* **2019**, 58, 5, 3338-3348.
13. Mils *et al. J. Am. Chem. Soc.* **2020**, 142, 4586-4591.

*Appendix H*

*Supporting Information for Chapter 9: Elucidation of Diverse Solid-State Packing in a Family of Electron-Deficient Expanded Helicenes via Microcrystal Electron Diffraction*

# General details

Commercial cerium ammonium nitrate (CAN) from Sigma-Aldrich was purified according to a literature procedure,[1] *o*-phenylenediamine was purified by sublimation under vacuum (15 mmHg, 50 °C). Compound **1a** was prepared according to the literature.[2] All other reagents and solvents were purchased from commercial suppliers and used as received. Mass spectrometry was performed by the QB3/Chemistry Mass Spectrometry Facility at the University of California, Berkeley. Preparatory thin layer chromatography was carried out using Analtech 1000-micron preparatory plates. Unless otherwise noted, NMR spectra were acquired at ambient temperature (~22 °C) using Bruker AV-700, AV-600, AV-500, DRX-500, AV-400, and AV-300 spectrometers. Chemical shifts (δ) are given in ppm and referenced to residual solvent peaks for $^1$H NMR spectra (δ = 7.26 ppm for chloroform-*d*) and for $^{13}$C{$^1$H} NMR spectra (δ = 77.16 ppm for chloroform-*d*).

# Synthetic procedures and characterization of compounds
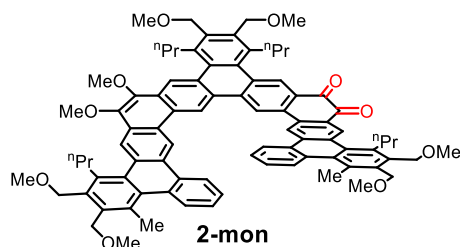


**Expanded [11]helicene monoquinone (2-mon).**
A 20 mL vial was charged with compound **1a** (100.0 mg, 0.076 mmol, 1.0 equiv) and $CH_2Cl_2$ (2.5 mL) to form a homogeneous solution, then the solution was diluted with MeCN (1.3 mL) (to avoid solubility issues, the order of addition is important). To the stirred solution was added a solution of cerium ammonium nitrate (251 mg, 0.458 mmol, 6.0 equiv) in water (4.6 mL). The biphasic mixture was stirred vigorously (*i.e.*, at a rate such that the phases become indistinguishable) for 3 h, then diluted with water (10 mL) and $CH_2Cl_2$ (50-60 mL, or until the organic layer became transparent). The layers were separated, and the organic layer was dried with $MgSO_4$, filtered, and the filtrate was concentrated by rotary evaporation. The residue was subjected to preparatory thin layer chromatography (15:1 $CH_2Cl_2$:MeCN) to afford **2-mon** (81 mg, 84%) as a red solid. $^1$H NMR (chloroform-*d*, 600 MHz): δ = 10.06 (s, 1H), 10.04 (s, 1H), 9.54 (s, 1H), 9.47 (s, 1H), 9.08 (s, 1H), 9.06 (s, 1H), 9.03 (s, 1H), 9.00 (s, 1H), 8.96 (d, J = 7.9 Hz, 1H), 8.91 (d, J = 7.9 Hz, 1H), 8.25 (dd, J = 12.9, 8.0 Hz, 2H), 7.64 – 7.40 (m, 4H), 4.83 (s, 2H), 4.82 – 4.78 (m, 6H), 4.77 (s, 2H), 4.73 (s, 2H), 4.21 (s, 3H), 4.19 (s, 3H), 3.62 (s, 3H), 3.61 (s, 3H), 3.61 (s, 6H), 3.57 (s, 3H), 3.57 (s, 3H), 3.52 – 3.41 (m, 4H), 3.35 – 3.24 (m, 4H), 2.98 (s, 3H), 2.97 (s, 3H), 2.17 – 2.08 (m, 4H), 2.01 – 1.91 (m, 4H), 1.19 – 1.12 (m, 6H), 1.08 (t, J = 7.3 Hz, 3H), 1.03 (t, J = 7.3 Hz, 3H); $^{13}$C{$^1$H} NMR (chloroform-*d*, 151 MHz): δ = 180.61, 180.48, 145.02, 143.81, 137.49, 137.19, 137.17, 137.11, 136.83, 136.83, 136.75, 136.62, 136.29, 136.13, 135.61, 134.93, 134.47, 134.41, 134.38, 133.51, 133.26, 132.97, 132.93, 132.82, 132.48, 132.42, 132.40, 132.32, 132.30, 132.00, 131.87, 131.73, 131.73, 131.57, 130.91, 130.24, 129.80, 129.79, 129.73, 129.62, 129.34, 129.05, 128.39, 128.21, 127.98, 127.93, 127.87, 127.44, 127.11, 126.42, 123.64, 123.08, 122.79, 122.78, 119.31, 119.05, 118.56, 117.37, 69.34, 69.29, 69.27, 69.07, 69.02, 68.98, 61.08, 61.04, 59.02, 58.99, 58.97, 58.94, 58.86, 58.82, 35.28, 35.19, 35.05, 34.99, 26.02, 25.97, 25.83, 25.77, 20.69, 20.68, 14.69, 14.68, 14.59, 14.58; HRMS-ESI (m/z): [M+H]$^+$ calcd. for $C_{86}H_{87}O_{10}$, 1279.6294; found, 1279.6288.
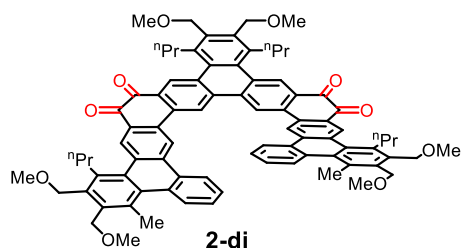
**Expanded [11]helicene diquinone (2-di).**
A 20 mL screw-cap vial was charged with compound **1a** (100 mg, 0.076 mmol, 1.0 equiv), $CH_2Cl_2$ (5.1 mL), and MeCN (2.5 mL) (to avoid solubility issues, the order of addition is important). To the stirred solution was added a solution of cerium ammonium nitrate (628 mg, 1.15 mmol, 15 equiv) in water (8.9 mL). The biphasic mixture was stirred vigorously (*i.e.*, at a rate such that the phases become indistinguishable) for 5 h, then diluted with $CH_2Cl_2$ (30 mL). The layers were separated, and the organic layer was dried with $MgSO_4$, filtered, and the filtrate was concentrated by rotary evaporation. The residue was subjected to preparatory thin layer chromatography (15:1 $CH_2Cl_2$:MeCN) to afford **2-di** (72 mg, 76%) as a red solid. $^1H$ NMR (chloroform-*d*, 500 MHz, [c] = 80 mM): δ = 9.39 (s, 2H), 9.14 (s, 2H), 9.02 (s, 2H), 8.78 (s, 2H), 8.64 (s, 2H), 8.22 (d, *J* = 7.8 Hz, 2H), 7.58 (q, *J* = 11.1, 9.0 Hz, 4H), 4.74 (s, 4H), 4.62 (s, 4H), 4.51 (s, 4H), 3.58 (s, 6H), 3.51 (s, 6H), 3.47 (s, 6H), 3.08 – 2.97 (m, 4H), 2.92 (s, 6H), 2.89 – 2.71 (m, 4H), 1.90 – 1.70 (m, 8H), 0.85 (s, 12H); $^{13}C\{^1H\}$ NMR (chloroform-*d*, 126 MHz, [c] = 80 mM): δ = 180.74, 180.24, 138.02, 137.27, 136.99, 136.89, 136.31, 135.48, 134.96, 134.40, 133.00, 132.64, 132.49, 132.43, 132.25. 132.19, 131.81, 131.80, 131.68, 131.50, 130.07, 130.06, 129.56, 128.79, 128.21, 127.93, 124.39, 119.72, 119.44, 69.30, 68.90, 68.57, 58.96, 58.85, 58.72, 35.06, 34.95, 25.64, 25.28, 20.66, 14.37, 14.15; HRMS-ESI (m/z): [M+H]$^+$ calcd. for $C_{84}H_{81}O_{10}$, 1249.5824; found, 1249.5848.
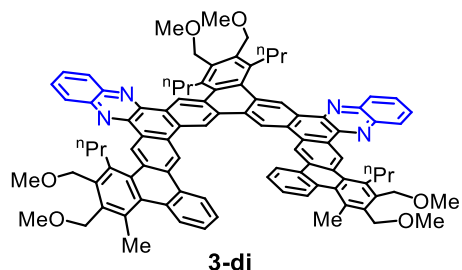


**Expanded [11]helicene diquinoxaline (3-di).**
A 20 mL screw-cap vial was charged with compound **2-di** (72 mg, 0.058 mmol, 1.0 equiv), *o*-phenylenediamine (125 mg, 1.15 mmol, 20.0 equiv), and 1,2-dichloroethane (4 mL). The vial was sealed, then the stirred mixture was heated at 80 °C for 16 h, brought to RT, and concentrated under reduced pressure. To remove excess *o*-phenylenediamine, the residue was dissolved in $CH_2Cl_2$ (3 mL), then the solution was diluted with MeCN (3 mL) and concentrated to ~2 mL *via* rotary evaporation. The resulting precipitate was collected by filtration, washed with MeCN (2 mL), and recrystallized from toluene (7 mL) at −25°C to afford **3-di** (70 mg, 89%) as a yellow needles.*
$^1H$ NMR (chloroform-*d*, 500 MHz, [c] = 24 mM): δ = 10.28 (s, 4H), 10.12 (s, 2H), 10.04 (s, 2H), 9.06 (d, *J* = 7.7 Hz, 2H), 8.32 (d, *J* = 9.7 Hz, 6H), 7.86 (dd, *J* = 6.4, 3.3 Hz, 4H), 7.57 (dt, *J* = 20.1, 7.2 Hz, 4H), 4.91 (s, 4H), 4.86 (d, *J* = 5.5 Hz, 8H), 3.65 (s, 6H), 3.63 (s, 6H), 3.60 (s, 6H), 3.49 (s, 8H), 3.02 (s, 6H), 2.51 (s, 8H), 1.28 – 1.19 (m, 12H); $^{13}C\{^1H\}$ NMR (chloroform-*d*, 151 MHz, [c] = 24 mM): δ = 143.01, 142.97, 142.17, 142.13, 136.91, 136.69, 136.43, 136.21, 135.05, 134.32, 133.89, 133.10, 132.70, 132.65, 132.00, 131.81, 131.54, 130.91, 130.75, 129.80, 129.74, 129.49, 129.47, 129.45, 129.45, 129.29, 129.18, 128.35, 128.02, 127.03, 126.83, 126.33, 122.95, 117.72,

117.13, 69.47, 69.18, 69.12, 58.82, 58.76, 58.65, 53.55, 35.67, 25.63, 25.34, 20.66, 15.37, 15.32; [M+H]$^+$ calcd. for $C_{96}H_{89}O_6N_4$, 1393.6777; found, 1393.6803.

*Crystals isolated in this way possess low kinetic solubility, requiring sonication or vigorous stirring to re-dissolve. Solutions of **3-di** in $CH_2Cl_2$ can be directly evaporated to yield a yellow amorphous film that is easily re-dissolved.
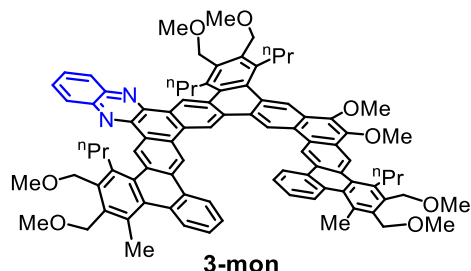


**3-mon**

## Expanded [11]helicene monoquinoxaline (3-mon).

A 25 mL Teflon-stoppered flask was loaded with compound **2-mon** (95 mg, 0.074 mmol. 1.0 equiv), *o*-phenylenediamine (40 mg, 0.37 mmol, 5 equiv), and 1,2-dichloroethane (5 mL). The flask was sealed, then the stirred mixture was heated at 70 °C for 2 h, brought to RT, and concentrated under reduced pressure. To remove excess *o*-phenylenediamine, the residue was dissolved in $CH_2Cl_2$ (5 mL), the solution was diluted with MeCN (3 mL), and the volume was reduced to ~2 mL *via* rotary evaporation. The resulting precipitate was collected by filtration, washed with MeCN (3 mL), and recrystallized from toluene at −25 °C to afford **3-mon** (67 mg, 67%) as a yellow microcrystalline solid.* $^1$H NMR (chloroform-d, 600 MHz, [c] = 62 mM): δ = 10.14 (s, 1H), 10.12 (s, 1H), 10.10 (s, 1H), 10.07 (s, 1H), 9.94 (s, 1H), 9.89 (s, 1H), 9.12 (s, 1H), 9.10 (s, 1H), 9.02 (dd, *J* = 7.3, 2.0 Hz, 1H), 8.98 (s, 1H), 8.27 (dd, *J* = 7.3, 2.0 Hz, 2H), 8.22 (dd, *J* = 17.1, 7.7 Hz, 2H), 7.85 – 7.78 (m, 2H), 7.59 – 7.53 (m, 4H), 4.88 (s, 2H), 4.85 (s, 2H), 4.84 – 4.81 (m, 6H), 4.79 (s, 2H), 4.24 (s, 3H), 4.23 (s, 3H), 3.63 (s, 3H), 3.61 (s, 6H), 3.60 (s, 3H), 3.60 (s, 3H), 3.58 – 3.51 (m, 7H), 3.41 (s, 4H), 3.02 (s, 3H), 2.99 (s, 3H), 2.40 (d, *J* = 37.1 Hz, 4H), 2.10 (q, *J* = 7.7 Hz, 4H), 1.26 (t, *J* = 7.3 Hz, 3H), 1.19 (t, *J* = 7.3 Hz, 3H), 1.15 (t, *J* = 7.3 Hz, 3H), 1.11 (t, *J* = 7.3 Hz, 3H); $^{13}$C{$^1$H} NMR (chloroform-d, 151 MHz, [c] = 62 mM): δ = 144.42, 144.21, 143.42, 142.44, 136.88, 136.58, 136.53, 136.53, 136.49, 136.36, 136.15, 136.15, 135.19, 134.85, 134.56, 134.47, 134.44, 134.21, 133.70, 133.41, 133.37, 132.84, 132.11, 132.11, 132.10, 131.99, 131.75, 131.70, 131.62, 131.52, 131.19, 131.09, 130.74, 130.35, 130.11, 129.73, 129.73, 129.72, 129.69, 129.63, 129.63, 129.59, 129.59, 129.49, 129.11, 128.74, 128.68, 128.04, 128.00, 128.00, 127.43, 127.40, 127.31, 127.15, 126.71, 126.38, 123.27, 123.19, 122.83, 122.68, 118.16, 117.98, 117.60, 117.47, 69.45, 69.39, 69.35, 69.24, 69.23, 69.18, 61.12, 61.09, 58.96, 58.92, 58.90, 58.86, 58.80, 58.74, 35.68, 35.53, 35.31, 35.25, 26.08, 25.90, 25.83, 25.61, 20.74, 20.72, 15.34, 15.29, 14.71, 14.70; [M+H]$^+$ calcd. for $C_{92}H_{91}O_8N_2$, 1351.6770; found, 1351.6773.

*Crystals isolated in this way possess low kinetic solubility, requiring sonication or vigorous stirring to re-dissolve. Solutions of **3-mon** in $CH_2Cl_2$ can be directly evaporated to yield a yellow amorphous film that is easily re-dissolved.

# $^1$H and $^{13}$C{$^1$H} NMR spectra
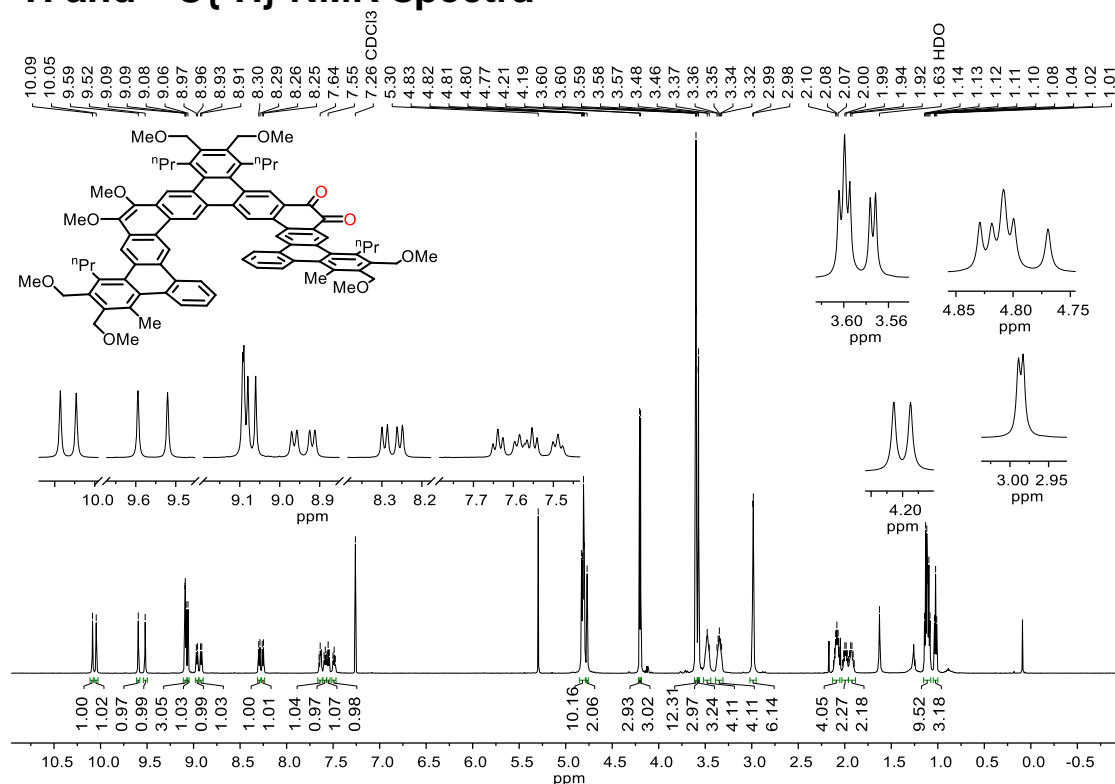


**Figure H.1.** $^1$H NMR spectrum (600 MHz, chloroform-*d*) of **2-mon**.
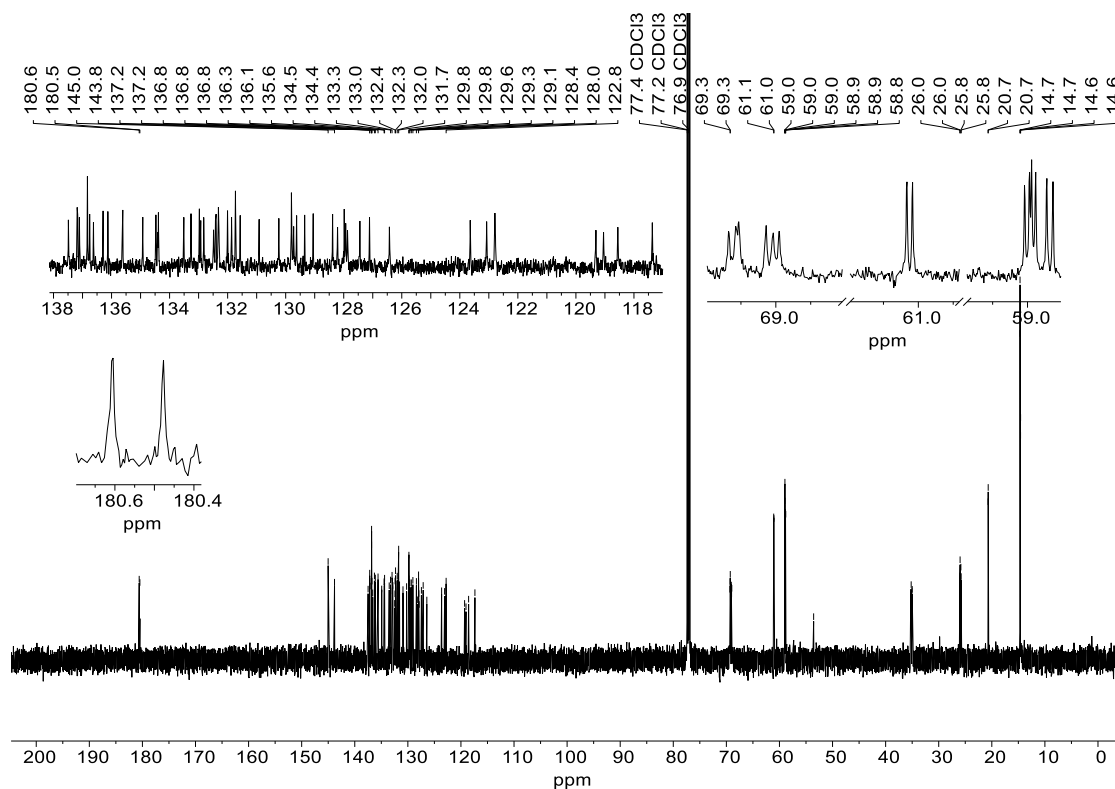


**Figure H.2.** $^{13}$C{$^1$H} NMR spectrum (151 MHz, chloroform-*d*) of **2-mon**.
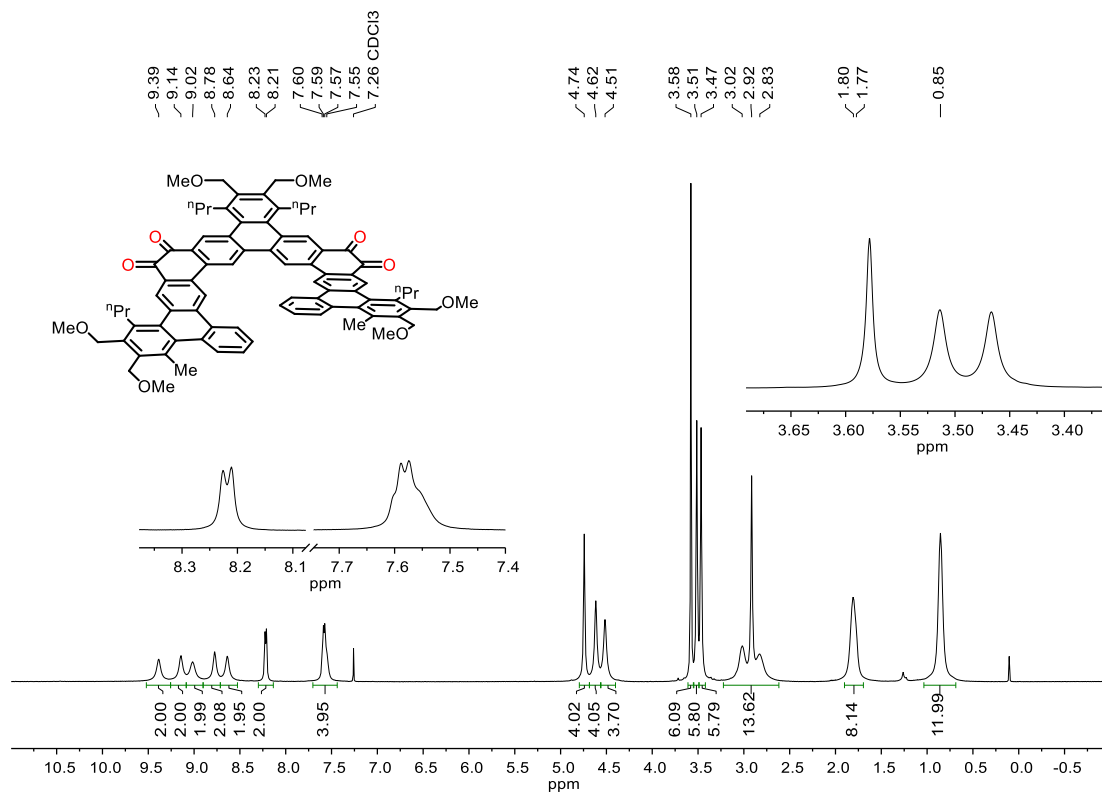
**Figure H.3.** $^1$H NMR spectrum (500 MHz, chloroform-*d*, [c] = 80 mM) of **2-di**.
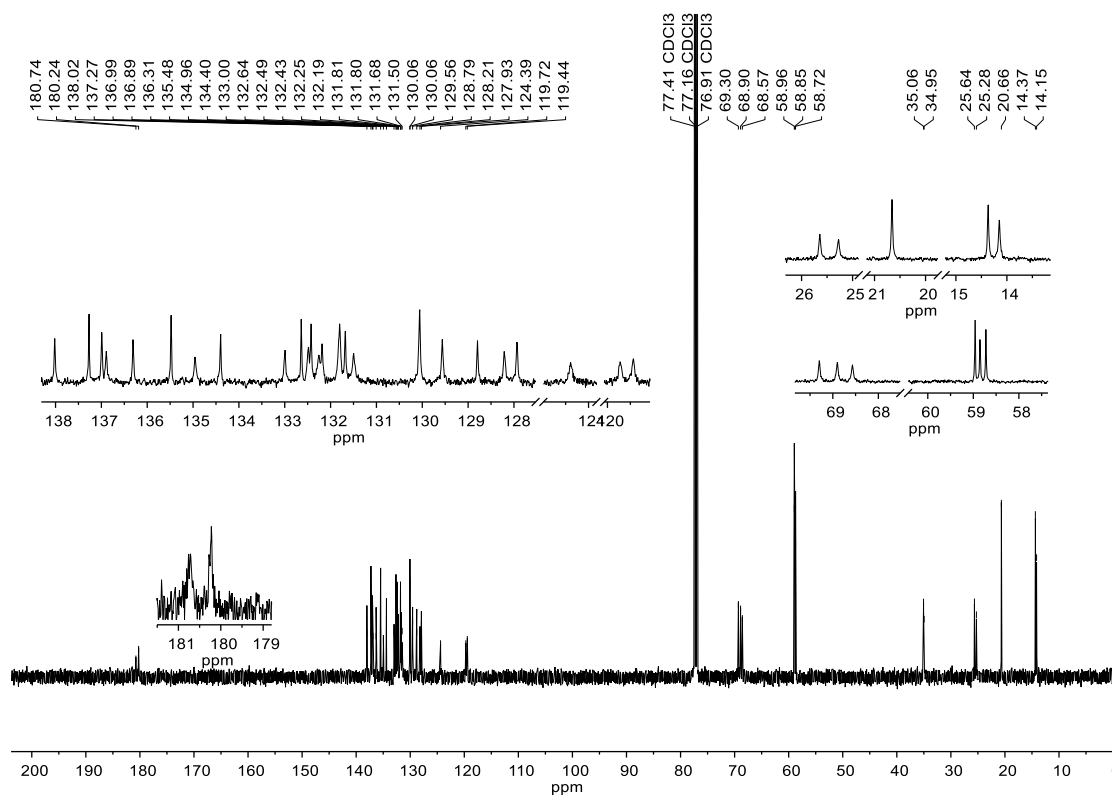


**Figure H.4.** $^{13}$C{$^1$H} NMR spectrum (126 MHz, chloroform-*d*, [c] = 80 mM) of **2-di**.
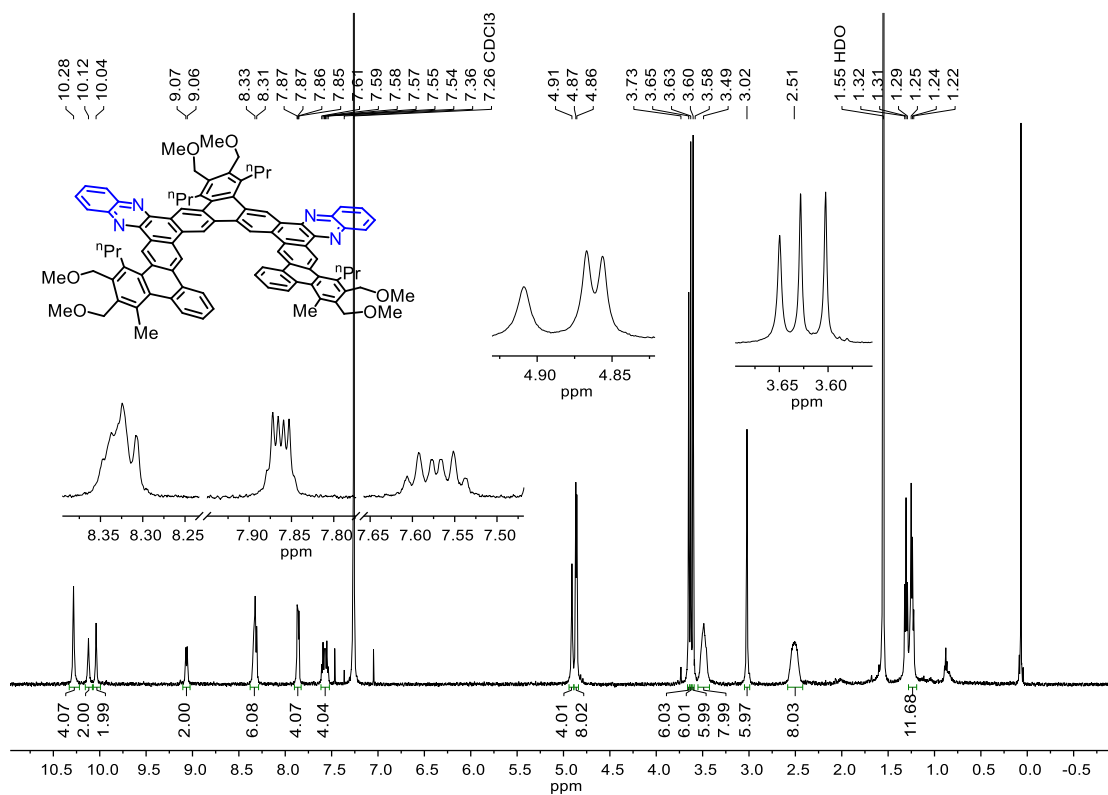
**Figure H.5.** $^1$H NMR spectrum (500 MHz, chloroform-*d*, [c] = 24 mM) of **3-di**.
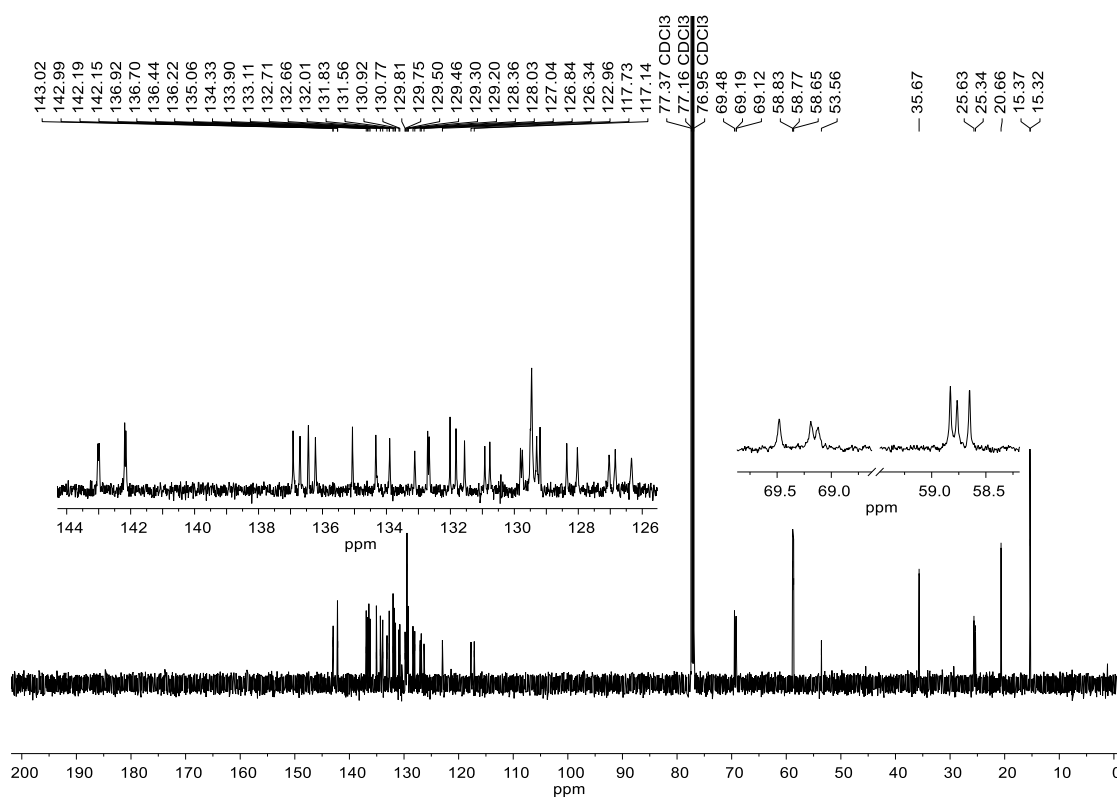


**Figure H.6.** $^{13}$C{$^1$H} NMR spectrum (151 MHz, chloroform-*d*, [c] = 24 mM) of **3-di**.
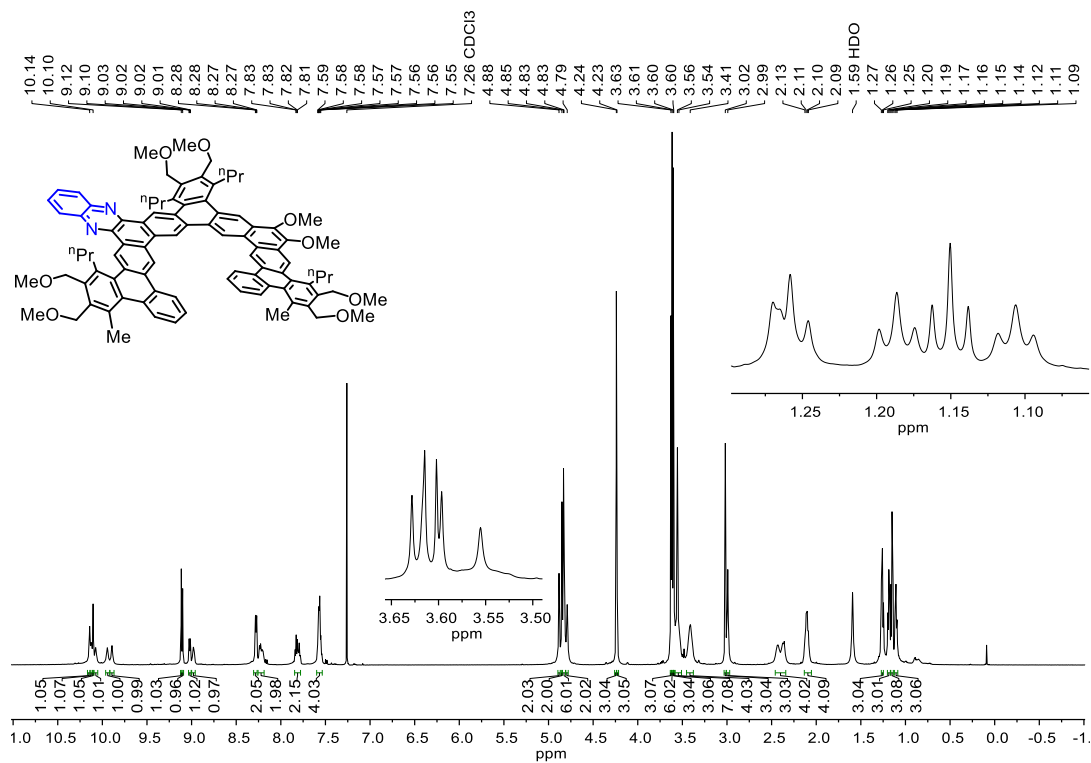
**Figure H.7.** $^1$H NMR spectrum (500 MHz, chloroform-*d*, [c] = 62 mM) of **3-mon**.
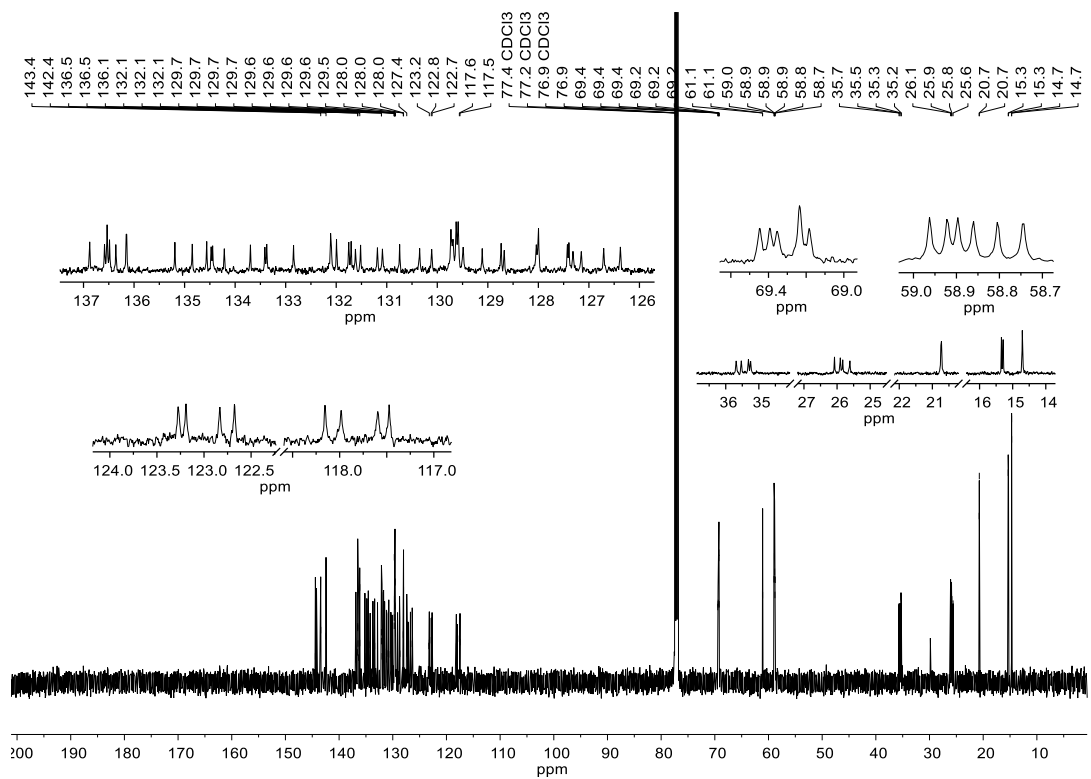


**Figure H.8.** $^{13}$C{$^1$H} NMR spectrum (151 MHz, chloroform-*d*, [c] = 62 mM) of **3-mon**.

# Variable concentration $^1$H NMR spectra
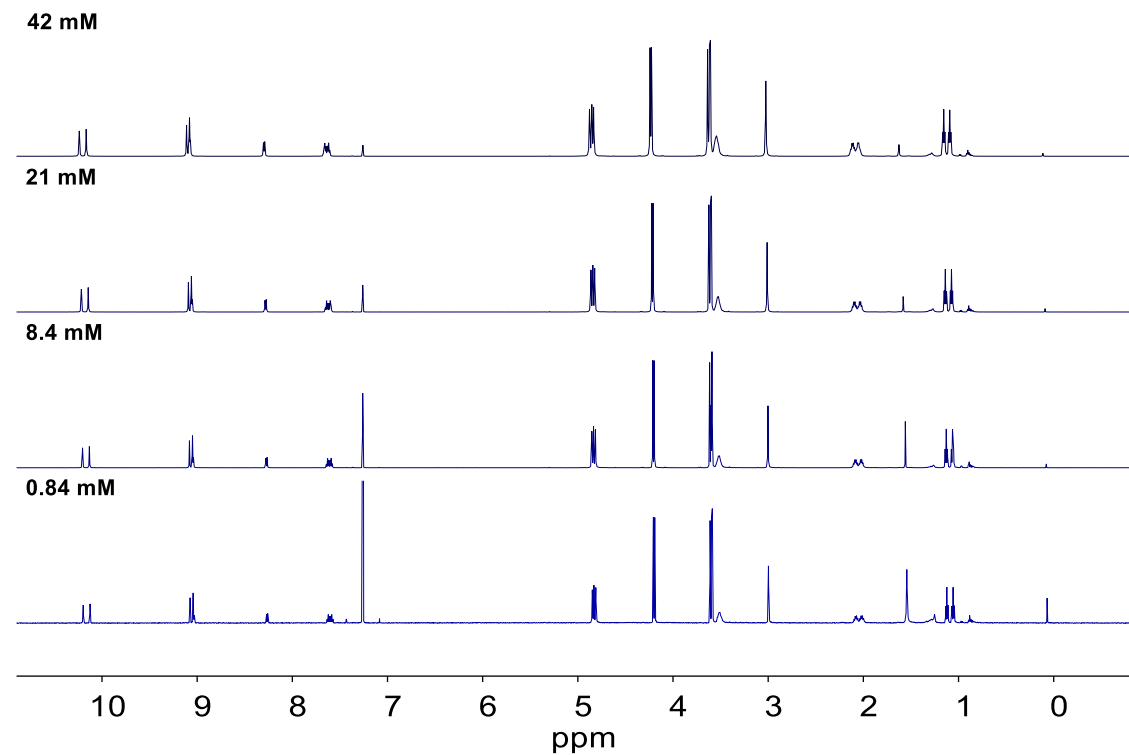


**Figure H.9.** Variable concentration $^1$H NMR spectra (600 MHz, chloroform-*d*) of **1a**.
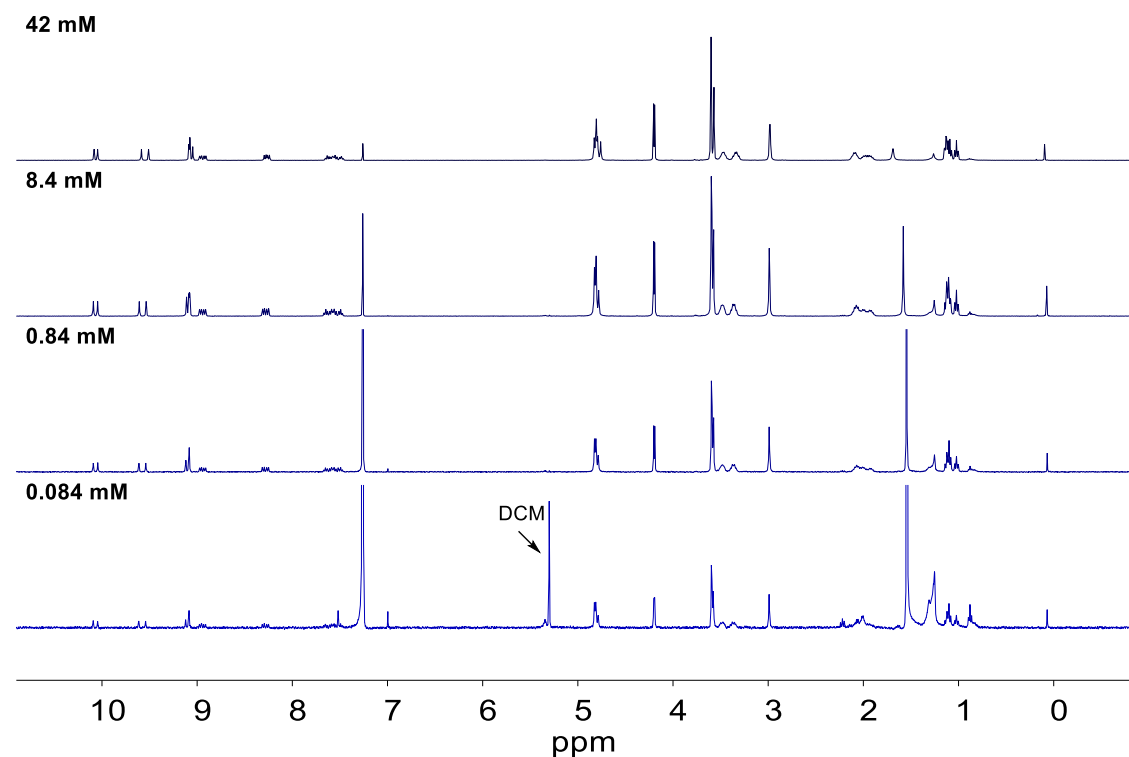


**Figure H.10.** Variable concentration $^1$H NMR spectra (400 MHz, chloroform-*d*) of **2-mon**.
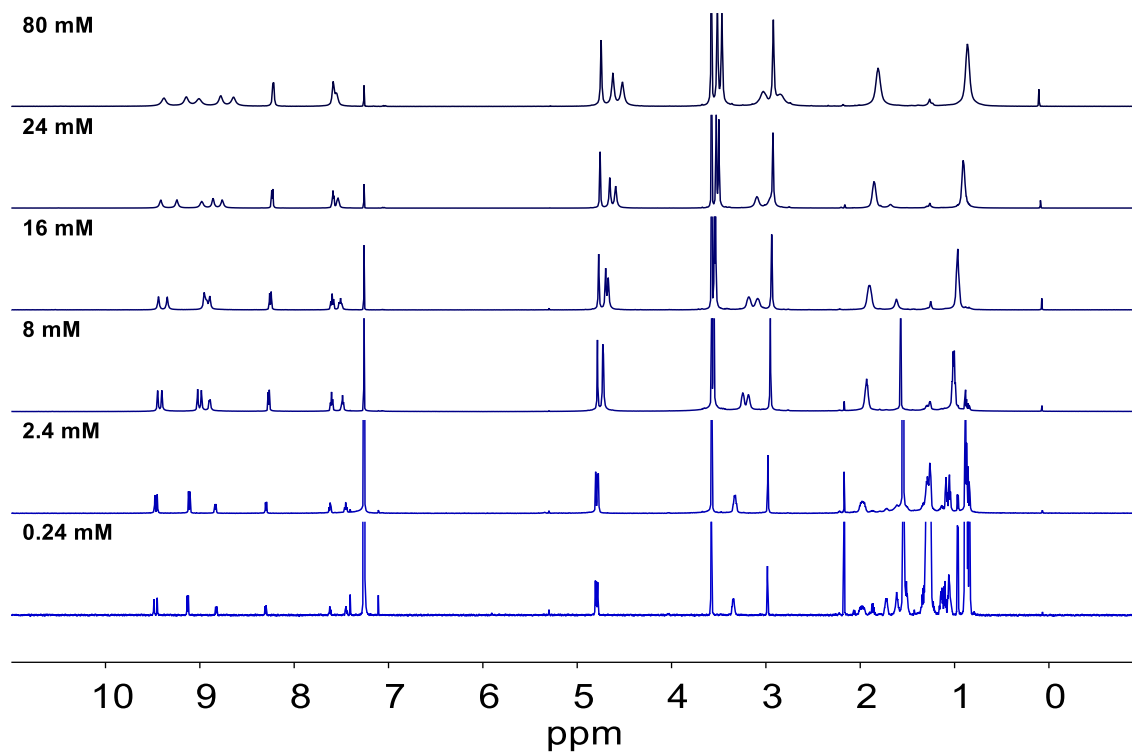
**Figure H.11.** Variable concentration $^1$H NMR spectra (700 MHz, chloroform-*d*) of **2-di**.
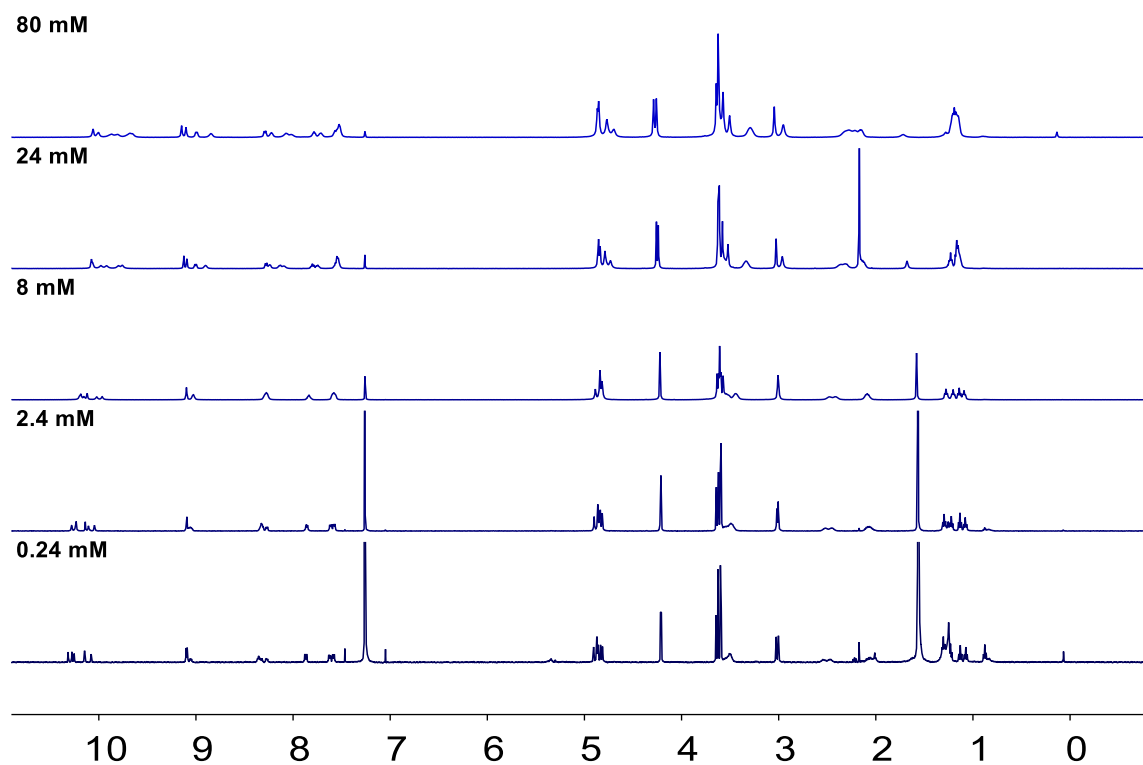


**Figure H.12.** Variable concentration $^1$H NMR spectra (500 MHz, chloroform-*d*) of **3-mon**.
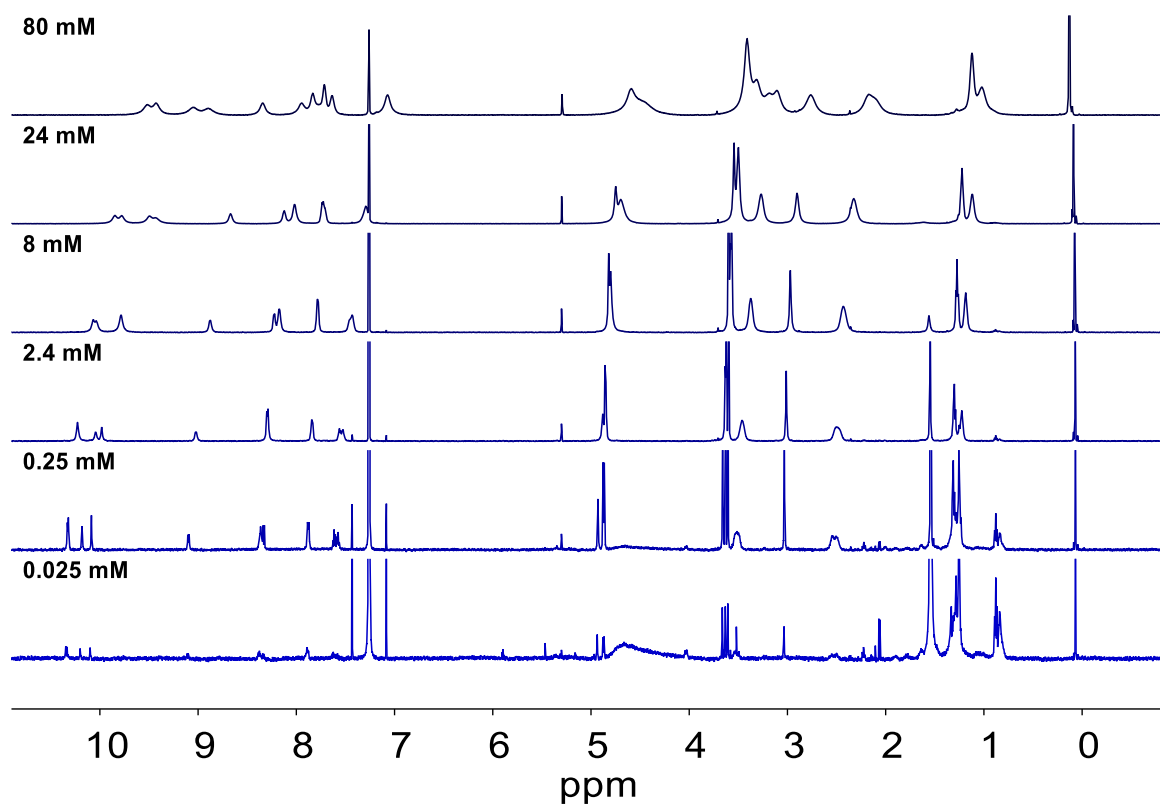
**Figure H.13.** Variable concentration $^1$H NMR spectra (600 MHz, chloroform-*d*) of **3-di**.

# MicroED experimental details

### Crystallization procedures
Samples were crystallized using the following procedures:

**1a**: Approximately 800 mg of **1a** was dissolved in $CH_2Cl_2$ (6mL). Hexanes (10 mL) was added and the total volume reduced to 8 mL, precipitating a yellow microcrystalline solid.

**2-di**: An approximately 1 mg/mL solution of **2-di** in ethyl acetate was vapor diffused with pentane at room temperature for 24 hours to yield orange needles.

**2-mon**: An approximately 1 mg/mL solution of **2-mon** in ethyl acetate was vapor diffused with pentane at room temperature for 24 hours to yield orange needles.

**3-di**: An approximately 1 mg/mL solution of **3-di** in benzene was sonicated for several hours until fully dissolved. The solution was evaporated slowly to yield yellow rods.

**3-mon**: An approximately 1 mg/mL solution of **3-mon** in benzene was sonicated for several hours and gently heated until sample was fully dissolved. The solution was slow evaporated to yield yellow rods.

### Sample preparation for electron diffraction
Samples were prepared using either Quantifoil or pure Carbon TEM grids. To prepare grids, approximately 2 µL of the mother liquor containing crystals were pipetted on to the surface of the TEM grid and excess solvent was wicked away using a Kimwipe. TEM grids were then placed in a Gatan 626 cryo-holder and frozen under liquid nitrogen.

### Instrument parameters
Data for **2-mon**, **2-di**, **3-mon**, and **3-di** were acquired on a Thermo Fisher Talos F200C electron microscope operating at an acceleration voltage of 200 KeV, corresponding to a wavelength of 0.0251 Å. Data for **1a** was acquired on an FEI Tecnai TF-30 electron microscope operating at ambient temperature with and operating voltage of 300 KeV, corresponding to a wavelength of 0.0196 Å. Screening of the TEM grids for micro crystals was done by operating the microscope in over focused diffraction mode to minimize diffraction and hysteresis between screening and diffraction operational modes.

### Electron diffraction data collection procedure
Electron diffraction data was collected using either Thermo-Fischer CetaD or TVIPS TemCam-XF416 CMOS 4k x 4k camera. Images were collected in a movie format as crystals were continuously rotated in the electron beam.[3] Typical data collection was performed using a constant tilt rate of 0.3°/s between the minimum and maximum tilt ranges of −72° to +72°, respectively. During continuous rotation the camera integrated frames continuously at a rate of 3 seconds per frame. The dose rate was calibrated to <0.03 e$^-$/Å$^2$ s. Crystals selected for data collection were isolated by a selected area aperture to reduce the background noise contributions and calibrated to eucentric height to stay in the aperture over the entire tilt range.

### X-ray crystallography
Synchrotron data for **3-mon** was collected on beamline 24-ID-C at the Advanced Photon Source at a wavelength of 0.7749 Å, Argonne National Laboratory, which is equipped with a single axis MD2 goniometer, X-ray diffractometer and a Dectris Eiger2 16M pixel array detector at a distance of 150 mm. This single axis goniometer limited our achievable value of sin(theta-max)/wavelength but did not affect the unambiguous determination of this structure.

**Crystallographic data processing**

All diffraction data were processed using the XDS suite of programs.[4] All structures were solved *ab initio* using direct methods in SHELXT[5] or SHELXD[6] and refined with SHELXL[7] using ShelXle.[8] Thermal parameters for **1a**, **2-di**, **3-di**, and **3-mon** were refined anisotropically for all non-hydrogen atoms. **2-mon** was refined isotropically due to disorder causing a significant portion of the atoms to become non-positive definite. For all structures, hydrogen atoms were assigned using the riding model. Due to inherent disorder within crystals, and the fact that several datasets must be merged to obtain solutions, structures obtained show high R-values and areas of residual density which is difficult to refine for. The data here is the best which could be obtained through electron or synchrotron sources yielding results which would otherwise be unobtainable through standard X-ray analysis. The identity of each compound was verified through spectroscopic analysis; thus, the primary purpose of crystallographic studies was to understand solid state packing characteristics, for which such data is sufficient.



**Figure H.14.** Microscope image of the crystals used to attain the MicroED structure for **2-di**.



**Figure H.15.** Microscope image of the crystals used to attain the MicroED structure for **3-mon**.

**Compound 1a: MicroED data**
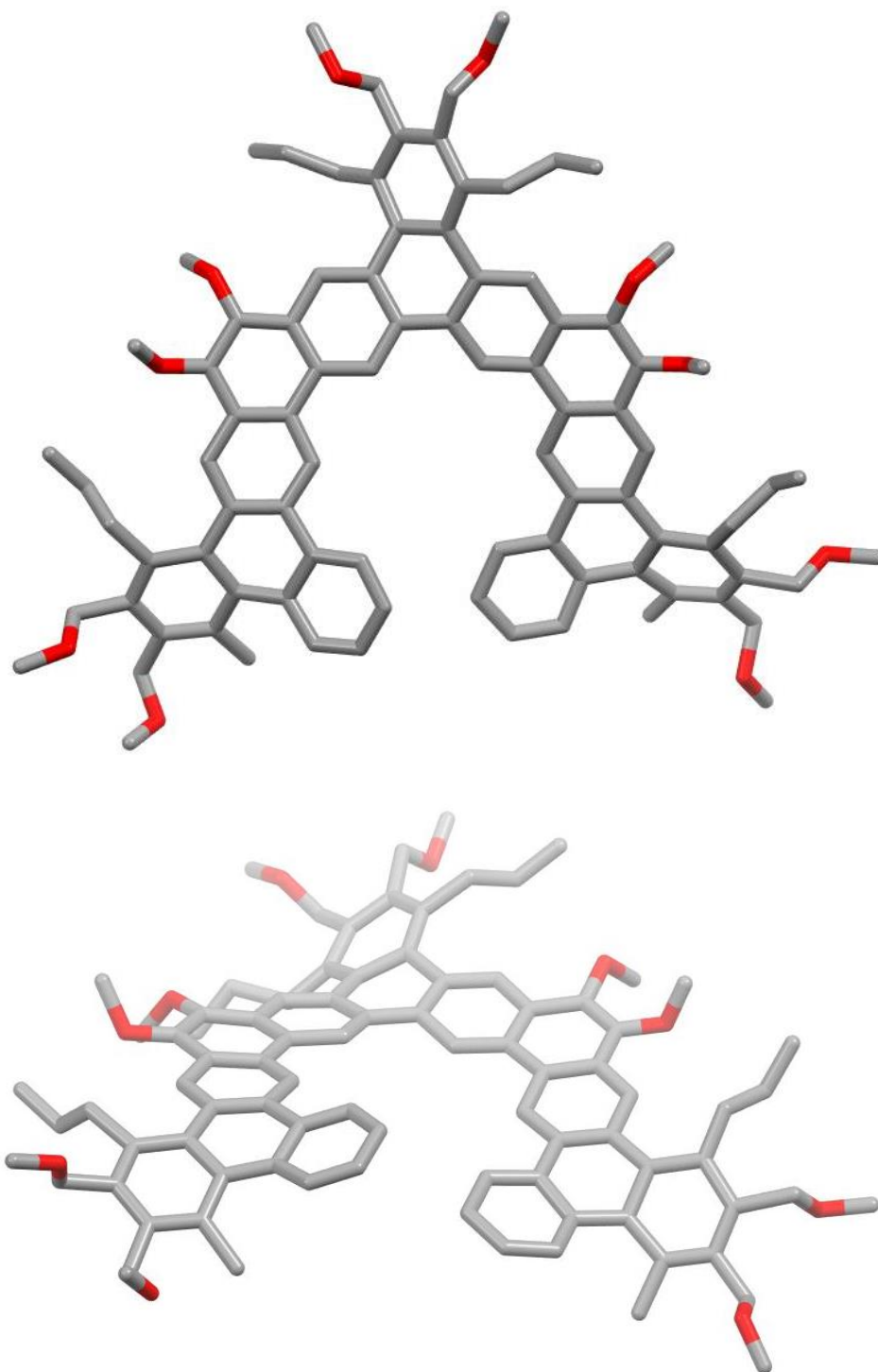


**Figure H.16.** MicroED structure for **1a** (CCDC 2026244).

| Structure | **1a** |
|---|---|
| Empirical formula | $C_{88}H_{92}O_{10}$ |
| Formula weight (g/mol) | 1279.62 |
| Crystal system | Orthorhombic |
| Space group | $P2_12_12_1$ (19) |
| Point group | 222 |
| Laue symmetry | mmm |
| Temperature (K) | 298 |
| Unit cell lengths a, b, c (Å) | 11.450(2), 18.420(4), 31.040(6) |
| Unit cell angles α, β, γ (°) | 90.000, 90.000, 90.000 |
| Unit cell volume (Å$^3$) | 6547(2) |
| F(000) | 289 |
| Z | 4 |
| Density (calculated) (g/cm$^3$) | 1.329 |
| Radiation source, wavelength (Å) | electron, 0.01969 |
| Resolution (Å) | 1.00 |
| Measured reflections | 31063 |
| Unique reflections | 5846 |
| Reflections with $I > 2\sigma(I)$ | 3977 |
| Completeness | 83.0% (4 merged datasets) |
| $I/\sigma$ | 7.38 |
| $\Theta_{max}$, $\Theta_{min}$ (°) | 0.57, 0.06 |
| Index ranges | $-11 \leq h \leq 11$, $-18 \leq k \leq 18$, $-26 \leq l \leq 26$ |
| Refinement method | Full-matrix least-squares on F$^2$ |
| H-atom treatment | H-atom parameters constrained |
| $R[F^2 > 2\sigma(F^2)]$ | 0.117 |
| $wR(F^2)$ | 0.264 |
| Goodness-of-fit on F$^2$ | 1.367 |
| $\Delta\rho_{max}$, $\Delta\rho_{min}$ (e/Å$^3$) | 0.16, −0.19 |

**Table H.1.** MicroED data for **1a** (CCDC 2026244).

**Compound 2-mon: MicroED data**
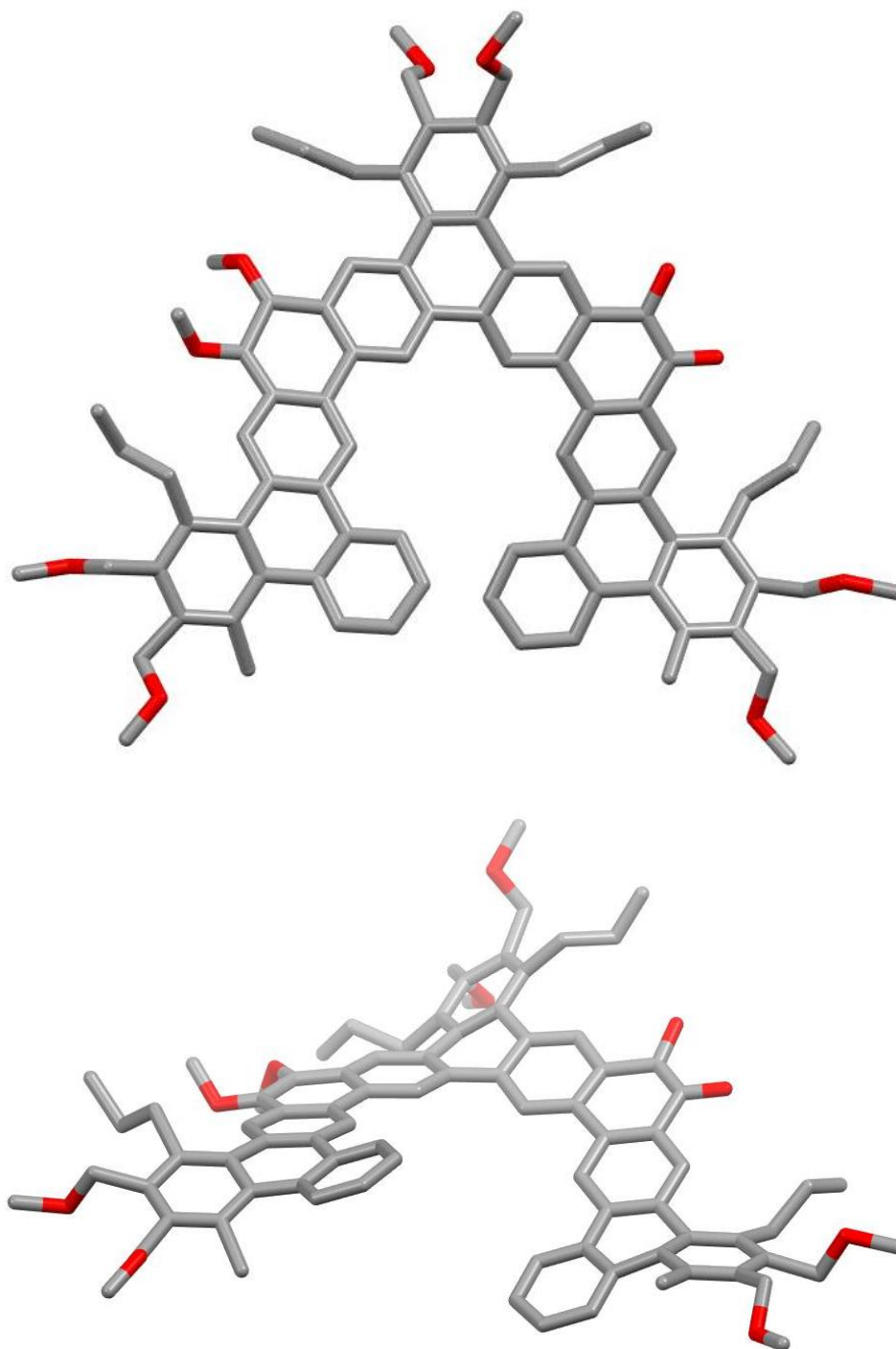


**Figure H.17.** MicroED structure for **2-mon** (CCDC 2026247).

| Structure | **2-mon** |
|---|---|
| Empirical formula | $C_{86}H_{86}O_{10}$ |
| Formula weight (g/mol) | 1279.62 |
| Crystal system | Orthorhombic |
| Space group | Iba2 (45) |
| Point group | mm2 |
| Laue symmetry | mmm |
| Temperature (K) | 100 |
| Unit cell lengths a, b, c (Å) | 47.570(2), 47.180(3), 8.190(3) |
| Unit cell angles α, β, γ (°) | 90.000, 90.000, 90.000 |
| Unit cell volume (Å$^3$) | 18381(7) |
| F(000) | 281 |
| Z | 8 |
| Density (calculated) (g/cm$^3$) | 0.925 |
| Radiation source, wavelength (Å) | electron, 0.02508 |
| Resolution (Å) | 1.10 |
| Measured reflections | 26331 |
| Unique reflections | 6674 |
| Reflections with $I > 2\sigma(I)$ | 4599 |
| Completeness | 90.7% (3 merged datasets) |
| $I/\sigma$ | 6.24 |
| $\Theta_{max}$, $\Theta_{min}$ (°) | 0.65, 0.08 |
| Index ranges | $-41 \leq h \leq 40$, $-42 \leq k \leq 42$, $-7 \leq l \leq 7$ |
| Refinement method | Full-matrix least-squares on $F^2$ |
| H-atom treatment | H-atom parameters constrained |
| $R[F^2 > 2\sigma(F^2)]$ | 0.163 |
| $wR(F^2)$ | 0.385 |
| Goodness-of-fit on $F^2$ | 1.721 |
| $\Delta\rho_{max}$, $\Delta\rho_{min}$ (e/Å$^3$) | 0.25, −0.26 |

**Table H.2.** MicroED data for **2-mon** (CCDC 2026247).

**Compound 2-di: MicroED data**
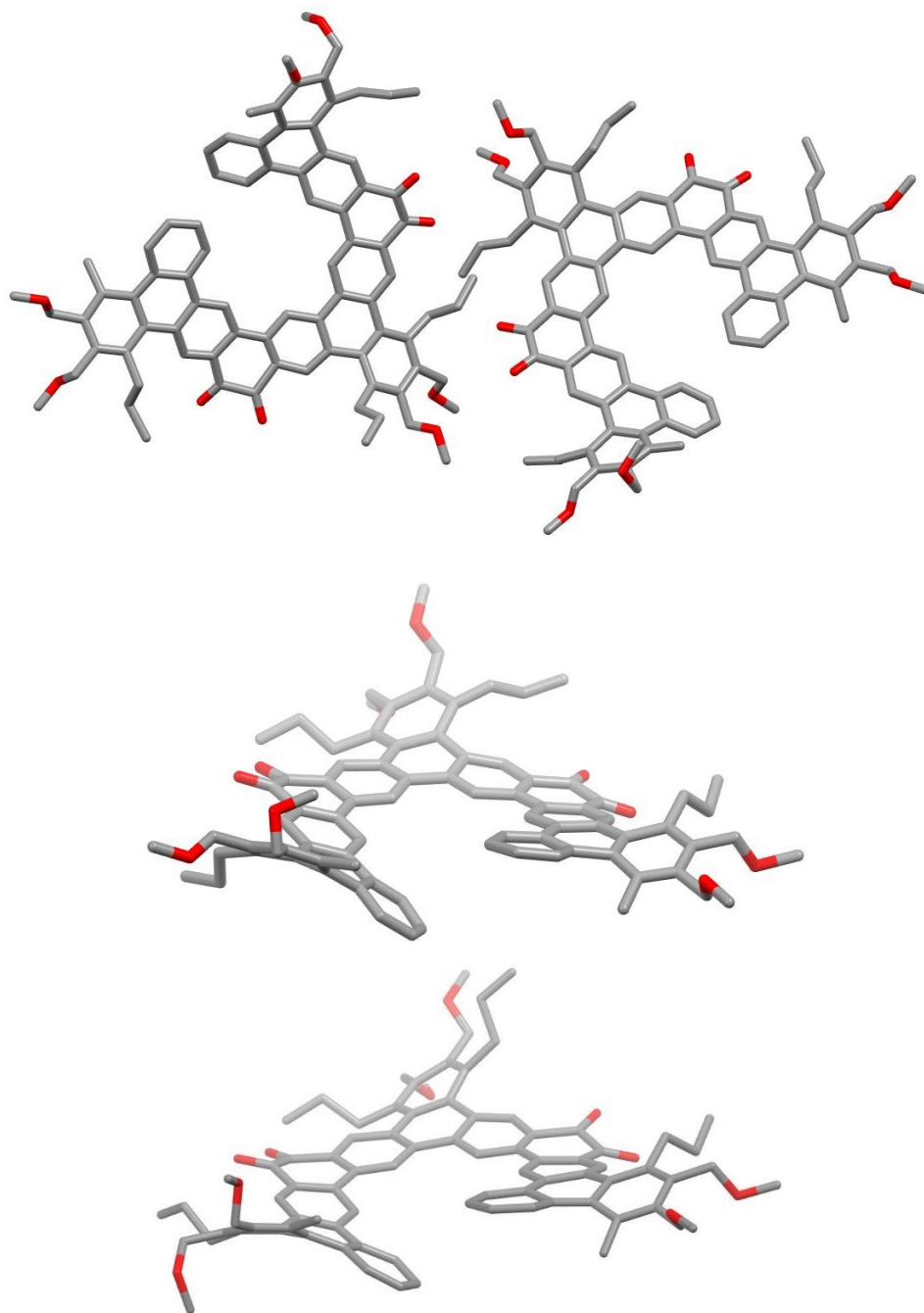


**Figure H.18.** MicroED structure for **2-di** (CCDC 2026249).

| Structure | **2-di** |
|---|---|
| Empirical formula | $C_{84}H_{80}O_{10}$ |
| Formula weight (g/mol) | 1249.55 |
| Crystal system | Triclinic |
| Space group | P-1 (2) |
| Point group | −1 |
| Laue symmetry | −1 |
| Temperature (K) | 100 |
| Unit cell lengths a, b, c (Å) | 8.030(2), 18.610(4), 45.130(9) |
| Unit cell angles α, β, γ (°) | 81.18(3), 89.13(3), 84.05(3) |
| Unit cell volume (Å$^3$) | 6629(3) |
| F(000) | 296 |
| Z | 4 |
| Density (calculated) (g/cm$^3$) | 1.324 |
| Radiation source, wavelength (Å) | electron, 0.02508 |
| Resolution (Å) | 1.00 |
| Measured reflections | 45615 |
| Unique reflections | 9966 |
| Reflections with $I > 2\sigma(I)$ | 6597 |
| Completeness | 72.0% (4 merged datasets) |
| $I/\sigma$ | 5.66 |
| $\Theta_{max}$, $\Theta_{min}$ (°) | 0.72, 0.08 |
| Index ranges | $-8 \leq h \leq 8$, $-16 \leq k \leq 16$, $-45 \leq l \leq 45$ |
| Refinement method | Full-matrix least-squares on F$^2$ |
| H-atom treatment | H-atom parameters constrained |
| $R[F^2 > 2\sigma(F^2)]$ | 0.172 |
| $wR(F^2)$ | 0.437 |
| Goodness-of-fit on F$^2$ | 1.588 |
| $\Delta\rho_{max}$, $\Delta\rho_{min}$ (e/Å$^3$) | 0.24, −0.20 |

**Table H.3.** MicroED data for **2-di** (CCDC 2026249).

**Compound 3-mon: MicroED and X-ray data**
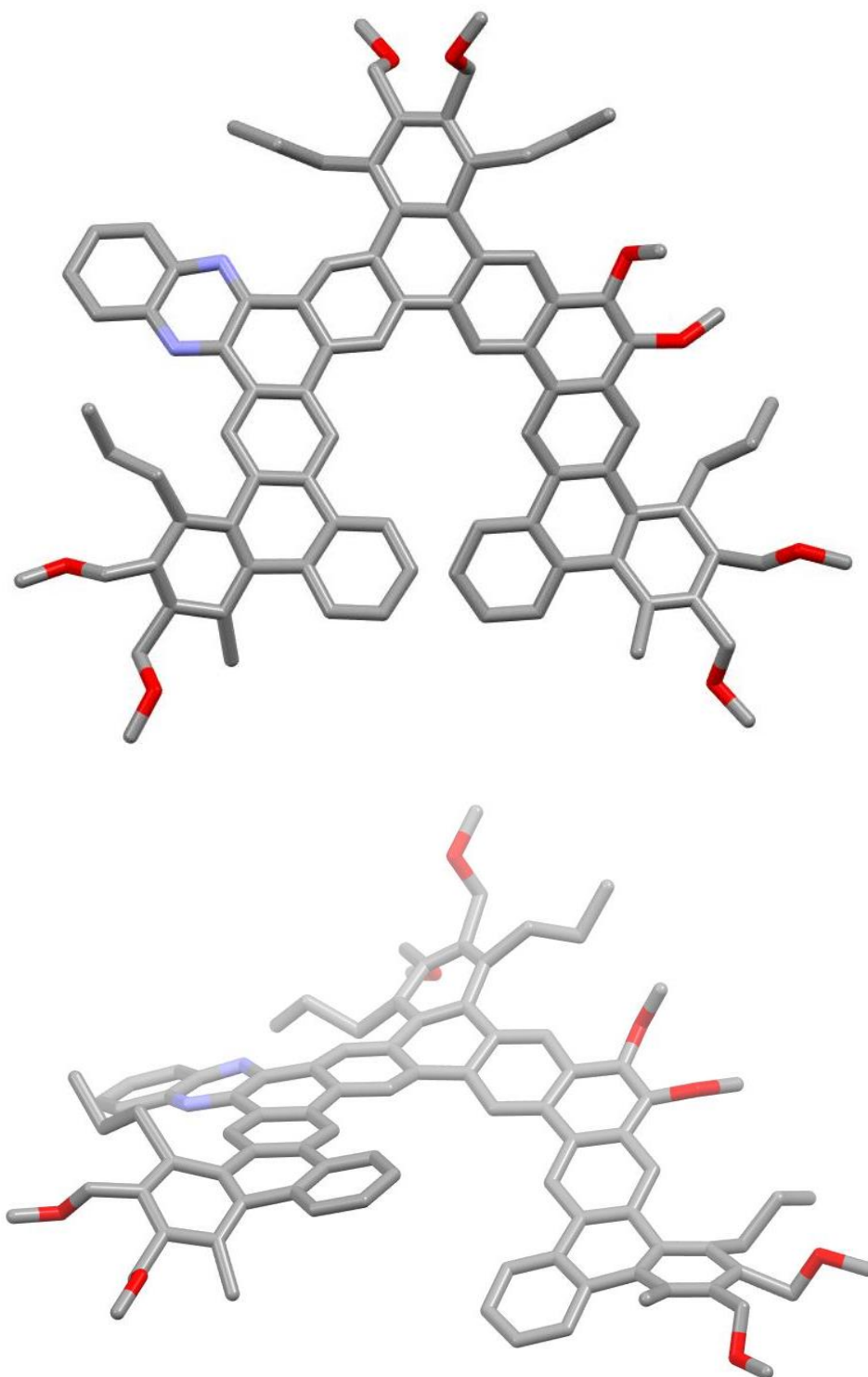


**Figure H.19.** MicroED structure for **3-mon** (CCDC 2026252).

| Structure | **3-mon** (electron) | **3-mon** (synchrotron) |
|---|---|---|
| Empirical formula | $C_{92}H_{90}N_2O_8$ | $C_{92}H_{90}N_2O_8$ |
| Formula weight (g/mol) | 1351.74 | 1351.74 |
| Crystal system | Orthorhombic | Orthorhombic |
| Space group | Iba2 (45) | Iba2 (45) |
| Point group | mm2 | mm2 |
| Laue symmetry | mmm | mmm |
| Temperature (K) | 100 | 100 |
| Unit cell lengths a, b, c (Å) | 48.29(5), 46.86(5), 7.970(8) | 47.750(2), 47.700(4), 8.220(6) |
| Unit cell angles α, β, γ (°) | 90.000, 90.000, 90.000 | 90.000, 90.000, 90.000 |
| Unit cell volume ($Å^3$) | 18035(32) | 18723(14) |
| F(000) | 295 | 720 |
| Z | 8 | 8 |
| Density (calculated) ($g/cm^3$) | 0.996 | 0.959 |
| Radiation source, wavelength (Å) | electron, 0.02508 | synchrotron, 0.77490 |
| Resolution (Å) | 1.00 | 1.05 |
| Measured reflections | 28118 | 111732 |
| Unique reflections | 9108 | 7747 |
| Reflections with $I > 2\sigma(I)$ | 4033 | 6600 |
| Completeness | 96.8% (3 merged datasets) | 91.1% (1 dataset) |
| $I/\sigma$ | 3.06 | 30.12 |
| $\Theta_{max}$, $\Theta_{min}$ (°) | 0.72, 0.08 | 21.68, 2.37 |
| Index ranges | $-46 \leq h \leq 46$, $-46 \leq k \leq 46$, $-7 \leq l \leq 7$ | $-45 \leq h \leq 45$, $-42 \leq k \leq 42$, $-7 \leq l \leq 7$ |
| Refinement method | Full-matrix least-squares on $F^2$ | Full-matrix least-squares on $F^2$ |
| H-atom treatment | H-atom parameters constrained | H-atom parameters constrained |
| $R[F^2 > 2\sigma(F^2)]$ | 0. 199 | 0.146 |
| $wR(F^2)$ | 0.492 | 0.357 |
| Goodness-of-fit on $F^2$ | 1.280 | 2.968 |
| $\Delta\rho_{max}$, $\Delta\rho_{min}$ ($e/Å^3$) | 0.21, −0.21 | 0.59, −0.44 |

**Table H.4.** MicroED (CCDC 2026252) and synchrotron (CCDC 2026253) data for **3-mon**.

**Compound 3-di: MicroED data**
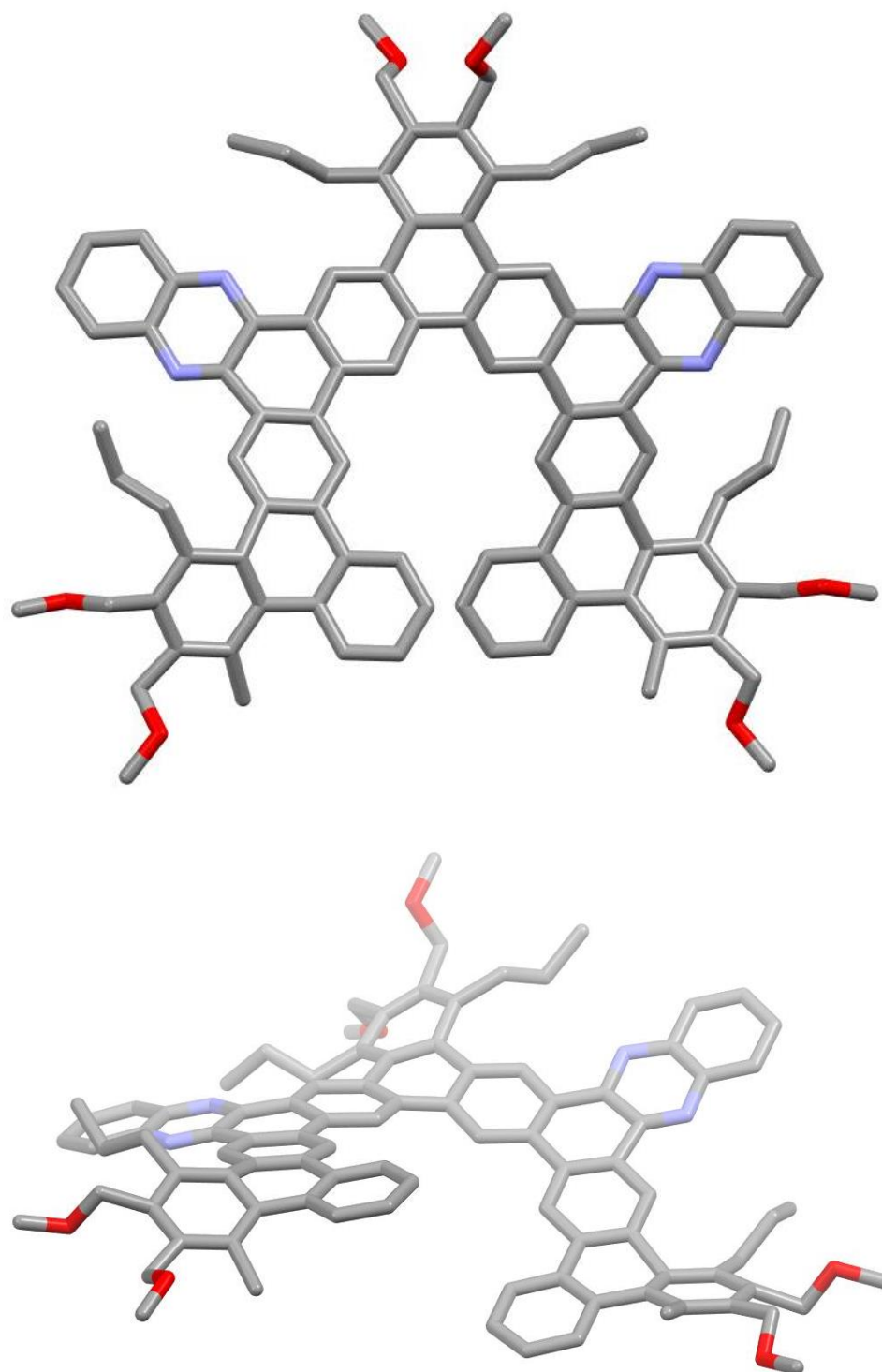


**Figure H.20.** MicroED structure for **3-di** (CCDC 2026251).

| Structure | **3-di** |
|---|---|
| Empirical formula | $C_{96}H_{88}N_4O_6$ |
| Formula weight (g/mol) | 1393.78 |
| Crystal system | Tetragonal |
| Space group | I-4c2 (120) |
| Point group | −42m |
| Laue symmetry | 4/mmm |
| Temperature (K) | 100 |
| Unit cell lengths a, b, c (Å) | 47.150(3), 47.150(3), 7.980(9) |
| Unit cell angles α, β, γ (°) | 90.000, 90.000, 90.000 |
| Unit cell volume (Å$^3$) | 17741(20) |
| F(000) | 308 |
| Z | 8 |
| Density (calculated) (g/cm$^3$) | 1.044 |
| Radiation source, wavelength (Å) | electron, 0.02508 |
| Resolution (Å) | 1.00 |
| Measured reflections | 10591 |
| Unique reflections | 4390 |
| Reflections with $I > 2\sigma(I)$ | 1917 |
| Completeness | 93.3% (1 dataset) |
| $I/\sigma$ | 3.37 |
| $\Theta_{max}$, $\Theta_{min}$ (°) | 0.72, 0.08 |
| Index ranges | $-34 \leq h \leq 35$, $-47 \leq k \leq 46$, $-7 \leq l \leq 7$ |
| Refinement method | Full-matrix least-squares on F$^2$ |
| H-atom treatment | H-atom parameters constrained |
| $R[F^2 > 2\sigma(F^2)]$ | 0.171 |
| $wR(F^2)$ | 0.416 |
| Goodness-of-fit on F$^2$ | 1.380 |
| $\Delta\rho_{max}$, $\Delta\rho_{min}$ (e/Å$^3$) | 0.18, −0.18 |

**Table H.5.** MicroED Data for **3-di** (CCDC 2026251).

## Photophysical characterization

Ultraviolet/visible (UV/Vis) absorption spectra were recorded on a Varian Cary 300 Bio UV-Visible spectrophotometer. Emission spectra were recorded on a Varian Cary Eclipse Spectrometer, and all compounds were excited at 335 nm. All compounds were prepared as described in the manuscript and used directly. For sample preparation, each analyte was weighed on an analytical balance and dissolved in the appropriate amount of spectroscopy-grade $CH_2Cl_2$ using a volumetric flask. All spectra are presented in the manuscript.

| Compound | Concentration ($\mu$M) | Absorption maximum, $\lambda_{max}$ (nm) | Absorption onset, $\lambda_{onset}$ (nm)[a] | Emission Maximum, $\lambda_{max}$ (nm) | Photophysical HOMO-LUMO gap, $E_g$ (eV)[b] |
|---|---|---|---|---|---|
| **1a** | 16 | 324 | 445 | 446 | 2.79 |
| **2-mon** | 13 | 333 | 595 | N/A[c] | 2.08 |
| **2-di** | 16 | 339 | 604 | N/A[c] | 2.05 |
| **3-mon** | 15 | 319 | 471 | 533 | 2.63 |
| **3-di** | 14 | 315 | 471 | 517 | 2.63 |

**Table H.6.** Summary of relevant photophysical properties in $CH_2Cl_2$ solvent. (a) Defined as $\varepsilon = 1000$ $M^{-1}cm^{-1}$; (b) Estimated from the absorption onset ($\lambda_{onset}$): $E_g = 1240/\lambda_{onset}$; (c) Non-fluorescent.

## Electrochemical characterization

Cyclic and square wave voltammetry were performed on a BASi EC Epsilon potentiostat/galvanostat with a PWR-3 Power Module using dry, oxygen-free solvents, a glassy carbon working electrode, Pt counter electrode, and Ag/Ag+ reference electrode.

| Compound | $E_{1/2}^{red}$ vs. Fc/Fc+ (V)[a] | $E_{1/2}^{ox}$ vs. Fc/Fc+ (V)[a] | Electrochemical HOMO–LUMO gap, $E_g$ (eV)[b] | LUMO (eV)[c] | HOMO (eV)[d] |
|---|---|---|---|---|---|
| **1a** | N/A | 0.66, 0.75 | N/A | −2.67[e] | −5.46 |
| **2-mon** | −1.15, −1.81 | 0.79, 0.98 | 1.94 | −3.65 | −5.59 |
| **2-di** | −1.08, −1.22, −1.81 | N/A | N/A | −3.72 | −5.77[e] |
| **3-mon** | −1.84 | 0.73, 0.97 | 2.57 | −2.96 | −5.53 |
| **3-di** | −1.85, −2.56 | N/A | N/A | −2.95 | −5.58[e] |

**Table H.7.** Summary of relevant electrochemical properties. (a) Reported values are for $E_{1/2}$ were measured with cyclic and square wave voltammetry in $CH_2Cl_2$ with 0.1M $^nBu_4NPF_6$ as the supporting electrolyte. Compounds that displayed no events for a given window are marked with "N/A"; (b) $E_g = E_{1/2}^{ox} - E_{1/2}^{red}$; (c) estimated using first reduction: $-(E_{1/2}^{red} + 4.80)$; (d) estimated using first oxidation: $-(E_{1/2}^{ox} + 4.80)$; (e) When $E_{1/2}^{red}$ or $E_{1/2}^{ox}$ were not available, these values were calculated using a combination of the photophysical $E_g$ and the available HOMO or LUMO energy level.
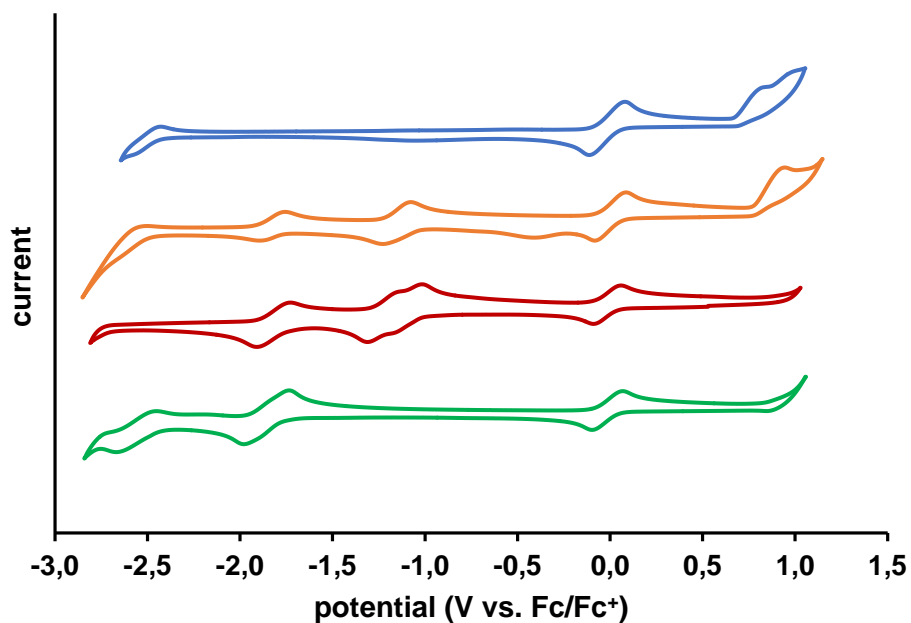
**Figure H.21.** Cyclic voltammograms of compounds **1a**, **2-mon**, **2-di**, **3-di** (from top to bottom) in THF (1.0 mM) with 0.1 M $^nBu_4NPF_6$ as supporting electrolyte, scanned at 100 mV/s.
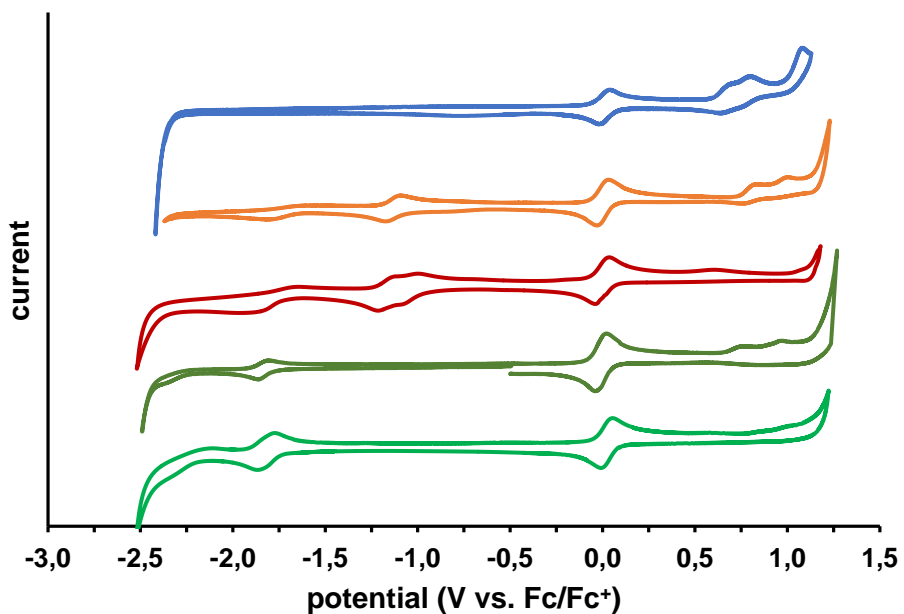


**Figure H.22.** Cyclic voltammograms of compounds **1a**, **2-mon**, **2-di**, **3-mon**, **3-di** (from top to bottom) in $CH_2Cl_2$ (1.0 mM) with 0.1 M $^nBu_4NPF_6$ as supporting electrolyte, scanned at 100 mV/s.

# Dynamic light scattering (DLS) characterization

Samples were analyzed using a ZetaPALS Zeta Potential Analyzer by Brookhaven Instruments, equipped for DLS measurements. Samples were freshly prepared in CDCl₃ and filtered through a 0.4 µm Teflon filter directly into a quartz cuvette before analysis. The sample holder was maintained at 25 ˚C, and samples were irradiated with 659 nm light with the detector at 90˚ from incident.
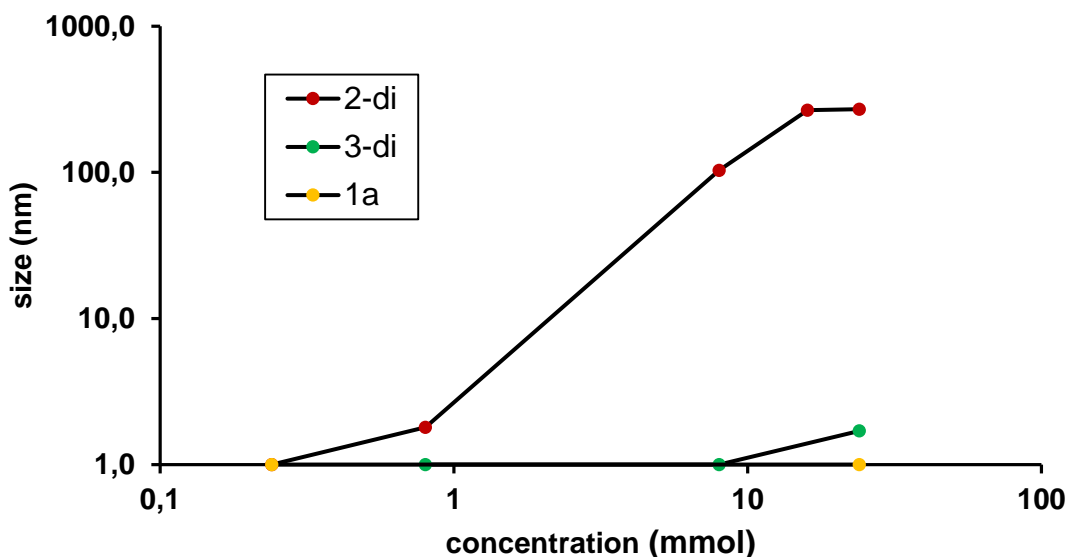


**Figure H.23.** Particle size versus concentration for respective helicenes. Values were determined by taking the size values at maximum peak height in Figure H.24.
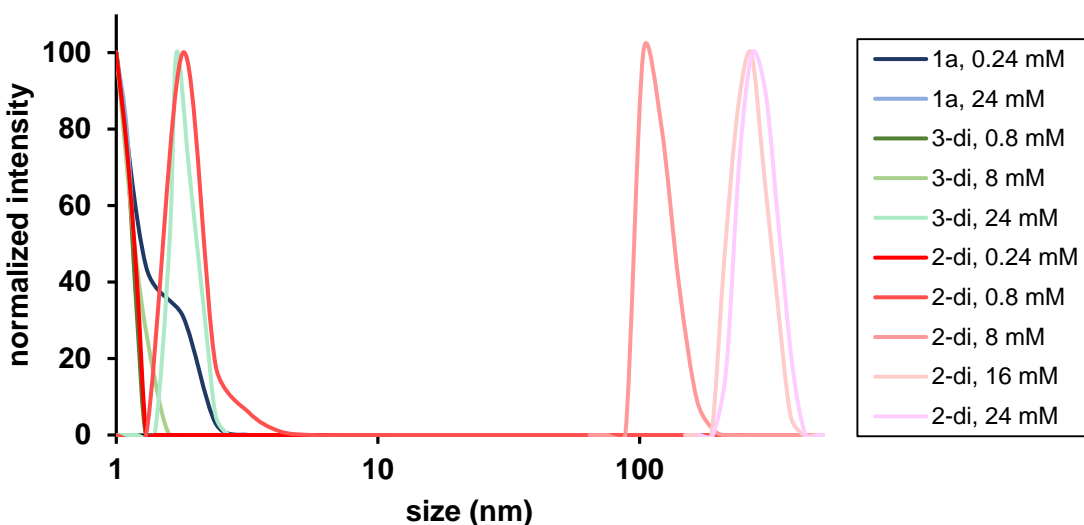


**Figure H.24.** Raw multimodal distributions for helicenes **1a**, **2-di**, and **3-di**, at various concentrations.

# Estimation of helical pitch

The pitch of a helix is defined as the height of one complete helical turn, measured parallel to the helical axis.[9] The expanded helicenes reported herein have highly distorted structures and short lengths (approximately one helical turn), which necessitates an approach for pitch estimation that averages out local conformational effects. For this purpose, we previously used the HELFIT program,[2,10] which employs a total least squares algorithm to estimate the parameters of a helix given a series of 3D coordinates as the input. Here, the use of this program for expanded helicenes is described in more detail, using compound **1a** as an example (Figure H.25). The coordinates used herein are those defined by the centroids of the rings on the expanded helicene core. First, attempts were made to perform the least-squares fit using the coordinates for the entire set of centroids (*i.e.*, all 11 of the centroids shown in Figure H.25a). Unlike for the previously-reported compounds, this gave an output that was physically unmeaningful. Thus, the centroids were broken up into two sets, inner and outer (red and blue, respectively, in Figure H.25a), and each set independently gave an excellent fit. The values for the inner and outer centroids were then averaged.

| | HELFIT data for 1a | | | |
|---|---|---|---|---|
| | **All centroids** | **Inner centroids** | **Outer centroids** | **Average of Inner & Outer** |
| Pitch (Å) | N/A[ii] | 3.24 | 4.17 | 3.71 |
| Data points (n) | 11 | 6 | 5 | 11 |
| Radius (Å) | N/A[ii] | 4.22 | 4.82 | 4.52 |
| RMSD/√(n-1)[i] | 0.9 | 0.04 | 0.06 | N/A |
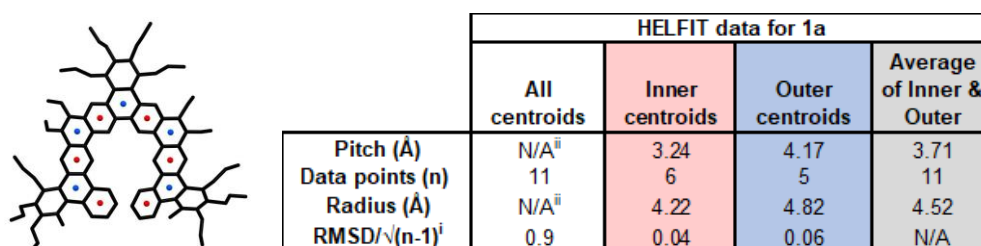
**Figure H.25.** Details of pitch calculation for compound **1a**. The molecular structure on the left depicts the inner (red) and outer (blue) centroids used as input for HELFIT, and the compiled data on the right are the results of the HELFIT calculation for the noted centroids. (i) This value describes the regularity of the helix independent of length, and larger values indicate a larger error between the data points and the best fit helix.[10] RMSD is the root-mean-square-distance of the data points to the best-fit helix and n is the number of data points; (ii) these values were not physically meaningful were thus not included.

For the purposes of comparison, best-fit helices were estimated as described above from crystal structure data for all new compounds (**1a**, **2-mon**, **2-di**, **3-mon**, **3-di**), the DFT-optimized structures (**2-mon-g**, **3-mon-g**, **3-di-g**, Figure H.27c), and all literature expanded helicenes for which crystal structures are available (**S1**, **1b-Dim**, **S2**, Figure H.26).[2,11] The remaining values are summarized in Table H.8.
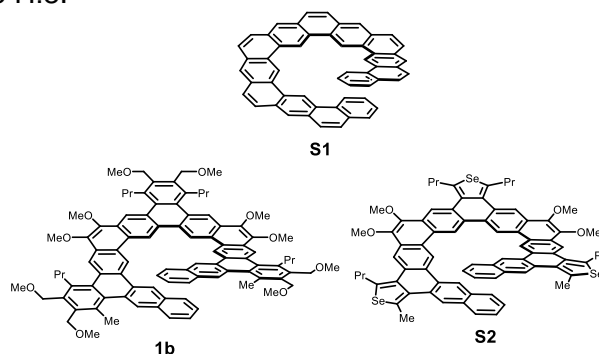
**Figure H.26.** Structures of literature compounds used for comparison.

| HELFIT data for 2-mon | | | |
|---|---|---|---|
| **All centroids** | **Inner centroids** | **Outer centroids** | **Average of Inner & Outer** |
| **Pitch (Å)** 6.31 | 5.95 | 7.58 | 6.77 |
| **Data points (n)** 11 | 6 | 5 | 11 |
| **Radius (Å)** 4.51 | 4.25 | 4.77 | 4.51 |
| **RMSD/√(n-1)** 0.11 | 0.05 | 0.01 | N/A |

| HELFIT data for 3-mon | | | |
|---|---|---|---|
| **All centroids** | **Inner centroids** | **Outer centroids** | **Average of Inner & Outer** |
| **Pitch (Å)** N/A | 6.01 | 7.59 | 6.80 |
| **Data points (n)** 11 | 6 | 5 | 11 |
| **Radius (Å)** N/A | 4.12 | 4.63 | 4.38 |
| **RMSD/√(n-1)** 1.02 | 0.04 | 0.01 | N/A |

| HELFIT data for 2-di (1)* | | | |
|---|---|---|---|
| **All centroids** | **Inner centroids** | **Outer centroids** | **Average of Inner & Outer** |
| **Pitch (Å)** N/A | 2.9 | 2.36 | 2.63 |
| **Data points** 11 | 6 | 5 | 11 |
| **Radius (Å)** N/A | 4.22 | 4.86 | 4.54 |
| **RMSD/√(n-1)** 0.93 | 0.04 | 0.05 | N/A |

| HELFIT data for 2-di (2)* | | | |
|---|---|---|---|
| **All centroids** | **Inner centroids** | **Outer centroids** | **Average of Inner & Outer** |
| **Pitch (Å)** 3.47 | 3.47 | 3 | 3.24 |
| **Data points** 11 | 6 | 5 | 11 |
| **Radius (Å)** 4.47 | 4.19 | 4.83 | 4.51 |
| **RMSD/√(n-1)** 0.11 | 0.04 | 0.04 | N/A |

| HELFIT data for 3-di | | | |
|---|---|---|---|
| **All centroids** | **Inner centroids** | **Outer centroids** | **Average of Inner & Outer** |
| **Pitch (Å)** 6.24 | 5.79 | 8.01 | 6.90 |
| **Data points** 11 | 6 | 5 | 11 |
| **Radius (Å)** 4.43 | 4.18 | 4.63 | 4.41 |
| **RMSD/√(n-1)** 0.11 | 0.04 | 0.01 | N/A |

| HELFIT data for 2-mon-g | | | |
|---|---|---|---|
| **All centroids** | **Inner centroids** | **Outer centroids** | **Average of Inner & Outer** |
| **Pitch (Å)** N/A | 3.54 | 4.3 | 3.92 |
| **Data points** 11 | 6 | 5 | 11 |
| **Radius (Å)** N/A | 4.34 | 4.98 | 4.66 |
| **RMSD/√(n-1)** 0.93 | 0.05 | 0.01 | N/A |

| HELFIT data for 3-mon-g | | | |
|---|---|---|---|
| **All centroids** | **Inner centroids** | **Outer centroids** | **Average of Inner & Outer** |
| **Pitch (Å)** N/A | 3.49 | 4.33 | 3.91 |
| **Data points** 11 | 6 | 5 | 11 |
| **Radius (Å)** N/A | 4.35 | 4.99 | 4.67 |
| **RMSD/√(n-1)** 0.93 | 0.05 | 0.01 | N/A |

| HELFIT data for 3-di-g | | | |
|---|---|---|---|
| **All centroids** | **Inner centroids** | **Outer centroids** | **Average of Inner & Outer** |
| **Pitch (Å)** N/A | 3.6 | 4.42 | 4.01 |
| **Data points** 11 | 6 | 5 | 11 |
| **Radius (Å)** N/A | 4.32 | 4.96 | 4.64 |
| **RMSD/√(n-1)** 0.93 | 0.04 | 0.01 | N/A |

| HELFIT data for S1 | | | |
|---|---|---|---|
| **All centroids** | **Inner centroids** | **Outer centroids** | **Average of Inner & Outer** |
| **Pitch (Å)** 3.23 | 2.81 | 3.39 | 3.10 |
| **Data points** 13 | 6 | 7 | 13 |
| **Radius (Å)** 4.63 | 4.29 | 4.91 | 4.60 |
| **RMSD/√(n-1)** 0.1 | 0.03 | 0.08 | N/A |

| HELFIT data for 1b-Dim | | | |
|---|---|---|---|
| **All centroids** | **Inner centroids** | **Outer centroids** | **Average of Inner & Outer** |
| **Pitch (Å)** 7.44 | 7.16 | 7.59 | 7.38 |
| **Data points** 13 | 6 | 7 | 13 |
| **Radius (Å)** 4.5 | 4.18 | 4.78 | 4.48 |
| **RMSD/√(n-1)** 0.09 | 0.04 | 0.03 | N/A |

| HELFIT data for S2 | | | |
|---|---|---|---|
| **All centroids** | **Inner centroids** | **Outer centroids** | **Average of Inner & Outer** |
| **Pitch (Å)** N/A | 3.65 | 3.73 | 3.69 |
| **Data points** 13 | 7 | 6 | 13 |
| **Radius (Å)** N/A | 4.39 | 5.05 | 4.72 |
| **RMSD/√(n-1)** 0.99 | 0.01 | 0.03 | N/A |

**Table H.8.** Compiled HELFIT data for relevant expanded helicenes. Data for **1a** is presented in a model calculation in Figure 25. *Compound **2-di** crystallized with two symmetrically inequivalent geometries, pitches were calculated for both and found to be different.

# DFT calculations

Density functional theory (DFT) calculations were performed using the Gaussian 16 software package.[12] Molecular mechanics calculations were used to generate starting geometries, and DFT optimization was carried out in $C_1$ symmetry in the gas-phase. Geometries were refined to meet standard convergence criteria, and confirmed to be local minima by normal mode frequency calculations. All DFT calculations were performed using the hybrid functional B3LYP, and the 6-311G(2d,p) basis set. This functional and basis set were chosen to maintain consistency with the only other published computational data on the structural flexibility of expanded helicenes.[11] For all calculations, *n*-propyl groups were truncated to methyl groups, and (methoxy)methyl groups were removed (specific structures are described in the following paragraph). These groups are not expected to affect the strain energy significantly and were altered to allow for reasonable calculation times.

To approximate the energetic cost of the structural deformation observed in the crystal structure for **2-mon**, **3-mon**, and **3-di** (Figure H.27a), two calculations were performed on truncated versions of each compound. The first calculation was a standard, unconstrained optimization to simulate the gas-phase minimum energy structure (**2-mon-g**, **3-mon-g**, and **3-di-g**, Figure H.27b). For the second calculation, two atoms on the terminal rings of the helicene were constrained to the distance observed in the crystal structure (**2-mon-x**, **3-mon-x**, and **3-di-x**, Figure H.27c). Thermally corrected enthalpy values were then compared between the unconstrained and constrained optimized geometries to determine the enthalpic cost associated with the helical pitch elongation observed in the solid state.
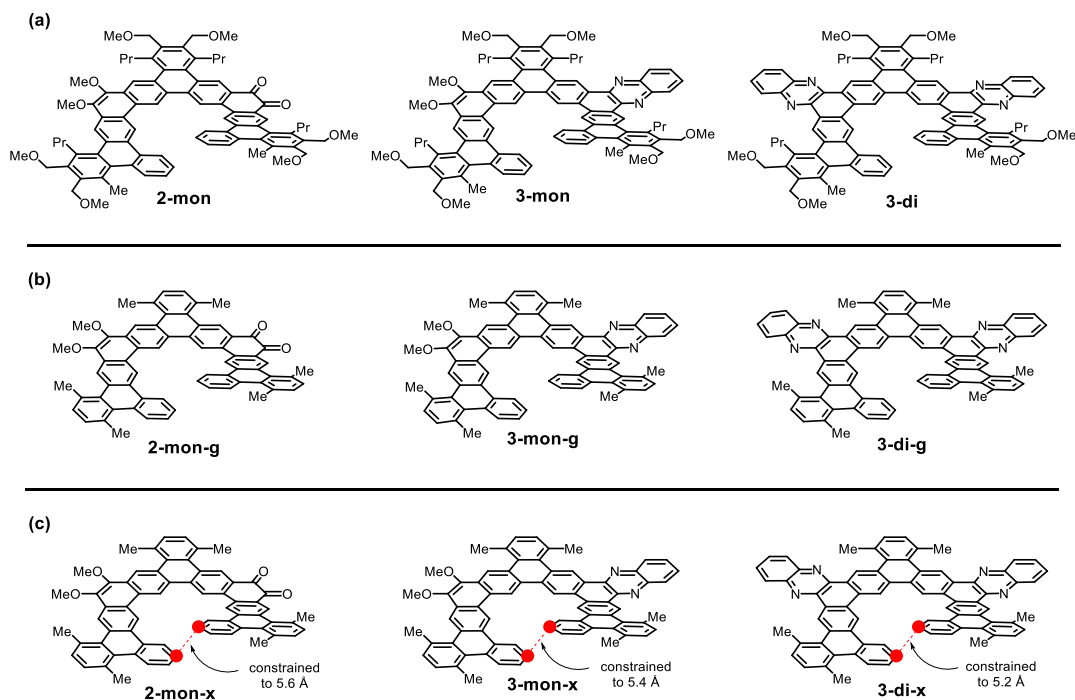


**Figure H.27**. Details of the structures used for DFT calculations: (a) Full structures; (b) Truncated structures for *unconstrained* optimization; (c) Truncated structures for *constrained* optimization.
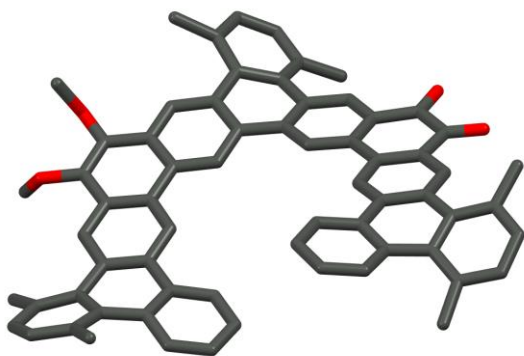
**Figure H.28**. DFT calculated structure of **2-mon-g**.

| | | | | | | | |
|---|---|---|---|---|---|---|---|
| C | 2.824 | 2.355 | -0.153 | C | 5.183 | 1.495 | -0.122 |
| C | 1.454 | 2.176 | -0.010 | C | 3.797 | 1.254 | 0.007 |
| C | 0.525 | 3.218 | -0.138 | C | 6.096 | 0.461 | 0.024 |
| C | 0.977 | 4.535 | -0.407 | C | 5.720 | -0.852 | 0.331 |
| C | 2.358 | 4.713 | -0.524 | C | 4.329 | -1.105 | 0.437 |
| C | 3.267 | 3.670 | -0.420 | C | 3.414 | -0.055 | 0.266 |
| C | -0.905 | 2.989 | 0.037 | C | 3.877 | -2.464 | 0.710 |
| C | -1.460 | 1.717 | -0.090 | C | 4.790 | -3.535 | 0.559 |
| C | -2.825 | 1.462 | 0.049 | C | 4.346 | -4.823 | 0.919 |
| C | -3.667 | 2.575 | 0.313 | C | 3.057 | -5.061 | 1.350 |
| C | -3.117 | 3.855 | 0.418 | C | 2.152 | -4.006 | 1.460 |
| C | -1.751 | 4.105 | 0.300 | C | 2.571 | -2.728 | 1.158 |
| C | -3.419 | 0.140 | -0.097 | C | -1.214 | 5.476 | 0.266 |
| C | -4.829 | 0.000 | -0.006 | C | 0.045 | 5.674 | -0.377 |
| C | -5.650 | 1.157 | 0.250 | C | -4.447 | -4.877 | -0.160 |
| C | -5.091 | 2.385 | 0.431 | C | -5.292 | -3.753 | -0.404 |
| C | -2.677 | -1.023 | -0.308 | C | 6.692 | -1.954 | 0.371 |
| C | -3.255 | -2.280 | -0.464 | C | 6.192 | -3.279 | 0.193 |
| C | -4.671 | -2.417 | -0.390 | C | 8.093 | -1.752 | 0.495 |
| C | -5.411 | -1.263 | -0.139 | C | 8.933 | -2.813 | 0.194 |
| C | -2.439 | -3.471 | -0.686 | C | 8.435 | -4.026 | -0.257 |
| C | -1.106 | -3.377 | -1.118 | C | 7.076 | -4.297 | -0.252 |
| C | -0.343 | -4.499 | -1.368 | C | -1.923 | 6.602 | 0.756 |
| C | -0.918 | -5.760 | -1.221 | C | -1.489 | 7.864 | 0.375 |
| C | -2.231 | -5.873 | -0.806 | C | -0.419 | 8.031 | -0.490 |
| C | -3.019 | -4.747 | -0.498 | C | 0.380 | 6.962 | -0.868 |
| C | 4.703 | 3.999 | -0.560 | C | -5.022 | -6.083 | 0.319 |
| C | 5.717 | 2.838 | -0.443 | C | -6.403 | -6.208 | 0.289 |

| | | | | | | | |
|---|---|---|---|---|---|---|---|
| C | -7.206 | -5.205 | -0.230 | H | 10.005 | -2.675 | 0.282 |
| C | -6.687 | -3.963 | -0.565 | H | 9.124 | -4.792 | -0.595 |
| C | -3.081 | 6.547 | 1.730 | H | -2.021 | 8.735 | 0.740 |
| C | 1.505 | 7.259 | -1.837 | H | -0.176 | 9.024 | -0.854 |
| C | 8.751 | -0.487 | 1.003 | H | -6.857 | -7.124 | 0.651 |
| C | 6.649 | -5.640 | -0.810 | H | -8.271 | -5.379 | -0.345 |
| C | -7.658 | -2.959 | -1.150 | H | -3.050 | 7.433 | 2.365 |
| C | -4.249 | -7.225 | 0.946 | H | -4.056 | 6.547 | 1.234 |
| O | 5.112 | 5.122 | -0.760 | H | -3.038 | 5.670 | 2.375 |
| O | 6.895 | 3.062 | -0.610 | H | 2.432 | 7.554 | -1.338 |
| O | -5.865 | 3.496 | 0.677 | H | 1.209 | 8.095 | -2.473 |
| C | -6.465 | 3.535 | 1.980 | H | 1.734 | 6.413 | -2.484 |
| O | -7.008 | 0.965 | 0.354 | H | 9.026 | 0.205 | 0.202 |
| C | -7.783 | 1.535 | -0.711 | H | 9.675 | -0.754 | 1.519 |
| H | 1.078 | 1.200 | 0.258 | H | 8.122 | 0.058 | 1.706 |
| H | 2.789 | 5.690 | -0.657 | H | 6.657 | -6.436 | -0.060 |
| H | -0.806 | 0.900 | -0.356 | H | 7.352 | -5.936 | -1.590 |
| H | -3.814 | 4.664 | 0.532 | H | 5.653 | -5.610 | -1.251 |
| H | -1.600 | -0.953 | -0.316 | H | -8.444 | -3.498 | -1.682 |
| H | -6.472 | -1.315 | 0.020 | H | -7.179 | -2.282 | -1.856 |
| H | -0.671 | -2.404 | -1.302 | H | -8.153 | -2.349 | -0.388 |
| H | 0.682 | -4.396 | -1.703 | H | -4.857 | -7.670 | 1.736 |
| H | -0.351 | -6.652 | -1.459 | H | -4.020 | -8.026 | 0.237 |
| H | -2.668 | -6.857 | -0.772 | H | -3.310 | -6.898 | 1.391 |
| H | 7.123 | 0.724 | -0.154 | H | -7.021 | 4.469 | 2.030 |
| H | 2.363 | -0.292 | 0.308 | H | -5.695 | 3.527 | 2.756 |
| H | 5.038 | -5.648 | 0.913 | H | -7.141 | 2.691 | 2.124 |
| H | 2.761 | -6.065 | 1.628 | H | -7.489 | 1.102 | -1.671 |
| H | 1.141 | -4.180 | 1.805 | H | -8.820 | 1.281 | -0.500 |
| H | 1.882 | -1.909 | 1.312 | H | -7.663 | 2.619 | -0.745 |

Electronic Energy: -2844.447121
Thermally Corrected Gibbs Free Energy: -2843.613809
Thermally Corrected Enthalpy: -2843.46627

**Table H.9**. Cartesian coordinates of calculated **2-mon-g**.
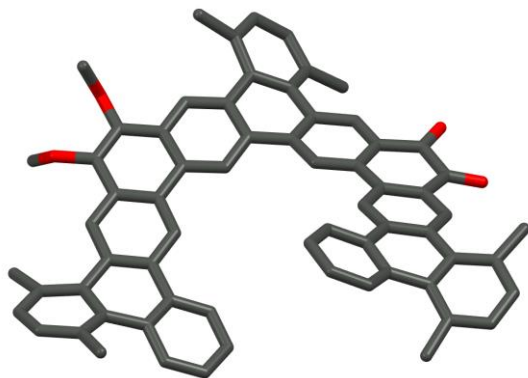
**Figure H.29**. DFT calculated structure of **2-mon-x**.

| | | | | | | | |
|---|---|---|---|---|---|---|---|
| C | -0.546 | -4.351 | -2.120 | C | -0.886 | 2.968 | 0.035 |
| C | -1.105 | -5.623 | -2.013 | C | -1.453 | 1.704 | -0.108 |
| C | -2.356 | -5.780 | -1.448 | C | 0.061 | 5.644 | -0.412 |
| C | -3.093 | -4.689 | -0.948 | C | -1.166 | 5.452 | 0.296 |
| C | -2.533 | -3.399 | -1.092 | C | 0.377 | 6.931 | -0.918 |
| C | -1.264 | -3.259 | -1.677 | C | -1.420 | 7.842 | 0.421 |
| C | -4.469 | -4.853 | -0.451 | C | -0.395 | 8.004 | -0.498 |
| C | -4.981 | -6.096 | 0.003 | C | -1.842 | 6.583 | 0.821 |
| C | -6.355 | -6.232 | 0.132 | C | -2.951 | 6.532 | 1.850 |
| C | -7.215 | -5.201 | -0.212 | C | 1.453 | 7.225 | -1.941 |
| C | -6.741 | -3.933 | -0.517 | C | 0.986 | 4.500 | -0.484 |
| C | -5.337 | -3.721 | -0.510 | C | 0.538 | 3.190 | -0.179 |
| C | -4.135 | -7.273 | 0.444 | C | 2.828 | 2.315 | -0.241 |
| C | -7.779 | -2.901 | -0.906 | C | 1.463 | 2.146 | -0.048 |
| C | -4.717 | -2.384 | -0.470 | C | 4.688 | 3.905 | -0.870 |
| C | -3.314 | -2.237 | -0.677 | C | 2.360 | 4.660 | -0.686 |
| C | -2.715 | -0.997 | -0.475 | C | 3.264 | 3.610 | -0.598 |
| C | -4.826 | 0.004 | 0.081 | C | 3.807 | 1.225 | -0.039 |
| C | -3.427 | 0.147 | -0.111 | C | 5.170 | 1.419 | -0.351 |
| C | -5.424 | -1.249 | -0.077 | C | 5.675 | 2.715 | -0.859 |
| C | -5.618 | 1.147 | 0.457 | C | 3.451 | -0.023 | 0.451 |
| C | -5.043 | 2.368 | 0.642 | C | 5.741 | -0.865 | 0.327 |
| C | -3.631 | 2.560 | 0.433 | C | 4.375 | -1.058 | 0.660 |
| C | -6.284 | 3.464 | 2.335 | C | 6.693 | -1.985 | 0.381 |
| C | -2.814 | 1.454 | 0.075 | C | 6.085 | 0.389 | -0.193 |
| C | -7.818 | 1.560 | -0.322 | C | 8.861 | -2.951 | -0.020 |
| C | -3.070 | 3.836 | 0.541 | C | 8.099 | -1.825 | 0.249 |
| C | -1.712 | 4.085 | 0.351 | C | 8.279 | -4.197 | -0.198 |

| | | | | | | | |
|---|---|---|---|---|---|---|---|
| C | 8.856 | -0.528 | 0.448 | H | -6.947 | 2.614 | 2.507 |
| C | 6.152 | -3.303 | 0.486 | H | -8.837 | 1.299 | -0.039 |
| C | 6.935 | -4.409 | 0.065 | H | -7.602 | 1.160 | -1.316 |
| C | 6.399 | -5.801 | -0.204 | H | -7.699 | 2.644 | -0.326 |
| C | 2.739 | -2.479 | 1.904 | H | -3.757 | 4.642 | 0.717 |
| C | 2.370 | -3.674 | 2.484 | H | -0.813 | 0.893 | -0.422 |
| C | 3.236 | -4.764 | 2.408 | H | -1.929 | 8.716 | 0.812 |
| C | 4.439 | -4.646 | 1.741 | H | -0.165 | 8.995 | -0.872 |
| C | 4.826 | -3.450 | 1.104 | H | -2.879 | 5.657 | 2.496 |
| C | 3.957 | -2.339 | 1.216 | H | -3.949 | 6.534 | 1.402 |
| O | -6.965 | 0.952 | 0.660 | H | -2.887 | 7.421 | 2.481 |
| O | -5.795 | 3.469 | 0.986 | H | 1.637 | 6.383 | -2.607 |
| O | 5.104 | 5.016 | -1.114 | H | 2.409 | 7.504 | -1.488 |
| O | 6.814 | 2.885 | -1.235 | H | 1.136 | 8.071 | -2.553 |
| H | 0.427 | -4.214 | -2.576 | H | 1.089 | 1.180 | 0.256 |
| H | -0.577 | -6.488 | -2.397 | H | 2.792 | 5.625 | -0.883 |
| H | -2.791 | -6.765 | -1.445 | H | 2.414 | -0.223 | 0.671 |
| H | -0.851 | -2.271 | -1.827 | H | 7.084 | 0.606 | -0.525 |
| H | -6.762 | -7.175 | 0.478 | H | 9.935 | -2.844 | -0.127 |
| H | -8.286 | -5.375 | -0.210 | H | 8.891 | -5.031 | -0.523 |
| H | -3.146 | -6.970 | 0.786 | H | 8.374 | 0.131 | 1.170 |
| H | -4.000 | -8.021 | -0.343 | H | 8.990 | 0.036 | -0.478 |
| H | -4.637 | -7.777 | 1.273 | H | 9.854 | -0.759 | 0.824 |
| H | -8.629 | -3.412 | -1.363 | H | 6.952 | -6.236 | -1.038 |
| H | -7.396 | -2.179 | -1.627 | H | 5.343 | -5.796 | -0.470 |
| H | -8.169 | -2.342 | -0.050 | H | 6.525 | -6.479 | 0.645 |
| H | -1.643 | -0.927 | -0.583 | H | 2.092 | -1.622 | 2.026 |
| H | -6.467 | -1.309 | 0.169 | H | 1.431 | -3.753 | 3.017 |
| H | -6.834 | 4.395 | 2.462 | H | 2.983 | -5.698 | 2.896 |
| H | -5.452 | 3.432 | 3.044 | H | 5.115 | -5.483 | 1.761 |

Electronic Energy: -2844.445891
Thermally Corrected Gibbs Free Energy: -2843.631993
Thermally Corrected Enthalpy: -2843.47129

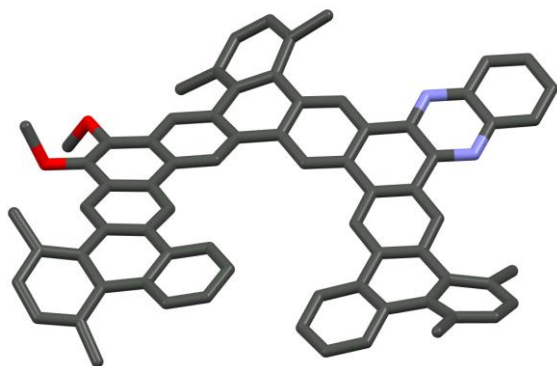**Table H.10**. Cartesian coordinates of calculated **2-mon-x**.

**Figure H.30**. DFT calculated structure of **3-mon-g**.

| | | | | | | | |
|---|---|---|---|---|---|---|---|
| C | -1.514 | -1.890 | -0.025 | C | 2.120 | 3.850 | 0.758 |
| C | -2.889 | -2.108 | 0.088 | C | 2.643 | 5.156 | 0.605 |
| C | -3.312 | -3.435 | 0.365 | C | 1.790 | 6.238 | 0.904 |
| C | -2.364 | -4.452 | 0.504 | C | 0.473 | 6.054 | 1.277 |
| C | -0.993 | -4.228 | 0.412 | C | -0.045 | 4.765 | 1.388 |
| C | -0.566 | -2.897 | 0.139 | C | 0.780 | 3.685 | 1.147 |
| C | -3.890 | -1.067 | -0.098 | C | -4.171 | 2.652 | -0.759 |
| C | -5.266 | -1.409 | -0.029 | C | -2.874 | 3.006 | -1.167 |
| C | -5.655 | -2.769 | 0.244 | C | -2.528 | 4.315 | -1.433 |
| C | -4.718 | -3.734 | 0.459 | C | -3.498 | 5.310 | -1.327 |
| C | -3.579 | 0.274 | -0.325 | C | -4.782 | 4.981 | -0.937 |
| C | -4.543 | 1.260 | -0.521 | C | -5.151 | 3.661 | -0.613 |
| C | -5.923 | 0.913 | -0.470 | C | -6.546 | 3.308 | -0.299 |
| C | -6.237 | -0.419 | -0.201 | C | -6.958 | 1.960 | -0.527 |
| C | 0.863 | -2.633 | -0.005 | C | -0.024 | -5.339 | 0.409 |
| C | 1.741 | -3.723 | -0.243 | C | 1.241 | -5.109 | -0.212 |
| C | 3.104 | -3.436 | -0.326 | C | -0.322 | -6.634 | 0.904 |
| C | 3.617 | -2.147 | -0.221 | C | 0.515 | -7.681 | 0.547 |
| C | 2.746 | -1.058 | 0.013 | C | 1.592 | -7.487 | -0.304 |
| C | 1.386 | -1.345 | 0.125 | C | 1.993 | -6.215 | -0.684 |
| C | 5.062 | -1.933 | -0.317 | C | -7.504 | 4.258 | 0.141 |
| C | 5.596 | -0.608 | -0.158 | C | -8.845 | 3.909 | 0.088 |
| C | 4.688 | 0.511 | 0.100 | C | -9.252 | 2.685 | -0.417 |
| C | 3.292 | 0.297 | 0.171 | C | -8.338 | 1.685 | -0.713 |
| C | 5.202 | 1.795 | 0.251 | C | 4.961 | 4.273 | 0.552 |
| C | 4.404 | 2.912 | 0.504 | C | 4.070 | 5.361 | 0.308 |
| C | 2.999 | 2.705 | 0.547 | C | 6.342 | 4.542 | 0.749 |
| C | 2.489 | 1.417 | 0.373 | C | 6.809 | 5.813 | 0.450 |

| C | 5.972 | 6.789 | -0.068 | H | -5.525 | 5.760 | -0.935 |
|---|-------|-------|--------|---|--------|-------|--------|
| C | 4.600 | 6.602 | -0.134 | H | 0.298 | -8.678 | 0.916 |
| O | -5.079 | -5.037 | 0.719 | H | 2.158 | -8.344 | -0.654 |
| C | -5.652 | -5.253 | 2.017 | H | -9.590 | 4.625 | 0.421 |
| O | -7.000 | -3.046 | 0.327 | H | -10.310 | 2.487 | -0.552 |
| C | -7.517 | -3.854 | -0.740 | H | 7.862 | 6.034 | 0.593 |
| C | -1.448 | -6.960 | 1.863 | H | 6.392 | 7.732 | -0.401 |
| C | 3.165 | -6.124 | -1.638 | H | -6.575 | -4.683 | 2.136 |
| C | 7.344 | 3.570 | 1.336 | H | -5.863 | -6.319 | 2.082 |
| C | 3.790 | 7.721 | -0.758 | H | -4.942 | -4.973 | 2.800 |
| C | -7.175 | 5.605 | 0.751 | H | -7.371 | -3.357 | -1.703 |
| C | -8.901 | 0.401 | -1.287 | H | -8.583 | -3.965 | -0.547 |
| N | 5.853 | -2.965 | -0.548 | H | -7.038 | -4.834 | -0.755 |
| C | 7.181 | -2.744 | -0.631 | H | -2.357 | -7.295 | 1.355 |
| C | 7.711 | -1.428 | -0.474 | H | -1.714 | -6.113 | 2.494 |
| N | 6.894 | -0.380 | -0.237 | H | -1.131 | -7.778 | 2.514 |
| C | 8.066 | -3.822 | -0.878 | H | 4.131 | -6.094 | -1.127 |
| C | 9.414 | -3.597 | -0.964 | H | 3.109 | -5.249 | -2.284 |
| C | 9.940 | -2.291 | -0.808 | H | 3.171 | -7.011 | -2.275 |
| C | 9.111 | -1.228 | -0.568 | H | 7.877 | 2.993 | 0.575 |
| H | -1.167 | -0.905 | -0.299 | H | 6.882 | 2.860 | 2.021 |
| H | -2.750 | -5.447 | 0.625 | H | 8.096 | 4.133 | 1.892 |
| H | -2.541 | 0.571 | -0.317 | H | 3.502 | 8.493 | -0.039 |
| H | -7.256 | -0.724 | -0.058 | H | 2.882 | 7.360 | -1.239 |
| H | 3.829 | -4.223 | -0.429 | H | 4.399 | 8.212 | -1.519 |
| H | 0.704 | -0.546 | 0.372 | H | -6.191 | 5.623 | 1.217 |
| H | 6.264 | 1.892 | 0.119 | H | -7.915 | 5.834 | 1.521 |
| H | 1.417 | 1.293 | 0.363 | H | -7.214 | 6.424 | 0.026 |
| H | 2.178 | 7.242 | 0.896 | H | -9.810 | 0.634 | -1.845 |
| H | -0.144 | 6.913 | 1.508 | H | -9.178 | -0.326 | -0.518 |
| H | -1.073 | 4.607 | 1.688 | H | -8.205 | -0.087 | -1.969 |
| H | 0.387 | 2.690 | 1.302 | H | 7.641 | -4.812 | -0.994 |
| H | -2.132 | 2.234 | -1.318 | H | 10.090 | -4.423 | -1.153 |
| H | -1.521 | 4.558 | -1.747 | H | 11.010 | -2.138 | -0.880 |
| H | -3.259 | 6.337 | -1.578 | H | 9.491 | -0.222 | -0.446 |

Electronic Energy: -3034.629832
Thermally Corrected Gibbs Free Energy: -3033.716155
Thermally Corrected Enthalpy: -3033.561714

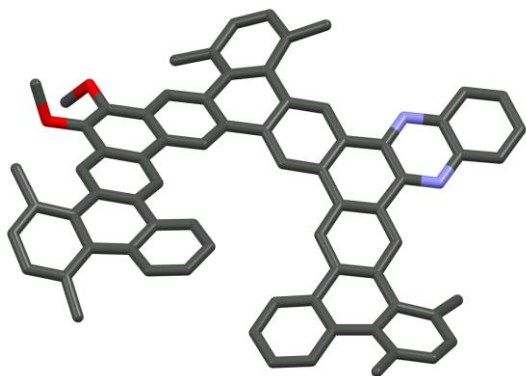**Table H.11**. Cartesian coordinates of calculated **3-mon-g**.

**Figure H.31**. DFT calculated structure of calculated **3-mon-x**.

| | | | | | | | | |
|---|---|---|---|---|---|---|---|---|
| C | 3.678 | 7.735 | -0.227 | | C | 7.106 | -2.750 | -0.948 |
| C | 4.566 | 6.588 | 0.212 | | C | 7.968 | -3.825 | -1.280 |
| C | 5.935 | 6.785 | 0.112 | | C | 9.304 | -3.598 | -1.471 |
| C | 6.833 | 5.786 | 0.454 | | C | 9.842 | -2.294 | -1.341 |
| O | -7.014 | -2.929 | 0.592 | | C | 3.059 | -3.443 | -0.366 |
| C | 6.410 | 4.494 | 0.730 | | C | 1.699 | -3.723 | -0.223 |
| O | -5.105 | -4.922 | 1.023 | | C | 0.839 | -2.624 | 0.035 |
| C | 5.017 | 4.222 | 0.693 | | C | 1.374 | -1.344 | 0.172 |
| C | 4.101 | 5.316 | 0.635 | | C | 1.186 | -5.103 | -0.156 |
| C | 7.484 | 3.500 | 1.119 | | C | 1.911 | -6.226 | -0.629 |
| C | 2.723 | 5.081 | 1.099 | | C | 3.055 | -6.166 | -1.620 |
| C | 1.924 | 6.131 | 1.594 | | C | 1.512 | -7.487 | -0.210 |
| C | 0.670 | 5.908 | 2.127 | | N | 6.855 | -0.393 | -0.493 |
| C | 0.167 | 4.611 | 2.204 | | N | 5.788 | -2.973 | -0.765 |
| C | 0.943 | 3.559 | 1.764 | | C | -6.990 | 5.766 | 0.181 |
| C | 2.220 | 3.765 | 1.213 | | C | -7.395 | 4.368 | -0.241 |
| C | 3.063 | 2.647 | 0.805 | | C | -8.742 | 4.054 | -0.150 |
| C | 4.456 | 2.862 | 0.624 | | C | -9.211 | 2.792 | -0.479 |
| C | 5.221 | 1.761 | 0.232 | | C | -8.342 | 1.740 | -0.730 |
| C | 4.688 | 0.487 | 0.058 | | C | -6.946 | 1.994 | -0.682 |
| C | 3.301 | 0.273 | 0.230 | | C | -6.494 | 3.348 | -0.640 |
| C | 2.529 | 1.375 | 0.588 | | C | -8.977 | 0.418 | -1.110 |
| C | 3.583 | -2.156 | -0.271 | | C | -5.122 | 3.627 | -1.098 |
| C | 5.019 | -1.944 | -0.456 | | C | -4.762 | 4.886 | -1.616 |
| C | 5.567 | -0.623 | -0.313 | | C | -3.509 | 5.131 | -2.144 |
| C | 2.734 | -1.068 | 0.032 | | C | -2.564 | 4.108 | -2.192 |
| C | 9.036 | -1.235 | -1.020 | | C | -2.904 | 2.853 | -1.729 |
| C | 7.649 | -1.436 | -0.815 | | C | -4.170 | 2.586 | -1.182 |

| | | | | | | | | |
|---|---|---|---|---|---|---|---|---|
| C | -4.547 | 1.244 | -0.749 | | H | 7.535 | -4.813 | -1.375 |
| C | -5.928 | 0.932 | -0.583 | | H | 9.963 | -4.420 | -1.725 |
| C | -6.243 | -0.362 | -0.173 | | H | 10.903 | -2.139 | -1.498 |
| C | -5.277 | -1.350 | 0.041 | | H | 3.775 | -4.230 | -0.513 |
| C | -3.901 | -1.035 | -0.110 | | H | 0.701 | -0.544 | 0.443 |
| C | -3.586 | 0.270 | -0.491 | | H | 2.983 | -5.307 | -2.287 |
| C | -3.332 | -3.371 | 0.502 | | H | 3.038 | -7.069 | -2.232 |
| C | -2.905 | -2.068 | 0.134 | | H | 4.036 | -6.127 | -1.138 |
| C | -1.529 | -1.866 | -0.003 | | H | 2.059 | -8.355 | -0.561 |
| C | -0.590 | -2.874 | 0.196 | | H | -7.656 | 6.099 | 0.980 |
| C | -1.022 | -4.191 | 0.519 | | H | -7.077 | 6.498 | -0.627 |
| C | -2.392 | -4.394 | 0.662 | | H | -5.969 | 5.808 | 0.557 |
| C | -4.737 | -3.644 | 0.667 | | H | -9.445 | 4.822 | 0.155 |
| C | -5.670 | -2.680 | 0.431 | | H | -10.279 | 2.610 | -0.508 |
| C | -7.590 | -3.792 | -0.400 | | H | -9.932 | 0.615 | -1.602 |
| C | -5.614 | -5.049 | 2.358 | | H | -9.192 | -0.217 | -0.246 |
| C | -0.061 | -5.310 | 0.512 | | H | -8.358 | -0.157 | -1.798 |
| C | -0.354 | -6.592 | 1.041 | | H | -5.493 | 5.676 | -1.659 |
| C | -1.453 | -6.889 | 2.040 | | H | -3.277 | 6.110 | -2.544 |
| C | 0.462 | -7.654 | 0.678 | | H | -1.583 | 4.284 | -2.616 |
| H | 4.177 | 8.278 | -1.033 | | H | -2.188 | 2.050 | -1.834 |
| H | 3.491 | 8.460 | 0.571 | | H | -7.257 | -0.639 | 0.044 |
| H | 2.713 | 7.396 | -0.600 | | H | -2.546 | 0.549 | -0.570 |
| H | 6.307 | 7.751 | -0.211 | | H | -1.174 | -0.897 | -0.322 |
| H | 7.894 | 6.007 | 0.475 | | H | -2.788 | -5.376 | 0.842 |
| H | 8.307 | 4.039 | 1.594 | | H | -8.648 | -3.872 | -0.154 |
| H | 7.906 | 2.967 | 0.262 | | H | -7.126 | -4.779 | -0.376 |
| H | 7.124 | 2.752 | 1.824 | | H | -7.480 | -3.356 | -1.397 |
| H | 2.313 | 7.135 | 1.615 | | H | -5.837 | -6.106 | 2.499 |
| H | 0.093 | 6.742 | 2.509 | | H | -6.522 | -4.457 | 2.487 |
| H | -0.811 | 4.423 | 2.632 | | H | -4.862 | -4.735 | 3.087 |
| H | 0.572 | 2.552 | 1.890 | | H | -1.688 | -6.029 | 2.665 |
| H | 6.267 | 1.862 | 0.012 | | H | -1.126 | -7.701 | 2.693 |
| H | 1.461 | 1.253 | 0.683 | | H | -2.382 | -7.220 | 1.565 |
| H | 9.425 | -0.229 | -0.915 | | H | 0.248 | -8.641 | 1.073 |

Electronic Energy: -3034.628702
Thermally Corrected Gibbs Free Energy: -3033.732856
Thermally Corrected Enthalpy: -3033.566814

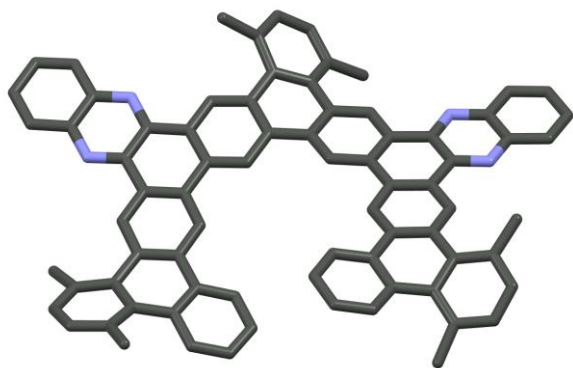**Table H.12**. Cartesian coordinates of calculated **3-mon-x**.

**Figure H.32**. DFT calculated structure of **3-di-g**.

| | | | | | | | | |
|---|---|---|---|---|---|---|---|---|
| C | -2.865 | -1.374 | 0.007 | | C | -3.647 | -0.144 | 0.195 |
| C | -1.474 | -1.409 | 0.097 | | C | -5.797 | 0.979 | 0.310 |
| C | -0.727 | -2.577 | -0.060 | | C | -5.214 | 2.219 | 0.577 |
| C | -1.394 | -3.808 | -0.300 | | C | -3.795 | 2.270 | 0.614 |
| C | -2.787 | -3.773 | -0.365 | | C | -3.060 | 1.099 | 0.414 |
| C | -3.525 | -2.600 | -0.234 | | C | -3.137 | 3.552 | 0.844 |
| C | 0.727 | -2.577 | 0.060 | | C | -3.888 | 4.744 | 0.712 |
| C | 1.474 | -1.409 | -0.097 | | C | -3.245 | 5.957 | 1.029 |
| C | 2.865 | -1.374 | -0.007 | | C | -1.916 | 6.008 | 1.400 |
| C | 3.525 | -2.600 | 0.234 | | C | -1.173 | 4.833 | 1.491 |
| C | 2.787 | -3.773 | 0.365 | | C | -1.788 | 3.626 | 1.231 |
| C | 1.394 | -3.808 | 0.301 | | C | 0.649 | -5.079 | 0.297 |
| C | 3.647 | -0.144 | -0.195 | | C | -0.649 | -5.079 | -0.297 |
| C | 5.059 | -0.187 | -0.136 | | C | 5.330 | 4.691 | -0.419 |
| C | 5.750 | -1.449 | 0.132 | | C | 6.009 | 3.456 | -0.648 |
| C | 4.986 | -2.652 | 0.313 | | C | -6.009 | 3.456 | 0.647 |
| C | 3.059 | 1.100 | -0.414 | | C | -5.330 | 4.691 | 0.419 |
| C | 3.794 | 2.270 | -0.613 | | C | -7.415 | 3.468 | 0.850 |
| C | 5.214 | 2.220 | -0.577 | | C | -8.106 | 4.637 | 0.571 |
| C | 5.797 | 0.979 | -0.310 | | C | -7.460 | 5.756 | 0.067 |
| C | 3.137 | 3.552 | -0.844 | | C | -6.077 | 5.822 | -0.003 |
| C | 1.788 | 3.626 | -1.230 | | C | 1.194 | -6.300 | 0.769 |
| C | 1.173 | 4.833 | -1.490 | | C | 0.557 | -7.480 | 0.413 |
| C | 1.916 | 6.009 | -1.398 | | C | -0.557 | -7.480 | -0.412 |
| C | 3.245 | 5.957 | -1.028 | | C | -1.194 | -6.301 | -0.768 |
| C | 3.888 | 4.744 | -0.712 | | C | 6.078 | 5.822 | 0.002 |
| C | -4.986 | -2.652 | -0.313 | | C | 7.461 | 5.756 | -0.068 |
| C | -5.750 | -1.449 | -0.132 | | C | 8.106 | 4.637 | -0.572 |
| C | -5.059 | -0.187 | 0.136 | | C | 7.414 | 3.468 | -0.851 |

| | | | | | | | | |
|---|---|---|---|---|---|---|---|---|
| C | 2.384 | -6.421 | 1.698 | | H | -1.464 | 6.962 | 1.645 |
| C | -2.384 | -6.421 | -1.697 | | H | -0.132 | 4.860 | 1.789 |
| C | -8.222 | 2.322 | 1.422 | | H | -1.222 | 2.716 | 1.371 |
| C | -5.486 | 7.078 | -0.610 | | H | -9.180 | 4.661 | 0.718 |
| C | 8.222 | 2.321 | -1.423 | | H | -8.046 | 6.612 | -0.251 |
| C | 5.487 | 7.078 | 0.610 | | H | 0.962 | -8.423 | 0.764 |
| N | -5.577 | -3.809 | -0.551 | | H | -0.962 | -8.423 | -0.762 |
| N | -7.070 | -1.461 | -0.199 | | H | 8.046 | 6.612 | 0.250 |
| C | -6.925 | -3.833 | -0.621 | | H | 9.180 | 4.661 | -0.719 |
| C | -7.684 | -2.637 | -0.443 | | H | 2.501 | -5.548 | 2.339 |
| C | -7.600 | -5.052 | -0.874 | | H | 3.328 | -6.568 | 1.167 |
| C | -8.967 | -5.076 | -0.946 | | H | 2.242 | -7.292 | 2.340 |
| C | -9.721 | -3.889 | -0.771 | | H | -2.242 | -7.292 | -2.339 |
| C | -9.097 | -2.695 | -0.524 | | H | -2.501 | -5.548 | -2.339 |
| N | 7.070 | -1.461 | 0.198 | | H | -3.328 | -6.568 | -1.166 |
| C | 7.684 | -2.637 | 0.442 | | H | -7.638 | 1.697 | 2.097 |
| C | 6.925 | -3.833 | 0.620 | | H | -8.644 | 1.669 | 0.653 |
| N | 5.577 | -3.809 | 0.551 | | H | -9.062 | 2.731 | 1.987 |
| C | 9.097 | -2.695 | 0.524 | | H | -5.340 | 7.879 | 0.121 |
| C | 9.721 | -3.889 | 0.770 | | H | -6.176 | 7.463 | -1.363 |
| C | 8.967 | -5.076 | 0.946 | | H | -4.529 | 6.895 | -1.096 |
| C | 7.600 | -5.052 | 0.873 | | H | 9.062 | 2.731 | -1.988 |
| H | -0.946 | -0.501 | 0.345 | | H | 7.637 | 1.697 | -2.098 |
| H | -3.359 | -4.677 | -0.471 | | H | 8.644 | 1.668 | -0.655 |
| H | 0.946 | -0.501 | -0.345 | | H | 4.530 | 6.895 | 1.096 |
| H | 3.359 | -4.677 | 0.471 | | H | 6.177 | 7.463 | 1.363 |
| H | 1.983 | 1.174 | -0.399 | | H | 5.340 | 7.879 | -0.121 |
| H | 6.860 | 0.883 | -0.185 | | H | -7.004 | -5.946 | -1.005 |
| H | 1.221 | 2.716 | -1.370 | | H | -9.483 | -6.008 | -1.140 |
| H | 0.132 | 4.860 | -1.788 | | H | -10.802 | -3.933 | -0.833 |
| H | 1.463 | 6.962 | -1.644 | | H | -9.653 | -1.776 | -0.387 |
| H | 3.809 | 6.874 | -1.037 | | H | 9.653 | -1.776 | 0.386 |
| H | -6.860 | 0.883 | 0.185 | | H | 10.802 | -3.933 | 0.832 |
| H | -1.983 | 1.174 | 0.400 | | H | 9.484 | -6.008 | 1.139 |
| H | -3.809 | 6.874 | 1.038 | | H | 7.004 | -5.946 | 1.005 |

Electronic Energy: -3144.978381
Thermally Corrected Gibbs Free Energy: -3144.059044
Thermally Corrected Enthalpy: -3143.905532

**Table H.13**. Cartesian coordinates of calculated **3-di-g**.
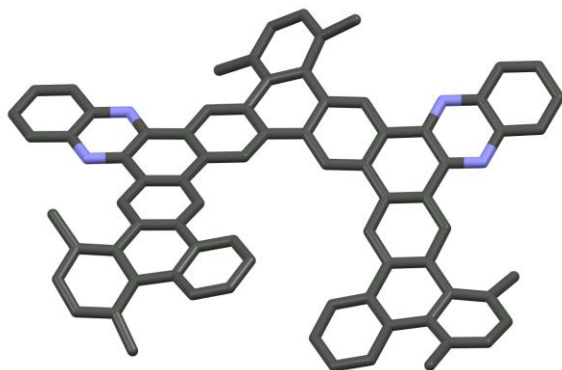
**Figure H.33**. DFT calculated structure of **3-di-x**.

| | | | | | | | |
|---|---|---|---|---|---|---|---|
| C | -0.341 | 5.305 | 7.146 | C | -1.979 | 9.558 | -3.769 |
| C | 0.024 | 6.001 | 5.851 | C | -0.647 | 2.739 | -3.748 |
| C | -0.152 | 7.376 | 5.810 | C | -0.435 | 1.360 | -3.792 |
| C | 0.119 | 8.104 | 4.662 | C | -0.116 | 0.720 | -2.566 |
| C | 0.395 | 7.478 | 3.456 | C | 0.014 | 1.477 | -1.401 |
| C | 0.435 | 6.059 | 3.430 | C | -0.362 | 0.616 | -5.062 |
| C | 0.450 | 5.345 | 4.667 | C | -0.885 | 1.111 | -6.284 |
| C | 0.703 | 8.382 | 2.280 | C | -1.926 | 2.203 | -6.405 |
| C | 0.989 | 3.975 | 4.661 | C | -0.467 | 0.512 | -7.464 |
| C | 1.549 | 3.399 | 5.818 | N | -0.934 | 6.998 | -1.401 |
| C | 2.151 | 2.156 | 5.801 | N | -1.187 | 5.484 | -3.749 |
| C | 2.234 | 1.440 | 4.609 | C | 0.341 | -5.305 | 7.146 |
| C | 1.731 | 1.997 | 3.452 | C | -0.024 | -6.001 | 5.851 |
| C | 1.109 | 3.257 | 3.449 | C | 0.152 | -7.376 | 5.810 |
| C | 0.632 | 3.869 | 2.214 | C | -0.119 | -8.104 | 4.662 |
| C | 0.375 | 5.267 | 2.190 | C | -0.395 | -7.478 | 3.456 |
| C | -0.080 | 5.805 | 0.984 | C | -0.435 | -6.059 | 3.430 |
| C | -0.247 | 5.049 | -0.173 | C | -0.450 | -5.345 | 4.667 |
| C | 0.000 | 3.658 | -0.148 | C | -0.703 | -8.382 | 2.280 |
| C | -0.558 | 3.484 | -2.575 | C | -0.989 | -3.975 | 4.661 |
| C | -0.819 | 4.924 | -2.610 | C | -1.549 | -3.399 | 5.818 |
| C | -0.685 | 5.700 | -1.408 | C | -2.151 | -2.156 | 5.801 |
| C | 0.421 | 3.110 | 1.061 | C | -2.234 | -1.440 | 4.609 |
| C | -1.596 | 8.967 | -2.595 | C | -1.731 | -1.997 | 3.452 |
| C | -1.316 | 7.579 | -2.557 | C | -1.109 | -3.257 | 3.449 |
| C | -0.192 | 2.855 | -1.363 | C | -0.632 | -3.869 | 2.214 |
| C | -1.440 | 6.809 | -3.753 | C | -0.375 | -5.267 | 2.190 |
| C | -1.838 | 7.451 | -4.953 | C | 0.080 | -5.805 | 0.984 |
| C | -2.100 | 8.795 | -4.956 | C | 0.247 | -5.049 | -0.173 |

| | | | | | | | |
|---|---|---|---|---|---|---|---|
| C | 0.000 | -3.658 | -0.148 | H | 0.576 | 2.044 | 1.124 |
| C | 0.558 | -3.484 | -2.575 | H | -1.496 | 9.531 | -1.675 |
| C | 0.819 | -4.924 | -2.610 | H | -1.925 | 6.847 | -5.848 |
| C | 0.685 | -5.700 | -1.408 | H | -2.404 | 9.285 | -5.873 |
| C | -0.421 | -3.110 | 1.061 | H | -2.193 | 10.620 | -3.797 |
| C | 1.596 | -8.967 | -2.595 | H | -0.845 | 3.298 | -4.644 |
| C | 1.316 | -7.579 | -2.557 | H | 0.331 | 0.969 | -0.503 |
| C | 0.192 | -2.855 | -1.363 | H | -2.581 | 2.253 | -5.536 |
| C | 1.440 | -6.809 | -3.753 | H | -2.547 | 2.002 | -7.280 |
| C | 1.838 | -7.451 | -4.953 | H | -1.490 | 3.196 | -6.546 |
| C | 2.100 | -8.795 | -4.956 | H | -0.855 | 0.881 | -8.407 |
| C | 1.979 | -9.558 | -3.769 | H | 1.165 | -5.845 | 7.617 |
| C | 0.647 | -2.739 | -3.748 | H | -0.479 | -5.290 | 7.869 |
| C | 0.435 | -1.360 | -3.792 | H | 0.663 | -4.276 | 6.989 |
| C | 0.116 | -0.720 | -2.566 | H | 0.479 | -7.893 | 6.706 |
| C | -0.014 | -1.477 | -1.401 | H | -0.081 | -9.187 | 4.696 |
| C | 0.362 | -0.616 | -5.062 | H | -1.137 | -9.311 | 2.656 |
| C | 0.885 | -1.111 | -6.284 | H | 0.187 | -8.657 | 1.707 |
| C | 1.926 | -2.203 | -6.405 | H | -1.415 | -7.937 | 1.587 |
| C | 0.467 | -0.512 | -7.464 | H | -1.565 | -3.957 | 6.739 |
| N | 0.934 | -6.998 | -1.401 | H | -2.581 | -1.756 | 6.711 |
| N | 1.187 | -5.484 | -3.749 | H | -2.716 | -0.471 | 4.581 |
| H | -1.165 | 5.845 | 7.617 | H | -1.861 | -1.463 | 2.520 |
| H | 0.479 | 5.290 | 7.869 | H | 0.358 | -6.840 | 0.908 |
| H | -0.663 | 4.276 | 6.989 | H | -0.576 | -2.044 | 1.124 |
| H | -0.479 | 7.893 | 6.706 | H | 1.496 | -9.531 | -1.675 |
| H | 0.081 | 9.187 | 4.696 | H | 1.925 | -6.847 | -5.848 |
| H | 1.137 | 9.311 | 2.656 | H | 2.404 | -9.285 | -5.873 |
| H | -0.187 | 8.657 | 1.707 | H | 2.193 | -10.620 | -3.797 |
| H | 1.415 | 7.937 | 1.587 | H | 0.845 | -3.298 | -4.644 |
| H | 1.565 | 3.957 | 6.739 | H | -0.331 | -0.969 | -0.503 |
| H | 2.581 | 1.756 | 6.711 | H | 2.581 | -2.253 | -5.536 |
| H | 2.716 | 0.471 | 4.581 | H | 2.547 | -2.002 | -7.280 |
| H | 1.861 | 1.463 | 2.520 | H | 1.490 | -3.196 | -6.546 |
| H | -0.358 | 6.840 | 0.908 | H | 0.855 | -0.881 | -8.407 |

Electronic Energy: -3144.977184
Thermally Corrected Gibbs Free Energy: -3144.070185
Thermally Corrected Enthalpy: -3143.911525

**Table H.14**. Cartesian coordinates of calculated **3-di-x**.

# Powder X-ray diffraction (PXRD) data

To verify substance uniformity, experimental PXRD data of bulk material was compared to predicted PXRD data derived from single-crystal structures. Predicted PXRD spectra were obtained in Mercury using the MicroED structures obtained for the respective helicenes. Experimental diffraction data were collected with 0.02° steps using a Bruker AXS D8 Advance diffractometer equipped with Cu−Kα radiation ($\lambda_{avg}$ = 1.5418 Å), a Göbel mirror, a Lynxeye linear position-sensitive director, and mounting the following optics: fixed divergence slit (0.6 mm), receiving slit (3 mm), and secondary beam Soller slits (2.5°). The generator was set at 40 kV and 40 mA. Samples were loaded on zero background sample holders for measurement.
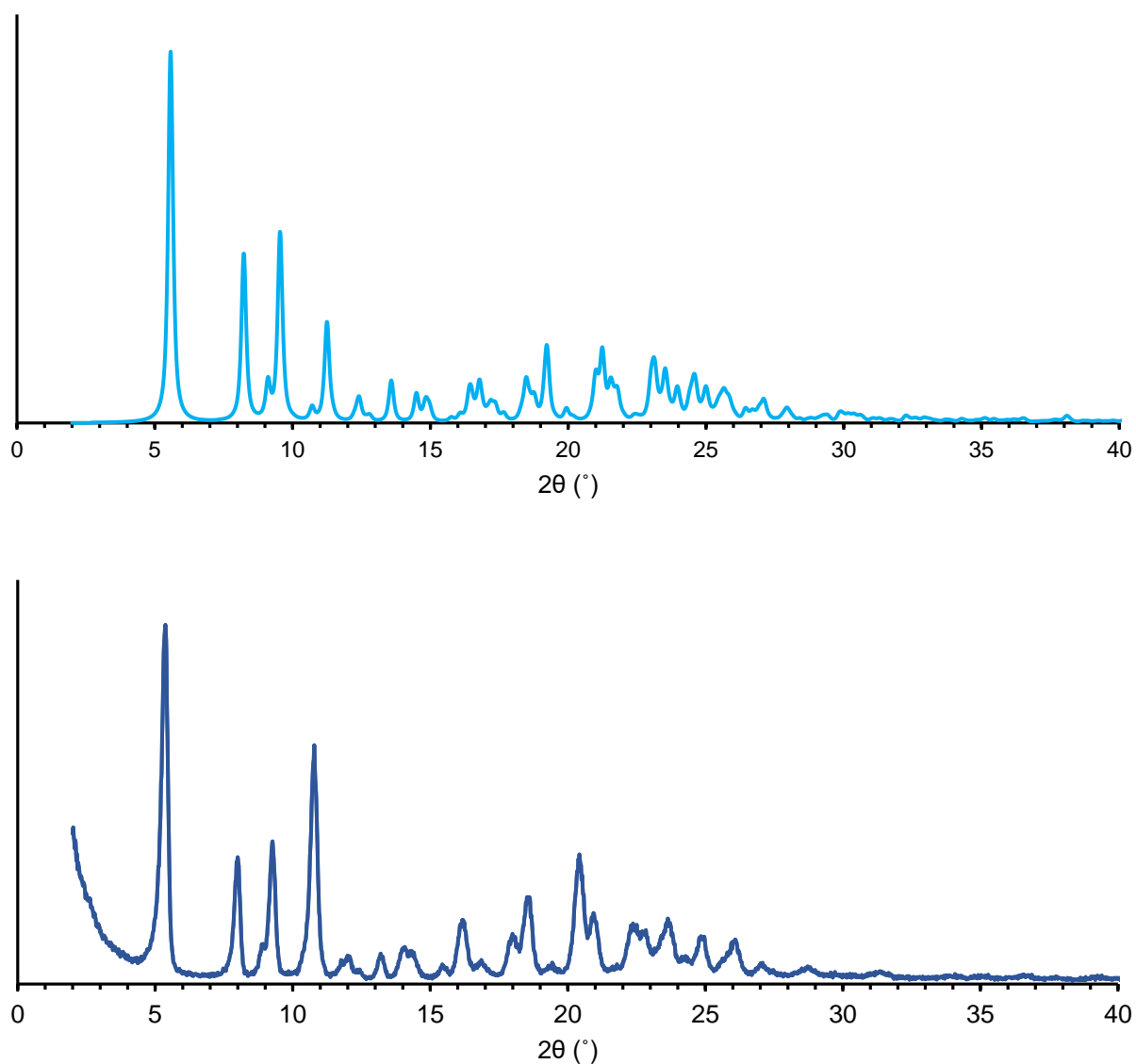
**Figure H.34**. Comparison of the predicted (light blue) and experimental (blue) powder X-ray diffraction patterns for **1a**.
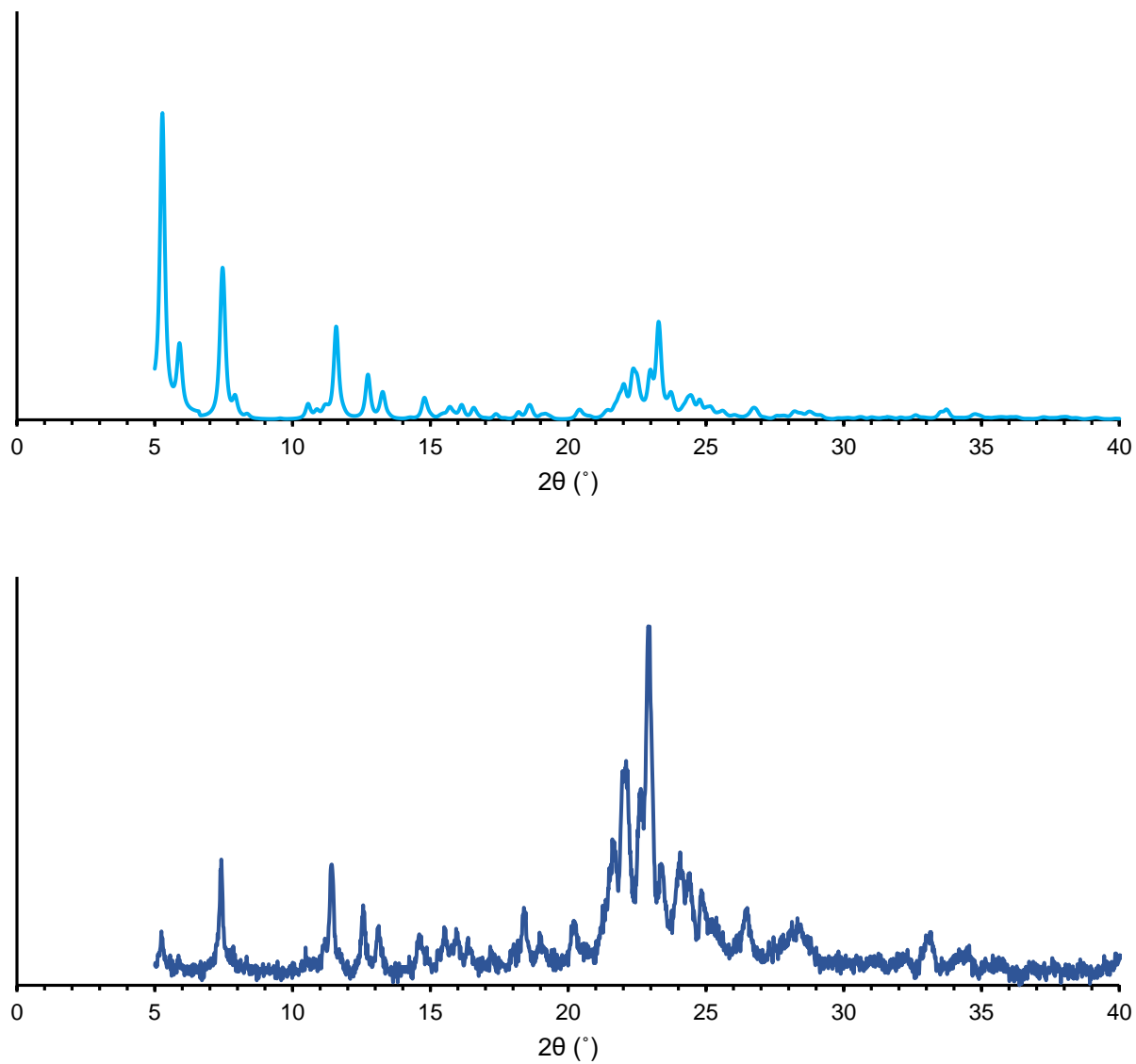
**Figure H.35**. Comparison of the predicted (light blue) and experimental (blue) powder X-ray diffraction patterns for **2-mon**.
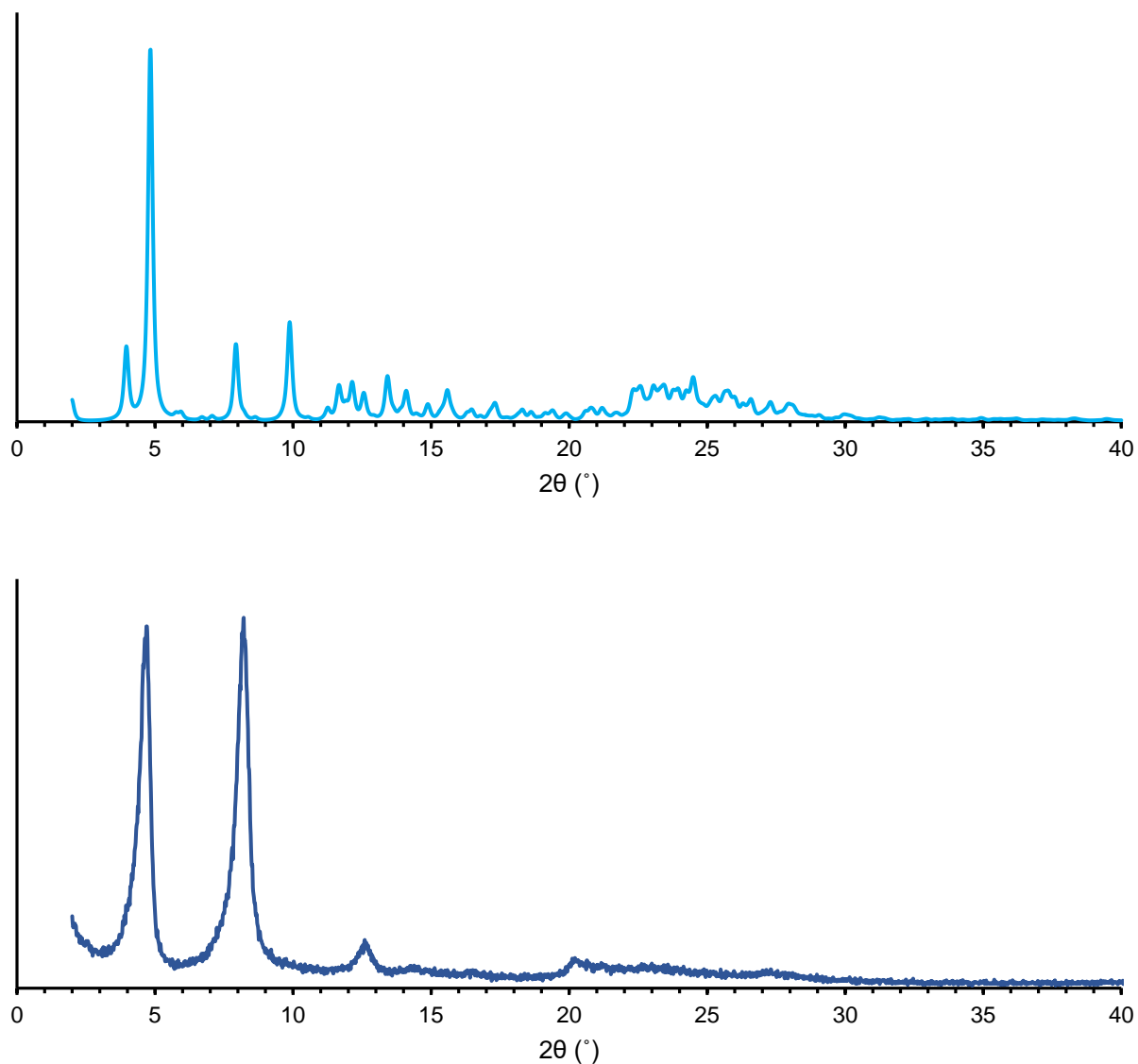
**Figure H.36**. Comparison of the predicted (light blue) and experimental (blue) powder X-ray diffraction patterns for **2-di**. We note that the two peaks at low angles line up with those at approximately 5° and 8° in the predicted pattern, though it does exhibit poor crystallinity that obscures observation of many other peaks. However, the peaks that are represented are consistent with preferred orientation along the (0 0 1) direction, in line with the needle-like crystal habit observed in the microED sample in Figure H.14.
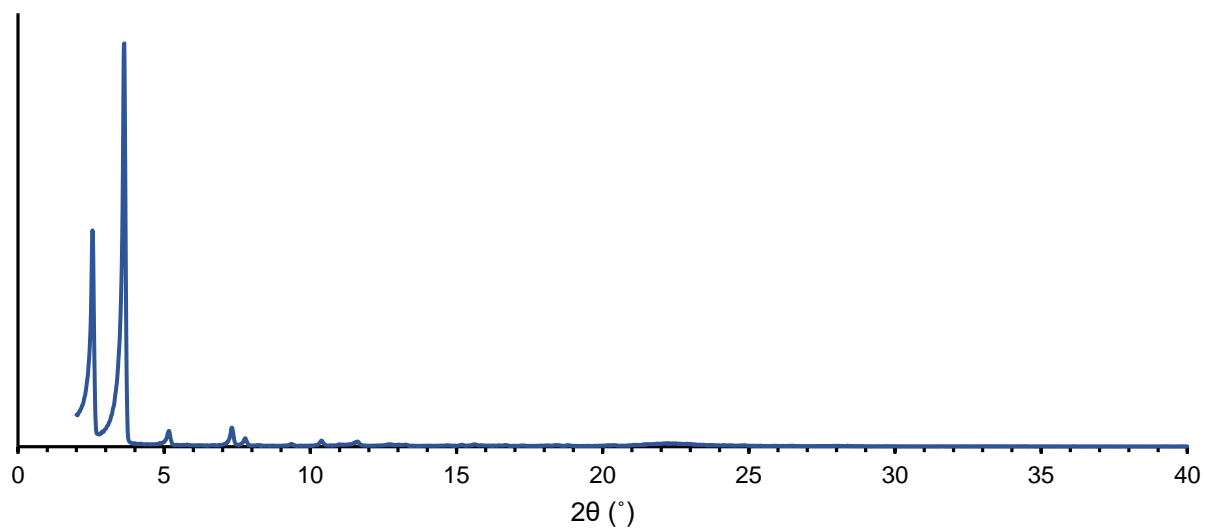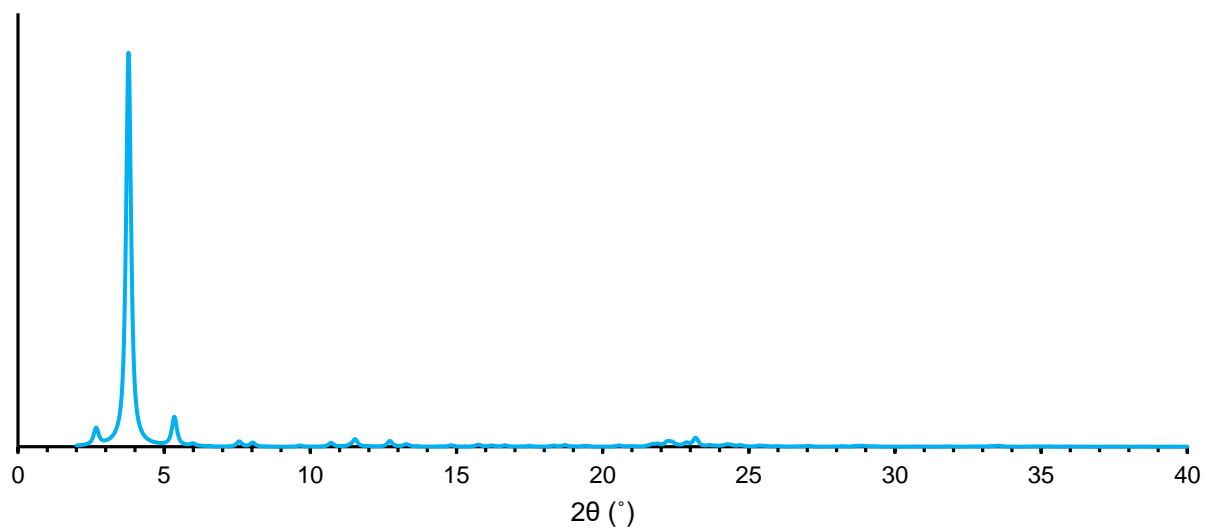
**Figure H.37**. Comparison of the predicted (light blue) and experimental (blue) powder X-ray diffraction patterns for **3-mon**.
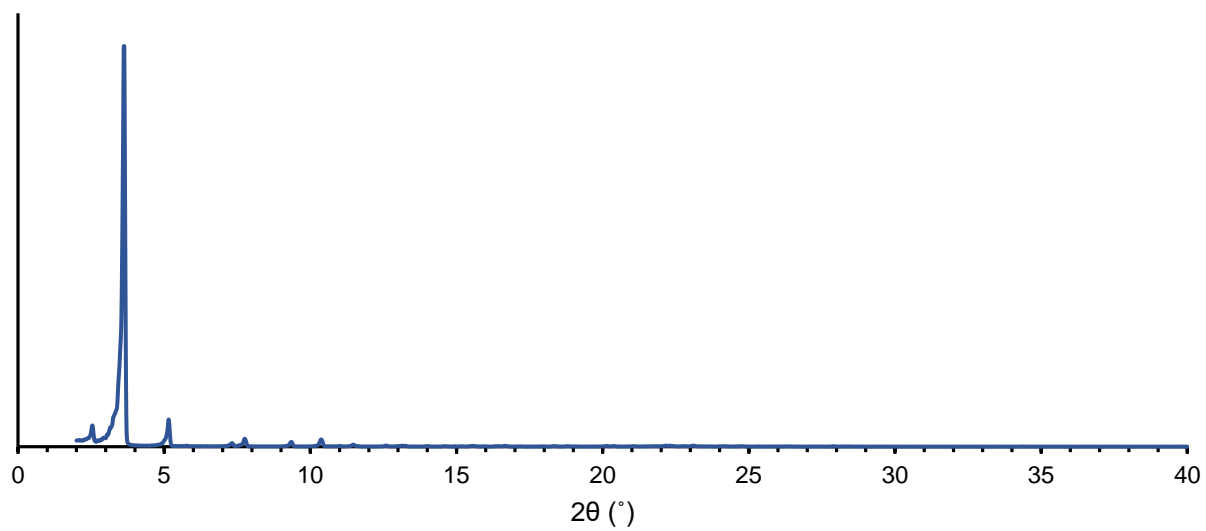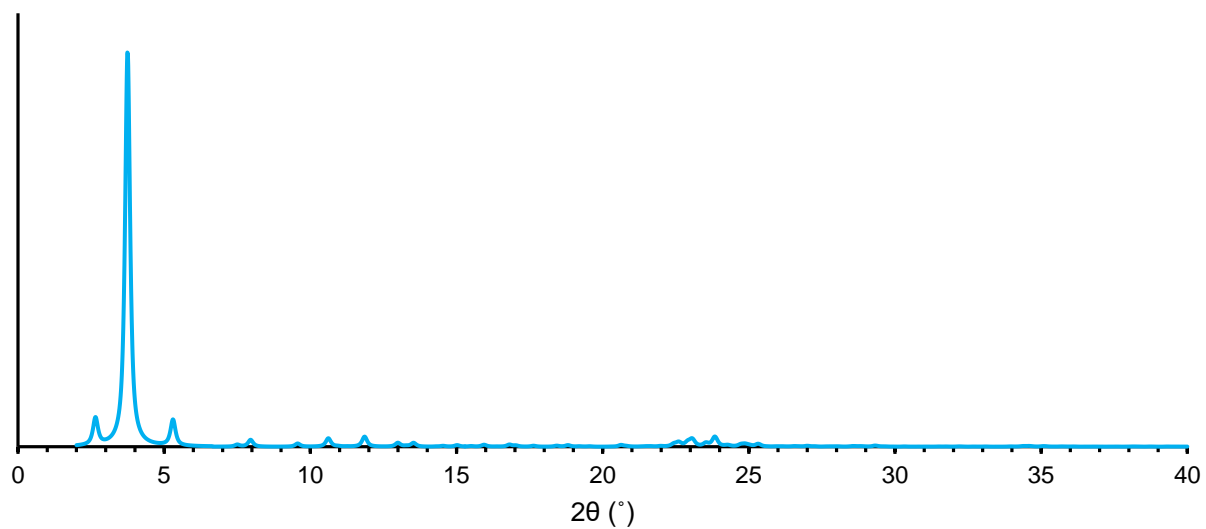
**Figure H.38**. Comparison of the predicted (light blue) and experimental (blue) powder X-ray diffraction patterns for **3-di**.

# References

(1)  Armarego, W. L. F.; Chai, C. L. L. Chapter 5 - Purification of Inorganic and Metal-Organic Chemicals: (Including Organic Compounds of B, Bi, P, Se, Si, and Ammonium and Metal Salts of Organic Acids). In *Purification of Laboratory Chemicals (Sixth Edition)*; Butterworth-Heinemann: Oxford, 2009; pp 445–576.

(2)  Kiel, G. R.; Patel, S. C.; Smith, P. W.; Levine, D. S.; Tilley, T. D. *J. Am. Chem. Soc.* **2017**, *139* (51), 18456–18459.

(3)  Nannenga, B. L.; Shi, D.; Leslie, A. G. W.; Gonen, T. *Nat. Methods* **2014**, *11* (9), 927–930.

(4)  Kabsch, W. *Acta Crystallogr. D Biol. Crystallogr.* **2010**, *66* (2), 133–144.

(5)  Sheldrick, G. M. *Acta Crystallogr. Sect. Found. Adv.* **2015**, *71* (1), 3–8.

(6)  Schneider, T. R.; Sheldrick, G. M. *Acta Crystallogr. D Biol. Crystallogr.* **2002**, *58* (10), 1772–1779.

(7)  Sheldrick, G. M. *Acta Crystallogr. Sect. C Struct. Chem.* **2015**, *71* (1), 3–8.

(8)  Hübschle, C. B.; Sheldrick, G. M.; Dittrich, B. *J. Appl. Crystallogr.* **2011**, *44* (6), 1281–1284.

(9)  Calio, F.; Alessandro Lazzari. *Elements of Mathematics with Numerical Applications*, 2nd ed.; Società Editrice Esculapio, **2017**.

(10) Enkhbayar, P.; Damdinsuren, S.; Osaki, M.; Matsushima, N. *Comput. Biol. Chem.* **2008**, *32* (4), 307–310.

(11) Nakakuki, Y.; Hirose, T.; Matsuda, K. *J. Am. Chem. Soc.* **2018**, *140* (45), 15461–15469.

(12) Gaussian 16, Revision C.01, Frisch, M. J.; Trucks, G. W.; Schlegel, H. B.; Scuseria, G. E.; Robb, M. A.; Cheeseman, J. R.; Scalmani, G.; Barone, V.; Petersson, G. A.; Nakatsuji, H.; Li, X.; Caricato, M.; Marenich, A. V.; Bloino, J.; Janesko, B. G.; Gomperts, R.; Mennucci, B.; Hratchian, H. P.; Ortiz, J. V.; Izmaylov, A. F.; Sonnenberg, J. L.; Williams-Young, D.; Ding, F.; Lipparini, F.; Egidi, F.; Goings, J.; Peng, B.; Petrone, A.; Henderson, T.; Ranasinghe, D.; Zakrzewski, V. G.; Gao, J.; Rega, N.; Zheng, G.; Liang, W.; Hada, M.; Ehara, M.; Toyota, K.; Fukuda, R.; Hasegawa, J.; Ishida, M.; Nakajima, T.; Honda, Y.; Kitao, O.; Nakai, H.; Vreven, T.; Throssell, K.; Montgomery, J. A., Jr.; Peralta, J. E.; Ogliaro, F.; Bearpark, M. J.; Heyd, J. J.; Brothers, E. N.; Kudin, K. N.; Staroverov, V. N.; Keith, T. A.; Kobayashi, R.; Normand, J.; Raghavachari, K.; Rendell, A. P.; Burant, J. C.; Iyengar, S. S.; Tomasi, J.; Cossi, M.; Millam, J. M.; Klene, M.; Adamo, C.; Cammi, R.; Ochterski, J. W.; Martin, R. L.; Morokuma, K.; Farkas, O.; Foresman, J. B.; Fox, D. J. Gaussian, Inc., Wallingford CT, 2016.

*Appendix I*

*Supporting Information for Chapter 10: A heterologous expression platform in*

*Aspergillus nidulans for the elucidation of cryptic secondary metabolism*

*biosynthetic gene clusters: discovery of the Aspergillus fumigatus sartorypyrone*

*biosynthetic pathway*

**Detailed structural characterizations of new compounds from this study**

Compound **1** has a molecular formula of $C_{26}H_{38}O_4$, as determined by its HRESIMS and $^{13}$C-NMR data, representing eight indices of hydrogen deficiency (IHD). $^1$H, $^{13}$C, and HSQC NMR spectra showed signals for five methyl groups [$\delta_H$ 0.67, 0.75, 0.98, 1.73, and 2.10 (each 3H, s)], one carbinol methine group [$\delta_H$ 3.18 (1H, dd, J = 10.6, 5.4 Hz, H-3); $\delta_C$ 78.3 (C-3)], one downfield methylene [$\delta_H$ 3.02 (1H, dd, J = 13.9, 6.9 Hz, H-15) and 3.11 (1H, dd, J = 13.9, 7.7 Hz, H-15); $\delta_C$ 22.9 (C-15)], one terminal alkene [$\delta_H$ 4.52 and 4.80 (each 1H, br s, H-25); $\delta_C$ 106.7 (C-25)], and the $\alpha$-pyrone moiety [$\delta_H$ 6.02 (1H, br d, J = 0.9 Hz, H-18), and 2.10 (3H, br s, H-20); $\delta_C$ 101.9 (C-16), 166.0 (C-17), 101.7 (C-18), 159.9 (C-19), 19.8 (C-20), and 167.4 (C-21)]. Besides the $\alpha$-pyrone moiety, there are four additional sp2 carbons [$\delta_C$ 135.4 (C-13), 123.7 (C-14), 149.4 (C-8), and 106.7 (C-25)]. Considering that there are eight IHD in compound **1** with only one $\alpha$-pyrone moiety and two olefins, compound **1** should contain a bicyclic diterpenoid moiety. Comparing the $^1$H and $^{13}$C NMR spectra of **1** with those of sartorypyrone D, the main differences are that one olefinic proton at ~ 5.03 ppm disappears, and one methyl group at ~ 1.59 ppm shifts to ~ 0.67 ppm in compound **1**, indicating the cyclization of one more ring in the diterpenoid moiety of compound **1**. In the HMBC spectrum, the long-range $^1$H-$^{13}$C correlations between H$_3$-24 and C-1, C-5, C-9, and C-10 confirm the connectivity of the bicyclic structure. The correlations of H$_2$-15 to C-13, C-14, C-16, and C-17 further connect the bicyclic diterpenoid and the $\alpha$-pyrone moiety to complete the planar structure of compound **1** (Table I.2 and Fig I.7-I.11). The relative stereochemistry was determined by analysis of the NOESY spectrum (Table I.2 and Fig I.12). The H-5 signal exhibits correlations to H-3, H-9, and H$_3$-22, while showing no correlations with the methyl group at C-10 (H$_3$-24), suggesting a trans-decalin ring junction. Furthermore, since the NOESY spectral data also show cross peaks of H-14 to H$_2$-12 and H$_2$-15, the configuration of double bond at C-13 is 13*E*.

Compound **4** has a molecular formula of $C_{28}H_{40}O_5$, as deduced from its HRESIMS and $^{13}$C-NMR data, implying nine IHD. The UV-Vis, $^1$H and $^{13}$C NMR spectrum were similar to those of compound **1**, indicating they are structural analogs. The main differences are the presence of an acetyl group [$\delta_H$ 2.00 (3H, s); $\delta_C$ 21.1, 170.8] and a mass difference of 42 units larger in compound **4**, suggesting compound **4** is an acetyl derivative of **1**. The COSY, HSQC, HMBC and NOESY spectrum analysis allowed the complete assignment of compound **4** as 3-O-acetylated compound **1** (Table I.5 and Fig I.17-I.22).

Compound **5** has a molecular formula of $C_{26}H_{36}O_5$, which was found by means of HRESIMS and $^{13}$C-NMR data, implying nine IHD. The UV-Vis, $^1$H and $^{13}$C NMR spectrum were similar to those of compound **6**, implying they are structural derivatives. The main differences are the disappearance of a methyl group [$\delta_H$ 1.65 (3H, s, H-27); $\delta_C$ 25.8 (C-27)] and the presence of a

carboxylic acid group [$\delta_C$ 169.2], suggesting compound **5** is a carboxylate derivative of **6** generated by carboxylation at C-27 (Table I.6 and Fig I.23-I.27). The chemical shift values of compound **5** at the H$_2$-19 methylene [$\delta_H$ 2.31 (2H, m)] and at the H-20 olefinic proton [$\delta_H$ 6.77 (1H, tq, J = 7.3, 1.4 Hz)] are in good agreement with those for asiaticusin A, indicating the double bond at C-20 is 20*E*.[1] The NOESY correlation between H$_2$-19 and H$_3$-26 further confirmed the 20*E* configuration (Fig I.28).

Compound **8** was determined to have a molecular formula of C$_{26}$H$_{38}$O$_4$, as determined through the utilization of HRESIMS and $^{13}$C-NMR data. This molecular formula suggests the presence of eight degrees of unsaturation (IHD). The UV-Vis, $^1$H, and $^{13}$C NMR spectra of compound **8** exhibited similarities to those of compound **6**, indicating a structural relationship between the two compounds. The chemical shift values of compound **6** at C-20 [$\delta_C$ 125.0] and C-21 [$\delta_C$ 131.6] were observed to shift to different values in compound **8** at C-20 [$\delta_C$ 64.0] and C-21 [$\delta_C$ 58.1]. These shift values along with the mass difference of 16 units indicate that compound **8** was formed through the epoxidation of compound **6** at C-20 and C-21. Moreover, the configuration at C-20 was deduced to be *S*, based on the biosynthetic relationship with compound **7** (Table I.9 and Fig I.33-I.37).

Compounds **9**, **10**, and **11** possess the molecular formulas C$_{21}$H$_{32}$O$_5$, C$_{22}$H$_{34}$O$_5$, and C$_{21}$H$_{30}$O$_4$, respectively, as determined through analysis of their HRESIMS and $^{13}$C NMR data. The UV-Vis, $^1$H, and $^{13}$C NMR spectra exhibited similarities among compounds **7-11**, while the mass differences of 68 units between compounds **9** and **7**, as well as between compounds **11** and **8**, suggested that compounds **9** and **11** have one less prenyl group than compounds **7** and **8**. Additionally, a comparison of the $^1$H and $^{13}$C NMR between spectra between **9** and **10** revealed that **10** has one more ether group [$\delta_H$ 3.16 (3H, s); $\delta_C$ 49.2] than **9**. HMBC correlations confirmed the assigned structure of **10**. The relative arrangement of compounds **9-11** was inferred from their derivatives **7** based on the biosynthetic association (Table I.10-I.12 and Fig I.38-I.52).

## Supplemental Materials and Methods

### Molecular genetic techniques and strain construction

Transformation procedures were generally as previously described[2–4] except that 100 mg/mL VinoTaste Pro (Novozymes) was used for protoplasting. Transforming fragments were generated by fusion PCR as previously described[2–4] with the following modifications. The DNA polymerase used was Q5 Hot Start High-Fidelity 2X Master Mix (New England Biolabs). The annealing temperature was Tm (for the lowest melting temperature primer) + 3-5ºC. Tm was calculated as previously described[3] where Tm is the melting temperature of the primer with the lowest melting temperature. Extension time was 30 seconds per kb. Flanking

regions were ~1 kb with slight variations consistent with primer design. For the refactored BGC, at the *yA* locus (Fig. 10.1B) the *spyA* overlap was 1012 bp and the *AtpabaA* overlap was 1197 bp. At the *wA* locus the *AtriboB* overlap was 1012 bp (see Fig. I.1). Miniprep DNA was prepared for diagnostic PCR following the procedure of Edgerton and Oakley.[5] The DNA polymerase was OneTaq Hot Start Quick Load 2X Master Mix (New England Biolabs). The annealing temperature was 55-60ºC and the extension time was one minute per kb. Multiple diagnostic PCR reactions were carried out for each gene. For the reconstruction of the BGC in *A. nidulans* (Fig. I.3), the Afu8g02420 overlap was 1013 bp, the *spyD* overlap was 1086 bp and the *spyA* overlap was 1003 bp. Both the refactored cluster and the reconstructed cluster were made in strain LO11098. *SpyB* was refactored using two different start codons. Site 1 is the site annotated in FungiDB (<u>ATG</u>TGCATGGACCGTCTTGT). Site 2 is 593 bp downstream of site 1 (<u>ATG</u>CCTAGAAGAGAGCGTAG).

For deleting the individual genes of the refactored BGC, ~1kb flanking fragments were fused to a selectable marker and the resulting fragment was used for transformation with selection for the marker on the transforming fragment. Transforming fragments were designed to remove the promoter driving the target gene as well as the coding sequence and 3' untranslated DNA. For example, to delete *spyA*, a ~1 kb *yA* flanking sequence was fused to *AfpyroA aldA*(p) (~300 bp) and ~700 bp of the N-terminal coding region of Afu8g02440. Transformation with this fragment resulted in removal of *AfpyrG* and *spyA*, but left Afu8g02440 intact and under control of *aldA*(p).

For expression of SpyA alone, a fragment consisting of ~1 kb of *yA* flank, *AfpyrG*, the *alcA* promoter and a 5' portion of the *spyA* coding region was created by fusion PCR. A second fragment consisting of an overlapping 3' portion of the *spyA* coding region plus 3' untranslated region and ~1 kb of *yA* 3' flank was generated by fusion PCR. The two fragments shared an overlap region of 1003 bp. The two fragments were co-transformed into strain LO11945 which is LO11098 with the promoter of the *alcR* transcription factor (which drives expression of *alcA* and *aldA*) under control of the strong constitutive *gpdA* promoter. The *Aspergillus terreus biA* gene (*AtbiA*) gene was used as a selectable marker for the replacement of the *alcR* promoter with the *gpdA* promoter. We designated the resultant *spyA* expressing strain LO12091.

**Fermentation and LC-MS analysis**
Liquid LMM medium (15 g/L lactose, 6g/L NaNO$_3$, 0.52 g/L KCl, 0.52 g/L MgSO$_4$·7H$_2$O, 1.52 g/L KH$_2$PO$_4$, 0.72 g/L fructose and 1 mL/L trace elements solution) was inoculated with $3 \times 10^7$ spores in a 30 mL volume and incubated at 37°C with shaking at 150 rpm in 125 mL flasks. Supplements such as riboflavin (2.5 mg/L), pyridoxine (0.5 mg/L), uracil (1 g/L), uridine (10 mM), p-aminobenzoic acid (1 mg/L), biotin (0.02 mg/L), L-lysine (200 mg/L) or choline HCl (20 mg/L) were added as needed. To induce *alcA*(p) and *aldA*(p), methyl ethyl ketone (MEK), was added into the medium at a final concentration of 50 mM, 42 hours after

inoculation. After 72 hours of MEK induction, the culture medium was collected by filtration and extracted with an equal volume of EtOAc. The mycelium was extracted with 30 mL 1:1 DCM/MeOH with 1 hour of sonication. The resulting extract was dried in vacuo to obtain an aqueous residue, which was then suspended in 30 ml $H_2O$ and partitioned with 30 ml EtOAc. To extract acidic phenolic compounds, the water layer was extracted with the same volume of EtOAc after acidification to pH 2. The EtOAc extract from culture medium, acidified culture medium or mycelium was evaporated in vacuo, re-dissolved in 1 ml of 20% DMSO in MeOH, and a portion (10 μL) was subjected to high performance liquid chromatography-photodiode array detection-mass spectroscopy (HPLC-DAD-MS) analysis.

The HPLC-MS analysis was performed using an RP C18 column (Phenomenex Luna Omega 3 μm Polar C18 100 × 2.1 mm) on a ThermoFinnigan LCQ Advantage ion trap mass spectrometer. The flow rate used was 125 μL/min. The solvent gradient consisted of 95% MeCN/$H_2O$ (solvent B) and 5% MeCN/$H_2O$ (solvent A), both containing 0.05% formic acid. The gradient was run under the following conditions: 0% solvent B from 0 to 5 min, 0–100% solvent B from 5 min to 35 min, 100–0% solvent B from 40 to 45 min, and re-equilibration with 0% solvent B from 45 to 50 min.

**Isolation and characterization of metabolites**

To purify metabolites, EtOAc was used to extract the broth from a 5 L culture. Mycelia were also extracted with 800 mL 1:1 DCM/MeOH at ambient temperature overnight, and the resulting extract was concentrated and re-extracted with EtOAc. Both of the extracts were subjected to silica-gel column chromatography followed by further separation through semi-preparative HPLC (Phenomenex Luna 5 μm C18 (2), 250 × 10 mm), with a flow rate of 4.0 mL/min and monitored using a UV detector set at 254 nm. NMR spectra were recorded using a Varian VNMRS-600 spectrometer, while a high-resolution electrospray ionization mass spectrometer (HRESI-MS) was used to obtain mass spectra, and optical rotations were measured on a JASCO P-1010 digital polarimeter. The identity of previously reported compounds, including sartorypyrones A, D, and E, and geranylgeranyl-triacetate acid lactone (designated compounds **2-3** and **6-7**), was confirmed by comparing their HRESIMS, UV-vis, and ^{1}H-NMR data with published information (as shown in Tables S3-4 and S7-8†).

**Purification conditions for compounds 1-4**

For structural elucidation, compounds **1-4** were purified from 5 L of LMM medium inoculated with LO11839, grown and induced with MEK and extracted with EtOAc as described above. The mycelia which also containing compounds **1-4** were soaked in 800 mL DCM/MeOH (1:1) overnight, and the resulting extract was evaporated and re-extracted with EtOAc. Both extracts were pooled to get 1.36 g of crude extract. This extract was then applied to a silica gel (Sigma-Aldrich 70-230 mesh, 63-200 μm) column and eluted with DCM-MeOH mixtures of increasing polarity (fraction A, 100:0, 300 mL; fraction B, 100:1, 300 mL;

fraction C, 50:1, 300 mL; fraction D, 25:1, 300 mL). Fraction B (160 mg), which contained compounds **3-4**, and Fraction C (59 mg), which contained compounds **1-2**, were further purified by reverse phase HPLC [Phenomenex Luna 5µm C18 (2), 250 × 10 mm] with a flow rate of 4.0 mL/min and measured by a UV detector at 254 nm. The gradient system was 95% MeCN/$H_2O$ (solvent B) in 5 % MeCN/$H_2O$ (solvent A). Fraction B was separated with the following gradient condition: 90 % B from 0 to 5 min, 90 to 100 % B from 5 to 15 min, maintained at 100 % B from 15 to 17 min, 100 to 90 % B from 17 to 18 min, and re-equilibration with 90 % B from 18 to 22 min. Sartorypyrone A (**3**, 29.0 mg) and sartorypyrone G (**4**, 25.0 mg) were eluted at 10.5 and 11.5 min, respectively. Fraction C was separated with the following gradient conditions: 80 % B from 0 to 5 min, 80 to 100 % B from 5 to 15 min, maintained at 100 % B from 15 to 17 min, 100 to 80 % B from 17 to 18 min, and re-equilibration with 80 % B from 18 to 22 min. Sartorypyrone F (**1**, 5.6 mg) and sartorypyrone G (**2**, 15.6 mg) were eluted at 7.5 and 8.5 min, respectively.

**Purification conditions for compounds 5-6**

For structural elucidation, compound **5** was purified from 5 L of LMM medium inoculated with LO12126, grown and induced, and extracted with EtOAc as described above. The medium was extracted with EtOAc three times and the combined EtOAc layer was then evaporated in vacuo to obtain 217 mg of crude extract. This extract was then applied to a silica gel (Sigma-Aldrich 70-230 mesh, 63-200 µm) column and eluted with DCM-MeOH mixtures of increasing polarity (fraction A, 50:1, 50 mL; fraction B, 25:1, 80 mL; fraction C, 9:1, 50 mL; fraction D, 4:1, 50 mL). Fraction B (94 mg), which contained compound **5** was further purified by reverse phase HPLC [Phenomenex Luna 5µm C18 (2), 250 × 10 mm] with a flow rate of 4.0 mL/min and measured by a UV detector at 254 nm. The gradient system was 95% MeCN/$H_2O$ (solvent B) in 5 % MeCN/$H_2O$ (solvent A). Fraction B was separated with the following gradient conditions: 40 % B from 0 to 4 min, 40 to 75 % B from 4 to 20 min, 75 to 40 % B from 20 to 21 min, and re-equilibration with 40 % B from 21 to 25 min. Compound **5** (60.2 mg) was eluted at 19.5 min.

The mycelia which contained compound **6** were soaked in 800 mL DCM/MeOH (1:1) overnight, and the resulting extract was evaporated and re-extracted with EtOAc to obtain 1.1 g of crude extract. This extract was then applied to a silica gel (Sigma-Aldrich 70-230 mesh, 63-200 µm) column and eluted with DCM-MeOH mixtures of increasing polarity (fraction A, 100:0, 200 mL; fraction B, 100:1, 200 mL; fraction C, 50:1, 200 mL; fraction D, 4:1, 300 mL). Fraction B (227 mg), which contained compound **6** was further purified by reverse phase HPLC [Phenomenex Luna 5µm C18 (2), 250 × 10 mm] with a flow rate of 4.0 mL/min and measured by a UV detector at 254 nm. The gradient system was 95% MeCN/$H_2O$ (solvent B) in 5 % MeCN/$H_2O$ (solvent A). Fraction B was separated using the following gradient conditions: 0 % B from 0 to 5 min, 0 to 100 % B from 5 to 35 min, maintained at 100 % B from 35 to 40 min, 100 to 0 % B from 40 to 41 min, and re-equilibration with 0 % B from 41

to 45 min. Compound **6** (12.2 mg) was eluted at 40.0 min.

## Purification conditions for compounds 7-8

For structural elucidation, compounds **7-8** were purified from 5 L of LMM medium inoculated with LO12107, grown, induced, and extracted with EtOAc as described above. The mycelia which also contained compounds **7-8** were soaked in 800 mL DCM/MeOH (1:1) overnight, and the resulting extract was evaporated and re-extracted with EtOAc. Both extracts were pooled to get 1.51 g of crude extract. This extract was then applied to a silica gel (Sigma-Aldrich 70-230 mesh, 63-200 μm) column and eluted with DCM-MeOH mixtures of increasing polarity (fraction A, 50:1, 300 mL; fraction B, 100:3, 300 mL; fraction C, 25:1, 300 mL; fraction D, 25:2, 300 mL; fraction E, 4:1, 300 mL). Fraction B (35.2 mg), which contained compound **8**, and Fraction D (311.1 mg), which contained compound **7**, were further purified by reverse phase HPLC [Phenomenex Luna 5μm C18 (2), 250 × 10 mm] with a flow rate of 4.0 mL/min and measured by a UV detector at 254 nm. The gradient system was 95% MeCN/$H_2O$ (solvent B) in 5 % MeCN/$H_2O$ (solvent A). Fraction B was separated with the following gradient condition: 40 % B from 0 to 4 min, 40 to 100 % B from 4 to 24 min, maintained at 100 % B from 24 to 25 min, 100 to 40 % B from 25 to 26 min, and re-equilibration with 40 % B from 26 to 30 min. Compound **7** (13.2 mg) was eluted at 22.0 min. Fraction D was separated with the following gradient condition: 45% B from 0 to 20 min, 45 to 100 % B from 20 to 21 min, maintained at 100 % B from 21 to 22 min, 100 to 45 % B from 22 to 23 min, and re-equilibration with 45 % B from 23 to 27 min. Compound **8** (142.3 mg) was eluted at 16.0 min.

## Purification conditions for compounds 9-11

For structural elucidation, compounds **9-11** were purified from 5 L of LMM medium inoculated with LO12117, grown, induced, and extracted with EtOAc as described above. The medium was extracted with EtOAc three times and the combined EtOAc layer was then evaporated in vacuo to obtain 690 mg of crude extract. This extract was then applied to a silica gel (Sigma-Aldrich 70-230 mesh, 63-200 μm) column and eluted with DCM-MeOH mixtures of increasing polarity (fraction A, 100:1, 150 mL; fraction B, 50:1, 150 mL; fraction C, 25:1, 150 mL; fraction D, 25:2, 150 mL; fraction E, 4:1, 150 mL). Fraction B (270 mg), which contained compounds **9-11** was further purified by reverse phase HPLC [Phenomenex Luna 5μm C18 (2), 250 × 10 mm] with a flow rate of 4.0 mL/min and measured by a UV detector at 254 nm. The gradient system was 95% MeCN/$H_2O$ (solvent B) in 5 % MeCN/$H_2O$ (solvent A). Fraction B was separated using the following gradient conditions: 50 % B from 0 to 3 min, 50 to 60 % B from 3 to 20 min, 60 to 100 % B from 20 to 21 min, maintained at 100 % B from 21 to 22 min, 100 to 50 % B from 22 to 23 min, and re-equilibration with 50 % B from 23 to 27 min. Compound **9** (55.6 mg), compound **10** (3.0 mg), and compound **11** (11.6 mg) were eluted at 6.7, 12.0, and 17.0 min, respectively.

**Crystallization of compound 1**

Compound **1** was crystallized by the hanging drop vapor diffusion crystallization method. First, compound **1** was dissolved in acetone at a concentration of 20 mg/mL. A series of polyethylene glycols (PEGs) ranging in mass from 300-20,000 were screened as precipitants at various concentrations (18, 25, and 32%). Vapor diffusion was set up by transferring 100 µL of PEG into each well of a 96-well plate. On a cover slip 0.4 µL of PEG precipitants from each reservoir was mixed with 0.4 µL of compound **1**. The cover slide was used to seal the reservoir using a silicone grease ring around the edge of the well. Crystals appeared in 1-3 days and drops containing crystals were harvested from multiple wells and combined for MicroED.

**Electron diffraction data collection, refinement, and statistics for compound 1**

A slurry of microcrystals was pipetted onto a lacey carbon grid and then briefly blotted using a Kimwipe. The grid containing dried crystals was mounted in a Gatan 626 cryo-holder at room temperature and inserted into a FEI Tecnai F200C transmission electron microscope prior to cooling the cryo holder to avoid icing. The microscope was operated at a voltage of 200 keV and a wavelength of 0.025 Å. After insertion, the sample was cooled down to a cryogenic temperature of 100 K. Data acquisition, conversion, and reduction were carried out as described previously,[6] and data from eight crystals were merged and scaled to obtain a complete data set for compound **1**. Diffraction data were indexed and merged using XDS Phases.[7] Compound **1** was solved using direct methods in SHELXD, and initial maps were refined in ShelXle with SHELXL,[8–10] where all non-hydrogen atoms were refined anisotropically, and hydrogen atoms were placed using the riding model.
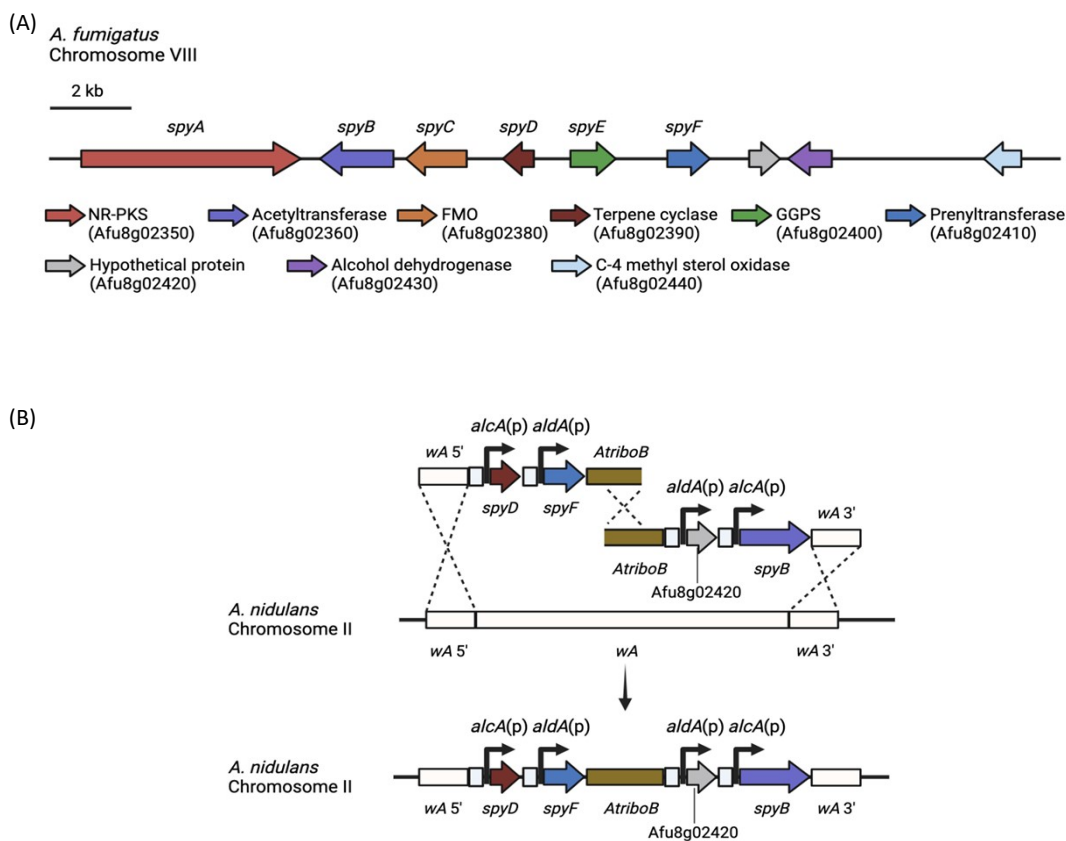
**Figure S1.** (A) The *spy* BGC from *A. fumigatus.* (B) Refactoring the *spyB, D* and *F* genes at the *wA* locus in *A. nidulans.* Afu8g02420 was also refactored at the *wA* locus, but it proved not to be a component of the *spy* BGC.
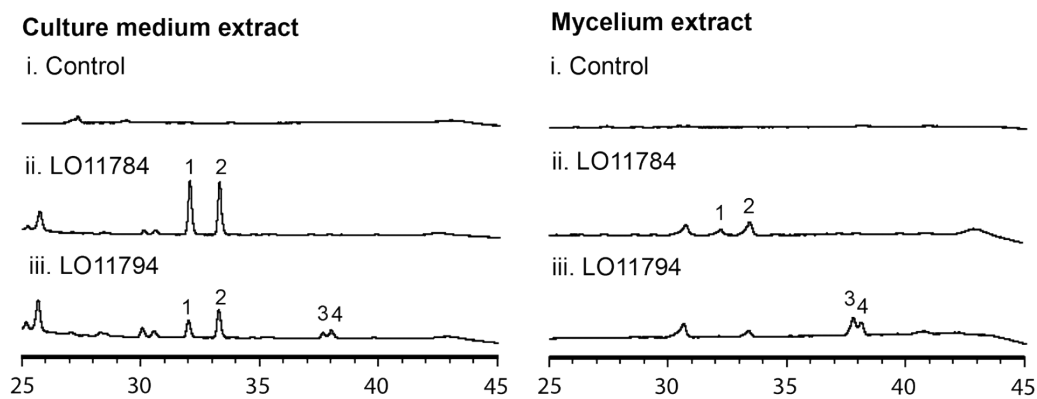
**Figure S2.** HPLC profiles of culture medium and mycelium extracts from *A. nidulans* transformants. Afu8g02360 (*spyB*) in LO11784 was refactored by fusing *alcA*(p) at start site 1; Afu8g02360 (*spyB*) in LO11794 was refactored by fusing *alcA*(p) at start site 2. The control strain is LO11098, which lacked the *A. fumigatus* BGC genes.
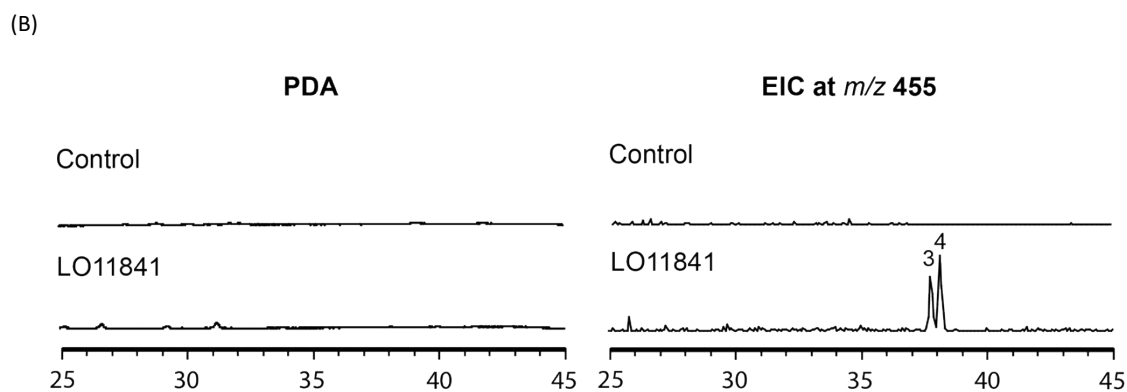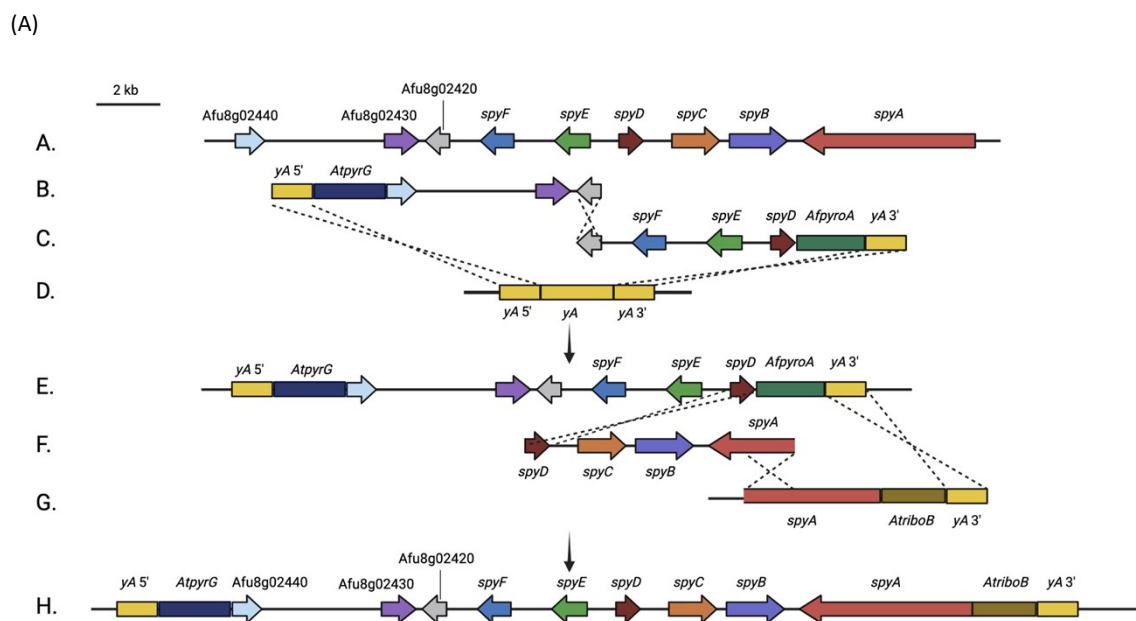
**Figure S3.** (A) Reconstructing the *spy* BGC from *A. fumigatus* into *A. nidulans.* The entire sequence transferred into *A. nidulans* was 25,832 bp. (B) HPLC profiles of extracts from the parental strain and a strain carrying the reconstructed BGC overexpressing *laeA* and *llmG* (LO11841) as detected by PDA and mass spectrometry in negative mode of extracted ion chromatogram (EIC) and *m/z* = 455.
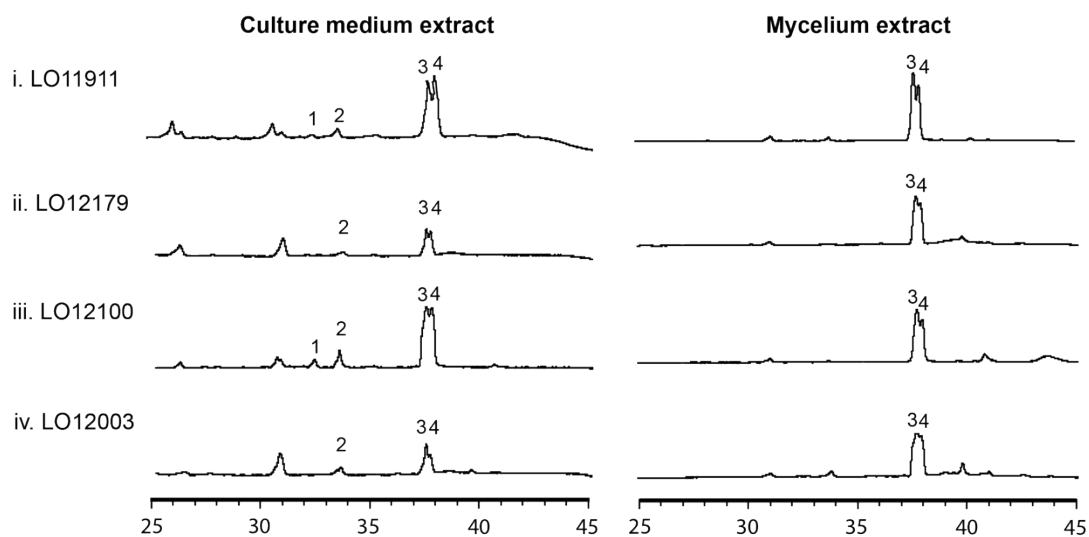
**Figure S4.** HPLC profiles of culture medium and mycelium extracts from *A. nidulans* transformants. LO11911 carried the entire *spy* BGC and three additional adjacent genes (Afu8g02420, Afu8g02430, and Afu8g02440); LO12179, LO12100, and LO12003 were Afu8g02420, Afu8g02430, and Afu8g02440 deletants from LO11911, respectively.
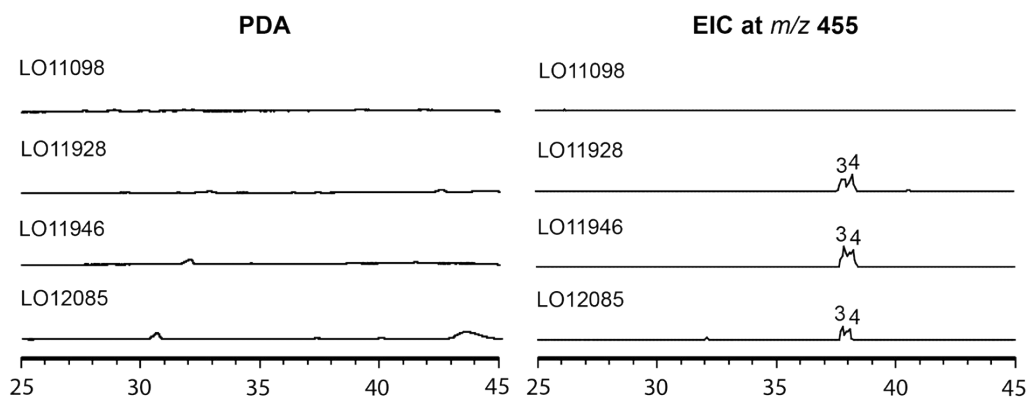
**Figure S5.** HPLC profiles of extracts from a control strain (LO11098), *spyA* deletant strain (LO11928), *spyA* /AN12440 double deletant strain (LO11946), and *spyA*/AN6448 double deletant strain (LO12085) as detected by PDA and mass spectrometry in negative mode of extracted ion chromatogram (EIC) and *m/z* = 455.

**Table I.1.** Strains used in this study. Some of the types of constructs are novel and there is no standard nomenclature for them. We have chosen to use brackets to indicate that multiple genes have been inserted or refactored at a particular locus. For example, [*wA*Δ:: *alcA*(p)*spyD, aldA*(p)*spyF, AtRiboB, aldA*(p)Afu8g02420, *alcA*(p)*spyB* start site 1], indicates that the *wA* gene has been replaced with *spyD* under control of the *alcA* promoter, *spyF* under control of the *aldA* promoter, the *Aspergillus terreus riboB* gene, Afu8g02420 under control of the *aldA* promoter, and *spyB* under control of the *alcA* promoter driving expression from start site 1.

| Strain | Description | Genotype |
|---|---|---|
| LO11098 | Multi-marker dereplication strain | *pyrG89, pyroA4, riboB2, pabaA*Δ, *biA*Δ, *lysB*Δ, *choA*Δ, *nkuA*Δ*::argB*, sterigmatocystin cluster (AN7804-AN7825)Δ, emericellamide cluster (AN2545-AN2549)Δ, asperfuranone cluster (AN1039-AN1029)Δ, monodictyphenone cluster (AN10023-AN10021)Δ, terrequinone cluster (AN8512-AN8520)Δ, austinol cluster part 1 (AN8379-AN8384)Δ, austinol cluster part 2 (AN9246-AN9259)Δ, F9775 cluster (AN7906-AN7915)Δ, asperthecin cluster (AN6000-AN6002)Δ. |
| | | |
| LO11784 - 11793 | Refactored *A. fumigatus* sartorypyrone cluster, with start site 1 for Afu8g02360 (*spyB*), in LO11098 | [*wA*Δ:: *alcA*(p)*spyD, aldA*(p)*spyF, AtRiboB, aldA*(p)Afu8g02420, *alcA*(p)*spyB* start site 1], [*yA*Δ*:: AfpyrG, alcA*(p)*spyA, aldA*(p)Afu8g02440, *alcA*(p)*spyE, AtpabaA, alcA*(p)*spyC, aldA*(p)Afu8g02430], *pyrG89, pyroA4, riboB2, pabaA*Δ, *biA*Δ, *lysB*Δ, *choA*Δ, *nkuA*Δ*::argB*, sterigmatocystin cluster (AN7804-AN7825)Δ, emericellamide cluster (AN2545-AN2549)Δ, asperfuranone cluster (AN1039-AN1029)Δ, monodictyphenone cluster (AN10023-AN10021)Δ, terrequinone cluster (AN8512-AN8520)Δ, austinol cluster part 1 (AN8379-AN8384)Δ, austinol cluster part 2 (AN9246-AN9259)Δ, F9775 cluster (AN7906-AN7915)Δ, asperthecin cluster (AN6000-AN6002)Δ. |
| | | |
| LO11794 - 11803 | Refactored *A. fumigatus* sartorypyrone cluster, with start site 2 for Afu8g02360 (*spyB*), in LO11098 | [*wA*Δ:: *alcA*(p)*spyD, aldA*(p)*spyF, AtRiboB, aldA*(p)Afu8g02420, *alcA*(p)*spyB* start site 2], [*yA*Δ*:: AfpyrG, alcA*(p)*spyA, aldA*(p)Afu8g02440, *alcA*(p)*spyE, AtpabaA, alcA*(p)*spyC, aldA*(p)Afu8g02430], *pyrG89, pyroA4, riboB2, pabaA*Δ, *biA*Δ, *lysB*Δ, *choA*Δ, *nkuA*Δ*::argB*, sterigmatocystin cluster (AN7804-AN7825)Δ, emericellamide cluster (AN2545-AN2549)Δ, asperfuranone cluster (AN1039-AN1029)Δ, monodictyphenone cluster (AN10023-AN10021)Δ, terrequinone cluster (AN8512-AN8520)Δ, austinol cluster part 1 (AN8379-AN8384)Δ, austinol cluster part 2 (AN9246- |

| | | AN9259)Δ, F9775 cluster (AN7906-AN7915)Δ, asperthecin cluster (AN6000-AN6002)Δ. |
|---|---|---|
| | | |
| LO11839 | *agsB*Δ::*ptrA* in LO11794 | *agsB*Δ::*ptrA* (pyrithiamine resistance gene from *Aspergillus oryzae*), [*wA*Δ:: *alcA*(p)*spyD*, *aldA*(p)*spyF*, *AtRiboB*, *aldA*(p)Afu8g02420, *alcA*(p)*spyB* start site 2], [*yA*Δ:: *AfpyrG*, *alcA*(p)*spyA*, *aldA*(p)Afu8g02440, *alcA(*p)*spyE*, *AtpabaA*, *alcA*(p)*spyC*, *aldA*(p)Afu8g02430], *pyrG89*, *pyroA4*, *riboB2*, *pabaA*Δ, *biA*Δ, *lysB*Δ, *choA*Δ, *nkuA*Δ::*argB*, sterigmatocystin cluster (AN7804-AN7825)Δ, emericellamide cluster (AN2545-AN2549)Δ, asperfuranone cluster (AN1039-AN1029)Δ, monodictyphenone cluster (AN10023-AN10021)Δ, terrequinone cluster (AN8512-AN8520)Δ, austinol cluster part 1 (AN8379-AN8384)Δ, austinol cluster part 2 (AN9246-AN9259)Δ, F9775 cluster (AN7906-AN7915)Δ, asperthecin cluster (AN6000-AN6002)Δ. |
| | | |
| LO11841 | Entire *A. fumigatus* sartorypyrone cluster, from 5' TTGGCTGTTGCCGC TGCG……to......GTG GCAACGCCCTGCCT T 3', replacing the *yA* coding sequence, *alcA*(p)*laeA*, *alcA*(p)*llmG* in LO11098 | *Atpaba-alcA*(p)*laeA*, *AtlysB-alcA*(p)*llmG*, [*yA*Δ::*AfpyrG*, Afu8g02440, Afu8g02430, Afu8g02420, *spyF*, *spyE*, *spyD*, *spyC*, *spyB*, *spyA*], *pyrG89*, *pyroA4*, *riboB2*, *pabaA*Δ, *biA*Δ, *lysB*Δ, *choA*Δ, *nkuA*Δ::*argB*, sterigmatocystin cluster (AN7804-AN7825)Δ, emericellamide cluster (AN2545-AN2549)Δ, asperfuranone cluster (AN1039-AN1029)Δ, monodictyphenone cluster (AN10023-AN10021)Δ, terrequinone cluster (AN8512-AN8520)Δ, austinol cluster part 1 (AN8379-AN8384)Δ, austinol cluster part 2 (AN9246-AN9259)Δ, F9775 cluster (AN7906-AN7915)Δ, asperthecin cluster (AN6000-AN6002)Δ. |
| | | |
| LO11911 | *AtbiA-gpdA*(p)*alcR* in LO11839 | *AtbiA-gpdA*(p)*alcR*, *agsB*Δ::*ptrA*, [*wA*Δ:: *alcA*(p)*spyD*, *aldA*(p)*spyF*, *AtRiboB*, *aldA*(p)Afu8g02420, *alcA*(p)*spyB* start site 2], [*yA*Δ:: *AfpyrG*, *alcA*(p)*spyA*, *aldA*(p)Afu8g02440, *alcA*(p)*spyE*, *AtpabaA*, *alcA*(p)*spyC*, *aldA*(p)Afu8g02430], *pyrG89*, *pyroA4*, *riboB2*, *pabaA*Δ, *biA*Δ, *lysB*Δ, *choA*Δ, *nkuA*Δ::*argB*, sterigmatocystin cluster (AN7804-AN7825)Δ, emericellamide cluster (AN2545-AN2549)Δ, asperfuranone cluster (AN1039-AN1029)Δ, monodictyphenone cluster (AN10023-AN10021)Δ, terrequinone cluster (AN8512-AN8520)Δ, austinol cluster part 1 (AN8379-AN8384)Δ, austinol cluster part 2 (AN9246- |

| | | AN9259)Δ, F9775 cluster (AN7906-AN7915)Δ, asperthecin cluster (AN6000-AN6002)Δ. |
|---|---|---|
| | | |
| LO11928 | *AfpyrG-alcA*(p)*spyA*Δ::*AtbiA* in LO11839 | *agsB*Δ::*ptrA*, [*wA*Δ:: *alcA*(p)*spyD, aldA*(p)*spyF, AtRiboB, aldA*(p)Afu8g02420, *alcA*(p)*spyB* start site 2], [*yA*Δ:: *AtbiA, aldA*(p)Afu8g02440, *alcA*(p)*spyE, AtpabaA, alcA*(p)*spyC, aldA*(p)Afu8g02430], *pyrG89, pyroA4, riboB2, pabaA*Δ, *biA*Δ, *lysB*Δ, *choA*Δ, *nkuA*Δ::*argB*, sterigmatocystin cluster (AN7804-AN7825)Δ, emericellamide cluster (AN2545-AN2549)Δ, asperfuranone cluster (AN1039-AN1029)Δ, monodictyphenone cluster (AN10023-AN10021)Δ, terrequinone cluster (AN8512-AN8520)Δ, austinol cluster part 1 (AN8379-AN8384)Δ, austinol cluster part 2 (AN9246-AN9259)Δ, F9775 cluster (AN7906-AN7915)Δ, asperthecin cluster (AN6000-AN6002)Δ. |
| | | |
| LO11945 | *AtbiA-gpdA*(p)*alcR* in LO11098 | *AtbiA-gpdA*(p)*alcR, pyrG89, pyroA4, riboB2, pabaA*Δ, *biA*Δ, *lysB*Δ, *choA*Δ, *nkuA*Δ::*argB*, sterigmatocystin cluster (AN7804-AN7825)Δ, emericellamide cluster (AN2545-AN2549)Δ, asperfuranone cluster (AN1039-AN1029)Δ, monodictyphenone cluster (AN10023-AN10021)Δ, terrequinone cluster (AN8512-AN8520)Δ, austinol cluster part 1 (AN8379-AN8384)Δ, austinol cluster part 2 (AN9246-AN9259)Δ, F9775 cluster (AN7906-AN7915)Δ, asperthecin cluster (AN6000-AN6002)Δ. |
| | | |
| LO11946 | AN12440Δ::*AtpyrG* in LO11928 | AN12440Δ::*AtpyrG, agsB*Δ::*ptrA*, [*wA*Δ:: *alcA*(p)*spyD, aldA*(p)*spyF, AtRiboB, aldA*(p)Afu8g02420, *alcA*(p)*spyB* start site 2], [*yA*Δ:: *AtbiA, aldA*(p)Afu8g02440, *alcA*(p)*spyE, AtpabaA, alcA*(p)*spyC, aldA*(p)Afu8g02430], *pyrG89, pyroA4, riboB2, pabaA*Δ, *biA*Δ, *lysB*Δ, *choA*Δ, *nkuA*Δ::*argB*, sterigmatocystin cluster (AN7804-AN7825)Δ, emericellamide cluster (AN2545-AN2549)Δ, asperfuranone cluster (AN1039-AN1029)Δ, monodictyphenone cluster (AN10023-AN10021)Δ, terrequinone cluster (AN8512-AN8520)Δ, austinol cluster part 1 (AN8379-AN8384)Δ, austinol cluster part 2 (AN9246-AN9259)Δ, F9775 cluster (AN7906-AN7915)Δ, asperthecin cluster (AN6000-AN6002)Δ. |
| | | |

| LO12003 | *aldA*(p)Afu8g02440Δ:: *AfpyroA* in LO11911 | *AtbiA-gpdA*(p)*alcR*, *agsB*Δ::*ptrA*, [*wA*Δ:: *alcA*(p)*spyD*, *aldA*(p)*spyF*, *AtRiboB*, *aldA*(p)Afu8g02420, *alcA*(p)*spyB* start site 2], [*yA*Δ:: *AfpyrG*, *alcA*(p)*spyA*, *AfpyroA*, *alcA*(p)*spyE*, *AtpabaA*, *alcA*(p)*spyC*, *aldA*(p)Afu8g02430], *pyrG89*, *pyroA4*, *riboB2*, *pabaA*Δ, *biA*Δ, *lysB*Δ, *choA*Δ, *nkuA*Δ::*argB*, sterigmatocystin cluster (AN7804-AN7825)Δ, emericellamide cluster (AN2545-AN2549)Δ, asperfuranone cluster (AN1039-AN1029)Δ, monodictyphenone cluster (AN10023-AN10021)Δ, terrequinone cluster (AN8512-AN8520)Δ, austinol cluster part 1 (AN8379-AN8384)Δ, austinol cluster part 2 (AN9246-AN9259)Δ, F9775 cluster (AN7906-AN7915)Δ, asperthecin cluster (AN6000-AN6002)Δ. |
| --- | --- | --- |
| | | |
| LO12085 | AN6448Δ::*AtpyrG* in LO11927 (sister transformant of LO11928) | AN6448Δ::*AtpyrG*, *agsB*Δ::*ptrA*, [*wA*Δ:: *alcA*(p)*spyD*, *aldA*(p)*spyF*, *AtRiboB*, *aldA*(p)Afu8g02420, *alcA*(p)*spyB* start site 2], [*yA*Δ:: *AtbiA*, *aldA*(p)Afu8g02440, *alcA*(p)*spyE*, *AtpabaA*, *alcA*(p)*spyC*, *aldA*(p)Afu8g02430], *pyrG89*, *pyroA4*, *riboB2*, *pabaA*Δ, *biA*Δ, *lysB*Δ, *choA*Δ, *nkuA*Δ::*argB*, sterigmatocystin cluster (AN7804-AN7825)Δ, emericellamide cluster (AN2545-AN2549)Δ, asperfuranone cluster (AN1039-AN1029)Δ, monodictyphenone cluster (AN10023-AN10021)Δ, terrequinone cluster (AN8512-AN8520)Δ, austinol cluster part 1 (AN8379-AN8384)Δ, austinol cluster part 2 (AN9246-AN9259)Δ, F9775 cluster (AN7906-AN7915)Δ, asperthecin cluster (AN6000-AN6002)Δ. |
| | | |
| LO12091 | *yA*Δ::*AtpyrG-alcA*(p) *spyA* in LO11945 | *yA*Δ::*AtpyrG-alcA*(p)*spyA*, *AtbiA-gpdA*(p)*alcR*, *pyrG89*, *pyroA4*, *riboB2*, *pabaA*Δ, *biA*Δ, *lysB*Δ, *choA*Δ, *nkuA*Δ::*argB*, sterigmatocystin cluster (AN7804-AN7825)Δ, emericellamide cluster (AN2545-AN2549)Δ, asperfuranone cluster (AN1039-AN1029)Δ, monodictyphenone cluster (AN10023-AN10021)Δ, terrequinone cluster (AN8512-AN8520)Δ, austinol cluster part 1 (AN8379-AN8384)Δ, austinol cluster part 2 (AN9246-AN9259)Δ, F9775 cluster (AN7906-AN7915)Δ, asperthecin cluster (AN6000-AN6002)Δ. |
| | | |

| | | |
|---|---|---|
| LO12096 | *alcA*(p)*spyB*Δ::*AtlysB* | *AtbiA-gpdA*(p)*alcR*, *agsB*Δ::*ptrA*, [*wA*Δ:: *alcA*(p)*spyD*, *aldA*(p)*spyF*, *AtRiboB*, *aldA*(p)Afu8g02420, *AtlysB*], [*yA*Δ:: *AfpyrG*, *alcA(p)spyA*, *aldA*(p)Afu8g02440, *alcA*(p)*spyE*, *AtpabaA*, *alcA*(p)*spyC*, *aldA*(p)Afu8g02430], *pyrG89*, *pyroA4*, *riboB2*, *pabaA*Δ, *biA*Δ, *lysB*Δ, *choA*Δ, *nkuA*Δ::*argB*, sterigmatocystin cluster (AN7804-AN7825)Δ, emericellamide cluster (AN2545-AN2549)Δ, asperfuranone cluster (AN1039-AN1029)Δ, monodictyphenone cluster (AN10023-AN10021)Δ, terrequinone cluster (AN8512-AN8520)Δ, austinol cluster part 1 (AN8379-AN8384)Δ, austinol cluster part 2 (AN9246-AN9259)Δ, F9775 cluster (AN7906-AN7915)Δ, asperthecin cluster (AN6000-AN6002)Δ. |
| | | |
| LO12100 | *aldA*(p)Afu8g02430Δ:: *AtlysB* in LO11911 | *AtbiA-gpdA*(p)*alcR*, *agsB*Δ::*ptrA*, [*wA*Δ:: *alcA*(p)*spyD*, *aldA*(p)*spyF*, *AtRiboB*, *aldA*(p)Afu8g02420, *alcA*(p)*spyB* start site 2], [*yA*Δ:: *AfpyrG*, *alcA*(p)*spyA*, *aldA*(p)Afu8g02440, *alcA*(p)*spyE*, *AtpabaA*, *alcA*(p)*spyC*, *AtlysB*], *pyrG89*, *pyroA4*, *riboB2*, *pabaA*Δ, *biA*Δ, *lysB*Δ, *choA*Δ, *nkuA*Δ::*argB*, sterigmatocystin cluster (AN7804-AN7825)Δ, emericellamide cluster (AN2545-AN2549)Δ, asperfuranone cluster (AN1039-AN1029)Δ, monodictyphenone cluster (AN10023-AN10021)Δ, terrequinone cluster (AN8512-AN8520)Δ, austinol cluster part 1 (AN8379-AN8384)Δ, austinol cluster part 2 (AN9246-AN9259)Δ, F9775 cluster (AN7906-AN7915)Δ, asperthecin cluster (AN6000-AN6002)Δ. |
| | | |
| LO12107 | *alcA*(p)*spyD*Δ::*AtlysB* in LO11911 | *AtbiA-gpdA*(p)*alcR*, *agsB*Δ::*ptrA*, [*wA*Δ:: *AtlysB*, *aldA*(p)*spyF*, *AtRiboB*, *aldA*(p)Afu8g02420, *alcA*(p)*spyB* start site 2], [*yA*Δ:: *AfpyrG*, *alcA*(p)*spyA*, *aldA*(p)Afu8g02440, *alcA*(p)*spyE*, *AtpabaA*, *alcA*(p)*spyC*, *aldA*(p)Afu8g02430], *pyrG89*, *pyroA4*, *riboB2*, *pabaA*Δ, *biA*Δ, *lysB*Δ, *choA*Δ, *nkuA*Δ::*argB*, sterigmatocystin cluster (AN7804-AN7825)Δ, emericellamide cluster (AN2545-AN2549)Δ, asperfuranone cluster (AN1039-AN1029)Δ, monodictyphenone cluster (AN10023-AN10021)Δ, terrequinone cluster (AN8512-AN8520)Δ, austinol cluster part 1 (AN8379-AN8384)Δ, austinol cluster part 2 (AN9246-AN9259)Δ, F9775 cluster (AN7906-AN7915)Δ, asperthecin cluster (AN6000-AN6002)Δ. |
| | | |

| | | |
|---|---|---|
| LO12117 | *alcA*(p)*spyE*, *AtpabaA*Δ::*AtlysB* in LO11911 | *AtbiA-gpdA*(p)*alcR*, *agsB*Δ::*ptrA*, [*wA*Δ:: *alcA*(p)*spyD*, *aldA*(p)*spyF*, *AtRiboB*, *aldA*(p)Afu8g02420, *alcA*(p)*spyB* start site 2], [*yA*Δ:: *AfpyrG*, *alcA*(p)*spyA*, *aldA*(p)Afu8g02440, *AtlysB*, *alcA*(p)*spyC*, *aldA*(p)Afu8g02430], *pyrG89*, *pyroA4*, *riboB2*, *pabaA*Δ, *biA*Δ, *lysB*Δ, *choA*Δ, *nkuA*Δ*::argB*, sterigmatocystin cluster (AN7804-AN7825)Δ, emericellamide cluster (AN2545-AN2549)Δ, asperfuranone cluster (AN1039-AN1029)Δ, monodictyphenone cluster (AN10023-AN10021)Δ, terrequinone cluster (AN8512-AN8520)Δ, austinol cluster part 1 (AN8379-AN8384)Δ, austinol cluster part 2 (AN9246-AN9259)Δ, F9775 cluster (AN7906-AN7915)Δ, asperthecin cluster (AN6000-AN6002)Δ. |
| | | |
| LO12126 | *AtpabaA-alcA*(p)*spyC*Δ::*AtlysB* in LO11911 | *AtbiA-gpdA*(p)*alcR*, *agsB*Δ::*ptrA*, [*wA*Δ:: *alcA*(p)*spyD*, *aldA*(p)*spyF*, *AtRiboB*, *aldA*(p)Afu8g02420, *alcA*(p)*spyB* start site 2], [*yA*Δ:: *AfpyrG*, *alcA*(p)*spyA*, *aldA*(p)Afu8g02440, *alcA*(p)*spyE*, *AtlysB*, *aldA*(p)Afu8g02430], *pyrG89*, *pyroA4*, *riboB2*, *pabaA*Δ, *biA*Δ, *lysB*Δ, *choA*Δ, *nkuA*Δ*::argB*, sterigmatocystin cluster (AN7804-AN7825)Δ, emericellamide cluster (AN2545-AN2549)Δ, asperfuranone cluster (AN1039-AN1029)Δ, monodictyphenone cluster (AN10023-AN10021)Δ, terrequinone cluster (AN8512-AN8520)Δ, austinol cluster part 1 (AN8379-AN8384)Δ, austinol cluster part 2 (AN9246-AN9259)Δ, F9775 cluster (AN7906-AN7915)Δ, asperthecin cluster (AN6000-AN6002)Δ. |
| | | |
| LO12178 | *aldA*(p)*spyF-AtriboB*Δ::*AfpyroA* in LO11911 | *AtbiA-gpdA*(p)*alcR*, *agsB*Δ::*ptrA*, [*wA*Δ:: *alcA*(p)*spyD*, *Afpyro*, *aldA*(p)Afu8g02420, *alcA*(p)*spyB* start site 2], [*yA*Δ::*AfpyrG*, *alcA*(p)*spyA*, *aldA*(p)Afu8g02440, *alcA*(p)*spyE*, *AtpabaA*, *alcA*(p)*spyC*, *aldA*(p)Afu8g02430], *pyrG89*, *pyroA4*, *riboB2*, *pabaA*Δ, *biA*Δ, *lysB*Δ, *choA*Δ, *nkuA*Δ*::argB*, sterigmatocystin cluster (AN7804-AN7825)Δ, emericellamide cluster (AN2545-AN2549)Δ, asperfuranone cluster (AN1039-AN1029)Δ, monodictyphenone cluster (AN10023-AN10021)Δ, terrequinone cluster (AN8512-AN8520)Δ, austinol cluster part 1 (AN8379-AN8384)Δ, austinol cluster part 2 (AN9246-AN9259)Δ, F9775 cluster (AN7906-AN7915)Δ, asperthecin cluster (AN6000-AN6002)Δ. |
| | | |

| LO12179 | *Atribo-aldA*(p)Afu8g02420Δ:: *AfpyroA* in LO11911 | *AtbiA-gpdA*(p)-*alcR*, *agsB*Δ*::ptrA*, [*wA*Δ*::* *alcA*(p)*spyD*, *aldA*(p)*spyF*, *AfpyroA*, *alcA*(p)*spyB* start site 2], [*yA*Δ*:: AfpyrG*, *alcA*(p)*spyA*, *aldA*(p)Afu8g02440, *alcA*(p)*spyE*, *AtpabaA*, *alcA*(p)*spyC*, *aldA*(p)Afu8g02430], *pyrG89*, *pyroA4*, *riboB2*, *pabaA*Δ, *biA*Δ, *lysB*Δ, *choA*Δ, *nkuA*Δ*::argB*, sterigmatocystin cluster (AN7804-AN7825)Δ, emericellamide cluster (AN2545-AN2549)Δ, asperfuranone cluster (AN1039-AN1029)Δ, monodictyphenone cluster (AN10023-AN10021)Δ, terrequinone cluster (AN8512-AN8520)Δ, austinol cluster part 1 (AN8379-AN8384)Δ, austinol cluster part 2 (AN9246-AN9259)Δ, F9775 cluster (AN7906-AN7915)Δ, asperthecin cluster (AN6000-AN6002)Δ. |
|---|---|---|

**Table I.2.** NMR data for sartorypyrone F (**1**)

$^1$H NMR spectrum (400 MHz), $^{13}$C NMR spectrum (100 MHz), acetone-$d_6$
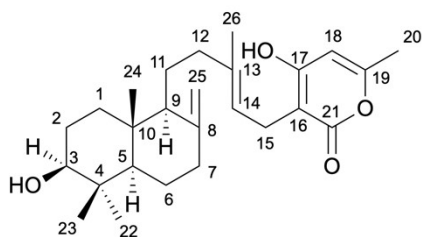


**Compound 1, Sartorypyrone F**
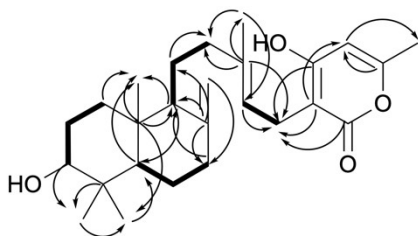


Key COSY (bold line) and HMBC

(arrow) correlations of **1**
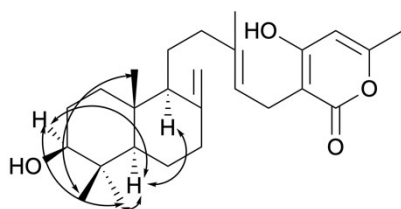


Key NOESY correlations of **1**

| position | $\delta_C$, type | $\delta_H$ mult (*J* in Hz) |
|---|---|---|
| 1 | 37.7, CH$_2$ | 1.13, m |
| | | 1.71, m |
| 2 | 28.8, CH$_2$ | 1.55-1.61, m |
| 3 | 78.3, CH | 3.18, dd (10.6, 5.4) |
| 4 | 39.9, qC | - |
| 5 | 55.4, CH | 1.08, dd (12.5, 2.7) |
| 6 | 24.9, CH$_2$ | 1.35, m |
| | | 1.71, m |
| 7 | 38.9, CH$_2$ | 1.90, m |
| | | 2.34, ddd (12.7, 4.2, 2.4) |
| 8 | 149.4, qC | - |
| 9 | 55.8, CH | 1.60, m |
| 10 | 39.8, qC | - |
| 11 | 22.4, CH$_2$ | 1.43, m |
| | | 1.58, m |
| 12 | 38.9, CH$_2$ | 1.81, m |
| | | 2.06, m |
| 13 | 135.4, qC | - |
| 14 | 123.7, CH | 5.20, dd (7.7, 6.9) |
| 15 | 22.9, CH$_2$ | 3.02, dd (13.9, 6.9) |
| | | 3.11, dd (13.9, 7.7) |
| 16 | 101.9, qC | - |
| 17 | 166.0, qC | - |
| 18 | 101.7, CH | 6.02, br d (0.9) |
| 19 | 159.9, qC | - |
| 20 | 19.8, CH$_3$ | 2.10, br s |
| 21 | 167.4, qC | - |
| 22 | 28.8, CH$_3$ | 0.98, s |
| 23 | 16.1, CH$_3$ | 0.75, s |
| 24 | 15.1, CH$_3$ | 0.67, s |
| 25 | 106.7, CH$_2$ | 4.52, br s |
| | | 4.80, br s |
| 26 | 16.4, CH$_3$ | 1.73, s |

HRMS-ESI (*m/z*) found 415.2846 [M+H]$^+$ (calculated for C$_{26}$H$_{39}$O$_4$, 415.2843).

Yellowish white amorphous; $[\alpha]_D^{27} = -9.87$ (c = 0.15, acetone).

**Table I.3.** Comparison of experimental and literature[11] NMR data for sartorypyrone D
(**2**) ^{1}H NMR spectrum (400 MHz), ^{13}C NMR spectrum (100 MHz), CDCl$_3$
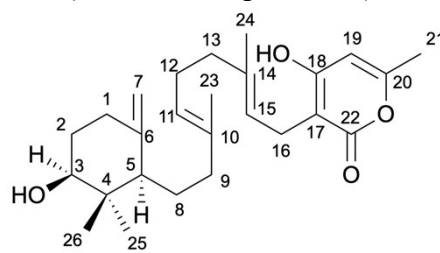


Compound 2, Sartorypyrone D

| position | Literature $\delta_H$ mult (*J* in Hz) | Observed $\delta_H$ mult (*J* in Hz) | Literature $\delta_C$, type | Observed $\delta_C$, type |
|---|---|---|---|---|
| 1 | 1.98, ddd (13.0, 12.0, 5.0) | 1.99, m | 32.4, CH$_2$ | 32.4, CH$_2$ |
| | 2.33, ddd (13.0, 5.0, 5.0) | 2.34, dt (13.2, 5.2) | | |
| 2 | 1.52, m | 1.52, m | 32.0, CH$_2$ | 32.0, CH$_2$ |
| | 1.86, dddd (13.0, 5.0, 5.0, 5.0) | 1.87, m | | |
| 3 | 3.43, dd (10.0, 5.0) | 3.43, dd (9.3, 4.2) | 77.3, CH | 77.2, CH |
| 4 | - | - | 40.4, qC | 40.4, qC |
| 5 | 1.63, br d (11.0) | 1.62, m | 51.2, CH | 51.2, CH |
| 6 | - | - | 147.3, qC | 147.3, qC |
| 7 | 4.60, s | 4.60, s | 108.5, CH$_2$ | 108.6, CH$_2$ |
| | 4.86, s | 4.86, s | | |
| 8 | 1.55, m | 1.57, m | 23.9, CH$_2$ | 23.9, CH$_2$ |
| | 1.60, m | 1.60, m | | |
| 9 | 1.75, m | 1.75, m | 38.6, CH$_2$ | 38.6, CH$_2$ |
| | 2.05, m | 2.05, m | | |
| 10 | - | - | 136.3, qC | 136.4, qC |
| 11 | 5.03, br t (7.0) | 5.02, m | 123.2, CH | 123.2, CH |
| 12 | 2.10, br t (7.0) | 2.11, m | 26.0, CH$_2$ | 26.0, CH$_2$ |
| 13 | 2.09, br t (7.0) | 2.09, m | 39.6, CH$_2$ | 39.6, CH$_2$ |
| 14 | - | - | 140.6, qC | 141.1, qC |
| 15 | 5.32, br t (7.0) | 5.33, br t (7.5) | 120.4, CH | 120.5, CH |
| 16 | 3.23, br d (7.0) | 3.24, d (7.5) | 22.9, CH$_2$ | 23.0, CH$_2$ |
| 17 | - | - | 100.7, qC | 100.6, qC |
| 18 | - | - | 165.8, qC | 165.7, qC |
| 19 | 5.82, s | 5.78, br d (1.0) | 100.7, CH | 100.6, CH |
| 20 | - | - | 160.3, qC | 160.3, qC |
| 21 | 2.18, s | 2.19, br s | 19.7, CH$_3$ | 19.7, CH$_3$ |
| 22 | - | - | 165.9, qC | 165.8, qC |
| 23 | 1.59, s | 1.59, s | 16.2, CH$_3$ | 16.2, CH$_3$ |
| 24 | 1.78, s | 1.78, s | 16.3, CH$_3$ | 16.4, CH$_3$ |
| 25 | 1.02, s | 1.02, s | 26.1, CH$_3$ | 26.1, CH$_3$ |
| 26 | 0.74, s | 0.74, s | 16.2, CH$_3$ | 16.2, CH$_3$ |

**Table I.4.** Comparison of experimental and literature NMR data for sartorypyrone A (**3**) $^1$H NMR spectrum (400 MHz), $^{13}$C NMR spectrum (100 MHz), CDCl$_3$
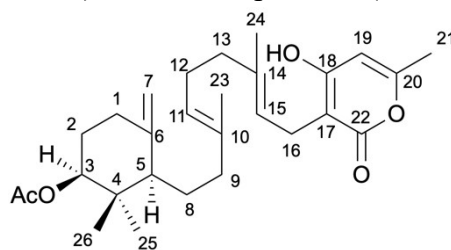


Compound 3, Sartorypyrone A

| position | Literature $\delta_H$ mult (*J* in Hz) | Observed $\delta_H$ mult (*J* in Hz) | Literature $\delta_C$, type | Observed $\delta_C$, type |
|---|---|---|---|---|
| 1 | 2.03, m | 2.03, m | 31.7, CH$_2$ | 31.8, CH$_2$ |
|   | 2.31, m | 2.31, m | | |
| 2 | 1.55, m | 1.56, m | 28.6, CH$_2$ | 28.6, CH$_2$ |
|   | 1.85, m | 1.83, m | | |
| 3 | 4.66, dd (8.9, 4.1) | 4.66, dd (9.0, 4.2) | 78.9, CH | 78.9, CH |
| 4 | - | - | 39.1, qC | 39.1, qC |
| 5 | 1.72, dd (9.1, 3.1) | 1.72, dd (9.9, 3.2) | 51.0, CH | 51.0, CH |
| 6 | - | - | 146.6, qC | 146.5, qC |
| 7 | 4.62, br s | 4.62, br s | 109.2, CH$_2$ | 109.1, CH$_2$ |
|   | 4.88, br s | 4.88, br s | | |
| 8 | 1.59, m | 1.58, m | 23.6, CH$_2$ | 23.5, CH$_2$ |
| 9 | 1.80, m | 1.78, m | 38.2, CH$_2$ | 38.2, CH$_2$ |
| 10 | - | - | 135.4, qC | 135.7, qC |
| 11 | 5.05, dd (5.6, 6.5) | 5.04, m | 124.1, CH | 123.8, CH |
| 12 | 2.08, m | 2.08, m | 26.3, CH$_2$ | 26.1, CH$_2$ |
| 13 | 2.04, m | 2.04, m | 39.7, CH$_2$ | 39.6, CH$_2$ |
| 14 | - | - | 138.2, qC | 139.4, qC |
| 15 | 5.29, ddd (7.2, 7.2, 1.0) | 5.32, tq (7.4, 1.3) | 120.5, CH | 120.4, CH |
| 16 | 3.20, d (7.2) | 3.22, d (7.4) | 22.4, CH$_2$ | 22.6, CH$_2$ |
| 17 | - | - | 101.7, qC | 101.2, qC |
| 18 | - | - | 166.1, qC | 165.7, qC |
| 19 | 6.00, d (0.7) | 5.92, br d (1.0) | 101.1, CH | 100.8, CH |
| 20 | - | - | 159.9, qC | 160.0, qC |
| 21 | 2.19, s | 2.19, br s | 19.6, CH$_3$ | 19.6, CH$_3$ |
| 22 | - | - | 166.8, qC | 166.2, qC |
| 23 | 1.58, s | 1.58, br s | 15.9, CH$_3$ | 15.9, CH$_3$ |
| 24 | 1.77, s | 1.77, br s | 16.3, CH$_3$ | 16.3, CH$_3$ |
| 25 | 0.94, s | 0.94, s | 26.0, CH$_3$ | 25.9, CH$_3$ |
| 26 | 0.79, s | 0.79, s | 17.5, CH$_3$ | 17.4, CH$_3$ |
| OAc | - | | 171.1, qC | 171.0, qC |
|   | 2.07, s | 2.07, s | 21.3, CH$_3$ | 21.3, CH$_3$ |

**Table I.5.** NMR data for sartorypyrone G (**4**)

$^1$H NMR spectrum (400 MHz), $^{13}$C NMR spectrum (100 MHz), acetone-$d_6$
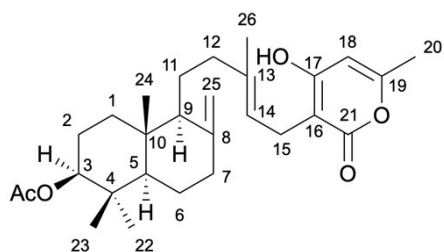


**Compound 4, Sartorypyrone G**
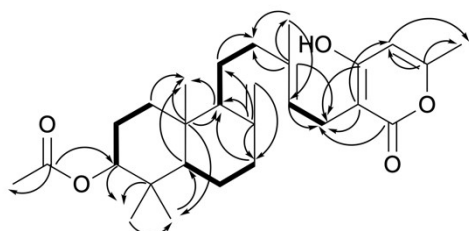


Key COSY (bold line) and HMBC (arrow)

correlations of **4**
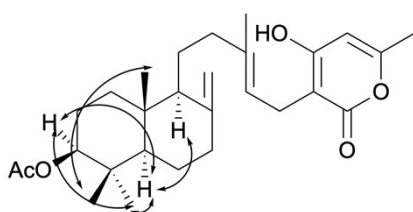


Key NOESY correlations of **4**

| position | $\delta_C$, type | $\delta_H$ mult (*J* in Hz) |
|---|---|---|
| 1 | 37.3, CH$_2$ | 1.17, m |
| | | 1.74, m |
| 2 | 25.1, CH$_2$ | 1.55-1.65, m |
| 3 | 81.0, CH | 4.47, dd (10.9, 5.5) |
| 4 | 38.7, qC | - |
| 5 | 55.3, CH | 1.18, m |
| 6 | 24.6, CH$_2$ | 1.36, m |
| | | 1.75, m |
| 7 | 38.7, CH$_2$ | 1.90, m |
| | | 2.35, ddd (12.8, 4.2, 2.5) |
| 8 | 148.9, qC | - |
| 9 | 55.3, CH | 1.65, m |
| 10 | 39.7, qC | - |
| 11 | 22.3, CH$_2$ | 1.45, m |
| | | 1.58, m |
| 12 | 38.7, CH$_2$ | 1.81, m |
| | | 2.05, m |
| 13 | 136.0, qC | - |
| 14 | 123.1, CH | 5.18, ddq (7.7, 6.8, 1.5) |
| 15 | 22.7, CH$_2$ | 3.02, dd (14.0, 6.8) |
| | | 3.12, dd (14.0, 7.7) |
| 16 | 102.6, qC | - |
| 17 | 165.1, qC | - |
| 18 | 100.7, CH | 6.04, br d (0.9) |
| 19 | 160.8, qC | - |
| 20 | 19.7, CH$_3$ | 2.13, br s |
| 21 | 165.6, qC | - |
| 22 | 28.6, CH$_3$ | 0.87, s |
| 23 | 16.9, CH$_3$ | 0.84, s |
| 24 | 15.1, CH$_3$ | 0.71, s |
| 25 | 107.1, CH$_2$ | 4.54, br s |
| | | 4.82, br s |
| 26 | 16.3, CH$_3$ | 1.73, s |
| OAc | 170.8, qC | - |
| | 21.1, CH$_3$ | 2.00, s |

HRMS-ESI (*m/z*) found 457.2950 [M+H]$^+$ (calculated for C$_{28}$H$_{41}$O$_5$, 457.2949).

Yellowish white plate, mp 175-177 °C; $[\alpha]_D^{27} = -12.34$ (c = 1.05, acetone).

**Table I.6.** NMR data for geranylgeranyl-triacetate lactone carboxylic acid (**5**)
$^{1}$H NMR spectrum (400 MHz), $^{13}$C NMR spectrum (100 MHz), acetone-$d_6$



**Compound 5**
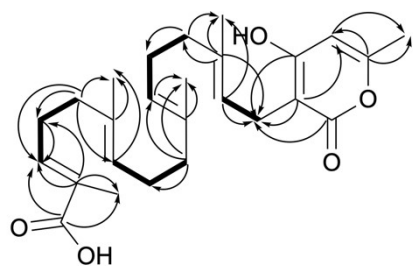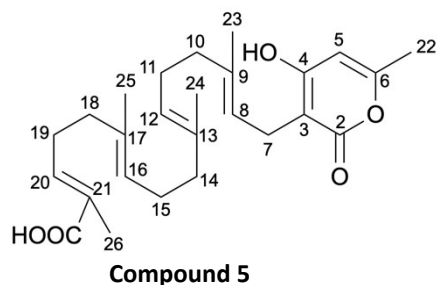


Key COSY (bold line) and HMBC (arrow)

correlations of **5**
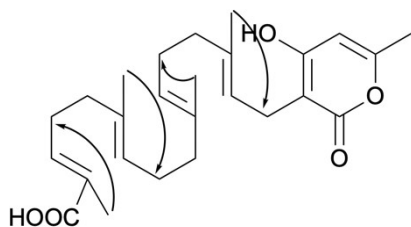


Key NOESY correlations of **5**

| position | $\delta_C$, type | $\delta_H$ mult (*J* in Hz) |
|---|---|---|
| 1 | | |
| 2 | 165.6, qC | - |
| 3 | 102.6, qC | - |
| 4 | 165.0, qC | - |
| 5 | 100.7, CH | 6.01, br s |
| 6 | 160.8, qC | - |
| 7 | 22.8, CH$_2$ | 3.08, d (7.2) |
| 8 | 122.6, CH | 5.23, m |
| 9 | 135.8, qC | - |
| 10 | 40.5*, CH$_2$ | 1.97, m |
| 11 | 27.3, CH$_2$ | 2.07, m |
| 12 | 125.2, CH | 5.12, tq (7.1, 1.4) |
| 13 | 135.4, qC | - |
| 14 | 40.4*, CH$_2$ | 1.97, m |
| 15 | 27.3, CH$_2$ | 2.07, m |
| 16 | 125.9, CH | 5.17, m |
| 17 | 134.7, qC | - |
| 18 | 39.0, CH$_2$ | 2.11, m |
| 19 | 27.9, CH$_2$ | 2.31, m |
| 20 | 142.8, CH | 6.77, tq (7.3, 1.4) |
| 21 | 128.4, qC | - |
| 22 | 19.7, CH$_3$ | 2.14, br s |
| 23 | 16.3, CH$_3$ | 1.73, br s |
| 24 | 16.1, CH$_3$ | 1.58, br s |
| 25 | 16.1, CH$_3$ | 1.63, br s |
| 26 | 12.5, CH$_3$ | 1.80, br s |
| COOH | 169.2, qC | - |

*The values are interchangeable

HRMS-ESI (*m/z*) found 429.2629 [M+H]$^{+}$ (calculated for C$_{26}$H$_{37}$O$_5$, 429.2636).
White amorphous powder.

**Table I.7.** Comparison of experimental and literature[13] NMR data for geranylgeranyl-triacetate lactone (**6**)

$^1$H NMR spectrum (400 MHz), $^{13}$C NMR spectrum (100 MHz), acetone-$d_6$
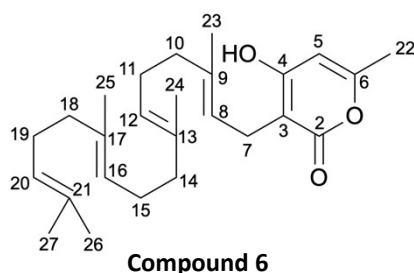


**Compound 6**

| position | Literature $\delta_H$ mult (*J* in Hz) | Observed $\delta_H$ mult (*J* in Hz) | Literature $\delta_C$, type | Observed $\delta_C$, type |
|---|---|---|---|---|
| 1 | | | | |
| 2 | - | - | 165.7, qC | 165.9, qC |
| 3 | - | - | 102.4, qC | 102.2, qC |
| 4 | - | - | 165.4, qC | 165.7, qC |
| 5 | 5.98, s | 6.01, br d (1.0) | 100.8, CH | 101.0, CH |
| 6 | - | - | 160.7, qC | 160.4, qC |
| 7 | 3.09, d (7.0) | 3.08, d (7.2) | 22.7, CH$_2$ | 22.8, CH$_2$ |
| 8 | 5.23, t (7.0) | 5.24, tq (7.2, 1.3) | 122.6, CH | 122.9, CH |
| 9 | - | - | 135.3, qC | 135.3, qC |
| 10 | 1.93, m | 1.97, m | 40.4, CH$_2$ | 40.4, CH$_2$ |
| 11 | 2.05, m | 2.05, m | 27.2, CH$_2$ | 27.3, CH$_2$ |
| 12 | 5.12, m | 5.11, m | 125.1, CH | 125.2, CH |
| 13 | - | - | 135.6, qC | 135.4, qC |
| 14 | 2.04, m | 2.05, m | 40.4, CH$_2$ | 40.4, CH$_2$ |
| 15 | 1.93, m | 1.97, m | 27.2, CH$_2$ | 27.3, CH$_2$ |
| 16 | 5.12, m | 5.11, m | 125.1, CH | 125.1, CH |
| 17 | - | - | 135.4, qC | 135.4, qC |
| 18 | 1.93, m | 1.97, m | 40.5, CH$_2$ | 40.5, CH$_2$ |
|  | 2.04, m | 2.05, m | | |
| 19 | 1.93, m | 1.97, m | 27.4, CH$_2$ | 27.4, CH$_2$ |
|  | 2.04, m | 2.05, m | | |
| 20 | 5.12, m | 5.11, m | 125.0, CH | 125.1, CH |
| 21 | - | - | 131.5, qC | 131.6, qC |
| 22 | 2.14, s | 2.12, br s | 19.6, CH$_3$ | 19.6, CH$_3$ |
| 23 | 1.59, s | 1.59, s | 16.1, CH$_3$ | 16.1, CH$_3$ |
| 24 | 1.59, s | 1.59, s | 16.1, CH$_3$ | 16.1, CH$_3$ |
| 25 | 1.74, s | 1.74, s | 16.3, CH$_3$ | 16.3, CH$_3$ |
| 26 | 1.59, s | 1.59, s | 17.7, CH$_3$ | 17.7, CH$_3$ |
| 27 | 1.65, s | 1.65, s | 25.8, CH$_3$ | 25.8, CH$_3$ |

**Table I.8.** Comparison of experimental and literature[14] NMR data for sartorypyrone E (**7**) ^{1}H NMR spectrum (400 MHz), ^{13}C NMR spectrum (100 MHz), CD$_3$OD
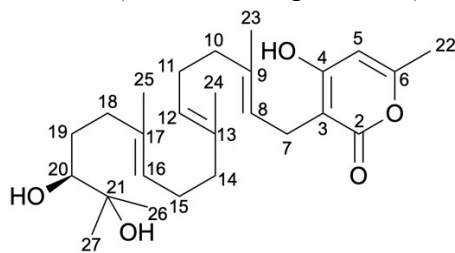


**Compound 7, Sartorypyrone E**

| position | Literature $\delta_H$ mult (*J* in Hz) | Observed $\delta_H$ mult (*J* in Hz) | Literature $\delta_C$, type | Observed $\delta_C$, type |
|---|---|---|---|---|
| 1 | | | | |
| 2 | - | - | 168.8, qC | 168.8, qC |
| 3 | - | - | 103.2, qC | 103.3, qC |
| 4 | - | - | 168.2, qC | 167.8, qC |
| 5 | 5.97, s | 5.97, br d (1.0) | 102.0, CH | 101.8, CH |
| 6 | - | - | 161.8, qC | 161.8, qC |
| 7 | 3.06, d (7.0) | 3.06, d (7.2) | 22.9, CH$_2$ | 22.9, CH$_2$ |
| 8 | 5.16, dt (7.5, 1.5) | 5.15, tq (7.2, 1.3) | 122.9, CH | 122.8, CH |
| 9 | - | - | 136.4, qC | 136.5, qC |
| 10 | 1.95, m | 1.95, m | 41.0, CH$_2$ | 41.0, CH$_2$ |
| | 2.03, m | 2.04, m | | |
| 11 | 1.98, m | 1.98, m | 27.9, CH$_2$ | 27.9, CH$_2$ |
| | 2.07, m | 2.07, m | | |
| 12 | 5.08, dt (7.0, 1.0) | 5.07, tq (7.1, 1.3) | 125.5, CH | 125.5, CH |
| 13 | - | - | 136.0, qC | 136.0, qC |
| 14 | 1.95, m | 1.95, m | 41.0, CH$_2$ | 41.0, CH$_2$ |
| 15 | 2.07, m | 2.07, m | 27.6, CH$_2$ | 27.6, CH$_2$ |
| 16 | 5.16, dt (7.5, 1.5) | 5.15, tq (7.2, 1.3) | 125.8, CH | 125.8, CH |
| 17 | - | - | 136.1, qC | 136.1, qC |
| 18 | 2.24, ddd (14.0, 9.5, 4.5) | 2.24, ddd (14.4, 10.3, 4.6) | 38.1, CH$_2$ | 38.1, CH$_2$ |
| | 2.00, m | 1.98, m | | |
| 19 | 1.70, m | 1.70, m | 31.0, CH$_2$ | 31.0, CH$_2$ |
| | 1.34, m | 1.34, m | | |
| 20 | 3.23, dd (10.5, 1.5) | 3.23, dd (10.6, 1.8) | 79.2, CH | 79.2, CH |
| 21 | - | - | 73.9, qC | 73.9, qC |
| 22 | 2.19, s | 2.18, br s | 19.8, CH$_3$ | 19.8, CH$_3$ |
| 23 | 1.73, s | 1.72, br s | 16.4, CH$_3$ | 16.4, CH$_3$ |
| 24 | 1.57, s | 1.57, br s | 16.3, CH$_3$ | 16.3, CH$_3$ |
| 25 | 1.61, s | 1.60, br s | 16.3, CH$_3$ | 16.3, CH$_3$ |
| 26 | 1.12, s | 1.12, s | 25.1, CH$_3$ | 25.1, CH$_3$ |
| 27 | 1.15, s | 1.15, s | 25.8, CH$_3$ | 25.8, CH$_3$ |

**Table I.9.** NMR data for epoxygeranylgeranyl-triacetate lactone (**8**)

$^1$H NMR spectrum (400 MHz), $^{13}$C NMR spectrum (100 MHz), acetone-$d_6$
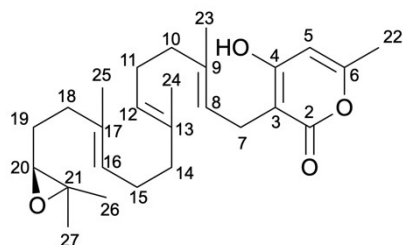


**Compound 8**
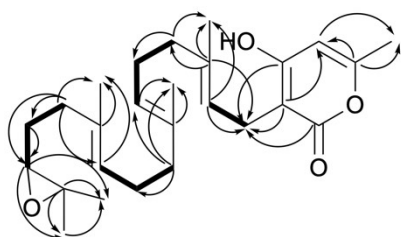


Key COSY (bold line) and HMBC (arrow)

correlations of **8**

| position | $\delta_C$, type | $\delta_H$ mult ($J$ in Hz) |
|---|---|---|
| 1 | | |
| 2 | 165.6, qC | - |
| 3 | 102.4, qC | - |
| 4 | 165.2, qC | - |
| 5 | 100.8, CH | 6.02, br s |
| 6 | 160.7, qC | - |
| 7 | 22.8, CH$_2$ | 3.08, d (7.2) |
| 8 | 122.7, CH | 5.23, tq (7.2, 1.3) |
| 9 | 135.6, qC | - |
| 10 | 40.5, CH$_2$ | 1.97, m |
| 11 | 27.3, CH$_2$ | 2.07, m |
| 12 | 125.1, CH | 5.12, m |
| 13 | 135.4, qC | - |
| 14 | 40.4, CH$_2$ | 1.97, m |
| 15 | 27.3, CH$_2$ | 2.07, m |
| 16 | 125.5, CH | 5.17, ddq (8.2, 6.9, 1.2) |
| 17 | 135.0, qC | - |
| 18 | 37.1, CH$_2$ | 2.09, m |
| 19 | 28.4, CH$_2$ | 1.58, m |
| 20 | 64.0, CH | 2.63, t (6.2) |
| 21 | 58.1, qC | - |
| 22 | 19.7, CH$_3$ | 2.13, br s |
| 23 | 16.3, CH$_3$ | 1.74, br s |
| 24 | 16.1, CH$_3$ | 1.59, br s |
| 25 | 16.1, CH$_3$ | 1.62, br s |
| 26 | 19.0, CH$_3$ | 1.21, s |
| 27 | 25.1, CH$_3$ | 1.22, s |

HRMS-ESI (*m/z*) found 415.2831 [M+H]$^+$ (calculated for C$_{26}$H$_{39}$O$_4$, 415.2843).

White amorphous powder; $[\alpha]_D^{20} = -5.94$ (c = 0.12, MeOH).

**Table I.10.** NMR data for dihydroxyfarnesyl-triacetate lactone (**9**)

$^{1}$H NMR spectrum (400 MHz), $^{13}$C NMR spectrum (100 MHz), CD$_3$OD
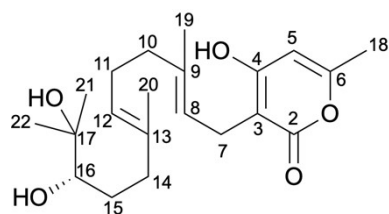


**Compound 9**
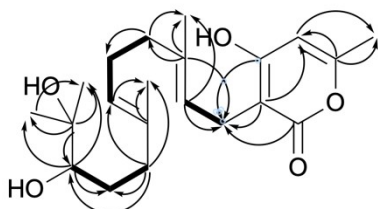


Key COSY (bold line) and HMBC (arrow)

correlations of **9**

| position | $\delta_C$, type | $\delta_H$ mult (*J* in Hz) |
|---|---|---|
| 1 | | |
| 2 | 168.8, qC | - |
| 3 | 103.2, qC | - |
| 4 | 167.9, qC | - |
| 5 | 101.9, CH | 5.99, br s |
| 6 | 161.8, qC | - |
| 7 | 22.9, CH$_2$ | 3.06, d (7.1) |
| 8 | 122.7, CH | 5.15, m |
| 9 | 136.6, qC | - |
| 10 | 41.0, CH$_2$ | 1.98, m |
| 11 | 27.7, CH$_2$ | 2.07, m |
| 12 | 125.7, CH | 5.15, m |
| 13 | 136.1, qC | - |
| 14 | 38.0, CH$_2$ | 1.98, m |
| | | 2.22, m |
| 15 | 30.9, CH$_2$ | 1.32, m |
| | | 1.69, m |
| 16 | 79.2, CH | 3.23, dd (10.5, 1.7) |
| 17 | 74.0, qC | - |
| 18 | 19.8, CH$_3$ | 2.19, br s |
| 19 | 16.5, CH$_3$ | 1.72, br s |
| 20 | 16.3, CH$_3$ | 1.59, br s |
| 21 | 25.1, CH$_3$ | 1.12, s |
| 22 | 25.8, CH$_3$ | 1.15, s |

HRMS-ESI (*m/z*) found 365.2324 [M+H]$^{+}$ (calculated for C$_{21}$H$_{33}$O$_5$, 365.2323).

Yellowish white amorphous powder; $[\alpha]_D^{20} =- 17.83$ (c = 0.12, MeOH).

**Table I.11.** NMR data for 17-methoxy-16-hydroxyfarnesyl-triacetate lactone (**10**)

$^1$H NMR spectrum (400 MHz), $^{13}$C NMR spectrum (100 MHz), acetone-$d_6$
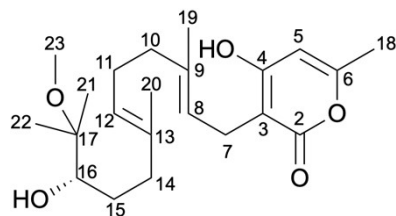


Compound 10
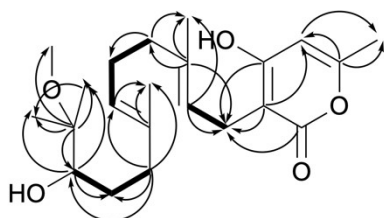


Key COSY (bold line) and HMBC (arrow)

correlations of **10**

| position | $\delta_C$, type | $\delta_H$ mult (*J* in Hz) |
|---|---|---|
| 1 | | |
| 2 | 166.2, qC | - |
| 3 | 102.1, qC | - |
| 4 | 165.8, qC | - |
| 5 | 101.2, CH | 6.02, br s |
| 6 | 160.4, qC | - |
| 7 | 22.8, CH$_2$ | 3.08, d (7.1) |
| 8 | 123.1, CH | 5.24, tq (6.4, 1.4) |
| 9 | 135.4, qC | - |
| 10 | 40.5, CH$_2$ | 1.98, m |
| 11 | 27.2, CH$_2$ | 2.07, m |
| 12 | 125.0, CH | 5.15, tq (6.8, 1.3) |
| 13 | 135.8, qC | - |
| 14 | 37.6, CH$_2$ | 1.98, m |
| | | 2.23, ddd (14.3, 9.7, 4.8) |
| 15 | 30.1, CH$_2$ | 1.31, m |
| | | 1.64, m |
| 16 | 76.4, CH | 3.35, dd (10.4, 1.8) |
| 17 | 77.9, qC | - |
| 18 | 19.7, CH$_3$ | 2.12, br s |
| 19 | 16.2, CH$_3$ | 1.73, br s |
| 20 | 16.3, CH$_3$ | 1.58, br s |
| 21 | 20.3, CH$_3$ | 1.07, s |
| 22 | 20.8, CH$_3$ | 1.10, s |
| 23 | 49.2, CH$_3$ | 3.16, s |

HRMS-ESI (*m/z*) found 379.2470 [M+H]$^+$ (calculated for C$_{22}$H$_{35}$O$_5$, 379.2479).

Yellow oil; $[\alpha]_D^{20} = -17.76$ (c = 0.07, MeOH).

**Table I.12.** NMR data for epoxyfarnesyl-triacetate lactone (**11**)

$^1$H NMR spectrum (400 MHz), $^{13}$C NMR spectrum (100 MHz), acetone-$d_6$
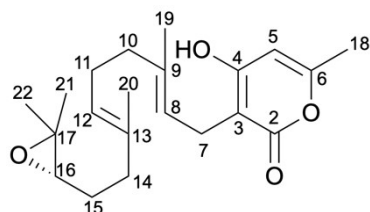


Compound 11
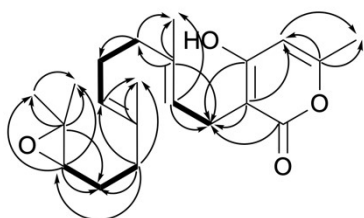


Key COSY (bold line) and HMBC (arrow)

correlations of **11**

| position | $\delta_C$, type | $\delta_H$ mult (*J* in Hz) |
|---|---|---|
| 1 | | |
| 2 | 165.6, qC | - |
| 3 | 102.5, qC | - |
| 4 | 165.2, qC | - |
| 5 | 100.7, CH | 6.02, br s |
| 6 | 160.8, qC | - |
| 7 | 22.8, CH$_2$ | 3.09, d (7.2) |
| 8 | 122.8, CH | 5.23, tq (7.2, 1.3) |
| 9 | 135.6, qC | - |
| 10 | 40.4, CH$_2$ | 1.98, m |
| 11 | 27.2, CH$_2$ | 2.08, m |
| 12 | 125.4, CH | 5.17, tq (7.1, 1.3) |
| 13 | 135.0, qC | - |
| 14 | 37.1, CH$_2$ | 2.08, m |
| 15 | 28.3, CH$_2$ | 1.57, m |
| 16 | 64.1, CH | 2.63, t (6.3) |
| 17 | 58.1, qC | - |
| 18 | 19.7, CH$_3$ | 2.15, br s |
| 19 | 16.3, CH$_3$ | 1.74, br s |
| 20 | 16.1, CH$_3$ | 1.61, br s |
| 21 | 19.0, CH$_3$ | 1.21, s |
| 22 | 25.1, CH$_3$ | 1.23, s |

HRMS-ESI (*m/z*) found 347.2210 [M+H]$^+$ (calculated for C$_{21}$H$_{31}$O$_4$, 347.2217).

White amorphous powder; $[\alpha]_D^{20} = -7.96$ (c = 0.09, MeOH).

**Table I.13.** Tabulated MicroED data statistics for sartorypyrone F (**1**)

| | |
|---|---|
| Stoichiometric Formula | $C_{26}H_{38}O_4$ |
| **Data Collection** | |
| Temperature (K) | 100(2) |
| Space group | C2 |
| Cell dimensions | |
| *a*, *b*, *c* (Å) | 50.1(2), 6.67(2), 12.670(10) |
| *α*, *β*, *γ* (°) | 90, 98.52(6), 90 |
| Resolution (Å) | 1.00 |
| Observed reflections | 13017 |
| Unique reflections | 2065 |
| $R_{obs}$ (%) | 13.7 |
| $R_{meas}$ (%) | 14.8 |
| I/σI | 8.22 |
| $CC_{1/2}$ (%) | 99.1 |
| Completeness (%) | 84.1 |
| **Refinement** | |
| $R_1$ | 0.1502 |
| $wR_2$ | 0.3363 |
| GooF | 1.285 |
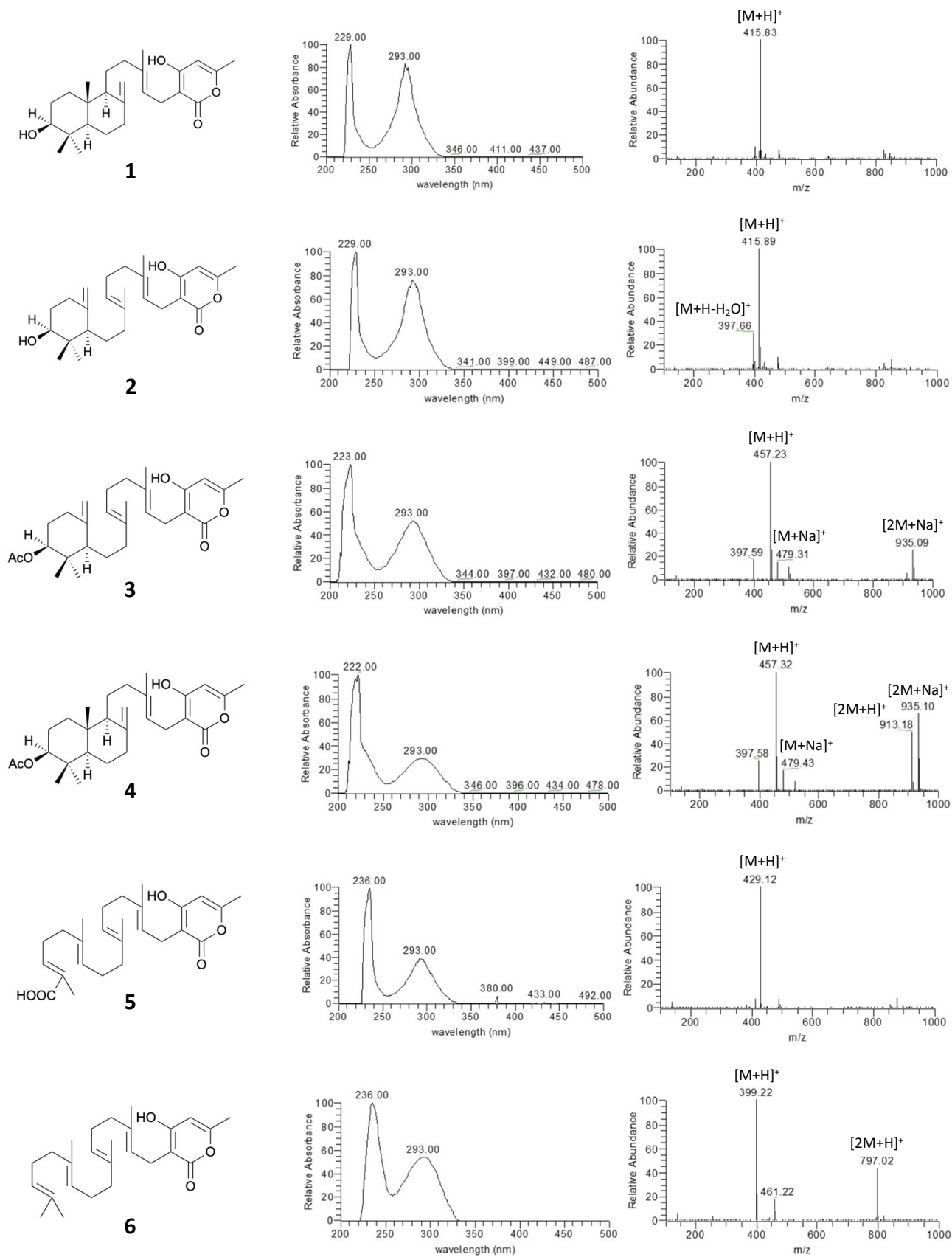
**Figure I.6.** UV-Vis and ESIMS spectra of compounds **1-12**
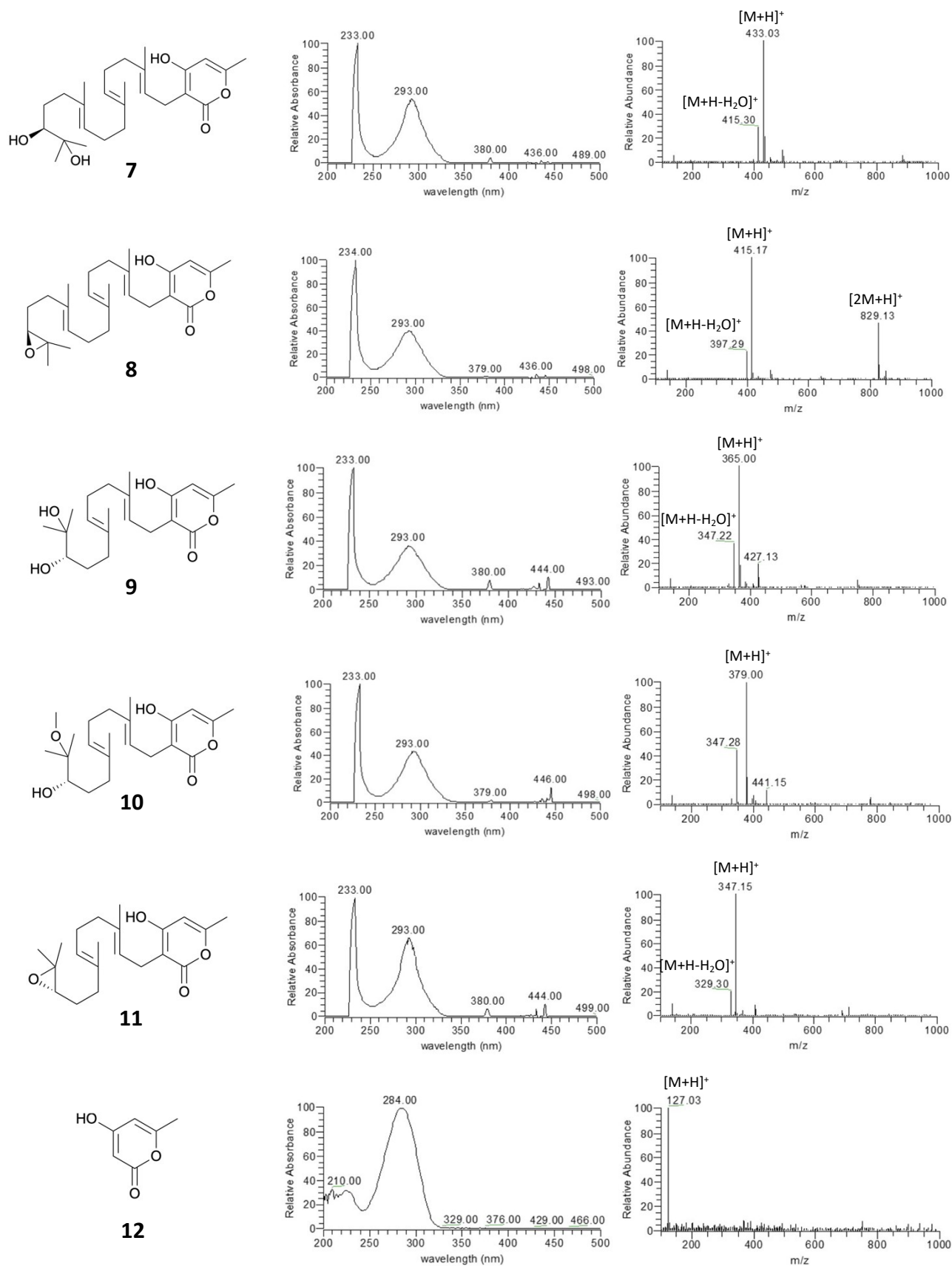
**Figure I.6.** UV-Vis and ESIMS spectra of compounds **1-12** (continued)

**Figure I.7.** $^1$H NMR of compound **1** in acetone-$d_6$

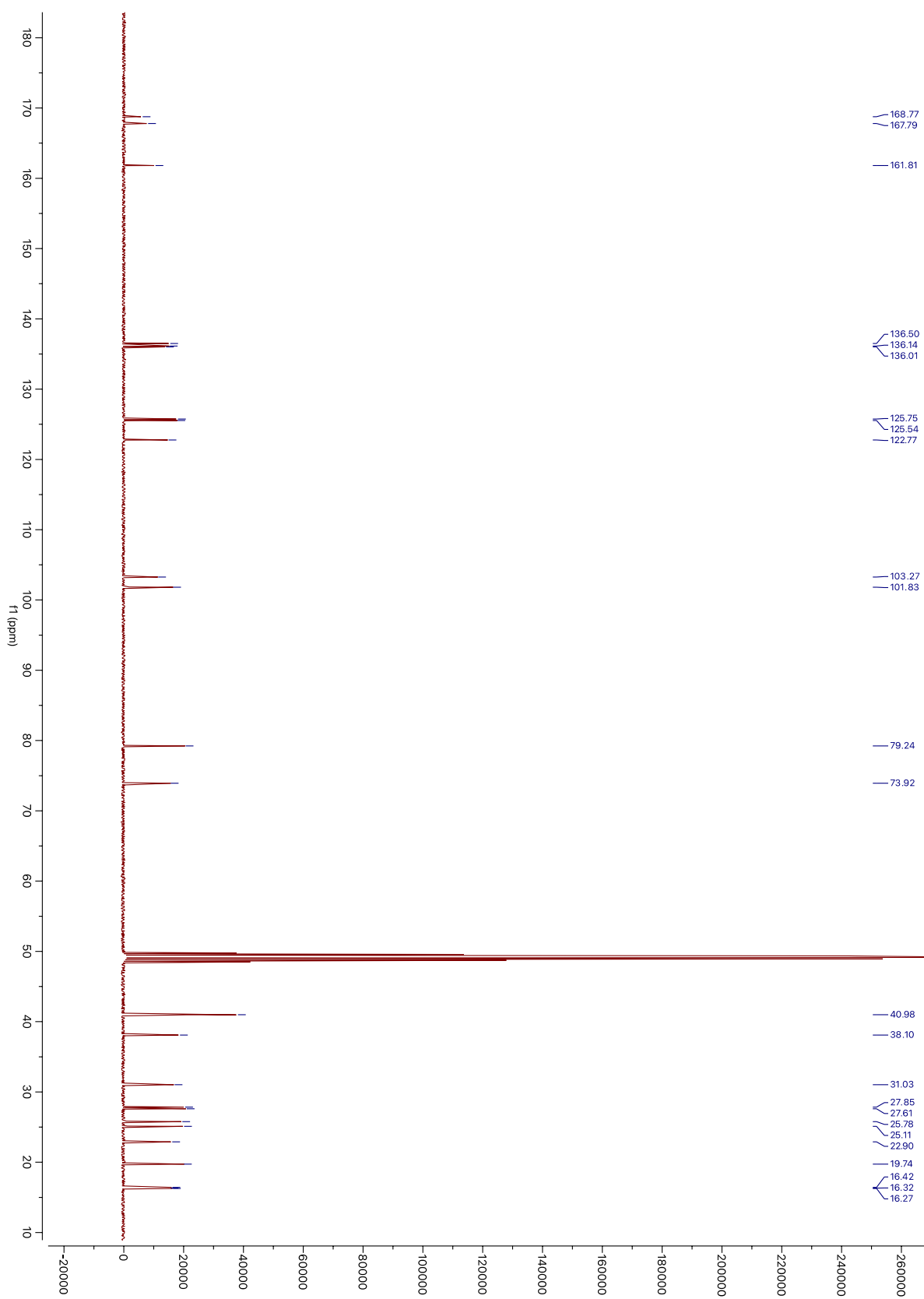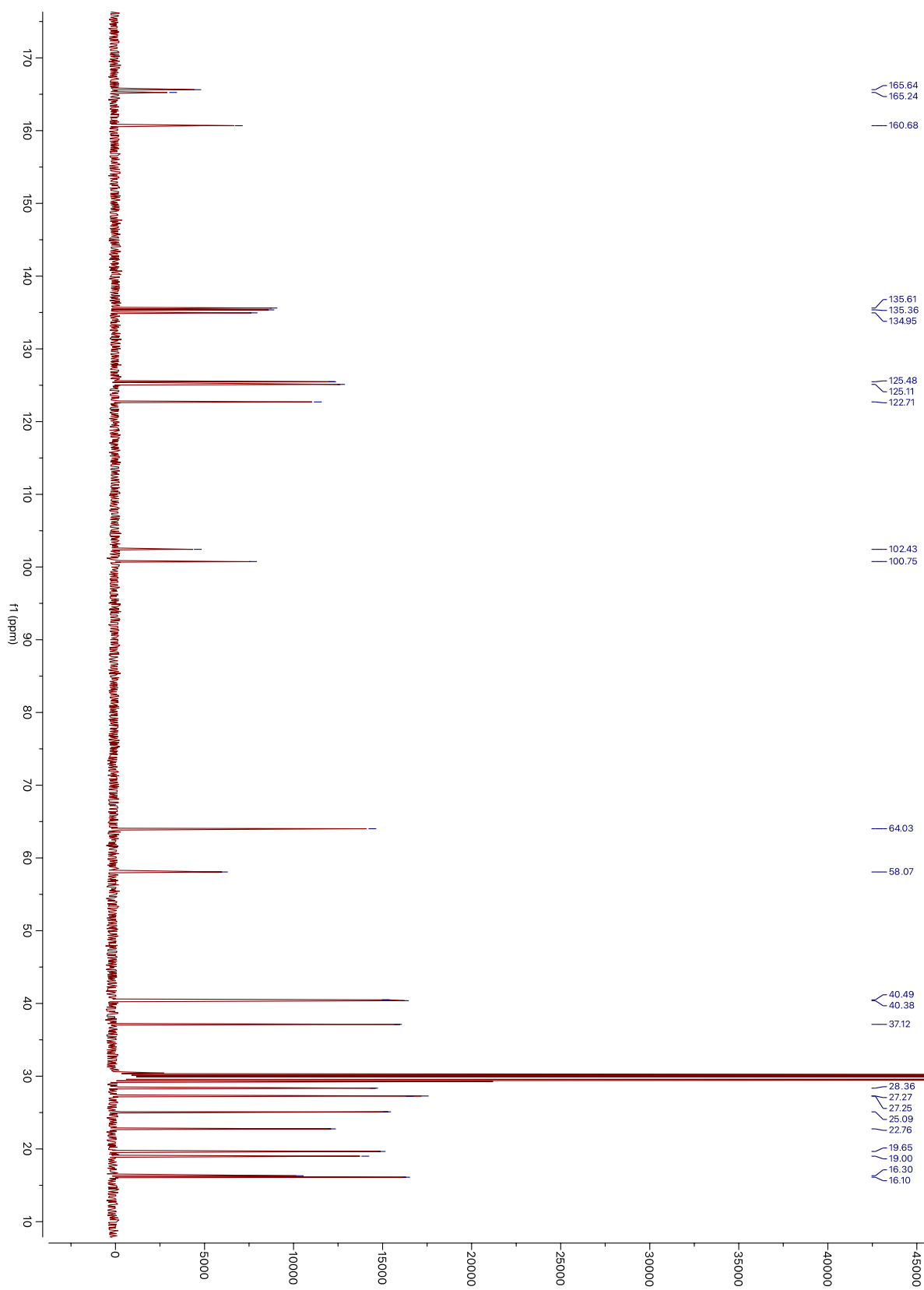**Figure I.8.** ¹³C NMR of compound **1** in acetone-$d_6$
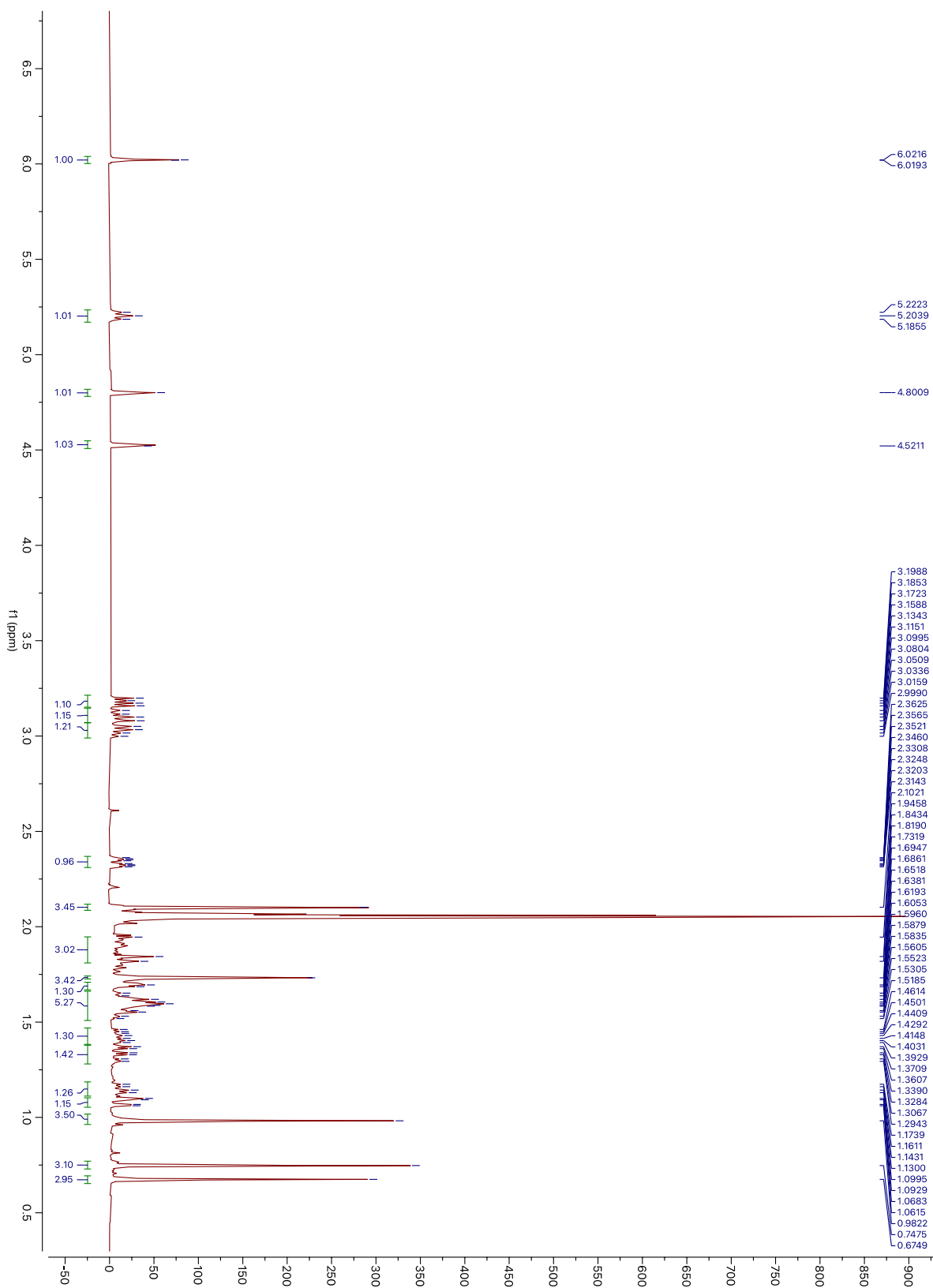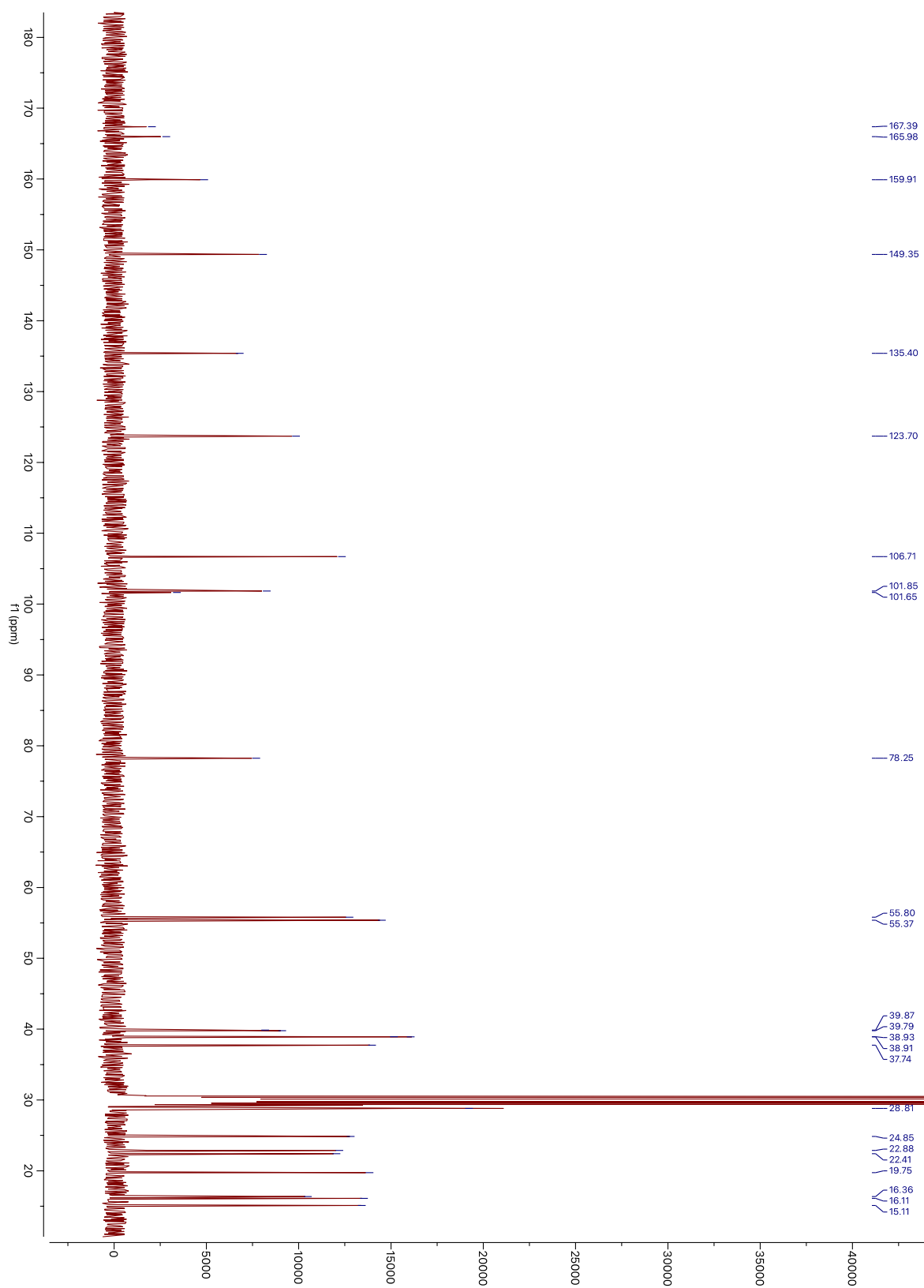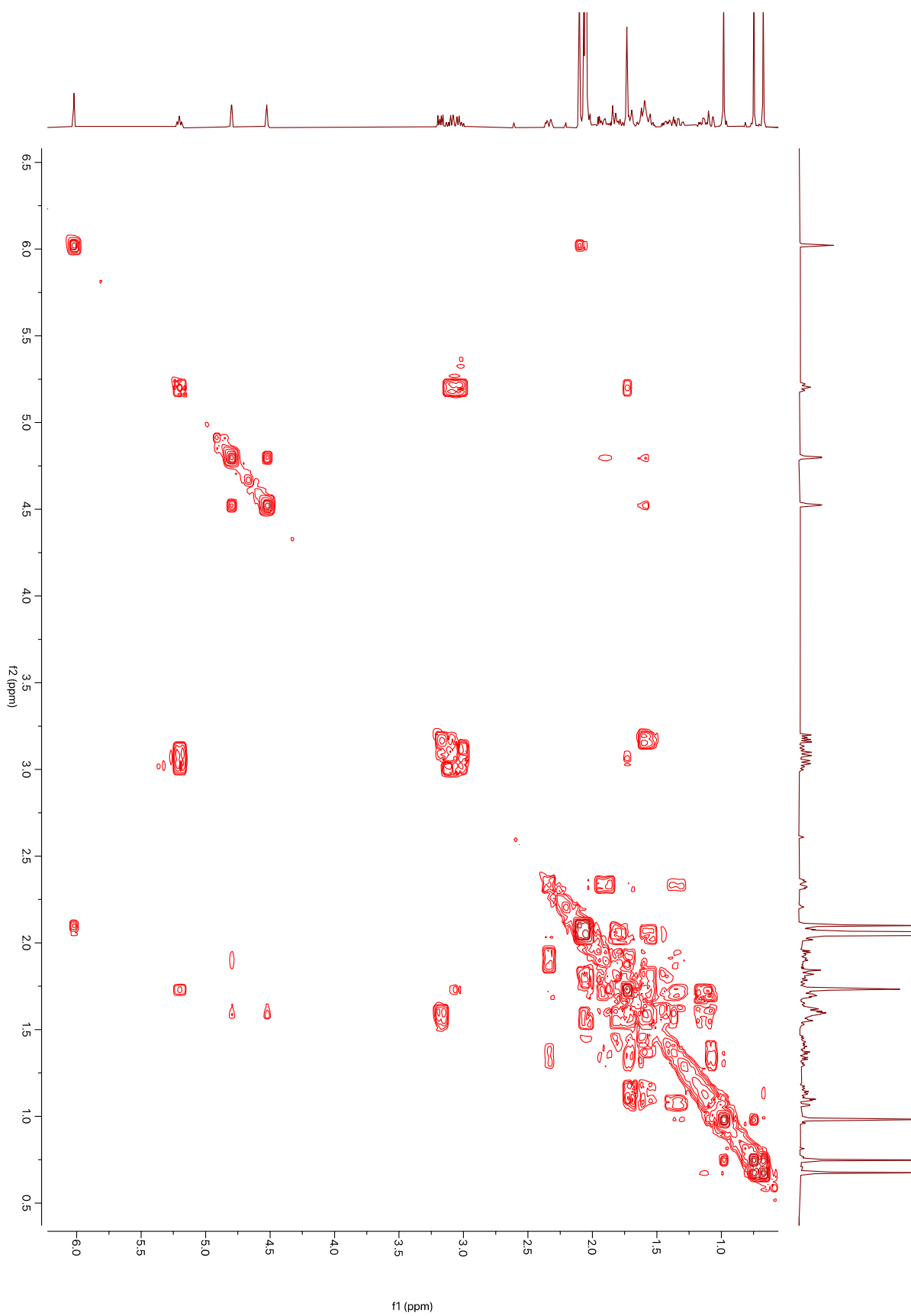
**Figure I.9.** COSY of compound **1** in acetone-$d_6$
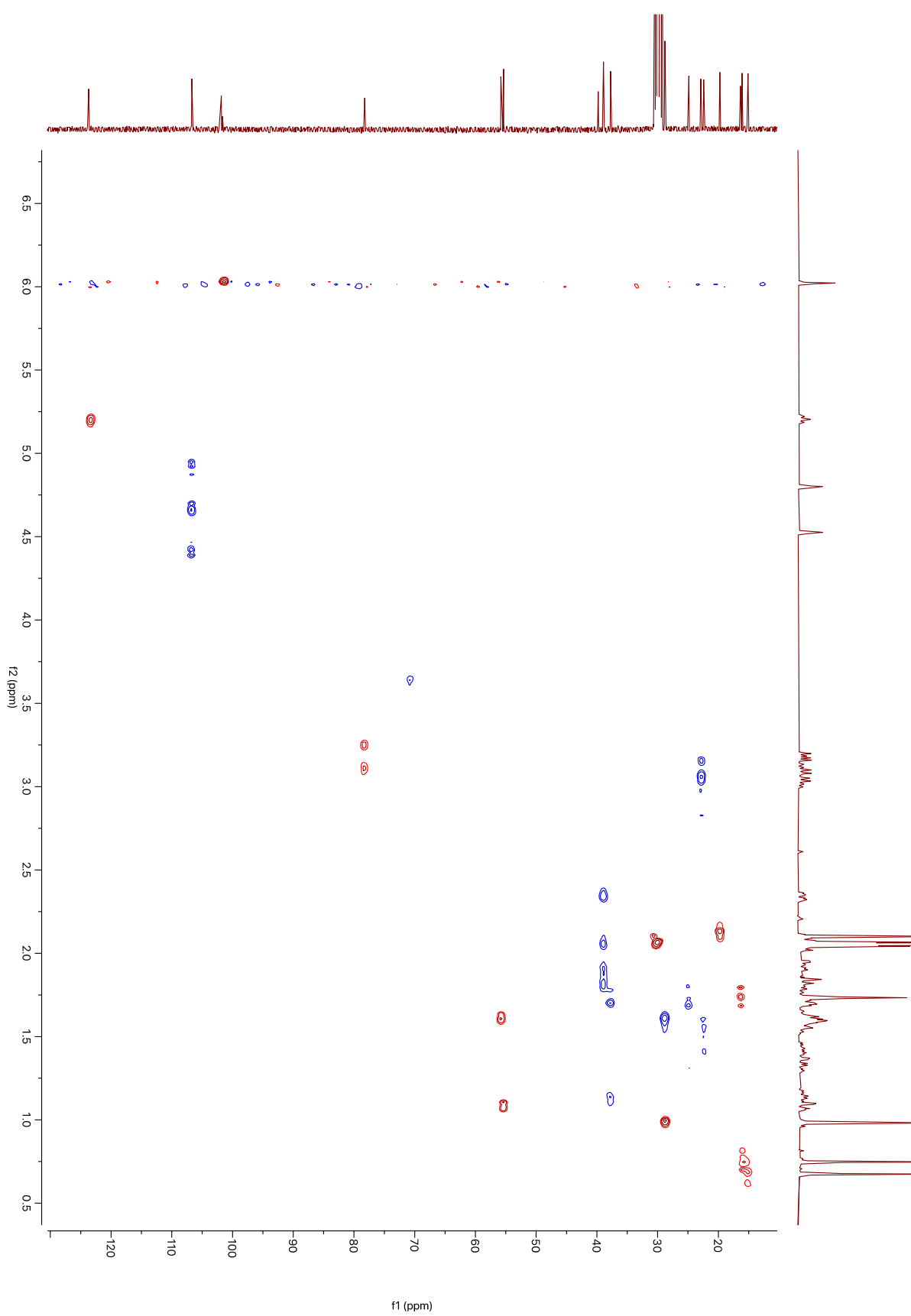
**Figure I.10.** HSQC of compound **1** in acetone-$d_6$
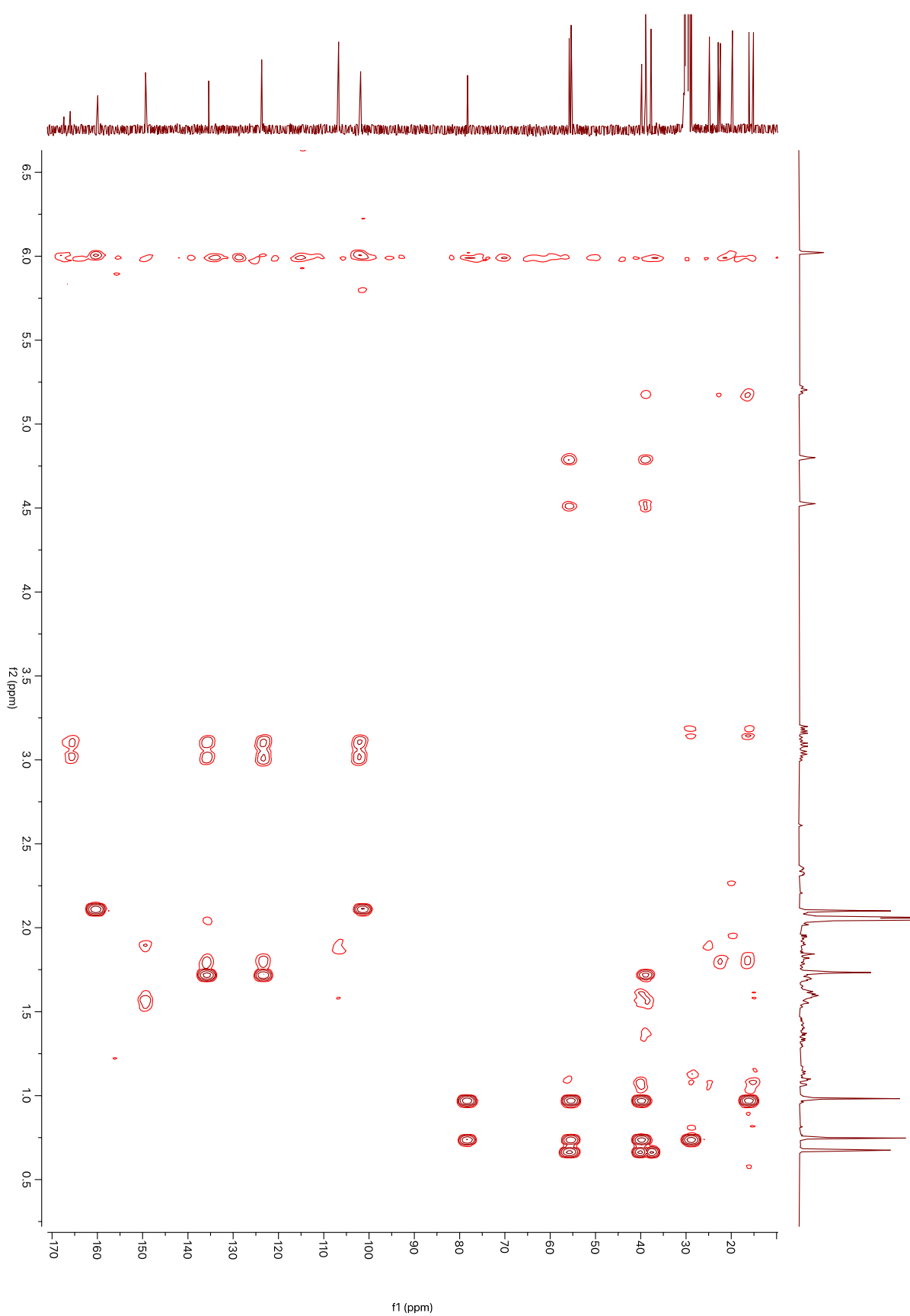
**Figure I.11.** HMBC of compound **1** in acetone-$d_6$
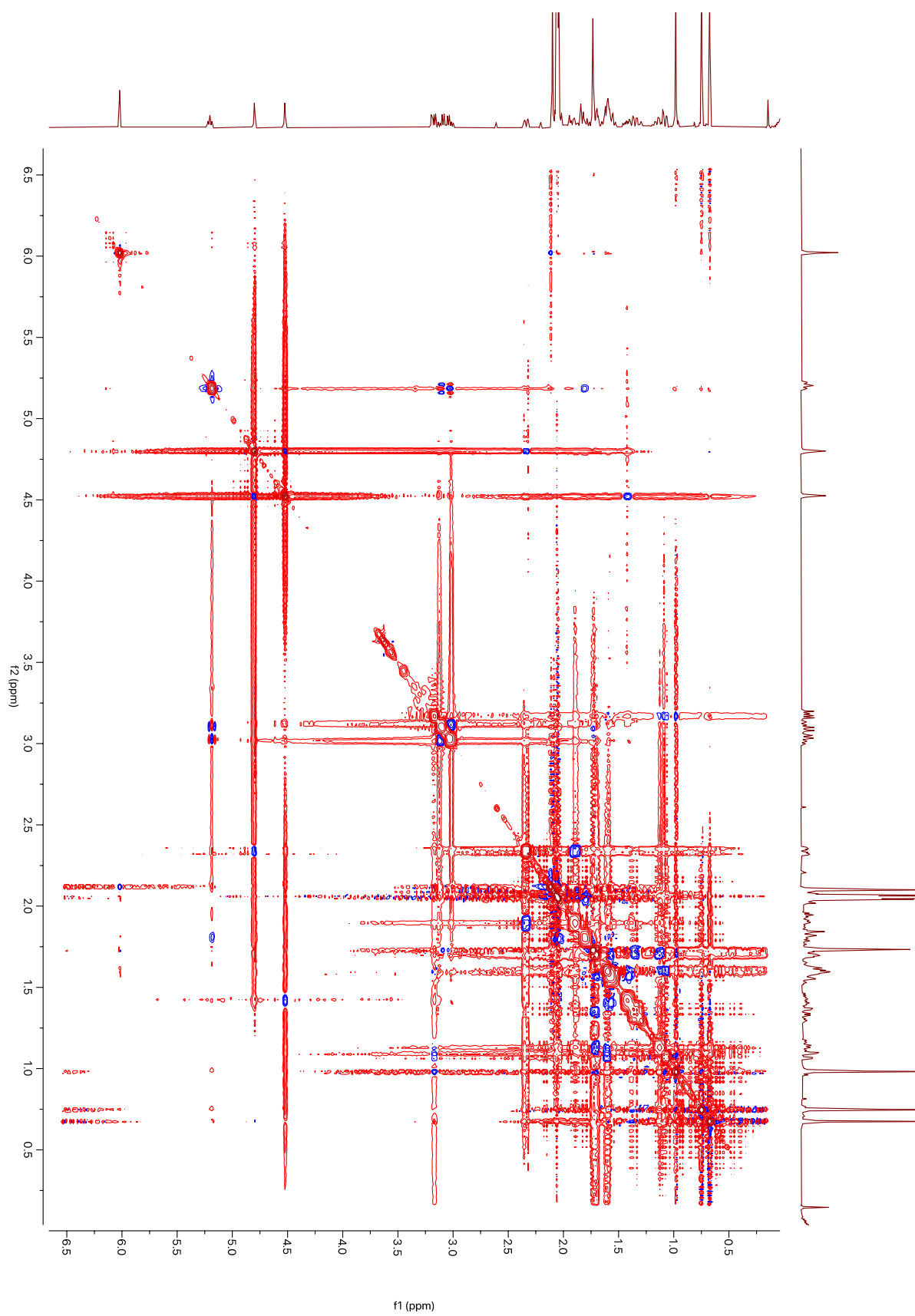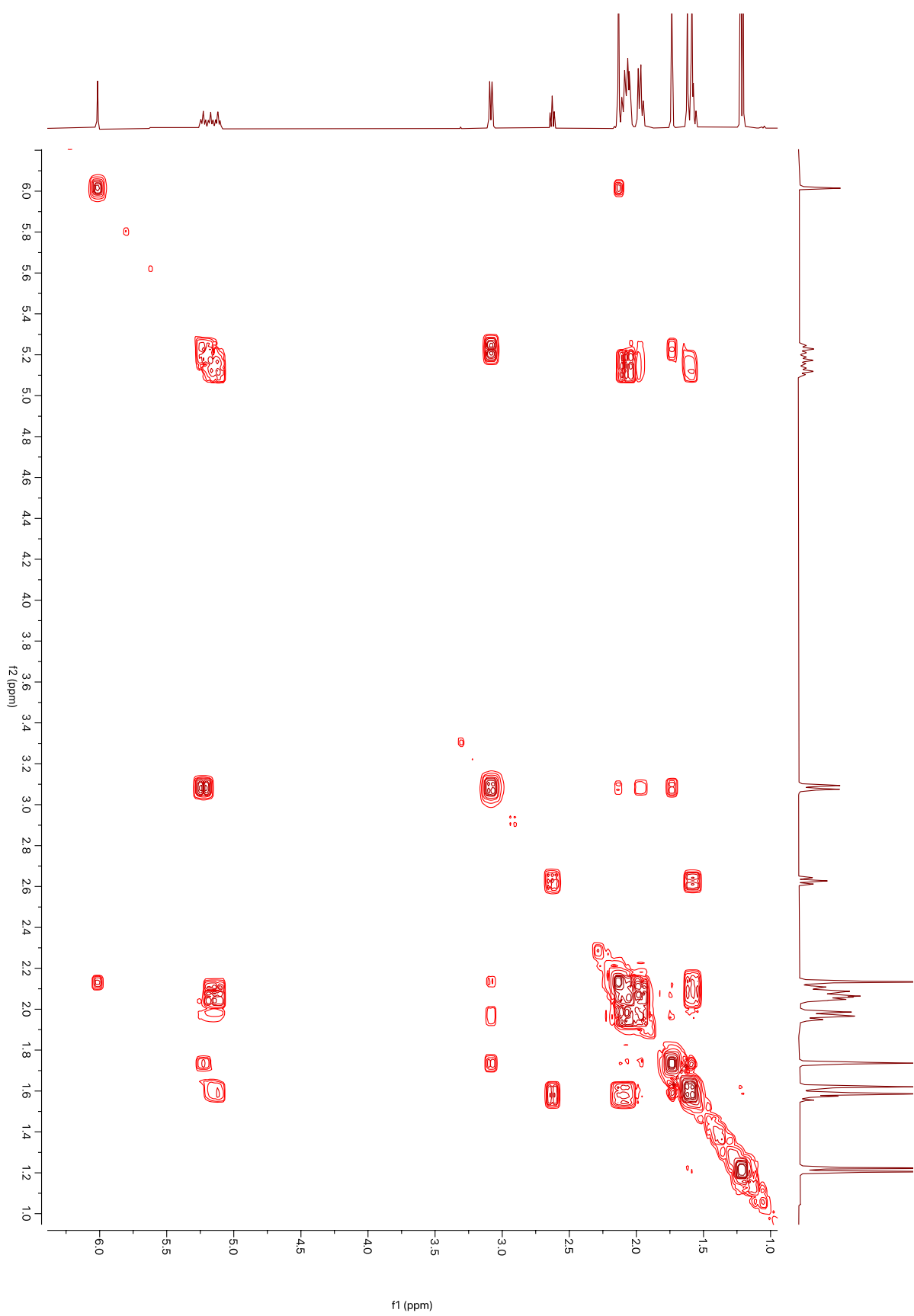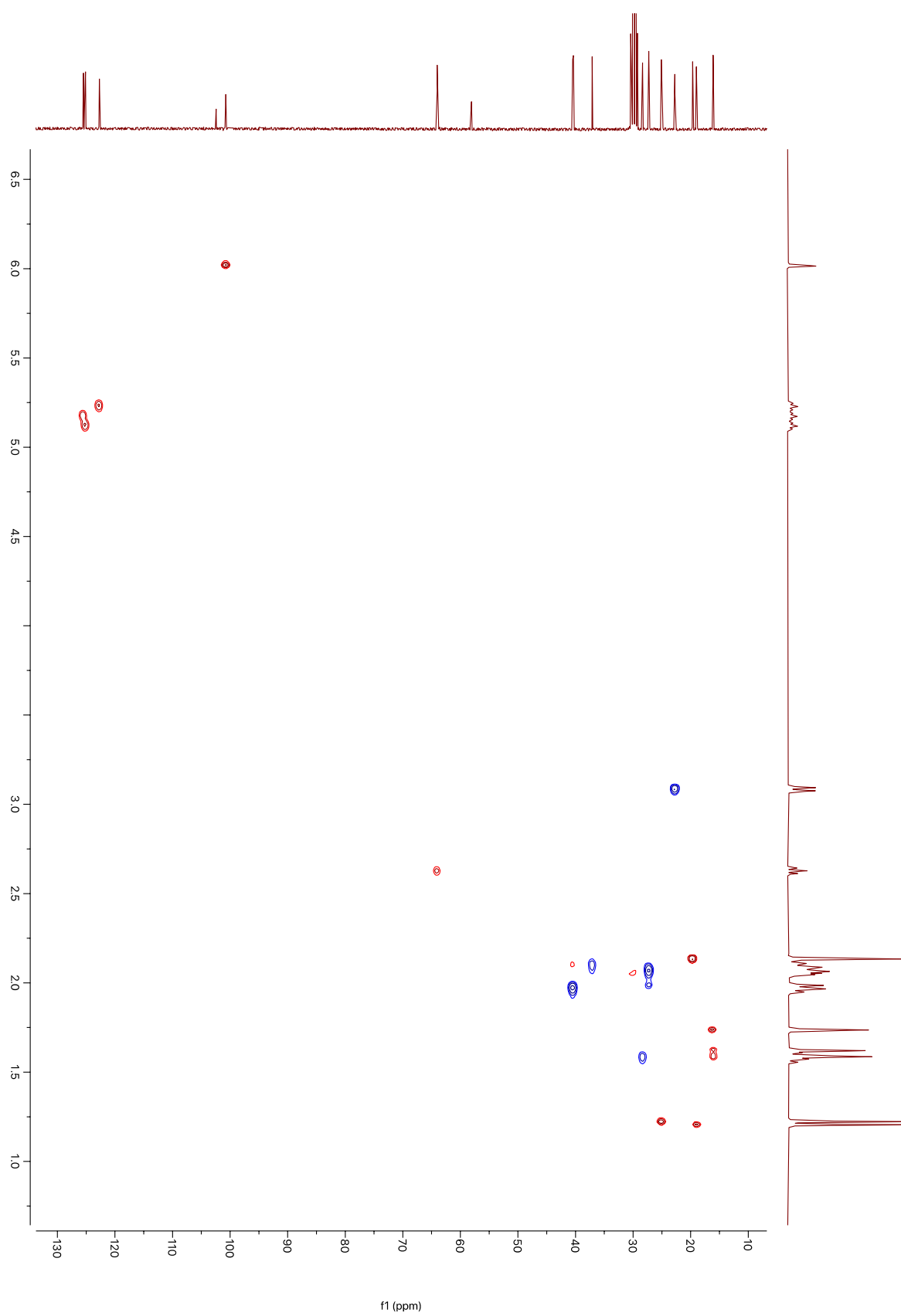
**Figure I.12.** NOESY of compound **1** in acetone-$d_6$

**Figure 1.13.** $^1$H NMR of compound **2** in CDCl$_3$
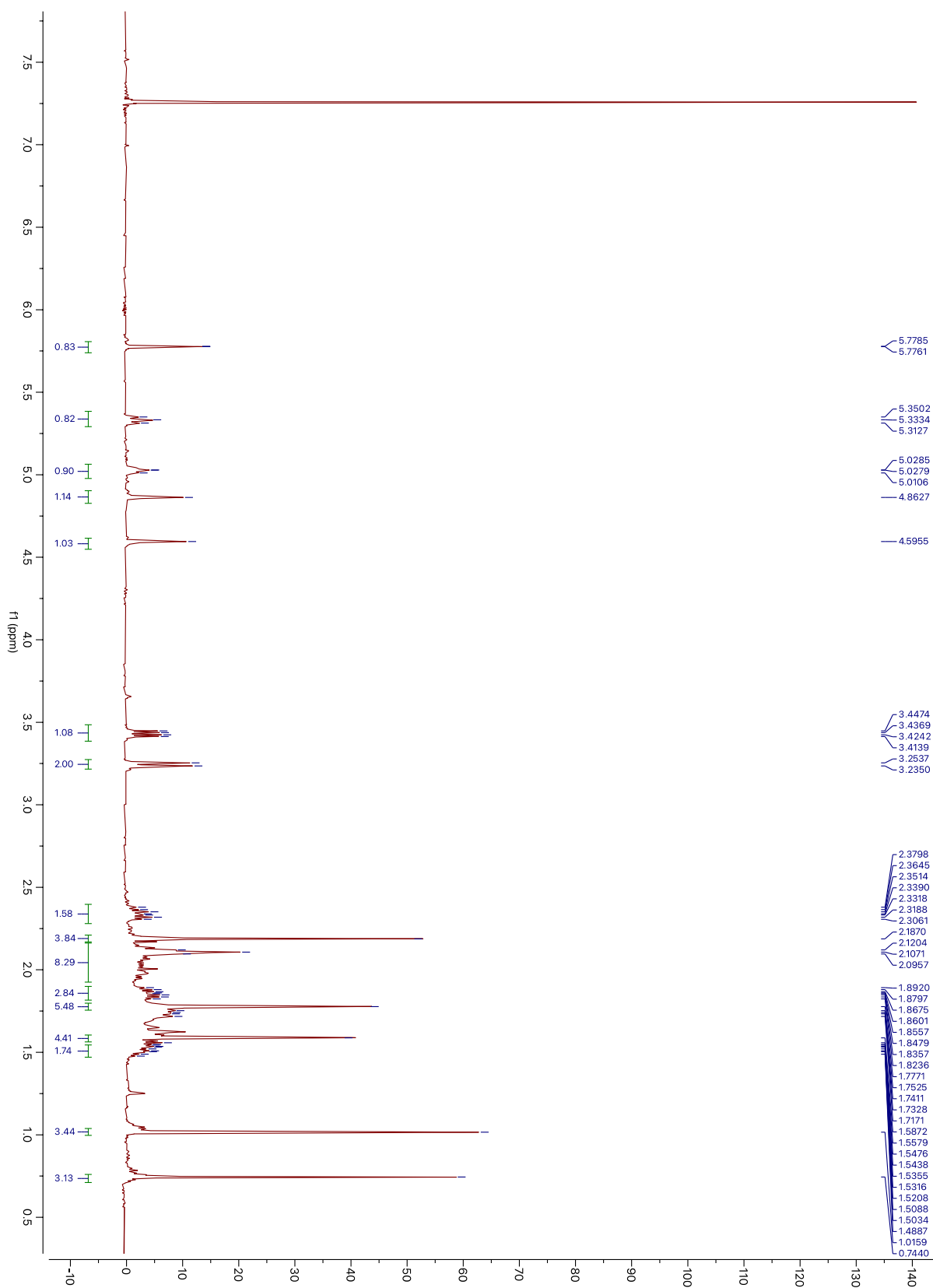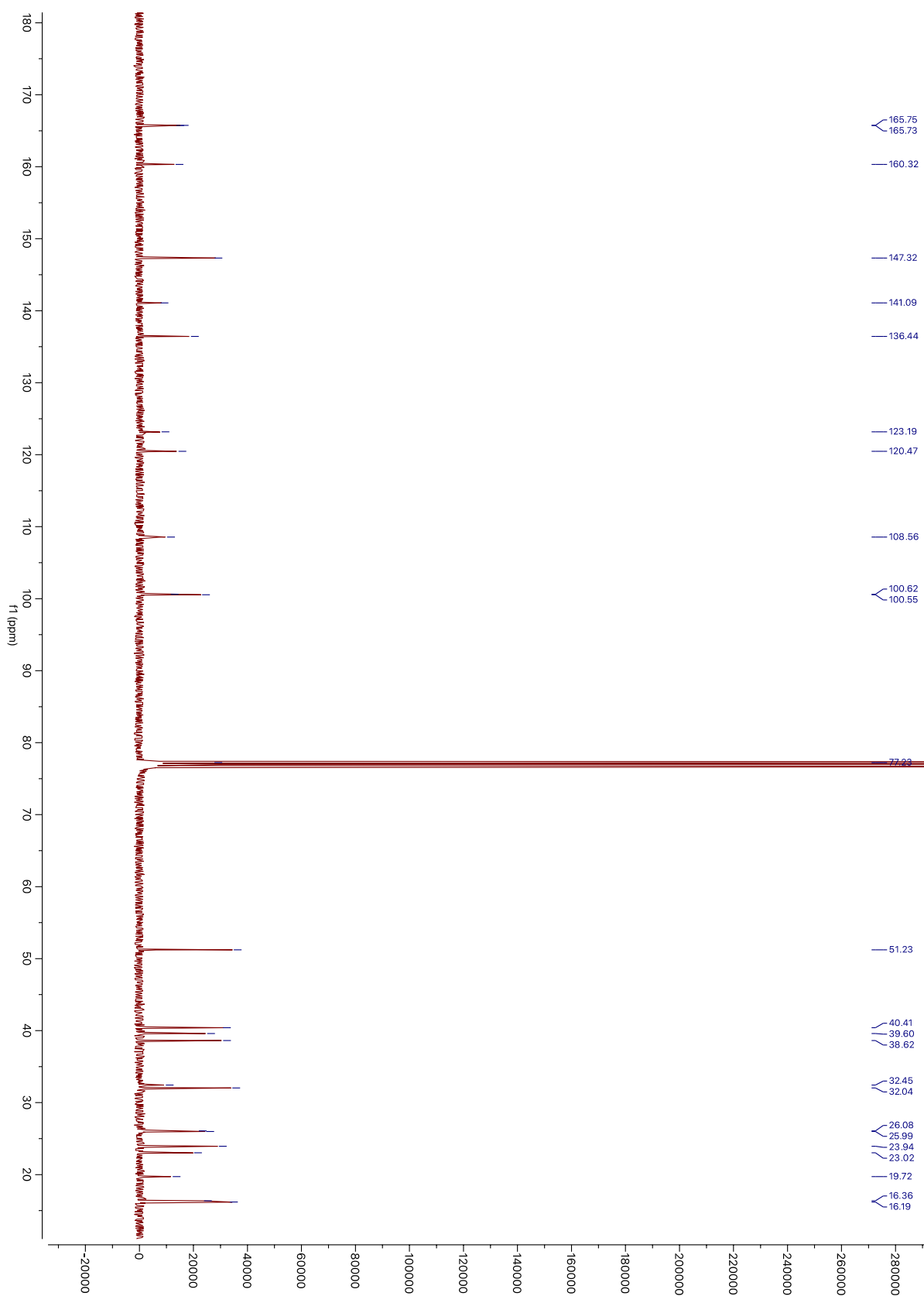
**Figure I.14.** $^{13}$C NMR of compound **2** in CDCl$_3$

**Figure 1.15.** $^1$H NMR of compound **3** in CDCl$_3$

**Figure 1.16.** $^{13}$C NMR of compound **3** in CDCl$_3$

**Figure I.17.** $^1$H NMR of compound **4** in acetone-$d_6$

**Figure 1.18.** $^{13}C$ NMR of compound **4** in acetone-$d_6$
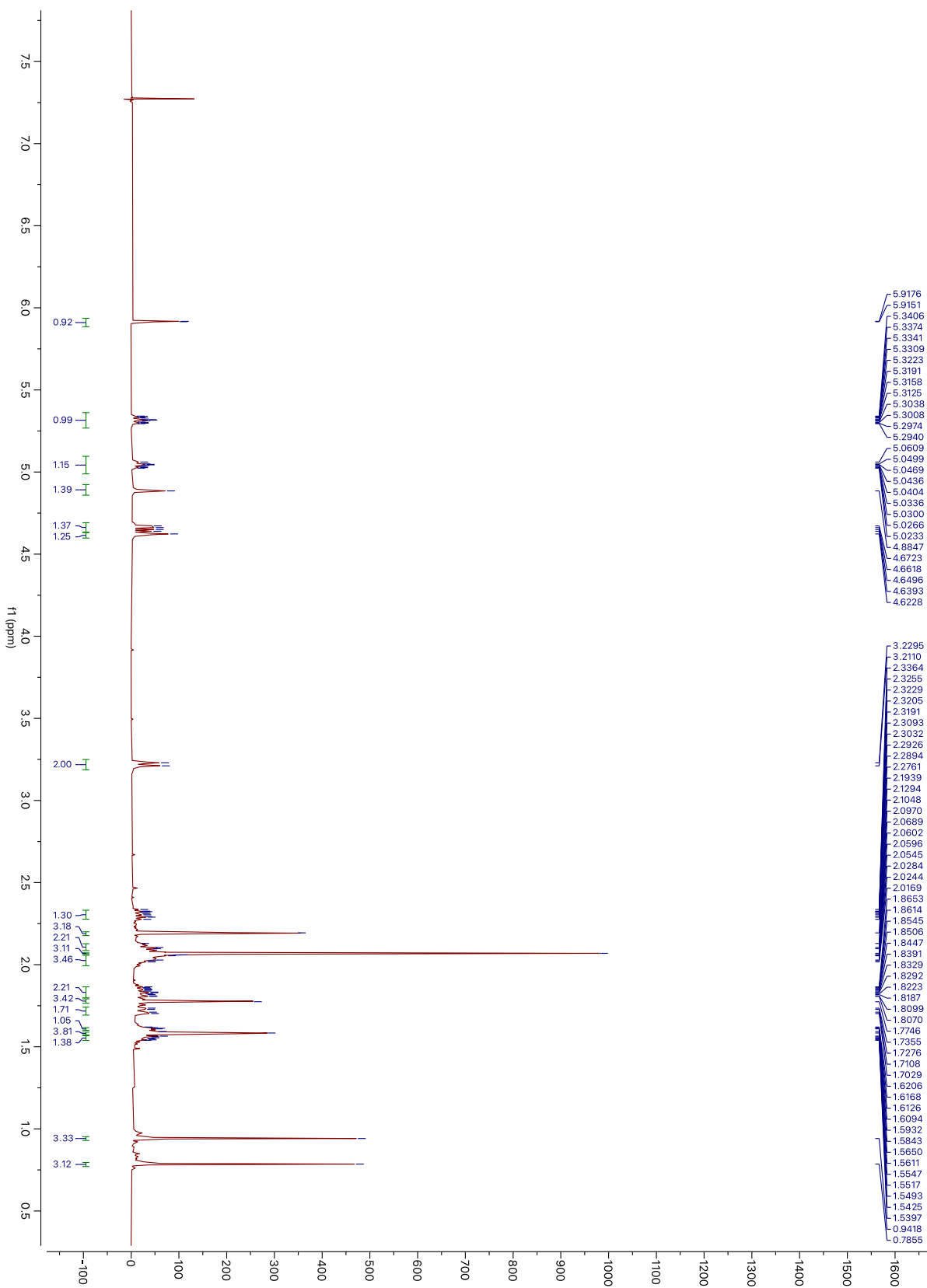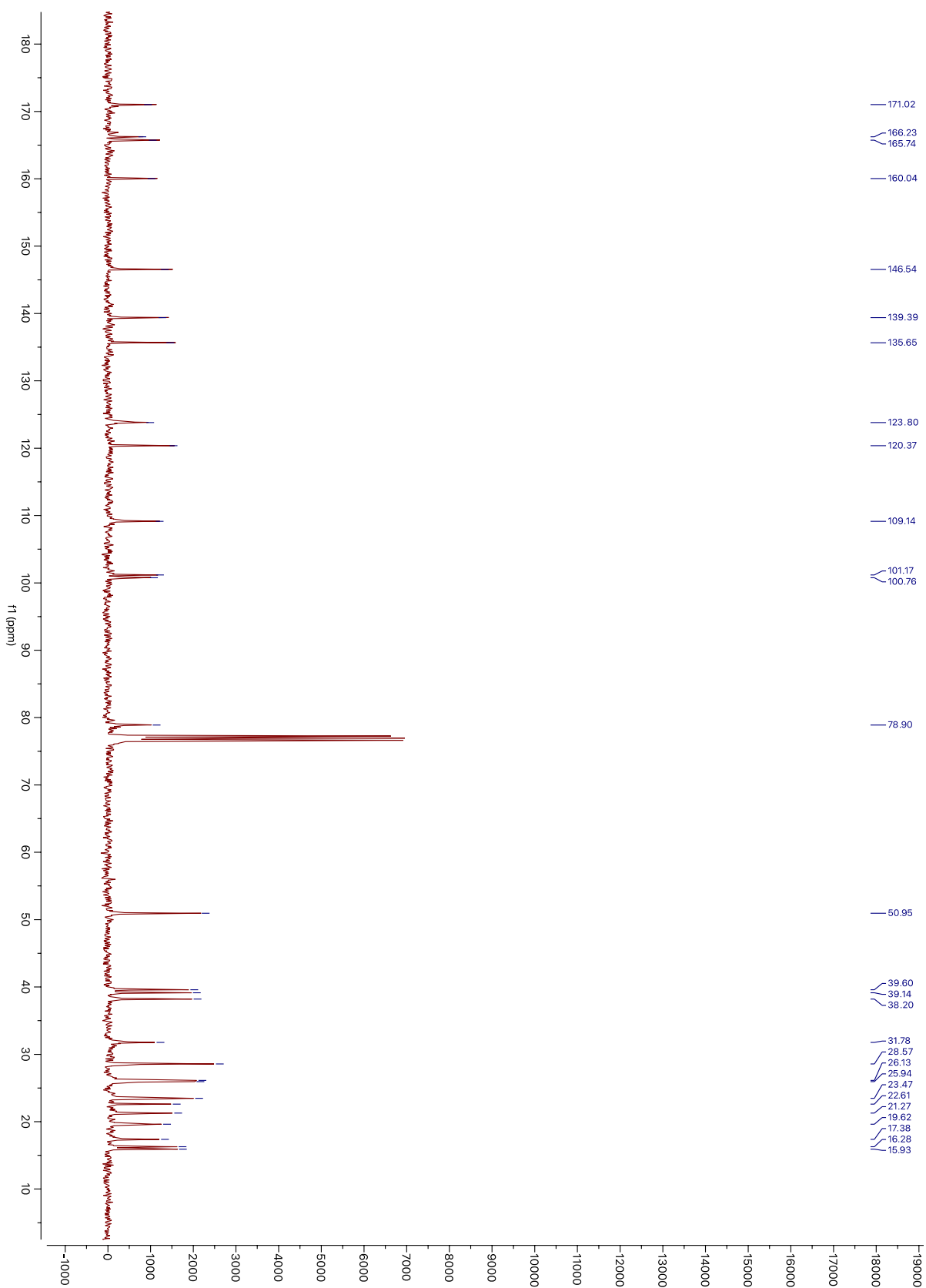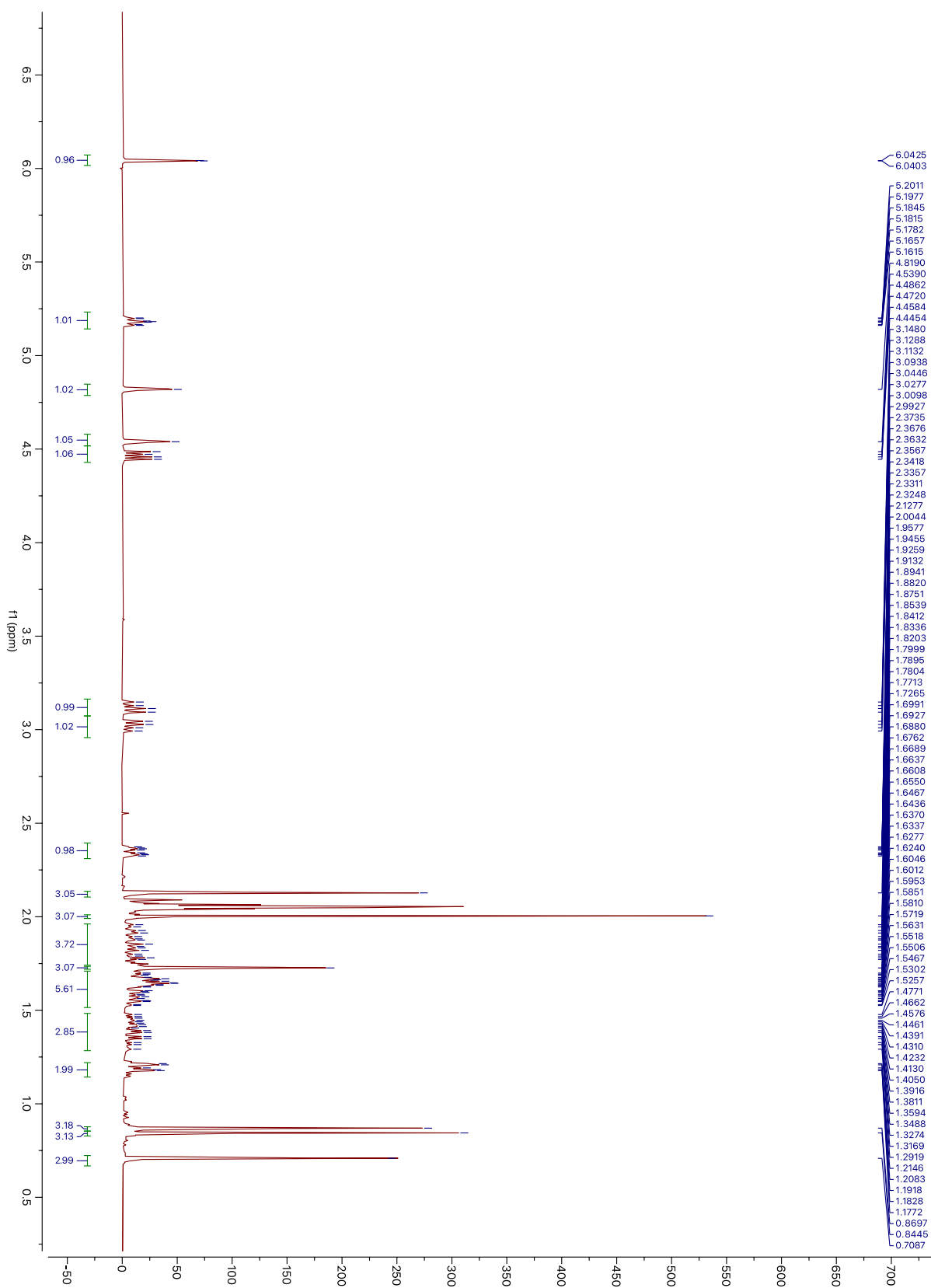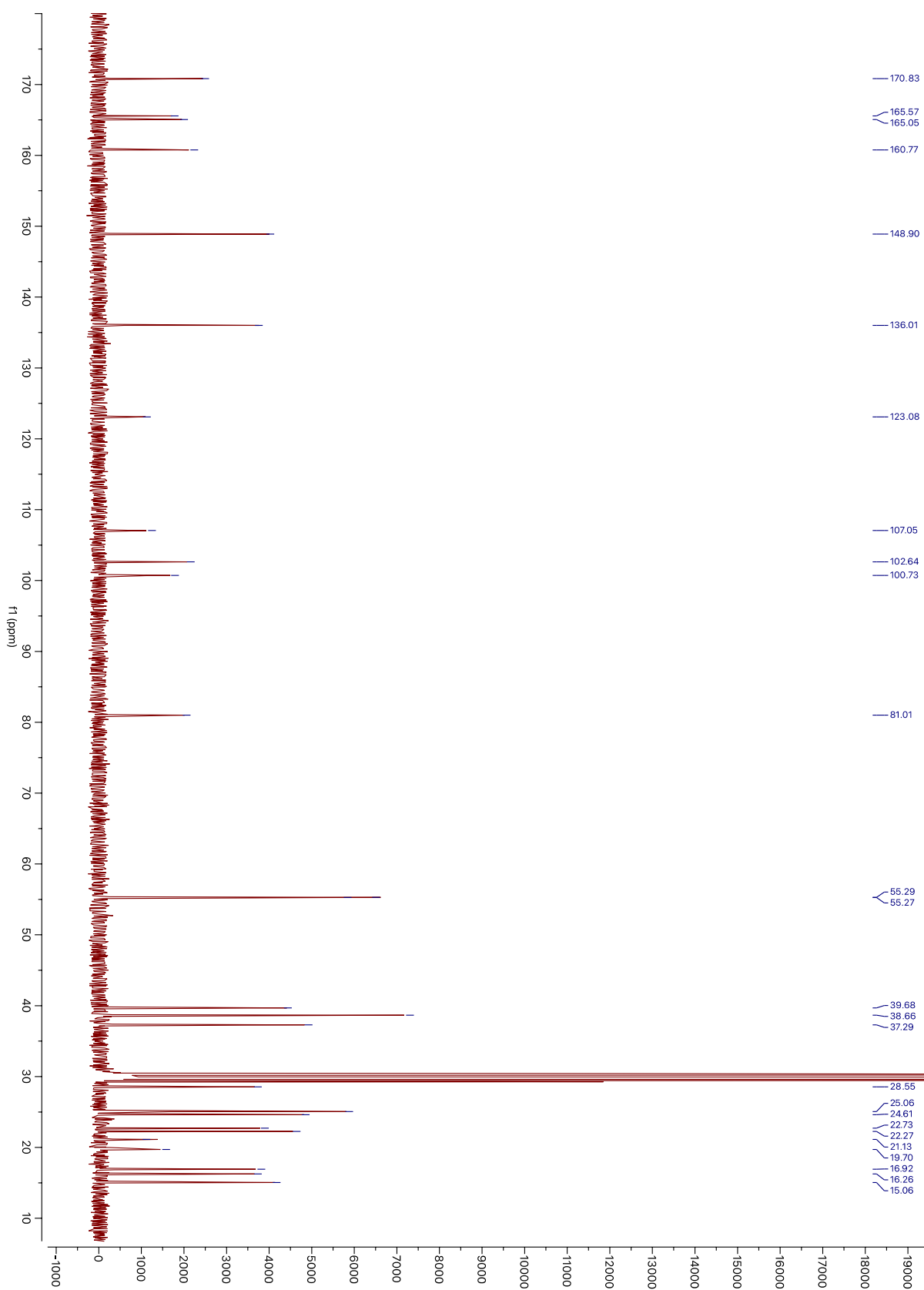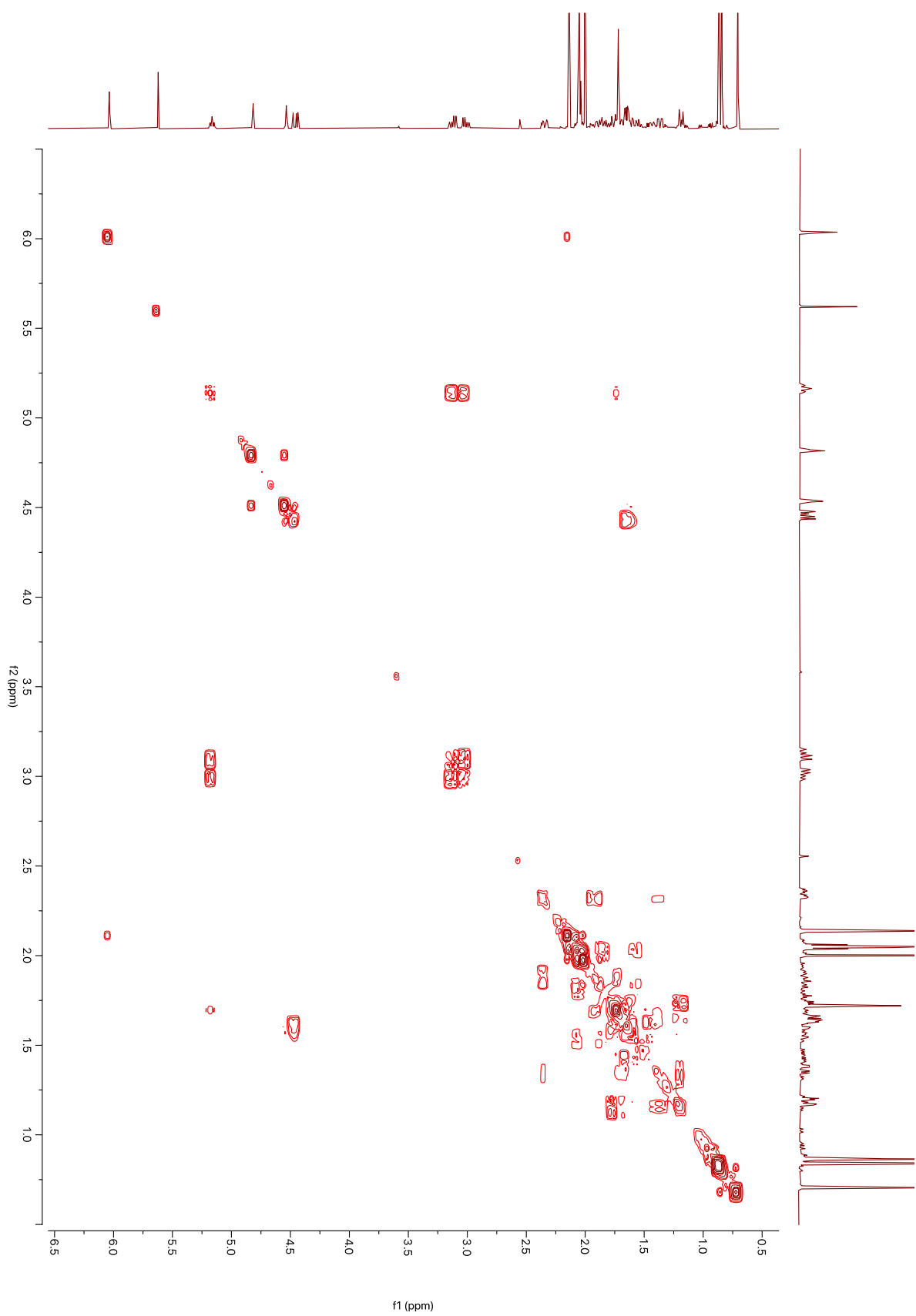
**Figure 1.19.** COSY of compound **4** in acetone-$d_6$
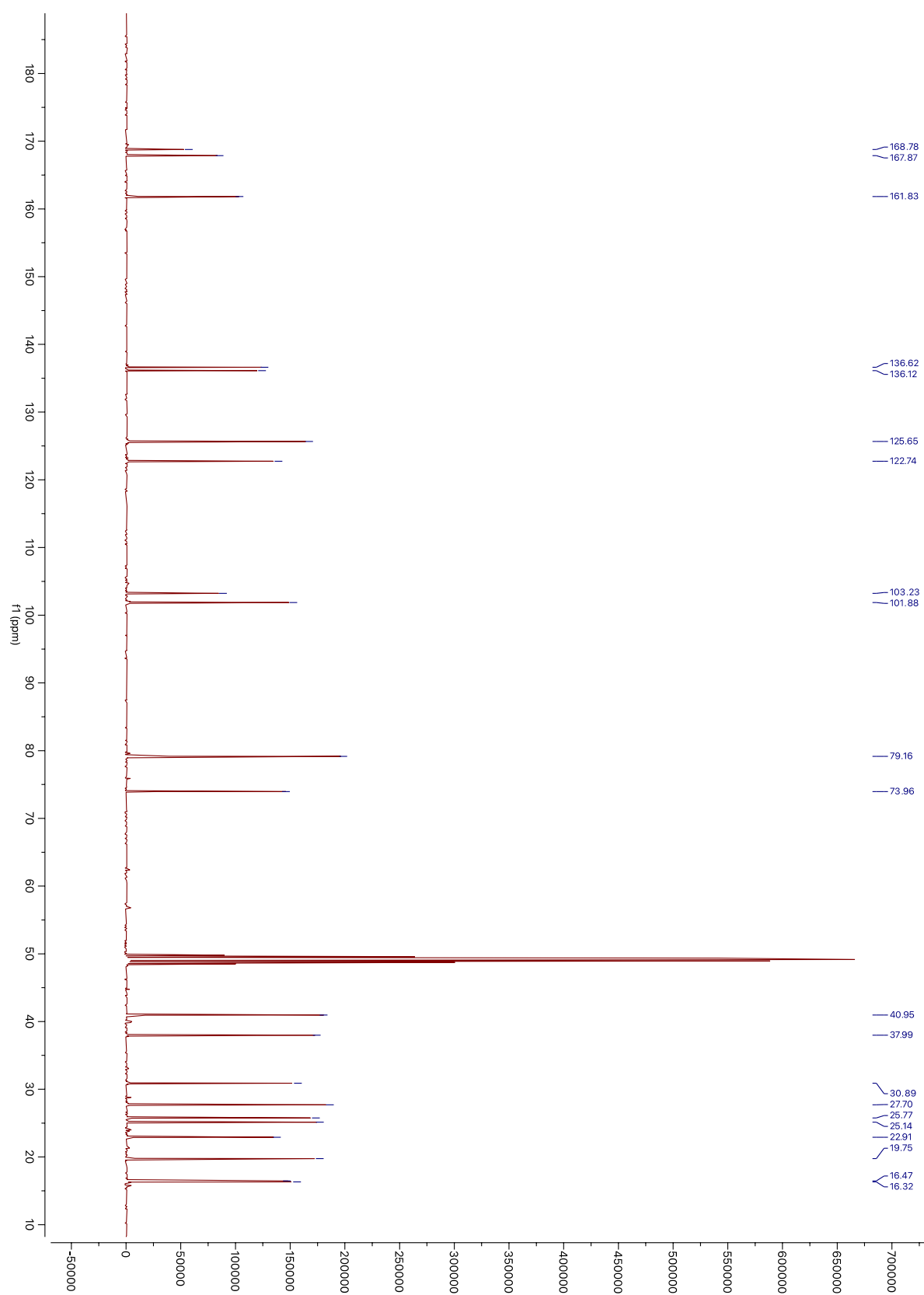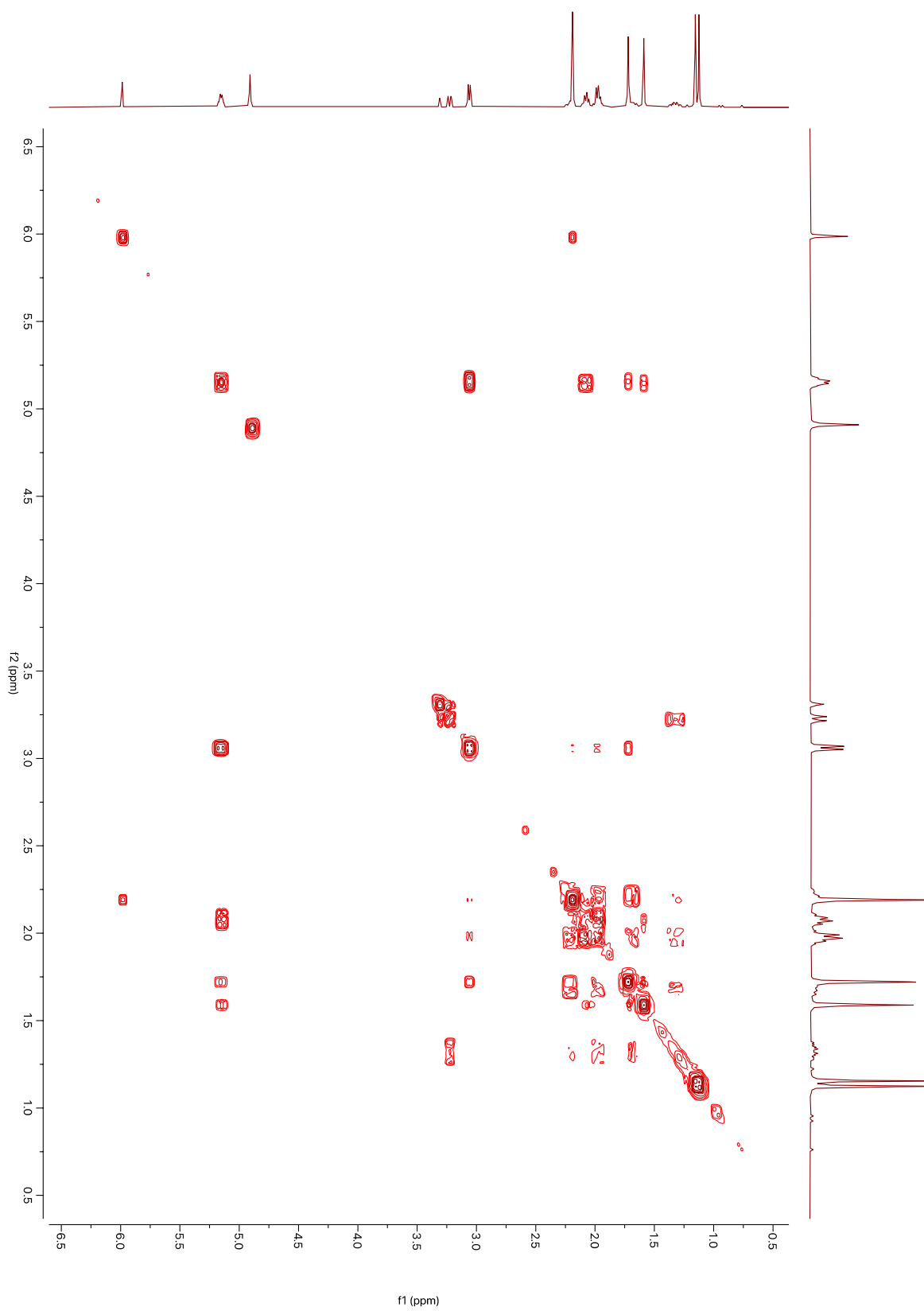
**Figure 1.20.** HSQC of compound **4** in acetone-$d_6$

**Figure 1.21.** HMBC of compound **4** in acetone-*d₆*

**Figure I.22.** NOESY of compound **4** in acetone-$d_6$

**Figure I.23.** $^1$H NMR of compound **5** in acetone-$d_6$
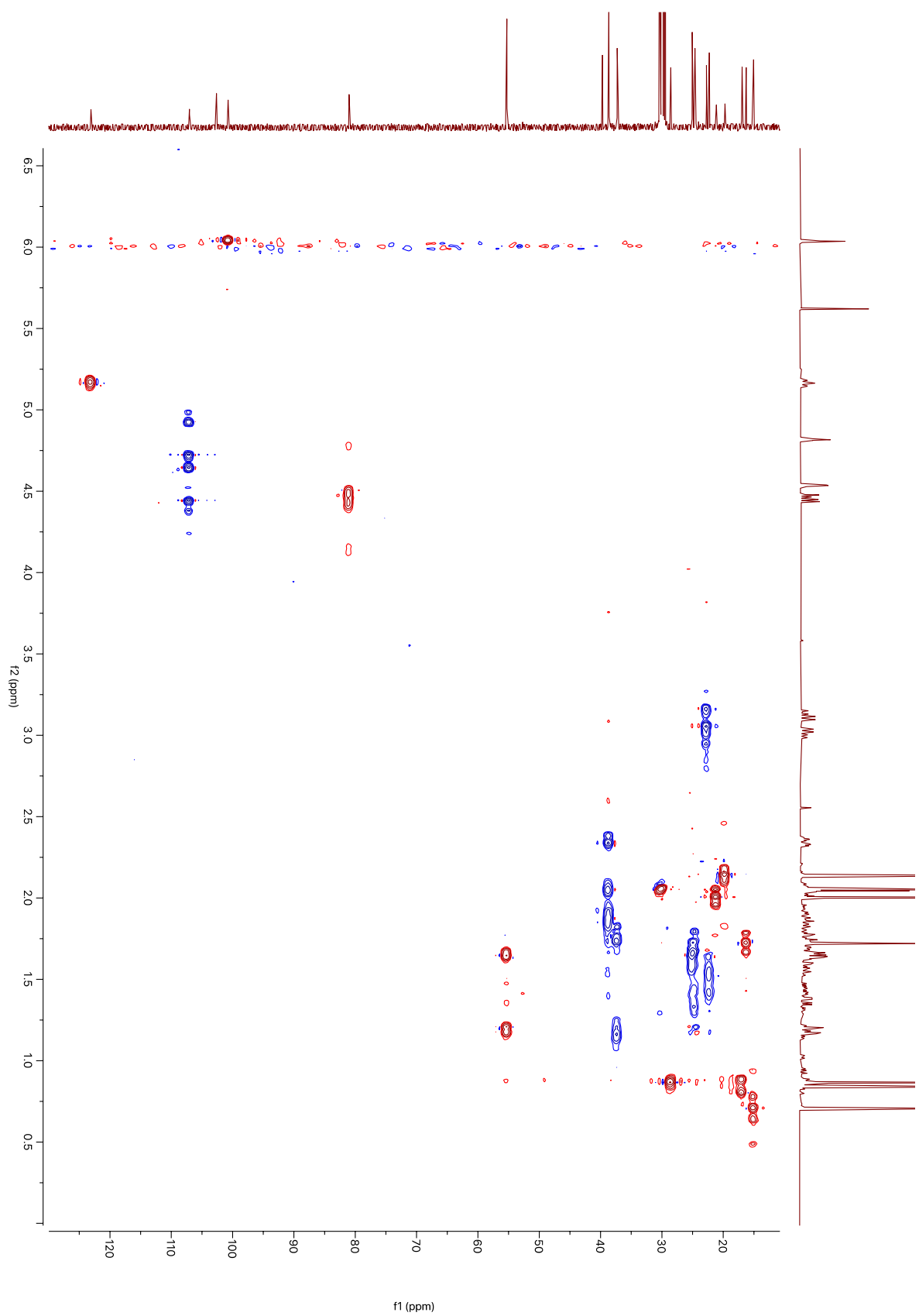
**Figure I.24.** $^{13}$C NMR of compound **5** in acetone-$d_6$
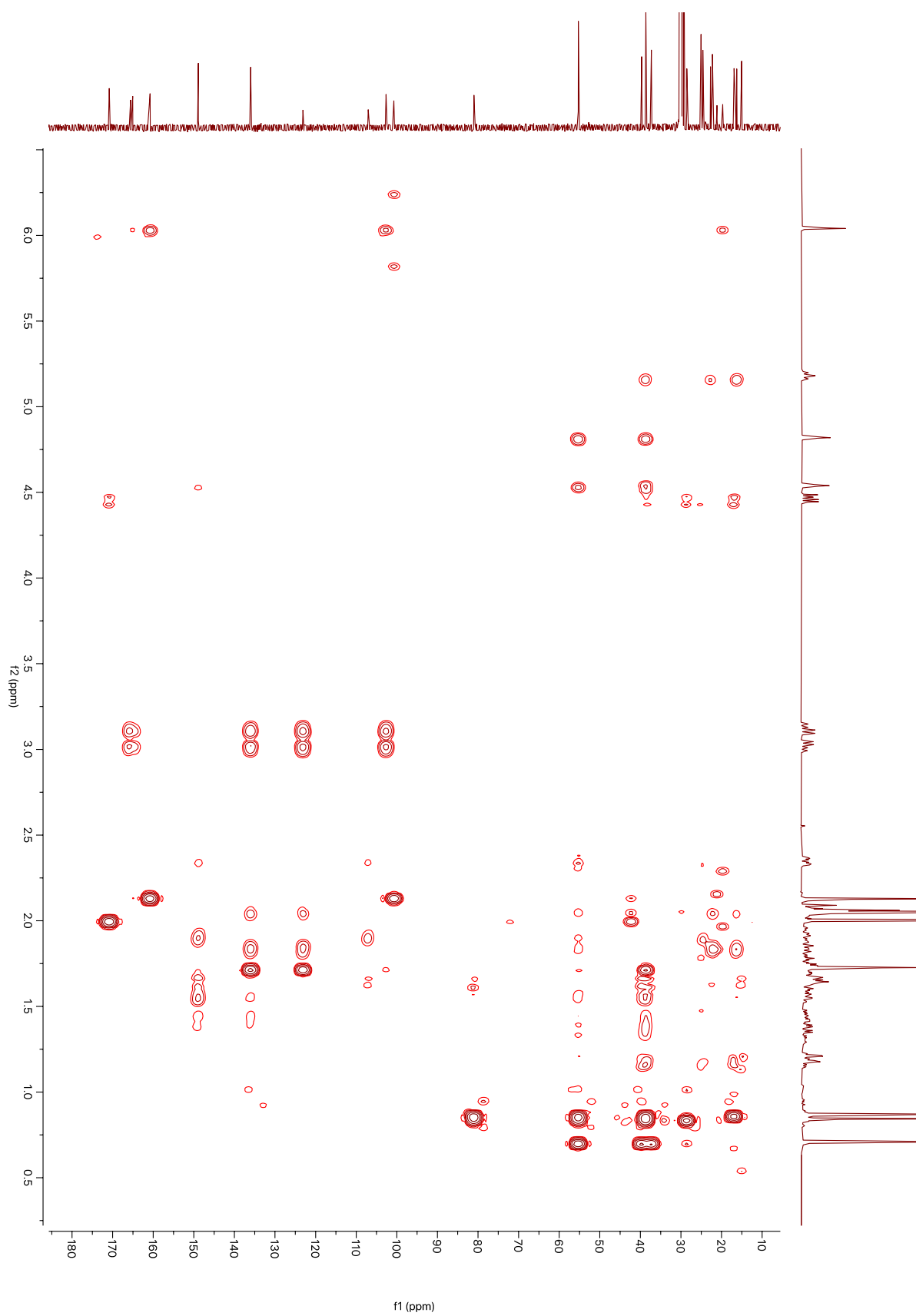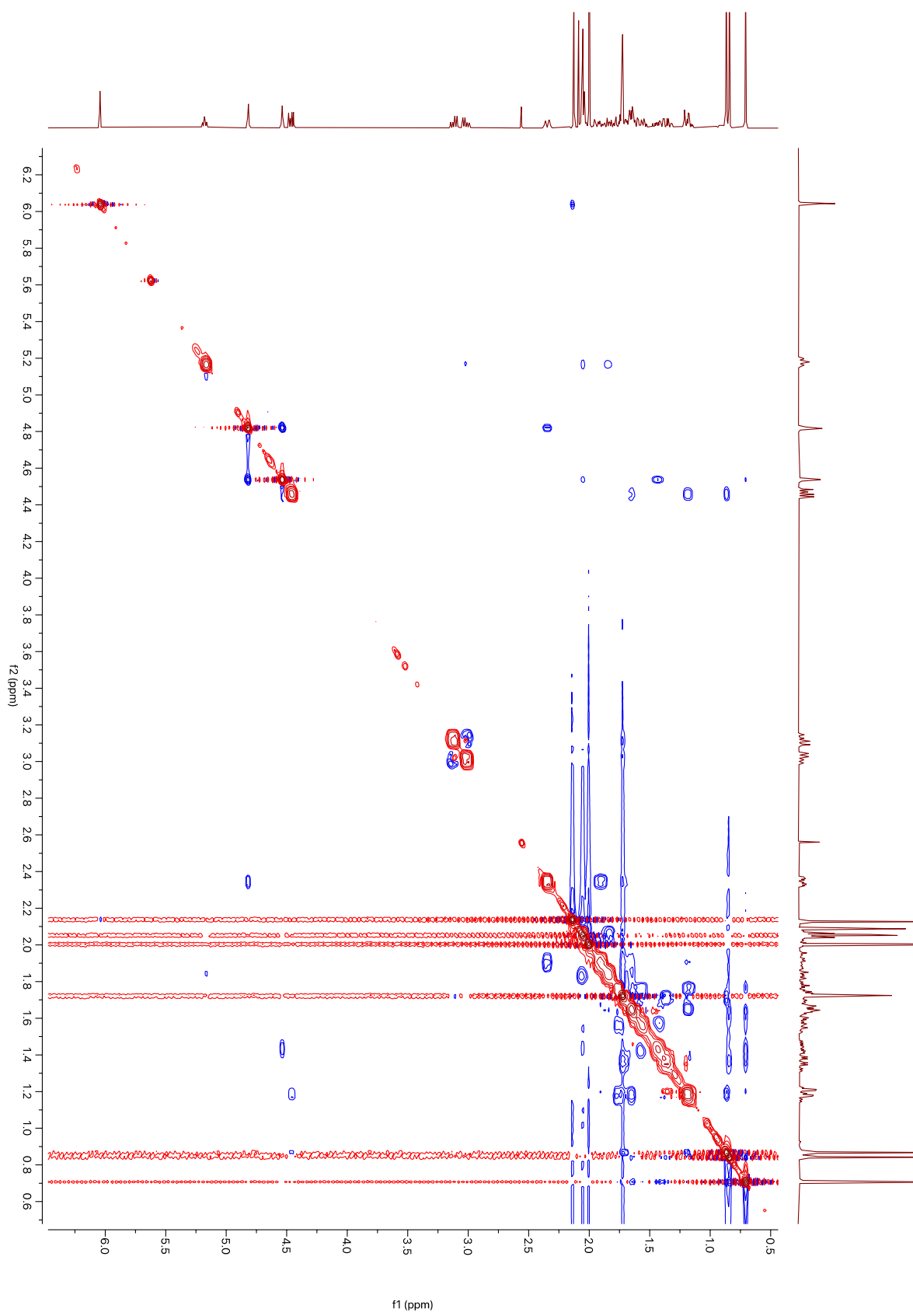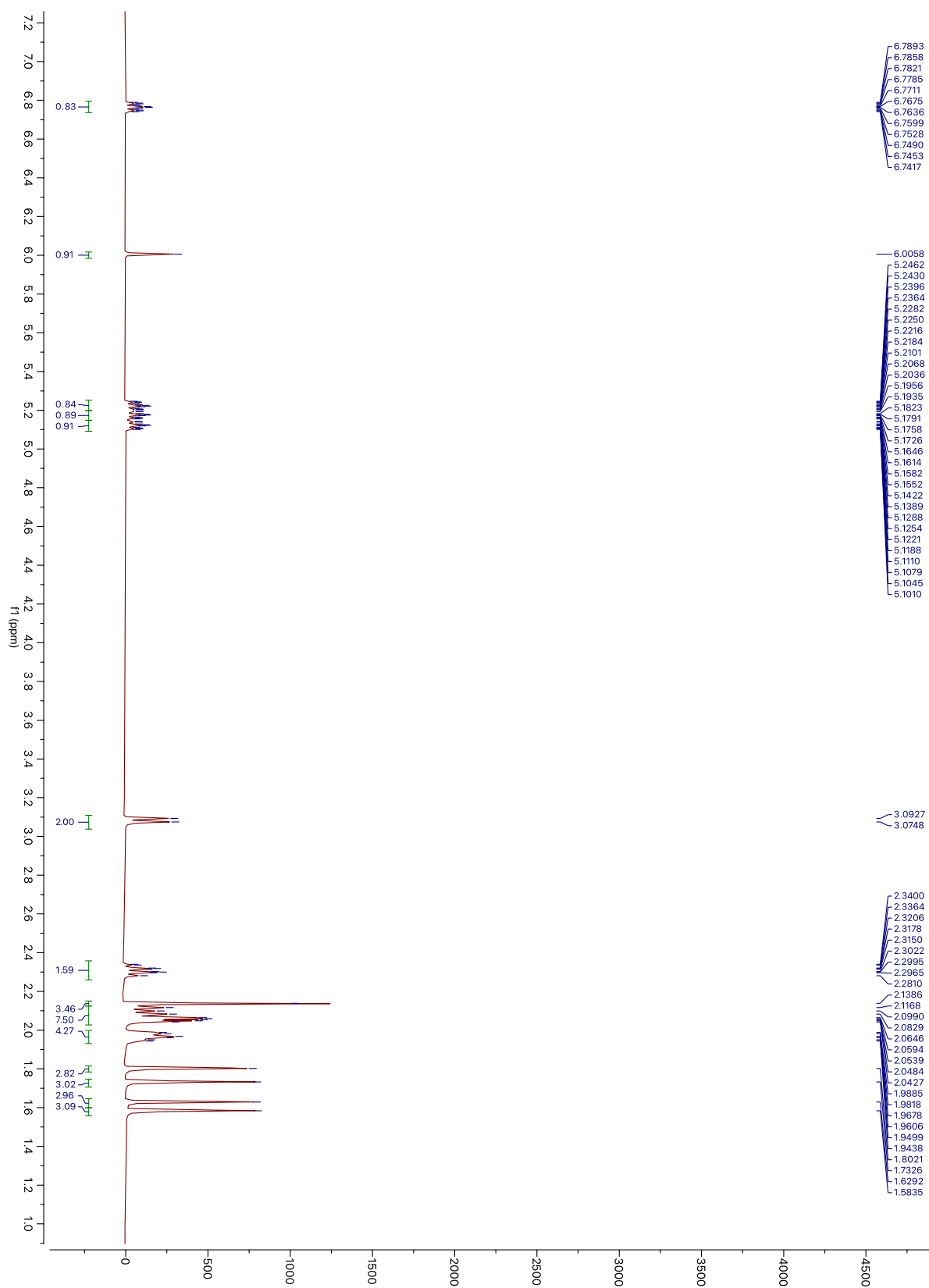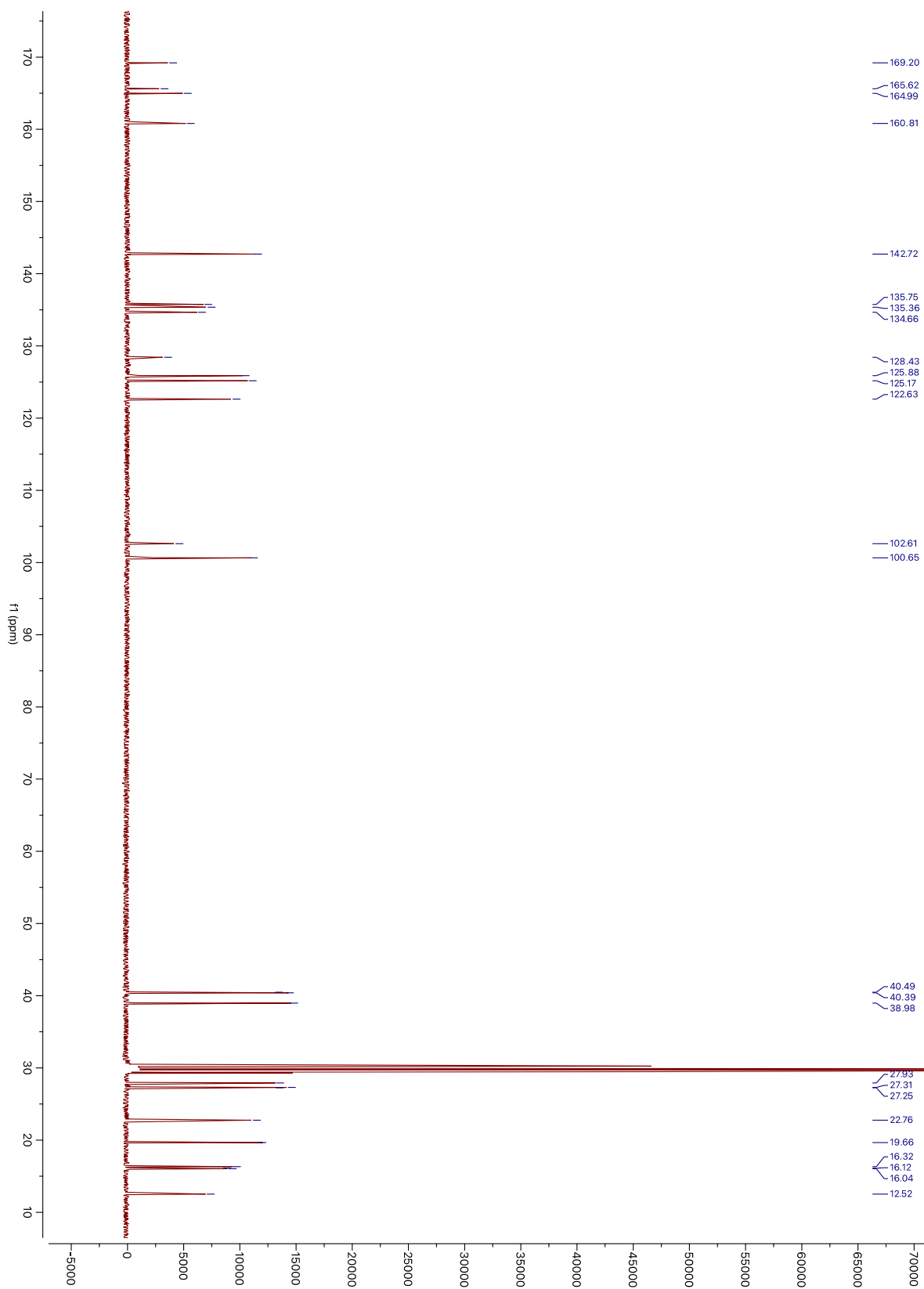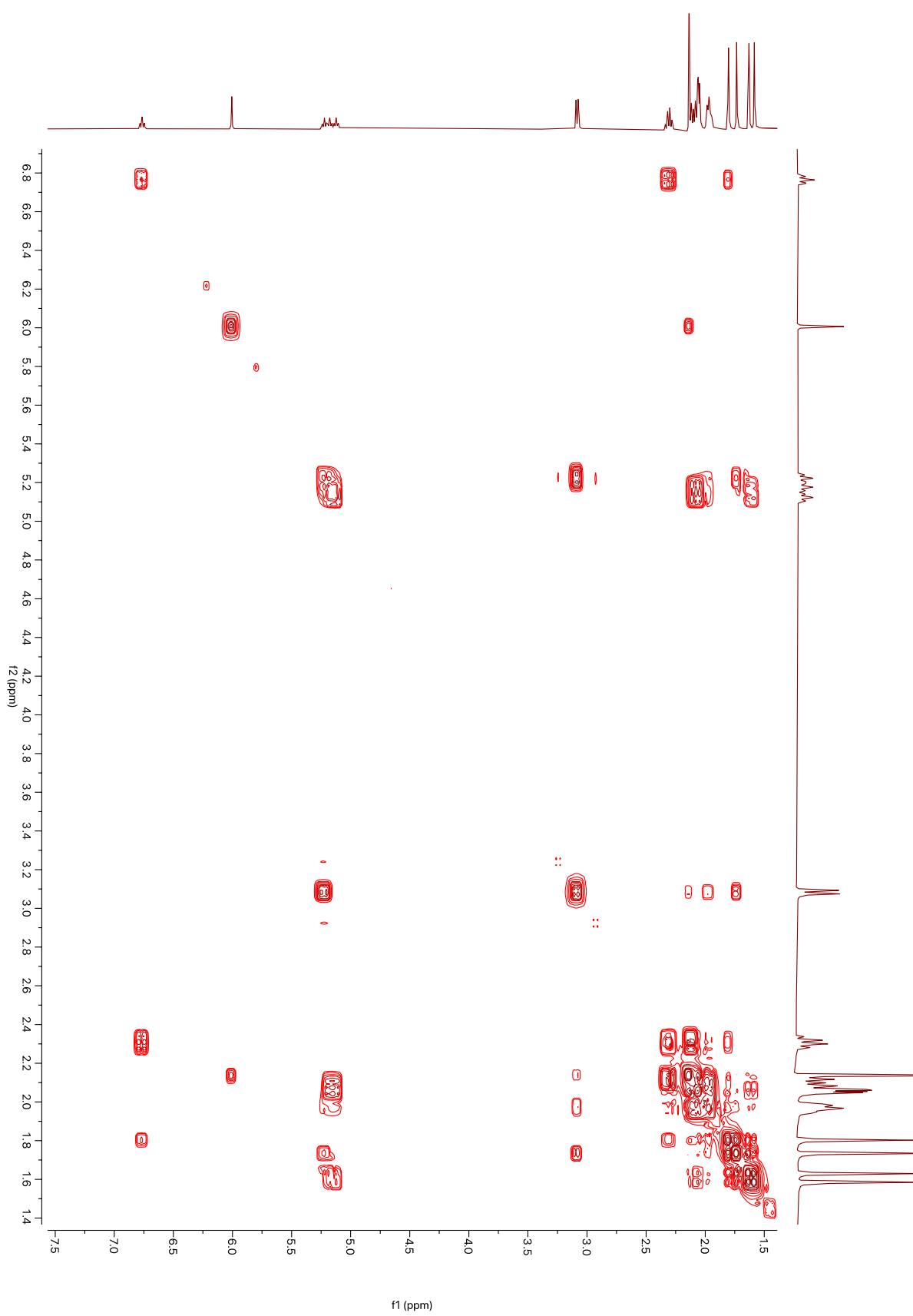
**Figure 1.25.** COSY of compound **5** in acetone-$d_6$
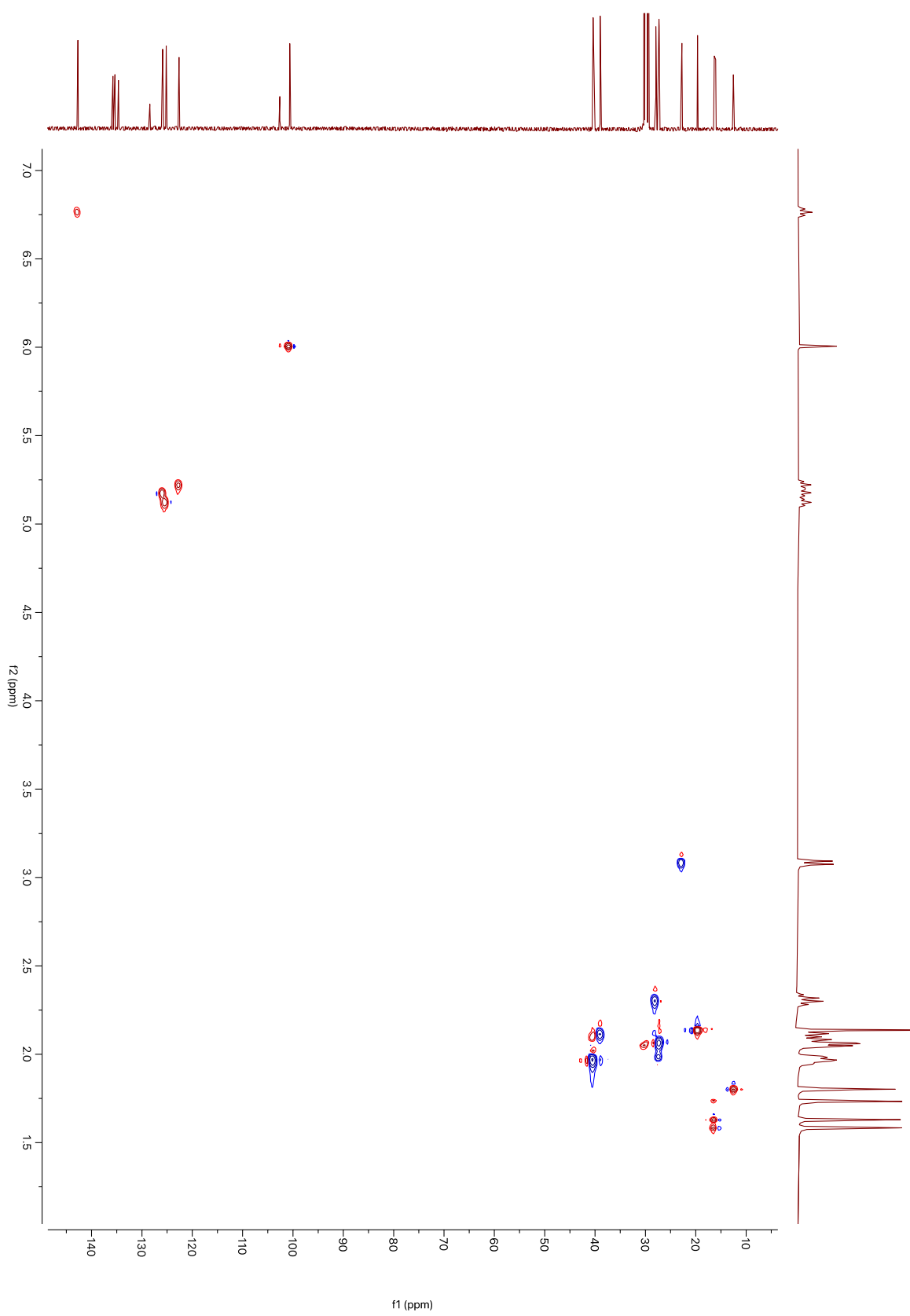
**Figure I.26.** HSQC of compound **5** in acetone-*d₆*

**Figure 1.27.** HMBC of compound **5** in acetone-$d_6$
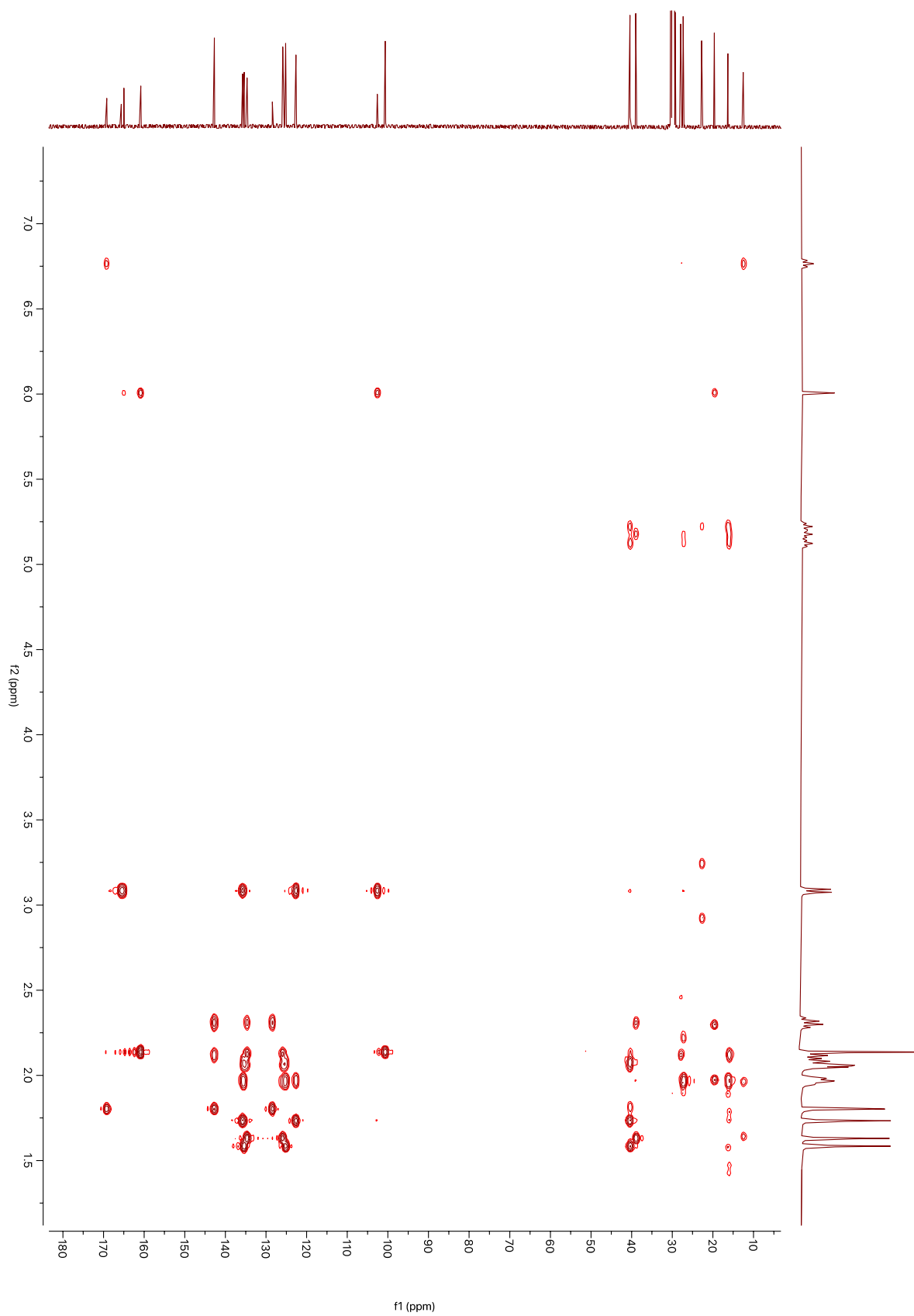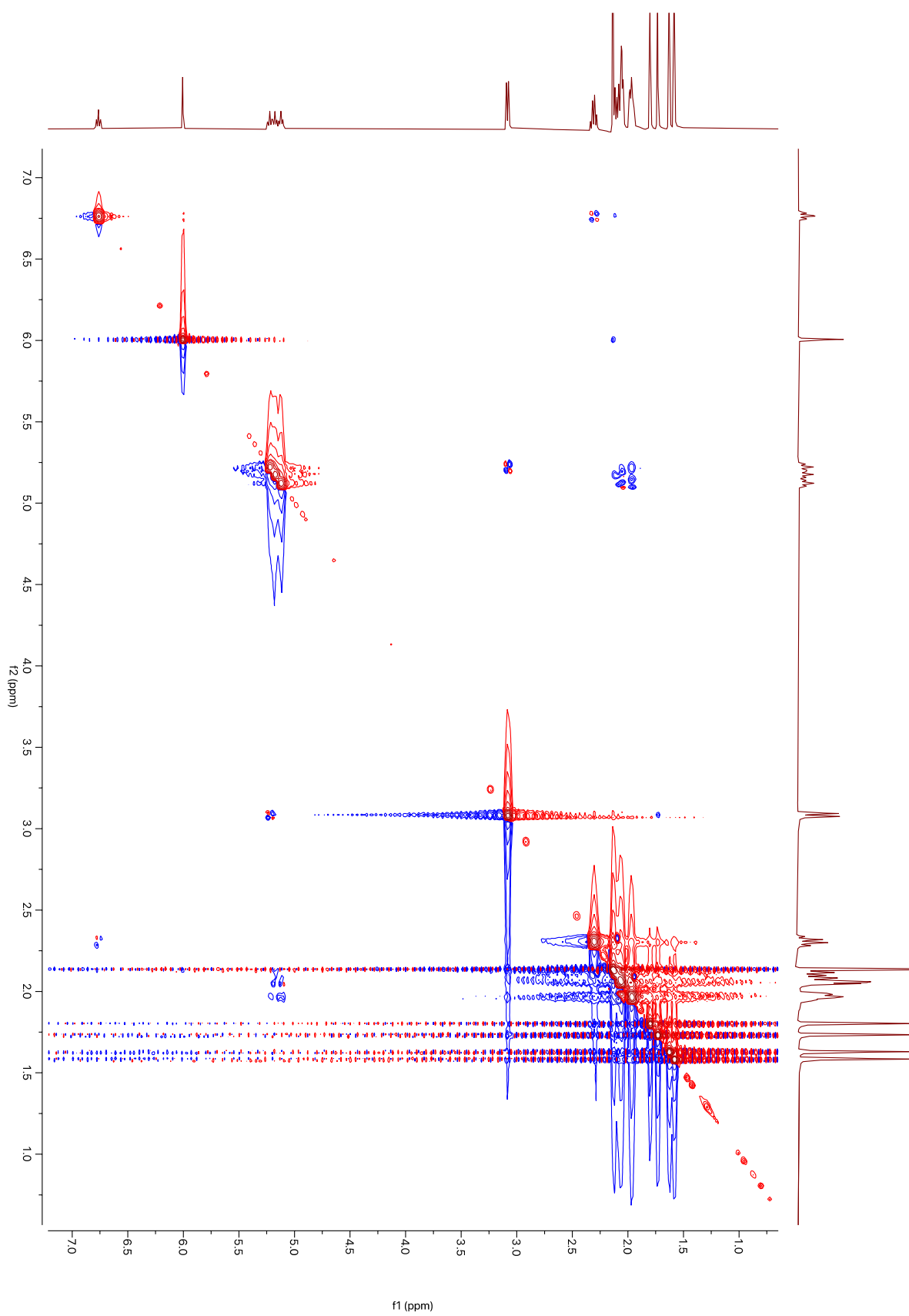
**Figure I.28.** NOESY of compound **5** in acetone-*d₆*

**Figure 1.29.** $^1$H NMR of compound **6** in acetone-$d_6$

**Figure I.30.** $^{13}$C NMR of compound **6** in acetone-$d_6$

**Figure I.31.** $^1$H NMR of compound **7** in CD$_3$OD

**Figure I.32.** $^{13}$C NMR of compound **7** in CD$_3$OD

**Figure I.33.** $^1$H NMR of compound **8** in acetone-$d_6$

**Figure I.34.** $^{13}$C NMR of compound **8** in acetone-$d_6$
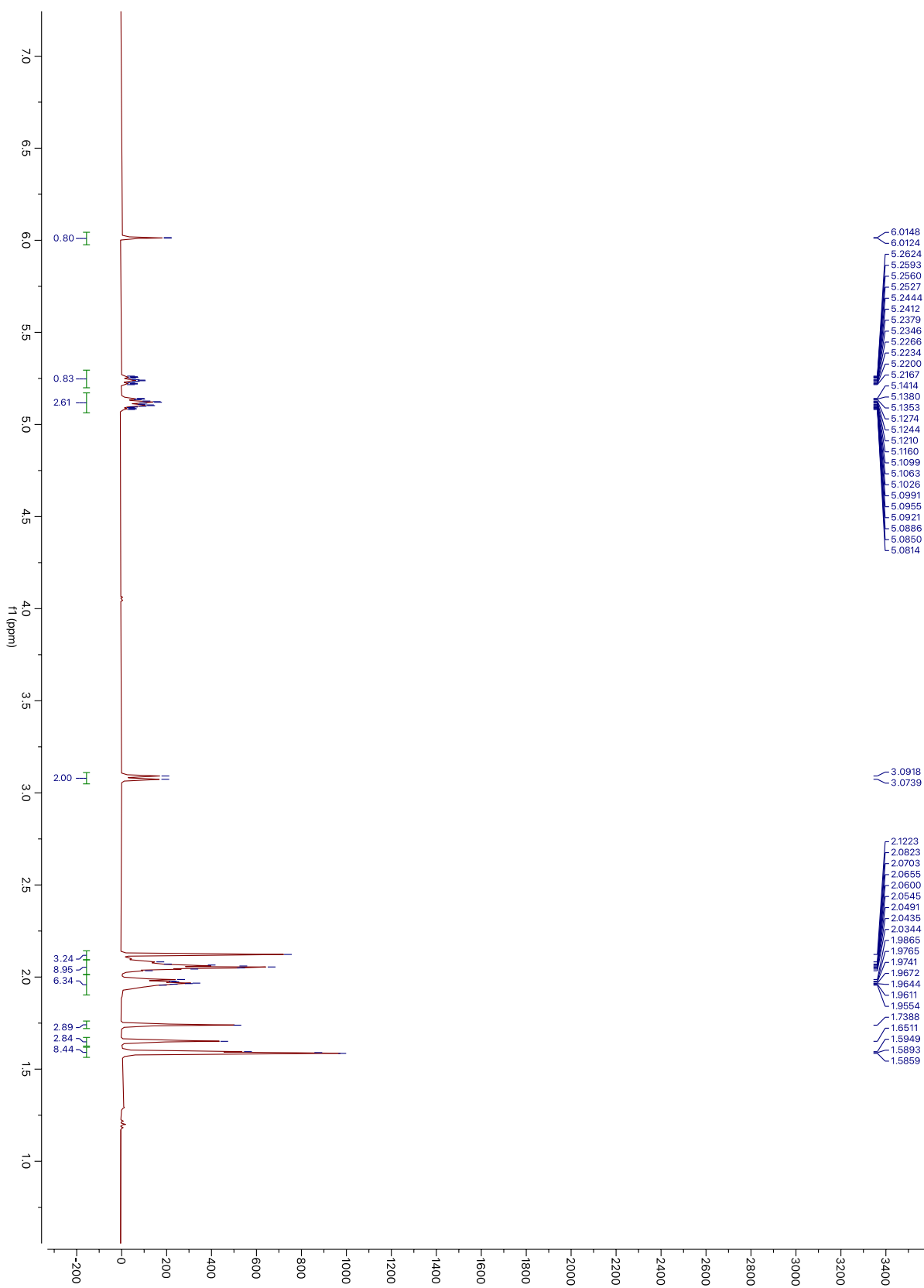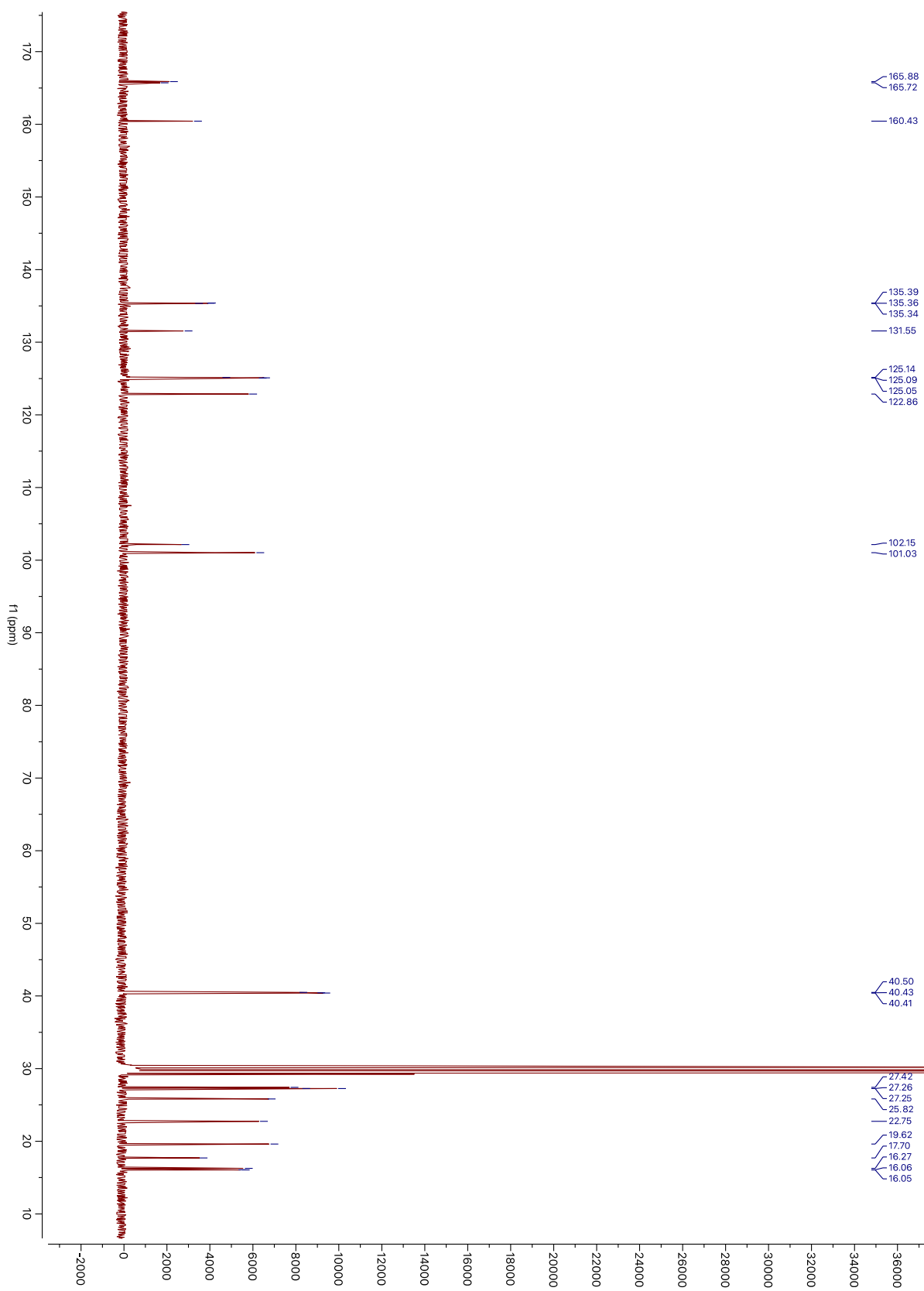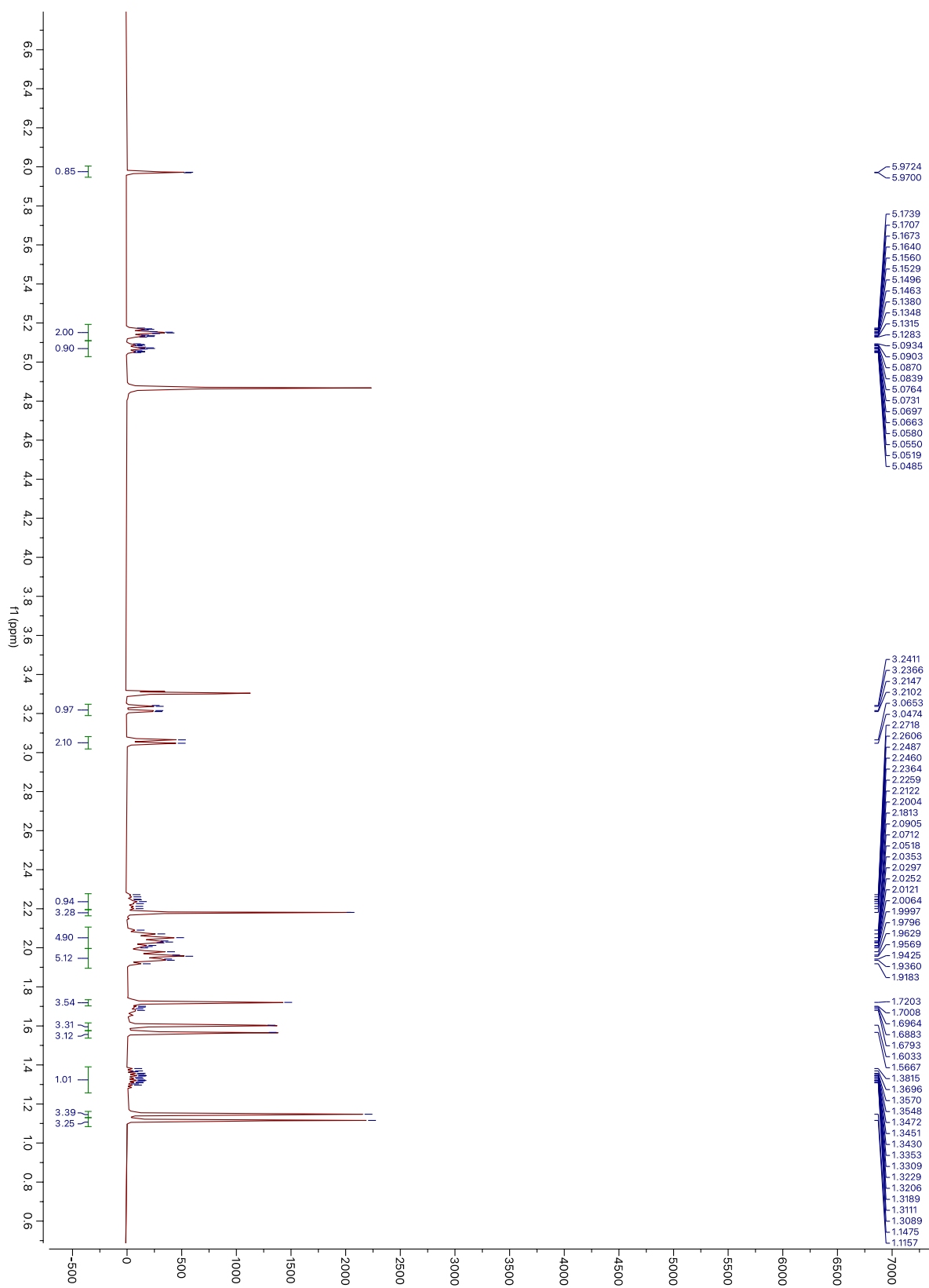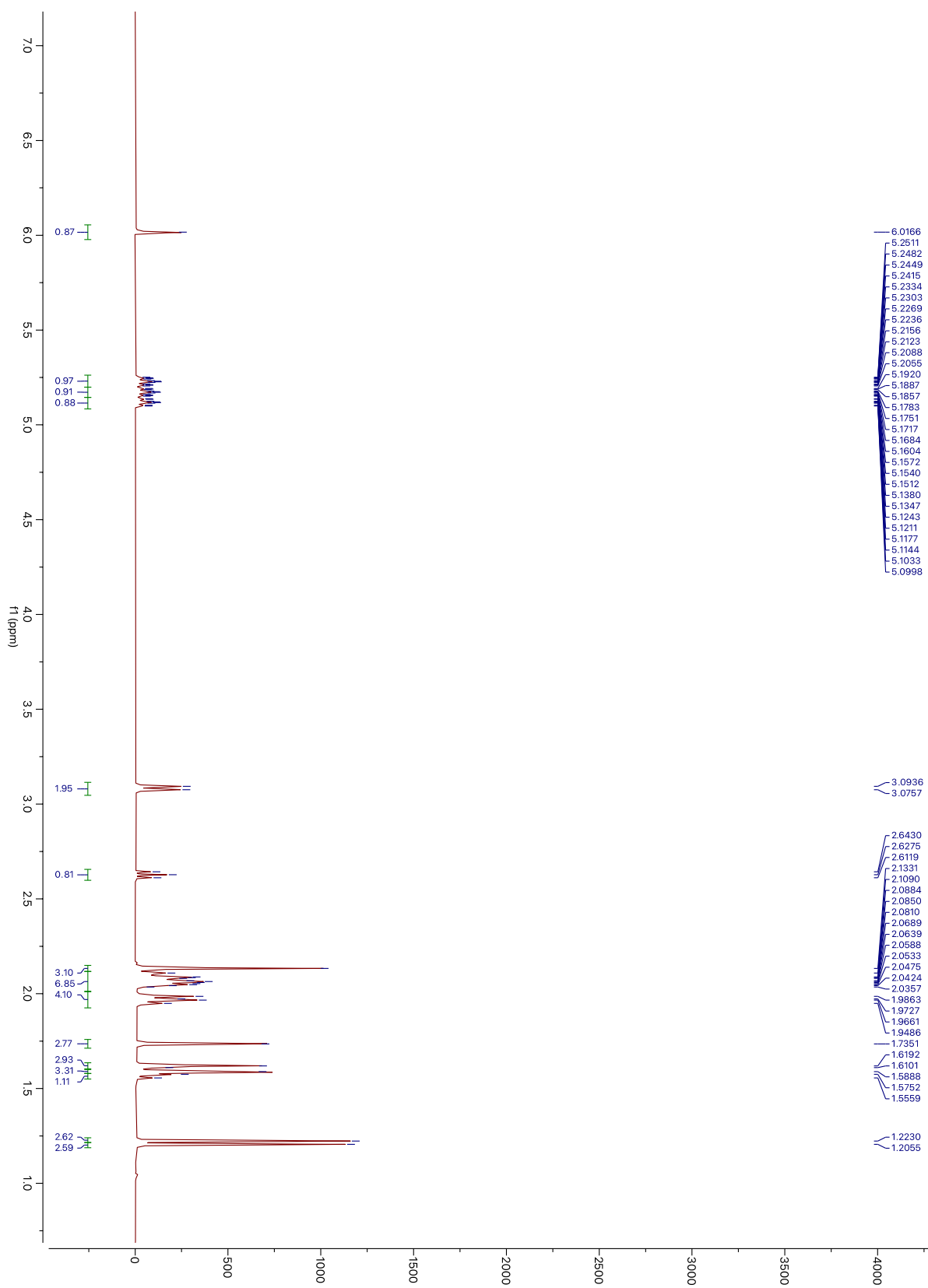
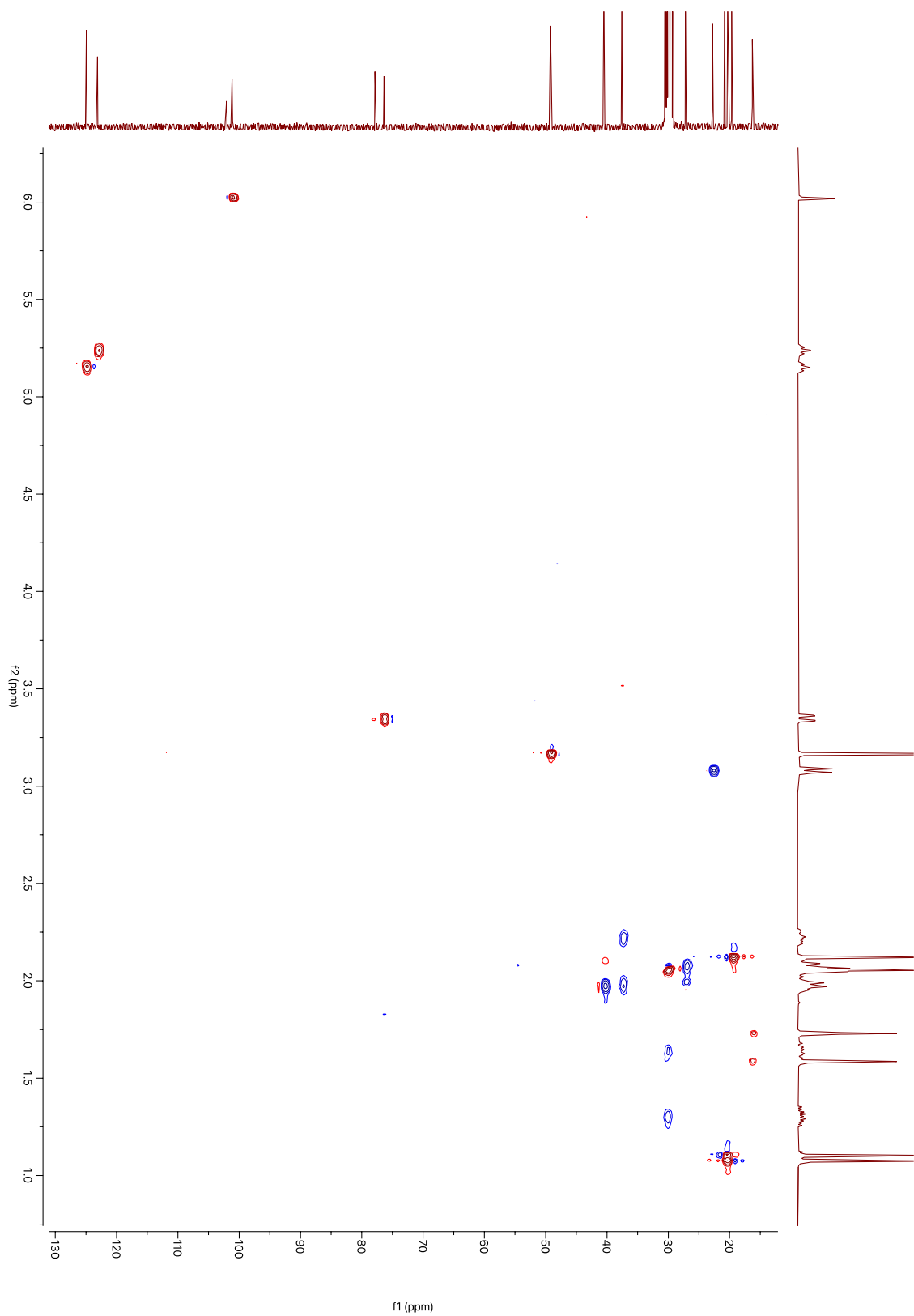**Figure 1.35.** COSY of compound **8** in acetone-*d*₆

**Figure I.36.** HSQC of compound **8** in acetone-$d_6$
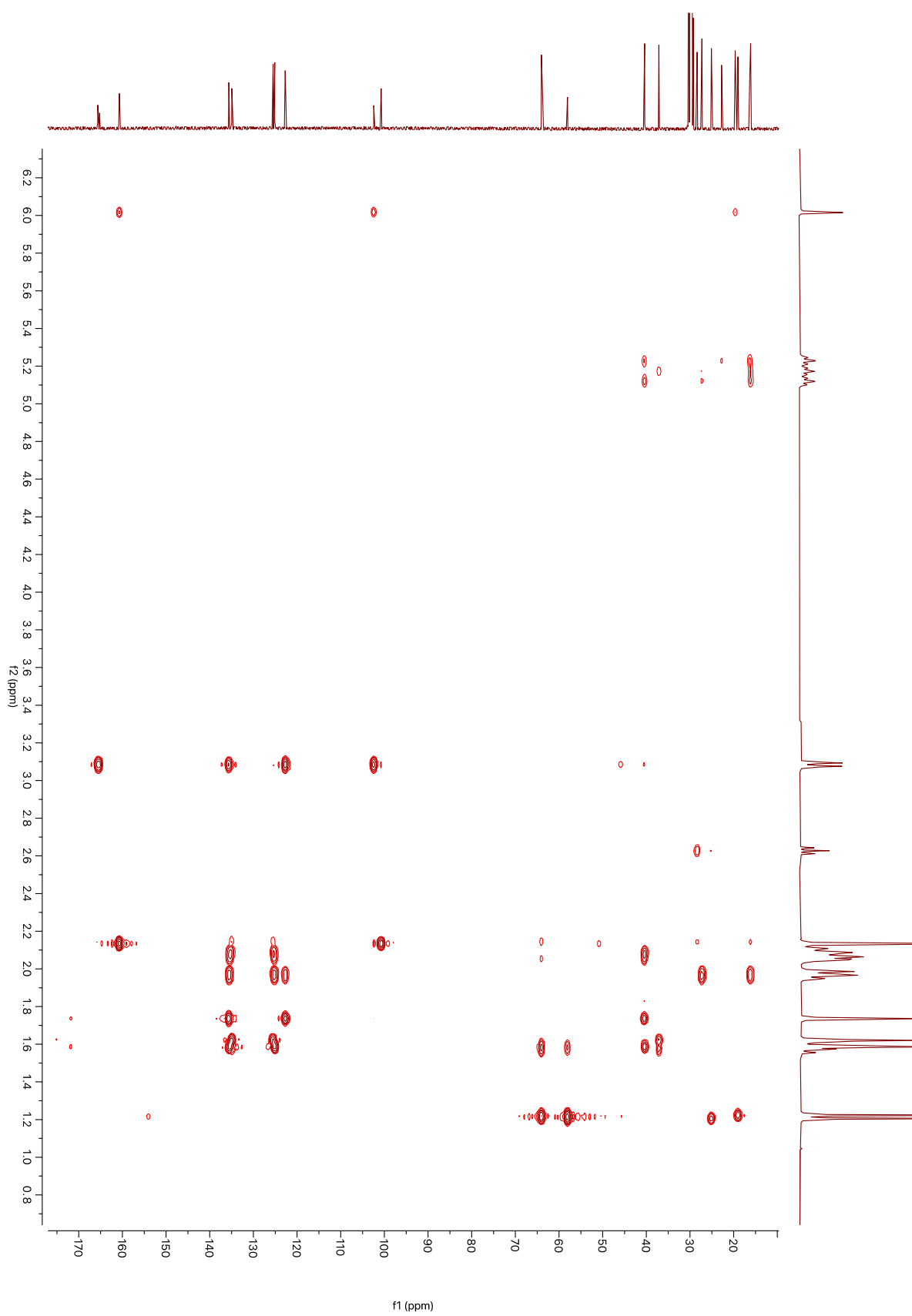
**Figure I.37.** HMBC of compound **8** in acetone-$d_6$

**Figure I.38.** $^1$H NMR of compound **9** in CD$_3$OD

5.9884

5.1789
5.1746
5.1642
5.1610
5.1572
5.1451
5.1306
5.1272
5.1245

3.2429
3.2386
3.2165
3.2122
3.0695
3.0517

2.2487
2.2372
2.2250
2.2135
2.1903
2.1069
2.0886
2.0699
2.0521
2.0137
1.9909
1.9722
1.9545
1.9378
1.7192
1.6988
1.6793
1.6750
1.6722
1.6674
1.6548
1.6494
1.5875

1.3732
1.3616
1.3499
1.3472
1.3388
1.3355
1.3274
1.3235
1.3155
1.3121
1.3037
1.3010
1.2889
1.2778
1.1547
1.1239

1.00
2.10
1.02
2.19
0.70
3.66
2.28
3.40
3.38
1.09
3.19
1.39
3.25
3.14

**Figure I.39.** $^{13}$C NMR of compound **9** in CD$_3$OD

**Figure 1.40.** COSY of compound **9** in CD$_3$OD

**Figure 1.41.** HSQC of compound **9** in CD$_3$OD

**Figure I.42.** HMBC of compound **9** in CD$_3$OD
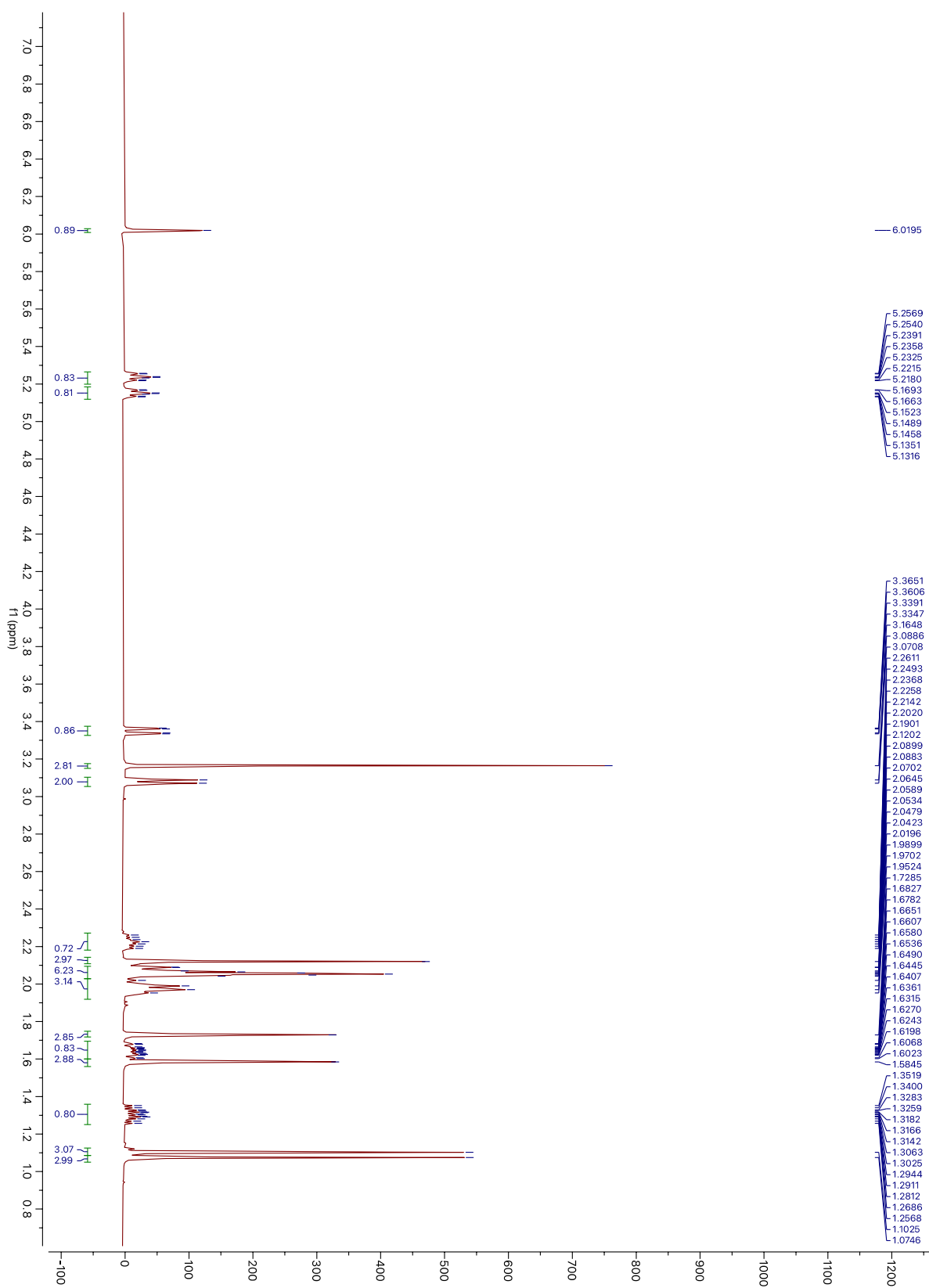
**Figure I.43.** $^1$H NMR of compound **10** in acetone-$d_6$

**Figure 1.44.** ¹³C NMR of compound **10** in acetone-$d_6$
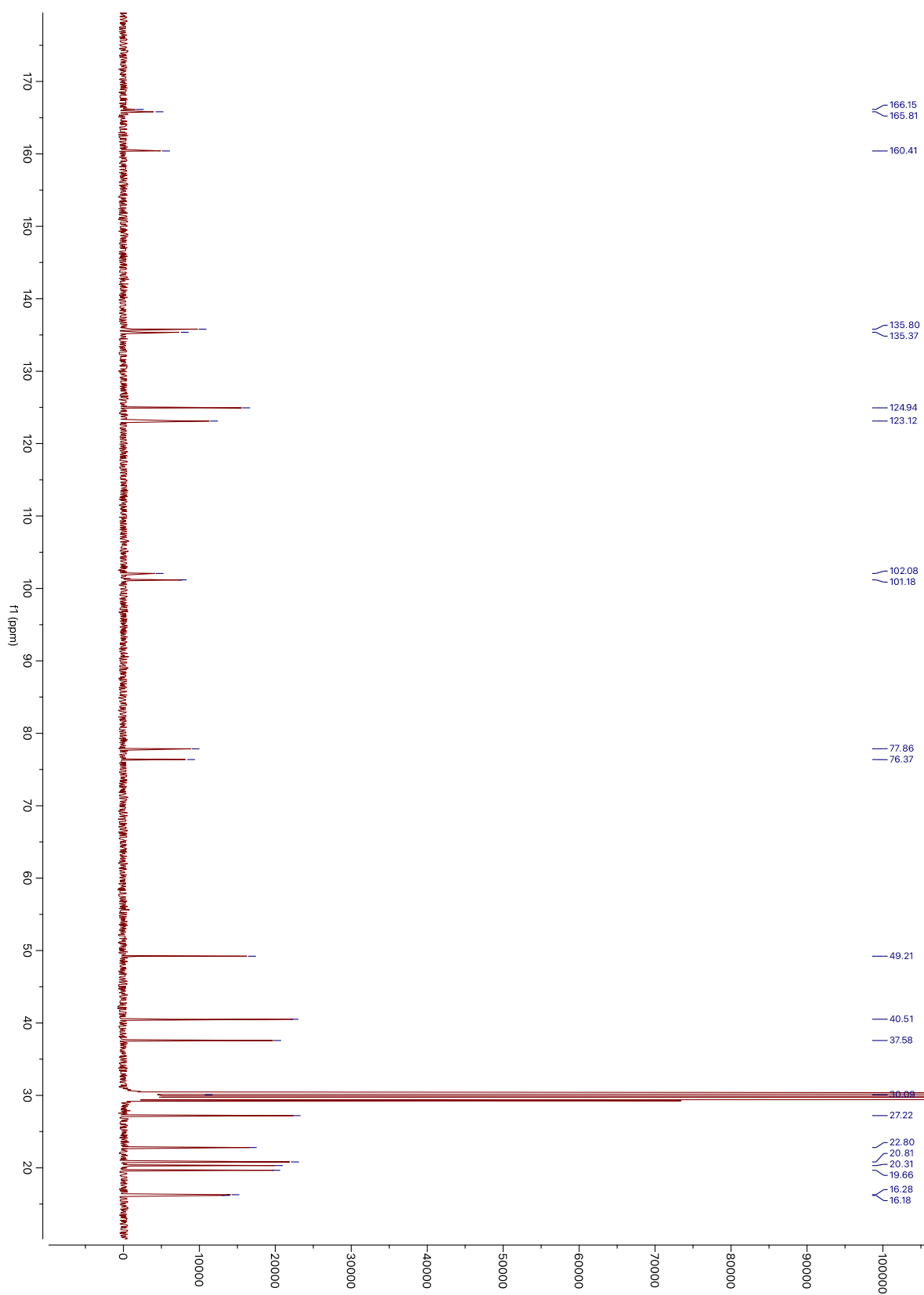
**Figure I.45.** COSY of compound **10** in acetone-$d_6$
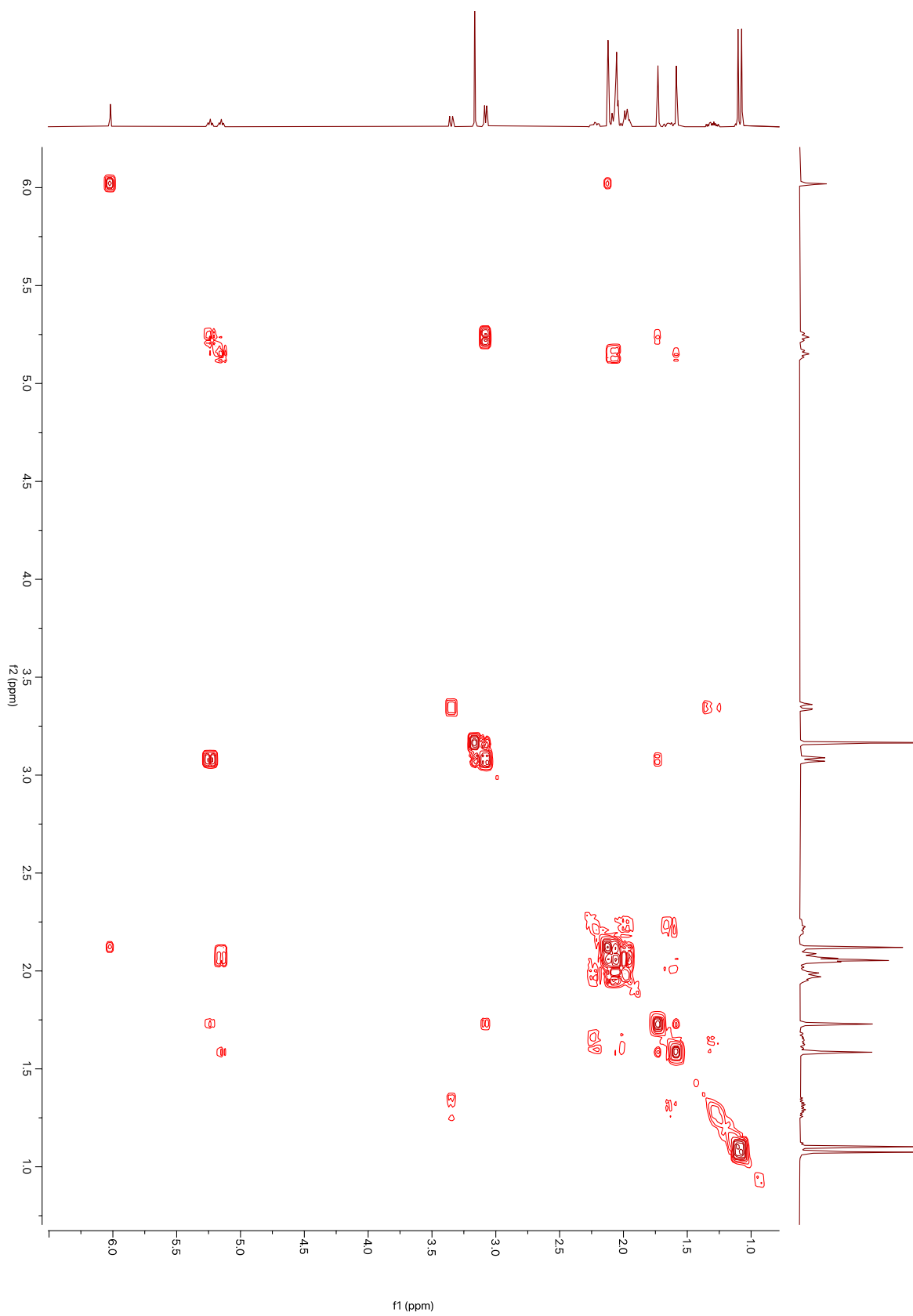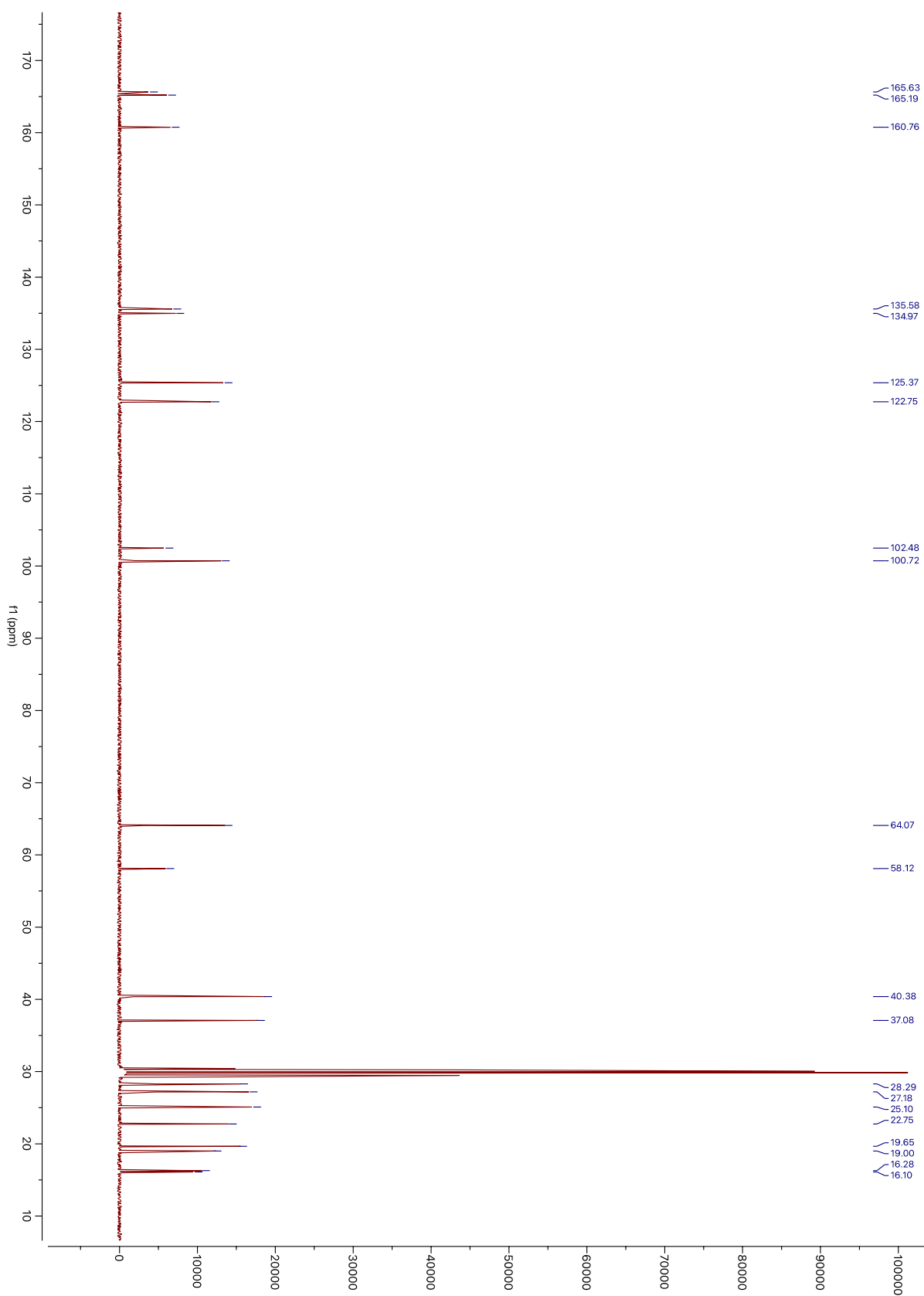
**Figure I.46.** HSQC of compound **10** in acetone-$d_6$
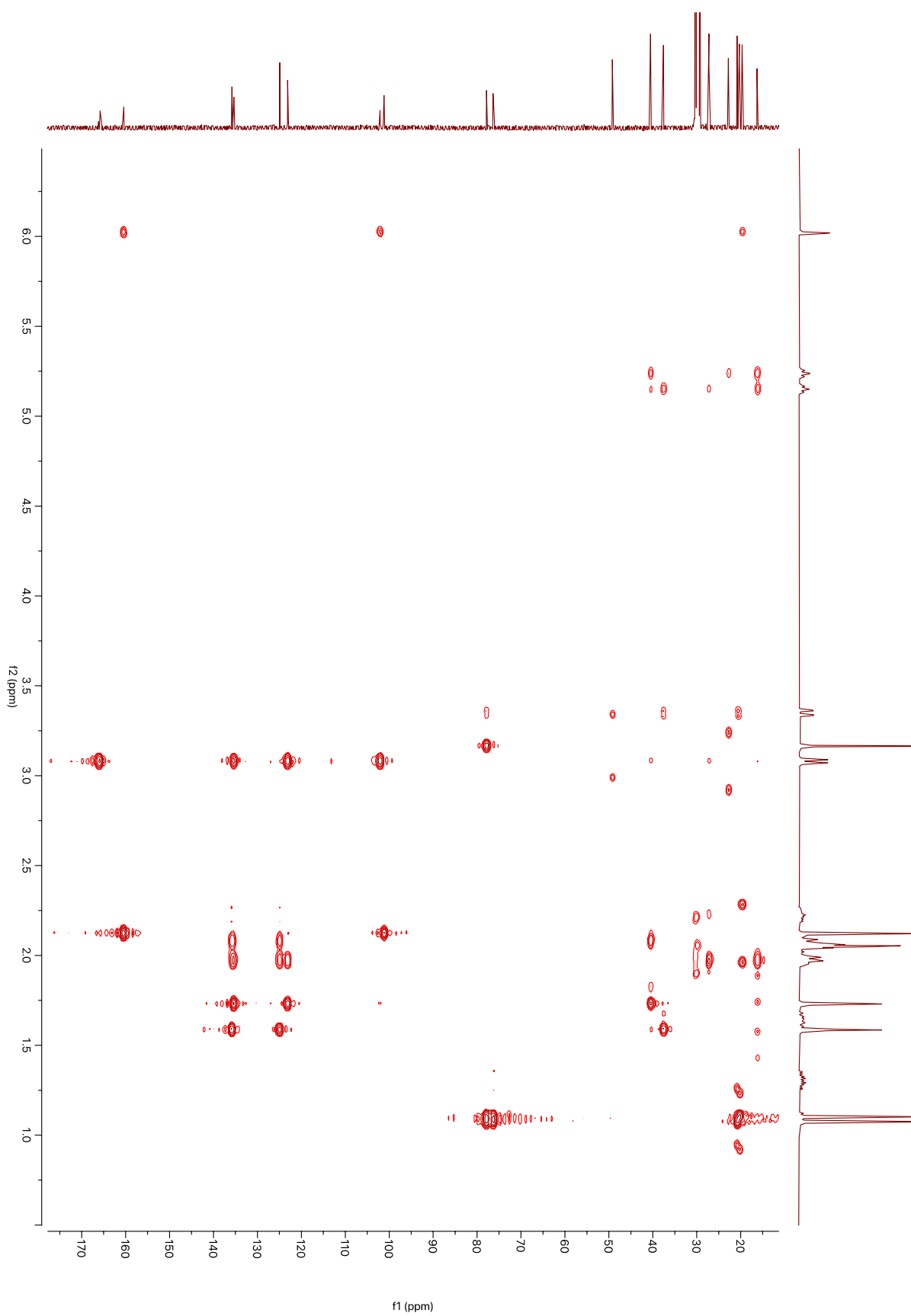
**Figure I.47.** HMBC of compound **10** in acetone-$d_6$

**Figure I.48.** $^1$H NMR of compound **11** in acetone-$d_6$

**Figure I.49.** $^{13}$C NMR of compound **11** in acetone-$d_6$
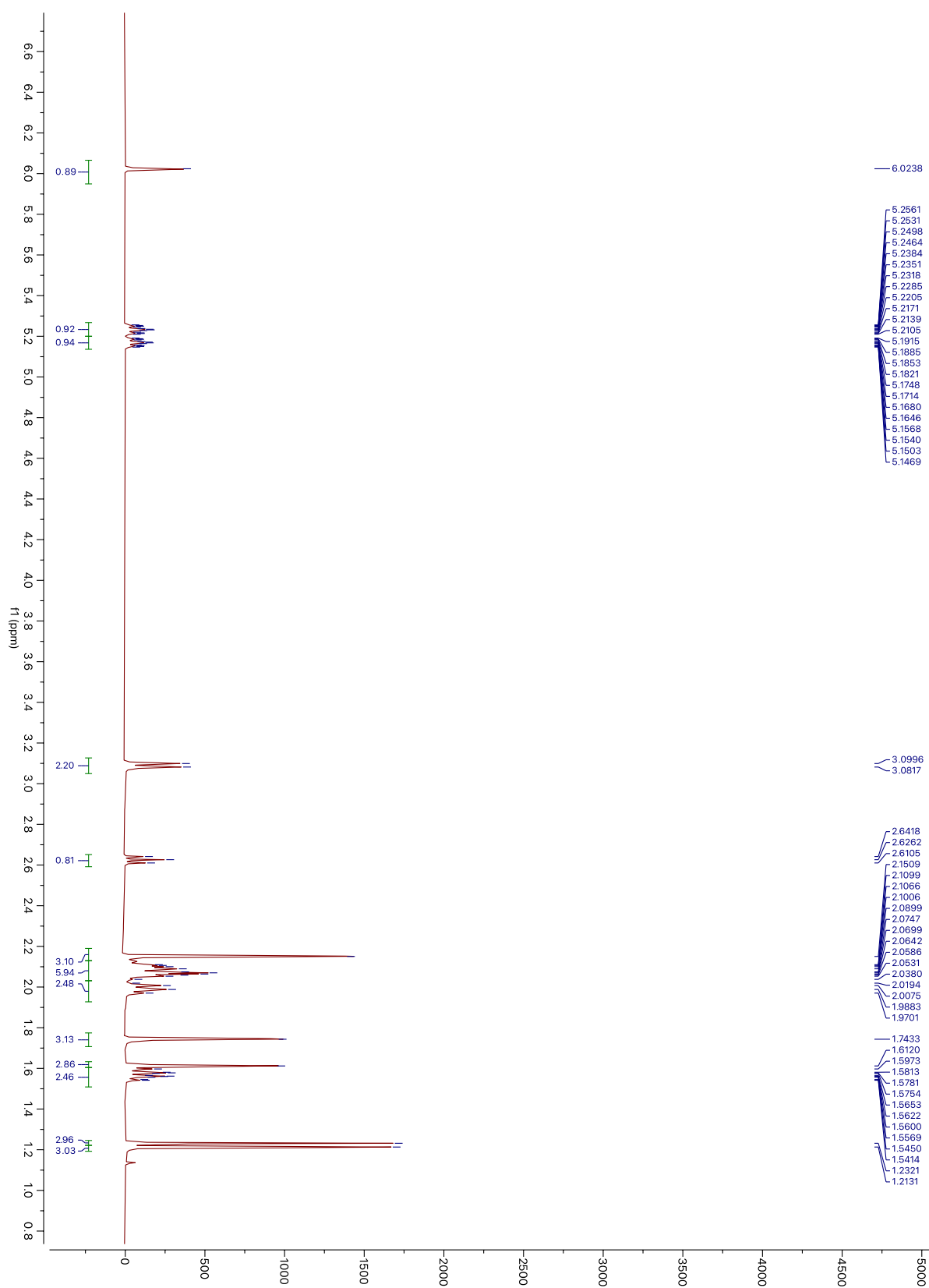
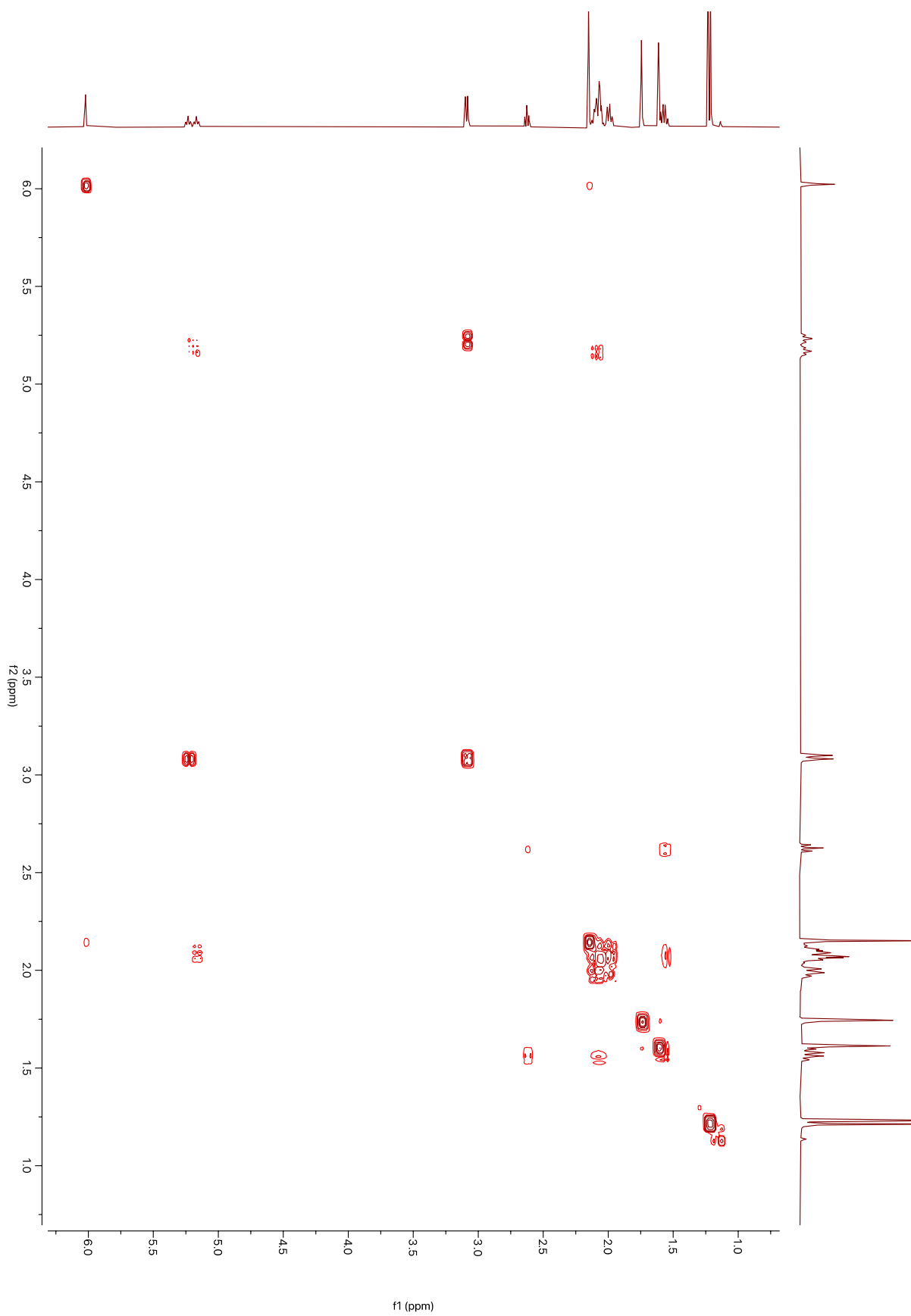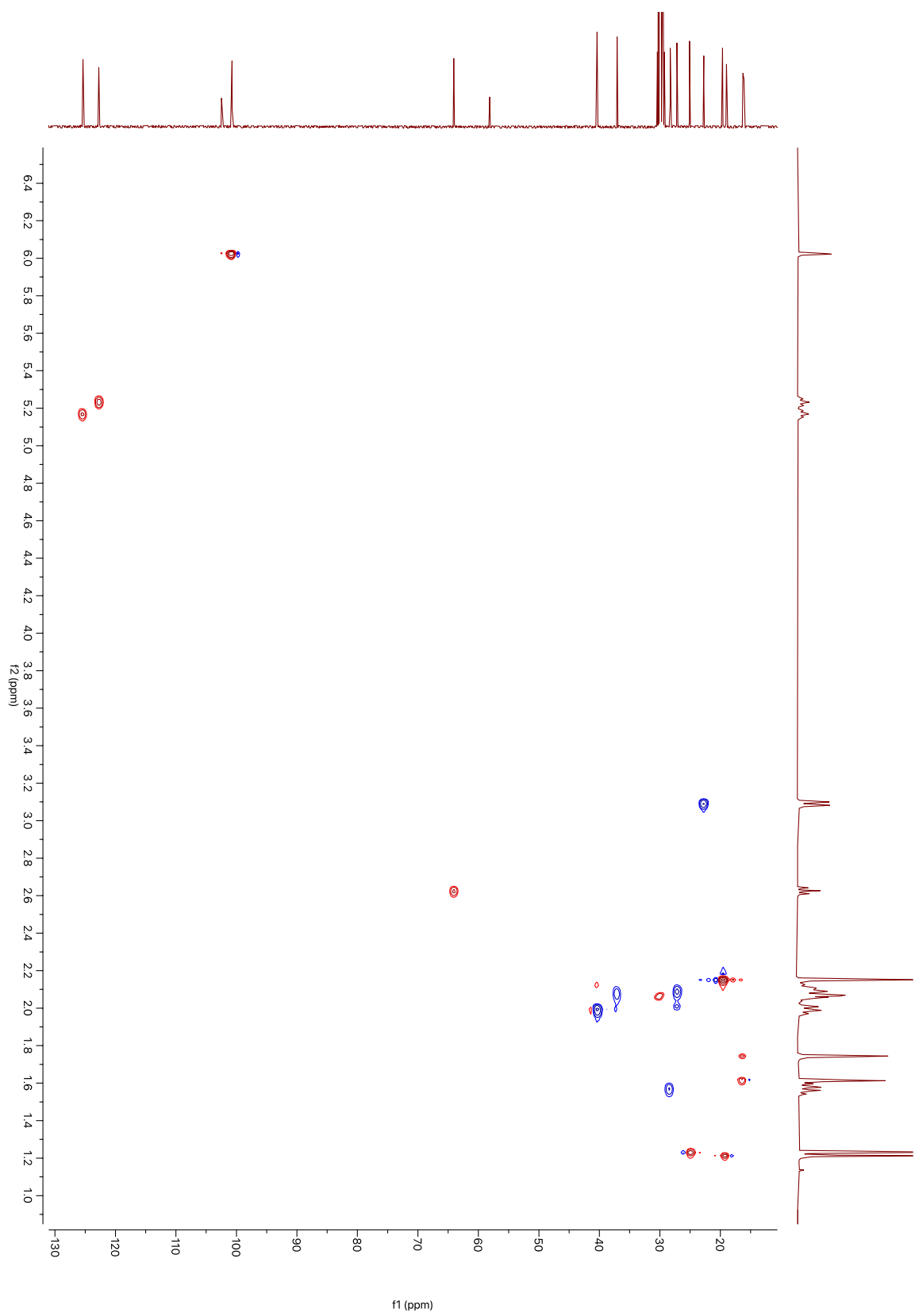**Figure I.50.** COSY of compound **11** in acetone-$d_6$

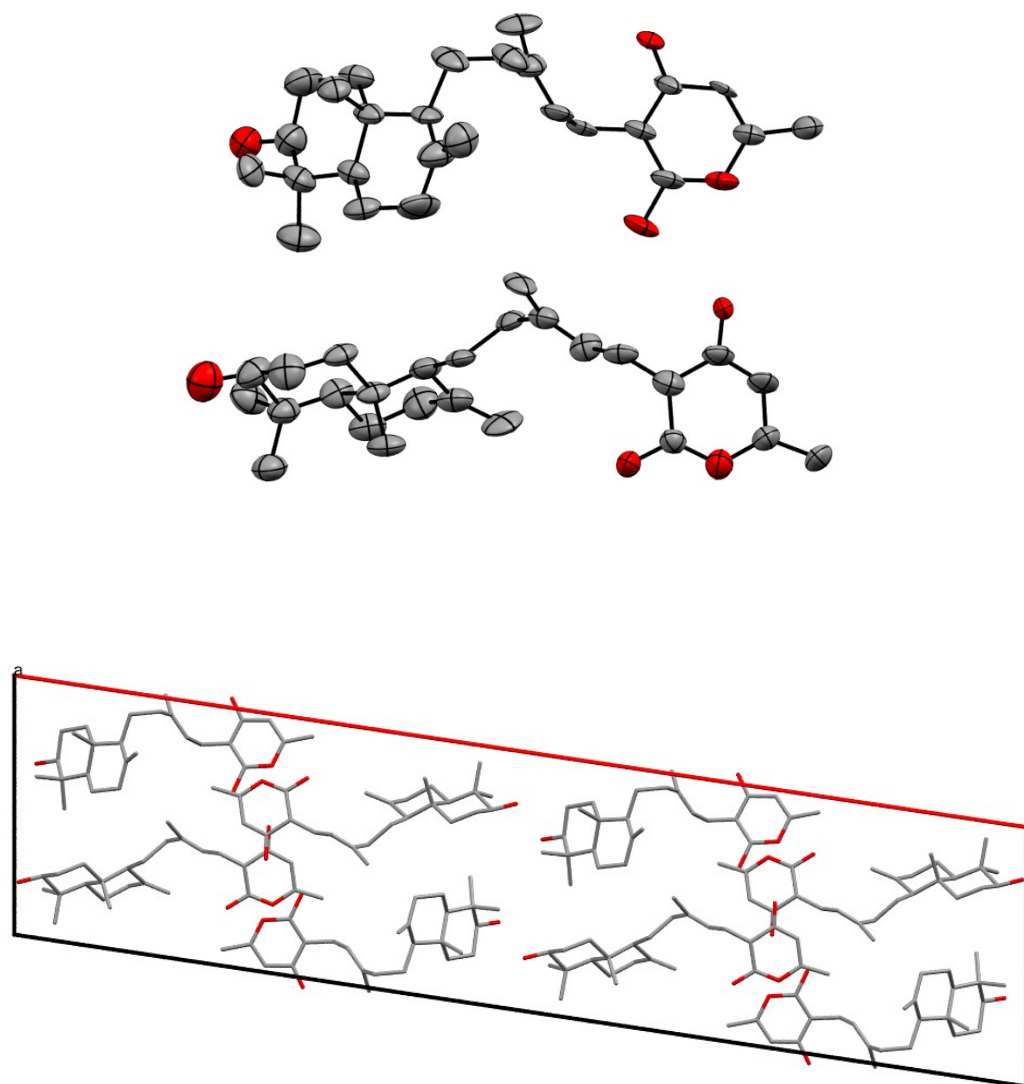**Figure I.51.** HSQC of compound **11** in acetone-$d_6$

**Figure I.53.** Crystal structure and unit cell packing of sartorypyrone F (**1**). Two molecules are present in the asymmetric unit. Thermal ellipsoids are drawn at 50% probability.

**References**

1    T. Wada, Y. Hayashi and H. Shibata, *Biosci. Biotechnol. Biochem.*, 1996, **60**, 120–121.

2    T. Nayak, E. Szewczyk, C. E. Oakley, A. Osmani, L. Ukil, S. L. Murray, M. J. Hynes, S. A. Osmani and B. R. Oakley, *Genetics*, 2006, **172**, 1557–1566.

3    E. Szewczyk, T. Nayak, C. E. Oakley, H. Edgerton, Y. Xiong, N. Taheri-Talesh, S. A. Osmani and B. R. Oakley, *Nat. Protoc.*, 2006, **1**, 3111–3120.

4    C. E. Oakley, H. Edgerton-Morgan and B. R. Oakley, in *Fungal Secondary Metabolism*, eds. N. P. Keller and G. Turner, Humana Press, Totowa, NJ, 2012, vol. 944, pp. 143–161.

5    H. Edgerton-Morgan and B. R. Oakley, *J. Cell Biol.*, 2012, **198**, 785–791.

6    L. J. Kim, M. Xue, X. Li, Z. Xu, E. Paulson, B. Mercado, H. M. Nelson and S. B. Herzon, *J. Am. Chem. Soc.*, 2021, **143**, 6578–6585.

7    W. Kabsch, *Acta Crystallogr D Biol Crystallogr*, 2010, **66**, 125–132.

8    G. M. Sheldrick, *Acta Crystallogr. Sect. A*, 2008, **64**, 112–122.

9    C. B. Hübschle, G. M. Sheldrick and B. Dittrich, *J. Appl. Crystallogr.*, 2011, **44**, 1281–1284.

10   G. M. Sheldrick, *Acta Crystallogr. Sect. C-Struc. Chem.*, 2015, **71**, 3–8.

11   S. Kaifuchi, M. Mori, K. Nonaka, R. Masuma, S. Ōmura and K. Shiomi, *J. Antibiot.*, 2015, **68**, 403–405.

12   A. Eamvijarn, N. M. Gomes, T. Dethoup, J. Buaruang, L. Manoch, A. Silva, M. Pedro, I. Marini, V. Roussis and A. Kijjoa, *Tetrahedron*, 2013, **69**, 8583–8591.

13   W.-G. Wang, L.-Q. Du, S.-L. Sheng, A. Li, Y.-P. Li, G.-G. Cheng, G.-P. Li, G. Sun, Q.-F. Hu and Y. Matsuda, *Org. Chem. Front.*, 2019, **6**, 571–578.

14   S. Bang, J. H. Song, D. Lee, C. Lee, S. Kim, K. S. Kang, J. H. Lee and S. H. Shim, *J. Agric. Food Chem.*, 2019, **67**, 1831–1838.